

Prashant M. Pawar ·
R. Balasubramaniam ·
Babruvahan P. Ronge ·
Santosh B. Salunkhe · Anup S. Vibhute ·
Bhuwaneshwari Melinamath *Editors*

Techno-Societal 2020

Proceedings of the 3rd International
Conference on Advanced Technologies
for Societal Applications—Volume 2

Techno-Societal 2020

Prashant M. Pawar · R. Balasubramaniam ·
Babruvahan P. Ronge · Santosh B. Salunkhe ·
Anup S. Vibhute · Bhuwaneshwari Melinamath
Editors

Techno-Societal 2020

Proceedings of the 3rd International
Conference on Advanced Technologies for
Societal Applications—Volume 2

 Springer

Editors

Prashant M. Pawar
SVERI's College of Engineering
Pandharpur, Maharashtra, India

Babruvahan P. Ronge
SVERI's College of Engineering
Pandharpur, Maharashtra, India

Anup S. Vibhute
SVERI's College of Engineering
Pandharpur, Maharashtra, India

R. Balasubramaniam
Precision Engineering Center
Bhabha Atomic Research Centre
Mumbai, Maharashtra, India

Santosh B. Salunkhe
SVERI's College of Engineering
Pandharpur, Maharashtra, India

Bhuwaneshwari Melinamath
SVERI's College of Engineering
Pandharpur, Maharashtra, India

ISBN 978-3-030-69924-6

ISBN 978-3-030-69925-3 (eBook)

<https://doi.org/10.1007/978-3-030-69925-3>

© The Editor(s) (if applicable) and The Author(s), under exclusive license to Springer Nature Switzerland AG 2021

This work is subject to copyright. All rights are solely and exclusively licensed by the Publisher, whether the whole or part of the material is concerned, specifically the rights of translation, reprinting, reuse of illustrations, recitation, broadcasting, reproduction on microfilms or in any other physical way, and transmission or information storage and retrieval, electronic adaptation, computer software, or by similar or dissimilar methodology now known or hereafter developed.

The use of general descriptive names, registered names, trademarks, service marks, etc. in this publication does not imply, even in the absence of a specific statement, that such names are exempt from the relevant protective laws and regulations and therefore free for general use.

The publisher, the authors and the editors are safe to assume that the advice and information in this book are believed to be true and accurate at the date of publication. Neither the publisher nor the authors or the editors give a warranty, expressed or implied, with respect to the material contained herein or for any errors or omissions that may have been made. The publisher remains neutral with regard to jurisdictional claims in published maps and institutional affiliations.

This Springer imprint is published by the registered company Springer Nature Switzerland AG
The registered company address is: Gewerbestrasse 11, 6330 Cham, Switzerland

Contents

Advanced Technology for Water, Energy, Transportation, Housing and Sanitation	
Optimal Time and EOQ for Inventory of Deteriorating Items with Variation and Leading Times	3
Abdullah Alshami and Aniket Muley	
Clustering and Association Rule Mining for Tree Species Plantation	17
Govind Kulkarni, Aniket Muley, Parag Bhalchandra, and Nilesh Deshmukh	
Behavior of Ammonia Borane as Solid-State Hydrogen Storage Material	29
Rohan Kalamkar, Vivek Yakkundi, and Aneesh Gangal	
Morphometric Analysis of Lendi River Basin Using Geographical Information System (GIS) Techniques	37
Gurav Chandrakant and Md. Babar	
Experimental Investigation of the Spinodal Decomposition in Cu-Ni-Cr Alloy for Corrosion Control in Marine Structure	47
S. C. Jirapure and Borade	
Enhanced Power Conversion Efficiency of the P3BT (Poly-3-Butyl Thiophene) Doped Nanocomposites of Gd-TiO₃ as Working Electrode	55
Vinayak Adimule, Santosh S. Nandi, and Adarsha Haramballi Jagadeesha Gowda	
A Facile Synthesis of Gadolinium Titanate (GdTiO₃) Nanomaterial and Its Effect in Enhanced Current-Voltage Characteristics of Thin Films	69
Vinayak Adimule, Santosh S. Nandi, and Adarsha Haramballi Jagadeesha Gowda	

Charge Pump Circuit Based Grid-Tied PV System for Single Phase Transformer Less Inverter Using Fuzzy Logic Controller	79
Anil Tekale and Swapna God	
Fabrication and Characterization of Composite Material Connecting Rod	87
G. G. Deshpande, H. P. Borate, and S. S. Wangikar	
Experimental Studies on RCCI Engine Powered with n-Butanol and Thevetia Peruviana Methyl Ester	97
P. A. Harari, V. S. Yaliwal, and N. R. Banapurmath	
Magneto Rheological Brake with Silicon Based Fluid and Hybrid of Silica Fumes with GO₂ as Additives	107
Vaibhav Vithal Shinde and Bhagyesh B. Deshmukh	
SCADA System Applied to Two-Wheeler Chassis Dynamometer	115
Sumedh Vidhate, Virendra Bhojwani, and Omkar Mobale	
Enhancement of Reliability and Efficiency of Solar Panel Using Cooling Methods	129
Nilesh Dhokane and S. Ramesh	
Design of Onboard Integrated Charger for Electric Vehicles Based on Split Three Phase Induction Motor	141
Ganesh Punjaram Thombre and S. V. Tade	
Performance Improvement and Cooling of the Solar Photovoltaic Panel by Using Fin and PCM Integrated Fin	151
Siddharth S. Patil, Sidalingagouda R. Patil, and Aniket B. Shedbale	
Performance Investigation of Photovoltaic-Thermal (PVT) Solar Collector Using Effective Cooling Techniques: Review	165
Nikhil K. Purwant and Avinash M. Badadhe	
Study the Impact of Gamification on Career Selection for Graduation—A Review	173
Deepali Bhalerao, Mahesh Deshpande, and Nachiket Thakur	
Numerical and Experimental Analysis of Magnetic Rheological Damper of Light Duty Load Carrying Vehicle	181
Pavan Kumar, Vatsal Bhat, Saurabh Shah, Rahul Raj, Balu Dome, M. Bhavana, and Malge Abhijeet	
Performance Enhancement of Multi-cylinder Four Stroke SI Engine Under the Effect of Magnetic Field	189
Nilesh Ramchandra Pawar and Sanjeev Reddy K. Hudgikar	
Thermo-Hydraulic Performance for an Electronic Cooling System Using Porous Material	197
Sumit Kumar Mehta and Sukumar Pati	

An Experimental Study on the Use of Industrial Wastes to Manufacture Light Weight Modular Bricks	205
Vikas V. Singh, K. M. Wagh, T. D. Agarwal, J. R. Sirsath, and S. B. Gorade	
Studies on Characteristics of Geo-Polymer Concrete Mix Design	215
Sandip Laxman Hake and Divakar Machhindra Waghmare	
Design of a Household Wet and Dry Waste Segregation Facilitator Dustbin	225
Sameer Joshi, Mihir Gharat, Suvinal Lagad, Sampada Khanvilkar, and Abhijeet Kore	
Thermal Analysis of Earth Air Tube Heat Exchanger for Cooling Tower	237
Nachiket Shende, Mayur Bhurle, Hrishikesh Bhagwat, Omkar Deokatte, and Rahul A. Patil	
Three Phase Z-Source Inverter Analysis Using Matlab Simulation	251
D. P. Narsale, A. M. Kasture, Akshay. A. Jadhav, and M. A. Deshmukh	
Utilization of Waste Plastic for Bituminous Mix for Improved Performance of Roads	259
Avinash B. Kokare, Abhinav S. Salunkhe, and Chetan R. Limkar	
Automatic Gas Fire Detection System Using IoT	267
Rupali Ramesh Shinde, Somnath B. Thigale, and Bhuvaneshwari C. Melinamath	
Assessment of Groundwater Quality from Warana River Basin, Kolhapur District, Maharashtra, India	275
S. V. Pathare, D. B. Panaskar, V. M. Wagh, and R. S. Pawar	
Study and Ergonomic Analysis of Automobile Engine Maintenance Workstation and Suggesting Improvements	285
Sagar Sul, Sameer Katekar, Ajinkya Gaikwad, Gururaj Inamdar, and Samadhan Mali	
Improving Plant Yield by Smart Irrigation System Using pH and NPK Sensors	293
Rahul Y. Pawar, Pramod B. Deshmukh, Vishakha A. Metre, and Swapnil V. Ghogardare	
Thermal Characterization of Solar Elliptical Dish Steam Generator	305
Ranjit Sawant, Kunal Hole, Swapnil Vhantale, Swapnil Yeutkar, and Rahul A. Patil	

Ecofriendly Road Construction by Using Industrial Waste (Spent Wash)	317
R. J. Salunkhe, N. A. Shinde, A. H. Kalubarme, H. D. Aiwale, and S. D. Patil	
Mitigation of Power Capacitor Switching Transient by Using RCSTL	329
Prakash Kadam, Sagar Ghodake, and Santosh Kolekar	
Holistic Approach for Sustainable Technology	
Performance of Conventional Concrete Integrated with RHA and GGBS As a Cementitious Material	341
Yogesh Tambe and Pravin Nemade	
Assessment of the Extent of ISO-QMS Implementation and Scope for Six Sigma—A Case from the Indian Textile Industry	355
S. S. More and B. P. Ronge	
Finite Element Analysis to Predict Performance of Flexure Bearing for Space Application	365
Suraj Bhojar, Virendra Bhojwani, Ganesh Khutwad, Gaurav Sawant, Jay Lad, and Stephen Sebastian	
Modal Characteristics of Composite Sandwich Structure with Intermediate Layer of Viscoelastic Material	375
Mayur M. Ghadage, Vishal B. Bhagwat, Shital R. Kadam, and Shrinivas V. Shelage	
Design and Weight Optimization of Critical Automobile Component—Steering Knuckle	385
Shital R. Kadam, Mayur M. Ghadage, and Prachi D. Kale	
Photovoltaic Power System with Battery Backup and Grid-Connection to Reduce Grid Dependency During Peak Demand Hours and Power Cuts	393
Vishal Rohilla, R. C. Rohilla, Prashant Thapliyal, Don Biswas, and Gambhir Singh Kathait	
Modeling and Simulation of Correlations of Porosity with Strength Development of GGBS Blend Cement Concrete	407
Sujata D. Ingale and Pravin D. Nemade	
Comparative Kinetic Study for Adsorption of Heavy Metals with Low-Cost Adsorbents—Sugarcane Baggase and Eggshell	417
Diksha Kadu, Siddhant Bhasarkar, and Sandeep P. Shewale	

Stress Analysis of Carbon Fiber Composite Rotating Blade Using COMSOL in Undamaged and Damaged Condition 427
 Avinash K. Parkhe, Sandeep S. Wangikar, Shashikant S. Jadhav, Shrikrushna B. Bhosale, and Prashant M. Pawar

Experimental Investigation on VCR Engine by Using Different Blend Proportions of Mexicana Oil Biodiesel 437
 Chhappare Shivkumar, Pandhare Amar, and Godse Mitesh

Estimation of Methane Generation Potential from Municipal Solid Waste by Using Bromatological Characteristics for Pimpri Chinchwad City 445
 Tanmay S. Khambekar and Sandip T. Mali

Investigation of Tube in Tube Helical Coil Heat Exchanger with Different Inner Tube Configuration 457
 Amol D. Shinde and Amarsingh B. Kanase-Patil

Analysis of Construction Labour Productivity for Indian States 467
 Rahul S. Chaudhari, Pankaj P. Bhangale, and Surabhi Sengar

Performance Analysis of Conical Journal Bearing with Different Configuration 475
 Sunil D. Bhingare, B. P. Ronge, Prashant M. Pawar, and U. B. Andh

Improving Cooling Performance of Deep Freezer by Incorporating Graphene Oxide Nanoparticles Mixed with Phase Change Materials During a Power Outage 485
 Avesahemad S. N. Husainy, Gajanan V. Parishwad, Sonali K. Kale, Siddhanath V. Nishandar, and Aishwarya S. Patil

Impact of Electric Vehicles on Electricity Power Demand in India 493
 Rahul Waghchaure and Pramod Kothmire

Computational Fluid Dynamics Simulation for the Prevention of Evapotranspiration from Agricultural Land Using Semi-Permeable Membrane 503
 Dhruv Singh and S. J. Pawar

Influence of Thermal Radiation on Natural Convection in a Square Enclosure 513
 Shantanu Dutta and Sukumar Pati

Evaluation of Lateral Stability of Cantilever Wall 525
 Pooja S. Lachyan, Prashant M. Pawar, M. M. Pawar, S. A. Gosavi, and A. B. Kokare

Application of Meta Heuristic Algorithms for Optimization of Inverse Kinematics of a 5D Robotic Manipulator 537
 V. B. Shinde and P. J. Pawar

Experimental Study of Behavior of Under-Reamed Stone Column in Black Cotton Soil	547
Prathmesh Solapure, Manasi Shinde, Shubhali Shete, Saurav Bachhav, and Shailendra Banne	
FE Analysis of the Glass/Jute/Polyester Bone Plate Versus Traditional Metal Plate for Ulna Bone Fracture	559
Rajkumar Deshmukh, Sudarshan Sanap, and Dineshsingh Thakur	
Dynamic Modeling and Experimental Study of Forced Convection Evacuated Tube Solar Collector Used for Grape Dryer	569
Amol Ubale, Dilip Panghavhane, and Parmeshwar Ritapure	
Effect Analysis of Process Parameters on Lubricated Sliding Wear of Al-25Zn-2Cu-2.5Si Alloy for Plain Bearing Application	581
Parmeshwar P. Ritapure, Y. R. Kharde, Amol Ubale, and B. D. Aldar	
Development of Air Controlled Cotton Cleaning Machine in Blow Room Part II Calculating Trash Content by Shirley Analyzer	593
P. S. Hibare and B. B. Deshmukh	
A Novel Scheme of Interleaved Flyback Inverter for Photovoltaic Application	603
Dhanraj D. Daphale and Mahesh S. Yadrami	
Experimental Analysis of Piezo-Beam in the Context of Vibratory Energy Harvesting	611
Rohan Nikam, Kanchan Bhosale, Sachin S. Pawar, Santosh B. Salunkhe, and Vaibhav S. Pawar	
Manufacturing and Fabrication Processes for Societal Applications	
Ergonomic Analysis Tools for Power-Loom Industry	623
Somnath Kolgiri, Rahul Hiremath, and Vaishali Kolgiri	
Role of Fillers in Controlling the Properties of Polymer Composites: A Review	637
K. B. Bommegowda, N. M. Renukappa, and J. Sundara Rajan	
Frequency Spectrum Analysis of Various Defects in Rolling Element Bearings Used in Heavy Load and High Speed Machinery	649
Prashant H. Jain and Santosh P. Bhosle	
Characterization of Hydroxyapatite-Titanium (HA-Ti) Samples Synthesized from Different Material Composition	665
Pranita Sawant, Vijaykumar Jatti, Swati Dhamale, and Meghna Gawade	

Performance Evaluation of Molybdenum Disulfide Based Cutting Fluids Under Near-Dry Machining as an Environment-Friendly Technique 675
 Shrikant U. Gunjal and Sudarshan B. Sanap

Investigation of Lubricant Condition and Machining Parameters While Turning of Steel 683
 L. B. Abhang, Mohd.Iqbal, and M. Hameedullah

A Short Spiral Conveyor Using Cut Flight Screw with Two Different Trough Cover of Different Height—A Comparative Study 695
 Debayan Mondal

Design Consideration of a Laboratory Size Screw Conveyor with Variable Speed for Experimentation Purpose—A Methodological Approach 705
 Debayan Mondal

Case Study Related to Volumetric Capacity, Mass Flow Rate and Filling Factor Against a Constant Trough Height As 180 mm for a Screw Feeder with Continuous Screw 715
 Debayan Mondal

CFD Investigation on Optimization of Pipe Pattern in Radiant Cooling System 725
 Prashant R. Nawale, Sudesh B. Powar, and Pramod P. Kothmir

Design and Simulation of Multiband, Circular Microstrip Patch Antenna for Wireless Applications 741
 Manoj Deshmukh, Ashish Jadhav, Nagashettappa Biradar, Husain Bhaldar, Mahesh Mathpati, and Renuka Wadekar

Portable UV-C 360 Degree Disinfection Chamber 753
 Dattatraya Anarse, Anjali Sakurkar, Mahadev Kadam, and Sonali Kale

Eco-friendly Soldering Technique 761
 Puskaraj D. Sonawwanay and V. K. Bupesh Raja

Friction Drilling an Emerging Technique in Hole Making Process 767
 Mathew Alphonse and V. K. Bupesh Raja

Statistical and Multi-attribute Analysis in Hardened Steel Turning Under Vegetable Oil-Based MQL 777
 A. A. Chavan and V. G. Sargade

Technology For Rural and Agricultural Employment Generation

Design and Analysis of Automated Detaching of Coconut and Branches from Tree Using a Robot 793

Ayush Narayan Malviya, Gokul Kumar Vishwanathan, Tejas walke, and Rahul K. Patil

An Economic Method for Fabrication and Calibration of Five-Hole Pressure Probes 805

Shrikant B. Taware and Chandrakant L. Prabhune

Lab Scale Batch Reactor Design, Fabrication and Its Application for Biodiesel Production 819

Niraj S. Topare, Kiran D. Patil, Satish V. Khedkar, and Nilesh Inamdar

Pest Management System Using Agriculture Robot 829

Anup S. Vibhute, Krishna R. Tate Deshmukh, Ravikant S. Hindule, and Sharad M. Sonawane

A Profound Approach Towards Rural Empowerment with the Aid of Solar Drying Technology 839

Asiya S. Pendhari, Nilprabha N. Yadav, M. Kaif R. Bagsiraj, Rajmati M. Patil, and Avesahemad S. N. Husainy

Chemical and Physical Processes

An Experimental Study of Dynamic Adsorption of Polymer in Alkaline Surfactant Polymer (ASP) Flooding for Heavy Oil 853

Siraj Bhatkar and Lalitkumar Kshirsagar

Analyzing Corrosion Prediction and Dose Optimization of Corrosion Inhibitor in Oil Field Production 861

Siraj Bhatkar, Niraj S. Topare, and Bashique Ahmed

A Study of Process Parameters for Adsorption of Textile Industry Wastewater Using Low-Cost Adsorbent (Bamboo Activated Carbon) 869

Shantini A. Bokil, Niraj S. Topare, and Satish V. Khedkar

Photodetection Performance of Sb³⁺ Doped Cd_{0.92} Hg_{0.08}S Based Electrochemical Cells 883

S. A. Lendave, S. T. Pawar, and L. K. Bagal

Facile Synthesis and Characterization of Pentanary Zn(Co, Cd, S)Se Semiconductor Thin Films 893

S. T. Pawar, S. A. Lendave, G. T. Chavan, V. M. Prakshale, S. S. Kamble, L. K. Bagal, and P. C. Pingale

Corrosion Prevention Study by Using Nano and Micro NiCrAlY Coating Over SA213 T22 Boiler Tube	901
Madhab Chandra Ghosh and Bappa Mondal	
Design and Development of Water Cooling System for Copper Mold	911
Shashikant S. Jadhav, Avinash K. Parkhe, Subhash V. Jadhav, and Samadhan J. Shinde	
Characterization of Calophyllum Oil Biodiesel—Alternative Fuel to Diesel Engines	921
Rahul Krishnaji Bawane, Chetan Choudhary, A. Muthuraja, and G. N. Shelke	
Performance and Emission Characteristics of CI Engine by Using Aluminium Nano Oxides with B40 Blended Bio Diesel in Diesel Fuel	937
Swapnil Vijay Ghogardare and Sanjeev Reddy K. Hudgikar	
Energy Recovery in Domestic Stove Using Thermosyphon	945
Balaji D. Kshirsagar, Zakeer S. Baig, Bait Shubham Ramesh, and Bagul Rahul Prakash	
Synthesis and Characterization of Copper(II), Cadmium(II) and Nickel(II) Complexes Containing 3-Amino-2-Methyl-4(3H)Quinazoline and Triphenylphosphine as Ligands	955
Panchsheela Ashok Ubale, Amit Arvind Kamble, Maina Machindra Awatade, and Vasant Baburao Helavi	
Analysis of Heat Transfer and Pressure Drop for Pressure Driven Flow of Non-Newtonian Fluids Through a Serpentine Channel: Influence of Prandtl Number	965
Sumit Kumar Mehta and Sukumar Pati	
Study of Transference Number and Dc Electrical Conductivity of Polianiline Composite	975
Sarika A. Khapre, Ramdas Biradar, and Sushil Deshpande	
Functionalization of Graft Copolymers of Poly (Ethyl Acrylate) and Cellulose by Post Polymer Reactions to Develop Reactive Metal Ion Sorbents	983
Suresh Kumar	
Effect of Finishing Chemicals on Fastness Properties in Reactive Dye of Cotton Fabric	995
Tushar A. Shinde, Sachin M. Munde, Leena N. Patil, K. K. Gupta, and Jitendra Sonawane	

Village Level Information System in South Solapur Tahsil Using Geoinformatics Approach, Maharashtra, India	1009
Prashant L. Unhale, D. D. Kulkarni, and R. S. Pawar	
Room Temperature Chemiresistive Properties of polypyrrole/Tin Oxide Hybrid Nanocomposites	1021
R. D. Sakhare, Y. H. Navale, Y. M. Jadhav, R. M. Mulik, and V. B. Patil	
Hydrothermally Synthesised ZnO Nanostructure: Highly Sensitive Towards NO₂ Gas	1031
P. R. Godse, Y. H. Navale, Y. M. Jadhav, R. N. Mulik, and V. B. Patil	
Indian Rural Challenges	
The Challenge of Unemployment and Entrepreneurship Before Rural India and Its Solution Through the Foundry Business Using Traditional Indian Knowledge System	1041
Ashutosh Dandekar, Akhilesh Joshi, Indraja Dandekar, Narayan Hargude, Amod Shrotri, and Satish Kulkarni	
Performance Investigation of Mitticool Refrigerator	1051
Nishigandha Patel, O. Mindhe, M. Lonkar, D. Naikare, S. Pawar, V. K. Bhojwani, and Sachin Pawar	
Impact of the COVID-19 Outbreak on Different Stakeholders of Hospitality and Tourism Management	1063
Brajesh Kumar Kanchan, Guddakesh Kumar Chandan, Roma Kumari, and Ojaswi Gautom	
Characterization of Groundwater Quality for Agricultural Purpose from Akkalkot MIDC, Solapur, Maharashtra, India	1075
A. D. Pathare, D. B. Panaskar, V. M. Wagh, S. B. Salunkhe, and R. S. Pawar	
Classification of Groundwater Quality for Drinking Purpose Concerning Industrial Effluent from Akkalkot MIDC, Solapur, Maharashtra, India	1085
D. V. Pathare, D. B. Panaskar, V. M. Wagh, S. B. Salunkhe, and R. S. Pawar	
Assessment of Rainwater Harvesting Potential in Tuljapur Tahsil, Osmanabad District, Maharashtra India Using Remote Sensing and GIS	1095
R. S. Pawar, S. A. Gosavi, S. V. Pathare, M. R. Chougule, and D. D. Kulkarni	
Women Journalists in India's Rural Areas: Social and Economic Conditions	1107
Md. Afsar and Suman Kumari	

Assessment of Godavari River Water Quality of Nanded City, Maharashtra, India	1117
P. R. Shaikh, Girish Deore, A. D. Pathare, D. V. Pathare, and R. S. Pawar	
Land Use Land Cover Detection from Naldurg Area of Osmanabad District, Maharashtra, India	1131
D. D. Kulkarni, Vijay Waghmare, A. D. Kokate, G. S. Pawar, and R. S. Pawar	

Advanced Technology for Water, Energy, Transportation, Housing and Sanitation

Optimal Time and EOQ for Inventory of Deteriorating Items with Variation and Leading Times



Abdullah Alshami and Aniket Muley

Abstract The proposed model represents the optimal time, EQO and optimal total cost, for two different time intervals as components of first run time under-considered constant demand, inventory is non-contact within the first component-time runs, constant within a second, purchasing cost is more than holding, the finite horizon planning, without shortage cost, replenishment required after the second component which is equal the first leading time of first run time. The inventory level is non-zero within a lengthier time on the horizon. Sensitivity analysis for the proposed model has represented the many values for varying demand; the deterioration rate lies in an assumed range. The represented figures explained the performance of optimal quantity and optimal total cost within the components of the first runtime (required time), the difference between the optimal total cost and the actual total cost was proposed.

Keywords Optimal of first run component time · Deterioration rate · Optimal leading time · Optimal total cost

1 Introduction

The inventory modeling, under special assumptions, was represented by many researchers as Abd [1] proposed optimal pricing and lot-sizing under conditions of perishability and partial back-ordering. Bierman and Thomas [2] urbanized inventory decisions under inflationary conditions. Chern, Teng, and Chan [3] considered that comparison among various inventory shortage models for deteriorating items on the foundation of maximizing profit. Dave and Patel [4] well-thought-out the policy of an inventory model for deteriorating items with time proportional demand. Friedman [5] accessible inventory lot-size models with general time-dependent and carrying

A. Alshami (✉)

Department of Mathematics, Thamar University, Thamar, Yemen

A. Muley

School of Mathematical Sciences, Swami Ramanand Teerth Marathwada University, 431606, Nanded, Maharashtra, India

cost function. Haneveld and Teunter [6] further extended the inventory model by developing EOQ within the effects of discounting and demand rate. Misra [7] offered optimal inventory management under inflation. Padmanabhan and Var [8] EOQ wrote a model to manage the models for perishable items under stock-dependent selling rate. Pal et al. [9] proposed a model for marketing-oriented with three-component demand rates dependent on the displayed stock level. Rong et al. [10], Sachan [11] residential the model policy for deteriorating items with time proportional demand. Umap [12] proposed model of multi-item under stock in demand, deterioration to i th item, solved the fuzzy non-linear programming. Waliv and Umap [13] developed the model of fuzzy stochastic to optimum the profit cost. Mishra et al. [14] applied the fuzzy non-linear programming intuitionistic fuzz optimization for multi-objective, inventory model, assumed the deterioration rate to i th item to represent numerical comparison the applied techniques of results. Waliv and Umap [15] the fuzzy inventory model developed through new assumptions as ramp demand, two-warehouses first own warehouse and second rented warehouse to achieve maximum profit cost. Waliv et al. [16] the model for deteriorating items improved within new assumptions as some represented parameters are vague other random with multi-objective, multi-item fuzzy stochastic inventory under demand in price, advertisement frequency. This paper considers the level of inventory to be not zero within variant-time of finite-horizon, the aim is to obtain the optimal components of the first runtime with realistic assumption purchasing cost is greater than holding cost. The inventory level is constant within the second components of the first run time before the replenishment, because in real life the level of inventory has to be nonzero with new technical software gave the alarm about inventory, the total inventory became 10% to order new quantities as replenishment, this consideration adopted in this paper, optimal time and optimal quantity of the inventory level should stay within a length of the horizon with taking the demand rate and required quantity as EOQ, leading time in the contemplation (Tables 1 and 2).

2 Materials and Methods

2.1 Assumptions

In this paper, the mathematical model is developed with the following assumptions

- (1) The Planning horizon is finite.
- (2) The replenishment rate is infinite.
- (3) Single item inventory control.
- (4) The demand and deterioration rates are constant.
- (5) Deteriorating occurs as soon as the items are received into inventory within $[0, t_n]$.
- (6) The Shortage is not allowed.
- (7) The leading time is nonzero.

Table 1 The sensitivity analysis when $k_1 < \theta$

θ	D	k_1	r_1	Q_1^*	t_1^*	t_{m1}^*	TC*
0.005	500	0.002503	0.500625	250.3127	1.003763	0.501882	12541.32
0.05	500	0.02532	0.506398	253.1992	1.039107	0.519554	12832.29
0.4	500	0.225352	0.563379	281.6896	1.454542	0.727271	15882.98
0.8	500	0.552429	0.690536	345.2681	3.085705	1.542852	23861.55
0.005	800	0.002503	0.500625	400.5003	1.003763	0.501882	20060.11
0.05	800	0.02532	0.506398	405.1188	1.039107	0.519554	20525.67
0.4	800	0.225352	0.563379	450.7034	1.454542	0.727271	25406.77
0.8	800	0.552429	0.690536	552.4289	3.085705	1.542852	38172.47
0.005	900	0.002503	0.500625	450.5628	1.003763	0.501882	22566.37
0.05	900	0.02532	0.506398	455.7586	1.039107	0.519554	23090.13
0.4	900	0.225352	0.563379	507.0413	1.454542	0.727271	28581.37
0.8	900	0.552429	0.690536	621.4825	3.085705	1.542852	42942.78
0.005	1000	0.002503	0.500625	500.6253	1.003763	0.501882	25072.63
0.05	1000	0.02532	0.506398	506.3985	1.039107	0.519554	25654.58
0.4	1000	0.225352	0.563379	563.3793	1.454542	0.727271	31755.97
0.8	1000	0.552429	0.690536	690.5361	3.085705	1.542852	47713.09

Table 2 The sensitivity analysis when $k_2 > \theta$

θ	D	k_2	r_2	Q_2^*	t_1^*	tm_1^*	TC*
0.005	500	1.997497	399.4994	199749.7	-801.004	-400.502	7.98E + 09
0.05	500	1.97468	39.4936	19746.8	-81.0391	-40.5196	77989188
0.4	500	1.774648	4.436621	2218.31	-11.4545	-5.72727	984387
0.8	500	1.447571	1.809464	904.7319	-8.0857	-4.04285	163783.5
0.005	800	1.997497	399.4994	319599.5	-801.004	-400.502	1.28E + 10
0.05	800	1.97468	39.4936	31594.88	-81.0391	-40.5196	1.25E + 08
0.4	800	1.774648	4.436621	3549.297	-11.4545	-5.72727	1575013
0.8	800	1.447571	1.809464	1447.571	-8.0857	-4.04285	262047.5
0.005	900	1.997497	399.4994	359549.4	-801.004	-400.502	1.44E + 10
0.05	900	1.97468	39.4936	35544.24	-81.0391	-40.5196	1.4E + 08
0.4	900	1.774648	4.436621	3992.959	-11.4545	-5.72727	1771889
0.8	900	1.447571	1.809464	1628.517	-8.0857	-4.04285	294802.2
0.005	1000	1.997497	399.4994	399499.4	-801.004	-400.502	1.6E + 10
0.05	1000	1.97468	39.4936	39493.6	-81.0391	-40.5196	1.56E + 08
0.4	1000	1.774648	4.436621	4436.621	-11.4545	-5.72727	1968764
0.8	1000	1.447571	1.809464	1809.464	-8.0857	-4.04285	327556.9

- (8) The purchasing cost is more than the holding cost.
 (9) The inventory level is constant within the second component of the first run time, non zero within the planning horizon.
 (10) The total relevant cost consists of fixed ordering, purchasing, and holding costs.

2.2 Notation

D	The demand rate quantity in the period $[0, t_n]$.
Q_1	The quantity through $[A, B]$.
Q_M	The quantity within $[0, A]$
t_1	The first component of the first runtime.
t_{w1}	The first leading time.
t_{m1}	The second component of the first runtime
Q	The total quantity within $[0, B]$.
TC_A	The total of fixed ordering cost during $[0, t_n]$.
I_h	The holding cost.
TC_h	The total holding cost during $[0, t_1]$.
TC_p	The total purchasing cost during $[0, t_1]$
TC	The total relevant cost during $[0, t_1]$.

2.3 Parameters

T	The length of the finite planning horizon.
$I_1(t)$	The inventory level at a time $[0, t_m]$.
$I_2(t)$	The inventory level at a time $[t_m, t_1]$.
t_1	The first run time of replenishment
θ	The constant deteriorating rate units/unit time during $[0, t_1]$.

3 Mathematical Model

Let $I(t)$ is the inventory level at any time

$$\frac{dI(t)}{dt} + \theta I(t) = -D_1, 0 \leq t \leq t_1, 0 \leq \theta \leq 1, I_0(t) = e^{-\theta t} \quad (1)$$

$$I_1(t) = I_0(t) \left[\int_t^{t_1} D e^{\theta u} \right] - b_1 t_1$$

$$\begin{aligned}
&= \frac{D}{\theta} (e^{\theta(t_1-t)} - 1) I_0(t) \\
&= e^{-\theta t_1} I_{01}(t) = e^{-\theta t_{m1}}
\end{aligned} \tag{2}$$

$$I_2(t) = I_{01}(t) \left[\int_{t_m}^{t_1} D e^{\theta u} \right] - Q_m t_{m1} = \frac{D}{\theta} (e^{\theta(t_1-t_{m1})} - 1) - \theta Q_m t_{m1} I_{01}(t) = e^{-\theta t_{m1}} \tag{3}$$

$$Q_1 = Q - Q_m$$

$$t_{w1} = t_1 - t_{m1}$$

Based in $ot_{m1}A$, ot_1B

$$Q_1 = \frac{Q}{2}, Q_m = Q_1 t_m = \frac{t_1}{2}$$

$$I(t) = \frac{D}{\theta} (e^{\theta(t_1-t)} - 1) - \frac{D}{\theta} (e^{\theta(t_1-t_{m1})} - 1) - \theta Q_m t_{m1} \tag{4}$$

$$I(0) = \frac{D}{\theta} (e^{\theta t_1} - 1) - \frac{D}{\theta} (e^{\theta(t_1-t_{m1})} - 1) - \theta Q_m t_{m1}$$

$Q_1 = \frac{D}{\theta} (e^{\theta t_1} - e^{\frac{\theta t_1}{2}}) - \frac{\theta Q_1 t_1}{2}$, series Talyors for $e^{\theta t_1} = 1 + \theta t_1$, $e^{\frac{\theta t_1}{2}} = 1 + \frac{\theta t_1}{2}$ about original point.

$$t_1 = \frac{2Q_1}{D - \theta Q_1}$$

3.1 Fixed Ordering Cost

The Fixed Ordering Cost in the Length of a Finite Horizon $[0, t_1]$.

$$TC_A = A \tag{5}$$

3.2 Purchasing Cost

According to Fig. (1) of inventory level the purchasing cost of

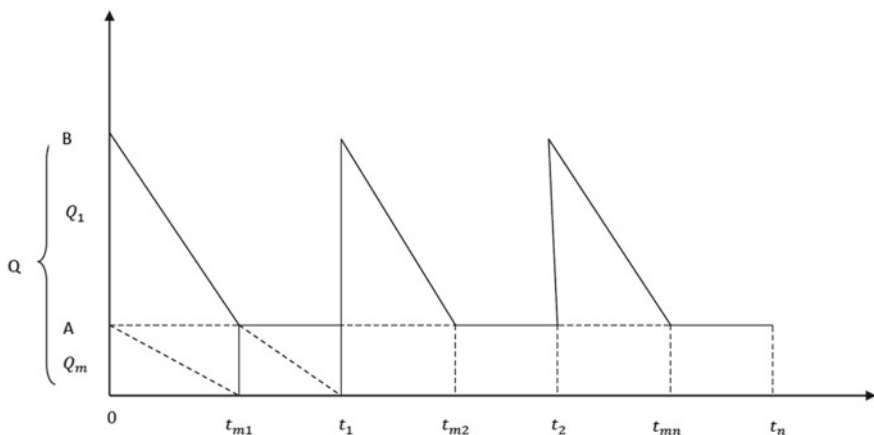


Fig. 1 Graphical demonstration of inventory control diagram

$$TC_P = \frac{CD(e^{\theta t_1} - e^{\frac{\theta t_1}{2}})}{\theta} - \frac{\theta Q_1 t_1}{2} \quad (6)$$

3.3 Holding Cost Excluding Interest Cost

We locate the average inventory quantity to obtain holding cost

$$\begin{aligned} TC_h &= I_h \left[\int_0^{t_1} I(t) dt \right] - \frac{I_h Q_1 t_1}{2} = \int_0^{t_1} \left[\frac{D(e^{\theta t_1} - e^{\frac{\theta t_1}{2}})}{\theta} \right] dt - \frac{I_h Q_1 t_1}{2} \\ &= \frac{I_h D}{\theta^2} \left(e^{\theta t_1} - 2e^{\frac{\theta t_1}{2}} + 1 \right) - \frac{\theta I_h Q_1 t_1}{2} \end{aligned} \quad (7)$$

3.4 Optimal Inventory Level and Optimal Time

To obtain the EOQ by optimizing the total cost

$$TC = TC_A + TC_h + TC_P \quad (8)$$

By substituting Eq. (5-7) in Eq. (8) we get,

$$TC = A + \left[\frac{CD(e^{\theta t_1} - e^{\frac{\theta t_1}{2}})}{\theta} - \frac{\theta Q_1 t_1}{2} + \frac{I_h D}{\theta^2} (e^{\theta t_1} - 2e^{\frac{\theta t_1}{2}} + 1) - \frac{\theta I_h Q_1 t_1}{2} \right] \quad (9)$$

Substitute $t_1 = \frac{2Q_1}{D - \theta Q_1}$ in Eq. (9)

$$TC = A + \left[\left(\frac{CDQ_1}{D - \theta Q_1} \right) - C \left(\frac{Q_1^2}{D - \theta Q_1} \right) - \frac{\theta I_h Q_1^2}{(D - \theta Q_1)} \right] \quad (10)$$

Deviating Eq. (10) with respect to Q_1

$$\begin{aligned} \frac{dTC_1}{dQ_1} = & CD \left(\frac{D}{(D - \theta Q_1)^2} \right) \\ & - C \left(\frac{2DQ_1 - \theta Q_1^2}{(D - \theta Q_1)^2} \right) - \theta I_h \left(\frac{2DQ_1 - \theta Q_1^2}{(D - \theta Q_1)^2} \right) = 0 \end{aligned}$$

$Q_1^* = \frac{D}{\theta} \left[1 - \left(1 - \frac{\theta C}{C + \theta I_h} \right)^{\frac{1}{2}} \right]$ alternatively we can obtained:

$$Q_1^* = \frac{D}{\theta} \left[1 + \left(1 - \frac{\theta C}{C + \theta I_h} \right)^{\frac{1}{2}} \right]$$

Lemma (1):

(a) If $0 \leq k_1 \leq 1$

(i) $D \leq Q_1^*$ If $Q_1^* = \frac{D}{\theta} \left[1 - \left(1 - \frac{\theta C}{C + \theta I_h} \right)^{\frac{1}{2}} \right]$

When $k_1 \geq \theta$, $0 \leq k_1 \leq 1$

(ii) $D > Q_1^*$ If $Q_1^* = \frac{D}{\theta} \left[1 - \left(1 - \frac{\theta C}{C + \theta I_h} \right)^{\frac{1}{2}} \right]$

When $k_1 < \theta$

b) $D < Q_1^*$ If $Q_1^* = \frac{D}{\theta} \left[1 + \left(1 - \frac{\theta C}{C + \theta I_h} \right)^{\frac{1}{2}} \right]$, where $k_2 > \theta$

Proof

Since

$$\theta C < C, 0 \leq \theta \leq 1$$

$$\theta C < C + \theta I_h$$

$$\frac{\theta C}{C + \theta I_h} < 1$$

$$0 < 1 - \left(1 - \frac{\theta C}{C + \theta I_h}\right) < 1, 0 < k_1 = \left[1 - \left(1 - \frac{\theta C}{C + \theta I_h}\right)\right]^{\frac{1}{2}} < 10 \leq k_1 \leq 1$$

So that: $D > Dk_1 = \theta Q_1^*$

There are two cases in this equality:

Case 1: If $k_1 \geq \theta$, then $D \leq Q_1^*$

Case 2: If $k_1 < \theta$, then $D > Q_1^*$

Similarly, $\frac{\theta C}{C + \theta I_h} < 1$

$$1 + \left(1 - \frac{\theta C}{C + \theta I_h}\right) > 1, k_2 = \left[1 + \left(1 - \frac{\theta C}{C + \theta I_h}\right)\right]^{\frac{1}{2}} > 1k_2 > 1$$

In order that, $D < D\left[1 + \left(1 - \frac{\theta C}{C + \theta I_h}\right)\right]^{\frac{1}{2}} = \theta Q_1^*$

$$D < k_2 D = \theta Q_1^*$$

If $k_2 \geq \theta$ then $Q_1^* > D$ Keep hold.

If $k_2 < \theta$ then $Q_1^* < D$ Keep hold.

$$t_1 = \frac{2Q_1}{D - \theta Q_1}$$

Theorem

$$(1) \text{ If } Q_1^* = \frac{D}{\theta} \left[1 - \left(1 - \frac{\theta C}{C + \theta I_h}\right)^{\frac{1}{2}}\right],$$

Then

TC is a maximum if $\frac{k_1}{\theta} = r_1 > 1$ when $k_1 \geq \theta$

TC is a maximum if $\frac{k_1}{\theta} = r_1, 0 < r_1 < \sqrt{2} - 1$ when $k_1 < \theta$

TC is a maximum if $\frac{k_1}{\theta} = r_1, \sqrt{2} - 1 < r_1 < 1$ when $k_1 < \theta$

TC is a minimum if $\frac{k_1}{\theta} = r_1, \sqrt{2} - 1 < r_1 < 1$ when $k_1 < \theta$

$$(2) \text{ If } Q_1^* = \frac{D}{\theta} \left[1 + \left(1 - \frac{\theta C}{C + \theta I_h}\right)^{\frac{1}{2}}\right]$$

Then

TC is a minimum if $\frac{k_2}{\theta} = r_2, r_2 > 1$

TC is a maximum if $\frac{k_2}{\theta} = r_2, 0 < r_2 < \sqrt{2} - 1$

TC is a maximum if $\frac{k_2}{\theta} = r_2, \sqrt{2} - 1 < r_2 < \frac{1}{2}$

TC is a minimum if $\frac{k_2}{\theta} = r_2, \frac{1}{2} < r_2 < 1$

Proof

The second order derivative of the total cost for the Q_1 as

$$\frac{dT^2C_1}{dQ_1^2} = \left(\frac{2\theta CD^2}{(D - \theta Q_1^*)^3} \right) - (C + I_h) \left(\frac{2}{(D - \theta Q_1^*)} + \frac{2\theta(2DQ_1^* - \theta Q_1^{*2})}{(D - \theta Q_1^*)^3} \right)$$

To prove that we need to show that

$$\frac{dT^2C_1}{dQ_1^2} = \left(\frac{2\theta CD^2}{(D - \theta Q_1^*)^3} \right) - (C + I_h) \left(\frac{2}{(D - \theta Q_1^*)} + \frac{2\theta(2DQ_1^* - \theta Q_1^{*2})}{(D - \theta Q_1^*)^3} \right)$$

$$\text{Let } f(D, Q_1^*) = \frac{dT^2C_1}{dQ_1^2} = \left(\frac{2\theta CD^2}{(D - \theta Q_1^*)^3} \right) - (C + I_h) \left(\frac{2}{(D - \theta Q_1^*)} + \frac{2\theta(2DQ_1^* - \theta Q_1^{*2})}{(D - \theta Q_1^*)^3} \right)$$

From Lemma (a) part (i)

$$D > Q_1^*, (D - \theta Q_1^*)^3 > 0$$

$$D = k_1 Q_1^*, \text{ if } k_1 \geq \theta$$

Let

$$2\theta CD^2 = (C + I_h) \left[2(D - \theta Q_1^*)^2 + 2\theta(2DQ_1^* - \theta Q_1^{*2}) \right]$$

$$2\theta CD^2 = (C + I_h) \left[2(D - \theta Q_1^*)^2 + 2\theta(2DQ_1^* - \theta Q_1^{*2}) \right]$$

$$2\theta CD^2 = (C + I_h) \left[2(D - \theta Q_1^*)^2 + 2\theta(2DQ_1^* - \theta Q_1^{*2}) \right]$$

$$\theta C k_1^2 = (C + I_h)(k_1^2 + 2\theta k_1 - \theta^2)$$

Let, $k_1 = r_1\theta$, $0 < \theta < 1$, $0 \leq k_1 \leq 1$ then $r_1 > 1$

$$r_1^2 C = (C + I_h)(r_1^2 + 2r_1 - 1)$$

$$(r_1^2 + 2r_1 - 1) > r^2$$

$r_1^2 C = (C + I_h)(r_1^2 + 2r_1 - 1)$, by assumption $C > I_h$, $C + I_h > C$

$r^2 C < (C + I_h)(r_1^2 + 2r_1 - 1)$, $f(D, Q_1^*) < 0$, That means that TC is a maximum.

When $0 < r_1 < 1$

$$D < Q_1^*(D - \theta Q_1^*)^3 < 0$$

From lemma (a) part (ii)

$k_1 = r_1\theta$, $0 < \theta < 1$, $0 \leq k_1 \leq 1$ then $0 < r_1 < 1$

If $0 < r_1 < \sqrt{2} - 1$ then: $r_1^2 C = (C + I_h)(r_1^2 + 2r_1 - 1)$

If $0 < r_1 < \sqrt{2} - 1$ then: $r^2 > (r_1^2 + 2r_1 - 1)$

$r_1^2 C = (C + I_h)(r_1^2 + 2r_1 - 1)$, by assumption $C > I_h, C + I_h > C$

$$r^2 C > (C + I_h)(r_1^2 + 2r_1 - 1), (D - \theta Q_1^*)^3 < 0$$

$$f(D, Q_1^*) < 0$$

That means that TC is a maximum.

If $\sqrt{2} - 1 < r_1 < \frac{1}{2}$

$$r_1^2 > (r_1^2 + 2r_1 - 1)$$

$r_1^2 C = (C + I_h)(r_1^2 + 2r_1 - 1)$, by assumption $C > I_h, C + I_h > C$

$$r_1^2 C > (C + I_h)(r_1^2 + 2r_1 - 1), (D - \theta Q_1^*)^3 < 0$$

$$f(D, Q_1^*) < 0$$

That means that TC is a maximum.

If $\frac{1}{2} < r_1 < 1$

$$r^2 < (r_1^2 + 2r_1 - 1)$$

$r_1^2 C = (C + I_h)(r_1^2 + 2r_1 - 1)$, by assumption $C > I_h, C + I_h > C$

$$r^2 C > (C + I_h)(r_1^2 + 2r_1 - 1), (D - \theta Q_1^*)^3 < 0$$

$$f(D, Q_1^*) > 0$$

Similarly

From lemma (b)

$$D < Q_1^*(D - \theta Q_1^*)^3 < 0$$

Let

$$k = r_2 \theta, 0 < \theta < 10 < k_2 < 1,$$

If $r_2 > 1$

By first part of Theorem

$$r_2^2 C < (C + I_h)(r_2^2 + 2r_2 - 1)$$

For the reason that $(D - \theta Q_1^*)^3 < 0$

Then

$$r_2^2 C < (C + I_h)(r_2^2 + 2r_2 - 1)$$

$$f(D, Q_1^*) > 0$$

TC is a minimum.

If $0 < r_2 < 1$

There are two cases as:

$$0 < r_2 < \sqrt{2} - 1$$

$$r_2^2 C > (C + I_h)(r_2^2 + 2r_2 - 1)$$

For the reason that $(D - \theta Q_1^*)^3 < 0$, then $r_2^2 C < (C + I_h)(r_2^2 + 2r_2 - 1)$

$f(D, Q_1^*) < 0$ TC is a maximum.

If $\sqrt{2} - 1 < r_2 < \frac{1}{2}$

$$r_2^2 C > (C + I_h)(r_2^2 + 2r_2 - 1)$$

For the reason that $(D - \theta Q_1^*)^3 < 0$, then $r_2^2 C > (C + I_h)(r_2^2 + 2r_2 - 1)$

TC is a maximum $f(D, Q_1^*) < 0$

If $\frac{1}{2} < r_2 < 1$

$$r_2^2 C < (C + I_h)(r_2^2 + 2r_2 - 1)$$

For the reason that $(D - \theta Q_1^*)^3 < 0$

$f(D, Q_1^*) > 0$ Then, TC is a minimum and second part hold.

4 Sensitivity Analysis

In the proposed model as: Optimal vary time and EOQ:

Example 1

$I_h = 0.05$ \$/perunit, $C = , 100$ \$/perunit, $A = 120$ \$/perunit

(a) When $D > Q_1^*$

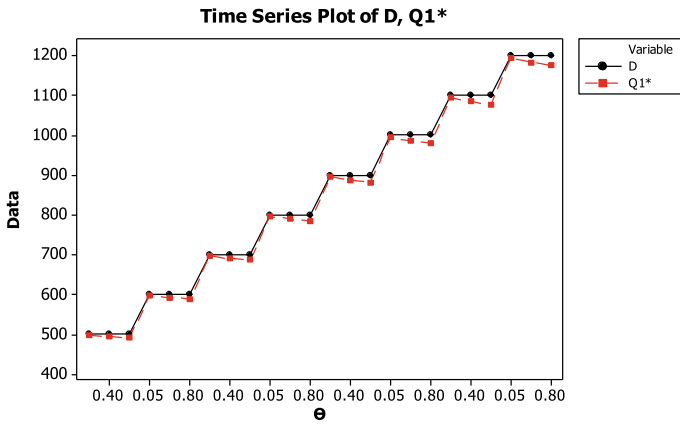


Fig. 2 The daily demand and EOQ versus deterioration rate

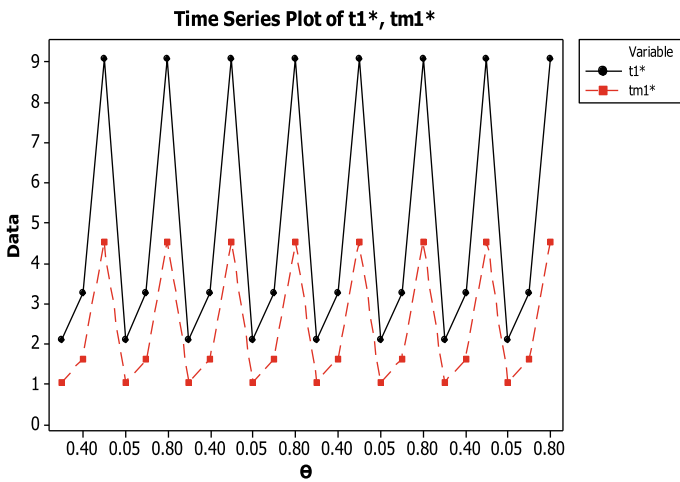


Fig. 3 The components of first runtime run optimal first runtime versus deterioration rate

$$(b) \text{When } D < Q_1^*$$

5 Conclusion

The crop of the planned model within two components of the first runtime as class intervals and leading time found out that, according to Fig. 2. Vary between demand rate and EOQ with deterioration rate anywhere demand rate and EOQ was decreased when the deterioration rate increased, Fig. 3. Illustrate that the deterioration rate was

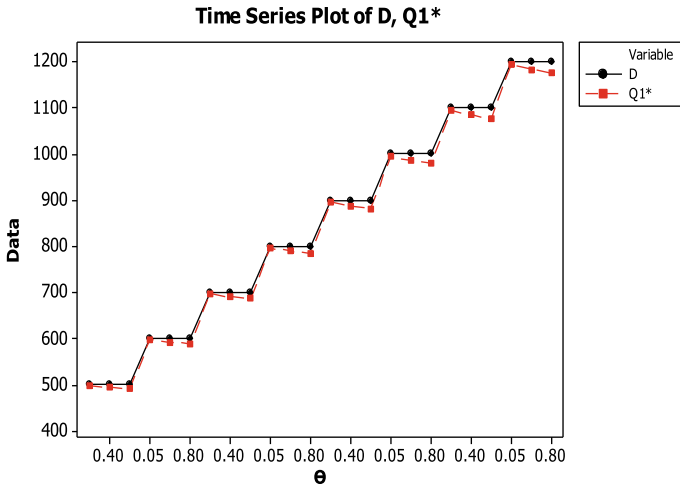


Fig. 4 The optimal total and actual costs versus deterioration rate within first runtime

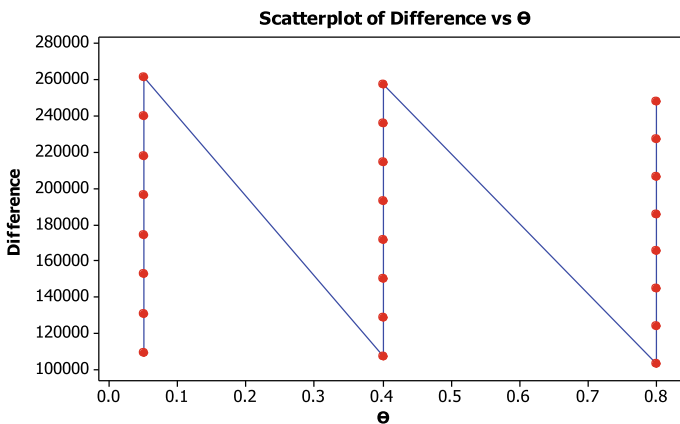


Fig. 5 The difference cost within optimal cost and actual total cost versus deterioration rate

increasing when components of first-run optimal time increased, Fig. 4. Represented the gap between actual total and optimal costs was high that made the proposed model is applicable deterioration rate increased while the total was decreasing. According to Fig. 5 the difference between actual total cost and the optimal total cost was decreased while the deterioration rate was increasing. The proposed model had stability when demand is higher than economic order quantity within the [A, B] time, that being making the model is supported to reduce the quantity in stock with higher demand. The proposed model can extend to inflation consideration also if the delay in payment is allowed; further, the variation in the level within each time run can take into consideration.

Acknowledgements We would like to thank the editor and referees for the important comments and suggestions that improved the paper, the thanking to Thamar University in Yemen for financially supporting also SRTM University in India. This work is supported by the Mathematical School of Sciences, India to develop the inventory model of deteriorating items.

References

1. Abd PL (1996) Optimal pricing and lot sizing under conditions of perishability and partial back ordering. *Manage Sci* 42:1093–1104
2. Bierman H, Thomas J (1977) Inventory decisions under inflationary conditions. *Decisions Sciences* 23:553–558
3. Chern, M.S., Teng, J.T., Chan, Y.L., (1999) A comparison among various inventory shortage models for deteriorating items on the basis of maximizing profit. *Asia-Pacific Journal of Operation Research* 5:1176–1182
4. Dave U, Patel, L.K., (1981) Policy inventory model for deteriorating items with time proportional demand. *J Oper Res Soc* 32:137–142
5. Friedman, M.F., (1982) Inventory lot size models with general time dependent and carrying cost function. *INFOR* 20:157–167
6. Haneveld, K.W.K., Teunter, R.H., (1992) Effects of discounting and demand rate variability on the EOQ. *International Journal of production economic* 54:173–192
7. Misra, R.B., (1979) A note on optimal inventory management under inflation. *Naval Research Logistics Quarterly* 26:161–165
8. Padmanabhan G, Var P (1995) EOQ models for perishable items under stock dependent selling rate. *Eur J Oper Res* 86:281–292
9. Pal, A.K., Bhunia, A.K., Mukherjee, R.N., (2005) A marketing oriented inventory model with three component demand rate dependent on displayed stock level. *Journal of the Operational Research Society*, 113–118
10. Rong, N.K., Mahapatra, N.K., Maiti, M., (2008) A two-warehouse inventory model for a deteriorating item with partially /fully backlogged shortage and fuzzy lead time. *Eur J Oper Res* 189:59–75
11. Sachan, R.S., (1984) Policy inventory model for deteriorating items with time proportional demand. *J Oper Res Soc* 35:1013–1019
12. Umap, H.P., (2014) Fuzzy Eoq Model for deteriorating items with exponential membership function. *American Journal of Applied Mathematics and Statistics* 2:203–206
13. Waliv, R.H., Umap, H.P., (2016) Fuzzy stochastic inventory model for deteriorating item. *Yugoslav Journal of Operations Research* 27:91–97
14. Mishra U, Waliv, R.H., Umap, H.P., (2019) Optimizing of multi-objective inventory model by different fuzzy techniques. *International Journal of Applied and Computational Mathematics* 5:136
15. Waliv RH, Umap, H.P., (2018) Multi item two-warehouse fuzzy inventory model. *International Journal of Procurement Management (IJPM)* 11, 443–454
16. Waliv, R.H., Mishra, U., Garg, H., Umap, H.P., (2020) A nonlinear programming approach to solve the stochastic multi-objective inventory model using the uncertain information. *Arab J Sci Eng* 45, 6963–6973

Clustering and Association Rule Mining for Tree Species Plantation



Govind Kulkarni, Aniket Muley, Parag Bhalchandra, and Nilesh Deshmukh

Abstract The present study focuses on greenery in an urban environment. Nowadays the concept of smart cities is a hot topic in the development of green space environment which helps to reduce the pollution level in the environment. Unsupervised K-means cluster analysis operation was performed to recognize the natural groups of instances of known soil dataset. Also, apriori algorithm applied on each individual cluster to find out the best possible combination of tree species in each respective cluster. The tree species were grouped with respective cluster based on the ideal soil pH. The result of this study will be helpful in designing green infrastructure policies. Furthermore, new planning strategies can be implemented for ecosystem services for the urban environment to target the green infrastructure at local as well as national level.

Keywords Association rule mining · K-means cluster · Nanded · Soil · Tree species · Urban environment

1 Introduction

Now day's rapid urbanization and uncontrolled industrialization are the serious threat in the 21st century. Expansion of population with increasing automobiles and demographic pressure exasperated the environmental problem in an urban region. The natural ecosystem has been affected due to rapidly increasing unnatural activities which demolished environmental quality. Hence, to overcome such a complex situation, it is highly recommended to increase the urban green space environment. Various studies have shown the importance of tree species which minimizes the negative influence and increases the positive effects. The appropriate selection of

G. Kulkarni
L.L.D.M.M, 431515 Parli Vajjnath, MS, India

A. Muley (✉)
School of Mathematical Sciences, S.R.T.M. University, 431606 Nanded, MS, India

P. Bhalchandra · N. Deshmukh
School of Computational Sciences, S.R.T.M. University, 431606 Nanded, MS, India

tree species is a complex process and it is based on several factors. These factors may include geographical nature of tree species, soil type, water quality in the region, the nature of pollution, the climate of the region, etc. Proper tree plantation is an effective way which has been widely accepted by the world [1]. The tree plantation in an urban environment makes our cities more enjoyable. The most appropriate tree species selection for plantation in urban environment reduces the unwanted noise level, absorbed air pollution and helps to reduce the human stress. Performed a multivariate statistical analysis method for selection of shrub and tree species in the study area [7]. Investigated the soil quality of the region with a standard reference value [9]. Cluster analysis was performed to identify similar character groups and classifies soil samples according to their homogeneity. Hierarchical clustering analysis method is applied to identify the correlation between physicochemical properties of collected soil samples [11]. Analyzed soil data type with the help of several data mining technique [10]. The major objective of their study was to predict the soil type nature. JRip, J48, and Naive Bayes classification algorithms were used for the extraction of knowledge from soil data. JRip classifier generated rules shown effectively and good performance as compare to other algorithms. Used data mining techniques i.e. latent class clustering (LCC) and k-modes clustering technique with association rule to identify the several factors associated with road accident to reduce the road accident in Haridwar [8]. Comparative analysis was performed with the help of LCC and k-modes clustering techniques and form several clusters. Association rule mining techniques for tree plantation site selection is used [12]. The unsupervised apriori association algorithm was applied to identify the best ideal location for tree species. The tree plantation locations were considered as target values for rule establishment. Validation part was considered for plantation site prediction. Introduced some innovative methods of data visualization in association rule by using R software for statistical computing with the help of R-package arules viz. the grouped based matrix methods were used to explore the complex scenario with interpretation [3]. The association rule was applied on hierarchical clustering to address the decision process and proposed framework was able to capture the pattern which visualizes coincidence of products categories. The group based visualization method found to be satisfactory with large database.

Applied the data mining techniques namely K-mode clustering, association rules and multi-criteria decision analysis approach to investigate the factors associated with the road accidents and to design conceptual framework for road safety policies [7]. Applied an improved apriori algorithm on mobile e-commerce shopping data to develop the recommendation system for mobile e-commerce community. The major objective of their study was to increase the efficiency of data that would achieve the unity of real time and recommendation accuracy [2]. The efficiency has been obtained by comparison method and conventional methods were used to predict the accuracy for mobile e-commerce business.

2 Materials and Methods

In this study cluster analysis and association rule mining technique is performed. the detailed explanation of proposed methodology is as follows.

2.1 Cluster Analysis

In cluster analysis, the dataset is treated as one group. It is a useful approach to recognize the homogenous collections of things known as the clusters. These clusters share many similar characteristics. Fundamental objective of cluster analysis is to identify the similar groups once we have decided the clustering variables the next procedure is to decide clustering procedure to form our groups of objects for analysis. The choice of variables is based on those clusters variable which proffers a clear contrast between sections of a particular managerial objective. The clustering operations are performed to identify the interesting groups from the data set. Further, the clustering operations find the optimal solution to given problems. The operative performance of cluster analysis method is recommended as all tents to be computationally effective and efficiently utilized on massive scale database. In present investigation soil parameters pH, Electrical conductivity, Magnesium, Calcium and Organic matter values were considered as data set on which K-means clustering algorithm available in the R programming environment with data mining package library cluster. The k-means clustering is well known reliable algorithm which is easy to implement on data set and freely available on R environment. The k-means algorithm is also known as the Centroid method. This algorithm follows the partitioning algorithm procedure which organizes the objects of data sets into some specific number of groups known as the clusters. In this study to execute the k-means clustering operation R3.4.1 version is used.

2.2 Association Rule Mining

The traditional data management system and relevant tools can only handle the storage and retrieval of explicitly stored data. The methods to descent the inclusion of knowledge entailed by large amount of data are highly desirable which put challenges on traditional database management system. Association rule mining analysis method is afloat technique most useful for new data set exploration to renders results to easy understand and easy to explain. The functional work of association rule mining is to find out the relationship in between the data set. The best known data mining technique is Association in which a pattern is discovered based on a relationship between items in the same transaction. Because of this reason the association mining is also known as the relation techniques. Association rules are the discovery

of community relations, various patterns or relationships among sets of objects or components in databases [7]. Association rules is one of the best data mining techniques which extract the meaningful hidden rules and relation between the attributes in large data set. The association rule mining technique is used to produce the set of rules which defines fundamental pattern in the given data set. We can define association rule for selection of possible combinations of tree species in urban environment as the associatively of two characteristics of trees is determined by the frequency of their occurrence together in the data set. For the identification of most important relationship association rules uses criteria support and confidence by investigation of data for frequent pattern. In Association rule support is used for the identification of frequently appeared item in a dataset, whereas Confidence is used for indication of number of times rule statements have been found to be true. Association rule mining apriori algorithm performs level-wise operations. The apriori algorithm is breadth—first algorithm used to count transactions of frequent item sets and to derive rules. Further, the group of such candidates are again tested the given data set. apriori algorithm uses bottom up approach by which frequent subsets are extended one item at one time to generate candidate. The general work flow of apriori Algorithm is as follows (Fig. 1):

In this study, grouped based matrix visualization, graph based visualization and scatter plot is used for the visualization of generated rules. The use of grouped based matrix visualization is to inspect the rules with possible combination with high granulated level. The highest lift value in top left corner in grouped based matrix shows the strong relationship with support value which is in the form of largest balloon as grouped matrix form uses balloon plot with antecedent groups as columns and consequents as rows. The color of each balloon represents the aggregative interest measure in the group and the size of the balloon shows the aggregated support.

Further, Graph based approach to highlight most important rules and is used to plot the rules in a concise manner than that of matrix view. As the number of items and

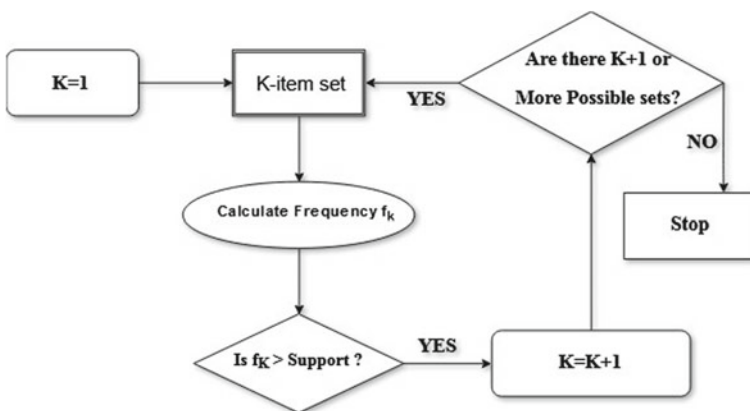


Fig. 1 Work flow of apriori algorithm

associations are increased in association rules then graph based visualization becomes cluttered. In graph based techniques each node represents the item; edges represent the relation among the left hand side and right hand side items. Support values of rules are encoded as area of node. Further, color represents the confidence measures. Important rules are added to the plot as labels on the edges, by notifying them with color or based on the width of the arrows which display the edges. In association rule mining graph based visualization techniques offer a strong representation of rules for small set of most important rules based on their corresponding lift score values. The association rule in R environment is executed with R library functions.

In this study, to generate rules apriori algorithm on each individual cluster. In order to generate rules on each cluster, 95% of confidence value is assumed. Further, these rules were evaluated on the basis of different support values and lift measures. Top rules were extracted on the basis of high lift values. In following association rule output on each individual clusters are discussed with possible combination of tree species for plantation in respective clusters.

2.3 Study Area

Nanded is positioned on the bank of Godavari River which splits the city into the North and south parts. Nanded is situated at latitude of 19.15 and a longitude of 77.30 [4]. The existing investigation is based on the North Nanded and is divided into six different regions [5]. A total of 25 soil samples have been collected from various parts of the study region. From 0 to 20 cm depth of composite surface soil is carried out for physiochemical analysis purposes with standard procedure. Figure 2 shows the areas of the soil units which were collected from the study region.

3 Result and Discussion

3.1 Clustering

The cluster analysis process was performed to classify the natural groups of instances of the provided data set. In this process, the dataset is considered as one group. It is a useful approach to recognize the homogenous groups of things known as the clusters. Fundamental objective of cluster analysis is to identify the similar groups once we have decided the clustering variables the next procedure is to decide clustering procedure to form our groups of objects for analysis. The choice of variables is based on those clusters variable which gives a distinct differentiation in segments regarding a specific managerial objective. In this study we applied k-means clustering algorithm on soil dataset obtained from the principle component analysis. By

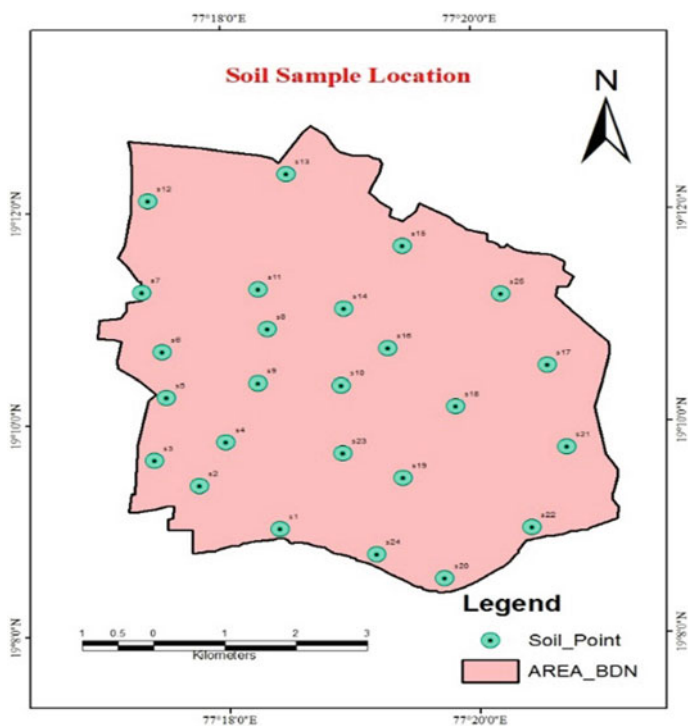


Fig. 2 Soil sample location

k-means clustering method we obtained 4 major clusters with 57.21% of point variability. The soil samples were classified based on K means clustering according to their similarity pattern and represented in Table 1. Further, the tree species have been classified according to the ideal pH range of respective soil samples.

In cluster 1, Neem and Chinch trees are most preferred trees. Table 2 explore classification of trees with ideal pH range. For sample location S1 Neem, Ashoka, Sisso, Shrish, Deris Indica, *Thesperia populnea*, Manikarna, Jambhul, Silky Oak, Gulmohar trees are more suitable and will be recommended. Further, location consist of S3 Ashoka, Sisso, Deris Indica, *T. populnea*, Pulmeria Rubra, Mango, and Silky oak. Sample location S13 cluster 2 suggested Ashoka, Sisso, Shrish, Deris Indica, *T. populnea*, Manikarna, Jambhul, Mango, Silky oak, Acacia catchu, Gulmohar.

Table 1 K-means cluster results

Cluster name	Sample in respective cluster
Cluster 1	S2, S7, S16
Cluster 2	S1, S3, S13, S14, S15, S21
Cluster 3	S4, S8, S11, S19, S20, S23
Cluster 4	S5, S6, S9, S10, S12, S17, S18, S22, S24, S25

Table 2 Association rule for cluster 1

lhs	rhs	Support	Confidence	Lift	Count
[1] {}	{Chinch}	1	1	1	3
[2] {}	{Neem}	1	1	1	3
[3] {Chinch}	{Neem}	1	1	1	3
[4] {Neem}	{Chinch}	1	1	1	3

Cluster 2 suggested Neem, Manikarna, Chinch, and Gulmohar for sample location S14. For cluster 3 k-means clustering algorithms found six soil samples with similar characters which include S4, S8, S11, S19, S20, and S23. The ideal location for Neem, Manikarna, and Chinch tree species found in sample location S4, S8, S11 and S19. Subabul, Neem, Shirish, Deris Indica, Manikarna, Jambhul, Silky oak, Acacia catchu, Chinch, Gulmohar tree were found most suitable in sample location S19. It is observed that, Ashoka, Sisso, Deris Indica, *T. populnea*, Manikarna, Mango, Silky Oak, and Gulmohar found to be ideal for plantation in sample location S20 and S23. Also Shirish, Jambhul and Acacia catchu tree species found to be ideal for plantation in sample location S19 and S23. Ten soil samples falls under cluster 4 with similar characters and the possible tree species will be suggested and represented in According to pH classification it is observed that, Neem, Manikarna, Chinch, Gulmohar tree species will be strongly recommended for plantation.

3.2 Association Rule Mining

Association rule for cluster 1 shows that Neem and Chinch trees are most preferred combination in cluster 1 which generates four rules with 95% of confidence value and support value 0.01. Following is the output of apriori algorithm in R environment for cluster 1.

Association rules for cluster 1 reveals that the group contain 4 rules with two possible consequents Neem and chinch (Table 2). Further, rules also states that Neem and Chinch tree can be planted individually or with the combination of Chinch and Neem tree in the sample region of cluster 1. The possible combination of rules represented for cluster 1 in the form of grouped matrix, Association rules for cluster 2: Table 3 shows that, while support value is lies between 0.10 and 0.30 it generates

Table 3 Association rules with different support value

Sr	Support	Constant	No. of rules
1	0.10–0.30	0.95	12,385
2	0.17–0.33	0.95	2232
3	0.34–0.50	0.95	77
4	0.51–1	0.95	0

12,385 rules. Further, it is observed that 2232 rules were generated if support value is within 0.17–0.33. Also, if support value is between the ranges viz. 0.34–0.50 has generated 77 rules. No rule was generated by assuming the support value within the range 0.51–1. We found that, most suitable rules were generated with support value ranges between 0.34 and 0.50.

Initially, top 10 rules extracted from 77 rules but not all of them were interested. Based on support, confidence and lift measurement was used to determine which rules were most interesting. Assuming support as 0.5 and confidence 1, it is observed that the rule is to be read as tree species *Deris Indica* is associated with the tree species *Silkyoak*. Alternatively, the first rule can also be interpreted as for an association rule *Deric Indica* \Rightarrow *Silky oak*. If the lift value is 1, it implies that *Deric Indica* and *Silky oak* are independent. Further, if the lift value is >1 , then based on rule 1 and 2 reveals that *Deric Indica* and *Silkyoak* are positively correlated. The rule 3–4, 5–6, 7–8, 9–10 also represents the association between the tree species. Also, it is observed that in all 10 rules, mostly *Deris Indica* tree species is highly correlated with other tree species. This suggests that *Deris Indica* should be considered for plantation in sample locations and represents the mostly associated trees suggested for plantation are: *Ashoka*, *Deris Indica*, *T. Populnea*, *Silkyoak* and *Sisso*.

Association rules for cluster 3: Table 3 show that, if support value is lies between 0.01 and 0.16 then it generates 14,933 rules. Further, it is observed that 769 rules were generated if support value is within 0.17–0.33. Also, if support value is between the ranges viz. 0.34–0.50 has generated 33 rules. Support value within the 0.51–0.66 range has generated 8 rules. We found that, most suitable rules were generated with support value ranges between 0.34–0.50. Table 4 shows the rules generated by apriori algorithm with constant confidence value with different support values.

Figure 3 shows that 33 rules were found in this experiment, but not all of them were interested. Based on support, confidence and lift measurement was used to determine which rules were most interesting. Further in these rules it is found that *Gulmohar*, *Deris Indica*, *Silkyoak* and *Manikarna* trees species have strong frequency occurrence in respective cluster. The result reveals that the most interesting rules were rule 1 to 10. Assuming support as 0.5 and confidence 1, it is observed that the rule 1 is to be read as tree species *Deris Indica* is associated with the tree species *Gulmohar*. Alternatively, the first rule can also be interpreted as for an association rule *Deric Indica* \Rightarrow *Gulmohar*. If the lift value is 1, it implies that *Deric Indica* and *Gulmohar* are independent. Further, if the lift value is >1 , then based on rule 1 and 2 reveals that *Deric Indica* and *Gulmohar* are positively correlated. The rule 3–4, 5–6, 7–8, 9–10 also represents the association between the tree species. Further, the rule 7 rule

Table 4 Association rules with different support value

Sr	Support	Constant	No. of rules
1	0.01–0.16	0.95	14,933
2	0.17–0.33	0.95	769
3	0.34–0.50	0.95	33
4	0.51–0.66	0.95	8



Fig. 3 Group matrix for 33 Rules

8 reveals that the Deris Indica, Gulmohar and Silky oak tree species have positive association within them. The rule 10 states that the Deric Indica and Manikarna have strong association with Gulmohar tree species. In this association rule we also observed that in all 10 rules, mostly Deris Indica tree species is positively correlated with other tree species and it is suggested that, Deris Indica should be considered for plantation in sample locations in respective cluster. Figure 4 shows the graphical representation of 10 rules.

For cluster 4, by putting support value within the range of 0.01–0.10 apriori algorithm have generated 11,305 rules. 16 rules were generated by support value of 0.11–0.20. With support value range within 0.21–0.30 we observed 12 rules generated by algorithm. Support values within 0.31–0.40 have generated 5 rules. Two rules were generated with the support value of 0.41–1. The investigation reveals that most suitable rules are generated with support value of 0.11–0.20 which generated 16 rules. Table 5 reveals the association rules with different support values.

For cluster 4 the association rule generated 16 rules with support value range within 0.11–0.20. In these rules it is also observed that the Neem, chinch and Manikarna tree have strong association the set. Based on support, confidence and lift measurement was used to determine most interesting rules. Further it is found

Table 5 Association rules with different support value

Sr	Support	Constant	No. of rules
1	0.01–0.016	0.95	14,933
2	0.17–0.33	0.95	769
3	0.34–0.50	0.95	33
4	0.51–0.66	0.95	8

that, Neem, Chinch and Manikarna trees species have strong frequency occurrence in respective cluster. These rules are represented in the form of grouped matrix in Fig. 4.

Assuming support as 0.2 and confidence 1, it is observed that the rule 1 is to be read as tree species Silkyoak is associated with the tree species Gulmohar. Alternatively, the first rule can also be interpreted as for an association rule $Silkyoak = = > Gulmohar$. If the lift value is 1, it implies that Silkyoak and Gulmohar are independent. Further, if the lift value is >1 , then based on rule 1 and 2 reveals that Silkyoak and Gulmohar are positively correlated. Further, the second rule states that tree species Manikarna and Silkyoak have strong association with Gulmohar tree species. The rule 3–4, 5–6, 7–8, 9–10 also represents the association between the tree species. Rule 9 and 10 reveals that Neem and Chinch tree species have association with each other. Here, in the extracted rule association rule have generated rules with different support value. Rules are considered on the basis of highest lift values. Positive association was found with tree species on the left hand side in rule 3–8 with Manikarna tree species. This suggests that Manikarna should be considered for plantation in sample locations in respective cluster.

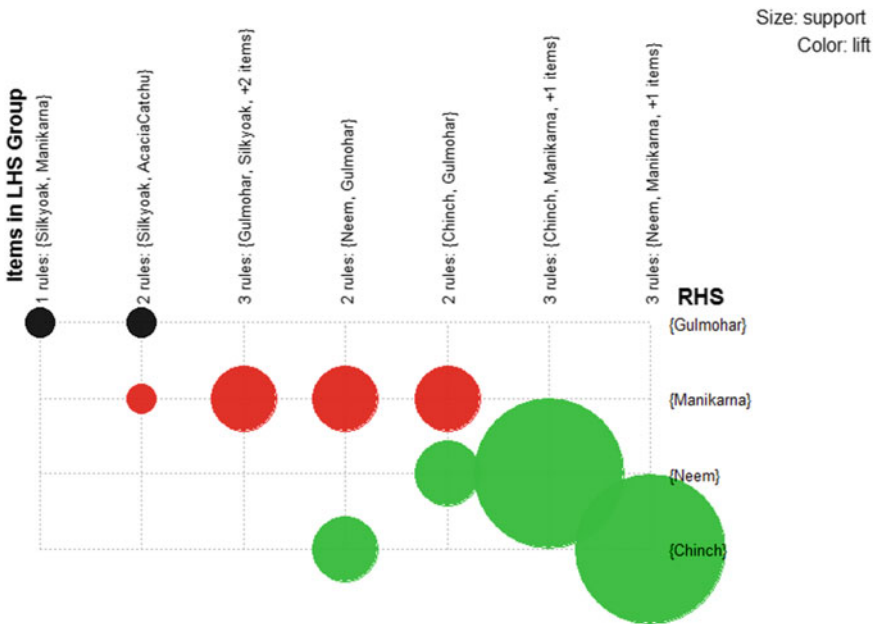


Fig. 4 Grouped matrix for cluster 4 (for 16 rules)

4 Conclusion

In this study, physicochemical analysis of soil sample is performed. This study, reveals the nature of the soil. Initially, correlation analysis is carried out and then principle component analysis operation was performed to identify the major soil parameters. Further, significant soil parameters were selected based on PCA results and expert opinion. Further, K-means cluster analysis was performed and 4 ideal clusters were obtained and soil samples were classified. By k-means clustering method 4 major clusters were obtained with 57.21% of point variability. Further, based on the cluster results the soil samples were classified with their respective cluster and tree species were grouped with respective cluster based on the ideal soil pH. It is observed that, the tree species were classified on the basis of ideal pH for each individual cluster. Association rule mining is used to identify the best possible combination of tree species for each individual clusters. Different support values were tested to generate most meaningful rules. For cluster 1 association rule generated 4 rules. Further, 77 rules were generated for cluster 2. Most meaningful 33 rules were generated for cluster 3. For cluster 4 16 rules were found ideal. For each individual cluster several support values were tested with 95% of confidence value to obtain the significant rule. Top rules were selected on the basis of highest lift values. The obtained rules were represented in scatterplot, grouped matrix form and in graph form. This study will be helpful for designing green infrastructure policies through which new planning strategies can be implemented for ecosystem services for urban area through the required planning process which target the green infrastructure at local and national level.

References

1. Faridi M, Verma S, Mukherjee S (2018) Integration of GIS, spatial data mining, and fuzzy logic for agricultural intelligence Soft computing theories and applications Springer Singapore 171–183
2. Guo Y, Wang M, Li X (2017) Application of an improved apriori algorithm in a mobile e-commerce recommendation system. *Ind Manag Data Syst* 117(2):287–303
3. Hahsler M, Karpienko R (2017) Visualizing association rules in hierarchical groups. *J Bus Econ* 87(3):317–335
4. Kulkarni GE, Muley AA, Deshmukh NK, Bhalchandra PU (2018) Multivariate statistical techniques for prediction of tree and shrub species plantation using soil parameters. *Model Earth Syst Environ* 4(1):281–294
5. Kulkarni GE, Muley AA, Deshmukh NK, Bhalchandra PU (2017) Investigation of noise pollution of Nanded city, Maharashtra case study using GIS and data mining technique. *Int J Future Revol Comput Sci Commun Eng* 3(11):01–06
6. Kulkarni G, Nilesh D, Parag B, Wasnik P, Hambarde K, Tamsekar P, Kamble V, Bahuguna V (2017) Effective use of GIS based spatial pattern technology for urban greenery space planning: a case study for Ganesh Nagar area of Nanded city. In: Deiva SP., Dash S, Das S, Panigrahi B (eds) *Proceedings of 2nd international conference on intelligent computing and applications. Advances in intelligent systems and computing*, vol 467. Springer, Singapore, pp 123–132

7. Kumar S, Toshniwal D (2015) A data mining framework to analyze road accident data. *J Big Data* 2(26):1–18
8. Kumar S, Toshniwal D, Parida M (2017) A comparative analysis of heterogeneity in road accident data using data mining techniques. *Evol Syst* 8(2):147–155
9. Rahman MM, Howladar MF, Faruque MO (2017) Assessment of soil quality for agricultural purposes around the Barapukuria coal mining industrial area, Bangladesh: insights from chemical and multivariate statistical analysis. *Environ Syst Res* 6(1):24
10. Rajeswari V, Arunesh K (2016) Analysing soil data using data mining classification techniques. *Indian J Sci Technol* 9(19):1–4
11. Reale R, Plattner SH, Guida G, Sammartino MP, Visco G (2012) Ancient coins: cluster analysis applied to find a correlation between corrosion process and burial soil characteristics. *Chem Cent J* 6(2):1–9
12. Vázquez HJ, Jaganaru-Mathieu M (2016) Exploring urban tree site planting selection in Mexico city through association rules. In *Proceedings of the 8th international joint conference on knowledge discovery, knowledge engineering and knowledge management*, vol 1, pp 425–430

Behavior of Ammonia Borane as Solid-State Hydrogen Storage Material



Rohan Kalamkar, Vivek Yakkundi, and Aneesh Gangal

Abstract The paper presents the characteristics behavior of Ammonia Borane (NH_3BH_3), which is an encouraging solid-state hydrogen storage material having theoretical 19.6 weight % hydrogen content. Ammonia Borane decomposes thermally between 373 to 473 K temperatures, and the limitations associated with the decomposition is slow kinetics with a warm-up period of 20 min. With the addition of the Silicon nanoparticle approach, the ball milling process was used to enhance the kinetics and suppress the warm-up period during the isothermal decomposition. The isothermal decomposition curve for silicon added ball-milled Ammonia Borane represents an enhancement in hydrogen uptake of about 9 wt % compared to the pure crystalline powder sample of Ammonia Borane. Fourier-transform infrared spectroscopy (FTIR) and Transmission electron microscopy (TEM) spectroscopy techniques validated the hydrogen released characteristics from the Ammonia Borane.

Keywords Hydrogen energy · Solid-state storage · Volumetric technique · Thermolysis

1 Introduction

The traditional forms of energy are depleted rapidly, and the combustion of fossil fuels disturbs the ecosystem's balance. Alternatives are taking the gap care for sustainable and continuous fuel supply in renewable energy to these fossil fuels. Among the different options, Hydrogen energy can be used as the future energy carrier for onboard and mobile applications. The hydrogen storage medium becomes impractically large is the most critical issue in developing hydrogen-based fuel systems. The

R. Kalamkar (✉)
Gharda Institute of Technology, Lavel, India

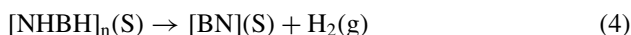
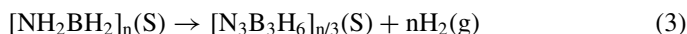
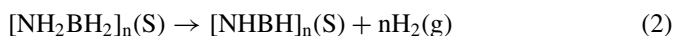
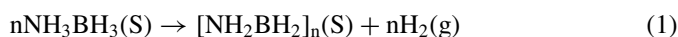
V. Yakkundi
Lokmanya Tilak College of Engineering, Koperkhairane, India

A. Gangal
SSPM's College of Engineering, Kankavalil, India

hydrogen storage system must have high gravimetric/ volumetric energy density to replace the conventional fuel system. Hydrogen has a 90 gm/m³ density with molecular weight 2.016 and has the best energy to weight ratio with an average heating value of hydrogen is 120 MJ per kg of H₂ [1, 2]. Hydrogen plays a significant role in lowering CO₂ emissions. The high pressure compressed hydrogen storage has issues concerning the tank's safety, and liquid storage suffers boil-off losses. Hydrogen storage in solid materials offers the potential for safe and efficient hydrogen storage. However, both these issues are addressed in solid-state hydrogen storage, where hydrogen combines either physically or chemically with some materials [3]. The research paper focuses on solid-state hydrogen storage powder material that can release hydrogen through the thermal decomposition route. The Ammonia Borane material (chemical hydride) is used for the research work to study the limitations associated with the dehydrogenation. The research study also proposes the ball milling process followed by a silicon metal doping to improve Ammonia borane's effectiveness by reducing decomposition temperature and enhancing hydrogen uptake.

2 Materials

Ammonia Borane (NH₃BH₃) is a fine powder material safely transported without hydrogen loss. NH₃BH₃ contains 19.6 wt% of hydrogen, and decomposes through thermal route in 100 and 120 °C temperature range to yield [NH₂BH₂]_n and it converts in [NHBH]_n between 120 to 200 °C and finally borazine [N₃B₃H₆] by releasing hydrogen in every step [4]. The decomposition of [NHBH]_n to BN occurs at temperatures over 500 °C as such, and this final step is not considered for practical applications for hydrogen storage, reaction [5, 6].



The issues with Ammonia Borane are high decomposition temperature, slow kinetics, and unwanted gaseous species formed during decomposition. The ball milling process and doping with a Silicon metal catalyst approach are used to suppress the warm-up period and lower the decomposition temperature. According to the literature survey, silicon can be used as a catalyst, and silicon metal has the capability of chemisorbing hydrogen. From the literature study, the silicon doping approach is

proposed in the decomposition of Ammonia Borane as it may pull out hydrogen from the NH_3BH_3 molecules. The Ammonia Borane and Silicon materials are procured from Sigma Aldrich.

3 Methods

The volumetric method is based on pressure measurement during hydrogenation and dehydrogenation to estimate the number of moles of hydrogen using van der Waals equation. Knowing the volume and temperature of the gas, the pressure change can be related to the number of moles of hydrogen with the van der Waals equation [7]. The Sievert's apparatus in Fig. 1 consists of a standard cell, a reactor, needle valves, and tubes made of stainless steel material. Tubing and tube fittings were purchased from Swagelok Inc. and were made of SS316 or SS316L grade stainless steel. They can withstand pressure up to 100 bar and can work in a reactive atmosphere. A pressure transmitter is used to measure hydrogen gas pressure from vacuum to 20 bar with an accuracy of 0.1% of full scale. The band heater temperature was controlled using a temperature controller device. The high vacuum system consists of a rotary pump and a diffusion pump and can maintain a vacuum of 10^{-3} mbar. The standard cell and reactor were designed to withstand 100 bar pressure represented in Fig. 1.

The thermal decomposition of ammonia borane is studied at isothermal and non-isothermal conditions. Characterization of NH_3BH_3 and the decomposition products was carried out using various techniques like FTIR and TEM. The decomposition of NH_3BH_3 is studied in the presence of a silicon metal catalyst. Initially, the sample material is weighed using a microbalance. The sample amount is taken approximately 500 mg. This sample is then kept in the sample holder, and the system is

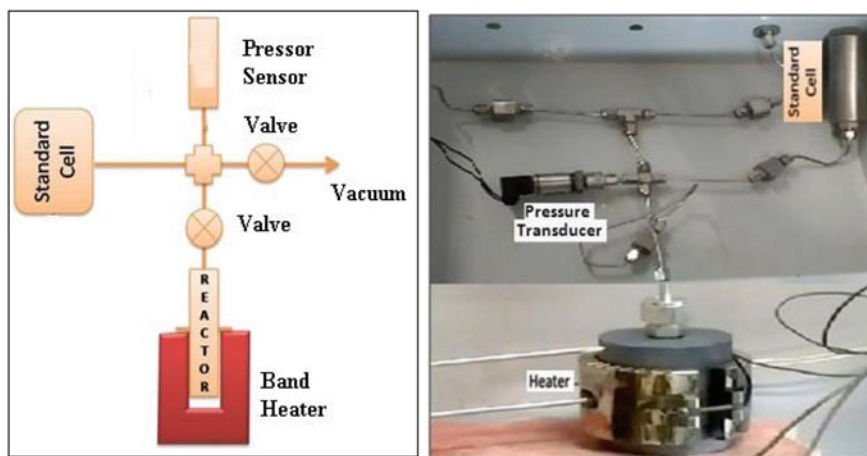


Fig. 1 Block diagram and Photograph of Sievert's type experimental setup

evacuated (vacuum) at 10^{-3} mbar before the actual test. The heater is switched on by setting the target temperature at which the decomposition is to be studied. As the heater attains the desired temperature sample cell is placed in the heater. As sample decomposes, hydrogen gas starts releasing from the NH_3BH_3 material. This released gas is then accumulated in the system causes increases in the system pressure until the equilibrium phase. The number of moles of hydrogen can be estimated using the van der Waals equation from the pressure and temperature reading data.

4 Result and Discussion

Isothermal decomposition of Ammonia Borane is studied in a Sievert's type apparatus. The apparatus involves volumetric measurement, and thus the gaseous products of decomposition remain in the device. In Fig. 2, the temperature of decomposition increases, the amount of gas released increases gradually. In the decomposition curve, Fig. 2 indicates a warm-up period of about 20 min. The warm-up period is the activation time required by the sample before the reaction [8]. During the warm-up period no gas released was observed. The second region is the acceleratory region in Fig. 2, where the rapid gas release was observed. The third region in Fig. 2 is when the reaction decelerates, making the curve flat. The amount of gas released in pure Ammonia Borane crystalline powder was found to be about 5 wt% at 473 K. The curve in Fig. 2 shows the presence of two plateaus for NH_3BH_3 sample material [9]. At a fixed temperature, initially, the release of hydrogen is fast, and after that, it slows down and takes time to reach equilibrium. The hydrogen helps in the passivation of silicon defects and improves its storage behavior [10]. The samples were prepared by mixing NH_3BH_3 and Si nanoparticles in a 10:1 ratio in a Fritsch pulverisette-6 ball mill. The homogeneous mixture was obtained by milling for one hour with a milling cycle of 10 min steps. Thermal decomposition was studied under isothermal conditions as well as transient temperature conditions [11].

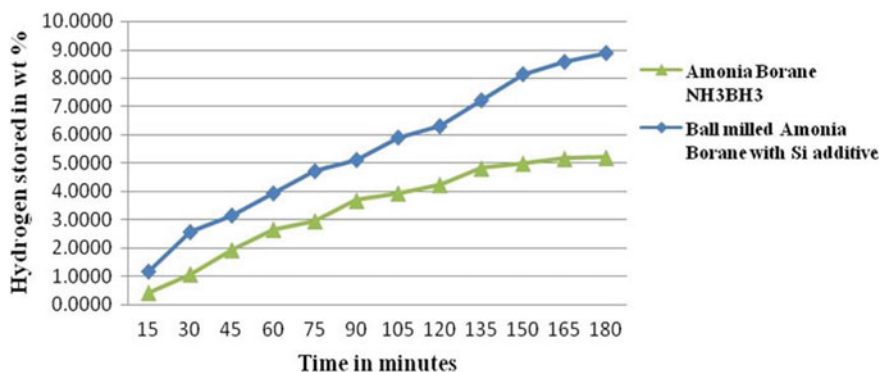


Fig. 2 Dehydrogenation data of Ammonia Borane with Si additive

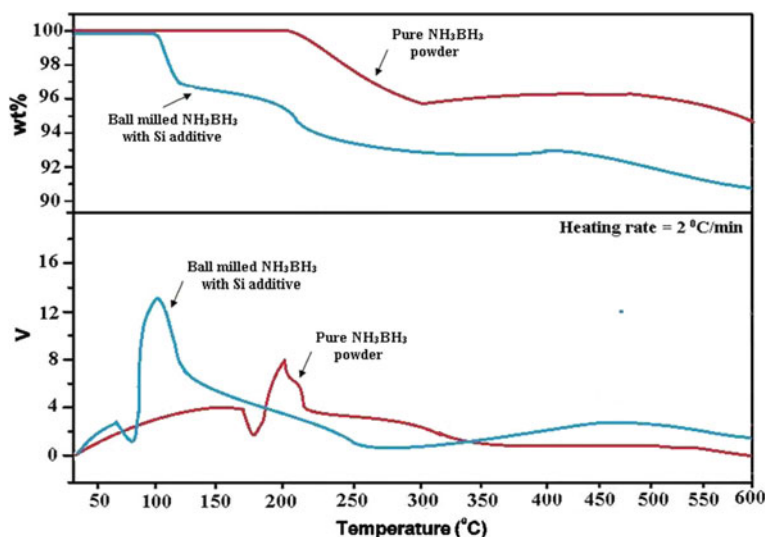


Fig. 3 TG-DTA study of Ammonia Borane samples

The Fig. 3 indicates TG-DTA study of Ammonia Borane sample to find out the decomposition temperature. The decomposition of Si added milled Ammonia Borane sample was initiated immediately as the heating started. The reaction is observed endothermic for Si added milled Ammonia Borane sample [12]. The amount of gas released in Silicon added ball-milled Ammonia Borane is found to be about 9 wt% at 373 K in Fig. 2. In short, it is observed that silicon doping assist in improving the decomposition behavior of Ammonia Borane which can be also verified from TG-DTA study. Silicon's decomposition temperature added ball-milled Ammonia Borane is lessening to 373 K compared to crystalline Ammonia Borane powder. Ball milling of Ammonia Borane with silicon nanoparticles not only results in a reduction of induction period but also enhances the amount of hydrogen released [13]. The warm-up period is observed negligible in the Silicon added ball-milled Ammonia Borane isothermal decomposition test, and wt% of released hydrogen is improved to 9 wt%. The isothermal decomposition of the Ammonia Borane study shows that kinetics and dehydrogenation behavior is improved on the addition of Silicon catalysts. The amount of gas released was reported 9 wt% from Fig. 2 for the Silicon added ball-milled Ammonia Borane. The noted gas released is significantly within the range of the amount of hydrogen present in Ammonia Borane, i.e., 19.6 wt% theoretical value. The decomposition curve at 373 K for from Silicon added ball-milled Ammonia Borane indicates zero warm-up periods. The suppression of warm-up period in the isothermal decomposition reaction of silicon added ball-milled ammonia Borane is a desirable phenomenon from an application point of view. Silicon added ball-milled Ammonia Borane shows faster gas release than pure crystalline powder Ammonia Borane samples initially up to about 120 min. The decomposition curve is seen to stabilize after 120 min, releasing 5 wt% of hydrogen

uptake for pure crystalline powder Ammonia Borane sample and 9 wt% of hydrogen released in Silicon's case ball-milled Ammonia Borane for 180 min.

5 Validation

The FTIR transmittance spectrum recorded using a Jasco FT/IR-6100A system [14]. In Transmission Electron Microscopy, an electron beam focused on the samples using the condenser lens system and magnified image and the X-ray produced through interaction were analyzed for evaluating the elemental composition [14]. The spectroscopy tests were performed at SAIF, IIT Bombay. Figure 4 shows an FTIR transmittance spectrum of pure Ammonia Borane crystalline powder before decomposition, FTIR transmittance spectrum of the solid residue of ball milled Ammonia Borane and Silicon added ball-milled Ammonia Borane after isothermal decomposition. The frequency bands of 500 to 3500 cm^{-1} are assigned to N–H, N–H₂ and N–H₃ stretch.

Figure 4 the transmittance spectra of ammonia borane before and after isothermal decomposition tests with additive silicon depicted that the frequencies are greatly affected, i.e., shrinking was observed transmittance intensities, 781 cm^{-1} , 1375 cm^{-1} , 2216 cm^{-1} , and 3323 cm^{-1} that reflects evolved hydrogen. As the decomposition temperature increases from 373 to 473 K, N–H, and B–H bands get minimize. FTIR spectra Fig. 4 of solid residue after tests do not show any bands corresponding to Silicon-H, which designate silicon additive do not take part in reactions. The

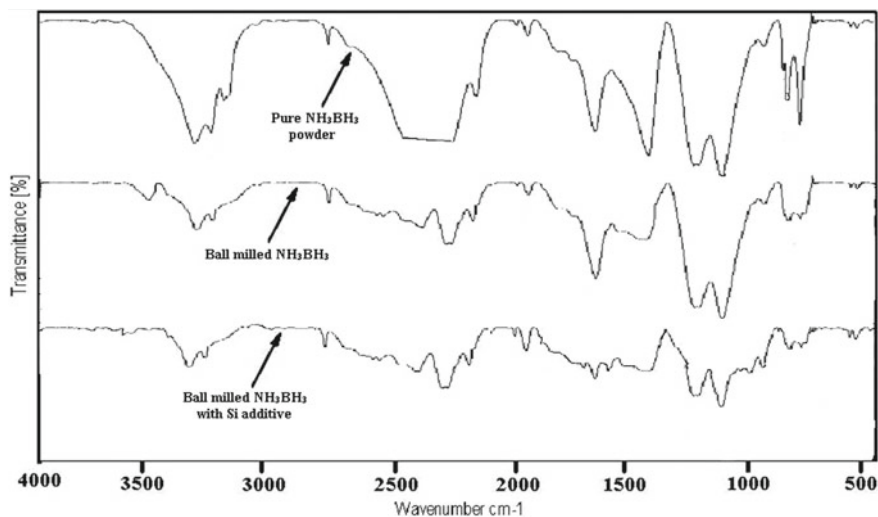


Fig. 4 FTIR of pure crystalline NH_3BH_3 powder and Si added ball milled NH_3BH_3 powder after isothermal decomposition

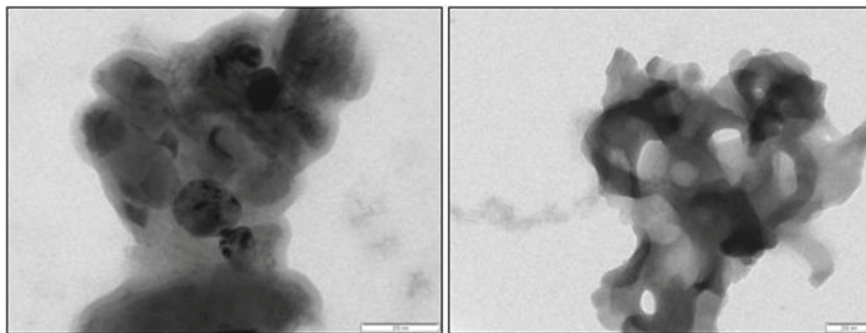


Fig. 5 TEM of NH_3BH_3 before and after isothermal decomposition

outcomes reported in Fig. 4 after the milling process of silicon added ammonia borane suggest that rapid decomposing occurs with a reduction in decomposition temperature by an amount of 100 K. These reported results matched with total suppression of a warm-up period in the dehydrogenation of Silicon-added ball-milled ammonia borane [2]. FTIR graphs don't show any transmittance peaks corresponding to silicon that designated silicon additive doesn't take part in the reaction but increase reaction [15]. Figure 5 shows TEM images of Ammonia borane sample materials before and after isothermal decomposition. TEM images before and after hydrogenation Fig. 5 indicates the depletion in the severity of pitch-black mark areas that describes hydrogen uptake during isothermal decomposition reaction. TEM figure of ball-milled ammonia borane with silicon catalysts reflecting rapid hydrogen released [16].

6 Conclusion

The pure Ammonia Borane decomposes thermally at 473 K temperature releases 5 wt% of hydrogen, and the limitations associated with it are slow kinetics with an observed warm-up period of 20 min. The non-isothermal decomposition study with the help of a TG-DTA system determines the decomposition temperature range 373 K to 473 K. In isothermal experiments, gaseous products of decomposition remain in the closed experimental system, unlike TG-DTA that supports chain branching or polymerization and suppressed the possibility of forming unwanted cyclic products of B:N:H compositions. In isothermal decomposition, initially, the release of hydrogen is fast up to 120 min, and after that, it slows down to reach equilibrium phase 180 min. The ball milling process of crystalline powder provides a wide surface to volume ratio that helps in the specimen's rapid activation. Due to silicon catalyst hydrogen's high porosity, hydrogen is readily chemisorbed on Si dangling bonds by breaking N-H and B-H bonds in Ammonia Borane. The breaking process of N-H and B-H bonds in NH_3BH_3 is because of the destabilizing effect of silicon doping, diminishing the decomposition temperature up to 100 K. Ball milled Ammonia Borane with

Silicon nanoparticles' addition describe hydrogen uptake of 9 wt% at 373 K with zero warm-up periods. The weight-loss event in TG–DTA for Si added ball-milled NH_3BH_3 sample is noted just after the melting of the sample confirms the warm-up period's suppression. The passiveness during hydrogenation in additives' surface increases desorption, reflecting in the shrinking edges of the transmittance spectra in FTIR. TEM outcomes are similar to observed investigational solutions that indicate demeaning in dense microstructure due to hydrogen released after decomposition. It can be noticed that the ball milling of NH_3BH_3 crystalline powder with silicon additive suppresses the induction period and enhances hydrogen release.

References

1. Manoharan Y, Hosseini S, Butler B (2019) Review: hydrogen fuel cell vehicles; current status and future prospect. *Appl Sci* 9(11):2296
2. Abe JO, Popoola API, Ajenifujii E (2019) Hydrogen energy, economy and storage: review and recommendation. *Int J Hydrogen Energy* 44(29):15072–15086
3. Gangal A, Sharma P (2013) Kinetic analysis and modeling of thermal decomposition of Ammonia Borane. *Int J Chem Kinet* 45:2–61
4. Zhitao X, Chaw KY, Guotao W, Ping C, Wendy S, Karmarkar A, Thomas A, Martin OJ, Simon RJ, Peter PE, William IFD (2018) High-Capacity hydrogen storage in lithium and Sodium Amidoboranes. *Nat Mater* 7:138–141
5. Frueh S, Kellett R, Mallery C, Molter T, Willis WS, King'ondeu C, Suib S L, (2011) Pyrolytic decomposition of Ammonia Borane to Boron Nitride. *Inorg Chem* 50:783–792
6. Shore SG, Parry RW (1955) The crystalline compound Ammonia Borane, $\text{1H}_3\text{NBH}_3$. *J Am Chem Soc* 77:6084–6085
7. Gangal A, Kale P, Edla R, Manna J, Sharma P (2012) Study of kinetics and thermal decomposition of ammonia borane in presence of silicon nanoparticles. *Int J Hydrogen Energy* 37(8):6741–6748
8. Aneesh C (2013) Gangal (2013) Ammonia Borane as Hydrogen Storage Material. Thesis, Department of Energy Science and Engineering, IIT Bombay
9. Rosalind D (2016) Lithium Amide Halides for Hydrogen Storage, Thesis, Centre for Hydrogen and Fuel Cell Research, School of Chemical Engineering, University of Birmingham (2016).
10. Kalamkar R, Gangal A, Yakkundi V (2017) Development of experimental setup for measurement of stored hydrogen in solids by volumetric method. In: Pawar P, Ronge B, Balasubramaniam R, Seshabhatter S (eds) *Techno-Societal 2016*. ICATSA 2016. Springer, Cham. 569–577
11. Gangal AC, Edla R et al (2015) Effect of mixed metal nanoparticles on thermal decomposition of Ammonia Borane, *J Res Nanotechnol*
12. Bor-Yih Yu (2013) Introduction to Aspen Plus, PSE Laboratory, Department of Chemical Engineering, National Taiwan University
13. Kalamkar R, Gangal A, Yakkundi V (2018) Hydrogen storage characteristics of mixture of Lithium Amide and Lithium Hydride using Severt's type apparatus. In: Pawar P et al (eds), *Techno-Societal 2018*, Springer, Cham
14. Kalamkar R, Gangal A, Yakkundi V (2020) Fabrication and analysis of apparatus for measuring stored renewable hydrogen energy in metal hydrides. RAM 2020. SVNIT, Gujarat
15. Edla R, Gangal A (2014) Kinetics and the thermal decomposition of Sodium Alanate in the presence of $\text{MmNi}_4.5\text{Al}_{0.5}$ nanoparticles. *Material Research Express*. IOP Science
16. Zulkarnain Jalil and Adi Rahwanto (2018) The use of nano-silicon carbide and nickel as catalyst in magnesium hydrides (MgH_2) for hydrogen storage material application. *Materials Research Express*. 5. IOP Science (2018)

Morphometric Analysis of Lendi River Basin Using Geographical Information System (GIS) Techniques



Gurav Chandrakant and Md. Babar

Abstract Present study is focusing on morphometric analysis of Lendi river a tributary stream of Manjra river in central Maharashtra. The main aims of this study are to understand the hydrological and morphological characteristics of Lendi river. For this, Remote sensing and Geographical Information System (GIS) techniques are used. Geologically, nearly 81.68% area of the basin is covered by Deccan Volcanic Basaltic (DVB) of late Cretaceous to early Eocene age and remaining 18.31% area covered by Peninsular Gneissic Complex (PGC) of Precambrian age. For present research, linear, areal and relief morphometric parameters are used. Based on these, found that basin is moderately elongated in shape. High drainage density and stream frequency indicates an area is impermeable in nature of lithology. Similarly, bifurcation ratio also shows drainages are geologically stable condition. The relief of the area is pointing towards moderate to gentle sloping surface in the basin.

Keywords Deccan basalt · Granite · Lendi river · Morphometry

1 Introduction

Drainage morphometry was first introduced by Horton [1]. It is important for understanding the underlain lithological structures, geomorphological formations, hydrological characteristics [2], soil types, and vegetation status [3] of any basin. The origin and development of drainage system depend upon three factors viz., underlain geology, endogenetic and exogenetic forces operating in the area [4]. The drainage morphometry give information about the hydrological and rock formation characteristics of the basin [5]. Morphometry is the measurement and mathematical analysis of the configuration of the earth's surface, shape and dimension of its landforms [6, 7]. Now days, Geographical Information System (GIS) techniques are used for study the morphometric parameters of the drainage basins, hydrogeology and tectonic study

G. Chandrakant (✉)

CTMD, CSIR-NEERI, Nagpur 440020, Maharashtra, India

Md. Babar

Department of Geology, Dnyanopasak College, Parbhani 431401, Maharashtra, India

© The Author(s), under exclusive license to Springer Nature Switzerland AG 2021

P. M. Pawar et al. (eds.), *Techno-Societal 2020*,

https://doi.org/10.1007/978-3-030-69925-3_4

37

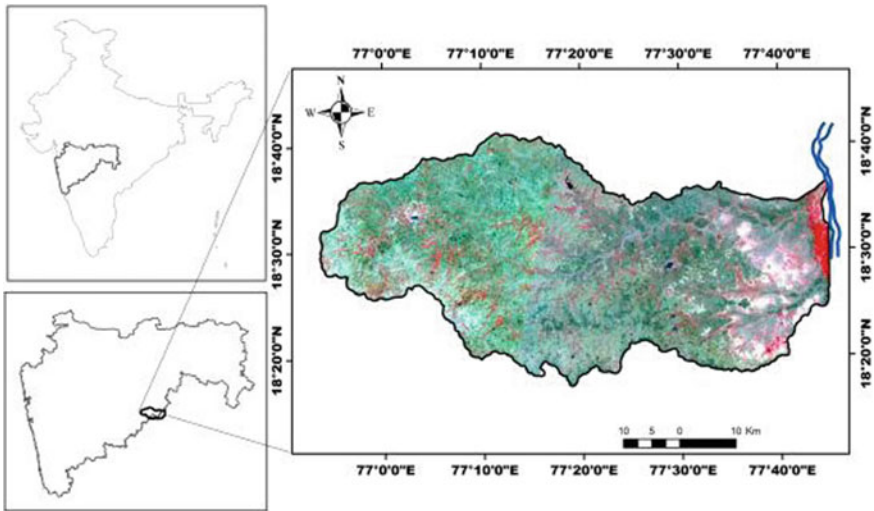


Fig. 1 Location map of the study area

[8–11]. The main objective of the present research is to study the hydrological and morphological characteristics of the Lendi river using GIS techniques. The present study area was previously studied for groundwater potential zone analysis using geology and geomorphology [12], NE-SW Strike-Slip faults evidences first reported in Granitoid zone [13] and Lendi river watersheds used for hydrogeomorphological study [8, 9].

2 Study Area

Lendi river, a tributary of Manjra river originates in Balaghat hill range on eastern slope. It confluence with Manjra river near Tamlur village in Degloor/Diglur tehsil in Nanded district of Maharashtra. The area is bounded by latitude $18^{\circ}17'20''\text{N}$ to $18^{\circ}41'26''\text{N}$ of longitude $76^{\circ}53'23''\text{E}$ to $77^{\circ}45'9''\text{E}$ covering an area of about 2536.3 sq km (Fig. 1). Climate of the area is semi-arid and receives rainfall primarily from sw monsoon between June to September.

3 Geology of the Area

Lendi river drains over three geological formations, viz., Deccan volcanic Basalt (DVB) of late Cretaceous to early Eocene age formation covers west and central part while Peninsular Gneissic Complex (PGC) Archaean–Palaeoproterozoic formation



Fig. 2 Geology formations in the study area. **a** Basaltic near Sangavi Badev village and **b** granitic formation near Degloor village

consists of granite and granite gneisses is on eastern part of the basin. The DVB covers 81.68% and PGC is 18.31% of the whole Lendi river basin (Fig. 4). The third formation is Quaternary sediments occurring along the main river and its tributary streams. It consists of fluvial sediments of sub-rounded gravels, pebbles, sand and silts of basalt and granitic rock fragments formed during early Quaternary to Holocene periods [13–15] (Fig. 2).

4 Methodology

Present research is carried using ArcGIS 10.3 software in the laboratory. Onscreen digitization process is used for this study. For morphometric study, Survey of India (SOI) topographic maps 56 B/14, 56 B/15, 56 F/3, 56 F/6, 56 F/7, 56 F/10, 56 F/11 and 56 F/14 on scale 1:50,000 were used for preparation of location map (Fig. 1) and drainage map (Fig. 4). The morphometric parameters such as linear, areal and relief are listed in Table 1 and formulas for their calculation are also represented in Table 1. As a first step the numbers of streams are counted as per the system of Strahler [16], and the data is presented in Table 1. In this method the smallest unbranched headwater stream is considered as a first order stream. The confluence of two first order streams is called the second order stream. Similarly, two second order streams unite to form the third order stream and so on. The lengths of each order are computed to get the total lengths of streams of the basin (L_u). The area of basin (A) is the total area that is covered by the drainage basin boundary. Basin perimeter (P) is the entire length of the basin boundary. Bifurcation ratio (R_b) is the ratio of the number of streams of any given stream order (N_u) to the number of streams in the next higher order ($N_u + 1$) as given Table 1. The elongation ratio is the ratio of diameter of a circle having same

Table 1 Morphometric analysis of Lendi river basin

Linear morphometric parameters					Areal morphometric analysis			
u	Nu	Rb	Lu	MSL	Pts	Ref	Formula	Values
01	4437		2638.0	0.60	A	–	–	2532.3
						P	–	–
02	1052		1035.9	0.98	Lb	–	–	90.59
						Dd	[1]	Lu/A
03	244		532.07	2.18	Fs	[21]	Nu/A	2.29
						Rt	[24]	Nu/P
04	55		292.31	5.32	Rf	[1]	A/Lb ²	0.31
						Rc	[17]	4πA/P ²
05	12		107.86	8.99	C	[18]	1/Dd	0.53
						Re	[16]	(2√A:√π)/Lb
06	05		113.56	22.71	Rb	[20]	Nu/Nu+1	
						Relief morphometric analysis		
07	01		63.85	63.85	HE	–	–	688 m
Sum	5806		4783.6	104.6	LE	–	–	343 m
Avg		4.16			H	[23]	HE–LE	345 m
					Rn	[22]	H*Dd	0.652

where, Pts—parameters, u—stream order, Nu—number of streams, Rb—bifurcation ratio, Lu—length of streams in km, MSL—mean stream length in km, A—area in sq km, P—perimeter in km, Dd—drainage density in km/km², Fs—stream frequency in streams/km², Rt—texture ratio in km⁻¹, Rc—circulatory ratio, Lb—basin length in km, Re—basin elongation ratio, Rf—form factor ratio, HE—highest elevation in m, LE—lowest elevation in m, H—basin relief in m, Rn—ruggedness number, Ref.—references and π = 3.14

area as the basin to the maximum length (Lb) of the basin [16]. It is calculated using formula is $Re = (2\sqrt{A}:\sqrt{\pi})/Lb$ (Table 1). The circularity ratio (Rc) is a numerical manifestation of the shape of the basin, which is represented by the ratio of basin area (A) to the area of circle, having the same perimeter (P) as the basin and given by formula $Rc = 4\pi A/P^2$ [17]. Drainage Density (Dd) is expressed as the ratio of the total stream lengths (Lu) of all orders in a basin to the total area of the basin (A). The stream frequency (Fs) is defined as the ratio of the total number of streams (Nu) in a basin to the total basin area (A). Drainage texture is calculated as the ratio of total number of streams of all orders with the basin perimeter (P). Form Factor (Rf) of a drainage basin is stated as the ratio amongst the area of the basin (A) and the square of the basin length (Lb). The parameter constant of channel maintenance (C) is the inverse of drainage density (Dd) [18]. Ruggedness number is the product of basin relief (H) with the drainage density (Dd). All these formulae and values as given in Table 1. The Shatter Radar Topographic Mission (SRTM) map downloaded from United States Geological Survey (USGS) used to calculate the relief of the area.

5 Result and Discussions

5.1 Linear Morphometric Analysis

In this study, stream order, number of stream, stream length and bifurcation ratio are calculated and semi-log graphs are prepared using the Table 1.

5.1.1 Stream Order (u)

The first step in morphometric analysis is ordering of streams. The highest order of Lendi river is found to be seventh order (Table 1).

5.1.2 Number of Stream (Nu)

It is number of streams present in each order. The first order streams are more in mountainous regions, whereas it is less developed in alluvial plain or pediplain areas of the basins [19]. Whole Lendi river basin has 5806 streams, of which 76.42% are the first order streams having 4437 segments. The second order streams are 1052 and accounted for 18.12%, third order stream are 244 and accounted for 4.20%, fourth order stream are 55 and accounted for 0.95%, fifth order stream are 12 and accounted for 0.21%, sixth order stream are 05 and accounted for 0.09%, seventh order stream is 01 and accounted for 0.02% (Table 1).

5.1.3 Stream Length (Lu)

The stream length is total length of each stream segment of each order. Stream length of any order depends on the relief of the area, slope and nature of rock formations [19]. In present study, total length of all orders of Lendi river basin is 4783.6 km of which 55.15% is the length of first order streams i.e. 2638.0 km. The second order streams length is 1035.9 km and accounted for 21.66%, third order stream length is 532.07 and accounted for 11.12%, fourth order stream length is 292.31 km and accounted for 6.11%, fifth order stream length is 107.86 km and accounted for 2.26%, sixth order stream length is 113.56 km and accounted for 2.37%, seventh order stream length is 63.85 km and accounted for 1.34% (Table 1).

5.1.4 Bifurcation Ratio (Rb)

The bifurcation ratio shows small range of variation for different regions or for different environment, if it is greater than 5 indicates structurally controlled drainage network, up to 2 for flat or rolling drainage basins, up to 3 or 4 for mountainous or

highly dissected drainage basins [20]. In the Lendi river basin Rb ranges from 2.40 to 5.00, an average is 4.16 (Table 1).

5.1.5 Semi-log Graph of Lendi River Basin

The relation of number of streams against stream order in the Lendi river basin (Fig. 3a) shows inverse geometric sequence by decreasing systematically with increasing order and conforms to the Horton’s [20] law of stream numbers. Lendi river basin has shown the negative correlation between stream number and stream order. The semi log plot of total lengths of stream of each order against stream orders (Fig. 3b) displays inverse geometric sequence for the area. This also conform the Horton’s [20] law of stream length. It is observed that the length of fifth order is slightly deviating from the regression trend line. The semi log plot of mean stream lengths is in direct geometric progression to stream orders (Fig. 3c). This plot conform the Horton’s [20] law of stream length. The mean stream length drawn against the streams order reflects the straight line trend.

5.2 Areal Morphometric Analysis

The areal aspects of the Lendi river basin are determined by using drainage density (Dd), stream frequency (Fs), drainage texture ratio (Rt), circulatory ratio (Rc), form factor ratio (Rf), constant of channel maintenance (C) and basin elongation ratio (Re).

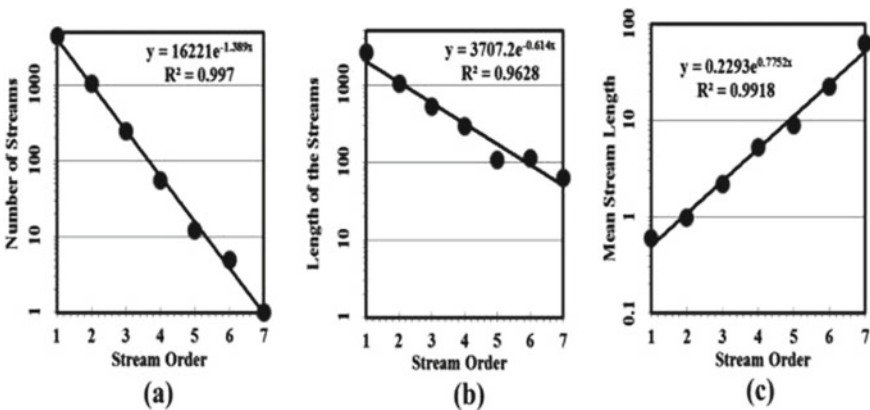


Fig. 3 Semi-log graphical representation of Lendi river basin. Graph (a) is stream order against number of streams, graph (b) is stream order against length of the streams and graph (c) stream order against mean stream length

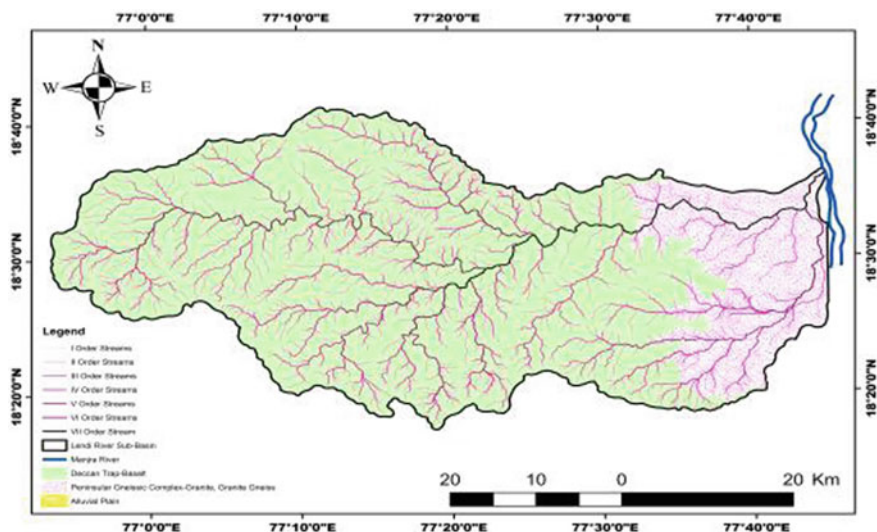


Fig. 4 Geology and drainage map of study area

5.2.1 Drainage Density (Dd)

It is the good indicator of knowing how much close the spacing between the channels, thus determines the time of travel by water [1]. It is calculated using the equation in Table 1. The value of drainage density of Lendi river basin is 1.89 km/km^2 in Table 1. Low drainage density occurs due to coarse drainage texture while high drainage density occurs due to fine drainage texture [16].

5.2.2 Stream Frequency (Fs)

The stream frequency is described as ‘the ratio of total number of stream segments of all orders to the total basin area’ [20]. It is calculated using the equation in Table 1 [21]. The stream frequency value of the Lendi river basin is $2.29 \text{ streams/km}^2$.

5.2.3 Texture Ratio (Rt)

Texture ratio is influence by underlying lithology, infiltration capacity and relief aspect of the terrain [21]. Smith [21] classified Rt ratio into five different textures from very course to very fine i.e. very course (<2), course (2–4), moderate (4–6), fine (6–8), and very fine (>8). It is calculated using the equation in Table 1. In the present study, texture ratio of the Lendi river basin is 21.54 km^{-1} , which indicates very fine texture and area under moderate relief (Fig. 4).

5.2.4 Circulatory Ratio (Rc)

It is influenced by the length, frequency and gradient of stream of various orders than slope conditions and drainage pattern of the basins [22]. It is calculated using the equation in Table 1 [1]. Circulatory ratio of Lendi river basin is 0.44, which is below 0.5 shows moderately elongated basin with semi permeable homogeneous lithology.

5.2.5 Form Factor Ratio (Rf)

Form factor ratio is the dimensionless ratio of the basin area to the square of basin length [1]. It is calculated using the equation in Table 1. The Rf value of the Lendi river basin is 0.31, which represents semi (moderately) elongated in shape.

5.2.6 Constant of Channel Maintenance (C)

The higher the drainage density lowers the constant of channel maintenance and vice versa [18]. It is calculated using the equation in Table 1. Regarding the Lendi river basin, the average constant of channel maintenance is 0.53 km²/km.

5.2.7 Elongation Ratio (Re)

Elongation ratio (Re) describes the shape of the basin quantitatively. It provides indirect information about the degree of maturity of the basin landscape. Schumm [18] defined 'it is the ratio between the diameter of a circle of the same area as the drainage basin and the maximum length of the basin'. The Re values are classified into three categories viz. circular (>0.9), oval (0.9–0.8), and elongated (<0.7) [15]. It is calculated using the equation in Table 1 [16]. The value of Re obtained from Lendi river basin is 0.63, indicates semi-elongated and slightly active basin.

5.3 Relief Morphometric Analysis

The relief parameters of the Lendi river basin are determined by using basin relief and ruggedness number.

5.3.1 Basin Relief (H)

Relief of the basin is vertical distance difference between point of maximum elevation and minimum elevation is the relief of basin. It is calculated using the equation in Table 1 [23]. The value of basin relief of Lendi river obtained is 345 m (Table 1).

5.3.2 Ruggedness Number (Rn)

Ruggedness number is the product of relief of basin (H) and drainage density (Dd). It is calculated using the equation in Table 1. The ruggedness number of Lendi river is 0.652 (Table 1) which indicates both relief and drainage density are moderate values. Moderate values are expected in a moderate to gently sloping region of tropical and sub-tropical climate with moderate rainfall [18].

6 Conclusion

GIS techniques are fast and give most acceptable morphometric characteristics results of Lendi river basin. The drainage density value of Lendi river is 1.89 km/km² and stream frequency value is 2.29 streams/km² point towards impermeable lithology and moderate to gently sloping area. The bifurcation ratio (Rb) ranges from 2.40 to 5.00, an average is 4.16 is the indicator of no strong structural in the study area. The values of form factor 0.31, circularity ratio 0.44 and basin elongation ratio 0.63 of the Lendi river basin indicates basin is moderately elongated in shape. The drainage texture ratio (Rt) of Lendi river is 21.6 km⁻¹ indicates the very fine drainage texture. The results can be used for sufficient hydrological and morphological planning in Lendi and adjoining area.

References

1. Horton RE (1932) Drainage basin characteristics. *Trans Am Geophy Union* 13:350–361
2. Morisawa M (1985) *Rivers-forms and process*. Longman Group, London
3. Jasmin I, Mallikarjuna P (2013) Morphometric analysis of Araniar river basin using remote sensing and geographical information system in the assessment of groundwater potential. *Arab J Geosci* 6:3683–3692
4. Reddy GPO, Maji AK, Gajbbiye KS (2004) Drainage morphometry and its influence on land-form characteristics in a basaltic terrain, Central India—a remote sensing and GIS approach. *Int J Appl Earth Observ Geoinf* 6(1):1–16
5. Singh P, Thakur JK, Singh UC (2013) Morphometric analysis of Morar River Basin, Madhya Pradesh, India, using remote sensing and GIS techniques. *Environ Earth Sci* 68(7):1967–1977
6. Agarwal CS (1998) Study of drainage pattern through aerial data in Naugarh area of Varanasi district U.P. *J Indian Soc Rem Sens* 26:169–175
7. Obi Reddy GP, Maji AK, Gajbbiye KS (2002) GIS for morphometric analysis of drainage basins. *Geol Surv India* 11:9–14
8. Chandrakant G, Babar Md (2016) GIS based hydrogeomorphological analysis of Tiru river sub-basin of Lendi river, Maharashtra, India. First Indian National Groundwater conference on sustainable development and management of groundwater resources in Arid and Semiarid regions. JNTU, Hyderabad, pp 90–100
9. Gurav C, Babar Md (2019) Hydro-geomorphological studies for groundwater potential of Mangyal nala watershed of Lendi river, Nanded district, Maharashtra *J Geosci Res* 2:61–66. Gondwana Geological Society, Nagpur

10. Chandrakant G, Babar Md, Ajaykumar A (2019) Morphometric analysis of Yelganga–Shiv-bhadra–Kohilla river basins in Aurangabad district Maharashtra India-using GIS techniques. *IJRAR* 6(1):250–257
11. Mahala A (2019) The significance of morphometric analysis to understand the hydrological and morphological characteristics in two different morpho-climatic settings. *Appl Water Sci* 10(1). <https://doi.org/10.1007/s13201-019-1118-2>.
12. Babar Md, Gurav C (2014). Influence of geological and geomorphological characteristics on groundwater potential in Lendi river sub-basin of Manjra river, Maharashtra, India. In: 4th ICHWAM, pp 103–109
13. Babar Md, Kaplay RD, Mukherjee S, Mahato S, Gurav C (2018) NE-SW strike-slip fault in the Granitoid from the margin of the South East Dharwar Craton, Degloor, Nanded district, Maharashtra India. In: Springer Geology, pp 115–134. https://doi.org/10.1007/978-3-319-99341-6_5
14. Madhnure P (2014) Groundwater exploration and drilling problems encountered in basaltic and Granitic terrain of Nanded district, Maharashtra. *J Geol Soc India* 84:341–351
15. Kaplay RD, Babar Md, Soumyajit M, Vijay Kumar T (2017) Morphotectonic expressions of geological structures in the eastern part of South East Deccan Volcanic province (around Nanded, Maharashtra, India). *Tectonics of the Deccan large Igneous province*. Geological society, London, Special publication, p 445
16. Strahler AN (1964) Quantitative geomorphology of drainage basin and channel network, handbook of applied hydrology
17. Schumm SA (1954) The relation of drainage basin relief to sediment loss, Pub. International association of hydrology, IUGG, Tenth gen. Assembly, Rose, 1, pp 216–219
18. Schumm SA (1956) Evolution of drainage system and slope in Badlands at Perth Amboy New Jersey. *Geol Soc Am Bull* 67:597–646
19. Babar Md (2005) Remote sensing and GIS applications in groundwater targeting for rural applications for rural development at NIRD, Hyderabad, pp 204–213
20. Horton RE (1945) Erosional development of streams and their drainage basins: hydrophysical approach to quantitative morphology. *Geol Soc Am Bull* 56:275–370
21. Smith KG (1950) Standard for grading texture of erosional topography. *Am J Soc* 5(298):655–668
22. Strahler AN (1957) Quantitative analysis of watershed geomorphology. *Trans Am Geophys Union* 38:913–920
23. Cox RT (1994) Analysis of drainage basin asymmetry as a rapid technique to identify areas of possible quaternary tilt-block tectonics: an example from the Mississippi embayment. *Geol Soc Am Bull* 106:571–581
24. Miller VC (1953) A quantitative geomorphic study of drainage basin characteristics in the Cinch mountain area. Virginia and Tennessee Technical Report 3

Experimental Investigation of the Spinodal Decomposition in Cu-Ni-Cr Alloy for Corrosion Control in Marine Structure



S. C. Jirapure and Borade

Abstract The use of spinodal decomposition including homogenization, solution heat treatment, aging heat treatment in Aragon atmosphere on Cu-Ni-Cr ternary alloy is proven and valuable new engineering method for corrosion resistant of Marine alloy. The present research proves the excellent performance of spinodal Cu-Ni-Cr alloy (Naval Alloy) in terms of corrosion resistance in marine (sea) environments. This also suggests ‘Naval alloy’ for offshore structure and ship hulls. This paper also reviews the different alloying combinations in sea environment and compares the present alloy used with ‘Naval alloy’.

Keywords Cu–ni–cr spinodal alloy · Heat treatment · Corrosion · Marine environment

1 Introduction

Marine engineering have tremendous problems in protecting Inshore, Offshore structures and ship hulls from corrosion. A broad range of alloy combinations, heat treatments, surface coatings are the most commonly used approaches for resisting corrosion in sea environment. Each and every approach is useful with its advantages and benefits [1–6]. The Copper-Nickel binary alloys are preferred for marine structure because they provide corrosion protection. The Copper-Nickel alloys are particularly attractive for sea water environment due to its strength and corrosion resistance property [7–12].

In sea environment, the majority of the most troublesome problems come across in contact with sea water, but atmospheric corrosion of metals exposed on or near coastlines and hot salt corrosion in engines operating at sea or taking in salt-laden air is equally problematic [13–15].

S. C. Jirapure (✉)

Mechanical Engineering Dept, Jawaharlal Darda Institute of Engineering & Tech., Yavatmal (MS), India

Borade

Government Polytechnic Gadchiroli, Yavatmal (MS), India

Long-term preservation is a difficult objective for ships in the sea environment. Wooden ships are often considered the most problematic due to insects, fungi, bacteria, and marine animals. Yet iron ships, while not subject to such organic attack, are hardly less temporary [16–18].

For marine applications, mild steel remains another option for constructional purposes by virtue of its relatively low cost, mechanical strength and ease of fabrication. Its main drawback is that it corrodes easily in seawater and unless adequately protected, rapidly loses strength which may result in structural failure [19].

Year upon year the cost of sea corrosion has increased until it is estimated today at 4% of the Gross National Product. So, there is a strong need to have such a material which minimizes the corrosion effect and have enough strength to mark it advisable.

2 Preparation of Material

2.1 Material

All the materials used in the preparation of the alloys are of good quality. The chromium is labelled 98.99 per cent. An analysis of one sample showed 98.2 per cent chromium with the remainder consisting largely of silica, slag, etc. The nickel was labelled 99.6 per cent with a small amount of iron, and only a trace of cobalt. Two different lots of copper are used.

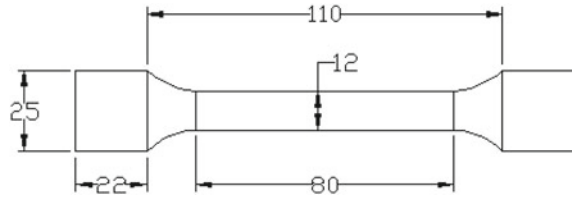
2.2 Spinodal Decomposition

The alloys were melted in electric arc furnace with water-cooled copper mold under argon atmosphere. Specimens were melted four times to ensure mixing. The temperature within the hot zone of the furnace was controlled to an accuracy of $\pm 5\%$. Homogenization was carried out at a temperature above the miscibility gap. The alloys were cooled down from the melt in 1–2 min to avoid the cracking caused by rapid quench. Subsequently annealing was performed at 550°C in air for up to 72 h. Aging heat treatment was carried out after the specimens were subjected to solution heat treatment. The microscopic examinations were conducted using Carl-Zeiss metallurgical microscope. Figure 1 shows the Design of casting of the Naval alloy.

2.3 Dimensional Specifications and Design of Casting of the Naval Alloy

See Fig. 1.

Fig. 1 Design of casting of the Naval alloy



2.4 Materials and Methods

The corroding reagents used were normal solutions of nitric acid, hydrochloric acid, sulphuric acid, sodium hydroxide, ammonium hydroxide, sodium chloride, and molten fatty acids. The normal solutions had been carefully standardized and were known to be reasonably accurate.

There does not seem to be any well-established method for making corrosion tests. Different investigators have used a variety of methods. For the present work, the scheme used has been reasonably satisfactory and it will be described somewhat in detail.

2.5 Solution and Temperature

The normal solutions were used for each test. No attempt was made to remove any dissolved gases, such as carbon dioxide. The solutions were contained in beakers of such size that they were filled almost to the top. Of course, the solutions changed slightly in concentration because of evaporation and of corrosion of the specimens, but that could not be avoided. The loss by evaporation was made very small by covering the beakers with watch glasses. With such a large volume of solution the change in concentration was not important in most cases. If it was observed that a specimen was dissolving very rapidly, it was removed and from the amount which had been corroded a calculation was made to find how much would have corroded in one week. One hundred grams of the fatty acids were taken for each of the tests that were made at 1050°C and 200 g for those made at 850°C.

The corrosion tests were made at the temperature of the laboratory. In order to be able to approximate the mean temperature, a maximum and minimum thermometer was kept on the desk where the tests were being made and readings were taken from time to time. A calculation showed that the mean temperature for the whole period of time was 20°C.

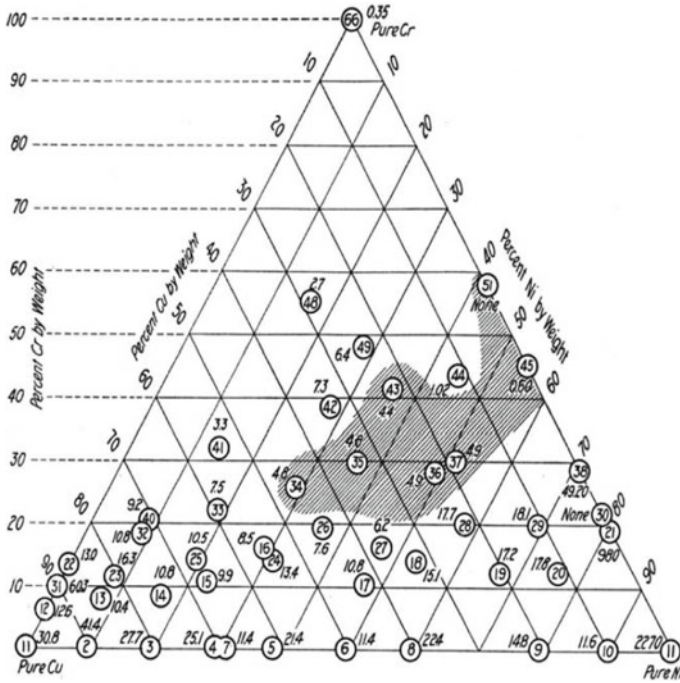


Fig. 2 Corrosion in Nitric acid solution

2.6 Time

It was intended to leave the specimens in the solutions for one week, but in some cases it was necessary to remove them before the end of that period.

3 Results and Discussions

The results of the corrosion tests are shown on tri-angular diagrams. In each diagram the loss in weight in milligrams per square inch per week for each alloy tested is shown above the circle, the centre of which represents the composition of the alloy. Areas of minimum corrosion are designated on the diagrams by shading.

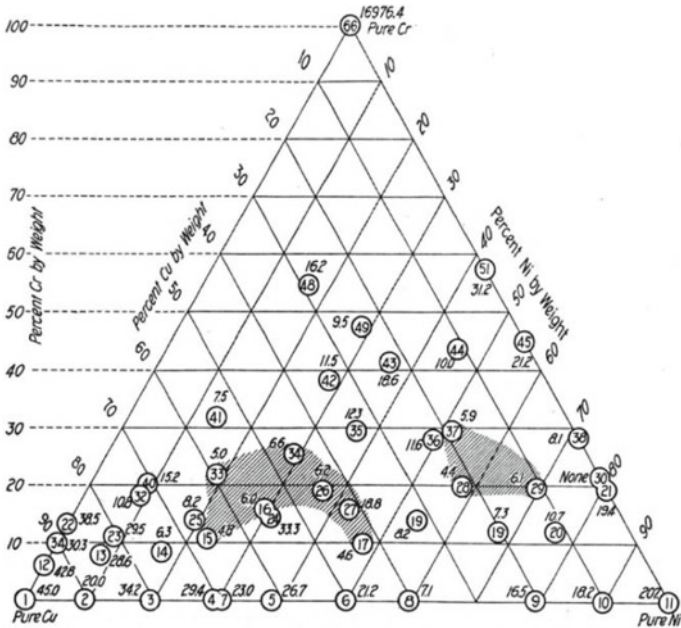


Fig. 3 Corrosion in normal hydrochloric acid solution

3.1 Nitric Acid

Figure 2 shows the results obtained with a normal solution of nitric acid. Nickel, especially, is attacked, and alloys with high percentages of this metal show great corrosion.

3.2 Hydrochloric Acid

The results from these tests are shown in Fig. 3. It is seen that all of the metals showed considerable corrosion in hydrochloric acid and that chromium was especially soluble in this acid. However, there is a fairly well-defined area in the triangle over which the corrosion was small.

3.3 Sodium Chloride

Losses in normal sodium chloride solution are, in general, small. These losses are largest for alloys near the copper corner of the triangle as shown in Fig. 4.

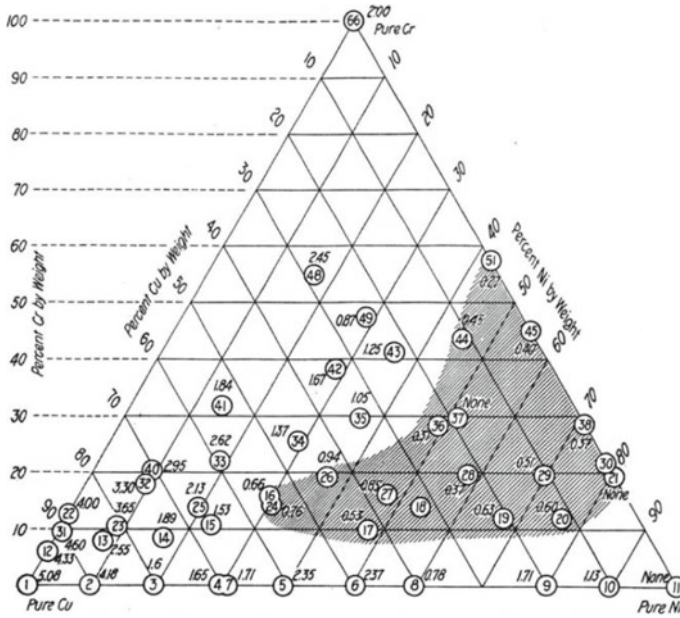


Fig. 4 Corrosion in normal sodium chloride solution

3.4 Fatty Acids

Some tests in fatty acids were made at 105° C by heating in an electric oven and some other tests were made at approximately 85° C by heating on a steam bath. The results are shown in Fig. 5. The greatest losses are near the copper corner of the triangle. This suggests that instead of using a copper container for fatty acids it might be advisable to use an alloy of copper and nickel, or possibly one containing copper and nickel with a little chromium.

4 Conclusions

Material is a key factor to prevent Marine corrosion. The properties of Cu-Ni binary as well as Cu-Ni-Cr ternary alloys were reviewed. Present research proves that the Cu-Ni-Cr ternary alloy with spinodal decomposition is having the better corrosion resistance than the present material used in marine environment.

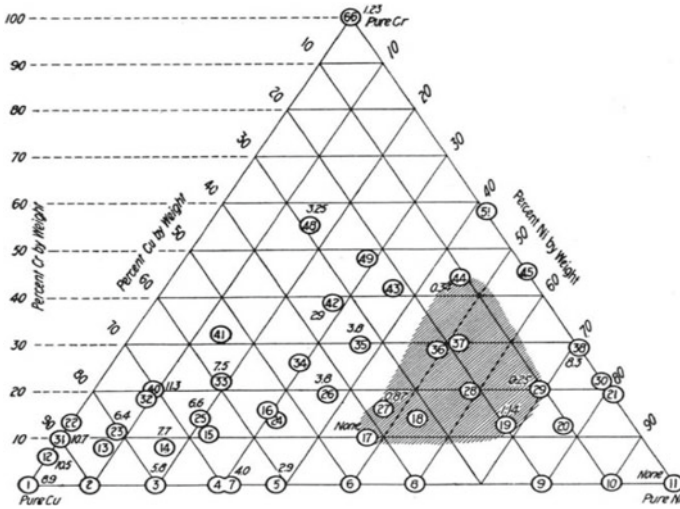


Fig. 5 Corrosion in fatty acids

Acknowledgements The authors are grateful to Heads & associates of Research lab, Mechanical Engineering Department, Engineering Metallurgy laboratory, JD Institute of Engineering & Technology, Yavatmal (MS), India to carry out the present work.

References

1. Antonov and Popov (1999) Model of spinodal decomposition of phases under hyperbolic diffusion. *Phys Solid State* 41(5):824–826
2. Barrett CS (1952) *Structure of Metals*. Metallurgy and Metallurgical Engineering series, Second Edition, McGRAW-Hill book Co, INC
3. Binder K, Billotet C, Mirolid P (1978) On the theory of spinodal decomposition in solid and liquid binary mixtures. *Zeitschrift fur Physik -Condensed Matter* 30(2):183–195
4. Cohen, A., “Copper Standards”, ASTM standardization news, pp. 34–43, (2006)
5. “Copper-Nickel Alloys, Properties and Applications” a handbook published by Copper Development Association, British Standards Institution, London W1A 2BS TN30 (1982)
6. “Copper – The Vital Metal” Copper Development Association, British Standards Institution, London W1A 2BS CDA Publication No. 121, (1998)
7. “Cost-Effective Manufacturing -Design for Production” a handbook published by Copper Development Association, British Standards Institution, London W1A 2BS CDA Publication No 97, (1993)
8. “Copper and copper alloys- compositions, applications and properties” a handbook published by Copper Development Association, British Standards Institution, London W1A 2BS publication No. 120 (2004)
9. Cribb, W. R and. John raka, “Copper Spinodal alloys”, *Advanced materials and processes*, AP0056, pp. 01–04, (2002)
10. Erukhimovich, Ya. and Prostomolotova, E.V., “New approach to the theory of spinodal decomposition”, *Journal of Experimental and Theoretical Physics*, Vol. 66, Issue 6, pp. 463–469, (1997)

11. Fehim Findik, "Modulated (Spinodal) Alloys", Periodicals Of Engineering And Natural Sciences Vol. 1 No. 1, ISSN 2303-4521, pp. 47-55, (2013)
12. Harald, P.C. and Schaftenaar, "Theory and Examples of Spinodal Decomposition in a Variety of Materials", Utrecht University, Padualaan 8, 3584 CH Utrecht, The Netherlands, pp. 1-17, (2008)
13. Kodgire V.D. and Kodgire, S.V., "Material Science and Metallurgy for Engineers", 30th Edition, A Text book published by Everest Publishing house with ISBN 8186314008, (2011)
14. Kuksin, A.Yu, Norman, G.E. and Stegailov, V.V., "The Phase Diagram and Spinodal Decomposition of Metastable States of Lennard-Jones System", High Temperature- Pleiades Publishing, Ltd, Vol. 45, No. 1, pp. 37-48, (2007)
15. Petrishcheva E, Abart R (2012) Ex-solution by spinodal decomposition in Multi-component mineral solutions. *Acta Mater* 60:5481-5493
16. Ramnarayan and Abhinandan (2003) Spinodal decomposition in fine grained materials. *Bull Mater Sci* 26(1):189-192
17. Jirapure, S.C. and Dr. Borade, A.B., "Measurement of Mechanical Properties and Microstructure of Cu-Ni-Cr Spinodal alloy", *International Journal of Advanced engineering and Management*, Vol.2(3), pp. 78-81, (2017)
18. Jirapure, S.C. and Dr. Borade, A.B., "A New Approach of Strengthening- Spinodal Decomposition", *Int. Journal of Applied Sciences and Engineering Research*, Vol. 3 (5), pp. 1021-1029, (2014)
19. Jirapure, S.C. and Dr. Borade, A.B., "Naval Corrosion- Causes and Preventions, *International Journal of Engineering Science & Research Technology*, Vol. 3(7), pp. 263-268, (2014)

Enhanced Power Conversion Efficiency of the P3BT (Poly-3-Butyl Thiophene) Doped Nanocomposites of Gd-TiO₃ as Working Electrode



Vinayak Adimule, Santosh S. Nandi,
and Adarsha Haramballi Jagadeesha Gowda

Abstract In this research, we described the enhanced PCE (power conversion efficiency) of the hybrid nanocomposites synthesized by co precipitation and ultrasonic assisted synthesis (UAS). The hybrid nanocomposites fabricated by varying the P3BT (poly-3-butyl thiophene) (5–10% wt ratio)/ Gd-TiO₃. Their characteristics features were understood by SEM–EDS and HR-TEM, compositional analysis by XRD and band gap calculations by UV–visible and cyclic voltammetry. The hybrid NCs were fabricated either by RF Sputtering with the top contact of Cu/Ag thin deposition, and in the present investigation it is made in the form of a pellet with varying concentrations of P3BT/Gd-TiO₃ which were (pelletized) made as layer of conducting surface with different thickness (100 nm, 250 nm and 550 nm). Photovoltaic (PV) current–voltage characteristics measured by Hg excitation method using Hg probe controller. The fabricated hybrid nanocomposites were studied their effect on the power conversion efficiency of the P3BT doped Gd-TiO₃ in dark and in light illumination. The photovoltaic and current–voltage characteristics is done using Hg-MDC probe controller with The PCE of the (10% wt ratio) of the P3BT doped with Gd-TiO₃ hybrid nanocomposites were 4.18% higher than inorganic Gd-TiO₃ nanocomposites as compared with the other working electrodes. The hybrid NCs showed excellent PV characteristics as compared with the existing inorganic/organic hybrid nanocomposites.

Keywords Hybrid Nanocomposites · Power conversion efficiency · Photovoltaic · Current–voltage characteristics · Co-precipitation

V. Adimule (✉)

Angadi Institute of Technology and Management (AITM), Savagaon Road, Belagavi 5800321, Karnataka, India

S. S. Nandi

Chemistry Section, Department of Engineering Science and Humanities, KLE Dr. M. S. Sheshgiri College of Engineering and Technology, Udyambhag, Belagavi 590008, Karnataka, India

A. H. Jagadeesha Gowda

Research Scholar, Centre for Research in Medical Devices, National University of Ireland, Gaillimh Galway-H91TK33, Ireland

e-mail: a.hj1@nuigalway.ie

1 Introduction

Nano particles isolated through surfactant and capping agents [1, 2], subsequent precipitation is a simple and cost effective method for the isolation of the uniform sized nanocomposites. The polymeric matrices preparation of nanocomposites are based on the structure of the polymer, solvent used such as tetra hydro furan, 1, 4-dioxan, methyl nitrile and acetone which are used in laboratory scale in the preparation of polymer nanocomposites [3–5]. Particle size of the majority nanoparticles mostly in the nanometers size ranging from 10 to 100 nm. The main advantage in the co precipitation method [6–8] is to maintain uniform particle size, solvent stability, stability of the isolated nanocomposites etc. The most of the organic/inorganic hybrid nanocomposites undergo self-assembling in its structure during precipitation, which results in particle agglomeration in the solution. Such hybrid nanocomposites [9, 10] were used most oftenly for solar cells [11], Bio imaging [12], photodiodes [13], sensors [14], dye encapsulates [15], drug delivery materials [16–18]. The imaging process nanoparticles dispersed in solution must have stability towards particle agglomeration, polymeric conjugated hybrid inorganic/organic nanoparticles have been used for photodiodes, batteries, solar cell applications [19, 20], but in contrast to their synthesis, towards isolation, purification and its stability several approaches were adapted for the dispersion of P3BT kind of molecules inside the inorganic particle matrix. The drawbacks of such P3BT: GT nanocomposite synthesis includes expensive processes, scaling up issues and difficult multistep synthesis [21–24]. The present research focuses the study to establish a simple protocol for the synthesis of P3BT: GT hybrid conjugated nanocomposites with highly conjugating donor molecule as P3BT (poly-3-butyl thiophene) and highly accepting inorganic matrix as GT (Gadolinium Titanate) by coprecipitation method under highly acidic condition at higher temperature [25–27]. The calcinated powders of different molar ratios of the P3BT doped hybrid nanomaterials were characterized by CV, SEM, XRD and studied I–V characteristics using Hg excitation method [28–30]. The hybrid nanocomposites also possess stability towards aqueous solution and mixed polar and non-polar solvents. A few current–voltage and capacitance voltage measurements carried out for the fabricated materials of 10% doped P3BT with different thickness of the pellet ranging from 100 to 550 nm in size. A nonlinear relation between the current and the voltage has been reported for the P3BT: GT nanocomposites as well as capacitance–voltage [31]. The assimilated values obtained from the graph was nonlinear and calculated admittance, power dissipation factor and PCE of the P3BT (10%) doped to GT nanocomposites and tabulated. High quantum yield, high solvent susceptibility, photo stability of the hybrid material is due to the dislocation of Π electrons into the inorganic tetrahedral structure and increased addition of P3BT resulted the increased electron carrier and dislocation capacity of the organic polymer in the form of Π - Π interactions [32, 33]. The hydrophobic interactions resulted the increased photoemission from the conducting surface of the 10% doped P3BT hybrid solar cells which combine both organic and inorganic semiconductors in an active layer due to increased electron excitation and dissociation at the interface, high stability,

inhibition towards the recombination of generated photo holes and the electrons. The distinct strategies involved in this research work open up varieties of electrical and electronic properties of the hybrid nanomaterials with unique properties. The material finds diversified applications in the solar cells, photodiodes, photo resistance, LEDs, micro sensors, diodes and super capacitor.

2 Materials and Methods

Starting chemicals, reagents purchased from e-Merck, India Ltd, Sigma-Aldrich India and from spectro chem. Ltd. JEOL instrument JSM IT-800 supported with hybrid lens and fitted versatile backscattered electron detector (VBED) was used to record the SEM morphology of the samples. XRD Instrument from Bruker D2 Phaser having reciprocal phase mapping and small angle X-ray scattering (SAXS), Cu-K α radiation ($\lambda = 0.1542$ nm) operating at 50 kV. CHI (Austin) instrument model D630 electrochemical analyzer used for recording CV spectrum and Specord 210 plus with variable resolution and double beam detection was used for optical absorptivity investigation. Pure and Gd doped NS coated as thin films and obtained these films by using electron beam evaporation and the distance between source and the target was 8 cm. the deposited thickness was measured. Mercury Probe Controller MDCs model 802 B was used for I–V of solar cell properties. The 99.98% pure P3BT has been procured from the Sigma Aldrich for doping into the inorganic NCs.

2.1 Hg Probe Station (Hg-Photovoltaic Current–Voltage Method)

Hg-probe is commonly used for I–V characterization because of its rapid and nondestructive nature. In order to measure the semiconductor properties especially current and voltage, the Hg probe finds its application otherwise classical fabrication was time consuming, needs metallic contact to be established and has several processing steps for the sample to be investigated. The entire processing takes usually several hours and affects the device performance under sun illumination. Hg-probe connects to the well-defined area of the flat sample and if the sample contact is rectifying it can be used to measure resistance, leakage currents etc. The thin films can be of any material either it may be metal, semiconductor or may be oxide. Typical Hg-probe can be used to measure I–V instead of fabricating material over ITO/FTO which intern reduces time and effort. Depending on the contact established between Hg and sample and obtained ohmic and added a value of Hg probe contact is that it is non-destructive and can be easily lifted from the sample.

2.2 Determination of I–V/C–V Using Hg-Probe (General Methodologies)

Two different ways of operating Hg-probe commonly categorized Front-Back Contact and Dual Front Contact. Back surface is coated with low resistance metal or alloy and top contact made with suction pump. Total connected area of Hg which is connected to LCR meter for I–V, C–V investigation. Commonly ohmic (rectifying) and non ohmic (Schoty) behavior studied using Hg probe.

Calibration of Hg-Probe.

Hg-probe usually calibrated by capacitance measurement on dielectric film of unknown thickness and permittivity. Hg forms MOS (metal oxide semiconductor structure) which is connected by shielded cables on the LCR meter which intern superimposes a small AC signal of 15 mV.

$$C = \epsilon_0 k A / d$$

K is relative permittivity of the dielectric sample, ϵ_0 permittivity of free space, A is the area of the dielectric sample and d is the thickness of the dielectric sample. The contact area of Hg can be calculated by.

$$A = C d / k \epsilon_0 .$$

3 Experimentation

3.1 Synthesis of Gd-TiO₃ NCs (Step 1)

Gd (NO₃)₃ · 6H₂O (10–40% molar wt. ratio) and TiCl₄ (titanium tetrachloride) were dissolved in 25 ml of deionized water (DM), treated with 10 ml of concentrated HCl under stirring, CTAB (0.210 g) and triethanol amine (0.5 mL) are added and reaction mixture (RM) was heated to 85°C for 2–3 h. RM was cooled, precipitate obtained after slow addition of NH₄OH solution was subjected to ultra-sonication for 2 h, precipitate was filtered, washed with cold water and dried at 100–200°C, calcinated at 800–850°C, grounded as powdered Gd-TiO₃ NS.

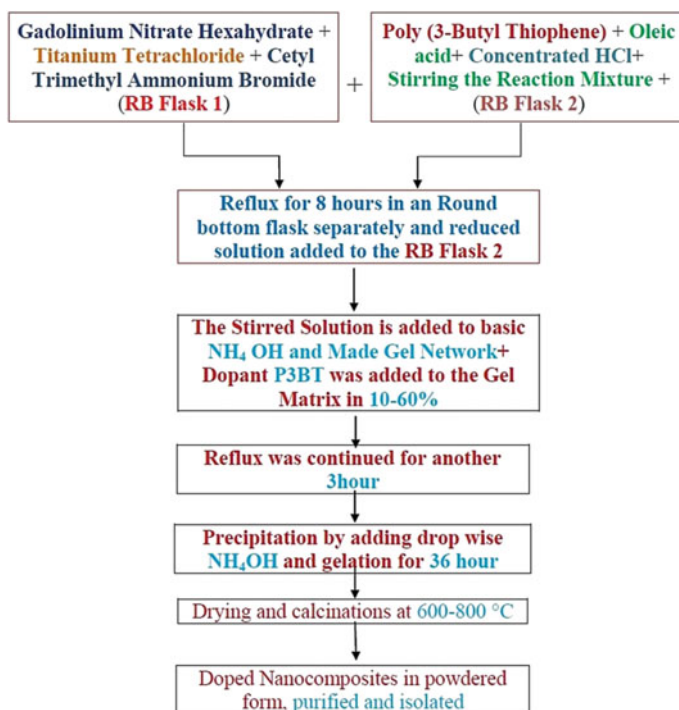


Fig. 1 Schematic reaction flow chart for the synthesis of P3BT: GTs of NCs

3.2 Doping of P3BT (Poly-3-Butyl Thiophene) to Gadolinium Titanate Nanomatrix (Step 2)

Gd TiO₃ (1.43 g, 1 molar ratio, step 1) mixed with P3BT (1.66 g, 10% molar ratio wt. ratio) in 50 ml deionized water and stirred continuously for 1 h. NaOH (4 M) solution was added drop wise up to pH = 9 and heated to 70 °C for 3–4 h. Finally the pale brown precipitate was filtered, washed with cold water, ethanol, dried at 100–200 °C, calcinated at 750–800 °C yielded as fine powders. Figure 1 indicates schematic Reaction Flow chart for the synthesis of P3BT: GTs of NCs.

4 Results and Discussion

4.1 BHJ Hybrid Working Principles

Solar cells composed off hybrid organic/inorganic nanomaterials reported in the literature generally consists of device architecture fabricated with active layers, top

contact and a bottom contact with the conducting polymer sandwiched in between active components (Fig. 2). Indium tin oxide (ITO) coated as conducting electrode behaving as anode with high work function over flexible plastic or a glass plate with $100 \Omega/\text{sq cm}^2$ resistance. The polymer poly (3, 4-alkenedioxythiophenes): poly (styrenesulfonate) (PEDOT: PSS) used as hole extractor in between the HTL and ETL layers coated either by spin coating over ITO substrate to form a thin film 100–200 nm thick. Al, Ag metal deposited over photo active layer as cathode and electrons, holes transported via percolating pathways. The holes are transported through the conjugated polymer, and the electrons are transported through the inorganic semiconductor (Fig. 3).

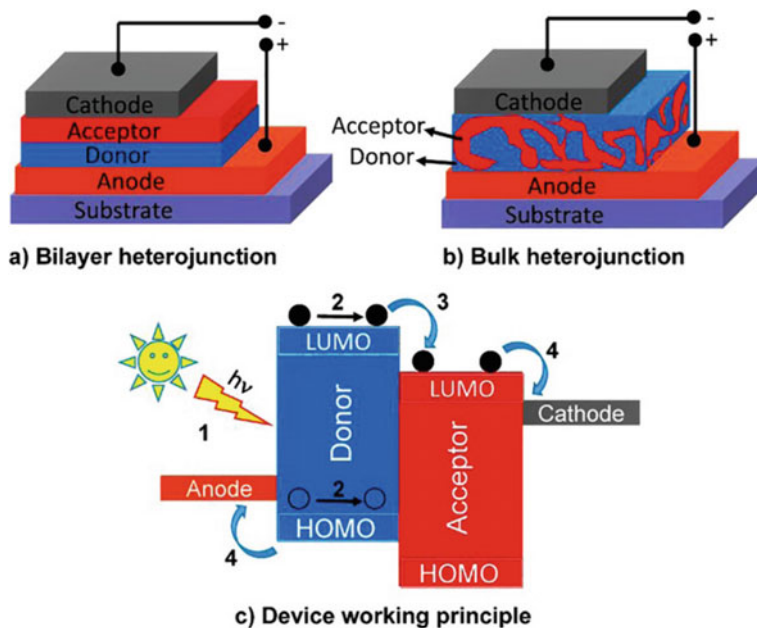


Fig. 2 Schematic conventional fabrication of the solar cell devices as reported in the literature

Fig. 3 Schematic illustration of the interface of the hole and electron charge carries at the boundary

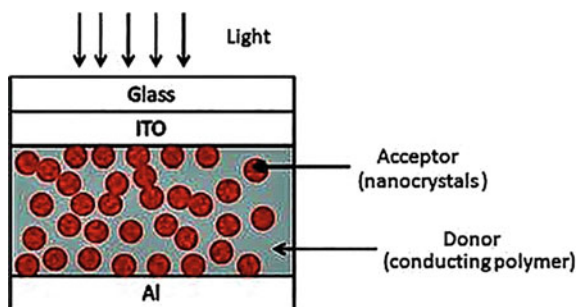
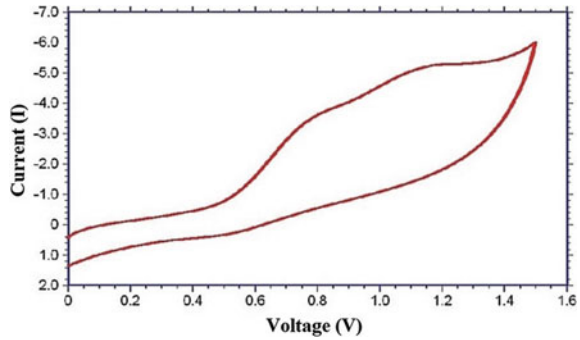


Fig. 4 Typical illustration of the 10% P3BT doped GT NCs CV spectrum



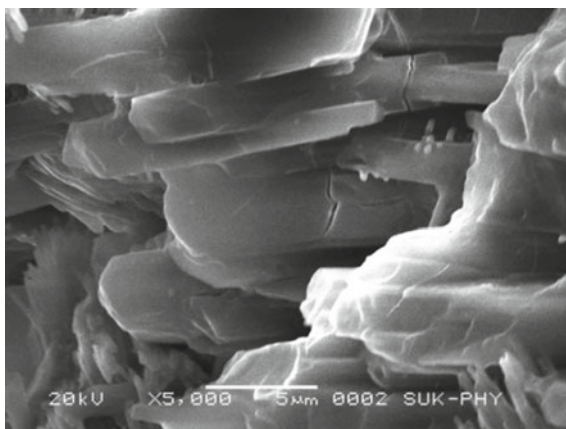
4.2 Electrochemical CV Measurements BHJ Hybrid Working Principles

Redox potentials were recorded using cyclic voltamogram (Fig. 4) the oxidation potential for the highest doped 10% of P3BT was found to be -0.44 eV and reduction potential of $+0.012$ eV. Applied voltage varied in between 0.5 and 1.4 V. HTL (hole transport layer) acting cathode material is GT and the acting anode material is P3BT (donor), due to the increased donating ability of the P3BT doped to the inorganic NCs which creates band gap of 0.97 eV. Due to electron releasing ability of P3BT organic compound which leads to more negative potential of the combined inorganic/organic NCs.

4.3 SEM Morphological Features

Scanning electron microscopic images (Fig. 5) of the 10% heavily doped GT NCs arrays and the picture depicts the pore diameter, wall thickness, inter pore distance, and the length of the P3BT: GT NCs are 100 nm, 75 nm, 40 nm and 55 nm respectively. The SEM and the particle configuration were obtained using focused ion beam (FIB). The grain size of the P3BT dispersed particle in the inorganic matrix was found to be 60 nm and the grain boundary distance is 100 nm. As seen from the Fig. 5 the increase in concentration of polymeric matrix, number of aggregates and agglomerates of gadolinium nanoparticles increases with the 10% addition the size of the nanoparticle is in between 30 and 55 nm at 5% it is in between 50 and 120 nm. The P3BT doping on the surface of the bulk hetero junction increases the surface conductivity, optical reflectivity and particles agglomerated inside the cavity of the NCs.

Fig. 5 Scanning electron microscopic images of the 10% P3BT doped GT NCs



4.4 X-ray Diffraction Spectroscopy

Figure 6 shows the X ray diffraction patterns (XRD) of the P3BT: GT NCs recorded after the thermal annealing at 800°C with diffraction peaks are absorbed at 2θ values. Prominent peak is utilized to estimate the grain size of the GdTiO_3 NPs with the help of Scherer equation $D = K\lambda/\beta\cos\theta$ where K is constant, $\lambda = 0.154 \text{ \AA}$ and θ is the diffraction angle. The hybrid perovskite layer was amorphous and the crystalline phase was (101), (007), (112), (121), (311), (401) at 2θ of 23, 24, 26, 27, 29, 31, 33, 36 respectively. The crystallinity and the tetragonal crystal structure of the 10% doped P3BT: GT NCs were confirmed by the dominant peak at (101), (112) corresponding to 2θ values of 29 and 31 respectively. XRD pattern of tetrahedral geometry of the intense peak TiO_3 is well matched with the JCPDS file number (39–1359). The formation of hybrid materials is confirmed by X-ray analysis which indicates the superimposition of the peaks of GT and P3BT in NCs.

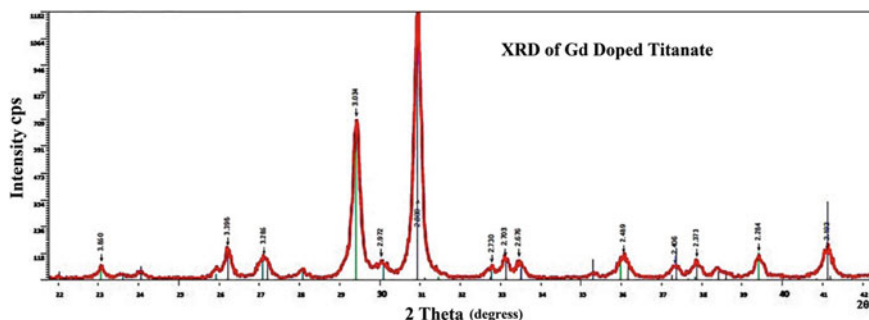
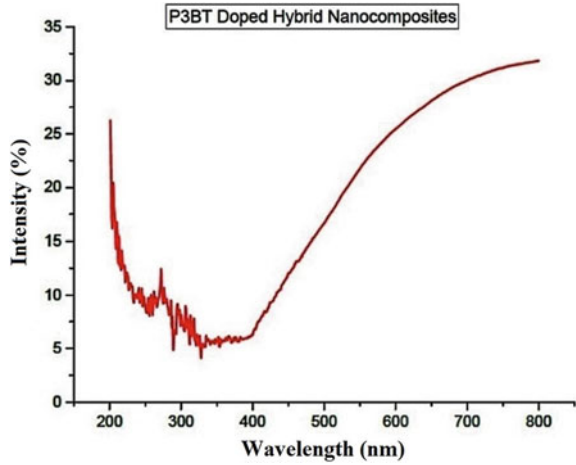


Fig. 6 XRD pattern of the 10% P3BT doped GT NCs

Fig. 7 UV–Visible spectrum of the P3BT: GT NCs



4.5 UV–Visible Characteristics

Optical absorptivity measured for 10% P3BT doped NCs using UV–Visible spectrophotometer (Fig. 7). NCs dissolved in methanol solvent at room temperature and kept in a special quartz cells irradiated with UV radiation in between 100 and 800 nm. Figure 7 shows the absorption spectra of the 10% P3BT doped GTs with absorptivity in between 450 and 800 nm stretching over end of the visible spectrum. Addition of P3BT (poly-3-butyl thiophene) to Gd-TiO₃ NCs displace the edge of the UV-spectrum and is due to agglomeration of the NPs. UV edge observed at 400 nm, at 305 nm to 400 nm and fall in the in the absorptivity is due to agglomeration of the GTs Chromosphere P3BT addition increases the absorptivity and can be clearly seen from 550 nm. Due to effect of addition of chromospheres P3BT into inorganic gadolinium nanocomposite. Band gap energy of the samples recorded and calculated by Kubeka Mulk model and the direct allowed transition calculated using the formula.

$$(\alpha' h \gamma)^2 = C (h \gamma - E_g).$$

C-is the absorption coefficient, $h\gamma$ -photon energy and E_g -optical band gap.

4.6 Photovoltaic Current–Voltage Characteristics

Pelletized sample of P3BT: GT NCs were studied for their photo current voltage characteristics and capacitance voltage characteristics using Hg probe, values are tabulated in Tables 1 and 2. The voltage is varied between -4.5 V and 4.5 V for the characteristics graphs to obtain which synchronized with our studies related solar cell properties of nanocomposites. The current gain varies non linearly form -1.36

Table 1 Depicting the values of current (I), voltage (V) and resistance (R) of the 10% doped P3BT: GT nanoparticles (Fig. 8)

Samples [P3BT, 10%]	Current gain [I]	Voltage applied [V]	Admittance [Ω]
P3BT: GT (P1)	-1.36×10^{-11}	-4.4	3.08×10^{-12}
P3BT: GT (P2)	-8.82×10^{-12}	-3.9	2.26×10^{-12}
P3BT: GT (P3)	1.99×10^{-12}	-1.3	-1.53×10^{-12a}
P3BT: GT (P4)	1.41×10^{-11}	3.0	4.70×10^{-12b}
P3BT: GT (P5)	1.48×10^{-11}	3.4	4.35×10^{-12}
P3BT: GT (P6)	1.89×10^{-11}	4.5	4.20×10^{-12}

^a(Lowest recorded admittance of the 10% doped GTs); ^b(highest recorded admittance for 10% doped GTs)

$\times 10^{-11}$ A to 1.99×10^{-12} A. The admittance calculated varies from -1.53×10^{-12} to 4.70×10^{-12} the highest recorded admittance in the present research work for the 10% doped organic material. The dissipation power as calculated varies from -2.59×10^{-12} to 8.51×10^{-11} . The lowest base line drawn from the summarized results to calculate the Fill factor, Open circuit voltage (V_{oc}) which are found to be 1.79 and 0.77 V respectively for the particular 10% doped P3BT material. The power conversion efficiency was found to be 15.2% which is which is 4–5 times higher than the commonly reported for the inorganic perovskite NCs.

5 Conclusion

Authors have synthesized the P3BT: GT NCs by co precipitation methods using surfactants and capping agents at high temperature and in highly acidic condition. The method employed by using magnetic stirrer and ultra-sonication and the reducing agent determines the size of the particles as well as the distribution of the particles in the organic/inorganic NCs by taking different wt. ratios of the organic material P3BT. Particle size, agglomeration, distribution and their density, shape was interpreted by SEM and XRD analysis, band gap, oxidation potential ability, reduction nature, absorptivity, optical properties of the doped material experimentally found by using CV and UV–Visible spectrophotometer experiments. Further Current–Voltage (I–V) performance of the 10% doped P3BT: GT NCs BHJ was investigated and after doping 10% wt. ratio of the P3BT to the GT Inorganic NCs showed more efficiency than the inorganic perovskite nanomaterials. The increased efficiency and the fill factor, power conversion efficiency is due to increased addition of P3BT into NCs This research work opens up to synthesize the novel small and large molecular weight of the thiophene compounds into inorganic NCs for efficient materials for the LEDs,

Table 2 Depicting the values of dissipations power, open circuit potential, Fill factor and efficiency of the maximum doped 10% doped P3BT: GT nanoparticles

Samples [P3BT, 10%]	Dissipation power	Voc [V]	FF	PCE [%]
P3BT: GT (P1)	5.97×10^{-11}	0.55	0.87	3.28
P3BT: GT (P2)	3.44×10^{-12}	0.88	1.62	4.12
P3BT: GT (P3)	-2.59×10^{-12}	0.61	0.47	6.38
P3BT: GT (P4)	4.24×10^{-11}	0.77	1.79	15.2
P3BT: GT (P5)	5.03×10^{-11}	0.78	0.95	7.89
P3BT: GT (P6)	8.51×10^{-11}	0.75	0.32	5.23

^a(Lowest recorded admittance of the 10% doped GTs); ^b(highest recorded admittance for 10% doped GTs)

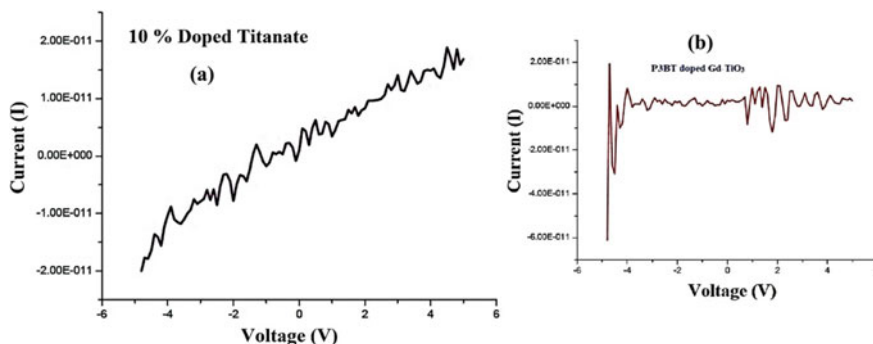


Fig. 8 a I-V Curve for the 10% doped P3BT: Gd-TiO₃ NCs b photovoltaic I-V Cure for the 10% doped P3BT to Gd-TiO₃ NCs

Photodiodes, sensors and other electrical and electronic components with variable properties.

Acknowledgements Author are thankful to KLE IT, Hubballi, CENSE, IISc, Bangalore, MSRIT, Bangalore India necessary experimentation during this research work.

References

1. Kim JY, Kim SH, Lee HH, Lee K, Ma W, Gong X, Heeger AJ (2006) New architecture for high-efficiency polymer photovoltaic cells using solution-based titanium oxide as an optical spacer. *Adv Mater* 18:572–576
2. Kim JY, Lee K, Coates NE, Moses D, Nguyen TQ, Dante M, Heeger AJ (2007) Efficient tandem polymer solar cells fabricated by all-solution processing. *Science* 317:222–225
3. Sharma GD, Suresh P, Sharma SK, Roy MS (2008) Photovoltaic properties of liquid-state photo electrochemical cells based on PPAT and a composite film of PPAT and Nano crystalline titanium dioxide. *Synth Met* 158:509–515
4. Trznadel M, Zagorska M, Lapkowski M, Louarn G, Lefrant S, Pron A (1996) UV–VIS–NIR and Raman spectro electrochemistry of regioregular poly (3-octylthiophene): comparison with its non-regioregular analogue. *J Chem Soc* 92:1387–1393
5. Shi CJ, Yao Y, Pei QB (2006) Regioregular copolymers of 3-alkoxythiophene and their photovoltaic application. *J Chem Soc* 128:8980–8986
6. Hwang SW, Chen Y (2001) Synthesis and electrochemical and optical properties of novel poly (aryl ether)s with isolated carbazole and p-terphenyl chromophores. *Macromolecules* 34:2981–2986
7. Antonis M, Demetrios B, Giannoulis A, Aquino SD (2016) Design of biodegradable bio-based equilibrium modified atmosphere packaging (EMAP) for fresh fruits and vegetables by using micro-perforated poly-lactic acid (PLA) films. *Postharvest Biol Tec* 111:380–389
8. Rhim JW, Hong SI, Ha CS (2009) Tensile, water vapour barrier and antimicrobial properties of PLA/nanoclay composite films. *Lwt-Food Sci Technol* 42:612–617
9. Reddy JP, Rhim JW (2014) Characterization of bio nanocomposite films prepared with agar and paper-mulberry pulp Nano cellulose. *Carbohydr Polym* 110:480–888

10. Atef M, Rezaei M, Behrooz R (2015) Characterization of physical, mechanical, and antibacterial properties of agar-cellulose bio nanocomposite films incorporated with savory essential oil. *Food Hydrocoll* 45:150–157
11. Choudalakis G, Gotsis AD (2009) Permeability of polymer/clay nanocomposites—a review. *Eur Polym* 45:967–984
12. Heng X, Liang M, Sun S, Shi Y, Ma Z, Sun Z, Xue S (2012) Synthesis and photovoltaic properties of organic sensitizers containing electron-deficient and electron-rich fused thiophene for dye-sensitized solar cells. *Tetrahedron* 68:5375–5385
13. Wang M, Xu M, Shi D, Li R, Gao F, Zhang G, Yi Z, Baker HR, Wang P, Zakeeruddin SM, Gratzel M (2008) High-performance liquid and solid dye-sensitized solar cells based on a novel metal-free organic sensitizer. *Adv Mater* 20:4460–4463
14. Lee MW, Kim JY, Lee DH, Ko MJ (2014) Novel D- π -A organic dyes with thieno [3, 2-b] thiophene-3, 4-ethylenedioxythiophene unit as a π -bridge for highly efficient dye-sensitized solar cells with long-term stability. *ACS Appl Mater Interfaces* 6:4102–4108
15. Paek S, Choi H, Choi H, Lee CW, Kang MS, Song K, Nazeeruddin MK, Ko J (2010) Molecular engineering of efficient organic sensitizers incorporating a binary π -conjugated linker unit for dye-sensitized solar cells. *J. Phys. Chem. C* 114:14646–14653
16. Lee MM, Teuscher J, Miyasaka T, Murakami TN, Snaith HJ (2012) Efficient hybrid solar cells based on meso-super structured organo metal halide perovskite. *Science* 338:643–647
17. Etgar L, Gao P, Xue Z, Peng Q, Chandiran AK, Liu B, Nazeeruddin MK, Gratzel M (2012) Mesoscopic $\text{CH}_3\text{NH}_3\text{PbI}_3/\text{TiO}_2$ heterojunction solar cells. *J Am Chem Soc* 134:17396–17399
18. Burschka J, Pellet N, Moon SJ, Humphry-Baker R, Gao P, Nazeeruddin MK, Gratzel M (2013) Sequential deposition as a route to high-performance perovskite-sensitized solar cells. *Nature* 499:316–319
19. Nie W, Tsai H, Asadpour R, Blancon JC, Neukirch AJ, Gupta G, Crochet JJ, Chhowalla M, Tretiak S, Alam MA (2015) High-efficiency solution-processed perovskite solar cells with millimeter-scale grains. *Science* 347:522–525
20. Mitzi DB, Feild C, Harrison W, Guloy A (1994) Conducting tin halides with a layered organic-based perovskite structure. *Nature* 369:467–469
21. Poglitsch A, Weber D (1987) Dynamic disorder in methylammoniumtrihalogenoplumbates (II) observed by millimeter-wave spectroscopy. *J Chem Phys* 87:6373–6378
22. Im JH, Chung J, Kim SJ, Park NG (2012) Synthesis, structure, and photovoltaic property of a nanocrystalline 2H perovskite-type novel sensitizer $(\text{CH}_3\text{CH}_2\text{NH}_3) \text{PbI}_3$. *Nanoscale Res Lett* 7:1–7
23. Baikie T, Fang Y, Kadro JM, Schreyer M, Wei F, Mhaisalkar SG, Graetzel M, White TJ (2013) Synthesis and crystal chemistry of the hybrid perovskite $(\text{CH}_3\text{NH}_3) \text{PbI}_3$ for solid-state sensitized solar cell applications. *J Mater Chem A*. 1:5628
24. Luk'yanchuk BS, Tribel'ski MI, Ternovski VV (2006) Light scattering at nanoparticles close to plasmon resonance frequencies. *J Opt Technol* 73:371–377
25. Ho WJ, Su SY, Lee YY, Syu HJ, Lin CF (2015) Performance-enhanced textured silicon solar cells based on plasmonic light scattering using silver and indium nanoparticles. *Materials* 8:6668–6676
26. Atwater HA, Albert P (2010) Plasmonics for improved photovoltaic devices. *Nat Mater* 9:205–213
27. Cotal H, Fetzer C, Boisvert J, Kinsey G, King R, Hebert P, Yoon H, Karam N (2009) Multifunction solar cells for concentrating photovoltaic. *Energy Environ Sci* 2:174–192
28. Yamaguchi M, Takamoto T, Araki K, Ekins-Daukes N (2005) Multi-junction III–V solar cells: current status and future potential. *Sol Energy* 79:78–85
29. Yamaguchi M (2002) Multi-junction solar cells and novel structures for solar cell applications. *J High Energy* 14:84–90
30. Pudasaini PR, Ayon AA (2013) Nanostructured plasmonics silicon solar cells. *Microelectron Eng* 110:126–131
31. Shishiyanu ST, Shishiyanu TS, Lupan OI (2006) Temperature effects on gas sensing properties of electrodeposited chlorine doped and undoped n-type cuprous oxide. *Sens Actuators B Chem* 113:468–476

32. White B, Yin M, Hall A (2006) Complete CO oxidation over Cu₂O nanoparticles supported on silica gel. *Nano Lett* 6:2095–2098
33. Dhas NA, Raj CP (1998) Synthesis, characterization, and properties of metallic copper nanoparticles. *Chem Mater* 10:1446–1452

A Facile Synthesis of Gadolinium Titanate (GdTiO_3) Nanomaterial and Its Effect in Enhanced Current-Voltage Characteristics of Thin Films



Vinayak Adimule, Santosh S. Nandi,
and Adarsha Haramballi Jagadeesha Gowda

Abstract The present research was carried out in understanding the enhanced efficiency of the I-V (current-voltage) properties of the novel inorganic nanocomposites (NCs) of Gd-TiO_3 . Nanocomposites of Gd-TiO_3 synthesized by precipitation technique incorporating CTAB (cetyl trimethyl ammonium bromide) as capping agent characterized by XRD (X-ray diffraction), UV Visible, CV (cyclic voltammetry) SEM (scanning electron microscopy) analytical techniques. Tetragonal close packing of Gd-TiO_3 NPs observed in XRD with particle overlay of Gd is 40 nm. Current-voltage properties studied with different concentration of Gd (10–40%) doped NS. The FF (fill factor) increases as the doping of Gd increases which indicates the increased charge dislocation inside the NCs of Gd-TiO_3 . The open circuit current (V_{oc}) and power maximum also increases as the gadolinium concentration increases. The effect of the loading of the Gd on the conductivity of the NCs was investigated. The filler loading up to 30% I-V characteristics was linear and the 40% it shows non linearity in the I-V characteristics which shows the ohmic nature of the NCs and the electrodes. Impedance value decreases with increase in applied voltage. Current-voltage behavior of NCs depends largely on the Gd content and 40% filler loaded TiO_3 showed better efficiency than the rest other NCs.

Keywords Current-Voltage characteristics · Nanocomposites · Co precipitation · Fill factor · Ohmic resistance

V. Adimule (✉)

Department of Chemistry, Angadi Institute of Technology and Management (AITM), Savagaon Road, Belagavi, Karnataka, India
e-mail: adimulevinayak@yahoo.in; researcher@vinayakadimule.in

S. S. Nandi

Department of Engineering Science and Humanities, KLE Dr. M. S. Sheshgiri College of Engineering and Technology, Udyambhag, Savagaon Road, Belagavi, Karnataka, India

A. H. Jagadeesha Gowda

Centre for Research in Medical Devices, National University of Ireland, Galway, Ireland
e-mail: a.hj1@nuigalway.com

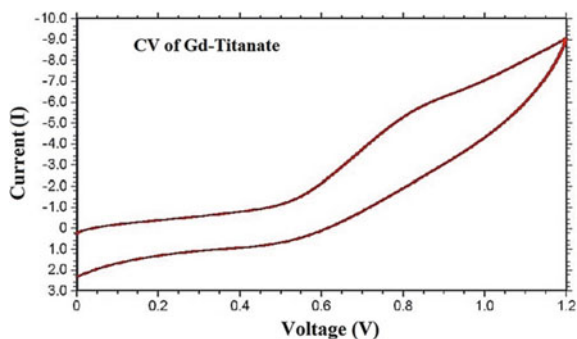
1 Introduction

In recent years nano science and nanotechnology [1–4] emerged as new materials and functional facilities. In recent times nano electronics [5, 6] one of the important growing area in nano chemistry, frequently nano metered sized particles, especially metallic particles show considerable change in the electrical and electronic properties [7–10] compared to bulk scale materials. Thus, these materials are designed and investigated largely. In order that the materials to show enhanced properties of the solar cells [11], sensors [12], optics [13], photodiodes [14], LEDs [15] etc. nano-materials synthesized in proper shape and size. Generally, specific size, shape and uniform distribution of the particle are achieved by varying the synthetic methods [16], different reducing agents, stabilizers etc. In the co precipitation method [17, 18] of chemical approach of the synthesis, metal cations and anions are combined and allowed to form clusters and aggregates. It is one of the classical methods to employ the different reducing agents like hydrazine hydrate, hydrogen, sodium cyno borohydride etc. in aqueous solutions [19, 20]. In this study, we present the unique method for the synthesis of nanomaterials from the existing co precipitation method using surfactants and capping agents [21–24]. In the first stage, the gadolinium nano particles are reduced at high temperature and in acidic condition and doped appropriately to the reduced nanomatrix of the titanate and obtained different compositional hybrids of the gadolinium titanate nanocomposites [25–28]. The purified and calcinated materials were characterized the distribution of the particles and the sizes by SEM and XRD, further the unique electrical and electronic properties are studied. In the present research work the current-voltage characteristics [29–35] of the 10%, 20%, 30% and 40% of the nanocomposite matrix is plotted and results of the obtained resistance, admittance, capacitance and power dissipation factor is summarized and elucidated in the results and discussion.

2 Materials and Methods

Starting chemicals, reagents purchased from e-Merck, India Ltd, Sigma-Aldrich India and from spectro chem. Ltd. JEOL instrument JSM IT-800 supported with hybrid lens and fitted versatile backscattered electron detector (VBED) was used to record the SEM morphology of the samples. XRD Instrument from Bruker D2 Phaser having reciprocal phase mapping and small angle X-ray scattering (SAXS), Cu-K α radiation ($\lambda = 0.1542$ nm) operating at 50 kV. CHI (Austin) instrument model D 630 electrochemical analyzer used for recording CV spectrum and Specord 210 plus with variable resolution and double beam detection was used for optical absorptivity investigation. Pure and Gd doped NS coated as thin films and obtained these films by using electron beam evaporation and the distance between source and the target was 8 cm. the deposited thickness was measured. Agilent B 1500 A series from keysight having source of 5 MHz with 10 ns pulsed resolution used for I-V investigation.

Fig. 1 Cyclic Voltamogram of the 40% Gd-TiO₃ NCs



3 Experimentation

3.1 Synthesis of Gd-TiO₃ NCs

Gd(NO₃)₃ · 6H₂O (10% to 40% molar wt. ratio) and TiCl₄ (titanium tetrachloride) were dissolved in 25 ml of deionized water (DM), treated with 10 ml of concentrated HCl under stirring, CTAB (0.210 g) and triethanol amine (0.5 mL) are added and reaction mixture (RM) was heated to 85 °C for 2–3 h. RM was cooled, precipitate obtained after slow addition of NH₄OH solution was subjected to ultra-sonication for 2 h, precipitate was filtered, washed with cold water and dried at 100–200 °C, calcinated at 800–850 °C, grounded as powdered Gd-TiO₃ NCs.

3.2 Cyclic Voltammetry

Redox potentials were recorded for 40% of Gd doped NS using instrument CV as shown in Fig. 1. Oxidation potential was found to be -0.34 eV, whereas reduction potential was +0.011 eV. Experiments performed by varying voltage in between 0.4 to 1.2 V. Increased electron donating ability of the Gd⁺³ ions caused more oxidation potential whereby creating lower band gap of 0.87 eV of the Gd-TiO₃ NS. Such increased negative electrode potentials commonly found in heavily doped rare earth NCs.

3.3 SEM Spectral Determination

Figure 2 show the SEM images of the 40% heavily doped Gd NCs arrays and the picture depicts the pore diameter, wall thickness, interpore distance, and the length of the GT NCs are 90 nm, 85 nm, 60 nm and 85 nm respectively. The SEM and

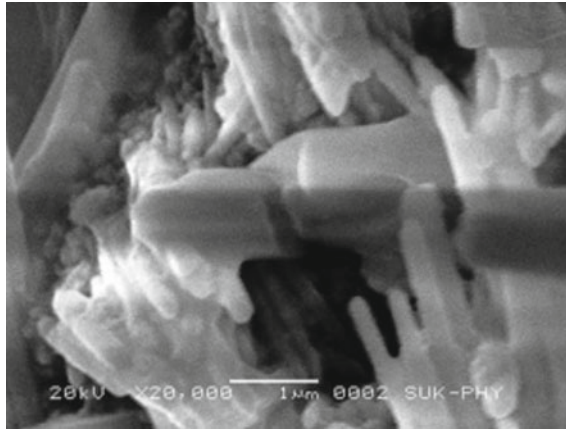


Fig. 2 SEM top view images of the Gd-TiO₃ NCs

the particle configuration were obtained using focused ion beam (FIB). The grain size of the Gd dispersed particle in the inorganic matrix was found to be 65 nm and the grain boundary distance is 90 nm. The Gd doping on the surface of the bulk hetero junction increases the surface conductivity, optical reflectivity and particles agglomerated inside the cavity of the NCs.

3.4 XRD Spectral Determination

Figure 3 shows the X ray diffraction patterns (XRD) of the Gd TiO₃ NCs recorded after the thermal annealing at 800 °C. The hybrid perovskite layer was amorphous and the crystalline phase was (112), (201), (211), (321), (311), (411) and (421) at 2θ of 22, 28, 29, 27, 30, 33, 35 respectively. The crystallinity and the tetragonal crystal

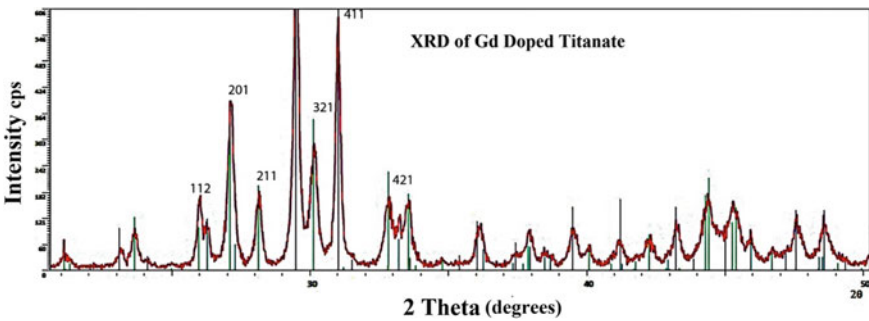
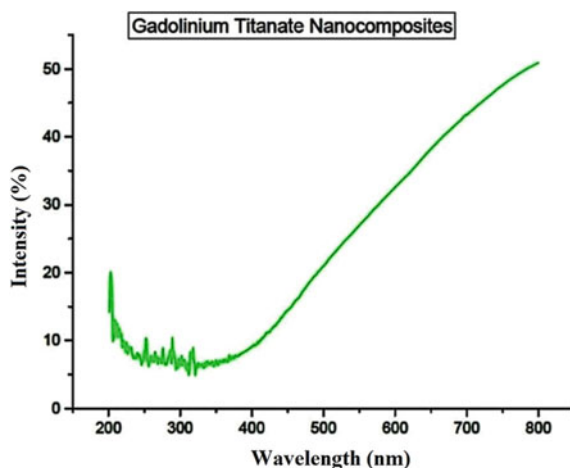


Fig. 3 XRD pattern of the 40% Gd-TiO₃ NCs

Fig. 4 UV-Visible spectrum of 40% GdTiO₃ NCs



structure of the 40% doped Gd NCs were confirmed by the dominant peak at (321), (411) corresponding to 2θ values of 30 and 33 respectively.

3.5 UV-Visible Characterization

Optical absorptivity of the 40% Gd doped NCs were recorded by using UV-Visible spectrophotometer (Fig. 4). NCs dissolved in solvent methanol and kept in a special quartz cells irradiated with UV radiation ranging in between 100 and 800 nm. The optical absorptivity of the 40% Gd-TiO₃ NS lies in between 450 nm to 800 nm spreading over broadly in visible region of the spectrum. Predominantly observed broad spectrum is due to small grain NPs and particle agglomeration. Edge displacement of the UV-Visible spectrum observed at shoulders 400 nm, at 205 nm to 300 nm and fall in the in the absorptivity is due to the dissociation of Gd⁺³ ions into the nano cavity of titanate clusters. Absorption intensity of 550 nm onwards increased effect of heavy doping of Gd was observed. Optical band gap, band energy, lattice parameters calculated by Kubeka Mulk model and the direct allowed transition calculated using the formula (Figs. 4, 5 and 6).

C -is the absorption coefficient, $h\nu$ -photon energy and E_g -optical band gap.

3.6 I-V (Current-Voltage) Characterization

I-V used to determine the total mobile charge carrier, leakage currents, resistance and time dependent conductivity performance of the sample. In rectifying mode I-V used to determine break down voltage and leakage current of dielectric films.

Fig. 5 Representing the I-V Characteristics of the 40% Gd TiO₃ NCs

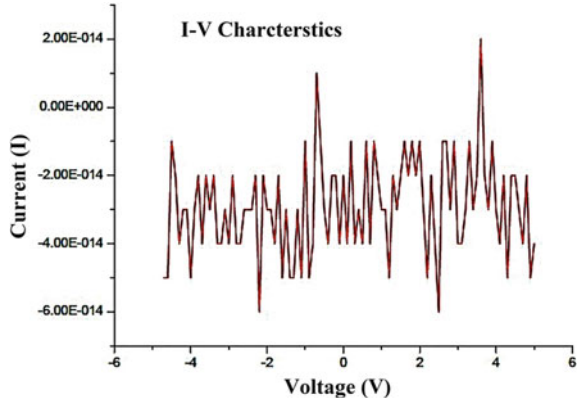
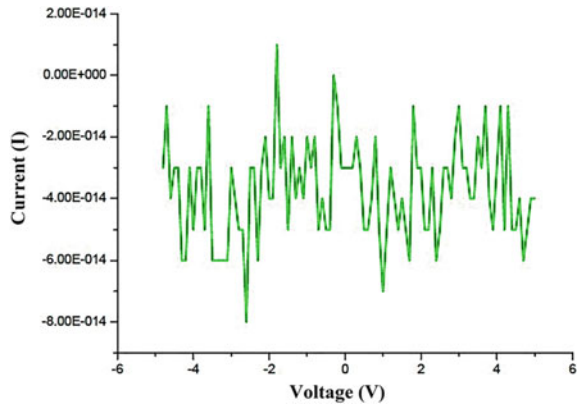


Fig. 6 Illustration of the 40% doped GT NCs I-V Curve



Leakage current can be of poole-frankel, fower-nordhein, ionic, space charge and Schooty. CV characteristics can be used to determine the permittivity and thickness and the amount of trapped and mobile charges of the sample. Dielectric Permittivity The method for the dielectric permittivity measurement is similar to the method mentioned for calibration

$$k = C d / \epsilon_0 A$$

Dielectric permittivity is proportional to capacitance which intern depends on the area of contact of Hg. This method has important applications when known new materials of known thickness are being investigated. Sample thickness measurements

$$D = k \epsilon_0 A / C$$

This method is useful when certain materials are being deposited or etched and the thickness of the film is unknown. In the present investigation, the pelletized sample of

Table 1 Conductance, Impedance and Admittance of the 40% Gd-TiO₃ NCs (Fig. 5)

Samples ^a	Voltage [V]	Conductance [S/m]	Impedance [Ω]	Admittance [S]
Gd TiO ₃	-4.5	2.20×10^{-15}	$4.50 \times 10^{+14}$	2.22×10^{-15}
Gd TiO ₃	-202	2.73×10^{-14}	$3.67 \times 10^{+14}$	2.73×10^{-14}
Gd TiO ₃	-0.7	-1.43×10^{-14}	$-7.00 \times 10^{+13}$	-1.43×10^{-14}
Gd TiO ₃	2.5	-2.40×10^{-14}	$-4.17 \times 10^{+14}$	-5.56×10^{-15}
Gd TiO ₃	3.6	5.56×10^{-15}	$1.80 \times 10^{+14}$	5.16×10^{-15}

^aSamples of Gd TiO₃ under different trails of I-V

Table 2 Conductance, Impedance, Admittance and power dissipation of the 40% Gd-TiO₃ NCs (Fig. 6)

Samples ^a	Voltage [V]	Conductance [S/m]	Impedance [Ω]	Admittance [Siemens]	Power dissipation
GdTiO ₃ (P1)	-3.6	2.77×10^{-15}	$3.60 \times 10^{+14}$	2.78×10^{-15}	3.60×10^{-14}
GdTiO ₃ (P2)	-1.8	-5.55×10^{-15}	$-1.80 \times 10^{+14}$	-5.56×10^{-14}	-1.80×10^{-14}
GdTiO ₃ (P3)	-0.3	5.06×10^{-15}	$-1.97 \times 10^{+14}$	-3.60×10^{-14}	-0.90×10^{-14}
GdTiO ₃ (P4)	1.8	-3.33×10^{-15}	$-3.00 \times 10^{+14}$	-5.60×10^{-15}	-1.80×10^{-14}
GdTiO ₃ (P5)	3.0	-2.70×10^{-15}	$-3.70 \times 10^{+14}$	-3.60×10^{-15}	-3.00×10^{-14}
GdTiO ₃ (P6)	3.7	-2.77×10^{-15}	$-4.10 \times 10^{+14}$	-2.70×10^{-15}	-3.70×10^{-14}
GdTiO ₃ (P7)	4.1	-2.43×10^{-15}	$-4.30 \times 10^{+14}$	-2.44×10^{-15}	-4.10×10^{-14}
GdTiO ₃ (P8)	4.3	-2.32×10^{-15}	$-4.40 \times 10^{+14}$	-2.33×10^{-15}	-4.30×10^{-14}

^aDifferent trials of the Gd TiO₃ nanocomposites of heavy (40%) doping

40% doped gadolinium was subjected for the I-V measurements and the summarized two best results are tabulated in the Table 1 and Table 2 respectively. The completely non linearity in the values of the current gain (J), Conductivity, Admittance and power dissipation factor was observed for the 40% doped gadolinium into the titante matrix. The experiments were carried out from voltage ranging from -4.5 V to +4.5 V while the total current gain varies non linearly. The conductivity value varies from 2.2×10^{-15} to 5.56×10^{-15} S and the Impedance of the sample vary from $4.50 \times 10^{+14}$ to $-7.00 \times 10^{+13}$ O. At 2.5 V the admittance value was found to be 5.56×10^{-15} , whereas the power dissipation factor varies from -0.90×10^{-14} to 3.60×10^{-14} . Increased negative potential observed with increase in applied voltage (3.0 V to 4.4 V) of the pelletized sample under investigation.

4 Results and Discussion

Rare earth doped inorganic hybrid NCs synthesized by low cost co precipitation method. In the present investigation Gd doped titanate NS prepared (10 to 40%) subsequently characterized by CV, SEM, XRD and UV-Visible spectroscopic techniques. Redox potentials, band gap, band energy calculated from CV and UV-visible spectroscopic analysis and optical band gap of 40% doped NS was found to be 0.89 eV. The particle size, grain boundary distance and the shape of the NCs determined from the SEM, XRD measurements. SEM revealed pore diameter, wall thickness, interpore distance, and the length of the GT NCs are 90 nm, 85 nm, 60 nm and 85 nm and XRD exhibited tetragonal crystal structure. I-V characteristics of the palatalized 40% Gd-TiO₃ exhibited non linearity in current gain, Impedance, conductance and power dissipation factor. All values related to the I-V varies non linearly, the conductivity value varies from 2.2×10^{-15} to 5.56×10^{-15} S/m and the impedance in between $4.50 \times 10^{+14}$ to $-7.00 \times 10^{+13}$ O. At 2.5 V the admittance value was found to be 5.56×10^{-15} , whereas the power dissipation factor fluctuate between -0.90×10^{-14} to 3.60×10^{-14} . Applied voltage varied between 3.0 V to 4.4 V. As the applied voltage increases power dissipation value tends to become more negative and varies non linearly from -3.00×10^{-14} to -4.30×10^{-14} .

5 Conclusion

In summary, Perovskite NCs of Gd-TiO₃ synthesized by co precipitation method and pelletized samples studied I-V properties. The 40% Gd doped NCs material was characterized by CV, SEM, UV-Visible, and I-V spectroscopic methods. Optical band gap of 0.89 eV calculated from UV-Visible spectrum, XRD exhibited tetragonal crystal structure and SEM showed grain and grain boundary distances of 85 nm and 90 nm respectively. I-V measurements of the powdered samples exhibited non-linear variation in current gain, capacitance, admittance and power dissipation due to heavily doping of Gd⁺³ ions over titanate NCs which results in facile transfer of electrons during surface conductivity of the NCs. Rare earth metal doped NCs finds applications in photodiodes, super capacitor and in the field of optoelectronics

Acknowledgements Authors are thankful to MSRIT, Bangalore, CENSE, IISc, Bangalore and Shivaji University, Kolhapur, Karnataka, India for their continuous support for all the needful experimentations and characterizations.

References

1. Smith TF, Waterman MS (1981) Identification of Common Molecular Subsequences. *J Mol Biol* 147:195–197

- Dang ZM, Shehzad K, Zha JW, Hussain T, Jun N, Bai J (2011) On refining the relationship between aspect ratio and percolation threshold of practical carbon nanotubes/polymer nanocomposites. *Jpn J Appl Phys* 50:8
- Chen Y, Wang S, Pan F, Zhang J (2014) A numerical study on electrical percolation of polymer-matrix composites with hybrid fillers of carbon nanotubes and carbon black. *J. Nanomater.* 614797:9
- Nanda GS, Sravendra R, Jae WC, Lin L, Siew HC (2010) Polymer nanocomposites based on functionalized carbon nanotubes. *Prog Polym Sci* 35:837–867
- Kim KS, Park SJ (2011) Influence of amine-grafted multi-walled carbon nanotubes on physical and rheological properties of PMMA-based nanocomposites. *J Solid State Chem* 184:3021–3027
- Cui LJ, Geng HZ, Wang WY, Chen LT, Gao J (2013) Functionalization of multi-wall carbon nanotubes to reduce the coefficient of the friction and improve the wear resistance of multi-wall carbon nanotube/epoxy composites. *Carbon* 54:277–282
- Guadagno L, De Vivo B, Di Bartolomeo A (2011) Effect of functionalization on the thermo-mechanical and electrical behavior of multi-wall carbon nanotube/epoxy composites. *Carbon* 49:1919–1930
- Wang Y, Rho WY, Yang HY, Mahmoudi T, Seo S, Lee DH, Hahn YB (2016) Air-stable, hole-conductor-free high photocurrent perovskite solar cells with $\text{CH}_3\text{NH}_3\text{PbI}_3$ -NiO nanoparticles composite. *Nano Energy*. 27:535–544
- Kojima A, Teshima K, Shirai Y, Miyasaka T (2009) Organometal Halide Perovskite as Visible-Light Sensitizers for Photovoltaic Cells. *J Am Chem Soc* 131:6050–6051
- Im, J.H., Lee, C.R., Lee, J.W., Park, S.W., Park, N.G.: 6.5% efficient perovskite quantum-dot-sensitized solar cell. *Nanoscale*. 3, 4088–4093 (2011)
- Lee MM, Teuscher J, Miyasaka T, Murakami TN, Snaith HJ (2012) Efficient hybrid solar cells based on meso-structured organometal halide perovskite. *Science* 338:643–647
- Etgar L, Gao P, Xue Z, Peng Q, Chandiran AK, Liu B, Nazeeruddin MK, Gratzel M (2012) Mesoscopic $\text{CH}_3\text{NH}_3\text{PbI}_3/\text{TiO}_2$ heterojunction solar cells. *J Am Chem Soc* 134:17396–17399
- Suresh, A.K., Pelletier, D.A., Wang, W., Morrell-Falvey, J.L., Gu, B.H., Doktycz, M.J.: Cytotoxicity induced by engineered silver nanocrystallites is dependent on surface coatings and cell types. *Langmuir*. 28, 2727–2735 (2012)
- Tabata Y, Ikada Y (1988) Macrophage phagocytosis of biodegradable microspheres composed of l-lactic acid/glycolic acid homo- and copolymers. *J Biomed Mater Res* 22:837–858
- Schlinkert P, Casals E, Boyles M, Tischler U, Hornig E, Tran N, Zhao J, Himly M, Riediker M, Oostingh GJ (2015) The oxidative potential of differently charged silver and gold nanoparticles on three human lung epithelial cell types". *J. Nanobiotechnology*. 13:1
- Tiyaboonchai W.: Chitosan nanoparticles: A promising system for drug delivery". *Naresuan University Journal*. 11, 51–66 (2003)
- Baker C, Pradhan A, Pakstis L, Pochan DJ, Shah SI (2005) Synthesis and antibacterial properties of silver nanoparticles". *J Nanosci Nanotechnol* 5:244–249
- Ladjouzi, S., Tala-Ighil, R., Iratn, A.: Ray irradiation effect on $\text{GdBO}_3/\text{silica}:\text{Ce}^{3+}$ others, – Ray irradiation effect on $\text{GdBO}_3/\text{silica}:\text{Ce}^{+3}$ composite prepared by sol gel method *Radiation Physics and Chemistry composite prepared by sol gel method. Radiat. Phys. Chem.* 114, 1–4 (2015)
- Nazaretski E, Merithew RD, Kostroun VO (2004) Effect of low-level radiation on the low temperature acoustic behavior of a SiO_2 . *Phys Rev Lett* 92:
- Wang T, Ma W, Shangguan J, Jiang W, Zhong Q (2014) Controllable synthesis of hollow mesoporous silica spheres and application as support of nano-gold. *J Solid State Chem* 215:67–73
- Li J, Feng Y, Zhang X (2015) Near-field radiative heat transfer across a pore and its effects on thermal conductivity of mesoporous silica. *Physica B Condens. Matter.* 456:237–243
- Dhas NA, Raj CP (1998) Synthesis, characterization, and properties of metallic copper nanoparticles. *Chem Mater* 10:1446–1452

23. Wang YQ, Nikitin K, Mc Comb DW (2008) Fabrication of Au–Cu₂O core–shell nanocube heterostructures. *Chem Phys Lett* 456:202–205
24. McFarland EW, Siripala W, Ivanovskaya A, Jaramillo TF, Baeck SH (2003) A Cu₂O/TiO₂ heterojunction thin film cathode for photo electro catalysis. *Solution Energy Materials Solution Cells*. 77:229–237
25. Li, D., Chien, C.J., Deora, S., Chang, P.C., Moulin, E., Lu, J.G.: Prototype of a scalable core-shell Cu₂O/TiO₂ solar cell. *Chem. Phys. Lett.* 501, 446–450 (2011)
26. Zainun, A.R., Tomoya, S., Noor, U.M., Rusop, M., Masaya, I.: New approach for generating Cu₂O/TiO₂ composite films for solar cell applications. *Mater. Lett.* 66, 254–256 (2012)
27. Liu J, Durstock M, Dai L (2014) Graphene oxide derivatives as hole- and electron-extraction layers for high-performance polymer solar cells, a Review. *Energy Environ Sci* 7:1297–1306
28. Yonghua C, Wei-Chun L, Jun L, Liming D (2014) Graphene oxide-based carbon interconnecting layer for polymer tandem solar cells. *Nano Lett* 14:1467–1471
29. Akimoto, K., Ishizuka, S., Yanagita, M., Nawa, Y., Paul, G.K., Sakurai, T.: Thin film deposition of Cu₂O and application for solar cells. *J. Sol. Energy*. 80, 715–722 (2006)
30. Izaki M, Mizuno K, Shinagawa T, Inaba M, Tasaka A (2006) Photochemical construction of photovoltaic device composed of p-copper (I) oxide and n-zinc oxide. *J Electrochem Soc* 153:C668–C672
31. Prasanta S, Mitali S (2015) Synthesis of zinc oxide nanoparticles using tea leaf extract and its application for solar cell. *Bull Mater Sci* 38:1–5
32. Monica D, Prasanta S, Mitali S (2015) Synthesis of ZnO nanocomposites for photovoltaic applications. *J Indian Chem Soc* 92:1–4
33. Johan MR, Wen KS, Hawari N, Aznan NAK (2012) Synthesis and characterization of copper (I) iodide nanoparticles via chemical route. *Int J Electrochem Sci* 7:4942–4950
34. Kim YH, Kang YS, Lee WJ (2006) Synthesis of Cu nanoparticles prepared by using thermal decomposition of Cu-oleate complex. *Mol Cryst Liq Cryst* 445:231–238
35. Murray IP, Lou SJ, Cote LJ, Loser S (2011) Graphene oxide interlayers for robust, high-efficiency organic photovoltaic. *J. Phys. Chem. Lett.* 2:3006–3012

Charge Pump Circuit Based Grid-Tied PV System for Single Phase Transformer Less Inverter Using Fuzzy Logic Controller



Anil Tekale and Swapna God

Abstract Nowadays leakage current is the challenge for the inverter circuit. Elimination of this current is necessary to prevent damage to such devices. Hence, in this article elimination of leakage current is presented where the charge pump circuit concept has been implemented with a fuzzy logic control strategy. At the time of the negative cycle, the charge pump circuit creates a negative output voltage for a proposed system. There are many advantages of the proposed plan: its compact size, minimum cost; the generated dc voltage of the proposed method is similar to the full-bridge inverter. The capability of grounding combination is fair, flexible, reactive power flow and better efficiency. Simulation results have been discussed for the proposed inverter, eliminating and also its real-time application in a grid-tied photovoltaic system is described. With the help of a fast Fourier transform, THD is measured and explained in the article.

Keywords Charge pumps · Fuzzy control · Photovoltaic systems · Pulse width modulation inverters · Leakage currents

1 Introduction

Photovoltaic (PV) systems have become quite widespread among renewable energy sources throughout the last two decades. In contrast, they produce electricity without mechanical parts, work quietly without pollution and require little maintenance [1, 2]. Distributed grid-connected PVs play an increasingly important role as an integral part of the electrical network. However, PV systems suffer from a standard high mode (CM) current due to the large stray capacitors between the PV panels and the ground, decreasing system performance and can cause safety issues such as electrical shock. Transformers are widely used in the PV network to provide galvanic insulation to remove the leakage currents. However, it possesses undesirable properties with significant losses, including wide-scale, rising cost and weight.

A. Tekale (✉) · S. God
University in Solapur, SVERI's College of Engineering, Punyashlok Ahilyadevi Holkar Solapur
University, Solapur 413304, Maharashtra, India
e-mail: aatekale@coe.sveri.ac.in

Therefore, eliminating the transformer is an excellent benefit for further increasing the overall device performance, reducing the size and weight [3]. The proposed topology consists of only four power switches, thereby minimising the semiconductors' cost and increasing the power quality by three-level output voltage to minimise the ripple of output current [4].

The current flows through two switches during the proposed inverter operation; hence, the conduction's loss is lower. The proposed inverter using dc voltage is the same as the FB inverter (as opposed to the NPC, ANPC, and half-bridge (HB) inverters) [5].

2 Transformer Less Inverter

Inverters are used to transform DC electricity into the AC electricity in PV systems. Low DC voltage (which could be 12 V, 24 V, 48 V,) is now mostly converted in PV systems to much higher AC voltage (around 230 V) than we can use in our electrical appliances. The transformer is present within the inverter to increase the voltage. An oversized transformer is current in the Low-Frequency Inverter. The low-frequency inverters are ideal for handling high impedance loads, such as pumping or compressor operations [7].

For a typical inverter, the internal transformer provides galvanic isolation. Conventional inverters are equipped with an internal transformer that synchronises the DC voltage with the AC output, the distinction between traditional and transformer fewer inverters is. Transformerless inverters use an automated multi-step process and electronic components to convert DC to high-frequency AC, back to DC and eventually to standard frequency AC [8].

3 Different Modes of Operation

Figure 1 Show a single-phase grid-tied transformerless inverter with CM current direction, where P and N are both positive and negative PV terminals. The leakage current ($i_{Leakage}$) flows between the filters (L1 and L2), the inverter, grid, and ground impedance (z_g) through a parasitic condenser (CP). This leakage current can cause safety issues, reduce the current injection quality to the grid, and decrease the system's efficiency [9].

The CM voltage (CMV) (v_{cm}) must be maintained constant during all operating modes according to [10] to remove the leakage present. The v_{cm} is determined as follows: with two filter inductors (L1, L2)

$$V_{cm} = \frac{V_{An} + V_{Bn}}{2} + \frac{(V_{An} - V_{Bn})(L1 - L2)}{2(L1 + L2)} \quad (1)$$

V_{An} and V_{Bn} are the difference in voltage between the inverter’s midpoints A and B to the dc bus minus terminal N. If $L1 = L2$ (asymmetric inductor), v_{cm} is measured as per (1), and the current of leakage appears due to a varying CMV. If $L1 = L2$ (symmetric inducer) simplifies the v_{cm} .

$$V_{cm} = \frac{V_{An} + V_{Bn}}{2} = Constant \tag{2}$$

The CMV is stable in this condition, and the current from the leakage is removed. Each filter change pump circuits While inductors is zero in certain systems, such as the virtual dc-bus inverter and the NPC inverter, and only each filter inducer is used. In this case, it will have a constant value according to (3) after simplification of v_{cm} , and the current of leakage will be removed.

$$V_{cm} = \frac{V_{An} + V_{Bn}}{2} + \frac{(V_{An} - V_{Bn})}{2} = Constant(L1 = 0)$$

Then,

$$V_{cm} = \frac{V_{An} + V_{Bn}}{2} - \frac{(V_{An} - V_{Bn})}{2} = Constant(L1 = 0) \tag{3}$$

4 Methodology

4.1 Charge Pump Circuit Concept

A charge pump is a DC to DC converter that uses energetic charge storage condensers to increase or decrease voltage. While being electrically simple circuits, Charge pump circuits are capable of high efficiencies, often as high as 90–95 per cent. It uses some form of switching devices to monitor supply voltage link via a condenser over a load. In a two-stage loop, the condenser is connected over the supply in the first stage, charging it to the same voltage [12]. The circuit is reconfigured in the second step so that the condenser is in series with the supply and the load. This doubles the voltage through the sum of the original supply and the capacitor voltages over the load. Using an output condenser also smoothes the pulsing nature of the higher voltage switched output.

Additional or secondary circuit power the switching up too many megahertz, usually at tens of kilohertz. The high frequency minimises the capacitance required, as lower charges must be stored and dumped in a shorter period. Charge pumps can double voltages, triple voltages, half voltages, invert voltages, multiply fractionally or scale voltages, and produce arbitrary voltages by swiftly switching modes, depending on the controller and topology of the circuits. They are widely used in low-power

electronics (such as cell phones) to boost and lower voltages for various parts of the circuitry and reduce power consumption by carefully regulating supply voltages.

The definition of a simple charge pump circuit for generating the inverter negative output voltage in the proposed topology is shown in Fig. 2. The course consists of two diodes (D1, D2) and two capacitors (C1, C2). This simple charge pump circuit gives a negative dc output voltage at C equal to point A [6].

The C1 condenser is used to connect the A voltage point to node D. The output voltage is pumped with two Schottky diodes D1 and D2. When the diode D2 is forward biased, the capacitor C1 is charged by diode D2. The diode D1 is reversed in this state. Once the D1 diode conducts, the C2 condenser is set via the C1 condenser using node n and the S2 switch. The negative charge pump circuit (vCn) can be generated in a steady state [11].

$$V_{cm} = -V_{dc} + V_{cut - in - D1} + V_{cut - in - D2} \tag{4}$$

V_{dc} is the voltage of the inputs, V_{cut - in - D1} and V_{cut - in - D2} are the voltages of the diodes D1 and D2, respectively. Such values can be marginal for high power applications. Using additional switching devices, the above concept

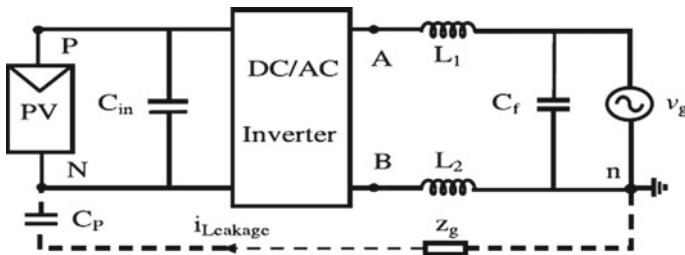


Fig. 1 Single Phase Grid Connected Transformer Less Inverter with a Leakage Current Path

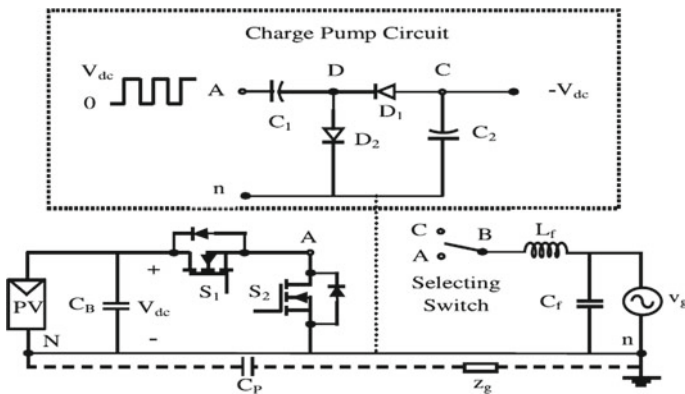


Fig. 2 Schematic diagram of the proposed inverter including the charge pump circuit

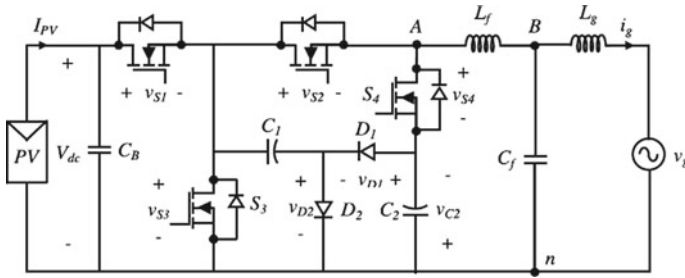


Fig. 3 Proposed single-phase transformer less grid suggested inverter voltage connected inverter

is incorporated into the proposed inverter. For the summary, the charging pump circuit in the less inverter transformer has the following characteristics for grid-tied applications.

1. This circuit has a standard line with the input dc voltage negative terminal and the grid neutral point which causes the leakage current to be removed.
2. The charge pump circuit does not have an active system, and the cost for grid-tied applications is smaller.

4.2 Proposed Topology

As illustrated in Fig. 3, The proposed topology consists of four power switches (S1 – S4), two diodes (D1, D2), two condensers (C1, C2) centred on the pump load circuit as defined in the previous section [13].

5 Simulation Results

The results of the proposed grid-connected inverter operation are shown in Fig. 4. Due to the three-level inheritance of the output voltage, the output current and the suggested inverter voltage are drain-source sinusoidal with low harmonic distortion. The condenser and diode strain stress is shown in Fig. 5.

Simulation outcomes for switch drain-source voltage are shown in Fig. 6.

6 Conclusion

This study uses a charging pump circuit design with the fuzzy controller to introduce a new single-phase transformer, less inverter for a grid-tied PV network. Therefore, the principal principle of the proposed device is to produce the negative output voltages

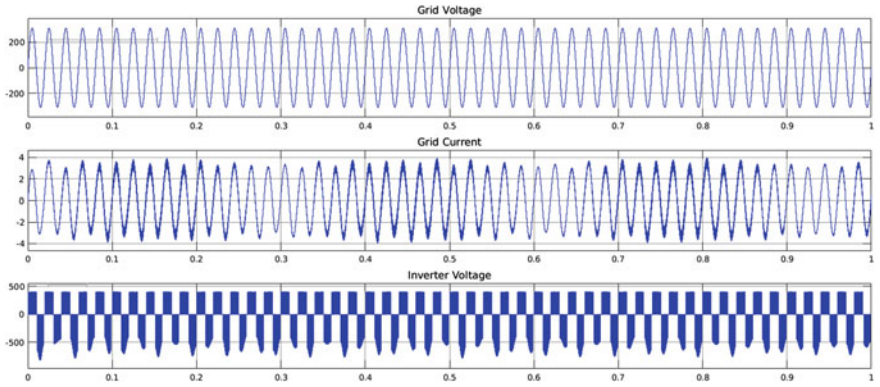


Fig. 4 Simulation results of the proposed topology (a) Grid Voltage V_g (b) Grid Current I_g (c) Inverter Voltage V_{An}

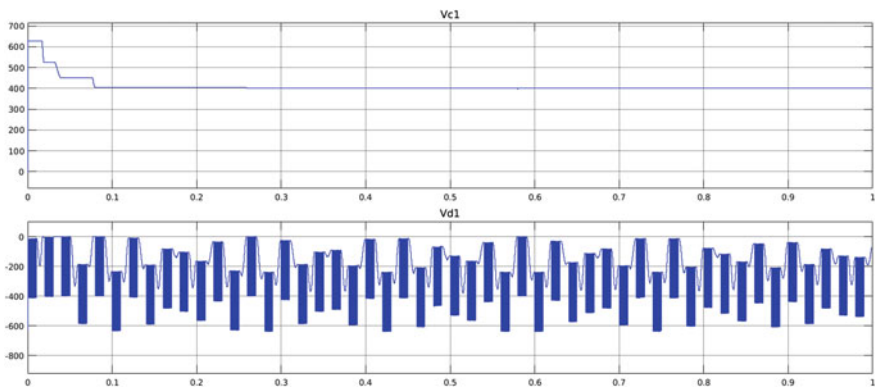


Fig. 5 Simulation results of the capacitor and diode voltages. **a** Capacitor Voltage **b** Diode Voltage

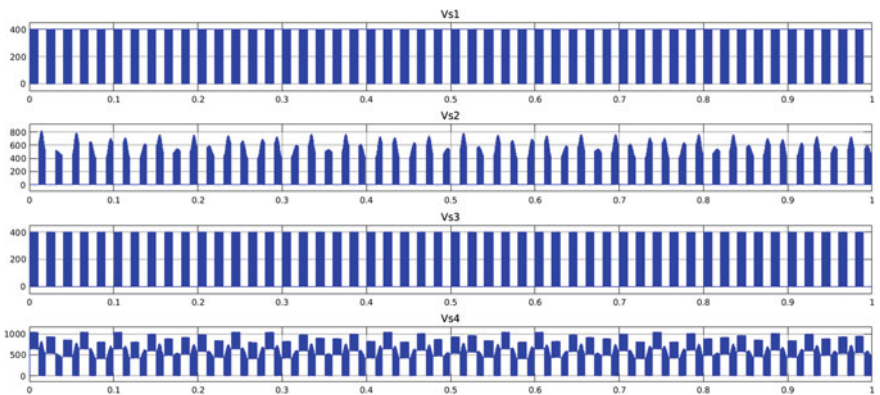


Fig. 6 Simulation results of the Switches **a** Vs1 **b** Vs2 **c** Vs3 **d** Vs4

generated in this proposed inverter. Consequently, we design the proposed topology close to the neutral line in the grid; thus, the leakage current will be suppressed, and the transformer is eliminated. Also, the proposed topologies have the potential to deliver the reactive power needed into the grid. The efficiency depicted by the proposed inverter is strong compared with other current Transformer, fewer topologies.

Thus, the proposed topology is used to realize the minimum number of components and achieve higher power density with lower design expense. Using the outcome of the simulation, we can check the device proposed.

References

1. S. B. Kjaer, J.K. Pedersen, and F. Blaabjerg, (2005) "A review of single-phase grid-connected inverters for photovoltaic modules," *IEEE Trans. Ind. Electron.*, vol. 41, no. 5, pp., 1292–1306.
2. Guo X, He R, Jian J, Lu Z, Sun X, Guerrero JM (2016) Leakage current elimination of four-leg inverter for transformerless three-phase PV systems. *IEEE Trans. Power Electron.* 31(3):1841–1846
3. Cha W-J, Kim K-T, Cho Y-W, Lee S-H, Kwon B-H (2015) Evaluation and analysis of transformerless photovoltaic inverter topology for efficiency improvement and reduction of leakage current. *IET Power Electron.* 8(2):255–267
4. Xiao H, Xie S (2010) Leakage current analytical model and application in single-phase transformerless photovoltaic grid-connected inverter. *IEEE Trans. Electromagn. Compact.* 52(4):902–913
5. Bruckner T, Bernet S, Guldner H (2005) The active NPC converter and its loss-balancing control. *IEEE Trans. Ind. Electron.* 52(3):855–868
6. L. C. Breazeale and R. Ayyanar, (2008) "A photovoltaic array transformerless inverter with film capacitors and silicon carbide transistors," *IEEE Trans. Power Electron.*, vol. 30, no. 3, pp. 1297–1305, Mar. 2015. F. Hong, R. Z. Shan, H. Z. Wang, and Y. Yangon, "Analysis and calculation of inverter power loss," *Proc. CSEE*, vol. 28, no. 15, pp. 72–78.
7. Tekale, Anil, et al. (2017) "A Review Paper on Power Quality Issues and Mitigation Strategies." *Journal for Advanced Research in Applied Sciences* 51–57.
8. Tekale, Anil, Radharaman Saha, Pratik Ghutke, and Swapna God, (2019) "Implementation of Fuzzy Based Grid-Tied PV System for Single Phase Transformer Less Inverter with Charge Pump Circuit Concept."
9. Potdar, A., Ghutke, P., Potdar, D., & Tekale, A. (2019). *Matlab Modelling and Simulation of Reconfigurable Solar Converter: A Single-Stage Power Conversion Pv-Battery System.* *Journal on Electrical Engineering*, 12(4).
10. M. Saitou and T. Shimizu, (2002) "Generalized theory of instantaneous active and reactive powers in single-phase circuits based on Hilbert transform," in *Proc. 33rd Annu. IEEE Power Electron. Spec. Conf.*, vol. 3, pp., 1419–1424.
11. Y. Yang, F. Blaabjerg, and H. Wang, (2014) "Low voltage ride-through of single-phase transformerless photovoltaic inverters," *IEEE Trans. Ind. Appl.*, vol. 50, no. 3, pp., 1942–1952.
12. J. M. Shen, H. L. Jou, and J. C. Wu, (2012) "Novel transformerless grid-connected power converter with negative grounding for photovoltaic generation system," *IEEE Trans. Power Electron.*, vol. 27, no. 4, pp., 1818–1829.
13. Y. Wang and R. Li, (2013) "Novel high-efficiency three-level stacked-neutral point-clamped grid-tied inverter," *IEEE Trans. Ind. Electron.*, vol. 60, no. 9, pp., 3766–3774.

Fabrication and Characterization of Composite Material Connecting Rod



G. G. Deshpande, H. P. Borate, and S. S. Wangikar

Abstract This paper mainly focuses on the fabrication and characterization of connecting rods made by composite material. This composite material is obtained by using E Glass fibre, Epoxy Resin, Fly Ash and MWCNT. There are three types of compositions observed for different testing. These compositions are C1 (Epoxy—70%, E-Glass—21%, Fly Ash—8%, MWCNT—1%), Composition C2 (Epoxy 52%, E-Glass—32%, Fly Ash—15%, MWCNT—1%), & Composition C3 (Epoxy—42%, E-Glass—42%, Fly Ash—15%, MWCNT—1%).

Keywords Design · Epoxy resin · E-glass fibre · Mwcnt · Forged steel · Solidworks

1 Introduction

The recent development in metallurgy or material science is to develop composite materials as the alternatives for recent one with enhanced properties. On the same basis, this paper presents a composite material using E-Glass Fibre, Epoxy Resin, Fly Ash, and MWCNT. This composite has been made in three types of compositions, through which the better one has been taken in consideration as an alternative for forged Steel by comparing these materials. The composite material is a homogeneous mixture of more than one material. The composite has specified enhanced properties as per the requirement for particular applications.

This paper has focused on such composite material made up as a connecting rod for different applications. The most common applications of connecting rods are in automobile engines, in electrical generators, and in turbines. In this project, this design and fabrication of the connecting rod does not focus on any of the specific applications. The main motto for developing this project is to suggest only alternatives for existing material. There is very less chance of engine failure due to breakage of

G. G. Deshpande (✉) · H. P. Borate
VPKBIET, Baramati, Maharashtra, India

S. S. Wangikar
SVERI's COE, Pandharpur, Maharashtra, India

connecting rod in general an automobile, but there is a large impact of connecting rod failure in other applications such as aerospace engines or electricity generators.

In this paper there are three types of composition are studied which are composition C1 (Epoxy—70%, E-Glass—21%, Fly Ash—8%, MWCNT—1%), Composition C2 (Epoxy 52%, E-Glass—32%, Fly Ash—15%, MWCNT—1%), & Composition C3 (Epoxy—42%, E-Glass—42%, Fly Ash—15%, MWCNT—1%). Then further the better one of these three C1, C2, and C3 has been used to compare with Forged Steel for results. Also this paper has a design of connecting rod using Solidworks and simulation for result and experimental validation of design against static conditions. The most common material for connecting rod is Forged Steel and hence there is comparison between composite and forged steel has been done.

2 Literature Review

Suraj Pal [1] In this paper Finite element analysis of single cylinder four stroke petrol engines is taken for the study; Structural systems of Connecting rod can be easily analyzed using Finite Element techniques. So firstly a proper Finite Element Model is developed using Cad software Pro/E Wildfire 4.0. Then static analysis is done to determine the von Misses stress, shear stress, elastic strain, total deformation in the present design connecting rod for the given loading conditions using Finite Element Analysis Software ANSYS.

Naga Malleshwara Rao [2] The main Objective of this work is to explore weight reduction opportunities in the connecting rod of an I.C. engine by examining various materials such as Genetic Steel, Aluminium, Titanium and Cast Iron. This was entailed by performing a detailed load analysis.

Sudershan Kumar [3] This paper describes modeling and analysis of connecting rod. In this project connecting rod is replaced by Aluminium reinforced with Boron carbide for SuzukiGS150R motorbike. A 2D drawing is drafted from the calculations. A parametric model of connecting rod is modeled using PRO-E 4.0 software. Analysis is carried out by using ANSYS software.

B. Anusha and C. VijayaBhaskar Reddy [4] In this paper a static analysis is conducted on a connecting rod of a single cylinder 4-stroke petrol engine. The model is developed using Solid modeling software i.e. PRO/E (Creo-parametric). Further finite element analysis is done to determine the von-misses stresses shear stress and strains for the given loading conditions.

B. Anusha and Dr. C. VijayaBhaskar Reddy [5]. The modeled connecting rod imported to the analysis software i.e. ANSYS. Static analysis is done to determine von-misses stresses, strain, shear stress and total deformation for the given loading conditions using analysis software i.e. ANSYS.

Mr. H. B. Ramani [6] In this study, detailed load analysis was performed on connecting rod, followed by finite element method in Ansys-13 medium. In this regard, In order to calculate stress in Different part of connecting rod, the total forces exerted connecting rod were calculated and then it was modeled, meshed and loaded

in ANSYS software. The maximum stresses in different parts of connecting rod were determined by Analysis. The maximum pressure stress was between pin end and rod linkages and between bearing cup and connecting rod linkage.

Dr. N. A. Wankhede [7], admits a paper attempts to design and analyze the connecting rod used in a diesel engine in context of the lateral bending forces acting along its length during cycle of it The lateral bending stress are commonly called as whipping stress and this whipping stress forms the base of evaluation of performance of various materials that can be used for manufacturing of connecting rod.

Bansal [8], conducted a dynamic simulation on a connecting rod made of aluminum alloy using FEA. In this analysis of connecting rod were performed under static load for stress analysis and optimization. Static load analysis was performed to determine the in von-mises stresses of the connecting rod.

3 Methodology

3.1 Problem Statement

The connecting rod of an engine or generator or turbine undergoes a number of stresses such as compressive force during expansion of gasses and tension force during work done on the gases. Also shear force occurs at the gudgeon pin at piston and shear force occurs at crank pin end of the connecting rod. In addition to this, thermal stresses are also produced when the engine is in working condition. These forces have a direct effect on engine speed. Generally these mentioned forces causes' failure of the connecting rod. This phenomenon is known as the throwing of connecting rods. There are many other reasons for failure such as improper alignment or lack of lubricant also may cause failure. Whether, it has a very less percentage of engine failure due to breakage of connecting rod. But it may be a great issue in a turbine or generator.

3.2 Design of Connecting Rod Using Solidworks

Solidworks is a design platform to produce various models with all necessary design aspects & also allows going for simulated analysis with different conditions like Static, Fatigue, Drop test etc. and many more. It also helps in design of very complex parts and assemblies. Figure 1 shows the CAD drawing of connecting rod.

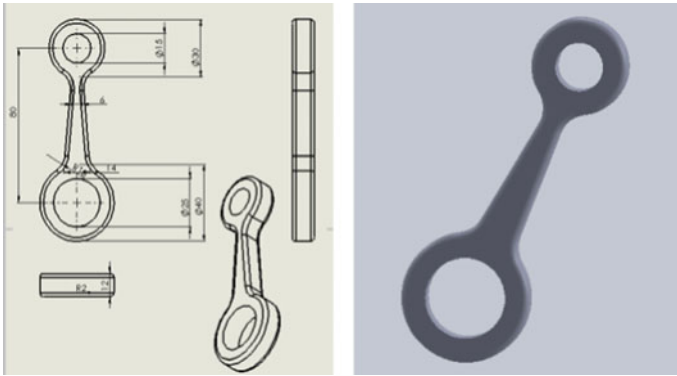


Fig. 1 Design of connecting rod using Solid Works

3.3 Model Making Procedure

- a. Prepare the mould as per the design with considering factors such as shrinkage allowance and distortion effect.
- b. Take the liquid epoxy in the required amount as per mentioned in composition.
- c. Then add hardener in the proportion as 1:3 to epoxy resin i.e. if epoxy is in 30 g then add 10 g of hardener to it.
- d. Then stir it well as a result the white viscous liquid forms as a homogeneous product.
- e. Take E-Glass, Fly Ash, and MWCNT in the proper amount as per the requirement in each composition.
- f. Mix well to become a proper mixture of these three materials.
- g. Put this mixture of each composition in the die or mould.
- h. Fill the die or mould completely with these materials.
- i. Pour the homogeneous mixture of epoxy and hardener in the mould cavity very carefully to avoid bubble formation.
- j. Press the mixture in die cavity well to fulfil the die or mould completely.
- k. Set the material and keep it solidified for a minimum 24 h.
- l. After 24 h, the components are ready for use.

3.4 Experimental Set Up

Figure 2 indicates the experimental set up.

1. Dimension of the test piece is measured at three different places along its height/length to determine the average cross-section area.
2. Ends of the specimen should be plain so that the ends are tested on a bearing plate.



Fig. 2 Experimental Testing Set Up

3. The specimen is placed centrally between the two compressions plates, such that the centre of moving head is vertically above the centre of specimen.
4. Load is applied on the specimen by moving the movable head.
5. The load and corresponding contraction are measured at different intervals. The load interval may be as 500 kg.
6. Load is applied until the specimen fails.

Type of Testing: Static Testing

Apparatus Used: Universal Testing Machine (UTM)

Number of Specimen: 03 Nos.

Number of Tests Conducted on each specimen: 04 Nos.

Tests carried out:

1. Compressive Strength Test
2. Tensile Strength Test
3. Torsion Test
4. Flexural Shear Test

4 Result and Discussion

Figures 3 and 4 demonstrates the results of the finite element analysis. Table 1 mentions the various properties of the materials used for the connecting rod during analysis.

5 Conclusion

- a. As result indicates, the prepared materials with the composition C1, C2, & C3; it has been found that the properties of Composition C3 are much better than other two (C1 & C2).
- b. Simultaneously, all of these compositions have higher strengths than that of conventional materials used for manufacturing of connecting rods.

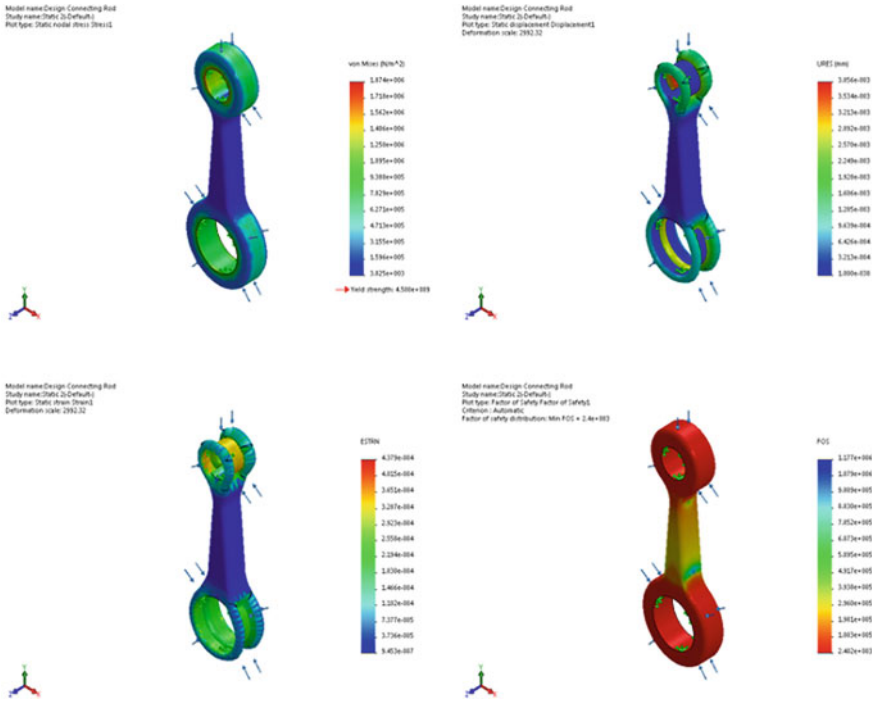


Fig. 3 Software Analysis of Forged Steel

- c. Also the weight of the component using composite material is almost equal to the forged steel so it won't matter the design of the engine.
- d. Also as compared to properties of Forges Steel, Powder metal and C-70 Alloy the composition C3 has more enhanced properties, which indicates the prepared composite can be a better alternative as a connecting rod material.

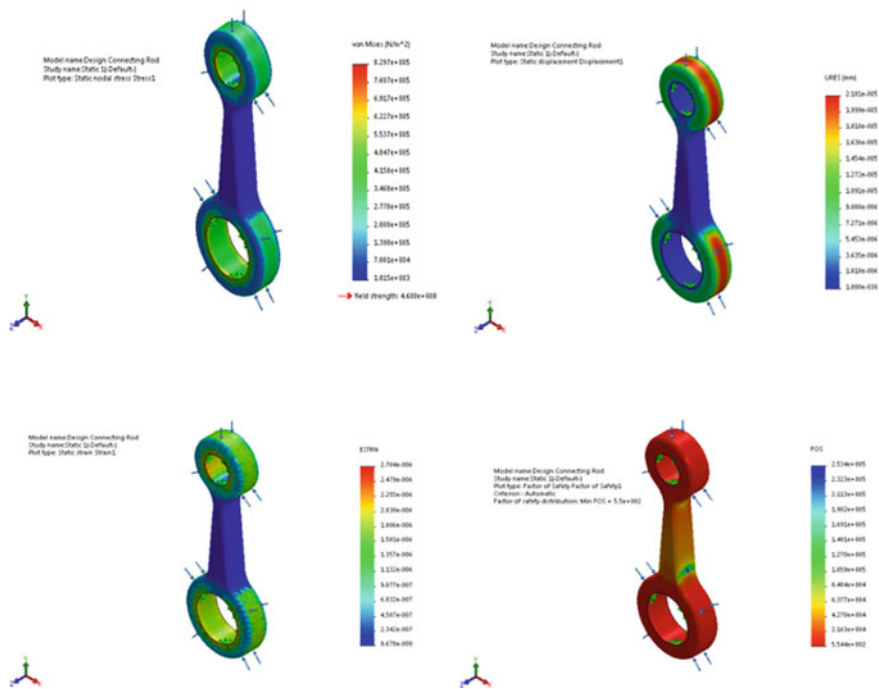




Fig. 4 Software Analysis of Composite Connecting Rod

Table 1 Properties of model

Model Reference	Properties	Component
	Name: AISI 4130 Steel Model type: Linear Elastic Isotropic Default failure criterion: Max von Mises Stress Yield strength: 4.6e+008 N/m ² Tensile strength: 7.31e+008 N/m ² Elastic modulus: 2.05e+011 N/m ² Poisson's ratio: 0.285 Mass density: 7850 kg/m ³ Shear modulus: 8e+010 N/m ²	Solid Body 1 (Fillet1) (Design Connecting Rod)
	Name: Glass Composite Model type: Linear Elastic Isotropic Default failure criterion: Max von Mises Stress Yield strength: 4.5e+009 N/m ² Tensile strength: 2.05e+009 N/m ² Compressive strength: 5e+009 N/m ² Elastic modulus: 2.875e+009 N/m ² Poisson's ratio: 0.23 Mass density: 2600 kg/m ³ Shear modulus: 3.6e+010 N/m ²	Solid Body 1(Fillet1) (Design Connecting Rod)

References

1. Suraj Pal: Design Evaluation and Optimization of Connecting Rod Parameters Using FEM, International Journal of Engineering and Management Research, Vol.-2, Issue-6, December 2012, ISSN No.: 2250-0758: 21-25.(2012)
2. G. Naga Malleshwara Rao: Design Optimization, and Analysis of a Connecting Rod using ANSYS, International Journal of Science and Research (IJSR), India Online ISSN: 2319-7064: vol2. issue7, pp. 225-229. (2013)
3. K. Sudershan Kumar: Modeling and Analysis of Two Wheeler Connecting Rod, International Journal of Modern Engineering Research (IJMER), Vol.2, Issue.5, Sep-Oct. 2012, pp-3367-3371. (2012)
4. B. Anusha, C.Vijaya Bhaskar Reddy, Modeling and Analysis of Two Wheeler Connecting Rod by Using Ansys, IOSR Journal of Mechanical and Civil Engineering (IOSR-JMCE), Volume 6, Issue 5 (May. - Jun. 2013), PP 83-87. (2013)
5. Mr. H. B. Ramani, Mr.Neeraj Kumar, Mr. P. M. Kasundra W. Li, D. Li and J. Ni: Analysis of Connecting Rod under Different Loading Condition Using Ansys Software, International Journal of Engineering Research & Technology (IJERT) Vol. 1 Issue 9, November- 2012 ISSN: 2278-0181. (2012)

6. Leela Krishna Vegi, Venu Gopal Vegi: Design and Analysis of Connecting Rod Using Forged steel, International Journal of Scientific & Engineering Research, Volume 4, Issue 6, June-2013. 2081 ISSN 2229–5518. (2013)
7. Prof. Vivek C. Pathade¹, Dr. Dilip S. Ingole: Stress Analysis of I.C.Engine Connecting Rod by FEM and Photoelasticity, IOSR Journal of Mechanical and Civil Engineering (IOSRJMCE) e-ISSN: 2278-1684 Volume 6, Issue 1 (Mar. - Apr. 2013), PP 117-125. (2013)
8. Kuldeep B, Arun L.R, Mohammed Faheem: Analysis and Optimization of Connecting Rod Using ALFASiC Composites, ISSN: 2319- 875, International Journal of Innovative Research in Science, Engineering and Technology, Vol. 2, Issue 6. (2013)

Experimental Studies on RCCI Engine Powered with n-Butanol and Thevetia Peruviana Methyl Ester



P. A. Harari, V. S. Yaliwal, and N. R. Banapurmath

Abstract In the present work, an attempt is made to study the effect of n-butanol as primary fuel along with diesel and thevetia peruviana methyl ester (TPME) as secondary fuels under reactivity controlled compression ignition (RCCI) mode of combustion. Experiments have been conducted on single cylinder compression ignition (CI) engine runs at 1500 rpm at 50% load for RCCI mode of operation by varying percentage of n-butanol in injected fuels. The results show that RCCI engine operated with 10% of n-butanol mixed with diesel exhibits higher brake thermal efficiency (BTE) as compared with other percentages of n-butanol in injected fuels. Nitric oxide (NO_x) and smoke emissions were reduced significantly for RCCI combustion mode. Beyond 10% n-butanol in injected fuels there is penalty of lower BTE and higher emissions.

Keywords Fuels · Low temperature combustion · Reactivity controlled compression ignition · Thevetia peruviana methyl ester

List of symbols

BTE	Brake thermal efficiency
CD	Combustion duration
CI	Compression ignition
CO	Carbon monoxide
CO ₂	Carbon dioxide
CP	Combustion phase
CRDI	Common rail diesel injection,
DF	Dual fuel

P. A. Harari (✉) · V. S. Yaliwal
SDM College of Engineering and Technology, Dharwad 580002, Karnataka, India

N. R. Banapurmath
BVB College of Engineering and Technology, KLE Technological University, Hubballi 580031, Karnataka, India

DFDI	Dual fuel direct injection
EGR	Exhaust gas recirculation
EGT	Exhaust gas temperature
HC	Hydrocarbon
HRF	High reactive fuel
HRR	Heat release rate
ID	Ignition delay
ITE	Indicated thermal efficiency
LRF	Low reactive fuel
LTC	Low temperature combustion
NOx	Nitric oxide
PODE	Poly oxymethylene dimethyl ether
PPR	Peak pressure rise
RCCI	Reactivity controlled compression ignition
TPME	Thevetia peruviana methyl ester

1 Introduction

Electric vehicles can be considered as a likely innovation to advance the change from regular portability to e-versatility. The genuine advantages regarding carbon dioxide (CO_2) emissions rely upon an incredible degree on their method of utilization, design of vehicle and power source. Over the most recent couple of years, progressed ignition modes as RCCI demonstrated extraordinary points of interest as far as soot and NOx emissions decrease [1]. In a RCCI combustion, when the premixed proportion of low reactive fuel (LRF) was high, inadmissible high peak pressure rise (PPR) consistently happened [2]. Dual fuel direct injection (DFDI) was one of the most encouraging approaches to control mixing process in a dual fuel (DF) engine [3]. Pan et al. [4] found that, compared with the diesel/gasoline RCCI burning mode, diesel/iso-butanol RCCI combustion mode had later combustion phase (CP), longer ignition delay (ID) and combustion duration (CD), higher indicated thermal efficiency (ITE), and lower PPR. Duraisamy et al. [5] found that, use of poly oxymethylene dimethyl ether (PODE) as high reactive fuel (HRF) with methanol as LRF under RCCI mode reduced the ID and resulted in shorter CD as compared with diesel/methanol RCCI mode of combustion. Raza et al. (2019) [6] found that, in-cylinder PPR and heat release rate (HRR) for RCCI were better by utilizing the physical and chemical properties of multi segment substitute fuel for both diesel and gasoline. Nazemian et al. (2019) [7] found that, with the expansion of the piston bowl diameter and piston bowl depth, because of higher heat transfer exergy expanded and total exergy diminished. Wang et al. [8] found that, thermal efficiency of gasoline/PODE RCCI combustion can be adequately improved with both intake air and exhaust gas recirculation (EGR). Yu et al. [9] found that, low temperature ignition kernels create in the n-heptane stream inside the mixing layer and advance into the low temperature flames, proliferating

Table 1 Properties of fuels

Fuels/Properties	n-Butanol	Diesel	B20	B100
Density (kg/m ³)	812	829	839	892
Kinematic viscosity at 40 °C (mm ² /s)	2.24	3.52	3.96	5.74
Flash point (°C)	37	53	77	178
Fire point (°C)	46	59	86	188
Calorific value (MJ/kg)	33.12	42.19	41.45	39.46

into moderately fuel rich mixtures. Dadsetan et al. [10] found that, minimum swirl proportion was the best for hydrocarbon (HC) and carbon monoxide (CO) decrease. The exhaust gas temperature (EGT) was most extreme around the swirl proportion of 1.2. The ideal swirl proportion for that engine was in the scope of 0.95 to 1.2 which prompts greatest efficiency and most reduced NO_x. Kakoe et al. [11] found that, high flame speed and high heating value hydrogen lead to expanding in-cylinder pressure and temperature. Because of the temperature increment of in-cylinder combustion, there was great consuming of methane and accordingly, there was a plummet of HC at 50% of hydrogen addition. Wenming et al. [12] found that, emissions of soot dropped fundamentally by 75% with the expansion of methanol rate from 0 to 60% because of better mixing between the fuel and air and more homogeneous burning cycle. Liu et al. [13] found that, initial low temperature combustion of RCCI was constrained by the HRF spray combustion process, with the essential heat release originating from the n-heptane low temperature combustion (LTC) process improved the system reactivity. Ebrahimi et al. [14] found that, adding hydrogen to landfill gas, the complete fuel mass per each cycle was decreased while the PPR was increased. Addition of hydrogen to landfill gas improved the methane dissociation rate subsequently the CD was diminished considerably. Zheng et al. (2018) [15] found that, expanding n-butanol proportion welcomed a decrease on soot emissions however prompts higher CO and HC emissions for RCCI mode. At low and medium loads, RCCI combustion followed lower HRR and ITE as n-butanol proportion was expanded.

2 Properties of Fuels

Four types of fuels were used in the present work viz., n-butanol, diesel, B20 and B100 blends of TPME. The fuels properties used are shown in Table 1.

3 Experimental Set up

1-Base, 2-CRDI engine, 3-Eddy current dynamometer, 4-Manifold injector ECU, 5-Crank angle sensor, 6-Air box, 7-Electric air heater, 8-Temperature controlling

unit, 9-Manifold fuel injector, 10-Diesel injector, 11-Computer interfaced to engine, 12-n-Butanol tank, 13-Injector driver for n-Butanol, 14-Diesel tank, 15-Biodiesel tank, 16-Calorimeter, 17-Exhaust gas analyzer, 18-Smoke meter.

Figures 1 and 2 shows the RCCI experimental setup used for the study. The n-butanol injector as shown in Fig. 3. Toroidal combustion chamber as shown in Fig. 4. The specifications of the engine test rig as shown in Table 2.

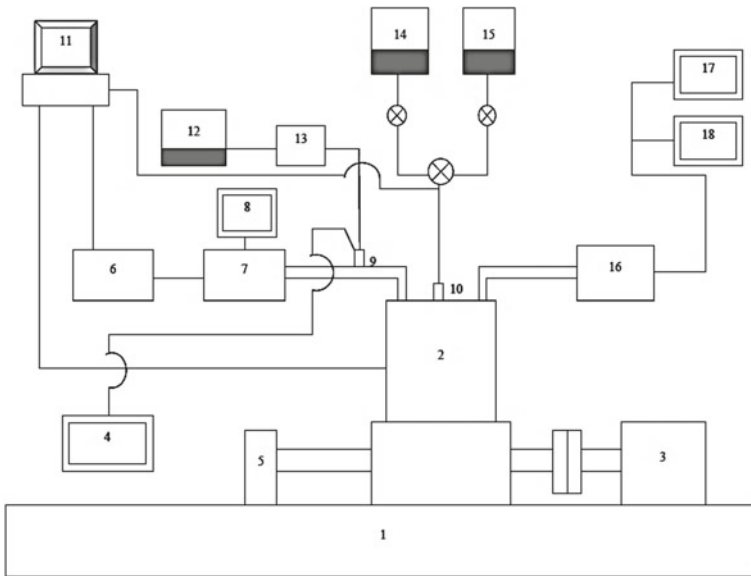


Fig. 1 Schematic representation of RCCI experimental setup

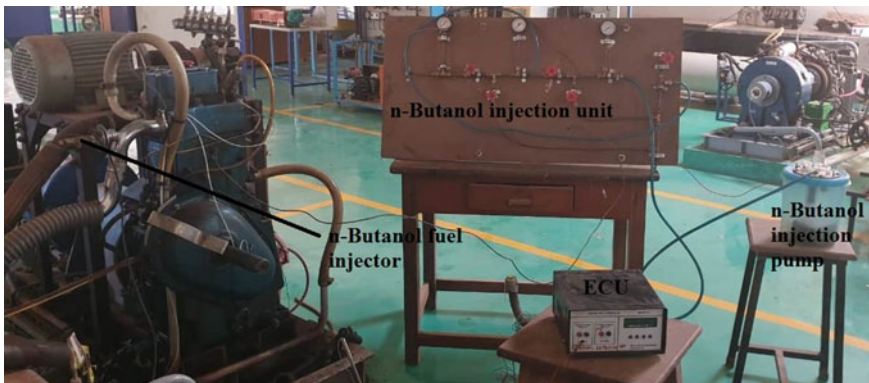


Fig. 2 Photographic representation of RCCI experimental setup



Fig. 3 n-butanol fuel injector

Fig. 4 Toroidal combustion chamber



4 Results and Discussion

Variation of BTE with n-butanol percentage for various fuels used as shown in Fig. 5. BTE decreased with the increase in n-butanol percentage. This is due to, formation of LTC inside the combustion chamber with the addition of n-butanol fuel. Highest BTE obtained for diesel and n-butanol fuel combination at 10% of n-butanol. This

Table 2 Test engine specifications

Engine parameters	Specifications
Engine	TV1 Kirloskar
Software used	Engine soft
No. of cylinder	1
No. of strokes	4
Bore × Stroke (mm)	87.5 × 110
Compression ratio	17.5: 1
Dynamometer	Eddy current
Combustion chamber	Toroidal
Governor type	Mechanical centrifugal type
Rated power	5.2 kW
Dynamometer arm length	0.180 m
Manifold injector opening pressure	5 bar
Direct injector opening pressure	900 bar

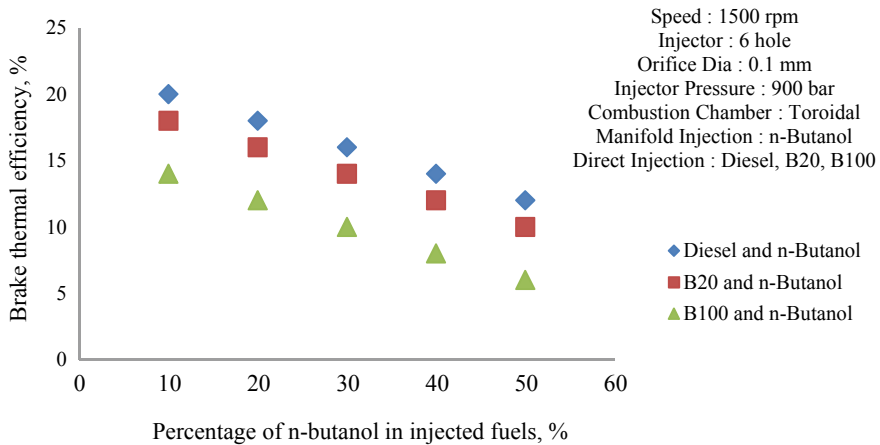


Fig. 5 Variation of BTE with n-butanol percentage

is due to, diesel had more calorific value which exhibits in better combustion as compared with biodiesel.

Variation of NOx emissions with n-butanol percentage for various fuels used as shown in Fig. 6. NOx emissions decreased with the increase in n-butanol percentage. Highest NOx emissions obtained for diesel and n-butanol fuel combination at 10% of n-butanol. This is due to, lean mixture formation of n-butanol with air which leads to lower reaction duration and hence NOx emissions decreased.

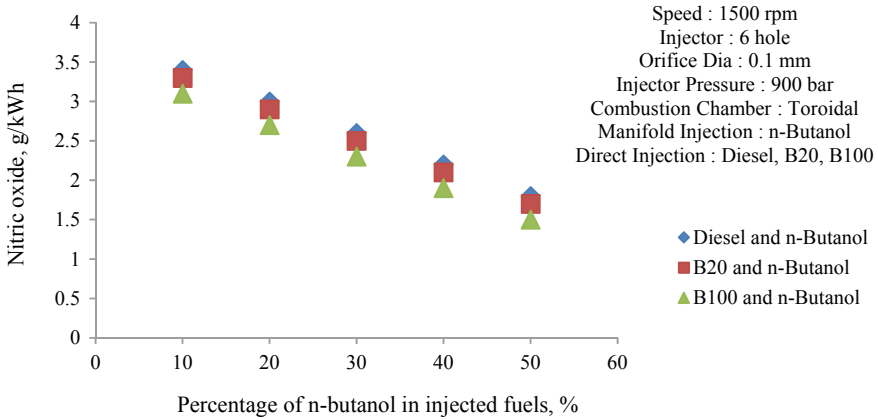


Fig. 6 Variation of NOx emissions with n-butanol percentage

Variation of HC emission with n-butanol percentage for various fuels used as shown in Fig. 7. HC emissions increased with the increase in n-butanol percentage. Lowest HC emissions obtained for diesel and n-butanol at 10% of n-butanol in injected fuels. This is due to incomplete combustion as the increase of n-butanol in injected fuels.

Variation of CO emissions with n-butanol percentage for various fuels used as shown in Fig. 8. The CO emissions increased with the increase in n-butanol percentage. Lowest CO emissions obtained for diesel and n-butanol at 10% of n-butanol in injected fuels. With the addition of n-butanol there is not enough availability of oxygen for complete combustion of fuel and air mixture which leads to higher CO emissions.

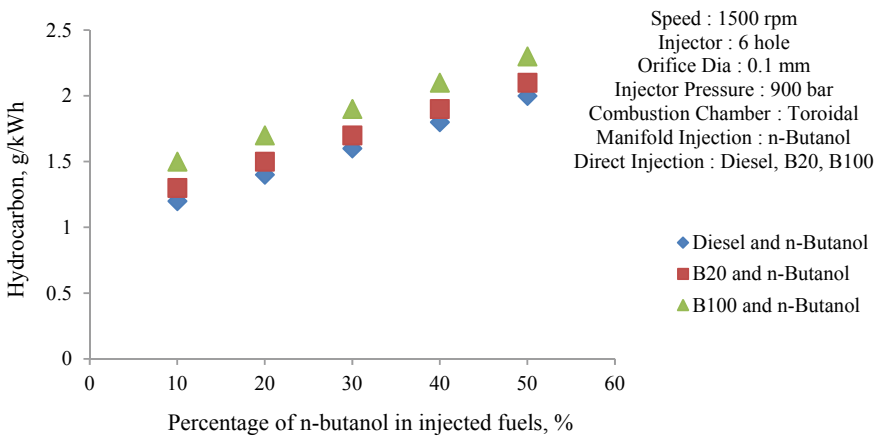


Fig. 7 Variation of HC emissions with n-butanol percentage

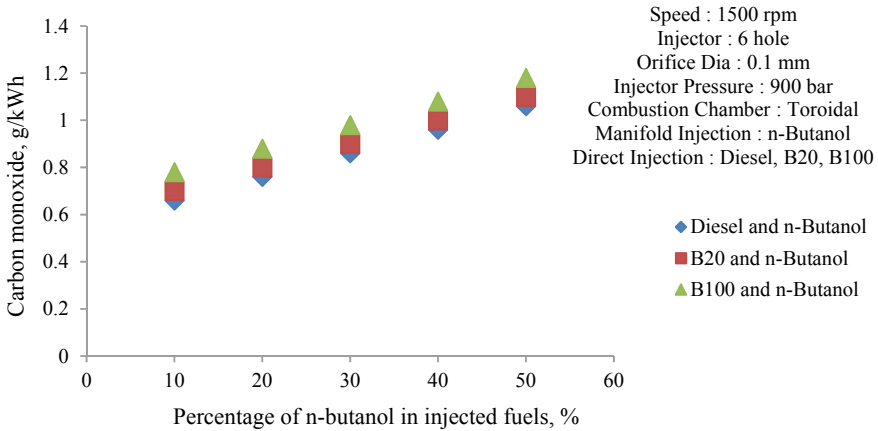


Fig. 8 Variation of CO emissions with n-butanol percentage

Variation of smoke emissions with n-butanol percentage for various fuels used as shown in Fig. 9. As the percentage of n-butanol increased smoke emissions decreased. Lowest smoke emissions obtained for diesel and n-butanol at 10% of n-butanol in injected fuels. Because of highly premixed n-butanol and more time of mixing for diesel, smoke emissions were very low.

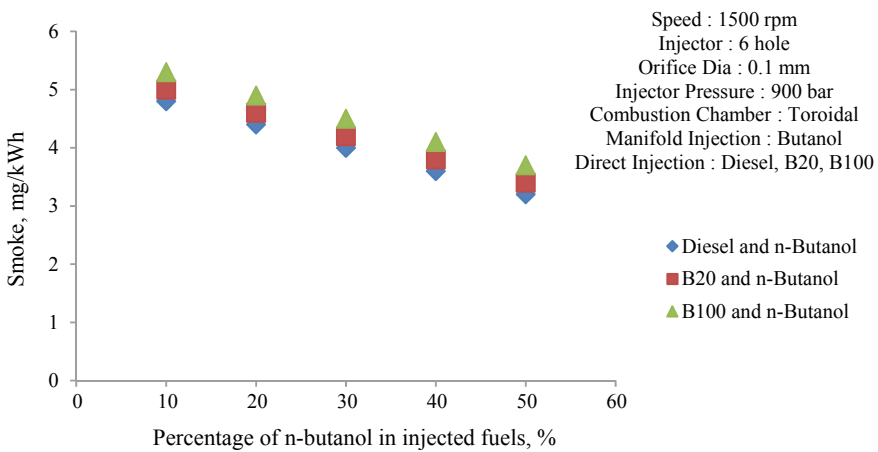


Fig. 9 Variation of smoke emissions with n-butanol percentage

5 Conclusions

Based on the test results following conclusions are made.

- As the percentage of n-butanol increases in injected fuels BTE decreases. Among various fuels combinations tested diesel and n-butanol gives higher BTE as compared with other fuels. At 10% n-butanol injection the highest BTE is obtained.
- As the percentage of n-butanol increases in injected fuels HC and CO increases.
- The NO_x and smoke emissions are reduced as the percentage of n-butanol increases in injected fuels.

References

1. Benajes J, Garcia A, Serrano JM, Boggio SM (2020) Emissions reduction from passenger cars with RCCI plug-in hybrid electric vehicle technology. *Appl Therm Eng* 164:
2. Li J, Yu X, Xie J, Yang W (2020) Mitigation of high pressure rise rate by varying IVC timing and EGR rate in an RCCI engine with high premixed fuel ratio. *Energy* 192:
3. Yang B, Duan Q, Liu B, Zeng K (2020) Parametric investigation of low pressure dual-fuel direct injection on the combustion performance and emissions characteristics in a RCCI engine fuelled with diesel and CH₄. *Fuel* 260:
4. Pan S, Liu X, Cai K, Li X, Han W, Li B (2020) Experimental study on combustion and emission characteristics of iso-butanol/diesel and gasoline/diesel RCCI in a heavy-duty engine under low loads. *Fuel* 261:
5. Duraisamy G, Rangasamy M, Govindan N (2020) A comparative study on methanol/diesel and methanol/PODE dual fuel RCCI combustion in an automotive diesel engine. *Renewable Energy* 145:542–556
6. Raza M, Wang H, Yao M (2019) Numerical investigation of reactivity controlled compression ignition (RCCI) using different multi-component surrogate combinations of diesel and gasoline. *Appl Energy* 242:462–479
7. Nazemian M, Neshat E, Saray RK (2019) Effects of piston geometry and injection strategy on the capacity improvement of waste heat recovery from RCCI engines utilizing DOE method. *Appl Therm Eng* 152:52–66
8. Wang H, Liu D, Ma T, Tong L, Zheng Z, Yao M (2019) Thermal efficiency improvement of PODE/Gasoline dual-fuel RCCI high load operation with EGR and air dilution. *Appl Therm Eng* 159:
9. Yu GH, Luong MB, Chung SH, Yoo CS (2019) Ignition characteristics of a temporally evolving n-heptane jet in an iso-octane/air stream under RCCI combustion relevant conditions. *Combust Flame* 208:299–312
10. Dadsetan M, Chitsaz I, Amani E (2019) A study of swirl ratio effects on the NO_x formation and mixture stratification in an RCCI engine. *Energy* 182:1100–1114
11. Kakoei A, Bakhshan Y, Gharehghani A, Salehi MM (2019) Numerical comparative study of hydrogen addition on combustion and emission characteristics of a natural-gas/dimethyl-ether RCCI engine with pre-chamber. *Energy* 186:
12. Wenming Y, Meng Y (2019) Phi-T map analysis on RCCI engine fueled by methanol and biodiesel. *Energy* 187:
13. Liu X, Kokjohn S, Li Y, Wang H, Li H, Yao M (2019) A numerical investigation of the combustion kinetics of reactivity controlled compression ignition (RCCI) combustion in an optical engine. *Fuel* 241:753–766

14. Ebrahimi M, Jazayeri SA (2019) Effect of hydrogen addition on RCCI combustion of a heavy duty diesel engine fuelled with landfill gas and diesel oil. *Int J Hydrogen Energy* 44:7607–7615
15. Zheng Z, Xia M, Liu H, Shang R, Ma G, Yao M (2018) Experimental study on combustion and emissions of n-butanol/biodiesel under both blended fuel mode and dual fuel RCCI mode. *Fuel* 226:240–251

Magneto Rheological Brake with Silicon Based Fluid and Hybrid of Silica Fumes with GO₂ as Additives



Vaibhav Vithal Shinde and Bhagyesh B. Deshmukh

Abstract Magneto Rheological Brake was designed with magneto rheological fluid based on silicon oil and hybrid of silica fumes with graphite oxide to give dispersion. This is original attempt made in order to investigate braking distance and stopping time for two wheelers with designed Magneto Rheological Brake. Magneto rheological fluid is prepared using Silicon oil as carrier fluid with silica fumes as surfactant and GO₂ as additive. When magnetic field is applied, it is assumed that particle forms single chain in direction of magnetic field. This hybrid mixture of suspension gives improved yield stress of magneto rheological fluid due to stronger chain formation process, which gives maximum braking torque. Volume of brake was investigated in order to estimate size of brake. Then maximum torque to volume ratio for Magneto Rheological Brake was calculated. In this way, brake was made compact and powerful by selecting proper torque to volume ratio. Torque to volume ratio is compared with other brake configurations in literature in order to estimate performance of Magneto Rheological Brake. Performance of Magneto Rheological Brake was decided based on Braking distance and Stopping time. Higher torque to volume ratio is expected to give better performance of Magneto Rheological Brake on Two-wheeler.

Keywords Magneto rheological brake · Magneto rheological fluid · Torque to volume ratio · Shear stress · Shear mode

1 Introduction

A branch of rheology that studies the flow and deformation of the materials upon the application of an applied magnetic field is known as magneto rheology. Magneto rheological fluids are suspensions of multi domain, non-colloidal, ferromagnetic particles with different morphologies, in a carrier liquid that is not magnetic (mineral oils, silicon oils, polyesters, watery solutions, gels, etc.) [1]. Magneto rheological

V. V. Shinde (✉)

Shri Vithal Engineering Research Institute, Pandharpur, India

B. B. Deshmukh

Walchand Institute of Technology, Solapur, India

fluid is intelligent material that changes its rheological properties on application of magnetic field. The volume fraction is taken as 0.55. This volume fraction is considered as high. Due to high density of magnetic particles, magneto rheological fluids are facing the problem of instability of the suspension caused by high settling rate.

While preparing and testing the magneto rheological fluids due to large density mismatch between the CI particle and carrier fluid, particles gets settle down with passage of time. Soft magnetic materials are considered as favorable magneto rheological candidates because of their ideal magnetic characteristics such as easiness to be magnetized and demagnetized, lower magnetic hysteresis and high magnetization saturation value.

Particle aggregation is due to Vander walls forces. Sedimentation is due to Gravity force and weight of particle [2]. Particles having cylindrical shape require to rotate at 90 degrees and octahedron shaped magnetic particles requires 45 degrees to rotate and spherical particle are ready to reorient in any direction hence in order to get quick response for Magneto Rheological Brake as to reduce braking time spherical particles are preferred.

As size of iron particles is increased the sedimentation increases hence it is prefer to use 8 micron size and 2 micron size surfactant layer over particles to get overall 10 micron size of particles. Particles are expected to float on hexagonal structure of precursor of graphite, which are added as additives. Field induced structure formation like single chain, multi chain, BCT and Hexagonal packed structure is possible with high volume concentration magneto rheological suspensions Here it is assumed that on application of magnetic field Single chains are formed which will enhance yield stress of magneto rheological fluid and then braking torque.

It was preferred to use combination of 40% Nano and 60% micrometer particle size to avoid sedimentation and aggregation. Optimized ratio of micrometer and Nano meter particle will give maximum yield stress. This is because Nano particles goes into interstitial sites of micrometer size iron particles and touch each other hence strengthening single chain formation when magnetic field is applied. Chain formation process is spontaneous and requires time in milliseconds, which gives better response time. Entropy of magneto rheological fluid is high at off state condition. When magnetic field is applied entropy of magneto rheological fluid becomes very low and ordered chains of iron particles are formed in magneto rheological fluid.

1.1 Magneto Rheological Fluid

Magneto Rheological fluid is treated as a brake lining material. This material does not wear away and provides desirable friction resistance by just controlling the Magnetic field passing through it. The rheological and magnetic properties of magneto rheological fluids are function of polarizable particle properties such as size, saturation magnetization, and shape.

The yield stress is one of the most important parameters that characterize visco-elastic properties of a Magneto Rheological fluid. The yield stress of Magneto Rheological fluid can be controllable by varying the applied current. Thus apparent yield stress will change within milli-seconds and fluids ability to transmit force can be controlled by magnetic field. Therefore, it is possible to control mechanical energy from magnetic energy with this Magneto Rheological fluid. From Fig. 1, it is clear that as particle size is increased from 2 micron to 10 micron braking torque increases from 20 Nm to 30 Nm.

If Gibbs free energy is considered for this spontaneous process its value will be negative. Stability of fluid particle in magneto rheological fluid can be determined from relation between particle size and free energy. Elastic response of any specimen is given by slope of stress strain curve at zero strain, which is defined as initial modulus or elastic modulus. Slope of stress–strain curve is obtained by differentiation of stress with respect to strain [3].

Surfactants like silica fumes are used to avoid aggregation and sedimentation of iron particles. However, at high speed fluid may disturb its flow but here we are adhered to general assumption that flow characteristics are linear. An increase of 60% in the on-state yield stress for Fe-GO2-silica fumes is expected here.

Magneto rheological fluid can be attributed to the gap filling by the hybrid additives during columnar-structure formation. Among two-dimensional (2D) materials, while graphene-oxide (GO) is a well-known 2D material with supreme mechanical properties like solid lubricant [4]. GO exhibits unique properties because of the oxygen functional groups on its basal plane and edge.

A plate-like structure of GO is used as the gap-filler to improve the sedimentation problem of CI-based magneto rheological fluid and the magneto rheological properties of pure CI particles and the CI/GO mixture-based magneto rheological fluids were evaluated.

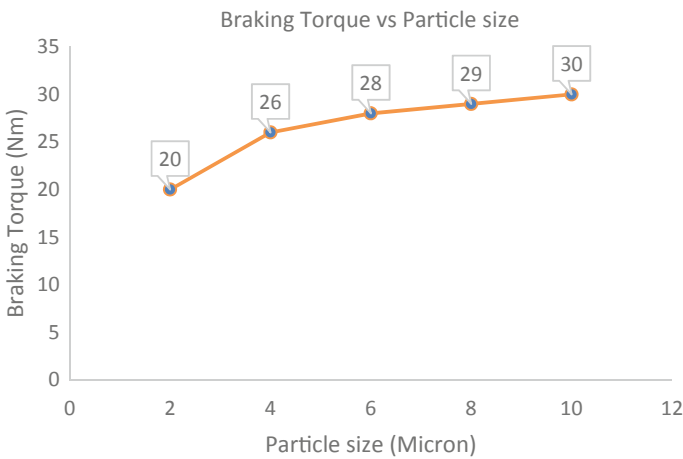
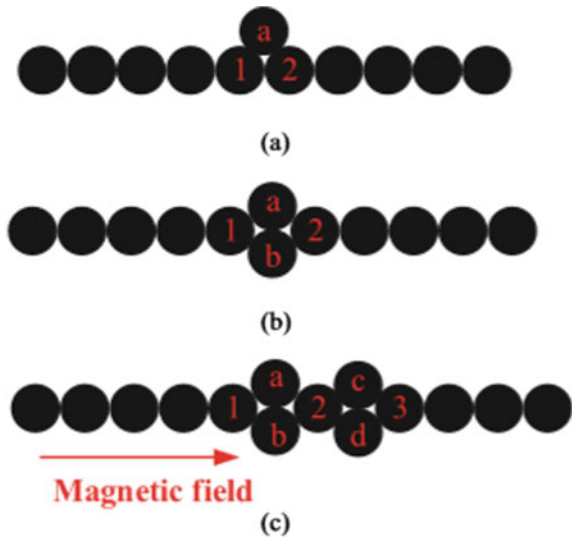


Fig. 1 Relation between particle radius and braking torque

Fig. 2 Typical defects in single chain formation process [5]. (a) Satellites (b) Cruciform (c) Multiple Cruciform



Here it was assumed that on application of magnetic field particle forms single chain due to the strong dipole–dipole interaction among the magnetic particles in silicon oil. Strength of chain decides value of yield stress. Therefore, defects in Single chain formation should be minimized to accurately predict yield stress value.

These defects are mainly considered as a. Satellite b. Cruciform and C. Multiple Cruciform as shown in Fig. 2. The magnetic moment of micronic particles in magneto rheological fluid is field induced and their Brownian motion is negligible. Particle aggregation processes are reversible and rather intense in magneto rheological fluids and are induced by the applied magnetic field, which is their key feature in developing field controlled flow behavior [6].

1.2 Yield Stress Model

Yield stress of Magneto Rheological fluid can be predicted by different approaches as shown in Table 1.

Table 1 Mathematical model for Yield stress

Sr. No.	Researcher	Yield Stress Equation	Approach
1	Ginder et al.	$\tau_y = \sqrt{6} \phi_s \mu_0 M_s H^{2/3}$	Finite Element Method
2	G. Song et al.	$\tau_y = V_{f1} \tau_{y1} s^{at} + V_{f2} \tau_{y2} s^{at}$	Constitute Model for State Transition
3	Bingham et al.	$\tau_y = \tau_y H + \mu_p \gamma$	Experimental Model

Suspension having Graphene has Hexagonal structure of carbon atoms. If iron particles are situated at center of atoms of each Hexagon of Graphene.

Then it is possible to apply Hexagonal packed chain model for obtaining yield stress of Magneto rheological Fluid, which was given by [7].

$$\tau_y = \frac{4H^2 a^3 \varphi \cdot \mu_0}{3k(2a + 2t + \delta)^3} \quad (1)$$

In above model H is magnetic field strength, a is particle radius, t is thickness of silica fumes coating on particles and δ is inter-particle distance.

Selection of Mathematical model for yield stress predictions are carried out by different researchers as shown in Table 1. It was decided to use Bingham model. By using this model it becomes easier to formulate the braking torque equation for Magneto Rheological Brake by integrating yield stress over the surface of disk. Therefore, Bingham model was selected for calculation of yield stress and Braking torque. Here for calculation of Braking torque at plastic viscosity of 0.218 pa-s, gap size of 0.001 m, angular velocity of disk is taken as 44.7 rad/s and Low shear rate up to 100 1/s is taken into consideration.

1.3 Magneto Rheological Brake

Magneto Rheological Brake is assembly of cylinder, casing, shaft, electromagnet, copper coil and magneto rheological fluid. As the power of the coil is turned on, a magnetic field is generated, and the Magneto Rheological fluid in the gap between the end-faces of the disc and the housing becomes solid instantaneously.

The shear friction between the rotating disc and the solidified magneto rheological fluid provides the required braking force to slow down and stop the shaft [8]. A brake naturally has a frictional behavior in an opposite direction of motion. This shear resistance against rotor motion provides the braking torque hence variable braking torque can be obtained by varying the value of supplied current to electromagnet [9]. The frictional characteristics of the proposed brake can be controlled by regulating the yield stress of the magneto rheological fluid as function of magnetic field [10]. Shear stress of the magneto rheological fluid generated on the surface of a disc (or a cylinder) is transformed into the braking torque. Magneto Rheological Brake can be used in control system. Accuracy of velocity control is about 15% and setting time is about 0.1 s.

Thus properties and behavior of Magneto Rheological Brake will be easy to adopt by changing software parameters and electrical outputs instead of adjusting mechanical components like changing number of springs. The disc type magneto rheological brakes cannot be operated at very high RPMs.

At higher angular velocities, the particles of the magneto rheological fluid that is between the rotor end faces and the housing, due to high centrifugal forces, can

separate from the working fluid and gather at the outer radius of the rotor and the brake can jam [11].

It has decided to select multiple disk four disk configurations because of higher yield stress and ease in manufacturing. For 3D cad model it was decided to develop Magneto Rheological Brake in Creo and NX due to their parametric nature in cad, assembly and drawing.

2 Volume of Magneto Rheological Brake

Our design intent was to maximize torque to volume ratio as high as possible. Maximization of torque was done using above selected yield stress Bingham model. Yield stress value is evaluated at magnetic field strength value. Where it was found that 35.5 Nm of torque was obtained using outer diameter of disk, inner diameter of disk and thickness of disk at given Magnetic field strength. Though Maximum torque can be highest with 132.39 KA/m of magnetic field strength. Torque required to stop vehicle was 35.5 Nm.

So here, 35.5 Nm torque is taken for calculation of torque to volume ratio. Volume of brake is calculated as follows in Table 2.

Volume of Magneto Rheological Brake is calculated by considering volume of cylinder which is given by $V = 3.14 \times (R_2 - R_1) \times L$. Where R_2 is considered as outer radius, R_1 is considered as inner radius and L is taken as length of brake. Different values are taken for casing outer radius are as shown in Table No.2 Outer casing radius is selected as 0.22 m. This is maximum possible radius of brake, which can be mounted on Two-wheeler with existing saree guard. If saree guard of vehicle is removed, Outer radius can be increased up to 0.35 m but will hamper aesthetics of vehicle. Here volume of brake is obtained using different values of radius of casing with constant length. If radius of casing is increased from 0.11 m to 0.399 m then it was found that volume of brake increased from 0.00227 m³ to 0.036 m³. Hence, 0.22 m casing radius and corresponding volume of brake i.e. 0.00911 m³ is selected for calculation of torque to volume ratio.

Table 2 Volume of magneto rheological brake

Sr. no.	Radius of casing (m)	Length (m)	Volume of brake (m ³)
1	0.11	0.060	0.00227
2	0.22	0.060	0.00911
3	0.299	0.060	0.0205
4	0.399	0.060	0.036

Table 3 Torque to volume ratio magneto rheological brake

Sr. No.	Objective function name	Symbol	Torque to volume ratio	Unit
1	Torque to volume ratio	T_v	3.89	KN/m ²

3 Torque to Volume Ratio of Magneto Rheological Brake

Comparison of Magneto Rheological Brake on basis of Torque to volume is required to decide compactness and power of brake. Hence, torque to volume ratio has been evaluated. Hence torque to volume ratio is taken as objective function and is optimized for inner disk radius, outer disk radius and Thickness of disk.

From Table 3 it was found that torque to volume ratio was calculated to 3.89 KN/m² using 35.5 Nm of torque and volume of 0.00911 m³.

Here optimization method followed for maximization of torque is iterative each iteration requires large number of calculations. These iterations are based on design update procedure where function values are evaluated at various disk radius and thickness values considered as candidate points.

Calculation of objective function and gradients for given constraints at current design point i.e. in our case $R_2 = 0.199$, $R_1 = 0.025$ and $t_d = 0.001$. Torque to volume ratio is evaluated at maximum torque developed, which is required for the two-wheeler.

4 Braking Time and Stopping Distance with Designed Magneto Rheological Brake

Magneto rheological brake was mounted on two-wheeler and tested for its braking distance and braking time. It was found that when electric current is applied to electromagnet of brake then 4.4. N of magnetic force was generated by chaining process of magneto rheological fluid on rotating disc of brake. This force is then converted to braking force by considering wheel radius and radius of brake disc and then braking distance and braking time is calculated.

From Table 4 It can be found that as vehicle speed increases stopping time increases and stopping distance also get increased. If braking force of 118 N is applied to vehicle with low speed 10 Km/h it will stop in 2 s. But when same braking force is applied at 50 Km/h it will take 6 s.

5 Conclusion

Magneto rheological fluid having silicon oil as carrier and GO₂ as additive and silica fume as surfactant will give improved yield stress which in turn provide maximum braking torque. Torque to volume ratio for designed magneto rheological brake is

Table 4 Braking time and stopping distance for two wheeler

Vehicle speed km/hr.	Magnetic force (N)	Braking force (N)	Stopping distance (m)	Stopping time (s)	Braking efficiency
10	4.4	118	0.5	2	50
20	4.4	118	2	3	64
30	4.4	118	4.5	4	76
40	4.4	118	8	5	81
50	4.4	118	12.5	6	84

3.89 KN/m² So designed Magneto Rheological Brake was compact and powerful. It has been shown that braking force generated by brake was successful in stopping vehicle with standard stopping distance and stopping time.

References

1. Barvinsch P (2018) Nano-Micro structured magneto rheological fluid and engineering applications. *J Rheol* 62(3):87–121
2. Vékás L (2008) Ferro fluids and Magneto rheological fluids. *Advanc Sci Technol* 54:127–136
3. Shekahar H, Sahasrabudhe A (2010) Maxwell Fluid Model for Generation of Stress-Strain Curves of Viscoelastic Solid Rocket Propellants. *Propellants, Explos, Pyrotech* 35:321–325
4. Ji Eun Kim et al (2018) Two dimensional rGo-Mos2 hybrid additives for high performance magneto rheological fluid, *Scientific report, Nature*,1–9, 8:12672
5. Wei S et al (2020) Influence of magnetic field, magnetic particle percentages, and particle diameters on the stiffness of magneto rheological fluids, *Journal of intelligent materials and structures*,1–14
6. DGuth, A Wiebe, J Maas, Ostwestfalen-Lippe, Design of shear gaps for high-speed and high-load Magneto rheological Brake and clutches, *Journal of physics, ERM, Conference series* 412,2013,012046,1–14, Germany. (2012)
7. Wanli song et al, Microstructure simulation and constitutive Modeling of Magneto Rheological Fluids based on Hexagonal close packed structure.,*Materials* 13,1674,1–20 (2020)
8. H. Zhang and D. Ning, Design and Testing of Novel two-way controllable overrunning clutch based Magneto Rheological Brake., *Smart material and structure*, IOP publication, 1–20, Australia. (2019)
9. Vijay kumar sukhwani and harish hirani, Comparative study of magneto rheological fluid brake and grease brake, *Tribology online* (3),1, pp 31–35,India. (2008)
10. Alireza Farjoud, Nader Vahdati and Yap Fook Fah, Mathematical Model of Drum-type Magneto Rheological Brake using Herschel- Bulkley Shear Model, *Journal of Intelligent material and structure*, Vol.19, Singapore (2018)
11. Nam et al, New Approach to Design MR Brake using a Small Steel Roller as a Large Size Magnetic Particle Materials, *International Conference on Control, Automation and Systems* Oct. 14–17, Seoul, Korea (2008)

SCADA System Applied to Two-Wheeler Chassis Dynamometer



Sumedh Vidhate, Virendra Bhojwani, and Omkar Mobale

Abstract This research paper presents the use of SCADA to control the Two-wheeler Chassis dynamometer parameters using PLC. A Two-wheeler chassis dynamometer is used to test two-wheelers performance where parameters like acceleration between two Speed points, maximum speed test, different gears speed test, load test, and fuel consumption tests. The focus of this is to simulate the working of the Dynamometer. The two-wheeler Chassis dynamometer consists of PLC from Mitsubishi which will be used to communicate with the sensors and this processed by the PLC microcontroller then this data is sent to the SCADA which monitors it and triggers an alarm if any parameter is out of limit. SCADA can simulate all the working conditions of the Dynamometer without having the real Dynamometer Built.

Keywords SCADA · Chassis dynamometer · Acceleration · Simulate · Mitsubishi · PLC · Microcontroller

1 Introduction

In INDIA from the total vehicle number of vehicles, there are around 70% of the two-wheeler. Most of the two-wheelers are from 100 to 350 cc class two-wheelers. There are many service stations which do maintenance two-wheelers which are third-party service station. The service station does not check the performance drop of the vehicle. The majority of the time they check is the oil level and fix some electronics issues which may occur over a while. The testbed is designed to be used in the medium-sized service station. The primary design requirements are compact in size, reduction of cost, less requirement for supporting system, easy interface so need to be highly educated to operate, it should be adaptive for a various test like emission

S. Vidhate (✉) · V. Bhojwani

Department of Mechanical Engineering, MIT School of Engineering, MIT ADT University, Loni Kalbhor, Pune, India 412201

O. Mobale

Research and Development Department, SAJ Test Plant Mundhwa, Pune, India 411036

test, wheel alignment, and mileage test [1]. Dynamometer is an energy absorption device which is used for vehicle testing. There are two mostly used dynamometer hydraulic dynamometer and eddy current dynamometer. A hydraulic dynamometer is used for a high power engine. It needs a different water system to arrange which makes it larger. The second type is Eddy current dynamometer, and it can be cooled by air available in the atmosphere and its compact in size to [2]. In our case, we are going to use an air-cooled eddy current dynamometer. The chassis dynamometer is used to simulate the real road conditions and driving conditions, which play an essential role in testing the engine parameters [3].

PLC helps to optimize the complete process. The monitoring of the process also becomes easier. The system becomes more optimized to use. All the enhancement is due to the Mitsubishi PLC [4]. For complex systems, PLC is the most cost-efficient system. They are a flexible system and can also be reapplied to other systems easily and quickly. The function of the Dynamometer is to apply load on the engine, which is used to measure the engine's power. The load is not put manually but using PLC and SCADA automatically [5]. Using SCADA, we can easily control the speed of any electrical system. The torque-speed characteristics also show the torque-speed control using the proposed mechanism [6]. SCADA system helps in real-time monitoring of the data, to test the system in different conditions without having the actual system installed the responses of the system are stored by the SCADA system which helps in analyzing the system performance[7]. The load cell is used to apply load on the wheeler through the Dynamometer. We are going to use the Parker drive 514C for applying load. For the industrial application, this is one of the best in the market. To protect the controller and the user, it should be mounted within an enclosure. There are terminals provided in the controller which should be permanently grounded. DC Shunt wound or permanent magnet motor is mostly controlled by the 514C controller. The motor speed in all 4 Quadrants of operation can be controlled by this controller. The controllers are designed to operate from a single-phase AC mains supply in the range of 110 Vac to 415 Vac at 50 or 60 Hz [8]. SCADA has many feature and advantages to it like the interface is amicable and easy to understand, it has a graphical interface which makes it more understandable. The data of the SCADA can be saved locally, which analyze the data very easy for further use [9].

The connection between the PLC and SCADA can be established using multiple methods like the CPU of the Mitsubishi connected to an Internet Hub and other engineering tools that are connected can be searched. The IP address of the displayed target device can be specified. The CPU of the PLC can also be connected directly via an Ethernet cable to a PC. It also has a Modbus protocol that helps implement RTU (Remote terminal unit) and TCP/IP (Transmission control protocol/internet protocol). It also can be prevented by passwords to prevent unauthorized access from outside [10].

2 Literature Survey

Vara Manthan Kantilal [11] Applied ZIGBEE based Wireless Monitoring and Controlling of Automation System using PLC & SCADA. Discuss the PLC is a controller-based system used for industrial automation. Both PLC and controller can control the equipment. The controller includes external communication hardware such as max 232, condensers, resistors, etc., while PLC is a system with a fully modular structure. This helps us to connect the input and output directly to the port provided in the PLC using PLC. SCADA is a software which works with PLC to remotely control the PLC-based system. Using SCADA, we can create an animated hardware file to be managed by a PLC to monitor and display the process in the SCADA program with ease. SCADA interacts with PLC.

Nakiya [12] it uses the processor is a solid-state device designed to replace relays, timers, counter, etc. Internal working of PLC also needs some power supply; this is given in current and Voltage. The input or output section is a field element that is interfaced to. Push buttons, limit switches, proximity switches, relay contacts, selector switches, thumbwheels are typical input or output section, specific input element. Solenoid valves relay coils, indicator lights LED displays are specific output elements. External plunge grinding machine is controlled using the PLC for Ease of use. Mitsubishi Q series PLC is used. In this control panel system. PLC controls all inputs and outputs. In external plunge grinding the wheel is directly feed into a workpiece.

Endi et al. [13] the research paper of “Three-Layer PLC/SCADA System Architecture in Process Automation and Data Monitoring. This paper presents the state-of-the-art and recent trends of SCADA system Architecture, which is typically three-layer SCADA system architecture based on open system technology rather than a vendor-controlled, proprietary technology A real-time industrial process (boiling system) is simulated, and a complete three-layer model SCADA system is built for this process, supervisory control layer. To construct the SCADA / HMI in the supervisory layer, National Instruments, Labview with the related data logging and supervisory control toolset is used.

John Robles et al. [14] architecture of Wireless Supervisory Control and Data Acquisition System. Discussing many HMI / SCADA third-party kits, providing builtin compatibility with most major PLCs, also entered the market, allowing mechanical engineers, electrical engineers and technicians to customize their own HMIs. The aim of human–computer interaction engineering is to create a user interface that makes running a system simple, effective and enjoyable in the manner that produces the desired result. In general, this means the operator must provide minimal input to achieve the desired output.

Table 1 Specification of the Mitsubishi PLC

No. of Inputs	16
No. of Outputs	16
Processing Speed	240 KB per Seconds
Operating Temperature	0° C to 55° C
Operating Ambient Humidity	5 to 95% RH
Rated Voltage	100 to 240 V AC
Communication Protocols	Ethernet port, RS485

3 Field Survey

We decided to have 2 wheelers of the range 100 cc to 350 cc. So, We decided to do collect some parameters of all the vehicles following into this category. We visited all the major 2-wheeler manufacturing brands and took a brochure of the respective vehicles.

List of the companies surveyed are- Honda, Hero, Vespa, Bajaj, Suzuki, KTM, Royal Enfield.

From this survey, we found out- max torque = 28 Nm, Max Power = 29 Hp, Wheelbase Length = 1412 mm and max weight = 192 kg. Specification of the Mitsubishi PLC is shown in Table 1.

4 Selection of Component

4.1 Mitsubishi PLC

Mitsubishi PLC of Fx 5u32mt Series is used for this project for the following reasons.

- Expanded input/output area for networks and complex applications
- Can be upgraded by combining with expansion modules
- Built-in SD card slot
- Run/Stop/Reset switch
- Built-in Ethernet port, RS485
- Displays the input and output states via LEDs
- Integrated real-time clock

4.2 RTD Temperature Sensor

The working temperature of the Dynamometer is around 60 °C to 70 °C, and the operating engine temperature is Around 105 °C. For this range, RTD fits perfectly

Table 2 Specification of RTD Temperature Sensor

Temperature range	-50 to + 250 °C
Accuracy	± 0.3 °C
Pressure range	Less than 25 Bar
Humidity	< 98% RH
Protection Class	IP 65

Table 3 Specification of Magnetic Pulse Pickup

Magnetic Pickup	Permanent magnet
Gear Pitch	24 dp
DC Resistance	1200 Ohms
Operating Temp	-73 ° C to 103 °C

and is low on the cost. The specifications of RTD temperature sensor is presented in Table 2.

4.3 Pulse Pickup

The rotor has a gear of 24dp, which makes it easy to use pulse pick of measuring the RPM. It can also withstand higher temperature up to 113 °C. The specifications of Magnetic Pulse Pickup are presented in Table 3.

4.4 Strain Gauge

The strain Gauge is used in torque meter to measure the torque of the bike, in our survey the maximum torque of the bike was 28 Nm hence less capacity strain gauge is sufficient for measuring the torque. The specifications of strain gauge are presented in Table 4.

Table 4 Specification of Strain Gauge

Measurable Strain	2 to 4% maximum
Temperature Range	-30 °C to + 80 °C
Substrate Thickness	20 microns
Cover Thickness	25 microns
Fatigue	10,000,000 Cycles

4.5 Load Drive

For applying load on the Dynamometer, we decided to go with Parker Drive 514C. Using Parker drive, we can control the Voltage of the stator pole windings which directly apply load on the engine. The specifications of Load drive are presented in Table 5.

5 Simulation in Scada

Wonderware Intouch SCADA software is selected for the following.

- Easy and Graphical interface with a more significant number of Symbols in Symbol Factory.
- It supports almost all the central PLC Brands Available.
- It has multilevel Security.
- It also has mobile access.
- Its open-source software which makes it very flexible.
- It supports all the communication Protocols like Ethernet, RS485 Microsoft SQL.
- Can run on less powerful Operating Systems too.
- Cost Efficient.

Table 5 Specification of Load Drive

Supply Voltage	110–500 V + 10% user selectable
Auxiliary supply	110/120 or 220/240 V + 10% user selectable. Single-phase 50-60 Hz + 10%
Ambient	0–40 °C - Altitude: up to 1000 m without derating
Overload	150% for 60 s

Table 6 Specification of KTM Duke 200 (www.ktm.com)

Dimension (LxWxH)	2002 × 873 × 1225
Engine displacement	200 cc
Transmission	6 speed
Power	25 hp
Torque	22 Nm

Table 7 Specification of Ns 200 (www.bajajauto.com)

Type	Petrol
Power	23.8 bhp
Torque	18.5 Nm
Emission standard	BS-VI
Displacement	200 cc

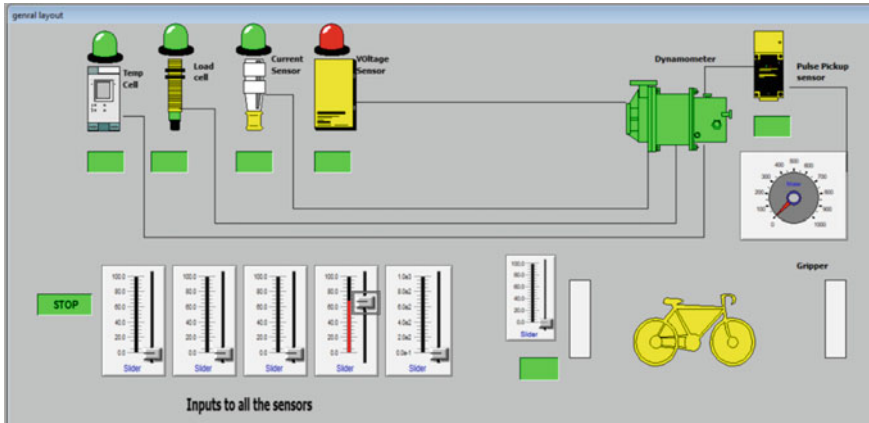


Fig. 1 Output screen for the General layout showing triggered alarm

5.1 General Layout

The screen is shown as a general layout of the systems. The design has different sensors such as the temperature sensor, load cell, current sensor, voltage sensor, and pulse pickup. All sensors have specific working limits that are specified in the above Tables 1, 2, 3, 4 and 5. If any of the sensors goes above the working boundary, it will trigger an alarm showcased by the light located below the sensor.

The pulse pickup is connected to a gear; the gear is the connector to the rotor. There is an air gap between gear teeth and pulse pickup. The calculation is done by using a gear tooth and the RPM. There is a gripper system used to hold the front tire; the gripper’s pressure can be adjusted according to our need. There is various temperature location for this, but the central temperature is to be monitored trunnion bearing and the heat produced in the winding. Tag name connects the virtual alarm to the virtual input. The alarm is connected to the slider which tag name is given as s1 in the software. As we move the slider, the input to the sensor will change. If there were real hardware, the sensor reading would automatically change according to the real-time condition. Figure 1 is a working example of the SCADA system as we are manually giving input if even if one slider, i.e. the sensor in hardware goes above the limit, the alarm will be the trigger.

5.2 Dynamometer Sensors

The rotor is a connector to the shaft this shaft rotates in turret housing. There are 2 housing each side of the shaft. This housing has born into it. The bearing temperature should be maintained at around 60 °C. For these, I am using RTD sensors to check the temperature. If the temperature goes above the limit, the software will trigger

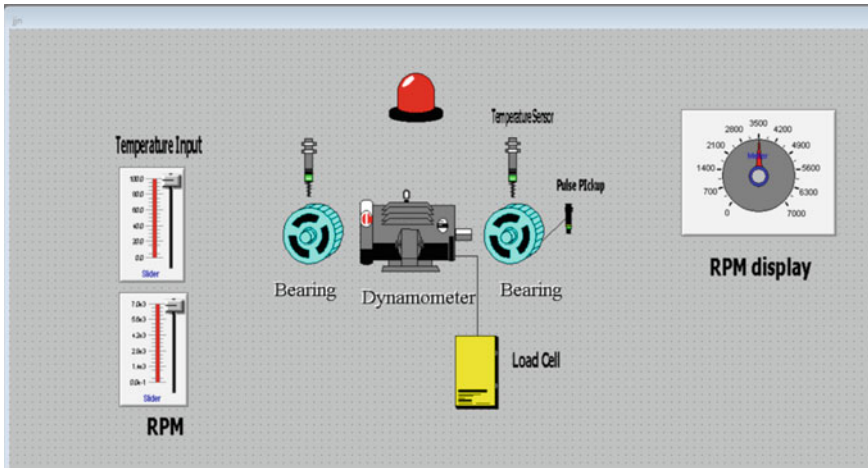


Fig. 2 Dynamometer sensor system

an alarm on the HMI. This screen also has a pulse pickup sensor which detects the RPM of the Shaft. The Dynamometer sensor system is illustrated in Fig. 2.

5.3 Output Graphs for Power and Torque

Mostly the output of the Dynamometer is expressed in real-time graphs. The input is taken by the rpm sensor and torque sensor. Using these inputs, I can calculate the horsepower as I did on the other screen before using a graph plotted of this power output on the HMI. The graphs can be saved locally. I can arrange for protecting the name of the customer, vehicle no. and bike model.

Figure 3 shows the output screen for the real-time graphs SCADA screen as you can see as the slider moves the same is plotted on the graph and shown in real-time. The sliders will be nothing be the rpm, and the torque input will be given by the sensor.

6 Results

Comparison of the graphs obtained by the software with already existing graphs of 4 models.

1. KTM Duke 200

Specification like the power and torque is given in Table 6.

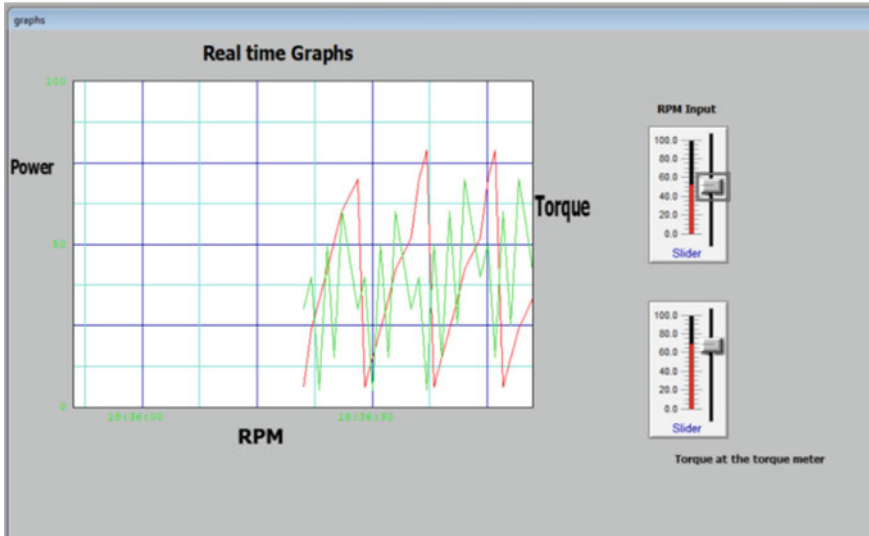


Fig. 3 Simulation of the real-time graph

Figure 4 performance graph of KTM 200 Duke. The graph is plotted between power and torque vs RPM. The graph shows Power and Torque as 7 hp and 14 Nm respectively for 1000 RPM. The graph shows Power and Torque as 25 hp and 18.2 Nm respectively for 10000 RPM.

The input to this simulation is RPM. As we input RPM, we get the power and torque Fig. 4 of the bike on the graph. If there were hardware attached to it, it would

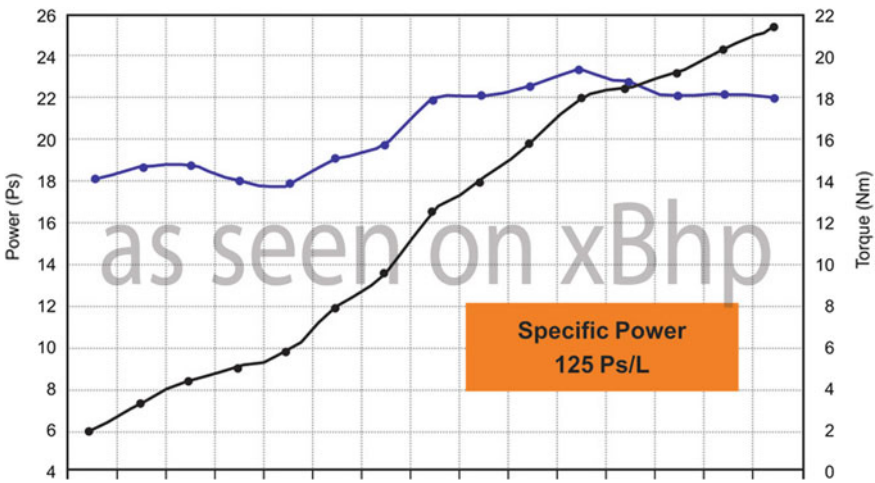


Fig. 4 Existing Performance Graph of KTM duke. (www.ktm.com)

take the reading of the power and torque at precisely 1000 rpm according to the program which is shown Fig. 5.

For validation, compared the performance graph for a total of 2 bikes.

We have designed a simulation for finding the graphical output of the performance of the bike. The input to this simulation is RPM. As we input RPM, we get the power and torque Fig. 5 of the bike on the respective graph.

2. Pulse 200 Ns.

Specification like the power and torque is given in Table 7.

Figure 6 performance graph of KTM 200 Duke. The graph is plotted between power and torque vs RPM. The graph shows Power 10 hp at 2000 RPM. The graph shows Power 23.8 hp for 8000 RPM.

Figure 7 the output of the Performance graph simulated by SCADA Software. According to the simulated graphs shows Power 11 hp at 2000 RPM. The graph shows Power 24.5 hp for 8000 RPM.

For a particular RPM, the engine produces torque. Along with the torque, there is power generated accordingly. Stimulation of the graphs of already existing performance graphs of these 4 bikes, got the almost identical Result which stated that the software program made was correct. Results were virtually the same power figures of the bikes at the respective RPM. The Result has Some Spikes to it as there is no physical hardware present. As these are real-time graphs, these graphs can be saved and viewed too.

Most of the Dynamometer in the market doesn't use an HMI they mostly have Pushbuttons, and we need to connect PC to extract data from the PLC. We are using SCADA for safety and monitoring purposes. Which makes it fully automated, and

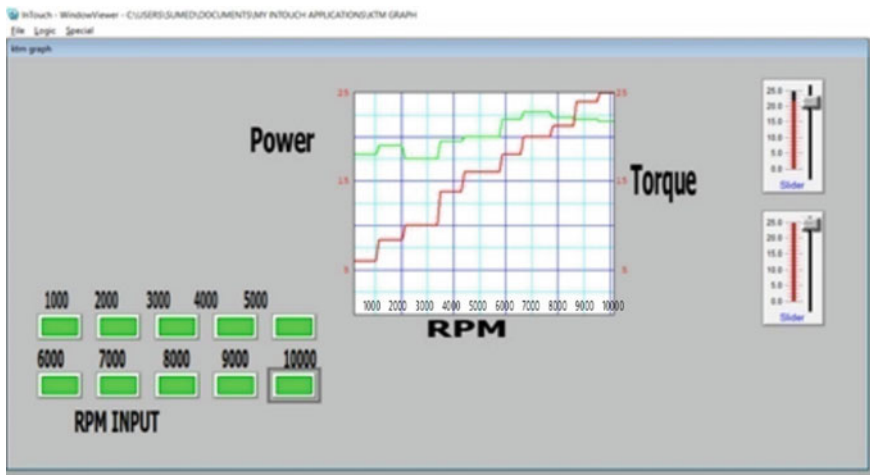


Fig. 5 Output for Performance Graph of KTM duke in SCADA

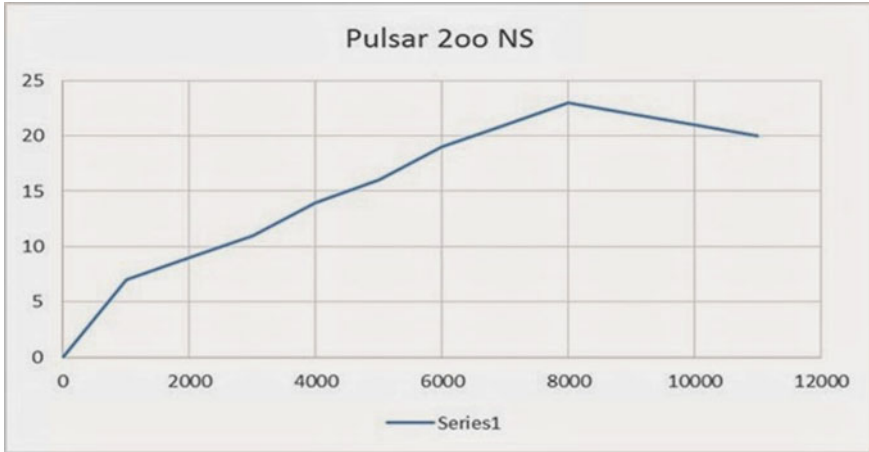


Fig. 6 Existing Performance Graph of NS 200 (www.xbhp.com)

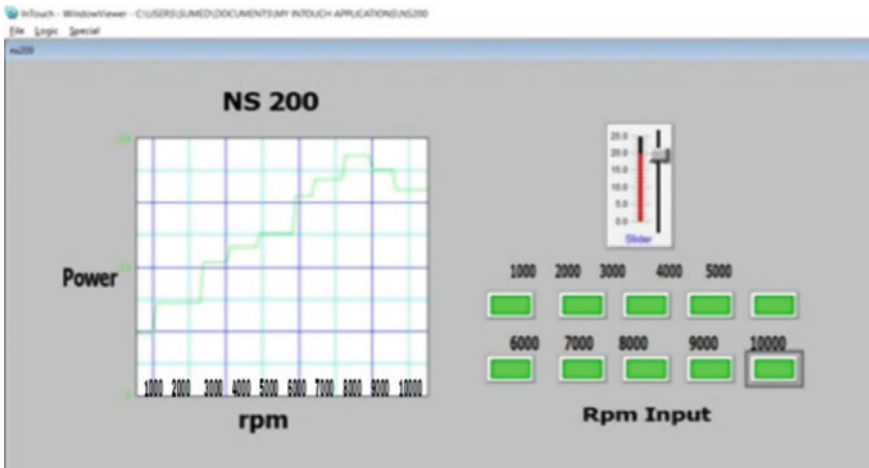


Fig. 7 Output for performance graph of NS 200 in SCADA

diagnostic becomes very easy. With SCADA real-time data is acquired, and with the alarm systems, we can get to know the problem where it exactly occurred.

The design perspective, made the Chassis dynamometer compact so it can be easily fit in a small garage. We added some wheels to make it a portable dynamometer. We also added some anti-vibration pads to it, so it does not vibrate a lot.

7 Conclusion

Successful incorporation of alarm system for safety. The temperature of the RTD temperature sensor located the bearing of the dynamometer alarm triggers after 65 °C. The current and Voltage sensors alarm triggers when it crosses 100 amp and 500 V respectively. If the Parker Drive crosses 550 V, then the alarm is triggered. Comparison of performance graphs obtained by InTouch SCADA Software with available two-wheeler models (less than 5% error was observed). In the simulation, there are spikes, and it's more of a straight line because the input is instant in the software. A graphical interface is implemented for observing real-time parameters/performance.

The SCADA system is one of the most useful systems as it can be applied to any complex system. The interface of the SCADA is easy, which is the primary advantage of it. The analysis of the system becomes easier as there is real-time monitoring done. We can change the input parameter to test the different operation conditions without installing the actual Dynamometer. The responses are stored in the SCADA database, which allows analysing the system performance. Moreover, it helps to develop an optimum system at a low cost which even making a prototype of the system.

With the visual/graphical interface of the SCADA, which makes it very friendly to use and understand. In the SCADA system, any auxiliary system is straightforward, which makes it flexible to use, no need to completely rewriting the whole program.

8 Future Scope

The following could be the scope for future work in the current investigation carried out,

- Wireless Sensor implementation using Ethernet PLC.
- Using wireless sensors, the complete system can be made wireless.
- The data of the bike can be saved on the cloud network for accessing data and report generation from anywhere.

References

1. Nilesh R. Mate, Prof. D. Y. Dhande.: Design and Development of Two-wheeler Retarder Type Dynamometer Portable Test Platform, International Journal of Engineering Research & Technology (IJERT) Vol. 3 Issue 2, February - 2014 ISSN: 2278-0181 IJERTV3IS20630
2. S.C. Kothale, V.P. Jagtap, C. S. Choudhari.: Design of Chassis Dynamometer for Light Motor Vehicle Service Stations, International Engineering Research Journal (IERJ) Special Issue Page 392-400, June 2016
3. Zhuo Yang, Baoqing Deng, Mengqi Deng and Shaojia Huang.: An Overview of Chassis Dynamometer in the Testing of Vehicle Emission, MATEC Web of Conferences 175, (2018)

4. Petru Pase Cristian Dumitru.: Energy Efficient street lighting using Mitsubishi Alpha 2 PLC Based Solution, 10th international conference in Interdisciplinary engineering
5. Matthias Markert, Hartmut Schmidt, Muhammad Faiz Rifqi Ardyatama.: Development of Load Characteristic of Main Engine and Its PLC Compatible Preparation in Cooperation with Water Brake as Generator, International Journal of Marine Engineering Innovation and Research, Vol. 1(4), Sept. 2017
6. Mihir K.Patel, Hemish R.Choksi.: Analysis of Induction Motor Speed Control Using SCADA Based Drive Operated System, IJSRD - International Journal for Scientific Research & Developmentl Vol. 3, Issue 10, 2015
7. Darko Babunski, Emil Zaev, Atanasko Tuneski.: Optimization Methods for a system using SCADA System, 2018 7th MEDITERRANEAN CONFERENCE ON EMBEDDED COMPUTING
8. Parker Drive 514C manual, <https://www.parker.com>
9. Gilberto Schneider, Vanessa F. de Lima, Lucas G. Scherer, Robinson F. de.: SCADA System Applied To Micro Hydropower Plant, IECON 2013 - 39th Annual Conference of the IEEE Industrial Electronics Society
10. MELSEC iQ-F FX5 User's Manual (Ethernet Communication) <https://dl.mitsubishielectric.com/dl/fa/document/manu>
11. Vara Manthan Kantilal.: Applied ZIGBEE based Wireless Monitoring and Controlling of Automation System using PLC & SCADA. 2006.
12. Arvind N. Nakiya, Mahesh A. Makwana, Ramesh R. Gajera.: An external plunge grinding machine with control panel automation technique based on Mitsubishi plc system, International Journal of electrical engineering and technology(ijeet), Volume 4, Issue 4 August 2013
13. Mohamed Endi, Y. Z. Elhalwagy.: Three-layer PLC/SCADA system Architecture in process automation and data monitoring, 2010 The 2nd International Conference on Computer and Automation Engineering (ICCAE)
14. Rosslin John Robles.: Architecture for SCADA with mobile remote components, 12th WSEAS International Conference on AUTOMATIC CONTROL, MODELLING & SIMULATION, May 2010

Enhancement of Reliability and Efficiency of Solar Panel Using Cooling Methods



Nilesh Dhokane and S. Ramesh

Abstract For Sustainable development of any country, electricity is the basic need for current civilization. Without hampering the environment, generation of electricity is very essential. Solar energy is completely natural, it is considered as clean energy source. In this work, an automatic system for solar panel cooling is proposed on the use of a commercial sensor with RISC based micro-controller. An electro-mechanism was designed and developed to enhance solar panel life time under different Sunlight Peak hours to evaluate its voltage efficiency. The impact on the overall performance of solar PV panel caused by different temperatures at Sunlight Peak hours is analyzed. The developed cooling system is innovative in relation to the unusual cooling system already existing in commercial units. A mini prototype model was designed and experimented, field results have proven good enhancement. With this automatic cooling technique, voltage efficiency is improved from 3% to 5%.

Keywords Automatic cooling technique · Solar energy · Solar PV panel · Temperature · Voltage efficiency · Sunlight peak hours

1 Introduction

The access to electricity determines the living standard of humans. One must realize that around 1.2 billion out of the 7 billion people worldwide still do not have access to the electricity grid the electricity worldwide is mainly generated from all coal, gas, nuclear and hydro power. The more advance in the use of solar energy, the brighter our future can be. The earth receives huge amount of energy directly from the sun. Using special scientific methods, we can utilize this solar energy. We can convert solar energy and to other useful forms of energy. For example we can convert solar energy into electrical energy and then we can convert electrical energy and to heat energy kinetic energy potential energy etc. Solar energy is the cheap source of energy which can be easily converted into other useful forms of energy. Solar energy reaches the earth as light travels in the form of waves. One meter square area of

N. Dhokane (✉) · S. Ramesh
University of Technology, Jaipur, India

the atmosphere receives one point four kilowatt energy which is also known as a solar constant. It means the solar energy absorption of our atmosphere is one point four kilowatt per meter square. We can convert solar energy into electrical energy through the use of semiconductor devices like silicon and these are called as solar cells. They are also called as photo voltaic (PV) cells made up of silicon electrons. The silicon gained energy from the sunlight to create the voltage. Each solar cell produces a very small amount of voltage. The high voltages can be derived from a large number of such solar cells are connected in series forming a solar panel. The applications of solar energy can be used power satellites having large solar panels which are keep facing the Sun. Solar watches and solar calculators are also in use nowadays solar energy is used in industrial zones for power generations. Nowadays, different developed countries have introduced cars that are completely running on solar energy. The solar energy is renewable energy which we can use again and again solar energy is environment-friendly source of energy. It means solar energy doesn't pollute our environment because it doesn't produce pollutant gas like carbon dioxide, sulphur dioxide, etc. Finally, solar energy is the energy of the Sun which we can use in different ways for long period of time without environmental hazards. That is why developed countries like China have invested billion dollars in renewable sources of energy. Solar energy is a renewable energy that will not cause any pollution in the environment. It is an energy extracted from the sun using solar power plants. Sun is the richest source of light energy and never has any scarcity. Approximately the energy delivered by the sun on the earth is more than sufficient to the energy requirement of the world for a year. Lack of sufficient electricity is always an immense problem in any developing country. So it is an efficient practice to store this energy instead of deriving it from non-renewable energy sources oil, gas, coal, etc. Shortage of electricity can be considered as the major problem in the developing and undeveloped countries. The utilization of energy from non-renewable energy resources will be expensive and exhaustive as they are limited in the nature. The efficient solution to this problem can be achieved by switching to the generation of energy from sunlight. Solar energy is always an effective option to generate the electricity due to its in-exhaustive and eco-friendly nature. Several countries have already adopted this technology to replace the crude oil in many industries. It is mainly due to the high cost of crude oil and its disastrous impact on environment. In the solar type of renewable energy, we use the photovoltaic (PV) cells as the primary and essential elements to efficiently convert the sunlight into electrical current, without any other form of mechanical or thermal interlink. Such 72 PV cells are connected together to make one module to generate a DC voltage between 23 and 45 V and a typical maximum power of 160 W, depending on temperature and solar radiation. The panel efficiency is dependent on the factors like solar intensity and temperature, and the dust will decrease its efficiency.

1.1 Problem Definition

A large amount of energy is available within the core of sun. If we are able to store at least 1% of this energy, then it can cater the need of our race for decades. Continuous efforts have been put to capture and store as much energy as possible. A few disadvantages of solar energy like expensive in capturing and storing process and its inconsistent availability are limiting its wide utilization in the market. In addition to this, the other problems like rise in the solar panel temperature can reduce its efficiency and lifetime as a result the system suffers from the reliability issues. This efficiency drop with temperature rise is approximately equal to $0.5\%/^{\circ}\text{C}$. So it will become a major drawback for the high rise in temperatures. In order to improve the efficiency and lifetime, we propose a cooling technique for the solar panel. The increment in the efficiency with the proposed cooling technique will be approximately equals to 3–5% of the overall efficiency. In water cooling technique, amount of water consumption plays an important role. So in this work, efficient water cooling technique is proposed to improve solar panel life time along with reduced power to drive the water cooling system.

1.2 Importance and Objective of This Research

The importance and objective of this research is to identify and solve the problems like solar panel lifetime, solar power efficiency, performance, and cooling system and dust cleaning within solar based system. These issues are raised from insufficient maintenance of solar panels and semiconductor photo voltaic cells. To solve these kinds of issues, maintenance of solar panel with less man power, water and power is needed. This reduction of power and water can improve the solar panel lifetime that leads to improvement in the solar system reliability. Also it can reduce the penalty of heat in high performance real-time solar systems. Based on above discussions, the objective of the work is summarized as follows:

- To design and implement a 20 w solar system with auto-cooling to reduce the temperature of solar panel at an acceptable level.
- It will definitely improve the life time of solar panel.

Amorphous silicon solar cell is considered in this work because it has lower life time compared to other solar cells.

2 Literature Review

Michaelo et al. [1] developed a technique to improve solar panel life span. The authors mentioned that the overheating of solar panel can form electric arcs which melts the metal fixtures and burns away its insulating materials [1]. Michaelo [1] used the hollow fiber (hollow tubes of 1 mm diameter attached behind solar PV panel) cooling system. But in these results were observed at temperature of 50 °C. It is too high i.e. 38 °C is STC (Standard Testing Temperature). Xiao Tang et al. [2] developed a novelty in their work to cool solar panels using micro heat pipe array. The air-cooling and water-cooling methods under nature convection condition were discussed in this paper. But they conclude that water cooling is the best technique to improve Solar PV panel efficiency. Mohd Ehtishaan et al. [3] developed a work to reduce temperature of solar panels. The temperature increase can reduce the band-gap of the semiconductor; as a result its material parameters will be affected. In a solar cell, the parameters generally influenced by the increase in temperature are the open circuit voltages [3]. As the temperature builds, the open-circuit voltage reduces, so it will decrease the fill factor and finally reduce the productivity of a solar cell. [3]. they have used the two cooling systems as Air cooled Systems and water or refrigerant cooled systems. They have implemented the model on MATLAB. Finally they conclude that cooling effect on PV panel improves efficiency. Sandeep Koundinya et al. [4] proposed a technique to improve the efficiency of PV panel. They have discussed that reflections from the top surface and the absorption of heat from the other parts of panel can reduce its efficiency. Also they have attempted to lessen the panel's temperature by cooling it with finned heat pipe. Computational Fluid Dynamics methods were adopted to design the solar panel model and its finned heat pipe assembly. This method decreases the temperature by a maximum of 20 K. Assembling of finned heat pipe is a complicated one. Koteswararao et al. [5] experimented a work to improve efficiency of solar system. Although we have the large amount of solar energy but we couldn't use it adequately because of its temperature variations in every while. In their research they found that the constant power was generated with the help of cooling. Also they have compared different cooling methods for solar panel. Ionel-Laurentiu, [6] the water cooling method uses the cross and parallel flows of water. When the panels are overheated then the thermal sensors will automatically switches on the motor to start the water cooling process. Then the parameters like efficiency and Fill Factor were calculated. Finally they have concluded that cooling system is compulsory one to improve PV panel efficiency. A. R. Amelia [7] In their work, they have shown that the efficiency of PV module with cooling system was increasing compared to PV module without cooling system; it is because the ambient temperature dropped significantly.

3 Proposed Methodology

Block diagram of proposed methodology is shown in Fig. 1. In these, three sensors are used to detect temperature, dust and output voltage of the panel. LCD module is used to display indication. DC motor, Fan & Pump are used as interface devices to do necessary action in this arrangement. SCU (Signal Conditioning Unit), Relay Driver Circuits, two 12v batteries are also connected in this setup. ARM processor is heart of this setup. Solar panel is tracked by tracking switch in various directions, at one direction; it gives maximum voltage that voltage is called as MPPT (Maximum Power Point Tracking) voltage. At that point, it stops tracking and the corresponding voltage is stored in ARM. Reference temperature is previously calibrated. Panel temperature is measured with temperature sensor, if it exceeds the reference temperature, pump will automatically power the water. According to temperature in the solar panel, water spraying is given by pump. Pump will be automatically off if panel temperature

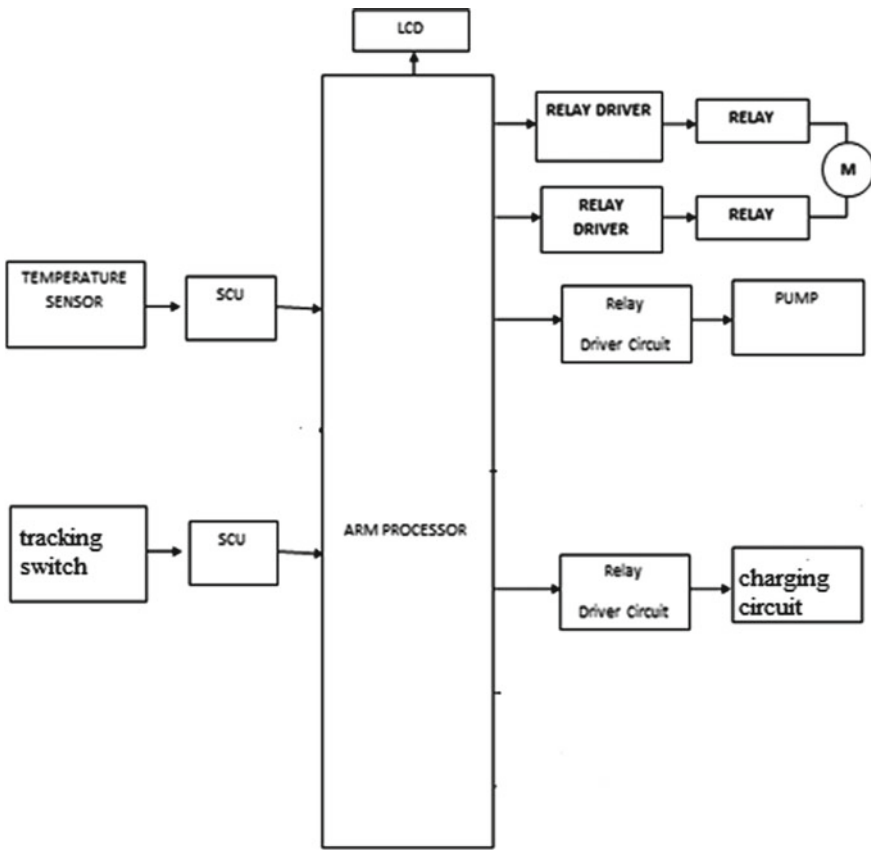


Fig. 1 Blocks diagram of proposed system

reduces below the reference level. Minimum enough temperature level to operate solar PV panel is setup in the microcontroller set-up circuitry. Measure temperature from solar panel is compared with preset temperature in controller circuit, according to control circuit decision in microcontroller circuit, water flow level is adjusted. This technique saves water and energy. It will leads to improvement of solar panel life. i.e. during unnecessary cooling time water flow will be stopped. MPPT voltage is stored in battery via charging circuitry and ARM 7 controller.

3.1 Interfacing Temperature Sensor LM35 with ARM7

It is a circuit for measuring temperature in the panel along with Data Acquisition System is shown in Fig. 2. Data acquisition block includes A/D converter, signal conditioning & amplifier. LM 35 temperature sensor is used to detect the panel temperature then it converts into voltage. This voltage is manipulated by signal conditioning unit for further stage of processing i.e. it pre-amplifies the sensor output. LM 35 output is given to p0.28 of ARM 7 micro controller. It is the ADC input of ARM 7.

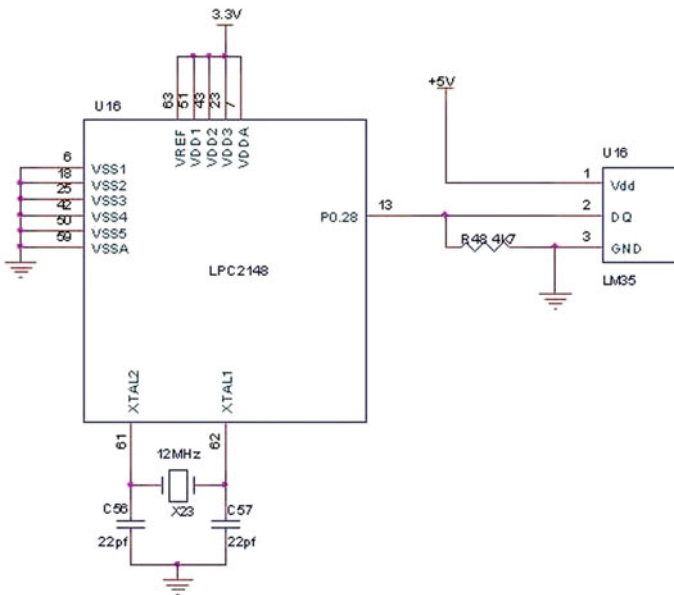
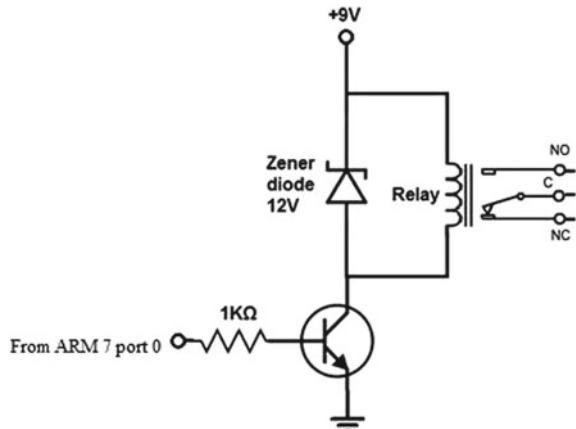


Fig. 2 Signal conditioning Unit with LM 35

Fig. 3 Relay Driver Circuit



4 Relay Driver Circuit

Relay Driver circuit is shown in Fig. 3. Whenever the relay coil receives the voltage at its terminals, it starts functioning. The required input DC voltage for the relay action is given by its DC voltage ratings. For the proper functioning of relay unit, the voltage spikes should be eliminated by connecting a zener diode in parallel to it. A transistor based circuit is used as the driver circuit for the relay unit as it draws very less power. As the base of the transistor is given with the sufficient voltage from the ARM 7 port, the transistor starts conducting. That makes the relay powered up and starts functioning according to the requirement.

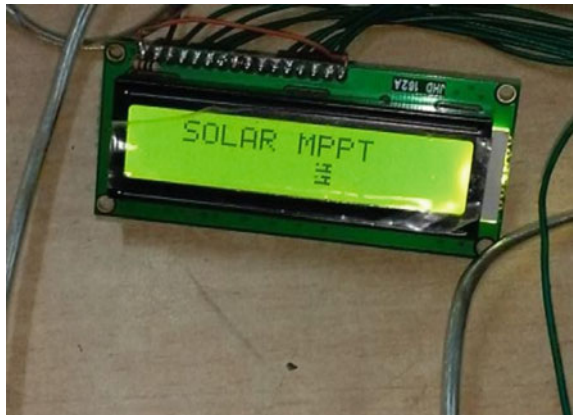
5 Results and Discussion

Home position of the panel is shown in Fig. 4. In this prototype model, we have to reduce the overheating of panel. First, the setup can be done and we set the reference temperature, at the time when it is reached the reference temperature, the water can flow around the panel to avoid excess of overheating in panel. According to the water flow we can avoid the overheating and improving the panel strength. According to panel voltage, solar panel is automatically tracked using servo motor. Initially the panel is on the home position see in the below diagram. The first step of the tracking is, determination of solar panel higher voltage. In this prototype model, we can give the manual panel voltage to the arm processor to track the corresponding voltage. Initially MPPT (Maximum Power Point Tracking) is tracked from the sunlight to track the maximum panel voltage obtained direction. This image is shown in Fig. 5. In LCD display Fig. 6, three indications are there. First one is panel temperature, second one is reference temperature which is preset in the ARM processor, and third one is panel voltage.

Fig. 4 Home Position of the Panel



Fig. 5 MPPT tracking



5.1 Measurement Setup

Panel voltage is measured at different intervals of Sunlight Peak hours. At 12.30 h, temperature is measured as 43° C. At that time corresponding panel voltage is 18.5 V for 21 V, 5 W solar panel. It is shown in Fig. 7. In this case reference voltage is set as 39° C. Measured temperature is higher than reference temperature. Now, water is sprayed through programmed pump over the surface of solar panel. It is shown in Fig. 8. Now panel voltage is displayed as 19.3 V, panel temperature becomes 38° C (Fig. 9). This is enough to work solar panel efficiently.

At 13.05 h, similar observations are monitored. Panel temperature is 43.3° C, panel voltage is 18.7 V. After cooling, panel temperature becomes 39° C, panel voltage is 19.3 v. Even though STC (Standard Testing Condition) is 43° C, amorphous silicon PV panel gives good performance at 38° C to 39° C). Therefore we conclude that we

Fig. 6 Indications of LCD Display



Fig. 7 At 12.30 h panel temperature



can improve amorphous silicon PV panel life time by auto water spraying method. Before cooling and after cooling measured voltages are tabulated in Table 1. Prototype model is only constructed here. Panel output voltage is measured in terms of no-load condition both before cooling and after cooling. No load voltage efficiency is improved from 88.04 to 91.9%.

Fig. 8 Automated water spraying on solar panel and panel voltage measurement

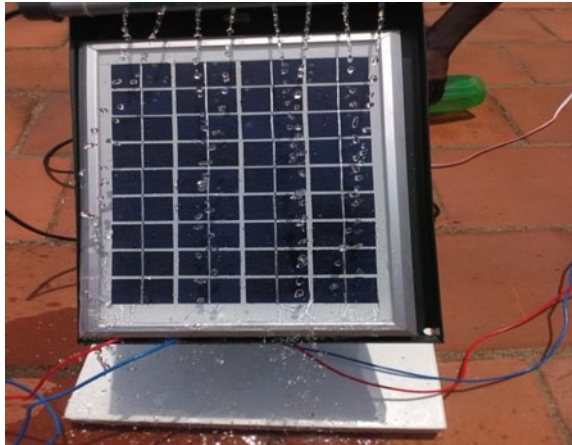


Fig. 9 After cooling panel voltage at 12.30 h



Table 1 Comparison of panel voltage before and after cooling

Sr. No.	Time	Panel temperature and voltage before cooling	Panel temperature and voltage after cooling	Efficiency improvement (%)
1	12.30 h.	43 C°, 18.5 V	38° C, 19.3 V	3.9
2	1.05 h.	43.3° C, 18.7 V	39° C, 19.3 V	3

6 Conclusion

This work was developed after conducting a number of simulations before finalizing the design. It reduces the bottleneck between hardware and software design. Entire simulation results are carried out using keil micro vision 7 in windows XP. After conducting experiments in various intervals of time it was concluded as it is an efficient technique to reduce solar panel temperature with minimum cost, power and water. No load voltage efficiency is improved from 88% to 91% with

our proposed auto water cooling technique. Further it was noted as if voltage efficiency of solar panel is improved, definitely lifetime/lifespan of solar panel will be definitely improved with minimum man power.

References

1. Schmidt Michaela (2016) Ilya Astrouski, Marcus Reppich, Miroslav Raudensky", Solar panel cooling system with hollow fibres. *Appl Solar Energy* 52(2):86–92
2. Tang Xiao, ZhenhuaQuan Yaohua Zhao (2010) Experimental investigation of solar panel cooling by a Novel Micro heat pipe array. *Energy Power Eng* 2:171–174
3. MohdEhtishaan, MdRizwanSaiffee (2016) Simulation Based Intelligent Water Cooling System For Improvement-The Efficiency of Photo-Voltaic Module. *Int J Comput Sci Mobile Comput* 5(7):535–544
4. SandeepKoundinya, Dr. A S Krishnan (2014) Computational Study of Cooling of PV Solar Panel Using Finned Heat Pipe Technology. *Int J Mech Eng Technol (Ijmet)*, 5:216–223
5. Koteswararao B, Radha Krishna K, Vijay P, Rajasurya N (2016) Experimental Analysis of solar panel efficiency with different modes of cooling. *Int J Eng Technol (IJET)*, Vol 8 No, pp 1451–1456
6. Ionel-Laurentiu, Gheorgh (2012) Automatic System For Cooling Of Photovoltaic Panel, Conferința Națională De AcționăriElectrice, Ediția Xvi, SUCEAVA
7. Amelia AR*, Irwan YM*, Irwanto M (2016) Cooling on Photovoltaic Panel Using Forced Air Convection Induced by DC Fan. *Int. J. Electr. Comput. Eng. (IJECE)*, Vol. 6, No. 2, pp. 526–534

Design of Onboard Integrated Charger for Electric Vehicles Based on Split Three Phase Induction Motor



Ganesh Punjaram Thombre and S. V. Tade

Abstract Today, as we knew that crude oil storage would vanish from the world due to the excessive use of various applications, the alternative energy source in multiple applications is becoming a must. The use of electric vehicles is the most prominent solution over conventional vehicles running on petrol, diesel etc. as they consume a substantial amount of crude oil. The most crucial factor in an electric vehicle is the design of a battery charging system. The battery charging system is an essential part of the electric vehicle. Therefore, the charger design by utilizing traction motor winding as an inductor filter reduces disturbance in input and keeps the vehicle as light as possible and cost-effective. The input filter in high power rectifier keeps line current distortion within the allowable limit. Simulation results for the proposed concept have been provided for comparing AC to DC converter with and without filter inductor and charging of the battery from the AC grid with the inductive input filter's effect across the battery.

Keywords Electric vehicle · Charging system · Traction motor · Inductor filter

1 Introduction

Today's trend in the market is to run the vehicle by using electrical energy. The hour's need is to develop a new energy source as crude oil supplies deplete every day and pollute the environment. Therefore, electric vehicles are the best option to replace conventional vehicles running on oil application. However, there are some difficulties in using electric vehicles like charging of electric vehicles battery time and charging station.

The use of electric vehicles instead of a conventional vehicle reduces pollution and dependency on crude oil [1, 2]. Therefore, most of the countries and their scientist are working on these issues. Most automobile industries are introducing new vehicles in the market day by day, which is getting charged very rapidly and giving a better response.

G. P. Thombre (✉) · S. V. Tade
Sinhgad Institute of Technology, Lonavala, India

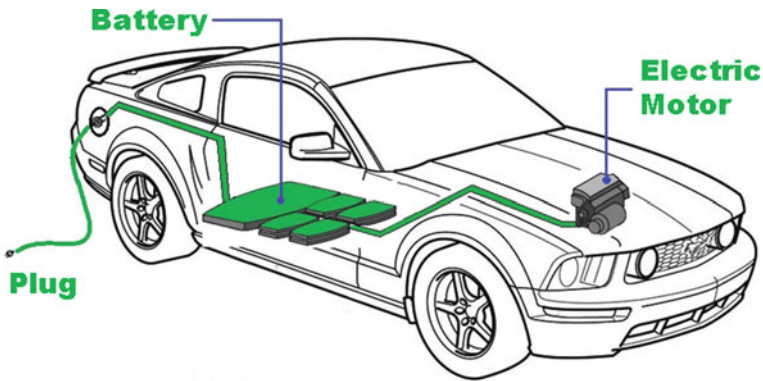


Fig. 1 Layout of electric vehicle

This paper motivates the design of a fast charger of an electric vehicle to make the electric vehicle comparable with the conventional vehicle in refuelling or recharging electric vehicle batteries [3].

2 Electric Vehicle Background

An electric vehicle uses one or more electric motors or traction motors for propulsion mainly classified as Hybrid electric vehicle, plug-in electric vehicle. As shown in Fig. 1, an electric vehicle uses the electric motor to run the vehicle, and electric supply to the motor has been given through the batteries. Batteries are charged using an onboard charging system or off-board charging system from the charging point provided at a different location [1, 3, 4, 6].

3 Methodology

To increase the electric vehicle's efficiency by reducing weight, volume and cost, traction motor is used to perform another independent operation when the vehicle parks [2]. Traction and charging are not simultaneous processes; the motor's induction motor and driving circuitry can be used in the charging circuit to form onboard integrated charger. While charging, when the vehicle at immobile state, we can use stator winding as an inductive filter at AC's input to DC converter.

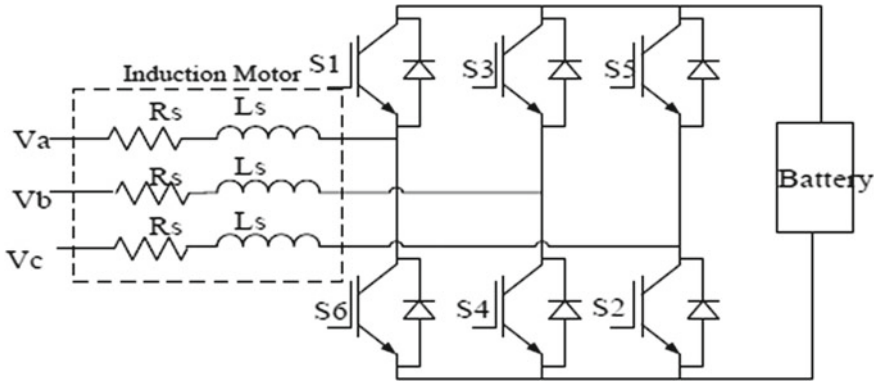


Fig. 2 Conventional Three Phase charging system

3.1 Conventional Electric Vehicle Charging System

In a conventional three-phase induction motor, we feed power to stator winding rotating magnetic field produce which rotates in the stator air gap at asynchronous speed. The conventional three-phase induction motor with inverter and battery are shown in Fig. 2.

When charging, the vehicle should be stationary, so the motor is stopped by applying mechanical brakes. Still, the application of mechanical brakes increases the stress on the motor shaft [5]. Another option is to use an extra clutch to rotate the motor freely. The above techniques have several disadvantages, such as increasing the magnetizing current, leading to the heating of motor and lower efficiency, and adding the mechanical hardware, which is not feasible options [1, 2].

A split three-phase induction motor can eliminate an above drawback. In a split three-phase induction motor, the induction motor’s winding is divided into two equal half portions with zero degrees displacement, sharing the same magnetic circuit. Here in split three-phase induction motor, each phase winding carries the same current, as well as each phase winding, produced the same magnetic field of the same magnitude, but in the opposite direction, so resultant is zero. Thus, no RMF, no torque and motor work as an inductive filter during charging.

3.2 MATLAB Simulation of the Converter Without Filter

The MATLAB simulation of proposed system without filter is shown in Fig. 3.

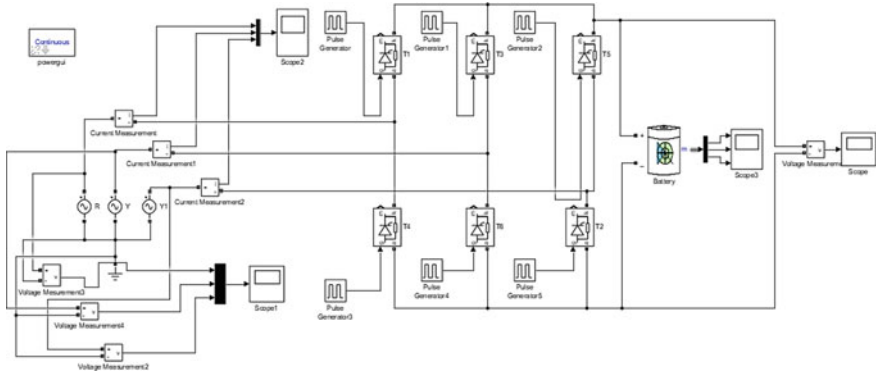


Fig. 3 Convention charging system with battery MATLAB simulation model

3.3 Proposed Design of Electric Vehicle Charger

In an integrated split three-phase induction motor charger, the same circuitry for charging and traction can be implemented. In charging mode, the battery's charging is done by closing switch G1, G2 and G3 for grid connection and moving the switch a, b and c toward 1, 2 and 3 to cancel the rotating magnetic field. The second mode is traction mode in which battery supplies the power to the traction motor, which can be achieved by moving switch a, b and c to 1' 2' and 3'. Making such type of arrangement winding of an induction motor goes in star connection and a motor capable of producing a rotating magnetic field.

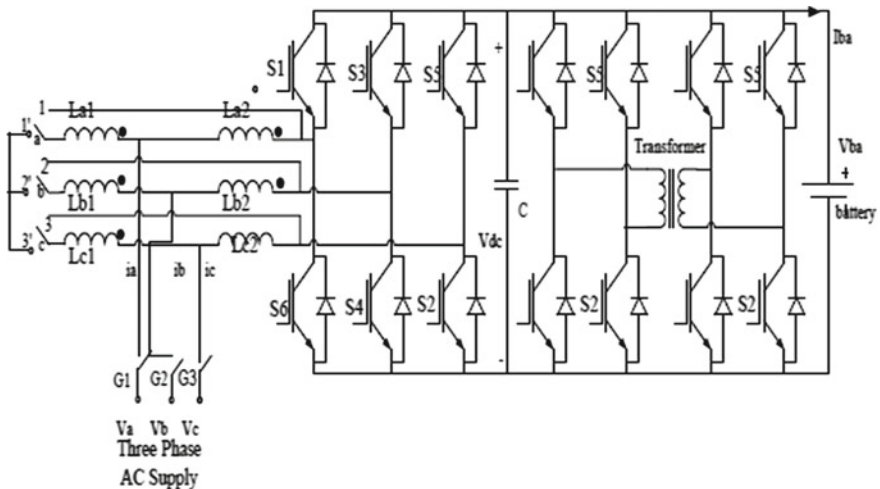


Fig. 4 Proposed designed charging system

The proposed system is shown in Fig. 4, input side 3- ϕ bridge ac to dc converter used for grid side power control, and the dual active bridge dc to dc converter used for controlling charging and discharging of the battery. Here V_a, V_b and V_c are the grid side voltage, and I_a, I_b and I_c are the grid side current V_{dc} is the dc side voltage. V_{ba} represents the battery side voltage, and I_{ba} represents the battery side current, R and L represent the induction motor's resistance and inductance, respectively. It can also be used to make buck/boost characteristics of the converter and obtain the converter's unity power factor and control the converter's bidirectional power [6, 7].

At the time of charging, power flows from grid to the battery where ac to dc converter work as the rectifier and dual active bridge dc to dc converter, the dc output voltage of the ac to dc converter at the desired voltage level required for battery, and also provide constant current and constant voltage charging of the battery.

When power flow reversed from battery side to the ac side during traction process, bidirectional dual active bridge dc to dc converter converts the battery voltage level required for dc to ac converter. That time ac to dc converter act as an inverter and supply power to the traction motor [4]. Instead, the dual active bridge dc to dc converter provides galvanic isolation and protects the system from switching surges and abnormal conditions. For simplicity, we have checked the effects of inductive filter on the performance of the Converter in MATLAB without DC to DC converter and inverter circuitry, as shown in Fig. 5.

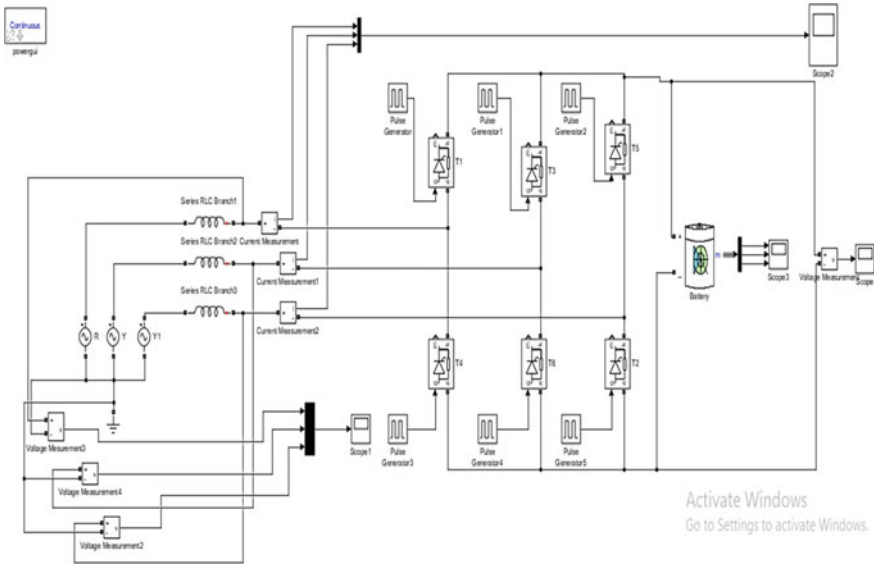


Fig. 5 The converter circuitry with inductive filter MATLAB simulation model

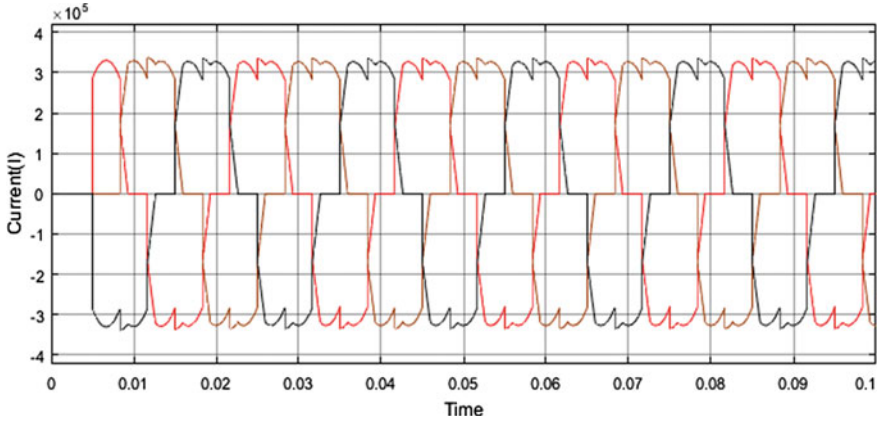


Fig. 6 Converter input Current waveform

3.4 MATLAB Simulation of Converter with Filter

See Fig. 6.

4 Results and Discussion

4.1 Converter Input Current Waveform Without Filter

It is observed from Fig. 6, that whenever we are using a supply from any source point directly to the load, the power factor of the system becomes low and absorbs more power due to the harmonics present in the supply current [7].

From the FFT analysis, it is clear that 49% THD is present in the input current waveform, as shown in Fig. 7, which ultimately causes low power factor and unnecessary absorption more power [1].

4.2 Converter Voltage Across the Battery Without Filter

The DC voltage available at the converter's output is less than the expected voltage because of the harmonics in the input supply, as shown in Fig. 8, which also affects the battery voltage and charging time [1].

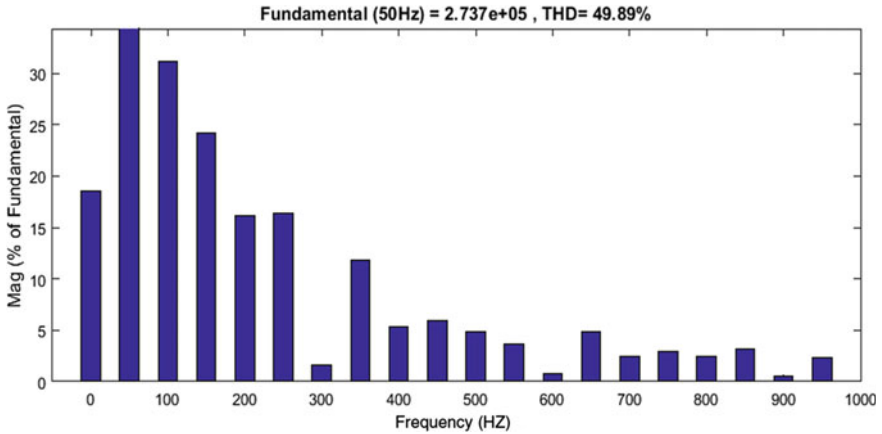


Fig. 7 FFT analysis without inductor filter

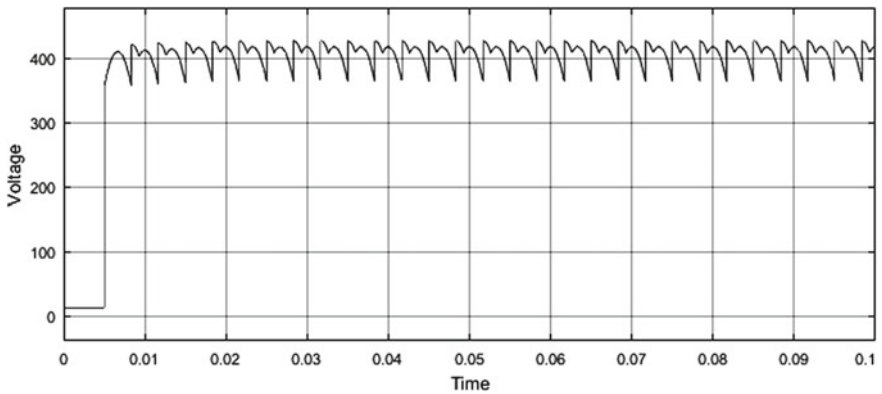


Fig. 8 Converter voltage across the battery

4.3 Filter Current Output Waveform

The inductor filter’s output current waveform shows that the current waveform becomes more sinusoidal, as shown in Fig. 9. Therefore, the harmonics component gets reduced, which improves the input power factor and low consumption of power [7].

The FFT analysis graph shown in Fig. 10 indicates that the inductor filter in the input circuit reduces THD up to 4.34%. Thus, the distortion in current becomes low, which increases the power factor of the system [7].

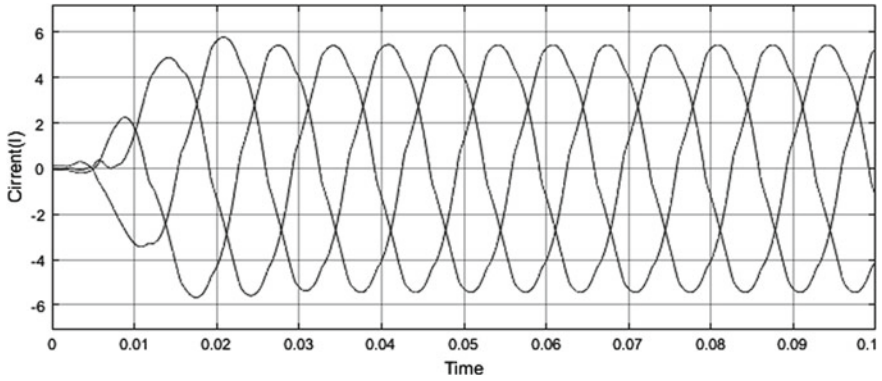


Fig. 9 Filter current output waveform

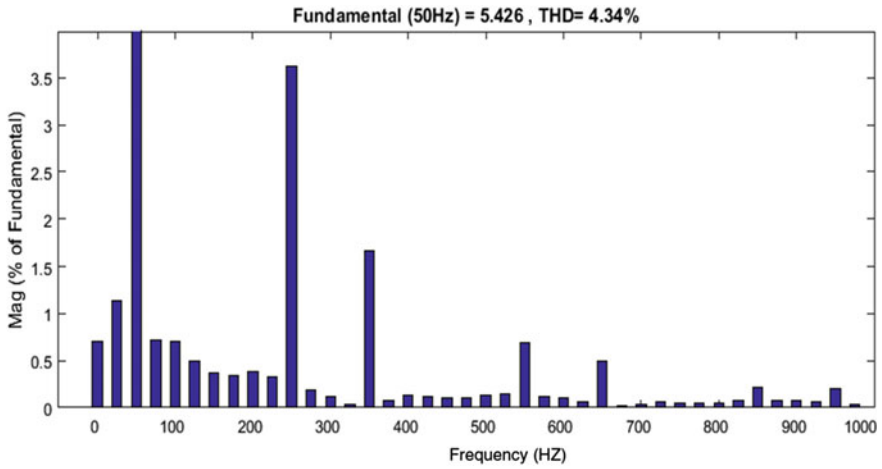


Fig. 10 FFT analysis of input current with inductor filter

4.4 Converter Output DC Voltage with Filter

Figure 11 shows that Converter with inductive filter draws sinusoidal current and provides regulated constant output DC voltage across the battery [1].

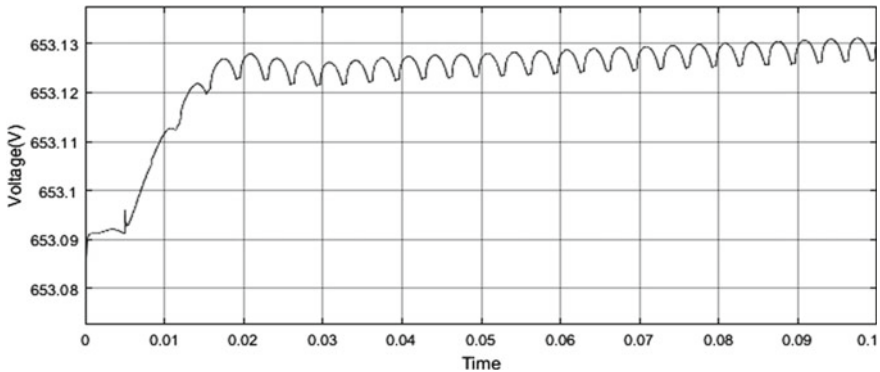


Fig. 11 Converter output DC voltage

5 Conclusions and Future Scope

The charging system's design with split-phase three-phase induction motor winding reduces the harmonics in the charging system and more effective use of induction motor winding to reduce harmonics in the input supply for the charging system. From simulation result and mathematical calculation, it is concluded that traction motor used in an electric vehicle can improve the power quality of input supply given to the Converter. Using traction motor stator winding as an inductor filter reduces the onboard weight of the battery charging system.

References

1. Nassary M, Orabi M, Ghoneima M, El-Nemr MK (2019) Single-phase isolated bidirectional AC-DC battery Charger for Electric Vehicle – Review. International Conference on Innovative Trends in Computer Engineering, Aswan, Egypt 2019:581–586
2. Yilmaz M, Krein PT (2013) Review of battery charger topologies, charging power levels and infrastructure for plug-in electric and hybrid vehicles. *IEEE Trans Power Electr* 28(5):2151–2169
3. Haghbin S, Lundmark S, Alakula M, Carlson O (2013) Grid-Connected Integrated Battery Chargers in Vehicle Applications: Review and New Solution. *IEEE Trans Industr Electron* 60(2):459–473
4. Arancibia Arnaldo (2013) A Unified Single- and Three-Phase Control for Grid-Connected Electric Vehicles. *IEEE Trans Smart Grid* 4(4):1780–1790
5. Lacressonniere F, Cassoret B (2005) Converter used as a battery charger and a motor speed controller in an industrial truck, European Conf. Power Electronics Applications, Dresden 2005:7
6. Haghbin S, Khan K, Zhao S, Alakula M, Lundmark S, Carlson O (2013) An integrated 20-kW motor drive and isolated battery charger for plug-in vehicles. *IEEE Trans Power Electron* 28(8):4013–4029
7. Varghese SS, George S (2013) Analysis of AC-DC Converter Based on Power Factor and THD. *Int J Emerg Technol Advanc Eng* 3(2):350–356

Performance Improvement and Cooling of the Solar Photovoltaic Panel by Using Fin and PCM Integrated Fin



Siddharth S. Patil, Sidalingagouda R. Patil, and Aniket B. Shedbale

Abstract Increasing photovoltaic (PV) cell temperature reduces the efficiency also PV cell durability. When the PV cell temperature is higher than its working condition, the PV cell efficiency decreases. The fundamental reason for this investigation is to moderate the PV panel temperature and keep it limited. The results of the overall study showed that when PCM and fin were used in conjunction with the PV panel, it was effective in keeping the PV panel temperature below 50 °C. Also, the use of fin and PCM has reduced the PV panel average temperature by 7–10 °C and this has increased the PV panel efficiency. The cooling system of fin and PCM has increased the PV panel efficiency by 1.4 to 4.6%.

Keywords Solar energy · Photovoltaic panel (PV) · Fin · Phase change material (PCM) · Thermal storage

1 Introduction

1.1 Significance

Nowadays the use of solar panels has increased tremendously in the country and the world. Solar panels are being used extensively for domestic as well as commercial purposes. Due to the increasing demand for energy, consumers and companies are turning to alternative energy sources for domestic and commercial purposes and looking at solar energy as a great alternative. In the world as well as in the country, more and more people are buying solar panels for domestic purposes and using them to generate electricity. With the increasing use of solar panels, the interest of researchers in making technical improvements for solar panels has increased. The main focus of the researchers is on cooling solar integrated panels as it is the main focus of private companies and consumers. When it comes to cooling solar integrated panels, the main focus is on the need for a different shape to fit the structure, and this is different from other cooling systems. An integrated panel is part of a building and

S. S. Patil (✉) · S. R. Patil · A. B. Shedbale
Padmabhooshan Vasantraodada Patil Institute of Technology, Budhgaon, Sangli, India

is not mounted on top of the building, making it difficult for air to play on the back of the panel [1].

The usage of renewable energy sources is on the rise due to limitations in the use of fossil fuels. With the rise in human residents as well as increasing demand for energy, a big question is what will happen after the exhaustion of fossil fuel reserves? Renewable energy sources can mainly use solar energy and solar energy can be an alternative to the use of fossil fuels. Once it approaches energy generation, it is important to focus on its efficiency. Energy can be generated in two ways, one is electrical energy and the other is thermal energy. Electrical energy is more valued and efficient than thermal energy due to its capability to simply transfer into work. Using solar radiance a PV cell is used to generate electrical energy. The efficiency of a PV cell ranges from 5 to 20% and is more than the indirect efficiency of wind and biomass energy [2].

However, researches have shown that a rise in cell temperature significantly decreases the efficiency of cells. The rate of deterioration of the efficiency of these cells is 0.25% to 0.5% per degree Celsius and it also depends on the material of the cell. Some research has shown that increases in temperatures significantly reduce the lifecycle and efficiency of the entire PV system. So the cooling system of the PV system has already been proposed and at the same time progress is being made in the cooling system. Numerous studies have shown that up to 5% extra power can be obtained when a cooling system is used with a PV system. However, about 87% of the total energy is changed into heat. In recent times, the focus has been on converting waste energy into usable thermal energy.

1.2 Execution of the PV System

The temperature has a big effect on PV panel performance. The PV panel which is not converted solar radiation into electricity is converted into heat energy. This heat energy increases PV panel temperature and reduces the overall PV panel efficiency. Some researchers have used various processes to improve PV panel performance and reduce the overall installation cost. Hosseini et al. [3] in this study water is used on PV panel surface. The use of water has succeeded in keeping the PV panel surface temperature low. A further system is used to facilitate the use of hot water on PV panel surfaces for other purposes. This overall system has been shown to reduce PV panel temperature and increase PV panel electrical efficiency. Furushima and Nawata [4] in this research, for cool the PV panel siphon age, has been used. The test is done in the summer. Studies have shown that lowering PV panel temperature has resulted in an increase in the generation of electrical energy and that water has been used for other purposes. Abdol Zadeh and Ameri [5] in this study cold water was sprayed on the PV panel surface to reduce PV panel temperature. A water pumping system is used for spraying water. Examination of the study noted an increase in overall system efficiency. Teo et al. [6] in this research, inlet and outlet manifold air duct has been used with PV panel backside to reduce PV panel temperature. The study found

that cold air reduced PV panel temperature and increased PV panel efficiency by 12 to 14%. Bahaidarah et al. [7] in this study heat exchanger is used with PV panel back surface. As a result, the heat exchanger absorbs PV panel temperature, which helps to PV panel cool. The hot water in the heat exchanger can be used for other purposes and the conclusion is that PV panel temperature has been reduced by 20% and PV panel efficiency has been increased by 9%. Gang et al. [8] in this heat pipe is used for PV panel cooling. The heat pipe is used with a PV panel back surface. The results show that the use of a heat pipe has reduced PV panel temperature and improved PV panel efficiency. Krauter [9] in this research, water flowing on the PV panel surface method is used to reduce PV panel temperature. As a result, PV panel temperature has come down to 22°C also the electrical yield has increased by 10.3%. Many researchers have used water as well as air to lower PV panel temperature. But the flow of air and water requires extra energy and this extra energy reduces the overall system efficiency. Hongbing Chen et al. [10] in this study fin are used with PV panel for cooling purpose. The study looks at how wind velocity, radiation, panel inclination, and temperature affect PV panel electrical efficiency as well as electrical energy generation

PCM in the passive cooling method does not need any external energy when used for cooling PV panels and this method is very convenient for cooling PV panels. It is very important to choose a good PCM for cooling PV panels. The best PCM has the properties of non-corrosive, great latent heat of fusion, non-toxic, chemically steady, melting temperature and subcooling temperature, and finally high thermal conductivity. Choosing the required PCM from these various properties is a very challenging task. Heat transfer can be increased by using fin in PCM. By takeout heat from the PV panel, the power output can be increased by getting the required temperature for the cells. The heat that is emitted from the PV panel when used for other subsequent applications is called PVT. Some studies show that PVT technology is very good and its use is probable to surge in the future. Various concepts of PV-PCM are available in the literature. Research on PV-PCM was done at the Dublin Institute of Technology. In this, they used four dissimilar PV panel cooling methods. Tests presented that the PV panel efficiency using PCM was greater than that of a normal PV panel and this was due to the PV panel's lower temperature as well as the lower cells temperature and the higher the decomposition of the resulting material.

1.3 Problem Identification

Considering the current world, the use of PV panels has increased in many countries. Many countries have started offering grants to encourage the use of PV panels. Many countries have started setting up large capacity solar plants. But when the PV panel temperature goes beyond its operating condition, its efficiency decreases. This means that the PV panel temperature wants to be kept low to increase its efficiency. Different methods are needed to cool PV panels in dissimilar parts of the world and studies and research on cooling methods are underway. If the PV panel can be cooled without any

financial loss, the PV panel efficiency will be increased and more renewable energy can be obtained. As the PV panel temperature and cells increases, their efficiency decreases. So our job is to cool the PV panel using fin and PCM.

1.4 Relevance

Increasing the photovoltaic (PV) cell temperature reduces the efficiency as well as durability of the PV cell. Therefore, many efforts are being made to keep the PV cell temperature low and to cool the PV panel. The main aim of this study is to reduce the PV panel temperature and keep it limited. In this study fin and PCM are limited. The focus of the work is to make an experimental setup and conduct tests to check the efficiency.

2 Experimental Setup and Methodology

2.1 Fin Modification

A test arrangement has been developed to test how using fin with PV panels affects the PV panel performance. Two PV panels have been used in the test arrangement and the PV panel area is 0.351 m^2 . A test arrangement is shown in Fig. 1. The maximum voltage and current 17.2 V and 2.3 A are developed by the PV panel at 1230 w/m^2 irradiance respectively. Experimental testing has been done at $31 \text{ }^\circ\text{C}$ ambient temperatures. The fin used for passive cooling is made of 0.8 mm thickness and is evenly glued to the PV panel rear surface. To increase the rate of heat transfer, a square cross-section shape fin has been added to the PV panel rear surface. A total of 14 fins are glued at 20 mm intervals each. The drill bit is drilled at the same distance

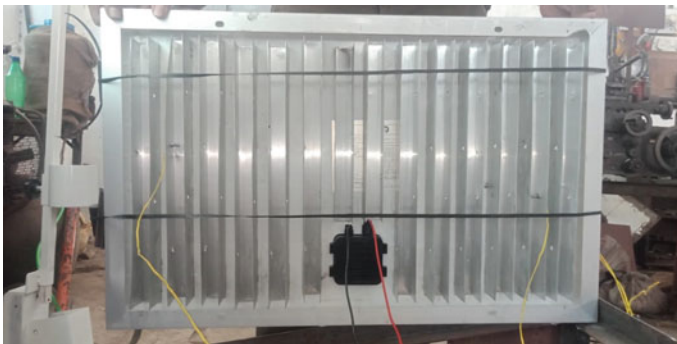


Fig. 1 Photos of Fin integrated experimental setup

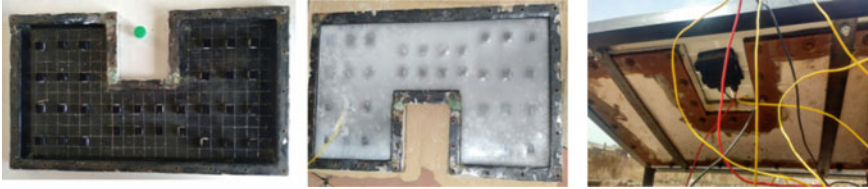


Fig. 2 Photos of PCM + Fin integrated experimental setup

with 10 mm drill bits. The tilt angle of the PV panel to the local latitude of Miraj (16.8222° N, 74.6509° E), India, is set to 21 with horizontal. Five thermocouples have been utilized to gauge the temperature in different parts of the PV panel. Two thermocouples are used on the PV panel top side and also two thermocouples are used on the PV panel bottom side and one thermocouple is used to measure the temperature of the fin. A pyranometer (flux meter) is used to measure the intensity of sunlight. A multimeter is used to measure the voltage as well as current. The experiment has been done every day for 6 days from 10 am to 4 am and the data entry has been done 15 times each.

A test arrangement has been developed to test how using PCM + fin with PV panels affects the PV panel performance. Two PV panels have been used in the test arrangement and the PV panel area is 0.351 m^2 . The test arrangement is shown in Fig. 2. The maximum voltage and current 17.2 V and 2.3 A are developed by the PV panel at 1230 w/m^2 irradiance respectively. Experimental testing has been done at 31°C ambient temperatures. The fin used for passive cooling is made of 0.8 mm thickness and is evenly glued to the PV panel back surface. P-70 Paraffin wax is used having melting point 48 to 50°C , Density 840 kg/m^3 , Latent heat of 148 kJ/kg , Thermal conductivity $0.4 \text{ W/m}^\circ\text{C}$. The tilt angle of the PV panel to the local latitude of Miraj (16.8222° N, 74.6509° E), India, is set to 21 with horizontal. K-type thermocouples have been used to measure the PV panel temperature. One thermocouple is used on the PV panel top side and also one thermocouple are used on the PV panels bottom side and one thermocouple is used to measure the fin temperature and one thermocouple is used to measure the PCM temperature. A pyranometer (flux meter) is used to measure the intensity of sunlight. A multimeter is used to measure the voltage as well as current. The experiment has been done every day for 6 days from 10 am to 4 am and the data entry has been done 15 times each.

2.2 PV Panel Efficiency

PV panel efficiency with fin and without fin was determined using Eq. (1). The equation shows that the PV panel efficiency depends on the PV panel temperature.

$$\eta_{PV} = \eta_{ref} [1 - \beta_{ref} (T_{PV} - T_{ref})]$$

$$\eta_{PV-fin} = \eta_{ref} [1 - \beta_{ref} (T_{PV-fin} - T_{ref})] \quad (1)$$

Improvement in PV panel efficiency with the fin is determined using Eq. (2)

$$\eta_{improvement} = \frac{\eta_{PV-fin} - \eta_{PV}}{\eta_{PV}} \times 100 \quad (2)$$

Improvement in PV panel performance with the fin is determined using Eq. (3)

$$\frac{\text{Temperature of the normal panel} - \text{Temperature of modified set}}{\text{up Temperature of normal panel}} \times 100 \quad (3)$$

3 Result and Discussion

3.1 Result for 6 Fin + Normal Set Up + PCM Implementation

6 fins experimental setup is shown in Fig. 3. The PV panel bottom surface temperature for three different experimental setups is shown in Fig. 4 and the figure shows the PV panel bottom surface temperature of normal setup is more than the fin setup and fin + PCM setup. The PV panel top surface temperature for three different experimental set up is shown in Fig. 5 and the figure shows the PV panel top surface temperature of normal setup is more than the fin setup and fin + PCM setup. The fin, PCM, and atmosphere temperature during the experiment are shown in Fig. 6, and the intensity of the sun during the experiment is shown in Fig. 7. The performance improvement

Fig. 3 Photos of 6 Fin integrated experimental setup



Fig. 4 The bottom temperature of the panel

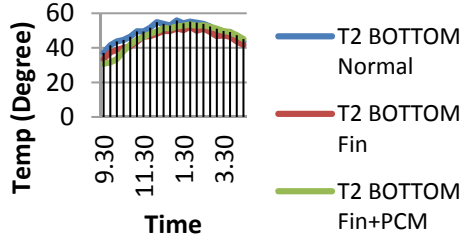


Fig. 5 Top temperature of the panel

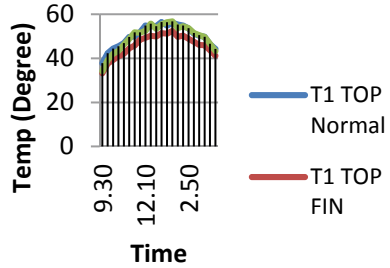


Fig. 6 The temp of the fin, PCM, and Atmosphere

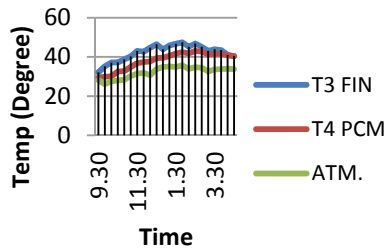
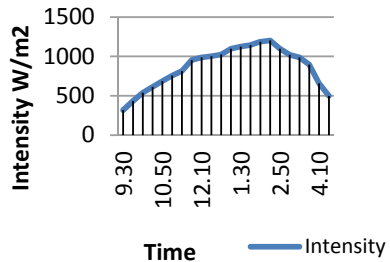


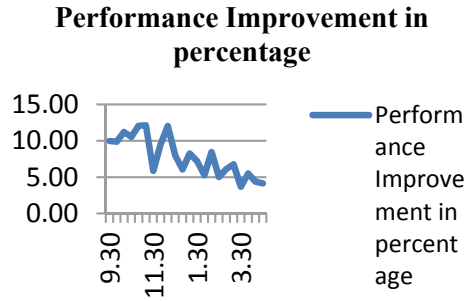
Fig. 7 Sun intensity



of the PV panel by using fin and fin + PCM over the normal PV panel is shown in Fig. 8.

Reading with the experimentation of 6 Fin + Normal set up + PCM implementation shows that it is possible to keep average temperature of front and back

Fig. 8 Performance Improvement in %



surface of PV panel at 46 °C by using fin and by using PCM average temperature is 45 °C. Whereas in a normal set up the average temperature of the front and back surface of the PV panel is 51 °C. The electrical conversion efficiency enhancement of 1.18–2.54% was achieved by the proposed cooling method.

3.2 Result for 10 Fin + Normal Set Up + PCM Implementation

10 fins experimental setup is shown in Fig. 9. The PV panel bottom surface temperature for three different experimental setup is shown in Fig. 10 and the figure shows the PV panel bottom surface temperature of normal setup is more than the fin setup and fin + PCM setup. The PV panel top surface temperature for three different experimental set up is shown in Fig. 11 and the figure shows the PV panel top surface temperature of the normal setup is more than the fin setup and fin + PCM setup. The fin, PCM, and atmosphere temperature during the experiment are shown in Fig. 12, and the intensity of the sun during the experiment is shown in Fig. 13. The performance improvement of PV panels by using fin and fin + PCM over the normal PV panel is shown in Fig. 14.

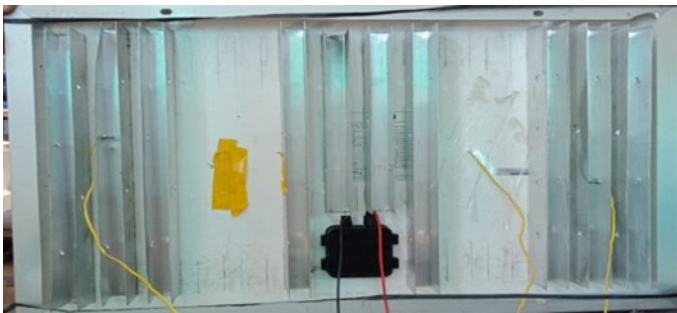


Fig. 9 Photos of 10 Fin integrated experimental setup

Fig. 10 The bottom temperature of the panel

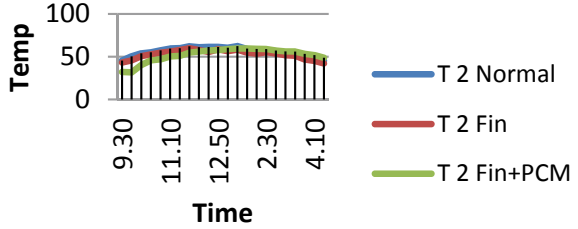


Fig. 11 Top temperature of the panel

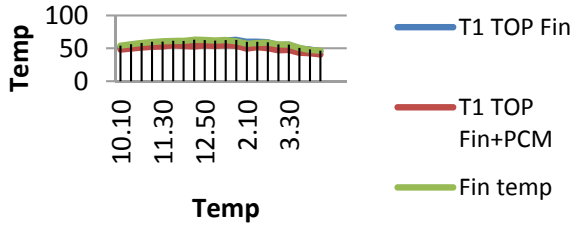


Fig. 12 The temperature of the fin, PCM, and Atmosphere

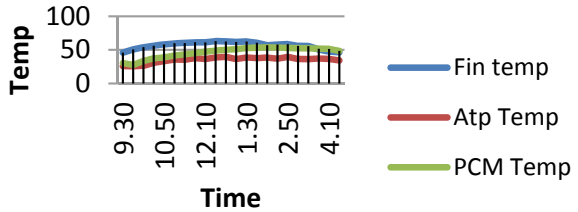


Fig. 13 Sun intensity

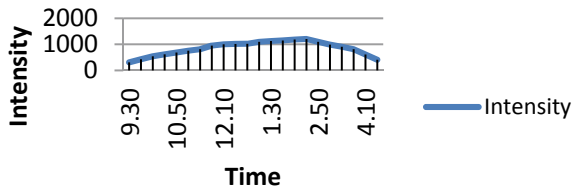
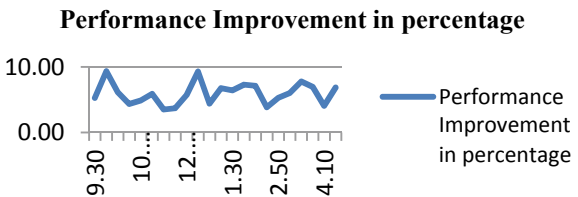


Fig. 14 Performance Improvement in percentage



Reading with the experimentation of 10 Fin + Normal set up + PCM implementation shows that it is possible to keep average temperature of front and back surface of PV panel at 50 °C by using fin and by using PCM average temperature is 52 °C. Whereas in a normal set up the average temperature of the front and back surface of the PV panel is 57 °C. The electrical conversion efficiency enhancement of 2.67-3.40% was achieved by the proposed cooling method.

3.3 Result for 14 Fin + Normal Set up + PCM Implementation

14 fins experimental setup is shown in Fig. 15. The PV panel bottom surface temperature for three different experimental setup is shown in Fig. 16 and the figure shows the PV panel bottom surface temperature of normal setup is more than the fin setup



Fig. 15 14 Fin integrated experimental setup

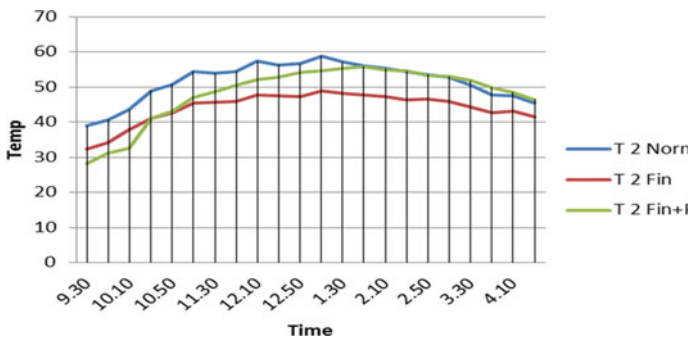


Fig. 16 The bottom temperature of the panel

Fig. 17 Top temperature of the panel

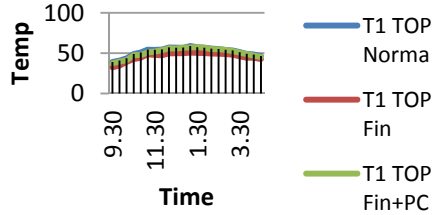


Fig. 18 The temp. of the fin, PCM, and Atm

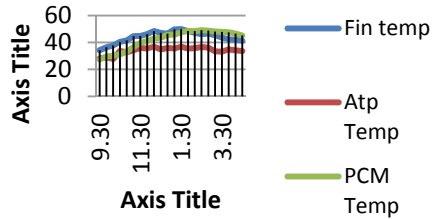
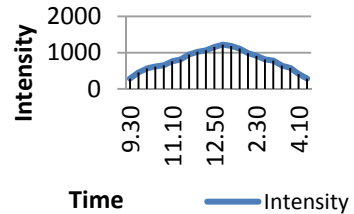


Fig. 19 Sun intensity



and fin + PCM setup. The PV panel top surface temperature for three different experimental set up is shown in Fig. 17 and the figure shows the PV panel top surface temperature of normal setup is more than the fin setup and fin + PCM setup. The fin, PCM, and atmosphere temperature during the experiment are shown in Fig. 18, and the intensity of the sun during the experiment is shown in Fig. 19. The performance improvement of PV panels by using fin and fin + PCM over the normal PV panel is shown in Fig. 20.

Reading with the experimentation of 14 Fin + Normal set up + PCM implementation shows that it is possible to keep average temperature of front and back

Fig. 20 Performance Improvement in %

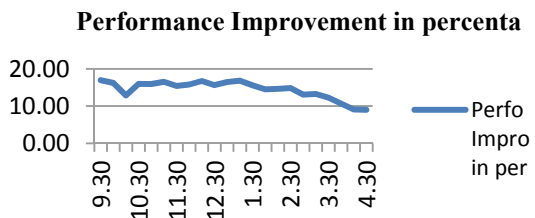
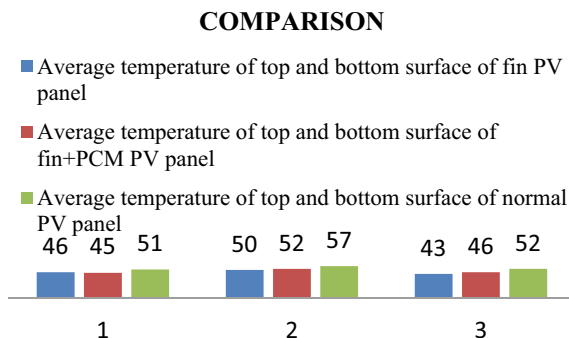


Fig. 21 Comparison based on Experimentation



surface of PV panel at 43 °C by using fin and by using PCM average temperature is 46 °C. Whereas in a normal set up the average temperature of the front and back surface of the PV panel is 52 °C. The electrical conversion efficiency enhancement of 3.7–4.61% was achieved by the proposed cooling method.

Following observations (refer Fig. 21) also recorded by experimentation.

4 Conclusion

In this work, an experimental study has been done on the PV panel electrical conversion efficiency also PV panel overall performance. In this study, fin and PCM have been used to increase PV panel efficiency and performance. Three PV panels have been used in the study and they are normal PV panels, PV panel with fin, PV panel with PCM. The results showed that when the PV panel was cooled naturally using fin and PCM, the PV panel was 1.4–4.6% has been improved. Also, the PV panel temperature is reduced to 7–10 °C due to the use of fin with the PV panel. When PCM was used with a PV panel, the PV panel temperature decreased to 4–6 °C. The overall use of fin and PCM has reduced PV panel temperature and increased PV panel efficiency. The reason for the decrease in temperature is that the heat from the sun increased PV panel temperature and due to natural convection it took a long time for the PV panel to cool down but when fin or PCM was used with the PV panel it helped to keep the PV panel temperature low. The use of fin helped in natural convection and PCM absorbed excess heat. This reduced the PV panel top temperature and bottom temperature and increased the PV panel efficiency.

Acknowledgements We would like to express our deep and sincere gratitude to my Guide Mr. S.R. Patil, Department of Mechanical Engineering, for guiding us to accomplish this project work. We are indeed grateful to him for providing the helpful suggestion, from time to time.

References

1. B.H. Khan: *Non-Conventional Energy Resources* (Tata McGraw Hill Publication) 5–21 (2006)
2. Adnan Ibrahim, Mohd Yusof Othman, Mohd Hafidz Ruslan, Sohif Mat, Kamaruzzaman Sopian: Recent advances in flat-plate photovoltaic/thermal (PV/T) solar collectors,; *Renewable and Sustainable Energy Reviews*, 15, 352–365 (2011)
3. R. Hosseini, N. Hosseini, H. Khorasanizadeh: An experimental study of combining a photovoltaic system with a heating system,; *World Renewable Energy Congress 2011 Sweden*, (8–13th May 2011)
4. K. Furushima, Y. Nawata,; Performance evaluation of photovoltaic power generation system equipped with a cooling device utilizing siphonage: *Journal Solar Energy Engineering ASME*, 128(2), 146–151 (2006)
5. M. Abdolzadeh, M. Ameri,; Improving the effectiveness of a PV water pumping system by spraying water over the front of photovoltaic cells,; *Renewable Energy*, 34, 91–96 (2009)
6. H.G. Teo, P.S. Lee, M.N.A. Hawlader: An active cooling system for photovoltaic modules,; *Applied Energy*, 90, 309–315 (2012)
7. H. Bahaidarah, Abdul Subhan, P. Gandhidasan, S. Rehman: Performance evaluation of a PV (photovoltaic) module by back surface water cooling for hot climatic conditions,; *Energy*, 59, 445–453 (2013)
8. P. Gang, Fu Huide, Z. Huijuan, JiJie: Performance study and parametric analysis of a novel heat pipe PV/T system,; *Energy*, 37(1), 384–395 (2012)
9. S. Krauter: Increased electrical yield via water flow over the front of photovoltaic panels,; *Solar Energy Materials & Solar Cells*, 82, 131–137 (2004)
10. Hongbing Chen, Xilin Chen, Sizhuo Li, Hanwan Ding: Comparative study on the performance improvement of the photovoltaic panel with passive cooling under natural ventilation,; *International Journal of Smart Grid and Clean Energy*, 3(4), 374–379 (2014)

Performance Investigation of Photovoltaic-Thermal (PVT) Solar Collector Using Effective Cooling Techniques: Review



Nikhil K. Purwant and Avinash M. Badadhe

Abstract The use of conventional fuel sources fulfils the energy requirements for all human activities and comfort. But the traditional fuel sources are limited and always have been a serious matter of concern. So it is essential to find an alternative source for energy generation to fulfil the energy requirements. Solar power is a non-traditional energy source, and it has great potential to be an alternative source of energy in the future. More solar radiation enters the atmosphere on earth than overall global energy consumption. So it is an abundantly and continuously available source of energy. Also, it is available free of cost. So it has good scope for energy production. Photovoltaic cells turn the solar irradiance into electric power. But they have very low conversion efficiencies. Generally, 0.45% reduction in the relative efficiency of PV panel with per degree rise in temperature. The rest of the energy is wasted as heat energy. Thus, it is essential to remove the PV system's heat to retain its optimum performance. Identified cooling technologies are proposed in-detail in this review paper.

Keywords Solar power · Photovoltaic (PV) panel · Cooling techniques

1 Introduction

After the first oil crisis of 1973, the word “power” started to appear extensively in the media and newspapers. And then the news is continuously dominated by the terms energy shortages & energy security. As a result, the deficit in oil supply increases prices. It's likewise evident that the fossil vitality period of nonrenewable assets is consistently concluding; the primary oil will be depleted, trailed by coal and natural gas [1]. India is confronting a significant vitality issue and for a long time, importing raw petroleum is expanding quickly, getting predominant in numerous such uses. There is also a need to research and analyse current and emerging energy options from various energy sources. A lot of innovative work exercises are now in progress toward this path.

N. K. Purwant (✉) · A. M. Badadhe
Rajarshi Shahu College of Engineering, Tathawade, Pune, India

One solution is to use renewable sources of energy derived from the sun more comprehensively. Solar power is a plentiful and potential energy resource on earth. In all solar power generation, the sun is a fundamental component. The quality and amount of sun oriented radiation at a specific area is of essential significance for improving any solar energy system.

The actual application utilises sunlight-based warm vitality for business and private space and water warming. Nonetheless, there are different applications past this lower temperature level. For cycles, for example, food, synthetic substances, petrochemicals, minerals, and so on., modern warmth request in Europe has been assessed at 300 TWh/year for the scope of temperature up to 250 °C, for example up to around 8% of absolute European last vitality utilisation. As of recently, this tremendous limit has generally been considered for sunlight based applications, even though this higher temperature can be acknowledged utilising exceptionally created sun oriented gatherers advancements [2].

2 Literature Review on Performance Investigation of PV Panel

A detailed literature survey was performed considering the design, material, performance, economics, and solar power application by different solar energy collectors. Literature deals with thermal performance improvement techniques and the application of photovoltaic in solar power were included.

Bahaidarah et al [3] studied the Efficacy of water to cool the PV system in Dhahran, Saudi Arabia's hot climate conditions. Water is the traditional cooling specialist utilised in numerous private and business applications, for example, inward burning motors, steam power plants, substance plants, and treatment facilities. Water is reasonable and non-harmful and has a high warmth stockpiling limit that fills the need for better cooling the PV module. A numerical model has been created, and the test results were discovered to be in an acceptable arrangement. Results indicated that water cooling brought down the PV surface temperature by 20%, which helped increment the PV board's proficiency by 9%.

Fudholi et al [4] had carried out a performance study of solar PVT water collectors and proved that the PV module's efficiency increases once the temperature drops. It was additionally demonstrated that temperature decline isn't direct with a mass stream rate increment.

Joy et al [5] conducted comparative research was on uncooled PV, water-cooled; ethylene glycol (EG) cooled, and water-EG blend cooled PV. The coiled tube design was utilised to catch heat from the PV unit, and yield is judged exclusively on thermal efficiency and electrical efficiency. It was indicated that PVT effectiveness increments exponentially with expanded coolant thermal conductivity.

Rahimi et al [6] developed a 0.667 mm hydraulically diameter micro-channel absorber to improve PVT heat transfer performance. A performance-based study

was conducted to assess the optimal generation of electric power. It was shown that the arrangement of micro-channel absorbers increased energy production by 30%.

Touafek et al [7] proposed a new layout of the PV for removing more heat was suggested by the theoretical model of the galvanised steel plate and incorporating the tube as an absorber for the extraction of heat and the quantified output with performance-based work. An absorber's updated design was distinguished by increased heat absorption potential and lower manufacturing costs and showed to be a reasonable alternative to the traditional PVT system.

Ben Cheikh El Hocine et al [8] conducted a low-cost analysis of galvanised steel to produce absorbers. They proposed a theoretical framework with two new absorber layouts, including a parallel vertical tube and a form of enclosure. Experimental analysis was carried out to test thermal and electrical parameters. The outcome supported something like an equal vertical tube absorber instead of a fenced-in area because of more significant power saving.

Astea et al [9] conducted heat-electrical optimisation of the fluid PVT collector setup, demonstrating that it is possible to optimise the PVT's efficiency by selecting the thermo-electrical configuration of the collector as necessary.

Jayasuriya et al [10] proposed a numerical model to evaluate the impact of design sensitivity, weather conditions, and operational conditions on PVT efficiency. Five different configurations were suggested depending on the cooling fluid and the organisation of Glass and Tedlar Plate. The various formats were Glass to glass PV system with air circulation just above the designed absorber plate, Glass to glass PV system with airflow just below the designed absorber plate, Glass to Tedlar PV system with airflow just below the designed absorber plate, Glass to glass PV system with water flow just below designed absorber plate and Glass to Tedlar PV system with water flow just below absorber plate. The results indicated that the Glass Tedlar Water emphasised as noticed to become a higher output design than the others. Researchers emphasised the significance of operational conditions such as wind speed, radiation from the sun, quantity flow rate of fluid, hotness of the liquid, and optimisation to obtain maximum efficiency.

An experiment conducted by Nyariki [11] to research the domestic operation of PVT in Kenya. They measured the daily customer demand for electric power and warm water for five people's families. The TRNSYS simulations are conducted to determine the appropriate flow rate of fluid to satisfy the guesstimated power requirements. It was observed that 25 LPH was an optimal flow rate offering a collection efficiency of 37-62% and a repayment period of 5 years.

Ondara et al [12] researched the techno-economic efficiency of PVT and correlated it to PV + SWH & Solar Water Heater (SWH). Researchers evaluated economic parameters such as Savings to Interest Ratio & Simple Payback Period, Internal Return Rate. This study presented that the PV + SWH method was marginally more favourable than PVT. Given the area requirement, the PV panel provided just about the same amount of power on 50% of the area needed by PV + SWH.

Aste [13] Overall Efficiency of uncovered & covered PVT is nearly 36% but Uncovered Electrical Efficiency is more. He used 2-Roll Bond Aluminum Absorber

Uncovered and Covered PVT with 0.055 & 0.066 kg/sec of mass flow rate and achieved an electrical efficiency from 6–14.2% and thermal efficiency of 29–21.8%.

Amma et al [14] uses rectangular copper pipes with 5.4lit/min of flow rate and achieved the electrical efficiency of 11.5–12.3% & also found that in general effectiveness diminishes when the temperature of PV Panel increments.

Evola et al [15] experiment with a square channel made of stainless steel with the polycrystalline cell with a mass flow of 80 kg/h/m³ and achieved an electrical efficiency of 13.5% and heat efficiency of 56.5%.

Ibrahim et al. [16] carried out an experiment using Rectangular and Circular Tubes of Stainless Steel in 7 different designs with a flow rate of 0.01 kg/sec, resulting in an electrical power conversion efficiency of 11.98% and a heat transfer of 50.12%, and also found that the model of Spiral flow with hollow rectangular tubes made of stainless steel has the highest thermal efficiency.

Chow et al [17] uses the aluminium alloy box structure with a flow rate of 75 to 95 kg/m³ and get an electrical efficiency of 9–11% and thermal efficiency of 45–50%.

Rajvikram et al [18] did the experimental investigation on PV/PCM panel with plain PV. They found that PV/PCM's output power increased by 2%, i.e. 19.2% due to a reduction in average temperature by 10.35 °C.

Wei [19] worked with an aluminium alloy flat box using a mass flow of 65.2 kg / m³ and obtained a performance of 3.96–5.42%. Also reported that with the addition of front glazing to the PV panel, heat loss could be reduced.

Rawat et al [20] tested the energy efficiency savings principle of the PV/T collector. A 37 W polycrystalline PV system is used to build an integrated photovoltaic thermal water collector system during the study. During the trial, the integrated photovoltaic thermal system's energy-saving efficiency was more significant than the traditional solar water heater's performance. The total understanding of the photovoltaic thermal design, which includes thermal and electrical conversion, was 57.61%, which is influenced by input variables like mass flow, fluid inlet temperature and fluid outlet temperature, and solar irradiance, atmospheric temperature, wind speed, system orientation.

Samson et al [21] performed the experimental investigation on PV panels with microchannel water-cooled flat plate heat pipe with back insulation. Results show that the electrical efficiency of hybrid PV panels with and without insulation was 11.98% and 12.19%.

Farkas et al [22] performed an empirical and energy efficiency evaluation of the photovoltaic thermal hybrid collector. The issue with excessive heating of the PV module was solved using a hybrid photovoltaic thermal solar collector. Glass coated photovoltaic thermal collector has the highest efficiency compared with various kinds of photovoltaic thermal hybrid collectors. During the measurement, it was found that if the PV temperature were decreased through 10 °C, it would result in a one percent improvement in performance.

Rajae et al [23] did the experimental study of the PVT system using cobalt oxide Nanofluid and PCM. Results indicate that 1% of Nanofluid with PCM gives the best results, i.e. up to 14.25% electrical efficiency.

Khalifa et al [24] performed research on the temperature rise in the atmosphere due to an increment of the PV system’s solar radiation to become less useful to stabilise them at operating temperature by cooling the PV system in the energetic analysis of the solar hybrid PV/T collector. During the investigation, he claimed that there must be a slight decrease in the direct cost by exploring the possibility of a combined application of the collector. Since the replication of several heat elements like covers & coating, reinforcement is usual to PV panels not necessary.

The thermal and electrical efficiency of the photovoltaic thermal collector was investigated by Engin et al [25] by building a numerical model and designing a prototype of the device. The efficiency of the system is checked under the condition of natural flow and forced flow. Durinof, the thermal collector’s output, working in the natural circulation mode, the heat efficiency was 41%, while the overall efficiency was 58.7% during the artificial circulation of a pump. The instantaneous efficiency of the photovoltaic thermal hybrid system under natural circumstances was observed to be 71%.

Mishra et al [26] performed a comparative analysis of the two cases of the PV system, case 1 (collectors partly shielded by PV system; 30% PV) & case 2 (collectors completely shielded by PV system) in 5 cities under four climate conditions. Research is focused on heat power, electric power, and exergy. The overall annual benefit is the highest for Jodhpur and the least for the city of Srinagar. The percentage difference between Jodhpur & Srinagar is 25% and 23.4% respectively, for situation one and situation 2. The annual benefit for New Delhi, Bangalore, & Mumbai is almost the same. The percentage difference between the 3 cities and Srinagar is 12%, 10.4%, & 15.2% respectively for case 1 and 10.2%, 9.3%, & 14% respectively for scenario 2.

3 Discussion

Figure 1 summarizes the average percentage improvement in the photovoltaic panel’s electrical efficiency using various cooling techniques, while Fig. 2 gives the details of electrical efficiency gain at different mass flow rates.

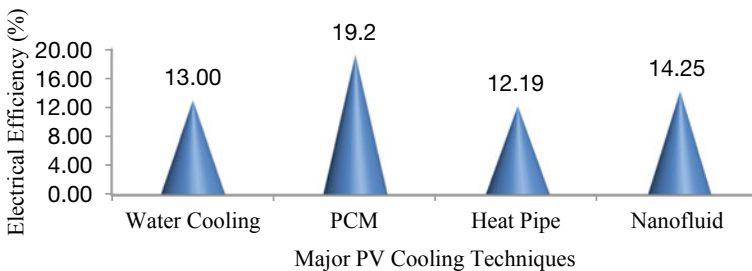


Fig. 1 Comparison of different PV cooling techniques

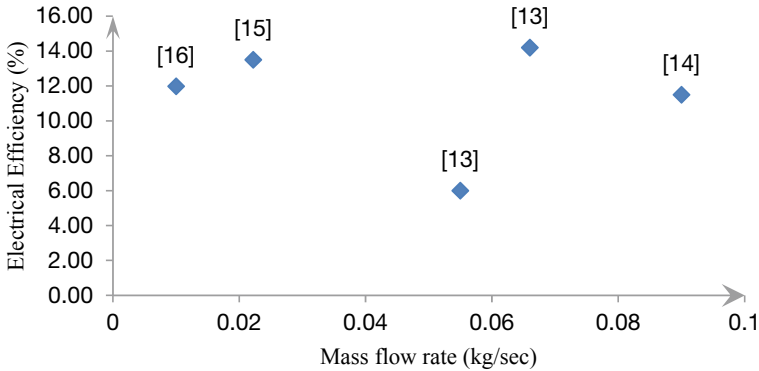


Fig. 2 Electrical efficiency gain at a different mass flow rate

As per Fig. 1, Phase change Material (PCM) indicates a maximum improvement in electrical efficiency, about 19.2%, whereas, heat pipe cooling technique shows minimum improvement, approximately 12.19%. Likewise, water cooling and Nanofluid show better performance, approximately 13.00% & 14.25% respectively.

Figure 2 suggests that maximum electrical efficiency will be achieved for the mass flow rate, between 0.06 kg/sec to 0.08 kg/sec.

4 Conclusion

From the literature survey, it has been observed that the Hybrid PVT Collectors need to be optimized to improve its thermal and electrical efficiencies. The electrical efficiency of the PV panel is to be improved with more effective cooling techniques. Studies on the effect of dust accumulation and its effect on performance and efficiency are concerns. Studies on the mass flow rate and its effect on the hybrid panel's efficiency need to be done thoroughly.

References

1. Agarwal RK, Garg H (1994) Study of a photovoltaic-thermal system—thermos phonic solar water heater combined with solar cells. *Energy Convers Manage* 35(7):605–620
2. Haurant P et al (2015) A numerical model of a solar domestic hot water system integrating hybrid photovoltaic/thermal collectors. *Energy Procedia* 78:1991–1997
3. Bahaidarah H et al (2013) Performance evaluation of a PV (photovoltaic) module by back surface water cooling for hot climatic conditions. *Energy* 59:445–453
4. Fudholi A et al (2014) Performance analysis of photovoltaic thermal (PVT) water collectors. *Energy Convers Manage* 78:641–651
5. Joy B et al (2016) Investigations on serpentine tube type solar photovoltaic/thermal collector with different heat transfer fluids: experiment and numerical analysis. *Sol Energy* 140:12–20
6. Rahimi M et al (2013) Heat transfer augmentation in a hybrid microchannel solar cell. *Int Commun Heat Mass Transfer* 43:131–137
7. Touafek K et al (2014) Theoretical and experimental study of sheet and tubes hybrid PVT collector. *Energy Convers Manage* 80:71–77
8. Ben Cheikh El Hocine H, Touafek K, Kerrou F (2017) Theoretical and experimental studies of a new configuration of photovoltaic-thermal collector. *J Sol Energy Eng* 139:021012-1–21017
9. Aste N, Del Pero C, Leonforte F (2012) Thermal-electrical optimisation of the configuration a liquid PVT collector. *Energy Procedia* 30:1–7
10. Jayasuriya WJA et al (2016) Performance analysis of Photovoltaic Thermal (PVT) panels considering thermal parameters. *ASME 2016 Power Conference*
11. Nyariki OW, David MM, David MM (2016) Design and characterization of a hybrid flat plate Photovoltaic-Thermal System. In: *Proceedings of the 2016 Annual Conference on Sustainable Research and Innovation*, 262–268
12. Nyariki O, Olusola OB, Serkan A (2016) Performance analysis and comparison of Photovoltaic, Solar Water Heating Photovolt Thermal Syst 978–1–5090–3784–1/16, 133–140
13. Aste N, Del Pero C, Leonforte F (2017) Water PVT collector's performance comparison, the 8th International Conference on Applied Energy – ICAE2016, *Energy Procedia* 105, 961–966
14. Amna AA, Nadine KB, Hind OH, Hamid AK (2014) Electrical/thermal performance of hybrid PV/T system in Sharjah, UAE. *Int J Smart Grid Clean Energy*
15. Evola G, Marletta L (2012) Exergy and thermos economic optimisation of a water-cooled glazed hybrid photovoltaic/thermal (PVT) collector. *Sol Energy* 107:12–25
16. Ibrahim A, Othman MY, Ruslan MH, Alghoul MA, Yahya M, Zaharim A, Sopian K (2009) Performance of Photovoltaic Thermal Collector (PVT) with different absorbers design, wseas transactions on environment and development
17. Chow TT, Ji J, He W (2007) Photovoltaic-Thermal Collector system for domestic application, *J Sol Energy Eng*
18. Rajvikram M, Leponraj S, Ramkumar S, Akshaya H, Dheeraj A (2019) Experimental investigation on the abasement of operating temperature in the solar photovoltaic panel using PCM and aluminium. *Sol Energy* 188:327–38
19. He W, Chow TT, Ji J, Lu J, Pei G, Chan LS (2006) Hybrid photovoltaic and thermal solar-collector designed for natural circulation of water. *Appl Energy* 83:199–210
20. Rawat P, Debarma M, Mehrotra S, Sudhakar K (2020) Design, development and experimental investigation of solar photovoltaic/thermal (pv/t) water collector system
21. Shittu S et al (2007) Experimental study and exergy analysis of photovoltaic-thermoelectric with flat plate microchannel heat pipe. *Energy Convers Manage* 207:112515
22. Farkas I, Kocsany I, Seres I (2010) Exergy based performance analysis of hybrid solar collectors
23. Rajae F et al (2020) Experimental analysis of a photovoltaic/thermoelectric generator using cobalt oxide nanofluid and phase change material heat sink. *Energy Convers Manage* 212:112780
24. Khelifa A, Touafek K, Benmoussa H (2013) Energetic study of hybrid solar PV/T collectors. *Revue Des Energies Renouvelables* 16(4):619–628

25. Dilsad E, Metin C (2012) Modeling and performance optimisation of photovoltaic and thermal collector hybrid system, Turk J Electr Eng Comput Sci
26. Mishra RK, Tiwari A (2012) Study of hybrid Photovoltaic Thermal (HPVT) solar water heater at constant collection temperature for Indian climatic conditions, Ashdin Publishing J Fundam Renewable Energy Appl 2, Article ID R120310

Study the Impact of Gamification on Career Selection for Graduation—A Review



Deepali Bhalerao, Mahesh Deshpande, and Nachiket Thakur

Abstract Gamification takes the best parts of games, such as competition, entertainment, and all the fun, and applies them to various real-world business processes, including learning and development. This paper emphasizes using serious games and the science of games to help young students figure out their interests, preferences, aptitude, and make significant career decisions. Subject matter experts, design engineers, instructional scientists, students can come together to develop a comprehensive game that facilitates career decision-making. It is proposed that an interactive, immersive, attractive, and thoroughly engaging game will help elucidate an optimistic and enthusiastic response from students. The use of games can significantly contribute to several aspects of career choice implementation, such as stress-free decision-making, good academic performance, commitment to the chosen study, and increased satisfaction and confidence. A detailed review of the literature is presented in this paper.

Keywords Serious games · Education · Career decisions · Guidance · Simulation · Interest identification · Immersion · Transformative decision-making

1 Introduction

Abt invented the idea of serious games first. As per Abt, serious games are carefully thought out for educational purposes and are not meant to be played purely for fun purposes. Inventive gaming strategies have been used to enhance physical and social science education, professional choice and training, government and business planning, and problem-solving [3].

A comprehensive understanding of self in terms of interests, strengths, values, personality, and skills is essential when choosing a career. Choosing a career after high school or junior college is a significant decision for all students and parents. At present, aptitude tests are widely used to help students make career decisions.

D. Bhalerao (✉) · M. Deshpande · N. Thakur
School of Management and Design, MIT Arts, Design and Technology University, Rajbaugh,
Pune, India

Aptitude tests act as an incentive for students to make a more intelligent choice about their future careers. The existing tests, however, have certain drawbacks. For instance, the tests are not tailored to the various career options available. Each profession requires a set of skills, and the test results must accurately portray those expectations. In addition, these tests require time to create and execute. It is vital to recognize that the tests must be kept current and relevant. As the nature of the jobs, the career opportunities available, the skill set, and expectations might change, the aptitude tests will have to change with current demand. The aptitude tests are administered in time-bound formats and in serious settings and ambiance. These make the test taker quite apprehensive and stressed, and such situations can significantly affect the outcome. It is essential to recognize that the aptitude tests emphasize the aptitude of the test takers as against the interest that they innately have. Because various factors, such as training, motivation, and interest, contribute to success in a course or career. Aptitude is not the sole deciding factor.

In line with the current trends and the prevalent digitalization, the study will primarily focus on designing a game-based test. The innovative system will help the test taker demarcate his or her interest and accordingly choose a career that is according to his or her innate inclination. The user-friendly and engaging test shall reduce the pressure that the exam-format testing uses and be more welcomed by students. Artificial intelligence and Machine Learning can help these game-based systems to learn from data, recognize patterns, and make decisions with little human intervention. When exposed to innovative data, these systems will be able to learn, grow, change, and develop by themselves. By using Machine Learning on a considerable scale, models that can evaluate more significant, more complex data and deliver accurate results can be generated quickly and automatically. Through such game-based precise models, students and parents can identify quickly and logically potential opportunities and avoid unidentified risks. Such data-driven decisions will help students to increasingly keep up with tough competition and challenges involved in career selection.

2 Literature Review

In [8], the author emphasizes that gaming gratifies intrinsic needs that may not be attainable in real lives; hence individuals like engaging in games. In the book, Jane shows how games' power can be leveraged to fix real-world social problems and familiarize readers with pioneering games.

School-aged children all over the world are growing up engaged in a media-rich, globalized world. Serious games are finding extensive applications in healthcare, military, public policy, well-being, advertisement, and corporate training, to name a few. Gamification is also widely used in education and other associated domains. Serious games have used the basic principles of entertainment, inventiveness, and experience to create games that achieve the goals needed in non-entertainment sectors such as corporate, government, etc. Also, gamification has the potential to boost

creativity and problem-solving, particularly when overcoming multiple barriers and dealing with complex rules. As highlighted by Faiella and Ricciardi [2], the students' capabilities are enhanced, as well as their feeling of achievement and optimism increases when playing games. Gamification often lacks the negative impact of wrong or unjustified decisions that enable disappointment and the strong desire to reframe failures vital in the learning process [1]. Ronda further highlights how the gamification concept can be used in career development and outlines the tactics for effectiveness. Using technologies from visual modeling and augmented reality contexts, serious games provide a delivery mechanism for the training and preparation of organizational video gaming. Designers may use a simulation approach to modeling and mimic thoughtful game form situations, presenting students/players with an immersive experience. Serious games are examples of experiential learning. They allow the conception of simulated illustrations of complex situations that learners can discover, understand and analyzed. These complex problems can be broken down into smaller pieces to illustrate the component's complexities and interactions. In comparison, video games manipulate visual communication, which has cognitive, affective, and behavioral effects [7, 12].

Gamification can increase student participation and awareness of career opportunities. To achieve success in student's ideal job prospects, student interest is vital. Recently, McGuire et al. [9] have developed a human-centered framework to enhance student engagement and knowledge of job prospects that focus on the user's needs while offering an immersive experience. This study uses gamification to explore student needs and to answer the following research question: "To what extent can a gamification framework help improve student interaction and what impact do specific elements have on user engagement?" Their mixed results suggest that a well-designed lesson is needed to ensure that the gamified cognitive system's intent is clearly conveyed to the participants. Empirical results also indicate that appropriate measurement tools are required to determine gamified knowledge systems' influence on job decisions compared to non-gamified structures.

For the success of educational institutions, the standard of teaching is incredibly important. In this sense, gamification is a technique frequently used to enhance the teaching-learning process by allowing both teachers and students to accomplish their short, medium, and long term goals. Considering the relevance of the subject in academia and society, Silva et al. [14] provided a comprehensive analysis of gamification literature as an instrument for improving the teaching process's quality.

Nah et al. [11] proposed a gamification framework comprising gamification principles, gamification elements, and user interaction dimensions to improve student participation and encouragement.

As the world population gets older exponentially, designers are increasingly striving to grasp and obtain real consumer insights into older people's design, wellness, and well-being. Comprehensive, empathetic, and responsive field studies are referred to as necessary in this respect, with ethnographies dominantly proclaimed for accomplishing this. However, it has been found that ethnography was not completely elucidated for design purposes, particularly for older people, because of its origins in anthropology. White [16] explains the steps and the methods needed

for the design of ethnography for the elderly. Similar techniques can be used in current research work. Such type of design model based on empathy and ethnography can be designed and used for the study of career selection among young students in the form of gamification [13].

Gamification may be carried out in the field of education increase educational efficiency. Much of the research report [4] has focused on identifying and evaluating gamification's role in the future of education as pedagogical innovation. This study answers four main questions: How is the evolution of gamification? What are the benefits and drawbacks of this? What policies are needed to effectively integrate gamification into education? And How was gamification applied?

As a novel and promising idea to recruit and pick prospective workers, gamification has recently gained increased interest from human resource professionals. Georgiou et al. [5] discussed a new form of gamified evaluation of employee selection. The results confirm the game components' applicability to a standard evaluation method designed to test applicants' soft skills.

Some representative existing tests and systems:

Jnanaprabodhini

Jnanaprabodhini, Pune [6] offers a well-known Aptitude Measurement and Career Guidance test. The objective test at Jnanaprabodhini to give a rational image of the strengths and limitations of a person. The test results are accompanied by sufficient feedback to ensure that the person suits in and thrives in the chosen field. The computerized exam, accompanied by an immediate student aptitude profile report, enables them to scientifically identify his/her aptitude and make sound career decisions.

The test consists of eight abilities and five orientations such as Knowledge Orientation, Practical Orientation, Artistic Orientation, Cognitive Ability, Reasoning Ability, Verbal Ability, Numerical Memory, to name a few. The student's aptitude profile is extensive with suggested career options followed by a thorough counseling session with an experienced academician, counselor, or professional. By capitalizing on their identified strengths and working upon their weaknesses, they can increase their competence for a career of their choice.

Pearson India Academy

The Pearson India Academy [15] provides a personality test to help young adults select the best career. "My Choice My Future (MCMF)" is an online scientific solution that lets individuals find the best career path in the Indian context. MCMF was developed and tested in association with senior professors and researchers from the Indian Institute of Technology, Madras. Post the online assessment, an automatic comprehensive and personalized Personality Report is generated. The test was statistically checked and confirmed in India with a comprehensive sample. Exhaustive career counseling by certified counselors follows the test and the results. The test is available in different languages such as Hindi, Bengali, Kannada, Malayalam, Tamil, and Telugu.

The assessments provide reliable evidence to increase human knowledge and provide greater insight into personality strengths and blind spots of job fields.

Mindler

Among other services, Mindler [10] offers career selection and planning for class 10–12. The advanced career assessment test helps students evaluate themselves on five dimensions essential for career success. The students are familiarized with their strengths and weaknesses through personalized reports, and developmental plans are provided to help them improve. The experienced and highly trained counselors counsel the students on their individual reports and help them plan their career development. The tests help students to choose careers from the identified top five careers suited best to their personality, aptitude, and attitude.

3 Similarities and Gaps in the Literature Review

3.1 Similarities

1. The use of game elements to increase motivation among students towards career awareness.
2. Students have a considerable interest in knowing what careers are available to them after they complete their college course as the opportunity for a better career is the primary motivator for students.
3. Gamification is recognized as a useful tool that effectively increases motivation, engagement, and learning.
4. Use of gamification for career awareness.
5. Use of gamification in the recruitment process and profile selection.
6. Use of gamification to develop new skills such as teamwork, critical thinking, innovation, and communication in the twenty-first century.

3.2 Gaps

1. Little research has been done around the use of gamification in the career selection process.
2. Use of Serious Game to evaluate and analyze the personal traits for better performance and future career.
3. Impact of different factors on career choices and the effect of that on career selection.
4. Lack of counseling tools based on scientific methodologies to understand career inclinations based on an individual's personality/interests/skills.
5. Designing a simple gamification tool to derive the algorithm from recommending a career path according to the personal inclination.

4 Conclusion

Gamification is gaining momentum by motivating and engaging students in their learning process. With gamified learning opportunities and career selection, learners will be able to choose their careers more widely. With improved usability, integration, user-system interaction, and education, a gamified career decision-making system can help make career selection an engaging process. While traditional career counseling and development is essential—in-person and in-group—today, learners need access to contemporary, quick, and relevant opportunities that accommodate their personal goals and interests. With a strong emphasis on gamification, the educational domain in entirety will catalyze creativeness and invention. There is a need to analyze the existing systems and help build on their positives to give young learners an engaging, encouraging, and exciting system and an unbiased decision-making tool.

References

1. Ansted R (2016) The gold star effect: the gamification of career decision-making. *Career Plan Adult Dev J* 32:3
2. Faiella F, Ricciardi M (2015) Gamification and learning: a review of issues and research. *J e-Learning Knowl Soc* 11(3):13–21
3. Fedwa L, Mohamad E, Saddik A (2014) Review article: an overview of serious games. *Int J Comput Games Technol* 14:1–15
4. Gamification and the future of education (2016) A report. World government summit, Oxford Analytica
5. Georgiou K, Gouras A, Nikolaou I (2019) Gamification in employee selection: the development of gamified assessment. *Int J Sel Assess* 00:1–13
6. Jnanaprobodhini, Pune <https://jpip.org/atcg-aptitude-testing-and-career-guidance/>
7. Khoo A, Gentile KA (2005) Problem-based learning in the world of digital games. In Tan O (ed) *Problem-based learning in eLearning Breakthroughs*. (pp 97–129) Singapore: Thompson Learning
8. McGonigal J, (2011) *Reality is broken: why games make us better and how they can change the world*
9. McGuire A, Broin Daire, White PJ (2017) Deevy colin and power ken increasing student motivation and awareness towards career opportunities through gamification. 11th European Conference on Games Based Learning, At Graz, Austria, 896–904
10. Mindler <https://www.mindler.com/career-counselling-for-class-10-11-and-12>
11. Nah FFH, Telaprolu VR, Rallapalli S, Venkata PR (2013) Gamification of education using computer games. In: Yamamoto S (eds) *Human Interface and the Management of Information. Information and Interaction for Learning, Culture, Collaboration and Business*. HIMI 2013. Lecture Notes in Computer Science, vol 8018. Springer, Berlin, Heidelberg
12. dos Santos D, Strada F, Bottino A (2019) Approaching sustainability learning via digital serious games. *IEEE Trans Learn Technol* 12:303–320
13. Shipepe A, Anicia Peters (2018) Designing an interactive career guidance learning system using gamification. In 2nd African Conference for Human Computer Interaction (Africhi '18), December 3–7, 2018, Windhoek, Namibia. ACM, New York, NY, USA, 4
14. Silva RJR, Rodrigues RG, Leal CT, Pereira, (2019) Gamification in Management Education: A Systematic Literature Review. *BAR-Brazilian Administration Review* 16(2):e180103

15. The Pearson India Academy <https://pearsonclinical.in/PAI/my-choice-my-future/>
16. White PJ (2013) Ethnography in Designing for Older People. Proceedings of the 2nd European Conference on Design for health 2013, Sheffield, UK, vol 3, 283–291

Numerical and Experimental Analysis of Magnetic Rheological Damper of Light Duty Load Carrying Vehicle



Pavan Kumar, Vatsal Bhat, Saurabh Shah, Rahul Raj, Balu Dome, M. Bhavana, and Malge Abhijeet

Abstract A Magneto rheological damper is one of the most advanced devices used in a semi-active control system to mitigate unwanted vibrations because the damping force can be controlled by changing the viscosity of the internal Magneto Rheological (MR) fluids. The most widely used configuration of MR Damper incorporates an annular gap through which the magnetically active MR Fluid is forced to flow. The numerical analysis was carried on a double slot piston rod of varying slot lengths. The analysis was done using COMSOL. The analysis showed that a double slot piston rod with equal slot dimensions was most feasible to be used for experimentation. The experimentation was carried on a typical double slot MR Damper with two coils in parallel connection. It has been experimentally seen that response of Magnetic Rheological fluid damper is better to 10 V (2 Hz) as compared to 5 V (1 Hz) frequency.

Keywords Magneto Rheology · Damping force · Magnetic flux · Viscosity

1 Introduction

Magnetic Rheological (MR) Damper is the most promising and up-coming area in automobile suspension protection field. These dampers normally use MR fluids to produce controllable damping coefficient [1]. The main issue that hampers the performance of an automobile is due to the most unanticipated cause and that is vibration. MR dampers are well known for their energy dissipating characteristic on the application of the magnetic field. The properties of the MR fluids can be instantly and reversibly modified or reorganized within milliseconds when a magnetic field is applied. In the absence of the applied field, the MR fluids behave like the Newtonian fluid. When a field is applied the suspended particles become polarized which further move so as to reduce the energy stored in the group. Magneto rheological materials are a class of smart materials whose rheological properties (viscosity) may be rapidly varied by applying a magnetic field. Under influence of magnetic field

P. Kumar · V. Bhat · S. Shah · R. Raj · B. Dome · M. Bhavana · M. Abhijeet (✉)
MIT Academy of Engineering, Alandi, India
e-mail: abhi.malge@gmail.com

the suspended magnetic particles interact to form a structure that resist shear deformation or flow. This change in materials appears as a rapid increase in apparent viscosity or in the development of a semi- solid state [1]. Damper offers an attractive solution of energy absorption in mechanical system and structures and can be considered as fail safe devices [2]. Magneto Rheological fluid has the extremely widespread application prospect in many fields including Aerospace automotive industry, hydraulic transmission, biotechnology and medical because of its characteristics of continuous reversible rapid and easy control [3]. The development of smart materials will undoubtedly be an essential task in many fields of Science and Technology such as information science, microelectronics, computer science, Medical treatment, Life science, energy, Transportation, Safety Engineering and Military technologies and the applications include Automotive primary suspensions systems control-by-via/tactile-feedback devices, Pneumatic control, Seismic mitigation and Human prosthetics [4]. The suppression of Mechanical and Structural vibration using semi-active control method has been actively worked upon by many researchers in last two decades. Recently, various semi-active Suspension systems featuring MR fluid damper have been proposed and successfully applied in the real field, especially in vehicle suspension systems [5]. Magneto rheological damper is becoming the most promising vibration controller in the intelligent suspension presently and it wins the favour of vehicle manufacturers, because it takes the advantages of high strength, good controllability, wide dynamic range, fast response rate low energy consumption and simple structure. A characteristic of MR damping fluid was studied to understand the damping behaviour pattern for different loads for suspension isolation or suppression of cars [6]. Material properties were also comprehensively studied to get optimal performance by proper balance [7]. Structural response due to seismic load was reduced by using clipped optimal control strategy based on acceleration feedback for controlling MR dampers [8]. Optimal design of MR damper was done by objective function consisting of dynamic force, dynamic range and inductive time constant. Also comparative study of damping force and time constant between the initial and optimal design was studied [9]. The squeeze mode of Magneto rheological fluid was studied by developing a unique model considering strain stiffening hysteresis behaviour [10]. Zhang et al. recommended a new semi-active controller based upon the inverse model and sliding mode control (SMC) strategies for the quarter-vehicle suspension with the Magneto-Rheological (MR) damper [11]. Oh et al. had developed a mathematical model of railway vehicle having 15 degrees of freedom to represent roll, yaw and mechanism [12].

In this research work an attempt is made to analyse the effect of number of slots on vibration damping, the numerical and experimental analysis was done on Double slot piston rod. The detailed effect of position of slots was studied numerically and the response of MR fluid to load was analysed experimentally.

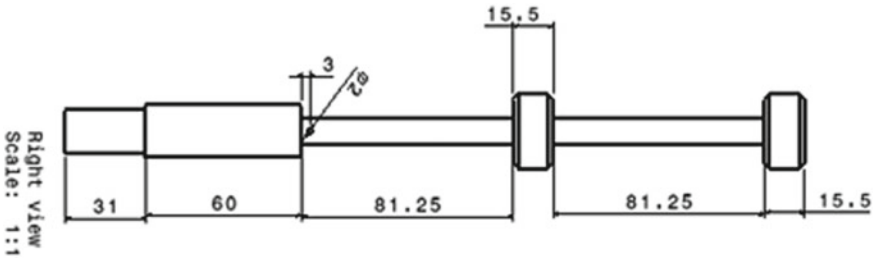


Fig. 1 Double slot piston rod

2 Numerical and Experimental Analysis

The numerical analysis was carried out on piston rod having two slots. Numerical simulations were carried out to locate the position and length of the slots. Figure 1 shows double slot piston rod. The length of piston rod is 284.5 mm. The piston rod used for simulation is of Light duty load carrying vehicle.

Double slot piston rod was modelled in CATIA V5 and then imported in COMSOL for analysis. The simulation was carried by varying current and varying number of turns of coil. The magnetic flux generated due to passing of current into the copper wires was simulated.

The double slot piston rod was simulated by keeping the current magnitude constant and varying the length of the slot and number of turns. As the length of the slots changes, correspondingly the number of turns changes. From the data it is seen that for length of slot of 82.5 mm, the number of turns are 154, for slot length of 123.5 mm the number of turns are 210 and for slot length of 41.25 mm the number of turns are 77. The simulation was carried out for piston rod divided into two slots of equal length 82.5 mm each, piston rod having slots of varying length of 123.5 mm and 41.25 mm.

3 Experimental Setup

Figure 2 shows double slot piston rod. The double slot piston was wound by copper wire on both the slots. One end of piston having thread M 14 × 2 to attach it with external set up which was a load cell of UTM. The other end of the piston was a cylindrical head. The cylinder is 205 mm in length & 2 mm thick. It is having 1 mm clearance with the piston head. It is sealed from the one end and other end having cylinder cap with centre hole for piston movement and washer to make it leak proof. The mounting has been taken from Omni suspension with 2 washers to restrict the movement of cylinder under the mountings on application of external force. The base plate was a mounting plate that was used to attach the suspension mounting with the piston cylinder assembly in it to the UTM base. The base plate was a rectangular



Fig. 2 The Piston rod of Omni light duty load carrying vehicle

block, made of mild steel, with an $M 27 \times 2$ mm internal threaded hole that was used to fix the base plate with the base of the UTM. Two more internally threaded holes of $M 10 \times 2$ mm were drilled for mounting the suspension assembly on the base plate. Dual output (DC) variable power source was used to provide power supply to the copper wires used to form electromagnet. Current range was from (0–3) A and voltage range was (0–30) volt.

Apparatus setup in UTM: The base plate of the model was attached to the hydraulic lift by means of screw of dimension $M 27 \times 2$. The upper part of the model was connected to the UTM by means of Nut and washer of Dimension $M 14 \times 2$. Copper wires are connected to external power source.

4 Experimentation

Figure 3 shows the experimental setup for testing the performance of MR fluid damping performance for light duty vehicles. External load is applied on the piston by the hydraulic jack of the UTM. Power stroke is given to damper in two cycles.

1. With a frequency of 1 Hz with ± 4 mm stroke length.
2. With a frequency of 2 Hz with ± 4 mm stroke length.

DC Voltage is given across the ends of the circuit with variable power source in stepped increment for each cycle and results are displayed on monitor.

The Magneto Rheological fluid was made with SAE40, 5 W as carrier fluid of volume 160 ml, Kinematic viscosity of $240.10 \text{ mm}^2/\text{s}$, dynamic viscosity-206.89 and density of 8545 g/cc^3 . Aerosil 200 as additive having 2% of oil and CI powder as magnetic particles having 40% of oil. The shape of CI powder used is having spherical shape. The Magneto Rheological fluid was prepared by stirring the carrier fluid with iron powder. Mechanical stirrer was used to maintain steady and constant speed of 700 rpm.

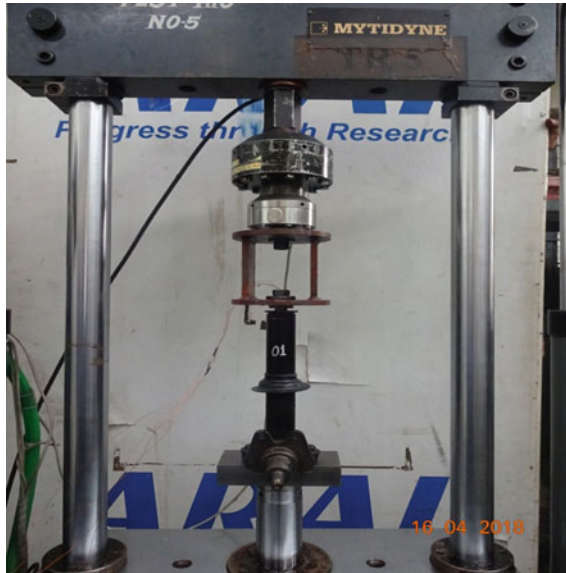


Fig. 3 Experimental set up

5 Results and Discussion

The Double slot piston rod is used for numerical and experimental analysis. The rod is having equal length of slot of dimension 82.5 mm. Numerical analysis was carried out by varying the lengths of slot and number of turns. Two different slot lengths were considered for simulations. The slot dimensions for first double slot piston rod are 82.5 mm and 82.5 mm respectively. The slot dimension for second double slot piston rod is 123.5 mm and 41.25 mm respectively.

Figure 4 shows the Magnetic Flux plot for Double slot piston rod with slot dimension 82.5 mm each. From the magnetic flux plot it is seen that the magnetic flux is generated equally on both the slots. The maximum magnitude of magnetic flux generated is 0.3×10^{-2} T and minimum flux generated is 4.210^{-13} T. The magnetic flux

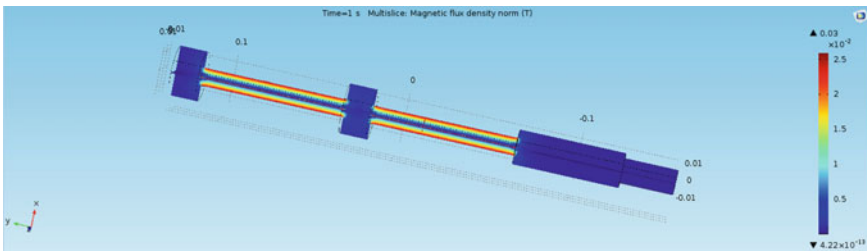


Fig. 4 Magnetic flux plot for double slot piston rod with slot dimension 82.5 mm each

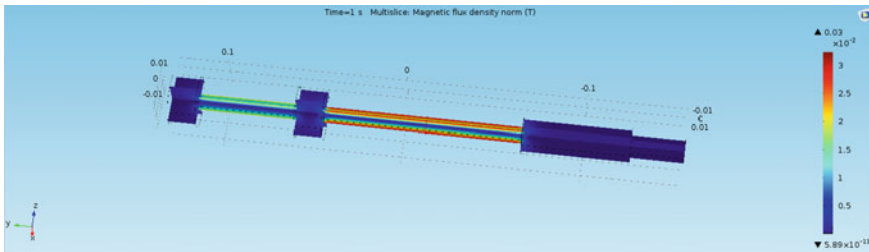


Fig. 5 Magnetic flux plot for double slot piston rod with slot dimension 123.5 mm and 41.25 mm each

magnitude generated on both the slots is of 0.3×10^{-2} T. The magnetic flux generated on other portion of piston rod is minimum of magnitude 4.210^{-13} T. The equal distribution of magnetic flux on the slot portion is due to equal number of turns of copper wire. Figure 5 shows the Magnetic Flux plot for Double slot piston rod with slot dimension 123.5 mm and 41.25 mm each. The magnitude of maximum flux generated is 0.3×10^{-2} T and minimum flux generated is 5.89×10^{-13} T. It is observed that magnitude of magnetic flux generated in slot having dimension 123.5 mm is 0.3×10^{-2} T, wherein the magnetic flux generated in slot having dimension 41.25 mm is $1.5\text{--}2 \times 10^{-6}$ T. The magnetic flux generated is more in 123.5 mm slot dimension as the number of turns is more as compared to 41.25 mm dimension slot. Thus from the numerical analysis, double slot piston rod with equal slot dimensions is finalised for experimentation.

Experimentation was conducted by fixing the damper having double slot piston rod fixed in Universal Testing Machine. The rod was subjected to tensile and compressive load of ± 4 mm stroke length with frequency of 1 and 2 Hz. DC voltage was given at the ends of circuit with variable power source in stepped increment for each cycle.

Figure 6 shows Load v/s Deflection graph for 5 V (1 Hz), tensile and compressive load of ± 4 mm deflection. From the graph the applied load magnitude range is from 0.15–0.24 kN. For on cycle load fluctuates between 0.125–0.15 kN and from 0.23–0.25 kN. The load magnitude for 5 V (1 Hz) fluctuates intermittently. Figure 7 shows the load and deflection graph for 10 V (2 Hz). From the graph it is seen that the load

Fig. 6 Load versus Deflection at 5 V(1 Hz)

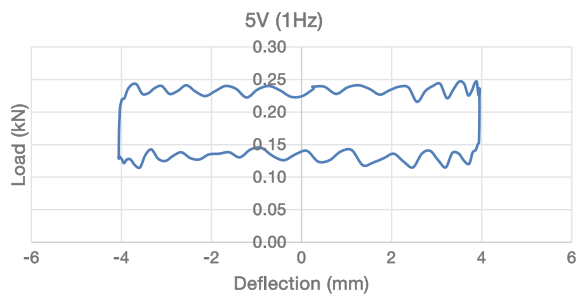
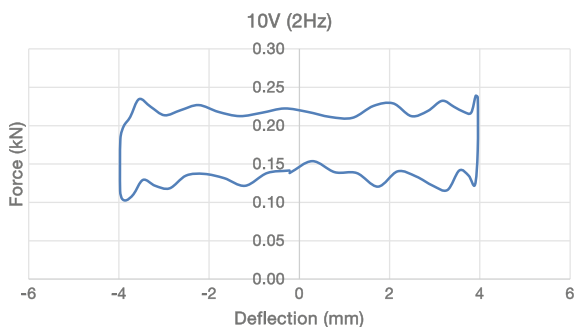


Fig. 7 Double slot piston rod having equal slot length



magnitude varies min between 0.11–0.15 kN and maximum between 0.22–0.23 kN. The load fluctuation is very less between the maximum and minimum range.

6 Conclusion

In this research work, Magnetic Rheological Fluid was used in damper of light load carrying vehicle to enhance the damping. Double slot piston rod with varying slot length was numerically analyzed. Further the double slot piston rod was experimentally analyzed for tensile and compressive load with deflection of ± 4 mm subjected to 5 V (1 Hz) and 10 V (2 Hz) frequency. From the numerical analysis double slot piston rod with equal slot length generated more magnetic flux as compared to varying slot dimensions piston rod. The load fluctuation for 10 V (2 Hz) frequencies is less as compared to 5 V (1 Hz).

References

1. Kciuk M, Turczyn R (2006) Properties and application of magneto rheological fluids. *JAMME* 18(1–2):127–130
2. Kolhe VP (2012) Advanced vibration control using magneto rheological fluid. *Int J Innovation Mech Automobile Eng, IJIMAE--II*, 115–121 ISSN: 2249–2968
3. Braz Cesar MT, Barros RC (2012) Experimental behavior and numerical analysis of MR damper. 15 WCEE LISBOA
4. Jiajia Z, Zhaochun L, JeongHoi K, Jiong W (2015) Magnetic circuit design and multiphysics analysis of a novel MR damper for applications under high velocity, *Adv Mech Eng*
5. Wang DH, Liao WH (2005) Semi active controllers for magneto rheological fluid dampers. *J Intell Mater Syst Struct* 16:983–993
6. Rashid MM, Hussain MA, Rahim N (2006) Application of magneto rheological damper for car suspension control, *J Appl Sci* 6(4):933–938
7. Jolly MR, Bender JW, Carlson JD (1998) Properties and applications of commercial magneto rheological fluids, *SPIE 5th Annual Symposium on Smart Structures and Materials*, San Diego, CA

8. Dyke SJ, Spencer BF Jr, Sain MK, Carlson JD (1996) Seismic response reduction using magneto rheological dampers, In: Proceedings of the IAFC World Congress; San Francisco, CA
9. Nguyen QH, Choi SB, Kim KS (2009) Geometric optimal design of MR damper considering damping force, control energy and time constant, *J Phys Conf Ser* 149, 012076
10. Yang MG, Li CY, Chen ZQ (2009) A new simple non linear hysteric model for MR damper and verification of seismic response reduction experiment. *Eng Struct* 522013:434–445
11. Zhang H, Wang E, Zhang N, Min F, Subash R, Su C (2015) Semi-active sliding mode control of vehicle suspension with magneto-rheological damper, *Chin J Mech Eng* **28**:63–75
12. Oh JS, Shin YJ, Koo HW (2016) Vibration control of a semi-active railway vehicle suspension with magneto-rheological dampers. *Adv Mech Eng* 8(4):1–13

Performance Enhancement of Multi-cylinder Four Stroke SI Engine Under the Effect of Magnetic Field



Nilesh Ramchandra Pawar and Sanjeev Reddy K. Hudgikar

Abstract The Strength of permanent magnets was used to improving the combustion of gasoline fuel results better performance of IC Engine by reducing exhaust emission up to certain level. The strong magnetic field was applied on fuel inlet pipe and manifold of four stroke gasoline engine and fuel flow through the pipes is under the influence of permanent magnetic effect. These experiments were frequently conducted at the different RPM and loads on engine. It has been observed that very fine droplets of fuel gives more atomization and decreases viscosity of fuel before entering into combustion chamber. Incomplete combustion of fuel occurs because of rich air–fuel mixture supplied to the combustion chamber. Because of strong and stable structure of fuel proper amount of oxygen was not provided during combustion of fuels results in excess emission of carbon monoxide, hydrocarbons and nitrogen oxides through exhaust causes more pollution for the atmosphere. Strong permanent magnetic flux around the fuel pipe will changes the steady fuel structure to improve air–fuel mixture and completely combines with oxygen. Ortho state divided gasoline fuel into finely particle having less intermolecular forces results to enhance in atomization for maximum burning of fuel. By applying permanent magnetic field and non-magnetic field around the gasoline fuel pipe it has been observed and comparing the results of combustion shows SI Engine generates more energy per specific volume of gasoline fuel and minimizes the atmospheric pollution under the influence of magnetic effect on fuel. The overall observations gives magnetic effect treatment on gasoline fuel improved fuel burning efficiency, decreases fuel consumption (Habbo ARA, Khalil RA, Hammoodi HS (2011) Effect of magnetizing the fuel on the performance of s.i. engine, *Al-Rafidain Engineering*, 19(6):84–90) [6] and reduction in exhaust pollutants.

Keywords Fuel consumption · Fuel line · Magnetic field · Stable structure · Para and Ortho state · Pollutants

N. R. Pawar (✉)

Visvesvaraya Technological University, Jnana Sangama, Belagavi, Karnataka, India

Assistant Professor, D Y Patil College of Engineering, Akurdi, Pune 411044, Maharashtra, India

S. R. K. Hudgikar

Lingaraj Appa Engineering College, Gornalli, Bidar, Karnataka, India

© The Author(s), under exclusive license to Springer Nature Switzerland AG 2021

P. M. Pawar et al. (eds.), *Techno-Societal 2020*,

https://doi.org/10.1007/978-3-030-69925-3_19

1 Introduction

The extremely wide use of automobiles all over the world in different sectors requires huge amount of fuel. This high demand as well as its consumption will be continuously goes on increasing day by day. It is very difficult to keep such high supply of fuel for automobiles in coming years and also tough to control on its pollution. Generally stationary and automobile IC engines released incompletely burned hydrocarbons, carbon monoxide and oxides of nitrogen which creates more smoke. From many years the attempts are going on to improving of fuel combustion either by modifying in the combustion chamber, change in engine design and to increase the inlet pressure of fuel for maximum atomization. This current study has concrete purpose and the invention is to add to the effectiveness of fuel combustion of fuel in IC Engines with upgrading of their environmental character. This arrangement is compact and very simple to apply and reliable. Processing and alteration of fuel before its reception into the combustion chamber of the internal-combustion engine. Objective of the present investigation to produce a regular magnetic field perpendicular to the direction of fuel flow to create a more laminar flow of the fuel in inlet manifold of an engine before admit into the combustion chamber. The function of such strong magnetic field shows a path how to reduce incomplete combustion and also offer to organized limits on combustion performance [1, 2, 5].

Modern studies imply that magnetic field having helpful effect on the performance of fuel burning system [7]. In molecules of fuel magnetic travel is already exist having positive and negative electrical charges but they are not properly aligned and not completely mixed with oxygen for completely burning hence it need to magnetized by permanent strong magnets by keeping around the fuel line [5]. Commonly fuels used for internal combustion engine are compound of molecules. Magnetic travels available in their particles so they already have positive and negative electrical charges. Though such particles have not been realigned hence the fuel didn't energetically inter-locked with O_2 during ignition so that the fuel particle or hydrocarbons must be ionized and realigned. These things are achieved by ionization as well as pre alignment of fuel molecules with the help of permanent magnet and its magnetic field. Objective of such strong magnetic flux effect on proper burning of fuel in SI engines.

Atmospheric air is polluted by number of reasons out of these reasons smoke exit from automobiles is also contributed because of improper burning of fuels which affects on eyes, throat and health of living things. To avoid such improper burning of fuel in combustion chamber many attempts are going on throughout the world. The output of all these efforts will to get better combustion, reduce the pollution hence ecofriendly and become more and more economical [4]. Some modern studies gives more efficient burning of fuel by arranging the fuel molecules in para state and ortho state by providing the strong magnetic flux around the fuel line of inlet port which helps to reduce the intermolecular attraction and resulting in more proper combustion of fuels hence reduced in smoke as well [3]. Fuel particles are widely separated so that maximum amount of oxygen is merged into fuel for better burning.

2 Methodologies

Majority fuels for IC engines are liquid, fuels didn't burn until they get atomized. The outcome results of strong magnetic flux provided on inlet port on fuel burning which was used for SI Engine and its possible impacts on exhaust gas were observed. Strong permanent magnets of intensity 2000 Gauss is used for this experimental setup. Testing is carried on Four-Stroke MPFI 3 cylinder water cooled gasoline engine of Maruti Suzuki 800 cc. It has fuel metering mechanism, self-governing panel box consisting of air container, fuel container, manometer, fuel measuring unit, digital speedometer and digital temperature gauge. Engine cooling water inlet—outlet and calorimeter temperature is shown on temperature gauge. Rota meter is used as cooling water and calorimeter flow measuring device. System enables study of engine for BP, BMEP, BTE, volumetric efficiency, SPC, AFR and heat balance.

3 Experimental Setup

Fill sufficient amount of fuel in fuel tank, ensure cooling water circulation for Hydraulic dynamometer, engine and calorimeter.

Start the Engine set up and run the engine on zero load at an idle speed for 05 min. 100 ml. fuel is taken before actual reading under the load and magnetic intensity. Gradually increase the load on the engine by rotating dynamometer load wheel. Wait for steady state for 05 min so that it will operate on its normal operating condition and collect the reading as per scheduled. Increase the engine throttle to any desired position and simultaneously load the engine to obtain desired speed for which power is to be calculated. First take all the readings by gradually increasing load without use of any magnet for 100 ml. fuel. Fill all the readings in observation table. Gradually decrease the load.

For further readings with one magnet fit one magnet before injector. Again increase the load gradually with magnet of intensity 2000 Gauss for 100 ml fuel. Fill all the readings in observation table. Again gradually decrease the load. Same procedure will repeat for all next readings without magnetic field and with magnetic field. Also fill all the readings in CO & HC Table with respective loads, rpm & number of magnets. Fill up all the observations in work sheet to get the results and performance plots.

Observations continuously recorded for different load conditions, different rpm, time required for combustion of fuel and at the same consumption of fuel was also noted. Several readings were noted for better accurate results. Exhaust gas temperature is also noted at various conditions. The exhaust gases during operation were measured, as well as the amount of consumed fuel after the end of the operation. Digital Exhaust Gas Analyzer is provided to analyze the exhaust gas. This gas analyzer can easily check the pollution level of burned fuel. Repeat this process for next readings for several times.

Fig. 1 Experimental engine setup

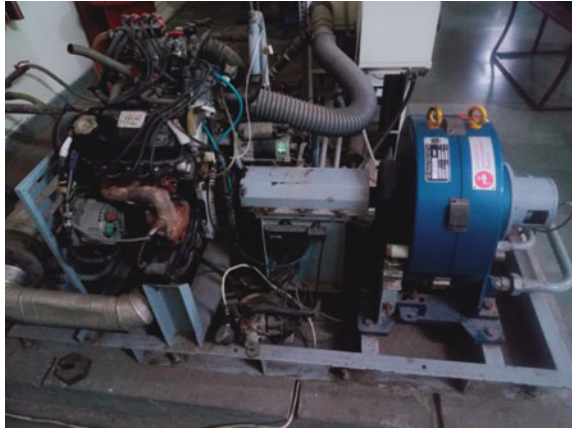
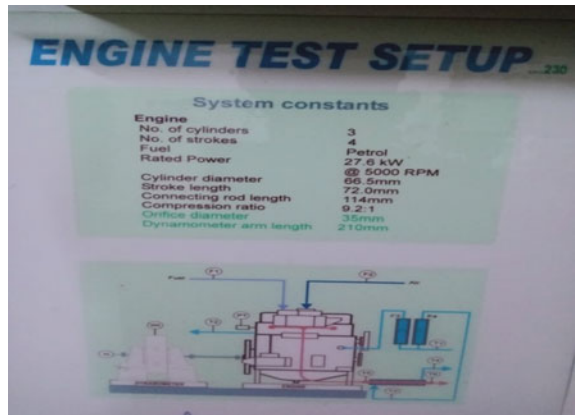


Fig. 2 Line diagram of setup



Figures 1 and 2 shows picture of experimental setup and permanent magnet fitted on fuel line of IC Engine. Intermittent observations were noted on an engine rpm. 2000, 3000 and 4000. By these observations required amount of fuel was also metered on each rpm. Readings also noted by providing 2000 Gauss magnets.

4 Experimental Results

The results are given in the following Tables 1 and 2.

Table 1 Engine rpm 3000-without magnet

BP (KW)	Torque NM	BSFC Kg/Kwh	B Th.Eff	Radiation %
11.3	39.2	0.393	19.94	18.3
12.6	43.2	0.371	20.83	25.3
13.8	47.1	0.353	21.51	28.9
14.0	51.0	0.332	22.64	24.7
15.3	54.9	0.328	23.33	29.3
16.5	58.9	0.320	24.99	26.8
17.7	62.8	0.393	25.85	28.7

Table 2 Engine rpm 3000 with 2000 Gauss magnet

BP (KW)	Torque NM	BSFC Kg/Kwh	B Th.Eff	Radiation %
12.3	39.2	0.400	20.45	20.9
13.6	43.2	0.378	21.66	28.1
14.8	47.1	0.360	22.72	29.6
16.0	51.0	0.354	23.14	28.6
17.3	54.9	0.343	23.86	31.7
18.5	58.9	0.343	23.86	31.0
19.7	62.8	0.322	25.45	31.4

5 Result Graphs

Figure 3 shows relationship between Brake Thermal Efficiency and Engine speed(rpm) By observation Brake Thermal Efficiency is led to improved because of maximize the fuel and air chemical reactions of burning of fuel causes rise in combustion chamber temperature.

Fig. 3 Brake Thermal Efficiency versus RPM. (At 3000 Engine RPM with 2000 Gauss magnet)

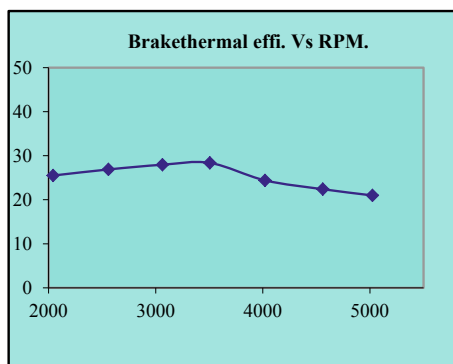


Fig. 4 BSFC versus RPM.
(At 3000 Engine RPM with
2000 Gauss magnet)

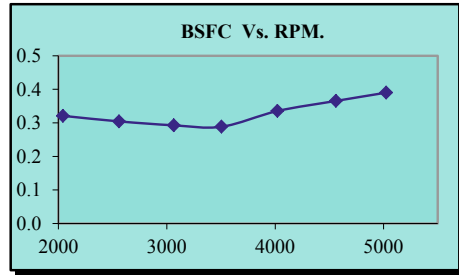


Figure 4 shows relationship between BSFC and RPM of engine. BSFC measures the efficiency after burning the fuel. Graph indicates how fuel supplied to engine is converted into maximum useful work. At the higher rpm and load, fuel burning and also temperature will be increased inside the combustion chamber hence enhance BSFC gradually.

6 Conclusions

Passage through which fuel passes was magnetized by strong permanent magnet by south and north opposite polarity for maximum burning of fuel available in combustion chamber producing better output of an engine, minimize quantity of unburned fuel hence reduces environmental pollution and better fuel economy.

Another advantage is to avoid carbon deposition in carburetor, fuel injector nozzle, on spark plug and in combustion area of engine hence improve the life of an engine. Maximize the chemical reactions of burning of fuel causes rise in combustion chamber temperature. In general performance of engine is better under the influence of magnetic flux. Exhaust emission of CO and HC were reduced and same time increased in percentage of CO₂ recorded in gas analyzer. Rate of consumption of fuel is also reduced because of proper air and fuel mixture. Oxidation rate of fuel was increased resulting in quicker and better combustion of fuels. Total influence on an engine performance is increased in power output and corresponding reduced in fuel consumption.

References

1. El Fatih FA, Saber GM (2010) Effect of fuel magnetism on engine performance and emissions. *Aust J Basic Appl Sci* 4(12):6354–6358
2. Faris AS, Al-Naseri SK, Jamal N, Isse R, Abed M, Fouad Z, Kazim A, Reheem N, Chaloob A, Mohammad H, Jasim H, Sadeq J, Salim A, Abas A (2012) Effects of magnetic field on fuel consumption and exhaust emissions in two stroke engine. *Energy Procedia* 18:327–338

3. Govindasamy P, Dhandapani S (2007) Performance and emissions achievements by magnetic energizer with a single cylinder two stroke catalytic spark ignition engine. *J Sci Ind Res* 66:457–463
4. Govindasamy P, Dhandapani S (2007) Experimental investigation of cyclic variation of combustion parameters in catalytically activated and magnetically energized two-stroke si engine. *J Energy Environment* 6(2007):45–59
5. Guo H, Liu Z, Chen Y, Yao R (1994) A study of magnetic effects on the physicochemical properties of individual hydrocarbons, Logistical Engineering College, Chongqing 400042, PR China, 216–220
6. Habbo ARA, Khalil RA, Hammoodi HS, (2011) Effect of magnetizing the fuel on the performance of s.i. engine, *Al-Rafidain Engineering*, 19(6):84–90
7. Okoronkwo CA, Nwachukwu CC, Ngozi LC, Igbokwe JO (2010) The effect of electromagnetic flux density on the ionization and the combustion of fuel (an economy design project). *Am J Sci Ind Res* 1(3):527–531

Thermo-Hydraulic Performance for an Electronic Cooling System Using Porous Material



Sumit Kumar Mehta and Sukumar Pati

Abstract The present study numerically investigates the thermo-hydraulic characteristics of an electronic cooling system having porous blocks between the two heating parts. To model the porous media flow, the Darcy-Brinkman-Forchheimer model is used. The streamlines distribution, temperature field, Nusselt number and performance factor are studied in the following range of Reynolds number (Re) and Darcy number (Da): $25 \leq \text{Re} \leq 200$ and $10^{-5} \leq \text{Da} \leq 10^{-1}$, respectively. It reveals that the maximum hot spot intensity decreases with the use of porous material. The average Nusselt number increases up to 40 to 50% for smaller Re, and 10 to 20% for higher Re with a higher value of Da. The performance factor is always higher for higher Darcy number ($\text{Da} = 10^{-2}$ and 10^{-1}) and greater than unity in the considered regime of flow.

Keywords Electronic-cooling · Nusselt number · Performance factor · Porous media

1 Introduction

The performance of the electronic components and integrated circuits depends on the operating temperature. The overheating of these circuits due to the compactness leads to heat generation which is in the order of kW/m^2 to MW/m^2 [1]. Therefore, to achieve a better performance of such devices, the cooling system with a higher heat transfer rate is needed, and in this regard, two methods of convective heat transfer enhancement are available. The first one is the active and another one is the passive method. The active method requires external power other than pumping power, whereas the passive method includes adding corrugation, waviness [2–8]. The passive method is relatively simple to implement and the addition of metallic porous media is more effective for such heat transfer enhancement as it enhances the effective thermal conductivity. Rachedi and Chikh [1] studied the mixed convective

S. K. Mehta (✉) · S. Pati

Department of Mechanical Engineering, National Institute of Technology Silchar, Silchar 788010, India

e-mail: sumit_rs@mech.nits.ac.in

© The Author(s), under exclusive license to Springer Nature Switzerland AG 2021

P. M. Pawar et al. (eds.), *Techno-Societal 2020*,

https://doi.org/10.1007/978-3-030-69925-3_20

197

electronics cooling system using foam with different thermal conductivity ratios and it is found that an increase in the thermal conductivity ratio of 2 to 10 decreases the maximum temperature up to 15%. Ould-Amer et al. [9] studied the forced convective electronic cooling system by placing partial part of the domain with a porous material. It is found that the inclusion of porous block decreases the maximum temperature intensity due to the higher effective thermal conductivity compared to the void domain. The heat transfer enhancement by the addition of porous media is achieved at the cost of pressure drop [1, 9]. To the best of the authors' knowledge, no study has been reported on the combined effect of heat transfer enhancement with pressure drop penalty, simultaneously to date. Hence, the objective is to analyse the thermo-hydraulic performance of an electronic cooling system using porous material.

2 Theoretical Formulation

The two-dimensional, steady, and incompressible forced convective flow of Newtonian fluid (air) through a partially filled porous channel with heated electronics blocks is considered as shown in Fig. 1. The porous material is assumed to be isotropic and homogeneous. There are five heated blocks with height and width $0.5H$ and H , respectively. The intermediate space between two is filled with the porous material with thickness $0.25H$. The total length of the channel is considered as $30H$. The inlet and outlet flat parts are having the length of $6H$ and $11H$, respectively. The thermo-physical properties of fluid and porous material are temperature independent, while the viscous and radiation effects are neglected. The Darcy-Brinkman-Forchheimer model is taken into consideration to mimic the porous media flow, accounting for the inertia and boundary effects. The local thermal equilibrium is assumed between the pore solid and fluid, as it is justified for the higher porosity of the porous material. Hence, for the present case, the porosity of the porous material is taken as 0.9.

Under the mentioned assumptions, the normalized governing equations are the following [9]:

$$\nabla \cdot \vec{U} = 0 \quad (1)$$

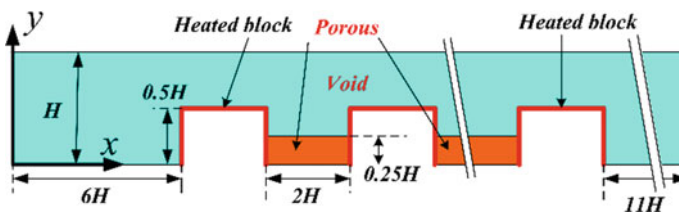


Fig. 1 Physical domain and co-ordinate

$$\frac{1}{\varepsilon^2} \left((\vec{\mathbf{U}} \cdot \nabla) \vec{\mathbf{U}} \right) = -\nabla P + \frac{1}{\varepsilon \text{Re}} \nabla^2 \vec{\mathbf{U}} + \zeta \left(-\frac{\vec{\mathbf{U}}}{\text{ReDa}} - \frac{C_f}{\text{Da}} |\vec{\mathbf{U}}| \vec{\mathbf{U}} \right) \quad (2)$$

$$\text{Re Pr} [\varepsilon + (1 - \varepsilon) \sigma] \vec{\mathbf{U}} \cdot (\nabla \theta) = \text{KR} \nabla^2 \theta \quad (3)$$

Here, ζ and ε are set to be zero and unity, respectively for the void region, while $\zeta = 1$ for the porous region; $\vec{\mathbf{U}}$ is the normalized volume-averaged velocity for the porous domain as well as fluid velocity in the void domain. The effective viscosity in porous media is assumed to equal to the fluid viscosity. The thermal conductivity ratio is defined as $(\text{KR}) = k_{\text{eff}}/k_f = [\varepsilon + (1 - \varepsilon)\Omega]$. The normalized velocity field is $\mathbf{U} = \mathbf{u}/u_r$ and $\vec{\mathbf{U}} = U\hat{i} + Y\hat{j}$, $\nabla = (\partial/\partial X, \partial/\partial Y)$, $X = x/H$, $Y = y/H$, normalized pressure is $P = p/\rho u_r^2$. Dimensionless temperature is defined as $\theta = (T - T_{in})k_f/qH$, where q is the heat flux at the heated blocks. The dimensionless numbers are defined as follows: Darcy number $\text{Da} = K/H^2$, Reynolds number $\text{Re} = \rho u_r H/\mu$, $C_f = 1.75/\sqrt{150\varepsilon^3}$. Prandtl number $\text{Pr} = \mu_f c_{pf}/k_f$, $\sigma = (\rho c_p)_s/(\rho c_p)_f$. The thermal conductivity ratio of the solid to fluid is given as $\Omega = k_s/k_f$. For the metallic porous foam, the value of Ω and σ are taken as 106 and 449.05, respectively [10]. The normalized Eqs. (1)–(3) are solved numerically using the following boundary conditions. At the inlet, uniform velocity ($U = 1$) is imposed with constant inlet temperature ($\theta = 0$). No-slip condition ($U = 0$) is imposed in all the walls. The blocks are heated with constant heat flux (For porous: $\text{KR}\partial\theta/\partial N = 1$, For void: $\partial\theta/\partial N = 1$; N is normal) and other walls are insulated ($\partial\theta/\partial N = 0$). The interfaces between the porous and void part follow the temperature, velocity, shear stress, and heat flux continuity. The gauge-pressure at the outlet is set to zero. The heat transfer enhancement is defined by the Nusslet number as [4, 5]:

$$\text{Nu} = hH/k_f = qH/(T - T_{in})k_f = 1/\theta_w \quad (4)$$

$$\text{Average Nusselt number } \overline{\text{Nu}} = (1/\text{number of blocks}) \left[\sum_{\text{number of blocks}_{\text{wall}}} \int_{\text{wall}} \text{Nu} d\Lambda / \int_{\text{wall}} d\Lambda \right] \quad (5)$$

Here, Λ is the direction along the heated block wall.

Percentage enhancement in heat transfer rate as compared to the void channel is termed as PE :

$$PE = 100(\overline{\text{Nu}}_{\text{porous}} - \overline{\text{Nu}}_{\text{void}})/\overline{\text{Nu}}_{\text{void}} \quad (6)$$

Relative enhancement in heat transfer rate to the relative increase in pressure-drop for the porous case is compared with that of the void case. This ratio is termed as performance factor PF [4]:

$$PF = (\overline{\text{Nu}}_{\text{porous}}/\overline{\text{Nu}}_{\text{void}})/(\Delta P_{\text{porous}}/\Delta P_{\text{void}})^{1/3} \quad (7)$$

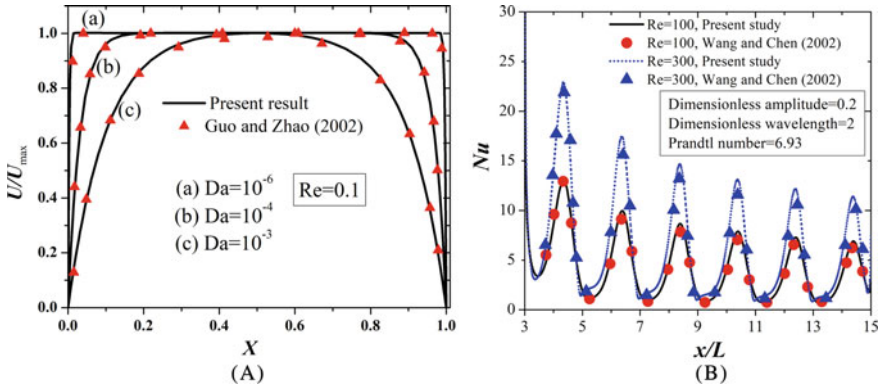


Fig. 2 **a** Comparison of flow velocity profile with Guo and Zhao [11] for generalized Poiseuille flow at different Darcy number with $\epsilon = 0.1$ and $Re = 0.1$, **b** Comparison of Nu with the results of Wang and Chen [12] for forced convective flow through a wavy channel with the limiting case of Darcy-Brinkman-Forchheimer model parameters $\epsilon = 1$, $Da \rightarrow \infty$ ($= 100$); implying that porous medium behaves as void

3 Numerical Methodology and Validation

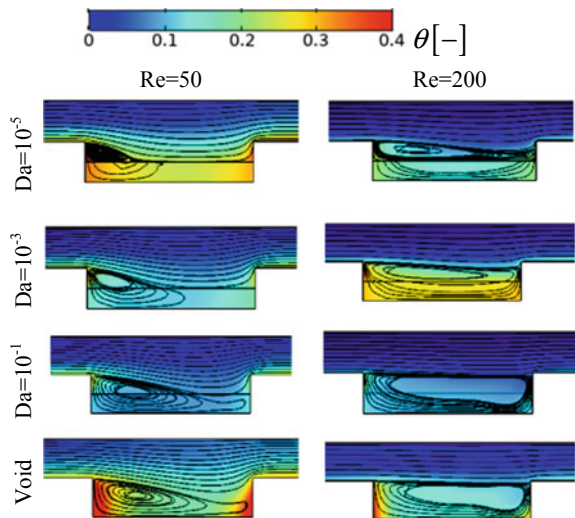
The finite element based numerical solver has been used to solve the governing transport equation numerically. The number of elements is taken as 102,942 ensuring the results are independent of grid lay-out. For these grids, \overline{Nu} is calculated and found that the percentage difference is less than 1% as compared to the very fine mesh. Validation is made with the numerical results of Gua and Zhao [11] by comparing the flow velocity for different Darcy number at $Re = 0.1$ and $\epsilon = 0.1$ as shown in Fig. 2a. The second validation is performed by comparing Nu with the result of [12] for flow through a wavy channel, as shown in Fig. 2b. For this validation, the porosity and the Darcy number are taken as 1 and 100, respectively essentially to mimic the void case as considered by Wang and Chen [12]. Both the comparisons show good agreement with the published results. Hence, our present model is acceptable for further numerical simulations.

4 Results and Discussion

The present work is focused on the thermo-hydraulic performance for electronic cooling using porous material. The distribution of streamlines, temperature field, Nusselt number (Nu), percentage enhancement in heat transfer (PE), and performance factor (PF) have been studied by varying Reynolds number (Re) and Darcy number (Da) in the range of $25 \leq Re \leq 200$ and $10^{-5} \leq Da \leq 10^{-1}$, respectively [1, 4, 5, 9].

To understated the mechanism of heat transfer in the domain, the streamline and normalized temperature contours are presented in Fig. 3 for $Re = 50$ (left) and 200 (right) for different values of Darcy number. The sudden change in flow area results in the formation of the recirculation zone [4, 13–17] near the block at the downstream. For $Re = 50$, the recirculation zone exists nearer the corresponding generating block, whereas at $Re = 200$, it is circulated intermediate region of the two blocks. It can be seen that for the void flow, the maximum temperature intensity is higher near the heated wall. For the porous cases as realized by varying magnitude of Darcy number (Da), the intensity of the hot spot is smaller because of the enhanced effective thermal conductivity in the porous region. It is interesting to see that the magnitude of the hot spot in the void-porous channel depends on the expansion of the recirculation zone between two heated blocks. For $Re = 50$, the size of the recirculation zone is limited to the corresponding block only. To mention, for $Re = 50$, the smaller flow velocity due to lower permeability (smaller Da) results in a hot spot near the heated wall. Whereas, an increase in Darcy number allows more convective strength of the recirculation being formed in the porous zone, and decreases the intensity of hot spot. For $Re = 200$, the recirculation zone forms only at the upper part of the porous zone and its shape is stretched in the axial direction at $Da = 10^{-5}$. Whereas, for $Da = 10^{-3}$, the increased permeability allows the higher size of the recirculation zone. This increase in the size makes the recirculation zone to be attached with the heated wall. The underlying phenomenon leads to an increase in the intensity of the hot spot. Further increase in Da allows more convective strength of air in the porous zone and results in a reduction in the temperature intensity. At higher Re ($=200$) and smaller Da , the temperature intensity in the intermediate part of two consecutive blocks is smaller for void flow as compared to that of the porous case.

Fig. 3 Streamlines and isotherms for $Re = 50$ (left) and 200 (right) for porous case with different Da and void case (bottom)



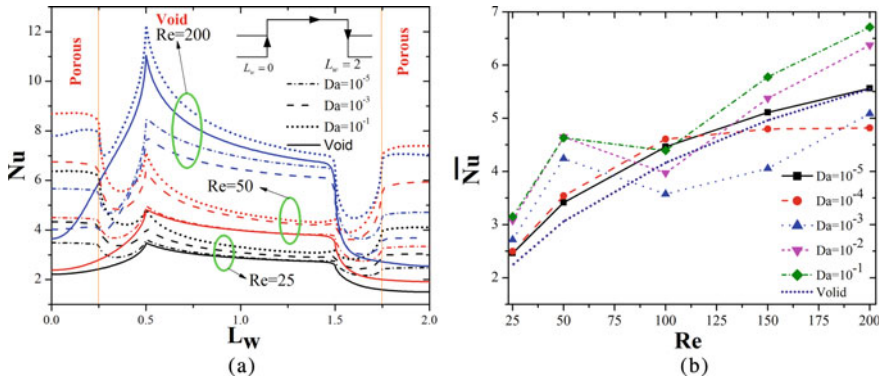


Fig. 4 Variation of **a** Nu at the second heated block for porous channel for different Darcy number and for void channel at Re = 25, 50 and 200. **b** \overline{Nu} vs. Re at different Darcy number for partially filled porous channel and for void channel

The variation of Nu at the second heated wall is presented in Fig. 4a for different Re and Da. It is noted that the variation of Nu is presented in the direction of L_w (direction of wall length along the heated block) as shown in the inset of Fig. 4a. For lower Re (=25 and 50), considerable enhancement in heat transfer rate is observed. This is due to the decrease in hot spot intensity as the effective thermal conductivity enhances. Also, Nu increases with Da as the hot spot intensity decreases for this case. Similarly, for the void part of the heated block, Nu is higher for the porous case as compared to the void case, and its magnitude increases with Da. At Re = 200, with a decrease in Da, Nu for the porous case becomes lesser as compared to that of the void case. This is attributed to the higher temperature intensity in the intermediate part of the heated blocks for porous cases (See Fig. 3). It is also noted that Nu is lower for $L_w < 0.5$ and $L_w > 1.5$ due to the presence of hot spot in the void part of the side wall of the heated block (See Fig. 3).

The overall effect of local heat transfer enhancement is presented in terms of average Nusselt number \overline{Nu} in Fig. 4b. For smaller Re, \overline{Nu} increases monotonically with Da. With increase in Re, \overline{Nu} decreases for higher Da as seen in Fig. 4b. This is because of the expansion of recirculation zone between the two heated blocks, enhancing the hot spot intensity (Fig. 3). Moreover, the convection strength increases with Re for higher Da, and a decrease in hot spot intensity again increases the value of \overline{Nu} with Re as seen in Fig. 4b.

The comparative analysis for enhancement in heat transfer rate for porous cases is compared with the void case and presented in terms of percentage enhancement parameter PE in Fig. 5a. The value of PE is found to be 40 to 50% for $25 \leq Re \leq 50$ with higher Da (Fig. 5a). The decrement in PE is found for intermediate values of Re for the porous case resulting in a negative value due to the decrease in \overline{Nu} for a porous case. Moreover, at Re = 200, PE again increases and attains a value up to 10 to 20% for Da = 10⁻² and 10⁻¹, respectively.

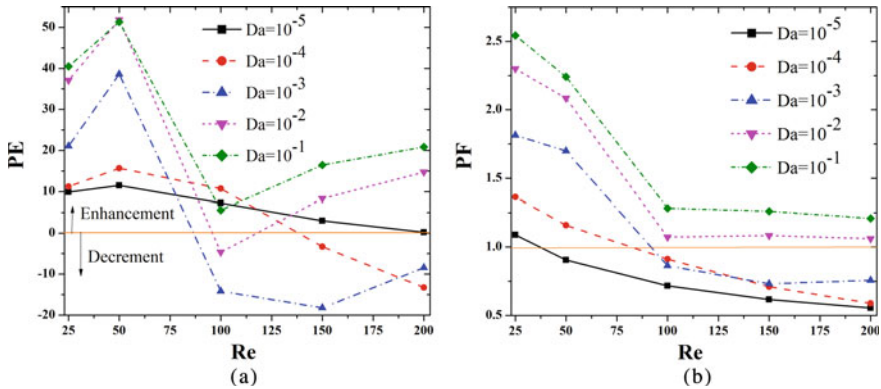


Fig. 5 **a** Percentage enhancement in heat transfer rate (PE) with Reynolds number in partially filled porous channel as compared to the void channel. **b** Variation of performance factor (PF) with Re for different Da

The relative enhancement in heat transfer rate with the corresponding pressure-drop for the porous case is compared to the void case and demonstrated through the variation of performance factor (*PF*) in Fig. 5b. The performance factor decreases with Re. This is due to the fact that the pressure-drop for porous case enhances more as compared to void case. It is found that *PF* becomes higher for $Da = 10^{-1}$. For $Re = 25$, the value of *PF* is higher than unity for all Da considered. On the other hand, at higher Re, the value of *PF* is higher than unity only for higher Da ($=10^{-2}$ and 10^{-1}).

5 Conclusions

The thermo-hydraulic characteristics for an electronic cooling system with the use of porous media have been studied in terms of streamlines, temperature contours, Nusselt number, percentage enhancement in heat transfer (*PE*), and performance factor (*PF*) by varying Re and Da in the range of $25 \leq Re \leq 200$ and $10^{-5} \leq Da \leq 10^{-1}$, respectively. The findings are summarized as follows: The maximum hot-spot intensity decreases with the use of porous media. At higher Re, the intermediate part of the heated blocks has higher temperature intensity as compared to the void case. The local Nusselt number increases with Da for smaller Re and becomes higher than that for the void case. At higher Re, the void case has a higher Nusselt number as compared to the porous case with smaller Da. The heat transfer enhances up to 40 to 50% for $Re = 25$, and up to 10 to 20% for $Re = 200$ at $Da = 10^{-2}$ and 10^{-1} , respectively. The performance factor (*PF*) is always higher for $Da = 10^{-1}$ in the considered regime. For smaller Re ($=25$), *PF* is always greater than unity for all porous cases. At higher Re ($=200$), *PF* factor becomes greater than unity only for higher Da ($=10^{-2}$ and 10^{-1}).

References

1. Rachedi R, Chikh S (2001) Enhancement of electronic cooling by insertion of foam materials. *Heat Mass Transf* 37:371–378
2. Mehta SK, Pati S (2018) Effect on non-uniform heating on heat transfer characteristics in wavy channel. Proceedings of the 5th International Conference on Computational Methods for Thermal Problems, IISc, Bangalore, 498–501. ISSN 2305–6924
3. Mehta SK, Pati S (2019) Analysis of thermo-hydraulic performance and entropy generation characteristics for laminar flow through triangular corrugated channel. *J Therm Anal Calorim* 136:49–62
4. Mehta SK, Pati S (2020) Numerical study of thermo-hydraulic characteristics for forced convective flow through wavy channel at different Prandtl numbers. *J Therm Anal Calorim* 141:2429–2451
5. Mehta SK, Pati S (2021) Thermo-hydraulic and entropy generation analysis for magnetohydrodynamic pressure driven flow of nanofluid through an asymmetric wavy channel. *Int J Numer Meth Heat Fluid Flow*. 31(4) 1190–1213
6. Pati S, Mehta SK, Borah A (2017) Numerical investigation of thermo-hydraulic transport characteristics in wavy channels: comparison between raccoon and serpentine channels. *Int Commun Heat Mass Transfer* 88, 171–176
7. Mondal PK (2013) Thermodynamically consistent limiting forced convection heat transfer in a asymmetrically heated porous channel: an analytical study. *Transp Porous Media* 100:17–37
8. Mondal PK, Dholey S (2015) Effect of conjugate heat transfer on the irreversibility generation rate in a combined CouettePoiseuille flow between asymmetrically heated parallel plates: the entropy minimization analysis. *Energy* 83:55–64
9. Ould-Amer Y, Chikh S, Bouhadek K, Lauriat G (1998) Forced convection cooling enhancement by use of porous materials. *Int J Heat Fluid Flow* 19:251–258
10. Dukhan N, ÖzerBağcı Ö, Özdemir M (2015) Thermal development in open-cell metal foam: an experiment with constant wall heat flux. *Int J Heat Mass Transfer*, 85:852–859
11. Guo Z, Zhao TS (2002) Lattice Boltzmann model for incompressible flows through porous media. *Phys Rev E* 66:036304
12. Wang CC, Chen CK (2002) Forced convection in a wavy-wall channel. *Int J Heat Mass Transf* 45:587–2595
13. Mondal B, Mehta SK, Patowari PK, Pati S (2019) Numerical study of mixing in wavy micromixers: comparison between raccoon and serpentine mixer. *Chem Eng Process: Process Intensification* 136:44–61
14. Mehta SK, Pati S (2021) Effect of non-uniform heating on forced convective flow through asymmetric wavy channel, Pandey KM et al (eds) Recent Advances in Mechanical Engineering, Lecture Notes in Mechanical Engineering, Springer Nature Singapore Pte Ltd. https://doi.org/10.1007/978-981-15-7711-6_34
15. Mehta SK, Pati S (2020) Thermo-hydraulic characteristics for MHD forced convective flow through raccoon channel. Jadavpur University, Kolkata, India, pp 501–504. ISBN 978–93–83660–56–8
16. Bhowmick D, Randive PR, Pati S (2020) Effect of thickness of porous layer on thermo-hydraulic characteristics and entropy generation in a partially porous wavy channel. In: Biswal B, Sarkar B, Mahanta P (eds) Advances in mechanical engineering. Lecture notes in mechanical engineering, Springer, Singapore. https://doi.org/10.1007/978-981-15-0124-1_13
17. Mehta SK, Pati S, Mondal PK (2021) Numerical study of the vortex induced electroosmotic mixing of non-Newtonian biofluids in a non-uniformly charged wavy microchannel: effect of finite ion size. *Electrophoresis* <https://doi.org/10.1002/elps.202000225>

An Experimental Study on the Use of Industrial Wastes to Manufacture Light Weight Modular Bricks



Vikas V. Singh, K. M. Wagh, T. D. Agarwal, J. R. Sirsath, and S. B. Gorade

Abstract In the world of construction, bricks are one of the oldest of all building materials which play a vital role. Traditionally, the term brick referred to a unit composed of clay, but it is now made of concrete materials and different other compositions. The sustainable development for construction involves the use of non-conventional and innovative materials in order to compensate the lack of natural resources and to find alternative ways conserving the environment. Since fly ash (FA) and rice husk ash (RHA) both are pozzolonic material. These pozzolonic material and construction and demolished (C&D) wastes are used to manufacture modular bricks. In this experimental work 4 proportions of brick had been manufactured and tested for water absorption, efflorescence, compressive strength and drop test.

Keywords Fly ash · Rice husk ash · C&D's waste · Recycled fine aggregate · Modular light weight brick

1 Introduction

Brick is the most important building material for the construction industry [10]. Anciently the bricks were produced by using clay and once they were dried, they are burnt into a kiln for final hardness and appearance. But, they caused serious environmental contamination by enormous emission of Green House Gases (GHG) resulted in unusual climate changes the consumption of earth-based material as clay resulted in resource depletion, environmental degradation and energy consumption [2]. The rapid growth in today's construction industry has obliged the civil engineers in searching for more efficient and durable alternatives of conventional bricks. Later the evolution of brick construction design led to development of concrete blocks. The current trend in brick manufacturing has major emphasis on the use of industrial by-products [4]. Fly-ash and Rice husk ash are one of the industrial by-products that are openly dumped on land and cause huge disposal problem and affects environment

V. V. Singh · K. M. Wagh · T. D. Agarwal · J. R. Sirsath · S. B. Gorade (✉)
Pimpri Chinchwad College of Engineering, Pune, Maharashtra, India

hazards. Therefore, in this experiment fly-ash, RHA and C&D waste had been used in manufacturing of modular bricks.

Fly ash is a by-product of burned coal from thermal power plants and in November 2018 PMO (INDIA) had proposed that use of fly ash bricks mandatory for all construction agencies of the Center such as state PWDs & CPWDs. In India, production of fly ash is approximately 197 million tons per year its production increasing each year. Out of which 63% is effectively utilized and the rest is dumped on open land as per 2018 data [8]. Such a huge quantity of fly ash causes challenging problems, in the form of land usage, health hazards and environmental dangers. Fly ash contains high amount of silica which acts as a pozzolona. When added in concrete, they improve the workability, strength and durability of concrete. The replacement of cement by fly-ash reduces the water demand for a given slump and it proves to be economical as fly ash is cost effective. Its maximum utilization varies from 0–25% by weight in bricks manufacturing [5]. To manufacture modular bricks, fly ash can be an alternative material to clay which can prove to be environment friendly [5].

India is a major country for rice cultivation. In power plant rice husk is directly used as a good fuel. Every year approximately 20MT RHA is produced. Dumping of RHA is a great threat to environment and surrounding area. The particle size of RHA is very much fine and it contains around 85–90% silica [3] (varies with burning temperature) and possess larger specific surface area. RHA utilization varies from 0–40% [6]. It improves the material properties as well as it also serve as a energy efficient material for building [4]. C&D waste management in India is a subject of concern in the construction market. C&D waste generation is about one third of the total municipal solid waste generated in India which is disposed either in designated landfills/dump sites or often in unauthorized places such as road sides, river beds and low lying areas causing safety and environmental problems. So, this C&D waste after segregating and crushing can be effectively utilized in mortar as fine aggregate. Therefore, we have used C&D waste as a replacement of crushed sand in manufacturing of modular bricks. The aim of this experimental work is to utilize the industrial wastes to manufacture modular bricks and also, to give a new way of research in construction industry.

2 Materials

The major materials used in this experiment are Cement, Fly-ash, RHA, C&D recycled fine aggregate and potable water.

2.1 Cement

Cement is a backbone of mortar or concrete. It binds the materials together and also strengthens them. OPC 53 grade cement is used in this experiment after performing

Table 1 Chemical composition of Fly ash (left) and RHA (right)

Compounds	Percentage	Compounds	Percentage
SiO ₂	55.23	SiO ₂	93.5
Al ₂ O ₃	26.56	Al ₂ O ₃	0.54
Fe ₂ O ₃	7.04	Fe ₂ O ₃	0.82
CaO (Lime)	8.95	CaO (Lime)	1.45
MgO	2.3	MgO	0.15
–	–	SO ₃	1.94

the all the cement test like fineness, initial and final setting time, soundness as per Indian Standard code (IS-4031).

2.2 Fly Ash

Fly ash is by-product of thermal power plant and inorganic material. It is very rich in silica content of different crystalline nature at different angle (θ) and wavelength as shown in graph. Fly ash-C class is used. It increases the later strength of brick mortar.

2.3 Rice Husk Ash (RHA)

After burning of rice husk at control temperature (400–600 °C) and atmospheric condition, rice husk ash is generated. The particle size of RHA is so much finer that it contains around 85–90% silica and have larger specific surface area as shown in graph. Since, it is also a pozzolonic material and very finer than fly ash and cement, it helps to improve the properties and fill the voids. It also reduces the carbon emission from mortar. The use of RHA in mortar provides an economical contribution and also serves as the energy efficient material for building (Table 1).

2.4 Construction and Demolished Waste

C&D waste segregation is done to remove all impurities like soil, dirt etc. Then, it is crushed and sieve analysis is done to use a specific fine aggregate grade. We have used aggregates which are passing from 4.75 mm and retained on 0.6 mm sieve. The density of C&D recycled fine aggregate (RFA) was 2.56 and water absorption was 5.15. In this experiment segregation and crushing of RFA is done manually (Table 2).

Table 2 Sieve analysis of C&D recycled fine aggregate

IS Sieve designation	Weight retained (in grams)	% of weight retained	Cumulative % of weight retained	% of passing
4.75 mm	0.064	3.2	3.2	96.8
2.36 mm	0.433	21.65	24.85	75.15
1.18 mm	0.518	25.9	50.75	49.25
600 μ	0.479	23.95	74.7	25.23
300 μ	0.254	12.7	87.4	12.6
150 μ	0.122	6.1	93.5	6.5
Pan	0.13	6.5	100	—

2.5 Brick Mould

The dimensions of brick mould are 215 mm \times 115 mm \times 75 mm as shown in Fig. 1.

Fig. 1 Dimensions of brick mould



Fig. 2 Casted samples



Fig. 3 Curing of samples with gunny bags



Table 3 Mix proportion of materials for casting modular bricks

Mix trail proportion	Cement %	Rice husk ash %	Fly ash %	Sand %	W/B ratio (by wt)	No. of specimen
1	30	15	25	30	0.5	6
2	30	15	15	40	0.5	6
3	30	20	20	30	0.5	6
4	30	25	15	30	0.5	6

3 Proportions of Material

The proportion of materials like FA and RHA had been decided after studying the literature. The four trial proportion had been fixed for experimental study (Table 3).

4 The Brick Making Process

All the materials as per its proportion by weight is taken into pan and mixed manually. Then the water was taken as per W/B ratio = 0.5 by weight and mixed with the materials to prepare mortar mix of brick for each trial proportion. Since casting of specimen was manual, the mortar was filled in the mould (oiling of mould is must for interior surface of mould) into 3 layers, to achieve proper compaction and smooth finishing of bricks. To remove air voids, vibration was given by vibrating table. Then

the top finishing was done. After giving vibration, the specimen was removed from mould. The casted specimen was kept for drying and after 4–5 h, curing was done by sprinkling water or covering the specimen with wetted gunny bag. The curing was done for 15 days. After removing from curing these bricks were kept for drying to lose its total moisture for the testing of bricks properties. Six specimens were casted for each trial proportion.

5 Tests on Modular Bricks

All the test on modular brick was carried out as per IS Code-3459 (Figs. 2 and 3).

5.1 Water Absorption Test: (IS-3459 Part2)

Lesser the water absorbed by the bricks, greater is the quality. The water absorption percentage was calculated by dividing the difference between after water absorption weight (W2) and initial weight (W1) to the initial weight (W1). As per IS 3459 part 2, water absorption must lie between 12 to 20% by its weight (Table 4).

Table 4 Observations of water absorption test

Specimen ID	Initial weight (W1) in Kg	Weight after water absorption (W2) in Kg	Water absorption %	Average %water absorption
1A	2595	2983.2	14.95	
1B	2519.5	3028.4	20.19	17.65
1C	2547.2	3001.5	17.83	
2A	2793.5	3167	13.37	
2B	2562.5	2945.8	14.96	14.76
2C	2536.2	2940.9	15.95	
3A	2543	2955.7	16.23	
3B	2329	2755.2	18.3	17.73
3C	2465	2925.7	18.68	
4A	2182.5	2649.3	21.4	
4B	1818	2196.7	20.83	20.82
4C	2075.5	2495.4	20.22	

Table 5 Observations of compression strength test

Specimen ID	Length (mm)	Width (mm)	Load (KN)	Compression Strength (N/mm ²)	Average strength (N/mm ²)
1A	215	115	126.19	5.10	
1B	215	115	136.48	5.52	5.218
1C	215	115	124.36	5.03	
2A	215	115	180.00	7.28	
2B	215	115	130.30	5.27	6.39
2C	215	115	163.38	6.62	
3A	215	115	92.22	3.73	
3B	215	115	90.98	3.68	3.55
3C	215	115	80.00	3.23	
4A	215	115	92.72	3.75	
4B	215	115	66.26	2.68	3.29
4C	215	115	85.55	3.46	

5.2 Compression Strength Test: (IS-3459 Part1)

Compression test was carried out for different proportions of bricks. The test was carried out under compression testing machine and the test results shown in Table 5.

5.3 Efflorescence Test: (IS 3459 Part3)

Take potable water in tray and immerse the specimen 25 mm deep from bottom of tray at room temperature. To avoid excessive evaporation, cover the tray. If the water is absorbed by brick and it appear dry then again place equal amount of water. After 24 h, observe the salt deposition or white patches on the surfaces of brick. If present, calculate the percentage of area covered by salt deposition.

6 Results and Discussion

6.1 Results of Water Absorption Test

Figure 4 shows the comparative result of water absorption for all four mix proportion of modular bricks. For first three mix proportion, water absorption was less than 20 % as per IS code. The average water absorption of mix 2 proportion gave best results i.e $14.76 \leq 20\%$.

Fig. 4 Water absorption test results of modular bricks

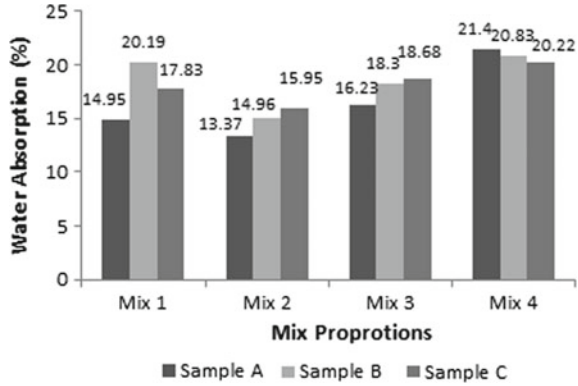
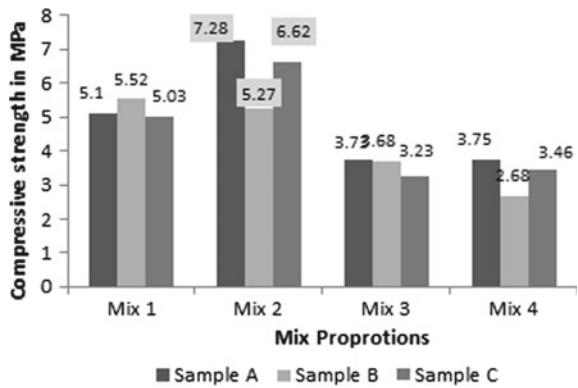


Fig. 5 Compression strength test results of modular brick



6.2 Results of Compression Strength Test

Figure 5 shows the compressive strength of all four mix proportion of modular brick. In Fig. 6 the mix 2 gives higher compressive strength as compare to remaining mixes. The average crushing strength of mix 2 is 6.39 N/mm².

7 Conclusions

1. This paper shows the effective use of industrial wastes (RHA, Fly Ash and C&D waste) gives better results compare to fly ash and burnt clay brick.
2. It was observed that increase in Fly ash and RHA in proportion, there was increase in water absorption.
3. Optimum proportion of bricks was observed at 15% RHA and 15% Fly ash and 40% RFA, as the bricks exhibited high compressive strength and less water absorption.

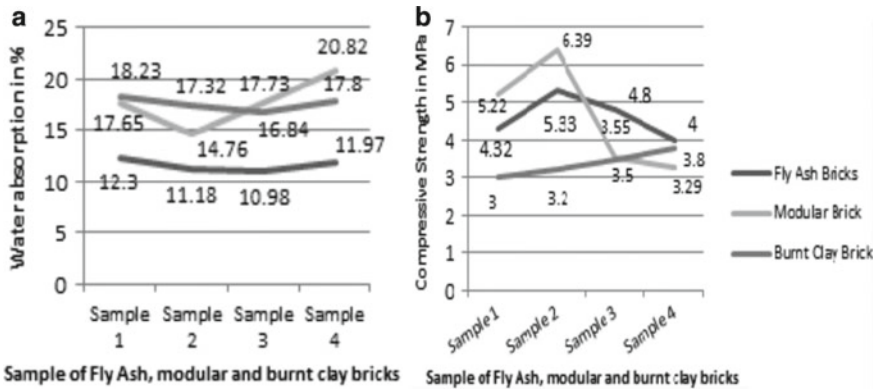


Fig. 6 Comparison of Fly ash, modular and burnt clay brick sample test results **a)** Water absorption test results **b)** Compression strength test results

4. RHA and Fly-ash being pozzolanic material does not contain soluble salts and there is no sign of efflorescence on bricks surfaces.
5. Fly-ash, RHA and C&D waste are light in weight, which in-turn reduces the weight of brick so the dead load of structure will be reduced.
6. Fly-ash, RHA and C&D waste RFA are industrial wastes which are available at low cost which makes the Modular bricks economical as compared to Fly ash and Conventional brick.
7. Brick surface is smooth and plaster requirement is less. After striking two bricks gives clear ringing sound which is sign of good quality brick.

References

1. Abbas S, Saleen MA, Kazmi MS, Munir MJ (2017) "Production of sustainable clay bricks using waste fly ash: Mechanical and Durability properties", *J Building Eng* 14:7–14
2. Gadling PP, Varma MB (2016) Comparative study on fly ash bricks and normal clay bricks, *Int J Sci Res Dev (IJSRD)*, 4(09)
3. Huq RS, Farhana C (2018) "Use of Rice Husk Ash as Substitute to Make Clay Bricks", *Int J Eng Res Appl (IJERA)*, 7(10)
4. Kanthe VN, Deo SV, Murmu M (2018) "Effect of Fly ash and rice husk ash on strength and durability of binary and ternary blend cement mortar", *Asian J Civ Eng* 19(8):963-970
5. Kumar R, Patyal V, Lallotra B, Ashish DK (2014) "Study of Properties of Light Weight Fly Ash Brick", *International Journal of Engineering Research and Applications (IJERA)*, 29. ISSN: 2248–9622
6. Mohan NV, Satyanarayana PVV, Srinivasa Rao K (2012) "Performance of Rice Husk Ash Bricks", *Int J Eng Res Appl (IJERA)*, 2(5):1906-1910. ISSN: 2248–9622
7. Muthadhi A, Kothandaraman S (2013) "Experimental Investigations of performance characteristics of Rice Husk Ash-Blended Concrete", *J Mat Civ Eng* 25(8)
8. Report on fly ash generation at coal/lignite based thermal power stations and it's utilization in the country (2018) Central Electricity Authority (CEA) New Delhi (India)

9. De Silva GHMJS, Perera BVA (2018) Effect of waste rice husk ash (RHA) on structural, thermal and acoustic properties of fired clay bricks, *J Build Eng* 18:252–259
10. Sutasa J, Manab A, Pitak L (2012) Effect of rice husk and rice husk ash to properties of bricks. *Procedia Eng* 32:1061–1067
11. Zareeia SA (2017) “Rice Husk Ash as a partial replacement of cement in high strength concrete containing micro silica”, *J Build Eng* 7

Studies on Characteristics of Geo-Polymer Concrete Mix Design



Sandip Laxman Hake and Divakar Machhindra Waghmare

Abstract Cement production and its use need to be controlled but not at the cost of halting the current pace of industrialization. Alternatives for cement are constantly being worked out. Flyash has evolved as a novel construction material which has huge potential to replace cement and manufacture cementless concrete. It is termed as geopolymer concrete. In present investigation, for preparing M45 grade concrete, Sodium silicate solution with $\text{Na}_2\text{O} = 16.57\%$, $\text{SiO}_2 = 34.25\%$ and $\text{H}_2\text{O} = 49.18\%$ and sodium hydroxide solution having 16M concentration were maintained constant throughout the experiment. Water-to-geopolymer binder ratio of 0.2, alkaline solution-to-fly ash ratio of 0.35 and sodium silicate-to-sodium hydroxide ratio of 2.5 by mass was fixed based on workability and cube compressive strength. Wet curing applied by immersing specimen in water and room temperature curing applied by keeping specimen at laboratory room temperature for specified time period and tested further. It is observed that the results of workability and compressive strength are well-matched with the required degree of workability and compressive strength. So, the proposed method is used to design normal and standard geopolymer concrete.

Keywords Flyash · Geopolymer concrete · Alkaline solutions

1 Introduction

One ton cement production emits equivalent one ton CO_2 in the atmosphere, whereby adopting geopolymer concrete will reduce the dumping of CO_2 in the atmosphere. CO_2 emission is due to two processes. Either due to the combustion of fossil fuel to run rotary kiln which is the largest source of CO_2 emission or due to chemical process to convert calcimine limestone into lime in cement kiln will produce CO_2 [8]. Cement production accounts for approximately 5 to 8% of total greenhouse gas emissions around the globe. It is about 1.35 billion tones of greenhouse emission annually [2]. With the current pace of cement production, Ordinary Portland cement

S. L. Hake · D. M. Waghmare (✉)

Vitthalrao Vikhe Patil College of Engineering, Ahmednagar, Maharashtra, India

use will add an extra 50% CO₂ of the current level by the end of 2020 [1]. As per ICC-2012 taking into an instance, every million tons of fly ash used instead of Portland cement will help to conserve one million tons of limestone, 0.25 million tons of coal from burning and over 80 million units of power. Also, avoid the emission of 1.5 million tons of CO₂ to the atmosphere. In terms of investment, ordinary cement requires huge capital investment for installation of a new plant whereas most of the geopolymer concrete ingredients are waste products of some or other processing units, which can be derived by spending only a few bucks. Kaolinite, clay consisting Si and Al are natural materials whereas flyash, silica flume, slag, rice husk ash, red mud are artificial byproducts of industrial or agricultural process which are best possible alternative to be used as binder for geopolymer concrete [3].

2 Literature Review

Contemporary work of other researchers in geopolymer mix design is simultaneously assessed in order to find out their assumptions and results to improvise the mix ratios and design processes in current research work. [7] Suggested the use of a trial and error approach to design a suitable mix for geopolymer concrete [6]. The used Granulated ground blast furnace slag (GGBS) as binder material. Naphthalene Sulphonate based superplasticizer added 4% of the binder by weight to increase workability and make concrete flow easily within the moulds during casting. Test results showed improvement in compressive strength for GGBS based geopolymer with an increase in NaOH molarity and the ratio of sodium hydroxide to sodium silicate concentration. Compressive, split, flexural strength increased by 13.82%, 18.23%, 30.19% as compared to conventional concrete [8]. The used GGBS in different proportions to replace flyash as a binder. By increasing alkaline activation proportion from 35 to 45% of total binder, setting time increases and at the same time compressive strength of Geopolymer concrete decreases. Also by adopting Na₂SiO₃ to NaOH ratio as 2.5 instead of 1.5 and 2, it reduces slump value and setting time. Geopolymer concrete was cured at room temperature by using Class F type fly ash as a binder [5].

3 Materials

Fly ash is recovered from thermal power plant consists of calcium which reacts with silicate and aluminate monomers to form calcium silicate hydrates and calcium aluminates to act as a binder for geopolymer concrete. Fly ash is the byproduct formed due to the combustion of pulverized coal during the generation of steam to run turbines for generating electric power at thermal power stations. Fly ash is collected through mechanical or electrostatic separators from the flue gases of a power plant. Low calcium class F fly ash was procured from Dirk India private limited Nashik. The specific gravity of the Fly Ash used is 2.26. XRF analysis of

Table 1 Optimized mix proportions for M45 grade geopolymer concrete (Kg/m³)

Parameters	Contents
Fly ash	408.89
Fine aggregates	554.4
Coarse aggregates	1293.3
NaOH concentration	40.89 (16 M)
Na ₂ SiO ₃	102.22
Extra water	–
Super plasticizer	Glenium(4%)
The ratio of mix proportions	1:1.36:3.16
Liquid to binder ratio	0.35
Water to geopolymer solids ratio	0.2

the fly ash sample performed to determine the amount of SiO₂, Al₂O₃, and Fe₂O₃ within fly ash. Chemical composition is given in Table 1. is extremely fine and spherical shaped fly ash particles help to improve workability and reduces extra water requirements during mixing. The alkaline solution is an expensive ingredient within overall geopolymer concrete. From an economic point of view, during mix design minimum to optimal to use of this component is important. Generally, the sodium-based solution is preferred over potassium-based solution due to its low cost. The viscosity of an alkaline solution is generally higher than water. It will form a gel after reacting with a binder. Sodium hydroxide solids of laboratory-grade in pellets form with 99% purity is obtained from local suppliers.

4 Methodology

In geopolymer concrete, the strength depends on the type and chemical composition of binder, types of activator solution, the ratio of Alkaline liquid to binders, Na₂SiO₃ to NaOH, NaOH molarity, water to binder ratio, curing temperature, curing method and rest period. In the investigated the Mix design procedure for Geopolymer concrete composite by adopted similar method that is used for Ordinary Portland cement concrete as per IS: 10262–2009 [4] by adopting few changes such as elevated temperature curing at 900C for early strength gain and improved compressive strength values as compared to its counterpart. M45 grade mix is designed as per the Rangan method for one cubic meter volume geopolymer concrete. NaOH concentration in the mix is measured in terms of molarity. The molecular weight of NaOH is 40. 1 M of NaOH is equal to the addition of 40 gm of NaOH flakes in 1l water. Therefore to get 16 M NaOH solution, take 16 × 40 = 640 gms flakes of NaOH and added inwater to get 1 L of 16 M NaOH solution.

4.1 Design Mix for M45 Grade Geopolymer Concrete

A. Design steps for mix design: (Subhash V. Patankar et al. 2015 (47))

1. Target mean strength is equal to characteristic compressive strength of geopolymer concrete (Fck)
 $F_{ck} = f_{ck} + 1.65 \times S$
 Where, S = standard deviation (Refer cl. 9.2.4.2 IS 456–2000 (48)).
2. Selection of fly ash based upon fineness and quality. Consider Alkaline solution to fly ash ratio 0.35 depending on previous work.
3. Calculate the quantity of alkaline activator solution consisting of sodium silicate and sodium hydroxide using sodium silicate-to-sodium hydroxide ratio equal to 1.0
4. Find the total quantity of solids in this mix consisting of fly ash and solid content of alkaline activators.
5. Find the quantity of water required for preparing the alkaline solution.
6. Calculate the correction of water content: extra water required to prepare the concrete mix.
7. Find the wet density of Geopolymer concrete based upon fineness.
8. Find the quantity of fine and coarse aggregates required for the mix. Find fine aggregate content using fine aggregate to total aggregate ratio.
9. Determine mix proportion in terms of fly ash.
10. Calculate the quantity of material required for casting one mould or quantity per cubic meters of concrete.

Mix design for M45 grade geopolymer concrete:

A. Preliminary data required:

B. Design procedure:

Unit weight of concrete = 2400 kg/m³.

Mass of Combined aggregate = 75–80% (take 77%) = $2400 \times 0.77 = 1848$ kg/m³.

Mass of Fly ash and alkaline Liquid = $2400 - 1848 = 552$ kg/m³.

Take alkaline liquid to fly ash ratio as 0.35.

Mass of fly ash = $(552)/(1 + 0.35) = 408.89$ kg/m³.

Mass of alkaline liquid = $552 - 408.89 = 143.11$ kg/m³.

Let us consider the ratio of NaOH to Na₂SiO₃ as 2.5.

Now mass of NaOH solution = $(143.11)/(1 + 2.5) = 40.89$ kg/m³.

Mass of Na₂SiO₃ solution = $143.11 - 40.89 = 102.22$ kg/m³.

Sodium Hydroxide solution (NaOH):

Considering 16 M concentration, consisting 44.4% of solids (pallets) and 63.5% of water.

Mass of solids = $(44.4/100) \times (40.89) = 18.16$ kg.

Mass of water = $40.89 - 18.16 = 22.73$ kg.

Sodium Silicate Solution (Na_2SiO_3):

The water content in silicate solution is 63.5%.

Mass of Water = $(63.5/100) \times (102.22) = 64.91$ kg.

Mass of solids = $102.22 - 64.91 = 37.31$ kg.

Total mass of water:

Mass of water in NaOH solution + mass of water in Na_2SiO_3 solution = $22.73 + 64.91 = 87.64$ kg.

Total mass of solids:

Mass of solids in NaOH solution + mass of solids in Na_2SiO_3 solution + mass of Fly ash.

= $18.16 + 37.31 + 408.89 = 464.36$ kg.

Ratio of water to Geopolymer Solids:

Ratio = $(87.64)/(464.36) = 0.18 \sim 0.20$.

Mixture proportion are shown in Table 1.

5 Results and Discussion

Selection of appropriate material in terms of fly ash quality and fineness, the molarity of NaOH solution, different ratios, Fine and coarse aggregate type and size, use of convenient Super plasticizer along with additional water has provided ease during mix design. The present investigation includes the addition of lime in different percentages by weight of bonder to decide the effectiveness of low calcium flyash along with alkaline activator to design M45 grade geopolymer concrete. The mixing procedure adopted for geopolymer concrete is quite similar to the conventional concrete mix. All ingredients were mixed in the laboratory at room temperature using tap water for preparing the alkaline solution. All ingredients were weighed to an accuracy of 1 gm and mixed as per the above-mentioned steps to get fresh, viscous, dark uniform colourgeopolymer concrete. After the initial workability test, the sample poured in mould and allowed to set for 24 h at room temperature. Hardened specimen demoulded after 24 h and tested further to determine short term and long term performance of concrete.

Figure 1 gives a graphical representation of compressive strength for M45 grade geopolymer concrete with different percentages of lime addition and cured at 90°C for 24 h. Cubes were kept for a rest period of 7 days before testing. The optimum value of compressive strength was found for 10% lime addition. For further trial M45 grade concrete with 10%, lime taken percentage by weight of binder was cured for different temperature values for 24 h. Later allowed to calm down for a rest period of 7 days and compressive strength values are determined. Maximum value obtained at 90°C . Hence as per Fig. 2 elevated temperature curing performed further at 90°C .

Fig. 1 Compressive strength of geopolymer concrete of grade M45 with addition of various percentages of Lime cured at 90 °C for 24 h

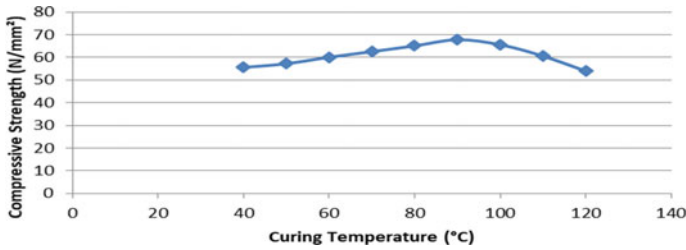
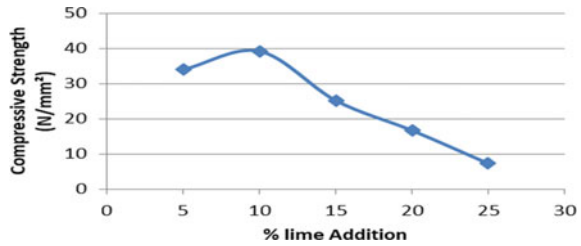


Fig. 2 Compressive strength of geopolymer concrete of grade M45 for 10% Lime addition and cured at varied temperature

Figure 3 represents an increase in compressive strength values with an increase in the rest period. The maximum compressive strength was achieved at 28 days. Investigation of 28th-day strength for concrete cured at room temperature, elevated temperature of 90°C and wet curing shows maximum strength is achieved at elevated temperature of 90°C. Concrete cured at elevated temperature has strength values 13% more than concrete adopting wet curing. Concrete consisting of 10% lime addition cured at room temperature shows strength values 10% more than wet cured concrete. The addition of lime reacts with water of alkaline solution to provide the desired degree of hydration and develops early strength. 98% percent of target strength achieved at 7th-day in case of elevated temperature curing as well as by adopting a 10% lime addition within concrete.

Split tensile strength is determined indirectly using a geopolymer concrete cylinder of 150 mm diameter and 300 mm length. Test procedure adopted in accordance with IS 5816–1999 (61). Geopolymer concrete cylindrical specimen is placed horizontally below load and gradually load is applied till failure. Split tensile strength is determined using the failure load. M45 grade concrete specimen is prepared for the test which consists of 10% lime addition and cured by three different curing methods. Specimen tested after completion of rest period ranging 7, 14, 21 and 28 days.

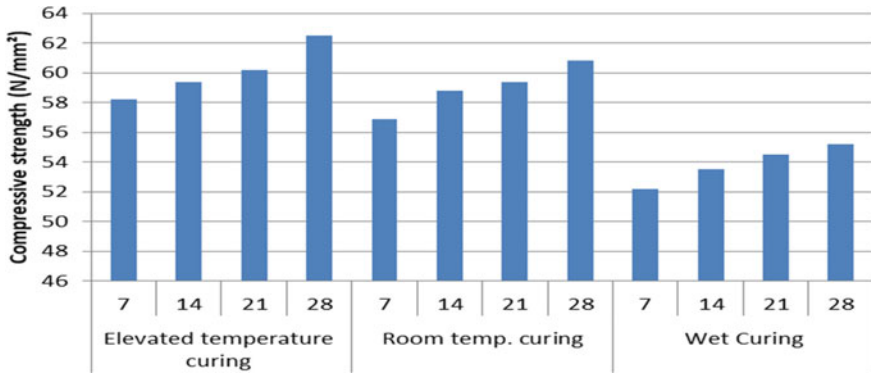


Fig. 3 Compressive strength of geopolymer concrete of grade M45 cured for 24 h with a varied rest period and different curing conditions

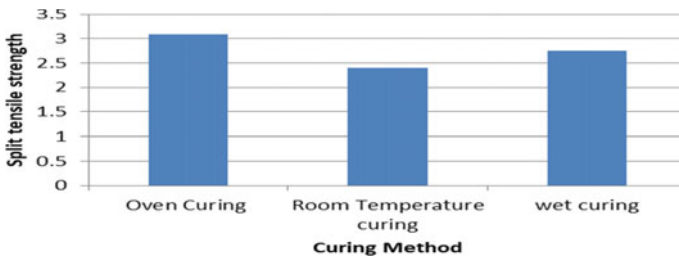


Fig. 4 Variation of split tensile strength by adopting different curing methods

The Fig. 4 shows split tensile strength values for different curing conditions. Concrete specimen adopting wet curing has a strength value of 15% more than specimen cured at normal room temperature. Whereas oven-cured sample has the highest split tensile strength value over the other two methods. It was 12% more than wet curing and 28.75% more than ambient room temperature curing.

Flexural strength gives intimation of failure of flexural/ slender concrete members upon the formation of cracks. A geopolymer concrete beam member of 100 cm length and 10 × 10 cm cross-section is placed below the loading device.

Figure 5 gives a graphical comparison of different flexural strength values for beam members subjected to curing at 900C, normal room temperature curing or wet curing. Flexural strength of beams subjected to wet curing is 11% more than the beam cured at normal room temperature.

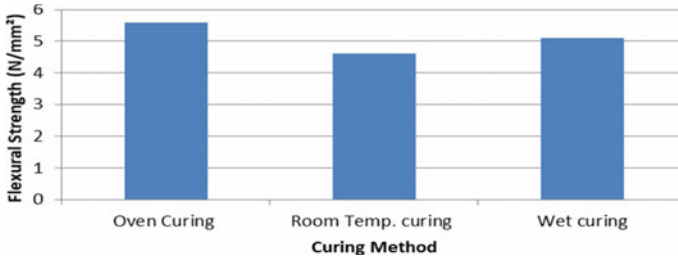


Fig. 5 Graph representing the variation of flexural strength by adopting different curing methods

6 Conclusions

Based on past research and present work attempts made to design geopolymer concrete for M 45 grade by deciding parameters like Class F flyash adopted by considering its fineness and quality. Other parameters were investigated such as quantity of water affecting workability, fine aggregate type and grading, fine-to-total aggregate ratio, water-to-geopolymer binder ratio as 0.35, sodium silicate-to-sodium hydroxide ratio as 1, molarity of Sodium hydroxide as 13 M and adopted ambient room temperature curing instead of oven heating at a temperature 60 °C for duration of 24 h and tested after test period of 7 days. Experimental results of short term and long term properties gives fair results. Promising results obtained in terms of workability and mechanical strength. Excellent properties like high compressive strength, negligible drying shrinkage, low creep, a good bond between flyash- activator and aggregates, good acid and sulfate resistance, fire resistance and excelled bond with old concrete makes geopolymer concrete a versatile material to be used extensively instead of OPC. Hence proposed design steps can be used to design concrete mix for geopolymer concrete similar to guidelines available for conventional OPC concrete. Geopolymer concrete is offering an alternative for reuse of flyash as binder material and eliminating the use of cement and water. This leads to a reduction in environmental pollution and conservation of natural resources.

References

1. Ahmed MF (2011) Nuruddin MF, Nasir S (2011) ‘Compressive strength and workability characteristics of low calcium fly ash-based self-compacting geopolymer concrete’. *World Academy of Science, Engineering and Technology* 74:8–14
2. Hardjito D, Wallah SE, Sumajouw DMJ, Rangan BV (2004) Factors influencing the compressive strength of fly ash-based geopolymer concrete. *Civil Engineering Dimension SIPIL* 6(2):88–93
3. Hardjito D, Wallah S, Sumajouw DMJ and Rangan BV (2004) “On the development of fly ash-based geopolymer concrete”, *ACI Mater J*, 101(6):467–472
4. IS:10262-2009 (2009) Recommended Guidelines for Concrete Mix Design, Bureau of Indian Standards, New Delhi, India

5. Javeed MA, Kumar MV and Narendra H (2015) Studies on mix design of sustainable Geo-Polymer concrete, *Int J Innovative Research Engineering & Management*, 2(4)9–14
6. Madheswaran CK, Gnanasundar G, Gopalakrishnan N (2013) “Effect of molarity in geopolymer concrete” *Int J Civ Struct Eng* 4(2)
7. Nath P, Sarker PK (2012) “Geopolymer concrete for ambient curing condition” Department of Civil Engineering, Curtin University, Kent Street, Bentley, WA, 6102, Australia
8. Srinivas Murthy TV, Ajeet Kumar Rai (2014) “Geopolymer concrete, an earth-friendly concrete, very promising in the industry” 5(7):113–122 ISSN 0976–6316

Design of a Household Wet and Dry Waste Segregation Facilitator Dustbin



Sameer Joshi, Mihir Gharat, Suvinal Lagad, Sampada Khanvilkar, and Abhijeet Kore

Abstract The design of an efficient, compact and self-sufficient household wet and dry waste segregation facilitator dustbin is discussed in detail in this paper. The components required and the mechanism for carrying out the segregation process are discussed and the equations required to find optimum dimensions of various dustbin components have been derived. Structural analysis of these components with the derived dimensions have been carried out and the results regarding the same have been displayed accordingly and the components are proved safe for the dimensions and materials considered for design. An efficient, sturdy, versatile and compact wet and dry waste segregation facilitator dustbin mechanism and design and its effects and socio-economic impact are discussed in this paper.

Keywords Waste segregation · Dustbin · Household waste · Wet waste · Dry waste

Nomenclature

x	Total Displacement covered by the piston
x_1	Distance between Lid surface and Piston head (Inner Piston)
x_2	Distance between Scrubber base and Piston head (Outer Piston).
r_1	Radius of Inner piston-cylinder arrangement.
r_2	Radius of Outer piston-cylinder Arrangement.
d_1	Total Distance covered by Piston 1 (Inner Piston).
d_2	Total Distance covered by Piston 2 (Outer Piston).
F_1	Force applied by the dustbin lid on the piston head of Inner Piston.
F_2	Force applied by the outer piston on the scrubber base.
E_{th}	Theoretical Energy required for efficient cleaning action by the scrubber.
E_{pr}	Actual amount of energy that is produced by the movement of the outer piston.

S. Joshi (✉) · M. Gharat · S. Lagad · S. Khanvilkar · A. Kore
Department of Mechanical Engineering, Pimpri Chinchwad College of Engineering, Pune, India
e-mail: smrjoshi13@gmail.com

1 Introduction

Urban India (about 377 million people) generates 62 million tonnes of municipal solid waste each year, of which about 43 million tonnes (70%) is collected and 11.9 million tonnes (20%) is treated [1]. With changing consumption patterns and rapid economic growth, there is a lot of variability in per capita waste generation in India, daily household municipal solid waste (MSW) generation ranges from 170 g per person in small towns to 620 g per person in large cities [2].

Different governments have tried different measures to segregate waste from the source but these methods are not even close to the expected results. According to a study conducted by Peng Jiang, Yee Van Fan, JiříJaromírKlemeš, social media was an impactful tool to increase household waste management awareness and bring about actual change in the masses [3]. With the mandatory implementation waste segregation and re-cycling Shanghai, compared to those in 2018, the average daily dry waste in 2019 was reduced by 17.5%, biodegradable food waste and recyclable waste were elevated by 88.8% and 431.8%, and the average number of views in the Shanghai Green Account was elevated by 138.5% [3]. This method focuses on increasing awareness and psychological drive amongst individuals towards household waste management.

In India, rag pickers play an important role in the recycling of urban solid waste. Rag pickers and conservancy staff have higher morbidity due to infections of the skin, respiratory, gastrointestinal tract and multisystem allergic disorders, in addition to a high prevalence of bites of rodents, dogs and other vermin [4].

The interest to design a wet and dry waste segregation facilitator dustbin for household or society based segregation purposes with easily available components and materials were as follows:

- a. Literacy rate amongst a large mass of the Indian population is less due to which creating social awareness becomes a difficult task and has not worked well in previous attempts.
- b. It can have a good social impact on creating more opportunities and jobs in the waste management sector and can introduce a sense of sophistication in this sector.
- c. Segregation at the source concept can be implemented well without catering to the human psychological factors that have to be taken care of in other methods of waste management.

The Dustbin works on the principles of torque induction and momentum and energy conservation. The working of the dustbin can be divided into two parts/mechanisms.

- a. Segregation of waste in contact with the dustbin.
- b. Cleaning of the residual waste that is in contact with the dustbin after the process of segregation.

A Lid is a functional unit of waste segregation in the dustbin. A Moisture sensor is placed at the centre of the lid and a servo motor is attached to one end of the

lid. When the waste is subjected to the lid, the moisture sensor senses the nature of waste and accordingly sends a signal to the microcontroller arrangement which in turn sends a signal to the servo motor to rotate either clockwise or anticlockwise depending upon kind of waste subjected(i.e. either wet or dry).

Once the waste drops into one of the compartments provided for segregation, there is some amount of residual waste that is left upon the lid. In case this waste is wet, the readings provided by the moisture sensor will be faulty. To prevent this from happening, a cleaning mechanism is attached to the other side of the dustbin which cleans and wipes the area surrounding the moisture sensor rendering it dry. The cleaning mechanism is a passive system and does not require any external power source to drive it. It makes use of the kinetic energy of the motion of the lid itself to actuate itself and carry out the cleaning action. The Dustbin lid while following its motion transfers some amount of kinetic energy to the piston head of the inner cylinder which in turn transfers some amount of energy to the Piston head of the outer cylinder through a fluid link between the two pistons. The outer piston then hits the base of a scrubber which is pivoted to the surface of the dustbin and carries out angular displacement. A soft scrubber type material is attached to the end of the scrubber rod so that effective cleaning action is carried out and no damage to the lid surface as well as to the moisture sensor occurs.

2 Methodology

A survey regarding the amount of household waste that is generated per household per day was carried out in five societies and these results were further compared to the results from similar surveys that were conducted on a larger scale by reputed institutes. Finally, an average of both these results was taken and final figures regarding the amount of waste generated per day per household were as follows:

- a. An average of 1.4 kg of waste gets generated per household every day [5].
- b. The average amount of wet waste generated in each house = 0.894 kg [5].

2.1 Equations

Calculation of Servo motor Power:

$$\text{Impact Force} = 1.5 \times \text{Normal Force} \quad (1)$$

Calculations for dimensions of cleaning mechanism components (Figs. 1 and 2).

$$x = \sqrt{0.3r_1 - r_1^2} \quad (3)$$

Fig. 1 Cleaning mechanism dimensions (Piston Assembly) dimensions (Lid Assembly)

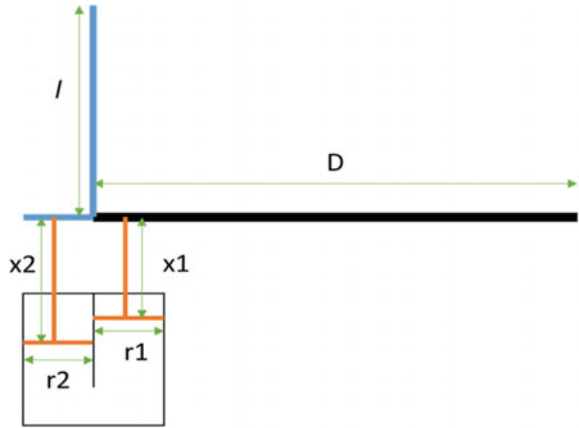
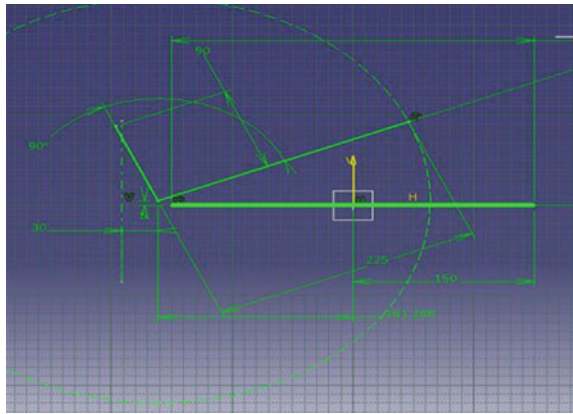


Fig. 2 Cleaning mechanism



$$d_1 = \sqrt{0.3r_1 - r_1^2} - 0.04 \tag{4}$$

According to the principle of energy conservation:

$$F_1d_1 = F_2d_2 \tag{5}$$

$$l = (r + 3) \tag{6}$$

The theoretical amount of displacement required to carry out the cleaning action:

$$d_{th} = r_2 * \sin(67) + 0.02 \tag{7}$$

The total energy required to carry out the displacement:

$$E_{th} = F_2 * d_{th} \quad (8)$$

Actual energy that is given out by actual displacement:

$$E_{pr} = F_2 * d_2 \quad (9)$$

2.2 Design of the Components

Initial Dimensions of the lid: Diameter –300 mm; Thickness –3 mm.

The lid dimensions including thickness are enough for an adequate clearance or interference fit with the shaft of the motor. The upper layer of the dustbin is layered with a low friction polymer such as polyethene so that the water and moisture do not stick to the lid surface.

Standard coefficient of friction of polyethene is around 0.18 to 0.2 [6].

The material is chosen for the dustbin lid and all other components were aluminium for the following reasons:

- a. The dustbin will be subjected to waste quite often which can cause corrosion and the oxide layer of aluminium will protect the dustbin from degrading.
- b. Aluminium gives more manufacturing flexibility and also provides the required sturdiness to the product.

2.3 Design Considerations and Parameters

The main considerations used for the design of the dustbin were effective segregation of the waste and effective cleaning of the dustbin lid after segregation. The other important consideration of the waste segregation was overall smooth functioning of the system as a whole. The parameters used for satisfying these conditions were the angular displacement and velocity of the dustbin lid concerning the pivot point. For the cleaning mechanism, design parameters considered were the amount of area covered by the scrubber for cleaning and the force by which it comes in contact with the dustbin lid.

The dustbin lid was powered by the servo motor whose power was fixed and hence, the only variable in the system was the amount of power that is transmitted to the scrubber through the pistons. Since the amount of time for which the cleaning action takes place is very short, the energy of the system was taken into consideration rather than the power. A theoretical amount of 67 degrees of scrubber displacement was needed to cover the maximum cleaning area. So, the theoretical amount of energy transfer to the scrubber was calculated by the above theoretical energy equation.

Then, different dimensions of the cylinder and piston rods were considered and the maximum energy that can be transferred by the pistons of these dimensions

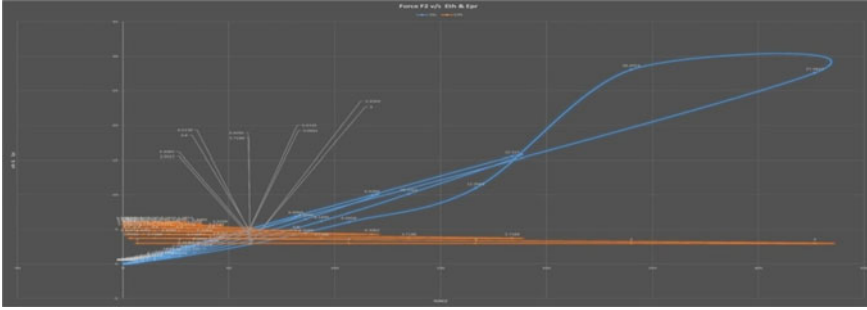


Fig. 3 Graph validation for calculated dimensions

was calculated and a graph was plotted between E_{th} and E_{pr} on the ordinate and force transmitted on the abscissa. The points where both the graphs coincided was considered as the piston dimensions.

From the graph in Fig. 3, it was inferred that the radii of both the inner and outer cylinders should be equal to transmit the required force to the base of the L-shaped scrubber. A MATLAB code was run which tested different dimensions of cylinders and the force transmitted by them. The results of the MATLAB code are depicted (Table 1).

Thus, the most suitable dimensions of the cylinders which were the main force-transmitting elements in the system were considered to be 30 mm (both inner and outer cylinders).

2.4 Structural Analysis of Piston Rods

The piston rods being the main elements transferring the force to the scrubber were to be ensured safe (Figs. 6 and 9) under the given values of force and this could be done by carrying out structural analysis on the rods.

The static structure analysis was performed by using the following steps:

- Geometry/3D model creation.
- Material selection and application.
- Defining boundary conditions.
- Defining structural loads (force, moments etc.)
- Generating mesh.
- Solving and interpreting the results.

By using Aluminium as the material for piston and scrubber mechanism and applying the necessary boundary conditions, structural loads resulted in very satisfying results. Using Von Mises Theory of failure the stress-induced are 5.5 and 0.8 MPa (Figs. 4 and 8 respectively) which is far less than the yield stress for the

Table 1 Result table from the Matlab graphs

T_1	F_1	r_1	A_1	r_2	A_2	F_2	d_1	d_2	d_{th}	E_{th}	E_{pr}
9.000	60.00	0.030	0.0028	0.010	0.0003	6.6667	0.050	0.4500	0.0292	0.1947	3.00
9.000	60.00	0.030	0.0028	0.020	0.0013	26.667	0.050	0.1125	0.0384	1.0243	3.00
9.000	60.00	0.030	0.0028	0.030	0.0028	60.000	0.050	0.0500	0.0476	2.8569	3.00
9.000	60.00	0.030	0.0028	0.040	0.0050	106.667	0.050	0.0281	0.0568	6.0608	3.00

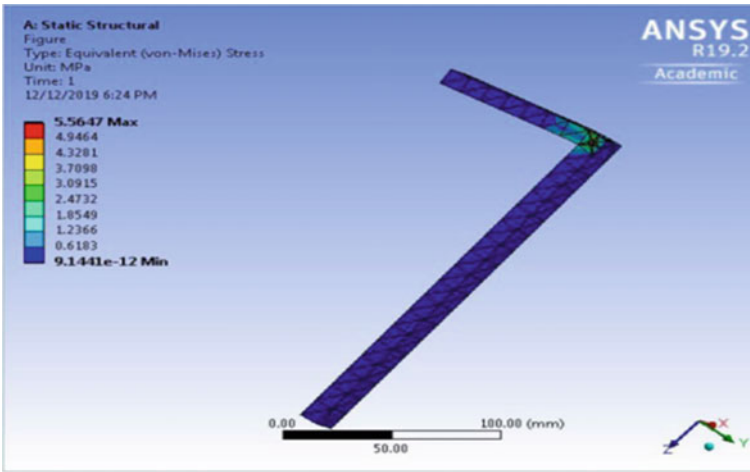


Fig. 4 Equivalent stress analysis scrubber mechanism

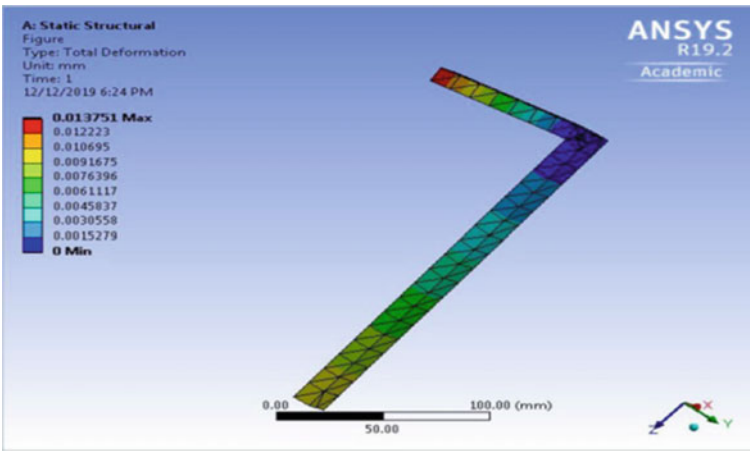


Fig. 5 Total deformation analysis scrubber mechanism

material whilst restricting the deformation of the components to less than 1 mm (Figs. 5 and 7) for the desired motion to be carried out.

2.5 Electronic Assembly Design

It includes:

1. Moisture Sensor

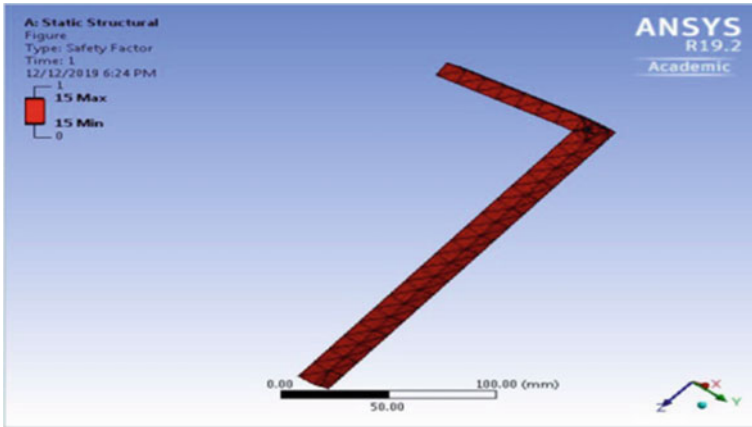


Fig. 6 Safety factor analysis scrubber mechanism

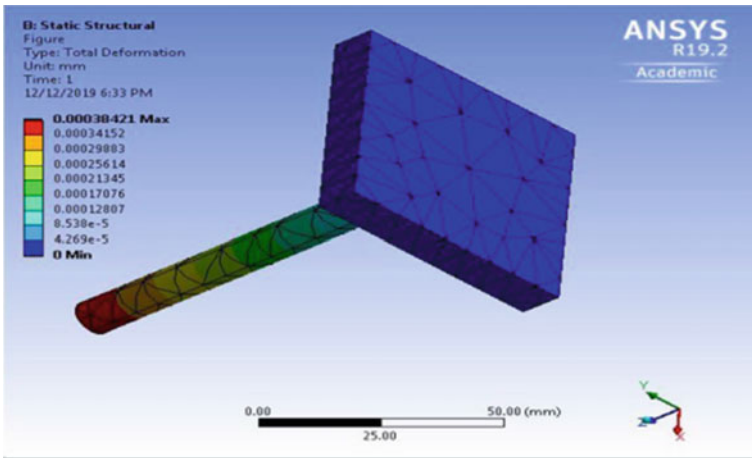


Fig. 7 Total deformation analysis piston assembly

- 2. Ultrasonic Sensor
- 3. Arduino Uno
- 4. Johnson's Motor
- 5. L298N
- 6. Battery.

The assembly is dependent on the Arduino. Sensors such as Moisture Sensor and Ultrasonic Sensor are used. Moisture Sensor detects the condition of the waste either DRY or WET respectively and sends the signals to Johnson's motor. The Ultrasonic Sensor is placed vertically facing the base of the dustbin which helps in knowing the amount of space left in the dustbin before it overflows. The Johnson's motor is

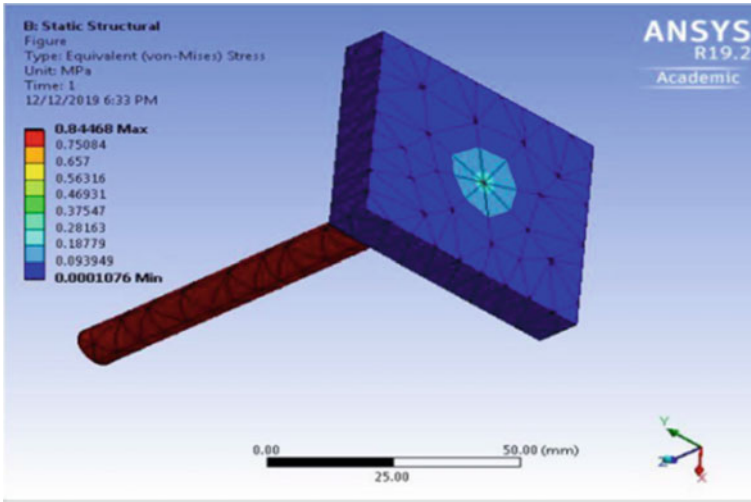


Fig. 8 Equivalent stress analysis piston assembly

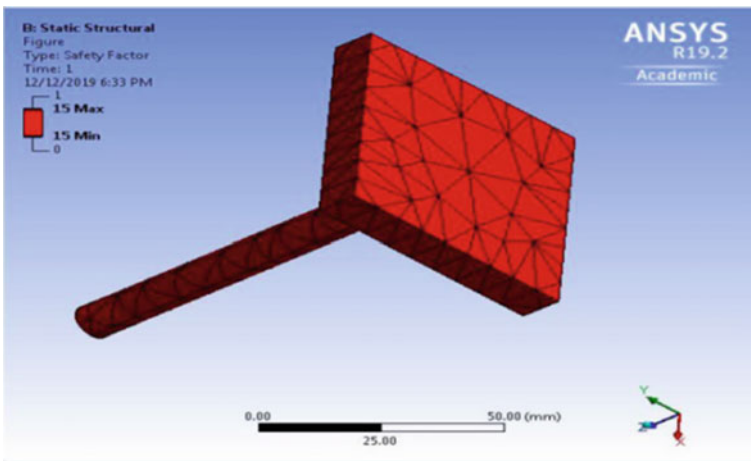


Fig. 9 Safety factor analysis piston assembly

coupled with the lid of the dustbin which helps in the rotation of the lid at particular angles. To get the perfect motion of the motor L298N motor driver module is used [7].

3 Estimated Impact of Project

According to our reports, every household on an average generates 1.4 kg of waste. If a considerably large area such as Pune is considered for a hypothetical implementation of the product, the following impact can be estimated. The total number of households present in Urban Pune is 1,371,531 [8]. Therefore approximate total waste generated: $1,371,531 \times 1.4 = 1,920,143.4$ kgs of waste generated per day. The current percentage of waste that is treated is 20% [9]. Out of this, the estimated amount of valuable treated waste generated can be calculated as:

$$\begin{aligned} \text{Total number of Households} &= \times \text{Amount of waste generated per house} \\ &\times \text{Percentage Amount of waste collected} \\ &\times \text{Percentage amount of waste treated} \quad (10) \end{aligned}$$

Applying the above equation to our figures:

$$1371531 * 0.894 * 0.6 * 0.2 = 147137.8457 \text{ kgs}$$

Consequently, the amount of dry waste that is generated can be calculated to 17445.87432 kgs.

A safe estimation of 50 per cent segregation facilitation can be assumed at this stage as a waste collection in a day happens only once. Hence, following the same calculations as mentioned above, of wet waste getting processed daily.

$$1371531 * 0.894 * 0.6 * 0.5 = 367844.6142 \text{ kgs}$$

Consequently, the amount of dry waste that is calculated comes up to 43,614.6858 kgs being processed per day. Thus, a safe estimation in the percentage increase of segregation efficiency is around 250% for both dry and wet waste as well.

The Socio-Economic impact of this system will be a reduction in the amount of manual effort required in waste segregation on dumpsites thereby reducing the chances of diseases spread by the same. Secondly, the product involves electronic components along with mechanical components which include manufacturing and maintenance which in turn can increase job opportunities amongst masses.

4 Conclusions

From the above information, the following points can be concluded:

1. Estimate the size of the cylinder diameter of the cleaning mechanism for a 300 mm dustbin diameter was calculated to be 30 mm which indicates a 1:10 ratio of the diameter of the cylinder to the diameter of the dustbin lid opening.

2. Stress-induced in the system is 5.5Mpa and 0.8Mpa which is far less than the yield stress of the system when the above-mentioned dimensions and materials are considered.
3. The approximate estimation of the impact that can be generated by the system, if it is implemented on a large scale, was calculated and the percentage increase in the dry waste processing efficiency was calculated to be around 250% for wet as well as dry waste when the approximate system efficiency is held to be 50%.

Thus, the wet and dry waste segregation facilitator dustbin was successfully designed.

References

1. Solid waste management rules (2016) Civildaily. <https://www.civildaily.com/solid-waste-management-rules-2016/> (Accessed 15 Sep 2020)
2. Kumar S et al (2017) Challenges and opportunities associated with waste management in India, *R Soc Open Sci* 4(3). <https://doi.org/10.1098/rsos.160764>
3. Jiang P, Van Fan Y, Klemeš JJ (2021) Data analytics of social media publicity to enhance household waste management, *Resour Conserv Recycl* 164:105146. <https://doi.org/10.1016/j.resconrec.2020.105146>
4. Chandramohan A, Mendonca J, Shankar NR, Baheti NU, Krishnan NK, Suma MS (2017) Automated waste segregator, In: *Proceeding—2014 Texas Instruments India Educators Conference TIIEC*, pp 1–6. <https://doi.org/10.1109/TIIEC.2014.009>
5. Swaminathan M (2018) How can India's waste problem see a systemic change? *Econ Polit Wkly* 53(16)
6. Friction and Friction Coefficients (2020) https://www.engineeringtoolbox.com/friction-coefficients-d_778.html (Accessed 15 Sep 2020)
7. Naveen B, Kavya GK, Kruthika SN, Ranjitha KN, Sahana CN (2018) AUTOMATED WASTE SEGREGATOR USING ARDUINO. *Int J Adv Eng Res Dev* 5
8. Directorate of Census Operations and Uttarakhand (2011) "District Census Handbook Pithoragarh," 2011, [Online]. Available: https://censusindia.gov.in/2011census/dchb/0507_PART_A_DCHB_PITHORAGARH.pdf.
9. "Government notifies new solid waste management rules." <https://www.downtoearth.org.in/news/waste/solid-waste-management-rules-2016-53443> (Accessed 04 Nov 2020)

Thermal Analysis of Earth Air Tube Heat Exchanger for Cooling Tower



Nachiket Shende, Mayur Bhurle, Hrishikesh Bhagwat, Omkar Deokatte, and Rahul A. Patil

Abstract This study focuses on the modified utilization of Earth Air Tube Heat Exchanger (EATHE) in the cooling of water supplied to cooling towers. The system involves the heat exchange process between the air and the soil using soil nature. The system can be installed before the cooling tower for the precooling of water. The design of the system includes a tube of 10.26 m in length and 0.15 m in diameter. To blow air through the tubes two blowers of 650 W can be used which will blow the air with a velocity of 4 m/s. The analytical study shows water temperature drop/rise of 4 to 7 °C. This system can be made portable for easy carrying and installation. This paper analyses the co-relation among different parameters of EATHE such as Temperature drop, NTU, Effectiveness, and Length of the tube, etc. to identify the best fit values in the selection of EATHE as a pre-cooler in a cooling tower.

Keywords Earth air tube heat exchanger · Cooling tower · Pre-cooling

N. Shende · M. Bhurle · H. Bhagwat · O. Deokatte
Student, School of Mechanical and Civil Engineering, MIT Academy of Engineering (MIT AOE)
Alandi (D), Pune, India
e-mail: npshende@mitaoe.ac.in

M. Bhurle
e-mail: mrbhurle@mitaoe.ac.in

H. Bhagwat
e-mail: hrbhagwat@mitaoe.ac.in

O. Deokatte
e-mail: oddeokatte@mitaoe.ac.in

R. A. Patil (✉)
Assistant Professor, School of Mechanical and Civil Engineering, MIT Academy of Engineering
(MIT AOE) Alandi (D), Pune, India
e-mail: rahul.patil@mitaoe.ac.in

1 Introduction

Earth air tubes are often a viable and economical alternative or supplement to conventional central heating or air conditioning systems since there are no compressors, chemicals, or burners and only blowers are required to move the air [18]. The ground temperature below the earth's surface is nearly constant after a certain depth depending upon the soil properties and climatic conditions. This property is being applied to cool or heat the ambient air for a very long time. This concept has been used to cool or heat the room air to reduce the load for cooling or heating by conventional methods [19].

The temperature of the ground remains constant after a specific depth. This is the main concept used while working on the current system. This system includes tubes under the soil through which the fluid will be flowing. In summer the surrounding ambient temperature will be more than the underground temperature, because of which the fluid flowing through tubes will be cooled. In the case of winter, the situation will be opposite to this. As the surrounding temperature will be less compared to the underground temperature, the fluid through tubes will be heated.

In most power plants supply water is used to absorb heat in the cooling tower. The simple concept applies that the cooler the water is, the lesser water will be consumed. In this system, the EATHE is used for pre-cooling of supply water so that we can decrease the temperature of supply water to some extent. As a result, with the help of a small quantity of supply precooled water, the efficiency of the cooling tower will increase. By supplying precooled water more heat transfer will occur from a mixture of steam and supply water. Comparing with the amount of energy used in power plants, the amount of energy used in the system of EATHE is negligible.

In this study, plastic tubes are considered to bury underground. The air is sucked from the surrounding using the blower and sent underground through the buried tubes. According to the principle of heat transfer, there will be heat transfer between the soil around the tubes and the air in the tubes. The type of soil plays a vital role and to decide which soil should be used, this paper further illustrates actual experiments and observations to select the best fit soil. After analyzing the results, sand (with some moisture content) was found as the best fit soil type.

This system is applied in cooling towers consisting of tubes carrying the fluid which will be surrounded by the tubes carrying the water in the loop form. There are two stages in this complete process. At the initial stage, the heat will be transferred from the water which is provided for cooling operation to the fluid flowing in EATHE. In the second stage, the heat will be transferred from the fluid flowing in EATHE to the ground. With increasing tube length, decreasing tube diameter, decreasing the mass flow rate of flowing air inside buried tube and increasing depth of ground up to 1.5 to 2 m performance of EATHE becomes better [6].

1.1 Literature Survey

Different analytical and practical experiments are performed by researchers which are discussed as follows.

Sharma A. et al. performed heat transfer analysis by CFD modeling and simulation of an Earth Tube Heat Exchanger (ETHE). The designed system includes the tube of length 1000 mm with inner and outer diameter 160 mm and 140 mm respectively on the ANSYS design modeler platform. Various materials were tested analytically which were involved in the setup whose thermal conductivities are Air (inside the tube) is 0.027 W/mK, Clay has 0.975 W/mK, Silica Sand (SiO₂), found on the beach, used for casting) has 1.3 W/mK, Sodium Chloride (NaCl) has 6.5 W/mK and at last, Graphite has a highest thermal conductivity of 320 W/mK being a highest grade of coal [18].

Agrawal K.K. et al. studied various horizontal EAHE tube structure like straight, U-shaped, Ring, Serpentine, Spiral and snail, Parallel and Grid, Wagon wheeler (or radial), Slinky coil and Helical coil, Multilayer tubes (with a distance between two layers must be at least 10 times the diameter of tubes), Vertical tube and plate type. This paper infers that tube diameter directly affects the pumping power of fluid hence ideally it should range from 0.1 m to 0.3 m [2].

Taguchi method approach was performed by Agrawal K.K. et al. for optimization of operating parameters of Earth Air Tunnel Heat Exchanger (EATHE) for space cooling. This study depicts material properties used in the simulation were air of 0.02 W/mK, the soil of 0.52 W/mK, and the PVC tube of 0.16 W/mK. It was concluded that by Taguchi optimization method inlet air temperature is most influencing (57.08%) control parameter in cooling mode for achieving maximum air temperature drop and tube diameter contribution of 53.28% in maximizing heat transfer rate [1].

Designing of an Earth Air Heat Exchanger system was performed by Ronge D. et al. in the hot and dry climate of Pandharpur (India). Researcher developed an Earth Air Heat Exchanger (EAHE) for power plant laboratory having 43 oC temperature with 16% relative humidity considering earth's undisturbed temperature (EUT). After theoretical calculation analysis, paper concluded that using NTU method for heat exchangers results in successful model for EAHE was proposed consisting of 100 mm diameter PVC pipe having length 35 m placed in serpentine manner having 2KW air blowers for blowing the air at a velocity of 4 m/sec. Further author suggests that the same system can be used for space heating in winter conditions when mean temperature is greater than inlet air temperature [16].

F. Tasdelen et al. performed a numerical investigation of thermal performance on Earth Air Heat Exchanger (EAHE). The analysis consists of thermal performance of EAHE at 3 different depths (1 m, 2 m, 3 m) designed to cool particular building. It is concluded that at 1 m, 2 m, 3 m depth for inlet temperature of 37 °C the outlet temperatures were 22.54 °C, 15.95 °C and 9.34 °C respectively. The researcher inferred that according to the experimented surroundings the comfort temperature ranges from 21 to 23 °C which falls under the condition of 1 m depth and hence 1 m

depth for other constant parameters would be effective in the intended region of stay [23].

1.2 Overview of Literature

As of now, the researcher's theoretical and practical inspection, experimentation, simulation, and observation systematic outputs were generated for implementing the system for thermal conditioning of a space or warehouse or used for the thermal comfort of human beings. According to the researcher's perspective, the acknowledged EATHE system has comparatively fewer components that are vulnerable to threat and payback period after the installation is reached within a few years. Hence this geothermal system is booming in the sector which requires rise and drop of temperatures which ranges from 4 to 7 °C concerning environmental conditions [1–3, 5, 6, 8, 14, 16–26, 28].

Considering the case of thermal power plants, use of economizers especially the pre-heaters for boilers have always elevated the efficiency of power plant conspicuously. Almost all thermal power plants utilize cooling towers to retrieve the temperature of the water which is used in the boiler for generating steam. When the cooling tower is taken into consideration the main issue addressed is of supply water which is supplied to cooling tower millions of gallons per day. On an average a cooling tower is supplied with 1001 cubic meters of water per day [9, 15, 27]. In such cases, researchers handed out designs of heat exchangers for pre-cooling of coolant or pre-cooling of water which can be inlet for cooling tower or outlet from the thermal power plant which backtracks itself to the water source [4, 7, 10, 11].

This paper provides an optimal solution for pre-coolers in the thermal power plant in the form of EATHE. This EATHE system can drop the temperature of the fluid up to 7 °C and when collaborated with a cooling tower for pre-cooling the supply water can save hundred's to thousand's gallons of water.

2 Construction and Working

EATHE consists of a blower, PVC tubes, soil, portable setup, and delivery chamber. The cycle operates on an open-loop system i.e. air is taken from the surrounding and delivered to the setup chamber employing blower. The schematic diagram as shown in Fig. 1 depicts the construction of this setup which is done in such a way that the blower is placed in the open environment whose inlet sucks the air and is delivered via a tube to setup chamber which can be named as the heat exchanger.

The portable setup consists of wet soil with intricate connectivity of tubes buried in the soil having a specific inlet and outlet. This whole setup can either be buried in the ground or can be kept on the earth's surface in the shaded area. The inlet of the setup is connected to the outlet of the blower which when operated passes the

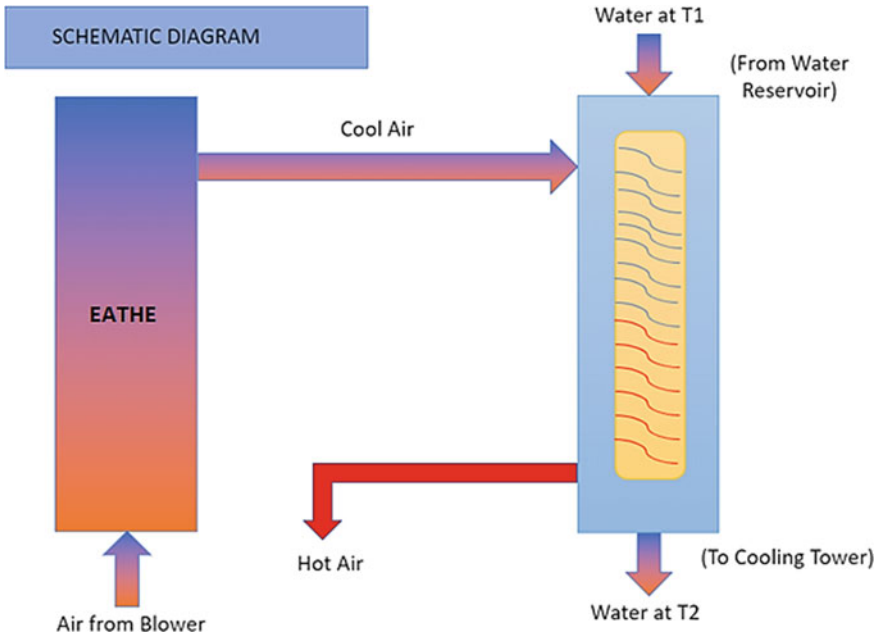


Fig. 1 Schematic diagram of heat exchange between portable EATHE and delivery setup

airflow through the tubes rejecting heat to the soil which is in the periphery of the tube.

The air which has dropped down by a certain degree Celsius needs to be passing at the delivery chamber which is placed at a certain distance from the outlet of the portable setup. As the fluid has dropped its temperature it has acquired the low pressure and because of which the system contains an additional blower to deliver the cooled air at delivery setup.

The delivery setup consists of inlet and outlet for the fluid which has to be cooled (in this case water going for the cooling tower) and zigzag tube system through which the cool air passes. With this interaction of water and air in delivery setup, the heat between the fluid exchanges and water can be cooled.

The outlet of water is further passed on to the cooling tower while the outlet of the air is given back to the surrounding. This is how we can construct the Earth Air Heat Exchanger which is used as a ‘Precooler’ for the cooling towers. According to the calculations performed, the length of the tube came out as 10.26 m with an inner diameter as 0.146 m and outer diameter as 0.15 m. The theoretical calculations resulted that a 10 °C drop can be measured with an airflow velocity of 4 m/s.

Figure 2 shows two heat exchangers 1 and heat exchanger 2 out of which heat exchanger 2 is above the ground providing a cooling effect to the water going in the cooling towers via cool air passed through the tube system in the exchanger and the heat exchanger 1 is below the ground absorbs heat from the hot air and dissipates it to the earth (soil).

The heat exchanger 1 is connected to a pump on the right-hand side which is used to suck the air. The air then passes through several coils in which the heat is dissipated into the earth. The cooled air at the outlet is then pumped to the heat exchanger 2 which is above the ground using the blower attached on the left-hand side (As shown in Fig. 3).

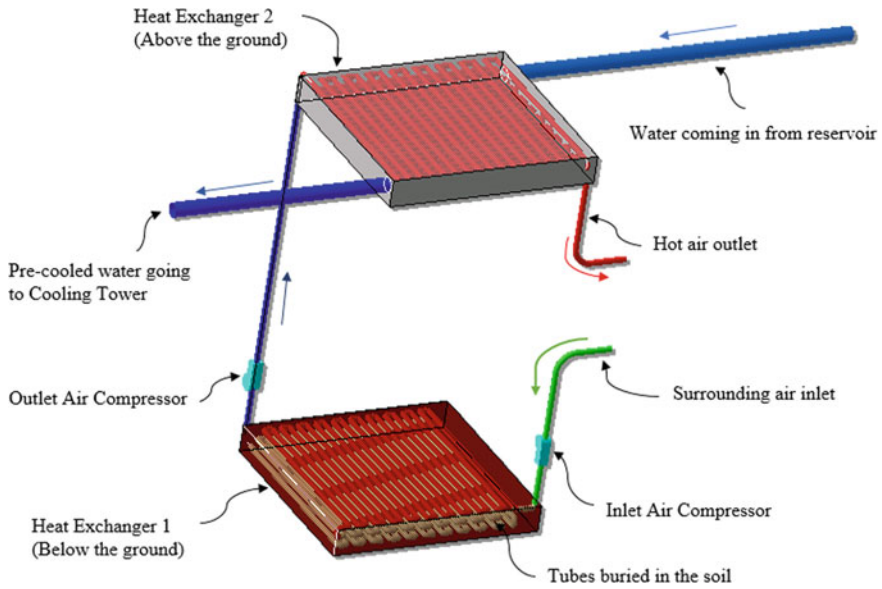


Fig.2 CATIA design of EATHE



Fig. 3 Experimental setup

Table 1 Soil selection observation table

Sr. No	Time allowed to settle the water	Type of soil	Temperature reading (Noted after 15 min.)	
			Without moisture	With moisture
1	15 min	Black Soil	25 °C	23 °C
2	15 min	Coarse Sand	25 °C	20 °C

3 Relative Conductivity of Soil

The experiment was performed for 2 different types of soil (a) black soil (b) Sand. Theoretically, the thermal conductivity of black soil ranges from 0.36 W/mK to 0.39 W/mK and that of sand ranges from 0.58 W/mK to 1.94 W/mK [12]. Also, the thermal conductivity of soil can be increased by 12% (max.) whenever it is mixed with bentonite extending mixture about 8–12% [13]. For sake of simplicity in an experiment, both mentioned soil were taken in two different chambers. Water was poured into the two different chambers and was allowed to settle for 15 min. The thermometer was used to measure the temperature of two different soils as shown in Fig. 3. It was observed that the sand showed more temperature drop compared to the black soil. Hence based on Table 1 conclusion was made that, it is better to use sand as the surrounding medium for the tubes for better transmission of heat in Earth Air Tube Heat Exchanger.

4 Design Calculations

In this section calculations are performed for two different types of heat exchangers;

- Large diameter tube ($D_i = 0.146$ m)
- Small diameter tube ($D_i = 0.02$ m).

The need of calculating various parameters for the different diameters is for making analytical conclusions for feasibility and effectiveness in installation in the view of concerning surroundings. One can conclude after scrutinizing these results that using larger diameter pipe would be more feasible as compared to smaller diameter pipe since it has length limitations for gaining the same temperature drop.

4.1 Assumptions [5]

Thermal conductivity of Air $K_a = 0.026$ W/mK.

Thermal conductivity of tube $K_t = 0.19$ W/mK.

Specific Heat of Air = $C_p = 1006$ J/kgK.

Dynamic Viscosity of Air = $\mu = 1.84 \times 10^{-5}$ N/ms.

Temperatures: $T_{in} = 35$ °C, $T_{out} = 25$ °C, $T_{wall} = 15$ °C, $\Delta T = T_{in} - T_{out} = 35 - 25 = 10$ °C.

Velocity = $v = 4$ m/s.

Friction factor (f) = 0.02345.

Volumetric air flow rate = velocity of air x area of tube = $4 \times \pi \times (R_i)^2 \times v = 0.06154$ m³/s.

Density of air = 1.1465 kg/m³.

Mass flow rate of air, $m_a =$ volumetric air flow rate \times Density of air = 0.07056 kg/s.

4.2 Thermal and Design Parameters

The NTU analysis has been performed. On the basis of assumptions and formulae, the values of various quantities have been obtained which are tabulated in Table 2, The Nusselt number correlation (Eq. 1) is used for predicting heat transfer coefficient (Eq. 2) and Overall heat transfer coefficient (Eq. 3) for NTU.

$$Nu = \begin{cases} \frac{\frac{f}{8} \times (Re - 1000) \times Pr}{1 + \left(12.7 \times \sqrt{\left(\frac{f}{8}\right) \times \left(Pr^{\frac{2}{3}} - 1\right)}\right)}, & Re > 2300, (Turbulent Flow) \\ 3.66, & Re < 2300, (Laminar Flow) \end{cases} \quad (1)$$

$$h = \frac{Nu \cdot \lambda}{D_i} \quad (2)$$

$$U_t = \frac{1}{\left[\frac{1}{h} + \frac{1}{2\pi k_t} \ln \frac{r_o}{r_i}\right]} \quad (3)$$

The effectiveness and NTU is calculated as follows;

$$\varepsilon = \frac{T_{(out)} - T_{(in)}}{T_{(wall)} - T_{(in)}} = (1 - e^{-NTU})NTU = -\ln(1 - \varepsilon) \quad (4)$$

$$NTU = \frac{U_t \cdot A}{m_a \cdot C_p} = \frac{U_t \cdot (\pi \cdot D_i \cdot L)}{m_a \cdot C_p} \quad (5)$$

Hence one can observe that the length of the tube plays a vital role while installing the setup as per Table 2. Practically implementing the tube length as 367 m would cost very high amount as compared to 10.27 m for obtaining equal temperature drop. Therefore, temperature drop varying from 10 to 19 °C the length of the tube was calculated which varies from 10 to 41 m.

Considering this fact, Table 3 signifies the values for required data which were reckoned from the inputs to deduce design parameters for EATHE for Constant Diameter of Tube (i.e. $D_i = 0.146$ m).

Table 2 Comparison chart between varying quantities with different diameter pipes

Sr. No	Quantities	Units	D _o = 0.15 m D _i = 0.146 m	D _o = 0.024 m D _i = 0.02 m
1	Reynolds number (Re)	–	36,373.04	4982.60
2	Prandtl number (Pr)	–	0.69	0.69
3	Nusselt number (Nu)	–	84.84	9.55
4	Convective heat transfer coefficient (h)	W/m ² K	15.11	3.53
5	Overall heat transfer coefficient per unit length (Ut)	W/m ² K	11.25	2.29
6	Heat exchanger effectiveness (ε)	–	0.5	0.5
7	Number of transfer units (NTU)	–	0.693	0.693
8	Length of tube (L)	Meters	10.27	367
9	Number of tubes (assuming one tube of 0.75 m length)	–	14	490

Table 3 Values of constant quantities with changing temperature drop

Sr. No	Quantities	Denoted by	Values	Units
1	Reynolds number	Re	36,388.91	–
2	Prandtl number	Pr	0.71	–
3	Nusselt number	Nu	86.01	–
4	Convective heat transfer coefficient	h	15.32	W/m ² K
5	Overall heat transfer coefficient per unit length	Ut	11.37	W/m ² K

5 Result and Discussions

The diameter of the tube, length of the tube, soil thermal conductivity, depth up to which tubes are buried, the material of tube, type of soil used, spacing between the tubes and the airflow rate inside the tube are different performance parameters for designing of EATHE. Additionally, the tubes having lower diameter shows more pressure drop which also generates turbulence in the flow considering Reynolds’s number for both the tubes. Turbulence results in more contact time between the fluid and the tube surface because of which the heat is transmitted more efficiently as compared to the laminar flow. Baffles can be used inside the tubes to create turbulence hence increasing the contact time. Varying parameters for designing EATHE considering constant diameter in the form of graphs are as follows,

Figure 4 depicts that for increasing temperature drop there is a linear increment in effectiveness with changing lengths of tube. It can be inferred that maximum effectiveness can be achieved for a 19 °C temperature drop. Hence the graph shows that effectiveness is directly proportional to the temperature drop.

Figure 5 represents that higher is the temperature drop, higher is the NTU. Therefore, achieving the maximum value of NTU temperature drop value should be 19 °C

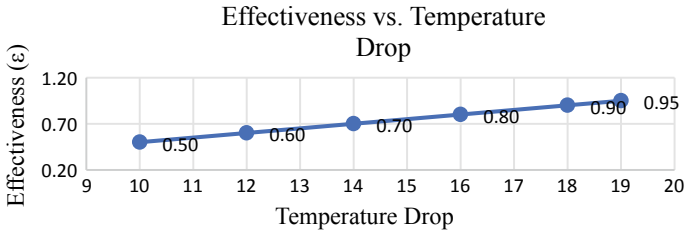


Fig. 4 Graph of Effectiveness versus Temperature Drop

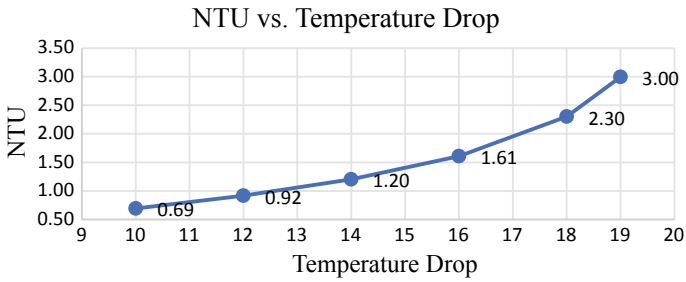


Fig. 5 Graph of NTU versus Temperature Drop

to enhance the heat transfer. Hence the graph shows exponential nature with respect to temperature drop.

Figure 6 denotes that if the mass flow rate is too high, there is less contact time between the air and the tube surface hence decreasing the heat transfer. A maximum temperature drop of 11.7 °C has been observed at a mass flow rate of 0.0196 kg/s for 10 m length of tube.

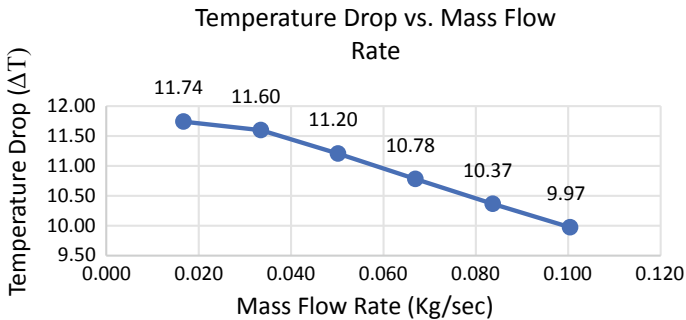


Fig. 6 Graph of Temperature Drop versus Mass Flow Rate

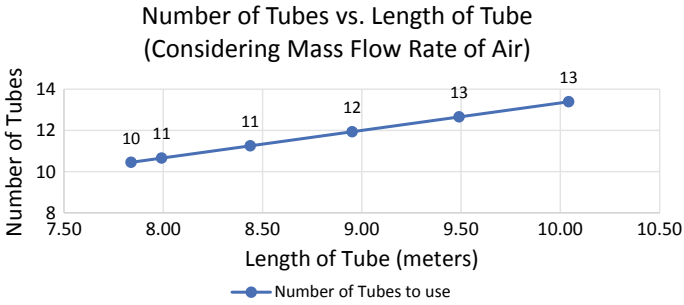


Fig. 7 Graph of Number of Tubes versus Length of Tube

5.1 Length of Tube versus No. of Tubes

Figure 7 shows the graph of mass flow rate and infers that for 8 m tube, minimum 10 tubes will be needed while for 10-m tube, minimum 13 tubes will be needed (when the available length is 0.75 m) which is a very slight change in the requirement of number of tubes when the mass flow rate is considered.

Figure 8 depicts the fact that, considering the inner diameter of 0.146 m the length of the heat exchanger required to obtain a temperature drop of 10 °C is 10.26 m hence if a tube of length 0.75 m with a mass flow rate of 10 kg/sec then 13 such tubes is needed. Graph of Temperature drop infers that minimum 13 and maximum 54 tubes are required to have increasing temperature drop.

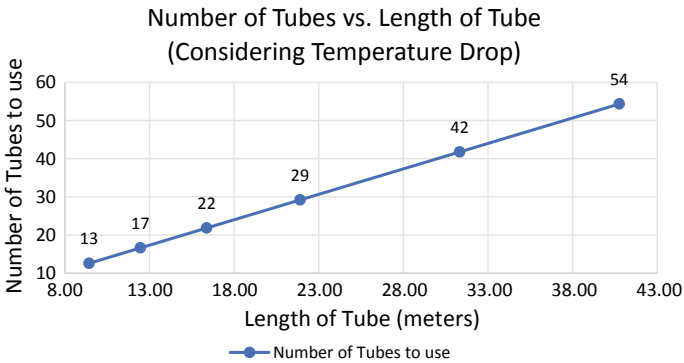


Fig. 8 Graph of Number of Tubes versus Length of Tube

6 Conclusion

Using NTU approach calculations were performed for two different diameters of the tube, which are 0.02 m and 0.146 m respectively. The required depth for placing an EATHE should range from 1.5 to 3 m as beyond this range ground temperature remains constant. The material covering the pipes plays a major role in heat dissipation, and from the studies it is clear that wet black soil with 8–12% of bentonite shows maximum heat dissipation [12]. Although, sand with water content of 18–20% can also be an alternative which gives an equivalent thermal conductivity as that of black soil and bentonite mixture.

For same temperature drop, it has been observed that tubes with an inner diameter of the order 10^{-2} m require very high length; hence it is suggested to use a tube of optimum diameter, varying from 0.100 m to 0.200 m. It is found that 50% and 95% efficient Heat Exchanger have length of tube varying from 10 to 41 m for the temperature drop of range 10 to 19 °C respectively. It suggests that system's temperature drop will increase with an increase in tube length.

For the proposed inner diameter of the pipe with 10 m length of tube, the maximum temperature drop is achieved at 0.0196 kg/s of mass flow rate. The number of tubes depends upon the availability of space, for a confined space it is suggested to use 13 tubes of length 0.76 m each.

The proposed dimension of an EATHE is capable to drop the temperature of working fluid at least 10 to 19 °C at most. This temperature drop is more than sufficient for a pre-cooler to achieve higher efficiency of the cooling tower. Also, the proposed EATHE is a portable system enabling it to be deployed under any shaded area nearby the plant. Hence keeping the design parameters and result oriented output of EATHE, it can be used as a pre-cooler for cooling tower in order to decrease the load on cooling tower in efficient manner which can save gallons of water per day.

References

1. Agrawal KK, Bhardwaj M, Misra R, Agrawal GD, Bansal V (2018) Optimization of operating parameters of earth air tunnel heat exchanger for space cooling: Taguchi method approach. In: *Geothermal Energy (Open Journal)* 6(10):1–17. Springer
2. Agrawal KK, Misra R, Agrawal GD, Bhardwaj M, Jamuwa DK (2019) Effect of different design aspects of pipe for earth air tunnel heat exchanger system: a state of art. *Int J Green Engy* 1–17
3. Atwany H, Hamdan M, Attom M, Abu-Nabah BA, Alami AH (2019) Performance of earth-water heat exchanger for cooling applications. *Int J E-Learning Educ Technol Digital Media* 5(1):17–21
4. Bisoniya TS (2015) Design of earth-air heat exchanger system. In: *Geothermal Energy (Open Journal)*. vol 3 18th edn, Springer, pp 1–10
5. Chauhan KM, Prajapati JG, Goswami NY, Patel SN, Patel KN (2018) Design and development of an earth air tube heat exchanger. *Int J Manag Tech Engg* 8(6):317–324
6. Dhruw HK, Sahu G, Sen PK, Sharma R, Bohidar S (2015) A review paper on earth tube heat exchanger. *Int J Rese Appl Sci Engg Tech* 3(11):415–417

7. Gad-Briggs A, Nikolaidis T, Pilidis P (2017) Analyses of the effect of cycle inlet temperature on the precooler and plant efficiency of the simple and intercooled helium gas turbine cycles for generation IV nuclear power plants. In: *Applied Sciences*. vol 7, 4th edn. MDPI, pp 1–20
8. Hamdan MO (2018) Tapping to geothermal energy through a high performance earth-to-water heat exchanger design. In: *5th International Conference on Renewable Energy: Generation and Applications*, IEEE, UAE, pp 207–210
9. Kumar V, Mathews R (2018) Performance analysis and optimization of cooling tower. *Int J Sci Res* 8(4):225–237
10. Manjunatha SG, Bobade KB, Kudale MD (2015) Pre-cooling technique for a thermal discharge from the coastal thermal power plant. In: *8th International Conference on Asian and Pacific Coasts*, Elsevier, pp 358–365
11. Mohammed JS, Hamdan AH, Mohammed R (2017) Design of pre-cooler for gas turbine at Garri (1and2) power station by using vapor compression refrigeration system. *Int J Sci Engg Sci* 1(12):1–7
12. Nidal H, Hamdeh A, Reeder RC (2000) Soil thermal conductivity: effects of density, moisture, salt concentration, and organic matter. *Soil Sci Soc Am J* 64:1285–1290
13. Omer A (2018) Soil thermal properties: effects of density, moisture, salt concentration and organic matter. In: *Euro-Mediterranean Conference for Environmental Integration*, Springer, Tunisia, pp 113–114
14. Rashid H (2014) Design and fabrication of a heating and cooling system using geothermal energy. In: *International Conference on Energy Systems and Policies*, IEEE, Islamabad, pp 207–213
15. Riguang W, Xuyang W, Jianqiang G, Minghao M, Zhongliang L (2016) Design of geothermal buried tube heat exchanger based on the double source heat pump systems. In: *International Conference on Power and Renewable Energy*, IEEE, pp 680–683
16. Ronge D, Kadam V, Shende S, Kate P, Waghmare V, Patil O (2020) Design of an earth air heat exchanger system for space cooling in hot and dry climate of Pandharpur, India. *Aegaeum J* 8(6):1594–1602
17. Rosa N, Santos P, Costa JJ, Gervásio H (2018) Modelling and performance analysis of an earth-to-air heat exchanger in a pilot installation, *J Buil Phy* 1–29
18. Sharma A, Srivastava S, Kumar S (2017) Heat transfer analysis of source/sink of an earth tube heat exchanger by CFD modelling and simulation. *Int J Mech Engg Tech* 8(7):1260–1271
19. Shelar SN, Patil SB, Ghuge NC (2016) A review on earth-air heat exchanger. *Int J Engg Res Tech* 5(2):1–5
20. Singh B (2018) Analysis of working parameters affecting the performance of earth-air tube heat exchanger (EATHE): a review. *Int Res J Engg Tech* 5(7):1254–1260
21. Singh SK, Sobati J (2015) Earth-air heat exchanger as a green retrofit for Chandigarh-a critical eeviw. In: *Geothermal Energy (Open Journal)*, vol 3(14), Springer, pp 1–9
22. Sogale N, Thombare S, Lopes I, Nair A (2017) Design and development of earth tube heat exchanger for room conditioning. *Int J Engg Sci Comp* 7(3):5039–5042
23. Tasdelen F, Dagtekin I (2018) A numerical investigation of thermal performance of earth-air heat exchanger. *Arabian J Sci Engg* 44:1151–1163
24. Tiwari GN, Singh V, Joshi P, Deo SA, Prabhakant Gupta A (2014) Design of an earth air heat exchanger (EAHE) for climatic condition of Chennai, India. In: *Open Environmental Sciences*, vol 8, Bentham Open, pp 24–34
25. Vlad G, Ionescu C, Necula H, Badea A (2011) Thermoeconomic design of an earth to air heat exchanger used to preheat ventilation air in low energy buildings. *International Conference on Energy. Environment, Entrepreneurship, Innovation*. SJR, US, pp 11–16
26. Yassine B, Ghali K, Ghaddar N, Chehab G, Srour I (2013) Effectiveness of the earth tube heat exchanger system coupled to a space model in achieving thermal comfort in rural areas. *Int J Sust Engy* 1–20

27. Yu Y, Li H, Niu F, Yu D (2014) Investigation of a coupled geothermal cooling system with earth tube and solar chimney. In: *Applied Energy*. vol 114, Elsevier, pp 209–217
28. Yusof TM, Ibrahim H, Azmi WH, Rejab MRM (2018) Thermal analysis of earth-to-air heat exchanger using laboratory simulator. In: *Applied Thermal Engineering*. vol 134, Elsevier, pp 130–140

Three Phase Z-Source Inverter Analysis Using Matlab Simulation



D. P. Narsale, A. M. Kasture, Akshay. A. Jadhav, and M. A. Deshmukh

Abstract This paper presents Matlab simulation analysis on the three-phase Z-Source inverter (ZSI) using simple boost (Pulse Width Modulation) PWM control method and maximum constant boost PWM control method with third harmonic injection. The ZSI is a new power conversion concept, used in all type of power conversion. The simulation of Z-Source inverter is performed using MATLAB/SIMULINK software. The simple boost control (SBC) and maximum constant boost control (CBC) with third harmonic injection, PWM control methods are utilized to generate sampled PWM signals. These PWM signal are used to trigger the switching devices. This paper represents the comparison of boost factor, voltage gain, voltage stress across switches, shoot through duty ratio and THD using different boosting techniques in Z-source inverter for fixed modulation index. The inverter is designed for a power rating of 100 W, RMS line voltage 230 V.

Keywords Traditional inverters · Z-source inverter · Third harmonic injection · Shoot through · Boost factor · Voltage gain · Voltage stress · Total harmonic distortion (THD)

1 Introduction

Inverters are the dc to ac converters. The input DC supply is either within the sort of voltage or current is converted into variable output AC voltage. There are two main types of three-phase inverters used, the voltage source inverter (VSI) and the current source inverter (CSI). In VSI, to obtain a constant voltage source, a capacitor is used in a DC link and in CSI, to get a constant current source a large inductor is used. Traditional inverters have certain limitations [4]. For buck (step down) DC to AC power conversion VSI is used. An additional DC-DC boost converter is required to spice up the AC voltage output. A different DC-DC boost converter is needed to spice up the AC voltage output. In DC to AC conversion, the CSI is used as a boost

D. P. Narsale (✉) · A. M. Kasture · Akshay. A. Jadhav · M. A. Deshmukh
SVERIs College of Engineering Pandharpur, Pandharpur, Maharashtra, India
e-mail: dpnarsale@coe.sveri.ac.in

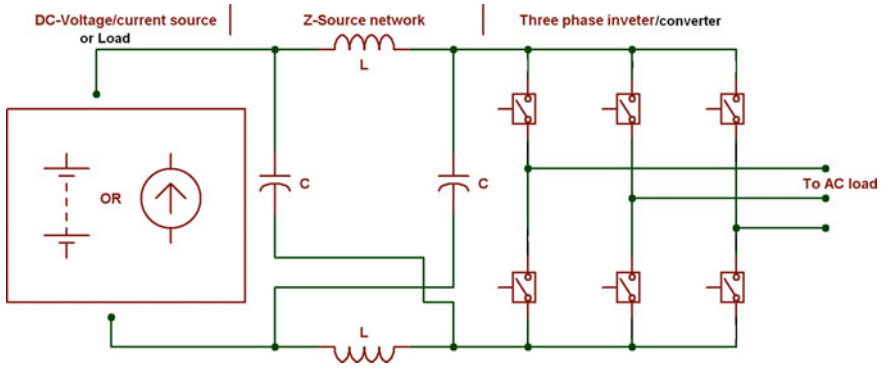


Fig. 1 Z-source inverter

inverter. For a change in voltage range, it also requires additional buck (or boost) DC-DC converters [8]. Hence, no traditional inverter can be employed only for a buck and boost simultaneously, without other DC link converters.

ZSI shown in “Fig. 1” has been recently developed and is being used in power converter applications for implementing all AC-to-DC, DC-to-AC, AC-to-AC, and DC-to-DC power conversion [4]. The ZSI make use of a unique impedance network to connect the primary converter circuit to the power source, load, or other converters, for providing unique features that cannot be observed in the traditional VSI and CSI. This paper represents the comparison of boost factor, voltage gain, voltage stress across switches, shoot through duty ratio and THD using different boosting techniques in Z-source inverter [6].

2 General System

The three-phase ZSI block diagram is shown in “Fig. 2”. The input DC supply source is acquired using single-phase rectifier and dc capacitor or by using DC source. The

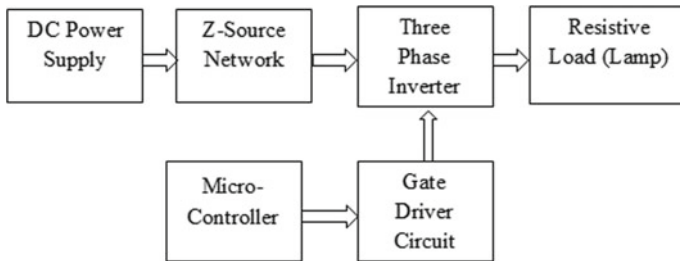


Fig. 2 Block diagram

DC voltage is then supplied to the Z-source circuit through a reverse blocking diode. Z-Source circuit consists of two capacitors and two inductors connected in such a way as to form a second-order filter. The output dc-link voltage is then used across the three-phase inverter. Then the three-phase output ac voltage is acquired at the output side [5]. The Microcontroller and driver circuit is used to control on/off time of switching devices in a proper sequence.

3 PWM Control of ZSI

The traditional PWM inverter topology results in high voltage stress to the switching devices [10]. The PWM inverter topology of DC to DC boosted can reduce the voltage stresses and limitations of VSI, but it affected by problems such as high cost and complexity related to the two-stage power conversion. Traditional PWM consists of six active states and two zero states. In traditional zero states, either upper three or lower three switching devices of inverter bridge are on and doesn't provide current to the load. Therefore the load voltage is almost zero within the zero state [3]. In the case of ZSI, additionally to 6 traditional active states and two zero states, it consists of 1 more condition called a shoot-through state. During a shoot-through state, both upper and lower switching devices during a single arm, our all the three components conducts simultaneously, hence producing short across load [1]. Therefore output voltage across the load remains zero within the shoot-through state. In Z-source inverter the part of zero conditions is changed into the shoot-through state, where both upper and lower switching device of one or all the three-arm of bridge inverter conducts simultaneously [2].

The following PWM control methods are used to control the ZSI:

1. Simple boost control
2. Maximum constant boost PWM control method with third harmonic injection.

The comparison of these PWM methods is presented in [7] and [11]. The simple boost control method produces higher voltage stresses across switching devices. The voltage stress across switching devices is reduced in maximum boost control method. The ultimate constant boost control with or without third harmonic injection method overcomes the limitations of simple boost control methods [9].

4 Implémentation of Z-Source Inverter in Matlab Simulink

4.1 Simulation Using Simple Boost Control Method

The complete simulation configuration and result waveforms of ZSI using SBC control method are shown in the "Fig. 3". The component values of ZSI depend

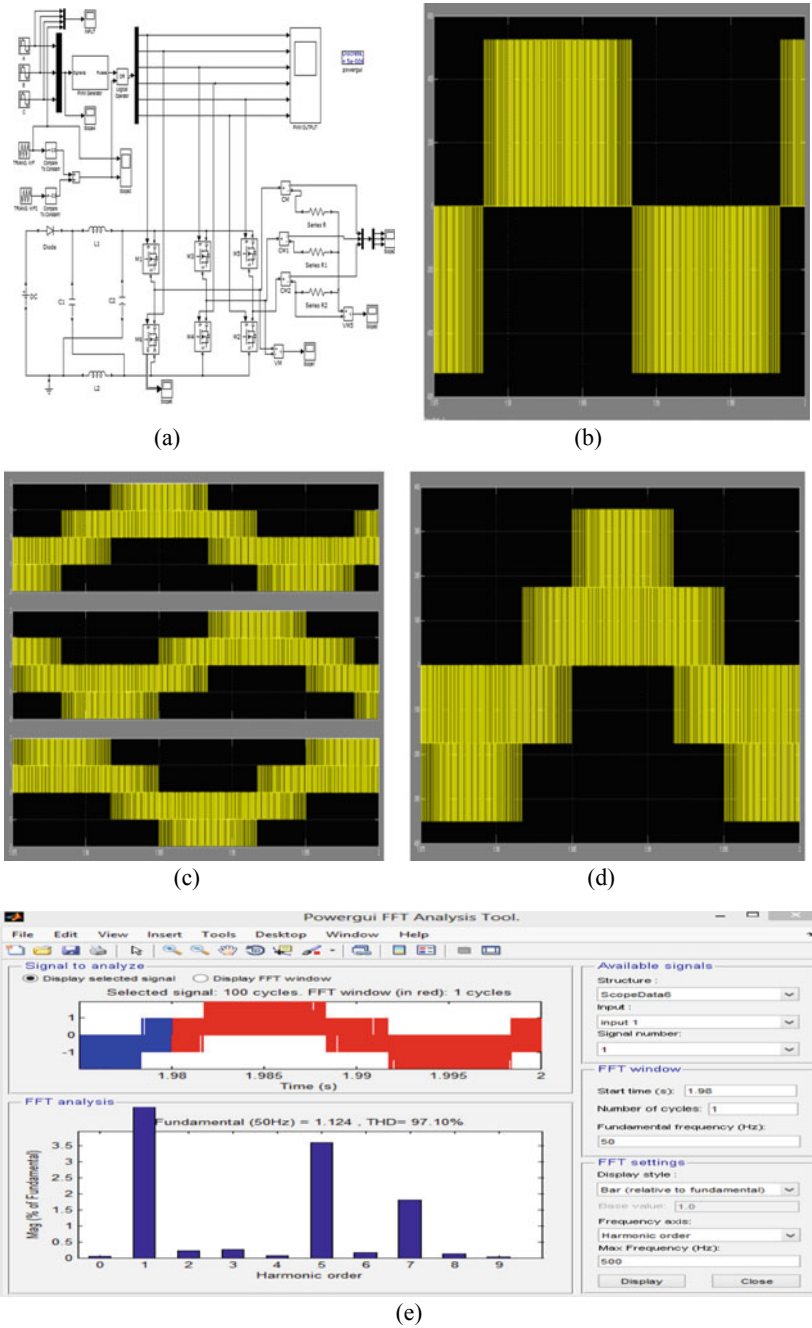


Fig. 3 a Simulation configuration of ZSI using SBC method b Waveform of SBC for line voltage c Waveform of SBC for phase voltage d Waveform of SBC for current through R load e FFT analysis of output current through R load

on switching frequency only. These component values are chosen as per design guidelines in [4]. For this circuit $L1 = L2 = 30\text{mH}$ and $C1 = C2 = 220\mu\text{F}$. The purpose of the system is to produce 230Vrms line voltage and 100 W power. For PWM generation the carrier frequency is set to 10 kHz, and modulating reference signal frequency is set to 50 Hz. The modulation index is 0.6932, and the input DC voltage is 211 V. Simple boost PWM signals are generated using PWM generator and logic circuit. The PWM generator block generates normal three-phase PWM waveforms for a given carrier frequency. Using the triangular function comparator and adder repeated shoot-through pulses are generated. These shoot-through pulses are evenly spread in all the three-phase PWM waveform using the OR logic function.

The capacitor voltage is the average dc-link voltage remains almost constant about 377 V. Thus the input voltage (211 V) is boosted (377 V) and applied as dc-link voltage. The peak value of this dc-link voltage appears as an input voltage across the primary inverter circuit. It is observed that during shoot-through state dc-link voltage becomes zero since all devices in the central inverter are switched on simultaneously, short-circuiting the dc link. Also, we can see that during the shoot-through period, the capacitor voltage becomes equal to the inductor voltage. The capacitor charges the inductor so that the inductor current increases during this time and releases its energy during the active state.

The detailed analysis is given below

1. Boost factor = $B = 2.58$
2. Peak dc link voltage = $2.58 * 211 = 545 \text{ V}$
3. Peak ac output voltage = $V_{ac} = 0.6932 * 2.58 * 211 / 2 = 188.6 \text{ V}$
4. RMS ac output voltage $V_{ac} = 133.4 \text{ V}$
5. RMS line voltage = $\sqrt{3} * 133.4 = 231 \text{ V}$.

4.2 Simulation Using Maximum Constant Boost PWM Control Method With Third Harmonic Injection

The complete simulation configuration and result waveforms of ZSI using CBC control method with third harmonic injection are shown in “Fig. 4”. The component values of Z-source inverter depends on switching frequency only. These component values are chosen as per design guidelines in [4]. For this circuit $L1 = L2 = 25 \text{ mH}$ and $C1 = C2 = 220 \mu\text{F}$. The purpose of the system is to produce 230Vrms line voltage and 100 W power. For PWM generation the carrier frequency is set to 10 kHz, and modulating reference signal frequency is set to 50 Hz. The modulation index is 0.7798, and the input DC voltage is 170 V. Constant boost PWM signals are generated using PWM generator and logic circuit. The PWM generator block generates normal three-phase PWM waveforms for a given carrier frequency. Using the triangular function comparator and adder repeated shoot-through pulses are generated. These shoot-through pulses are evenly spread in all the three-phase PWM waveform using the OR logic function. The capacitor voltage is the average dc-link voltage remains

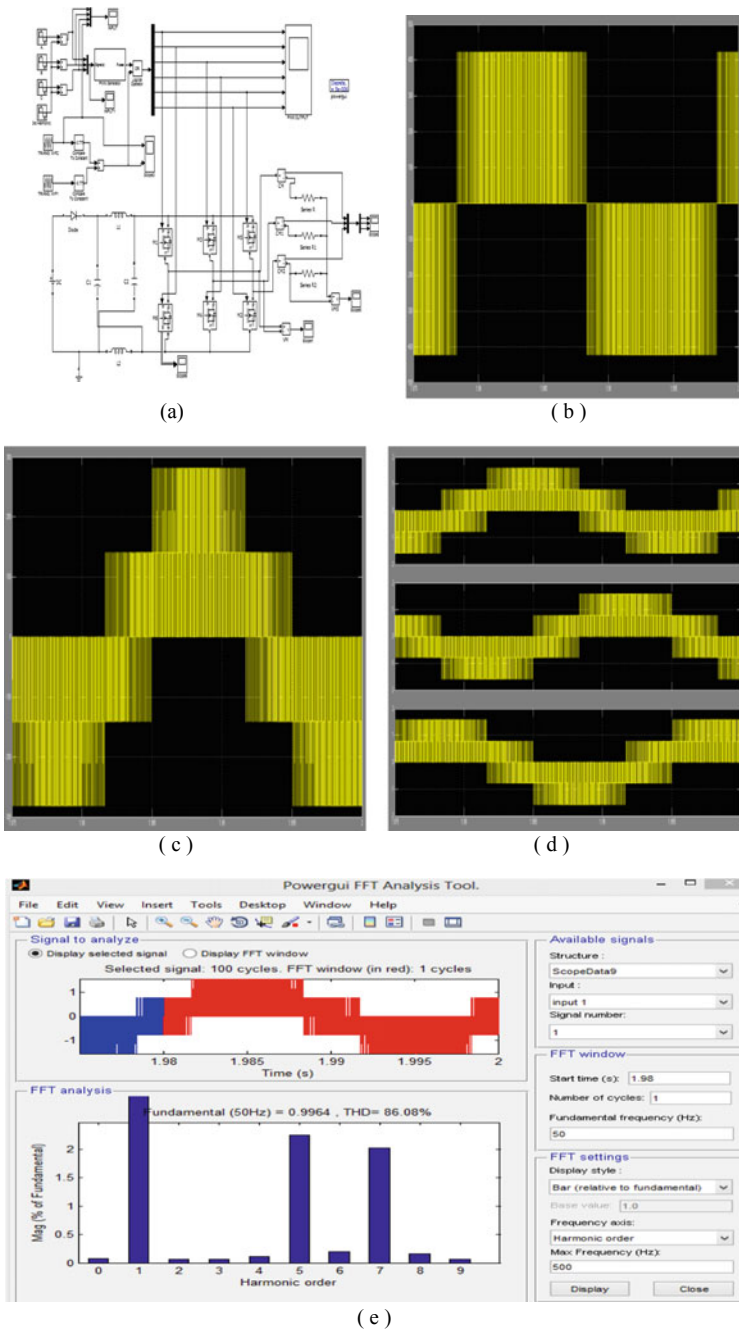


Fig. 4 a Simulation configuration of ZSI using CBC method b Waveform of CBC for line voltage c Waveform of CBC for phase voltage d Waveform of CBC for current through R load e FFT analysis of output current through R load

almost constant about 327 V. Thus the input voltage (170 V) is boosted (327 V) and applied as dc-link voltage.

The detailed analysis is given below

1. The boost factor = $B = 2.85$
2. Peak dc link voltage = $2.85 * 170 = 485 \text{ V}$
3. Peak ac output voltage = $V_{ac} = 0.7798 * 2.85 * 170 / 2 = 188.9 \text{ V}$
4. RMS ac output voltage $V_{ac} = 133.5 \text{ V}$
5. RMS line voltage = $\sqrt{3} * 133.5 = 231.3 \text{ V}$.

5 Results and Discussion

Maximum constant boost control PWM control method with third harmonic injection is more advantageous PWM control method among the other PWM control methods shown in Table 1. It increases output voltage boost while minimizing voltage stresses across switching devices. It allows over-modulation where modulation index can be varied from 0.57 to 1.154. Parameter Analysis shown in “Fig. 5”.

Results of simulation are compared with traditional PWM inverter.

Following results are observed,

1. Shoot-through state is allowed by switching on all devices in the central inverter; this shoot-through state does not allow in the traditional inverter.
2. Output voltage can be boosted to any desired value by varying shoot-through period.

Table 1 Parameter analysis for PWM control methods

Methods	ZSI using the simple boost control method	ZSI using constant boost control method with third harmonic injection
Parameters		
Input voltage	211	170
RMS phase voltage	133.4	133.5
RMS line voltage	231	231.3
Boost factor (BF)	2.58	2.85
Voltage gain(G)	1.79	2.22
Voltage stress(V_S)	545	485
Duty ratio(D_0)	0.3060	0.3246
THD for R load	97.10%	86.08%
THD for RL load	3.04%	2.17%

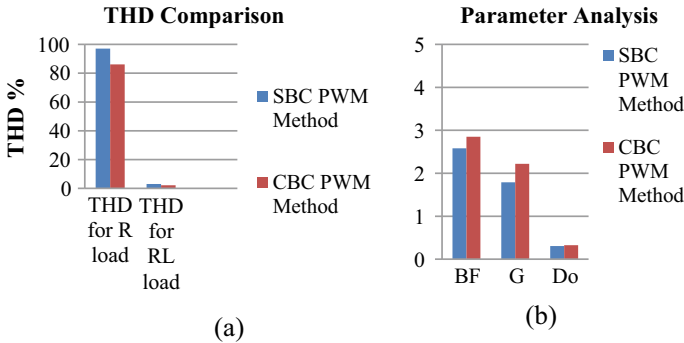


Fig. 5 a THD comparison b Parameter Analysis

6 Conclusion

The Z-source converter overcomes the limitations of the traditional VSI and CSI. The Z-source inverter system can produce an output voltage more remarkable than the dc input voltage by controlling the shoot-through duty ratio. In this work, different PWM techniques and their comparison are presented in MATLAB simulation.

References

1. Ellabban O, Mierlo J, Lataire P (2009) Comparison between different pwm control methods for different z-source inverter topologies, IEEE Conference of emerging trends in electrical and computer technology, pp 1–11
2. Ellabban O, Van Mierlo J, Lataire P (2010) Comparison between different PWM control methods for different Z-source inverter topologies. IEEE Trans Ind Appl 39:11–17
3. Huang Y, Shen M, Peng F (2006) Z-source inverter for residential photovoltaic systems. IEEE Trans Power Electron 21(6):1776–1782
4. Peng F (2003) Z-source inverter. IEEE Trans Ind Appl 39:504–510
5. Peng F, Shen M, Qian Z (2005) Maximum boost control of the z-source inverter. IEEE Trans Power Electron 20(4):3514–3522
6. Rajakaruna S, Jayawickrama Y (2007) Designing impedance network of z-source inverters, IEEE Trans Ind Appl 1217–1222
7. Rathika S, Kavitha J, Paranjothi S (2010) Embedded controlled z source inverter fed induction motor drive. IEEE Trans Ind Appl 32(2):4417–4422
8. Shen M, Wang J, Joseph A, Peng F (2006) Constant boost control of the z-source inverter to minimize current ripple and voltage stress. IEEE Trans Ind Appl 42(3):4013–4018
9. Sutar AR, Jagtap SR (2015) Performance Analysis of Z-source Inverter Fed Induction Motor Drive. Int J Sci Eng Res 03:2229–5518
10. Tao Y, Lee H, Song J, Song D, Park S (2008) Psim and Matlab simulations analysis on 3-phase Z-source inverter, IEEE Conf Devices Circuits Syst 978–983
11. Vidhyarubini N, Rohini G (2011) Z-source inverter based photovoltaic power generation system, IEEE Conf Emerg Trends Electr Comput Technol 29–34

Utilization of Waste Plastic for Bituminous Mix for Improved Performance of Roads



Avinash B. Kokare, Abhinav S. Salunkhe, and Chetan R. Limkar

Abstract Plastic use in road construction is not new. It is already in use as PVC or HDPE pipe mat crossings built by cabling together PVC (polyvinyl chloride) or HDPE (high-density poly-ethylene) pipes to form plastic mats. The plastic roads include transition mats to ease the passage of tyres up to and down from the crossing. Both options help protect wetland haul roads from rutting by distributing the load across the surface. But the use of plastic-waste has been a concern for scientists and engineers for a quite long time. Recent studies in this direction have shown some hope in terms of using plastic-waste in road construction i.e., Plastic roads. A Bangalore-based firm and a team of engineers from R. V. College of engineering, Bangalore, have developed a way of using plastic waste for road construction. An initial study was conducted in 1997 by the team to test for strength and durability. Plastic roads mainly use plastic carry-bags, disposable cups and PET bottles that are collected from garbage dumps as an important ingredient of the construction material. When mixed with hot bitumen, plastics melt to form an oily coat over the aggregate and the mixture is laid on the road surface like a normal tar road.

Keywords Waste plastic · Plastic road · Re-cycled polyethylene etc.

1 Introduction

The debate on the use and abuse of plastics in relation to environmental protection can go on, without yielding results until practical steps are initiated at the grassroots level by everyone who is in a position to do something about it [5]. The plastic wastes could be used in road construction and the field tests withstood the stress and proved that plastic wastes used after proper processing as an additive would enhance the life of the roads and also solve environmental problems [6]. The present write-up

A. B. Kokare (✉) · C. R. Limkar
SVERI's College of Engineering, Pandharpur, Maharashtra, India
e-mail: abkokare@coe.sveri.ac.in

A. S. Salunkhe
Civil Engineer & Business Partner At Raut Salunkhe Associates, Solapur, Maharashtra, India

highlights the developments in using plastics waste to make plastic roads. Plastic is everywhere in today's lifestyle. It is used for packaging, protecting, serving, and even disposing of all kinds of consumer goods [1]. Studies have linked the improper disposal of plastic to problems as distant as breast cancer, reproductive problems in humans and animals, genital abnormalities and even a decline in human sperm count and quality. If a ban is put on the use of plastics on emotional grounds, the real cost would be much higher, the inconvenience much more, the chances of damage or contamination much greater [4]. The risks to the family health and safety would increase and, above all the environmental burden would be manifold. Hence the question is not 'plastics vs no plastics' but it is more concerned with the judicious use and re-use of plastic-waste [8]. A Bangalore based company M/s K.K. Poly Flex Pvt., Ltd., supplied the proceed plastic materials and they also hoped the centre for developing some additional facility to test the bituminous mix specimens under controlled temperature [7]. Polymer blended Bitumen shows higher Softening point, lower penetration point, and better ductility [2]. Polymer coated aggregate blended with Bitumen shows higher Marshall value and better stripping value showing that the mix is more suited for road laying [3].

2 Process of Making Plastic Bitumen Road

1. Segregation
 - a. Plastic waste collected from various sources must be separated from other waste.
 - b. Maximum thickness of 60 microns.
2. Cleaning process
 - a. Plastic waste get cleaned and dried.
3. Shredding process
 - a. Plastic will be shredded or cut into small pieces.
 - b. The different types of plastic wastes are mixed together
4. Collection process
 - a. The plastic waste retaining in 2.36 mm is collected (Fig. 1).

3 Materials and Methods

- Aggregate of 20 mm, 10 mm, Stone Dust and Lime as Filler.
- 60/70 grade bitumen.
- Waste plastic in the shredded form.



Fig. 1 Process of making plastic

In Fig. 2 we have carried out some tests on modified bitumen at K K Polyflex, Bangalore as well as at our college laboratories. Also we obtained the test results from various literatures.

Table 1 shows the physical properties of waster plastic and Table 2 shows the volumetric properties of modified and conventional mix properties of bitumen. Properties of modified mixes are better than the conventional waste plastic mixes 8% by weight of bitumen.

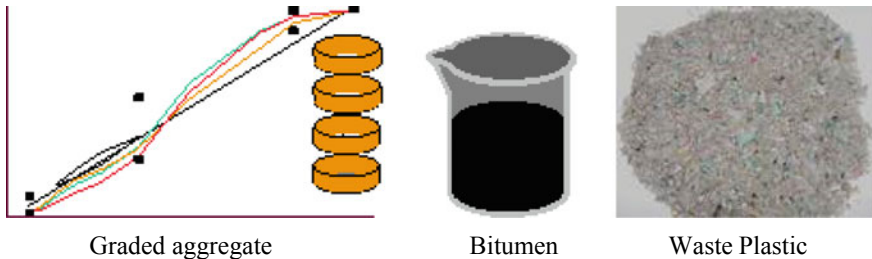


Fig. 2 Properties on re-cycled plastic

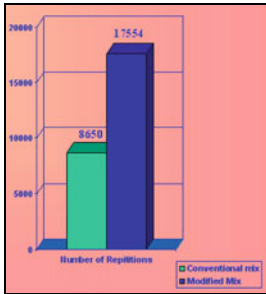
Table 1 Physical properties of waste plastic

Description	Range
Specific gravity	1.03
Melting temperature	75–138 °C
Weight loss (6%)	200–400 °C

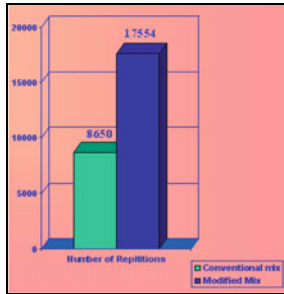
Table 2 Volumetric property of BC Mixes

Properties	Modified mix (Waste plastic) 8% by wt of bitumen	Conventional mix
Marshal stability (kg)	1700	1350
Bulk density (g/cc)	2.374	2.350
Air voids (%)	4.4	3.5

Indirect Testing Machine



Fatigue Test



Rutting Test

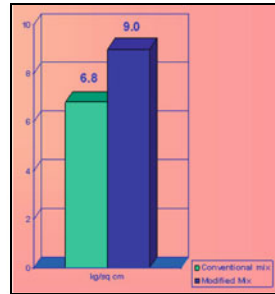


Fig. 3 Comparison of conventional mix versus modified mix

4 Result and Discussion

Performance Studies of the Plastic Mixes

Figure 3 shows the comparative result of conventional mix and modified mix indirect test, fatigue test and rutting test and modified mix results are more than the conventional mix up to 8% addition of waste plastic. Figure 4 shows the comparative result of conventional mix and modified mix for binder vs bulk density, stability, flow, air voids and VFB and modified mix results are satisfactory with the conventional mix up to 8% addition of waste plastic. Figure 5 shows the optimum use of waste plastic i.e. 8% by weight of bitumen.

5 Economics of Plastic Road Construction

a. Materials:

For 1000 M × 3.75 M (25 mm) Road: 11.250 tons (60/70 grade) bitumen needed.

Road:

Shredded Plastics Required: 10% by weight (passing 4.74 mm sieve & retaining 2.36 mm).

Bitumen replaced (saved) by 10% Plastics: 1.125 tons.

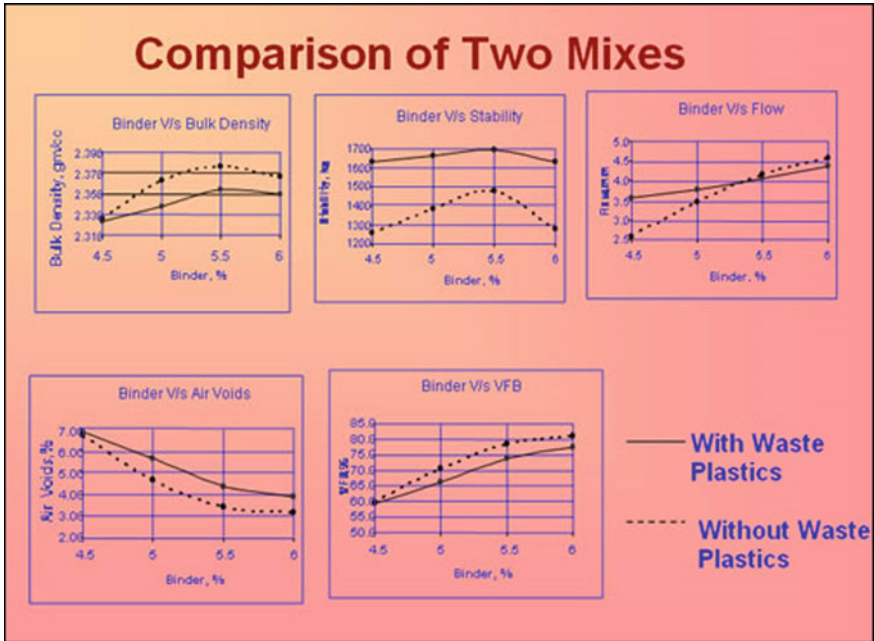


Fig. 4 Comparison of conventional mix versus modified mix

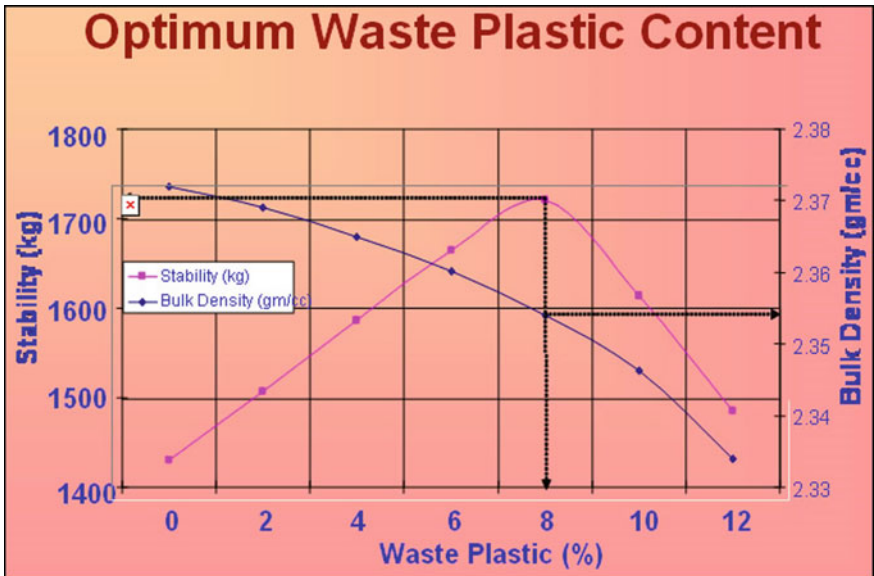


Fig. 5 Optimum use of Waste Plastic

Actual Bitumen Required:	10.125 tons.
Aggregate (11.2 mm):	70.875 Cu.M.
Aggregate (6.7 mm):	43.125 Cu.M.
Aggregate Dust:	23.625 Cu.M.

b. Cost: The total cost including material as mentioned above, labour charge etc. (At Madurai) is approx. 5.00 lakh, however, the cost may be different from place to place and have to be calculated accordingly. The cost break-up is given below:

(i) Collection of littered plastics:	Rs. 0.50 lakh.
(ii) Cost of shredder and other equipment:	Rs. 0.50 lakh.
(iii) Laying of road with material, labour etc.:	Rs. 4.00 lakh.
Total:	Rs. 5.00 lakh.

- Ultimately it saves up to Rs. 15,000/- for a road of 1000 m × 3.75 m.
- 8% by weight of plastic waste in bitumen = a saving of 0.4% of bitumen by weight in roads.

- Expected saving by use of waste plastic instead of bitumen

Area of the road as project to be covered =	100.00 km × 12 m wide.
Volume of bitumen concrete wearing =	10,000 × 12 × 0.05.
Coat –50 mm thick =	60,000 cum.
Therefore Expected need of bitumen of =	10 kg per cum × 60,000 cum.
80/100 grade =	600,000 kg.
Considering 8% use of waste plastic =	600,000 × 8/100.
Instead of bitumen =	48,000 kg.
As rate per kg of bitumen =	Rs 17/- per kg.
Rate per kg. of waste plastic =	Rs. 02/- per kg.
Saving of in cost of bitumen by using coast = 17 – 2 =	Rs. 15/- plastic in roads.

- Gross saving by using waste plastic in roads in % = $720,000 \times 100 / 600,000 \times 17 = 7.058\%$

- Net saving by costs plastic = 720,000 – installment of loan.
= 720,000 – 150,000.
= 5,70,000/-
= 5.588%.

- Rate of saving = @ 5.50% & also solving the problem of pollution say = 5.50% by waste plastic.

6 Conclusion

1. Plastics will increase the melting point of the bitumen. The use of the innovative technology not only strengthened the road construction but also increased the road life as well as will help to improve the environment and also creating a source of income.
2. Plastic roads would be a boon for India's hot and extremely humid climate, where temperatures frequently cross 50 °C and torrential rains create havoc, leaving most of the roads with big potholes.
3. It is hoped that in near future we will have strong, durable and eco-friendly roads which will relieve the earth from all type of plastic-waste.

References

1. Amjad K, Gangadhar MM, Vinay R (2011) "Effective Utilisation of Waste Plastics in Asphaltting of Roads". Project Report prepared under the guidance of R. Suresh and H. Kumar, Dept. of Chemical Engg., R.V. College of Engineering, Bangalore.
2. An article 'Riding on Plastic' by Jayanthi Narayan in Construction World magazine, April 2010.
3. Research Work at the Centre for Transportation Engineering, Bangalore University (March, 2001) and the Seminar Report on "Study of the Effect of Plastic Modifier on Bituminous Mix Properties" by V.S. Punith, II Semester, M.E. (Civil) Highway Engg., Dept. of Civil Engineering, Bangalore University.
4. Flynn L (1993) Recycled Plastic Finds Home in Asphalt Binder. Journal, Roads and Bridges
5. Justo CEG, Honorary Professor, Bangalore University Bangalore and Dr. A. Veeraragavan Co-ordinator (2013) A paper on 'Plastic Road.' Centre for Transportation Engineering, Bangalore
6. Schroeder RL (2015) "The Use of Recycled Materials in Highway Construction", Journal, Public Roads, Vol. 58, No. 2
7. Vasudevan R, Nigam SK, Velkennedy R, Undara Kannan RCSB, Department of Chemistry, Department of Civil Engineering, Thiagarajar College of Engineering, Madurai, Central Pollution control Board, New Delhi respectively (2009) 'Utilization of Waste Polymers for Flexible Pavement and Easy Disposal of Waste Polymers' In Proceedings of the International Conference on Sustainable Solid Waste Management, Chennai, India. pp 105–111
8. Zoorob SE, Suparma LB (2000) Laboratory design and investigation of proportion of bituminous composite containing waste recycled plastics aggregate replacement (Plastiphalt). CIB Symposiumon Construction and Environment Theory into Practice, Sao Paulo, Brazil

Automatic Gas Fire Detection System Using IoT



Rupali Ramesh Shinde, Somnath B. Thigale,
and Bhuvaneshwari C. Melinamath

Abstract Nowadays, human life becomes very automatic and busy. Due to the work stress, people can't remember many things like switch off the nob of the cylinder, switch off the lights, fan, AC. Fire and gas accidents are very dangerous issues and may occur in homes, industrial areas, crowded areas like temple places, and hotel kitchens. Accidents involving gas cylinders can cause severe injury or even death and loss of property. To avoid all these consequences, we have to alert and have proper provision for detecting gas leakage and fire situations. One of the preventive measures to avoid these type of consequences is to install the automatic Gas fire detection kit at such places. The purpose of the research is to avoid fire and gas accidents through some automated actions. We are using various sensors for detecting gas leakage and fire. If the gas sensor detects the Gas then automatically it shuts off the gas supply, thereby stopping the further leakage. It also starts exhaust fan to suck out all the Gas. If the fire is detected by the fire sensor, then it shuts off the gas supply.

Keywords Fire sensor · DC motor · Exhaust fan · Gas sensor

1 Introduction

To control fire and gas accidents, we are developing a safe and secure automatic system without any cause of human Gas, and fire accidents are becoming a major problem in society. There may be chances of accidents and blasting and explosion of Gas. The aim of our system is to avoid fire and gas accidents. In our system, we use the fire and gas sensors for detecting the fire and Gas. When the Gas is detected, it shuts off the gas supply using DC motor, and it starts the exhaust fan to suck off the Gas from the room. It is not only for the Gas it is also used for the fire accidents when the fire sensor detects the fire, it shuts off the gas supply to avoid the explosion of Gas and starts the exhaust fan to suck out all the smoke.

R. R. Shinde (✉) · S. B. Thigale · B. C. Melinamath
Department of Computer Science and Engineering, SVERI's College of Engineering, Punyashlok
Ahilyadevi Holkar Solapur University, Solapur, Maharashtra, India
e-mail: rshinde@coe.sveri.ac.in

Today, automation is the trend of industries, and Internet application development is very important. So IoT is a significant domain by which we can develop various useful internet applications. Basically, IoT is a network in which all physical objects are connected to the internet through network devices or routers and exchange data. IoT allows objects to communicate with each other, controlled remotely across the existing network infrastructure. IoT is a very good and intelligent methodology which reduces human effort as well as easy access to physical devices.

In the upcoming years, IoT-based technology will offer advanced levels of services and practically change the way people lead their daily lives. In a span of coming ten years, IoT devices will grow from 75 billion to more than 100 billion, and the improvement from 4 to 5G in terms to grow IOT is most important. Today's 4G network can support up to 5500 to 6000 NB-IOT devices on a single cell. Advancements in medicine, power, gene therapies, agriculture, smart cities, and smart homes are just a very few of the categorical examples where IoT is strongly established.

2 Literature Survey

- (1) K. Padmapriya et al. [1] Proposed the design of wireless LPG monitoring system for home safety. This system detects the gas leakage and alerts the user through SMS, and the power supply is turned off. It automatically monitors the level of the Gas. So if the Gas is around 2 kgs, it automatically books the cylinder using a GSM module. This project is implemented using ARM 7 processor and simulated using Keil software.
- (2) Prof. Pankaj C. Wardle et al. [2] LPG Detection, Metering and Control System Using Microcontroller proposed a system which contains a buzzer will alarm the user when the gas unit comes to the edge of the end. The user can see the unit (kg) of Gas remained for use on the LCD display. When the Gas is detected, it starts a buzzer and sends a notification to a user.
- (3) V. Ramya et al. [3] Proposed the design of microcontroller-based toxic gas detecting and alerting system. The hazardous gases like LPG and propane were sensed and displayed in the LCD display each and every second. Whenever the LPG leakage is detected, an alarm is generated immediately and also sends an alert message to the authorized person through the GSM.
- (4) Aastha Singh et al. [4] Proposed the design of Detection of Liquefied petroleum gas using sensor through Arduino Uno microcontroller. In this system MQ-2 sensor is used to detect the Gas. Whenever the Gas is detected the installation generates a sound alert using a buzzer and with the help of the GSM module, it is capable of broadcasting messages to the stakeholders about the LPG leak.
- (5) Pooja Bhamare et al. [5] Proposed the design of GASBO for LPG Gas Detection and Controlling Using Mobile App. Whenever the gas leakage is detected, it sends an alert message to the owner for safety using an android app and Buzzer blows on Gas detection. For closing the valve, automatic action is taken.

3 Existing System

There are some existing methods for Gas and fire accident avoiding. It sends the only SMS to the user and fire officer. If they are near to the place, then they can stop the accident. Otherwise, they can't do anything even if they know about the incident. So, here only monitoring is possible and no automatic control.

The second existed method raise the only alarm whenever Gas is detected at any place. Due to this alarm, people create faired situation start to run haphazardly. As a result worker in the factory gets injured severely. Sometimes people do not realize the intensity of the fire, and they can't escape from the fire affected building quickly.

Drawbacks in the existing system:

- (a) The intimation is possible.
- (b) Automation is not possible.
- (c) Can't detect the intensity of the fire.

4 Proposed System

Here we are developing a system called gas fire detection system that smartly avoids fire as well as gas accidents by detecting fire and gas leakages and taking corrective action to avoid any accidents from happening. The system consists of gas fire sensors for detection purpose. If the system detects a gas leakage, the system first shuts off the gas supply and starts an exhaust fan. The system also has a fire sensor to detect fires.

Advantages in the proposed system

- (a) Automation is available.
- (b) Monitoring and as well as controlling also possible.
- (c) No need for Human Interaction.
- (d) Less maintenance.
- (e) No Possibility of Manual Errors.
- (f) Simple & Economical.

5 Methodology for the Proposed System

Gas sensor and fire sensor are connected to the IoT based automation system. It detects the harm and perform some automatic actions like shuts off gas supply by using DC motor, starts an exhaust fan on. To make the entire system works, the user needs to supply the power to the system (Fig. 1).

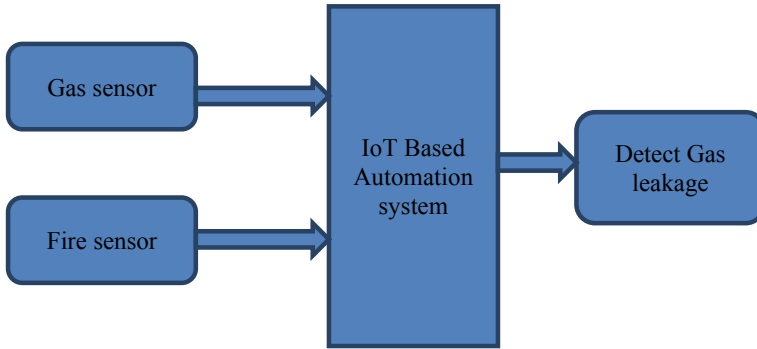


Fig. 1 The basic flow of the system

6 MODULES

The different modules used in our project are:

- a. Gas and Fire Detecting Module
- b. Analysis Module
- c. Action Module.

a. **Gas and Fire Detecting Module**

Gas Sensor: The gas sensor is a sensor which detects the presence of gases in an area, often as part of a safety system. When the gases is detected, the sensor will give value as one, and if no particular gas is detected, it returns zero. Refer Fig. 2 for sample Gas Sensor.

Fig. 2 Gas sensor

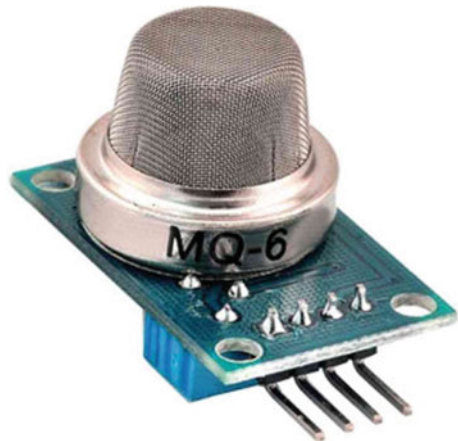


Fig. 3 Fire sensor



Fire Sensor: A fire detector is a sensor designed to detect and respond to the presence of a flame or fire, thus preventing the fire from spreading further and avoiding any chances of explosions. Refer Fig. 3 for sample fire Sensor.

b. **Analysis Module**

IoT Based Automation system is less Integrated circuits. This development kit that plays a vital role in designing a proper IoT product. The module is mainly based on ESP8266, that is a low-cost Wi-Fi microchip. The ESP8266 Node MCU is a complex device, which combines some features of the ordinary Arduino board with the possibility of connecting to the internet.

c. **Action module**

Exhaust fan: Whenever the Gas is detected, the system starts an exhaust fan to suck out all the leaked Gas from the room.

DC motor: If the system detects the gas leakage, the system first shuts off the gas supply using a DC motor without any human interaction to avoid more gas leakage.

7 Flow chart

A proposed system flow chart can be represented, as shown in Fig. 4.

8 Working Model and Procedure

In the proposed system, fire and Gas sensors are connected to the IoT based automatic system. Those sensors sense and send the result to the IoT based automatic system. IoT based automatic system analyses the results and detect whether there is any harm

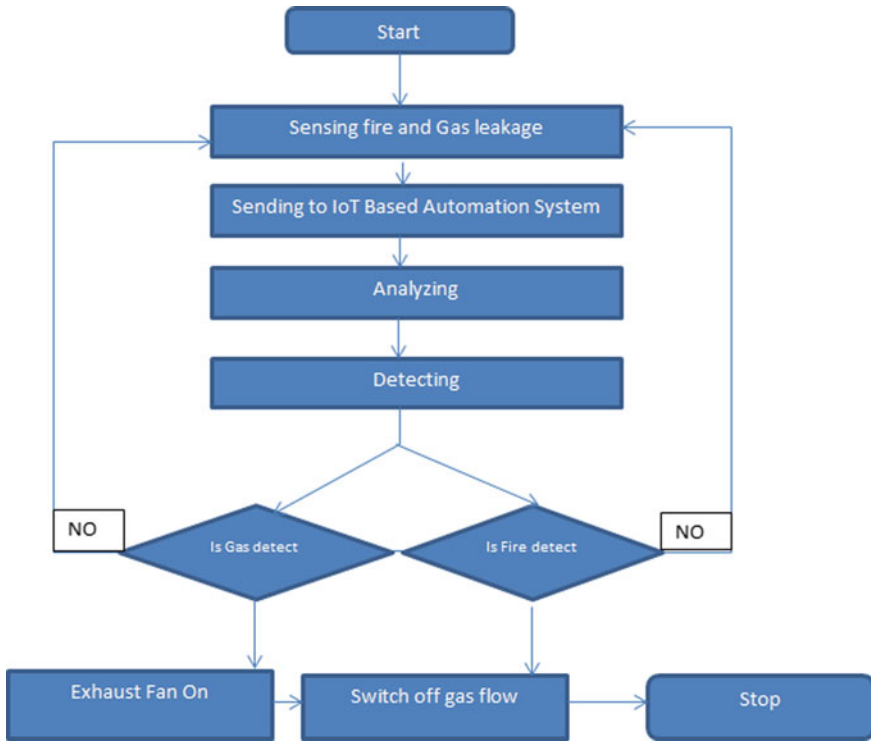


Fig. 4 Flowchart

are not. If harm is detected, then it checks whether it is gas leakage or fire. If gas leakage is detected, it shuts off the gas supply using DC Motor, starts an exhaust fan. If a fire is detected, then it shuts off the gas supply.

9 Conclusion and Future Scope

In the previous system, there is a human interference so the possibility of manual errors. But the current system is fully automated with no possibility of manual errors. It provides safety and security. In the future plan we have to send SMS to the user by using the App. Or we want to develop a system which sends the messages directly to the user mobile without using any app. However, notifications sent to the user are just for intimating the user about the incident, but the users need not perform any actions. So it is not much considerable. This project definitely helps the people to protect their lives, home and hotel kitchens from gas leakages.

References

1. Priya KP, Surekha M, Preethi R (2014) Smart gas cylinder using embedded system, published in 2014
2. Ramya V, Palaniappan B (2012) Embedded system for Hazardous Gas detection and Alerting, published in 2012
3. Wardle PC, Upadhyay S, Shelke SS, Khandade SK (2016) LPG detection, metering and control system using microcontroller, published in 2016
4. Singh A, Verma M, Sahu L (2017) Detection of liquefied petroleum gas using sensor through arduino uno microcontroller, published in 2017
5. Bhamare P, Dalvi S, Bhamare M, Bhonsle M (2017) GASBO for LPG Gas and Controlling Using Mobile App, published in 2017

Assessment of Groundwater Quality from Warana River Basin, Kolhapur District, Maharashtra, India



S. V. Pathare, D. B. Panaskar, V. M. Wagh, and R. S. Pawar

Abstract The present study was carried out in Warana River basin for the assessment of groundwater geochemistry. The study mainly focused on impact of intensive agricultural practices on groundwater regime of the study area. Methodology was adapted to know the local environmental components influencing the groundwater quality. Groundwater samples were collected from dug/bore wells during pre-monsoon and post-monsoon season and analyzed for physicochemical characteristics. The suitability of groundwater quality by collecting 65 representative samples from bore wells and dug wells covering in the rural areas of the Warana River Basin, Kolhapur District. Warana River Basin is situated in the northern side of the Kolhapur District. The groundwater from the study area have been classified for domestic and irrigation purpose on the basis of Sodium Absorption Ratio (SAR), Kelly's Ratio (KR), Soluble Sodium Percentage (SSP), Residual Sodium Carbonate (RSC), Percent Sodium (% Na), Magnesium Hazard (MH), Magnesium Ratio (MR) and Permeability Index (PI). The values of majority of groundwater samples for SAR, KR, SSP, RSC, % Na, MH, MR and PI are within permissible limit indicating excellent quality for irrigation purpose.

Keywords Groundwater quality · Domestic purposes · Irrigation purposes · Permissible limit etc.

S. V. Pathare

Department of Geology, Rajaram College, Kolhapur, Maharashtra, India

D. B. Panaskar · V. M. Wagh

School of Earth Sciences, SRTM University, Nanded, Maharashtra, India

R. S. Pawar (✉)

SVERIs College of Engineering Pandharpur, Solapur, Maharashtra, India

e-mail: rspawar@coe.sveri.ac.in

1 Introduction

India covers 2.4% of total geographical area of the world and has population of about 1.30 billion, the second largest populous nation. India supports 20% livestock population of the world. India receives annual precipitation of approximately 4000 km³ including snowfall. Monsoon accounts for 3000 km³ of precipitation. Rainfall in India mainly occurs due to South-West and North-East monsoon winds. India is blessed with 20 major rivers and their tributaries. Some of the major rivers like Ganga, Brahmaputra and Indus originating from Himalayas are perennial. On the other hand, most of the peninsular rivers are seasonal. In India more than 50% water resources are located in river tributary systems. The water potential in Himalayan rivers is double than peninsular rivers [1]. National Commission for Integrated Water Resources Department has estimated that the basin wise average annual flow is 1953 km³ and utilizable flow is 690 km³. Conversely the annual groundwater recharge is 432 km³ in India. Total water storage capacity in major and minor dams is ca 225 km³. In addition, the ongoing projects are estimated to contribute 171 km³. Thus, ca. 396 km³ of water storage will be available in future. Apart from freshwater resources of the country, groundwater is an important source for human needs. Groundwater meets 80% domestic need and 45% irrigation requirement in the country. In India net groundwater availability is 399 bcm. The annual groundwater draft is 231 bcm. Of this 213 bcm is used for irrigation and 18 bcm is utilized for domestic and industrial purposes. According to international norms, if per capita water availability is less than 1700 m³/yr then the country is categorized as water stressed. If per capita water availability is less than 1000 m³/yr than the country is classified as water scarce country [2]. Present study was conducted with a focus on assessment of groundwater quality from Warana river basin, covering two districts viz. Kolhapur and Sangli from Maharashtra. For the present study, 65 groundwater samples were collected from places so as to cover the whole section of the Warana River basin during the post-monsoon season in 2012. The focus of study was assessment of groundwater quality. The study also aims to find out the influence of geological processes on the groundwater quality of the study area. Such an approach is expected to help in developing management plans for improving groundwater quality in affected areas of Warana river basin.

1.1 Study Area

For the present study, Warana River Basin has been selected. The Warana River flows through three districts of Maharashtra viz. Satara, Kolhapur and Sangli. The study area is located between 16°47' to 17°15' N latitude and 73°30' to 74°30' E longitude as shown in Fig. 1. Drainage of Warana is relatively narrow but is a well developed basin from north-west to south-east (Fig. 1). Total length of the river system is approximately 170 kms. There are around 86 villages on the banks of the

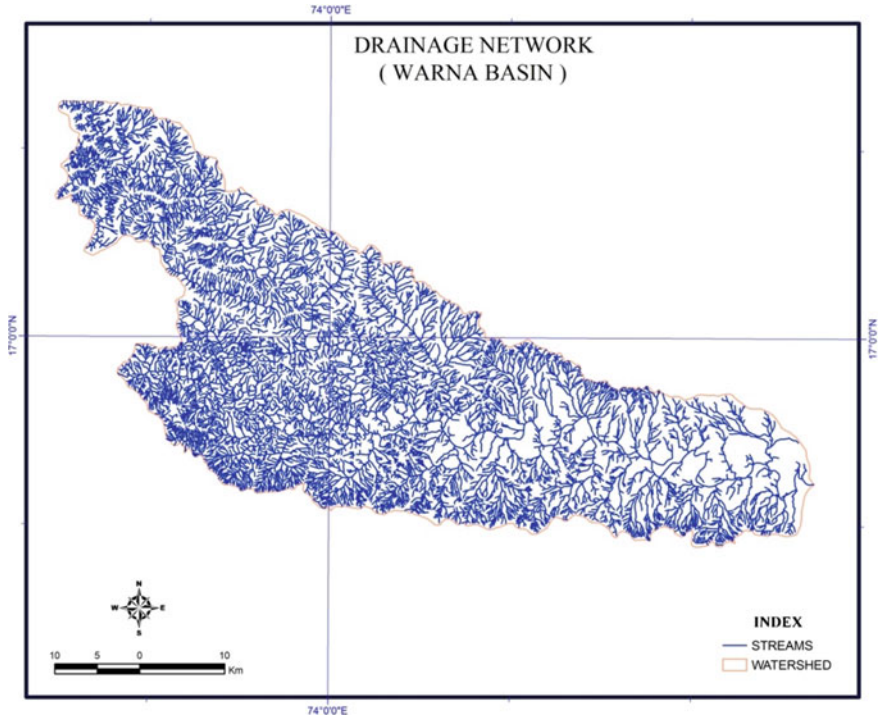


Fig. 1 Location map of study area

river and its tributaries. The river originates about 2 kms to the west of Patherpunj village at an altitude of 914 MSL in Patan tehsil of Satara district. After flowing most of its course along the boundary of Kolhapur and Sangli districts for over 149 kms, Warana meets river Krishna near Haripur village in Sangli district. Kolhapur district is located between 15°40', 17°15' north latitudes and 73°30', 74°45' east longitudes. It is divided into 12 tehsils viz. Karvir, Panhala, Shahuwadi, Kagal, Hatkanangale, Shirol, Gadhinglaj, Chandgad, Ajara, Bhudargad, Radhanagari and Gaganbavada. The district has total area of 7620 sq.km. The Warana River flows through Shahuwadi, Hatkanangle and Shirol tehsils. Sangli district is located between north latitudes 16°43', 17°38' and east longitudes 73°41', 75°41'. The district is divided into 10 tehsils viz. Shirala, Walwa, Palus, Khanapur, Atpadi, Jat, Kadegaon, Miraj and Kavathemahankal. The district occupies a total area about 8572 sq.kms. Warana River flows through Shirala tehsil before joining the Krishna River at Haripur near Sangli. The terrain is made up of basalt and its weathering product-laterite. Lithology has also been found to be responsible for quality of groundwater [3].

2 Review of Literature

In case of Warana River basin, related groundwater study is very restricted. GSDA and CGWB have investigated only few samples from representative villages. CGWB carried out studies of groundwater for parameters viz. TH, NO_3 and F in Kolhapur and Sangli districts. According to them concentrations of most of the parameters are within desirable limits except nitrates exceeding in few samples. The parameter EC was studied to determine the dissolved salts and their concentrations. 57% samples were found to be medium saline and 30% samples low saline in Kolhapur district. In Sangli district, 62% samples fall under high salinity, while 7% fall in very high salinity category. Review of literature provided information concerning previous groundwater studies, present status of research and current development in the context of groundwater quality. These studies give a direction and helped to recognize the gaps in the work done as well as outlined a standard methodology for fulfilling the objectives specified. In this perspective, a few studies related to the proposed work are reviewed in this chapter. Review of literature includes information on groundwater depletion and quality aspects, health related issues, soil quality, groundwater suitability for different purposes, water quality index, etc.

Panaskar, et al. [4] studied the hydrochemical characteristics of groundwater in Nanded tehsil, Maharashtra, for its suitability for different purposes. The analytical results compared with the WHO and BIS concluded that TH, TDS, Ca, Mg, Na, Cl parameters exceed the safe limit. In the study area the groundwater is alkaline and moderately hard to very hard in nature. The cation and anion dominance are $\text{Na} > \text{Ca} > \text{Mg} > \text{K}$ and $\text{HCO}_3 > \text{Cl} > \text{CO}_3 > \text{SO}_4$ respectively. The groundwater suitability for irrigation was evaluated from SAR, EC, TDS, RSC and percent Na which revealed that majority of the samples confirm their fitness; however, MAR and KR ratio showed that 36% groundwater samples were unsuitable for irrigation.

3 Material and Methods

The study area was divided into grids for facilitating collection of representative groundwater samples. A total of 65 representative groundwater samples were collected from different dug/bore wells during post-monsoon season for the period of 2011. After systematic collection of groundwater samples brought to analytical laboratory and stored at 4 °C temperature to avoid any contamination. Major ions like calcium (Ca), magnesium (Mg), carbonate (CO_3), bicarbonate (HCO_3) and chloride (Cl) were analyzed in the laboratory by gravimetric analysis following the standard methods of American Public Health Association [5, 6]. The sodium (Na) and potassium (K) ions was determined using flame photometer (ELICO CL 361). The sulphate (SO_4), phosphate (PO_4) and nitrate (NO_3) were determined by using spectrophotometer (Shimadzu UV-1800). Fluoride (F) was determined by SPNADS method.

The ions were converted from milligram per liter (mg/L) to mill equivalents per liter (meq/L).

4 Data and Results

The quality of groundwater is very important because it decides it's suitable for domestic, industrial and agricultural purpose. Physicochemical parameters of groundwater samples from Warana River Basin were determined and assessed in order to understand the variations in different parameters and their interrelationship of various locations. Data obtained during the course of both field and laboratory analyses of groundwater samples during the post monsoon season 2012 have been given in the Table 1. The minimum, maximum, average and standard deviation of the parameters, with locations and with WHO standards [7] have been discussed here [8].

4.1 Hydrogen Ion Concentration (pH)

pH of groundwater varies from 6.57 to 7.96 in the post monsoon season 2012. The minimum pH has been recorded from sample no. 13, while maximum pH has been recorded from sample no.37. The average pH standard deviation of the groundwater is 7.03 and 0.28 respectively.

Table 1 Physicochemical parameters of groundwater samples

Sr. No	Parameter	Unit	Min	Max	Avg	StDev
1	pH	—	6.57	7.96	7.03	0.28
2	EC	μS/cm	362	3420	1094.8	617.9
3	TDS	mg/L	231.68	2188.8	700.7	395.48
4	TH		100	1400	341.8	227.5
5	Ca		27.25	366.52	87.15	58.48
6	Mg		2.92	144.79	32.72	22.96
7	Na		3.48	57.49	16.57	9.96
8	K		0.2	75.54	5.61	12.30
9	Cl		117.04	688.7	115.1	99.57
10	TA		40	500	205.2	102.4
11	SO ₄		48.7	227.17	79.75	33.24
12	NO ₃		0	73.98	10.64	18.56
13	PO ₄		0	2	0.14	0.29

4.2 *Electrical Conductivity (EC)*

Electrical conductivity of groundwater samples varies from 362 to 3420 uS/cm for post monsoon season 2012. The minimum EC has been recorded from sample no. 13, while maximum EC has been recorded from sample no.45. The average EC and standard deviation value of the groundwater is 1094.8 uS/cm and 617.9 respectively.

4.3 *Total Dissolved Solids (TDS)*

TDS of groundwater samples measured during post monsoon season of 2012 ranges from 231.68 to 218.8 mg/l. The minimum TDS was recorded from sample no. 13, while maximum TDS was recorded from sample no.45. The average TDS and standard deviation value of the groundwater is 700.7 mg/l and 395.48 respectively.

4.4 *Total Hardness (TH)*

Hardness of groundwater samples in the post monsoon 2012 varies from 100 to 1400 mg/l. The minimum TH was recorded from sample no. 13, while maximum TH was recorded from sample no.45. The average Hardness and standard deviation value of the groundwater is 341.8 mg/l and 227.5 respectively.

4.5 *Calcium (Ca)*

Calcium of groundwater samples varies from 27.25 to 366.52 mg/l in the post monsoon season 2012. The minimum Ca has been recorded from sample no.5, while maximum Ca has been recorded from sample no.45. The average Calcium and Standard deviation value of the groundwater is 87.150 mg/l and 58.48 respectively.

4.6 *Magnesium (Mg)*

Magnesium of groundwater samples in the post monsoon season of 2012 ranges from 2.92 to 144.79 mg/l. The minimum Mg was recorded from sample no. 7, while maximum Mg was recorded from sample no.45 the average magnesium and standard deviation value of the groundwater is 32.72 mg/l and 22.96 respectively.

4.7 Sodium (Na)

Sodium of groundwater samples in the post monsoon season of 2012 ranges from 3.48 to 57.49 mg/l. The minimum Na was recorded from sample no. 8, while maximum Na was recorded from sample no.42. The average sodium and standard deviation value of the groundwater is 16.57 mg/l and 9.96 respectively.

4.8 Potassium (K)

Potassium of groundwater samples in the post monsoon season of 2012 ranges from 0.2 to 75.54 mg/l. The minimum K was recorded from sample No.50, while maximum K was recorded from sample no.65. The average potassium and standard deviation value of the groundwater is 5.61 mg/l and 12.30 respectively.

4.9 Chloride (Cl)

Chloride of groundwater samples in the pre monsoon season of 2012 varies from 17.04 to 688.7 mg/l. The Minimum chloride was recorded from Sample No. 17 while maximum chloride was recorded from Sample No. 45. The average chloride and Standard Deviation value of the groundwater is 115.1 mg/l and 99.57 respectively.

4.10 Alkalinity (TA)

Alkalinity of groundwater samples in the post monsoon season of 2012 varies from 40 to 500 mg/l. The minimum alkalinity was recorded from Sample No. 5, while maximum alkalinity was recorded from Sample No. 42. The average total alkalinity and Standard Deviation value of the groundwater is 205.2 mg/l and 102.4 respectively.

4.11 Sulphate (SO₄)

In post monsoon season of 2012, Sulphate content of groundwater samples varies from 48.7 to 227.17 mg/l. The minimum SO₄ has been recorded from Sample No. 4, 54 and 65, while maximum SO₄ has been recorded from Sample No. 42. The average sulphate and Standard Deviation value of the groundwater is 79.75 mg/l and 33.24 respectively.

4.12 Nitrate (NO_3)

In post monsoon season of 2012, Nitrate of groundwater samples varies from 0 to 73.98 mg/l. The minimum NO_3 has been recorded from sample No. 39, 43, 47 and 53, while maximum NO_3 has been recorded from Sample No. 21. The average Nitrate and Standard Deviation value of the groundwater is 10.64 mg/l and 18.56 respectively.

4.13 Phosphate (PO_4)

In post monsoon season of 2012, Phosphate of groundwater samples varies from 0 to 2 mg/l. The minimum PO_4 has been recorded from Sample No. 6, 25, 30, 31 and 32, while maximum PO_4 has been recorded from Sample No. 10. The average phosphate and Standard Deviation value of the groundwater is 0.14 mg/l and 0.29 respectively.

4.14 Irrigation Water Quality Ratios.

The characteristic ratios of the groundwater in the Warana River Basin are shown in Table 2. These ratios like Sodium Absorption Ratio (SAR), Kelly's Ratio (KR), Soluble Sodium Percentage (SSP), Residual Sodium Carbonate (RSC), Percent Sodium (%Na), Permeability Index (PI), Magnesium Hazard (MH) and Mg/Ca ratio evaluate the groundwater quality for the irrigation purposes.

From Fig. 2a, b and c shows that the SAR, KR, SSP, RSC, %Na, MH and Mg/Ca Ratio values for groundwater of the study area are less than 10, 01, 50, 1.25, 60%, 50 and 01 respectively, therefore indicates excellent quality for irrigation purpose. Based on the Doneen [9] chart, PI content of all the groundwater samples in the study area are unsuitable for irrigation purpose [10].

Table 2 Irrigation quality ratios of Warana river basin of post monsoon season 2012

S. N	SAR	KR	SSP	RSC	%Na	PI	MH	Mg/Ca ratio
Min	0.07	0.37	1.45	-23.96	1.58	11.19	8.87	0.10
Max	1.22	0.99	38.68	-0.69	39.48	68.32	49.41	0.98
Avg	0.42	0.88	10.96	-3.68	12.63	37.30	37.63	0.63
StDev	0.26	0.14	7.82	3.62	9.07	11.70	8.49	0.20

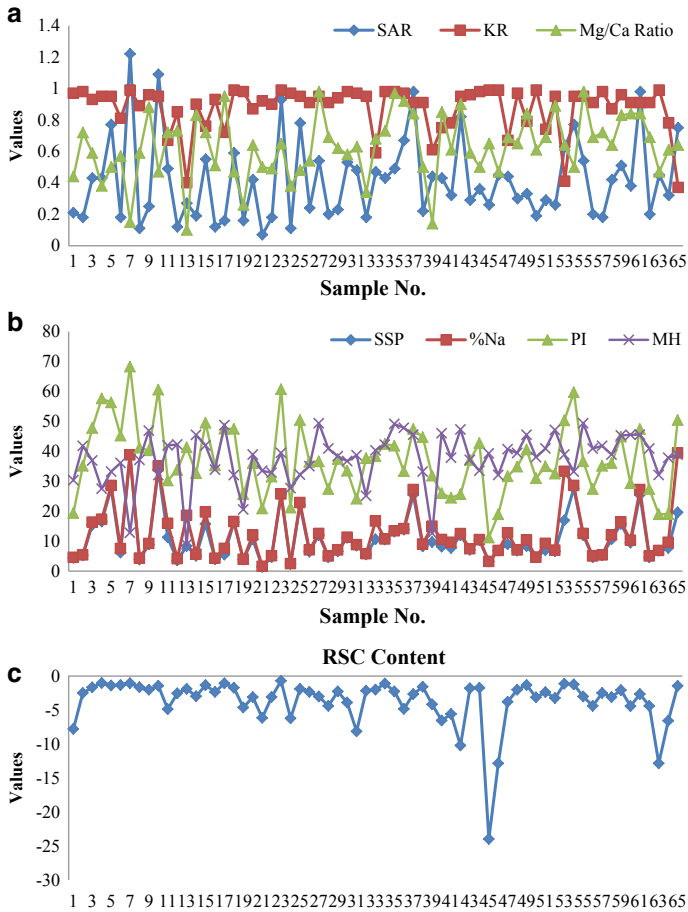


Fig. 2 a Graphical representation of irrigation quality ratios of study area b Graphical representation of irrigation quality ratios of study area c Graphical representation of irrigation quality ratios of study area

5 Conclusion

The pH content of groundwater samples is alkaline in nature. Majority of groundwater sample EC, TDS, TH, Cl and NO₃ content is higher than the permissible limit. The SAR, KR, SSP, RSC, %Na, MH and Mg/Ca Ratio values for groundwater of the study area are less than 10, 01, 50, 1.25, 60%, 50 and 01 respectively, therefore indicates excellent quality for irrigation purpose except PI.

References

1. Lal M (2001) Climate change-implications for India's water resources. *J Indian Water Resour Soc* 21:101–119
2. CWC (Central Water Commission) (2010) Water and related statistics. Water Planning and Project Wing, Ministry of Water Resources, Government of India, New Delhi, p 2010
3. Pawar RS, Panaskar DB (2014) Characterisation of groundwater in relation to domestic and agricultural purposes, Solapur Industrial Belt, Maharashtra, India. *J Environ Res Dev (JERAD)* 9(01):102–112
4. Panaskar DB, Wagh VM, Muley AA, Mukate SV, Pawar RS, Aamalawar ML (2016) Evaluating groundwater suitability for the domestic, irrigation, and industrial purposes in Nanded Tehsil, Maharashtra, India, using GIS and statistics. *Arab J Geosci* 9(13):615
5. APHA, (1985). Standard methods for the estimation of water and wastewater, Washington DC, pp 6–187
6. Trivedi RK, Goel PK (1986) Chemical and biological methods for water pollution studies. Environmental publication, Karad
7. World Health Organization (WHO) (2002). Guideline for Drinking Water Quality, 2nd ed, Health Criteria and other supporting information (pp 940–949) Geneva: World Health Organization
8. Panaskar DB, Wagh VM, Pawar RS (2014) Assessment of groundwater quality for suitability of domestic and irrigation from Nanded Tehsil, Maharashtra, India. *SRTMUS J Sci* 3(2):71–83
9. Doneen LD (1964) Notes on water quality in agriculture, Published as a water science and Engineering, paper 4001. University of California, Davis
10. Raghunath HM (1987) Groundwater. Wiley Eastern, New Delhi

Study and Ergonomic Analysis of Automobile Engine Maintenance Workstation and Suggesting Improvements



Sagar Sul, Sameer Katekar, Ajinkya Gaikwad, Gururaj Inamdar, and Samadhan Mali

Abstract To retain a system in normal state during the life cycle, Maintenance is essential. This is basically of two types one is corrective and second is preventive maintenance; both the methods of maintenance consist of different maintenance activities which are performed by a worker to bring a system at its working state. Ergonomics shows a substantial role in worker's efficiency, and to enhance efficiency is a vital aspect of every industry, by considering the ergonomic growth of the country, optimum utilization of resource with minimum possible time are the backbone of productivity. As India is a developing country and common problem found in Indian related to workers is Musculoskeletal disorders (MSDs) in industries specifically in small scale industries or workstations, i.e. the experience of the worker to MSDs risk is high. The workers complete maximum work manually as an effect of manual workload can cause MSDs of the workers. Absence of ergonomic characteristics of the workstation design is the basic reason for the (MSDs) problem. The use of systematic ergonomic principles in maintenance operations and maintenance workstation helps to reduce worker fatigue, injury during working time monotonous of work etc. The research extends to the study of existing maintenance workstation analysis for ergonomics and suggested improvements in the workstation, based on the results obtained by RULA analysis using CATIA software. The result shows that there is a need for modification in the maintenance workstation as the score is 7, for the chosen posture of a case study.

Keywords Ergonomics · Musculoskeletal disorders · RULA analysis · Maintenance · Efficiency

1 Introduction

The maintenance work plays an vital role in any segment of Engineering, as a role of activity is to recover a system in operational state when system fails due to some reasons, and a human interface in this activity is one of the unavoidable situations,

S. Sul (✉) · S. Katekar · A. Gaikwad · G. Inamdar · S. Mali
SKN Sinhgad College of Engineering, Korti, Panntharpur, Maharashtra, India

Mainly in production industries, Assembly industries, human interface is mores in maintenance activity which requires the technical skill with the ability of works to reach maintenance point and work at its position, sometimes the defective part may be taken to workplace too for repairing [5]. Which cause the unwanted movement, or posture of workers, as a result, the worker may suffer from MSDs, from literature it is found that for assembly of parts, production, etc., the ergonomic considerations have been made, still, research is scarce at the place of maintenance workstation of different sectors from ergonomic point of view [9]. Here the automobile maintenance workstation (MSRTC Bus Maintenance workshop) is chosen for the study as the activity is run by a government society, and we found that the workers are doing maximum work manually and there is no provision of proper maintenance workstation to perform the task related to maintenance activity and analysis of the workstation through ergonomic principles. The maintenance workstation has various sections station form staff car repair to paint repaired Bus, among the all stations the gear box maintenance workstation is chosen for the study as the activity is consist more critical and bent postures [2–4, 10].

2 Methodology

The work is having four fragments. The first is a study of various maintenance activities are occurring in the workshop, second taking photos of the working conditions, the third study the existing maintenance workstation modeled with various postures of the operator taken during maintenance of the system with CATIA software. Present maintenance workstation Ergonomic analysis of the possible postures attained by maintenance person throughout the activity of maintenance is the last fourth one and addressed suggestions for enhancement (Fig. 1).

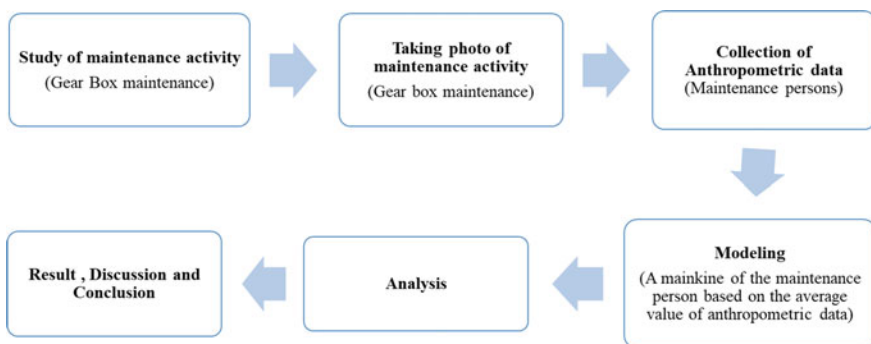


Fig. 1 Methodology

Table 1 Demographic details for 5 subjects who participated in the study

Person No	Age (Years)	Height (cm)	Weight (Kg)
1	25	165.5	58.9
2	30	150.8	57
3	35	181.7	63
4	40	163.3	72
5	45	157.5	76
Mean		163.76	65.38

Table 2 Anthropometric parameters of male maintenance person obtained from anthropometric data analysis Sheet of above (Table 1) five workers for sitting posture

Sr. No	Description	CATIA index	Values (cm)	
			Mean Value	SD
1	Stature	us100	163.76	6.3
2	Sitting height	us94	91.39	3.56
3	Eye height	us50	79.2	3.42
4	Foot breadth	us51	10	0.53
5	Hip breadth, sitting	us67	36.68	5.14
6	Shoulder elbow length	us92	36.9	1.79

2.1 Anthropometric Data

The anthropometric data of the maintenance person is taken using measuring devices with error of $\pm 2\%$ shown in Table 1 for five persons. The mean value is taken for the analysis. Table 2 indicates the anthropometric parameters considered for study. Figure 2 demonstrates the various postures of the maintenance personnel while actual working.

2.2 Manikin Posture Modeling at Workplace

There are various maintenance activities carried out in the workshop, from those activities one is chosen for the study based on the requirement of workshop in-charge and workers, i.e. maintenance of gear box of Bus, as shown in Fig. 2d, Posture 4 is taken for the study based on the requirement of the maintenance supervisor and modelled in CATIA V5R17 (Fig. 3). The parts in the work atmosphere specially gear box (in simple rectangular box type) are modeled [6]. With the help of Anthropometric dimensions (Table 2), the manikin modelled using CATIA's human builder section. Using human measurements editor workbench, dimensions of maintenance people were updated.



Fig. 2 Postures attained by a maintenance person

Fig. 3 Modelled posture 4 attained by a maintenance person



2.3 RULA Analysis

For the modelled manikin RULA analysis is done, it does manikin upper limbs analysis based on parameters as like weight, distance, and frequency. It is used to work on several characteristics of manikin posture with reference to several variables and worker in formation, as like object weight, lifting distance, action interval, lowering distance, and frequency of task. Analysis yield carefulness of work precise variables such as the manikins outer support, the manikin’s stability and manikin’s arms orientation with respect to the feet and body [7]. Therefore, the RULA analysis supports to adjust manikin posture causing in improved intended and extensively supposed yields and workstations. RULA analysis executed for the one frequently accomplished posture by maintenance personas shown in Fig. 2. Posture 4. It is observed that has to bent and perform the maintenance of gear box. There are total four postures are attended by the workers shown in Fig. 2, with request and the frequency, interval of activity of posture is found critical so the posture taken for the study [1, 8].

Table 3 Interpretation of RULA score in basic mode

Sr. No	Score	Colour	Meaning
1	1 and 2	Green	The posture is acceptable if it is not retained or repeated for longer period
2	3 and 4	Yellow	Further investigation is required and changes may also be required
3	5 and 6	Orange	Investigation and changes are needed soon
4	7	Red	Investigation and changes are needed immediately

Figure 3 is the postures modelled of maintenance activity done by worker shown in Fig. 2d. Posture 4, with the help of Digital Human Modelling technology. Maximum attention was given while to modelling the posture attained during work by the operator.

2.4 RULA Score

The score of RULA analysis gives the score between 1 to 7, which represents the risk associated with the different parts of the body individually as well as it gives an average posture score between the same range as mentioned above i.e. 1 to 7, the detailed importance of the value and its meaning is provided in Table 3.

3 Result and Discussion

RULA analysis window for left side and right side for Posture 4 is shown in Fig. 3. Table 4 presents RULA score for the posture 4 taken for the study.

In the posture taken for study, the operator is required to forward/lateral bend or flex/extend hands at sitting position, twist the wrist/spine etc. for performing the maintenance activity.

The analyzed score of posture 4 presented in Table 4, illustrates that present work posture of the maintenance person is highly dangerous (score 6 and 7) and must be altered by detailed study of workplace to hold off the maintenance person by musculoskeletal disorder. Figure 4 shows the RULA analysis window.

Gear box is placed on a ground while performing a maintenance activity as there is no proper workstation to hold, position the object, also the worker does not have

Table 4 RULA score of posture (A) while doing maintenance of ST Bus Gear Box

Posture	RULA Score	
	(Left side)	Score (Right side)
A	7	7

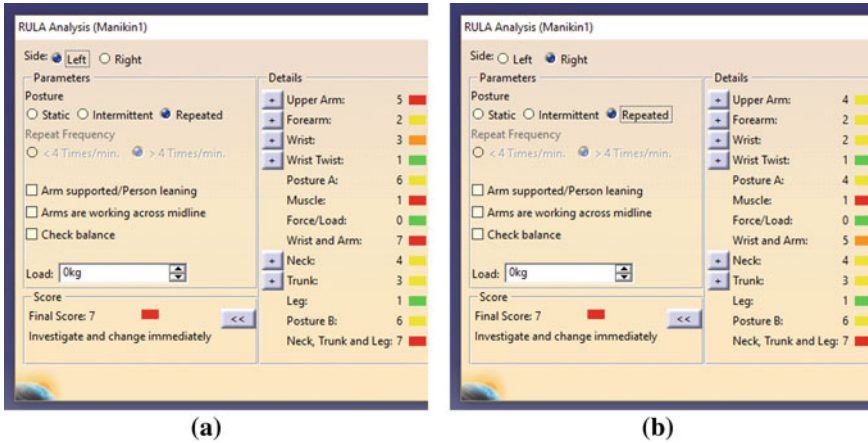


Fig. 4 RULA analysis window a For left side of body b For right side of body

a proper sitting arrangement while performing maintenance operation, by designing a proper maintenance workstation the workstation can be improved.

As the 5 to 10 gear box are maintained by worker in a day so, it is advisable to develop a low cost box holding and worker sitting mechanism wherein reduced human intervention is required such using fixtures to hold the job and use of new technological tools for maintenance. This will reduce the drudgery caused and cost of operation.

4 Conclusions

While studying maintenance activities performed in the workshop, it is observed that, the maintenance person attains number of uncooperative postures, which result in physical stress on the maintenance person, and these uncooperative postures frequency is also below average. And this scenario needs to be analysed and improvement in it to have an increase in efficiency of the work and reduce the stress coming on maintenance person.

Thus, by using anthropometric data of user population with the help of Digital Human Models technique ergonomically sound yields can be build. Moreover, the RULA analysis of present workstation gives 7 score, for both 5 and 95 percentiles. Which tells that there is essential of immediately investigation and alteration the existing maintenance station. The ergonomically designed machines/equipment's can reduce the stressed work, and increase safety, comfort and efficiency of the activity.

References

1. Bhuse PK, Vyavahare RT (2014) Ergonomic evaluation of knapsack sprayer used in agricultural application. *Int J Sci Eng Res* 5(12):903–907
2. Bloswick D (1990) An ergonomic analysis of the ladder climbing activity. *Int J Ind Ergon* 6:17–27
3. Ghugare BD, Adhao SH, Gite LP, Pandya AC, Patel SL (1991) Ergonomic evaluation of a lever-operated knapsack sprayer. *Appl Ergon* 22(4):241–250
4. Grandjean E (1988) *Fitting the task to the man*. Taylor and Francis, London
5. Kumar A, Mohan D, Patel R, Varghese M (2002) Development of grain threshers based on ergonomic design criteria. *Appl Ergon* 33(5):503–508
6. Meyers J (1995) Using ergonomics in the prevention of musculoskeletal cumulative trauma injuries in agriculture: learning from the mistakes of others. *J Agromedicine* 2(3):11–24
7. Ren J, Xiao D (2009) Ergonomic simulation and evaluation of elliptical trainer with CATIA V5. *CADDM* 19(1):81–86
8. Sanjog J, Karmakar H, Agarwal C, Patil D (2012) Designing and ergonomic evaluation of a shoe-rack in CAD environment. *Int J Comput Appl* 49(20):38–41
9. Singh A, Gautam US, Pannase S, Singh A (2010) Ergonomic evaluation of farm women during maize shelling. *Indian Res J Ext Edu* 10(3):41–44
10. Somasundaram A, Srinivasan P (2010) Design optimization of dosa making workstation for smooth ergonomic interface. *J Sci Ind Res* 69:221–224

Improving Plant Yield by Smart Irrigation System Using pH and NPK Sensors



Rahul Y. Pawar, Pramod B. Deshmukh, Vishakha A. Metre,
and Swapnil V. Ghogardare

Abstract Agriculture could be a major supply of earning of Indians and agriculture has created a giant impact on India's economy. The event of crops for a far better yield and quality deliver is exceptionally needed. So, appropriate conditions and appropriate wetness in beds of crop will play a significant role for production. An automated irrigation system for economical water management and intruder detection system has been planned. Soil Parameters like pH, soil moisture, humidity are measured and therefore the Pressure detector and therefore the perceived values are displayed in LCD. The GSM module has been accustomed establish a communication link between the farmer and also the field. The present fields standing are going to be intimated to the farmer through SMS. The farmer will access the server regarding the sphere condition anytime, anywhere thereby reducing the man power and time.

Keywords Internet of things (IoT) · Agriculture technologies · Soil health · PH sensor · NPK sensors · Arduino

1 Introduction

The agriculture system is plagued with issues surrounding wastage of water as well as extra usage of water than required. These issues have often led to damage to crops further leading to humongous losses to the farmers. Apart from insufficient or excessive water distribution, crop health has been a matter of great concern. As crops are grown, it is not known for sure whether the conditions are adequate for healthy yield. With the advent and growth of technologies in recent years, Internet of Things has been of great support to varying fields in the market and the entire world.

This paper deals with how IoT (Internet of Things) can help and alleviate the problems in Agricultural system to ensure less wastage of resources, healthier yield and consequently extraction of as many profits as possible. The technology of IoT has been put to use with the use of different types of hardware and that enable and embed

R. Y. Pawar · P. B. Deshmukh (✉) · V. A. Metre · S. V. Ghogardare
D. Y. Patil College of Engineering, Akurdi, Pune 411044, India

certain features into the Agricultural procedure which are not possible in the normal procedure. For this setup, we have made use of Arduino kit along with four major sensors: Moisture Sensor, Temperature Sensor, pH Sensor and Nitrogen Phosphorus Potassium (NPK) Sensor. Whenever we talk about India, horticulture turns out to play a major role in the country's economic backbone. Horticulture, the cultivation of plants, serves as an earning means for around 70% of India's population of over 1.3 Billion people.

The objective of this paper is to help ease the Agricultural process throughout the country and at the same time, ensuring less wastage water resources. This project will help farmers as well as the general public in providing them with a better Agricultural objective procedure. This paper proposes such a programmed irrigation system which will lead to reduced manual labor, better optimized water usage as well as increased productivity of crops. We make use of sensors and the IoT technology to form a framework that will help the farmer to automatically provide water to a plant as needed along with maintaining proper pH levels and proper level of nutrients ensuring healthy yield. Moisture Sensors are buried in soil to notify the system with information on moisture level present in soil of a crop. These levels are checked with a simple program and predefined threshold values. If moisture level is less than the required amount of water, water is distributed over the crops with the help of a motor. As soon as the crops attain its required moisture level, the motor shuts down, hence ensuring there's no wastage of water. Similarly, Temperature Sensor is used to continually check the current temperature of soil. The findings are then compared with threshold values stored in the system and if temperature exceeds the required temperature level, just adequate amount of water is sprinkled over the crops to bring the temperature down. pH Sensor is used to ensure that the crops are in proper pH conditions to maintain the health of the crops and ascertain a healthy yield. pH sensor is used to measure the pH values of the soil. If the pH value is reported as below a certain range under 7, the soil is considered acidic. The values are compared with threshold values for crop and as required, the adequate amount of alkaline is sprinkled over the crop to balance out the acidic part. However, if value is reported above a certain range over 7, soil is considered alkaline and is treated with an acidic solution of Mono-Ammonium Phosphate $[(NH_4)H_2PO_4]$. NPK Sensor comes into the picture as we need to measure the contents of essential nutrients NPK in the soil and consequently maintain the adequate amount of these nutrients. NPK Sensor is implemented with the help of an optical transducer which ascertains on how much of these nutrients are required in the soil to make it fertile enough. Optical Transducer is implemented as a detection sensor which uses three LEDs (Blue, Yellow and Red) for light sources and a photodiode for light detection.

2 Background Study and Related Work

There has been good amount of research work on the topic of automating agricultural practices. Use of different microprocessors and different algorithms has taken place in the past to achieve the same goals. Scientists have tried out different approaches to

tackle automated water sprinkling or water system framework. An article, published in 2014, takes into account how water sprinkling can be automated in order to use water cautiously and consequently save water. It discusses on important aspects of water conservation including equal and strictly sufficient distribution of water, goes in depth on discussing the technological needs of automatic water distribution system followed by methods of achieving it, and it's followed by different methods and are discussed to achieve increased performance in the agenda of automatic water supply [1]. pH Measurement has been tackled using technologies like an ion-sensitive field effect transistor (ISFET) based sensor, along with EC sensor and a p-n diode temperature sensor. Such a framework focuses on particularly improving the productivity of crops and obtaining a stable production of high quality fruits and vegetables. Making use of Electrical Conductivity, salt substance concentration of soil is calculated which consequently helps in monitoring the health conditions of plants by monitoring and dealing with nutrients in the plants in a quantitative manner [2]. The process of drip irrigation has been studied and implemented combining IoT technologies with Image Sensing technologies. A database of predefined soil moisture values is used with moisture sensor and an Android app to form an interface with the farmer. Apart from the moisture sensor, a camera is used to click pictures of the leaves of plants. The results are compared with the results of healthy plant leaves already available in a database, which helps in identifying whether the plant or a part of plant is diseased or not [3]. Another framework has been implemented which involves Arduino-UNO for the first time to carry out automated irrigation. Apart from the Arduino-UNO embedded system, moisture sensors with WiFi module are used. All of these are used together in a well formed network to carry out a procedure which tackles the distribution of water over crops by making it automatic [4]. BARC developed field testing kit called Soil Organic Carbon Detection Kit [5]. To ensure healthy yield of crops, it is important to check and maintain presence of adequate amount of Nitrogen, Phosphorus and Potassium nutrients. NPK sensor is built with the help of an Optical Transducer. Optical Transducer involves an implementation as a detection sensor using three LEDs as light source and a photodiode for light detection. An Arduino micro-controller is involved for data acquisition and analog to digital data conversion [6].

3 Experimental Design

3.1 Problem Statement

IoT based system of irrigation works in co-operation with sensors on Arduino kit; all its functioning is shown in Fig. 1. First counting on would like of crop a threshold worth is ready on wetness detector. Then incessantly wetness browse by detector is checked against the edge values.

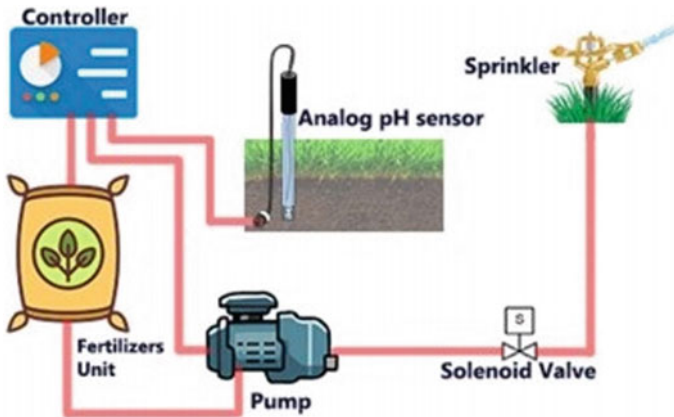


Fig. 1 Architecture of the system

If the humidity value is a smaller amount than threshold then still irrigation is sustained. Once the edge price is reached then the pump is changed mechanically by causation signals through the Arduino kit.

Arduino microchip board is connected with a bread board to increase the connections, for connecting the pump with microchip. Soil moisture sensors are connected with Arduino kit to urge readings of moisture of soil of farm. Then these gathered values are compared with threshold values of moisture levels and consequently pump is being operated switched on or off. Xiangpei HU et al. Review of operational management in intelligent agriculture based on IoT 317 on modern information technology [7].

3.2 Components Required

(a) Arduino

Arduino is basically an electronic platform that's built on easy to use and easily available hardware. The software is made open source by the creators [8]. We make use of Arduino Nano which is the one of the lower cost versions of Arduino. It is an embedded system. The various pins available on Arduino are used to read and write values on to the system. We make use of Arduino as it is.

- More affordable
- Cross Platform (Windows, Mac OS, Linux)
- Open Source
- Extensible hardware and software.

(b) Soil Moisture Sensor

Soil Moisture Sensor, also referred to as SMS, measures soil dampness content dynamically in a repetitive cycle and impedes the cycle if the dampness or moisture is over a characteristically set threshold value. Working: SMS work on the concept of Dielectric Permittivity. Dielectric Permittivity is basically the amount of electricity that can be passed through soil. It acts as a function of water content present in the soil. Threshold value of a particular crop is decided after following these steps:

- The soil moisture sensor is buried in the soil of the crop and water has to be applied to the soil. It is recommended that at least one inch of standing water is applied.
- Then, the soil is just left untouched along with the SMS for duration of twenty four hours. It is to be noted that if it rains within this period, the entire process has to be started over.
- After the twenty four hour duration is up, the value of soil moisture is read. This value is set as the threshold value for that crop.

Soil Moisture Sensors follow a basic working methodology. It measures the soil dampness or moisture value in short periods and if the value exceeds the threshold value, the relay is switched on which in turn switches on the motor of the Water tank. Water is distributed over the crops and as soon as the moisture value returned by the sensor reaches the threshold value, the relay is switched off and the water motor is switched off.

(c) Temperature Sensor

Temperature Sensors are used to ensure that the overall temperature of soil of a crop stays under a particular threshold temperature, crossing which might result in unhealthy yield. Again, a database of threshold temperature values for required crops is maintained and the temperature sensor is deployed. It is programmed such that as soon as the temperature of soil crosses the threshold temperature, with the help of a relay device, the water sprinklers are turned on. Adequate water is sprinkled and this in turn, cools down the temperature and brings it to the appropriate soil temperature required for healthy yield.

(d) pH Sensor

pH Sensor is the most important sensor deployed that deals with the biological health of a crop. It is dipped into the soil of a crop and it measures the pH value of the soil.

- If the value is found to be between 7.9 to 9.4, the soil is deemed on the alkaline side, and to balance it out, with the help of a relay, the motor of the tank of acidic solution of Mono-Ammonium Phosphate $[(\text{NH}_4)\text{H}_2\text{PO}_4]$ is turned on. Hence, the adequate amount of this acidic solution is sprayed until the pH Sensor returns an appropriate pH value.
- On the contrary, if the value is found to be between 5.0 and 6.0, the soil is deemed on the acidic side, and similarly, to balance it, a relay is used

to switch on the motor attached to the tank of alkaline Potassium Nitrate (KNO_3).

Thakur et al. mentioned the selection of sensors in exactness agribusiness is to upgrade the general creation of harvests. Sensors can help for estimating different boundaries of horticulture land like dampness, soil dampness, climatic condition, interruption recognition; water level which encourages that can prompt better creation [9].

(e) NPK Sensor

Nitrogen Phosphorus Potassium (NPK) Sensor is essential to measure and maintain the required nutrients of the soil which in turn helps in healthy yield of crops. NPK Sensor is implemented with the help of an Optical Transducer which acts as a light detection sensor. To carry out light detection, it is necessary to have a light source and a light detector. In this NPK Sensor, 3 LEDs (of colours Blue, Yellow and Red) are used as light sources and BH 1750 digital light sensor is used for light detection. The lights are used as such because the blue light is absorbed by Nitrogen nutrients in the soil, the yellow light is absorbed by Phosphorus nutrients in the soil and the red light is absorbed by Potassium nutrients in the soil shown in Fig. 2.

The measure of these nutrients is calculated on basis of wavelength difference. The wavelength at which each light is transmitted is noted. Then, the received wavelength of each light (after a specific amount being absorbed by the particular nutrient) is noted. This wavelength difference gives us a clear idea of the amount of nutrients present in the soil. The NPK Sensor is held over the soil to carry out this measurement.

It works in the following steps:

- The LEDs continuously emit the required lights towards the soil; some amount of each light is absorbed by the particular nutrient. Using transmitted and received wavelength values, the required wavelength difference is calculated.

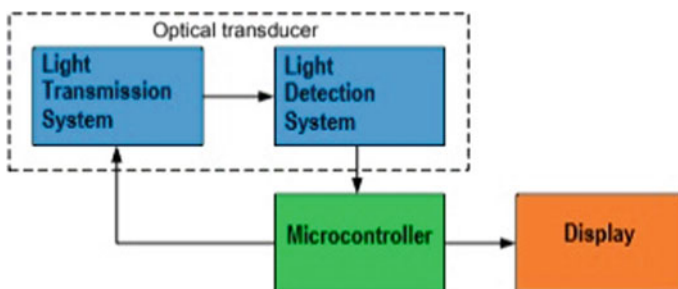


Fig. 2 Block diagram of integrated optical transducer with microcontroller

- For a healthy yield, the wavelength difference for blue light (Nitrogen) should be 3.5 units, for yellow light (Phosphorus), it should be 2.46 units and for red light (Potassium), the difference should be 1.6 units.
- The acquired values are compared to the required values and if found lacking, with the help of a relay, the motor is switched on and an NPK solution is distributed over the crops until the nutrients in soil reach the adequate amount required.

(f) LED Display

The Arduino Nano board is also connected to a small LED display. It is used to simply display all the values that are acquired from the deployed sensors. In case of pH Sensor, the display is also used to show in text, whether the soil is Acidic or Alkaline alongside the actual pH values.

4 Result and Discussion

4.1 Moisture Module

In this working module we are focusing on monitoring of crops, irrigation management of crops, environmental parameters for crops, and to renew the existing smart irrigation systems. The vast majority of the farmers utilize massive pieces of farming area and it turns out to be frightfully inconvenient to prevail in and track each side of tremendous grounds. Ordinarily there’s a break of lopsided water sprinkles. This prompts undesirable quality yields that extra winds up in cash misfortunes, during this circumstance, the reasonable Irrigation System exploitation the most current IoT innovation is valuable and winds up in simple farming.

Figure 3 shows Block diagram Irrigation System includes a wide scope to modify the entire irrigation system. Here we tend to area unit building associate IoT primarily based Irrigation System using ESP8266 Node MCU Module and DHT11 Sensor. It won’t exclusively precisely flood the water upheld the dampness level inside the dirt anyway conjointly send the data to give Speak Server to remain track of the

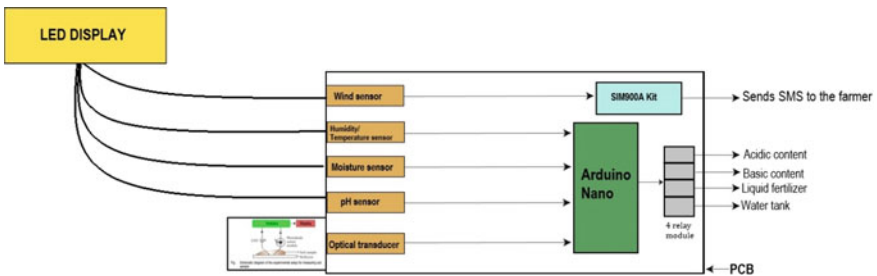


Fig. 3 Block diagram of the system



Fig. 4 Implemented smart irrigation system using pH and NPK sensors

land condition. The System can incorporate a siphon which can be wont to sprinkle water on the land depending upon the land status like dampness, Temperature, and Humidity.

Figure 4 shows Implemented Smart Irrigation System using pH and NPK Sensors, we also implemented with antecedently builds an identical Automatic Plant Irrigation System that sends alarms on versatile anyway not on the IoT cloud. but this, Rain caution and soil dampness locator circuit may likewise be valuable in building an astute Irrigation framework. Prior to starting, it's important to see that very surprising the different harvests need diverse Soil moisture, Temperature, and Humidity Condition. Along these lines during this instructional exercise,, we have a tendency to square measure mistreatment such a crop that may need soil moisture of concerning 50–55%. therefore once the soil loses its moisture to less than 50% then the Motor pump can activate automatically to sprinkle the water and it'll still sprinkle the water till the moisture goes up to 55% and subsequently, the pump are turned off. The detector information are sent to issue Speak Server in an exceedingly outlined interval of your time so it is monitored from anyplace within the world.

4.2 Nitrogen Contains Module

In the planned Irrigation system IoT is enforced, during this system all the knowledge that's received from the sensors and also the numerous parameters area unit given to the arduino-UNO microcontroller as AN analog input. A predetermined price of soil wet device is mounted in microcontroller and additionally for fencing. Table 1 shows that a various nutrients like Nitrogen (N), Phosphorus (P), and Potassium (K) are available in soil sample. Every nutrient is having its own property as far as absorption is concerned.

In light spectrum different lights are having their own wavelength these lights are absorbed by the nutrients from the soil. In experimental analysis three different LED emitting light are used which are having same level wavelength as nitrogen, phosphorus and potassium. Optical transducer used for transmission and reception of a light after reflection shown in the Table 2.

Table 1 Optical characteristics of NPK soils and LED remittance

Sr. No	Nutrient	Absorption wavelength (nm)	LED type	Wavelength (nm)
1	Nitrogen (N)	438–490	LED 1	460–485
2	Phosphorus (P)	528–579	LED 2	500–574
3	Potassium (K)	605–650	LED 3	635–660

Table 2 Threshold value of low, medium and high nutrient in soil sample

Sr. No	Nutrient	Low (V)	Medium (V)	High (V)
1	Nitrogen (N)	$3.5 < \times < 3.8$	$3.8 < \times < 4.1$	$\times > 4.2$
2	Phosphorus (P)	$2.45 < \times < 2.8$	$2.9 < \times < 3.3$	$\times > 3.4$
3	Potassium (K)	$1.6 < \times < 2.2$	$2.3 < \times < 2.8$	$\times > 2.9$

When it goes on the far side the actual threshold price water is mechanically irrigated to the crops and once the specified quantity of water is consummated it stops. The Microcontroller transmits that info on the net through a network of IoT within the style of WiFi module ESP8266 that's hooked up to that. This enhances machine-driven irrigation because the pump are often switched on or off through info given to the controller. This planned Irrigation system is employed to induce the pigment content and gas content of the leaf victimization LDR and optical device. This approach is for the advancement of the irrigation method by the automated technique while not personnel by measure numerous parameters associated with the sphere and so improves irrigation.

4.3 pH Module

pH SENSOR: pH is the proportion of corrosiveness or alkalinity of water arrangement which is controlled by the general number of hydrogen (H⁺) or hydroxyl (OH⁻) particles present. The pH esteem (under 7) is supposed to be acidic and (over 7) is supposed to be essential. The pH of an answer can change with temperature individually.

Table 3 Technical specification of pH sensor

Sr. No	Characteristics	Value
1	pH range	0 to 14 pH
2	pH resolution	0.01 pH
3	pH accuracy	0.02 pH
4	Temperature range	–5.0 to 60.0 °C
5	Response time	<= 1 min

Table 4 Threshold value of low, medium and high nutrient in soil sample

Sr. No	pH value	Nitrogen content %	Phosphorus content %	Potassium content %
1	4.5 (extremely acidic)	30	23	33
2	5 (very strong acid)	53	34	52
3	5.5 (strong acid)	77	48	77
4	6 (medium acid)	89	52	100
5	7 (neutral)	100	100	100

Table 3 shows technical specification of pH Sensor with different values respectively and Table 4 shows threshold value of low, medium and high nutrient in soil samples and with different pH values like extremely acidic, very strong acid, strong acid, medium acid, and neutral.

4.4 GSM Module

GSM (Global System for Mobile Communication) could be a customary developed by the European Telecommunication Standards Institute (ETSI) to explain protocols for second-generation (2G) digital cellular networks employed by mobile phones. GSM describes a digital, circuit-switched network optimized for full-duplex voice telecommunication and conjointly expanded to incorporate knowledge communications, packet knowledge transport via GPRS (General Packet Radio Services). The longest distance the GSM specification supports in sensible is thirty five kilometers. Hence better usage of above smart automation system in agriculture definitely helps to improve the yield of the crops [10].

5 Conclusion

This paper proposes the novel automated Smart Irrigation System, the use of sensors, Arduino under the IoT technology ensures that the crop yield of a farmer is improved, healthier as well as also ensures conservation of our most vital natural resource, water designed system can irrigate field with lesser amount of water. In addition to that, basic application of this system such as Diagnosis of diseases, Auto spreading, Crop yield analysis, Soil erosion, Field monitoring, Water stress, Variable rate of fertility. The biological health of the crop is taken great care of with the help of pH Sensor and NPK Sensor. With the help of pH Sensor, accompanied with other necessary

hardware, the pH levels of the crops are always kept in control and in a suitable range. Similarly, with the help of NPK Sensor, the amounts of Nitrogen, Phosphorus and Potassium in the soil are well regulated and maintained. Overall, it results into a completely better process with the focus on using just the right amount of resources and achieving the healthiest possible yield.

References

1. Bhawarkar NB, Pande DP, Sonone RS, Aaquib M, Pandit PA, Patil PD (2014) "Literature Review for Automated Water Supply with Monitoring the Performance System", *Int J Curr Eng Technol* 4(5):3328–3331
2. Izumi R et al (2017) Biological information (pH, EC) sensor device for quantitatively monitoring plant health conditions, *IEEE SENSORS. Glasgow* 1–3. <https://doi.org/10.1109/ICSENS.2017.8234170>
3. https://igin.com/article-218-drip_irrigation_water_conserving_solution.html
4. Mishra D, Khan A, Tiwari R, Upadhyay S (2018) Automated irrigation system-IoT based approach. In: 3rd International Conference on internet of things: smart innovation and usages (IoT-SIU). Bhimtal 1–4. <https://doi.org/10.1109/IoT-SIU.2018.8519886>
5. Mehetre ST, Chattopadhyay S (2018) Role of BARC technologies in agriculture for benefit of farming community in India. In: Pawar P, Ronge B, Balasubramaniam R, Seshabhatter S (eds) *Techno-Societal 2016. ICATSA 2016*. Springer, Cham. https://doi.org/10.1007/978-3-319-53556-2_2
6. Masrie M, Rosman MSA, Sam R, Janin Z (2017) "Detection of nitrogen, phosphorus, and potassium (NPK) nutrients of soil using optical transducer," In: 2017 IEEE 4th International Conference on smart instrumentation, measurement and application (ICSIMA), Putrajaya, pp 1–4. <https://doi.org/10.1109/ICSIMA.2017.8312001>
7. Hu X, Sun L, Zhou Y, Ruan J (2020) Review of operational management in intelligent agriculture based on the internet of things. *Front Eng Manage* 7. <https://doi.org/10.1007/s42524-020-0107-3>
8. <https://www.arduino.cc/en/Guide/Introduction>
9. Thakur D, Kumar Y, Kumar A, Singh P (2019) Applicability of wireless sensor networks in precision agriculture: a review. *Wireless Pers Commun* 107. <https://doi.org/10.1007/s11277-019-06285-2>
10. Raju KL, Vijayaraghavan V (2020) IoT technologies in agricultural environment: a survey. *Wireless Pers Commun* 113:2415–2446. <https://doi.org/10.1007/s11277-020-07334-x>

Thermal Characterization of Solar Elliptical Dish Steam Generator



Ranjit Sawant, Kunal Hole, Swapnil Vhantale, Swapnil Yeutkar,
and Rahul A. Patil

Abstract Concentrated Solar Thermal (CST) Collector system is used for steam generation in process heat applications. Elliptical Dish Steam Generator (EDSG) is a CST device having concentrating reflector and receiver. The overall EDSG performance depends on receiver's thermal efficiency. In order to improve the receiver's efficiency, it is necessary to modify the affecting parameters. The purpose of this paper to present an analytical study on thermal characterization of a receiver to improve overall performance of solar EDSG. Sun rays are concentrated at focus point of elliptical dish. Receiver is used as steam generator cum steam storage device. The thermal efficiencies are determined at steam pressure at 1 bar and 2 bar for both receivers. The analytical result shows that performance parameters such as collector area, shape of receiver, and average solar irradiation affects thermal efficiency of receiver. Study shows that the cylindrical receiver has higher average thermal efficiency than conical.

Keywords Elliptical steam generator · Cylindrical receiver · Conical receiver · Thermal efficiency

R. Sawant · K. Hole · S. Vhantale · S. Yeutkar · R. A. Patil (✉)

School of Mechanical and Civil Engineering, MIT Academy of Engineering (MITAOE), Alandi (D), Pune, India

e-mail: rahul.patil@mitaoe.ac.in

R. Sawant

e-mail: rssawant@mitaoe.ac.in

K. Hole

e-mail: kghole@mitaoe.ac.in

S. Vhantale

e-mail: spvhantale@mitaoe.ac.in

S. Yeutkar

e-mail: sdyeutkar@mitaoe.ac.in

1 Introduction

Solar thermal energy is a crucial source of energy that has been utilized to meet human needs. The most used solar dish concentrators technologies are linear Fresnel collectors (LFR), parabolic trough collectors (PTC), and elliptical dish collectors. LFRs and PTCs have linear focus technology with an operating temperature range of up to 5000C. The elliptical dish concentrator has a point focus with a high operating temperature range of working fluid [1].

Elliptical shaped dish collector is a perfect alternative for supplying medium (100 °C–250 °C) and warmth (250 °C–400 °C) processing heat for various applications like solar cooling, washing equipment [2]. The elliptical dish comprises of vinyl tape adhered to its surface, which reduces the weight of the concentrator. The dish concentrator locates itself for reflection the sun rays to a water containing receiver that to be heated. Figure 1 shows, tracking mechanism of elliptical dish concentrator. This dish often tracks the sun in E-W direction for whole day is a single axis tracker system which can be manually or automatically operated. For seasonal tracking, the reflector position is often positioned manually by adjusting telescopic clamps. Scheffler dishes with automatic N- S direction adjustment has also been introduced in India. In an Elliptical dish collector system, a receiver could be a significant factor. The receiver is employed for heating water using concentrators and producing steam for various process heat applications. The performance of the Elliptical dish steam generator depends on receiver’s thermal efficiency, and the receiver’s thermal efficiency varies in line with parameters like the shape of the receiver, solar irradiation,

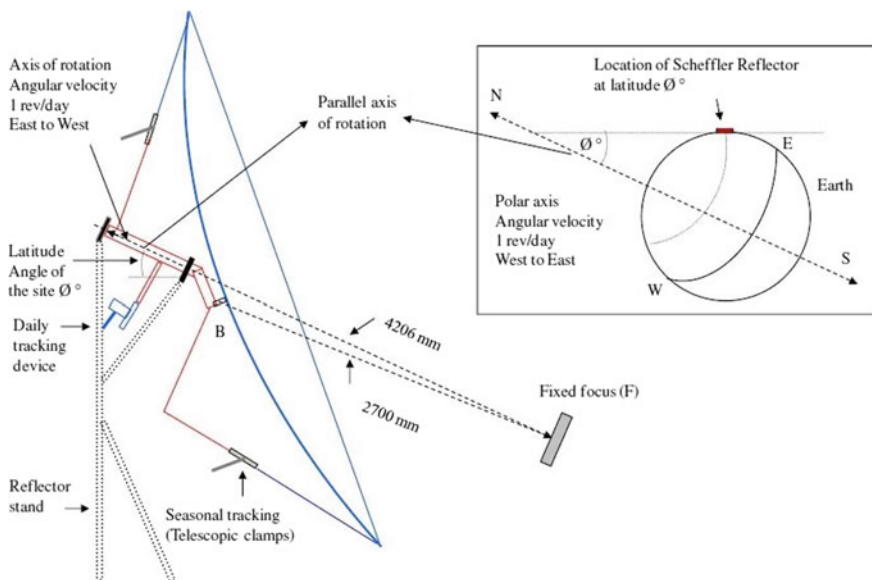


Fig. 1 Elliptical dish concentrator schematic [3]

and ambient temperature. The most typically used solar receiver for a solar dish concentrator is cylindrical. The optimal thermal efficiency with an area of 2.7 m^2 for conical and cylindrical receivers with 8-liter capacity is 38.24% and 52.03%, respectively [3].

The primary purpose of this study for domestic applications so small-scale systems. The overall performance of the system relies on the receiver's thermal efficiency. This analytical study focuses on optimization of thermal efficiency considering performance parameters such as shape, size, and steam pressure.

Elliptical dish concentrator of area 1.25 m^2 has been taken for analytical study. The cylindrical and conical shaped receiver of 4-liter capacity has been used for thermal characterization, which serves the binary purpose of absorber and steam storage. The paper is focused on the thermal characterization of the elliptical dish steam generator to improve efficiency.

2 Literature Survey

Until now, many researchers have researched on solar thermal collector by considering various parameters such as the area of a collector, wind speed, shape of a receiver, solar irradiation, the capacity of the receiver, and inlet water temperature. Various analytical and experimental models have been made by researchers, which are explained in the following.

Kasim [1] investigated the performance of the Parabolic trough solar furnace (PTSC). It was the primary try for local collector fabrication and evolution in environment of Iraq. Considering this condition, the results are relatively accepted. The technical adequacy of using PTSC results in thermal energy at $150 \text{ }^\circ\text{C}$ for average solar irradiance of 450 W/m^2 . Scheffler reflector is suitable for low pressure—temperature steam generation [2]. The receiver's efficiency depends on the receiver's shape, inlet water temperature, tilt angle, and glass cover. Efficiency can be increased by preheating the inlet water and coating the receiver by black paint. As wind speed increases, the conical receiver shows more efficiency than cylindrical. The optimal thermal efficiency of a cylindrical receiver is 51.90% and, in the case, of the conical receiver, it is 78.13%. When the steam temperature drops below $37 \text{ }^\circ\text{C}$ the thermal efficiency becomes low [3].

M. Prakash et al. published a paper on occurring heat losses within the solar cavity receiver. The paper says that the receiver system has mainly two losses, viz. radiative and convective. The radiative losses depend on the wall's temperature, the form factor, and, therefore, the receiver wall's absorptivity/emissivity. The convective losses are directly proportional to the mean receiver temperature and inversely to receiver inclination. The parabolic dish collector is the best design for concentrating the upper temperature because it comprises a reflector within the kind of a dish. Therefore, the primary target is receiver. From the results, it's concluded that the total deviation occurred in experimental and theoretical calculations is 14% [4]. Using the same type of dish concentrator, R. Loni et al. studied the performance of

Solar ORC on the open-cavity receiver. It was concluded that to increase the overall efficiency and efficiency of collector, a high rise in mass flow rate is required. Along with this inlet temperature of thermal oil should be kept low. Parabolic shaped dish concentrator is used for reflecting the sun rays and concentrating on the aperture of receiver. This results in the absorption of solar heat by the receiver's inner walls and sent to working fluid (thermal oil) [5]. The results about the smaller cavities show that the heat flux intensity at upper surface is more than the intensity at the sides of the cavity. It was concluded that the improvement in efficiency is done by decreasing the inlet temperature and runner tube diameter; also increase in mass flow rate causes efficiency improvement.

2.1 Literature Overview

Many researchers have worked on the performance of parabolic collectors and solar cavity receivers with the tilt angle [6–10]. So far, the studies on collectors do not include an elliptical dish collector and regular positions of the receiver. Here, in this research study, the efficiencies of conical and cylindrical receivers are compared considering various parameters like outer surface temperature, steam pressure, solar irradiation. In this case, the incident solar radiation, the mass flow rate of steam, ambient temperature, and reflectivity of material is considered as an independent factor. These factors are considered for the optimization of efficiency. The study is performed on an elliptical dish of 1.25 m² with the receiver of 4-liter capacity kept at a focus point. The receiver considered have no heat loss. The thermal efficiencies are calculated at 1 bar, 2 bar steam pressure for 30 days durations.

Here, the mathematical model is formed using factors such as the average incident solar radiation, the mass flow rate of steam, ambient temperature, and reflectivity of a material. The generated values are plotted against each other, and comparison is done with the help of graphs.

3 Construction and Working

3.1 Schematic of System

The Fig. 2 shows the Elliptical Dish collector steam generation process and its use for various applications. As the solar thermal energy falls on the collector, solar radiation gets focused on a single point due to the elliptical nature of the collector. When the solar radiation falls on the receiver, the temperature of the receiver increases. The receiver gets heated up and water as well. The steam generation takes place. Generated steam can be utilized for various applications such as process heat cooking,

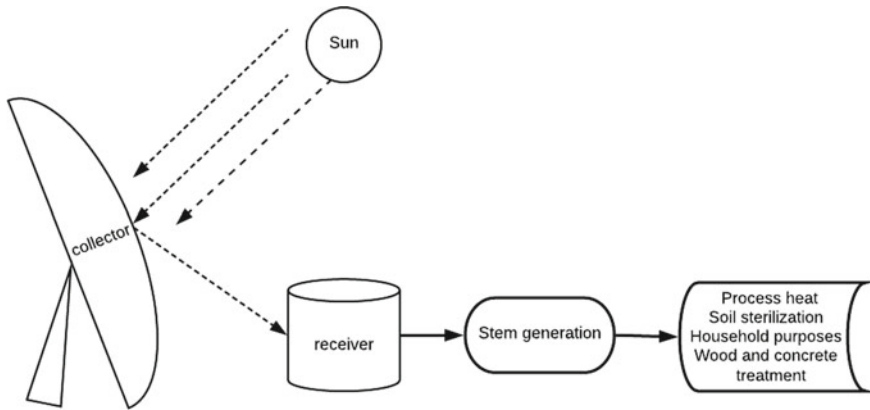


Fig. 2 Schematic of elliptical steam generator

bathwater, absorption cooling, soil sterilization, lifting gas, wood and concrete treatment.

3.2 Reflector Frame and Reflective Material

The solar collector collects the radiations and reflects it to the fixed point on the receiver. Every 15 min, the sun changes their position, so there is a need for solar tracking in our solar collector system.

Reflective material is used to reflect solar radiation. The main task to select a material having maximum reflectivity to increase the performance of the system. We selected vinyl tape as a reflecting material shown in Fig. 3 The vinyl tape used has properties of both glass and aluminium foil. i.e., high reflectivity as glass and high concentration focus point as aluminium foil. Also, the drawback of aluminium foil was not in vinyl tape; hence we placed it on the dish.

3.3 Receiver

The receiver has been made to store the working fluid having inlet and outlet valves for the circulation of the water. The receivers used are cylindrical (Fig. 4) and conical (Fig. 5). It is kept at the focus of the collectors (Fig. 5) as per the design of the system. The solar radiations are concentrated on the receiver to increase the temperature of the working fluid. After heating working fluid, steam is transferred through a pipe to the turboexpander for electricity generation or as hot water for other purposes.

The selected material is cast iron. The receiver is coated by insulating material, glass wool to minimize the heat loss from the system, which is useful to improve the

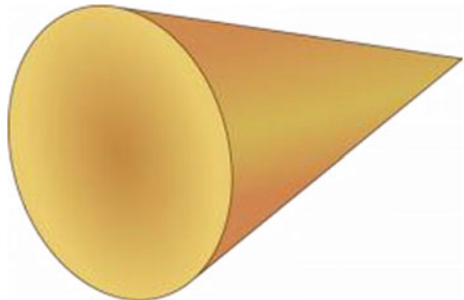
Fig. 3 Reflector with vinyl type



Fig. 4 Cylindrical receiver



Fig. 5 Conical receiver



efficiency of the system. The thickness of a material used for the receiver is 1–2 mm for maximum heat transfer to the water from outside.

4 Methodology

The material selection consists of a selection of reflector frame, reflective material, and various types of receivers. After material selection, the data collection is done which consists of finding an area of dish, finding the receiver’s capacity and surface area, and collecting monthly data of average solar radiation and wind speed (Table 1).

4.1 Aperture Area Calculation

To calculate the aperture area firstly finds the declination angle, then the aperture area by using the formula

Declination Angle [3]:

$$(\delta) = 23.45 \times \sin \left[\frac{360}{365} \times (284 + n) \right] \tag{1}$$

Table 1 Nomenclature [3]

Symbol	Explanations
A_{dish}	Area of dish
A_p	Apertures area
D	Characteristic focus diameter
A_s	Area of focus
T_{osurf}	Outside temperature of a wall
T_{isurf}	Inside temperature of a wall
T_{sat}	Saturation temperature
T_e	change in temperature
Σ	Stefan Boltzmann constant
Δ	Delectionation angle
N	number of the day in the year
I	Avg. solar radiation
Q_{conv}	Heat transfer by convection
Q_{rad}	Heat transfer by radiation
Q_{cond}	Heat transfer by conduction
m_s	Mass of steam
R	Reflectivity of material

Aperture area [3]:

$$(A_p) = A_{\text{dish}} \times \cos \left[\left(\frac{43.20^\circ - \delta}{2} \right) \right] \quad (2)$$

Total radiation from the sun is the first incident on the collector then reflected the receiver with 80% reflectivity of the material. The whole surface of the receiver gets heated. inside of receiver, the heat transfer occurs through the convection as the receiver is 50% filled. The convective heat transfer occurs only through a 50% surface area (i.e. only in which water is filled.). Therefore, for finding the outer surface temperature using a formula given below by equating Heat input and radiative heat transfer [11].

$$\text{Heat Input} = I \times A_p \times R \quad (3)$$

$$Q_{\text{rad}} = \sigma \times \epsilon \times A_r (T_{\text{osurf}}^4 - T_a^4) \quad (4)$$

4.2 Heat Transfer Coefficient

In calculation of heat transfer coefficient, find inner surface temperature using the formula given below by equating conductive and Heat input [11].

$$Q_{\text{cond}} = \frac{K \times A_s \times (T_{\text{osurf}} - T_{\text{isurf}})}{t_{\text{wall}}} \quad (5)$$

After finding the inner surface temperature, find heat transfer coefficients for convection and radiation using these formulas given below. All the unknown variables in the below formulae are taken from the stream table [11].

$$h_{\text{conv}} = 0.62 \times \left[\frac{K_v^3 \times \rho_v (\rho_l - \rho_v) g (h_{\text{fg}} + 0.4 C_{\text{pv}} \times T_c)}{\mu_v \times D \times T_e} \right]^{\frac{1}{4}} \quad (6)$$

$$h_{\text{rad}} = \frac{5.67 \times 10^{-8} \times \epsilon (T_{\text{Isurface}}^4 - T_{\text{sat}}^4)}{(T_{\text{Isurface}} - T_{\text{sat}})} \quad (7)$$

The overall heat transfer coefficient required to find heat transfer by convection is calculated from the given formulae [11].

$$h = h_{\text{conv}} + \frac{3}{4} \times h_{\text{rad}} \quad (8)$$

$$Q_{\text{conv}} = h \times A_s (T_{\text{isurf}} - T_{\text{sat}}) \quad (9)$$

The convective heat transfer is in watts which are converted into KJ using given formulae.

$$q = Q_{\text{conv}} \times \frac{3600}{1000} \quad (10)$$

4.3 Mass Flow Rate Calculation

To calculate the mass flow rate [11], the formula used is

$$m_s = q \times h_{fg} \quad (11)$$

After all the calculation to find the thermal efficiency [3] the universal formula is

$$\text{Heat Input} = I \times A_p \times R \times \frac{3600}{1000} \quad (12)$$

$$\text{Heat Output} = m_s \times h_{fg} \quad (13)$$

$$\eta = \frac{\text{heat output}}{\text{heat input}} \times 100 \quad (14)$$

The system is to be made as per the design and do the analysis by experimenting and validate the system design.

5 Results and Discussion

Figure 6 shows the analytical result of Thermal Efficiency for Cylindrical and Conical receiver at 1 bar and steam pressure. For a cylindrical receiver, maximum thermal efficiency is 30.5727%, whereas for conical receiver maximum thermal efficiency is 25.63% in the general case at 2 bar steam pressure. This value of thermal efficiency depends upon aperture area, heat input, the outer surface temperature of receiver, mass flow rate of steam. The overall performance is better for the cylindrical receiver.

Figure 7 shows the variation of thermal efficiency with an outer surface temperature of a cylindrical receiver, which states that thermal efficiency decreases with an increase in the outer surface as outer surface temperature increases conductive losses increase. Hence there is a slight change in thermal efficiency.

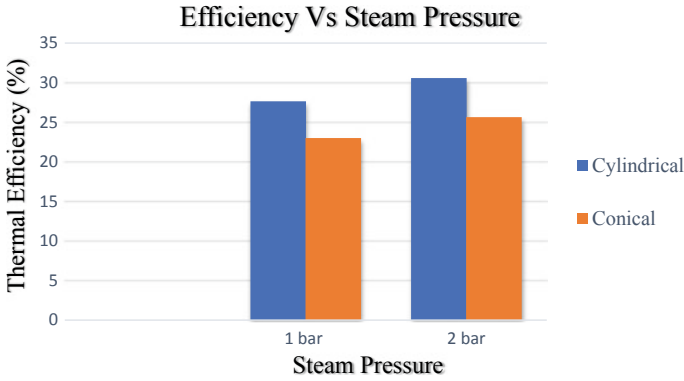


Fig. 6 Thermal efficiency for cylindrical and conical receiver

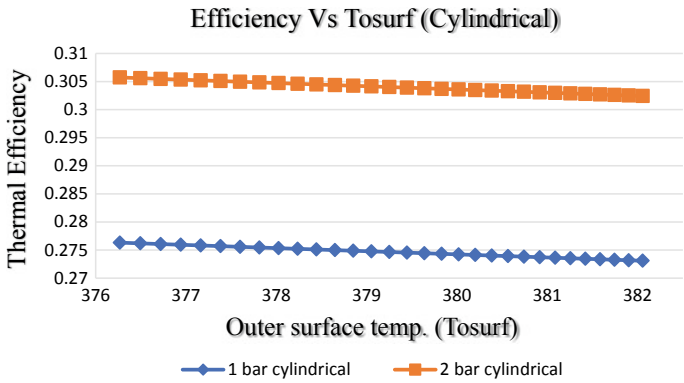


Fig. 7 Variation of thermal efficiency with outer surface temperature for cylindrical receiver

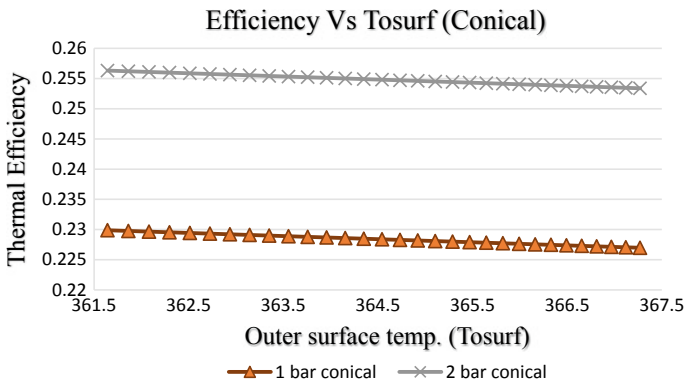


Fig. 8 Variation of thermal efficiency with outer surface temperature for conical receiver

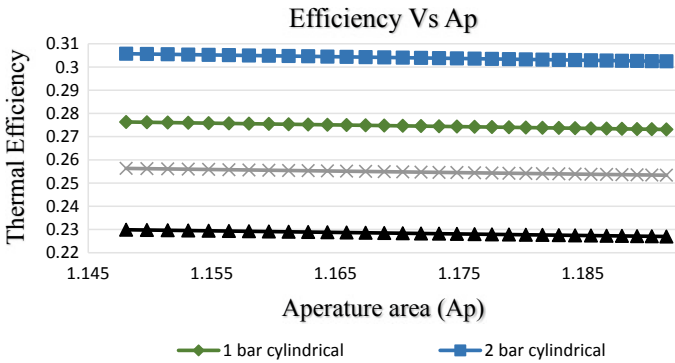


Fig. 9 Variation of thermal efficiency with aperture area for cylindrical and conical receiver

Figure 8 shows the variation of thermal efficiency with an outer surface temperature of a conical receiver which states that thermal efficiency decreases with an increase in the outer surface.

Figure 9 shows the variation of thermal efficiency against the aperture area. The graph shows that the decrease in thermal efficiency with increases in aperture area at a higher value of aperture area convective and radiative losses increases. This causes decreases in heat by the receiver.

6 Conclusion

The thermal efficiency of the receiver depends on the shape of the receiver, inlet temperature of the water, and also steam pressure. The thermal efficiency increases with an increase in steam pressure. At 1 bar steam pressure, the overall thermal efficiency for cylindrical and conical receiver is 27.46% and 22.83% respectively. At 2 bar steam pressure, the overall thermal efficiency for cylindrical and conical receiver is 30.39% and 25.47% respectively. With an increase in steam pressure, there is a significant increase in the thermal efficiency of a cylindrical receiver as compared to a conical receiver. Hence for higher steam pressure, the cylindrical receiver can be preferred over conical.

The coating of black paint on receivers increases thermal efficiency due to the increase in heat absorptivity. The reflector area, receiver surface area, and receiver's capacity have a significant effect on thermal efficiency. As the percentage of water-filled decreased to 50%, there is an increase in efficiency by 65.82%. Hence, as the percentage of water filled in receiver increases, the steam generation is less, which results in a decrease in thermal efficiency. The optimized efficiencies for cylindrical and conical receiver is 30.39% and 25.47% respectively.

References

1. Kasim NK, Design and fabrication of parabolic trough solar collector for thermal energy applications. Rep. Iraq Mins. High. Edu. and Sci. Res. Univ. Baghdad
2. Bhasme Swati (2016) Comparative evaluation of parabolic collector and scheffler reflector for solar cooking. *Int J Eng Res Technol* 6:1–16
3. Patil RA, Nene AA (2015) Design optimization and parametric variation on receiver of Scheffler solar concentrator. *Int Eng Res J* 2:4252–4258
4. Prakash M, Kedare SB, Nayak JK (2009) Investigations on heat losses from a solar cavity receiver. *Sol Energy* 83:157–170
5. Loni R, Kasaeian AB, Askari Asli-Ardeh E, Ghobadian B, Le Roux WG (2016) Performance study of a solar-assisted organic rankine cycle using a dish-mounted open-cavity tubular solar receive. *Appl Therm Eng.* <http://dx.doi.org/10.1016/j.applthermaleng.2016.08.014>
6. Mokhtari A, Yaghoubi M, Kanan P, Vadiiee A, Hessami R (2007) Thermal and optical study of parabolic trough collectors of Shiraz solar power plant. In: 3rd International conference on thermal engineering: theory and application, Jordan, pp 65–70
7. Jing Li, Gang Pei, Jie Ji (2010) Optimization of low temperature solar thermal electric generation with organic rankine cycle in different areas. *Appl Energy* 87:3355–3365
8. Alawneh F, Geuder N, Bataineh SM, Ghermandi A (2018) Concentrating solar power-driven desalination for communities in Israel and Jordan. ResearchGate
9. Qiu Shoufeng, Ruth Matthias, Ghosh Sanchari (2015) Evacuated tube collectors: a notable driver behind the solar water heater industry in China. *Renew Sustain Energy Rev* 47:580–588
10. Baccioli M, Antonelli U (2017) Desideri, Dynamic modeling of a solar ORC wit compound parabolic collectors: Annual production and comparison with steady-state simulation. *Energy Convers Manag* 148:708–723
11. Rajput RK (2012) Heat and mass transfer, Revised edn. S. Chand, pp 13–19. ISBN 8121926173

Ecofriendly Road Construction by Using Industrial Waste (Spent Wash)



R. J. Salunkhe, N. A. Shinde, A. H. Kalubarme, H. D. Aiwale, and S. D. Patil

Abstract The work is carried out to study deals with the blending spent wash in water on index properties of black cotton soil and plastic limit soil. Road transport plays important role in development of country. Developing an honest network of road in villages in India may be a challenging problem because it needs stabilization of sub grade and sub base with economical option. Spent wash is distillery wasteproduct of sugar industry and harmful if not properly treated and dispersed in water. It is often economic and environmentally friendly replacement choice to water with improvement in index properties of plastic limit soil and black cotton soil.

Keywords Spent wash · Black cotton soil · Plastic limit soil · Road construction

1 Introduction

Roads play a imperative role of transportation system for sending the agricultural crop the market place and supporting the Fanner lives. Thus, a key of advancement of a nation is great street network. About 69,000 miles of these roads in India are stabilized with crushed limestone or gravel due their small traffic doesn't legitimize clearing with tock-top or Portland concrete cement. With the expanded worldwide interest for the energy and a growing local requirement for aggregates, it has become costly from material cost to eliminate substandard soils and restore them with foreign soil which can more suitable for it. Thus, it is necessary to amend the characteristics of locally accessible soil to the degree that it tends to be utilized in the development of streets to limit the expense of development of streets and for making the best use of different industrial by-products such fly ash and spent wash as a soil stabilizing agents [1]. Spent wash and fly debris are being delivered in adequate amount in Maharashtra and there is no doubt about its availability. In this work, it is planned to consider different properties of spent wash as soil replacement or as restricting material particularly in the development of streets. More in recent times, the higher

R. J. Salunkhe (✉) · N. A. Shinde · A. H. Kalubarme · H. D. Aiwale · S. D. Patil
SVVERIs College of Engineering (Poly), Pandharpur, India

costs of waste discarding techniques have proved an interest in the probable utilization of waste materials like steel slag, fly ash, lignin, waste tires, spent wash etc.

2 Role of Transportation

There is good contribution of transportation in the industrial, economic, cultural and social development of any country. For the economic growth of any region, transportation plays a noteworthy role as every commodity produced whether it is clothing, food, medicines or industrial products desires transport at the various stages of production. In production stage, transportation is essential for carrying raw materials such as cotton, seeds, sugarcane, steel, coal, etc. Transportation is needed from the production centres viz: factories and farms to marketing centres for delivery to every household in the distribution stage [2]. The inadequate transportation facilities act as a constraining factor in the procedure of socio-economic growth of the country.

2.1 Importance of Highway Transportation

The media of distribution between shops, homes, factories, etc. is the highway transportation. The significance of highway transportation can be simply referred from following determinations of roads:

1. They enable conveyance of raw materials, goods, manufactured articles, people, etc. quickly and easily in the various part of the country.
2. The roads perform as only media of communication in areas of high altitudes which is in hilly regions.
3. Highway Transportation aid in development of trade and further economic activities in and outside the villages and towns by creating contact between villages and towns.
4. The streets assist in providing effective supply of natural resources and agricultural products across the country.
5. Transportation support in price stabilization of commodities because of agility of products within the country.
6. They offer more employment opportunities.
7. The transportation improves land value and therefore carry well revenue.
8. They aid in social and cultural progress of people and creating the villagers active and alert affiliates of community.
9. They aid in endorsing the social and cultural ties amongst people in various regions of the country and consequently reinforce the national unity.
10. They serve enhanced medical amenities.

2.2 Sugar Industrial Waste

Pollution because of the industrial wastes [3] is intricate and tenacious problem that require consideration and further action such wastes from industries are discarded into the soil to recycle it naturally. Industrial wastes turn out to be an energy supply to the micro-organisms of soil, the nutrient cause for the development of plant and further aid as an adjustment for the challenging soils. Challenging soils contains saline soils, sodic soils, soils of acidic nature, etc. These soils are capable for the production of crop when these are ameliorated or reclaimed [4]. Hence, above and beyond general adjustments, character of wastes in amending soils was recognized and endeavoured. Substantial sum of molasses, sulphuric acid, phospho-gypsum, press mud (by-products and wastes from smelters, petroleum industries, and dairies) and sugar factory lime, shale ash, spent wash, slags, etc. are being unconfined each year that are responsible for the atmosphere pollution.

2.3 Spent Wash

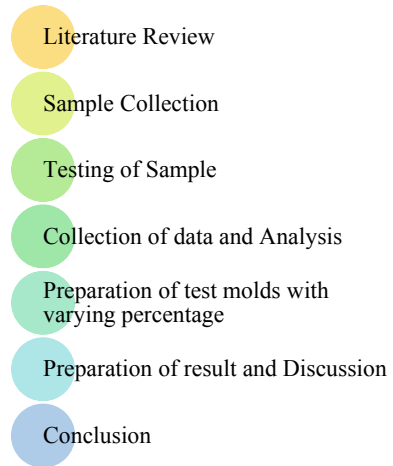
The alcohol distilleries byproduct is the spent. It is acidic in nature yet wealthy in potassium, magnesium, and calcium. The expansion of spent wash [5] deprived of weakening was exceptionally successful in expanding the water admission pace of sodic calcareous soil. The utilization of spent wash trailed by water system was compelling than application upon weakening in the recovery of sodic soils. The influence of flocculating of salt in unadulterated spent wash are accountable for expanding the porousness if contrasted with its weakened ranch. Hence, higher concentration assists more noteworthy trade of calcium for sodium. A mix of spent wash (75 tone/ha) and farmyard manure (10 tone/ha) verified being better than the utilization of gypsum (2.5 tone/ha) in addition to green manure (30 tone/ha). In the moderate system, the free acidity of spent wash counteracts carbonates and bicarbonates existing in sodic soil, other than killing dirt alkalinity. Calcium in addition to magnesium substance of spent wash straightforwardly substitutes sodium from exchange complex and enhances the state of being of sodic soil. The supplements like 4 nitrogen, zinc and phosphorous in the spent wash assists with improving the richness status of sodic soil.

3 Methodology

3.1 Materials

The materials utilized in this analysis were black cotton soil [2], murum and spent wash. The soil for experimental investigation was collected from Someshwarnagar,

Fig. 1 Flow chart of methodology



Tal Baramati. An oven dried black cotton soil sample was used for geotechnical properties. The spent wash was collected from Someshwar Sahakari Sakhar Karkhana, Someshwarnagar, Tal-Baramati. The methodology is depicted in Fig. 1.

3.1.1 Black Cotton Soil

Soil is one of foremost soil credits of India. Soils display high rate of bump and shrinkage if exposed to variations in the content of moisture and henceforth have been noted to be the utmost worrying form engineering consideration. The montmorillonite rate is higher in the black cotton soil that roots expansiveness and subsequent cracks happens in the soil deprived of any warning, which is hazardous for the construction. Distillery wastes water [6] with hostile odour stances a solemn threat to water superiority in different regions of the world. The ever-increasing generation of distillery spent wash on the one hand and strict legislative regulation of its discarding on the other has enthused the requirement for evolving new technologies to progress this effluent competently and economically. The Characteristics of Black Cotton Soil are presented in Table 1.

3.1.2 Murum

Mumm is the battered rock fragments [7] that are sternly and whose nature is non-plastic. The granulated murum is taken from Waki Tal-Baramati, and analyzed in laboratory for un-soaked California Bearing Ratio test. The water in and underneath a road pavement has a key influence on the performance of road [8] and its survivability a clean and potable water is used for the testing. The Spent wash Constituent Amount's Chemical Analysis is shown in Table 2.

Table 1 Characteristics of black cotton soil

Sr. No.	Properties	Value
1	Liquid limit	73.88%
2	Plastic limit	40.39%
3	Shrinkage limit	84.64%
4	Plasticity index	33.09%
5	Consistency limit	1.23
6	Specific gravity	2.59
7	Maximum dry density	1.4048
8	Optimum moisture content	29.91

Table 2 Spent wash constituent amount's chemical analysis

Sr. No.	Details of constituent	Amount
I	pH	5.0
II	EC (Electric Conductivity) (dsm-l)	75
III	Calcium + Magnesium (m/l)	160
IV	Sodium (mg/l)	10.9
V	Potash (%)	1
VI	Zinc (ppm)	3.7
VII	Organic Carbon	133

4 Experimental Analysis

In this paper, various tests on soil were conducted discover the stabilization of sub base utilizing the spent wash. Different tests performed for checking the characteristics [9] of stabilized black cotton soil and murum are as follows,

- a. Plastic Limit Test.
- b. Liquid Limit Test.

4.1 Determination of Mastic Limit of Soil [IS: 2720 (Part 5)—1985 (Reaffirmed-2006)]

4.1.1 Required Equipment

- I. Porcelain evaporating dish with diameter approximately.
- II. A Spatula.
- III. A Container for determining the content of moisture.
- IV. Balance with (0.01 g) accuracy.
- V. An Oven.
- VI. 20 cm × 15 cm Ground glass plate.
- VII. A Rod with diameter 3 mm and length approx. 1 cm.

4.1.2 Sample Preparation

At first, take 30 g of air-dried soil from a systematically mixed sample by passing throughout 425 gm IS Sieve. Blend soil with purified water in porcelain evaporating dish and keep the soil mass for certain time (can be for 24 h) so that it will become mature.

4.1.3 Process

- A. An Approximately 8 g soil is required to be taken and further required to roll using fingers with about 80–90 strokes per minute, on a plate of glass for getting diameter of 3 mm.
- B. The diameter may be decreased lesser than 3 mm, without any cracks present in the thread, it indicates that the content of water content is higher than its plastic limit. Further, it is required to massage the soil for decreasing the content of the water content.
- C. The above process alternative rolling and kneading is needed to be repeated till the thread crumbled.
- D. Further, accumulate and preserve the crumbled soil pieces in a porcelain container.
- E. Then, repeat the above process for minimum two times by taking fresh samples of plastic soil every time.

The plastic limit test details are demonstrated in Figs. 2 and 3.

Fig. 2 Plastic limit test

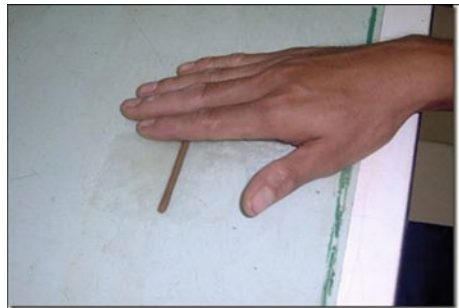


Fig. 3 Performing plastic limit test



4.2 Determination of Liquid Limit of Soil [IS: 2720 (Part 5)—1985-Reaffirmed-2006]

4.2.1 Equipment

- I. Casagrande's liquid limit device.
- II. A Casagrande's grooving tool.
- III. An Oven.
- IV. An evaporating dish.
- V. A spatula.
- VI. IS Sieve with size 425 gm.

4.2.2 Sample Preparation

- (1) At firsts-dry the sample of soil and then split the clods. Further, take away the organic matter such as brake pieces, roots of tree, etc.
- (2) Approximately 100 g of specimen passing throughout tlr 425 gm IS Sieve is blended systematically with the purified water and further keep for soaking for about 24 h.

4.2.3 Process

1. Put a portion of paste in a cup of liquid limit apparatus.
2. Level the blend for getting 1 cm as highest.
3. By holding the tool at right angles to the cup, demonstrate a grooving tool throughout a sample along the symmetrical axis of the cup.
4. Casagrande's apparatus (shown in Fig. 4) is employed for standard fine grained soil for cutting groove 2 mm broad at the base, 1110 broad at the peak and 8 mm deep.
5. Later than the soil pat was cut by a appropriate grooving tool, handle is rotated with a pace of 2 rps and the number of blows measured, until the two parts of soil sample come into contact approximately for a length of 10 mm.

Fig. 4 Casagrande's apparatus for liquid limit test



Fig. 5 Performing liquid limit test



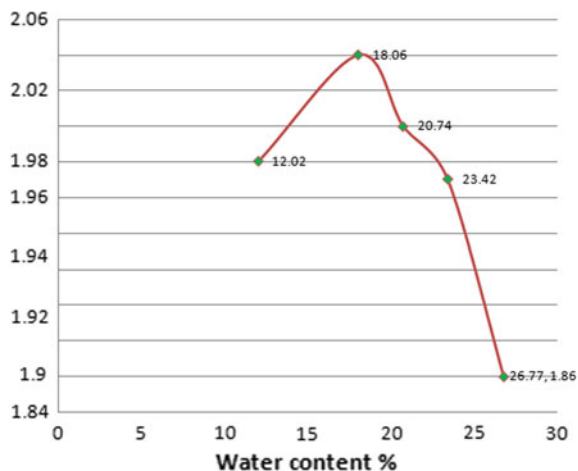
6. Take approx. of soil close groove and find out its water content.
7. Then, the soil other cup is transported to a dish including the paste of soil and blended uniformly later than adding up some amount of water. Repeat the tee.
8. By changing the soil water content and repeating the preceding operations, get at least 5 readings within range of 15–35 blows. Don't blend dry soil to modify its constancy.
9. The liquid limit (for test- refer Fig. 5) is decided by drawing a 'flow curve' on a semi-log graph, with no. of blows as abscissa (log scale) and the water content as ordinate and sketching the finest straight line through the plotted point.

5 Results and Discussion

The present moisture content defines tie plastic limit and uttered as a percentage of oven dried soil at a certain stage such that the soil can be rolled into the threads one eighth inch in a diameter devoid of soil breaking into pieces. This is also the moisture content of a solid at which a soil changes from a plastic State to a semi solid state.

Table 3 Soil + Spent wash mix (5%)

Sr. No.	Parameters	Test results				
1	Dry density (gm/cm ³)	1.98	2.04	2.0	1.97	1.86
2	Moisture content (%)	12.02	18.06	20.74	23.42	26.77

Fig. 6 OMC and MDD curve for 5% spent wash mix

The results of plastic limit for black cotton soil without and with 5% spent wash are presented in Table 3.

5.1 The Results for Different Percentage of Spent Wash with Black Cotton Soil Are as Follows

See Fig. 6.

When soil is added with the 5% spent wash, it observed that nature of dry density is increased up to some limit, further increase of water content decreases dry density. From above graph maximum dry density is 2.04 at optimum moisture content is 18.06% (Tables 4 and 5).

5.2 Liquid Limit of Soil

See Tables 6 and 7.

Table 4 Plastic limit test on black cotton soil with water

Sr. No.	Description	Trial 1	Trial 2	Trial 3
1	Container No.	2	5	6
2	Wt. of container + lid (W1)	63.77	71.53	75.86
3	Wt. of container + lid + wet sample (W2)	73.96	86.21	95.07
4	Wt. of container + lid + dry sample (W3)	70.99	82.00	89.48
5	Wt. of dry sample = (W3 – W1)	7.22	10.47	13.62
6	Wt. of water in the soil = (W2 – W3)	2.97	4.21	5.59
7	Water content (%) = [(W2 – W3)/(W3 – W1)] × 100	41.13	40.21	41.04
8	Average plastic limit (%)	40.79		

Table 5 Plastic limit test on black cotton soil with water +5% spent wash

Sr. No.	Description	Trial 1	Trial 2	Trial 3
1	Container No.	1	4	–
2	Wt. of container + lid (W1)	63.10	68.92	–
3	Wt. of container + lid + wet sample (W2)	74.22	78.56	–
4	Wt. of container + lid + dry sample (W3)	70.89	75.73	–
5	Wt. of dry sample = (W3 – W1)	7.79	6.81	–
6	Wt. of water in the soil = (W2 – W3)	3.33	2.83	–
7	Water content (%) = [(W2 – W3)/(W3 – W1)] × 100	42.75	41.55	–
8	Average plastic limit (%)	42.15		

Table 6 Liquid limit test on black cotton soil with water

Sr. No.	Determination number	Trial 1	Trial 2	Trial 3
1	Container number	3	4	7
2	Weight of container (W1)	72.27	63.18	119.60
3	Weight of container + wet soil (W2)	138.32	109.73	194.27
4	Weight of container + dry soil (W3)	110.85	89.95	162.20
5	Weight of water (Ww = W2 – W3)	27.47	19.78	32.07
6	Weight of dry soil (Ws = W3 – W1)	38.58	26.77	42.60
7	Moisture content (%) = (Ww/Ws)	71.20	73.88	75.28
8	No. of blows	34	25	22

5.3 Test Summary

See Table 8.

Table 7 Liquid limit test on black cotton soil with water +5% spent wash

Sr. No.	Determination number	Trial 1	Trial 2	Trial 3
1	Container number	2	3	6
2	Weight of container (W1)	63.75	74.21	75.85
3	Weight of container + wet soil (W2)	87.34	101.28	120.80
4	Weight of container + dry soil (W3)	78.40	90.70	102.27
5	Weight of water ($W_w = W_2 - W_3$)	8.94	10.58	18.53
6	Weight of dry soil ($W_s = W_3 - W_1$)	14.65	16.49	26.42
7	Moisture content (%) = (W_w/W_s)	61.02	64.16	70.13
8	No. of blows	28	26	20

Table 8 All test summary

Sr. No.	Description	Water	Water + Spent wash	
1	For Black cotton soil	Optimum moisture content	29.91	24.58
		Maximum dry density	1.4048	1.4769
		CBR	14.33	19.2
		Plasticity index	33.09	22.95
		Consistency limit	1.23	1.84
2	For Murum	Optimum moisture content	29.47	23.64
		Maximum dry density	1.4559	1.5731
		CBR	15.3	22.17

6 Conclusion

From the present experimental study, it can be concluded that 5% for stabilization of black cotton soil and murum respectively.

1. The plastic limit and liquid limit for black cotton soil increases with increases in percentage of spent wash.
2. Consistency limit increases for black cotton soil with increase in percentage of spent wash.
3. There is an appreciable improvement in the optimum moisture content and maximum dry density. For the black cotton soil and murum treated with industrial waste (spent wash).
4. Stabilization with 5% of spent wash with water was effective for black cotton soil.

References

1. Roy A (2014) Soil stabilization using rice husk ash and cement. *Int J Civ Eng Res* 5(1). ISSN 2278-3652
2. Mehta A, Parte K, Rupprai BS (2013) Stabilization of black cotton soil by Fly Ash. Special issue for National conference on recent advances in technology and management for integrated growth 2013 (RATMIG 2013)
3. Mathura BS (1999) The pollution of water resources due to rural industrial waste. Paper published by, 'Chemistry and Chemical Engineering Department of the Indian Institute of Technology', Delhi, pp 310–314
4. M'Ndegwa JK (2011) The effect of cane molasses on strength of expansive clay soil. *J Emerg Trends Eng Appl Sci (JETEAS)* 2(6):1034–1041. © Scholarlink Research Institute Journals
5. Arunvivek GK, Saravanakumar R, Senthilkumar M, Logesh Kumar M (2013) Experimental study on plasticizing effects of distillery Spent wash in concrete. *Int J Civ Struct Environ Infrastruct Eng Res Dev (IJCSEIERD)* 3(5). ISSN (P): 2249-6866; ISSN (E): 2249-7978
6. Adams Joe M, Maria Rajesh A (2015) Soil stabilization using industrial waste and lime. *Int J Sci Res Eng Technol (IJSRET)* 4(7). ISSN 2278 – 0882
7. Malhotra M, Nava S (2013) Stabilization of expansive soils using low cost materials. *Int J Eng Innov Technol (IJEIT)* 2(11)
8. Arockiadoss T (2012) Green cement for sustainable construction. United States patent application publication pub. No.: us 2012/0145043 a1 pub. Date: Jun. 14, 2012. *Sens Actuators A: Phys* 113(2):226–235 (2004)
9. Elias N (2015) Strength development of soft soil stabilized with waste paper sludge strength. *Int J Adv Technol Eng Sci* 03(01)

Mitigation of Power Capacitor Switching Transient by Using RCSTL



Prakash Kadam, Sagar Ghodake, and Santosh Kolekar

Abstract This paper presents the study of a new resistive capacitor switching transient limiter (RCSTL) to reduce the risk of losses due to the power capacitor switching transients. The RCSTL consist of the three limiting resistors, a three-phase full-bridge diode rectifier, a thyristor and a three-phase coupling transformer. The limiting resistor is in series with the capacitor bank, and the thyristor connected at dc side of the diode rectifier. During the process of the capacitor bank energizing, the thyristor is in OFF state. The coupling transformer's secondary side behaves as open circuit due to which high impedance with the transformer. Magnetic reactance remains parallel with the limiting resistor, which is in the series in the capacitor bank. Under such condition the limiting resistor restrains the capacitor switching transients. The control system triggers the thyristor, and the coupling transformer acts as a short circuit in a steady-state state. The limiting resistors bypassed by coupling transformer, and therefore RCSTL has no significant effect on the course. To describe the different operating mode of proposed RCSTL analytical analysis is performed.

Keywords Potential transformer · MATLAB software · Microcontroller Atmega-328L · Damping resistor 50 Ohm · 1000 W · SCR-BT16 · 16A · 800 V · C.T 30A ACS712

1 Introduction

Transients are power quality disturbances that involve high destructive magnitudes of current and voltage or even both. It may reach thousands of volts and amps even in low voltage systems. However, such phenomena only exist in a concise duration from less than 50 ns to as long as 50 ms. This is the shortest among power quality problems, hence, its name. Transients usually include abnormal frequencies, which could reach as high as 5 MHz. When a capacitor bank switched on, an unwanted, high-frequency inrush current and transient overvoltage may appear during the energizing

P. Kadam (✉) · S. Ghodake · S. Kolekar
Department of Electrical Engineering, Shri Vithal Education and Research Institute College of
Engineering Polytechnic, Pandharpur 413304, India
e-mail: pdk542@gmail.com

process. These transients lower the capacitor banks' lifetime and can damage the electromagnetic switches such as circuit breakers. Customer's electrical apparatus might be damaged during such phenomenon as well [1].

Since the surge current needs and effectively discharged, system grounding issues are must be considered in this method. These methods utilize power electronics components and comprise other control systems, which increase the complexity and the cost of the system and thus, they have less economic justification. In this context, we introduced two methods [2].

When a capacitor bank switched on, an unwanted, high-frequency inrush current and transient overvoltage may appear during the energizing process. These transients lower the capacitor banks' lifetime and can damage the electromagnetic switches such as circuit breakers. Customer's electrical apparatus might be damaged during such phenomenon as well. Since the surge current needs to discharge effectively, system grounding issues considered in this method, these methods utilize power electronics components and comprise different control systems [3].

2 Proposed System

The block diagram of the proposed system for mitigation power capacitor switching transient shown in Fig. 1.

The RCSTL operation can be divided into two different states as follows: (i) Limiting mode: During the energization process, since the capacitor bank initial voltage is zero, the positive terminal of the comparator is less than the negative terminal. Therefore, the comparator's output is equal to $-VCC$, grounded, as shown in

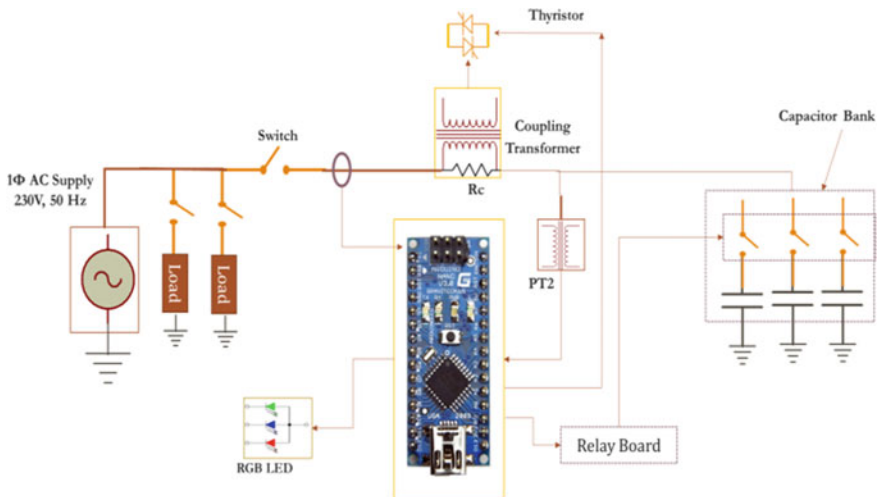


Fig. 1 Block Diagram of the proposed system

Fig. 2. In this condition, the thyristor is off, and the coupling transformer's secondary side is open. In other words, a high impedance of the core magnetizing reactance reflects at the primary side. Since this impedance is significantly greater than the limiting resistor, the line current flows through the limiting resistor. Consequently, the switching transient can considerably suppress by the limiting resistor. Figure 3 shows the RCSTL operation in the limitation mode. (ii) Steady-state mode: When the capacitor bank charged, the positive terminal of the comparator is greater than the negative terminal, and hence, the output of the Op-Amp is equal to +VCC [4].

The R-L circuit sends a pulse to the gate of the thyristor. Consequently, the thyristor turns on, and the secondary side of the coupling transformer acts as short-circuits. Thus a low impedance is reflected the primary side of the coupling transformer. This impedance is relevant to the coupling transformer's primary and secondary windings'

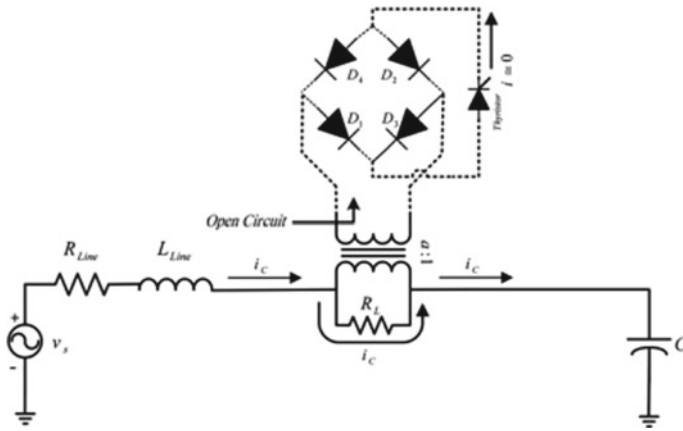


Fig. 2 RCSTL behaviour in the limiting mode

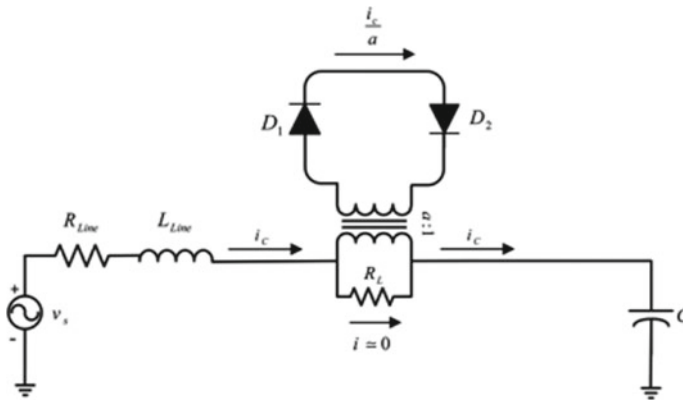


Fig. 3 RCSTL behaviour in steady-state mode

leakage inductances and resistances. The coupling transformer windings designed to have a few numbers of turns [4].

3 Components Selections

3.1 *Arduino Nano*

Arduino Nano is a surface-mount version with the integrated USB port. It is the smallest, complete, and breadboard-friendly. It comes with eight analogue input pins and onboard +5 V AREF. Nano doesn't have a power jack. The Nano is automatically sensing and switch to the higher positive voltage source of power [5].

Arduino Nano got a pin layout that works well with the Basic Stamp (TX, R.X., ATN, and GND on one top layer, power and ground on the other). This version comes with Atmel's 8-bit AVR ATmega328 microcontroller in a pint-sized TQFP (Thin Quad Flat Package) package having low power and high performance. Atmega328P offer more programming and data memory space. The Nano is designed and has manufactured by Gravitech.

3.2 *Thyristor TYN16-600CT*

Planar passivity Silicon Controlled Rectifier (SCR) SOT78 (TO-220AB) plastic package intended for use in applications requiring high thermal cycling performance and high junction temperature capability ($T_j(\max) = 150\text{ }^\circ\text{C}$).

High junction operating temperature capability High thermal cycling performance High voltage capability planar passivity for voltage ruggedness and reliability [5].
Type number: TYN16-600CT, Package version: SOT78, Package name: TO-220AB, VDRM [max] (V): 600, VRRM [max] (V): 600, IT(RMS) [max] (A): 16, IGT [max] (mA): 15, ITSM [max] 50 Hz (A): 180, T_j [max] ($^\circ\text{C}$): 150.

3.3 *Current Transformer*

In electrical engineering, a current transformer is in series for the measurement of electric current. Current transformers, together with voltage transformers (V.T.) potential transformers (P.T.), are known as instrument transformers. When the current in a circuit is too high to apply to measuring instruments directly, a current transformer produces a reduced current accurately proportional to the load current in the course, conveniently connected to measuring and recording devices. A current transformer also isolates the measuring instruments from a very high voltage in the monitored

circuit. Current transformers commonly used in metering and protective relays in the electrical power industry. For PCB mount, allows your microcontroller to monitor AC Current drawn on a line. Simple Current Transformer with a 1000/1 ratio. Measures current up to 10 A Max. [5]. Input current: 10 A, Output current: 10 mA.

3.4 Potential Transformer

Potential transformers are step-down transformers, also called voltage transformers with extremely accurate turn's ratio, and step-down voltage is measured with a standard measuring instrument. These transformers have a large number of primary turns and the smaller number of secondary turns.

A potential transformer typically expressed in primary to secondary voltage ratio. For example, a 600:120 P.T. would mean the voltage across secondary is 120 volts when the primary voltage is 600 volts.

In an ideal potential transformer or voltage transformer, when the rated burden gets connected across the secondary; the ratio of a transformer's primary and secondary voltages is equal to the turn's balance. The two-terminal voltages are distinct phase opposite to each other. But there must be an error in the voltage ratio and the phase angle between primary and secondary voltages in the actual transformer [5].

3.5 Relays

The relays can also be useful to switch high current, and high voltage A.C. and D.C. devices using An electromechanical relay contain an electromagnetic coil (right side of the image above) moves a metal arm to make and break an electrical connection. Electromechanical relays are useful for switching high current and A.C. devices that provide electrical isolation between the control signal and the load and are relatively low cost. No standard ground connection between the control signal and gear is needed. A typical digital logic GPIO output pin does not supply enough current to drive a relay coil directly. Logic signals for control.

When using logic signals to control a relay, a driver circuit can boost the current needed to energize the relay's electromagnetic coil. The load switches made on and off using the relay's metal contacts that move when a coil gets energized. Since the metal contacts touch, relays will have less voltage drop across the switch point than transistor circuits. They are sometimes used to switch regulated power supplies on and off. Relays tend to more resistant to a failure caused by high voltage surges than semiconductor devices [5].

3.6 Bridge Rectifier

A bridge rectifier is an arrangement of four or more diodes in a bridge circuit configuration which provides the same output polarity for either input polarity. The primary application of bridge rectifiers is converting an alternating current (A.C.) input into a direct current (D.C.) output. All electronic devices require direct current, so those bridge rectifiers installed inside the power supplies of almost all electronic equipment [5].

3.7 16x2 Characters LCD

LCD (Liquid Crystal Display) screen is an electronic display module and find a wide range of applications. They come in many sizes 8x1, 8x2, 10x2, 16x1, 16x2, 16x4, 20x2, 20x4, 24x2, 30x2, 32x2, 40x2 etc.

Many multinational companies like Philips Hitachi Panasonic make their particular kind of LED's are suitable in their products. All the LED's performs the same functions (display characters). Their programming is also the same, and they all have 14 pins (0–13) or 16 pins (0–15) [5].

3.8 Coupling Transformer

A coupling transformer is a transformer used to transfer electrical power from a source of alternating current (A.C.) power to some equipment or device while isolating the powered device from the power source, usually for safety reasons.

Isolation transformers provide galvanic isolation and are used to protect against electric shock, suppress electrical noise in sensitive devices, or transfer power between two circuits that must not be connected. A transformer sold for isolation is often built with superior insulation between primary and secondary and is specified to withstand a high voltage between windings. Coupling transformers block transmission of the D.C. component in signals from one circuit to the other but allow A.C. components to pass. Transformers with a ratio of 1 to 1 between the primary and secondary windings are often used to protect secondary circuits and individuals from electrical shocks between energized conductors and earth ground. Suitably designed coupling transformers block interference caused by ground loops [5].

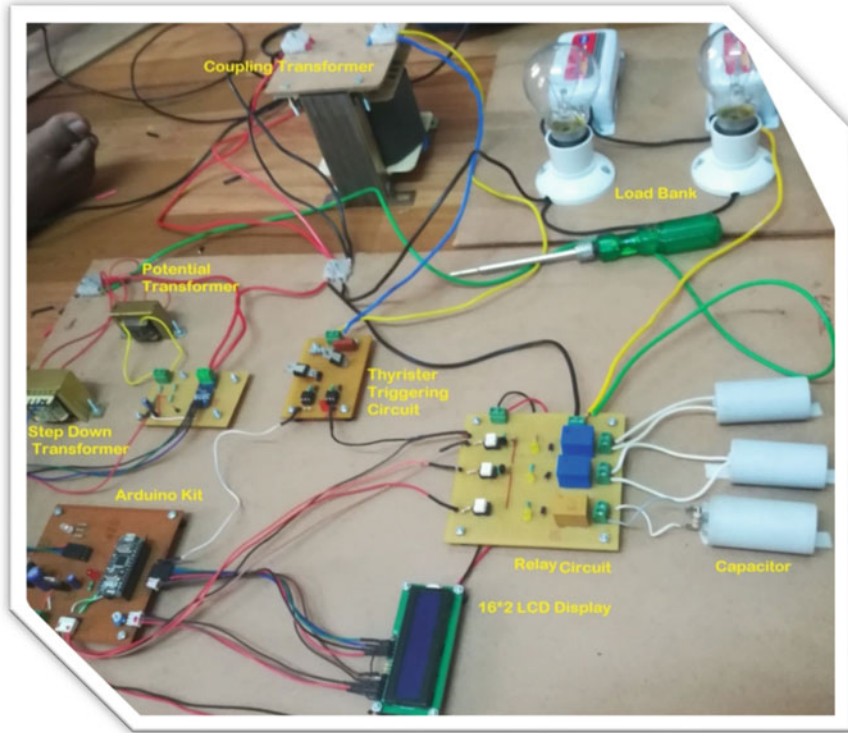


Fig. 4 Hardware setup of the proposed system

4 Results and Discussions

4.1 Hardware Setup and Output

The hardware set of the proposed system is shown in Fig. 4. The readings measured through digital meters for the transient current flowing through limiting resistor before and after by digital meters are shown in Fig. 5.

4.2 MATLAB Results

The MATLAB model for the proposed system is as shown in Fig. 6 [6]. The transient capacitor switching current and transient limited current are shown in Figs. 7 and 8.

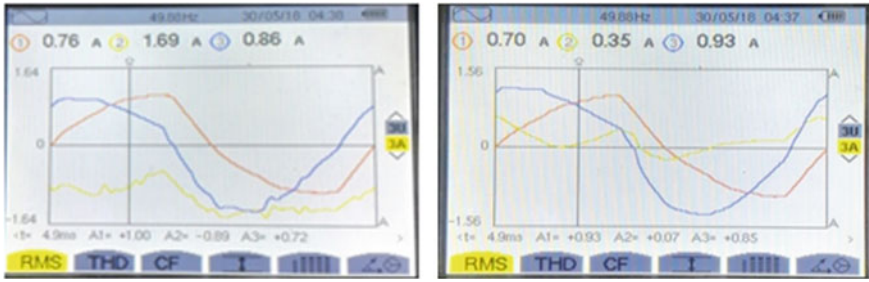


Fig. 5 Transient current flow through limiting resistor before and after limiting

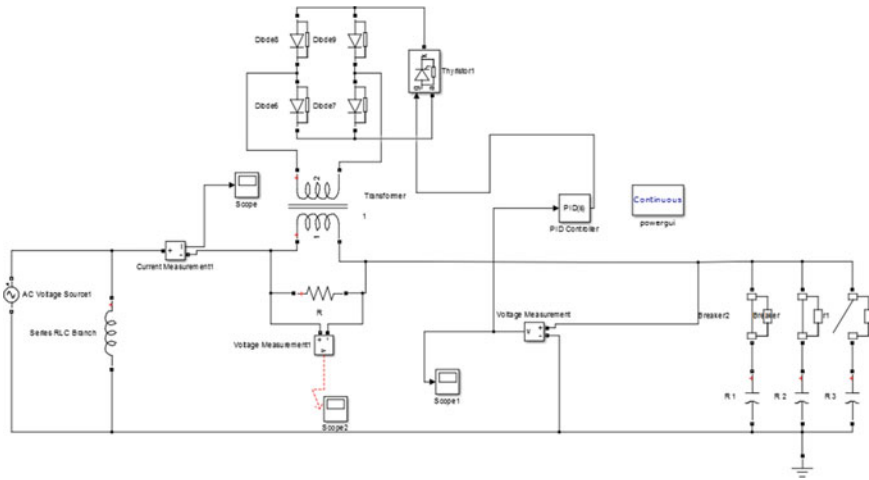


Fig. 6 MATLAB setup of the proposed system

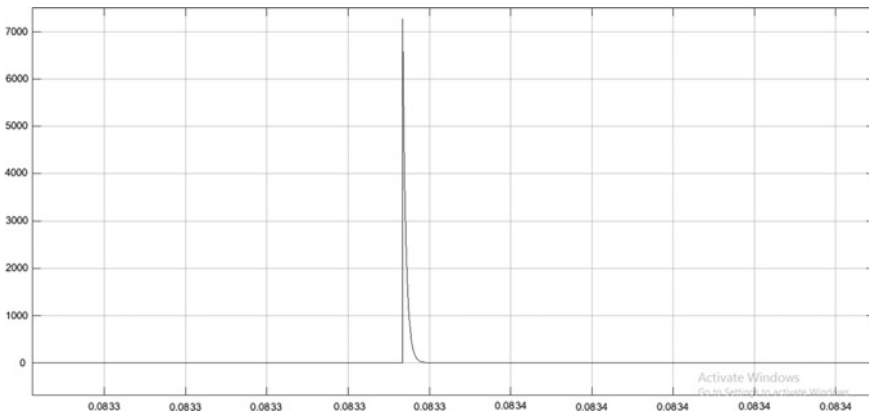


Fig. 7 Capacitor switching transient result

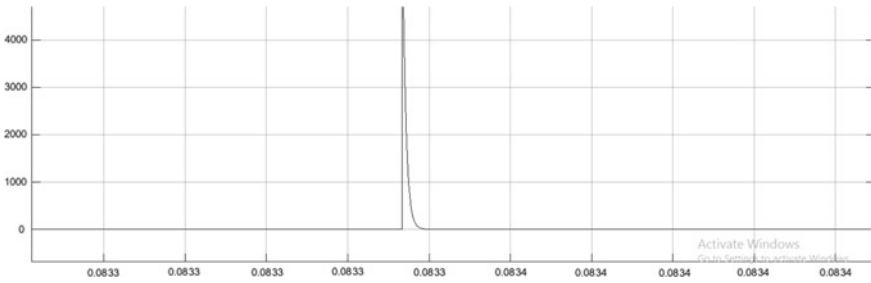


Fig. 8 Limited current transient result

5 Conclusion

A single-phase resistive, and capacitive switching transient limiter is proposed and designed correctly.

The RCSTL mitigates the switching transients by limiting resistors in series with the capacitor bank. In steady-state a thyristor installed at the secondary side of the coupling, the transformer switched on. Hence, the limiting resistors bypassed through the coupling transformer. The MATLAB Simulation results and Prototype hardware of products RCSTL results compared, and statistical results show the current limiting resistor is 1.69 A before bypassing it through coupling transformer. After ignoring it, it is 0.35 A.

References

1. Miller TJE (1982) Reactive power control in the electric system. John Wiley and Sons Inc. Press, pp 204–214
2. Garcia O, Cobos JA, Prieto R (2001) Power factor correction: a survey. In: 2001, IEEE Proc, PESC, vol 1, pp 8–13
3. IEEE Standard (2011) IEEE guide for the application of shunt power capacitors. IEEE Std 1036-2010 (Revision of IEEE Std 1036-1992), 17 January 2011, pp 1–88
4. Blooming TM, Carnovale DJ (2008) Capacitor application issues. IEEE Trans Ind Appl 44(4):1013–1026
5. Skeans DW (1995) Recent development in capacitor switching transient reduction. In: Proceedings of T&D World Expo. Substation Section, March 1995, pp 1–13
6. Chandwani H, Upadhyay CD, Vahora A (2013) Mitigation of switching overvoltage by application of surge arrester on capacitor bank. J Electric Energy Technol 4(2):37–45

Holistic Approach for Sustainable Technology

Performance of Conventional Concrete Integrated with RHA and GGBS As a Cementitious Material



Yogesh Tambe and Pravin Nemade

Abstract Sustainable development becomes necessary to protect our existing environmental conditions. The agricultural and metal industry produces various residues which are having prospective to be utilized as a supplementary for the cement. Rice husk ash (RHA) minimizes the carbon footprint emissions and achieves green effect in the existing environment. Ground Granulated Blast Furnace Slag (GGBS) is utilized as an alternative to the cement which helps in reducing CO₂ emissions and minimizes the consumption of non-renewable resources of lime stone. The corresponding study insights the usage of supplementary materials like GGBS and RHA into the production of concrete matrix. Also, the aim of this study is to achieve sustainable development incorporating the agricultural and industrial wastes into concrete industry, which can be beneficial for the nation and less the effect on natural ingredients on conventional concrete. The present study is carried out to optimize percentages of RHA and GGBS after the replacement to the cement such as 0, 5, 10, 15, 20, 25 and, 30% interval. Also, to evaluate the compression and split-tensile strength of conventional concrete with different ages of 7 and 28 days under normal curing conditions. The prediction model for compression strength is prepared using statistical analysis.

Keywords RHA · GGBS · Compressive strength · Split tensile strength · Prediction model

Y. Tambe (✉)

Department of Civil Engineering, Dr. D.Y. Patil Institute of Technology, Pimpri, Pune, India

e-mail: yhtcivil.svpm@gmail.com

Y. Tambe · P. Nemade

Savitribai Phule Pune University, Pune, Maharashtra, India

e-mail: pravin.nemade@gmail.com

P. Nemade

S. B. Patil College of Engineering, Indapur, Pune, India

1 Introduction

The primary building material is concrete consumed in large quantity by the construction industry. In construction industry due to urbanization the need of concrete has been increased rapidly therefore, the new supplementary materials for cement should be developed for the manufacturing of conventional concrete. The concrete industry is continually in search of advanced supplementary materials consisting pozzolanic properties with the purpose of minimizing the residues disposal problems [1]. Concrete has basically consisted of ingredients as cement, sand, aggregate and water. Primarily, cement is crucial component of concrete mix design. During cement manufacturing severe environmental pollution caused and leads to carbon dioxide (CO_2) emissions up to almost 6–8% [2]. The various environmental issues are resulted from cement production has become a worldwide major concern today. To achieve a sustainable development it is encouraged to minimize the use of such construction materials that can affect the environment [3]. The residual waste disposal of materials are poses serious problems to the environment [4, 5]. Due to increasing worldwide consciousness of environmental pollution and, increasing residues disposal issues, it is now challenge for researchers to design and produce cementitious materials with less clinkers and incorporating them into concrete for sustainable development. The various researchers concluded that, the conventional concrete properties can be improved with various supplementary binders namely, fly ash (FA), waste paper sludge (WPS), metakaolin (MK), silica fume (SF), ground granulated blast furnace slag (GGBFS) and rice husk ash (RHA) in quantified percentages as a replacement to the cement [6]. The use of a steel industrial residue, GGBS is effectively accepted binder for various cementitious applications which attains durability including high sulphate attack resistance, penetration of chlorides and, protection in case of alkali-silica reaction [7]. Also, RHA is an agricultural residue which is produced annually in large quantity. The fineness of RHA is more than cement and contains large amount of silica percentage which indicates such material is having potential for pozzolanic actions [8]. Nearly, 1 tonne of CO_2 is evolved in the production of each tone of Portland cement, which is harmful for environment so for that, it becomes essential to find out alternative materials which attain properties similar to cement [9]. Therefore, to tackle with these problem effective materials such as GGBS and RHA adopted in this research. This study experimentally investigates, the influence of RHA and GGBS as a partially substituted with cement on mechanical behavior of conventional concrete at 7 and 28 days.

2 Ingredients of Conventional Concrete

The ingredients used in the production of conventional concrete were 53 grade OPC with a specific gravity of 3.15, specific gravity of F.A. and C.A. is 2.65 and 2.7 with zone III respectively, water, GGBS and, RHA. The Fig. 1a, b represents the



Fig. 1 a GGBS and b RHA

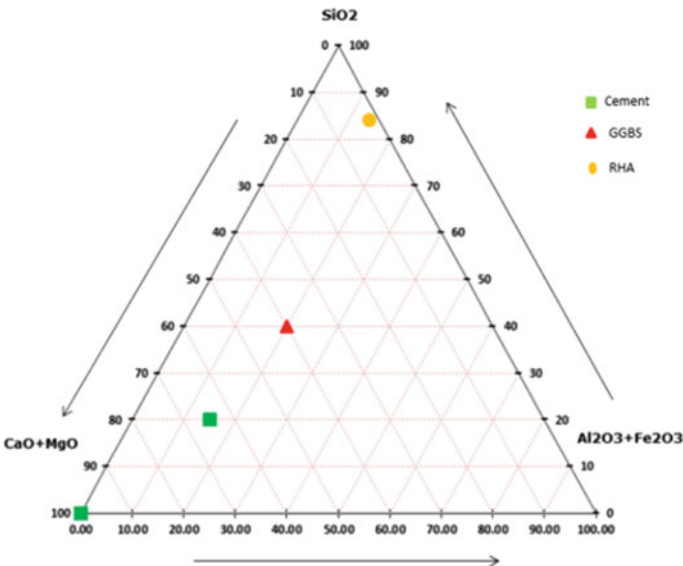


Fig. 2 Ternary diagram

residual waste materials adopted in this research. Figure 2 shows ternary diagram which represents the chemical compositions of the residual wastes utilised in concrete matrix. The chemical and physical properties of RHA and GGBS are represented in the following Tables 1 and 2.

3 Concrete Mixture Proportion

The IS code method (IS 10262-1982) has adopted for the trail mix designs. This method consists of determining the water content and fine aggregates percentage

Table 1 Comparison of chemical properties of RHA and GGBS with cement

Components	Cement	RHA	GGBS
Sio ₂	±19.65	±83.87	±33.46
Al ₂ O ₃	±5.25	±2.35	±15.19
Fe ₂ O ₃	±3.68		
CaO	±62.9	±0.2	±25.08
MgO	±2.54	±0.52	±7.97
SO ₃	±2.72	±0.11	±0.85
K ₂ O	±0.9	±0.13	±1.31
Na ₂ O	±0.25	±0.16	±1.32

Table 2 Comparison of physical characteristics of RHA and GGBS

Properties	RHA	GGBS
Colour	Blackish white	White
Shape	Irregular	Spherical
Specific gravity	2.1–2.33	2.6–2.77
Bulk density (kg/m ³)	22	1040–1090
Appearance	Powder form	Powder form

corresponding to nominal size of aggregate for the various values of workability w/c ratios and the grading of F.A. (Tables 3 and 4).

1. 28 days characteristic compressive strength = 20 MPa
2. Max. Agg size. = 20 mm

Table 3 Proportion of design mix for M-20 grade

Mix M-20	Water	Cement	F.A.	C.A.
By weight (kg/m ³)	186	413.33	674.6	1121.84
Proportion	0.45	1	1.63	2.71

Table 4 Mixes for different proportion of RHA/GGBS for 1 m³

Replacement percentage (%)	OPC (kg)	RHA/GGBS (kg)	F.A. (kg)	C.A. (kg)	Water (l)
0	413.33	0	674.60	1121.84	186
5	392.64	20.69	674.60	1121.84	186
10	371.95	41.33	674.60	1121.84	186
15	351.26	62.02	674.60	1121.84	186
20	330.62	82.33	674.60	1121.84	186
25	309.93	103.02	674.60	1121.84	186
30	289.31	123.71	674.60	1121.84	186

3. Deg. of quality = Good
4. Condition = Mild exposure
5. Method of concrete mixing = Hand mixing
6. Sp. gravity OPC grade 53 = 3.15
7. Sp. gravity of C.A. = 2.7
8. Sp. gravity of F.A. = 2.65 (Zone-III)

Mix design calculations

1. Target mean strength—

$$F_t = F_{ck} + KS$$

$$= 20 + 1.65 \times 4$$

$$= 26.60 \text{ N/mm}^2$$
2. W/C ratio
 Based on experience and trials
 Select W/C = 0.45
 Max. W/C ratio = 0.55
 Selected W/C ratio = 0.45
3. Water content
 (Ref. T-5 IS456-2000 page no. 20)
 Degree of workability – compaction factor = 0.8
 Slump = 25
 Max. C.A. size = 20 mm
 Water quantity = 186 kg/m³
4. Applying correction for water content
 Correct quantity of water = 191.5 kg/m³
5. Cement quantity
 W/C ratio = 0.45
 Cement = 186/0.45 = 413.33 kg/m³
 From IS recommendations, min. cement content = 220 kg/m³ (mild exposure condition)
6. Proportion of volume of C.A. and F.A. for zone 3
 Ref. T-3 Page No. 3 IS 10262 – 2009
 Size of agg. 20 mm with zone 3 of C.A & F.A. = 0.62
 Vol. of C.A. per unit Vol. = 0.62
 Vol. of F.A. = 1 – 0.62 = 0.38
 - (a) Vol. of concrete = 1 m³
 - (b) Vol. of cement = 413.33/3.15 × 1000 = 0.13 m³
 - (c) Vol. of water = 186/1 × 1000 = 0.186 m³
 - (d) Vol. of [C.A. + F.A.] = a – [b + c] = 1 – [0.1312 + 0.186] = 0.6828 m³
 - (e) Mass of C.A. = 0.6828 × 2.65 × 0.62 × 1000 = 1121.84 kg
 - (f) Mass of F.A. = 0.6828 × 2.7 × 0.38 × 1000 = 674.60 kg

Fig. 3 Compression test on cube



4 Experimental Procedure

4.1 Compressive Strength of Concrete

The investigation was carried out for concrete grade of M-20 mix proportion with 0, 5, 10, 15, 20, 25, 30% of cement partially replaced with RHA and GGBS. The 78 number of cubic samples of size 150 mm were casted and tested using CTM to estimate the strength of matrix in compression at 7 and 28 days. To achieve uniform consistency all the concrete ingredients thoroughly mixed in concrete mixer. The cube specimen was compacted layer by layer properly while filling in mould. The casted specimens were separated from the mould after 24 h and kept in the water tank for the period of 7 and 28 days for curing under normal temperature. The compression testing was performed using CTM having 2000 KN capacity refer Fig. 3. The gradually uniform loading was applied on the specimen until the failure takes place. The testing specimen was kept horizontal in between loading planes of the CTM and the application of loading is uniform without causing disturbance until the failure occurs.

4.2 Split-Tensile Strength of Concrete

The cylinder specimens 78 in number of size 150 mm in diameter and 300 mm height with M-20 grade of concrete were casted to evaluate the split-tensile strength

Fig. 4 Testing on cylindrical sample



of conventional concrete. In a concrete mixer uniform consistency of concrete is achieved by thoroughly mixing of concrete ingredients. During casting of cylinder specimens properly compaction of concrete was carried out and specimens removed from the mould after 24 h of casting. For curing purpose the casted cylindrical samples were kept in water under normal temperature for a period of 7 and 28 days. The sample was kept horizontal in between the surfaces of loading of the CTM along with wooden strips placed at top and bottom of the specimen shown in Fig. 4. The application of loading was gradual without vibrations until the failure of the sample takes place.

5 Result and Discussion

The mechanical properties of conventional concrete in hardened state were discussed in accordance with compressive strength and split-tensile strength for the period of 7 and 28 days. The detailed discussion on compressive and split-tensile strength of concrete matrix is as follows.

5.1 Compressive Strength

The most crucial characteristic of concrete matrix is strength in compression which measures the amount of load sustained by the concrete structure before failure. The following figures show that, the compression strength of concrete cube specimens at the age of 7 and 28 days with respect to replacement percentage of cement 5, 10, 15, 20, 25, and 30% of RHA and GGBS mix proportion. The trend line equations for 7 and 28 days compressive strength represent better performance with the values of R^2 nearly equal to 0.98 as a regression coefficient.

The compressive strength testing results were shown in Figs. 5 and 6. The obtained results conclude that, the increment in the RHA percentage as replacement to the cement causes reduction in compression strength of concrete matrix. Figures 5 and 6 shows that, the RHA of 10% as a replacement to the cement is optimum and appreciable in terms of compressive strength. In case of RHA as the age of concrete increases, the compressive strength is reduced up to nearly 15%. But in case of GGBS the results are different, which shows increasing percent of GGBS as replacement to

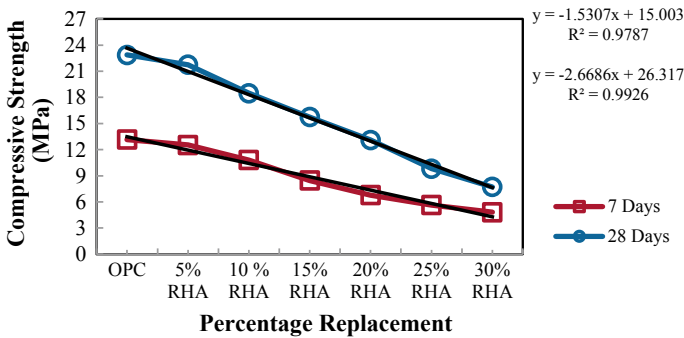


Fig. 5 Compressive strength versus Percentage replacement with RHA

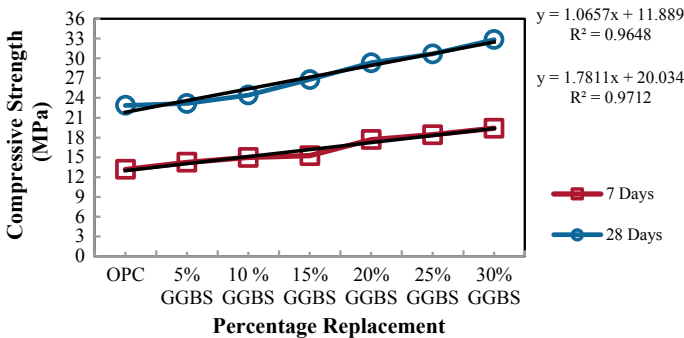


Fig. 6 Compressive strength versus Percentage replacement with GGBS

the cement increases strength of concrete in compression. The cement replacement up to 30% with GGBS is optimum and acceptable with respect to concrete compression strength. The compression strength is nearly increased up to 6–7% with increase in the age of concrete matrix. The developed model is used for the prediction of the concrete matrix compression strength containing supplementary cementitious materials (SCM) provides a useful design tool and, promotes environmental friendly concrete.

5.1.1 Binder Reactivity Effects with SCM on Strength of Concrete Matrix in Compression

The ordinary Portland cement and SCMs consists varying chemical compositions because of variation in their sources and types [10]. The above ternary diagram represents the chemical composition range based on percentage weight ratio for various types of binders. The diagram compares the chemical composition of SCMs with OPC and highlights the difference between compositions. When modeling the mechanical properties or proportioning design mix for conventional concrete, it becomes necessary to study the reactivity of binder materials. Practically, based on the experimental studies it can be observed that, the oxides of CaO, SiO₂, Al₂O₃, and Fe₂O₃ mainly contributes in the process of hydration for OPC [11–14]. The GGBS consists of comparable chemical composition with OPC and primarily contains CaO, SiO₂, Al₂O₃, and Fe₂O₃ oxides allowing GGBS with its self-binding properties [15].

5.1.2 Reactivity Assessment for SCMs

The reactivity for single SCM was effectively quantified considering following indices: Reactivity Modulus (RM), Silica Modulus (SM) and, Alumina Modulus (AM) represented in the following Eqs. (1), (2) and (3) respectively [15–18].

$$RM = \frac{[CaO + MgO + Al_2O_3]}{SiO_2} \quad (1)$$

$$SM = \frac{SiO_2}{[Al_2O_3 + Fe_2O_3]} \quad (2)$$

$$AM = \frac{Al_2O_3}{Fe_2O_3} \quad (3)$$

It can be noted that, the index RM evaluates the self-binding characteristics and AM and SM characterizes the pozzolanic reactivity of SCMs. The compressive strength of concrete (Fc) increases with an increase in the binder reactivity and minimizes with rise in the w/b ratio utilizes for the mix. The reactivity modulus of overall binder estimated by using following Eqs. (4)–(6);

Table 5 Results of compressive strength

SCM	Average compressive strength (28 days)	
	Experiment	Model
RHA	15.64	14.62
GGBS	27.15	26.13

$$RM = \frac{\sum_{k=1}^n [RM_k w]}{100} \tag{4}$$

$$SM = \frac{\sum_{k=1}^n [SM_K w]}{100} \tag{5}$$

$$AM = \frac{\sum_{k=1}^n [AM_K w]}{100} \tag{6}$$

where, RM_k and w is the modulus of hydration for each binder and, its weight. The combination of modulus showing pozzolanic and hydraulic behavior with w/b factor represents reactivity index (γ) as follows:

$$\gamma = \frac{[W_1 RM + W_2 AM + W_3 SM]}{(w/b)} \tag{7}$$

where, W_1, W_2 and W_3 are empirical constants with values 1.796, 0.002 and, 0.011 respectively. Depending on statistical analysis, the correlation uniting reactivity indices and the strength of concrete in compression including SCMs shown below [18];

$$F_c = U \cdot \gamma^V \tag{8}$$

The values of U and V are considered as empirical constants used in the above Eq. (8).

$U_{RHA} = 14.1$ and $V_{RHA} = -1.2$ and $U_{GGBS} = 5.3$ and $V_{GGBS} = 1$. The present study concludes that, the strength of concrete matrix in compression incorporated with SCMs is not only dependent on w/b factor of mix but also, based on their binder’s reactivity (Table 5).

5.2 Split Tensile Strength

The split-tensile strength is an important property of conventional concrete because concrete structures are highly vulnerable to tensile cracking due to various kinds of effects and applied loading. The following graphs shows that, the split-tension strength for cubes at 7 and 28 days strength with respect to 0, 5, 10, 15, 20, 25, 30% of RHA and GGBS mix proportion. The trend line equations for 7 and 28 days

split-tensile strength represent better performance with the values of R^2 nearly equal to 0.96 as a regression coefficient.

The obtained results of split-tension test on concrete samples with RHA and GGBS as partially replaced with cement were shown in Figs. 7 and 8. The split tensile strength of conventional concrete whose cement is replaced by GGBS reduces with rise in percentage GGBS for 28 days, while in case of 7 days for concrete matrix the split tensile strength attains maximum values with rise in replacement percentages of GGBS. In case of RHA, as the age of concrete increases the split tensile strength is reduced consistently. The concrete becomes harsh with increase in percentage replacement of cement using RHA and GGBS. Based on the experimental investigations, it was concluded that, to maintain concrete strength and workability the most optimized percentages as replacement to the cement by GGBS is 30% and in case of RHA is 10%.

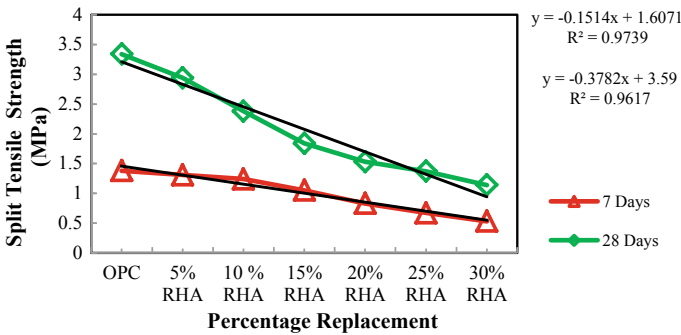


Fig. 7 Split-tensile strength versus Percentage replacement with RHA

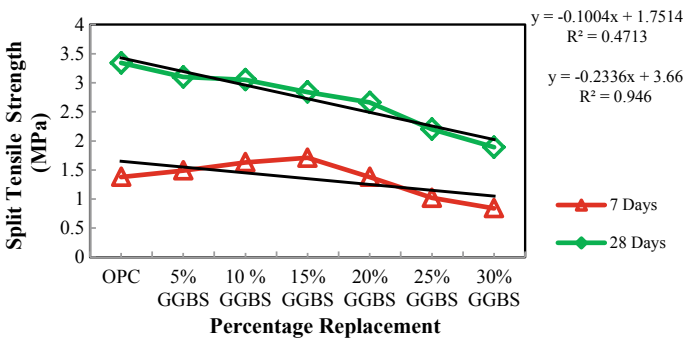


Fig. 8 Split-tensile strength versus Percentage replacement with GGBS

6 Conclusions

Depending on the experimental study on conventional concrete with RHA and GGBS, the notable conclusions are reported that, the GGBS and RHA are the appropriate cement replacement materials in order to safeguard environment from bitter effects of cement manufacturing process. The cement replacement using GGBS not only accelerates the compression strength but also, reduces the cement content which diminishes emission of CO₂. The strength of concrete in compression attains higher values with the addition of GGBS up to certain extent but in case of addition of RHA, it is discovered that, compressive strength of concrete decreases. The performance of the concrete is exceptionally magnificent in case of compressive and split tensile strength of concrete. However, beyond 30% of replacement of GGBS and 10% of replacement of RHA the strength decreases as well as performance of concrete dwindles. The experimental study represents that, most optimized percentages of replacement for cement by GGBS as 30% and in case of RHA, it is found to be 10%. Therefore, the partially replacement of ordinary Portland cement using GGBS & RHA is not only economical but also, makes provision for environmental friendly disposal of agricultural and an industrial residue which attains sustainable development in concrete industry. Thus, the incorporation of RHA and GGBS in concrete matrix proved suitable for sustainable development, as a result solving the adverse impacts during cement preparation like emission of CO₂, consumption of resources, economy and, problems regarding waste disposal for agricultural and industrial wastes to a certain limit. The developed model is used for the prediction of the concrete matrix compression strength containing supplementary cementitious materials (SCM) provides a useful design tool and, promotes green concrete applications and contributing to experimental friendliness.

Acknowledgements The authors would like to express deepest appreciation for getting the support and motivation for this research from Dr. D.Y. Patil Institute of Technology, Pimpri, Savitribai Phule Pune University, Pune.

References

1. Gadpalliwar SK, Deotale RS, Narde AR (2014) To study the partial replacement of cement by GGBS and RHA and natural sand by quarry sand in concrete. *IOSR J Mech Civ Eng* 2(2):69–77
2. Veena K, Pradeep Kumar BK, Gyanen T (2017) Sustainable studies on structural performance and thermal cycle on cement concrete pavement with using GGBS. *Int J Adv Sci Res Eng* 3(1):392–398
3. Tadepalli DB, Etaveni M, Adil SE (2016) Strength and workability Properties of GGBS and RHA. *Int J Eng Res Gen Sci* 4(2):157–161
4. Aprianti E, Shafigh P, Bahri S, Nodeh J (2015) Supplementary cementitious materials origin from agricultural wastes – a review. *Constr Build Mater* 74:176–187
5. Madurwar MV, Ralegaonkar RV, Mandavgane SA (2013) Application of agro-waste for sustainable construction materials: a review. *Constr Build Mater* 38:872–878

6. Tambe YH, Nemade PD (2020) Efficacy of cementing materials in proportioning and optimization of foamed concrete design mix-a review. *J Seybold Rep* 15(9):4148–4162
7. Vinod V, Susheel B, Mahindra K (2017) Study on strength properties of concrete by partially replacing cement with GGBS. *Int J Civ Eng Technol* 8(4):2044–2048. Article ID IJCIET1804233
8. Shashikant D (2016) Replacement material in concrete: review. *J Res Sci Technol* 3
9. Mokashi SC, Daule SN (2017) Study of partial replacement by GGBS and RHA and natural sand by quarry in sand concrete. *IRJET* 4(3):2618–2623
10. Xie T, Visintin P (2018) A unified approach for mix design of concrete containing supplementary cementitious materials based on reactivity moduli. *J Clean Prod* 203:68–82. <https://doi.org/10.1016/j.jclepro.2018.08.254>
11. Alam M, Singh G, Bahaa B, Sahar M (2013) Acceptability of demolished concrete waste aggregate in making high strength self-compacting concrete. *Int J Civ Eng* 2(3):1–12
12. Alnahhal MF, Alengaram UJ, Jumaat MZ, Alqedra MA, Mo KH, Sumesh M (2017) Evaluation of industrial by-products as sustainable pozzolanic materials in recycled aggregate concrete. *Sustainability* 9(5):767. <https://doi.org/10.3390/su9050767>
13. Ann KY, Moon H, Kim Y, Ryou, J (2008) Durability of recycled aggregate concrete using pozzolanic materials. *Waste Manag* 28(6), 993–999. <https://doi.org/10.1016/j.wasman.2007.03.003>
14. Aprianti E, Shafiqh P, Bahri S, Farahani JN (2015) Supplementary cementitious materials origin from agricultural wastes a review. *Constr Build Mater* 74:176–187. <https://doi.org/10.1016/j.conbuildmat.2014.10.010>
15. Behim M, Beddar M, Clastres P (2013) Reactivity of granulated blast furnace slag. *Slovak J Civ Eng* 21(2):7–14
16. Binici H, Temiz H (2007) The effect of fineness on the properties of the blended cements incorporating ground granulated blast furnace slag and ground basaltic pumice. *Constr Build Mater* 21(5):1122–1128. <https://doi.org/10.1016/j.conbuildmat.2005.11.005>
17. Darquennes A, Espion B, Staquet S (2013) How to assess the hydration of slag cement concretes? *Constr Build Mater* 40:1012–1020. <https://doi.org/10.1016/j.conbuildmat.2012.09.087>
18. Xie T, Visintin P (2018) A unified approach for mix design of concrete containing supplementary cementitious materials based on reactivity moduli. *J Clean Prod.* <https://doi.org/10.1016/j.jclepro.2018.08.254>

Assessment of the Extent of ISO-QMS Implementation and Scope for Six Sigma—A Case from the Indian Textile Industry



S. S. More and B. P. Ronge

Abstract The ISO quality management system (ISO-QMS) has proven its application in Manufacturing and Service industry. However, ISO certification of the Indian Textile Industry has shown a marginal level impact on productivity improvement. This study was focused on evaluation of the ISO-QMS implementation and detecting scope for Six Sigma as a Continuous Improvement (CI) Quality Tool and Technique (QTT) in the textile sector. Questionnaire survey methodology has applied in this study. The respondents expressed a high level of importance for ISO-QMS implementation but a low satisfaction level for its impact. The findings of surveyed textile industries pointed-out that, ISO-QMS was not delivering significant consequences and also neglecting the use of most crucial CI QTTs like Six Sigma for improvement. The trend of results depicted an immense need for applying QTTs such as Six Sigma along with the existent ISO-QMS of an enterprise to improve overall productivity.

Keywords ISO-QMS · CI · QTT · Six sigma · Indian textile industry

1 Introduction

The foundation of the industrial revolution in India was laid by the Textile Industry. The Indian textile industry is highly localized in the western part of the country at Ahmedabad and Mumbai, and also exists in other regions along-with Calcutta, Kanpur, Indore, Coimbatore and Solapur. Textile Industries in India holds a prominent place in the economy. Its contribution is 4% to GDP, 14% to total industrial production, and 15% of the total export. It also provides the second-largest employment sector. World Trade Organization (WTO) regime created opportunities in the world market but also resulted in a cut-throat competition.

The observations indicated that the Indian Textile Industry is lagging in performance and competitiveness when compared with competitor countries.

S. S. More (✉) · B. P. Ronge
SVERI's College of Engineering, Pandharpur, India
e-mail: ssmore81@gmail.com

Many of the Indian textile industries had ISO certification. The reasons for ISO certification were found as mandatory for export and the government policy. Ideally, the objectives of ISO-QMS implementation were to establish standard procedures, guidelines, documentation procedure for production data in order to improve productivity, product quality, to achieve a high level of customer satisfaction, and improvement in profit. But the literature showed that the adoption of ISO-QMS for ISO certification was failed to achieve significant improvement in productivity. ISO certified Indian Textile Industries were experiencing only a marginal level impact on productivity improvement and imparting the burden of documentation on a large scale.

The objective of this study is to investigate the impact of ISO-QMS in different leading subsectors of the Indian Textile Industry in terms of Motives, Benefits, Development of ISO-QMS implementation and to find scope for different Quality Management Tools & Techniques. The questionnaire survey method was used for fact realisation.

In this study, a questionnaire was designed by conforming to the guidelines by Dillman (1991). This questionnaire contained two sections: the first section collected demographic information of the respondent, and the second section had extensive questions in four parts to achieve the study objectives. The group of respondents consists of ISO-QMS certified textile industries from Solapur District along with other ISO-QMS certified textile industries from the Maharashtra State.

2 Literature Review

Last 15 years show considerable growth in the adoption of ISO 9001 certification, globally [1]. In the Indian textile industry ISO standard-based Quality Management System was extensively implemented in recent years. As per the Textiles Committee, currently 286 Units procured certification of ISO-9000, 19 units of ISO-14000, 16 units of SA-8000 and 09 units of OHSAS-18000. Out of these ISO Certified Textile Manufacturing Organizations, 25 were located in Maharashtra, and 9 were sited at SOLAPUR [2]. Results of a case study by R. R. Gorakhia (1997) showed a marginal level of improvement after implementation of ISO-QMS [3]. It was extensively agreed that implementation of QMS is possible in any organization despite of its type and size. In spite of benefits, due to the expenses of implementation and challenges in maintenance, small and medium sized enterprises (SMEs) in the Textile Industry show less concern towards the implementation of ISO-QMS. Developed countries have highly accepted and implemented ISO-QMS whereas in a developing country like India a huge gap was seen in the acceptance and true implementation [4]. Towers and McLoughlin (2005) carried a survey at a textile SMEs situated in UK to analyze the effect of QMS implementation on the cost of a product, quality and productivity, this study showed that above 67% of the SMEs carefully thought about QMS as a developer of raised customer satisfaction, quality awareness and organizations teamwork [5].

Further, the effectiveness of ISO-QMS could be enhanced by integrating different tools and techniques. In manufacturing industries, the concept of integrating ISO-QMS with other Continuous Improvement (CI) Quality Tool and Technique (QTT) like Six Sigma, Lean Six Sigma and Lean manufacturing is widely used to enhance its effectiveness [6–9]. A case study conducted by Hussain (2014) for exploring the Six Sigma application has shown improvement in the process sigma level by resulting increased profit worth \$26,000 per month [10]. Hayajneh (2014), applied “DMAIC” (Define-Measure-Analyze-Improve-Control) tools based on Six Sigma methodology to minimise production-related defects in manufacturing of textiles at Jordan, resulting in reduced rejection from 7.7 to 2% [11]. Atwell (2010) conducted a case study in an apparel manufacturing plant, he found that it is impossible to manufacture to 100% specification. A study exhibited that an improvement of just a single Process Sigma level resulted in savings of \$10,000 to \$20,000 [12]. Krishnaraj (2009), found that Six Sigma is capable of analyzing a huge amount of data and deliver the right information for identifying and validating root causes to make better factual decisions for business [13].

R. Senthil Kumar and S. Sundaresan (2010) [14], implemented Six Sigma methodology in an apparel manufacturing industry. He stated the fact that variation in specifications of every garment is inherent in the manufacturing and is unavoidable. Pfeifer et al. (2004) integrated Six Sigma to ISO-QMS and revealed that both philosophies could be used as management techniques to succeed [15]. Dey (2008) compared Six Sigma with ISO 9001 to find out the relationship between them, and found that Six Sigma can fulfill the requirements of eight ISO principles if introduced properly [16].

All these studies suggest for developing an integrated model to use tools like Six Sigma for improving ISO-QMS effectiveness. Hence, the Indian Textile Industry needed to go beyond ISO-QMS and utilize different proven tools and techniques like Six Sigma. However, the literature review does not provide any evidence of a comprehensive study for assessing the extent of the impact of ISO-QMS and also Scope for Six Sigma.

The objective of the present study was an assessment of the extent of the ISO-QMS implementation and identification of Scope for Six Sigma. Hence, an investigation study carried out in the weaving sector of Indian Textile Industry for assessment of the four dimensions given below:

- Motives for ISO-QMS
- Benefits of ISO-QMS
- Development of ISO-QMS implementation
- Scope for different Quality Management Tools & Techniques.

3 Research Methodology

In order to reach the objectives of the research, a survey questionnaire was developed and used for collecting data from the Textile Industries of Maharashtra State. The questionnaire had two sections: the demographic information of respondents was

Table 1 Respondent's demographics

Characteristics	Category	Frequency	Percentage
Location	Mumbai	8	29
	Nagpur	8	29
	Sangli	2	8
	Solapur	11	40
Gender	Male	24	86
	Female	5	18
Designation	General Manager/Senior Manager	6	22
	Deputy Manager	9	33
	Assistant manager/Officer/Trainee engineer	14	40
Department	QA/QC/Industrial Engineering	7	25
	Marketing/Production	14	50
	/Merchandising	8	29
Industry Sector	Weaving	10	36
Type	Spinning, Ginning & Pressing	8	29
	Home Textiles, Handloom, & Madeups	6	22
	Composite (Knitting & Processing)	2	8
	Trading, Business Operations	3	11
Total Respondents	29		

gathered in the first section (Table 1), the second section had extensive questions in four parts related to the objectives of the study. About 58 Textile Industries from Maharashtra State were selected for data collection. Around 58 questionnaires were circulated, out of which 34 were responded and after scrutiny 29 were considered for further analysis. Response rate of 50% was observed. A custom made analysis programme in MS Excel was used to analyse data obtained.

Goodness-of-Fit (GOF) and reliability of dataset were assessed before analyzing the results of survey. GOF was checked by carrying out the chi-square (χ^2) test and reliability of data by Cronbach's α test. The Statistical tool ANOVA was applied to test the null hypothesis. Statistics of χ^2 test for variables is shown in Table 2, with respect to significant p-values. As shown in Table 3, a value of 0.80 is obtained for Cronbach's α indicates acceptable reliability and internal consistency of the dataset.

4 Results and Discussion

The findings of the survey concerning the objective of the study, are described in four sections comprising four dimensions viz, Motives for ISO-QMS, Benefits of

Table 2 Results of Chi-square (χ^2) test

Test Statistics	Chi-Square (χ^2)	df	p-value
Top management decision	7.85	1	0.003
Improving productivity	56.18	3	0.000
Maintaining and/or increasing market share	8.56	1	0.003
Improvement in image and reputation	28.15	1	0.000
Improved profitability	10.02	1	0.002
Increased customer satisfaction	39.82	1	0.000
Improved product/process/service quality	39.82	1	0.000
ISO-QMS uses time and resources of company	53.89	1	0.042
ISO-QMS creates unnecessary burden	8.94	1	0.003
Scope for Six Sigma	88.92	3	0.000
Scope for Quality cost analysis	39.92	1	0.000
Scope Quality circle	39.15	2	0.000

Table 3 Results of Cronbach's α test

Cronbach's alpha	N of items
0.800	56

ISO-QMS, Development of ISO-QMS implementation, Scope for different Quality Management Tools & Techniques.

Each dimension has different attributes. The dimension Motives for ISO-QMS possess 11 attributes, Benefits of ISO-QMS possess 17 attributes, Development of ISO-QMS implementation possess 16 attributes, and Scope for different Quality Management Tools & Techniques possesses 12 attributes. All these 56 attributes were assessed by understanding responses from the questionnaire survey.

4.1 Hypothesis Testing

A single factor ANOVA was applied in this study; one can use either 'F' test or 'p' test or both methods.

Table 4 ANOVA of satisfaction level of motives/reasons for iso implementation

Source of variation	SS	df	MS	F	P-value	F critical
Between groups	11.2727	8	1.4090	4.4711	0.00013	2.04298
Within groups	28.3636	90	0.31515			
Total	39.6363	98				

Table 5 Mean and rank values of significant attributes

Attribute No.	Attributes	Satisfaction mean	Importance mean
A1	Top management decision	2.78	3.56
A2	Improving productivity	1.45	3.45
A4	Maintaining and/or increasing market share	1.67	3
A12	Improvement in image and reputation	1.89	3.12
A13	Improved profitability	1.78	3.56
A14	Increased customer satisfaction	2.78	4
A16	Improved product/process/service quality	1.56	3.56
A32	ISO-QMS uses time and resources	1.78	1.56
A37	ISO-QMS creates unnecessary burden	2.78	1.34
A51	Scope for Six Sigma	1.12	4
A54	Scope for Quality cost analysis	1.45	2.67
A55	Scope Quality circle	1.45	2.67

Table 4 of the ANOVA test shows that for the corresponding alpha (α) level of 0.05 the 'F' value was more than the critical value. Hence the null hypothesis was rejected.

4.2 Ranking of Attributes

The mean and rank values of various attributes were obtained from the survey, and mean and rank values of most significant attributes are given in Table 5.

4.3 Importance Satisfaction (I-S) Model

The Importance-Satisfaction (I-S) model is used to interpret the responses of organizations. Yang et al. (2003) importance satisfaction model presents four areas as an excellent, to be improved, surplus and careless [17]. Figure 1 shows the I-S model developed by Yang. Decisions of improvement are comparatively easy for management, so the I-S model focuses on Area-II (to be Improved Area). Necessary improvements must have carried out for identified attributes or factors located in Area II.

The outcome of the survey was interpreted from the mean values for importance and satisfaction level of dimensions. The I-S Plots were drawn for attributes and dimensions separately by using the data. Figure 2 shows an I-S Plot representing the

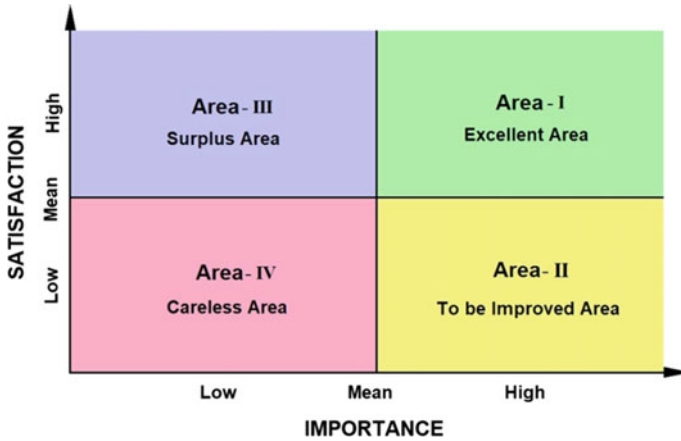


Fig. 1 Importance satisfaction model [17]

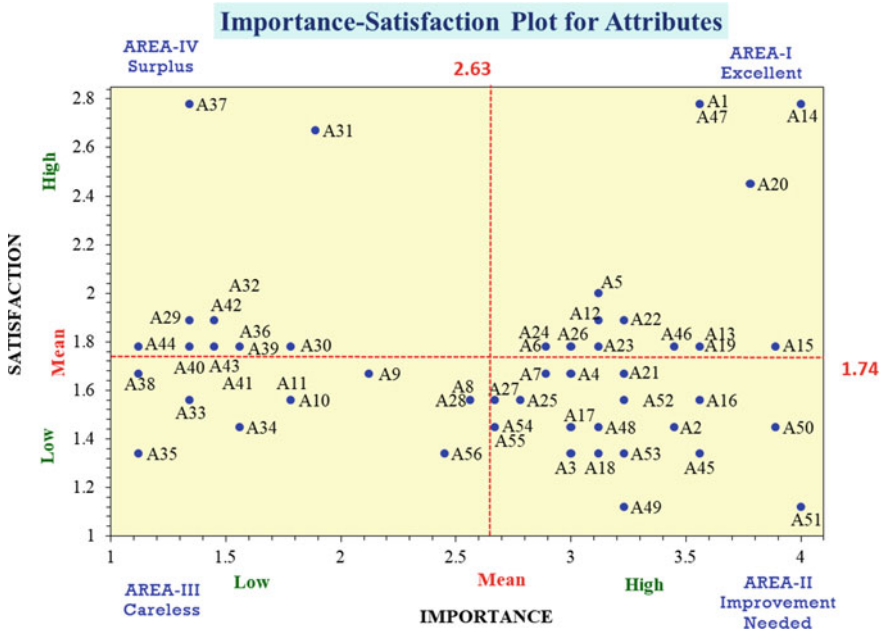


Fig. 2 Outcome of I-S survey for attributes

mean values of importance and satisfaction for attributes obtained from the analysis of survey data (significant attributes were shown in Table 5). Table 6 indicates the mean values of importance and satisfaction for various dimensions of assessment and Fig. 3 represents the I-S plot of these dimensions.

Table 6 Mean values for four dimensions

Dimension of attributes		Mean values	
		Importance	Satisfaction
D1	Motives for ISO-QMS	2.75	1.74
D2	Benefits of ISO-QMS	3.24	1.79
D3	Development of ISO-QMS implementation	1.44	1.85
D4	Scope for different Quality Management Tools & Techniques	3.26	1.51
Average of averages		2.68	1.73

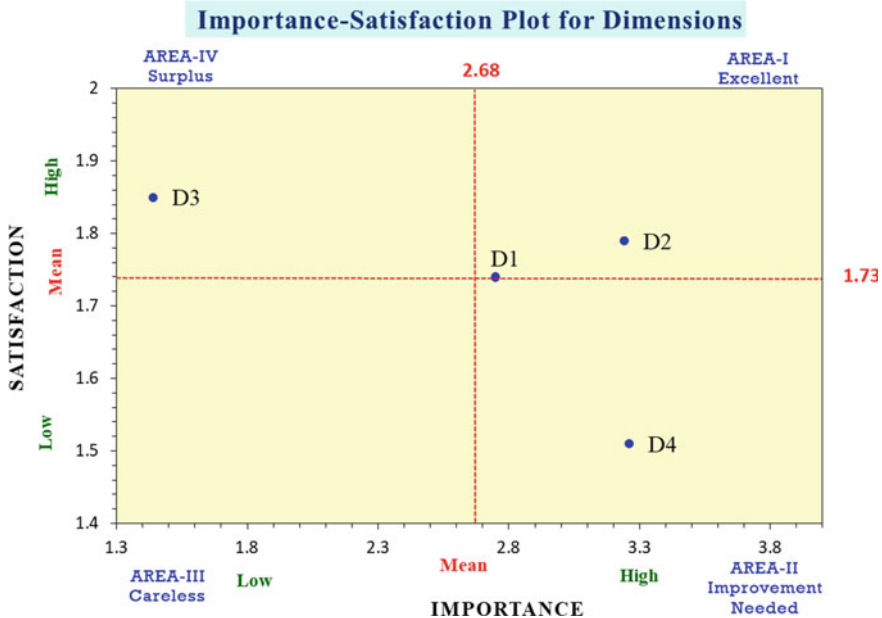


Fig. 3 Outcome of I-S survey for four dimensions of assessment

From the plot of Fig. 2, it was seen that the respondents shown dissatisfaction but gave more importance for the attributes of improving productivity, developing internal markets or expansion, maintaining and increasing market share, pressure from a customer for quality assurance, regarding the dimension of motives for ISO implementation.

It was observed that the attribute from the dimension of "development of ISO-QMS Implementation" has given lower importance compared to the dimension of "benefits of ISO-QMS". These attributes were, improved product or process quality, an improved advantage over competitors, an effective tool of marketing

promotion, improved quality awareness of employee, communication improvement within the organization and mutual co-operation improvement. On the other hand, they gave more importance to the attributes related to the dimension of "scope for different Quality Management Tools and Techniques", like Benchmarking, Failure mode and effect analysis, Fault tree analysis, Sampling techniques, Six Sigma, Lean concept, Kaizen, Quality cost analysis and Quality improvement teams or Quality circle.

Immediate improvement was needed for the attributes which were situated in the critical area. As reported by the respondents, there was enormous scope for implementing other Quality Management Tools & Techniques like particularly Six Sigma in the textile industry of India to achieve overall productivity improvement.

From the plot of Fig. 3, it was seen that the respondents shown dissatisfaction but gave more importance to the dimension of "Scope for different Quality Management Tools & Techniques". The respondents indicated a huge scope for the use of QTTs like Six Sigma and were expecting much more improvement.

5 Conclusion

Organization's satisfaction is very important at the end of the implementation of ISO-QMS, as they are the ultimate customers of the ISO certification process. The satisfaction will be more if ISO certification will produce a more overall improvement in productivity. The facts identified from the survey were given below,

- The Dimension, "Motives for ISO-QMS" or important reason of ISO-QMS implementation found were mostly internal such as, top management decision, improving productivity, developing internal markets or expansion, maintaining and increasing market share than external reasons like customer requirement related to assurance of quality, an act to impress suppliers about the quality, reducing cost of customer complaints. Moderate importance and low satisfaction level was seen for this dimension.
- The Dimension, "Benefits of ISO-QMS implementation", such as improved product or process quality, gaining an advantage over competitors, effective tool of marketing promotion, improvement in quality awareness of employee, communication improvement within an organization, were associated with internal operational issues. However, the benefit of improvement in mutual co-operation with suppliers and customers was associated with the external operational issue. High importance level and moderate satisfaction level was seen for this dimension.
- The Dimension, "Development of ISO-QMS implementation" was seen at a non-critical level. This dimension was situated in the 'surplus area' of I-S plot, which indicates the burden of documentation with having low importance. It shows that most of the respondents were using the company's ISO-QMS documents for them as their daily practices without any value addition.

- The Dimension, "Scope for different quality management tools and technics (QTT)" was situated in the area 'to be improved' of I-S plot. The respondents gave a higher level of importance but expressed a lower level of satisfaction to the scope for CI-QTTs .

The questionnaire survey indicated that implantation of ISO-QMS was not showing a remarkable improvement in overall productivity of Indian Textile Industry; at the same time, negligence towards using proven quality tools and techniques like Six Sigma for continuous improvement was observed. Hence, to improve overall productivity, the need identified is to use different Quality Management Tools and Techniques in-particular Six Sigma, synchronously with the existent 'ISO-QMS' of company.

References

1. International Organization for Standardization. <https://www.iso.org>
2. Gorakhia RR (1997) Implementation of ISO 9000 quality systems in textile industry, Colourage, Dec97 Supplement, vol 44, p 25
3. Ministry of Textiles, Government of India, Textile committee, case studies. <http://www.textil.escommittee.nic.in/services/case-studies-1>
4. Scott L, Collins P (1998) Evaluation of the ISO 9000 series: benefits and problems of implementation and maintenance in production companies. *J Text Inst* 89(1):90–109
5. Towers N, McLoughlin J (2005) Effective total quality management in the textile fashion retail supply chain: a pilot survey of the UK textile manufacturers. *J Text Inst* 96(2):87–92
6. Chiarini A (2011) Integrating lean thinking into ISO 9001: a first guideline. *Int J Lean Six Sigma* 2(2):96–117
7. Karthi S, Devadasan SR, Muruges R (2011) Lean six sigma through ISO 9001 standard-based quality management system: an investigation for research. *Int J Prod Qual Manag* 8(2):180–204
8. Karthi S, Devadasan SR, Muruges R (2011) Integration of lean six-sigma with ISO 9001: 2008 standard. *Int J Lean Six Sigma* 2(4):309–331
9. Karthi S, Devadasan R, Muruges C, Sreenivasa SN (2012) Global views on integrating six sigma and ISO 9001 certification. *Total Qual Manag Bus Excell* 23(3–4):237–262
10. Hussain T (2014) Reducing defects in textile weaving by applying six sigma methodology: a case study. *Int J Six Sigma Compet Adv* 8:95
11. Hayajneh MT (2010) Applying six sigma methodology based on "DMAIC" tools to reduce production defects in textile manufacturing. In: *Recent advances in industrial and manufacturing technologies*. ISBN: 978-1-61804-186-9
12. Atwell R, Six sigma for the apparel industry. <http://www.yoda.gen.tr>
13. Krishnaraj G, 6 sigma: tool for profit strategy in apparel industry - not a myth. <https://www.fibre2fashion.com>
14. The Indian Textile Journal. <https://indiantextilejournal.com>
15. Pfeifer T, Reissiger W, Canales C (2004) Integrating six sigma with quality management systems. *TQM Mag* 16(4):241–249
16. Dey P, How to complement ISO 9001:2000 with six sigma. <https://vietnamwcm.wordpress.com>
17. Yang CC (2003) Establishment and applications of the integrated model of service quality measurement. *Manag Serv Qual: Int J* 13(4):310–324

Finite Element Analysis to Predict Performance of Flexure Bearing for Space Application



Suraj Bhojar, Virendra Bhojwani, Ganesh Khutwad, Gaurav Sawant, Jay Lad, and Stephen Sebastian

Abstract Finite Element Analysis of a flexure bearing used in a cryocooler for space application is a very critical component in determining the working life of cryocoolers. The present study analyzes various significant parameters using the finite element analysis to achieve finite-fatigue life. The infinite fatigue life is necessary to ensure that cryocooler does not fail during the mission life of the satellite. Flexure bearing serves two purposes—(a) maintaining a mean position of a free-piston in linear compressor by providing desired stiffness and (b) avoiding radial deflection of the piston leading to wear and tear. The flexure bearing also ensures oil-less operation of linear compressor since the use of oil in cryocooler may lead to severe damage to the heat exchanger by freezing at cryogenic temperature. This paper considers various essential parameters optimized to achieve—(a) high stiffness (b) load stresses and (c) infinite fatigue life necessary for space application.

Keywords Finite element analysis · Flexure spring · Cryocooler compressor · Stiffness · Space application · Fatigue life

1 Introduction

A bearing is utilized to approbate the relating movement between two surfaces. In this process, a shaft needs to turn about its casing or a piston needs to slide about the cylinder. For the smallest frictional losses to happen, both of them require relative movement. Cryocoolers actually require performance reliability and elevated operational life. Linear motors are preferred to rotary compressors because large radial forces are exerted by rotary compressors and cause a large amount of wear and require lubrication as well. The common pain point in cryocoolers is lubrication. A special purpose flexure spring is designed for maintenance-free operation and longer life for cryocoolers. Thus, flexural bearing in this sort of utilization is better. A spring that permits movement by bending a heap constituent is called a flexure bearing. An

S. Bhojar (✉) · V. Bhojwani · G. Khutwad · G. Sawant · J. Lad · S. Sebastian
Department of Mechanical Engineering, MIT-ADT University, Pune 412201, India
e-mail: suraj.bhojar@mituniversity.edu.in

Fig. 1 Special flexure bearing



average flexure spring is only one part joining two different parts. Flexure direction have the edge over most different bearings that they are simple and accordingly affordable. They are often compact, lightweight and have low friction and are simpler to fix without a particular gear. The researchers plan to design, examine and manufacture flexure bearing which will enhance the productivity of systems by lessening frictional just as well as mechanical losses. The flexure spring acts as a spring in axial direction (exhibiting low stiffness) and it acts as a bearing in radial direction (exhibiting high stiffness) [1–16].

An exceptional unit of a flexure bearing utilized in the cryocooler compressor is presented in Fig. 1. Every unit is like a thin flat metal disc with three spiral openings, and three spiral arms which sustain the spiral and the pivotal loads. Every spiral sweeps a point of 560° . The external diameter of the disc is 69 mm and the P.C.D. of the external holes is 61 mm. The focal gap has a 3.1 mm breadth [1]. On the other hand, the external clamped 12 holes have a measurement of 6 mm and the thickness of the circle is 0.7 mm. The spirals are situated 10 mm separated from the center point of the disc. The spiral arm has an equivalent to a thickness of 0.7 mm.

2 Methodology

The present study follows a methodology based on the FEA approach using Ansys package in which the analysis is divided into five major steps as depicted below (Fig. 2).

The parametric analysis was performed primarily for space applications to satisfy the life criteria of cryocooler compressors. To define the ideal geometrical configuration, the parameter study approach was deployed; and it was accomplished through the Ansys package and checked through the experimental results.



Fig. 2 Steps in FEA

Table 1 The pre-processing inputs

Sr. No.	Parameters	Details
1	Element type	Structural–Spiral
2	Real constant thickness	0.7 mm
3	Material	Beryllium copper
4	Young’s modulus	130×10^3
5	Poisson’s ratio	0.3

The preferred way to achieve high operating life and reliability, as described, is to refrain from physical interaction between the compressor’s piston and cylinder. Using flexure springs, the helping weight of the piston to the front complemented with strong radial stiffness at the back side will be the most competent way to do the same.

The following research approach has been considered in this study investigation:

1. Compact size to achieve greater mechanical spring stiffness.
2. Infinite life to achieve lower operational stresses free from fatigue
3. Identification of an optional material with better mechanical properties
4. Selection of best geometric configuration

2.1 Pre-processing

Pre-processing for linear flexure under investigation is an integral step in the present study. Table 1 represents the preprocessor data.

In the first step, the Finite Element model is developed by modeling geometry, choosing element type, real constant and material properties. The FEA package element library consists of various types of structural, thermal and fluid elements. Under structural type beam, plane, solid, shell elements are available that are to be selected depending on the analysis type and geometry.

2.2 Number of the Spiral Arms

Material—Beryllium Copper (UNS C 17200) has displacement of –5 mm from the mean position and thickness of 0.3 mm. The analysis has been carried out by varying

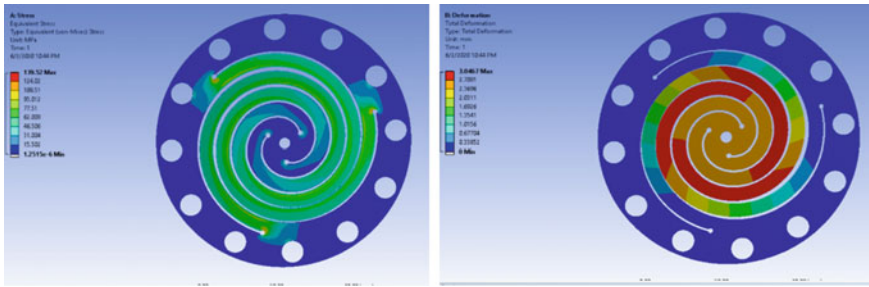


Fig. 3 Equivalent Stress = 139.52 MPa and Stiffness = 0.3289 N/mm for 3 Spiral arms

Table 2 The results for no. of spiral arms

Number of spiral arms	2	3	4
Displacement (mm)	5	5	5
Stress (MPa)	170.8	139.52	132.6
Force (N)	1	1	1
Deformation (mm)	2.38	3.04	3.51
Stiffness (N/m)	418.55	328.22	284.75

the number of arms on the flexure i.e. 2, 3 and 4. The Fig. 3 depicts Number of Spiral Arms (Stress) (Table 2).

2.3 Stress Against the Spiral Arm

If the minimum stress criterion is considered, number four of the spiral is suitable. If the maximum stiffness criterion is considered, number two of the spiral arms is suitable. Therefore, by considering both the parameters, number three of the spiral arm has been selected for the best results (Fig. 4).

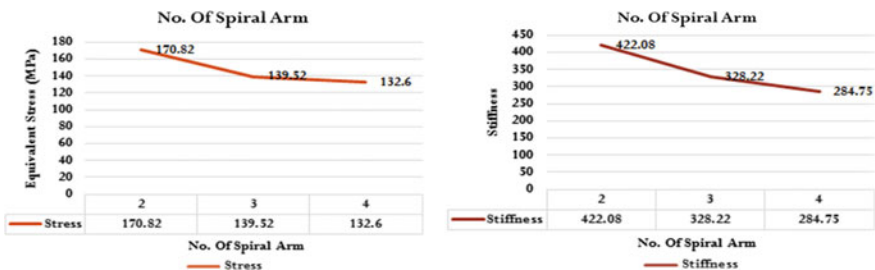


Fig. 4 No. of spiral arms versus equivalent stress and stiffness

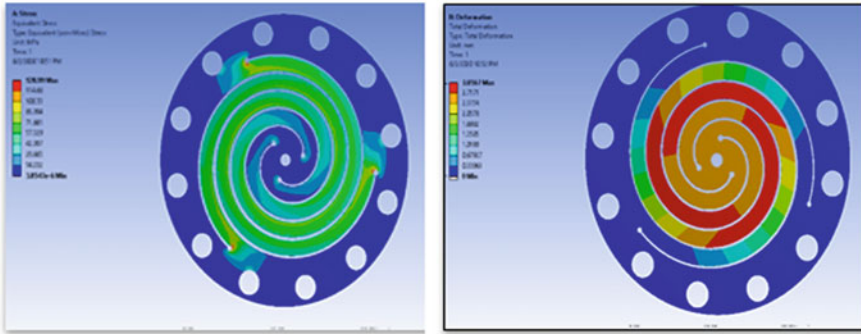


Fig. 5 Equivalent Stress: 129 MPa and Stiffness = 0.3278 N/mm

Table 3 The results for width of spiral cut

Width of cut	0.2	0.4	0.6	0.8	1
Thickness (mm)	0.3	0.3	0.3	0.3	0.3
Displacement (mm)	5	5	5	5	5
Stress (MPa)	143.24	138.85	129	128.26	121.47
Force (N)	1	1	1	1	1
Deformation (mm)	2.88	2.96	3.05	3.15	3.25
Stiffness (N/m)	346.68	337.05	327.15	317.21	307

2.4 Width of the Cut-off Spiral Arm

Material—Beryllium copper (UNS C 17200), Displacement –5 mm from the mean position, thickness—0.3 mm. The number of spiral arms-3 (Fig. 5 and Table 3).

The flexure is composed by a chemical etching process, and the limitation in this process is that it is not possible to cut the spiral slot up to 0.4 mm. As a result, the suitable width for the spiral cut is 0.6 mm. Therefore, 0.6 mm has been taken as a suitable width for the spiral cut.

2.5 Stress Against the Width of the Cut

The width of the spiral cut constantly increases. Stiffness and equivalent stress both however decrease gradually. The criteria for ideal design, are maximum value of stiffness accompanying minimum value of stress through 0.6 mm width of the spiral cut has been taken (Fig. 6).

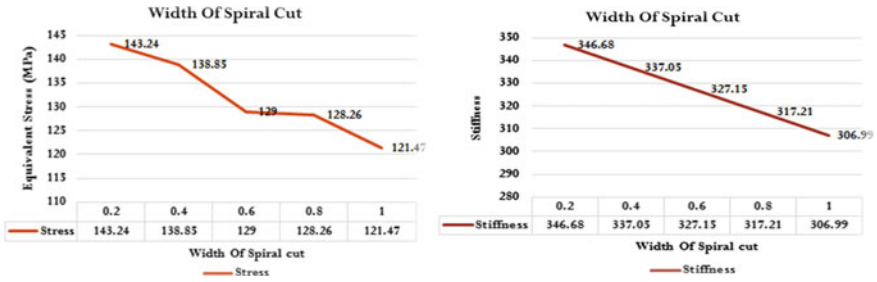


Fig. 6 Width of spiral cut versus equivalent stress and stiffness

2.6 Impact of the Spiral Angle

Material Beryllium copper (UNS C 17200 (TH02)), Displacement –5 mm from mean position, thickness—0.3 mm. Number of spiral arm-3 (Fig. 7 and Table 4).

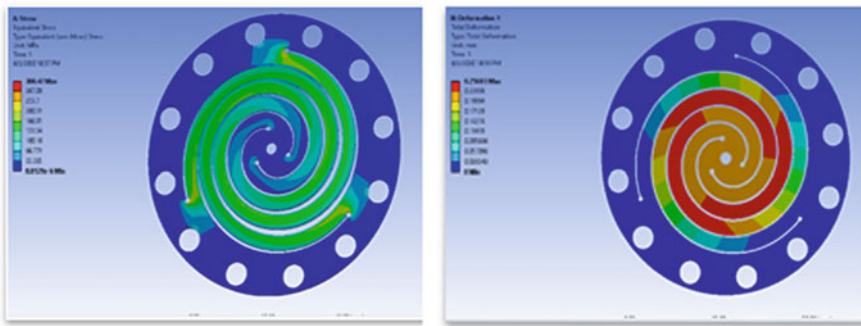


Fig. 7 Equivalent Stress = 300.47 MPa and Stiffness = 3.906 N/mm

Table 4 The results for spiral angle

Spiral angle	360°	420°	480°	540°	560°	570°
Thickness(mm)	0.7	0.7	0.7	0.7	0.7	0.7
Displacement (mm)	5	5	5	5	5	5
Stress (MPa)	645.32	467.76	372.75	328.94	300.47	310.69
Force (N)	1	1	1	1	1	1
Deformation (mm)	0.069	0.115	0.168	0.231	0.256	0.27
Stiffness(N/m)	14310.45	8685.07	5927.68	4322.45	3892.11	3750.09

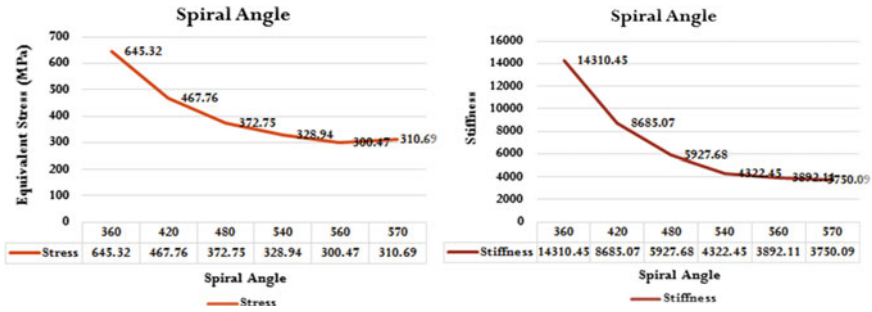


Fig. 8 Stress versus spiral angle and stiffness versus spiral angle

2.7 Stress Against the Width of the Cut

The graph given above clearly shows that for 560° spiral angle, minimum stress (300.47 MPa) has been obtained and the corresponding stiffness is 3892.11 N/m. through 560° spiral angle is suitable for flexure bearing (Fig. 8).

2.8 Stress Against the Width of the Cut

Material—Beryllium copper (UNS C 17200 (TH02)), Displacement −5 mm from mean position, thickness—0.3 mm. Number of spiral arm-3 (Fig. 9, Tables 5 and 6).

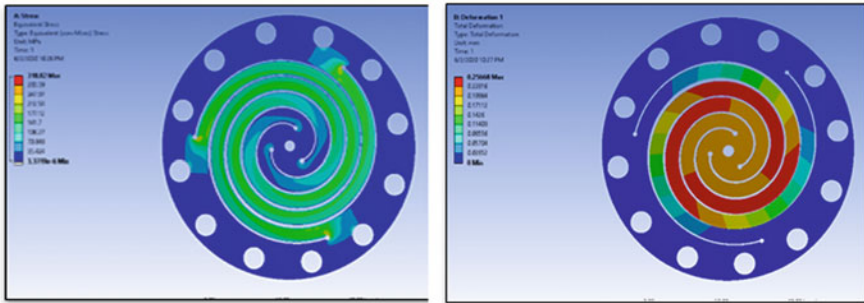


Fig. 9 Equivalent Stress = 318.8 MPa and Stiffness = 3.906 N/mm

Table 5 The results for disc thickness

Thickness (mm)	0.3	0.5	0.7	1	1.25
Displacement (mm)	5	5	5	5	5
Stress (MPa)	138.5	227.53	300.47	439.2	517.66
Yield stress (MPa)	965	965	965	965	965
FOS	2.2	2.2	2.2	2.2	2.2
Allowable stress	438.6	438.6	438.6	438.6	438.6

Table 6 The results for disc thickness & deformation

Thickness (mm)	Deformation (mm)	Stiffness (N/m)
0.3	3.0567	327.15
0.7	0.256	3895.90

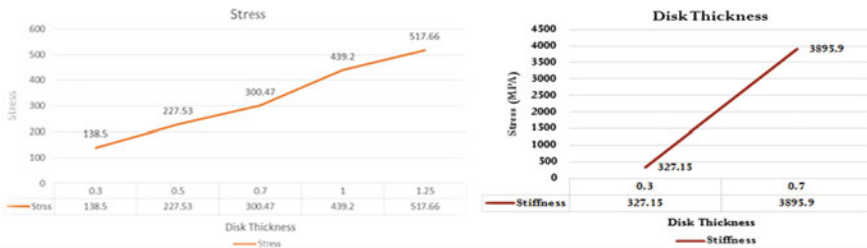


Fig. 10 Stress versus Disc Thickness & Stiffness versus Disc Thickness

2.9 Stress Against Disc Thickness

From the table and the graph presented above, it can be resolved that stiffness in flexure spring having thickness as 0.7 mm gets more as compared to thickness value of 0.3 mm (Fig. 10 and Table 7).

3 Conclusion

From the analysis of various diameters of the flexure spring, 69 mm diameter of the founds within the factor of safety 2.2 and the outcome from the is shown below. The output is as follows from the finite element analysis performed:

- Flexure spring geometry: Spiral with helical arms
- Material—Beryllium copper UNS C17200 (TH02)
- Number of arms—3
- Width of cut for the spiral arm—0.6 mm
- Traverse angle for spiral arms—560°
- Disc thickness—0.7 mm thick.

Table 7 The outcomes of the FEA

Parameters	Value	Remarks
Flexure Arm	Spiral type	Lower stress values
Material	Beryllium copper UNS	High factor of safety
No. of spirals	3	Lower stress values
Width of cut	0.6 mm	Feasibility for manufacturing
Angle of traverse	560°	Low induced stress values
Disc thickness	0.7 mm	Max. stiffness

The specification given above has been investigated for static stress conditions as well as stiffness only. The flexure spring is exposed to periodic loading. It becomes essential to investigate whether the discussed parameters would sustain to fatigue. Reference to the above specification CAD model has been prepared and analysis is carried out to find final stress. The stress found in the analysis is then compared by the S-N curve of the material.

Acknowledgements The research was funded by Research and Consultancy Cell, MIT-ADT University, Pune, India. Also, the research work would not have been possible without the inputs and resources provided by Dr. Sudarshan Sanap.

References

1. Bhojar S, Bhojwani V, Sanap S (2020) Parametric design and comparative analysis of a special purpose flexure spring. In: E3S Web of Conferences, vol 170, p 02013. <https://doi.org/10.1051/e3sconf/202017002013>
2. Jomde A, Anderson A, Bhojwani V, Kharadi F, Deshmukh S (2017) Parametric analysis of flexure bearing for linear compressor. Science Direct, Material Today: Proceedings, vol 4, pp 2478–2486
3. Zhou WJ, Wang LY, Gan ZH, Wang RZ, Qui LM, Pfothenauer JM (2012) The performance comparison of Oxford and triangle flexure bearings, advances in cryogenic engineering. AIP Conf Proc 1434:1149–1156
4. Gawali BS, Atrey MD, Narayankhedkar KG (2002) Performance prediction and experimental investigation on orifice pulse tube cryocooler, ICEC-19, pp 391–394
5. Al-Otaibi ZS, Jack AG (2007) Spiral flexure springs in single phase linear-resonant motors. In: Proceeding of 42nd international universities power engineering conference, pp 184–187
6. Davey C (1981) The Oxford University miniature cryogenic refrigerator. In: International conference on advanced infrared detectors and systems, London, p 39
7. Wong TE, Pan RB, Johnson AL (1992) Novel linear flexure bearing. In: Proceedings of 7th International Cryo Conference, pp 675–698

8. Marquardt E, Radebaugh R, Kittel P (1992) Design equations and scaling laws for linear compressors with flexure springs. In: Proceedings of 7th International Cryo Conference, pp 783–804
9. Wong TE, Pan RB, Marten HD, Sve C, Galvan L, Wall TS (1995) Spiral flexural bearing. In: Proceedings of 8th Cryo Conference, pp 305–311
10. Gaunekar AS, Goddenhenrich T, Heiden C (1996) Finite element analysis and testing of flexure bearing elements. *Cryogenics* 36:359–364
11. Lee CC, Pan RB (1997) Flexure bearing analysis procedures and design charts. In: *Cryocoolers*, vol 9. Plenum Press, New York, pp 413–420
12. Simcock CJ (2007) Investigation of materials for long life, high reliability flexure bearing spring for Stirling Cryocooler Applications. In: *Cryocoolers*, vol 14, pp 335–343
13. Qi Y, Wu Y, Zhang H, Chen X (2009) Simulation of deformation of diaphragm spring grooved with spiral slits by FE method, DETC2009-86371, ASME International Conference, IDETC/CIE
14. Beadshaw CR (2012) A miniature-scale linear compressor for electronics cooling. Publications of the Ray W. Herrick Labs
15. Lee H, Ki S, Kang J-H, Yang S-M, Rhee W-H (2008) Noise characteristics of linear compressor for refrigerators. Digital Appliance Research Laboratory, LG Electronics Inc. Seoul, Korea, pp 153–802
16. Phadkule S, Inamdar S, Inamdar A, Jomde A, Bhojwani V (2019) Resonance analysis of opposed piston linear compressor for refrigerator application. *Int J Ambient Energy* 40:7, 775–782. <https://doi.org/10.1080/01430750.2017.1421574>

Modal Characteristics of Composite Sandwich Structure with Intermediate Layer of Viscoelastic Material



Mayur M. Ghadage, Vishal B. Bhagwat, Shital R. Kadam,
and Shrinivas V. Shelage

Abstract Structural foundations are used for the provision of support to engine, motor, pump, and machines in industrial units. The present investigation has been done to increase the dynamic properties of laminated sandwich composites in which the structural damping is premeditated with micro-mechanical analysis approach. A sandwich structure was manufactured by adhesively adding viscoelastic material into the various astonishing composite laminates. Materials that have their high stiffness and high damping are impracticable. Surface damping treatment has been done on a composite sandwich structure to provide large amount of damping to the structures. The damping characteristics of the sandwich structures were calculated concerning the ply orientation of the composite laminates. Modal analysis of composite sandwich structures has been performed in ANSYS v19 and it has very good covenant with experimental results. It has been observed that the free natural frequencies of CFRC structure have 4–10 times increases while inserting viscoelastic material into CFC structure.

Keywords Dynamic properties · Mode shapes · Natural frequency · Stiffness · Fiber orientation · Viscoelastic material · Modal analysis

1 Introduction

Plates are the straight, flat surface structure where other dimensions of the plates are greater than its thickness of the plate. There are mainly 3 types of boundary conditions applied on the plate for its vibration analysis, they are clamped edge condition, simply supported edge condition and free edge condition. One another type is mixed edge condition, which is combination of above-mentioned boundary conditions. From these boundary conditions there are such a 21 combinations are obtained [1]. Plates are subdivided into 4 types based on their structure; that are Stiff plates, Membranes, Flexible plates, and Thick plates. The stiff plates are thin plates carry a load two- dimensionally and it also consist flexural rigidity (D). Membranes

M. M. Ghadage (✉) · V. B. Bhagwat · S. R. Kadam · S. V. Shelage
Department of Mechanical Engineering, VPKBIET, Baramati, India

are also thin plates but they carry lateral loads axially without flexural rigidity. The example of membrane is a network of stressed cables. Flexible plates are the combination of stiff plates as well as membranes and they carry an external load by two-dimensionally as well as lateral loads axially. A thick plate carries internal stress within the structure [2]. Many materials available in recent years, but composite materials are better than conventional materials. Every material has own dynamic properties. That means each can be vibrating at its highest itself frequencies, when the natural frequencies matches with an excitation frequencies of the vibrating structure then Resonance will occur. Due to resonance problem the component gets cracked or some time damaged. There are many methods to prevent resonance but one among the most known methods is it can be avoided with the help of natural frequency of the vibrating structure. We must know the natural frequencies of the vibrating structure for avoiding the resonance problem. There are many techniques to determine the free natural frequencies of vibrating structure concerning its mode shapes [3]. Composite materials have better mechanical properties such as high strength, high stiffness and many more. These composite materials are used in advance structures mainly in the aerospace industry, shipbuilding, robot structures and many more. Nowadays, plates are mostly used in various engineering fields such as hydraulic structures, containers, missiles instruments, engine support, machine parts, architectural structures, etc. [4]. Composites are the combination of various materials gives better mechanical properties to the structure. These composite materials are often prepared by putting two or more dissimilar materials in such a way that they act as mechanically one unit. Composite material is usually man-made and those are chemically distinct from each other having higher properties than of its constituents. They have better flexibility as compared to other conventional materials. In the present work, we used carbon fiber epoxy composite (CFC) material; it has high mechanical as well as dynamic properties. Carbon fiber epoxy composite has higher damping as compared to conventional materials, since it does not only absorb noise and vibration of the structure but also it improves the fatigue lifetime of the material. Carbon fiber composite have manufactured in sandwich construction and which provides good properties with light weight construction [5]. Nowadays, advanced composites are used as alternatives for conventional materials because of its properties, and addition of the viscoelastic composite material makes them suitable for high performance and better efficient in structural application. In the present work, the viscoelastic material is used as silicon rubber sheet [6]. The structural foundation requires more attention due to the transfer of dynamic forces in the earth with the addition of a static load of a machine part, machine accessories. Over a long period of dynamic load, the foundation behavior changes, and deformation will be increased due to cyclic loading. In the design of the machine foundation, it is necessary to determine the amplitude and natural frequencies of structure to increase the fatigue life of the system. There are many techniques used for structural foundations that are spring foundation, plate foundation, etc. but the plate foundation is identical to implement due to its high static stiffness, and plates are designed with composite structures in the concrete very comfortable [7–9]. The best design criterion of structural foundations is that no resonance, it can be obtained by tuning of foundation. Structural damping treatment has been done by

adjusting the natural frequencies of the structure. The machine foundation has done for the vertical machine center the innovative machine foundation absorbs the vibrations better than the previous technique used in the workshop. The CFRC composite sandwich has more effective for structural foundation due to its dynamic properties.

2 Finite Element Analysis of Sandwich Structures

The modal analysis was done in ANSYS v19 software to compute the natural frequencies of the composite sandwich plate structures. The designs of sandwich plates are done in CATIA V5 software. Figure 1 shows the geometry of the composite sandwich structures. In the present fig the first structure have only layers of carbon fiber and second sandwich structure is made up by inserting rubber sheet into the two carbon fiber laminates. The results obtained from FEA for sandwich structures have discussed in the Sects. 2.1 and 2.2. Modal analysis is one of the powerful numerical methods which predict the natural frequencies of the structure with respect to its mode shapes.

2.1 Epoxy Carbon Fiber Sandwich Structure

The FEA analysis has done on sandwich plate using various parameters. The fiber orientation [90 0] shows the better results for both sandwich plate structures. At the [90 0] fiber orientation the natural frequencies are more while the insertion of rubber sheet into the plate structure. In the present work, the structural foundation is used for simple machine application; boundary conditions are considered using this machine application. From the simulation results various mode patterns are obtained and they are shown in Figs. 2 and 3 for the sandwich plates respectively. The various mode shapes visualize the plate vibrates in different patterns. For the first carbon fiber plate has two bending and three twisting patterns that are shown in Fig. 2. The mode 1 and mode 2 consist bending transformation while mode 2, 3 and mode 5 shows twisting transformation. The maximum deformation occurs at mode 3.

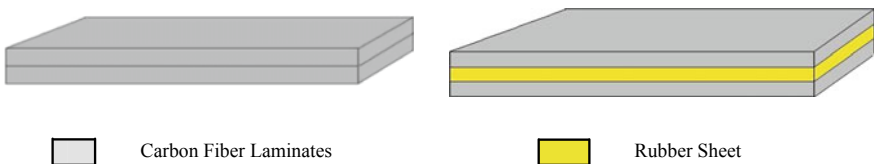


Fig. 1 Geometry of composite sandwich structure

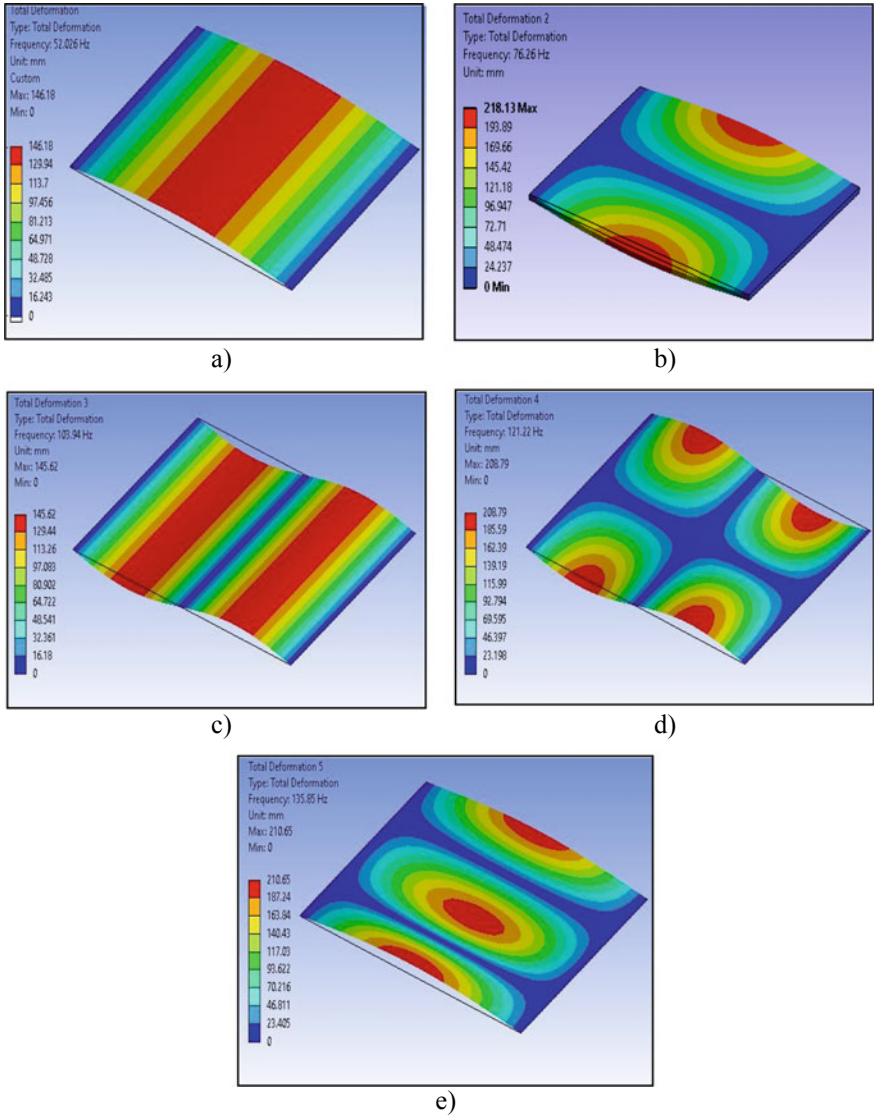


Fig. 2 Modal analysis of carbon fiber plate structure: **a** Mode 1st; **b** Mode 2nd; **c** Mode 3rd; **d** Mode 4th; **e** Mode 5th

2.2 Epoxy Carbon Fiber Rubber Sandwich Structure

See Fig. 3.

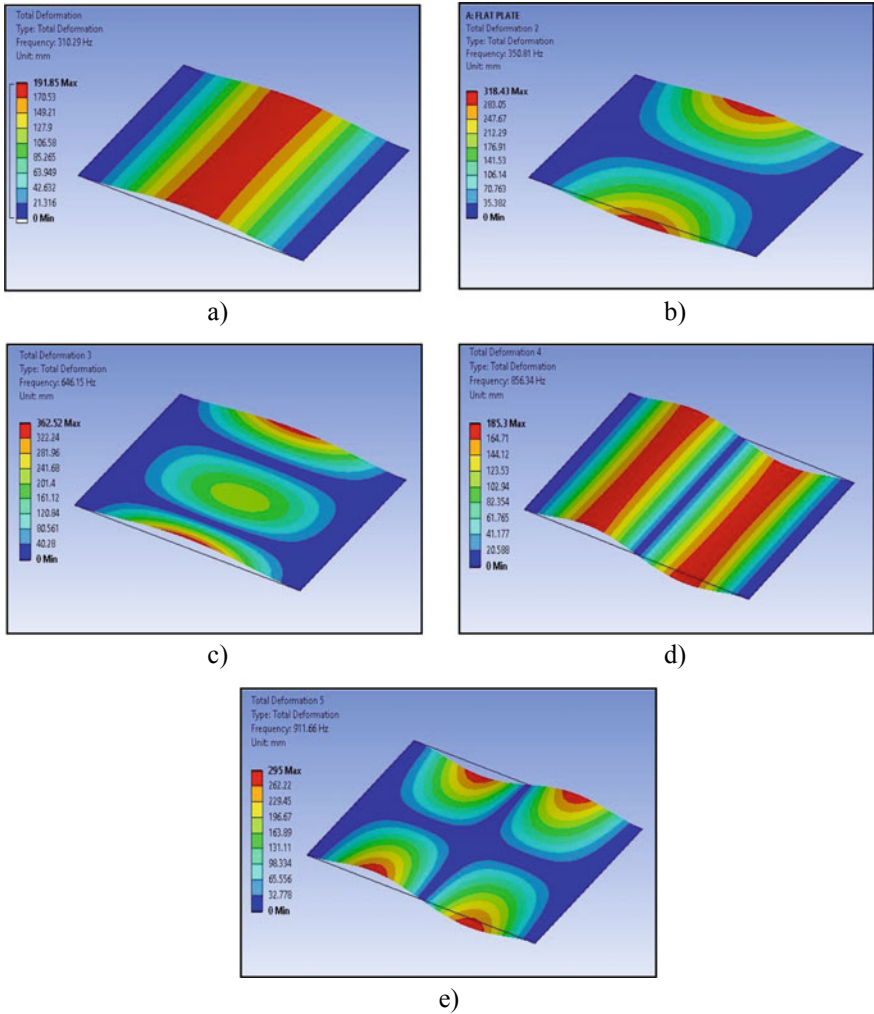


Fig. 3 Modal analysis of carbon fiber plate structure: a) Mode 1st; b) Mode 2nd; c) Mode 3rd; d) Mode 4th; e) Mode 5th

3 Manufacturing and Experimental Testing

The hand lay-up method is a type of open molding method. This technique is mostly used due to the easy steps of its manufacturing process. This is suitable for making large verities of simple as well as tiny products due to this method is preferred for making composite material. The Tables 1 and 2 show the material properties of carbon fiber and silicon rubber respectively. In free vibration tests, the system

Table 1 The properties of UD epoxy/carbon fiber composite laminate material

Symbol	Value	Property
ρ	1490 kg/m ³	Density
t	1 mm	Ply thickness
E_x	121 GPa	Longitudinal modulus in X direction
E_y, E_z	8.6 GPa	Transverse modulus in Y and Z direction
ν_{xy}, ν_{xz}	0.27	Poisson's ratio along XY, and XZ plane
ν_{yz}	0.4	Poisson's ratio along YZ plane
G_{xy}, G_{xz}	4.7 GPa	Shear modulus in XY, and XZ plane
G_{yz}	3.1 GPa	Shear modulus in YZ plane

Table 2 The material properties of silicon rubber sheet

Symbol	Value	Property
ρ	980 kg/m ³	Density
E	0.45 MPa	Young's modulus
ν	0.3	Poisson's ratio
K	0.375 MPa	Bulk modulus
G	0.17308 MPa	Shear modulus

is subjected to free vibrations using the impact hammer. The resulting free vibrations are recorded using accelerometers and FFT analyzers, from which the information recording the natural frequency and damping parameters can be obtained. For measurement of the natural frequency of both specimen (carbon fiber epoxy and carbon fiber epoxy with viscoelastic material), we create a fixture for mounting purposes. After that, we measure natural frequency by using the FFT analyzer and Impact hammer. Rectangular shaped composite plates are selected as per particular material (Carbon fiber epoxy and Carbon fiber epoxy- rubber) having dimensions as per design and accelerometer transducer chosen. The boundary conditions are applied on the plate here the two sides of plates were clamped. An accelerometer has located at the center of the specimen, to detect the free vibration response (acceleration). The accelerometer and impact hammer sensor are attached to the data acquisition DAQ unit with respective port 1 to port 8. DAQ is connected to the desktop with the help of a USB port and opening the DEWSOFT software. Accelerometers are placed on both plates with respective mode shapes 1 and impact hammer is hammer on the surface of the specimen for giving initial displacement. The data was recorded from the accelerometer transducer has in form of graph (Acceleration vs. Frequency). This experimental procedure was again repeated up to 2 times to check the precision of the experimental results. The whole set of data was recorded in a database, and

Fig. 4 Experimental specimen setup



Fig. 5 Experimental specimen testing



finally experimental results are getting with the help of the FFT analyzer. The setup of experimental has shown in Fig. 4 and testing has shown in Fig. 5.

4 Result and Discussion

The results obtained from experimental testing have shown in Figs. 6 and 7. The results from simulation and experimental has found good correlation. The Tables 3 and 4 shows the comparison of natural frequencies with its mode shapes between

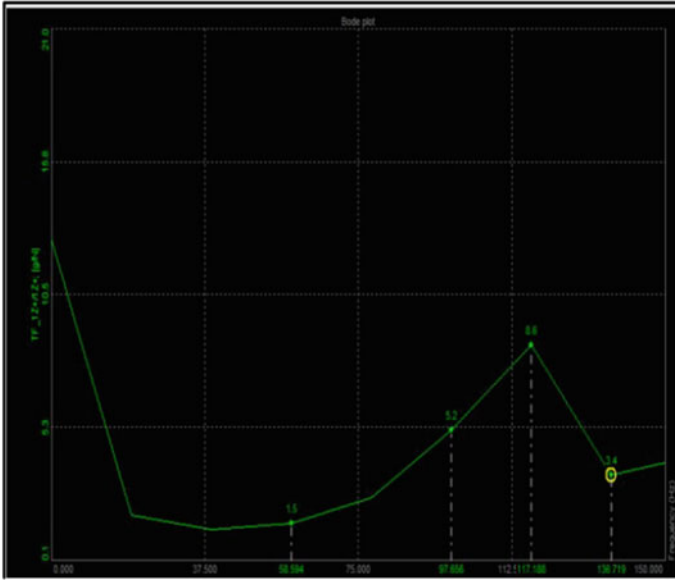


Fig. 6 Frequency spectrum of CFC plate structure

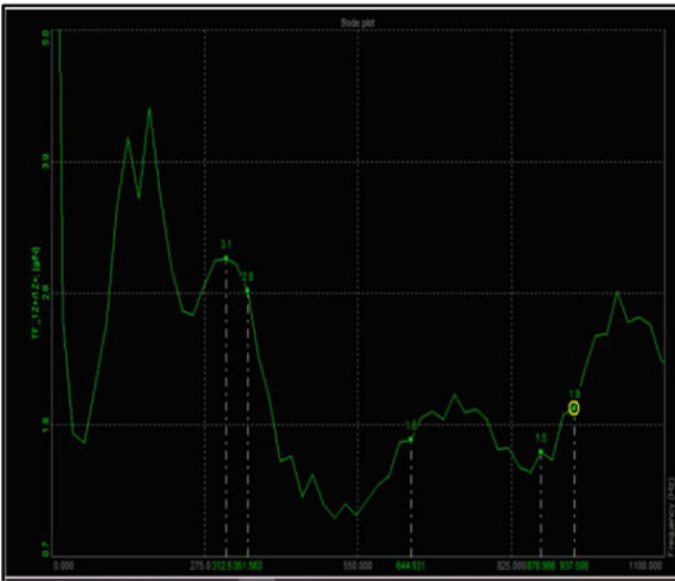


Fig. 7 Frequency spectrum of CFRC plate structure

Table 3 Comparative results of epoxy carbon fiber composite plate

Mode shape	Simulation results (Hz)	Experimental results (Hz)	% Error
1	52.02	58.59	11.21
2	76.26	75.00	1.652
3	103.94	97.66	6.041
4	121.22	117.18	3.332
5	135.85	136.71	0.629

Table 4 Comparative results of epoxy carbon fiber rubber composite plate

Mode shape	Simulation results (Hz)	Experimental results (Hz)	% Error
1	310.29	312.53	0.716
2	350.81	351.56	0.213
3	646.15	644.53	0.25
4	856.34	878.90	2.566
5	911.16	937.50	2.809

the experimental and simulation results of CFC and CFRC plate structure. The % of error between experimental and simulation results for carbon fiber epoxy composite plate has 0 to 11%. The % of error between experimental and simulation results for carbon fiber rubber composite plate has 0 to 3%. The overall comparison of both sandwich plates has shown in Fig. 8.

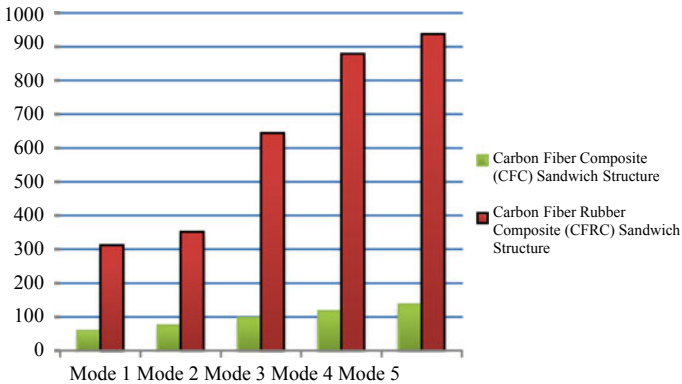


Fig. 8 Comparison of experimental results between both composite plates

5 Conclusions

In this research, the composite sandwich structures for the structural foundation were designed and manufactured with carbon fiber and with viscoelastic material which was inserted to 1 mm thickness into the carbon fiber laminates. The viscoelastic material provides large amount of damping to the structure comparatively carbon fiber structure. The damping characteristic of the CFC sandwich and CFRC sandwich structures were analyzed through simulation results and tested with ply orientation. The damping is anisotropic in nature and it's depending upon the micromechanical, physical structure of the material. The CFRC sandwich structure has great dynamic properties as well as high damping than the CFC sandwich structure. From the experimental vibration test, it was found that the natural frequency of CFRC structure has a 4-10 times increases while inserting viscoelastic material into CFC structure. The CFRC sandwich structure has better dynamic properties than of CFC sandwich structure. CFRC structures has successfully replaced with previous structural foundation for vertical machine center of milling machine operations.

References

1. Leissa AW (1973) The free vibrations of rectangular plates. *J Sound Vib* 31:257–293
2. Ma L, Chen Y-L, Yang J-S, Wang X-T, Ma G-L, Schmidt R, Schroder K-U (2018) Modal characteristics and damping enhancement of carbon fiber composite auxetic double-arrow corrugated sandwich panels. *Compos Struct* 203:539–550
3. Talekar N, Kotambkar M (2020) Modal analysis of four layered composite cantilever beam with lay-up sequence and length-to-thickness ratio. *Materials Today: Proceedings*, vol 21, pp 1176–1194
4. Kumar TP, Dwivedy SK (2016) Dynamic analysis of MRE embedded sandwich plate using FEM. *Proc Eng* 144:721–728
5. Lee DG, Chang SH, Kim HS Damping improvement of machine tool columns with polymer matrix fiber composite material. *Compos Struct* 43:155–163 (1998)
6. Klimenda F, Soukup J (2017) Modal analysis of thin aluminum plate. *Proc Eng* 117:11–16
7. Jung DS, Seung HC, Lee DG, Choi JK, Park BS (2001) Damping characteristics of composite hybrid spindle covers for high- speed machine tools. *J Process Technol* 113:178–183
8. Manoharan R, Kurhe NM, Shedbale IB, Charapale UD (2018) Modal analysis of hybrid laminated composite sandwich plate. *Mater Today Proc* 5:1245–1246
9. ANSYS workbench user manual. <http://www.ansys.com>

Design and Weight Optimization of Critical Automobile Component-Steering Knuckle



Shital R. Kadam, Mayur M. Ghadage, and Prachi D. Kale

Abstract In automobile, vehicle consist of many basic and critical components of system. Steering knuckle comes under suspension system of vehicle. Its design is an important aspect of the efficient working phase. This paper focuses on steering knuckle weight optimization criteria without compromising their static mechanical properties and efficiency enhancement. The steering knuckle is manufactured by aluminum alloy 7075 T6 material in place of cast iron. With the help of CATIA, software design has been done and structural characterization has been carried out by using ANSYS software. On the basis of ansys result, for affirmation aluminium steering knuckle has manufactured and strain gauge testing has done. Laser cutting and brazing processes are used for manufacturing steering knuckles. The result obtained from strain gauge testing and analysis is compared and encouraged using aluminum alloy for steering knuckle with a weight reduction of almost 71%.

Keywords Steering knuckle · Suspension system · Optimization criteria · Static mechanical properties · Efficiency enhancement · Structural characterization · Strain gauge

1 Introduction

A vehicle is fundamentally larger than the basic summation of its components. In vehicle every single component influence on other component and so that it a couple on multiple main systems and another branch subsystem. In the suspension system of a vehicle steering knuckle is some of the critical parts which accommodates the wheel hub or wheel spindle. The steering knuckle is the supporting plug of the steering and suspension system. It's also called as steering knuckle as well as steering upright and spindle [1]. The assembly of tire and wheel attached to the hub/spindle of the steering knuckle. The wheel revolves while being kept in a constant plane of motion

S. R. Kadam (✉) · M. M. Ghadage
ME Design, VPKBIET, Baramati, India

P. D. Kale
Department of Mechanical Engineering, VPKBIET, Baramati, India

by the suspension system. Steering Knuckle is an essential part of the car, its main role is to load steering, which supports the body weight, handover switch to withstand the front brake torque and braking torque so on. When we decrease the mass of car components it automatically decreases the mass of the car and reduces its energy intake demand so that this will increase its fuel efficiency and also material capitals will be set aside [2]. The main goal of supporting the study examination and design of automobile steering knuckle is to what significance of steering knuckle in the automobile suspension system and how we can create an appropriate design with the essential material. In this research, from other suspension system components, we have selected the steering knuckle as a research component. In demand to succeed superior performances with reducing weight, a new design approach is needed to create vehicle structure design. To accomplish our goal we have to interchange traditional material with lightweight material. Therefore, we have used aluminum alloy T6 material for manufacturing steering knuckles instead of cast iron material [3]. There are various optimization methods, tools exist in the market, because of high speed computing and software improvement from that we selected topology optimization which provides the finest use of material for a vehicle structure. Topology optimization is a beneficial tool for designers that create the best conceptual shape of a mechanical structure. Topology optimization is a scientific way of determining the best structural design for a given set of loads and boundary conditions [4]. Bhardwaj et al. Explained about steering knuckles is a critical component in the automotive suspension system. They studied on different materials for making a decision matrix for the optimized design of steering knuckle. Vijayarangan et al. Studied on alternative material for manufacturing steering knuckle is aluminum alloy reinforced with titanium carbide particulate. Wang Chun Yana et al. analyzed steering modality for multi-objective optimization and conclude that the NSGA-II algorithm can better to avoid resonance to improve the steering performance. Kumar et al. focused on the optimization of steering knuckle weight optimization. Dumbre et al. [5] studied unsprung mass reduction of vehicles, so the efficiency of a vehicle is increased. d'Ippolito et al [6] in the overall performance of a vehicle and their lifetime is calculated by its fatigue life and various physical parameters effect on fatigue life so that he focused on the improvement of fatigue life with the optimization approach. Kashyzadeh et al. [7] explained about fatigue life of automobile safety components with various axial amplitude loading situations. The Fourier curve fitting method was used here to articulate the probability distribution function. Tagade et al. [8] focused on the optimization of steering knuckle weight by using shape optimization which gives the best use of material for knuckle. David et al. [9] reported a review related to the Topology and shape optimization methods by employing evolutionary algorithms.

2 Material Selection

For the manufacturing of automobile steering knuckle, various materials are used like gray cast iron and forged steel is also used for manufacturing knuckle. The steering knuckle which we have selected for the comparative study is made up of cast iron. The automobile industry is focused on light weight material as an alternative for such type of applications so that aluminum alloys 7075 T6 is a good alternative material. Because of the light weight of material, it will reduce fuel consumption and emission as well as improve the efficiency and performance of a vehicle. In this study initially, we took two materials for analysis that are cast iron and aluminum alloy 7075 T6. In finite element analysis, we have check total deformation, equivalent stress, and maximum principal strain. Then we have select aluminum alloy for manufacturing steering knuckle and carried out experimental testing on it. Aluminum alloy 7075T6 is the cheapest material as compared to other materials for study purposes also it is a more ductile material and other parameters such as material properties are better as compare to other aluminum series. 7075 aluminum having zinc is the primary element that is strong and good strength compare with other steel.

3 Design of CAD Model

CAD model of automobile steering knuckle was created in 3D modeling software CATIA V5. The FEA analysis has done on cast iron and aluminum alloy steering knuckle using various parameters. There are two kinds of force acting on steering knuckle i.e. breaking force and steering force. For finding breaking force stand on one wheel we need to distribute the overall weight of the vehicle on four wheel. So that weight on one wheel is 384 kg. The breaking force was calculated by using the following formula

$$\text{Breaking force} = 1.5 g$$

$$\text{Breaking force} = 5640 \text{ N}$$

The below image shows applied boundary conditions on steering knuckle. Here steering force we have considered as 100 N.

Point A is fixed support and breaking force is applied at point B and steering force is at point C. At the connecting point of the brake caliper, there is a degree of freedom is zero as shown in Figure (a). The total deformation of component & directional deformation is common parameters in finite element methods regardless of software being applied. Directional deformation can be set as the displacement of the coordination in a specific axis or operator distinct direction. The total deformation of cast iron steering knuckle is shown in Figure (b), in that maximum deformation under static condition was 0.15261 mm. Maximum equivalent stress of cast iron steering knuckle was found that 219.95 MPa which is shown in Figure (c). FEA analysis of cast iron steering knuckle is shown Fig. 1. And for aluminum alloy is in Fig. 2. Total maximum deformation of aluminum steering knuckle is 0.3299 mm.

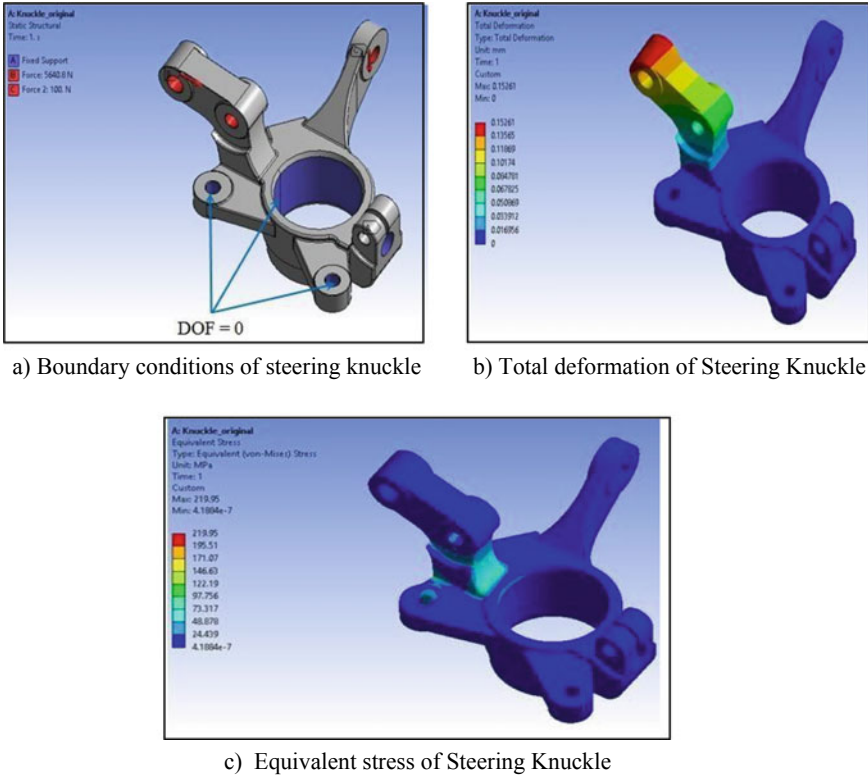


Fig. 1 FEA analysis of cast iron steering knuckle

The maximum equivalent stress has 182.18 MPa for aluminum alloy steering knuckle which is shown in Fig. 2. The results achieved from structural analysis are equated with existing steering knuckles and it is detected that the stress values are fewer than their permissible yield stress values. So, our design is safe.

4 Manufacturing and Experimental Testing

In this analysis, for education automobile steering knuckle is castoff as a component. Regarding the weight decrease, the development field is by far-off wider. In real it has been established that weight reduction has a robust effect on fuel utilization decrease if seen not only the particular vehicle but allowing for the fleet economy. For the manufacturing of aluminum alloy steering knuckles for our research, we have used the advance process. In that first we take aluminum alloy material sheet as per dimension then drafting has done on this sheet for making components. After that we have done laser cutting of that sheet material then this part is joined by using the

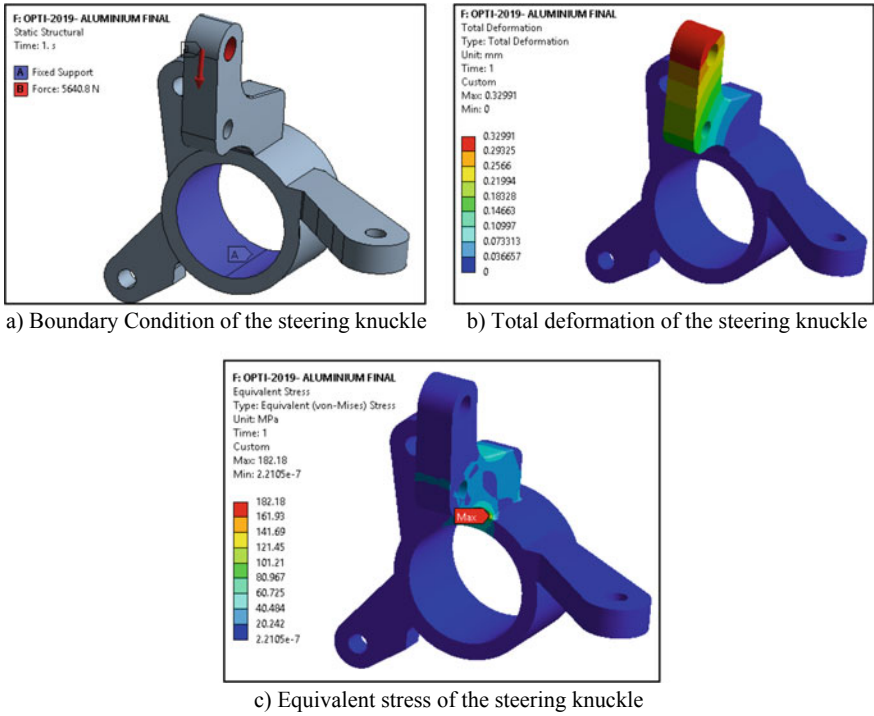


Fig. 2 FEA analysis of the aluminum steering knuckle

brazing process then the final component is ready for testing. The final component of aluminum alloy steering knuckle is shown in below Fig. 3.

Fig. 3 Aluminum alloy steering knuckle



4.1 Strain Gauge Testing

The fixture is manufactured according to the component designed. Single force is applied as per FEA analysis and reanalysis is performed to determine strain by numerical and experimental testing. The strain gauge is applied as per FEA results to the maximum strained region and during experimental testing; force is applied as per numerical analysis to check the strain obtained by analytical and experimental results. During the strain gauge experiment, two wires connected to the strain gauge are connected to the microcontroller through the data acquisition system and DAQ is connected to the laptop. Strain gauge values are displayed on a laptop using DEWE-SOFT software which is shown in Fig. 4 and total experimental testing is shown in Fig. 5.

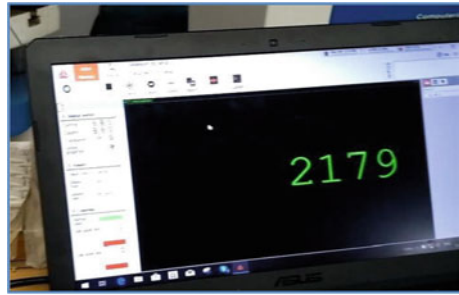


Fig. 4 Strain gauge testing



Fig. 5 Experimental testing

Fig. 6 Experimental result



5 Result and Discussion

For validation of FEA result need to calculate design parameter, so compare strain value from FEA result to Experimental strain value. For this purpose, strain gauge testing has been carried out. Result obtained from strain gauge testing and compressive testing on aluminum alloy 7075 T6 steering knuckle is shown in below Fig. 6.

From FEA it concluded that Maximum Principle strain of aluminum steering knuckle 2053 micro strain. By performing UTM test on aluminum knuckle it concluded that strain of aluminum steering knuckle is 2179 micro strain.

$$\text{Percentage error} = \frac{\text{Experimental value} - \text{FEA value}}{\text{Experimental value}} \times 100$$

$$\text{Percentage error} = \frac{2179 - 2053}{2179} \times 100$$

$$\text{Percentage error} = 5.7\%$$

The value of strain from FEA and strain gauge testing is near about the same. The percentage of error occurs during the FEA strain value and the experimental strain value is 5.7% for the aluminum alloy steering knuckle. From these result we conclude that the aluminium alloy is convenient material for steering knuckle in automobile.

6 Conclusion

The automobile steering knuckle component has been modeled using CATIA V5 and analyzed using ANSYS 19.0. The several parameters such as total deformation of steering upright, directional deformation of steering upright, maximum principal stress And Maximum Shear Stress are entirely analyzed. The results achieved from structural analysis are equated with existing steering knuckles and it is detected that

the stress values are fewer than their permissible yield stress values. So, our design is safe. The topology optimization method is used in this study for reducing the mass of knuckles by 71%. After the successful implementation of aluminium alloy steering knuckle it was concluded that, this invented steering knuckle can be used in the future for weight optimization purpose. For validation of FEA result need to calculate design parameter, so compare strain value from FEA result to Experimental strain value. For this purpose, strain gauge testing has been carried out.

References

1. Bhardwaj S, Ashok B, Lath U, Agarwal A (2018) Design and optimization of steering upright to reduce the weight using FEA. SEA Technical paper 2018-28-0081
2. Vijayarangan S, Sivananth V, Rajamanickm N (2013) Evaluation of metal matrix composite to exchange graphite iron for a critical component, steering knuckle. *Mater Des* 43:532–541
3. Wang CY, Zhang Y, Zhao WZ (2018) Multi-objective optimization of a steering system considering steering modality. *Adv Eng Softw* 126:61–74
4. Kumar CS, Kumar BK (2017) Design optimization of a steering knuckle component using conventional method of finite element analysis. *Int J Res Appl Sci Eng Technol* 5(XI):525–532
5. Dumbre P, Mishra AK, Aher VS, Kulkarni SS, Structural analysis of steering knuckle for weight reduction. *Int J Adv Eng Res Stud*. E-ISSN 2249–8974
6. d'Ippolito R, Hack M, Donders S, Hermans L (2009) Improving the fatigue life of a vehicle with a reliability-based design optimization approach. *J Stat Plann Inference* 139:1619–1632
7. Kashyadash RK, A new algorithm for fatigue life assessment of automotive safety components based on the probabilistic approach: the case of the steering knuckle. *Eng Sci Technol Int J* 23(2):392–404
8. Tagade PP, Shau AR, Kutaramane HC, Optimization and finite element analysis of steering knuckle. *Int J Comput Appl ICQUEST2015* (0975-8887)
9. David JM, Gareath AV, Graent PS (2015) *Topology and shape optimization methods using evolutionary algorithms: a review*. Springer, Berlin

Photovoltaic Power System with Battery Backup and Grid-Connection to Reduce Grid Dependency During Peak Demand Hours and Power Cuts



Vishal Rohilla, R. C. Rohilla, Prashant Thapliyal, Don Biswas,
and Gambhir Singh Kathait

Abstract Sun is considered as best and cleanest renewable energy source. This energy can be converted into electrical energy using array of solar cells. The generated electrical energy thus can be utilized to run the electrical appliances. Running these electrical appliances inevitably depends on the availability of utility grid. Sometimes the geographical, environmental and societal conditions affect the availability of utility grid; that's why the battery backed inverters are becoming one of the must have amenity at homes and offices. In the present research work, we have converted this battery backed inverter to the solar PV powered battery backed system in order to reduce grid dependency for charging the batteries and reducing the utility bill. The system is designed, tested and installed for a 2 BHK house situated in civil hospital complex, Panipat at Latitude 29.401, Longitude 76.971 and Elevation 232 m, in the Haryana State of Northern India. Panipat city is in the National Capital Region (NCR) and have capability to represent approximately 1.6 million houses in the entire region including states Punjab, Haryana, Delhi, western part of Uttar Pradesh State and Eastern part of Rajasthan State. Total energy demand for peak hours i.e. from 6:00 PM to 10:00 PM for total 4 h comes out to be 2250 Wh/day. So, the system was designed according to 2250 Wh/day. System's cost was, Rupees Sixty Thousand Four Hundred (Rs. 60,400/-). System is working without losing power on a single day and producing electricity. Normally, the billing without installing the system was approximately, Rupees One Thousand Four hundred (Rs.1,400/-) for 350 units (1 unit = 1 kWh).

Keywords Battery backed · Charge controller · Design · Peak demand hours · PV · Photovoltaic solar · Utility grid

V. Rohilla (✉) · P. Thapliyal · D. Biswas · G. S. Kathait
Department of Instrumentation Engineering-USIC, H.N.B., Garhwal University, Garhwal,
Srinagar 246174, Uttarakhand, India

R. C. Rohilla
P.W.D. B&R, Panipat 132103, India

1 Introduction

Sun is a readily available source of renewable energy. It spreads life giving energy on every creature in the solar system. Due to its abundance and availability to all without any bias, it is considered to be the best and cleanest renewable energy source also, as it is available to everyone so, he/she is free to utilize according to needs and capabilities. Using the photo voltaic technology one can harness its capability of producing electrical energy. The generated electrical energy thus can be utilized to run the electrical appliances designed to make life and living comfortable.

In the present scenario, electrical energy for the consumers is provided through utility grid so, the availability of electrical energy for running the loads/appliances that one has, inevitably depends on the availability of utility grid in the vicinity of house/work place. Sometimes, the geographical, environmental, and societal conditions affect the availability of utility grid.

According to government of India and ministry of power , electrical energy requirement of country was 12,74,595 MU and the availability was 12,67,526 MU for the year 2018–19. Total deficit was only 0.6%, while calculating the deficit total installed capacity was considered it doesn't include the power stations running in under capacity mode. So, in real time this deficit is far more [1]. However, it has been seen that housings in the planned localities as well as housings near to them witness the frequent power cuts. That's why the battery backed inverters are becoming one of the must have amenity. Power cuts and unavailability of grid, this situation is not limited to the unplanned housings but also in Planned housing societies, Metro cities, Small cities, Towns as well as in Villages. It may be due to lack in the demand and supply ratio, faults in distribution system and many other known and unknown causes. System is designed and installed at the location within the Panipat city, Haryana State of Northern India. While designing the proposed solar PV system it has been kept in mind that, the grid is mostly unavailable during the peak demand hours in summer season i.e. from 6:00 PM to 10:00 PM in the evening. It is the time when most of the people arrive from their workplace to home and they get relax, entertainment, cook meals, and start their sleep in the night. Since, it becomes dawn and tually night during these hours most of the lightening, cooling, and entertainment appliance came up in the operation mode so, electricity demand gets increased by many folds.

As far as the Indian power sector is concerned, the power generation is first from thermal (Coal, Gas and Oil) 64.1%. Second is from other renewable sources 20.8%. Third is the hydro power (renewable) 13.1% and at last from nuclear 2.0% [1].

Thermal power generation is a costly technology. Hence, the electricity generated is costly in terms of price per unit of consumption. This cost ultimately incurred from the consumers. With the advancement in technologies in the distribution system, "Smart Grid" concept is now in starting phase of its adaptation. One of the attribute is that, the user will be charged for the consumption according to demand and supply ratio. Price of electricity will vary throughout the day and in the peak demand hour's, consumers have to pay more price for the consumption.

Solar Photovoltaic energy production technology is now matured enough and commercialized [2]. Many design strategies like hybrid, standalone and grid connected as well as optimization of system components have been proposed in literature [3]. Our work is to demonstrate the system based on the use of existing methods, tools, and techniques to reduce the dependency on grid and further, bring down the utility bills. Hence, the residents may adopt the proposed system, and get benefited from our design.

2 Methodology

2.1 Solar Resource Assessment

First thing is to assess the solar resources available throughout the year at that place where the system is to be installed. This can be done through meteorological data that is being made available in public domain by many government agencies of the world like, Ministry of New and Renewable Energy India, NREL, Department of Energy US and many more international solar alliance [4–7]. Data collected from the ground station or the form the Meteosat satellite [8]. Some well-known online tools and software are also available like pvgis, VAISALA, solargis, nrgsystems, PVSYST, homer etc. [9–14]. Some have inbuilt applications to find the Latitude, Longitude and Elevation of that place and use them for assessing the availability of solar radiations throughout the year for different tilt angel of solar panels.

The system is designed, tested and installed for a 2 BHK house situated in Civil hospital complex, Panipat at Latitude 29.401, Longitude 76.971 and Elevation 232 m, in the Haryana state of Northern India [9], which is in the National Capital Region [15]; and have the capability to represent the entire region including states Punjab, Haryana, Delhi, western part of Uttarpradesh state and Eastern part of Rajasthan state. Solar resource availability was assessed by PVGIS online [9] and PVGIS-SARAH dataset, which have used images capturing the solar surface irradiance and cloud albedo from Meteosat satellite to construct this data set [16].

2.2 Optimum Solar Tilt Angle

PV panels to capture maximum solar radiations can be mounted either on sun tracking platform with capability to track sun by change one axis, two axis or fixed. Sun tracking arrangement is costly, so that, in our design we have not used it. Instead we have chosen to mount PV panels fixed at an optimum tilt angle. For optimizing, the tilt angle findings of several researchers have been reviewed; and concluded the simplest way to choose it [17, 18]. We found that sum of Latitude angle of that place and 5° i. e. $34.4^\circ \pm 4^\circ$ is optimum for winters as well as summers [19]. The found angle

Table 1 Monthly Global horizontal irradiation (kWh/m²) data obtained Minimum in any month of a year at optimum tilt angle

SARAH data set year for selected location	Monthly global horizontal irradiation (kWh/m ²) minimum	At optimum tilt angle 34.4° ± 4°	Month of minimum global horizontal irradiation (kWh/m ²)
2005	108	155	January
2006	105	157	December
2007	111	165	December
2008	105	155	December
2009	108	153	January
2010	85.6	113	January
2011	107	150	January
2012	97.8	141	December
2013	101	141	January
2014	93.5	127	January
2015	82.7	109	January
2016	94.7	130	January

gives Global horizontal irradiation above 1 kWh/m² as per calculations from PVGIS online tool Table 1 summarizes the obtained values .

The observed data conform the feasibility of operation of the system throughout the year. Solar resource availability varies from 109 kWh/m²–165 kWh/m². Year wise variations in minimum resource availability varies from 82.7 kWh/m² to 111 kWh/m².

2.3 Load Estimation

Next step is to estimate the load of appliances, a small 2 BHK house with appliances is summarized in Table 2. It is chosen because it represents the maximum number of housings and the minimum load requirements in the entire NCR region. Temperature in summers may go up to 45 °C when fans are needed and in winters goes below up to 12 °C when no need of fans only lightings are required.

Total energy demand of a day is coming out to be 8,953 Wh. the maximum load at any time is 670 W. Total energy demand for peak hours i.e. from 6:00 PM to 10:00 PM total 4 hours comes out to be 2250 Wh/day. So, the system was designed according to 2250 Wh/day.

Table 2 Estimation of load of appliances to be run. TL = Tube light (22 W); LE1 = Led B22 Bulb (10 W); EF = Exhaust Fan (50 W); CF = Ceiling Fan (75 W); MC = Mobile Charger (10 W); TV = Television Set (100 W); STB = Set Top Box (20 W); LE2 = Led B22 Bulb (8 W)

Time	Appliances in															Total power												
	Kitchen			Bed room 1			Bed room 2			Drawing/Living room			Toilet/Bathroom		Lobby/Dining room			Entrance		Balcony								
	TL	LE1	EF	TL	LE1	CF	MC	TL	LE1	CF	MC	TL	LE1	TV	STB	CF	AS	LE2	EF	TL	LE1	CF	TL	LE1	TL	LE1	LE1	
6	0	10	0	0	10	75	10	0	10	100	20	75	0	8	0	0	0	0	0	0	10	75	0	10	0	10	0	458
7	0	10	0	22	0	75	0	0	10	100	20	75	0	8	0	0	0	0	0	0	10	75	0	10	0	10	0	340
8	22	0	50	22	0	75	0	22	0	100	20	75	0	8	50	0	0	0	50	22	0	75	0	0	0	0	0	638
9	22	0	50	0	0	75	0	22	0	100	20	75	0	8	50	0	0	0	50	22	0	75	0	0	0	0	0	586
10	22	0	0	0	0	75	0	0	0	100	20	75	0	8	0	0	0	0	0	22	0	75	0	0	0	0	0	472
11	0	0	0	0	0	75	0	0	0	0	0	0	0	75	40	0	0	0	0	0	0	75	0	0	0	0	0	340
12	0	0	0	0	0	0	0	0	0	0	0	0	0	40	0	0	0	0	0	0	0	75	0	0	0	0	0	115
13	0	0	0	0	0	0	0	0	0	0	0	0	0	0	0	0	40	0	0	0	0	0	0	0	0	0	0	40
14	0	0	0	0	0	75	0	0	0	0	75	0	0	0	75	40	0	0	0	0	0	0	0	0	0	0	0	265
15	0	0	0	0	0	75	0	0	0	100	20	75	0	0	0	0	0	0	0	0	0	75	0	0	0	0	0	420
16	0	0	0	0	0	75	0	0	0	100	20	75	0	0	0	0	0	0	0	0	0	75	0	0	0	0	0	420
17	0	0	0	0	0	75	0	0	0	100	20	75	0	0	0	0	0	0	0	0	0	75	0	0	0	0	0	420
18	0	0	0	0	0	75	0	0	0	100	20	75	0	0	0	0	0	0	0	0	0	75	0	0	0	0	0	420
19	22	0	0	0	10	75	0	0	10	75	0	22	0	8	0	0	0	0	0	0	0	75	0	0	0	10	0	502
20	22	0	50	22	0	75	0	22	0	100	20	75	0	8	50	0	0	0	50	22	0	75	0	0	0	10	10	658
21	22	0	50	22	0	75	0	22	0	100	20	75	0	8	50	0	0	0	50	22	0	75	0	0	0	10	10	670
22	22	0	0	22	0	75	0	22	0	100	20	75	0	8	0	0	0	0	0	0	22	0	75	0	0	0	0	570
23	0	10	0	0	0	75	10	0	0	100	20	0	0	0	0	0	0	0	0	22	0	75	0	22	0	10	0	539

(continued)

Table 2 (continued)

Time	Appliances in																							Total power			
	Kitchen			Bed room 1			Bed room 2			Drawing/Living room			Toilet/Bathroom		Lobby/Dining room			Entrance		Balcony							
	TL	LE1	EF	TL	LE1	CF	MC	TL	LE1	CF	MC	TL	LE1	TV	STB	CF	AS	LE2	EF	TL	LE1	CF	TL		LE1	LE1	
0	0	0	0	0	0	75	10	0	0	0	75	10	0	0	0	0	0	0	0	0	0	0	0	0	10	0	180
1	0	0	0	0	0	75	10	0	0	0	75	10	0	0	0	0	0	0	0	0	0	0	0	0	10	0	180
2	0	0	0	0	0	75	10	0	0	0	75	10	0	0	0	0	0	0	0	0	0	0	0	0	10	0	180
3	0	0	0	0	0	75	10	0	0	0	75	10	0	0	0	0	0	0	0	0	0	0	0	0	10	0	180
4	0	0	0	0	0	75	10	0	0	0	75	10	0	0	0	0	0	0	0	0	0	0	0	0	10	0	180
5	0	0	0	0	0	75	10	0	0	0	75	10	0	0	0	0	0	0	0	0	0	0	0	0	10	0	180
																											8,953
																										Total	

2.4 Inverter Selection

Inverter is required to convert DC voltage stored in the batteries to AC voltage similar to the voltage that comes to a house from Utility Grid, so that appliances may function smoothly. Inverters with high efficiency greater than 90% are readily available in the market. Keeping in view the efficiency, availability in market and system voltage, 1100 VA Single Phase inverter with option to connect 24 V battery bank with efficiency greater than 90% (assumed 93%) was purchased from old appliances market due to cost constraints.

Inverter has to supply the power in the cabling to which load is connected. There may be 2% power loss is assumed so, inverter output energy should be 2% greater than 2250 Wh/day i.e. 2296 Wh/day.

Calculated Input Energy to the inverter from Battery Bank = (Inverter output energy/inverter efficiency) = $(2296/0.93) = 2468.81$ Wh/day.

2.5 Battery Bank Design

Output voltage of Battery Bank was chosen as 24 V. Some of the energy from battery to inverter may get lost this was assumed to be 2%.

Output energy from battery was calculated to be $(2468.81/0.98) = 2519.20$ Wh.

Capacity of battery is the ampere hour (Ah) capacity and depends upon the output energy required, output voltage and the depth of discharge of battery (DoD). DoD was assumed as 50%.

$$= (\text{Energy required} \times \text{Day of Autonomy}) / (\text{output voltage} \times \text{Depth of Discharge}) \\ = (2519.20 \times 1) / (24 \times 0.50) = 209.93 \text{ Ah.}$$

In the market, 12 V/ 200 Ah lead acid batteries are readily available at fair price. Since, the output voltage was chosen as 24 V so, two batteries of 12 V 200 Ah each were connected in parallel to achieve the 24 V, 200 Ah.

Battery will be charged via Solar panels through charge controller and in absence of solar energy can be charged through utility grid. Battery charging system for solar photovoltaic system is different from conventional charging system. Because, energy harvested from solar panels is neither provide constant charging current nor the constant voltage. Therefore, a charge controller is required.

Total energy required at input of the battery bank depends on how efficiently the battery bank gets charged from its lowest state of charge to full charge.

We have assumed the Lead Acid Battery bank as 70% efficiency [20].

So, input energy = (Output energy/efficiency)

$$\text{Input energy} = (2519.20 \text{ Wh}/70\%) = 3598.85 \text{ Wh.}$$

Table 3 Specifications of charge controller

Nominal battery voltage	24 V
Maximum battery current rating	30–50 A
Input PV voltage range, Voc	40–85 V
Power conversion efficiency	>96%
Charge regulation	Four stage charging algorithm: bulk, absorption, float and equalization
Float voltage	27 V
Reverse current flow protection	Yes
PV High voltage charging disconnect and its recovery	Yes
PV high current regulation	If battery current ≥ 30 A

2.6 Charge Controller Selection

Battery charging can be controlled via two types of technologies available one is Pulse-Width Modulation (PWM) technology and another is Maximum Power Point Tracking (MPPT) technology. Both the technologies have their own benefits and drawbacks. In MPPT, there is a programmable chip which is usually used to switch on the DC-DC convertor according to the algorithm and fused into chip. When solar panel output voltage is higher than the required DC voltage, the DC-DC convertor takes high DC voltage at input and maintain a required constant lower DC voltage at the output. This extra voltage is converted into the current. When the solar panel output voltage decreases below the required voltage, the DC-DC converter takes lower DC voltage at input and convert it into higher DC voltage by compensating the current.

Charge controller also works as a reverse blocking system that prevents the flow of charge from battery to solar panels. MPPT charge controller was chosen in this system. However, cost of MPPT charge controller is higher than PWM Charge controller. But due to its various advantages like efficiency, battery life enhancement feature and availability at affordable price, makes it a popular controller. The MPPT charge controller with capability of controlling the battery charging via solar panel as well as via grid was selected in our system. Specifications of charge controller are summarized in Table 3.

2.7 Solar Panel Estimation

Solar panels need to be connected with battery bank via charge controller so, there will be some energy loss in wires from panel to charge controller, charge controller

Table 4 Specifications of solar panel provided by manufacturer

Cells type	Poly crystalline
Capacity	315 W
Voltage at Max Power (Vmax)	36.75 V
Open Circuit Voltage (Voc)	45.25 V
Current at Max Power (Imax)	8.58 A
Short Circuit Current (Isc)	9.29 A

to battery bank and within the charge controller itself. We have assumed the cabling loss is 2% in either direction.

Energy at the charge controller output after 2% cable loss = $(3598.85 \text{ Wh}/0.98) = 3672.30 \text{ Wh}$.

Input energy required to the charge controller from solar panel side = $(3672.30 \text{ Wh}/\text{charge controller efficiency}) = (3672.30 \text{ Wh}/97\%) = 3785.87 \text{ Wh}$.

Solar panel output required at input of charge controller after 2% cable loss = $(3785.87/0.98) = 3863.14 \text{ Wh}$.

Output of Solar panels while assuming 5 h of sunshine = $(3863.14 \text{ Wh}/5 \text{ h}) = 772.62 \text{ W}$.

Module retarding factor due to panel soiling, shading, mismatch and temperature difference were assumed as 30%.

So, module output power required = $(772.62 \text{ W})/(100 - 30)\% = 1103.75 \text{ W}$.

Module aging factor was also considered as 10%.

Final module power required = $(1103.22 \text{ W}/90\%) = 1226.39 \text{ W}$.

Four solar panels of 315 W each were chosen to provide the required energy from the available choices in the market. Specifications of solar panel as provided by manufacturer summarized in the Table 4.

3 Results and Discussion

The block diagram representation of the system is summarized in Fig. 1. Four solar panels of 315 watt each are connected with wire in parallel to achieve final module power required at the input of charge controller as per calculations. All connections with solar panels were constructed by 6 mm² copper wire, charge controller in this system works as master for all the system components solar panels, battery bank, inverter mains input and AC mains (grid input). Battery bank is connected parallel to both charge controller and inverter. Inverter mains input comes from charge controller which is being utilized to charge batteries if not fully charged, via grid, in case of absence/insufficient solar power. Inverter output is connected with the load. The designed system is similar to the popularly known retrofitted system as propagated by the charge controller manufacturers [21, 22]. According to the specifications, it is easy to connect with battery backed inverter system. The actual designed system is depicted in Figs. 2, 3, 4 and 5. System is working without losing power on a single

Fig. 1 Block diagram representation of the designed system

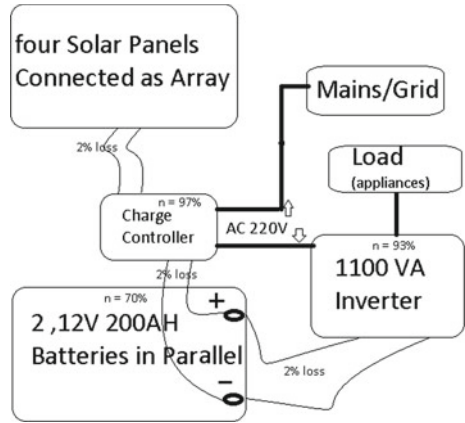


Fig. 2 Installed system (inverter and batteries)



Fig. 3 Solar Charge Controller



day and producing electricity. Daily, at the time of peak demand hours, the house owner himself switches off the mains/grid.

The installed system can provide three fold benefits in terms of power saving. The first benefit, it doesn't require power from utility grid to charge batteries. second

Fig. 4 4 Solar panels connected in parallel of 315 Watt each



Fig. 5 Solar panels mounted at optimum angle



benefit, during day time surplus energy can run the electrical appliances or fed to the grid. third benefit, it can run the electrical appliances during peak hours and power cut. Hence, the system is capable of reducing the monthly electricity bill. The money saved can be accounted for the recovery of the cost of installed system.

4 Conclusions

The designed system for Assessment of electricity savings utility bills is reviewed. In Panipat city the electricity distribution and its monthly billing is maintained by Uttar Haryana Bijli Vitran Nigam (UHBVN). It's official website contains latest orders and circulars that governs the tariff and charges for the computation of monthly electricity bills [23]. The monthly savings of electricity by utilizing the designed system comprises of electricity generated from the solar panels during 5 sun shine hour (electricity used in charging batteries and surplus power, power delivered to load during 4 peak demand hours).

$$\text{Savings} = (3598.85\text{Wh} + 2250\text{Wh}) = 5848.85 \text{ Wh}$$

Approximately, 6 kWh/day and in a month it comes out to be 180 kWh.

Table 5 Actual cost of the system

Sr. No.	Material/Equipment	Charges in Rupees
1.	1100 VA inverter	2,000
2.	Two batteries of 12 V, 200 Ah	22,000
3.	Charge controller 24 V	3,500
4.	4 Solar Panels of 315 W each	29,900
5.	Other expenses (cables, stand and labor)	3,000
	Total	60,400

Normally the billing without installing the system was approximately Rupees, One thousand Four hundred (Rs. 1,400/-) for 350 units (1 unit = 1 kWh). After installing the system monthly electricity bill is now approximately Rupees, Five Hundred (Rs.500/-). Clearly it leads to savings of approximately Rupees One thousand (Rs.1,000/-).

Actual cost of system is summarized in Table 5.

References

1. CEA (2020) "Power sector at a glance ALL India" ministry of power powermin.nic.in. <https://powermin.nic.in/en/content/indian-electricity-scenario>
2. Chapman RN (1987) Sizing handbook for stand-alone photovoltaic/storage systems, SAND87-1087, Sandia National Laboratories, Albuquerque, New Mexico
3. Egido M, Lorenzo E (1992) The sizing of stand-alone PV systems: a review and a proposed new method. *Sol Energy Mater Sol Cells* 26:51–69
4. Bibek B, "INDIA SOLAR RESOURCE MAPS" Ministry of New and Renewable Energy Government of India. <https://mnre.gov.in/india-solar-resource-maps>
5. Department of Energy U.S. (2020) Solar resources. <https://www.energy.gov/>. Accessed 1 Jan 2020
6. NREL (2020) "Solar Resource Data, Tools, and Maps" nrel.gov.in. <https://www.nrel.gov/gis/solar.html>. Accessed 1 Jan 2020
7. Google.com searched term solar resource maps, 1 January 2020
8. Wikimedia Foundation (2020) "Meteosat" Wikipedia.org. <https://en.wikipedia.org/wiki/Meteosat>. Accessed 1 Jan 2020
9. European Commission (2019) "EU Science Hub/ PVGIS/Interactive tools". https://re.jrc.ec.europa.eu/pvg_tools/en/tools.html. Accessed 9 Apr 2019
10. VAISALA (2019) "Vaisala Forecaster" vaisala.com. <https://www.vaisala.com/en/products/renewable-energy/forecaster>. Accessed 9 Apr 2019
11. Suri M (2019) "Prospect data forecast" solargis.com. <https://apps.solargis.com/prospect/map?> Accessed 9 Apr 2019
12. Vogel E (2019) "SOLAR RESOURCE ASSESSMENT" nrgsystems.com. <https://www.nrgsystems.com/products/applications/solar-resource-assessment>. Accessed 9 Apr 2019
13. Andre M et al (2019) "A full package for the study of your photovoltaic system" pvsyst.com. <https://www.pvsyst.com/>
14. Homer energy team (2019) "Homer pro software" homerenergy.com. <https://www.homerenergy.com/products/pro/index.html>. Accessed 9 Apr 2019

15. NCR planning board (2019) "NCR Constituent Areas" National Capital Region Planning Board (Ministry of Housing and Urban Affairs, Government of India). <http://ncrpb.nic.in/ncrconstituent.html>. Accessed 9 Apr 2019
16. Müller R, Trentmann J, Trager-Chatterjee C, Pfeifroth U (2015) Sarah-a new homogeneous climate data record of surface radiation. In: EGU general assembly conference abstracts, vol 17, p 2009
17. Benganem M (2011) Optimization of tilt angle for solar panel: case study for Madinah, Saudi Arabia. *Appl Energy* 88:1427–1433
18. Mohd Azmi bin Hj Mohd Yakup, Malik AQ (2001) Optimum tilt angle and orientation for solar collector in Brunei Darussalam. *Renew Energy* 24(2):223–234
19. Zobia AF, Bansal RC (2011) Handbook of renewable energy technology (Chap. 9). World Scientific, p 217
20. Stevens JW, Corey GP (1996) A study of lead-acid battery efficiency near top-of-charge and the impact on PV system design. Sandia National Laboratories, Specialists Conference, IEEE, Washington, DC
21. Schneider-electric (2019) "C12 PWM Charge Controller" solar.schneider-electric.com. <https://solar.schneider-electric.com/product/conext-c12pwm-charge-controller/>. Accessed 9 Apr 2019
22. Smarten power systems (2019) Prime series r-mPPT charge controller. <http://www.smartenpowerversystems.com/pdf/Prime-series-MPPTController.pdf>. Accessed 9 Apr 2019
23. Chief Engineer/Commercial (2019) UHBVN, Panchkula "Tariffs" uhbvn.org.in. <https://uhbvn.org.in/staticContent/documents/Tariff.pdf>. Accessed 9 Apr 2019

Modeling and Simulation of Correlations of Porosity with Strength Development of GGBS Blend Cement Concrete



Sujata D. Ingale and Pravin D. Nemade

Abstract By-product of iron industry that is GGBS is suitable material used in manufacturing cement and concrete. The concrete mix and their types both contributes vital role in producing strength of concrete. This paper addresses how the pores in concrete structure relate with its strength of compression. Experimentally obtained results of pore volume and compressive strength are comparing with the calculated value. For predictions, the model SP-24 for compressive strength, and the Powers–Brownyard model for pore volume are used. Predicted value with both models gives roughly the same values as reported values

Keywords GGBS · Concrete · Pore volume · Compressive strength

1 Introduction

GGBS is broadly used as a partial replacement of cement to increase in the strength and to reduce in the water demand. It play important role in minimizing resistance to chloride attack, causes lower in porosity. Also by using GGBS as cementitious material, gain high strength at an increase of age [1]. Optimum % replacement of cement with GGBS is a crucial factor [2, 3]. It is a source of Alumino-silicate, used as a binder material [4]. To manufacture enduring cement concrete with all depositories should minimize its voids, to have a minimum of 28 days strength. This condition can reduce either by an increase in the amount of cement in prevailing concrete or by introducing micro-particles in it [5]. GGBS concrete has higher compressive strength than OPC, when after almost completion of hydration and pozzolanic reactions [6]. Specimens made with suitable cement in addition to GGBS and gypsum produce minimum stresses and resistance to abrasion after drying the specimen.

S. D. Ingale

Department of Civil Engineering, Dr. D.Y. Patil Institute of Technology, Pimpri, Pune, India

S. D. Ingale (✉) · P. D. Nemade

Savitribai Phule Pune University, Pune, Maharashtra, India

P. D. Nemade

S. B. Patil College of Engineering, Indapur, Pune, India

Table 1 Chemical compositions (%) of binding material

References	Cementitious material	CaO	SiO ₂	Al ₂ O ₃	Fe ₂ O ₃	MgO	SO ₃
Vasugi and Elavenil [23]	GGBS	58.6	26.6	11.4	0.4	2	–
Xie et al. [21]	OPC	62–67	20–24	7-Apr	6-May	0.9	2.12
	GGBS	35.05	35.52	13.6	0.61	9.58	1.72
Yong et al. [22]	Fly ash	1.59	65.9	24	2.87	0.42	–
	GGBS	42.6	36	13.8	0.3	5.8	0.56
Shahab et al. [24]	GGBS	40	35	16	3	6	–

Consequently, the specimen shows a decrease in voids and their volume at the ages of different curing conditions [7]. With decreasing the porosity, increasing values of the compressive strength [8, 9]. GGBFS having pozzolanic reactivity, used as a replacement of cement in cement concrete, causes the gain of strength as an increase in the age of curing [10]. Exothermic process of cement hydration produce a significant amount of heat. As cement concrete has minimum conductivity in thermal, at beginning of processes cause a substantial change in temperature near the surface and high internal temperature. [11]. GGBS as partial replacement material with cement in concrete can considerably minimize the liability of attack of sulfate, penetration of chloride, and the reaction of alkali-silica [12]. GGBS is by-product coming from furnace slag which is used to manufacture Iron. It is high in calcium silicate hydrate, which cause increase in strength and durability. Mainly the composition of GGBS, are CaO, SiO₂, and Al₂O₃ which are same as composition of cement. Thus, use of GGBS as partial replacements of cement, which result in minimize demand of cement consequently decrease in environmental pollution, as production of cement goes on decreasing (Table 1).

2 Experiments

2.1 Materials

Material reported by [13] were PC (ASTM Type 1), GGBS having finesse 4000 cm²/g, the size of coarse aggregate was 20 mm, for fine aggregate finesse modulus was 2.96, and super plasticizer C494 G-type which fulfill requirements.

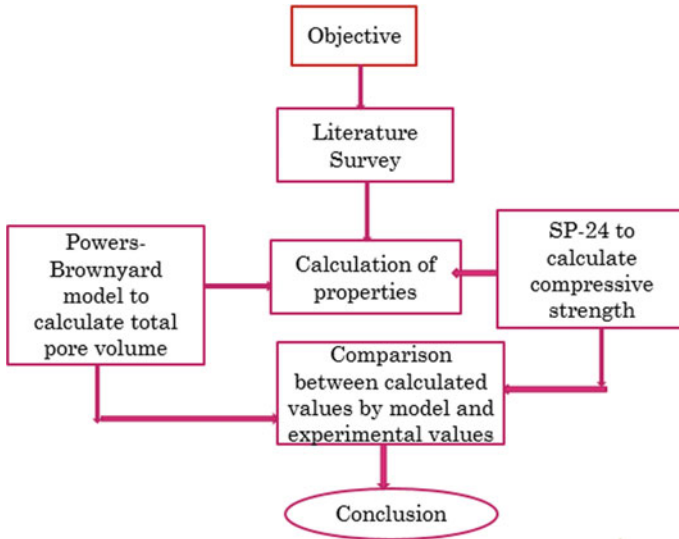


Fig. 1 Systematic representations of methodology

2.2 Methodology

2.3 Drying Technique

Microstructure plays important role in drying processes thus identification of microstructure of cementitious material is very important. Galle [14] has reported four drying methods namely as first oven drying at 60 °C, second oven drying at 105 °C, third one is drying processes in vacuum, and fourth one is freeze-drying. For oven drying, ventilated ovens were used for placing paste samples, which was readjusted at 60 °C and 105 °C ± 1 °C. Well-controlled conditions were achieved at 7 days of drying operation. The drying techniques were not affected by total mercury porosity values. In these method vacuum desiccators were connected to trap, dry ice-alcohol bath temperature was used for this technique, similar to the drying method [15]. In this process, the first sample was frozen (-195 °C) for 5 minutes by immersing in liquid nitrogen, to prevent the enhancement of large ice cube which cause large pore formation [16].

3 Results and Discussions

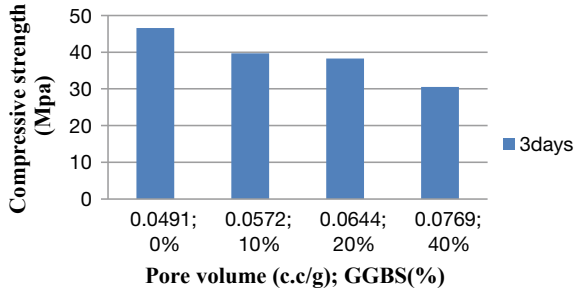
3.1 *Relation Between Pore Parameters and Compressive Strength*

Ordinary cement concrete has less drying shrinkage as compare to alkali activated slag concrete, even though in case of ordinary Portland cement, there is large amount of moisture loss at the time of drying [17, 18]. GGBS added in cement concrete can improve the concrete strength in compression and split tensile, which produces better grain size distribution and pozzolanic effect as compared to the specimen with cement alone. [7, 19]. When water and cement both come in contact with each other, start the process of hydration of cement. Water present in the cement paste is of two natures, evaporable and non-evaporable. The non-evaporable water chemically reacts with the cement, called as bound water. In further hydration process, contributes only capillary water [11]. Chemical reactions between alkaline activators solution and pozzolanic material both cause denser amorphous products which lead to rise in load-carrying capacity and correspondingly rise in its compressive strength [4, 13]. Finer particle size of particle could not effects on autogenously shrinkage of materials [20]. Hydration processes are closely related to the inner product, as it produces resistance to ion movement, this resistance depends upon properties of C-S-H as well as thickness [1]. Main constitute in the strength development are the type of the mixed proportion of slag in concrete and its characteristics. The pozzolanic reactivity of GGBFS gains strength at a later age [10]. Figure 2a shows that, at 3 days of curing, pore volumes are more than that at 28 days of curing. Also at early age, strength decreases with an increase in % of slag. That means, strength is inversely correlated with substitution ratio. It is because; at early age cement hydration causes strength. As pore volume decreases with an increase in age, the pozzolanic reaction gets apparent which results in higher strength. Figure 2b shows that at maximum % of replacement of cement by GGBS that is 40%, pore volume for the same matrix is 0.0141 c.c/g which is less as compares to other matrix, and having maximum compressive strength that is 59.77 MPa [13]. From the above discussion, it has been clear that pore can fill effectively by adding GGBS into concrete.

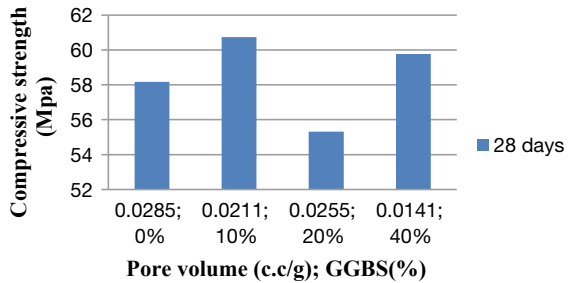
3.2 *Prediction of Porosity Measurement*

The materials pore space was measured by measuring free water pore and MIP tests. As MIP measurement processes not liable to give the appropriate value of total porosity, as it has limitation to pore size range nearly about 375 to 0.003 μm . Whole water porosity (ϕ_w) is equal to net quantity of water drawn out through water soaking specimen after process of one and all drying up to constant loss of mass and is given by Eq. (1) [14].

Fig. 2 Strength versus capillary pore volume of GGBS concrete: **a** strength at 3 days, and **b** strength at 28 days



(a)



(b)

$$\varnothing_w = \frac{m_s - m_d}{v\rho} \tag{1}$$

where, \varnothing_w is the total water porosity, m_s is the specimen water-soaking mass (kg), m_d is dried mass of the specimen (kg), v is volume of the specimen (m^3), and ρ is the density of water at 20 °C (kg/m^3).

The Powers–Brownyard model, total porosity (\varnothing_t) is equal to the sum of hydrate porosity and capillary porosity (Eqs. (2)–(7)).

$$\varnothing_t = \varnothing_0 - 0.55m(1 - \varnothing_0) \tag{2}$$

where, \varnothing_t , is equal to total porosity, \varnothing_0 is the pilot porosity, and m is hydrate rate. If saturation of cement material is considered under water, then complete hydration cannot occur. So take $m = 0.38$.

$$\varnothing_0 = \frac{w/c}{(w/c + 0.313)} \tag{3}$$

Total porosity-theoretically given by,
 Total pore volume (cm^3);

$$v_{p,tot.} = w_0 - 0.19 \alpha \quad (4)$$

Where, $\alpha = 1$

$$v_{p\ tot\ gel} = 0.197 \alpha c \text{ (cm}^3\text{)} \quad (5)$$

Capillary porosity is the difference between total porosity and gel porosity.

$$P_{cap} = \frac{(w/c)_0 - 0.39 \alpha}{(w/c)_0 + 0.32} \quad (6)$$

$$\text{In general } P_{cap} = \frac{(w/c)_0 - k \alpha}{(w/c)_0 + 0.32} \quad (7)$$

K is coefficient of the order 0.36–0.42.

Figure 3 shows comparative result of reported and calculated porosities. As w/c is an integral criterion in the Powers–Brownyard model, experimental values, and calculated values at w/c ratio 0.34–0.57, 10% relative discrepancy occurs. Table 2 shows that, at w/c ratio 0.5–0.83, there is a 30–40% relative discrepancy between calculated and experimental values.

3.3 Comparison Between Compressive Strength Reported in [13] and Predicted Values with SP-24

SP-24 suggest the following equation for compressive strength with time of concrete cube [10]

$$(f_c)_t = \left(\frac{t}{4.7 + 0.83t} \right) (f_c)_{28} \quad (8)$$

Where $(f_c)_t$ is strength in compression of concrete cube at any time in N/mm^2 , t indicate time in days and $(f_c)_{28}$ is strength in compression of cube at 28 days in N/mm^2 .

Figure 4a indicates, the strength for replacement of cement with 20% GGBS at early age that is from 0 to 7 days, reported in Cheng et al. [13] are higher than the strength calculated with the model given in SP-24. While at 28 days both calculated and reported values are the same for 20 and 40% replacement of cement by GGBS. Figure 4b, For 40% GGBS, strength at 1 day, and 56 days, both reported and calculated values are the same, for other ages that is for 3 and 7 days both calculated and reported values are round about the same.

Fig. 3 Comparison between capillary pore volume reported in Cheng et al. and estimated by the Powers–Brownyard model: a, b, and c for 0.35 w/b

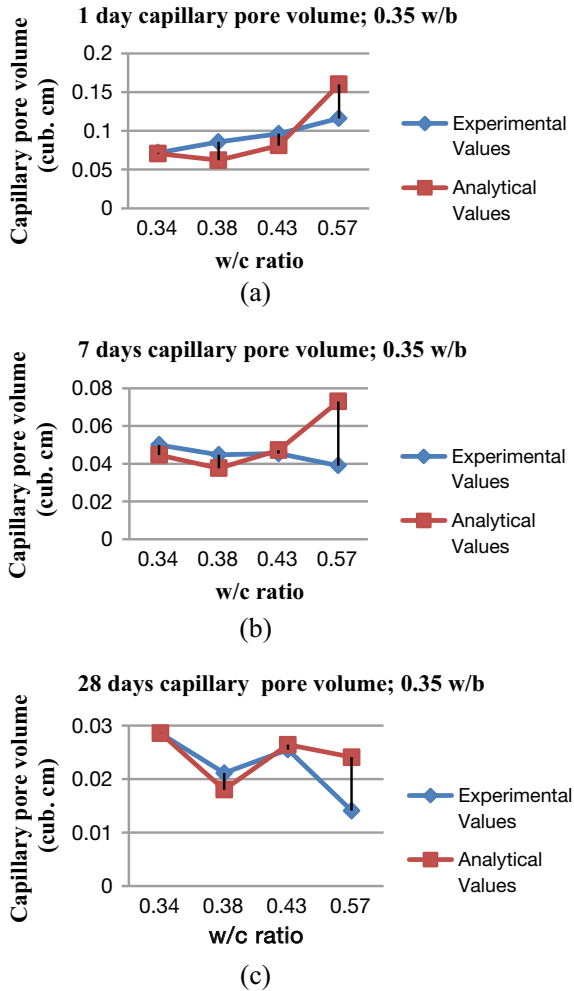
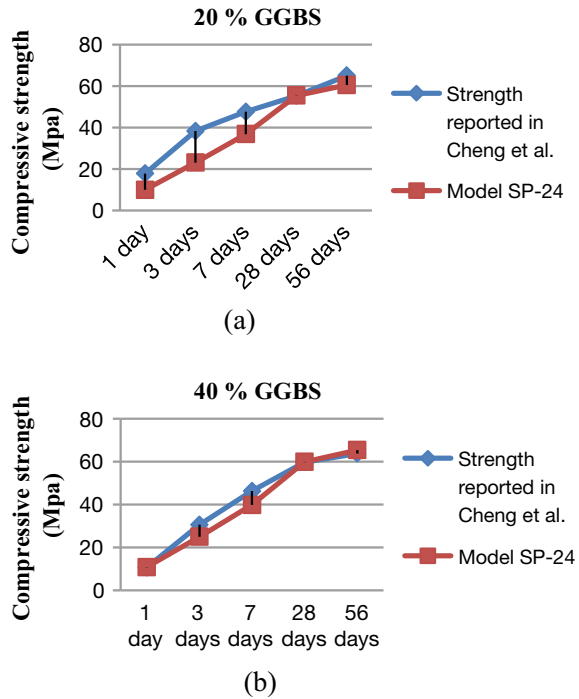


Table 2 Comparison between Capillary pore volume (c. c./g) reported in [13] and calculated by the Powers–Brownyard model

Capillary pore volume (c.c./g)	w/c ratio							
	0.5	0.55	0.62	0.83	0.5	0.55	0.62	0.83
	1 day				28 days			
Cheng et al. [13]	0.1207	0.121	0.1266	0.129	0.0617	0.0508	0.055	0.023
The Powers–Brownyard model	0.1219	0.138	0.1382	0.1818	0.0629	0.0672	0.062	0.037

Fig. 4 Comparison between compressive strength reported in Cheng et al. [13] and estimated with the model SP-24: **a** 20% replacement of cement with GGBS; **b** 40% replacement of cement with GGBS



4 Conclusion

Predicated on the above study conclusions are as below:

The strength in compression of GGBS concrete with the SP-24 model have found to be a good agreement with reported value.

The proposed model for predicting Capillary pore values, w/c ratio is an essential parameter for that; possess agreement between reported and calculated values is almost perfect for w/c ratio range between 0.35 and 0.56. For the w/c ratio 0.5–0.83, there is a deviation of about 30–40%.

Also result shows that, in the case of GGBS strength increases with an increase in curing age of concrete, as pore size decrease with an increase in age of curing.

References

1. Yao L, Tetsuya I, Toyoharu N, Takahiro S (2012) Enhanced model and simulation of hydration process of blast furnace slag in blended cement. *J Adv Concr Technol* 10:1–13
2. Lee H-S, Wang A-Y, Zhang L-N, Koh K-T (2015) Analysis of the optimum usage of slag for the compressive strength of concrete. *Materials* 8:1213–1229

3. Xie T, Yang G, Zhao X, Xu J, Fang C (2020) A unified model for predicting the compressive strength of recycled aggregate concrete containing supplementary cementitious material. *J Clean Prod* 251
4. Krishnan V, Solaiyan E (2020) Study of engineering and micro structural properties of ambient cured GP concrete produce from GGBS and M-sand. *J Crit Rev* 7(7)
5. Balayssac JP, Detriche ChH, Grandet J (1995) Effect of curing upon carbonation of concrete. *Constr Build Mater* 9(2):91–95
6. Lee J, Lee T (2020) Durability and engineering performance evaluation of CaO content and ratio of binary blended concrete containing ground granulated blast-furnace slag. *Appl Sci*
7. Jiang C, Zhou X, Tao G, Chen D Experimental study on the performance and microstructure of cementitious material made with due sand. *Adv Mater Sci Eng* (2016)
8. Yazdi MA, Liebscher M, Yang J, Mechtcherine V (2018) Correlation of micro structural and mechanical properties of geopolymers produced from fly ash and slag at room temperature. *Constr Build Mater* 191:330–341
9. Hilal El-H, Kianmehr P (2018) Pervious concrete pavement incorporating GGBS to alleviate pavement runoff and improve urban sustainability. *Road Mater Pavement Des* 19(1):167–181
10. Shariq M, Prasad J, Masood A (2010) Effect of GGBFS on time dependent compressive strength of concrete. *Constr Build Mater* 24:1469–1478
11. Wang X-Y, Lee H-S (2010) Modeling the hydration of concrete incorporating fly ash or slag. *Cem Concr Res* 40:984–996
12. Divsholi BS, Lim TYD, Teng S (2014) Durability properties and microstructure of ground granulated blast furnace slag cement concrete. *Int J Concr Struct Mater* 157–164
13. Cheng A-S, Yen T, Liu Y-W, Sheen Y-N (2008) Relation between porosity and compressive strength of slag concrete. Crossing. In: Structures congress 2008, Vancouver, British Columbia, Canada
14. Galle C (2001) Effect of drying on cement-based materials pore structure as identified by mercury intrusion porosimetry: A comparative study between oven-, vacuum-, and freeze-drying. *Cem Concr Res* 31:1467–1477
15. Zhang L, Glasser FP (2000) Critical examination of drying damage to cement paste. *Adv Cem Res* 12(2):79–88
16. El-Died AS, Hooton RD (1994) Evaluation of the Katz-Thompson model for estimating the water permeability of cement-based materials from mercury intrusion porosimetry data. *Cem Concr Res* 24(3):443–455
17. Collins F, Sanjayan JG (2000) Effect of pore size distribution on drying shrinkage of alkali activated slag concrete. *Cem Concr Res* 30:1401–1406
18. Wenyan Z, Yukio H, Seung HN (2015) Drying shrinkage and micro structure characteristics of mortar incorporating ground granulated blast furnace slag and shrinkage reducing admixture. *Constr Build Mater* 93:267–277
19. Oner A, Akyuz S (2007) An experimental study on optimum usage of GGBS for the compressive strength of concrete. *Cem Concr Compos* 29:505–514
20. Sharmilan S, Yuya T (2020) Experimental study on autogenous shrinkage behaviors of different Portland blast furnace slag cements. *Constr Build Mater* 230
21. Xie J, Wang J, Rao R, Wang C, Fang C (2019) Effects of combined usage of GGBS and fly ash on workability and mechanical properties of alkali activated geopolymer concrete with recycled aggregate. *Compos B Eng* 164:179–190
22. Yong H, Zhuo T, Wengui L, Yunan L, Vivian WY (2019) Physical-mechanical properties of fly ash/GGBFS geopolymer composites with recycled aggregates. *Constr Build Mater* 226:139–159
23. Vasugi K, Elavenil S (2020) Study on engineering and micro structural properties of ambient cured GP concrete produce from GGBS and M-sand. *J Crit Rev* 7(7):499–506
24. Shahab S, Shah A, Limbachiya M (2017) Strength development characteristics of concrete produced with blended cement using ground granulated blast furnace slag (GGBS) under various curing conditions. *Indian Acad Sci* 42(7):1203–1213

Comparative Kinetic Study for Adsorption of Heavy Metals with Low-Cost Adsorbents—Sugarcane Baggase and Eggshell



Diksha Kadu, Siddhant Bhasarkar, and Sandeep P. Shewale

Abstract Heavy metals present in wastewater are toxic and have an adverse effect not only on human health but the whole ecosystem. The removal of toxic heavy metals from wastewater is of great concern from the environmental point of view. Here, sugarcane bagasse is used as an adsorbent for the removal of heavy metals along with eggshell. The experimentation was carried out using the conventional batch process as well as with ultrasonication. The ultrasonication creates cavitation which results in breaking of bond and creating more area for adsorption. Various process parameters such as contact time, pH, particle size, etc. were investigated, optimized and studied to get maximum adsorption. It was found that Ultrasonication shows maximum %removal of Zinc than the batch process. Effects of %removal of zinc concerning time, uptake capacity concerning time were plotted. The isotherms were plotted for kinetic study shows that the Langmuir isotherm is best suitable.

Keywords Heavy metals · Sugarcane bagasse · Batch process · Ultrasonication · Kinetic study

1 Introduction

Most of the heavy metals are released into the surrounding through the different sources such as manufacturing processes, domestic effluents, drainage water, business effluents, atmospheric deposition, and traffic-related emissions and are reflected determined environmental pollutants as they cannot be diminished naturally. Toxic metal ions (for example Zn, Ni, Cr, Cu, Cd, Pb, As, etc.) are the source of physical discompose and sometimes deadly infection with permanent harm to the crucial body organ. Deposition of heavy metal ions in the surrounding is acquired and are signified beside the food series [1, 2]. The harmful heavy metals, actual in large or even in small concentrations, must be efficiently removed from the wastewaters by the efficient method. Surrounded by all these toxic metals, zinc has many adverse effects on the environment like it cause phytotoxicity, Anaemia and lack of muscular

D. Kadu · S. Bhasarkar · S. P. Shewale (✉)
School of Chemical Engineering, MIT Academy of Engineering Alandi, Pune 412105, India

coordination etc. The WHO, BIS and USEPA permissible limit of zinc in drinking water is 0.5 mg/L. The maximal allowable limit of zinc in the inward surface water is 5.0 mg/L by central pollution control board (CPCB), India. The maximal allowable limit of zinc in industrial wastewater is 5.0 mg/L by USEPA. Processes such as wetness, ion exchange, thickening, connection, reverse osmosis, electro-winning, adsorption etc. have been established for heavy metal elimination from the wastewater however utmost practices have some restrictions for instance to the necessity of numerous pre-operation and added actions [3, 4]. Besides, some of them are less effective and require high capital. Among these adsorptions is widely used because of its high selectivity compared with other separation techniques, cost-effectiveness and relatively high sorption capacity for pollutants even at low concentration. There are various adsorbents like nano adsorbents, Modified natural materials, Industrial by-products, Modified biopolymers, agricultural waste and hydrogels but their application is not conjoint and limited to the exceptional conduct because of high fixing and operative cost. Amongst all these systems, biosorption might be used in agricultural waste has gained considerable attention because of high efficiency, minimal operating cost, more accessibility and simplicity of usage. Biosorption exploits biological constituents as adsorbents and this technique has been investigated by numerous investigators as a substitute for traditional methods for the elimination of heavy metals from wastewater [5–7]. Amongst all these techniques and process for selection adsorbent, sugarcane bagasse (SCB) is used widely as it is an inexpensive agriculture waste product attained from the remaining cane pulps used later the sugar extraction. It is essentially together of fat, cellulose, ash, lignin and waxes silica. The agriculture waste (SCB) comprises of different functional groups like as carbonyl, phenolic and amine faction that can be associated with usage new composites with many substances [8, 9]. In the present study, removal of zinc has been studied using sugarcane bagasse as an adsorbent along with eggshell for comparative study. Ultra-sonication and batch processes have been studied and compared. Several experimental parameters like pH, adsorbent dosage, interaction time, particle size, adsorbent concentration, were inspected. Effects of %removal of zinc to time, uptake capacity to time were plotted. SEM investigation previously and subsequently portion of zinc in contact with sugarcane bagasse was similarly accomplished to estimate the system of adsorption. The kinetic study is also done using Langmuir and Freundlich isotherm.

2 Materials and Methods

2.1 Materials

Raw eggshell was collected from a local bakery shop. The raw sample was washed with definite times with the distilled water to remove contamination and some resistance of salt and organic material. Afterwards, the eggshell sample was transferred

to a dry oven for 24 h at 100 °C and then purifying the sample. Then the calcinations of broken dried sample was finished in the furnace at 250 °C for 20 min. Lastly, the sample material was ground and sieved through different mesh sizes. This portion was relative to 60% of the available total dried sample. Then the adsorbent prepared was used for further experiment. Sugarcane bagasse was procured from a Sant. Tukaram Maharaj sugar industry, Pune. The available bagasse was dehydrated under sun and pith was removed manually. The segregated and clean pith was boiled with distilled water for about 35 min to eliminate soluble sugars available in it. The substantial charge obtained was further dried at 125 °C in a hot air type of oven for 1 day, and afterwards, the material was ground and sieved over different mesh sizes. The prepared adsorbent is now can be used for further experimentation. SEM analysis was done from Pune university before adsorption. Different concentration of zinc solutions was processed by dissolving zinc acetate in distilled water and the solution was heated at 60 °C. The pH of the solutions was regulated by 0.01 M NaOH/0.01 M HCl by applying a pH meter. Different particle size adsorbents were obtained by using different mesh sizes. Analysis of samples after studying different parameters was carried out in UV-Visible spectrophotometer.

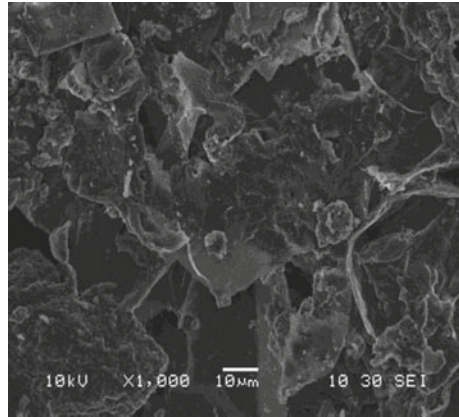
2.2 Adsorption Experiments

Batch and ultrasonication experiments were performed for both the prepared adsorbents and various parameters like pH (2–6), adsorbent dose (0.25–2 g), particle size (0.106, 0.212, 0.3 mm) were studied for a contact time of 60 min. For a batch experiment, 250 ml closed batch reactor which has provision for collecting the sample at regular interval of time was taken and placed with an overhead stirrer along with it. Now, 200 ml of 200 ppm zinc solution (prepared by adding 0.04 g of zinc acetate in distilled water) was taken and 1 g of adsorbent was added. Now, set the desired agitation speed (rpm). Collect the sample solution after every 5 min. of starting the agitation speed in sample bottles. For ultrasonication, 250 ml volumetric flask was taken and 200 ml of 200 ppm zinc solution (prepared by adding 0.04 g of zinc acetate in distilled water and solution was kept for heating at 60 °C) were added with 1 g adsorbent. Now, start the ultrasonicator and collect samples after every 5 min. in a sample bottle. Repeat the procedure same for optimising different parameters. Analysis of samples was carried out in UV-Visible spectrophotometer and absorbance was measured at 213 nm, further calculation and graphs were calculated using the absorbance value. The removal percentage ($R\%$) of zinc was estimated for each experimental run by the below equation [10, 11]:

$$R(\%) = \left[\frac{C_i - C_e}{C_i} \right] \times 100 \quad (1)$$

Here C_i and C_e were the starting and lateral concentration of zinc in the available solution. The adsorption quantity of an adsorbent that is attained through the mass

Fig. 1 SEM analysis before adsorption



balance (M) on the sorbate in a integrate with solution volume V is usually used to achieve the experiential adsorption isotherms [12–15]. Under the experiential conditions, the adsorption quantity of all the adsorbents for every single concentration of zinc ions at equilibrium was examined by

$$q_e(\text{mgg}^{-1}) = \left[\frac{C_i - C_e}{M} \right] \times V \quad (2)$$

3 Results and Discussions

3.1 Characterization of Adsorbent

Analysis of adsorbent (sugarcane baggase) before and after adsorption of zinc was shown by SEM. It gave us a clear idea about the availability of sites present for the adsorption at various magnifications. It was observed from Figs. 1 and 2 that the perforated one before the adsorption was coated with zinc after the adsorption. The SEM morphology can be seen

3.2 Effect of Contact Time on Adsorption (Eggshell Adsorbent)

The effect of contact time on zinc metal ion (Zn^{+2}) adsorption by eggshell adsorbent was studied taking the time of 120 min for batch and 60 min for ultrasonication with the metal ions available concentration of 200 ppm, pH 6, particle size 0.106 and

Fig. 2 SEM analysis after adsorption

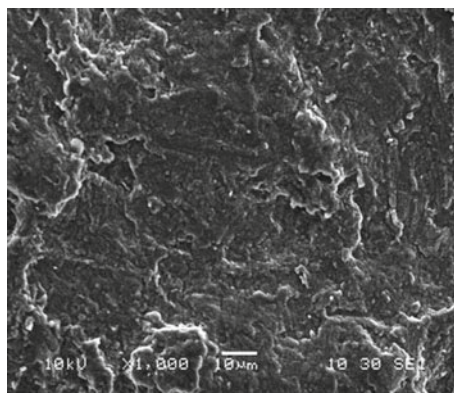
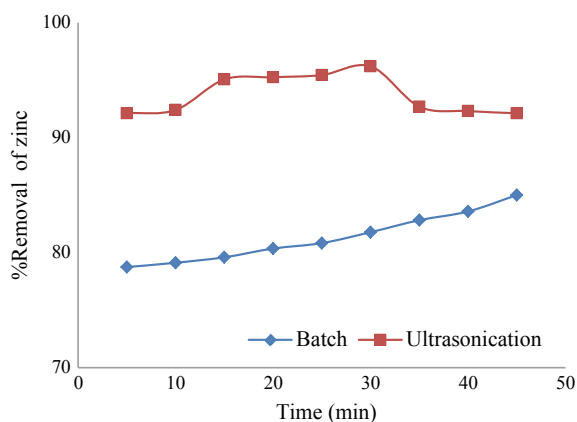


Fig. 3 Comparative study between batch and Ultrasonication process



adsorbent dosage 1 g. As shown in Fig. 3 It was found that the Ultrasonication shows better adsorption than the batch process and with an optimum time of 30 min.

3.3 Effect of Particle Size: (Eggshell Adsorbent)

The experiment was carried (Fig. 4) out using eggshell adsorbent using a mesh size of 0.106, 0.212 and 0.3 mm. As the particle size decreases the rate of adsorption increases this because of the rise in the available surface area. As the surface area increases the rate of adsorption increases and can be seen in fig. that 0.106 mm gives maximum zinc removal when compared with 0.212 and 0.3 mm

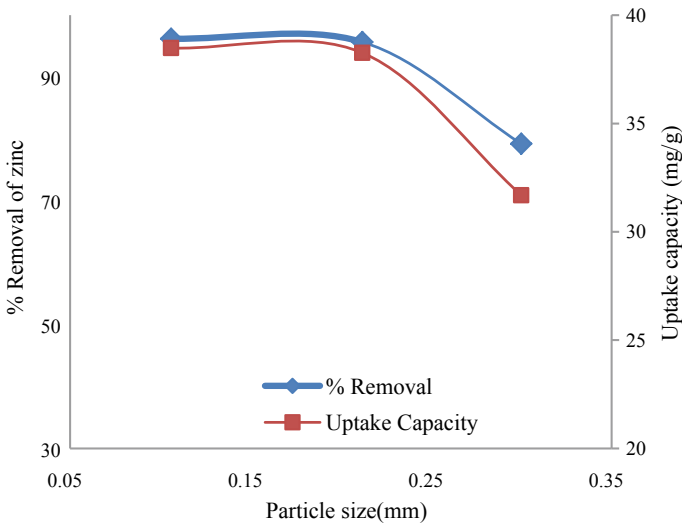


Fig. 4 Effect of particle size on %removal and uptake capacity at 200 ppm, pH 6 and 1gm of an adsorbent

3.4 Effect of Contact Time on Adsorption (Sugarcane Baggase)

The effect of contact time on zinc metal ion (Zn^{+2}) adsorption by SCB adsorbent was studied by taking the time of 120 min for batch and 60 min for ultrasonication to the metal ions available concentration of 200 ppm, pH 6, particle size 0.106 and adsorbent dosage 1 g. As shown in Fig. 5, it was found that the ultrasonication shows better adsorption than the batch process and with an optimum time of 30 min.

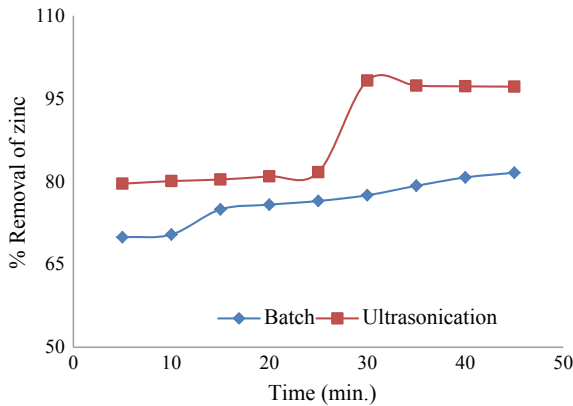


Fig. 5 Comparative study between batch and ultrasonication

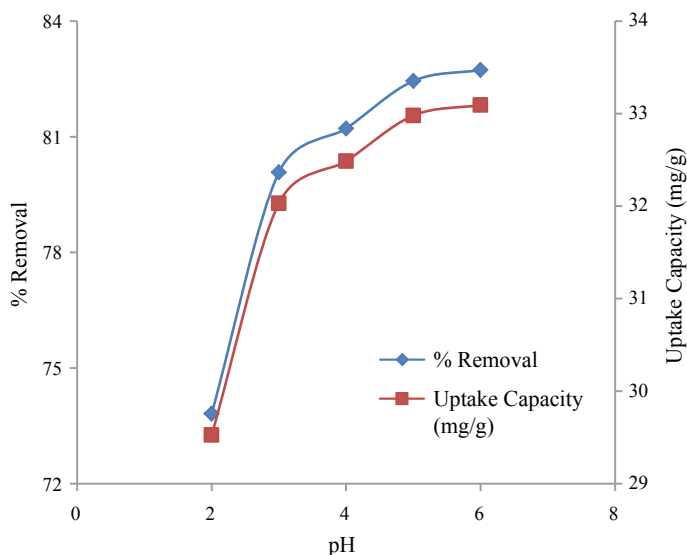


Fig. 6 Effect of pH on %removal and uptake capacity

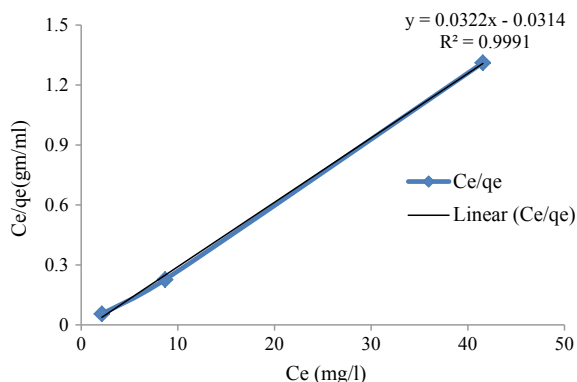
3.5 Effect of PH (for Sugar Cane Baggase)

The pH of an aqueous solution is an essential parameter that can limit the adsorption system. Also, the pH of the solution influences the metal ion category and the surface imputation state of the adsorbent precisely. The effect of pH was studied by varying pH 2 to 6 while keeping other parameters constant. The interrelation amongst the starting values of pH and quantity of heavy metal was conferred in Fig. 6 at pH reduce than 6, simultaneously lower the adsorption of metal ions. The reason for this phenomenon is due to minimal pH, the proton concentration is above than the particular of a metal ion. Accordingly, the adverse sites of the Zinc will be engaged by proton ions to prevent the metal ions adsorption and it will be diminished.

3.6 Adsorption Isotherm Models

The adsorption considerations were accomplished to the different parameters i.e. introductory adsorbate concentration, pH, adsorbent dosage. As shown in Fig. 7 the values were accepted for the applicability to the Langmuir isotherm and Freundlich isotherms. From the R^2 values, the data obtained fitted well into the Langmuir adsorption isotherm for changes to all the parameters by using the equation.

Fig. 7 Langmuir isotherm model



4 Conclusion

Adsorbent prepared from sugarcane baggase and eggshell can be used for removal of zinc from wastewater. The preparations of adsorbents were performed and the study of the adsorbents before adsorption and after adsorption was done by SEM. The experiment was performed by both batch experimentation as well as Ultrasonication. The comparative study was carried out using batch adsorption as well as ultrasonication and was found out that the Ultrasonication is the best way for adsorption because it gives maximum adsorption in less time. Various parameters were studied and optimized i.e., particle size, contact time and pH. The %removal versus time, uptake capacity v/s time and a plot between uptake capacity, %removal and the optimizing parameter were drawn and studied. For eggshell, as particle size increases adsorption decreases. For sugarcane bagasse, we got optimum pH is 6, as metal ion concentration increases adsorption decreases and as adsorbent dosage increases, absorption also increases. The adsorption process was described by Langmuir isotherms as it shows good agreement with equilibrium data obtained for changes in all parameters i.e. contact time, particle size, adsorbent dosage, pH, particle size as it fit with the experimental data.

References

1. Barakat MA (2011) New trends in removing heavy metals from industrial wastewater. Arab J Chem 4:361–377. <https://doi.org/10.1016/j.arabjc.2010.07.019>
2. Hegazi HA (2013) Removal of heavy metals from wastewater using agricultural and industrial wastes as adsorbents. HBRC J 9:276–282. <https://doi.org/10.1016/j.hbrj.2013.08.004>
3. Hussain AZ, Sheriff KMM (2014) Removal of heavy metals from wastewater using low cost adsorbents. Arch Appl Sci Res 6:52–54
4. Jai PH, Wook JS, Kyu YJ, Gil KIMB, Mok LEES (2007) Removal of heavy metals using waste eggshell. J Environ Sci 19:1436–1441

5. Karami H (2013) Heavy metal removal from water by magnetite nanorods. *Chem Eng J* 219:209–216. <https://doi.org/10.1016/j.cej.2013.01.0227>
6. Lata S, Samadder SR (2016) Removal of arsenic from water using nano adsorbents and challenges: a review. *J Environ Manag* 166:387–406
7. Yogeswari E, Vashantha R, Samuel J (2016) Removal of toxic bivalent ions from wastewater by adsorption on bioadsorbents-a short overview. *Arch Appl Sci Res* 8:20–23
8. Chitaranjan D, Ramakar J, Desai VR (2015) Rice husk and sugarcane baggase based activated carbon for iron and manganese removal. *Aquat Proc* 4:1126–1133. <https://doi.org/10.1016/j.aqpro.2015.02.143>
9. Ihsan U, Raziya N, Munawar I, Qaisar M (2013) Biosorption of chromium onto native and immobilized sugarcane bagasse waste biomass. *Ecol Eng* 60:99–107. <https://doi.org/10.1016/j.ecoleng.2013.07.028>
10. Saswati C, Vinod T (2006) Role of various parameters in synthesis of insoluble agrobased xanthates for removal of copper from wastewater. *Biores Technol* 97(18):2407–2413. <https://doi.org/10.1016/j.biortech.2005.10.010>
11. Umesh G, Kaur MP, Jawa GK, Dhiraj S, Garg VK (2008) Removal of cadmium (II) from aqueous solutions by adsorption on agricultural waste biomass. *J Hazard Mater* 154(1–3):1149–1157. <https://doi.org/10.1016/j.jhazmat.2007.11.040>
12. John Kwame B, Wei W, Sok K, Yeung-Sang Y (2015) Removal of heavy metals from aqueous phases using chemically modified waste Lyocell fiber. *J Hazard Mater* 299:550–561. <https://doi.org/10.1016/j.jhazmat.2015.07.033>
13. Dhiraj S, Garima M, Kaur MP (2008) Agricultural waste material as potential adsorbent for sequestering heavy metal ions from aqueous solutions – a review. *Biores Technol* 99(14):6017–6027. <https://doi.org/10.1016/j.biortech.2007.11.064>
14. Ioannis A, Amit B, Bassim H, Yong Sik O, Michalis O (2017) A review on waste-derived adsorbents from sugar industry for pollutant removal in water and wastewater. *J Mol Liq* 240:179–188. <https://doi.org/10.1016/j.molliq.2017.05.063>
15. Misbah A, Haq Nawaz B, Munawar I, Saima N, Sana S (2017) Biocomposite efficiency for Cr(VI) adsorption: Kinetic, equilibrium and thermodynamics studies. *J Environ Chem Eng* 5(1):400–411. <https://doi.org/10.1016/j.jece.2016.12.002>

Stress Analysis of Carbon Fiber Composite Rotating Blade Using COMSOL in Undamaged and Damaged Condition



Avinash K. Parkhe, Sandeep S. Wangikar, Shashikant S. Jadhav, Shrikrushna B. Bhosale, and Prashant M. Pawar

Abstract Rotating beams play an important role in engineering structure such as turbine blades, airplane propellers and robot manipulators. Composite materials are widely used in aircraft industries. In helicopter rotor application composite material bring additional features like drastic reduction in number of parts and bulkiness, especially for rotor hub system which is typical large source of profile drive. In this paper the dynamic analysis of composite blade is carried out to find the stresses induced in beam at different locations. The dynamic stress analysis has carried out on composite blade in undamaged and damaged condition to check the increase in stress value due beam damages at different locations. The composite blade is made by Carbon Fiber with 8 layers in 0° and 90° orientation of fibers. This stress analysis is carried out using COMSOL Multiphysics analysis software. The beam has rotated at different RPM and accordingly the stresses are calculated near fixed end, at mid point and at free end.

Keywords Stress · Composite blade · Undamaged · Damaged · COMSOL

1 Introduction

Composite materials have been used over the past few decades in a variety of structures. Thin-walled structural shapes made up of composite materials, which are usually produced by pultrusion, are being increasingly used in many engineering fields. Composite materials are widely used in the aircraft industries because of their superior fatigue characteristics, greater damage tolerances, and larger stiffness-to-weight ratios as compared with their metal counterparts [1, 2]. In helicopter rotor applications, composite materials can bring additional features like drastic reduction in the number of parts and bulkiness, especially for the rotor hub system, which is typically a large source of the profile drag. During manufacturing of composite blades material uncertainty remains present in it due which delamination of blade

A. K. Parkhe (✉) · S. S. Wangikar · S. S. Jadhav · S. B. Bhosale · P. M. Pawar
SVERI's College of Engineering, Pandharpur, Maharashtra, India
e-mail: akparkhe@coe.sveri.ac.in

will be taking place which creates error during testing [3, 4]. This paper aims the dynamic analysis of composite blade is carried out to find the stresses induced in beam at different locations. The dynamic stress analysis has carried out on composite blade in undamaged and damaged condition to check the increase in stress value due beam damages at different locations [5–7]. This stress analysis is carried out using COMSOL Multiphysics analysis software. The beam has rotated at different RPM and accordingly the stresses are calculated near root, at mid and at tip. In this paper internationally we have damaged the blades by producing cracks at different locations to compare results with results of undamaged blades.

2 Stress Analysis in Undamaged Condition

2.1 Specification of Problem

The Composite beam has a ply lay-up $[0_3/90]_s$ on all four sides the composite beam contain 8 layers. With the help of solid mechanics module in the COMSOL Multiphysics Stress is calculated. Figures 1 and 2 shows geometry of undamaged—damaged composite blade used for rotating condition analysis. The beam is damaged at three different locations like near root, at mid and at tip shown in Fig. 1 [8, 9].

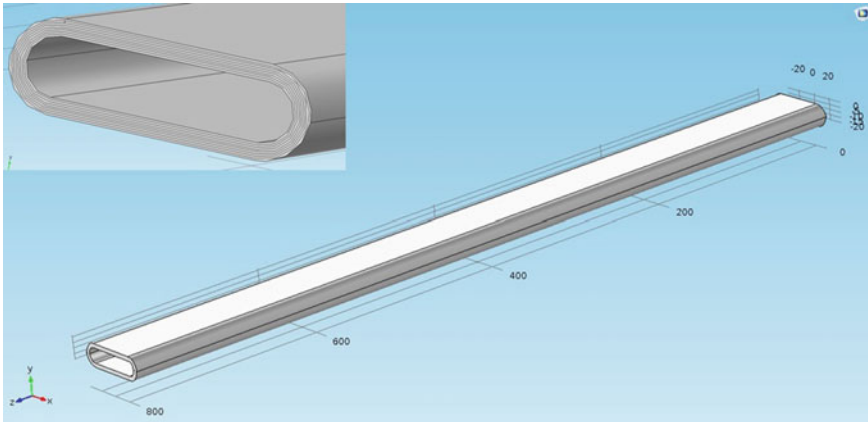


Fig. 1 Geometry of undamaged composite blade

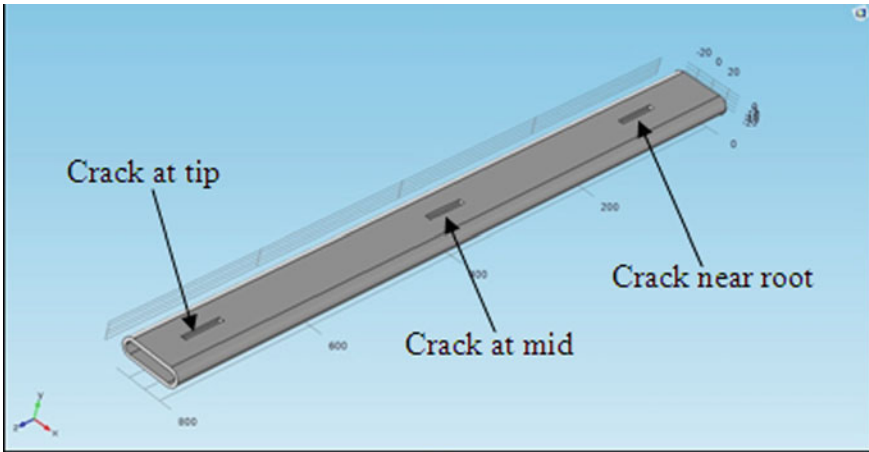


Fig. 2 Geometry of damaged composite blade at root, mid and at tip

2.2 Boundary Conditions

The Composite blade is considered as cantilever type. Hence fixed at one end and rotating at different rpm i.e. from 100 to 500 rpm shown in Fig. 3.

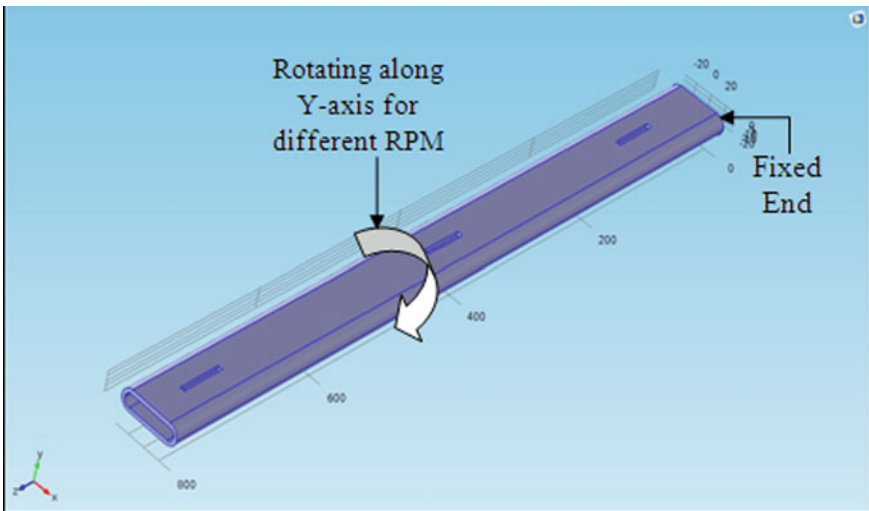


Fig. 3 Boundary conditions applied to blade

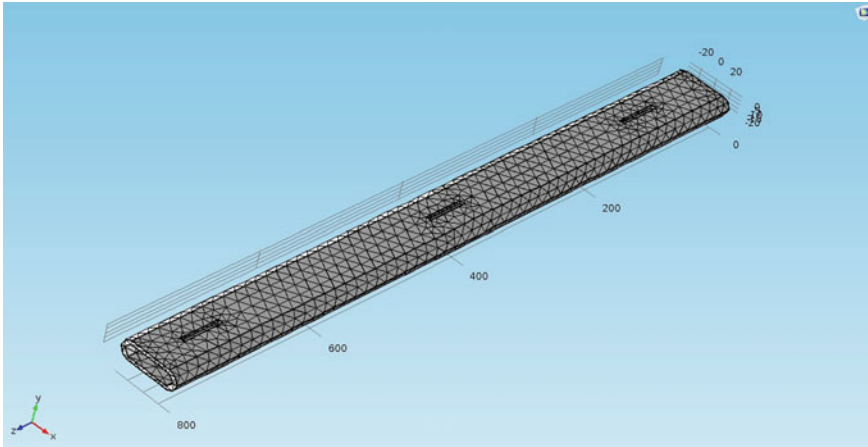


Fig. 4 Meshing of damaged composite blade

2.3 Meshing of Geometry

Meshing method is used for meshing the geometry in COMSOL Multiphysics. The geometry of composite blade with extremely coarse mesh is shown in Fig. 4.

2.4 Numerical or Simulation Result

Simulation is done for Rotating Composite blade for different rpm using COMSOL Multiphysics analysis software. Due to the rotation of blade for different RPM the stresses are induced at different locations which shown by following Fig. 5 [10, 11]. Following three figures represents the stresses induced in undamaged blade for 100 rpm. The 1st figure represents the stress induced near the fixed end, 2nd represents stress induced at mid and 3rd figure represents the stress induced at tip of the blade.

The stress analysis was carried for undamaged blade. Then for further analysis the blade is damaged at three different locations like near fixed end, at mid and at tip and again it is rotated at different rpm. Due the blade damages its stiffness gets loosed and stresses in the blade get increases is shown by following Fig. 6. The following three figures represents the stresses induced in damaged blade at three different locations [12, 13].

If damaged blade is rotating for different rpm stresses values will get changed i.e. increases which is shown by above Fig. 6. The stresses induced in undamaged and damaged blade for other rpm are represented by following Table 1 to find the stress difference at different locations due to blade damage [14].

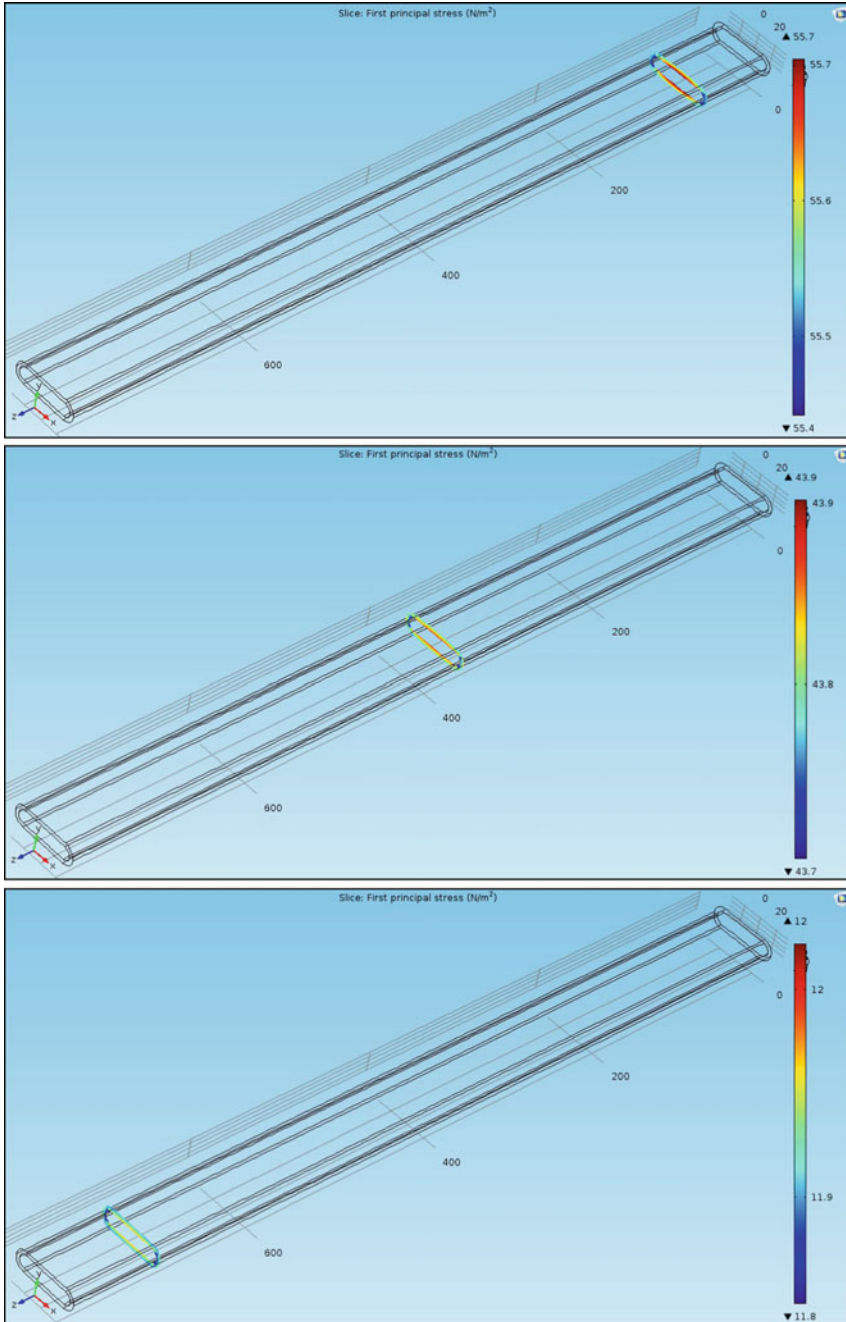


Fig. 5 Stresses results for undamaged rotating blade near root, at mid and at tip for 100 RPM

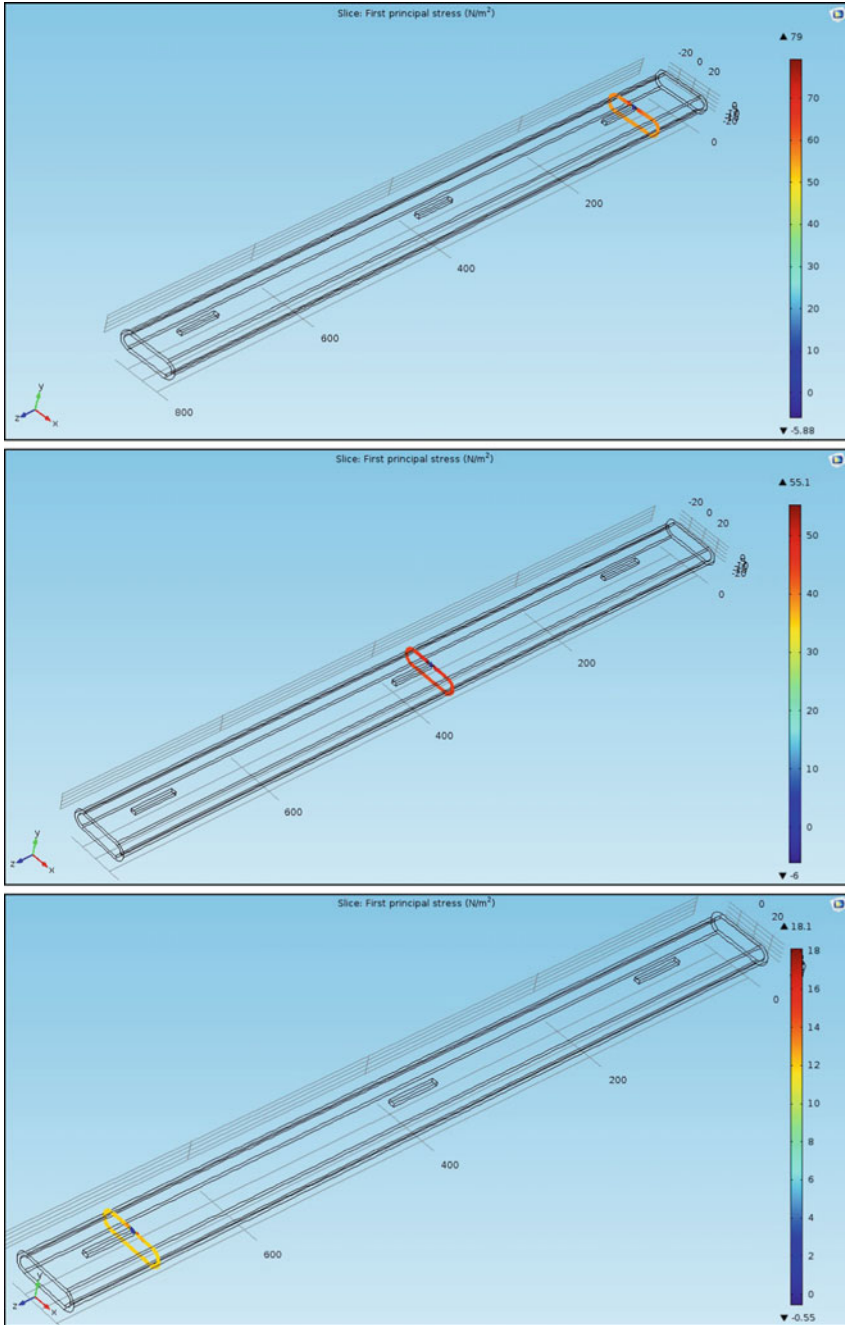


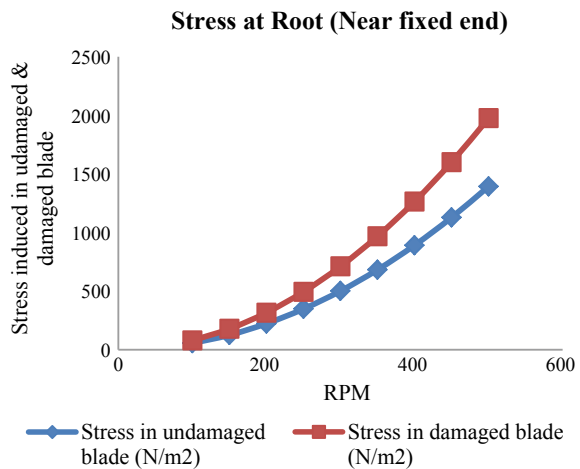
Fig. 6 Stresses results for undamaged rotating blade near root, at mid and at tip for 100 RPM

Table 1 Simulated stress results for undamaged and damaged rotating blade for different RPM and locations

RPM	Stress in undamaged blade (N/m ²)			Stress in damaged blade (N/m ²)		
	Root	Mid	Tip	Root	Mid	Tip
100	55.7	43.9	12	79	55.1	18.1
150	125	98.8	27	178	124	40.6
200	223	176	48.1	316	220	72.3
250	348	274	75.1	494	344	113
300	501	395	108	711	496	163
350	682	538	147	968	675	221
400	891	702	192	1264	881	289
450	1128	889	247	1600	1116	366
500	1393	1098	301	1975	1377	452

After analysis of all the above Figs. 7, 8, and 9 it has been observed that due to increase in rpm the stress value in rotating blade is also get increases and it always maximum at root of blade and it get decreases at tip of the blade because its free end. The above three figures indicates the increased stress value with increase in RPM along with different locations like near root, at mid and at tip of the blade [15, 16]. The overall graph of rpm versus stresses induced in undamaged and damaged blade at different locations (i.e. near root, at mid and at tip) is shown in Fig. 10.

Fig. 7 Graph of RPM versus Stress induced in undamaged and damaged composite blade at Root of blade



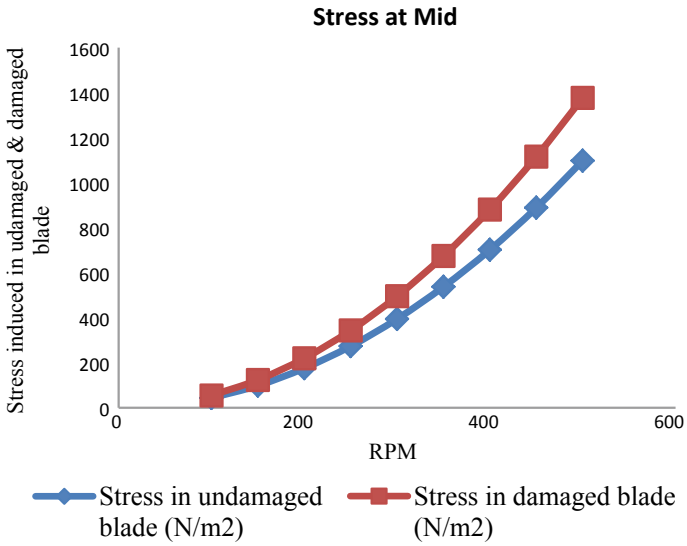


Fig. 8 Graph of RPM versus Stress induced in undamaged and damaged composite blade at Mid of blade

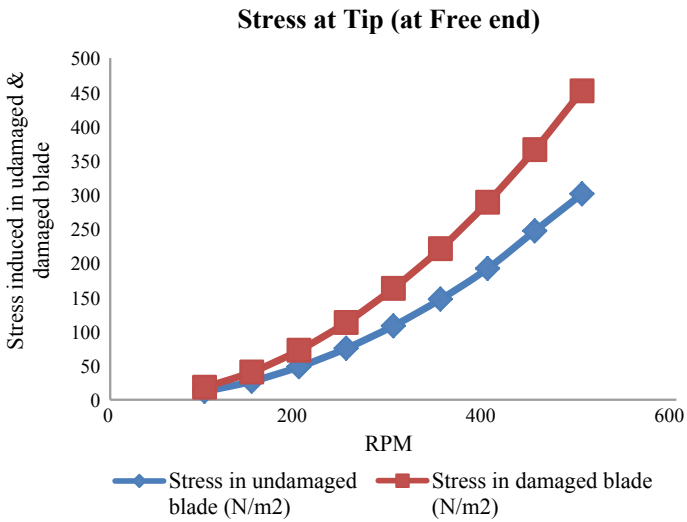


Fig. 9 Graph of RPM versus Stress induced in undamaged and damaged composite blade at Tip of blade

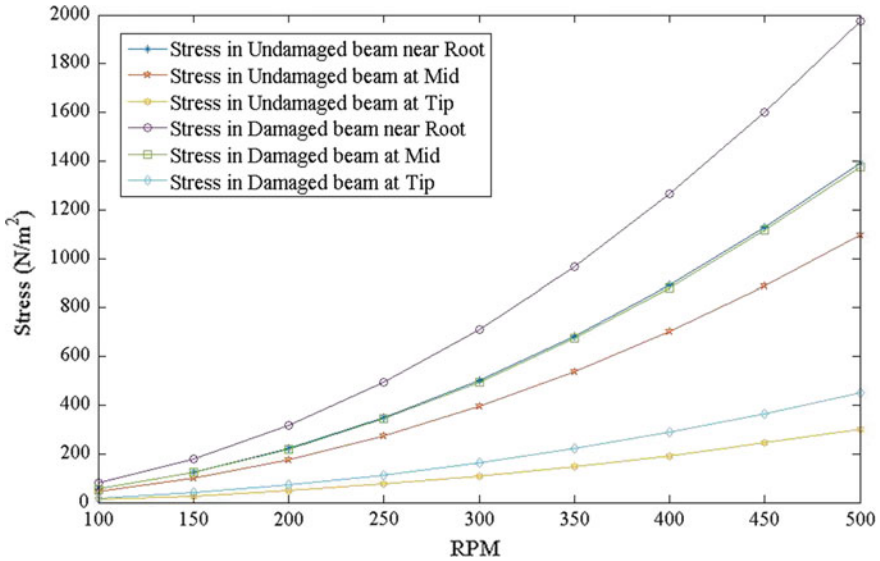


Fig. 10 Graph of RPM versus Stress induced in undamaged and damaged composite blade at different locations under different RPM

3 Conclusion

By making the comparison between the stresses induced in undamaged and damaged composite blade using COMSOL following conclusions are made:

1. Stress value has increased for damaged blade than undamaged blade and will continuously increases with increase in rpm.
2. The stress value is Maximum near the root crack than mid and tip for both undamaged and damaged blade. By this simulated results it has observed that after damaging of blade stress value is increased by 29–30% more than undamaged blade.

References

1. Chung J, Yoo HH (2002) Dynamic analysis of a rotating cantilever beam by using the finite element method. *J Sound Vib* 249:147–164
2. Jafari TR, Della C (2015) Dynamic behavior of a rotating delaminated composite beam including rotary inertia and shear deformation effects. *Ain Shams Eng J* 6:1031–1044
3. Sakara G, Sabuncu M (2008) Dynamic stability analysis of pretwisted aerofoil cross-section blade packets under rotating conditions. *Int J Mech Sci* 50:1–13
4. Lin SC (2001) Vibration analysis of a rotating Timoshenko beam. *J Sound Vib* 240:303–322

5. Ronge BP, Pawar PM, Parkhe AK (2018) Experimental analysis of composite rotor blade models for damage identification. In: *Advances in science and engineering technology international conference*, pp 1–7
6. Parkhe AK, Shinde AB, Sawant NS, Pawar PM, Haridas PD (2018) Experimental estimation of material uncertainty of composite beam using hall effect sensor. *Techno-Soc* 1:263–270
7. Hake AA, Ronge NS, Bhingare VA, Parkhe AK, Bhuse PK, More SN (2019) Static & dynamic research of composite blade using condition monitoring method. *Int J Recent Technol Eng* 8:2145–2149
8. Sina SA, Haddadpour H (2014) Axial–torsional vibrations of rotating pretwisted thin walled composite beams. *Int J Mech Sci* 80:93–101
9. Rao SS (2001) Finite element vibration analysis of rotating Timoshenko beams. *J Sound Vib* 242:103–124
10. Pawar PM, Ganguli R (2007) Fuzzy-logic-based health monitoring and residual-life prediction for composite helicopter rotor. *J Aircr* 44:981–986
11. You Y, Jung S, Pawar PM, Kim C (2010) Effect of uncertainty on hub vibration response of composite helicopter rotor blades. *J Aircr* 47:151–160
12. Kachare PS, Parkhe AK, Utpat AA, Salunkhe SY (2019) Health monitoring of static composite beam for material uncertainty and its numerical validation. *Int J New Technol Res* 5:79–83
13. Parkhe AK, Haridas PD, Kapurkar RB, Pawar PM (2015) Experimental study on natural frequency of composite box beam for multiple. *Int J Res Aeronaut Mech Eng* 3:20–25
14. Yao MH (2012) Nonlinear vibrations of blade with varying rotating speed. *Nonlinear Dyn* 68:487–504
15. Parkhe AK, Wangikar SS, Patil PK, Vhare CK, Kashid DT, Pawar PM (2020) Analytical and numerical stress analysis of composite box beam in dynamic condition and validation with COMSOL multiphysics software. *AEG. J* 8:380–387
16. Kachare PS, Parkhe AK, Utpat AA (2019) Free vibration analysis of rotating composite box beam using GY-521 accelerometer. *Int J Sci Res Publ* 9:281–289

Experimental Investigation on VCR Engine by Using Different Blend Proportions of Mexicana Oil Biodiesel



Chhappare Shivkumar, Pandhare Amar, and Godse Mitesh

Abstract Biodiesel has been proven one of the best alternatives because of its performance parameters and exhaust emissions comparable to diesel. The experimental investigation of Mexicana oil with different blend proportions with diesel carried out and found that the Hydrocarbon emissions were almost similar for all the Mexicana oil blends (7.89 ppm) compared to conventional diesel fuel (7.8 ppm). Carbon monoxide (CO) emissions were lower for all the Mexicana oil blends (0.036 ppm) compared to conventional diesel fuel (0.038 ppm). As the blend proportion increased, Nitrogen oxide emissions increased but NO_x emissions can be reduced by proper combustion cycle. The BTE increased by 2.37% for biodiesel blended up to 30% (D70B30). The Brake specific fuel consumption required was slightly higher for all the blends (0.28 kg/W-h) compared to diesel fuel (0.267 kg/W-h). Blend ratio D80B20 found the best diesel-biodiesel ratio to replace pure diesel fuel in CI engines.

Keywords Variable compression ratio (VCR) · Argemone mexicana biodiesel · Brake specific fuel consumption · Brake thermal efficiency · BHP · BMEP

1 Introduction

The growth of Indian oil demand has been increased with the increase in Indian economy in past 10–20 years. India is depending on other countries for petroleum products to fulfil energy scarcity of the country. To overcome this problem, India has to be focus on alternative options like biodiesel. Biodiesel is produced by esterification and trans-esterification with the help of alcohols like methanol or ethanol and catalysts like Sodium hydroxide or Potassium hydroxide. FME refers to Methanol based vegetable oil biodiesel while FEE refers to Ethanol based vegetable oil biodiesel [1–3].

Different blends of biodiesel are prepared for experimentation purposes.

C. Shivkumar (✉) · P. Amar
Sinhgad College of Engineering, Pune 411041, India

G. Mitesh
Vishwakarma Institute of Information Technology, Pune 411037, India

- 80% diesel, 20% biodiesel is referred as D80B20
- 70% diesel, 30% biodiesel is referred as D70B30.

It was found that the Carbon monoxide emission and Hydrocarbon emission are produced because of incomplete combustion. As Mexicana oil percentage increased, both CO and HC emissions decreased. The unburned hydrocarbon emissions decreased as the load increased. Higher in-cylinder temperature of engine resulted into increase in NO_x emission [4, 5]. As the load increased, BTE increased and BSFC decreased. Many researchers had carried out experimentation with different biodiesels like Jatropa, Soybean, Karanja, Mahua oil [6–8]. The performance parameters and exhaust emission analysis of diesel engine with Argemone Mexicana has not carried out yet to the best results. The argemone biodiesel can also be good alternative fuel to tackle the current global fuel scarcity.

2 Methodology

2.1 Material and Method

In esterification, 2 ml of H₂SO₄ is added with 20 ml of methanol and 100 ml of preheated oil. The complete mixture is heated at 60 °C for 60 min. The oil is allowed to settle in a funnel for 24 h.

In trans-esterification, 0.8gms of KOH is added to mixture of 100 ml of oil and 20 ml of methanol then heated on a magnetic stirrer for 90 min. at a temperature of 60 °C. The mixture is allowed to settle on a funnel for 24 h. The glycerol is now separated. Small quantity of water is added in the oil and mixture is kept aside for 24 h for separation of biodiesel. The separated oil is then removed. This separated oil is washed 2–3 times with water for purification of biodiesel. The moisture from biodiesel is removed by heating at 55–60 °C to get final trans-esterified oil [3, 9, 10].

2.2 Experimental Setup

A Kirloskar single cylinder, 4-stroke, water-cooled agriculture diesel engine with 1500 rpm, 3.5 kW power was used as shown in Fig. 1. The load on engine was controlled by eddy current dynamometer. The in-cylinder pressure is measured with the help of piezoelectric pressure transducer while inlet and outlet temperature of water was measured using thermocouples. AVL di gas analyzer is used to measure the emissions. The engine testing was done at atmospheric conditions. Initially, engine was warmed using diesel fuel and later it was switched to blends.

The various Argemone Mexicana biodiesel blends tested on this are B10, B20, B30, B50. During every test, the engine rpm was kept constant.

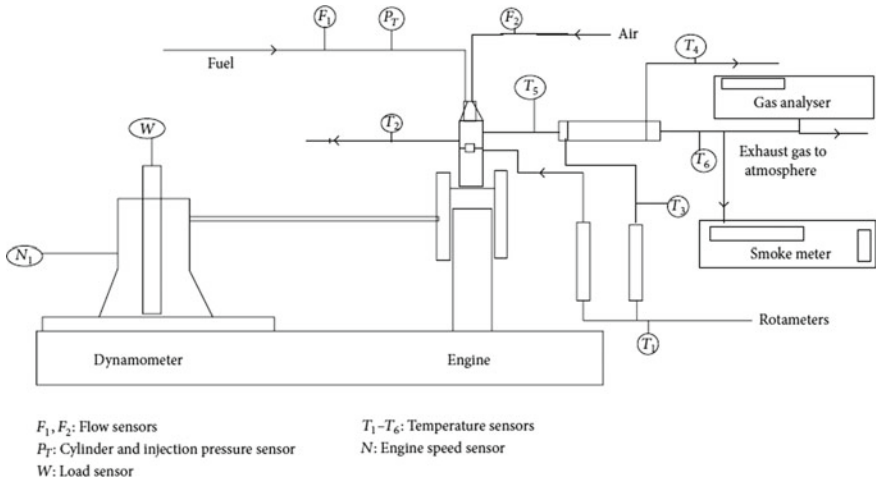


Fig. 1 Schematic diagram of test setup [10]

3 Results and Discussions

3.1 Engine Exhaust Emissions

HC emissions: As the blend proportion increased up to 20% (D80B20), HC emission decreased as shown in Fig. 2. At low load conditions, injected fuel results to formation of rich mixture zones, which results to increase in HC emissions [11].

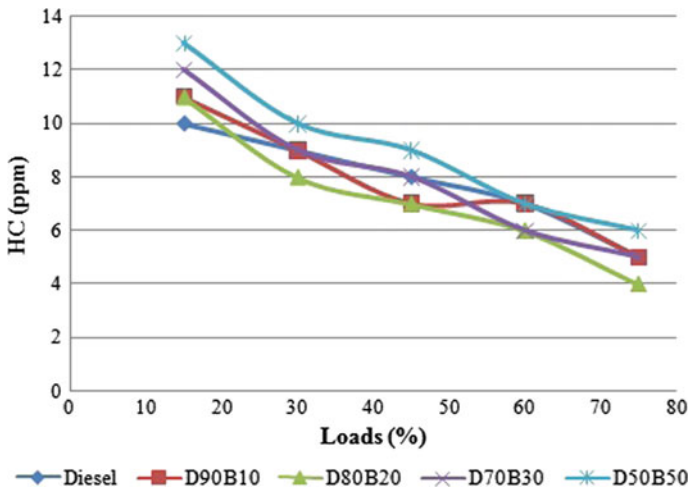


Fig. 2 Variation of Mexicana biodiesel blends on HC emissions with different loads

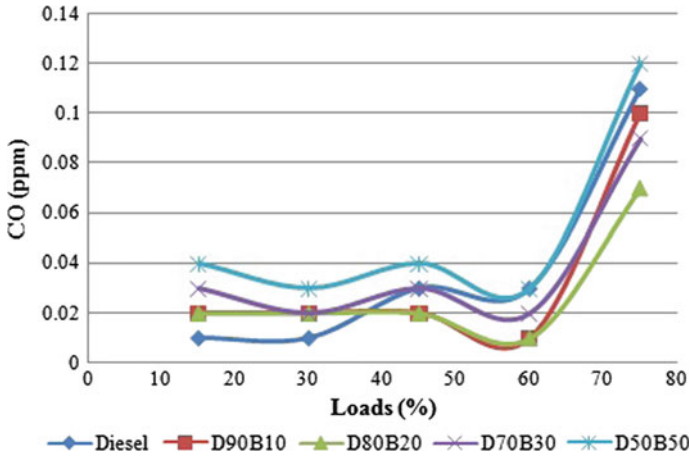


Fig. 3 Variation of Mexicana biodiesel blends on CO emissions with different loads

The unburned hydrocarbon produced was almost similar at various blends (7.89 ppm) compared to conventional diesel fuel (7.8 ppm). The in-cylinder temperature rise at low load results in HC emission reduction for D90B10 and D80B20 fuel.

CO emissions: As the blending of Mexicana oil biodiesel is increased up to 20% (D80B20), CO emissions decreased. The higher oxygen content is the responsible factor for CO emissions reduction [5]. During the combustion process, carbon monoxide produced combines with oxygen molecules to form CO₂. The percentage of CO produced was less for all Mexicana biodiesel blends (0.036 ppm) as compared to conventional diesel fuel (0.038 ppm). The Higher viscosity of the D50B50 reduces the injection angle of fuel spray that results to higher CO emissions [6]. CO emission increased suddenly beyond 60% load as shown in Fig. 3.

NOx emissions: As the load increases, Nitrogen Oxide emission increases as in Fig. 4. NOx emissions due to biodiesel blends (753 ppm) were higher than diesel fuel (755 ppm). As the Mexicana biodiesel blend increases, NOx emission decreases. Nitrogen Oxide emissions occurs mainly because of higher in-cylinder temperature of engine. Because of higher oxygen content in biodiesel blends, the in-cylinder temperature rises due to which nitrogen oxide emission increases. During the testing at low loads, there is lesser heat release rates due to which NOx emissions decreased [7].

3.2 Performance Parameters for Engine

Thermal Efficiency (BTE): BTE variation with increase in load is shown in Fig. 5. As load increases, the power produced in engine also increases which results to increase

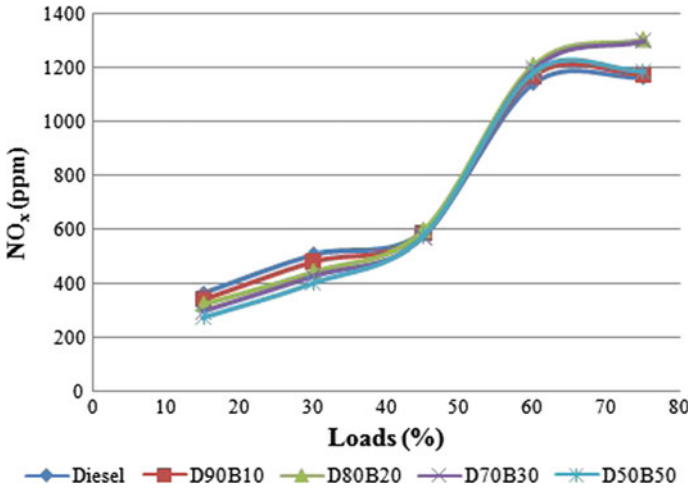


Fig. 4 Variation of Mexicana biodiesel blends on NOx emissions with different loads

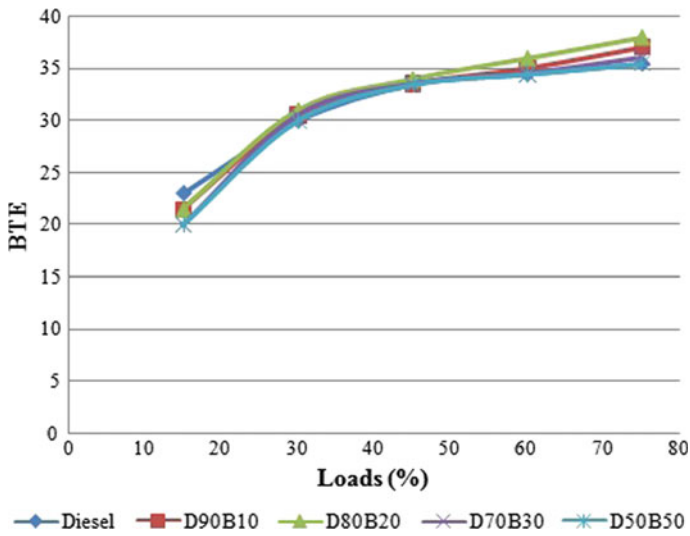


Fig. 5 Variation of Mexicana biodiesel blends on BTE emissions with different loads

in BTE [9]. The highest BTE was observed for 20% blend (D80B20), which was 38%. The BTE increased by 2.37% for biodiesel blended with 30% (D70B30).

The maximum BTE for Mexicana biodiesel blend B50, B30, B20 and B10 were 35.5%, 36%, 38% and 37% respectively at maximum loads. BTE decreases beyond D70B30 blend ratio due to reduction in calorific value and rise in viscosity.

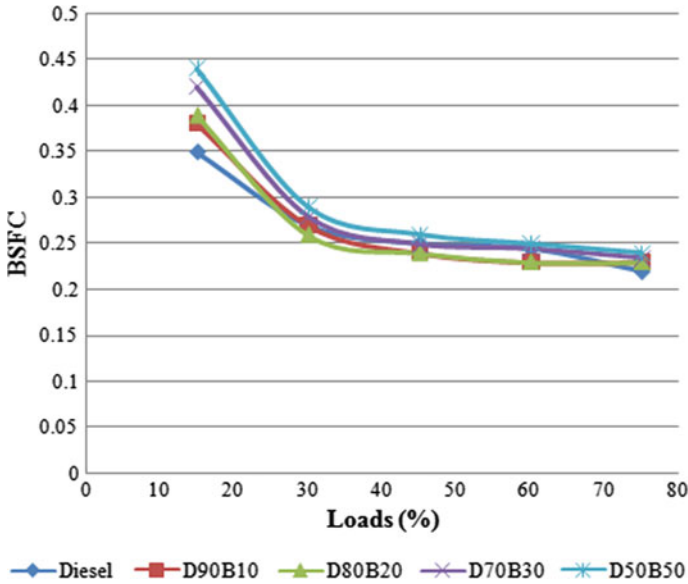


Fig. 6 Variation of Mexicana biodiesel blends on BSFC emissions with different loads

Specific fuel consumption (BSFC): Fig. 6. represents effect of load on BSFC. The BSFC decreased as the load rises with blends. BSFC was slightly higher for all the blends (0.28 kg/W-h) compared to diesel fuel (0.267 kg/W-h). The increase of Argemone Mexicana results to rise in BSFC.

4 Conclusions

The conclusions drawn from experimental investigation of 3.5 kW single cylinder diesel engine are:

- (i) As the load increases, HC emission decreases. However, beyond D80B20, as the blend proportions of argemone Mexicana biodiesel increases, HC emission rises.
- (ii) Up to 60% load, lower CO emissions were observed. CO emission increased drastically beyond 60% load. However, these emissions rise along with rise in blend beyond D80B20.
- (iii) The rise in Nitrogen Oxide emission along with rise in blend proportion and % of load was noted.
- (iv) The BTE increased by 2.37% for biodiesel blended up to 30% (D70B30). BTE increased with increase in % of loads as well as increase in blend proportions of biodiesel.

- (v) BSFC decreased along with rise in % of loads. However it rises with rise in blend proportions of biodiesel beyond D80B20.

Blend ratio D80B20 found the best diesel-biodiesel ratio to replace pure diesel fuel in CI engines.

References

1. Parida M, Joardar H, Rout A, Routaray I, Mishra B (2019) Multiple response optimizations to improve performance and reduce emissions of argemone Mexicana biodiesel-diesel blends in a VCR engine. *Appl Therm Eng* 148:1454–1466
2. Uyumaz A (2018) Combustion, performance and emission characteristics of a DI diesel engine fueled with mustard oil biodiesel fuel blends at different engine loads. *Fuel* 212:256–267
3. Thangaraj S, Govindan N (2018) Evaluating combustion, performance and emission characteristics of diesel engine using karanja oil methyl ester biodiesel blends enriched with HHO gas. *Int J Hydrog Energy* 43:6443–6455
4. Singh M, Sandhu S (2020) Performance, emission and combustion characteristics of multi-cylinder CRDI engine fueled with argemone biodiesel/diesel blends. *Fuel* 265:117024–117030
5. Uludamar E, Yıldızhan A, Aydın S, Özcanlı M (2016) Vibration, noise and exhaust emissions analyses of an unmodified compression ignition engine fuelled with low sulphur diesel and biodiesel blends with hydrogen addition. *Int J Hydrog Energy* 41:11481–11490
6. Appavu P, Ramanan V, Venu H (2019) Quaternary blends of diesel/biodiesel/vegetable oil/pentanol as a potential alternative feedstock for existing unmodified diesel engine: Performance, combustion and emission characteristics. *Energy* 186:115–156
7. Ashour M, Eldrainy Y, Elwardany A (2018) Effect of cracked naphtha/biodiesel/diesel blends on performance, combustion and emissions characteristics of compression ignition engine. *Energy* 132:86–98
8. Thiyagarajan S, Sonthalia V, Geo E, Prakash T, Karthickeyan V, Ashok B (2020) Effect of manifold injection of methanol/n-pentanol in safflower biodiesel fuelled CI engine. *Fuel* 261:116–138
9. Kumar R, Singh M (2019) Experimental investigation of performance and emission characteristics of DI CI engine with dual biodiesel blends of Mexicana Argemone and Mahua. *Mater. Today: Proc.* 16:321–328
10. Pandhare A, Padalkar A (2013) Investigations on Performance and Emission Characteristics of Diesel Engine with Biodiesel (Jatropha Oil) and Its Blends. *J Renew Energy* 2013:1–12
11. Celebi K, Uludamar E, Özcanlı M (2017) Evaluation of fuel consumption and vibration characteristic of a compression ignition engine fuelled with high viscosity biodiesel and hydrogen addition. *Int J Hydrog Energy* 42:23379–23388

Estimation of Methane Generation Potential from Municipal Solid Waste by Using Bromatological Characteristics for Pimpri Chinchwad City



Tanmay S. Khambekar and Sandip T. Mali

Abstract Landfilling is the cheapest and unscientific way of disposal of municipal solid waste (MSW) practiced in developing countries. Apart from the other environmental concerns, emission of landfill gas containing methane which is a green house gas is the serious problem. The quantity of methane emitted from the Moshi landfill site located in Pimpri Chinchwad city in Pune district in Maharashtra state of India have been calculated in the study presented. The limited information of the total waste generation and composition of the waste in the city was used to find the yearly waste generation, yearly quantities of the components in the MSW and quantities of the elements like carbon, hydrogen, oxygen, nitrogen and sulphur. The quantities of the carbohydrates, proteins and fats present in the organic fraction of municipal solid waste (OFMSW) were also estimated and were further used to calculate the theoretical methane yield (TMY). The TMY values varied as 156.81–315.39 ml of CH₄/g of VS. TMY values were further used to calculate the methane values in MT. These values ranged between 7048.23 and 10888.01 MT.

Keywords Municipal solid waste · Elemental composition · Bromatological properties · Theoretical methane yield

1 Introduction

Uncontrolled population and rapid urbanization are providing huge challenges for municipal solid waste management in developing country like India. The municipal solid waste generation in India by 2051 will be 300 million tons per annum which will require 1450 km² of the land for systematic disposal [1, p. 3]. The level of urbanization increased from 27.8 to 31.6% during the year 2001–2011 and is estimated to reach

T. S. Khambekar (✉)

Research Scholar, Department of Civil Engineering, Sinhgad College of Engineering, Savitribai Phule Pune University, Pune, Maharashtra, India

S. T. Mali

Department of Civil Engineering, Pimpri Chinchwad College of Engineering, Pune, Maharashtra, India

50% in next 10 years [2, p. 1] [3, p. 1]. Landfilling is the most practiced method for MSW disposal as it is most economical and can be practiced with unskilled personnel. The collection efficiency in Tier I cities reported is 70–90% and that in Tier II and III reported is less than 50% [4, p. 1]. Global percentage of organic fraction of municipal solid waste (OFMSW) in municipal solid waste (MSW) is 44% [5, p. 29]. The disposal of these biodegradables in the landfills leads eventually for generation of landfill gas (LFG). Methane (CH_4) is the major constituent of the LFG and has 40–60% of percentage in LFG and thus the open landfills are acting anthropogenic source of the green house gas (GHG) emission. 29% of India's GHG emission is accounted to landfills which is higher than the global average of 15% [6, p. 2]. CH_4 is known to have good calorific value which makes it a potential source of energy. Estimation of the CH_4 values will help evaluate the potential of CH_4 from LFG as the energy source.

Methods like default method by Intergovernmental Panel on Climate Change (IPCC), Triangular Model, Modified Triangular Model, Landfill gas emission model by US (LandGEM), First order Decay Model, EPER model by Germany and France, Stoichiometric model, GasSim, TNO have been used for estimating or calculating methane depending upon the data available and the accuracy of the results desired. Landfill Degradation Transport Model (LDAT) was used to estimate the bromatological properties by Manjunatha et al. [7, p. 8]. LDAT model estimates the quantities of carbohydrates, proteins and fats in MSW. Further the bromatological properties calculated for OFMSW can be used to calculate the theoretical methane yield [8, p. 4].

The objective of study is to find the potential methane generation from the MSW at the landfill site at Moshi in Pimpri Chinchwad city in Pune district of Maharashtra state in India for the years from 2012 to 2019 by using the bromatological characteristics. The components of MSW taken into consideration are food and garden waste (F&G), wood, metal, paper, plastic, rubber, cloth and inert material.

2 Materials and Methods

2.1 Study Area

Pimpri Chinchwad is the twin city industrial township located in South-East of Mumbai and in the North quadrant of Pune. It covers 181 sq.km area and currently houses approximately more than 21 lakhs population. According to the Solid Waste Management (SWM) Annual Report, 2019 published by Maharashtra Pollution Control Board, Pimpri Chinchwad Municipal Corporation (PCMC) generates 1050 metric tonne per day (MT/day) of MSW. The per capita waste generation is approximately 450 gm/day. Currently, PCMC uses the waste depot located at Moshi as shown in Fig. 1 which is 20 km from city limits and has an area of 32.8 hectares for management of MSW. Moshi waste depot is operational since 1999–92 and has received approximately 3.35 lakhs MT of MSW till March, 2019.

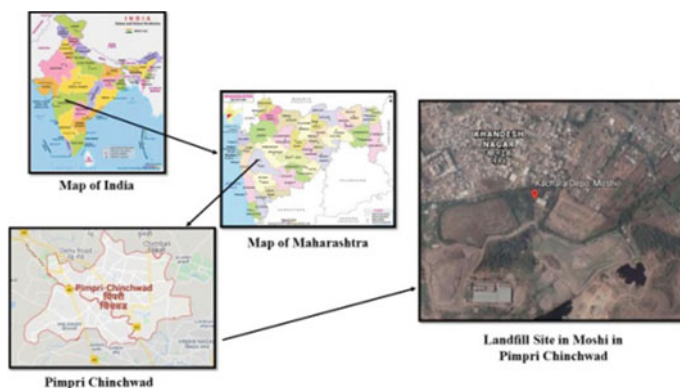


Fig. 1 Location of Moshi landfill site in Pimpri Chinchwad

2.2 Data Collection

The data was collected from the Environmental Status Reports (ESR) published by PCMC. The total waste generation of MSW and the physical composition values of MSW were extracted from the ESR published by PCMC for the years 2012–13, 2015–16 and 2018–19.

2.3 Calculation of Total Waste Generation of MSW

The values of total waste generation and physical composition published by PCMC in ESR for the years 2012–13, 2015–16 and 2018–19 were used to calculate the total waste generation and physical composition for the years 2013–14, 2014–15, 2016–17 and 2017–18.

The values of total waste generation per day are represented graphically in Fig. 2. Considering the calculated values of per day waste generation, the total waste generated for the years 2012–13, 2013–14, 2015–16, 2016–17, 2017–18, 2018–19 is tabulated in Table 1.

2.4 Calculation of Physical Composition of MSW

The percentage composition of the MSW for the year 2012–13, 2015–16 and 2018–19 was published by PCMC in ESR. The percentage composition of the MSW for the years 2013–14, 2014–15, 2016–17 and 2017–18 were calculated. The graphical representation of the percentage composition of MSW for all the years is presented in Fig. 3.

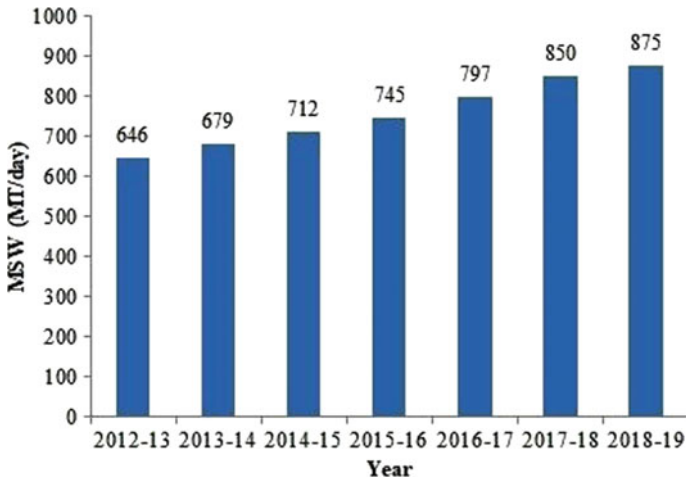


Fig. 2 Waste generated per day

Table 1 Waste generation in a year

Year	Total MSW production for the year (MT)
2012-13	235,790
2013-14	247,835
2014-15	259,880
2015-16	271,925
2016-17	290,905
2017-18	310,250
2018-19	319,375

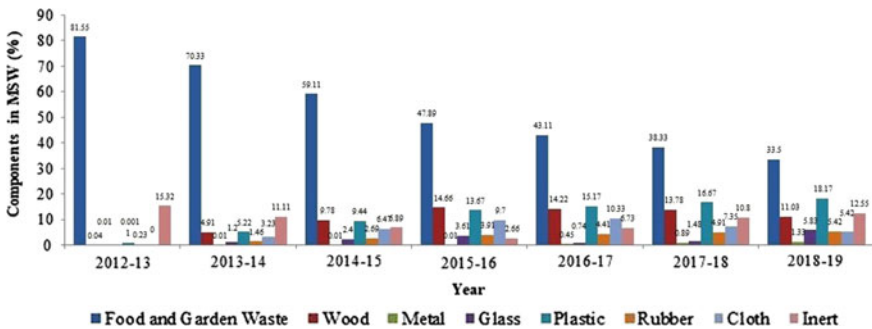


Fig. 3 Percentages of the components in the daily waste

Table 2 Variation in the percentages of the components of the MSW

Year	Percentage (%) Variation								Total
	F&G	Wood	Metal	Paper	Plastic	Rubber	Cloth	Inert	
2012–13	81.55	0.04	0.01	1.85	1	0.23	0	15.32	100
2013–14	70.33	4.91	0.01	2.53	5.22	1.46	3.23	11.11	100
2014–15	59.11	9.78	0.01	3.21	9.44	2.69	6.47	6.89	100
2015–16	47.89	14.66	0.01	3.89	13.67	3.91	9.7	2.66	100
2016–17	43.11	14.22	0.45	4.84	15.17	4.41	10.33	6.73	100
2017–18	38.33	13.78	0.89	5.79	16.67	4.91	7.35	10.8	100
2018–19	33.5	11.03	1.33	6.75	18.17	5.42	5.42	12.55	100

Table 3 Quantity of the components

Component (MT)	2012–13	2013–14	2014–15	2015–16	2016–17	2017–18	2018–19
F&G	192,287	174,302	153,615	130,225	125,488	118,919	106,991
Wood	94	12,169	25,416	39,864	41,393	42,752	35,227
Metal	24	25	26	27	1310	2761	4248
Paper	4362	6270	8342	10,578	14,089	17,963	21,558
Glass	2	2974	6237	9816	2154	4592	18,620
Plastic	2358	12,937	24,533	37,172	44,158	51,719	58,030
Rubber	542	3618	6991	10,632	12,837	15,233	17,310
Cloth	0	8005	16,814	26,377	30,069	22,803	17,310
Inert	36,120	27,534	17,906	7233	19,590	33,507	40,082
Total	235,790	247,835	259,880	271,925	291,088	310,250	319,375

2.5 Calculation of Yearly Waste Generation and Quantity of the Components

Variation in the percentage of individual components in the MSW for the years 2012–13, 2013–14, 2015–16, 2016–17, 2017–18 and 2018–19 is calculated and presented in Table 2. Also, the quantities of the components in MT for the individual year is calculated and presented in the tabular form in Table 3.

2.6 Estimation of Carbon (C), Hydrogen (H), O Oxygen), Nitrogen (N) and Sulphur (S) Quantities in MSW

Determination of the elemental composition is done on the basis of the dry weight. The PCMC ESR has reported the percentage of the components for the year 2012–13, 2015–16 and 2018–19. For theoretical calculation of the elemental composition,

the percentage moisture content (MC) of each of the components was obtained by the literature review and is presented in the Table 4. The typical values of the MC of each of the component was used for determination of the dry weight. According to the previous research, the typical data on the ultimate analysis of the components in the residential MSW is presented in the tabular form in Table 5. The reported values are used to estimate the C, H, O, N and S quantities for each day and further for a individual year.

Table 4 Moisture content of the components of MSW

Component	Range (%)	Typical (%)
Wood	15–40	20
Food Wastes	50–80	70
Paper	4–10	6
Plastics	1–4	2
Textiles	6–15	10
Rubber	1–4	2
Leather	8–12	10
Metal	2–4	2
Glass	1–4	2
Dirt, ashes, etc.	6–12	8

(Source [9, p. 70])

Table 5 Elemental composition of the components of the MSW

Component	Percent by weight dry basis					
	C (MT)	H (MT)	O (MT)	N (MT)	S (MT)	Ash
<i>Organic</i>						
Food Waste	48.0	6.4	37.6	2.6	0.4	5.0
Paper	43.5	6.0	44.0	0.3	0.2	6.0
Plastics	60.0	7.2	22.8	–	–	10.0
Textiles	55.0	6.6	31.2	4.6	0.15	2.5
Rubber	78.0	10.0	–	2.0	–	10.0
Leather	60.0	8.0	11.6	10.0	0.4	10.0
Wood	49.5	6.0	42.7	0.2	0.1	1.5
<i>Inorganic</i>						
Glass	0.5	0.1	0.4	<0.1	–	98.9
Metal	4.5	0.6	4.3	<0.1	–	90.5
Dirt, ash, etc.	26.3	3.0	2.0	0.5	0.2	68.0

(Source [9, p. 81])

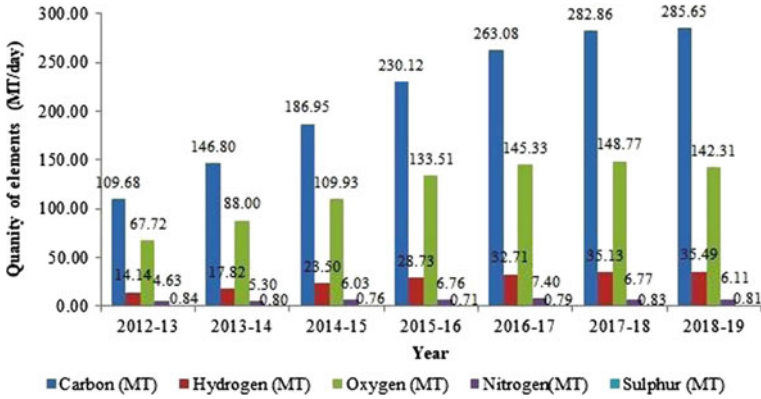


Fig. 5 Quantity of C, H, O, N and S

Table 6 Quantity of C, H, O, N and S in a year

Year	C (MT)	H (MT)	O (MT)	N (MT)	S (MT)
2012–13	40,032.48	5159.76	24,719.28	1689.22	305.53
2013–14	53,583.56	6505.89	32,119.25	1936.00	292.40
2014–15	68,237.65	8577.43	40,123.24	2199.49	276.50
2015–16	83,994.50	10,486.23	48,731.63	2467.50	257.76
2016–17	96,023.48	11,940.93	53,043.68	2702.41	287.73
2017–18	103,244.57	12,820.78	54,300.36	2471.58	303.80
2018–19	104,260.93	12,952.55	51,942.92	2230.31	294.74

The quantity of the elements C, H, O, N & S in MSW calculated for a day is represented graphically in Fig. 5 and the values of quantities of C, H, O, N and S for the years under consideration is represented in the Table 6.

2.7 Estimation of Bromatological Properties of MSW

Amongst all the components in the MSW, F&G, paper and wood are considered as organic fraction and mainly contribute for LFG generation because of anaerobic conditions developed in landfill. The carbohydrates, proteins and fats present in the organic fraction of municipal solid waste (OFMSW) is found using following equations of LDAT model.

$$\text{Carbohydrates} = 0.31a_F + 0.67a_G + 0.83a_P + 0.45a_T \tag{1}$$

$$\text{Higher Carbohydrates} = 0.40a_F + 0.08a_G + 0.45a_T \tag{2}$$

$$Protein = 0.18a_F + 0.33a_G \tag{3}$$

$$Fat = 0.11a_F \tag{4}$$

where, a_F = Dry mass fraction of food waste
 a_G = Dry mass fraction of garden waste
 a_P = Dry mass fraction of paper waste
 a_T = Dry mass fraction of textile waste

As only OFMSW is to be considered, all other values related to non-organic fraction in the formula are neglected. The quantity of carbohydrates, proteins and fats for a day is represented graphically in Fig. 6 and the quantities of carbohydrates, proteins and fats for the years under consideration is tabulated in Table 7.

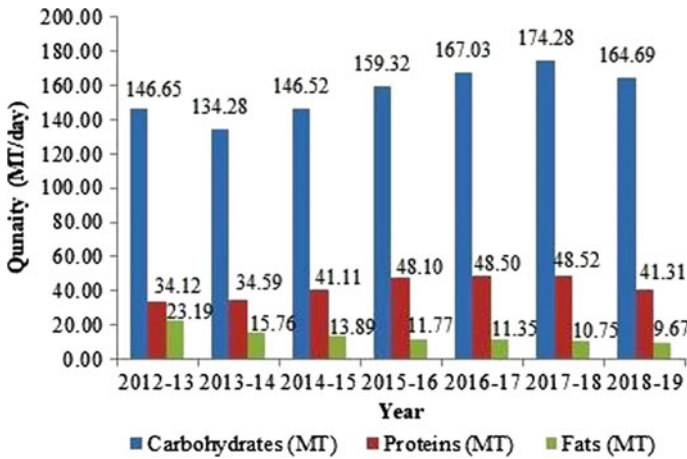


Fig. 6 Quantity of carbohydrates, proteins and Fats

Table 7 Quantity of carbohydrates, proteins and fats in a year

	2012-13	2013-14	2014-15	2015-16	2016-17	2017-18	2018-19
Carbohydrates (MT)	53,527.25	49,012.2	53,479.8	58,151.8	60,965.95	63,612.2	60,111.85
Proteins (MT)	12,453.80	12,625.35	15,005.15	17,556.5	17,702.5	17,709.8	15,078.15
Fats (MT)	8463.79	5752.4	5069.85	4296.05	4142.75	3923.75	3529.55

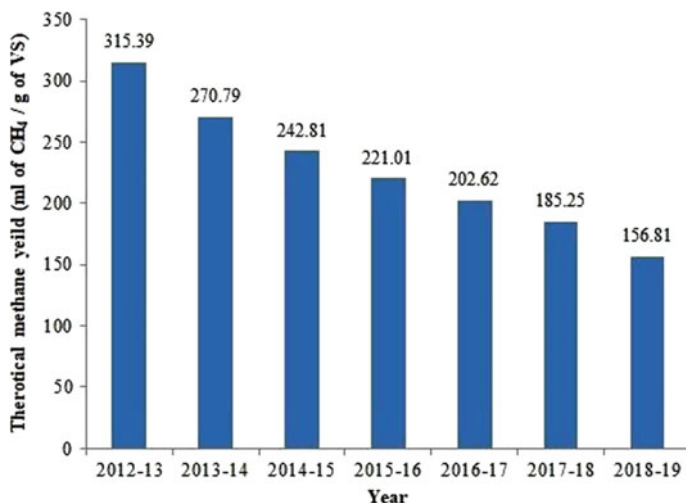


Fig. 7 Theoretical methane yield in (ml of CH₄/g of VS)

2.8 Estimation of Theoretical Methane Yield Form the OFMSW by Using Bromatological Properties

The theoretical methane yield (TMY) from OFMSW is calculated by using the percentage of the carbohydrates, proteins and lipids or fats in the dry matter of OFMSW. TMY is calculated using the percentages of carbohydrates, proteins and lipids or fats by using Eq. 5.

$$TMY(\text{ml of } CH_4/\text{g of VS}) = (415 \times \% \text{Carbohydrates} + 496 \times \% \text{Proteins} + 1014 \times \% \text{Lipids}) \quad (5)$$

TMY value for the years considered is represented graphically in Fig. 7. As per the literature survey, the quantity of volatile solids in the OFMSW averages out to be 89.94%. Considering the same value, the VS content of the OFMSW was calculated with reference to the dry weight for estimating the quantity of methane generated in a year. The values are tabulated in Table 8.

3 Results and Discussions

From the calculated values of the daily MSW generation, it was observed that due to the rapid urbanization, the total generation of daily MSW has seen a continuous increase. The average percentage increase every year is approximately 5.19%.

Table 8 Quantity of methane generated in a year

Year	VS received/day (MT)	Methane Yield (ml of CH ₄ /g of VS)	Methane (L) produced from of MSW in a year	Methane (MT) produced from of MSW in a year
2012–13	143.9602	315.39	16,572,315,033	10,888.01
2013–14	158.0575	270.79	15,622,138,850	10,263.75
2014–15	172.8102	242.81	15,315,416,210	10,062.23
2015–16	188.269	221.01	15,187,407,466	9978.13
2016–17	195.4871	202.62	14,457,506,042	9498.58
2017–18	201.9088	185.25	13,652,318,294	8969.57
2018–19	187.4339	156.81	10,727,901,828	7048.23

Lower percentage increase of 2.94% was observed for year 2018–19 and the highest percentage increase of 7.05% was observed for year 2016–17.

The calculated percentage of the various components in the MSW as represented in Fig. 3 indicates the decline in the percentage of food & garden waste by 44.36%. Components like metal, paper, plastic and rubber have shown steady increase in the composition of MSW. Considering 2012–13 to 2018–19, metal, paper, plastic and rubber in MSW increased by 99.5%, 79.76%, 95.93% & 96.85% respectively. Percentage of cloth increased from year 2012–13 to 2016–17 and then reduced for further years till 2018–19. The percentage of inert material in MSW was found decreasing for the years 2012–13 to 2015–16 and then increased till 2018–19. This changes in the composition of the MSW are interrelated. Various factors that may have brought these changes are awareness about food wastage amongst residents, reduction in the garden area due to urban infrastructure development, increase in the demand of packaged food, increase in the use of online shopping resulting into increase of packaging material, easy available and less durable products usage, etc.

Considering the estimated quantities of elemental analysis, the quantity of C has been noted to be highest and continuously increasing for all the years.. However, the percentage increase in C has fall from 33.85 to 0.98% from years 2012–13 to 2018–19 the reason being the reduction in the F&G waste component over the year which is highest contributor of the C. O quantity increased at a rate of 17.5% till 2017–18 and then reduced by 4.35% for 2018–19. The H percentage in the MSW increased with average of 17.07%. Also, N was found to be increasing till 2016–17 at an average rate of 12.48% and reduced thereafter till 2018–19 at average rate of 9.15%. S was found to be both increasing and decreasing from 2012–13 to 2018–19. S quantity decreased at a average rate of 5.50% till 2015–16, increased at rate of 8.6% till 2017–18 and decreased at rate of 2.98% for year 2018–19.

The quantity of the carbohydrates was initially found to decreased for year 2013–14 by 8.43% and then increased at an average rate of 6.76% till 2017–18 and then finally reduced by 5.50% for 2018–19. For proteins, the quantity increased at an average rate of 7.62% till 2017–18 and then reduced with the rate of 14.86% for 2018–19. Average reduction of 13.0% every year in the quantity of the fat was

found. As the percentage of the OFMSW is reducing in the MSW composition, the percentages of carbohydrates, proteins though increasing have been associated with reduction in percentage increase for every year and for some years decrease in their quantities have been noted.

The theoretical methane yield calculated from the bromatological characteristics of the OFMSW suggests the decrease in their estimated quantities. The reason being the reduction in the fraction of OFMSW over the years.

4 Conclusion

The theoretical methane yield (TMY) potential of the OFMSW has been calculated. The range of the TMY found was 156.81–315.39 ml of CH₄/g of VS. TMY values have been noted to decrease from 2012 to 2019. TMY values were further used to calculate the methane values in MT. These values ranged between 7048.23–10888.01MT. The results obtained from this method yields values on higher side as it considers complete conversion of carbohydrates, proteins and fats into the methane. This method assumes conversion of the carbohydrates, proteins and fats into methane in a single year whereas the methane will be generated over the period of years through it. Though the method is crude, it provides guiding value to get a glimpse of the huge emission of methane that happens through the landfills and asserting the role of the open landfills in the emission of the methane which is GHG into the atmosphere and thus resulting for environmental problems.

References

1. Joshi R, Ahmed S (2016) Status and challenges of municipal solid waste management in India: a review. *Cogent Environ Sci* 2(1):1139434
2. Syamala Devi K, Swamy AVVS, Nilofer S (2016) Municipal solid waste management in India—an overview. *Asia Pac J Res* 1:118–126
3. Gupta B, Arora SK (2016) Municipal solid waste management in Delhi—the capital of India. *Int J Innov Res Sci Eng Technol* 5(4):5130–5138
4. Sharma A, Ganguly R, Gupta AK (2018) Matrix method for evaluation of existing solid waste management system in Himachal Pradesh, India. *J Mater Cycles Waste Manag* 20(3):1813–1831
5. Kaza S, Yao L, Bhada-Tata P, Van Woerden F (2018) What a waste 2.0: a global snapshot of solid waste management to 2050. The World Bank
6. Singh CK, Kumar A, Roy SS (2018) Quantitative analysis of the methane gas emissions from municipal solid waste in India. *Sci Rep* 8(1):2913
7. Manjunatha GS, Chavan D, Lakshmiathan P, Swamy R, Kumar S (2020) Estimation of heat generation and consequent temperature rise from nutrients like carbohydrates, proteins and fats in municipal solid waste landfills in India. *Sci Total Environ* 707:135610
8. Nielfa A, Cano R, Fdz-Polanco M (2015) Theoretical methane production generated by the co-digestion of organic fraction municipal solid waste and biological sludge. *Biotechnol Rep* 5:14–21
9. Tchobanoglous G, Theisen H, Vigil S (1993) Integrated solid waste management: engineering principles and management Issues. McGraw-Hill

Investigation of Tube in Tube Helical Coil Heat Exchanger with Different Inner Tube Configuration



Amol D. Shinde and Amarsingh B. Kanase-Patil

Abstract The aim of study is to experimentally investigate the effect of number of inner tubes as a geometric parameter on thermal and hydrodynamic performance. Three heat exchangers (TTHC) with different parameters like tube side coil pitch, curvature ratio and number of coiled tubes were tested for counterflow configuration. The measuring parameters like flow rate, inlet-outlet temperatures and head loss across coil were measured by using suitable calibrated instruments. Tube side and annulus side Nusselt numbers are to be calculate by using Wilson plot technique. In results, tube side and annulus side convective heat transfer coefficients, Nusselt number, Dean number, effectiveness, friction factor and pumping power were calculated. It is observed that tube side Nusselt number increases with increase in tube side flow rate whereas it decreases with increase in annulus side flow rate.

Keywords Tube in tube helical coil (TTHC) · Heat transfer · Counterflow · Nusselt number (Nu) · Dean number (De)

1 Introduction

Heat exchanger is a mechanical device used to transfer heat energy from one fluid to another fluid. It works on the principle of conservation of energy which follows first law of thermodynamics. Heat exchangers are commonly used in process industries, power industries, food processing, refrigeration and HVAC's etc. The requirements of heat exchanger are changes with respect to time, as compactness and heat transfer rate should be high. Curve coil tube has an advantage of secondary flow pattern, due to the centrifugal forces. This secondary flow generates dean vortices (two semicircular profiles) perpendicular to the direction of the flow. These helical coils are compact in size and have high heat transfer capacity [1].

Helical coil multipass arrangements give rise to complex internal heat flow paths which helped to transfer heat rapidly. Martin et al. [2] presented a work, had such

A. D. Shinde (✉) · A. B. Kanase-Patil
Sinhgad College of Engineering, Pune 411041, Maharashtra, India
e-mail: shinde2996@gmail.com

flow paths which were modelled using a simplified methodology that breaks up the complex flow and represents it as a network of simple arrangements in counter flow and parallel flow. The network is then solved to determine outlet temperatures from where the rate of heat transfer is determined.

Numerical model of shell and helical tube heat exchanger was investigated by Mir and Seyed [3] to assess heat transfer coefficient and exergy loss. Result was indicated the tube diameter and cold flow rate are the most significant design parameters of heat transfer and exergy loss, respectively. It is also seen the heat transfer coefficient was reduced by increasing pitch of coil. The optimum levels for heat transfer coefficient are: pitch 13 mm, tube diameter 12 mm, cold and hot flow rate 4 LPM.

Majidi et al. [4] studied and experimentally investigated the overall heat transfer coefficient of air in a double-pipe helical heat exchanger. New method was suggested to obtain the heat transfer coefficients of double-pipe helical heat exchangers for internal tube and annulus section by combining of the previously proposed approaches. The effect of the installed fin on the heat transfer coefficient of the annulus section was also been investigated and resulting in the enhancement of overall heat transfer capacity due to the presence of the fin in the annulus.

2 Coil Configurations

The coil configurations are to be constructed from standard copper materials i.e. tubing and connections. In coil 1, single helical coil inserted in annulus side concentrically with same pitch ratio and curvature ratio. In coil 2, two helical coils inserted in outer single helical tube which is having same pitch and curvature ratio. The outer coil is maintained zero coil pitch distance and same curvature ratio. In coil 3, three helical coils inserted with optimum tube diameter inside the outer tube. All the three coils have same coil pitch ratio. Three inner helical coils are mounted in triangular pattern as shown in Fig. 1.

Outer tube surface is to be drilled by small holes and tapped with insert screws in order to support inner tubes and position them at the required Pitch Circle Diameter (PCD). Fine sand was filled in these tubes before bending to give a desired pitch circle diameters. The single, double and triple coiled bundle is mounted concentrically

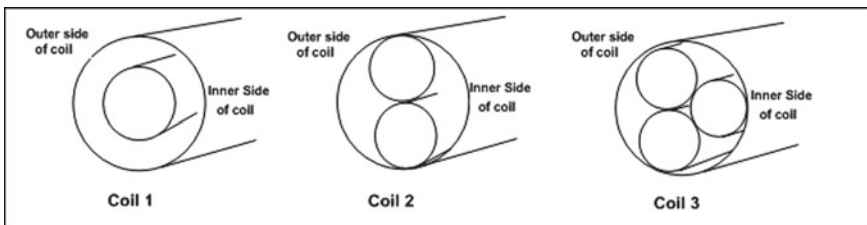


Fig. 1 Geometries of coiled tube

inside the annulus region. The inner coil concentricity and position in annulus region is maintained as per requirement.

3 Experimental Setup and Methodology

The schematic experimental set-up is shown in Fig. 2. Setup consist two storage tanks i.e. hot water tank, cold water tank for storage and continue supply of hot and cold water respectively. First feed water pump is required at inlet supply, to send a hot and cold water at high pressure and velocity. Heater (1.5 kW) is provided at hot water tank to heat up the water. Flow control valves are fitted at every inlet of hot and cold water supply to restrict the flow. At every inlet point of heat exchanger in both side flow meters are placed to calculated flow rate. Pressure gauge is fitted only at inlet of hotter side to calculated inlet pressure of water. At every inlet as well as outlet of hot water and cold water thermocouples are fitted for senses of the temperature within the time intervals.

3.1 Procedure

Experiment carried out for counter flow configuration. Firstly, annulus side cold water (25°) flow rate was kept constant (100 LPH) and tube side hot water (60°) flow rates varied from 60 to 200 LPH for each configuration run.

Further, tube side hot water (60°) flow rate was kept constant (60LPH) and annulus side cold water (25°) flow rates varied from 100 to 300 LPH for each configuration run. Temperature readings are recorded after every 10 s to achieve stability.

Fig. 2 Experimental set-up



Total eight flow rates maintained at annulus side and ten flow rates on tube side likewise eighty observations were taken for each heat exchanger configuration.

3.2 Heat Transfer Analysis

This experimental study is performed to find out the relationship of helical coil's inner tube and outer tube to make coil design easy and safe. To get relationship it is important to find heat transfer capacity of coil and friction factor, because they are important parameters in heat transfer [5].

Tube side heat transfer rate;

$$Q_t = m_t C p_t (T_{hi} - T_{ho}) \quad (1)$$

Annulus side heat transfer;

$$Q_a = m_a C p_a (T_{co} - T_{ci}) \quad (2)$$

The average heat transfer rate;

$$Q_{avg.} = \frac{Q_t + Q_a}{2} \quad (3)$$

Overall heat transfer coefficient;

$$U_o = \frac{Q_{avg.}}{A_s * LMTD} \quad (4)$$

LMTD (log mean temperature difference) for counter flow;

$$LMTD = \frac{(\Delta T_2 - \Delta T_1)}{\ln(\Delta T_2 / \Delta T_1)} \quad (5)$$

In above equation, ΔT_1 , is temperature difference of inlet hot water and outlet cold water. ΔT_2 , is temperature difference of outlet hot water and inlet cold water.

Overall heat transfer coefficient is to be related to inner and outer heat transfer coefficient by equation;

$$\frac{1}{U_o} = \frac{A_o}{A_i h_i} + \frac{A_o \ln(d_o / d_i)}{2\pi K L} + \frac{1}{h_o} \quad (6)$$

To find unknowns h_i and h_o , which are convective heat transfer coefficient for inner and outer side of tubes respectively, by taking mass flow rate in annulus side is to constant and varying mass flow rate from tube side. h_i and h_o are calculate by use of Wilson plot method.

$$\text{For tube side Nussult Number, } Nu_i = \frac{h_i d_i}{k} \quad (7)$$

$$\text{For annulus side Nussult Number, } Nu_o = \frac{h_o d_o}{k} \quad (8)$$

3.3 Pressure Drop Analysis

In pressure drop analysis taking equivalent diameter of tube D_e , are different in all 3 experimental cases. It is calculated from equation;

$$D_e = \frac{4 * \text{flow area}}{\text{Wetted Perimeter}} \quad (9)$$

The tube side and annulus side fanning friction factors are determined as,

$$f = \frac{\Delta P D_e}{2\rho V^2 L} \quad (10)$$

4 Results and Discussion

In this experimental study, trails were conducted on water to water heat transfer application (i.e. single-phase helical coil heat exchanger) to test multiple helical coils to analyze in terms of temperature variation, heat transfer analysis, effectiveness, friction factor and pumping power.

4.1 Nusselt Number (Nu) Versus Dean Number (De)

Figure 3 represents the contrast of inner side Nusselt number with annulus side Dean number for constant tube side flow rate. Due to the increase in temperature drop at each section, tube side Nusselt number decreases with increase in cold water flow rate for constant hot water flow rate.

Figure 4 shows the contrast of annulus side Nusselt number with annulus side Dean number for constant annulus side flow rate for various coiled heat exchanger. The annulus side Nusselt number decreases with decrease in number tubes; this is due to convective surface exposure to annulus side. It is seen that, the effect of secondary flow in coil 3 is greater than coil 2 and 1. From the Fig. 4, also it is seen that the annulus side Nusselt number increases with annulus Dean number. It appears that,

Fig. 3 Inner Nusselt number versus annulus side dean number

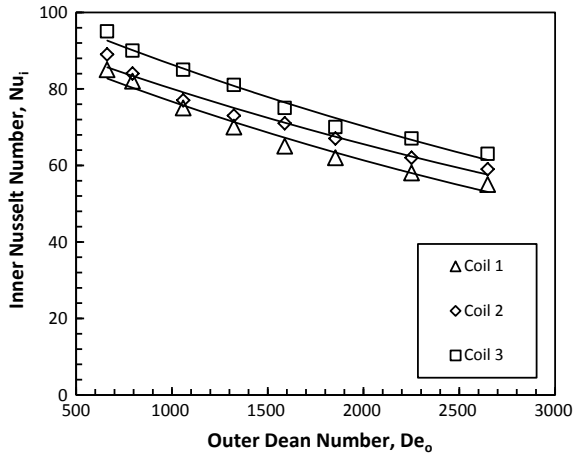
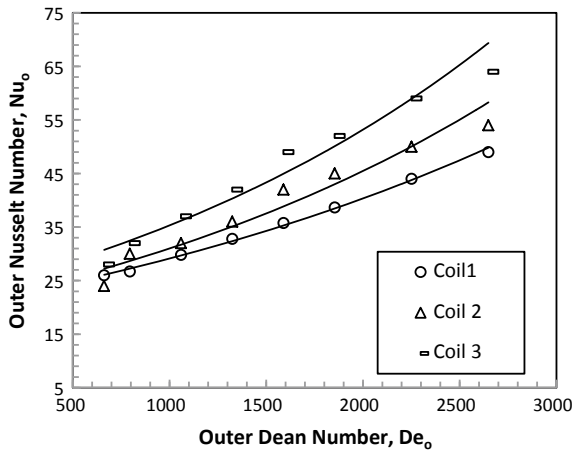


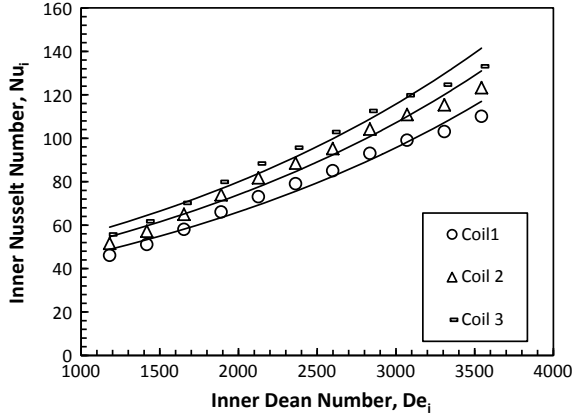
Fig. 4 Outer Side Nusselt number versus outer side dean number



mounting number of tubes in annulus side results increase in the annulus side Nusselt number. The heat transfer enhancement observed in coil1, coil 2 and coil 3 because more secondary flow and turbulence developed in annulus region. The annulus side Nusselt numbers is to be calculated at the modified Dean number which is the concept of equivalent diameter.

Figure 5 represents the contrast of tube side Dean number to tube side Nusselt number for the constant tube side flow rate. In coil 1, due to centrally located inner coiled tube, the time taken for circulation of fluid in annulus region is large. Due to increasing in number of inner coiled tubes, increases fluid circulation in annulus region and the annulus surface is affected to the extra effective heat transfer rate therefore more heat transfer will takes place in less time.

Fig. 5 Inner Nusselt number versus inner dean number

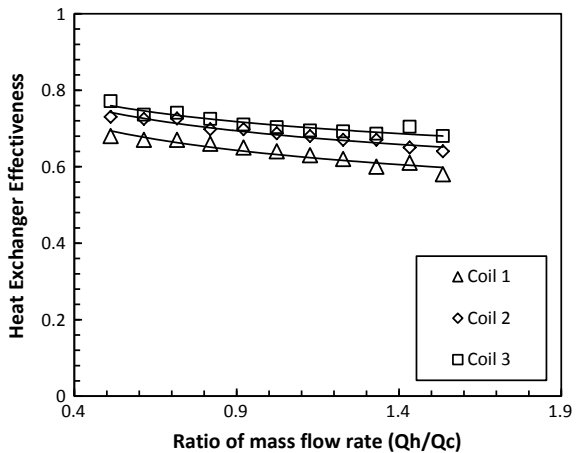


4.2 Effectiveness

Effectiveness is defined as the ratio of actual heat transfer rate to the maximum heat transfer rate. Figure 6 shows the contrast of effectiveness of the heat exchanger with ratio of mass flow rate of hot water to cold water (m_h/m_c) for all three heat exchangers.

It was observed while experimentation that effectiveness of heat exchangers are to be decreasing with increasing in the ratio of mass flow rate (Q_h/Q_c). For same annulus side, mass flow rate is rapidly decreases with increase in hot side mass flow rate, but for particular tube side mass flow rate at constant inlet hot water and cold water temperatures, the effectiveness is to be increases with increase in annulus side mass flow rate.

Fig. 6 Heat exchanger effectiveness versus ratio of mass flow rate



4.3 Inner and Outer Side Friction Factor

Figures 7 and 8 indicate the contrast of friction factor in tube side and annulus side with Dean number of tube side and annulus side respectively. Both the figures shows annulus side and tube side friction factor is higher for coil 3 and lower for coil 1. It was seen that, coil induces centrifugal force which causes to the development of the secondary flow. This secondary flow enhances fluid mixing and rate of heat transfer. Curvature ratios in all three coil tubes are considerably same, due to that development of secondary flow increases with increase in no of concentrated tubes in coils.

It was found that from Figs. 7 and 8 that the friction factor tends to decrease rapidly for low Dean number and slowly decreased for high Dean number. It is to be observed from present work, friction factor value is higher in coil 3 and this effect

Fig. 7 Inner friction factor versus inner dean number

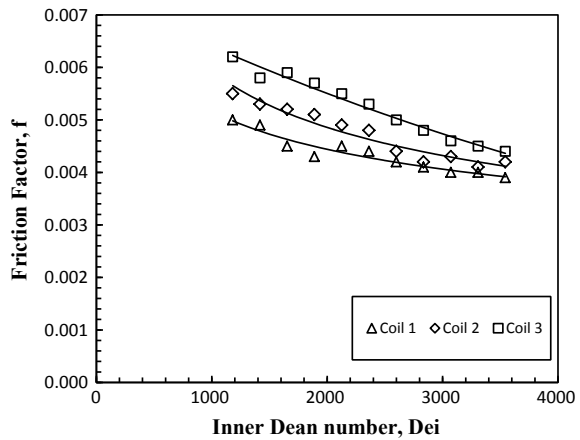


Fig. 8 Outer friction factor versus outer dean number

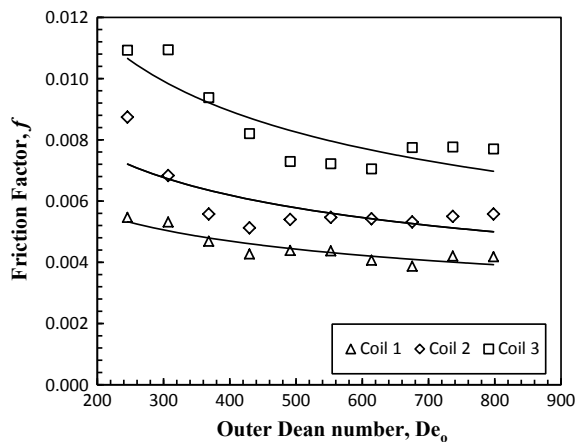
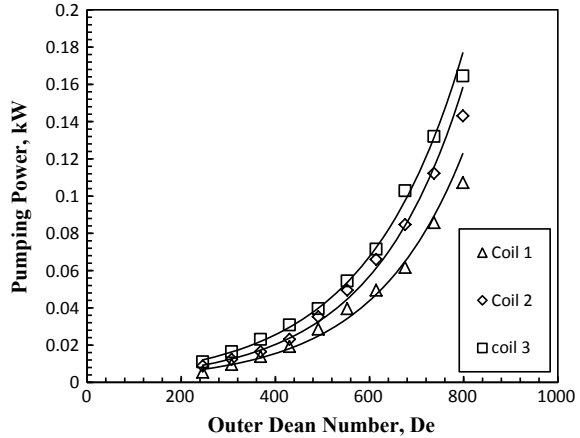


Fig. 9 Pumping power versus outer dean number



is observed due to more tube side surface are exposed to annulus region and inner surface area of coil.

4.4 Pumping Power

The pumping power is directly proportional to mass flow rate and pressure drop across coiled tube. Figure 9 shows the variation of pumping power with outer Dean Number. In that considering the coil 1, coil 2 and coil 3 experimentally and investigate the variations in all three coils.

From Fig. 9 it is clearly shows that, as the increasing in outer side Dean Number pumping power is also increasing in all three coils. But for same Dean Number required pumping power is different in all three coils, as coil 1 required less pumping power then other two coils, coil 2 required more power than coil 1 but less power than coil 3 and coil 3 took up more power than other two coils.

5 Conclusion

Study of helical coil heat exchanger using concentrated pipe is to be performed by using multiple no of coiled configured heat exchanger set up. The mass flow rate of inner tube and annulus tube with varied counterflow configurations were tested. On the basis of experimental analysis, the following conclusions are to be drawn,

1. An annulus side, outlet cold water temperature was increased with increasing in hot water mass flow rate.
2. Heat transfer capacity using multiple tubes was higher than the single tube for same cold water mass flow rate.

3. An average rate of heat transfer increase with the increase in hot and cold water mass flow rate
4. The effectiveness and friction factor of coiled tube heat exchanger decreases with increasing in hot water mass flow rate.
5. The rate of heat transfer and effectiveness of coiled tube increase with increasing in number of coiled tubes.

References

1. Pawar SS, Shriyan N, Vedpathak A, Mule S (2015) A review on heat transfer of fluids in curved and coiled geometries. *Elixir Mech Eng* 89:36998–37007
2. Martin PN, Jorge GC, Benjamin AB (2016) Thermo-hydraulic design of single and multi-pass helical baffle heat exchangers. *Appl Therm Eng* 17:21–27
3. Mir ME, Seyed AHB (2017) Numerical investigation and optimization of heat transfer and exergy loss in shell and helical tube heat exchanger. *Appl Therm Eng* 121:294–301
4. Majidi D, Alighardashi H, Farhadi F (2018) Experimental studies of heat transfer of air in a double-pipe helical heat exchanger. *Appl Therm Eng* 133:276–282
5. Rajput RK (2015) A textbook of heat and mass transfer. S. Chand Publishing, India

Analysis of Construction Labour Productivity for Indian States



Rahul S. Chaudhari, Pankaj P. Bhangale, and Surabhi Sengar

Abstract United Nation has done a survey in 2017 and found that 59.24% of the population resides in a rural area in India. This needs to develop the required infrastructure and real estate sector to fulfill the needs of the huge population. Nearly 5.10 Cr, construction workers are working in this sector out of which approximately 3.5 Cr. Construction workers have registered with the board. In this study out of 28 states only 17 states are considered for study as data is not available for other states. It is observed that construction labour productivity is highest in the states like Maharashtra, Meghalaya and Gujrat in 2016–2017 but reduced in 2017–2018. Also, the lowest labour productivity was observed for states like Odisha, West Bengal. Cumulative variation in labour productivity was observed for all the zones. Positive variation is observed for south (14.53) and east zone (4.52). But negative variation was observed for the other zones like north (–1.983), west (–98.402), central (–33.415), and northeast (–44.346). The variation is observed may have problems like low wages, working conditions, welfare facilities provided, method of construction and most important motivation of the workforce.

Keywords Labour Productivity · Construction sector · Analysis of productivity

1 Introduction

During the year 2011–2015, the growth rate of the construction industry in India was 2.9% which was expected to increase up to 5.6% by 2016–2020. In 2019, it was contributed over 2.7 trillion Indian rupees in GDP which is highest recorded till date. This mainly includes the growth of rural areas [1]. The growth of the industry mainly depends upon the factors like skill of labours, nature of the project, duration

R. S. Chaudhari (✉)

Shri Satya Sai University of Medical Sciences and Technology, Sehore, India

P. P. Bhangale

Civil Engineering Department, SSGB COE and T, Bhusawal, India

S. Sengar

Pimpri Chinchwad College of Engineering, Pune, India

© The Author(s), under exclusive license to Springer Nature Switzerland AG 2021

P. M. Pawar et al. (eds.), *Techno-Societal 2020*,

https://doi.org/10.1007/978-3-030-69925-3_46

467

of the project, wages provided to the labours, facilities provided to the labour etc. As India is a country with 28 states and nearly 135 Cr. of the population. This arises a huge demand for shelters, infrastructure in the country and is provided by the construction sector. To improve the productivity Prime Ministers Shram Award Scheme was started by Government of India. In 2016, a total of 32 awards was given to 50 workers or groups of workers working in productive processes and manufacturing (Ministry of labour and employment, Annual report 2017–2018) [2–4].

According to Human resources and skill required in Building construction and real Estate Sector (2013–2022) By Government of India skill Development and entrepreneurship, construction industry creates 45 million jobs in various classes Directly or indirectly in the country which is expected to 76 million by 2022 [5, 6] (Table 1).

In 2012–2013 capital investment was 651 billion USD which was increased to 1181 Billion in 2019–2020. Percentage of unskilled workers is nearly 83.30%, and skilled workforce is 9.14% only. This affects productivity in this sector. Heavy investment in real estate was concentrated around tier1 cities like Mumbai, Delhi and NCR.

As India is one of the fastest developing countries, the awareness between the labours for registration at the government office is very less. In this country, workers can register themselves as a construction worker under “Building and other Construction Worker Act 1996” (BOCW) to get the benefit related to wages, welfare, continuous employment etc. But due to lack of awareness and due to negligence of the employer (Pity contractors etc.) those are not getting registered. In this study, the data is collected from various official publications related to the number of labours registered under BOCW and amount of work done in the respective states to calculate labour productivity. In India development is not uniform in all the states therefore migration of workers from one state to other takes place [7, 8].

In this paper following points are addressed,

1. State wise construction workers productivity in India.
2. Correlation of productivity According to zone.
3. Coefficient of variation for two successive financial years.

Table 1 Employment projection in construction sector

Sector	Employment base in Million		
	2013	2017	2022
(A) Building construction and real estate	40.14	51.95	66.62
(B) Infrastructure	5.28	7.45	9.93
Total (A + B)	45.42	59.40	76.55

2 Literature Survey

At present, in the construction industry, labour productivity is measured by using various major factors which are again subdivided into sub factors. Methods like Relative Importance Index (RII) are calculated and factors affecting labour productivity are summarized. According to Ayele, Selam Y. and Fayek, Aminah Robinson (2017) there are various formulae available to calculate labour productivity.

1. Total Factor Productivity = Total output/Labor + Material + Equipment + Energy + Capital)
2. Labor Productivity = Total Output/Labor (Direct Work hours)
3. Total Productivity = Total Tangible Output (Unit)/Total Tangible Inputs
4. Labour Productivity = Total Tangible Output (Unit)/Labour Inputs
5. Capital Productivity = Total Tangible Output (Unit)/Capital Inputs
6. Material Productivity = Total Tangible Output (Unit)/Material Inputs
7. Energy Productivity = Total Tangible Output (Unit)/Energy Inputs [9]

Chaudhari and Bhangale [10] has summarized sector wise various methods used for finding loss of labour productivity in construction projects for various countries. According to Annual Report from the Ministry of Labour and Employment Government of India, 2018–2019, the construction sector is one of the sector having unorganized workers whose monthly income is less than Rs.15000/- and are not covered under the Employees’ State Insurance Corporation (ESIC) scheme or Employees’ Provident Fund Organization (EPFO), New Pension Scheme (NPS) may also one of the reasons for getting less productivity at the construction site. Fah Choy, Chia, Skitmore, Martin, Runeson, Goran, and Bridge, Adrian (2012) has found that the productivity of the construction industry has a significant impact on the development of the nation. For this productivity, indicators shall be examined.

For Malaysia, results show that there is an improvement in labour productivity but value-added contents are declining. According to Dharani [11] Indian construction sites having problems like low wages, issues related to safety, welfare issues etc. are not fulfilled by small firms hence affecting labour productivity. The observations are summarized factors into zero, high and Very high variance of contractors view and labours view (Refer to Table 2).

Table 2 Variance and factors considered for productivity

Zero variance	Work Experience, types of labour
Low variance	Medical aid
High variance	Training, working environment
Very high variance	Wages

3 Data Collection Process

As mentioned earlier some important factors play a very important role in data collection of any study. India is one of the fastest developing countries in which the construction sector is one of the largest unorganized sectors. While data collection, census reports were considered. The latest report contains data up to the year 2017–2018 which is available on the official websites. Some issues faced by Government.

While data collection is, 1. Companies does not submit or upload their data on the government website on time. 2. Companies miscode their entries. For data collection, various reports from Reserve Bank of India, Annual reports from Ministry of labour and employment, Annual reports were studied. Data for some states is not available are not considered in this study. The data was collected and sorted for 17 different states.

In India, development is not uniform, therefore, workers migrate from one place to another for getting bread butter and not getting registered. Mainly the migration is from the states like Bihar, Uttarakhand, Uttar Pradesh and Madhya Pradesh towards Maharashtra, Delhi, and Gujrat etc.For getting details of wages of workers, official gazettes and websites were referred.

4 Data Analysis

As per the above discussion, data is not available for all states. So, the following states are considered for this study. Table 3 includes Zone wise Distribution of states by the Indian Government which are considered for the study. As per various formulae available for calculation of labour productivity, following equation is used. The analysis was carried out based on the data available on official websites.

$$\text{Sub-sector } LP_i = \frac{\sum_{j=1}^{17} VC_{ij}}{\sum_{j=1}^{17} NCW_{ij}}$$

Table 3 Zone wise distribution of states by indian government assessing macroeconomic labor productivity

Zone wise distribution of states by Indian Government					
North	South	East	West	North East	Central
Rajasthan	Tamil Nadu	Bihar	Maharashtra	Meghalaya	Uttar Pradesh
Himachal Pradesh	Andhra Pradesh + Telangana	West Bengal	Gujarat	Sikkim	Delhi
	Karnataka	Jharkhand			Uttarakhand
	Pondicherry	Odisha			

In this equation,

L_{Pi} the labor productivity of i (state j),

V_{Cij} the value of construction work in rupees (i in state j), and.

NCW_{ij} the number of construction workers of industry i in state j. (Registered).

Table 4 gives details related to State wise labour productivity for 2016–2017 and 17–18.

Based on the data collected from the states, it was observed that Tamil Nadu is having maximum Sectoral gross state domestic product at factor cost for construction (for 2016–2017 (12,629,839) and for 2017–2018(13,569,487) and Registered workers with the board (BOCW) is also maximum as 2016–2017 (2,700,749) and for 2017–2018 (2,853,544) But the labour productivity was observed as 2016–2017 (4.6769) and for 2017–2018 (4.755). The maximum value was observed for Maharashtra and minimum for Odisha. Figure 1 shows state wise variation in labour productivity in India.

Following three different cases are observed after data analysis,

Case No 1:

1. In Adhra pradesh the registered construction workers in 16–17 are 27,52,748 and in 17–18 was 29,91,420. But the productivity observed as only 2.66 and 2.88.

Table 4 State wise labour productivity

States/Union territories	labour Productivity in Lac	
	2016–2017	2017–2018
Andhra Pradesh + Telangana	2.868	2.887
Bihar	4.101	4.279
Himachal Pradesh	6.937	5.874
Jharkhand	2.934	2.344
Karnataka	5.268	4.183
Maharashtra	17.960	11.963
Meghalaya	11.601	7.513
Odisha	1.398	1.227
Rajasthan	3.591	3.082
Sikkim	2.882	3.091
Tamil Nadu	4.676	4.755
Uttar Pradesh	3.303	3.029
Uttarakhand	8.062	6.276
West Bengal	1.833	2.399
Delhi	4.501	4.583
Pondicherry	8.337	8.926
Gujarat	10.046	8.980

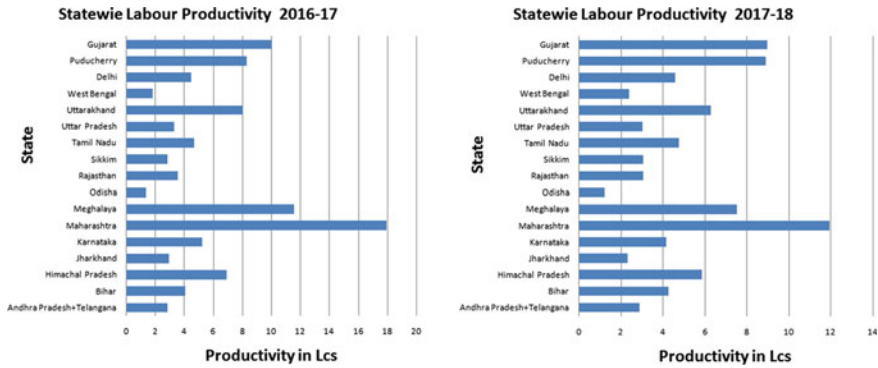


Fig. 1 State wise Labour Productivity in India for 2016–17 and 2017–18

Case No 2:

In Maharashtra, the registered construction workers in 16–17 are 6,10,715 and in 17–18 was 9,89,018. And the productivity observed as only 17.96 and 11.96. which is maximum value was observed.

Case No 3:

3. In Odisha the registered construction workers in 16–17 are 1,840,000 and in 17–18 was 2,234,569. But the productivity observed as only 1.39 and 1.22.

Macroeconomic Labor Productivity is represented in graphical form in Fig. 1 for the financial year 2016–2017 and 2017–2018. In the financial year 2016–2017, highest productivity is observed in Maharashtra (17.96035) and the minimum was observed at Odisha (1.398497). Similarly, for the financial year 2017–18, highest productivity is observed in Maharashtra (11.96321) and the minimum was observed at Odisha (1.2269932) again. The average productivity of labour in the year 2016–17 was (5.8998) and for 2017–2018 was (5.0231).

Geographically India is country where culture, population, income and development changes drastically. As previously mentioned, complete data is for all states is not available. For those states (17) zone wise distribution is given in table no 3, and standard deviation (SD), Mean value of productivity and Coefficient of variation (CV) is calculated. The details are given Table No 5.

1. For **South zone**, the Coefficient of variation (CV) in labour productivity for the financial year 2016–17 and 17–18 was observed as + 14.531% which shows improvement in the productivity.
2. For **North zone**, the Coefficient of variation (CV) in labour productivity for the financial year 2016–17 and 17–18 was observed as -1.983% which shows reduction in the productivity.
3. For **East zone**, the Coefficient of variation (CV) in labour productivity for the financial year 2016–17 and 17–18 was observed as -4.525% which shows slight increase in the productivity.

Table 5 Standard Deviation (SD) Mean and Coefficient of variation (CV) between 2016–2017 and 2017–2018

Zone	2016–2017		2017–2018		Coefficient of variation (CV) between 2016–2017 and 2017–2018
	S.D	Mean	S.D	Mean	
South	2.275	5.287	2.612	5.188	14.531
North	2.366	5.264	1.974	4.478	-1.983
East	1.210	2.567	1.265	2.562	4.525
West	5.596	14.003	2.109	10.472	-98.402
Central	2.475	5.288	1.624	4.630	-33.415
North East	6.165	7.241	3.127	5.302	-44.346

4. For **West zone**, the Coefficient of variation (CV) in labour productivity for the financial year 2016–17 and 17–18 was observed as -98.402% which shows drastically decrease in the productivity.
5. For **Central zone**, the Coefficient of variation (CV) in labour productivity for the financial year 2016–17 and 17–18 was observed as -33.415% which shows decrease in the productivity.
6. For North East zone, the Coefficient of variation (CV) in labour productivity for the financial year 2016–17 and 17–18 was observed as -44.346% which shows decrease in the productivity (Table 5).

5 Conclusion

1. It was observed that the labour productivity in Maharashtra is highest whereas lowest in Odisha. The reason may be,
 - Migration of labors from state to state,
 - Skill of labour Force,
 - Facilities provided by the employer on the construction site,
 - Wages labour getting in the respective states.
2. Meghalaya and Gujrat states is also having better labour productivity in 2016–2017 but reduced in the financial year 2017–2018.
3. Benefits construction labours get under Building and other Construction workers act required registration of labours to the office.
4. Highest number of labours registered at Andhra Pradesh and Telangana states. But the labour productivity is observed as 2.86 and 2.88. The reason for less productivity may be migration to the states like Maharashtra, Gujrat etc.

6 Future Scope

1. In the study cumulative value of sectoral gross state domestic product at factor cost - construction (the amount is in Lakh) was considered. But the study can be carried out in detail by considering individual sectors like infrastructure, housing etc.
2. Study shall be carried out by considering wages of labours in the states

References

1. Annual Report (2017–2018) Ministry of Labour and Employment Government of India. 68–100, Website: <https://www.labour.nic.in>
2. Annual Report (2016–2017) Ministry of Labour and Employment, Government of India, 73–114. Website: <https://www.labour.nic.in>
3. Annual Report (2018–2019) Ministry of Labour and Employment, Government of India, 34–92. Website :<https://labour.gov.in/annual-reports>
4. India Wage Report (2018) Wage policies for decent work and inclusive growth, International Labour organization.
5. Human Resources and skill requirements in Building construction and rural estate sector 2013–22,national skill development corporation (NSDC), Government of India, Ministry of Skill Development and Enterprenurship, 24–50
6. Education, Skill Development and Labour Force (2013–14), Government of India, Ministry Of Labour and Employment, Labour Bureau Chandigarh
7. Indian Labour Statistics (2017) Government Of India, Ministry Of Labour And Employment, Labour Bureau, Shimla. Volume III
8. Report Q (2016) On Employment Scenario (New Series), Government of India. Ministry of Labour and Employment, Labour Bureau, Chandigarh
9. Choi K, Haque M, Lee HW, Cho YK, Kwak YH (2013) Macroeconomic labor productivity and its impact on firm's profitability. *J Oper Res Soc* 1–33
10. Chaudhari RS, Bhangale PP (2020) An analytical approach by researchers to find factors affecting labour productivity in the construction industry-a review. *J Emerg Technol Innovat Res* 7(4):1–6. (ISSN: 2349–5162)
11. Dharani K (2015) Study on labours productivity management in construction industry. *Int J Latest Trends Eng Technol (IJLTET)* 6(1):278–284

Performance Analysis of Conical Journal Bearing with Different Configuration



Sunil D. Bhingare, B. P. Ronge, Prashant M. Pawar, and U. B. Andh

Abstract The space between the shaft and the bearing is called lubrication gap and is filled with lubricant. Journal bearing test rig is used to test the 40 mm diameter and 28 mm long bearing. The bearing is loaded mechanically. The bearing is tested under various parameters like type of lubricant, loading conditions, speeds etc.... in the last, experimental results are compared with the simulation results by using COMSOL software and results are found satisfactory. The setup consists of a bearing journal driven by an electrical motor and the freely moving bearing housing. The bearing is loaded with different, interchangeable weights. Both the radial and axial distribution of pressure can be recorded in the bearing gap at two measuring points around its perimeter and four along the length. The pressure readings are recorded with the help of pressure sensors. Pressure distribution in the bearing without adding surface features on the journal is first recorded and then by adding different surface features, the results are taken and the difference of the results are satisfactory. Surface features are created on the journal by using Photo chemical machining (PCM). It is clear that the measured oil film pressure in case of journal with surface features is clearly wider than that of journal without surface features.

Keywords Journal Bearing · Pressure · Surface features · PCM

1 Introduction

Now-a- days, there is a great increase in industrial demands to cater the need for high speed applications; hybrid journal bearings are most suitable for high load carrying capacity and long life. Conical journal bearing is a radial–thrust hybrid bearing which offers distinct advantages over the cylindrical journal bearing. The main advantage of the conical hydrostatic/hybrid journal bearing is that it can carry radial as well axial load at the same time, thereby eliminating the need for separate thrust and journal bearing. Further, conical journal bearings are applied both in low speed

S. D. Bhingare (✉) · B. P. Ronge · P. M. Pawar · U. B. Andh
Department of Mechanical Engineering, SVERI's College of Engineering, Pandharpur, India
e-mail: sdbhingare@cod.sveri.ac.in

heavy load machine and high speed high precision machine. Conical journal bearing is designed by using different micro features like pillars, walls, circumferential ribs, circumferential slots, etc. [1].

It is fabricated by one of the methods like Photo Chemical Machining (PCM). After designing of conical journal bearing with micro features, various parameters is studied for different loading conditions, different speeds. Effect on development of fluid film pressure is studied for above different conditions. Simulation is carried out by using numerical based software like COMSOL MUTIPHYSICS, then the above said simulation and experimental results obtained for different types of hydrodynamic conical journal bearing is compared, considering different parameters like speed, load carrying capacity and viscosity.

2 Experimentation

2.1 Photo Chemical Machining (PCM)

Photo chemical machining is used to fabricate the metal sheets by using photo resist and etchants. This technology was developed in 1960s. With the help of this technology, we can produce very complicated parts with greater accuracy. This technology can be the best alternative to other expensive processes like laser cutting, electric discharge machining etc. Various researchers have reported the fabrication of microchannels, heat sinks, microfeatures and micro textures using photochemical machining [2–12].

Modified configurations of journal bearing are done by adding features on the surface of journal shaft with the help of PCM as shown in Figs. 1 and 2.

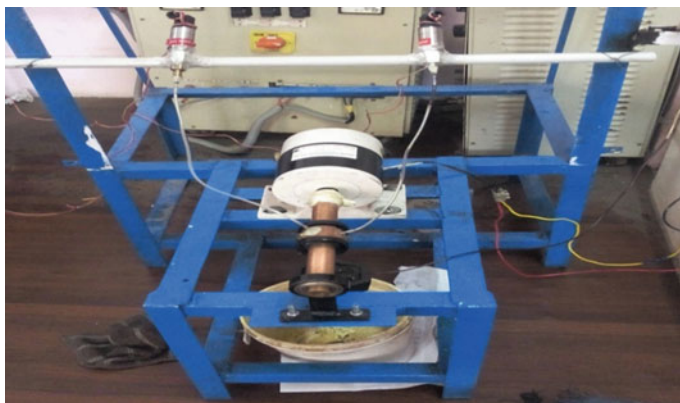
Fig. 1 Journal Shaft with Surface features after PCM



Fig. 2 Copper Bearing

2.2 Layout of Experimental Set up

It consists of a copper Bearing mounted freely on a stainless steel and copper journal shaft. This journal shaft is fixed between one pedestal bearings and connected to motor shaft through the coupling. The speed of DC motor is finely controlled by speed control unit. The journal bearing has two equiv.-spaced pressure tapings around its circumference. Clear flexible plastic tubes are connected to the tapings at one end while the other ends to the pressure sensors. The oil reservoir can be adjusted at required height and is connected to the bearing by flexible plastic tubes [1]. From this reservoir SAE 40 oil enters the bearing. Provision is made to drain the collected oil which can again be supplied to supply tank as shown in Fig. 3.

**Fig. 3** Mounting of Conical Journal Bearing set-up

3 Results and Discussions

3.1 Experimental Results

Table 1 indicates the values of pressure for load of 1.5 kg and at 2000 rpm.

In Fig. 4, it is observed that, as equilibrium conditions reaches, positive fluid film pressure increases. The blue color line is for pressure distribution for conical journal bearing with surface textures. Red color line is for pressure distribution for conical journal bearing without surface textures. It is observed that, development of fluid film pressure is more in case of conical shape journal bearing with surface textures than the without texturing for load 1.5 kg and speed 2000 RPM.

Table 2 indicates the values of pressure for load of 1.5 kg and at 2000 rpm.

In Fig. 5, it is observed that, as equilibrium conditions reaches, positive fluid film pressure increases. The blue color line is for pressure distribution for conical journal

Table 1 Pressure readings for load 1.5 kg Speed 2000 rpm

Sr. No		1	2	3	4	5	6	7	8	9
Positive pressure in KPa	Without texture	0	2	7.1	10.2	18	22	26.2	25	24.6
	With texture	0	4	9	11	17	21.2	31.2	30.1	30
Negative pressure in KPa	Without texture	0	0.2	0.7	1	1.8	2.7	3.4	3.2	3.7
	With texture	0	0.4	0.9	1.2	4.7	6.2	7	8.5	9

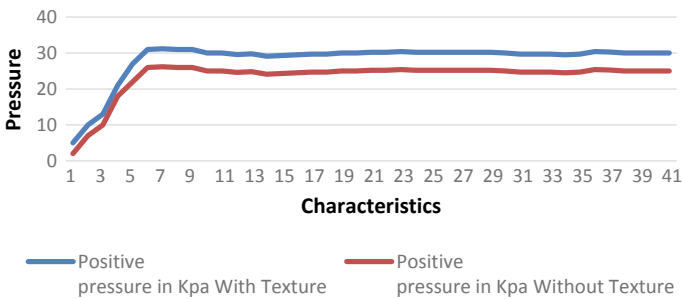


Fig. 4 Radial pressure profile comparison

Table 2 Pressure Readings for load 3.5 kg speed 1500 rpm

Sr. No		1	2	3	4	5	6	7	8	9
Positive pressure in KPa	Without texture	0	8	33.1	50.2	73.8	77.8	79	80.1	79.2
	With texture	0	18	45	62.2	84	84.1	84.4	84.9	85
Negative pressure in KPa	Without texture	0	1.3	7.1	7.5	12	13.1	13.5	13.8	14
	With texture	0	2.3	11.3	11.5	17.1	17	17.2	17.5	17.8

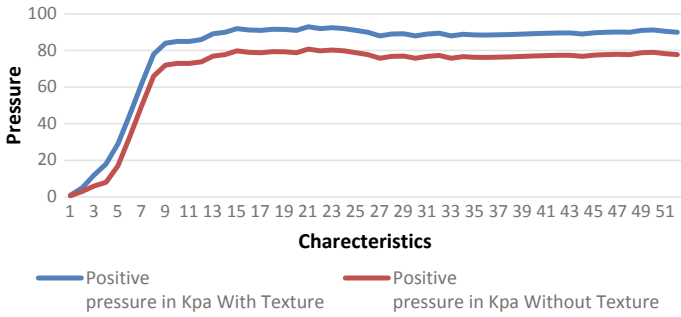


Fig. 5 Radial pressure profile comparison

bearing with surface textures. Red color line is for pressure distribution for conical journal bearing without surface textures [13, 14].

It is observed that, development of fluid film pressure is more in case of conical shape journal bearing with surface textures than the without texturing for load 3.5 kg speed 1500 rpm.

Table 3 indicates the values of pressure for load of 3.5 kg and at 2000 rpm.

In Fig. 6, it is observed that, as equilibrium conditions reaches, positive fluid film pressure increases. The blue color line is for pressure distribution for conical journal

Table 3 Pressure Readings for Load 3.5 kg Speed 2000 rpm

Sr. No		1	2	4	6	7	9	11	12	13
Positive pressure in KPa	Without texture	0	8	28	72	82	94	102	102.1	101.9
	With texture	0	7.1	35.2	102.2	112	119	119	120	120
Negative pressure in KPa	Without texture	0	1.5	5.1	12.3	16.4	20.2	21.1	21	21.2
	With texture	0	2	9.8	14.1	16.2	24.3	26.3	27.1	27.2

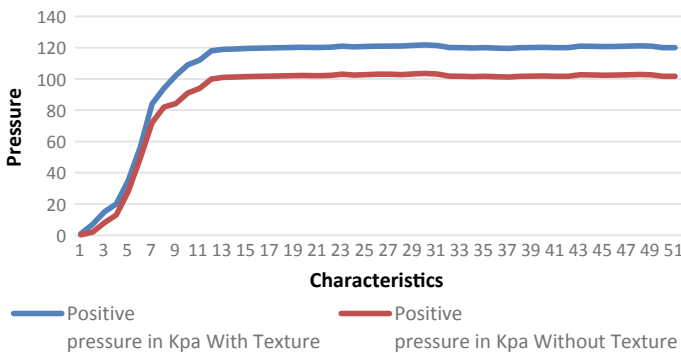


Fig. 6 Radial pressure profile comparison

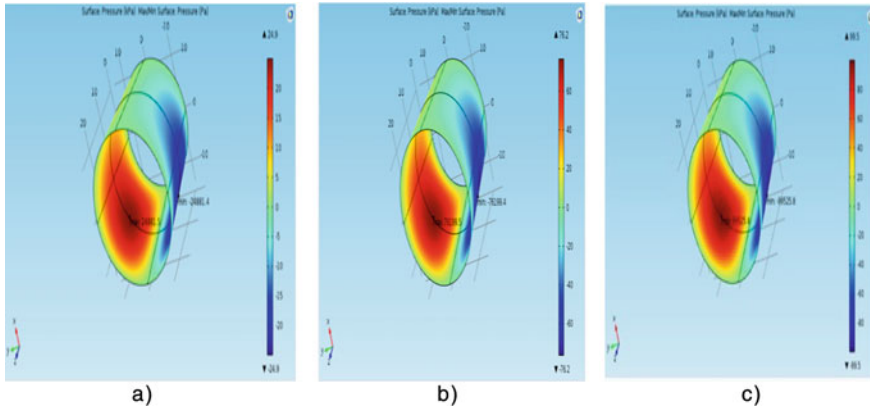


Fig. 7 Pressure Readings for Load in kg and Speed in rpm on COMSOL Multi-physics

bearing with surface textures. Red color line is for pressure distribution for conical journal bearing without surface textures. It is observed that, development of fluid film pressure is more in case of conical shape journal bearing with surface textures than the without texturing for load 3.5 kg and speed 2000 rpm [15].

3.2 Results of Finite Element Analysis

In Fig. 7a, it is observed that, pressure analysis with loading condition at 2000 rpm. The bearing without texture has been compared with each other while running the shaft at 2000 rpm and subjected to the load of 1.5 kg. The radial pressure profile is gate up to 24.9 kPa [16].

In Fig. 7b, it is observed that, pressure analysis with loading condition at 1500 rpm. The bearing without texture has been compared with each other while running the shaft at 1500 rpm and subjected to the load of 3.5 kg.

The radial pressure profile is gate up to 76.2 kPa. In Fig. 7c, it is observed that, pressure analysis with loading condition at 2000 rpm. The bearing without texture has been compared with each other while running the shaft at 2000 rpm and subjected to the load of 3.5 kg. The radial pressure profile is gate up to 99.5 kPa. The red zones are the maximum positive fluid film pressure and support to external load and the blue zones are the maximum negative fluid film pressure [16–18].

3.3 Comparison of Experimental and Simulation Results

The main result of this study is the measurement of realistic oil film pressure in real type hydrodynamic conical journal bearings at various operating points across the

Table 4 Comparison of Experimental and Simulation results

Characteristics	Experimental results (Pressure) Kpa	Simulation results (Pressure) Kpa	% Error
Load 1.5 kg and Speed 2000 rpm	26.2	24.9	1.3
Load 3.5 kg and Speed 1500 rpm	80.1	76.2	3.9
Load 3.5 kg and Speed 2000 rpm	102.1	99.5	2.6

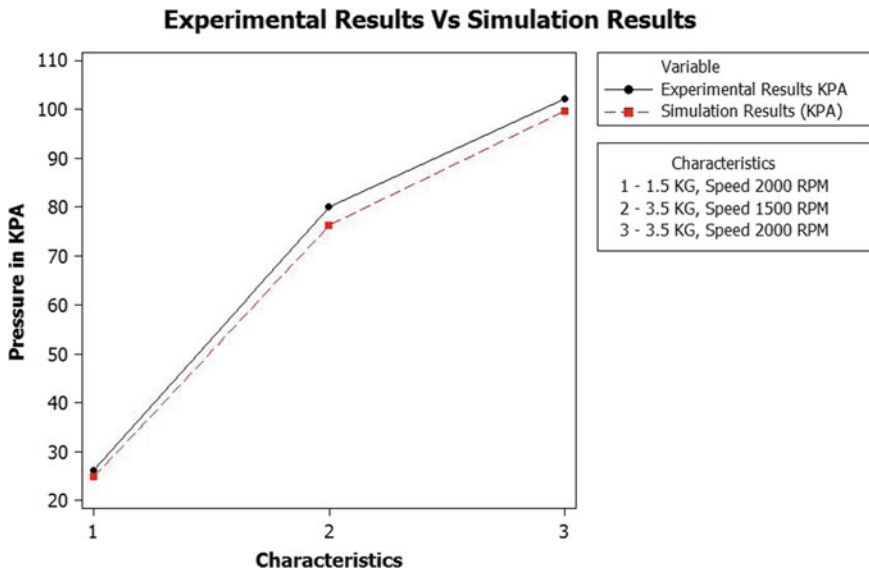


Fig. 8 Comparison of Experimental and Simulation result by using graph

realistic operating range and that certain significant differences between the measured and simulated data were found. Table 4 demonstrates the comparison of the results of experimental and finite element analysis.

From the above recorded data and Fig. 8 it is clear that the measured oil film pressure in case of journal with texture is clearly wider than that of journal without textures.

4 Conclusions

The fluid film pressure distribution and load carrying capacity of the hydrodynamic journal bearing lubricated with oil under steady state is analyzed. Based on the numerical results, following conclusions made for conical shape journal bearing were studying. Using Reynolds equation, present model of conical shape journal bearing

is simulated. In the analysis of conical shape journal bearings, influence of different journal speed on performance characteristics like fluid film pressure distribution and load carrying capacity etc. were studied.

- From analysis, it is found that maximum fluid film pressure developed (102 kPa) for high journal speed (2000 rpm and 3.5 kg load)
- From experimental, it is found that the measured oil film pressure in case of journal with surface features is clearly wider than that of journal without surface features.

References

1. Meruane V, Pascual R (2008) Identification of nonlinear dynamic coefficients in plain journal bearings. *Tribol Int* 41:743–754
2. Das SS, Tilekar SD, Wangikar SS, Patowari PK (2017) Numerical and experimental study of passive fluids mixing in micro-channels of different configurations. *Micros Technol* 23:5977–5988
3. Wangikar SS, Patowari PK, Misra RD (2018) Numerical and experimental investigations on the performance of a serpentine microchannel with semicircular obstacles. *Micros Technol* 24:3307–3320
4. Wangikar SS, Patowari PK, Misra RD (2017) Effect of process parameters and optimization for photochemical machining of brass and german silver. *Mater Manuf Proces* 32:1747–1755
5. Wangikar SS, Patowari PK, Misra RD (2016) Parametric optimization for photochemical machining of copper using grey relational method. In: 1st techno-societal, international conference on advanced technologies for societal applications. Springer, Berlin, pp 933–943
6. Wangikar SS, Patowari PK, Misra RD (2018) Parametric optimization for photochemical machining of copper using overall evaluation criteria. *Mater Tod Proceed* 5:4736–4742
7. Wangikar SS, Patowari PK, Misra RD, Misra ND (2019) Photochemical machining: a less explored non-conventional machining process. In: Non-conventional machining in modern manufacturing systems. IGI Global, pp 188–201
8. Kulkarni HD, Rasal AB, Bidkar OH, Mali VH, Atkale SA, Wangikar SS, Shinde AB (2019) Fabrication of micro-textures on conical shape hydrodynamic. *J Bearing Int J Tre Eng Technol* 36:37–41
9. Raut MA, Kale SS, Pangavkar PV, Shinde SJ, Wangikar SS, Jadhav SV, Kashid DT (2019) Fabrication of micro channel heat sink by using photo chemical machining. *Int J New Technol Res* 5:72–75
10. Patil PK, Kulkarni AM, Bansode AA, Patil MK, Mulani AA, Wangikar SS (2020) Fabrication of logos on copper material employing photochemical machining. *Nov MIR Res J* 5(6):70–73
11. Wangikar SS, Patowari PK, Misra RD, Gidde RR, Bhosale SB, Parkhe AK (2020) Optimization of photochemical machining process for fabrication of microchannels with obstacles. *Mater Manuf Proces* <https://doi.org/10.1080/10426914.2020.1843674>
12. Chavan NV, Bhagwat RM, Gaikwad SS, Shete SS, Kashid DT, Wangikar SS (2019) Fabrication and Characterization of Microfeatures on PMMA Using CO₂ Laser Machining. *Int J Tre Eng Technol* 36:39–32
13. Bang KG, Lee DG (2002) Thrust bearing design for high-speed composite air spindles. *Compo Struct* 57:149–160
14. Isea T, Aritaa N (2014) Development of externally pressurized small-size conical-shaped gas bearings for micro rotary machines. *Preci Engg* 38:506–511
15. Glavatskih WS, Cervantes MJ (2009) 3D thermohydrodynamic analysis of a textured slider. *Tribol Int* 42:1487–1495

16. Stolarski TA (2010) Numerical modeling and experimental verification of compressible squeeze film pressure. *Tribo Int* 43:356–360
17. Deligant M, Podevin P, Descombes G (2011) CFD model for turbocharger journal bearing performances. *App Therm Eng* 31:811–819
18. Gertzos KP, Nikolakopoulos PG, Papadopoulos CA (2008) CFD analysis of journal bearing hydrodynamic lubrication by Bingham lubricant. *Tribo Int* 41:1190–1204

Improving Cooling Performance of Deep Freezer by Incorporating Graphene Oxide Nanoparticles Mixed with Phase Change Materials During a Power Outage



Avesahemad S. N. Husainy, Gajanan V. Parishwad, Sonali K. Kale, Siddhanath V. Nishandar, and Aishwarya S. Patil

Abstract The aim of this research is to improve the cooling performance of deep freezer by prolonging the cut off period of the compressor, and also maintain a constant temperature inside the freezer cabinet by using different combinations of Nano-phase change material (Nano-PCM), viz. (graphene oxide + KCl and graphene oxide + NaCl) by considering water as a base fluid. In this work, an attempt has been given to reduce the temperature fluctuation that occurred by a power outage as well as frequent opening and closing of the door of the deep freezer. The experimental results show that the freezer cabinet temperature remains stable and is maintained between 3 and 7 °C for 6 to 7 h even though a power outage exists when Nano-PCM is used. It will help to reduce the wastage of perishable products. Hence thermal energy storage by using Nano-PCM could be the most appropriate way to correct the gap between the demand and supply of energy.

Keywords Food safety · Cooling effect · Temperature fluctuations · Cold chain

A. S. N. Husainy (✉) · S. V. Nishandar
Ph.D Research Scholar, Shivaji University, Kolhapur, Maharashtra, India

G. V. Parishwad
Director, Pimpri Chinchwad College of Engineering, Pune, Maharashtra, India

S. K. Kale
Assistant Professor, Department of First Year Engineering, Pimpri Chinchwad College of Engineering, Pune, Maharashtra, India

A. S. Patil
M. Tech Research Scholar, Department of Technology, SPPU, Pune, Maharashtra, India

1 Introduction

According to the global chest freezer market survey, the deep freezer market is going to cross 2.2 billion United States dollars (USD) with an improvement in the compound annual growth rate of 3.8% [1]. A deep/chest freezer is a well-insulated refrigeration system that is mainly used to store various temperature sensitive products for a longer duration of time and maintain the temperature between -18 and $+8$ °C. Various products like fruits, vegetables, vaccines, meat, medicines, and milk products are required to preserve under lower temperatures. In recent decades improvement has been made in the agricultural process, even though food losses and food safety are still common problems in cold chain processes [2]. Also in India power outage is very common because of wind, storm, high power demand, earthquake, maintenance, excavation digging, etc., which affects the food quality as well as refrigeration system performance. The phase change material store latent heat during charging mode and dissipate that energy during off-peak load and change its phase from liquid to solid or solid to liquid. Phase change material is attractive technology in the cold chain process because of lower dependency on fossil fuel, availability in a wide range of lower temperature, no harmful effects, etc. The advantage of phase change materials for the cold chain process is to improve food safety, food loss, reduce temperature fluctuations, and keep freezer temperature for a longer duration of time even though power outage exists. Major lacuna of phase change material is poor thermal conductivity and diffusivity, so it is decided to use graphene oxide nanoparticles in phase change material [3]. The compressor operates in normal deep freezer is ON–OFF mode. During compressor ON mode, refrigerant flowing inside the copper tube of evaporator absorb heat in the freezer section and during OFF mode temperature start rising inside the freezer cabinet [4]. In experimentation different mass fraction of phase change materials like (NaCl and KCl) mixed with nanoparticles (graphene oxide) used as a thermal energy storage. The main advantages of the nano phase change material integrated deep freezer are less power consumption, fewer compressor problems, good thermal stability, less maintenance, etc. This Nano-PCM used in the evaporator section of deep freezers improve the performances of the refrigeration system by increasing compressor cut OFF time and thereby decreasing power usage. Selection of suitable phase change material for each specific application for lower temperature application is an important matter [5]. So, the reduction of temperature fluctuation and improvement of refrigeration cooling performances is the reason for using Nano-PCM. Nano materials like graphene oxide, CuO, TiO₂, CNT, Al₂O₃ nanoparticles were commonly used for incorporation with phase change materials, which improves their thermo-physical properties like thermal conductivity, diffusivity, specific heat and latent heat capacity, and heat transfer rate [6].

Many investigators given their attempts to increase the performance of refrigeration system by implementation of phase change materials for lower temperature applications. Li Huang et al. [7] developed an insulated containers integrated with phase change material in a temperature range of 2 to 8 °C. The outcome of this research work is to maintained internal freezer temperature maintained at 4 to 5 °C by using a phase change material with a melting/freezing point of 5 °C, while the container presented a sub cooling effect in a range of -1 to 2 °C by using water as phase change material. Saurav Negi et al. [8] identified important aspects related to food losses and wastage in the fruits and vegetables in cold chain process and motivate farmers, transporters, stakeholders, researchers, and cold storage owners to regulate the risk of losses and wastage. Singh et al. [9] studied some important aspects that obstruct the full exploitation of temperature regulating material technology within the food packaging industry. Researchers focus on making packaging systems commercially viable. Veerakumar et al. [10] noticed recent developments on cold thermal energy storage using phase change materials. Also, different applications where the phase change material can be employed for cold energy storage such as passive cooling of buildings, air-conditioning, refrigerated trucks, and cold packing are listed and focused. Du et al. [11] studied phase change materials and their applications for heating, cooling, and electricity generation according to their working temperature ranges from (-20 °C to 200 °C). In this paper low-temperature application range (-20 °C to +5 °C), medium-low temperature application range (5 °C to 40 °C), medium high-temperature application range (40 °C to 80 °C), and high-temperature application range (80 °C to 200 °C) review show that energy saving of up to 12% can be achieved and a reduction of the cooling load of up to 80% can be obtained by PCMs in the low to medium-low temperature range. Sharma [12] focused on the assessment of the thermal properties of various PCMs for solar water and air heating systems, solar cooking, buildings, off-peak electricity storage systems application.

In order to improve the performance of refrigeration system a deep freezer of 200 L capacity is used. The Nano-PCM containers made by stainless steel materials are used in the freezer cabinet of deep freezer as shown in Fig. 3. During experimentation different combinations of Nano-PCM like 3% NaCl + 0.5% graphene oxide, 5% NaCl + 0.5% graphene oxide, 3% KCl + 0.5% Graphene oxide, 5% KCl + 0.5% Graphene oxide are considered. During ON mode of compressor Nano-PCM inside the container charged and changes its phase from liquid to solid and when temperature fluctuations occurs due to power outage at that time Nano-PCM start changing phase from solid to liquid and keeps freezer cabinet temperature constant for longer duration of time.

2 Applications of Phase Change Materials for Lower Temperature

In below Fig. 1 the important applications of phase change materials for lower temperature are discussed.

1. Food packaging

The packaging is one of the most important methods to protect food commodities for a longer duration of time and implementation of phase change material as thermal storage in packaging container will help to prolong the heating/cooling effect without disturbing the food quality.

2. Refrigeration transportation

PCM integrated panels are integrated into refrigerated trucks, food packaging, and medical product, for a better thermal buffering capacity to enhance the thermal protection of perishable products.

3. Cold storage/Cold room and Pre-cooling chamber

It is impossible to operate a working cold room for 24 h without electricity. Alternately, diesel generators are used as a power source, which incurs huge costs and is unviable as well. Phase change material is a novel option to reduce a load of vapor compression refrigeration cycle during off peak hours.

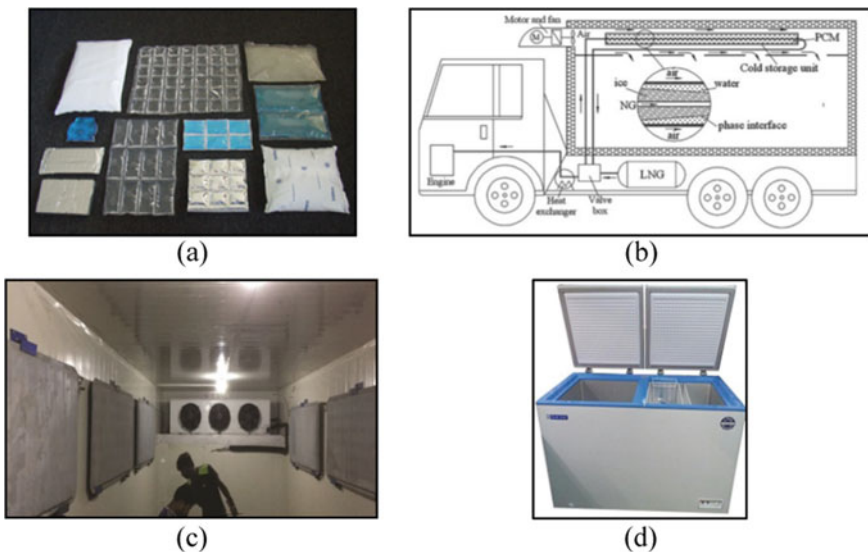


Fig. 1 a PCM pouches for food packaging [13], b PCM integrated refrigerated truck [14], c PCM based cold room, d PCM enhanced deep freezer.

4. Deep freezer/Chest coolers

A deep freezer is used mostly to preserve temperature sensitive products like Ice-cream, cold drinks, fruits and vegetables, milk products, medicines, vaccines, etc. In India still, we are facing power outage problems in urban and rural areas.

3 Experimental Investigation

The experimental set up consists of test facilities like pressure gauge, energy meter, LP, and HP cut-off as shown in Fig. 2. The freezer space is enclosed with Nano-PCM containers (refer Fig. 3). The mixing of graphene oxide and phase change materials is done with the help of ultrasonic agitator as shown in Fig. 4. The experiment is started by filling the Nano-PCM compartments with the different combinations of Nano-PCM viz. (graphene oxide as a nanoparticle + KCl and NaCl as a phase change material) by considering water as a base fluid. The volume concentration of the nanoparticles plays a vital role in enhancing the thermal conductivity of the phase change material. For experimentation, graphene oxide nanoparticles are selected

Fig. 2 Nano-PCM enhanced deep freezer

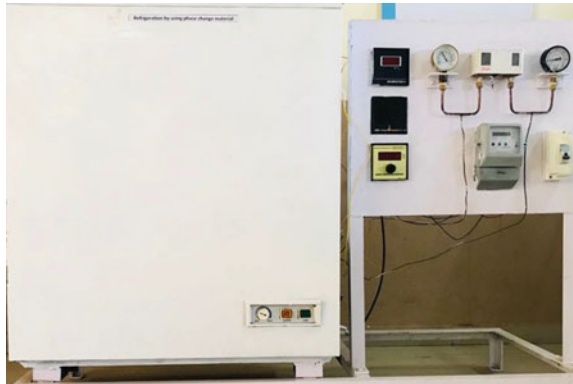


Fig. 3 Nano-PCM container



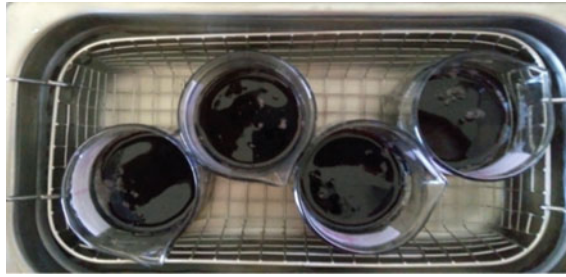


Fig. 4 Mixing of graphene oxide nanoparticles in phase change material

because it has a very good density of 3600 kg/m^3 , thermal conductivity 3000 W/m K and latent heat 250 J/kg K . $30\text{--}50 \text{ nm}$ graphene oxide particles were selected because it will give good thermal stability and doesn't allow the particles to settle down. Hence, the implementation of Nano-PCM will improve the performance of the refrigeration system by extending the OFF time of the compressor in case of temperature instability as well as during power outage situations. Initially, 10 readings are taken during power ON condition and 20 readings are taken after power OFF conditions at 15 min interval to check the temperature stability by consideration of Nano-PCM. From all the tests conducted, gathered all the data of evaporator inlet, outlet pressure, and temperature, condenser inlet, outlet pressure, and temperature, a number of blinks. The same experimental methodology is repeated for different combinations of Nano-PCM and graphs of temperature vs. time have been drawn and compare its results with normal readings (without Nano-PCM) during power OFF condition.

By using NaCl (3 and 5%) + graphene oxide (0.5%) combinations it is possible to maintain evaporator temperature from 3 to 5°C for 6 to 7 h span as shown in Fig. 5. By use of NaCl + graphene oxide (Nano-PCM) will keep evaporator temperature

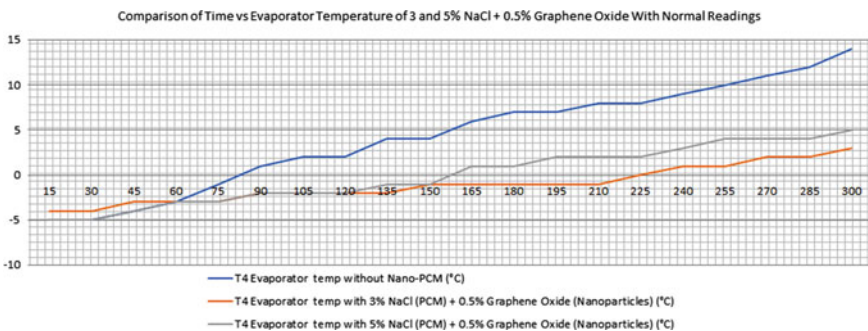


Fig. 5 Comparison of time with evaporator temperature of 3 and 5% NaCl + 0.5% graphene oxide with absence of Nano-phase change material

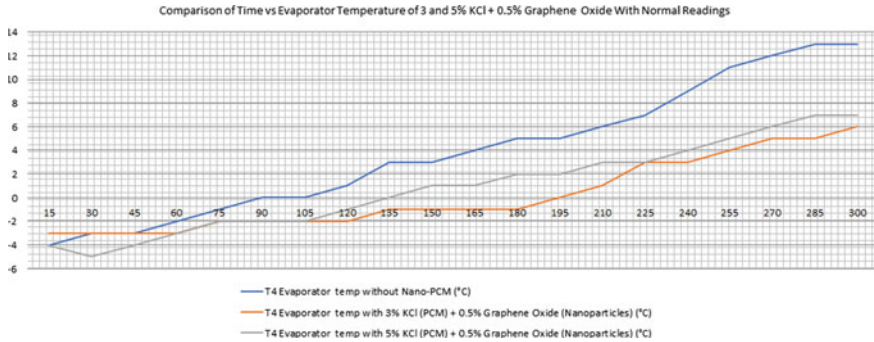


Fig. 6 Comparison of time with evaporator temperature of 3 and 5% KCl + 0.5% graphene oxide with absence of Nano-phase change material

constant for longer duration of time and after 300 min temperature of evaporator cabinet start rising.

By using KCl (3 and 5%) + graphene oxide (0.5%) combinations we can maintain evaporator temperature from 6 to 7 °C for 6 to 7 h span as shown in Fig. 6. By use of KCl + graphene oxide (Nano-PCM) will keep evaporator temperature constant for longer duration of time and after 300 min temperature of evaporator cabinet start rising.

4 Conclusions

Experimentation had been carried out to investigate the performance of a deep freezer using different combinations and mass fractions of Nano-PCM during power outages. The use of NaCl and KCl as phase change material mixed in graphene oxide nanoparticle imposes a great impact on reducing temperature fluctuation during a power outage as well as frequent opening and closing the door of the system. Using Nano-PCM materials it is possible to achieve a noticeable change in temperature which can be utilized for cooling effect. By using 3 and 5% NaCl + 0.5% graphene oxide (Nano-PCM) combinations, it has been possible to maintain evaporator cabinet temperature from 3 to 4 °C and 3 to 5 °C respectively for 6 to 7 h span. By using 3 and 5% KCl + 0.5% graphene oxide (Nano-PCM) combinations, it has been possible to maintain evaporator cabinet temperature from 5 to 6 °C and 6 to 7 °C respectively for 6 to 7 h span. After 300 min the temperature of the evaporator section starts rising. The power consumed with the advancement in setup is lesser than that of the conventional one. The maximum COP improvement is around 12% for a eutectic solution by using the water + KCl + graphene oxide combinations. It has been found that the addition of graphene oxide nanoparticles in phase change material results in an enhanced conduction heat transfer from the cooling cabinet of the deep freezer. From experimentation, it has been proven that the use of Nano-PCM on the evaporator side

maintained a constant temperature for a longer duration of time (6–7 h) after power failure. Still in future work focus will be given to selection on the optimum quantity of Nano-PCM for improving the overall performance of the refrigeration system.

References

1. Value Market Research report, <https://www.valuemarketresearch.com>
2. Liddiard R, Gowreesunker BL, Spataru C, Tomei J, Huebner G (2017) The Vulnerability of Refrigerated Food to unstable Power Supplies. *Energy Proced* 123:196–203
3. Saxena R, Dwivedi C, Dutta V, Kaushik SC, Rakshit D (2020) Nano-enhanced PCMs for low temperature thermal energy storage systems and passive conditioning applications. *Clean Technologies and Environmental Policy*
4. Khan MIH, Afroz HM (2014) Diminution of temperature fluctuation inside the cabin of a household refrigerator using phase change material. *Int J Rec Adv Mech Eng* 3:43–52
5. Oró E, De Gracia A, Castell A, Farid MM, Cabeza LF (2012) Review on Phase Change Materials (PCMs) for cold thermal energy storage applications. *Appl Ener* 99:513–533
6. Kaviarasu C, Prakash D (2016) Review on phase change materials with nanoparticle in engineering applications. *J Eng Sci Technol Rev* 9:26–36
7. Huang L, Piontek U (2017) Improving performance of cold-chain insulated container with phase change material: an experimental investigation. *Appl Sci* 7:1288
8. Negi S, Anand N (2016) Factors leruits and vegetables seading to losses and wastage in the supply chain of fctor in India. *Energy Infrast Transp Challe W Forw I*. 80–105
9. Singh S, Gaikwad KK, Lee M, Lee YS (2018) Temperature regulating materials for advanced food packaging applications: a review. *J Food Meas Charact* 12:588–601
10. Veerakumar C, Sreekumar A (2016) Phase change material based cold thermal energy storage: materials, techniques and applications—a review. *Int J Refrige* 67:271–289
11. Du K, Calautit J, Wang Z, Wu Y, Liu H (2018) A review of the applications of phase change materials in cooling, heating and power generation in different temperature ranges. *Appl Energy* 220:242–273
12. Sharma A, Tyagi VV, Chen CR, Buddhi D (2009) Review on thermal energy storage with phase change materials and applications. *Renew Sustain Energy Rev* 13:318–345
13. PCM Products. <https://www.pcmproducts.net>
14. Tan H, Li Y, Tuo H, Zhou M, Tian B (2010) Experimental Study on Liquid/Solid Phase Change for Cold Energy Storage of Liquefied Natural Gas (LNG) Refrigerated Vehicle. *Energy* 35:1927–1935

Impact of Electric Vehicles on Electricity Power Demand in India



Rahul Waghchaure and Pramod Kothmire

Abstract An electric vehicle is the future of transportation. An electric vehicle is exactly you can think of like a small electric toy car much more complicated system. It is propelled by an electric motor instead of petrol, diesel engine. In this paper various areas related to the electric vehicle are studied. The power generation scenario of India is studied to have an idea about the power generation sector and to know the available power and peak load that can be taken by the power generation sector. Then automobile sector trends have been studied. Installed capacity for manufacturing of internal combustion vehicles also production and sales of different types of vehicles like two-wheelers, 3 wheelers, passenger vehicles, and commercial vehicles have been studied. After that increase in sales of electric vehicles is studied. The government's vision to adopt electric vehicles by the year 2030 is 30% of total vehicles. Power requirement if 30% of the vehicle running are an electric vehicle by the year 2030 and % increase in power requirement of the total power generation.

Keywords Electric vehicles · India · Power demand · Automobile · Industry · EV · Transportation · Infrastructure · Charging stations

1 Introduction

Power plants generate the power that we use for day to day life and for the industrial purpose as electric power. The sources from which this power is extracted the renewable and nonrenewable sources. The battery is an important part of solar energy extraction also plays a major role in the electronics and electrical fields. The transportation sector is mainly dependent on the crude oils that are responsible for rising global earth temperature. Modifying fuel by adding additives or using more from renewable sources can largely reduce emissions. Internal combustion engines are used in vehicles for over 100 years. Inventions are going on for electrical vehicles as alternatives for combustion engines. The transition from a combustion engine vehicle

R. Waghchaure (✉) · P. Kothmire
MIT Academy of Engineering, Alandi, India
e-mail: waghchaure Rahul8@gmail.com

to a battery-powered electric vehicle is challenged by vehicle performance and its cost.

The first electrical vehicle is manufactured between the years 1832–1839. In 1900 first mass-produced electrical vehicle appeared in America. EVs use electrical energy and convert it into mechanical energy by using an electric motor or traction motors. EV uses batteries to store electrical energy. Due to battery charging and life issues, electric vehicles were taking market very slowly but nowadays a lot of research is going on batter recharge cycles, battery capacity, and battery life. India is aiming to have at least 15% of the vehicles on its roads to be electric in the coming five years. It will not take too much time to come in general use.

An electric vehicle is the future of transportation. The electric vehicle is exactly you can think of like a small electric toy car much more complicated system. It is propelled by an electric motor instead of petrol, diesel engine. There are a few types of EV technology, the most common are plug-in electric hybrid vehicles (PHEV), range extender electric vehicles (REEVs), and battery electric vehicles (BEVs). A battery pack is used to power the electric vehicle motor. The battery pack can be charged at home or at a charging station by plugging in the charger.

So before that proper charging infrastructure to be developed to cope up with the requirements of electric vehicles. So a major factor in using the electrical vehicle is recharging time and recharging stations. For recharging stations, a proper power management system should be developed. Because recharging of the electrical vehicles may increase the demand for peak load on power stations.

So in this paper, with a proper introduction to the problem, the impact on power demand due to electrical vehicles in India will be studied.

2 Literature Review

2.1 Modeling Energy and Power Requirements of Electric Vehicles

In this paper [1] author has studied the performance of the electric vehicle model. The performance study of the electric vehicle later used to calculate the power requirements of vehicles in different driving conditions. Basic vehicle parameters were used for developing the vehicle model and then it is studied with the simple model of the battery. For the same driving conditions, results of energy requirement and effective range obtained for the electric vehicle are compared with the internal combustion engine.

2.2 Technical Research Report: The Electric Vehicle

The author has begun the paper [2] with the history of the electric vehicle. Subsequent section technical description of the electric vehicle is given including all basic terms like parts of electric vehicle function of the part and theory of operation. Information about hybrid cars is also given in the next section of this report. Based on the working principles and parameters, the author has compared the internal combustion engine, the hybrid engine, and the electrical engine in terms of efficiency, speed, acceleration, maintenance, mileage, and cost. This paper states the merits and demerits of the electric vehicle comparing with internal combustion engine vehicles.

2.3 Review of Battery Charger Topologies, Charging Power Levels, and Infrastructure for Plug-In Electric and Hybrid Vehicles

This paper [3] reviews the current status and implementation of battery chargers, charging power levels, and infrastructure for plug-in electric vehicles and hybrid vehicles. There are two categories of charger systems off-board types and onboard types with unidirectional or bidirectional power flow. The availability of charging infrastructure reduces onboard energy storage requirements and costs. Battery performance depends on various factors like the design of the battery, cooling system, type of battery, and also it depends upon the charger characteristics and charging infrastructure.

3 Power Generation Scenario in India

The total power generation capacity of India is about 3,71,977 MW.

In India, there are 3 modes of power generation.

a. Thermal power plant

In thermal power plants, it is subcategorized on the basis of fuel used to fire boiler-coal, gas, and diesel. The installed capacity of the coal used power plant is 200704 MW, the gas used power plant is 24937 MW and diesel-powered power plant is 637 MW.

b. Nuclear power plant

The nuclear power generation capacity of India is 6.78 GW which is about 2% of the total installed power generation capacity.

c. Renewable Energ

Table 1 Total Installed Capacity (As on 31.07.2020)

Sector	MW	% of total
Central sector	94,027	25.3
State sector	1,03,652	27.9
Private sector	1,74,298	46.9
Total	3,71,977	

Source Central Electricity Authority

From renewable sources like hydro, solar, wind, biomass, geothermal, tidal, India has a power generation capacity of 69.05 GW from non-conventional renewable sources and 45.29 GW from conventional renewable sources.

Electricity providers can be divided into three categories like central sector, state sector, and private sector. Table 1 gives the power generation quantity of each sector and also the % of total power generation of each sector.

As an electric vehicle is going to take the market, the additional power requirement must be satisfied by all three sectors simultaneously as they serve in non-intersecting regions.

As there are different electricity providing sectors in India, there are also different regions defined geographically. Table 2 gives the information about region-wise energy requirement, installed capacity in the region also information about whether installed capacity meeting energy requirements. Also, there is information about peak load needed and available peak load and whether the required peak load meeting available peak load. The Eastern region has less available power than required. Also looking at power scenario based on peak load northern region is not meeting requirements.

4 Automobile Industry and Number of Vehicles in India

The automobile industry in India stands 4th largest in the world. It is expected to reach Rs 16.16–18.18 Trillion by 2026. According to the Department of Promotion of Industry and Internal Trade (DPIIT), the Indian automobile industry has received \$ 24.21 billion in Foreign Direct Investment from April 2000–March 2020. 26.36 million Vehicles were being manufactured in FY 2020 and also sales increase by 1.29% with 21.55 million vehicles were sold in FY2020. The Electric Vehicle market will be Rs 50,000 crore in India by 2025. The Indian government is encouraging to sell only electric vehicles. The electric vehicle is implemented in city public transport in 11 major cities of India. The Indian government has also declared an income tax deduction of 1.5 lakh on the loan taken for buying an electric vehicle. As a result, sales of an electric vehicles is increased by 20% in FY 2020 excluding e rickshaws. 156 lakh units of electric two-wheelers have been sold in FY20.

Table 2 Total Installed Capacity (As on 31.07.2020).

State/Region	Energy			Peak		
	Requirement	Availability	Surplus/Deficit	Demand	Availability	Surplus/Deficit
Northern	414,450	483,195	68,195	65,700	71,480	5780
Western	407,350	413,581	6231	57,083	58,529	1446
Southern	382,120	396,219	14,099	53,967	55,675	1708
Eastern	171,807	160,775	-11,032	25,897	27,863	1966
North-Eastern	19,176	21,522	2347	3264	3013	-250
All India	1,394,904	1,475,292	80,388	189,951	205,870	15,919

Source Central Electricity Authority

Table 3 Automobile production trends

Category	Production trends			Sales trends		
	2017–2018	2018–2019	2019–2020	2017–2018	2018–2019	2019–2020
Passenger Vehicles	4,020,267	4,028,471	3,434,013	3,288,581	3,377,389	2,773,575
Commercial Vehicles	895,448	1,112,405	752,022	856,916	1,007,311	717,688
Three Wheelers	1,022,181	1,268,833	1,133,858	635,698	701,005	636,569
Two Wheelers	23,154,838	24,499,777	21,036,294	20,200,117	21,179,847	17,417,616
Quadricycle	1713	5388	6095	0	627	942
Grand Total	29,094,447	30,914,874	26,362,874	24,981,312	26,266,179	21,546,390

In Table 3, the production trend for the last three years is given. In India total of 26,362,282 vehicles produced which includes the various categories of vehicles such as Passenger Vehicles, commercial vehicles, three-wheelers, two-wheelers, and quadricycles in 2019–2020 which were less than the previous year 2018–2019 by 14.73% [4]. In the table, in other section, it is given the sales trends of the vehicles for the same years. As we can see passenger vehicle sales decrease by 17.88% in 2019–2020 than the previous year, commercial vehicle sales decrease by 28.75%, sales of three-wheeler decreased by 9.19%, two-wheeler sale decreased by 17.76%. There can be too many reasons for decreasing the sale. Some of them can be unclear government policies, increasing IC engine vehicle prices due to environmental norms, or due to economic slowdown.

In the year 2019–2020 export from the automobile industry increases by 2.95%. Commercial and three-wheeler export went down by 39.25% and 11.54% respectively but two-wheeler and passenger vehicle export registered a growth of 7.30% and 0.17% respectively in the same year 2019–2020 [5].

5 Increasing Sales of Electric Vehicles in India

The electric vehicle industry is growing in India. Sales are less than 1% of total automobile sales but it can grow up to 5% in upcoming years. Presently there are 5 lakh electric two-wheelers and a few thousand electric cars running on Indian roads. Electric vehicle sales grew by 20% excluding e-Rickshaws in years 2019–20. Sales are directly affected by the fluctuation in the incentives given by the government in each state. Many manufacturing organizations like Hero, Ather, Electrotherm, Avon, Lohia, Ampere, etc. are trying to achieve the goal of increasing sales and to attract people towards electric vehicles under the Society of manufacturers of electric

vehicles (SMEV). The electric vehicles running on the roads are mostly (90%) low-speed electric vehicles [6, 7]. Low-speed vehicles have a speed range of 0–25 km/hr. so they don't need the permission and license. The industry is almost ready to hit the market and show its historical growth over some short period. This industry will play a very important role in controlling carbon footprints, reduce the import of crude oil, generating employment, and developing advanced technology.

6 Power Demand After Electric Vehicle Takes the Market

The Indian government has set a target for 30% adoption of electric vehicles by 2030. electric vehicle sales are expected to grow 36% annually from 2019 to 2026. Installation of charging infrastructure is projected to grow at 42.38% annually. Alongside the vehicle and charging infrastructure, the market of an electric vehicle batteries is expected to grow at a rate of 60.15% annually as the local battery manufacturer TATA chemicals and BHEL enter the market. Under the government scheme FAME II (Faster adoption and manufacture of electric vehicles) subsidy of Rs. 20,000 is given for the 1million two-wheelers powered by new advanced technology battery of 2KWHr.

The power requirement of the different types of an electric vehicle is given in Table 4.

Based on the travel demand survey in the NCT in 2008, the average Vehicle Kilometers Traveled (VKTs) in a year by two-wheelers is 2,942 km/yr, and that by cars are 2,893 km/yr. As per the data given by the Road and Transport ministry, there were 253 million vehicles in operation in India in 2017.

As there are 81% two-wheelers mean 204.93million two-wheelers, 3% three-wheelers mean 7.59 million, 13% passenger vehicles that mean 32.89 million. This data is up to the year 2017 [9]. Still, if we continue with calculations we can approximately predict the power demand required to switch from ICEV to EVs.

So the government is planning to take 30% of market by electric vehicle.

Total two wheelers in electric vehicles = $204.93 * 0.30 = 61.479$ million.

Total three wheelers in electric vehicles = $7.59 * 0.30 = 2.277$ million.

Total four wheelers in electric vehicles = $32.89 * 0.30 = 9.867$ million.

Table 4 Electrical consumption range of each vehicle [8]

Electrical Consumption(Wh/km)			
	Average city	Average Hwy	Range
Scooter	33	38	31–40
3 wheeler	61	85	53–97
Low power EV	84	133	70–192
High power EV	123	164	101–224

The number will be bigger than this at the end of 2030, but we are just taking the minimum to just understand the impact of electric vehicles. So the power requirement by this vehicle in a year will be.

Formula for power calculations will be

$$\text{Power} = \text{Number of Vehicles} * \text{Average travel Distance (km/yr)} * \text{Electrical Consumption (Wh/km)}$$

Consider average energy consumption between city and highway.

$$\begin{aligned} \text{Total Power required by two wheelers} &= 61.479 * 2942 * 35.5 \\ &= 6,420,928.24 \text{ million Wh} \end{aligned}$$

$$\begin{aligned} \text{Total Power required by three wheelers} &= 7.59 * 2893 * 73 \\ &= 1,602,924.51 \text{ million Wh} \end{aligned}$$

$$\begin{aligned} \text{Total Power required by four wheelers} &= 32.89 * 2893 * 124 \\ &= 11,798,695.48 \text{ million Wh} \end{aligned}$$

$$\begin{aligned} \text{Total power required as per data from 2017} &= 19,822,548.23 \text{ million Wh} \\ &= 19,822.54823 \text{ million kWh} \\ &= 19,822.548 \text{ million unit of power} \end{aligned}$$

From the table 3 data total number of vehicles sold in 2017–18, 2018–19, 2019–2020.

$$= 72,793,881 = 72.7938 \text{ millions.}$$

Considering the average, we can approximately predict number of vehicle in year 2030.

$$\begin{aligned} \text{Total number of vehicle in year 2030} &= 253 + 72.7938 + 24.264627 * 10 \\ &= 568.4398 \text{ million} \end{aligned}$$

Above power calculation was for 253 million vehicles.

So now predicting that data for 568.4398 million.

$$= 19,822.548 * 568.4398 / 253.$$

$$= 44,537.25384 \text{ million Units.}$$

This is 3% of the total power generation of India and vehicle adoption is only 30%. This calculation indicates very ideal condition, at the actual condition the requirement will be even more than this because we have excluded heavy vehicles, public transport buses which also will be electric vehicles and also we don't have assumed increase in vehicle sales over the period so the number of vehicles will be more than calculated.

7 Conclusion

The electric vehicle industry is a growing industry in India and it is the future of the automobile industry and transportation. As we know, electric vehicles have many advantages and benefits over the internal combustion engine and hybrid vehicles. As long as power distribution is concerned India doesn't have enough infrastructure. Advertisement of an electric vehicle, development of infrastructure, efficiency and smart chargers and improved charging technologies will have a very large impact on the success of the electric vehicle. In this paper, we have studied the power generation scenario in India. So as a large number of an electric vehicles will start to come on the road, necessary charging stations and power distribution infrastructure is needed and also EV power requirement can strain the local power grid system. Also, we have studied the automobile industry scenario in India. India is fourth-largest manufacturer of automobiles and necessary components. Investors have invested too much in internal combustion research and manufacturing so they can't abandon it right away, there must clear vision from the government to motivate investors and industrialists to do so. Then we have studied increasing EV sales and power demand. As we have seen power demand will rise by a minimum of 3%. But as it will be hit the road, it will be very hard to come up with. So there is too much investment needed in the infrastructure and power generation sector.

References

1. Blair PD (1978) Modelling energy and power requirements of an electric vehicle. *Energy Conversion* 18:127–134
2. Argueta R (2010) A Technical Research Report: The Electric Vehicle
3. NYilmaz M, Krein PT (2013) Review of battery charger topologies, charging power levels, and infrastructure for plug-in electric and hybrid vehicles. *IEEE Trans Power Electron* 28(5). Member, IEEE
4. Park W-J, Song K-B, Park J-W (2013) Impact of electric vehicle penetration-based charging demand on load profile. *J Electr Eng Technol* 8(2):244–251
5. Tiewsoh LS, Jirásek J, Sivek M (2019) Electricity Generation in India: Present State, Future Outlook, and Policy Implications. *Energies MDPI*.
6. Load Generation Balance Report 2019–20- Central Electricity Authority: <https://www.cea.nic.in/reports/annual/lgbr/lgbr-2019.pdf>
7. Ministry of Power: <https://powermin.nic.in/en/content/power-sector-glance-all-india>
8. Saxena S, Gopal A, Phadke A (2014) Electrical consumption of two-, three- and four-wheel light-duty electric vehicles in India. *Appl Energy*
9. Indian Brand equity foundation: <https://www.ibef.org/industry/automobiles-presentation>

Computational Fluid Dynamics Simulation for the Prevention of Evapotranspiration from Agricultural Land Using Semi-Permeable Membrane



Dhruv Singh and S. J. Pawar

Abstract Water is the absolute necessity of every living being on the earth and in the current context, saying that it is a scarce resource will not be a far-fetched statement. The problem of evaporation of water from open agricultural fields is taken into consideration in this work. A simulation of evaporation in an open field and when a semi-permeable membrane is used to cover the field is performed in an open-source simulation software named OpenFOAM. The simulation is performed for total evapotranspiration considering a mean temperature for the month of May at Prayagraj, India. It is seen from the result that the semi-permeable membrane has intensely decreases the evapotranspiration rate from the surface of the agricultural land even in the hottest month. The amount of water that was prevented from evaporating ranged from 75–84% at a different time of a day/month/year. Thus, semipermeable membrane is found to reduce evapotranspiration rate and also regulates the temperature.

Keywords Ecology · Evaporation · Evapotranspiration · Semi-permeable membrane · Thermodynamics

1 Introduction

As per the estimate, about 45% of the Indian working population is employed in the Agricultural Sector, making it the primary occupation in India. This estimate inevitably means that India's economic and environmental well-being depends heavily on its water management. There is a well-defined water conservation program with various community members interested in water conservation, including residential water consumers, commercial water consumers, industrial water consumers, recreational water users, agricultural users, etc. All these members have specific requirements and constraints. Developing a water system profile is crucial in taking inventory of the existing resources and conditions, which helps systems assess their

D. Singh (✉) · S. J. Pawar
Motilal Nehru National Institute of Technology Allahabad, Prayagraj 211004, India
e-mail: iamdhruv283@gmail.com

present circumstances and design strategies to meet emerging needs [1]. There are plans for numerous water conservation underway, including constructions of the canal, irrigation channels, dams construction, etc. Still, not much work is done to prevent the evaporation of water from the land's surface. This problem is of significant importance, especially in India's arid regions and for crops like paddy, which requires standing water in the field to grow and thrive. The strategy to tackle this problem and keeping in mind the ecological balance at the same time is necessary.

The work focuses on water conservation in the agricultural sector. Different types of evaporation which affect the total rate of evaporation were identified as (a) Soil Evaporation—(i) Bare soil and (ii) Soil under a canopy and (b) Evaporation via wet foliage [2]. Bare soil evaporation is the major contributor to the annual evaporation. It is of immense importance in precipitation and pre-irrigations when a crop is still not grown properly. It may extend more than the 5–10 cm limit, which is traditionally considered in many irrigation scheduling and simulation models. Wet-foliage evaporation ranges from small percentages to more than 50% of the irrigation water used. The effect is most prominent in short irrigation cycles, which frequently occurs in a short time-span, especially in hot and dry regions. Three components (Interception, Evaporation, Transpiration) regarding the total evapotranspiration are to be taken into consideration to achieve optimum results [3]. Interception loss is that a portion of the precipitation returned to the atmosphere through evaporation from the plant surfaces. Evaporation from the soil surface, as well as the rate of transpiration, are taken into consideration. In 1948, Penman combined the mass transfer method and energy balance to derive an equation from computing the evaporation from an open water surface from standard climatological records of sunshine, temperature, humidity, and wind speed [4].

Many countries, like the United States, Israel, Japan, and Russia, have been working on the topic of evaporation prevention for a long time [5, 6]. A recent study for using plastic sheet mulch to prevent evapotranspiration and soil erosion shows that the evapotranspiration shall prevent 50–55% of the water evaporation from the field [7, 8]. The major problem was the degradation of crops due to the lack of proper air-flow and perspiration in the soil. Also, the plastic being non-biodegradable can cause environmental damage and maybe an ineffective in hot and arid regions because it was observed that it melts if exposed to direct sunlight for a long time.

A semi-permeable membrane is a biological or synthetic membrane that is polymeric. It allows specific molecules or ions to pass through it by means of diffusion while preventing others or, in exceptional cases, by more specialized processes such as passive or active transport and facilitated diffusion. In more straightforward terms, it works as a very fine sieve and holds promise to prevent evapotranspiration and maintain a proper balance of air and humidity for proper plant growth without causing any damage to the crop. Many notable works have been done in semi-permeable membranes, a study of the osmosis process through the membranes [9], use of a membrane in desalination [10]. Some latest works involve high power densities in Pressure-Retarded Osmosis in non-ideal semi-permeable supported membranes [11].

The current research focuses on increasing the certainty of assessing the rate of evapotranspiration from an agricultural field and simulating the effect of using a

semi-permeable membrane to reduce this evapotranspiration in conserving water. It presents a simulation of evapotranspiration from an agricultural plot with and without semi-permeable membranes using OpenFOAM. For computational fluid dynamics-based simulation of total evapotranspiration, climatic conditions of the month of May at Prayagraj, UP, India are taken as a standard case, which have been obtained from the Meteorological Department. Penman–Monteith equation is modelled for the simulation of total evapotranspiration in this work. The results are then compared, and detailed conclusions are made considering various factors of importance.

2 Methodology

The methodology adopted in this work involves mathematical modeling of the evapotranspiration and its simulation in OpenFOAM.

2.1 Mathematical Modeling

After accessing different literature sources, Total Evapotranspiration is found out to be dependent on interception, evaporation, and transpiration losses. The equation for the total transpiration is

$$T_{ETR} = IL + EL + TL \quad (1)$$

where, T_{ETR} is the total evapotranspiration, IL is the interception loss, EL is the evaporation loss, and TL is the transpiration loss.

Penman–Monteith equation [4] is incorporated into the code for simulation in the OpenFOAM file of governing equations. The equation considers various factors to accommodate the variables in computing the total evapotranspiration from an open field. It requires daily mean temperature, wind speed, relative humidity, and solar radiation as the inputs in terms of energy flux rate (Eq. 2(a)) and volume flux rate (Eq. 2(b)).

$$\lambda_v E = \frac{\Delta(R_n - G) + \rho_a c_p (\delta_e) g_a}{\Delta + \gamma(1 + g_a/g_s)} \quad (2a)$$

$$ET_0 = \frac{\Delta(R_n - G) + \rho_a c_p (\delta_e) g_a}{(\Delta + \gamma(1 + g_a/g_s))L_v} \quad (2b)$$

where, λ_v is the latent heat of vaporization in Jg^{-1} , E is the mass water evapotranspiration rate in $\text{gs}^{-1} \text{m}^{-2}$, Δ is the rate of change of saturation specific humidity with air temperature in PaK^{-1} , R_n is the net irradiance, the external source of energy

Table 1 Values of properties used in simulation [14]

S. No	Properties	Value
1	Daily mean temperature (T_m)	35.7 °C
2	Wind Speed (v_a)	8.87 kmph
3	Relative Humidity	0.80
4	Solar irradiation (R_n)	70 kWh/m ²
	Ground heat flux (G)	474.32 W/m ²
6	Dry air density (ρ_a)	1.225 kg/m ³
7	Specific heat capacity of air (c_p)	1.00 kJ/kg
8	Psychrometric Constant (γ)	0.4 (g _{water} /kg _{air})K ⁻¹
9	Latent heat of vaporization (λ_v)	2,260 kJ/kg
10	Specific Humidity (δ_e)	0.016

flux in Wm⁻², G is the ground heat flux, usually difficult to measure Wm⁻², ρ_a is the dry air density in kgm⁻³, c_p is the specific heat capacity of air in Jkg⁻¹ K⁻¹, δ_e is the vapor pressure deficit or specific humidity in Pa, g_a is the conductivity of air, atmospheric conductance in ms⁻¹, γ is the psychrometric constant in K⁻¹, g_s is the conductivity of stoma, surface conductance in ms⁻¹, ET_0 is the water volume evapotranspired in mms⁻¹, and L_v is the volumetric latent heat of vaporization in MJm⁻³.

The physical measurement of evapotranspiration (T_{ETR}), evaporation (E), and transpiration (T) requires numerous complex, expensive instruments, complicated data interpretation techniques and costs a fair amount of computational power. Using the energy balance equation is a convenient method [12].

$$LE + H = R_n^s - G \quad (3)$$

where, LE is the latent heat flux in, H is the sensible heat flux in, and R_n^s is the net irradiation.

The computational fluid dynamics-based simulation is carried out in this work. The analysis is performed considering an open agricultural field, and the climatic values are taken analogous to Prayagraj, Uttar Pradesh, India, for the month of May. The standard values for the computation and simulation are taken from the Meteorological Department [13], as given in Table 1.

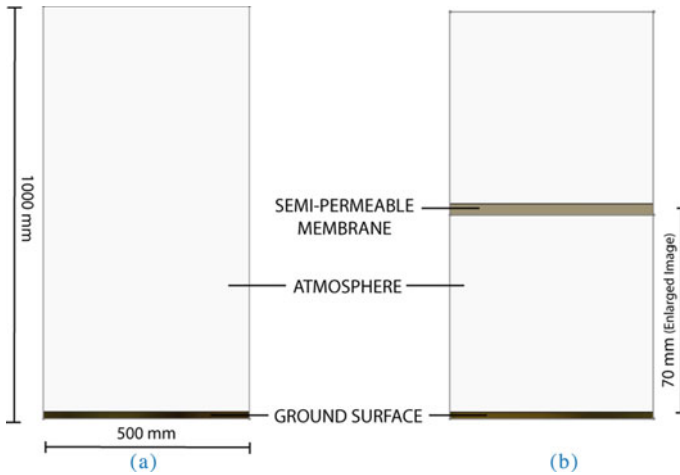


Fig. 1 Simulation domain of open field. **a** Without any covering and **b** With semi-permeable membrane

2.2 Model Description

The simulation domain is $0.5 \times 1.0 \text{ m}^2$ space. The lowest layer of the simulation domain is the topsoil cover of the agricultural farm, and the topmost layer represents the atmosphere, which is assumed at a distance of 1 m from the bottom. The properties of the material space are altered, and a multi-physics problem is computationally solved with OpenFOAM. The results are viewed in paraView. Figure 1a gives a pictorial presentation of the evapotranspiration model from an open-field with no covering. Figure 1b presents the model with the semi-permeable (at 70 mm from the bottom) membrane cover over the field.

3 Results and Discussion

The real-time simulation of land covered with a semi-permeable membrane versus the bare land is given in Figs. 2 and 3. The total evapotranspiration report is generated considering a mean temperature for the month of May at Prayagraj, India. It is evidently visible from the figures that the semi-permeable membrane dramatically reduces the evapotranspiration rate from the surface of the agricultural land even in the hottest month at Prayagraj. The temperature range is regulated across the day for more realistic results. The evapotranspiration rate is found to strongly depends on the time during day, mainly due to temperature variations. The values of E are taken at an interval of 2 h for a full day, keeping the mass water evapotranspiration rate (E) as the decisive quantity. The tabular data is obtained from the simulation results. It is found that E without any covering (Table 2) is lowest at 12 mid-night and increases slowly

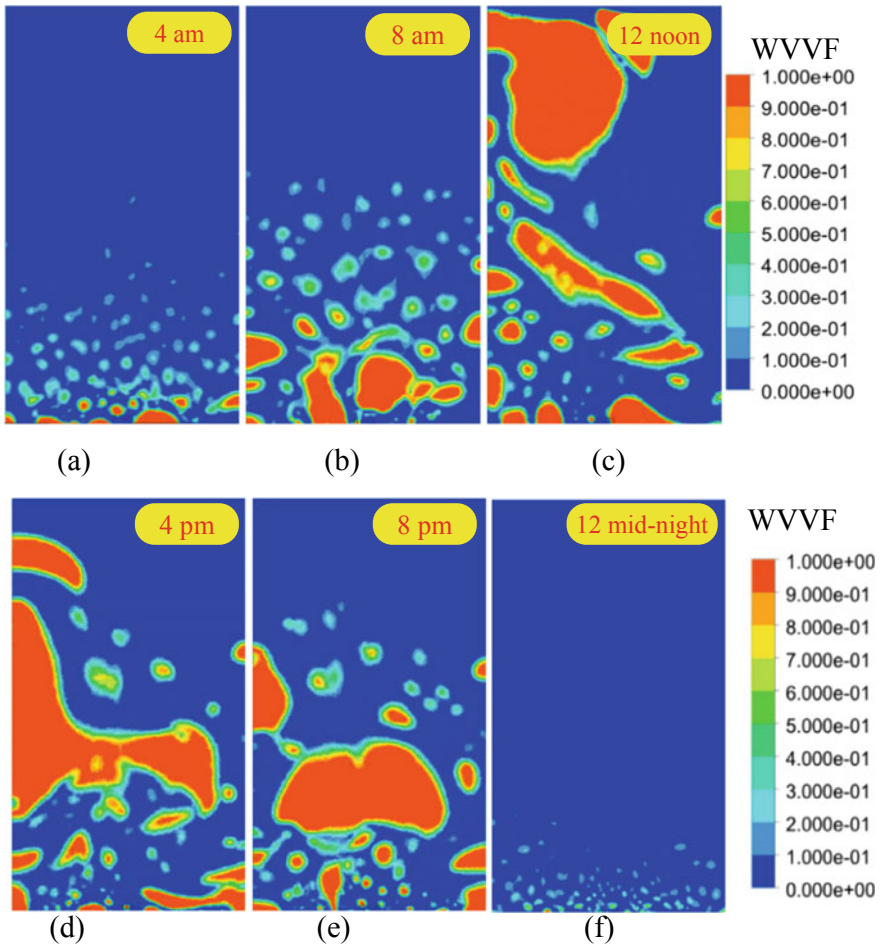


Fig. 2 Simulation results of uncovered land at **a** 4 am, **b** 8 am, **c** 12 noon, **d** 4 pm, **e** 8 pm, and **f** 12 mid-night. (WVVF—Water Vapour Volume Fraction)

till 6 am. It further rises at increasing rate till 10 am with sunrise. However, with more sun rays the same shows more increase till 10 am. The E rises sharply at 12 noon and remains high till 4 pm (highest). The maximum reduction in evapotranspiration rate is found between 4 and 6 pm. Similarly, it is observed from the simulation that E with semi-permeable covering (Table 2) is lowest at 12 mid-night and increases slowly till 6 am and it then shows steady upswings till 10 am. A sharp rise in the evapotranspiration rate is found from 10 am to 12 noon. Between 12 noon to 4 pm the magnitude of the E remains highest. The sharp drop in E is seen between 4 to 6 pm. Asymmetric nature of the variation between E (with and without covering) and time during day is found from the simulation. When, E values with covering and without covering are compared, it is found that there is appreciable reduction in

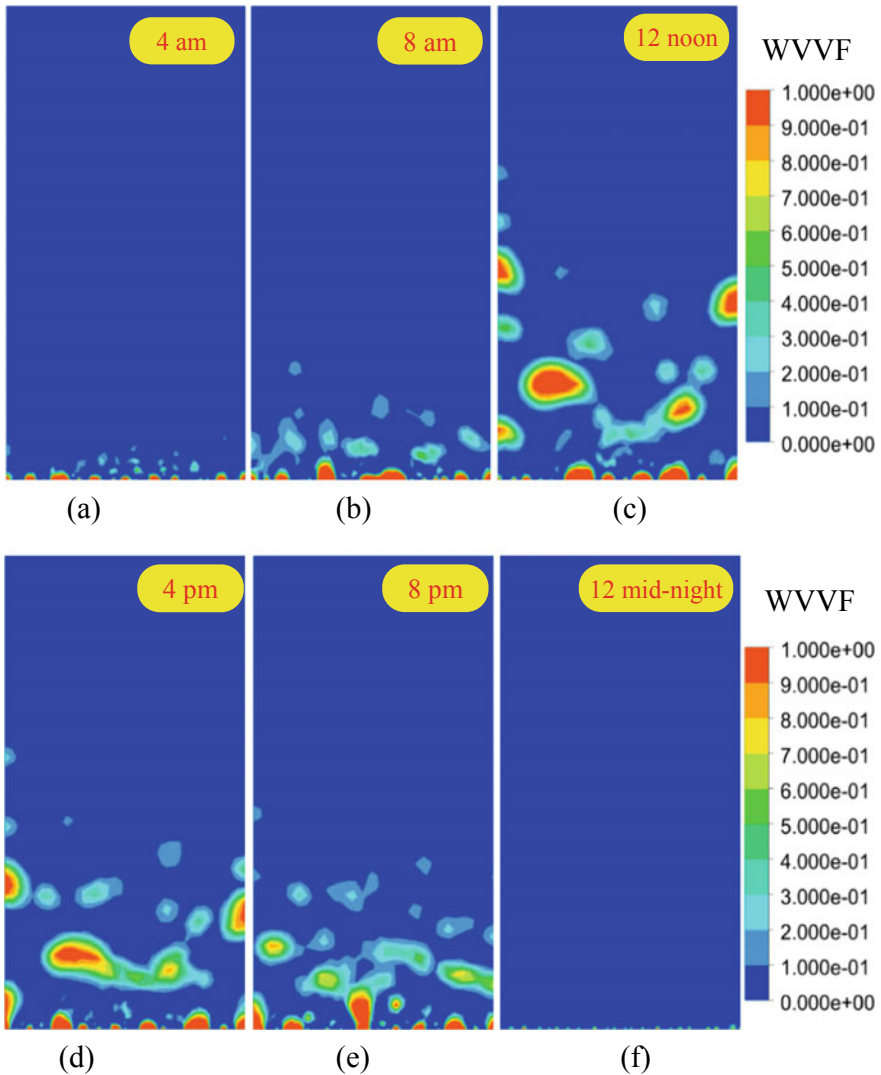


Fig. 3 Simulation results of semi-permeable membrane covered land at **a** 4 am, **b** 8 am, **c** 12 noon, **d** 4 pm, **e** 8 pm, and **f** 12 mid-night. (WVVF—Water Vapour Volume Fraction)

the evapotranspiration rate throughout the day time. The maximum reduction in E is found at 12 mid-night and minimum reduction is found at 4 pm. The computational results show that the rate of evapotranspiration is reduced by 77.36% in the time range of 12 noon to 2 pm in the month of May. The average lies at 80.79% across the year, and the range is 74.91–83.93%. The temperature distribution inside the semi-permeable membrane typically necessitates the need to include the heat loss from the soil at the time of sunset. This results in the variation of the trend, that is,

Table 2 Simulation Results for E with and without covering and percentage reduction

S. No	Time during day	$E_{\text{Without any covering}} \text{ (gs}^{-1} \text{ m}^{-2}\text{)}$	$E_{\text{With Semi-permeable membrane}} \text{ (gs}^{-1} \text{ m}^{-2}\text{)}$	% $E_{\text{Reduction}}$
1	12 mid-night	5.321	0.855	83.93
2	2 am	7.516	0.1242	83.47
3	4 am	10.278	1.861	81.91
4	6 am	13.823	2.399	82.64
5	8 am	19.245	4.018	79.12
6	10 am	25.964	5.538	78.67
7	12 noon	43.217	10.225	76.34
8	2 pm	49.634	10.731	78.38
9	4 pm	51.975	13.040	74.91
10	6 pm	23.671	4.978	78.97
11	8 pm	11.874	2.479	79.12
12	10 pm	9.678	1.873	80.64

the slope of evapotranspiration increases at a higher rate in the case of the semi-permeable membrane in contrast to uncovered land from 4 to 6 pm [9]. During the hottest hours of the day, the rate of condensation in the semi-permeable membrane becomes significant and this directly affects the rate of evapotranspiration due to the increased pressure difference.

The Indian subcontinent typically hosts two sub-types of tropical climate - monsoon and wet-dry. The values which are taken from the meteorological department inculcate this climate trend and hence, the simulation gives a realistic picture of the actual evapotranspiration in the country to a reasonable degree. The semi-permeable membrane is also found to regulate the temperature between the land surface and the membrane. It maintains a uniformly distributed temperature profile, which provides better growth conditions for the crops. Table 2 gives a detailed comparison of the hour-wise rate of evapotranspiration with and without the semi-permeable cover over the farming land. Moreover, the reduction in the evapotranspiration due to semi-permeable membrane can reduce the water requirement of the crop appreciably, thus water can be conserved effectively. This study could possibly help in better water management for the crop considering the local Meteorological data, water requirement for the crop, water availability, further this study could also help for better crop management across the region. The cost analysis has not been carried out in this work, however, the result shows that, the cost analysis may yield fruitful results. As in the market, biodegradable semi-permeable membranes are available and the life of similar membranes are sufficiently long, the issues of cost and sustainability could be better without any burden of disposal of used semi-permeable membrane.

4 Conclusion

The results clearly indicate that using a semi-permeable membrane as a cover over the agricultural land reduces the evapotranspiration rate drastically and, hence, conserves water that otherwise would have evaporated in an open field. The temperature profile regulation between the membrane and soil surface proves to be a medium of accelerated growth for the crops. The membrane allows even distribution of fertilizers and pesticides and does not hinder any natural process. It is also environmentally favorable due to its sufficiently long life and production of numerous biodegradable semi-permeable membranes. It is advisable to make it a removable arrangement so that the membrane could be removed at times of tilling or ploughing. The above study holds promise for use in large scale and small scale farming and can be easily inculcated in the traditional agricultural practices. Better water and crop management could be achieved with the use of semi-permeable membrane without any burden of used membrane disposal.

References

1. U.S. Environmental Protection Agency Water Conservation Plan Guidelines. In: Part 3 Basic Guideline for Preparing Water Conservation Plans
2. Evaporation from Irrigated Agricultural Land in California, ITRC Report R 02–001 (2002)
3. Merta M, Seidler C, Fjodorowa T (2006) Estimation of evaporation components. *Agricul Crop Biol* 61:S280–S283
4. Allen RG (2005) Penman-Monteith Equation. *Encyc Soil, Environ*
5. Frenkiel J (1965) Evaporation reduction—physical and chemical principles and review of experiments. *Unit Natl Edu Sci Cult Organiz* 50–80
6. Nguyen TBT, Nguyen THN, Pham QT (2020) Water loss due to evaporation from open reservoirs under weather conditions in Vietnam. *Asia-Pacific J Chem Eng* 15:42–52
7. Wang Z, Gao Y (2013) Effect of plastic sheet mulch, wheat straw mulch, and maize growth on water loss by evaporation in dryland areas of China. *Agricul Water Manage* 39–49
8. Majmundar B, Patel JN (2016) Different methods for evaluating evaporation losses from the open water surface in semi-arid area of Gujarat, India
9. Xu S, Eisenberg B, Song Z, Huang H (2018) Osmosis through a semi-permeable membrane: a consistent approach to interactions
10. Woo YC, Kim HS, Shon HO, Tijing LD (2019) Introduction: membrane desalination today, past, and future. *Curr Tren Futu Develop Bio-Membranes* 1–45
11. Yaroshchuk A (2017) “Breakthrough” osmosis and unusually high power densities in pressure-retarded osmosis in non- ideally semi-permeable supported membranes. *Sci Rep* 7:45168
12. Meng W, Sun X, Ma X, Guo X, Zheng L (2019) Evaporation and soil surface resistance of the water storage pit irrigation Trees in the loess plateau. *Water* 11:648
13. India Meteorological Department. <https://mausam.imd.gov.in>
14. Centre for Environment and Energy Development (CEED): Uttar Pradesh: Uncovering Solar Rooftop Potential in Urban Cities

Influence of Thermal Radiation on Natural Convection in a Square Enclosure



Shantanu Dutta and Sukumar Pati

Abstract Numerical investigations are carried out to analyze the pre-emergence of after-effects characterized by thermal radiation coupled with natural convection in a two-dimensional square enclosure. The square enclosure has an adiabatic top and bottom wall with side walls being administered at consistent temperature with different values. The mathematical equations of this present research have been solved by applying a finite element strategy. A broad in content parametric research investigation is executed to assess the confrontation of Rayleigh number (Ra) along with radiation criterion (R_d) on the fluid-transport eventuation. The numerical simulations demonstrate that Nusselt number (Nu) is an augmenting function of Ra and R_d . Consequential changes in streamlines along with isothermal contours for high Ra are realized. The present numerical investigations are applicable to solar collecting design devices, fire modelling in compartment, etc.

Keywords Free convection · Square cavity · Radiation heat transfer

1 Introduction

Natural convection continues to be accounted for in several heat transfer investigation and has substantial utilization in desiccant and dehumidification technologies [1], photo electronic PCB constituents [2], lead-chemical acid-batteries [3], thermo-repository configuration [4], etc. because of its simplicity and cost aspects. The concerted natural convection in presence of radiation has an important applications in solar collectors, electronic device cooling systems, modern energy-saving buildings and fire and plume assemblies, to name a few. The demand for appropriate design and optimization of these aforesaid important implorations has generated

S. Dutta (✉)

Department of Mechanical Engineering, PS: Ghola, Elitte College of Engineering PO: Karnamadhapur, Sodepur, Kolkata 700113, India

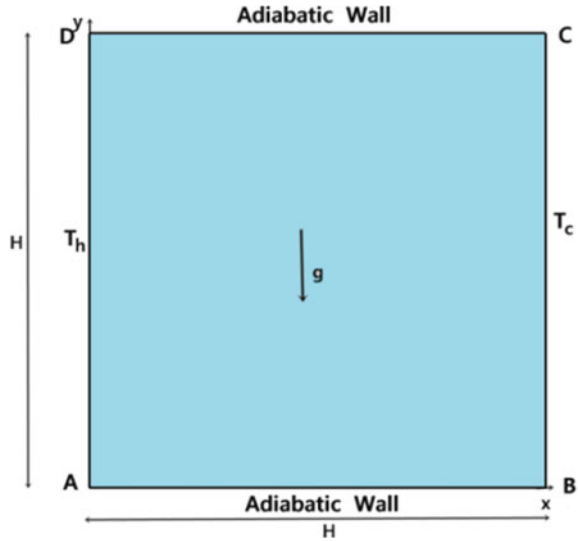
S. Pati

Department of Mechanical Engineering, National Institute of Technology Silchar, Silchar 788010, India

the progress of advanced numerical approaches which have led to the modification, development and blending of the radiation transport equations. Further, under different circumstances, numerical investigations due to amalgamation of radiation heat transportation with conduction and or convection are also of prime importance being the result of the fact that the aftermath of the heat transfer achieved by radiation is of paramount importance in the existence of a presence of medium. This medium could be participative in nature and further it was also found out that heat transfer can be enhanced noticeably with the active wall emissivity in enclosure study as well [5]. Bouali et al. [6] investigated natural convection fluid thermal heat transportation in a rectangular cavity with an inclination in existence of radiation. Bahlaoui et al. [7] performed a numerical analysis on natural convection confederate with surface thermal radiation presence in an enclosure with an inclination in presence of discrete heaters and communicated that the radiation subdues the natural convection predominance although it augments the overall heat transfer appearing inside the cavity as well.

In the last few decades, several researchers have performed experimental as well as numerical simulations pertaining to natural convection heat transfer in uniform square geometries by taking into account isothermal contours, streamlines and Nusselt number (Nu). These numerical investigations have customarily taken into consideration two situations, namely, bottom wall heated enclosures and differentially heated enclosures. Several numerical investigations can be found in literature pertaining to convection heat transport in enclosures for different geometric configurations and boundary conditions [8–11]. Lari et al. [12] scrutinized natural convection in association with radiation heat transfer inside a square enclosure considering ambient conditions. They carried out their investigation for a wide-ranging value of Ra and optical thickness (Radiative heat transfer under diffusive condition) in their research article. Balaji and Venkateshan [13] had performed numerical investigations in reference to natural convection considering square enclosure. The authors had solved the paper utilizing Gosman's FVM (finite-volume). The radiation model was based on distinctive emissivities considering vertical walls and simultaneously it considers the top and bottom walls as well. The authors investigated for surface radiation and heat transportation attribute of the enclosure. Their calculations demonstrated that there is a lot of the emphasis, that can be attributed to surface radiation associated with small emissivities and temperature levels and the authors have also provided an interpretation of the inconsistencies between the theoretical as well as experimental interrelationships. Sharma et al. [14] analysed conjugate natural convection and additionally accounted for surface radiation (radiosity–irradiation formulation) in a rectangular enclosure subjected to bottom heating while the other walls were maintained at cold temperature. A comprehensive investigation of the domination of the wall emissivity and the external heat transfer coefficient was also accounted for, by them. Ridouane et al. [15] investigated the actualization of thermal radiation on account of natural convection in a heated enclosure and demonstrated that the presence of radiation strongly affected the rate of heat evolution from the horizontal wall of enclosure. Saravanan and Raja [16] investigated natural convection inclusive of radiation inside a square enclosure by accounting for heating the enclosure by dual

Fig. 1 Schematic of the enclosure



discrete heaters. In the results, the authors indicated that the two different discrete heating arrangement resulted in two distinguishing exhibition of radiative fluxes at the insulated walls at the lesser Ra whereas for larger Ra , the thermal radiation resulted in two contrasting effect at the top and bottom adiabatic wall of enclosure. In recent times, Dutta et al. [17] had executed a numerical analysis to investigate two-dimensional natural convection inside a porous quadrantal enclosure. Dutta et al. [18] had carried out a numerical investigation in a rhombic cavity considering Cu-water nanofluid and magnetic field in the horizontal direction.

To the authors' knowledge, not much attention has been given to square enclosure subjected to thermal radiation considering differential heating to be the heating strategy, which is the motivation of this research article. The present numerical investigation intents to explore the conception approach of convection heat transfer inside a square enclosure in the subsistence of thermal radiation. The fluid flow, temperature fields, local and average Nusselt number along with the velocity plots, were obtained by solving the mathematical equations by COMSOL, finite element analysis software.

2 Geometry Interpretation with Mathematical Formulation

2.1 Specification of the Problem

We consider the square geometric as per the schematic 2D model which is depicted in Fig. 1. The regimentation region examined numerically comprehends two dimensional laminar incompressible, steady buoyancy induced fluid flow inside the square enclosure as depicted. The operative fluid being considered inside the enclosure is air (Prandtl number (Pr) = 0.71). The left wall is administered an uniform high temperature of T_h while the right wall is enforced to a lower temperature T_c . The parallel bottom and top walls are in adiabatic condition while the no slip condition on all enclosure walls is also enforced.

2.2 Governing Equations

The Boussinesq approximation (linear model) is contemplated and categorically it means that density alteration of the fluid flow (air) is only mathematically accounted for by administering the buoyancy force term. Viscous dissipation effects are also disregarded in this study.

Further, the radiation heat flux is taken into account by Rosseland diffusion approximation approach [19]:

$$q(x,y) = q(q_{rx}, q_{ry}) \tag{1}$$

$$q_{rx} = -\frac{4\sigma}{3\beta} \frac{\partial T^4}{\partial x} \quad q_{ry} = -\frac{4\sigma}{3\beta} \frac{\partial T^4}{\partial y} \tag{2}$$

Applying the Taylor series, we carry out expansion of T^4 considering the terms for the lesser right wall cold temperature T_c and further excluding the higher order terms in the equation, we arrive at:

$$T^4 \approx 4TT_c^3 - 3T_c^4 \tag{3}$$

Now utilizing the above equation and with the bolstering of the radiation heat flux factors in the expressions the equations are reduced to:

$$q_{rx} = -\frac{16\sigma T_c^3}{3\beta} \frac{\partial T}{\partial x}, \quad q_{ry} = -\frac{16\sigma T_c^3}{3\beta} \frac{\partial T}{\partial y} \tag{4}$$

The appropriate dimensionless mass, momentum along with the energy equations can now be demonstrated into attaining the conformation arrangement [20]:

$$\nabla \cdot v = 0 \quad (5)$$

$$\text{Pr} \cdot \nabla^2 v = -\nabla p + (v \cdot \nabla)v - Ra \text{Pr} \theta + v_\tau \quad (6)$$

$$\frac{\partial \theta}{\partial \tau} + v \cdot (\nabla \theta) = \left(1 + \frac{4R_d}{3}\right) \nabla^2 \theta \quad (7)$$

To further simplify the above governing equations, it is prudent to familiarize to the ensuing important dimensionless criterions:

$$\tau = \frac{tu_0}{L}, X = \frac{x}{L}, Y = \frac{y}{L}, U_x = \frac{u}{u_0}, U_y = \frac{v}{v_0}, \theta = \frac{T - T_c}{T_h - T_c}, P = \frac{p_0}{u_0^2 \rho_f}, R_d = \frac{4\sigma T_c^3}{k\beta}, \quad (8)$$

Here τ accounts for non-dimensional time, X and Y refers to the non-dimensional cartesian coordinate system, U_x and U_y refers to non-dimensional velocity components, θ refer to non-dimensional temperature, P refer to non-dimensional pressure while the T_h along with T_c refers to temperature pertaining to the vertical wall of square enclosure.

While considering Eq. (6), Ra , R_d and Pr refer to Rayleigh number, Radiation parameter and Prandtl number respectively and are delineated, as follows:

$$Ra = \frac{g\beta(T_h - T_c)L^3 \text{Pr}}{\nu_f^2}, \text{Pr} = \frac{\nu_f}{\alpha_f}, R_d = \frac{4\sigma T_c^3}{k\beta} \quad (9)$$

The appropriate boundary conditions for this present numerical investigation are described which follow:

$\theta = 0$ on the right hand wall of the enclosure (side BC).

$\theta = 1$ on the left hand wall of the enclosure (side AD).

$\frac{\partial \theta}{\partial n} = 0$ on the top and bottom horizontal walls (along side AB and CD).

2.3 Nusselt Number

Nusselt number is expressed in terms of local along with average heat transfer rate and they are determined respectively and as follow:

$$Nu = -\left[1 + \frac{4R_d}{3} \left(\frac{\partial \theta}{\partial X}\right)_{x=0}\right] \quad (10)$$

$$\text{Average Nusselt number } Nu = -\int_0^1 \left(\frac{\partial \theta}{\partial X}\right) dY \quad (11)$$

2.4 Grid Independency

It is also important to indicate that comprehensive grid sensitivity numerical experiments have been carried out in square enclosure adopting a non uniform temperature on the left and right wall following [21], to ensure that the results do not depend on the number of elements used. The detailed grid independency test can be found out in Table 1.

The values of \overline{Nu} on the non-uniformly heated left wall for different grid systems for water ($Pr = 7$) and for $Ra = 10^5$ are presented in Table 1. We use 17,650 elements for the present numerical simulations of this paper, because of the logical reasoning that when there is augmentation in the number of finite elements from 17,650 to 24,876 the maximum relative difference is less than 2%.

3 Numerical Strategy and Validation

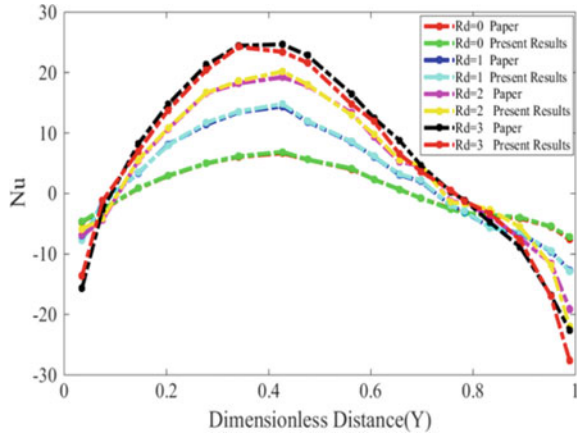
The mathematical governing equations in-consistent with the boundary conditions have been interpreted by implementing a finite element based COMSOL Multi-physics, version 5.5 [22].The Galerkin weighted residual approach is utilized to remodel the governing mathematical equations into a constitution of integral mathematical equations. The validation of this paper is performed by comparing local Nusselt number with the published results [21].

The local Nusselt number depicted along left wall for $\theta = \sin(\pi Y)$, $Ra = 10^5$, $\alpha = 0$ (no rotation), φ (volume fraction) = 0.04, $\tau = 200$ s and for distinctive value of radiation parameters(R_d) from [21] are presented as can be referred in Fig. 2. It can be clearly observed from the results, that the present computational code acquiesces very well with the published literature, demonstrating the accuracy of the present code for the present simulation.

Table 1 Comparison of \overline{Nu} on left heated wall for various grid systems with $Ra = 10^5, \tau = 200$ for the present enclosure design and BCs adopted from Sheremet et al. [21]

R_d	\overline{Nu}			Relative difference % (max-min)/max
	No. of elements			
	6922	17,650	24,876	
0	3.0693	3.069	3.067	0.07
1	5.386	5.284	5.285	1.8
2	7.190	7.110	7.098	0.012
3	8.989	8.979	8.896	1.03

Fig. 2 Validation of Nu for various radiation parameter with [21] considering the left heated wall for $Ra = 10^5$, $\alpha = 0$ (no rotation), $\phi = 0.04$, $\tau = 200$ s



4 Results and Discussion

The investigation of thermal transport for natural convection within a square enclosure considering radiation for a side length of 15 cm is presented now. The effects of natural convection heat transfer is demonstrated through Ra and the range being chosen as: ($Ra = 10^4 - 10^6$) and thermal radiation criterion ($R_d = 0-2$) taking into account $Pr = 0.71$. The accomplished results are illustrated in the concoction of streamlines (ψ), isothermal contours (θ), and as well as local and average Nusselt number.

4.1 Streamlines and Isotherms

Figure 3 delineates the fluid-flow pattern (streamlines), isothermal contours for $R_d = 1, 2$ and $Ra = 10^5$. The dominion of significance considered is for uniform heating of the left heated wall of the square geometry under analysis, where the temperature distributions along the right wall (cooled) are also kept uniform.

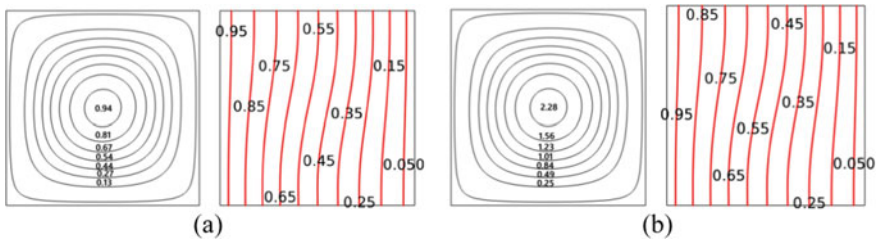


Fig. 3 Streamlines (ψ), Isotherms (θ) for $Ra = 10^5$, $Pr = 0.71$ **a** $R_d = 1$, **b** $R_d = 2$

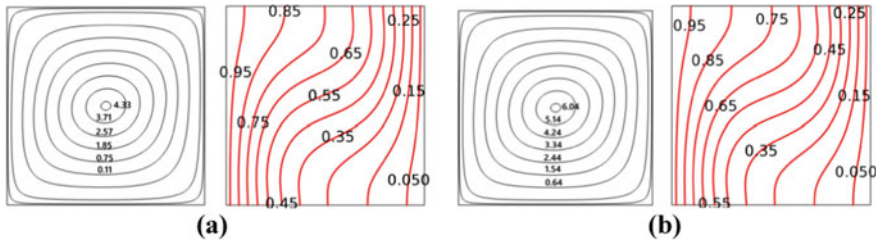


Fig. 4 Streamlines (ψ), Isotherms (θ) for $Ra = 10^6$, **a** $R_d = 1$, **b** $R_d = 2$, $Pr = 0.71$

A single enlarged convective cell of strength 0.94 is observed for $R_d = 1$ and it increases to 2.28 for $R_d = 2$. This is developed at the center of the enclosure and the fluid-flow circulations are seen to occupy the entire square geometry to approximately 85%. The isotherms are also seen to be uniformly spread out along the entire geometric configuration and are mostly uniform in nature with a very slight twisting. The isotherm patterns cannot be distinguished from each other from the results of $R_d = 1$ from $R_d = 2$.

Figure 4 delineates the numerical interpretation for fluid-flow pattern (streamlines), isotherms for $R_d = 1, 2$ and considering the higher $Ra = 10^6$. It is clearly seen from the figures that the fluid particle velocity progressively intensifies when Ra aggravates to 10^6 , which is on account of substantial buoyancy force in relation with regard to viscous force inside the square enclosure [23–29].

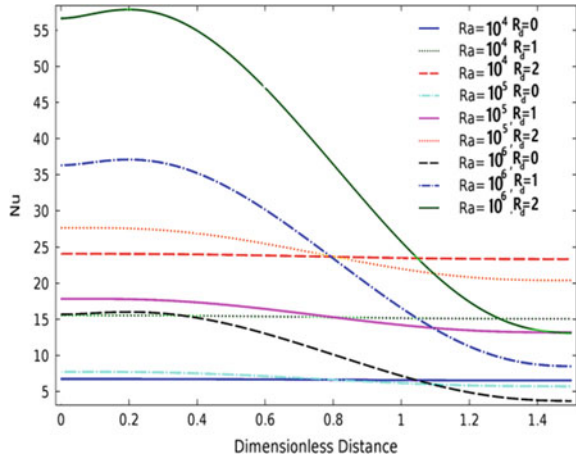
A single enlarged convective cell of strength 4.33 is observed for $Ra = 10^6$ (for $R_d = 1$) and this increases to 6.04 for $Ra = 10^6$ ($R_d = 2$) and this is developed at the center of the enclosure and the fluid-flow circulations are seen to occupy the entire square geometry to approximately 95%. An appreciable change in streamline pattern, isotherm contours are observed for the larger Ra . Considering $Ra = 10^6$, a vehement intensification of fluid motions are created and the isotherms are found to be twisted towards the left cold wall. The heat transportation is seen to be primarily materializing from the hot left vertical wall approaching the cold right vertical wall of the enclosure.

4.2 Nusselt Number

In this section we highlight the manifestation on account of radiation number R_d and natural convection criterion, Ra on local Nusselt number along the left wall of square enclosure and this is illustrated in Fig. 5.

The values of Nu for $R_d = 1$ and 2 for $Ra = 10^6$ are maximum for dimensional distance (Y) = 0.3 and its value is 38 for $R_d = 1$ and around 58 for $R_d = 2$. The corresponding value for Nu without considering radiation is only 18 for the same Ra . So applying radiation results in a 111% increase of Nu for $R_d = 1$. For $R_d = 2$ the increase of percentage is of the order of 222%. The corresponding

Fig. 5 Nu all along the left heated wall for distinctive values of Ra considering $R_d = 0, 1, 2$



maximum value of Nu considering $Ra = 10^5$ and $R_d = 1$ is 17 and it is around 28 for $R_d = 2$. Thus it is seen that there is a progressive magnification of Nu with intensification of R_d , demonstrating that preminent heat transfer occurs from heated left wall of enclosure to the fluid (air) in enclosure considering a larger radiative heatflux.

To further portray the effects of heat transfer on account of radiation in enclosure, we have also demonstrated the effects of surface velocity in this section. Figure 6 shows the surface velocity in the enclosure corresponding to $Ra = 10^5$ and 10^6 for $R_d = 2$. The range of velocities for $Ra = 10^6$ are found to be nearly more than 7 times the value of $Ra = 10^5$.

The effects of radiation parameter and Ra on average Nusselt number are shown in Table 2. It is clearly realized from the table, that all \overline{Nu} are positive on the left

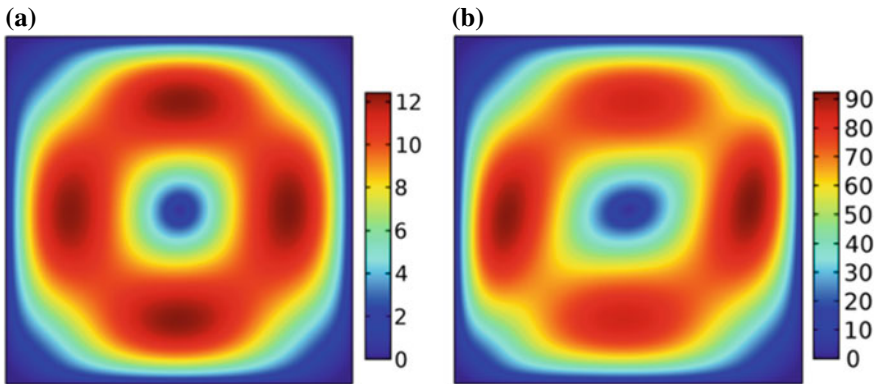


Fig. 6 Surface velocity plot inside the enclosure considering different numerical values of Ra for $R_d = 2, Pr = 0.71$ **a** $Ra = 10^5$ **b** $Ra = 10^6$

Table 2 Comparison of \overline{Nu} along left heated wall for various Ra with for the present enclosure design

Ra	R _d	\overline{Nu}		Relative difference of \overline{Nu} % for left wall (Value-Value (R _d = 0))/Value (R _d = 0)
		Average Nusselt number		
		Left wall	Right wall	
10 ⁴	0	1.002	-1.002	-
	1	2.298	-2.368	129.8
	2	3.557	-3.777	254.99
10 ⁵	0	1.016	-1.016	-
	1	2.336	-2.406	130.91
	2	3.616	-3.836	255.91
10 ⁶	0	1.565	-1.565	-
	1	3.617	-3.687	131.12
	2	5.629	-5.849	259.68

wall and maximum \overline{Nu} is obtained for Ra = 10⁶ and R_d = 2 and its value is 5.63 and the corresponding \overline{Nu} is 3.62 for R_d = 1. The minimum \overline{Nu} is obtained for Ra = 10⁴ considering R_d = 1(2.29) and considering R_d = 2, it is 3.56.

A relative difference column in the table also gives an idea about the percentage increase of \overline{Nu} on addition of radiation parameter (R_d). All values of \overline{Nu} are negative for right wall leading to the situation that heat is transferred on to the wall from the fluid in these situations.

5 Conclusion

Natural convection heat transfer and fluid flow coupled with radiation heat transfer is investigated in an air-filled square enclosure of side length 15 cm by FEM strategy. The left wall of the square enclosure is enforced to a constant high temperature (T_h) while we enforce the right vertical wall to a fixed and constant low temperature (T_c), whilst, the top and bottom walls are held to adiabatic conditions. The numerical results have demonstrated that Nu and flow velocity are small considering low Ra = 10⁴. Contrarily, circulation and temperature stratification are observed at larger Ra (= 10⁶). Also the Nusselt numbers are augmenting function of Ra and R_d. Heat transfer mechanism coupled with radiation as per this model is used extensively in several applications such as solar energy system and the present numerical investigations are applicable to solar collecting design devices, fire modelling, etc.

Future scope of work The analysis of this paper was restricted only to square enclosure. The future scope of work will be considered in different non uniform enclosure design with or without the effects of porosity and nanofluids.

References

1. Pangavhane DR, Sawhney RL, Sarsavadia PN (2002) Design, development and performance testing of a new natural convection solar dryer. *Energy* 27(6):579–590
2. Fetecau C, Akhtar S, Pop I, Fetecau C (2017) Unsteady general solution for MHD natural convection flow with radiative effects, heat source and shear stress on the boundary. *Int J Numer Methods Heat Fluid Flow* 27(6):1266–1281
3. Malekshah MH, Malekshah EH, Salari M, Rahimi A, Rahjoo M, Kasaeipoor A (2018) Thermal analysis of a cell of lead-acid battery subjected by non-uniform heat flux during natural convection. *Thermal Sci Engg Progr.* 5:317–326
4. Sheremet MA, Pop I (2018) Natural convection combined with thermal radiation in a square cavity filled with a viscoelastic fluid. *Int J Numer Methods Heat Fluid Flow* 28: 624–640
5. Ayachi RE, Raji A, Hasnaoui M, Naïmi M, Abdelbaki A (2012) Combined effects of radiation and natural convection in a square cavity submitted to two combined modes of cross gradients of temperature. *Numer Heat Transf Part A: Appl* 62(11):905–931
6. Bouali H, Mezrhah A, Amaoui H, Bouzidi M (2006) Radiation-natural convection heat transfer in an inclined rectangular enclosure. *Int J Thermal Sci* 45(6):553–566
7. Bahlaoui A, Raji A, Hasnaoui M (2006) Combined effect of radiation and natural convection in a rectangular enclosure discretely heated from one side. *Int J Numer Methods Heat Fluid Flow* 16(4):431–450
8. Dutta S, Goswami N, Pati S, Biswas AK (2020) Natural convection heat transfer and entropy generation in a porous rhombic enclosure: influence of non-uniform heating. *J Therm Anal Calorim.* <https://doi.org/10.1007/s10973-020-09634-7>
9. Dutta S, Biswas AK, Pati S (2018) Natural convection heat transfer and entropy generation inside porous quadrantal enclosure with nonisothermal heating at the bottom wall. *Numer Heat Transf Part A: Appl* 73(4):222–240
10. Dutta S, Biswas AK, Pati S (2019) Analysis of natural convection in a rhombic enclosure with undulations of the top wall—a numerical study. *Int J Amb Energy* <https://doi.org/10.1080/01430750.2019.1630304>
11. Dutta S, Biswas AK (2019) A numerical investigation of natural convection heat transfer of copper-water nanofluids in a rectotrapezoidal enclosure heated uniformly from the bottom wall A numerical investigation of natural convection heat transfer of copper-water nanofluids in a rectotrapezoidal enclosure heated uniformly from the bottom wall. *Math Model Eng Prob.* 6(1):105–114
12. Lari K, Baneshi M, Nassab SG, Komiya A, Maruyama S (2011) Combined heat transfer of radiation and natural convection in a square cavity containing participating gases. *Int. J. Heat Mass Transf.* 54(23–24):5087–5099
13. Balaji C, Venkateshan SP (1993) Interaction of surface radiation with free convection in a square cavity. *Int J Heat Fluid Flow* 14(3):260–267
14. Sharma AK, Velusamy K, Balaji C, Venkateshan SP (2007) Conjugate turbulent natural convection with surface radiation in air filled rectangular enclosures. *Int J Heat Mass Transf* 50(3–4):625–639
15. Ridouane EH, Hasnaoui M, Amahmid A, Raji A (2004) Interaction between natural convection and radiation in a square cavity heated from below. *Numer Heat Transf Part A: Appl* 45(3) 289–311
16. Saravanan S, Raja N (2020) Combined radiation-convection in an air filled enclosure with in-line heaters. *Int. Comm. Heat Mass Transf* 110:104399
17. Dutta S, Biswas AK, Pati S (2019) Numerical analysis of natural convection heat transfer and entropy generation in a porous quadrantal cavity. *Int J Num Meth Heat Fluid Flow* 29:4826–4849
18. Dutta S, Goswami N, Biswas AK, Pati S (2019) Numerical investigation of magnetohydrodynamic natural convection heat transfer and entropy generation in a rhombic enclosure filled with Cu-water nanofluid. *Int J Heat Mass Transf* 136:777–798

19. Magyari E, Pantokratoras A (2011) Note on the effect of thermal radiation in the linearized Rosseland approximation on the heat transfer characteristics of various boundary layer flows. *Int Commun Heat Mass Transf* 38(5):554–556
20. Sheremet MA, Pop I (2018) Natural convection combined with thermal radiation in a square cavity filled with a viscoelastic fluid. *Int J Numer Methods Heat Fluid Flow*
21. Sheremet MA, Pop I, Rosca AV (2018) The influence of thermal radiation on unsteady free convection in inclined enclosures filled by a nanofluid with sinusoidal boundary conditions. *Int J Numer Methods Heat Fluid Flow*
22. Introduction to COMSOL Multiphysics; COMSOL: Stockholm, Sweden (2019)
23. Bhowmick D, Randive PR, Pati S, Agrawal H, Kumar A, Srivastava PK (2020) Natural convection heat transfer and entropy generation from a heated cylinder of different geometry in an enclosure with non-uniform temperature distribution on the walls. *J Therm Anal Calorim* 141:839–857
24. Bhowmick D, Chakravarthy S, Randive PR, Pati S (2020) Numerical investigation on the effect of magnetic field on natural convection heat transfer from a pair of embedded cylinders within a porous enclosure. *J Therm Anal Calorim* 141:2405–2427
25. Pal GC, Goswami N, Pati S (2018) Numerical investigation of unsteady natural convection heat transfer and entropy generation from a pair of cylinders in a porous enclosure. *Numer Heat Transf Part A: Appl* 74(6):1323–1341
26. Meshram P, Bhardwaj S, Dalal A, Pati S (2016) Effects of inclination angle on natural convection heat transfer and entropy generation in square porous enclosure. *Numer Heat Transf Part A: Appl* 70:1271–1296
27. Bhardwaj S, Dalal A, Pati S (2015) Influence of wavy wall and non-uniform heating on natural convection heat transfer and entropy generation inside porous complex enclosure. *Energy* 79:467–481
28. Dutta S, Pati S, Biswas AK (2020) Thermal transport analysis for natural convection in a porous corrugated rhombic enclosure. *Heat Transf* 49:3287–3313
29. Goswami N, Randive PR, Pati S (2021) Natural convection from a pair of heated cylinders in a square cavity with non-uniform temperature on the side walls. *J Inst Eng India Ser C* 102(2):389–396

Evaluation of Lateral Stability of Cantilever Wall



Pooja S. Lachyan, Prashant M. Pawar, M. M. Pawar, S. A. Gosavi, and A. B. Kokare

Abstract Brick masonry constitutes the vital part of building construction globally. As they are in elastic and have non-homogenous material properties, the analysis for evaluating the performance of brick masonry is intricate. For numerical investigations, identifying the constitutive material properties is essential to study their behavior. The experiments are performed to determine the material properties such as compressive strength, modulus of elasticity and stress- strain characteristics of brick units, mortar cubes. Finite element modeling is carried out for numerical analysis using ANSYS. Considering the material properties from experimental results, the interface properties, stress distribution and failure criteria for brick masonry are studied in ANSYS. In this Present work, we have observed that when applied pressure increases then there is increase in maximum deformation and equivalent stresses. The study proves that for single brick wall and double brick wall of various dimensions, there is increase in maximum deformation and also in equivalent stresses due to increase in applied pressure.

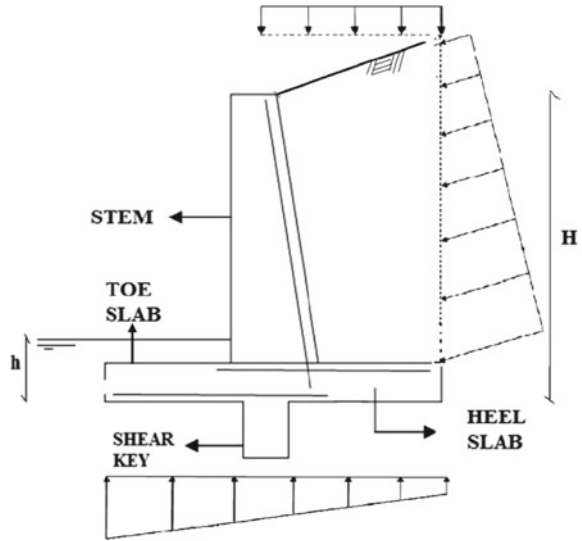
Keywords Brick Masonry · Finite Element Modeling · Material Properties · Single brick wall · Double brick wall etc.

1 Introduction

The cantilever wall generally consists of a vertical stem, and a base slab, made up of two distinct regions, viz. a heel slab and a toe slab. All three components behave like one-way cantilever slabs the stem acts as a vertical cantilever above the lateral earth pressure; the heel slab and the toe slab acts as a horizontal cantilever under the action of the resulting soil pressure. The walls will provide long-standing stability and serviceability [1]. These walls are constructed of reinforced concrete. This wall consists of a thin stem and base slab. The base of this retaining wall is divided into two parts namely the heel and the toe. The concrete cantilever wall can be defined

P. S. Lachyan (✉) · P. M. Pawar · M. M. Pawar · S. A. Gosavi · A. B. Kokare
SVERIs College of Engineering Pandharpur, Solapur, Maharashtra, India
e-mail: pslachyan@coe.sveri.ac.in

Fig. 1 Cantilever wall



as a construction of reinforced concrete to support backfill soil by cantilever action. The base slab serves as a permanent support and prevents against overturning and sliding. The cantilevered stem portion is rigid at the bottom and is free at the top. The walls will provide long-standing stability and serviceability [2]. Retaining walls are structures that are used to retain earth (or any other material) in a position where the ground level changes abruptly. They can be of many types such as gravity wall, cantilever wall, counter fort wall and buttress wall among others. The lateral force due to earth pressure is the main force that acts on the retaining wall which has the tendency to bend, slide and overturn it [3].

The present research focuses on designing the cantilever type of wall for overturning, sliding and bearing. The main considerations are the external stability of the section with the help of codal provision i.e. IS: 456:2000 Satisfying the external stability criteria is primarily based on the section giving the required factor of safety. The heel is a part of the base under the backfill. This wall uses much less concrete than retaining walls but it needs careful construction and design. It's usually economic till 25 ft in height ref Fig. 1. And these walls can either be precast in a factory or formed on the site. The Cantilever Wall is the most common type of retaining structure and is generally economical for height up to about 8 m.

1.1 Size of Brick

The two sizes of bricks are commonly used in practice. conventional size bricks having dimensions 230 mm × 115 mm × 76 mm (9" × 4.5" × 3") including the joint thickness, and (ii) modular size bricks of dimension 200 mm × 100 mm ×

100 mm including joint thickness. The present study the brick which are used for construction of single brick wall and double brick wall having size $4 \times 4 \times 9$ inch and 25.4 mm [4].

1.2 Types of Walls

1. **Permanent or Temporary Walls:** All walls can be divided into permanent or temporary walls, depending on project application. Permanent walls have a typical designed life of 75 years. The temporary walls are designed for a service life of 3 years, or the intended project duration, whichever is greater. Temporary wall systems have less restrictive requirements for construction, material and aesthetics.
2. **Bottom-up or Top-down Constructed Wall:** This wall classification method refers to the method in which a wall is constructed. If a wall is constructed from the bottom of the wall, upward to the top, it is considered a bottom-up type of wall. Examples of this include CIP cantilever, MSE and modular block walls. Bottom-up walls are generally the most cost effective type. If a wall is constructed downward, from the top of the wall to the bottom, it is considered a top-down type of wall. This generally requires the insertion of some type of wall support member below the existing ground, and then excavation in front of the wall to the bottom of the exposed face. Examples of this include soil nail, soldier pile, cantilever sheet pile and anchored sheet pile walls. These walls are generally used when excavation room is limited.
3. **Mass Gravity Walls:** A mass gravity wall is an externally stabilized, cast-in-place rigid gravity wall, generally trapezoidal in shape. The construction of these walls requires a large quantity of materials so these are rarely used except for low height walls less than 8.0 feet. These walls mainly rely on self-weight to resist external pressures and their construction is staged as bottom up construction, mostly in fill or cut/fill situations.
4. **Masonry or concrete walls:** The stem of a masonry wall is usually constructed of either 8" or 12" deep concrete masonry block units. The cells are partially or solid grouted, and are vertically reinforced. An eight-inch block is generally adequate to retain up to about six feet, and a twelve-inch block up to ten to twelve feet. The stems of a concrete wall must be formed, and can be tapered for economy, usually with the taper on the inside (earth side) to present a vertical exposed face. Hybrid walls, with both concrete and masonry, can also be constructed using formed concrete at the base, where higher strength is required, then changing to masonry higher up the wall. A variation for masonry cantilever walls uses spaced vertical pilasters (usually of square masonry units) with in-filled walls of lesser thickness, usually 6" masonry. The pilasters cantilever up from the footing and are usually spaced from four to eight feet on center. These walls are usually used where lower walls are needed-under about six feet high.

5. Counter fort walls: As shown in the counter fort wall having figure (d). Counter fort cantilevered retaining walls incorporate wing walls projecting upward from the heel of the footing into the stem. The thickness of the stem between counter forts is thinner (than for cantilevered walls) and spans horizontally, as a beam, between the counter fort (wing) walls. The counter forts act as cantilevered elements and are structurally efficient because the counter forts are tapered down to a wider (deeper) base at the heel where moments are higher. The high cost of forming the counter forts and the infill stem walls make such walls usually not practical for walls less than about 16 feet high.
6. Cantilever wall: As shown in the cantilever wall having figure (c). Composed of stem and base slab. It is constructed from reinforced concrete, precast concrete, or prestress concrete. Cantilever retaining wall is the most common type used as retaining walls. Cantilever retaining wall is either constructed on site or prefabricated offsite i.e. precast. The portion of the base slab beneath backfill material is termed as heel, and the other part is called toe. Cantilever retaining wall is economical up to height of 10 m. It requires smaller quantity of concrete compare with gravity wall but its design and construction shall be executed carefully. Similar to gravity wall, sliding, overturning, and bearing pressure shall be taken into consideration during its design [5].

2 Methodology

2.1 Analysis of Lateral Stability of Brick Wall

The lateral stability of Brick wall analyzed for using Load cell, the wooden bearing plate is clamped on the entire height of wall. The horizontal force is applied on center of wall. The displacement meter attach to the machine shows weight to be carried out by the wall for successive interval of dial gauge readings which are converted into the lateral pressure. The maximum value of the lateral pressure is considered as a lateral stability of brick wall without failure.

2.2 Critical Failure Locations

Failure location of wall is evaluated from the graph of displacement verses force. It is observed that the critical location is at junction of wall and foundation at the maximum value of force. This shows that the wall fails due to overturning moment and not due to faulty material. It is observed that strength of the wall decreases with increases in height of the wall.

2.3 Experimental Analysis of Stability of Wall

An experimental analysis of 1 m wide brick wall having height variation as 1 m, 1.5 m and 2 m are tested for gradually applied horizontal loads. The ultimate load where the brick wall fails is evaluated from this experiment. Maximum displacement is calculated at certain interval. An experimental analysis of 1 m wide brick wall having height variation as 1 m, 1.5 m and 2 m are tested for gradually applied vertical loads. The ultimate load where the brick wall fails is evaluated from this experiment. Also maximum displacement is calculated at certain interval [6, 7].

3 Experimental Procedure

Figure 2 shows the picture of actual experimental setup which is explained below:

1. This device has a portable cantilever column which will be fixed near the walls parallel to the walls.
2. The height of the column is about 1.5 m which helps in varying the height of the
3. Lateral point where load can be applied with respect to LG of wall based on the Height.
4. Horizontal hydraulic jack is connected perpendicular to the wall connecting to the vertical column. This jack is useful for applying the horizontal load.
5. There is a load cell connected between wall and loading jack which measures the amount of load applied.
6. Dial gauge is also connected between wall and vertical cantilever column to measure the deflection of wall.

Fig. 2 Actual experimental setup



Fig. 3 Failure of double brick wall 1.0 m height



Fig. 4 Failure of double brick wall 1.5 m height



Fig. 5 Failure of double brick wall 2 m height



4 Result and Discussion

4.1 Failure Pattern Observed for Various Heights of Walls

The following Figs. 3, 4 and 5 shows the failure pattern of double brick wall for various heights.

4.2 Finite Element Approach for Brick Wall Analysis

Figure 6 shows the Engineering data input Mortar material properties below. The primary material properties that we need to specify are the.

1. Brick Density = 2132Kg/m^{-3}
2. Poisson's Ratio, $\nu = 0.165$ Pa.
3. Young Modulus = $2.65\text{E} + 09$ (pa) 4) Bulk modulus = $1.3184\text{E} + 09$ (pa)
4. Shear Modulus = $1.1373\text{E} + 09$ (pa)
5. Tensile Ultimate strength = $5\text{E} + 06$
6. Compressive Ultimate strength = $4.1\text{E} + 07$

Figure 7 shows the Engineering data input Brick material properties below. The primary material properties that we need to specify are the.

1. Brick Density = 1612.3 kg/m^{-3}
2. Poisson's Ratio, $\nu = 0.213$ Pa.
3. Young Modulus = $3.5\text{E} + 10$ (pa)
4. Bulk modulus = $2.0325\text{E} + 10$ (pa)

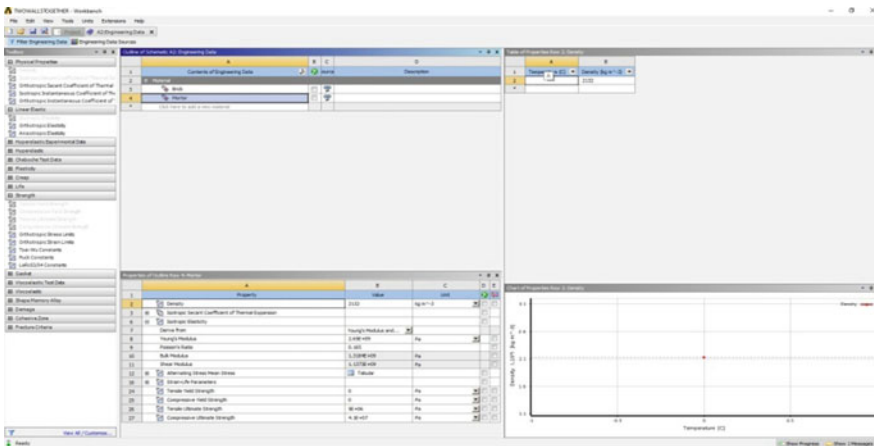


Fig. 6 Engineering data input mortar material properties

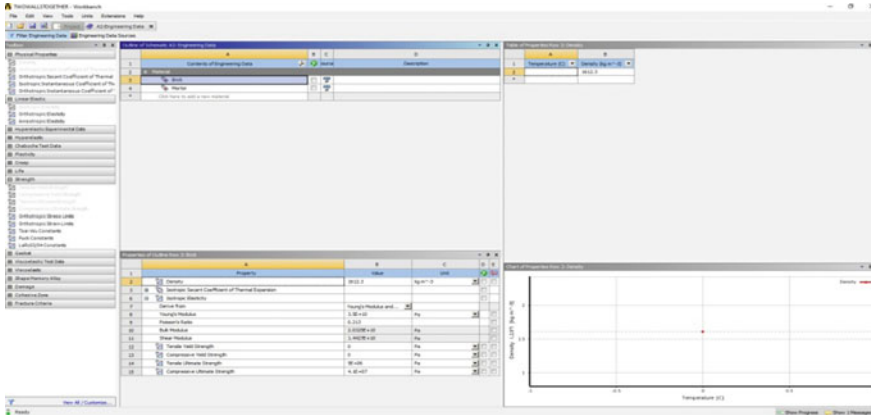


Fig. 7 Engineering data input brick material properties

- 5. Shear Modulus = $1.4463E + 10$ (pa)
- 6. Tensile Ultimate strength = $5E + 06$
- 7. Compressive Ultimate strength = $4.1E + 07$

Save the changes with Save. To return to the Project tab either close the A2: Engineering Data (X) tab or click on the grayed-out Project tab to the left of the A2: engineering Data tab and leave the Engineering Data tab open, but hidden. This action will take you back to the overall ANSYS project window. The Engineering Data cell in your Axial Bar System menu should now have a green check mark next to it. The total deformation and equivalent stress is shown in Figs. 8 and 9.

4.3 Double Brick Wall Ansys Model

Finite element Analysis of three walls heights of 1, 1.5 and 2.0 m is performed and results are shown below ref Figs. 10, 11, 12, 13, 14 and 15.

5 Conclusion

In this thesis detailed analysis of failure of brick walls due to lateral pressure is carried out Using experimental approach, analytical approach and numerical approach. The conclusions of the study are summarized below:

- 1. The analytical approach was utilized to find out the cause of the failure wall under the lateral Pressure gendered due to wind pressure. This shows that the failure of wall was due to increased Wind pressure as compared the design wind

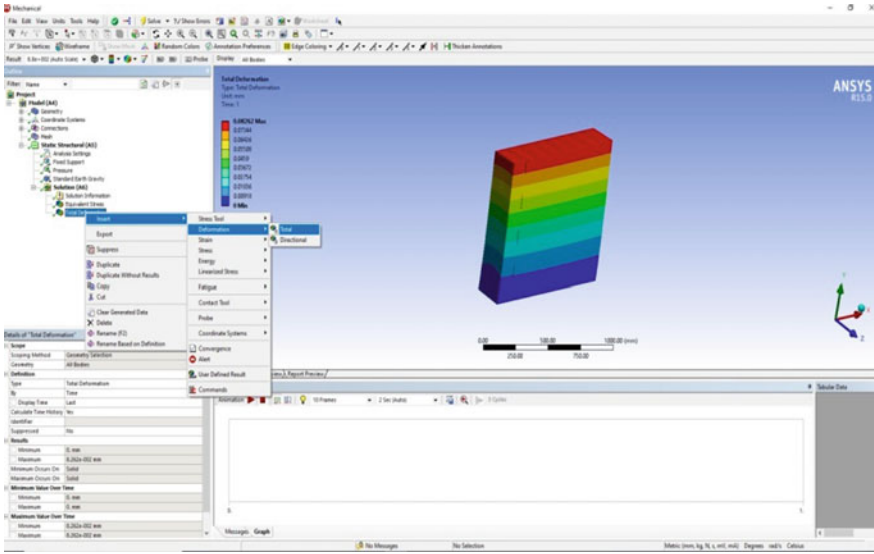


Fig. 8 Total deformation

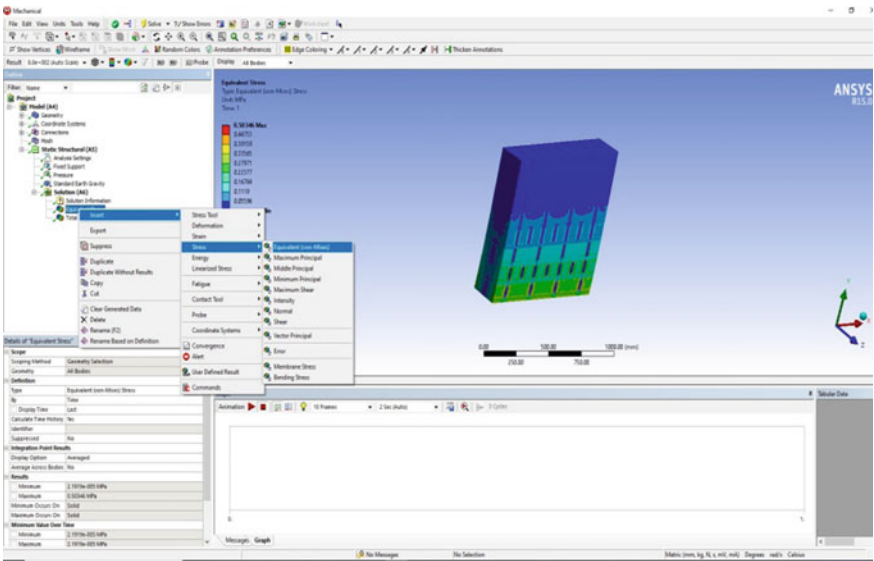


Fig. 9 Equivalent stress

Fig. 10 Max. Deformation versus Applied Pressure for wall of 1 m height

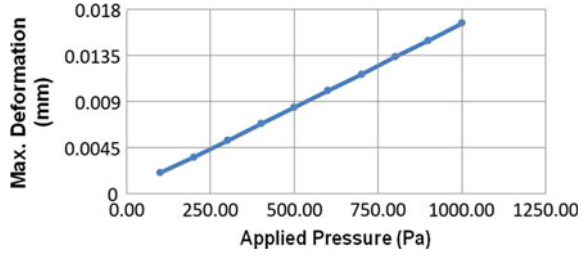


Fig. 11 Equivalent Stress versus Applied Pressure for wall of 1 m height

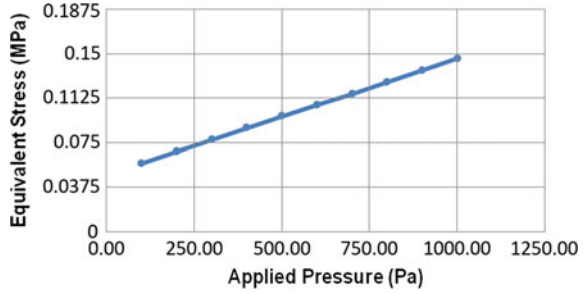


Fig. 12 Max. Deformation versus Applied Pressure for wall of 1.5 m height

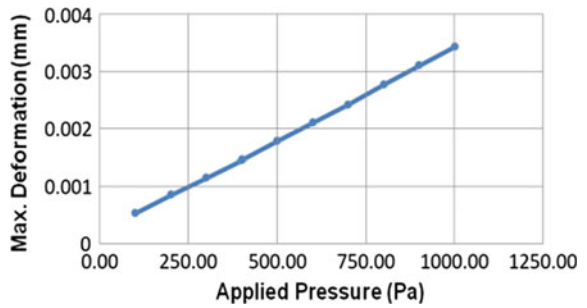


Fig. 13 Equivalent Stress versus Applied Pressure for wall of 1.5 m height

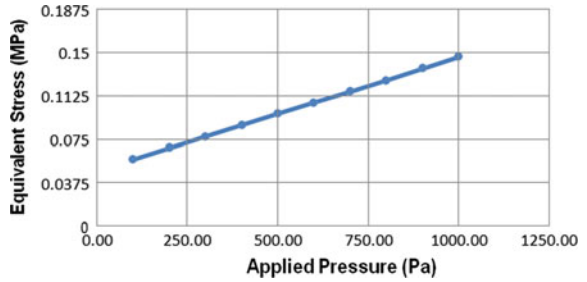


Fig. 14 Max. Deformation versus Applied Pressure for wall of 2.0 m height

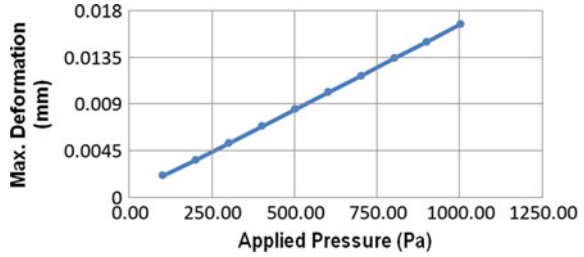
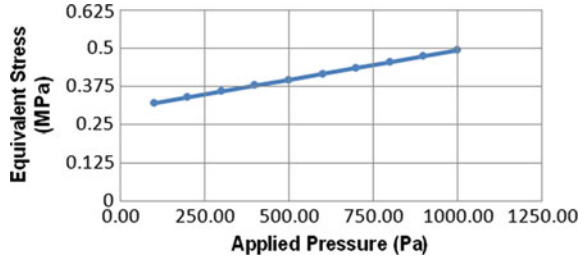


Fig. 15 Equivalent Stress versus Applied Pressure for wall of 2.0 m height



pressure. Further, it shows that with reduced height, This failure could have been avoided even for the increased with pressure.

2. An experimental setup is developed to perform the experiments to demonstrate failure of walls due to wind pressure. This shows that the nearly linear force displacement till the failure of the wall. After the first failure in the wall, force requirement start reducing with increase in displacement of wall.
3. Experimental results of the walls shows that all the three walls of heights 1, 1.5 and 2.0 m, Fails at the junction foundation and superstructure of the walls. The superstructure wall show not Signature of failure. It was also observed that with increase the height of the wall with same width. The amount of failure pressure requirement reduces.
4. Finite element models developed of brick walls shows similar trends of force-displacement relations. The stiffness values obtained from the force-displacement results show that with increase in height of the wall the stiffness values decreases.
5. The stress analysis results of by finite element methods also show similar failure patterns by showing highest stresses at junction of the wall and foundation which the cause of failure of walls.

References

1. Ravi S, Viswanathan S, Nagarajan T, Srinivas V, Narayanan P (2014) Experimental and numerical investigations on material behaviour of Brick Masonry. In: 2nd international conference on research in science, engineering and technology (ICRSET''2014). Dubai (UAE)
2. Sharma C, Baradiya V (2014) Evaluation of the effect of lateral soil pressure on cantilever retaining wall with soil type variation. *J Mech Civil Eng (IOSR-JMCE)* 11(2) Ver. III:36–42
3. Neha S, Ali D, Bhutekar SB, Domale AP (2015) Evaluation of suitability of retaining wall for different height's. *IOSR J Eng (IOSR JEN)*, 44–47
4. Narayanan SP, Sirajuddin M, Properties of Brick Masonry for FE modeling. *Am J Eng Res (AJER)* 1:06–11
5. Chaliawala Y, Solanki G, Chandiwala AK (2015) Comparative study of cantilever and counter fort retaining wall. *Int J Adv Eng Res Dev* 2:221–224
6. Sobana U, Gayathri S (2018) Design and analysis of lateral earth pressure effect on cantilever retaining wall, *Int J Innovat Res Sci Eng Technol* 7(Special Issue 5). An ISO 3297: 2007 Certified Organization
7. Naraine K, Sinha SN (1989) Behavior of Brick Masonry under cyclic compressive loading. *J Struct Eng ASCE*

Application of Meta Heuristic Algorithms for Optimization of Inverse Kinematics of a 5D Robotic Manipulator



V. B. Shinde and P. J. Pawar

Abstract Traditional methods of optimization are more complex and quite expensive for solving inverse kinematics problems when the degree of freedom of a robot increases. In the present work, forward and inverse kinematic model of five degree of freedom (5D) industrial manipulator for various applications, is developed using the homogeneous transformation matrices and the Denavit-Hartenberg (DH) parameters. The objective of such non-standard 5D robot is to reduce the positional error among the specified target points and robot end-effector positions, with reference to the joint angular displacements which are employed for translating the robot end-effector to the target points in the Cartesian space. Different traditional and meta-heuristic algorithms (MH) are employed to solve the problem and the obtained results are compared for the positional error of end-effector. From the results, it is found that simulated annealing performs better for the positional error of end-effector than sequential quadratic programming and genetic algorithm.

Keywords Multi-objective optimization · Sequential quadratic programming · Genetic algorithm · Simulated annealing · Positional error

1 Introduction

A variety of industrial robots applications in the field of manufacturing are increasing due to their autonomy, flexibility, and autonomous work in different environments. Typical applications such as, drilling, material transfer and machine loading and unloading, processing, assembly and inspection, welding, spray coating, machining operations, etc. In order to perform repetitive kind of task industrial robots are designed. To perform these operations different configurations are required. The work is carried out by allowing the robot to move the body, arm and wrist during a series of motions and positions. The end-effector attached to the wrist is used by the robot to complete specific task and joint motions are associated with degrees of

V. B. Shinde (✉) · P. J. Pawar

Department of Production Engineering, K. K. Wagh Institute of Engineering Education and Research, Nasik, Maharashtra, India
e-mail: vilas.shinde@avcoe.org

freedom. The robot's motions are carried out using powered joints. The joints are normally associated with the action of body, and arm and number of joints are used depends upon the complexity of the task to be performed.

One of the toughest challenges for growing industrial robotics field is high investment involvement in adoption, lack of trained workforce and ease of availability of hardware components. In most of industrial applications robots has to perform the tasks under the conditions of restrictions. This motion control is achieved by solving the inverse kinematics (IK) of the redundant manipulator. The important issue of such redundant manipulators are highly nonlinear with multiple solutions [1]. Similarly, infinite number of IK solutions are obtained and difficult to get closed form solutions [2]. The kinematics of the rotational robot is more difficult to analyze than the linear robot. It is reported that due to the occurrence of singularity in analysis of robotic position by employing traditional approaches such as a geometric technique [3], and algebraic technique [4, 5]. Furthermore, a classical iterative methods are depends on an initial solution and are time consuming [6]. Therefore, it is quite interesting and challenging to solve such kind of IK problem of a redundant robot with different methods.

Forward-kinematics (FK) problem consist of finding the end-effectors position and orientation using the joint angles. Using link parameters and joint variables of a robot, FK of a robotic manipulator can be solved easily, while the IK are nonlinear and configuration dependent problem with multiple solutions.

To begin with MHs alone, the singularity problem can be eliminated when employing IK problem based on FK. The MHs are flexible as there is no need of data training. The MH are a global search optimization techniques which considers variety of objectives and design parameters [7]. Hence, the MHs are applied for different applications like structural optimization [8], job shop scheduling [9], a traveling salesman problem [10], etc. Further, it is also used for solving the IK problem of redundant manipulators through FK analysis [7]. The solution of IK problem of redundant robotic manipulator is scarce using MH due to search convergence rate and consistency.

In such kind of problems, several objectives and constraints are considered. The search space becomes large for finding optimum solution and the problem becomes more complex to solve by exact methods. Significant research is reported in the literature [11] that the conventional optimization techniques such as Powell's technique, Fletcher-Reeves technique, Dynamic programming technique, and the reduced gradient technique etc. have been employed for such kind of problems. Still, such techniques lack to perform well over a wide range of problem areas. In addition, these techniques give local optimal solution and are not robust. With these issues as an input, several researchers have attempted to model and optimize the complex problem using MH. The most frequently used non-traditional optimization method is Genetic Algorithm (GA). GA is powerful technique having large search space without local optimum solution but it has reduced convergence properties. Thus, there is an ardent requirement to control the robot redundant manipulator parameters using more recent and robust method for optimization. Particle Swarm Optimization (PSO) is one of the nontraditional optimization techniques reported as better

algorithm for the nonlinear functions and complex problems with good convergence properties [12]. Simulated Annealing (SA) is capable to give global optimum solution for the problem under consideration which presents a very good and reliable solution to the inverse kinematics problem (IKP), by dealing with singularities and easily scalable as well [13]. The objective of present work is to reduce a positional error among the target points and the calculated points obtained using joint angles.

Developing robust solutions for solving complex inverse kinematics problem related to manufacturing engineering is a key issue to deal with various aspects like path planning optimization, smooth trajectory generation and optimization of robot control parameters. Although few attempts have been made to resolve these issues, it is revealed from literature review and industrial survey that accuracy, robustness and cost effectiveness are still remaining issues in which improvement can be sought. Moreover, as an attempt to make industrial robots more flexible and adaptable, multi-objective optimization to improve overall performance of industrial robot with respect to above mentioned issues. Hence, in the present work, F_{\mincon} , GA and SA algorithms have used in MATLAB environment for minimization of positional error of end-effector at specified targeted points.

2 Kinematic Modeling of 5D Manipulator

Robot manipulator arm is created using joints and links as open-loop chain mechanism, as FK problem. The end-effector position in Cartesian space is calculated using joint angles. The problem can be written using Eq. (1) as:

$$x(t) = f(\theta(t)) \quad (1)$$

where θ is joint angles and x is end effector position. The IK problem is reverse of the FK using Eq. (2) as:

$$\theta(t) = f'(x(t)) \quad (2)$$

The Denavit Hartenberg (DH) notations and methodology is employed for obtaining the kinematics of 5D robot manipulator [14]. The coordinate frame represents the local coordinate frames at 5 joints and at the end-effector respectively as depicted in Fig. 1. The DH parameters for 5D robot manipulator is shown in Table 1, where θ_i shows rotation with reference to the Z-axis, d_i transition along the Z-axis, α_i rotation with reference to the X-axis, and a_i translation along the X-axis.

With the help of DH parameters, the transformation matrix (TM) from joint i to joint $i-1$ is shown in Eq. (3) as:

TM for 5D Robot manipulator

Fig. 1 A five (5D) joint robotic arm

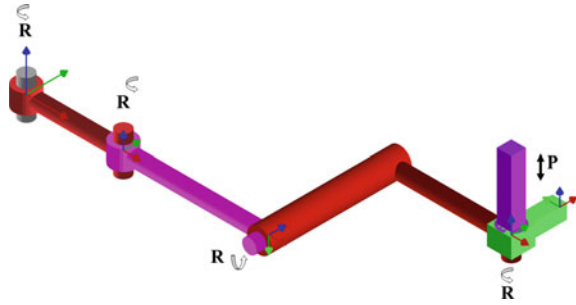


Table 1 DH Parameters for the 5D Robot

Joint i	θ_i°	d_i (cm)	α_i°	a_i (cm)	Operating range
1	30	0	0	2	$\pm 180^\circ$
2	120	0	-90	3	$\pm 180^\circ$
3	0	2.5	90	2.5	$\pm 180^\circ$
4	$\theta + 90$	0	90	0	$\pm 180^\circ$
5	0	$3.5 + d$	0	0	± 2 cm

$${}^{i-1}A_i = \begin{bmatrix} \cos \theta_i & -\sin \theta_i \cos \alpha_i & \sin \theta_i \sin \alpha_i & a_i \cos \theta_i \\ \sin \theta_i & \cos \theta_i \cos \alpha_i & -\cos \theta_i \sin \alpha_i & a_i \sin \theta_i \\ 0 & \sin \alpha_i & \cos \alpha_i & d \\ 0 & 0 & 0 & 1 \end{bmatrix} \quad (3)$$

By adding the DH parameters from Table 1 in Eq. (3), the individual TMs A_1 to A_5 can be achieved. The general TM from the first to the last manipulator joint is obtained by multiplying all the individual TMs to get $({}^0T_5)$. The TMs of each joint is written using following Eqs. (4-8).

$$\begin{bmatrix} C_1 & -S_1 & 0 & 2C_1 \\ S_1 & C_1 & 0 & 2S_1 \\ 0 & 0 & 1 & 0 \\ 0 & 0 & 0 & 1 \end{bmatrix} \quad (4)$$

$${}^1T_2 = \begin{bmatrix} C_2 & 0 & -S_2 & 3C_2 \\ S_2 & 0 & C_2 & 3S_2 \\ 0 & -1 & 0 & 0 \\ 0 & 0 & 0 & 1 \end{bmatrix} \quad (5)$$

$${}^2T_3 = \begin{bmatrix} 1 & 0 & 0 & 2.5 \\ 0 & 0 & -1 & 0 \\ 0 & 1 & 0 & 2.5 \\ 0 & 0 & 0 & 1 \end{bmatrix} \quad (6)$$

$${}^3T_4 = \begin{bmatrix} -S_3 & 0 & C_3 & 0 \\ C_3 & 0 & S_3 & 0 \\ 0 & 1 & 0 & 0 \\ 0 & 0 & 0 & 1 \end{bmatrix} \quad (7)$$

$${}^4T_5 = \begin{bmatrix} 1 & 0 & 0 & 0 \\ 0 & 0 & 0 & 0 \\ 0 & 1 & 1 & 3.5 + d \\ 0 & 0 & 0 & 1 \end{bmatrix} \quad (8)$$

where, $C\theta_i$ is $\cos\theta_i$ ($i = 1$ to 5), $S\theta_i$ is $\sin\theta_i$ ($i = 1$ to 5). Finally, the TMs of the end-effector can be calculated as:

$${}^0T_5 = {}^0T_1 * {}^1T_2 * {}^2T_3 * {}^3T_4 * {}^4T_5 = \begin{bmatrix} n_x & o_x & a_x & p_x \\ n_y & o_y & a_y & p_y \\ n_z & o_z & a_z & p_z \\ 0 & 0 & 0 & 1 \end{bmatrix} \quad (9)$$

where (p_x, p_y, p_z) be the positions and $\{(n_x, n_y, n_z), (o_x, o_y, o_z) \text{ and } (a_x, a_y, a_z)\}$ represents the end-effector orientations. The end-effectors position and orientation is determined using following matrix as:

$${}^0T_5 = \begin{bmatrix} -S_3C_{12} - S_{12}C_3 & 0 & C_{123} - S_{123} & (C_{123} - S_{123})(3.5 + d) + 2.5(C_{12} - S_{12}) + 3C_{12} + 2C_1 \\ C_{123} - S_{123} & 0 & S_{12}C_3 + C_{12}S_3 & (C_{123} - S_{123})(3.5 + d) + 2.5(C_{12} - S_{12}) + 3C_{12} + 2C_1 \\ 0 & 1 & 0 & 0 \\ 0 & 0 & 0 & 1 \end{bmatrix} \quad (10)$$

where, $C\theta_i$ is $\cos\theta_i$ ($i = 1$ to 5), $S\theta_i$ is $\sin\theta_i$ ($i = 1$ to 5), C_{12} is $\cos\theta_1 * \cos\theta_2$, S_{12} is $\sin\theta_1 * \sin\theta_2$, C_{123} is $\cos\theta_1 * \cos\theta_2 * \cos\theta_3$, S_{123} is $\sin\theta_1 * \sin\theta_2 * \sin\theta_3$.

3 Methodology

The objective of this work is to reduce the positional error P_e .

$$\text{Minimize } Z = P_e \quad (11)$$

Quadratic programming Algorithm in Matlab environment is then applied to solve the above mentioned optimization model.

3.1 Determination of Positional Error

As defined above positional error P_e that is the distance among initial end effector positions and the targeted point which is the function of link angles. The decision parameters considered are the link angular positions $(\theta_1, \theta_2, \dots, \theta_n)$, where n represents the number of links. The objective function is given as:

$$\text{Min.error}(P_e) = \sqrt{(P_x - p_x)^2 + (P_y - p_y)^2 + (P_z - p_z)^2} \quad (12)$$

where $[P_x, P_y, P_z]$ be the end effector current position and $[p_x, p_y, p_z]$ be the desired end position. p_x, p_y , and p_z are written in terms of joint parameters as:

$$p_x = (\cos(\theta_1 + \theta_2) \cos \theta_3) - \sin(\theta_1 + \theta_2) \sin \theta_3 (3.5 + d) + 2.5(\cos(\theta_1 + \theta_2) - \sin(\theta_1 + \theta_2)) + 3 \cos(\theta_1 + \theta_2) + 2 \cos \theta_3 \quad (13)$$

$$p_y = (\sin(\theta_1 + \theta_2) \cos \theta_3) + \cos(\theta_1 + \theta_2) \sin \theta_3 (3.5 + d) + 2.5(\sin(\theta_1 + \theta_2) + \cos(\theta_1 + \theta_2)) + 3 \sin(\theta_1 + \theta_2) + 2 \sin \theta_3 \quad (14)$$

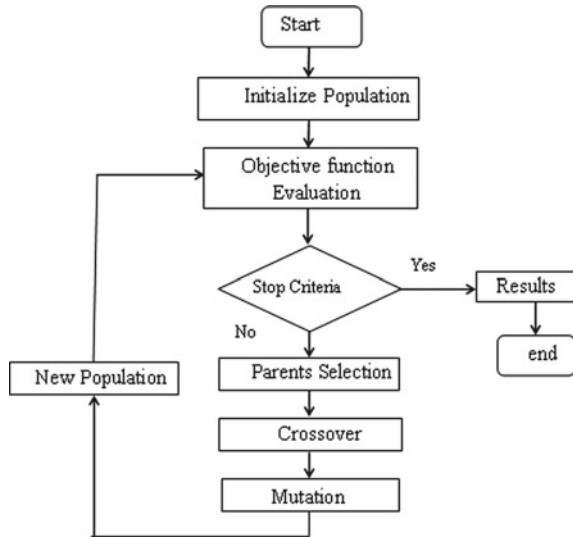
$$p_z = 0 \quad (15)$$

where, d_i is the prismatic joint variable parameter i.e. stroke. In the next section, the MH methods are presented.

3.2 Meta-Heuristic Methods

In present work, most recent and commonly employed MHs are applied and evaluated using IK problem. For this using Eq. (12) and the constraints from the DH parameter Table 1, we obtained $\theta_1, \theta_2, \theta_3, d$ and objective function. By solving Eqs. (12–15), the values for p_x, p_y and p_z is determined by using considered MH algorithms. Finally, the positional error P_e is calculated and the method which gives least values of objective function will be the best method.

Fig. 2 Flowchart of genetic algorithm



3.2.1 Genetic Algorithm

GA is powerful non-traditional optimization technique having large search space without local optimum solution. The GA offers the best solution from the population of individuals (solutions) which are promoted to allow for the next generation [15].

The functioning of the GA is shown in Fig. 2. In this case, the population is a set of individuals, each one formed by the angles θ_1, θ_2 and θ_3 , the initial population consists of individuals close to the found values by applying IK, the result of the IK will be starting point of the GA. Each individual will be evaluated using fitness function. The fitness function is used in a first step using kinematics Eqs. (13–15), then the individual’s position is compared to the get position using Eq. (2). Individual’s crossover was done heuristically using higher fitness function. To ensure convergence of the algorithm, mutation is commonly employed [16, 17] to get the desired target solution.

3.2.2 Simulated Annealing (SA)

SA is reported better optimization technique for continuous and discrete optimization problems [18]. The SA technique is a probabilistic search technique capable of searching the global minimum amongst multiple local minima, explicitly where traditional techniques fail. The SA optimization algorithm is demonstrated as shown in the Fig. 3.

SA works on randomly aggravating the decision variables and observes the best objective function for every randomized variable sets. After number of iterations, a set which produces the best objective function value is selected as the center about which

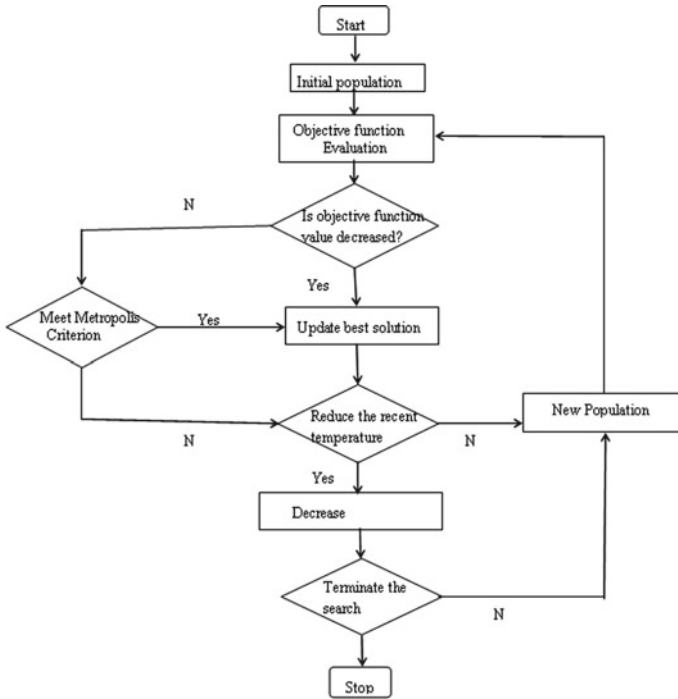


Fig. 3 Flowchart of SA algorithm

disruption will take place for the next temperature. The temperature (the standard deviation of the random number generator) is then reduced, and new iterations are performed [19]. The SA optimization algorithm is demonstrated as shown in the Fig. 3.

4 Results

After doing optimization for the 10 test runs for the IK problem, the accuracy of the MH is calculated based on end-effectors positional error i.e. objective function (values) and the results are shown in Tables 2. Using present methods, the method gives smaller values of positional error is the best method while the method which requires less number of function computation is said to be the faster method. It is observed that, the best algorithm in terms of positional accuracy is SA while the second best is F_{mincon} .

Table 2 Summary of objective function (values)

Sr. No	Fmincon	Genetic Algorithm	Simulated Annealing
1	3.16×10^{-6}	1.15×10^{-5}	2.46×10^{-6}
2	4.39×10^{-6}	5.41×10^{-6}	7.34×10^{-7}
3	2.06×10^{-5}	2.69×10^{-5}	6.73×10^{-8}
4	1.71×10^{-5}	5.31×10^{-6}	1.23×10^{-6}
5	1.64×10^{-5}	5.21×10^{-6}	7.76×10^{-8}
6	1.46×10^{-5}	1.23×10^{-4}	1.80×10^{-8}
7	1.87×10^{-5}	2.22×10^{-5}	1.21×10^{-6}
8	2.23×10^{-5}	2.67×10^{-5}	2.17×10^{-8}
9	1.32×10^{-5}	3.40×10^{-6}	8.42×10^{-5}
10	4.96×10^{-6}	1.43×10^{-5}	5.88×10^{-6}
Average error	1.35×10^{-5}	2.441×10^{-5}	9.594×10^{-6}

5 Conclusions

In this work, different meta-heuristic algorithms (MH) are employed and compared for solving the inverse kinematics (IK) of a robotic manipulator using forward kinematics (FK). The objective of such non-standard 5D robot is to reduce the positional error between the user defined points and end-effector positions, with reference to the joint angle movements which are employed for moving a robotic end-effector to the target points in Cartesian space. Most recent and commonly employed MH has been applied and the results evaluated in terms positional accuracy based on solving the IK problem. It is observed that, the best algorithm in terms of positional accuracy is SA while the second best is F_{\mincon} . This work is yet to be considered as real dynamic one as here the pre-defined target points were considered before running algorithm. Application of additional numerical approaches such as PSO, CSO techniques, the outcome of these algorithms could still be improvised considering restriction viz. environment, energy consumption etc.

References

1. Wang H, Li R, Gao Y, Cao C, Ge L (2016) Comparative study on the redundancy of mobile single- and dual-arm robots. *Int J Adv Robot Syst* 13:1–19
2. Zacharia PT, Aspragathos NA (2005) Optimal robot task scheduling based on genetic algorithms. *Robot Comput Integr Manuf* 21:67–79
3. Liu S, Qiu Z, Zhang X (2017) Singularity and path-planning with the working mode conversion of a 3-DOF 3-RRR planar parallel manipulator. *Mech Mach Theory* 107:166–182
4. Manocha D, Canny JF (1994) Efficient inverse kinematics for general 6R manipulators. *IEEE Trans Robot Autom* 10:648–657
5. Duffy J (1980) *Analysis of mechanisms and robot manipulators*. Wiley, New York

6. Zhang Q, Zhao MY (2016) Minimum time path planning of robotic manipulator in drilling/spot welding tasks. *J Comput Des Eng* 3:132–139
7. Saka MP, Hasançebi O, Geem ZW (2016) Metaheuristics in structural optimization and discussions on harmony search algorithm. *Swarm Evol Comput* 28:88–97
8. Jian X, Wenyi Q, Bin L, Cheng L (2007) Inverse kinematics problem for 6-DOF space manipulator based on the theory of screws. In: *IEEE international conference on robotics and biomimetics (ROBIO)*. Sanya, China, pp 1659–1663
9. Liu B, Wang L, Jin YH (2007) An effective PSO-based memetic algorithm for flow shop scheduling. *IEEE Trans Syst Man Cybern Part B Cybern* 37:18–27
10. Held M, Karp RM (1970) The traveling-salesman problem and minimum spanning trees. *Oper Res* 18:1138–1162
11. Rao RV, Pawar PJ (2010) Parameter optimization of a multi-pass milling process using non-traditional optimization algorithms. *Appl Soft Comput* 10:445–456
12. Pawar PJ, Rao RV, Davim JP (2010) Multiobjective optimization of grinding process parameters using particle swarm optimization algorithm. *Mater Manuf Process* 25:424–431
13. Pawar PJ, Rao RV, Davim JP (2010) Optimisation of process parameters of mechanical type advanced machining processes using a simulated annealing algorithm. *Int J Mater Prod Technol* 37:83–101
14. Jha P, Biswal BB, Sahu OP (2015) Inverse kinematic solution of robot manipulator using hybrid neural network. *Int J Mater Sci Eng* 31–38
15. Köker R (2013) A genetic algorithm approach to a neural-network-based inverse kinematics solution of robotic manipulators based on error minimization. *Inf Sci (Ny)* 222:528–543
16. da Graça Marcos M, Machado JT, Azevedo-Perdicoúlis TP (2009) Trajectory planning of redundant manipulators using genetic algorithms. *Commun Nonlinear Sci Numer Simul* 14:2858–2869
17. Nearchou AC (1998) Solving the inverse kinematics problem of redundant robots operating in complex environments via a modified genetic algorithm. *Mech Mach Theory* 33:273–292
18. Dutra MS, Salcedo IL, Margarita L, Diaz P (2008) New technique for inverse kinematics problem using simulated annealing. *Eng Optim* 1–5
19. Goldenberg AA, Benhabib B, Fenton RG (1985) A complete generalized solution to the inverse kinematics of robots. *IEEE J Robot Autom* 1:14–20

Experimental Study of Behavior of Under-Reamed Stone Column in Black Cotton Soil



Prathmesh Solapure, Manasi Shinde, Shubhali Shete, Saurav Bachhav, and Shailendra Banne

Abstract The stone column is a ground improvement technique mainly used for enhancing the properties of soft soils. Provision of the under reaming to stone column increases the bearing capacity of the soil and it also reduces the settlement in soil. The study deals with determining the effect of the under-reamed stone column on black cotton soil, the effect of variation of aggregate sizes in stone column and effect of position of the under-reamed bulb on the settlement. Also, it deals with determining the bearing capacity of black cotton soil with a stone column. The laboratory model test has been performed by using an under-reamed stone column of diameter (D) 50 mm, bulb diameter 2.5D and height 300 mm and varying aggregate sizes at each bulb position. The experimental analysis gives results that position of the bulb at center results in the lesser settlement of soil than the position of the bulb at bottom.

Keywords Black cotton soil · Under-reaming · Stone column · Settlement · Bearing capacity · Bentonite slurry · Etc

1 Introduction

The stone column technique is one of the ground improvement techniques which is used to increase the strength and also decreases the compressibility of silty sand and cohesive soil or loose fine graded soil. The stone column technique helps in the densification of the soil and also improves the drainage functions. A stone column is a column made up of aggregates or stone which is inserted in soil deposits to improve ground characteristics or soil conditions. It is one of the easiest and effective techniques used for ground improvement. The Indian black cotton soil consists of various features which are low bearing capacity, high swelling and shrinkage properties, and also high compressibility. For soft soil similar to black cotton soil which consists of low safe bearing capacity, the stone column technique was found to be economical and rapid for construction. Usually, the stone column is loaded over an area greater than its own which helps in reducing bulging leading to increase ultimate

P. Solapure · M. Shinde · S. Shete · S. Bachhav · S. Banne (✉)
Department of Civil Engineering, Pimpri Chinchwad College of Engineering, Pune, India

bearing capacity and also reduces the settlement as the load is carried by both the soil as well as the stone column. The stone column also works as a drainage system which decreases the consolidation time in saturated cohesive soil. The stone column in cohesive soil or silty sand acts similar to pile foundation except that there is no pile cap or structural connections. The stone columns techniques consist of various advantages like the construction of stone column is simple and cost-effective, resist lateral loads, reduces settlement, increases bearing capacity.

1.1 Literature Review

In the literature, Golait et al. [1] concluded that the provision of a semi-rigid floating type of under-reamed stone column is used for economical and effective improvement of soft soil. It also revealed that both settlement and bearing capacity characteristics improved significantly. “S. Siva Gowri Prasad et al. show that the inclusion of a stone column increases the load-carrying capacity of soil by about 117% by densifying the soil; also stiffness can be increased by lateral reinforcement of column using geogrid” [2]. “Anand Kumar et al. have explained the mechanism of ground improvement techniques and mechanism including the important factors that will help engineers in judging and adopting a particular technique in fields” [3]. “Marina Miranda et al. investigated the three series of tests i.e. one with non-encased and the other two with different geotextile encasements and it clearly shows that encased columns were most effective than non-encased so it gives a brief idea for stabilization of external walls of the stone column” [4]. “Jorge Castro simplified the concept regarding area replacement ratio and column length. He concluded that the critical length of the column is $1.5-2B$ for non-encased stone columns, where B is the size of footing” [5]. Das et al. [6], have investigated the load-carrying capacity of treated and untreated soil on soft soil. They show the failure of bulging occurs within the entire column area. It was also helpful for experimental setup and procedure for measurement of displacement. Golait et al. [7], describes that the provision of bulbs to the simple cemented stone column shows effective performance in case of settlement. Also, investigate the well suitable positioning of the bulb and found the bulb at the intermediate level gives better results than the bulb at bottom of the stone column. Kalantari et al. [8], shows that to support isolated footing in soft cohesive soil, the stone column technique is frequently implemented. They give a brief idea about the stone column and methods for the installation of a stone column on the field. “K. Ali et al. have investigated that the performance of stone columns can be improved either by encasing them or by the inclusion of geosynthetic material within the stone column. The model tests and results on short, floating, and fully penetrating single column with and without reinforcement” [9]. “Mohmoud Ghazavi et al. show that the lateral bulging of the stone column reduces by frictional and interlocking effects with the stone column by the inclusion of aggregates. Also performed a test on the stone column with horizontally layered geosynthetic reinforcement” [10]. Fattah et al. [11], derived the equation which can be adopted for estimation of bearing capacity of

single and group of stone columns. They also prove that the area replacement ratio is the controlling parameter for bearing capacity. Lajevardi et al. [12], compared single and grouped stone columns with geotextile and it is observed that bearing capacity increases in both cases. Mehrannia et al. [13], utilized reinforced and unreinforced granular blankets to solve the problems on soft soil. Singh and Sahu [14] give a review on a review on stone columns used for ground improvement of soft soil. Bouziane et al. [15] conducted tests on crushed sand and coarser granularity with reinforcement and the results were relevant to predict the improvement of granular soils of medium density.

1.2 Under-Reamed Stone Column

The under-reamed stone column is a bored stone column having one or more number of bulbs formed by enlarging the column stem. The bearing capacity characteristics and settlement parameters of soft ground are improved by the utilization of under-reamed stone columns instead of utilizing regular stone columns. These under-reamed stone columns are best suited in soils where considerable ground movement occurs due to seasonal variation. The arrangement of an enlarged bulb in the stem found either at lower part of the column or at some appropriate middle of the level can have extra helpful impacts because of expanded bearing zone. In the case of conventional stone columns, lateral bulging takes place under axial load which restricts its load-carrying capacity. Therefore to reduce the bulging to some extent and enhance the load-carrying capacity of the stone column under-reamed stone column is used. The use of fill material in the column is helpful for soil stabilization. Bentonite slurry is used as fill material which is very cost-effective compared to other filler materials and it also stabilized the soil by applying it on the inner side of the column. The under-reamed stone column has a provision of an enlarged bulb located at the bottom of the column or the intermediate height. The installation of an under-reamed stone column of stem diameter (D) 50 mm forming an enlarged bulb of a diameter of 2.5 times the diameter of column stem and height of the column is 300 mm with varying bulb position.

2 Materials and Equipments

2.1 Black Cotton Soil

The black cotton soil as shown in Fig. 1 is collected from the Jambhe farm, Tathwade, Pimpri Chinchwad, Maharashtra. The soil sample was collected from the depth of one meter below the ground level avoiding the surface soil by open excavation. Table 1 shows the index and engineering properties of black cotton soil.



Fig. 1 Black cotton soil

Table 1 Index and engineering properties of soil

Parameters	Engineering properties of soil
Water content	35%
Specific gravity	2.186
Liquid limit	73%
Plastic limit	60.7%
Flow index	13.28%
Plasticity index	12.3%
Toughness index	0.92
OMC	34.5%
MDD	1.365 g/cc
Cohesion	1.05 kg/cm ²
Angle of internal friction	7.96°

2.2 Aggregate

The stone column is prepared using various sizes of aggregates. Project work consists of testing of a stone column under various sizes of aggregate and behavior of aggregates under cumulative loading and knowing the corresponding settlement. Aggregate sizes being tested in the under-reamed stone column are 8, 12, 20 mm.

2.3 Bentonite Slurry

Bentonite slurry is used for experimental investigation as a binder and also for stabilization of the inner sides of the column. Bentonite slurry is a combination of sodium bentonite and water. The combination is generally used to form a protective barrier in the ground.

2.4 Under-Reamer

For the provision of the under-reamed portion in the stone column, the instrument as shown in Fig. 2 can be used. The vertical metal rod of 9 cm is provided at the bottom to place the bulb at intermediate height. The square shape arrangement is made to get 2.5D (Diameter) i.e. 12.5 cm diagonal of the bulb. These rods are well jointed to each other and the top and bottom rods with nuts and bolts. T-shape is given to the top for rotating the instrument to excavate the required size of the bulb.

3 Experimental Set-Up and Methodology

To investigate the effectiveness of under-reamed stone columns in black cotton soil, laboratory model tests were carried out. The under-reamed stone column model tests are quite convenient and economical because the construction of stone column, design, and operation of the model can be altered several times to minimize the defects of the model while carrying out the test. The model test results have to be used furthermore on site for construction, but they have to be utilized with caution while predicting the performance of the prototype. The model tests were carried out to determine the ultimate bearing capacity of the column and evaluate the reduction in settlement of a single unit cell of the under-reamed stone column. Also, the model test was conducted to check the feasibility of the stone column on the Black cotton soil.



Fig. 2 Under-reamer

3.1 Methodology

The test bed was prepared in rectangular shape acrylic mould with dimensions 800 mm × 400 mm × 400 mm. Black cotton soil was filled layer by layers up to 350 mm in height. To maintain the controlled conditions throughout the investigation the mould is emptied and refilled for each test. The column was positioned on the soil bed at the desired height. The following seven tests were conducted on the black cotton soil:

1. Bare soil.
2. Under-reamed stone column bulb at the center.
 - (a) With 8 mm size aggregate.
 - (b) With 12 mm size aggregate.
 - (c) With 20 mm size aggregate.
3. Under-reamed stone column bulb at the bottom.
 - (a) With 8 mm size aggregate.
 - (b) With 12 mm size aggregate.
 - (c) With 20 mm size aggregate.

3.2 Test Procedure

For carrying out the above tests mould was filled with black cotton soil up to 350 mm height and it consists of an under-reamed stone column of 50 mm diameter and 300 mm height with bulb diameter 2.5 times diameter of the stone column. With the help of an under-reamer, the bulb was created at desired locations i.e. at the centre and bottom. Bentonite slurry was applied slightly on the inner sides of the column which helps in the stabilization of soil which is shown in Fig. 3. Further the aggregates



Fig. 3 Application of Bentonite Slurry



Fig. 4 A column filled with aggregates

were poured and simultaneously tamping was carried out for removal of voids and a stone column of the desired height was obtained.

Before starting the test the top surface of the soil was made horizontal plain surface for maximum surface contact of the load with soil. Figure 4 shows that aggregates were filled up to the top of the soil surface.

The stone column was loaded with a total load of 30 kg for measurement of settlement. The load was placed exactly on top of the stone column. Loading was done by placing circular weights. While loading the weights were kept carefully and by slowly making them touch with the soil surface to avoid jerk and impact effect on the stone column. Dial gauges were fixed on the shaft as shown in Fig. 5.

The settlement was measured using a dial gauge. The settlement readings were taken at 1, 5, 10, 20, 40, 60, 120, and 720 min. The time for recording the settlement is similar to that of the plate load test. A similar procedure was conducted for each bulb positioned and aggregate size test and respective results were noted down carefully.



Fig. 5 Testing setup

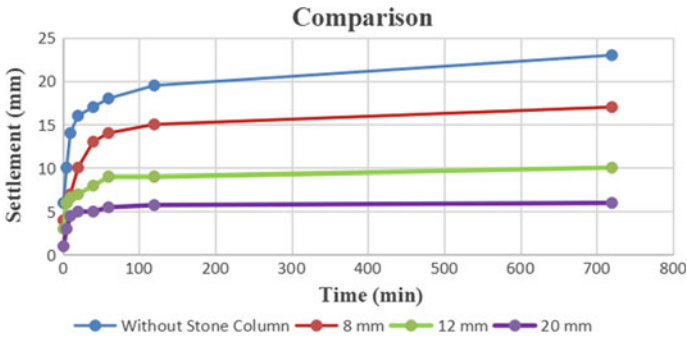


Fig. 6 Time versus settlement comparative study curve for bulb at the centre

4 Result and Discussion

The testing was done with bulb position at center and bottom with varying the sizes of aggregates. From the several test results, a comparative study of the under-reamed stone column with different aggregate sizes was done. This gives the settlement behavior of stone columns and surrounding soil.

4.1 Comparative Study for Bulb at Centre

This includes a comparative study of the three tests carried out for the position of a bulb at centre shown in Fig. 6 i.e. for 8 mm size aggregate, for 12 mm size aggregate, and 20 mm size aggregates. The Time-Settlement curve for various aggregate size stone column.

4.2 Comparative Study for Bulb at Bottom

This includes a comparative study of the three tests carried out for the position of a bulb at the bottom i.e. for 8 mm size aggregate, for 12 mm size aggregate, and 20 mm size aggregates. The Time-Settlement curve for various aggregate size stone columns. Figure 7 shows that there is a considerable decrease in settlement for 20 mm aggregate size with a bulb at the centre.

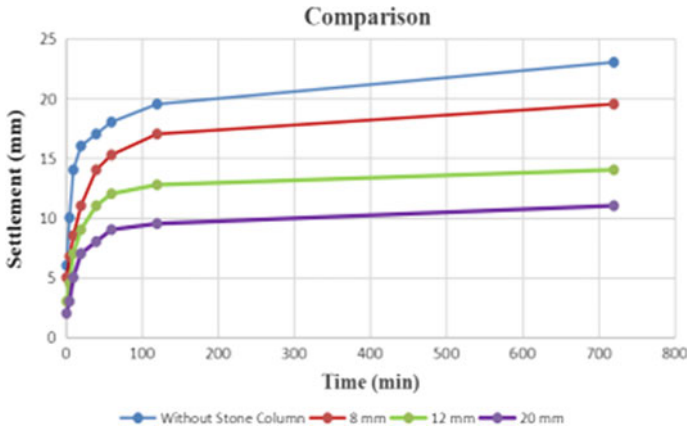


Fig. 7 Time versus settlement comparative study curve for bulb at the bottom

4.3 Percentage of Settlement Reduction

The testing results of settlement reduction were calculated to know the effective aggregate size and effective position of the bulb. From the above results, the position of a bulb at the centre gives less settlement as compared to the position of a bulb at bottom of the under-reamed stone column. So the percentage of settlement reduction evaluated for the position of a bulb at centre. Figure 8 shows that 20 mm size of aggregates gives more percentage of reduction in settlement than other sizes of

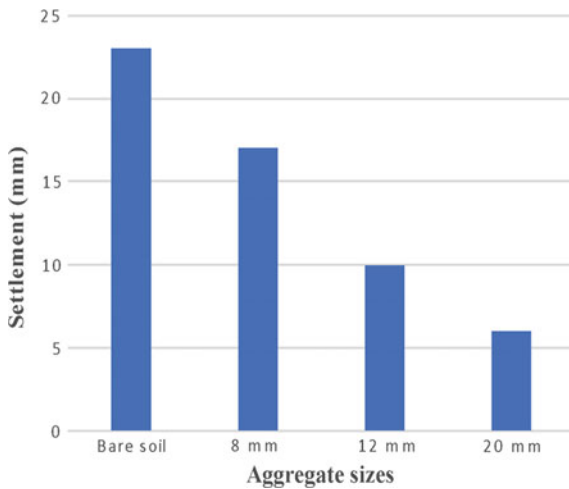


Fig. 8 Settlement versus aggregate sizes

Table 2 Percentage reduction for each aggregate

Sr. No	Size of aggregate (mm)	Settlement (mm)	Percentage reduction (%)
1	Without stone column	23	–
2	8	17	26.09
3	10	10	56.52
4	20	6	73.91

aggregates. Table 2 shows the final settlement and percentage reduction in each size of aggregate.

4.4 Estimation of Bearing Capacity

Construction of stone columns in soft clay under an embankment is a common economical method to increase the Bearing Capacity of the soil. The bearing capacity (Fattah et al. [11]) is calculated by the formula given below:

$$(Q_u) = 15.34 \times C_u^{0.401} \times A_s^{0.266} \times N_s^{0.084} \times (L/D)^{0.526} \quad (1)$$

where, C_u = Undrained shear strength, A_s = Area replacement ratio, N_s = No. of stone column, L/D = Length to diameter ratio.

The area replacement ratio can be defined as the ratio of the area of a stone column to a total area of the unit cell or footing of diameter 100 mm.

$$A_s = A_c / A_f$$

(a) **Estimation of Bearing Capacity of the Black Cotton Soil using circular stone column:**

From the formula of area replacement ratio, it was found to be 0.249 for the circular stone column of diameter 50 mm. The bearing capacity of the circular stone column was calculated by Eq. (1) and it gives the value of bearing capacity is 174.45 KN/m².

(b) **Estimation of Bearing Capacity of the Black Cotton Soil using under-reamed stone column:**

The formula of area replacement ratio was found to be 0.727 for the under-reamed stone column of diameter 50 mm and bulb diameter 125 mm. The bearing capacity of the under-reamed stone column was calculated by Eq. (1) and it gives the value of bearing capacity is 231.98 KN/m². The above results indicate that the most controlling parameter is the area replacement ratio. As the area of an under-reamed column

is greater than the area of a circular stone column, the bearing capacity is also greater for the under-reamed stone column.

5 Conclusion

Based on experimental work carried out in the present study, the following conclusion is drawn out.

1. The present study shows that an under-reamed stone column is an effective ground improvement technique which reduces settlement in the soft sensitive soil such as Black Cotton Soil.
2. Settlement in the under-reamed stone column is less as compared to settlement in a circular stone column and without a stone column in Black Cotton Soil.
3. The various aggregate sizes used for experimental analysis of under-reamed stone column in Black Cotton Soil shows that 20 mm aggregate size is most effective such that it gives a maximum reduction in the settlement.
4. Settlement in Black Cotton Soil with the under-reamed stone column is reduced up to 73.91% by using bulb at centre whereas it reduces up to 52.17% by using bulb at the bottom. Therefore the position of the bulb at centre gives less settlement as compared to the position of the bulb at the bottom.
5. An under-reamed stone column with a position of a bulb at centre results in the maximum percentage of settlement reduction in 20 mm size aggregates is 73.91% whereas it is 56.52% and 26.09% for 12 mm and 8 mm size aggregates respectively. Similarly, the maximum percentage of settlement reduction for the position of the bulb at the bottom is 52.17% for 20 mm size aggregates whereas it is 39.13% and 17.39% for 12 mm and 8 mm size aggregates respectively.
6. The bearing capacity of black cotton soil is increased by using the stone column ground improvement technique. General bearing capacity of black cotton soil is 150 KN/m², by use of circular stone column the bearing capacity has increased to 174.45 KN/m², and using under reamed stone column the bearing capacity has increased to 231.98 KN/m²

References

1. Golait YS, Satyanarayana V, Raju SSV (2009) Concept of under reamed cemented stone column for soft clay ground improvement. IGS 356–360
2. Gowri Prasad SS, Satyanarayana PVV (2016) Improvement of soft soil performance using stone column improved with circular geogrid disc. Indian J Sci Technol 2:1–6
3. Kumar A, Rajput S, Kumar S (2016) Working model and analysis on innovative stone column encasement. In: 3rd international conference on recent development in engineering, science, management and humanities, pp 121–125

4. Miranda M, Da Costa A, Castro J, Sagaseta C (2017) Influence of Geotextiles Encasement on the Behaviors of stone column. Laboratory Study. *Geotextiles Geomembrane* 45(1):14–22
5. Castro J (2017) Group of encased stone column Influence of column length and arrangement. *Geotextiles Geomembrane* 45(2):68–80
6. Das P, Pal SK (2013) A study on behavior of stone column in local soft and loose layered soil. *EJGE* 18:1777–1786
7. Yadav SG, Padade AH (2018) Enhancement in effectiveness of cemented stone columns for soft clay ground improvement by providing under-reamed bulbs. *Int J Geomech* 18(11):1–15
8. Mokhtari M, Kalantari B (2012) Soft soil stabilization using stone column- a review. *EJGE* 17:1659–1666
9. Ali K, Shahu JT, Sharma KG (2012) Model tests on geosynthetic-reinforced stone columns: a comparative study. *Geosynth Int* 19(4):292–305
10. Ghazavia M, Yamchia AE, Afsharb JN (2018) Bearing Capacity of horizontally layered geosynthetic reinforced stone columns. *Geotextiles Geomembranes* 46.3:312–318
11. Fattah MY, Al-Neami MA, Al-Suhaily AS (2017) Estimation of bearing capacity of floating group of stone columns. *Eng Sci Technol* 20(3):1166–1172
12. Lajevardi SH, Enami S, Shamsi HR, Hamidi M (2019) Experimental study of single and groups of stone columns encased by geotextile. *Amirkabir J Civil Eng* 50(6):337–340
13. Mehrannia M, Kalantary F, Ganjian N (2018) Experimental study on soil improvement with stone columns and granular blankets. *J Central South Univ* 25:866–878
14. Singh I, Sahu AK (2019) A review on stone columns used for ground improvement of soft soil. *Int J Innovat Technol Exploring Eng* 8:7C2
15. Bouziane A, Jamin F, Mandour A, Omari A, Bouassida M, Youssoufi M (2020) Experimental Study on a scaled test model of soil reinforced by stone columns. *Eur J Environ Civ Eng* 1964–8189:1–21

FE Analysis of the Glass/Jute/Polyester Bone Plate Versus Traditional Metal Plate for Ulna Bone Fracture



Rajkumar Deshmukh, Sudarshan Sanap, and Dineshsingh Thakur

Abstract Stress shielding is a mechanical concept generally observed in fracture fixation bone plates. Distinction in material properties among the human bone and the metallic bone plates prompts to stress shielding phenomenon. In the current analysis, glass/jute/polyester and commonly used titanium were chosen as bone plate material. Ideal structure was hypothetically gotten that displays mechanical properties near to the characteristic human bone. Fracture fixation plate was intended for ulna utilizing solid works software. Finite element (FE) analysis was embraced to dissect the distribution of stress in the bone fixed with plate under static loading. Bone plate by four screws was modeled with solid works software and simulated utilizing FEA. Analysis was likewise made taking into account titanium as fixing plate and compared with the current composite material researched. Hybrid polymer matrix composite (HPMC) has demonstrated material properties near the bone contrasted with titanium. The outcomes have obviously demonstrated that the von-Mises stresses initiated in the ulna bone by HPMC plates was expanded contrasted and the bone fixed with titanium. From the current analysis, it is certainly exhibited that the hybrid composites of glass/jute/polyester can be a proper material suggestion for ulna bone fracture fixation plate with diminished stress shielding problem.

Keywords FEA · Bone plate · Composite material

R. Deshmukh (✉) · S. Sanap
MIT ADT University, Pune, India

D. Thakur
Defence Institute of Advanced Technolgy, Pune, India

1 Introduction

As the proposed composite material should use as a bone plate to fix bone fracture inevitably, main purpose of the present work was to investigate the distribution of stresses in the fractured ulna bone and composite bone plate in examination with ordinary metallic bone plate. It was speculate that stress incited in the bone with composite bone plates was expanded contrasted and the metallic bone plate [1, 2]. Stress shielding phenomenon is biomechanical impression generally observed in metallic bone fracture fixation plates. Mismatch in material properties of human bone and metallic bone plates prompts stress shielding issue [3, 4].

Composite materials are a class of materials which show combined properties when compared with their contributing materials. Due to this specialty, composite material implants considered as alternative option to the metallic implants in biomedical field.

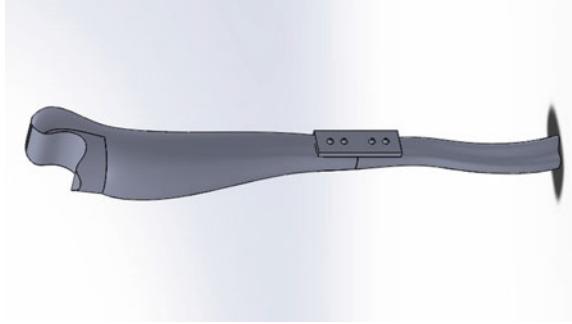
Mainly in fracture repairing plates, composites are the optimums option as the exhibit orthotropic nature same as human bone. The recent studies revealed that composites are the best alternatives for bone plate application by stress distribution and healing rate perspective. Recently, Dhason et al. [12] studied polymer matrix composite materials to fix femur B1 type fracture by finite element software gives feasible outcomes to design the composite fracture fixation plates.

In the current examination, glass/jute/polyester hybrid polymer matrix composite (HPMC) and glass/polyester polymer matrix composite (PMC) materials were developed which shows mechanical properties near that of human ulna bone. Fracture fixation plate, screws and ulna bone model was designed utilizing solid works software. FE analysis was executed to inspect the distribution of stress in the fractured bone fixed with bone plate in static loading [5]. The outcomes have obviously indicated that the amount of von-Mises stress increased in the bone with authors newly developed hybrid composite bone plate compared to the bone fixed by metallic plate. Strikingly, hybrid polymer matrix composites exhibited maximum stresses in the bone than polymer matrix composite material. From this current study, hybrid composite of glass and jute fiber can be potential choice for ulna bone fixation plates.

2 Design and Analysis

The same geometry of ulna bone, fracture fixation plate and screws has been modeled by adopting SOLID WORKS CAD software as shown in Fig. 1. The shape of the bone have been tried to match with the actual shape to facilitate accuracy in the results. During the current modeling, four screws were inserted by considering the fracture in the ulna shaft at the mid portion (weakest portion). Total three geometric models i.e. bone, plate and screws were assembled to obtain 3D structure. The geometry of bone model was designed with 265 mm length, 32 mm distal radial width 32 mm and 24 mm radial head width. Thickness of bone plate has taken as 3 mm; width is

Fig. 1 Modeling of Ulna bone in SOLIDWORKS



15 mm and 62 mm long. Four drills of 4 mm width were penetrated on the bone plate to furnish arrangement to fix the plate with bone by utilizing cortical screws.

2.1 Elements and Meshing

The CAD model assembly of fractured bone fixed with bone plate and screw was exported to ANSYS workbench 16.0 program for FE analysis. Then, auto-meshing preference was chosen for dividing CAD model into discrete elements. For proper contact, congruity was set up between the mating surfaces during meshing. When plate was screwed through the bone fracture, a strong bond was generated through the Workbench simulation module among the plate and the tissue. Every slight movement involving in the implant plate with tissue affects the rate of healing process. Therefore, the contact between the bone and bone plate was considered as a No-Separation contact. Because of the applied load, growth of bone tissues over the bone plate may allow easy sliding of the bone plate as a result of dissimilarity in the compressive strains among the bone and bone plate. The kind of fracture of the bone was considered as two divided parts with no sliding development. Thus, automatic bonded type contact between plate-screw and bone-screw was considered. Further, the contact between plate and bone was chosen as friction less automatic. Other studies also adopted similar considerations for their FE models of bone fractures. The element type considered for meshing the ulna bone and bone plate was tetrahedral type. The number of nodes and elements are 234,055 and 156,009.

2.2 Material Properties

Material properties are the important input quantities in FE analysis before applying boundary conditions (Table 1). The nature of human bone is highly nonlinear, so it is difficult to assign material properties along each direction of bone model. The

Table 1 Input material properties for FE analysis

Material	E_x (GPa)	E_y (GPa)	ν_{xy}	G_{xy} (GPa)	$\rho(\text{g/cm}^3)$	E (GPa)	ν	References
Bone	–	–	–	70	2000	2.13	0.3	[1]
Titanium	–	–	–	45	4.26	116	0.34	[1]
HPMC 1	14.13	14.13	0.39	3.33	1.46	–	–	–
HPMC 2	12.65	12.65	0.54	2.27	1.46	–	–	–
PMC	24.89	24.89	0.34	1.52	1.97	–	–	–

glass/jute/polyester (HPMC) and glass/polyester (PMC) composites were considered as orthotropic material. For metal fixation plate and screws titanium material is considered for analysis. It should be noted that the properties for composite material bone plate were considered for analysis were without holes. However, the existence of the bored holes on the plates for screw insertion may change composite plate material properties.

2.3 Loading and Boundary Conditions

To avoid rigid body motion, the displacement of the ulna bone was restricted at fixed support. A static compression load of 750 N was applied on the each end of the ulna bone by taking into account the patient weight and the reactive force from the opposite side of the bone. Using FE analysis, the values of the Von Misses Stress was calculated.

3 Results

In the current work, compressive loads were applied over the ulna bone model because of the patient weight (750 N). Because of patient self-weight impact of bending was thought to be insignificant. The load applied toward the end of the bone is move to the fracture fixation plates through the interface of the bone with screw. It was hypothesize that, the stress induced in the fractured bone due to composite material bone plate is maximum as compared to metallic plate. For proper healing process of bone stress generation in the bone is required. In current study FE analysis was done to investigate the distribution of stresses in bone-plate assembly.

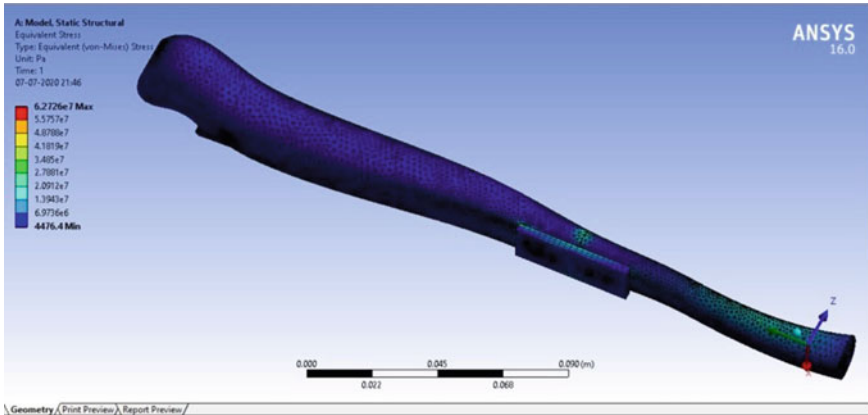


Fig. 2 Von-mises stress distribution in titanium bone plate and bone

3.1 Distribution of Stress in the Bone and Metallic Bone Plate

For FE analysis of plate and bone assembly first study was carried out on commercially used Titanium metallic plate. After the application of load the von-Mises stress distribution in the bone and titanium bone plate is shown in the Fig. 2. The variation of stress was found in between 55.75 MPa and 6.97 MPa. The amount of stress distribution was found minimum in bone and in bone plate maximum amount of stress distribution was observed. This difference in stress distribution is evident as the titanium metal bone plate has more Young’s modulus as compared to bone.

3.2 Distribution of Stress in the Bone and Composite Bone Plates

Further FE analysis of plate and bone assembly was carried out on authors newly developed composite material bone plates as shown in Figs. 3, 4 and 5. Total three types of composite plates have been made, out of which two plates are of hybrid type i.e. glass/jute/polyester (HPMC 1 and HPMC 2) and third type was made of glass/polyester (PMC) material. The same amount of load was applied to find the distribution of von-Mises stress in the bone and HPMC 1 bone plate. The maximum amount of stress (48.56 MPa) was found in the bone and minimum amount of stress (5.39 MPa) was found in the bone plate and some regions of bone also. For second sample of composite plate (HPMC 2) the maximum amount of stress (42.42 MPa) was found in the bone and minimum amount of stress (6.06 MPa) was found in the bone plate. The third type of composite (PMC) shown maximum amount of stress (38.76 MPa) was found in the bone and minimum amount of stress (5.54 MPa) was found in the bone plate.

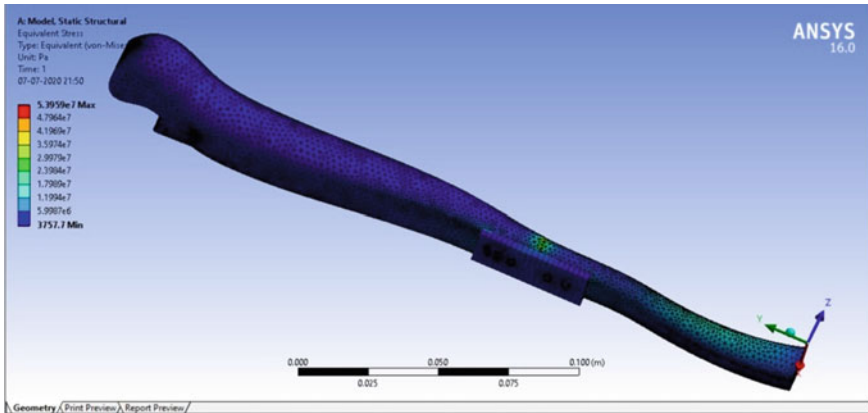


Fig. 3 Von-mises stress distribution in HPMC 1 and bone

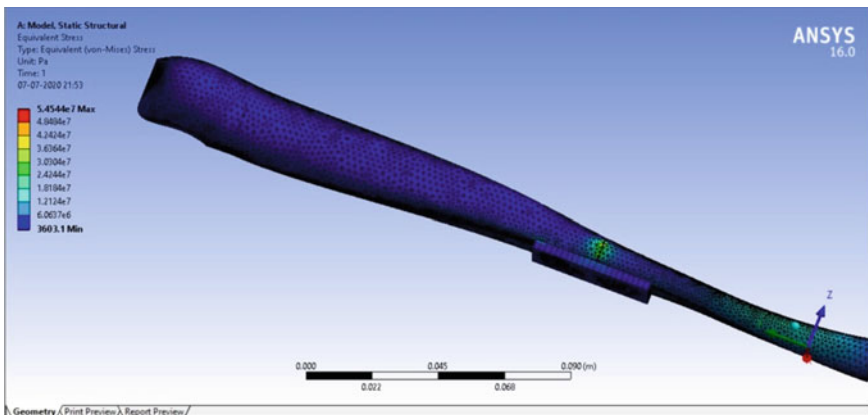


Fig. 4 Von-mises stress distribution in HPMC 2 and bone

4 Discussion

From the results the maximum von-Mises stress was observed lesser in glass/jute/polyester hybrid composite bone plate as compared to the maximum stress induced in titanium metal bone plate. Remarkably, the stress developed in the fractured bone with hybrid composite bone plate was found to be greater compared with the stress developed at the fractured bone fixed by titanium metal bone plate. Therefore, as mentioned in previous studies [6–9, 11] the bone redevelopment during healing process is greatly influenced by stress induced at the fractured area of the bone as the stress observed at the fractured area which is fixed with hybrid composite bone plate. The maximum amount of stress in Glass/Polyester composite (38.76 MPa) was observed slightly decreased compared with Glass/Jute/Polyester hybrid composite.

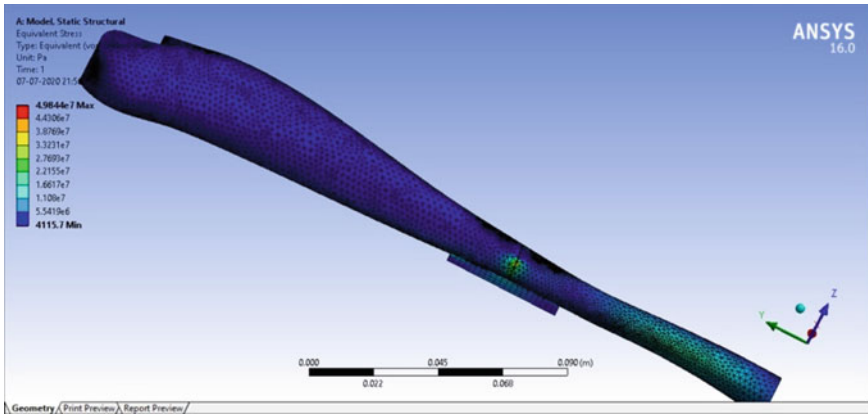


Fig. 5 Von-mises stress distribution in PMC and bone

Minimum amount of stress (6.97 MPa) was found to be in fractured bone with titanium bone plate which is lesser compared with the composite when bone is fixed with HPMC and PMC bone plates. All these results clearly revealed that maximum amount of stress can be developed in the bone at fractured area where maximum growth of bone redeveloping is anticipated by implementing the proposed glass/jute/polyester bone plate. The comparison of von-Mises stresses in various materials of fracture fixation plates are shown in Fig. 6.

In the current FE analysis the maximum stress was lowered to 16.99% in both HPMC and PMC bone plates compared with the titanium metal bone plate. On the other hand, from the stress analysis it has been clearly observed that the fractured bone with HPMC bone plates has maximum stress in comparison with the bone with titanium metal fixation plate. As a result, fractured bone fixed with HPMC plate can be evidence for increased densities as loss of mass because of bone resorption process is decreased in comparison with the fractured bone fixed with titanium metal plate. This is because as per Wolf’s law, bone regeneration and remodeling rate is high

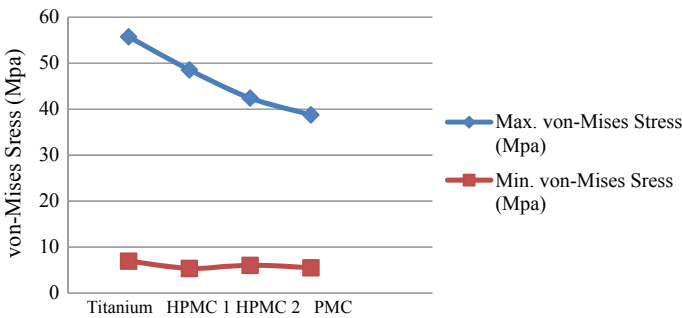


Fig. 6 Comparison of von-Mises stresses in various materials of fracture fixation plates

under high stress conditions during healing process [10]. Therefore, authors derived HPMC having a potential to minimize the effect of stress shielding and improve the healing rate of the fractured ulna bone. Though, complexity in developing desired shape of HPMC plates is more. By implementing advanced processing technique like additive manufacturing to develop suitable composite with strong fiber matrix bonding strength can be explored to produce composite material in future.

5 Conclusions

Glass and jute fibers with polyester matrix material were selected for the analysis of composite material fracture fixation plate. The derived composition of material was chosen from the design rules consideration along with implant requirements to mimic the structure and mechanical properties with natural bone. Bone with HPMC fixation plate has shown greater von-Mises stress in comparison with the fracture bone fixed with titanium metal bone plate. Therefore, it tends to be proposed that the HPMC can be an ideal decision as bone plate material to reduce the stress shielding problem with improved fracture healing rate.

References

1. Senthil PS, Maheswaran R, Vasanthanathana A (2013) Numerical analysis of fractured femur bone with prosthetic bone plates. *Procedia Eng* 64:1242–1251
2. Mehboob H, Chang SH (2015) Optimal design of a functionally graded biodegradable composite bone plate by using the taguchi method and finite element analysis. *J Comput Struct* 119:166–173
3. Naidubabu Y, Mohanarao G (2017) Design and simulation of polymethyl methacrylate-titanium composite bone fixing plates using finite element analysis: optimizing the composition to minimize the stress shielding effect. *J Mech Eng Sci* 231:4402–4412
4. Dhanopiya A, Bhargava M (2017) Finite element analysis of human fractured femur bone implementation with PMMA thermoplastic prosthetic plate. *Procedia Eng* 173:1658–1665
5. Ramírez TM, Doño MA (2017) Analysis of bone plate with different material in terms of stress distribution. *J Defect Diffusion F* 371:18–24
6. Baruaa E, Das S, Deoghare AB (2018) Development of computational Tibia model to investigate stress shielding effect at healing stages. *Matrl Today: Proc* 5:13267–13275
7. Sayed MS, Ahmed SA (2018) Optimum design and FEA of Tibia fracture composite bone plate. *J Eng Trends Technol (IJETT)* 57:89–97
8. Haka DJ, Banegasa R (2018) Evolution of plate design and material composition. *Int J Care Injured* 49:S8–S11
9. Fouda N, Mostafa R (2019) Numerical study of stress shielding reduction at fractured bone using metallic and composite bone-plate models. *J A S Eng* 10:481–488
10. Yan L, Lim JL (2019) Finite element analysis of bone and implant stresses for customized 3d-printed orthopaedic implants in fracture fixation. *J Med Biol Eng Comput* <https://doi.org/10.1007/s11517-019-02104-9>

11. Dhason R, Roy S, Datta S (2020) A biomechanical study on the laminate stacking sequence in composite bone plates for vcouver femur B1 fracture fixation. *J Comput Methods Prog* 196:1–7
12. Mehboob A, Mehboob H, Changa S (2020) Evaluation of unidirectional BGF/PLA and Mg/PLA biodegradable composites bone plates-scaffolds assembly for critical segmental fractures healing. *J Comput Part a*. 135:1–11

Dynamic Modeling and Experimental Study of Forced Convection Evacuated Tube Solar Collector Used for Grape Dryer



Amol Ubale, Dilip Panghvhane, and Parmeshwar Ritapure

Abstract The two dimensional performance model, analyzing evacuated tube solar collector system, used for grape drying is developed. A Solar collector is designed and fabricated to dry 10 kg of Thompson seedless grapes efficiently, under the forced convection heat transfer. But this article is restricted to discussion on solar collector and its thermal performance only. The collector setup consists of ten evacuated tubes of outer diameter 58 mm and length 1800 mm arranged parallel. This solar system's performance is tested experimentally and an analytical thermal model is developed by solving coupled linear differential equations using Rung-Kutta's fourth order method. The experimental data of the solar collector is compared with the analytical data of thermal model. It is observed that the developed model predicts the behavior of the actual system accurately with average percentage error in the range of 2.45–4.6% with coefficient of determination $R^2 = 0.957–0.98$. The experimental thermal efficiency of the system is observed as high as 31.2% which is higher than the thermal efficiency of the flat plate collector solar system (15%). Theoretically calculated and experimentally measured results of air outlet temperature from solar collector shown a good agreement.

Keywords Evacuated tube solar collector · Forced convection · Runge–kutta method

Nomenclature

C_f	Sp. Heat of working fluid (J/kgK)
H_{con}^{r-f}	Heat transfer coeff. betn absorber and working fluid (W/m ² k)
T_r	Absorber surface temperature (k)

A. Ubale (✉) · P. Ritapure
Zeal Education Society's College of Engineering and Research, Pune, India
e-mail: amol.ubale@zealeducation.com

D. Panghvhane
Government College of Engineering, Awsari, Pune, India

T_f	Working fluid temperature (k)
R_e	Renold's number
D	Diameter of air flow pipe (m)
T_g	Outer glass temperature (k)
H_{con}^{g-a}	Heat transfer coeff. betn outer tube and atmosphere (W/m ² k)
T_a	Atmospheric temperature (k)
μ	Viscosity of working fluid
I_G	Global solar radiation (W/m ²)
m	Mass flow rate of working fluid (kg/s)

1 Introduction

For minimizing the convective heat loss to the surrounding from the solar collector now a day evacuated tube solar collector is being used widely. A twin-glass evacuated tube is made up of strong material like; transparent borosilicate glass with the outer surface of inner tube is coated with a special selective coating (Al-Ni/Al). This coat is having excellent solar heat absorption and minimal heat reflection features. The top of the two tubes is fused together and evacuated. The sunlight enters through the outer glass tube; the heat generated is absorbed by the selective coatings and subsequently transferred to the circulating working fluid. Since evacuated tube collectors can operate under cloudy conditions, they are more efficient throughout the year and can achieve higher temperature with higher efficiency as compared to flat plate collectors.

However, evacuated tube collector is more expensive than flat plate collector [17–7]. Yadav Kumar [18] studied experimentally the performance of an evacuated tube solar air collector for different air mass flow rates. Air was used as a working fluid in the several experiments and tested in Indian climatic conditions. Sabiha [1] has thoroughly reviewed comprehensive literature on, why evacuated tube collector is preferable, its types, structures, applications and challenges. Applications of evacuated tube solar collectors in water heating, air conditioning, heat engines, solar cooker, swimming pool heating, steam generation and solar drying for industrial as well as residential sectors have been summarized and presented. Philippe [6] have developed a dynamic model of a solar evacuated tube collector under variable weather conditions to predict the performance of the system theoretically. They have validated this mathematical model with experimental results and parametric sensitivity analysis was applied to the model to improve the accuracy. Sharma [14] has studied the thermal analysis of a novel solar collector with mini channel with the help of numerical method. The novel solar collector was fabricated by using a U-shaped flat-tube absorber with the selective coating on its external surface. The working fluid was circulated inside the array of mini channels which were located at the cross-section of the absorber and along the length of evacuated tube. Two dimensional mathematical models were developed to compare the performance of the system

with experimental results. Rushi [12] has investigated experimentally an air heating system using one ended evacuated tubes powered by solar energy. The solar collector system containing forty evacuated tubes was used for air heating purpose. Naik [9] presented the analytical model of a U type evacuated tube solar collector for heating Aqueous lithium chloride solution (LiCl-H₂O), water and air used as working fluid. The developed mathematical model predicted the outlet temperature and net heat gain by the working fluid with high accuracy with that of experimental results.

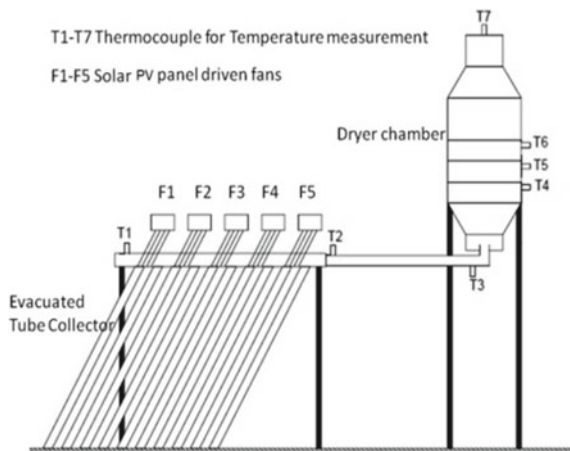
Two dimensional thermal model of the system is developed under transient conditions. Air is used as a working fluid so as to avoid freezing, overheating of working fluid. Another advantage of air as working fluid is that it can be used in an open loop cycle and risk of getting contaminated is eliminated. Variations of ambient temperature, solar radiation, mass flow rate of working fluid, and wind speed are considered in this model for the analysis of collector outlet temperature. The developed thermal mathematical model depends on the equations of energy conservation to a small control volume along the longitudinal axis of the evacuated tube. The first order differential equations for each control volume are obtained and solved by using a fourth order Runge–Kutta algorithm. In particular, dynamic modelling predicts the behaviour of collectors significantly. The experimental setup has been validated to assess the predictions given by the thermal model.

2 Materials and Methods

2.1 Experimental Setup

Evacuated tubes are made up of two coaxial borosilicate glass tubes, joined at the top and sealed at the bottom which contains a vacuum as shown in Fig. 1. The outer

Fig. 1 Solar ETC system with forced circulation (Schematic)



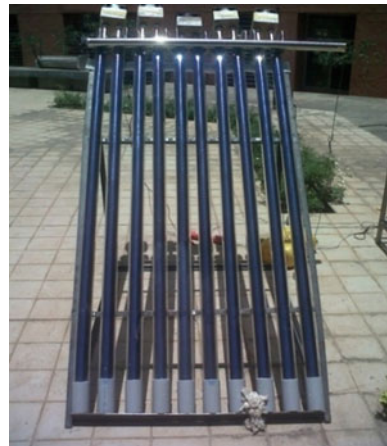
tube is a transparent tube of 58 mm in diameter and 1800 mm in length, called as cover tube. Whereas, the inner tube is of 47 mm in diameter and 1750 mm in length, which is called as Absorber Tube. The thickness of the inner tube and the outer tube is 1.6 and 2.00 mm respectively. The working fluid is circulated through the inner tube which absorbs the solar energy. The outer part of the inner tube is coated with a selective coating material (Aluminium Nitrite) for absorbing the incident solar radiation further it is transmitting to working fluid flowing through it. As the space between the outer and the inner tube is evacuated, hence it works as a thermal insulator which prevents heat losses primarily due to conduction and convection.

Thus the trapped solar energy absorbed and transmitted to a working fluid, gets prevented from escaping back to the environment (green house phenomena). Based on the design the required area of solar collector is 1.51 m^2 to collect the solar energy to dry 10 kg of Thompson seedless grapes. According to the selected size of the evacuated tube, it requires 9.28 tubes to make 1.51 m^2 exposed area of the collector.

Hence ten evacuated tubes are arranged parallel to each other and to collect the output of the individual tube, a perpendicular tube is arranged at the top of all evacuated tube. This central tube is of stainless steel material of 60 mm diameter. It is further connected to the bottom of the dryer to give the output hot air to dryer chamber.

From the literature, it is found that the angle of inclination of the solar collector is kept at a longitudinal value of location $+15^\circ$. In this setup array of tubes is inclined 45° to horizontal on a steel frame to gain maximum solar beam radiation and absorb diffused radiation as well. All the time the collector area is measured which is exposed to the direct sunlight and it is found as 1.61 m^2 . The contacting area between the supportive frame and the evacuated tube is insulated with polyethylene foam sheet with the thermal conductivity of 0.04 W/m-k , to minimize the heat losses (not shown in above Fig. 2). Forced air circulation is provided with the help of 12 V/1A five fans which run on the 15 W solar panel.

Fig. 2 Actual solar ETC system



2.2 Thermal Model of Solar ETC System

The air mass flow rate is the very important parameter which acts on the defined performance indicators. The higher is the airflow, better is the thermal efficiency but lower is the outlet working fluid temperature.

Figure 3 shows the thermal model of the evacuated tube exposed to the solar radiation. At the bottom of evacuated tubes large pressure drop is observed due to 180° change in the direction of the air flow [3–7].

The following assumptions are made to solve the set of equations,

- Heat transfer in the system is considered in one-dimension which is along the radial coordinate and axis symmetric.
- Diffused radiation gained by the actual system is neglected.
- Finite differential equation is solved for single evacuated tube and uniformity is considered to all tubes with constant mass flow rate.
- For any axial position on the tube and the cover, heat distribution is equal in azimuth direction.
- As the walls are thin, the resistances due to conduction in the glass walls are assumed negligible.
- There is only one temperature that characterizes the inner and outer surface of glass tubes and the temperature varies in the axial direction which is essential because of the heat gained by the fluid.
- The temperature dependent data for variable thermal properties with air temperature is readily available.

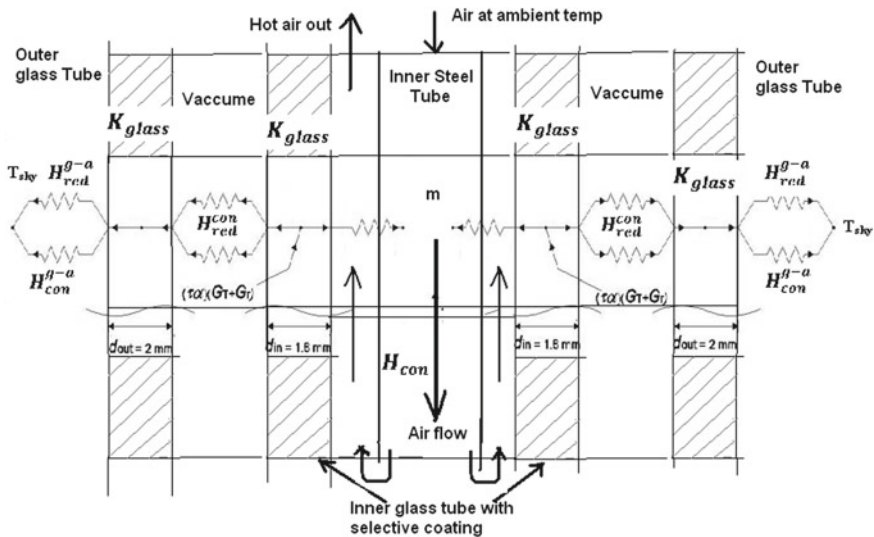


Fig. 3 Thermal model of the ETC exposed to solar radiation

Because the flow in an evacuated tube collector is completely enclosed, energy balance equation can be applied to determine the variation in mean temperature of working fluid. Also the temperature at different positions along this tube and the total convection heat transfer is related to the difference in tube inlet and outlet temperatures. For the constant mass flow rate heat gained by the working fluid is given by following equation, [8, 10, 11, 13–16]

$$C_f \left(\frac{\partial T_f}{\partial t} + u \frac{\partial T_f}{\partial x} \right) = \{H_{con}^{r-f} (T_r - T_f)\} \quad (1)$$

The evacuated tube is divided in to ‘n’ (180) segments along its longitudinal direction, the velocity of the working fluid is more as compared to the width of each segment, and hence change in fluid temperature is negligible. The velocity of the working fluid, ‘u’ is assumed to be constant, thus equation above reduces to,

$$C_f \left(\frac{\partial T_f}{\partial t} \right) = \{H_{con}^{r-f} (T_r - T_f)\} \quad (2)$$

It is considered that the heat transfer coefficient is zero due to convection, in between the inner to outer glass, as the vacuum is present. Heat transfer coefficient due to convection between working fluid and receiver is calculated by Reynolds number and Nusselt number (Nu) as follows,

$$Re = \frac{4m}{\pi D \mu} \quad (3)$$

For the turbulent flow region ($Re > 6000$), it recommended to use the correlation obtained from the relationship of Reynold number and Prandtl number (Pr), [3],

$$Nu = \frac{\frac{f}{8} (Re - 1000) Pr}{1 + 12.7 \sqrt{\frac{f}{8}} (Pr^{2/3} - 1)} \quad (4)$$

The Darcy friction factor (f) for the setup can be obtained from:

$$f = (0.79 \log Re 1.64)^{-2} \quad (5)$$

and

$$H_{con}^{r-f} = \frac{Nu k}{D} \quad (6)$$

Heat transfer to the receiver is given by the equation,

$$C_r \left(\frac{\partial T_r}{\partial t} \right) = \{ \tau \alpha I_G + \varepsilon_g \sigma (T_g^4 - T_r^4) + H_{con}^{r-f} (T_f - T_r) \} \quad (7)$$

where the product ‘ $\tau\alpha$ ’ is the transmittance absorptivity of the evacuated tube collector, ϵ_g is Emmisivity of the receiver and σ is the Stufen Boltzman constant.

Temperature of the receiver tube at the end is calculated as;

$$T_r = \frac{q^{con}}{H_{con}^{r-f}} + T_f \tag{8}$$

The outer glass tube temperature is calculated as;

$$C_g \left(\frac{\partial T_g}{\partial t} \right) = \{ \epsilon_g \sigma (T_a^4 - T_g^4) + \epsilon_g \sigma (T_r^4 - T_g^4) + H_{con}^{g-a} (T_g - T_a) \} \tag{9}$$

Equation (9) stats the change in cover temperature which is proportional to the difference between net heat gain rate by the receiver to the heat losses to the environment by radiation and convection.

The convective heat transfer coefficient between the atmosphere and the outer glass is given by the equation,

$$H_{con}^{g-a} = 5.678 + 3.8v \tag{10}$$

where, ‘ v ’ is ambient air velocity in m/s.

Finite difference method is used to solve this system. In this system, the collector is defined as a single fluid channel and it is divided into ‘ n ’ segments ($n = 180$). The single order differential equations are solved for each segment in the time domain using a 4th order Runge–Kutta method. A MATLAB-14B program is developed to solve this set of equations simultaneously. At first iteration boundary conditions like the glass temperature T_g and air temperature T_a is considered as the same.

Equations 1, 7 and 9 are solved simultaneously for the first segment (that is. $n = 0$ node). The output of the first segment is passed as an input for the next segment and so on. The last segment gives the output temperature of the outer glass tube, inner glass tube and the outlet temperature of the working fluid. Total tube length is divided in 180 segments.

Table 1 Solar ETC data for day one

Time Hrs	Solar radiation W/m ²	Ambient		Collector outlet Temp	Velocity of air m/s	Mass of air kg/s	Heat gain J/s	Thermal efficiency
		Temp	% RH					
9.00	409	23.4	32	31.2	2.3	0.01092	85.68442	13.09
10.00	649	30.8	25	51.8	2.4	0.011394	240.7188	23.18
11.00	810	31.6	22	61.2	2.5	0.011869	353.4363	27.27
12.00	847	32.5	21	67.5	2.4	0.011394	401.198	29.60
13.00	960	34.5	21	73.1	2.6	0.012344	479.336	31.21
14.00	850	35.8	19	73.5	2.3	0.01092	414.1414	30.45
15.00	780	34.8	22	68.1	2.3	0.01092	365.8066	29.31
16.00	610	32.8	25	61.3	2.2	0.010445	299.4656	30.68
17.00	490	29.8	28	51.2	2.2	0.010445	224.8619	28.68
18.00	320	25.6	31	41.2	2.1	0.00997	156.4672	30.56

Table 2 Solar ETC data for day two

Time Hrs	Solar radiation W/m ²	Ambient		Collector outlet Temp	Velocity of air m/s	Mass of air kg/s	Heat gain J/s	Thermal efficiency
		Temp	% RH					
9.00	411	23.5	29	32.1	2.4	0.010852	93.8858	14.28
10.00	651	29.7	24	52.1	2.4	0.010852	244.540	23.48
11.00	809	31.8	21	62.1	2.5	0.011304	344.566	26.62
12.00	845	32.8	20	68.2	2.7	0.012208	434.768	32.16
13.00	915	34.6	19	73.5	2.6	0.011756	460.059	31.42
14.00	880	35.7	19	73.6	2.4	0.010852	413.752	29.39
15.00	720	35.1	20	67.9	2.3	0.0104	343.156	29.79
16.00	610	33.1	23	61.2	2.3	0.0104	293.984	30.12
17.00	490	29.8	26	51	2.4	0.009948	212.153	27.06
18.00	324	25.4	31	41.3	2.4	0.009948	159.115	30.69

3 Results and Discussion

3.1 Experimental Results

Tables 1 and 2 shows the sample experimental data for a particular test. The experiments are conducted under the uncontrolled conditions of the environment. The forced air is generated by DC fans run on the solar 15 W panel. The fan speed is the function of the solar radiation, as more is the beam radiation more will be a PV panel current and voltage and hence more air is circulated through the system. The

air velocity at the exit to the solar collector is measured from 2.1 m/s to 2.7 m/s. Based on the discharge the instantaneous mass flow rate is calculated and tabulated.

The temperature of air at the inlet and outlet of the collector is measured and recorded for every hour during the test. The diurnal variation of the solar radiation ambient air temperature (T_{sky}) and relative humidity, collector outlet temperature, mass flow rate and instantaneous thermal efficiency of the ETC system is shown in Tables 1 and 2.

During the test time, solar radiation varies from 380 to 925 W/m², with the average solar radiation value 730 W/m² in the month of April where as it rises to the average value of 830 W/m² with highest solar radiation of 1050 W/m² in the month of May during the year 2013–2015. The ambient air temperature varies in the range of 23–35 °C in the month of April and it goes up to the maximum ranges from 35.8 °C to 38.3 °C in the month of May.

The minimum average temperature range is 24.3–25.9 °C during the test time. The maximum gain in the temperature is observed to 42 °C, which is quite high as compared to other type of solar collector. The maximum collector outlet temperature reached to 80.5 °C to a mass flow rate of air 0.0113Kg/s with average out let temperature of collector is 55.1 °C. The mass flow rate is directly proportional to the voltage generated by the solar PV panel. This voltage is a function of the solar radiation. Hence the mass flow rate in the afternoon is observed higher during 12 noon to 2 pm.

3.2 Simulated Collector Output

Below Tables 1 and 2 gives the detail about the thermal properties of the solar ETC system along with their properties. The program out is calculated for a single evacuated tube and it considered as same for all the tubes.

As all the ten tubes are arranged as parallel to each other, together the mass flow rate will be increased and temperature output of all tubes will remain the same as no considerable changes are observed in input parameters to each tube.

The Tables 3, 4 and Figs. 4, 5 illustrates the software calculated values of collector outlet temperature.

Figure 4 is a plot of the single day collector outlet working fluid temperature variation. This shows simultaneously the outlet temperature values measured using accurate measuring instruments and analytically calculated values at the same point. Last column in the Tables 3 and 4 demonstrates the percentage error in individual reading, which is observed in the range of 1.07–6.98% with the total average percentage error of 2.46% which is well within the acceptable limit.

Similar kinds of results are observed for all experimental data when analyzed theoretical as explained in the Fig. 5 with the percentage error between experimental and analytical collector outlet temperature in the range of 1.5–7.06%. The total average percentage error is 3.55% with $R^2 = 0.985$, which is also well within the acceptable limit. The Fig. 5 shows the plot of actual/experimental versus predicted

Table 3 Experimental and theoretical collector outlet temperature

Time in Hrs	Solar radiation	Ambient temp	Collector outlet Temp. (Actual)	Collector outlet Temp (Analytical)	% error
9.00	411	23.5	32.3	31.8	1.57232
10.00	651	29.7	52.3	54.8	4.56204
11.00	809	31.8	62.3	65.4	4.74006
12.00	845	32.8	68.3	71.3	4.20757
13.00	915	34.6	73.8	77.3	4.52781
14.00	880	35.7	73.4	76.1	3.54796
15.00	720	35.1	67.6	71.4	5.32213
16.00	610	33.1	63.4	62.2	1.92926
17.00	490	29.8	54.3	57.2	5.06993
18.00	324	25.4	40.8	43.9	7.0615
Average % error					3.5537

Table 4 Experimental and Theoretical collector outlet temperature

Time in Hrs	Solar radiation	Ambient temp	Collector outlet Temp (Actual)	Collector outlet Temp (Analytical)	% error
9.00	409	23.4	32.1	30.6	4.90196
10.00	649	30.8	52.1	54.5	4.40367
11.00	810	31.6	62.1	65.4	5.04587
12.00	847	32.5	68.2	71.4	4.48179
13.00	920	34.5	73.5	74.6	1.47453
14.00	850	35.8	73.6	74.4	1.07527
15.00	713	34.8	67.9	70.3	3.41394
16.00	530	32.8	63.2	61.9	2.10016
17.00	464	29.8	54.1	57	5.08772
18.00	320	25.6	41.3	44.4	6.98198
Average % error					2.496

Fig. 4 Diurnal Collector outlet temperature experimentally and theoretically

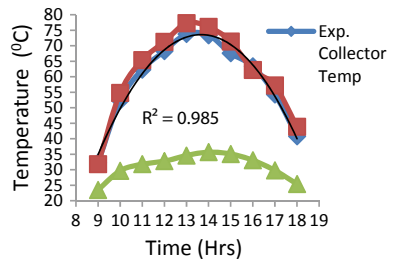
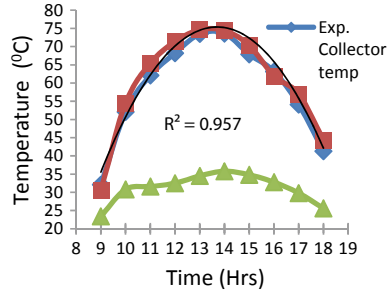


Fig. 5 Diurnal Collector outlet temperature experimentally and theoretically



collector outlet working fluid temperature for a single day. It is observed that the predicted and experimental values are in good agreement with $R^2 = 0.984$. Similar kinds of results are observed in all experimental and predicted values. It indicated that the simulated mathematical model is accurate.

4 Conclusion

The performance of solar evacuated tube collector is studied analytically and experimentally. A set of single order differential equations are formed which simulates the performance of the system. These equations are solved numerically by 4th order Runge–Kutta method with the help of MATLAB program. To simulate the flow analysis certain assumptions are made and collector outlet fluid temperature is calculated for a single tube, by considering there will not be much variation in physical data like mass flow rate and solar radiations, among all evacuated tubes. The validation of the simulated results is done with the experimental values. It is observed that the average percentage error in the actual collector outlet temperature and simulated or analytically calculated value is in the range of 2.45–4.6% with average coefficient of determination $R^2 = 0.973$ to for all experiments. Hence it is concluded that the actual collector outlet working fluid temperature has good agreement with calculated collector outlet working fluid temperature with developed thermal model.

References

1. Aed IO, Mohd T, Hassan I, Husan S (2014) The heat losses experimentally in the evacuated tube solar collector system in Baghdad-Iraq climate. *Int J Res Eng Technol* 2:13–23
2. Ayyappan S, Mayilsamy K (2010) Experimental investigation on a solar tunnel drier for copra drying. *J Sci Ind Res* 69:635–638
3. Belessiotis V, Delyannis E (2011) Solar drying. *Sol Energy* 85:1665–1691
4. Duffie J, Beckman W (2013) *Solar engineering of thermal processes*, 5th. Wiley, New York

5. Gang P (2012) Comparative experimental analysis of the thermal performance of evacuated tube solar collector system with and without mini compound parabolic concentrating reflector. *Energy* 3:911–924
6. Jean P, François (2005) Dynamic modeling and elements of validation of solar evacuated tube collectors. In: Ninth international IBPSA conference, pp 15–18
7. Lamnatou C, Papanicolaou E, Belessiotis V, Kyriakis N (2012) Experimental investigation and thermodynamic performance analysis of a solar dryer using an evacuated-tube air collector. *Appl Energy* 94:232–243
8. Mahesh A, Sooriamoorthi C, Kumaraguru A (2012) Performance study of solar vacuum tubes type dryer. *J Renew Sustain Energy* 4:13–19
9. Naik K, Varshey A (2016) Modelling and performance analysis of U type evacuated tube solar collector using different working fluids. *Energy Proce* 90:227–237
10. Pangavhane D (2002) Comparative drying performance study of natural convection solar dryer with traditional grape drying method. *Int J Energy* 3:13–22
11. Pannlal S (2011) Silk cocoon drying in force convection solar dryer. *Appl Energy* 88:1720–1726
12. Rushi P (2012) Performance analysis of the solar water heater with flat plate collector using computer program. *Int J Eng Res* 1:67–79
13. Shah L (2007) Theoretical flow investigations of an all glass evacuated tubular collector. *Sol Energy* 81:822–828
14. Sharma N (2011) Performance analysis of a novel evacuated solar tube collector based on micro channels. *Sol Energy* 85:881–890
15. Taha A, Eissa A (2009) Simulation model of flat plate solar collector performance. In: *Proceeding of the first scientific conference for marketing the applied university research*, pp 421–429
16. Ubale A, Pangavhane D, Auti A (2017) Performance analysis of forced convection evacuated tube solar collector used for grape dryer. *J Eng Sci Technol* 12:42–53
17. Walker A, Mahjouri F (2004) Evacuated-tube heat-pipe solar collectors applied to the recirculation loop in a federal building. *Am Sol Energy Soc Conf Proceed* 1–6
18. Yadav A, Bajpai V (2011) An experimental study on solar tube collector used for air heating in India. *Int J Mech Aero Ind Mechatr Manuf* 5:1188–1193

Effect Analysis of Process Parameters on Lubricated Sliding Wear of Al–25Zn–2Cu–2.5Si Alloy for Plain Bearing Application



Parmeshwar P. Ritapure, Y. R. Kharde, Amol Ubale, and B. D. Aldar

Abstract The present study is an attempt to model lubricated sliding wear of Aluminum Zinc alloy and wear parameters. The effect of wear parameters like applied load, sliding speed and sliding time (distance) on the lubricated sliding wear of the alloy have been investigated using pin-on-disc tribometer with EN24 shaft steel disc as per Taguchi L_9 orthogonal array. The analysis of variance and developed regression equations were used to investigate the influence of parameters on the wear of alloy. The pin temperature is identified as the most influencing factor for the wear and friction characteristics of the composites. The developed linear and Non-linear regression models were found capable for predicting the lubricated sliding wear behavior of the alloy. Finally, confirmation tests were conducted to verify the experimental results foreseen from the mentioned correlations.

Keywords Aluminium Zinc alloy · Analysis of variance · Confirmation test · Orthogonal array · Sliding wear · Wear parameters

1 Introduction

Implementation of Tribology provides economic and environmental benefits by reducing energy loss due to friction and wear, loss due to breakdowns, depreciation of machinery and overall global carbon emissions. The wear and friction at tribo-contact can be reduced successfully by the use of novel materials, low viscosity lubricants, material treatment, surface modification and material coating [1].

Tribological performance of Zn-Al alloy have been tested and applied in a variety of engineering applications. These alloys were found to be superior to the traditional bearing materials including bronze [2], cast iron [3], steel, plastics etc. as far as their high resistance to wear, high strength, low density, low cost and low coefficient of

P. P. Ritapure (✉) · A. Ubale · B. D. Aldar
Department of Mechanical Engineering, Zeal College of Engineering and Research, Pune, India
e-mail: ritapurep@yahoo.co.in

Y. R. Kharde
Department of Mechanical Engineering, Pravara Rural Engineering College, Ahmednagar, India

friction concerned. However, these alloys have limited applications involving high stress conditions due to its lower creep resistance, compared to traditional aluminum alloys and other structural materials, especially at temperatures above 100 °C [4]. The second important problem relating to zinc–aluminum alloys refers to dimensional instability and lower ductility [5]. It has been shown that this problem could be reduced through alloying with different elements such as Cu, Si, Ni, Mn and Mg etc. [6, 7]. Also, it has been shown that zinc-based alloys can be successfully replaced by aluminum based alloys for tribological applications. Aluminum Zinc (AZ) alloy was found to be superior to bearing bronzes and comparable to the zinc-based commercial alloys as far as their mechanical and tribological properties concerned [4, 8, 9]. Also, Silicon was found to be most effective alloy addition towards improving mechanical and tribological properties of AZ alloys. It has been shown that the highest wear resistance was obtained with Al–25Zn–2Cu–2.5 Si alloy [10, 11]. However; the effect of process parameter on lubricated sliding wears of Al–25Zn–2Cu–2.5 Si alloy has not been investigated. Therefore, the aim this research work was to investigate the effect of wear parameters such as sliding speed, pressure, sliding time (distance) on lubricated sliding wear behavior of the Al–25Zn–2Cu–2.5 Si alloy and to establish correlation between them.

2 Experimental Studies

2.1 Alloy Preparation

Al–25Zn–2Cu–2.5Si was prepared from commercially pure aluminium (99.2%), high purity Zinc (99.8%), electrolytic copper (99.97%). Alloys were melted in an electric furnace and poured at a temperature of 680 °C into a steel mould at room temperature. The mould had a cylindrical shape with a length of 155 mm and diameter of 18 mm. The chemical compositions of the alloys were determined by atomic absorption analysis method.

2.2 Wear Test Experimental Setup

The friction and wear tests were carried out using single pin type “Pin-on-disc friction and wear monitor TR20”, Ducom make, Bangalore. Tests were carried out at the room temperature under wet operating condition. Lubrication was provided by dropping SAE 20 W/40 oil on to the revolving disc at the rate of 1.5 cm³/h. The cylindrical Pin flat ended specimens of size 10 mm diameter and 25 mm length were tested against EN-31 steel disc (0.62%Si–0.35Mn–1.02C–1.05Cr–0.3Ni). The average

surface Roughness value Ra of disc before test was measure as 0.5 μm . Measurement of Ra value was obtained by using “Taylor-Hobson: Surtronic-10”, Denmark instrument with least count of 0.1 μm .

2.3 Plan of Experiments

The experiments were conducted as per the $L_9 3^3$ orthogonal array. The selection of the orthogonal array was based on the condition that the degrees of freedom for the orthogonal array should be greater than or equal to sum of those wears parameters. The wear parameters chosen for the experiments and their levels are shown in Table 1.

3 Results and Discussions

On conducting the experiments as per orthogonal array, the wear results for various combinations of parameters were obtained and are shown in Table 2.

Both linear as well as nonlinear regression analysis have been carried out, based on the data collected as per design of experiments, which are discussed below. To establish the correlation between sliding wear and the wear parameters, a multiple linear regression models is obtained using statistical software “Design Expert”. The

Table 1 Process parameters and their levels

Level	Speed V (m/s)	Load P (MPa)	Sliding time T (min.)
-1	1.0472	0.3747	30
0	2.0944	0.3747	60
1	3.1416	1.1421	90

Table 2 Orthogonal array $L_9 (3^3)$ of Taguchi with actual values

Test Run	Velocity (m/s)	Pressure (MPa)	Time (min.)	Wear (micron)
1	1.0472	0.3747	30	21
2	1.0472	0.7584	60	50.5
3	1.0472	1.1421	90	94
4	2.0944	0.3747	60	40
5	2.0944	0.7584	90	82
6	2.0944	1.1421	30	29
7	3.1416	0.3747	90	70
8	3.1416	0.7584	30	15
9	3.1416	1.1421	60	70

Table 3 Model fit summary

Source	Sum of squares	DF	Mean square	F value	p-value Prob > F	
Mean versus Total	24,701.4	1	24,701			
Linear versus Mean	6119.2	3	2039.7	51.9	0.0003	Suggested
2FI versus Linear	191.1	3	63.7	22.9	0.0421	
Quadratic versus 2FI	5.6	2	2.8			Aliased
Cubic versus Quadratic	0	0				Aliased
Residual	0	0				
Total	31,017.3	9	3446.4			

Table 4 Model Summary Statistics

Source	Std. Dev	R-squared	Adjusted R-squared	Predicted R-squared	Press	
Linear	6.27	0.969	0.95	0.874	798.6	
2FI	1.67	0.999	0.996	0.945	344.5	Suggested
Quadratic					+	Aliased
Cubic					+	Aliased

terms that are statistically significant are included in the model. From Tables 3 and 4 it is observed that for predicting the wear behaviour of material the 2FI (Factorial interaction) Model is better as compared to the Quadratic, Cubic Model. Hence 2FI Model is used for linear regression analysis.

3.1 Linear Regression Analysis for 2FI Model

The statistical analysis is carried out for a level of significance of 5% i.e. the level of confidence 95%. In Table 5 the F-value of 378.6 implies the model is significant. There is only a 0.26% chance that a “Model F-Value” this large could occur due to noise. Values of “Prob > F” less than 0.050 indicate model terms are significant. In this case B, C, AC and BC are significant model terms. Values greater than 0.10 indicate the model terms are not significant.

The last column in Table 5 shows the percentage contribution of each factor on the total variation indicating their degree of influence on the result. One can observe that the influence of sliding time (65.1%), pressure (24.8%) and sliding speed (4.5%) on the wear. The interaction between the parameter does not have significant influence on the wear. Also, individual and interaction effect of process parameter on wear has

Table 5 ANOVA results for 2FI Model

Source	Sum of squares	DF	Mean square	F Value	p-value Prob. > F	% contribution
Model	6310.3	6	1051.7	378.6	0.0026	Significant
A-velocity	6.5	1	6.5	2.3	0.2662	4.5
B-pressure	512.8	1	512.8	184.6	0.0054	24.8
C-time	2503.3	1	2503.3	901.2	0.0011	65.1
AB	2.4	1	2.4	0.9	0.4523	0.2
AC	61.9	1	61.9	22.3	0.042	2
BC	51.5	1	51.5	18.5	0.0499	1.6
Residual	5.6	2	2.8			
Cor. Total	6315.9	8				

been shown in Figs. 1, 2, 3, 4 and 5. Table 6 shows the predicted R-squared of 0.95 is in reasonable agreement with the adjusted R-squared of 0.91. Adequate precision measures the signal to noise ratio. A ratio greater than 4 is desirable [12, 13]; the ratio of 52.93 indicates an adequate signal.

Final Equation in Terms of Coded Factors:

$$Wear = 52.39 + 1.57A + 13.98B + 30.88C + 1.43AB + 7.29AC + 6.64BC \quad (r^2 = 95.12) \quad (1)$$

Fig. 1 Effect of velocity on wear of material

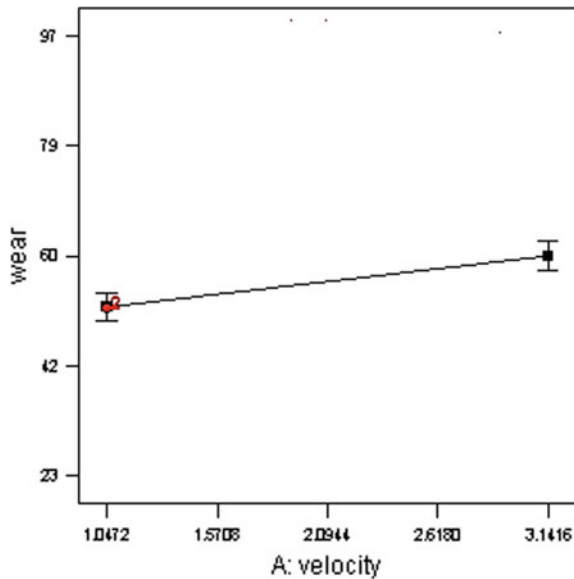


Fig. 2 Effect of pressure on wear of material

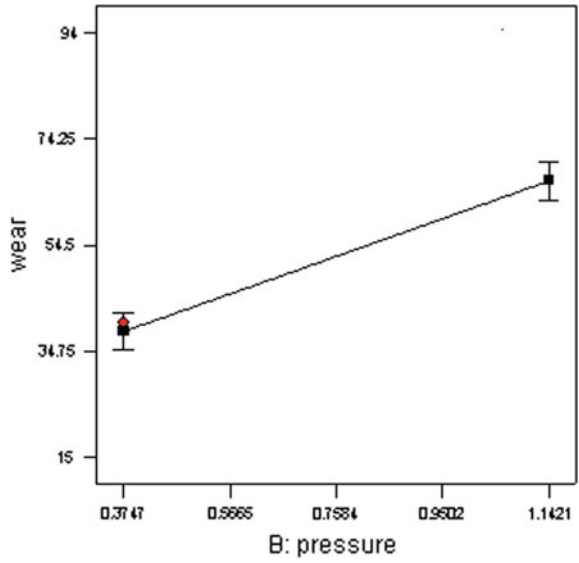
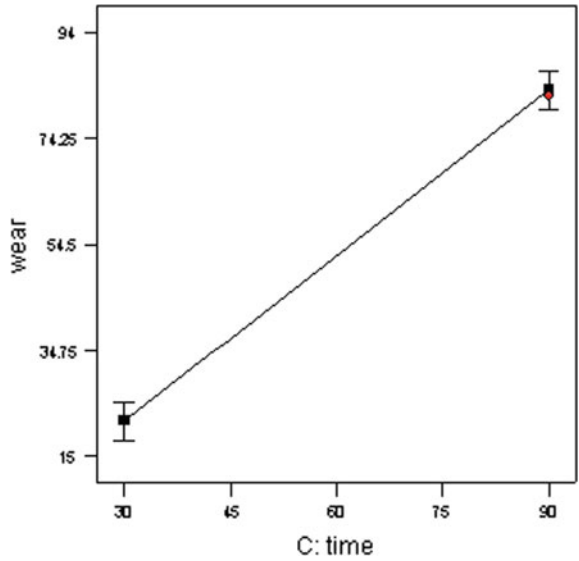


Fig. 3 Effect of time on wear of material



Final Equation in Terms of Actual Factors:

$$\begin{aligned} \text{Wear} = & 20.9 - 15.11 \times V + 5.64 \times P + 0.10 \times T + 3.5 \times V \times P \\ & + 0.23 \times V \times T + 0.57 \times P \times T \end{aligned} \tag{2}$$

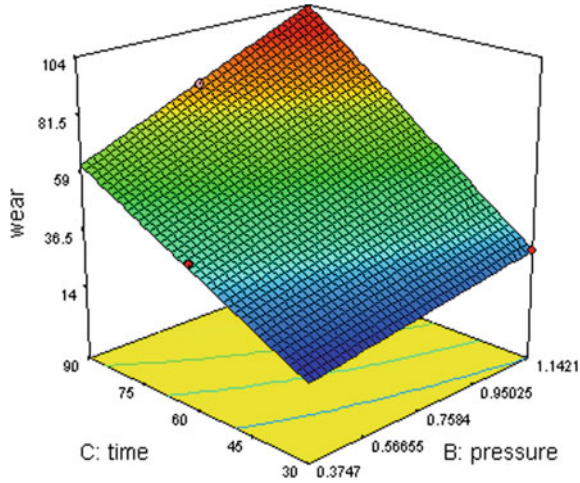


Fig. 4 Interaction effect of pressure and time on wear

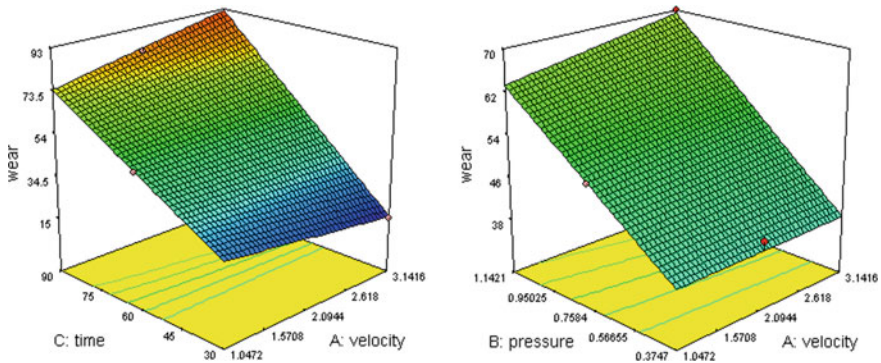


Fig. 5 Interaction effect of time and velocity and pressure and velocity on wear of material

Table 6 Model statistics for 2FI Model

Std. Dev	1.7	R-squared	0.95
Mean	52.4	Adjusted R-squared	0.91
C.V. %	3.2	Predicted R-squared	0.87
Press	344.5	Adequate precision	52.93

If we substitute the recorded values of the variables in the above equation the sliding wear of the alloy can be calculated. The positive value of the coefficient suggests that the sliding wear of material increases with their associated variables. Whereas the negative value of the coefficient suggest that the sliding wear of the material will decreases with the increase in associated variables [14].

Table 7 Regression Variable results for nonlinear model

Variable	Value	Std.d error	t-ratio	Prob.(t)
a	0.1192	3.8E-02	3.1	0.02688
b	0.3945	4.1E-02	9.6	0.0002
c	1.0613	5.3E-02	20.1	0.00001
k	0.735	2.3E-01	-1.3	0.24423

Table 8 ANVOA for nonlinear model

Source	DF	Sum of squares	Mean square	F ratio	Prob.(F)
Regression	3	5405	1801.8	238.3	1.00E-05
Error	5	38	7.6		
Total	8	5443			

Coefficient of Multiple Determination (R²) = 0.90

Adjusted coefficient of multiple determination (Ra²) = 0.92

3.2 Nonlinear Regression Analysis

Non-linear regression analysis can be carried out of its different forms, such as quadratic, cubic, power, and others. In the present Model the input–output relationships are assumed to follow the form given below.

$$Wear = K \times P^a \times V^b \times T^c \tag{3}$$

where k is constant and a, b, c are the coefficients of the model under consideration and these are obtained using the statistical software. The equation obtained is as follows

$$Wear = 0.735 P^{0.119} V^{0.394} T^{1.0613} \tag{4}$$

Substitute the recorded values of the variables in the above equation the sliding wear of the material can be calculated. Tables 7 and 8 shows regression variable and ANVOA for Nonlinear model.

3.3 Comparison of 2FI and Nonlinear Model

Wear values obtained from experimentation and predicted by statistical software were compared for the set of 9 randomly generated tests as shown in Table 9. The percentage deviations in the wear values were determined by using the Eq. 5 which

Table 9 Comparison between 2FI and Nonlinear Model

Run order	Wear value (micron)			% deviation in wear value	
	Experimental	Predicted by 2FI model	Predicted by nonlinear model	Experimental and Predicted by 2FI model	Experimental and Predicted by nonlinear model
1	21	21.32	18.55	-1.51	11.69
2	50.5	50.82	51.11	-0.63	-1.21
3	94	93.6	92.38	0.42	1.73
4	40	38.41	42.04	3.97	-5.09
5	82	83.27	85.37	-1.55	-4.11
6	29	28.84	31.27	0.55	-7.82
7	70	69.37	67.84	0.91	3.08
8	15	15.79	15.97	-5.29	-6.3
9	70	69.37	68.48	0.91	2.17

is shown in Table 9.

$$\% \text{deviation} = \frac{(\text{Actual value} - \text{Predicted value})}{(\text{Actual value})} \times 100 \tag{5}$$

Figure 6 shows the deviation for the 9 test trial. From Fig. 6, it is observed that the 2FI model has small deviation from the mean as compared with the nonlinear models. Also from the ANOVA of both the models (Tables 6 and 8) R² value of 2FI model is 0.95 and for nonlinear model 0.90. From the above discussion; it can be observed that the 2FI model is more accurate than the non-linear models for the prediction of wear of the alloy.

Table 10 Parameters for confirmation wear test

Test	Speed (m/s)	Load (Mpa)	Time (min.)
1	1.57	1.124	30
2	0.52	0.999	30
3	2.61	0.5	30

Table 11 Confirmation test results

Test	Predicted wear (micron)	Experimental wear (micron)	Error %
1	315	338	6.79
2	362	376	3.67
3	176	189	6.8

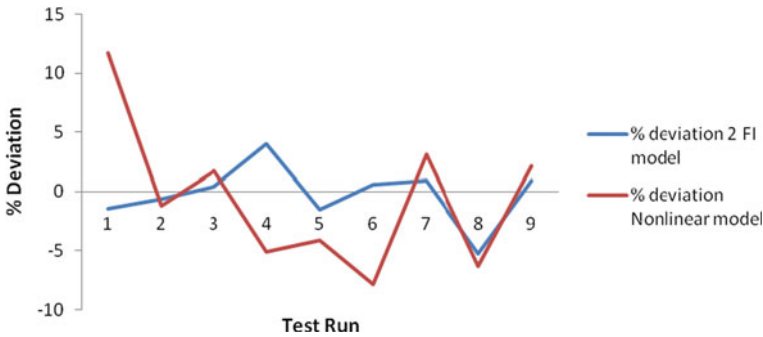


Fig. 6 Comparison of 2FI model and nonlinear model

3.4 Confirmation Test

To test the accuracy of the model the confirmation test were performed by selecting the set of parameters as shown in Table 10. The wear values obtained from the confirmation tests were compared with wear values calculated using Eq. 2 for the set of parameters which are shown Table 11.

From the analysis of Table 11, we can observe that the calculated error varies from 3.67% to 6.8% for wear. Therefore the multiple regression Eq. 2 derived above correlate the evaluation of wear in the alloy with the degree of approximation.

4 Conclusions

The following are the conclusions drawn from this study:

1. The lubricated sliding wear rate of material is dominated by process parameters in the order of sliding time, pressure and sliding speed.
2. The interaction between the parameter does not have significant influence on the wear.
3. The 2FI model is found more accurate as compared with the non-linear model for the prediction of wear of material
4. From the confirmation test result, it is observed that the calculated error varies from 3.67% to 6.8% for the wear. Therefore the multiple regression equation derived; correlate the evaluation of wear in the alloy with the degree of approximation.

References

1. Kenneth H, Ali E (2019) The impact of tribology on energy use and CO₂ emission globally and in combustion engine and electric cars. *Tribo Int* 135:389–396
2. Prasad BK, Yegneswaran AH (1997) Influence of the nature of micro constituents on the tensile properties of a zinc-based alloy and a leaded-tin bronze at different strain rates and temperatures. *J Mater Sci* 3:1169–1175
3. Prasad BK (2007) Dry sliding wear response of zinc-based alloy over a range of test speeds and loads: a comparative study with cast iron. *Tribo Lett* 25(2):103–115
4. Gencaga P, Temel S, Samuel M (2002) Dry sliding friction and wear properties of zinc based alloys. *Wear* 252:894–901
5. Temel S, Osman B, Yasin A (2009) Developing aluminium–zinc-based a new alloy for tribological applications. *J Mater Sci* 44:1969–1976
6. Ahmet T, Mehmet DE (2007) The effect of manganese on the microstructure and mechanical properties of zinc–aluminum based ZA-8 alloy. *J Mater Sci* 42:8298–8305
7. Babic M, Slobodan M (2010) The influence of heat treatment on the sliding wears behavior of a ZA-27 alloy. *Tribol Int* 43:16–20
8. Perrin C, Shenton P (2001) Aidan Dana Corporation.: Aluminum alloy and method for production thereof. Patent No. WO 01/34330 A1
9. Kang HS (2014) Hyundai Motor Company, Seoul (Kr) Wear resistant alloy having complex microstructure. Application No. 14/270,674, Patent No. US2014/0334970A1
10. Temel S, Zeki A (2008) An investigation of lubricated friction and wear properties of Zn–40Al–2Cu–2Si alloy in comparison with SAE 65 bearing bronze. *Wear* 264:920–928
11. Ali PH, Merve C (2020) Effects of titanium addition on structural, mechanical, tribological and corrosion properties of Al-25Zn-3Cu and Al-25Zn-3Cu-3Si alloys. *Trans Nonferr Met Soc China* 30: 303–317
12. Holman JP (1994) *Experimental methods for engineers*, 6th edn. McGraw Hill, Inc., Singapore, pp 34–10
13. Basavarajappa S, Chandramohan G (2005) Wear studies on metal matrix composites: a taguchi model. *J Mater Sci* 21:815–850
14. Gupta SP (2004) *Statistical methods*. Sultan Chand, New Delhi, pp 436–476

Development of Air Controlled Cotton Cleaning Machine in Blow Room Part II Calculating Trash Content by Shirley Analyzer



P. S. Hibare and B. B. Deshmukh

Abstract In textile industries cleaning of cotton is important thanks to impurities which are present within the cotton such as firestones, leaves; seeds etc. fiber cleanliness influences the process ability of cotton and yarn [1]. Conventional machineries used for cleaning uses mechanical beaters for opening and cleaning of fibers. The change in the settings of beaters at different stages of blow room changes the cleanliness of fibers. This paper deals with the air controlled cotton cleaner whose main advantage is that it doesn't varies the setting in the least and also the compressed air which is available in mill premises itself and also it requires less maintenance.

Keywords Firestone · Opening · Cleanliness · Process ability

1 Introduction

The staple for the manufacture of cotton yarn comes generally within the sort of highly compressed bales of cotton. Each bale consists of a really sizable amount of tightly packed layers of tufts of cotton and every tuft contains hundreds and thousands of fibers [2]. The cotton tufts contain, compressed between the fibers, an outsized quantity of foreign matter, leaves and cotton seed particles. It is the matter for the spinner to open out these cotton bales, eliminate trash content as far as possible and prepare a good strand of carded sliver [3]. High degree of cleaning of fibers is important permanently quality yarn but how does this cleaning occur is additionally equally important [4]. This paper represents the method of cleaning of cotton in blow room, in blow room the cottons are available bales which weighs approximately 150 kg through bale plucking machine, it feeds the cotton into cleaner where with the help from beaters the fibers get opened and cleaned and waste is collected.

P. S. Hibare (✉) · B. B. Deshmukh

Department of Mechanical Engineering, Walchand Institute of Technology, Solapur, Maharashtra, India

1.1 Problem Identification

In conventional cotton cleaner in blow room the opening is completed with the assistance of mechanical beaters. Thanks to impurities which are present within the cotton, when it gets beaten on the the surface of the beaters it makes thudding sound also affects the standard of the fibers. Thanks to pebbles which are present within the cotton it also causes fire hazards and jamming of beater [5]. To beat the above problems this projects are undertaken to develop air controlled cotton cleaner by using the existing compressed air which is in company premises itself. This project will reduce power consumption and improves the standard of fiber.

1.2 Findings from Literature

From previous researches we have observed that the amount of trash present within the cotton influences the formation of faults during spinning process. The common faults during spinning are lap weight variation, neps formation etc. [6]. A higher degree of opening in blow room, good cleanliness and maintenance of machinery reduce the fault formation. The common faults during blow room are neps formation, lap licking and curly cotton etc. [7]. The heavy particles such as pebbles which are present in the cotton are the main reason behind the often breakdowns and reduction of quality [8].

2 Calculating Trash with Shirley Analyzer

2.1 Introduction of Shirley Analyzer

The measurement of trash or non-lint content is extremely important in assuring the lint quality of cotton sample. The Shirley Analyzer is a laboratory machine developed at the Shirley Institute, Manchester, England, provides an effective method for trash analysis of waste in cotton lint. The Shirley analyzer separates the trash from the lint. This is probably the nearest approach to perfect separation of lint and foreign matter. The following Fig. 1 shows the Shirley analyzer.

2.2 Working Principle of Shirley Analyzer

The Shirley analyzer works on the principle of air flotation principle by air currents. The Shirley analyzer consists of a feed roller, licker, the cylinder and a blower to open the fibers and separate lint and trash. The cotton is fed slowly to the licker and, it



Fig. 1 Shirley analyzer

is broken up, the air current carries the lint around the bottom of the float plate and up to the condenser. Trash and heavy particles drop into the waste collection. The machine is so made that not only raw cotton but also various waste products are continuously analyzed. The working analogous that of miniature carding machine.

2.3 Procedure of Analysis

- Clean the instrument and therefore the containers
- Shake the specimen in order that large particles of waste materials etc. are runaways from the specimen.
- Open out the hard lumps of fibers, if present
- Spread the cotton sample on the feed plate with the sort of an same layer
- Start the machine and let the lint content and trash collect in their chambers
- Take out the waste lint from the lint chamber and pass it again through the machine without any changes the waste matter within the settling chamber
- Stop the machine and collect the primary lint (L1) from the lint chamber and keep it separate.
- Remove all the waste particles containing lint sample from the tray and settling chamber and again pass it through the machine.
- Collect the lint secondary (L2) and keep it during a separate chamber. Collect all the discarded matter (T1) in the tray, settling chamber and any seeds clinging to the wires of the licker the cylinder and combine them
- Weigh the discarded matter (T1), which contains lint again through the machine and ignore the waste matter collect. Collect the final lint (L3) and keep it during a separate container. Weigh the final lint (L3) with an accuracy of 10 mg
- Mix all the portions of lint (L1, L2, and L3) and weight with accuracy of 10 mg.
- Continue the equivalent process for more accuracy

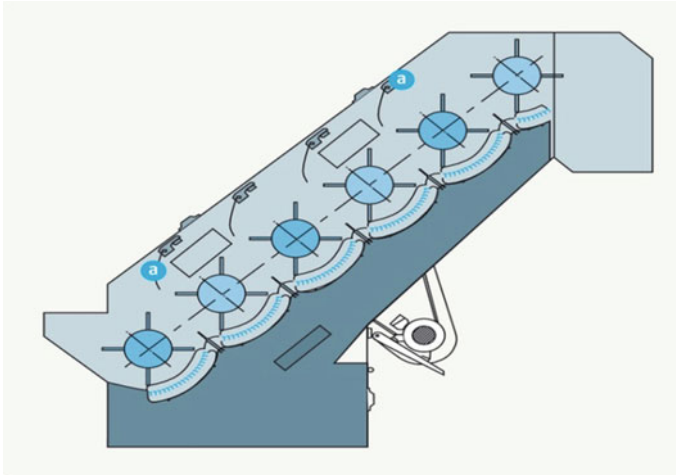


Fig. 2 Conventional cotton cleaner in blow room [8]

2.4 Conventional Cleaner in Blow Room

Firstly the fabric falls into the feed hopper and passes through the primary beater. After that carried above by the six beaters, each carrying grid bars and therefore the beaters are arranged on a line inclined upward at 45°. Elimination of waste particles takes place from the continual passage of the fabric over the grid bars arranged underneath the rollers [9]. Some step cleaners have a high flow chamber with special baffle plates (a) to enhance cleaning intensity. The grids are adjustable. The following Fig. 2 shows the conventional cotton cleaner used.

2.5 Cleaning Efficiency of Conventional Cotton Cleaner

The cleaning efficiency of blow room is defined as the difference between the percentage of trash in the bale cotton fed to blow room and percentage of trash in the lap delivered as percentage of trash in cotton [10]. For this purpose the machinery is use this Shirley analyzer which directly shows the percentage of trash present in the cotton. For this process total 3 no of samples were taken from lap fibers. In this machine the cotton is fed into the feeding tray where it performs its operation on the raw or processed cotton and shows the result with the help of calculations. This analyzer is present in the statistical quality control department of the company.

In this process 3 samples of 100 gm were taken from different bales of cotton and trash percentage and cleaning efficiency is calculated.

Sample 1

We determined these quantities from Shirley analyzer,

$$L_2 \text{ (Pure Lint)} = 74.48 \text{ gm.}$$

$$L_4 = 10.08 \text{ gm.}$$

$$L_5 = 4 \text{ gm.}$$

$$T_5 \text{ (Total trash)} = 9.2 \text{ gm}$$

$$\begin{aligned} \text{Lint Percentage} &= L_2 + L_4 + L_5 = 74.48 + 10.08 + 4 \\ &= 88.56 \end{aligned} \quad (1)$$

$$\text{Trash Percentage} = T_5 = 9.2\%$$

$$\begin{aligned} \text{Cleaning efficiency} &= [(T_5 - L_5)100] \div T_5 \\ &= [(9.2 - 4)100] \div 9.2 \\ &= 56.52\% \end{aligned} \quad (2)$$

Sample 2

We determined these quantities from Shirley analyzer,

$$L_2 \text{ (Pure Lint)} = 71.29 \text{ gm.}$$

$$L_4 = 9.56 \text{ gm.}$$

$$L_5 = 3.4 \text{ gm.}$$

$$T_5 \text{ (Total trash)} = 8.5 \text{ gm}$$

$$\begin{aligned} \text{Lint Percentage} &= L_2 + L_4 + L_5 = 71.29 + 9.56 + 3.4 \\ &= 84.25 \end{aligned}$$

$$\text{Trash Percentage} = T_5 = 8.5\%$$

$$\begin{aligned} \text{Cleaning efficiency} &= [(T_5 - L_5)100] \div T_5 \\ &= [(8.5 - 3.4)100] \div 8.5 \\ &= 60.00\% \end{aligned}$$

Sample 3

We determined these quantities from Shirley analyzer,

$$L_2 \text{ (Pure Lint)} = 71.53 \text{ gm.}$$

$$L_4 = 9.42 \text{ gm.}$$

$$L_5 = 3.7 \text{ gm.}$$

$$T_5 \text{ (Total trash)} = 8.9 \text{ gm}$$

$$\begin{aligned} \text{Lint Percentage} &= L_2 + L_4 + L_5 = 71.53 + 9.42 + 3.7 \\ &= 84.65 \end{aligned}$$

$$\text{Trash Percentage} = T_5 = 8.9\%$$

$$\begin{aligned} \text{Cleaning efficiency} &= [(T_5 - L_5)100] \div T_5 \\ &= [(8.9 - 3.7)100] \div 8.9 \\ &= 58.42\% \end{aligned}$$

2.6 Air Controlled Cotton Cleaner in Blow Room

In conventional cotton cleaner unit the fibers are opened and cleaned with the help of mechanical beaters which tends to damage the fibers and also a chance of break down due to the foreign particles which are present in it but in air controlled type there are no any mechanical parts the opening and cleaning happens in cylindrical compartment which set at a different heights from each other due to which when bale cotton comes from inlet pipe and flows towards outlet pipe vortex is created in the chamber due to which cotton gets opened and all the trash goes towards the trash compartment where it gets separated. The main parts of this type of machine are as following Fig. 3 shows the air controlled cotton cleaner's model.

- [A] Cylindrical Chamber.
- [B] Inlet Pipe.
- [C] Outlet Pipe.

2.7 Cleaning Efficiency of Air Controlled Cleaner

In this process same samples of 100 gm were used as we were analyzing conventional cotton cleaner. Trash percentage and cleaning efficiency is calculated.

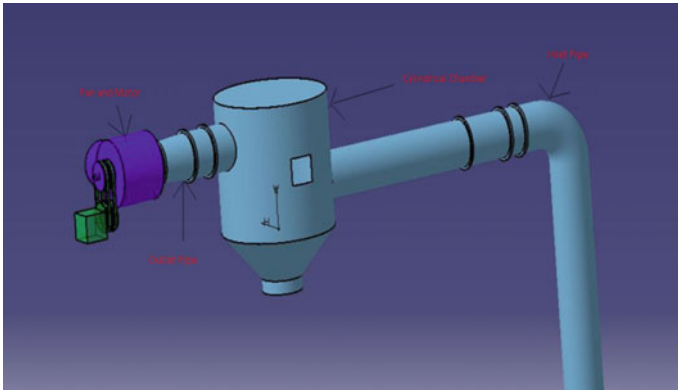


Fig. 3 Model of air controlled cotton cleaner in blow room

Sample 1

We determined these quantities from Shirley analyzer,

$$L_2 \text{ (Pure Lint)} = 73.86 \text{ gm.}$$

$$L_4 = 9.06 \text{ gm.}$$

$$L_5 = 3.2 \text{ gm.}$$

$$T_5 \text{ (Total trash)} = 9.2 \text{ gm}$$

$$\begin{aligned} \text{Lint Percentage} &= L_2 + L_4 + L_5 = 73.86 + 9.06 + 3.2 \\ &= 86.12 \end{aligned}$$

$$\text{Trash Percentage} = T_5 = 9.2\%$$

$$\begin{aligned} \text{Cleaning efficiency} &= [(T_5 - L_5)100] \div T_5 \\ &= [(9.2 - 3.2)100] \div 9.2 \\ &= 65.21\% \end{aligned}$$

Sample 2

We determined these quantities from Shirley analyzer,

$$L_2 \text{ (Pure Lint)} = 74.59 \text{ gm.}$$

$$L_4 = 10.23 \text{ gm.}$$

$$L_5 = 3.1 \text{ gm.}$$

$$T_5 \text{ (Total trash)} = 8.5 \text{ gm}$$

$$\begin{aligned}\text{Lint Percentage} &= L_2 + L_4 + L_5 = 74.59 + 10.23 + 3.1 \\ &= 87.92\end{aligned}$$

$$\text{Trash Percentage} = T_5 = 8.5\%$$

$$\begin{aligned}\text{Cleaning efficiency} &= [(T_5 - L_5)100] \div T_5 \\ &= [(8.5 - 3.1)100] \div 8.5 \\ &= 63.52\%\end{aligned}$$

Sample 3

We determined these quantities from Shirley analyzer,

$$L_2 \text{ (Pure Lint)} = 72.43 \text{ gm.}$$

$$L_4 = 9.46 \text{ gm.}$$

$$L_5 = 3.5 \text{ gm.}$$

$$T_5 \text{ (Total trash)} = 8.9 \text{ gm}$$

$$\begin{aligned}\text{Lint Percentage} &= L_2 + L_4 + L_5 = 72.43 + 9.46 + 3.5 \\ &= 85.39\end{aligned}$$

$$\text{Trash Percentage} = T_5 = 8.9\%$$

$$\begin{aligned}\text{Cleaning efficiency} &= [(T_5 - L_5)100] \div T_5 \\ &= [(8.9 - 3.5)100] \div 8.9 \\ &= 60.67\%\end{aligned}$$

3 Results

For cleaning efficiency firstly total 3 samples were taken from 3 different bales and then they processed at conventional cleaner at plant no 1 and also at air controls cleaner at plant no 2 and results of conventional cleaner are as shown in following Tables 1 and 2 respectively.

Results of air controlled cleaner are as following.

As we can see tables above the air controlled cleaner has higher cleaning efficiency than that of conventional cleaner.

Table 1 Cleaning efficiency of conventional cleaner

Sample no	Trash in bale cotton (In gm)	Trash in lap cotton (In gm)	Cleaning efficiency (%)
1	9.2	4.0	56.52
2	8.5	3.4	60.00
3	8.9	3.7	58.42

Table 2 Cleaning efficiency of air controlled cleaner

Sample no	Trash in bale cotton (In gm)	Trash in lap cotton (In gm)	Cleaning efficiency (%)
1	9.2	3.2	65.21
2	8.5	3.1	63.52
3	8.9	3.5	60.67

4 Conclusion

There is no fiber damage during the cleaning of cotton as there are no mechanical parts and it saves energy as it is operated on compressed air available in a mill. As we seen from above that there is a rise in cleaning efficiency. Due to less mechanical parts there are less chances of break down. We can conclude that from this method we can get better cleaning efficiency with less fiber damage.

References

1. Gupta N, Bharti PK (2013) State of art on yarn manufacturing process and its defects in textile industry. *Int J Comput Eng Res* 3:129–135
2. Gupta AK, Garde AR, Grover JM (1978) Cleaning at blow room and cards in relation to the nature of trash in cotton part I- assessment of trash content. *Ind J Ttxtl Res* 3:29–35
3. Sule D, Bardhan MK (2001) Recycling of textile waste for environment protection an overview of some practical cases in the textile industry. *Ind J Fib Ttxtl Res* 26:223–232
4. Venkatakrisnan S, Shanmugam N, Kalyana Kumar M (2014) Effectiveness of cotton trash parameters measured by AFIS In comparison with gravimetric and HVI methods. *Cott Res J* 6:53–65
5. Ratnam TV, Chellamani KP (2003) Maintenance management in spinning. *SITRA Manograph*
6. Gupta N (2014) Analysis on the defects in yarn manufacturing process and its prevention in textile industry. *Int J Eng Invent* 2:45–67
7. Huang V, Chen V, Chang T (2010) An Application of DMADV Methodology for Increasing The Yield Rate of Surveillance Cameras. *Microelec. Reli.* 50:266–272
8. Dhayaneswaran Y, Ashok Kumar V (2013) A study on energy conservation in textile industry. *J Inst Eng India Ser B* 53–60
9. Lorde P (1981) The economies, science and technology of yarn production. *Txtl Inst* 10 Black friars Manchester, England 149–171
10. Vijay Kumar T (2007) Report on experience with the Rieter C 60 CARD. *Link* 19(51):3–6

A Novel Scheme of Interleaved Flyback Inverter for Photovoltaic Application



Dhanraj D. Daphale and Mahesh S. Yadrami

Abstract Electricity demand is continuously increasing everywhere in the world. The best way to get out of this problem is the use of renewable energy sources. Solar energy is one such type of life which gives more efficiency. This study represents inverters' the analysis and design for the photovoltaic application by using the interleaved flyback topology. The other main aim of this study is to reduce the system's cost, which will help achieve more efficiency. This cost reduction is possible by using the converter topology, using the small size of the converter. Ripples can be easily removed using this technique which plays a vital role in the system's design. Maximum efficiency and near about unity power factor is possible by using this scheme.

Keywords Photovoltaic (pv) · Discontinuous current mode (DCM)

1 Introduction

The Controller Area Network Bus is an everlasting version of the communication bus systems utilized in the automotive industry. CAN-BUS may be a serial digital communication protocol invented by German BOSCH Corporation within the early 80 s to understand the info exchange between numerous controllers and measuring instruments in modem automobile. It's a multi-master bus; the communication medium is often a double-stranded wire, coax or optical fiber. Communication speed is up to 1MBPS. Bus communication interface integrates the CAN protocol physical level. Therefore, the link-layer function can complete the framing of the communication of knowledge processing, including the position filled, the block data code, the circulation parity checks, the priority distinguished and other works. CAN communication protocol feature is to encode the info block? Length of the info is up to eight bytes, which may meet the electrical bus control commands, working status and

D. D. Daphale (✉) · M. S. Yadrami
SVERIs College of Engineering, Pandharpur, Maharashtra, India
e-mail: dddaphale@coe.sveri.ac.in

test data requirement. Meanwhile, the 8 bytes won't take the bus for an extended time, so it ensures real-time communication [1].

In this paper, two major automotive applications, namely engine temperature monitoring and airbag deployment mechanism are implemented. The project consists of two nodes, namely sensing node and therefore the controlling node. The sensing node and therefore the controlling node consists of the ARM7 based microcontroller (with inbuilt CAN Controller) and may Transceiver each. The microcontroller LPC2129 processes the critical time data from sensors of the sensing node. The CAN Controller takes care of the CAN broadcast message data. This data is then sent onto the CAN Bus. The controlling node then receives this data from the CAN bus. The controlling node then further takes appropriate action. For controlling the temperature, a lover is often used; while the airbag deployment mechanism is usually achieved by turning on a relay connected to the controlling node.

This ensures the engine temperature being monitored and controlled further and therefore, the driver's safety; that has drawn particular attention thanks to increasing number of accidents day by day caused by risky high speeds. Thus the essential CAN protocol has been implemented for real-time embedded automotive applications.

2 System Design

The system block diagram is shown below.

The sensing node and therefore, the controlling node consists of LPC2129 microcontroller each shown in Fig. 1. The sensing node senses the sensor data. The sensed data is then sent onto the bus. The controlling node then receives this data. The controlling node then takes the controlling actions accordingly. Here the fans often wont to control the engine's temperature while the relay depicts the airbag's

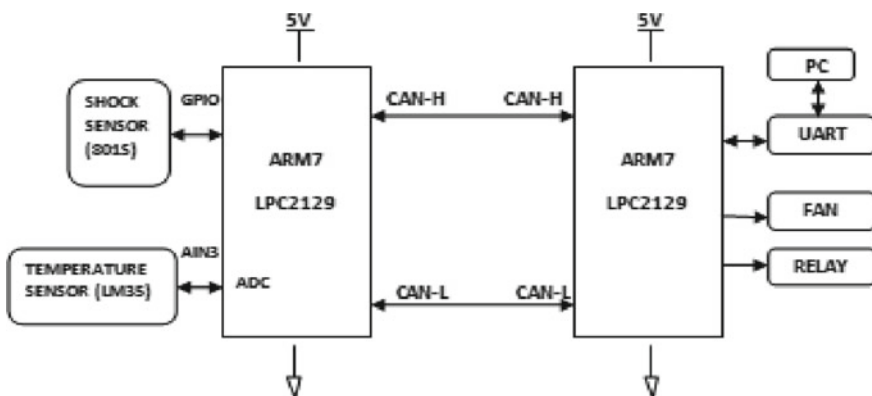


Fig. 1 Block diagram

deployment. The number of nodes is usually added to the bus to extend the number of applications served.

2.1 System Hardware Components

A CAN bus automotive electronic system consists of every controller through the CAN bus interconnected to exchange information (such as speed, engine speed, engine ambient temperature etc.). This mutual connection helps the controllers to use the info at an equivalent time. On the opposite hand, it helps extend the throughput of the system, to develop updated features within the system and reduce the system cost.

Electronic automotive instrument cluster nodes can fully reflect the car factor, product design and technical standards. Intelligent sensor nodes accurately receive various sorts of signals and at an equivalent time can eliminate interference signals [2].

- (1) CAN Bus Electrical Characteristics: CAN transmission medium formed by the two is called high-level transmission line CANH, and the other one is called low-level transmission line CANL.
- (2) Hierarchical structure of CAN protocol based BUS: According to the CAN-BUS network structure, classified into the following five levels, as shown in Fig. 2.
- (3) CAN Message Transmission and Frame Type: CAN message use frame as a transmission unit. In the CAN 2.0B specification is provided in a standard format data frame, given in two different 2.0B frame formats, the difference

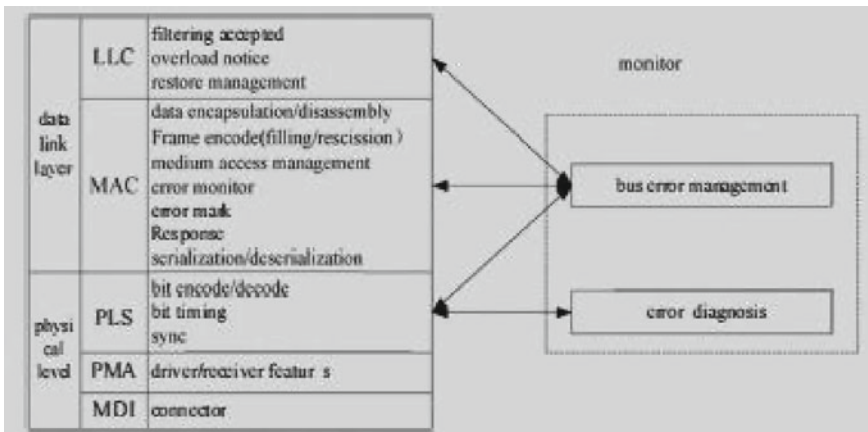


Fig. 2 Hierarchical structure of CAN bus

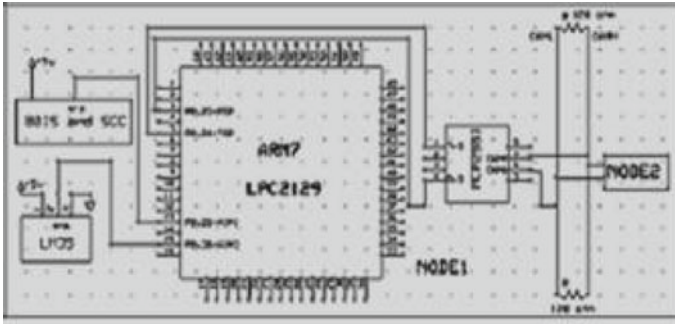


Fig. 3 Circuit design of CAN node

is the length of other identifiers: Frame with an n-bit identifier called the standard frame, the contains 29 identifiers is called an extended frame. Message transmission has the following four different types of structures: data frame, remote frame, error frame, overload frame [3].

- (4) **CAN BUS NODE DESIGN:** The CAN Bus node consists of two nodes, namely the sensing node and the controlling node. The sensing node consists of the following sensors: temperature sensor and a shock sensor. The real-time data from the sensors is sent to the ARM7 based LPC2129 microcontroller and then to the CAN Bus via CAN Transceiver MCP2551. The controlling node then receives this data, and appropriate action is taken. Thus the ambient temperature of the engine can be monitored. Also, to control it further, a cooling fan can be started. The other application is the Airbag deployment mechanism. As soon as the data is received from the shock sensor, the controlling node takes appropriate action. The action can be making a relay on as a way to deploy the airbag further.

As shown ion Fig. 3, the sensor used for sensing temperature is LM35 while the sensor used for shock sensing is 801S. The shock sensor is a micro-vibration detection sensor and is useful for the demo purpose.

The microcontroller used for the node is LPC2129 (ARM7 based and Philips made microcontroller). It has several advantages including inbuilt CAN Controller, supports high speed CAN operation, the low power consumption etc. The CAN Transceiver plays a significant role here. It is used for communication between the node and the CAN bus and then the other nodes. The data is sent onto the bus via the high-speed CAN Transceiver. The CAN Transceiver MCP2551 is compatible with CAN 2.0B. It can provide differential transmit capability to the bus and differential receive qualification to the CAN controller. The chip was initially designed for high-speed automotive communications fully compatible with ISO/DIS standard, and the moment of interference in the anti-car environment, protecting the bus's ability. It is compatible with ISO-11898 standard at speeds up to 1 Mb/s and can resist the substantial interference at the moment of interference such as the automotive environment. General internal bus of circuit protection and limiting circuit has a

low current standby mode and slope control to reduce radio frequency interference [4]. The sensing node may control the temperature by turning a cooling fan on. Also, the airbag deployment is depicted by turning on a relay. Thus two applications, namely engine temperature monitoring and airbag deployment mechanism have been implemented.

3 System Software Components

The system software is written in embedded C and is compiled using ARM Keil Microvision v4 software. Flash Magic is used to upload the program to the microcontroller chip. The software flow consists of CAN transmission and reception of messages. The flow is depicted in Figs. 4 and 5 with the aid of flowcharts.

(1) *Transmission flow:*

Fig. 4 Transmission flow

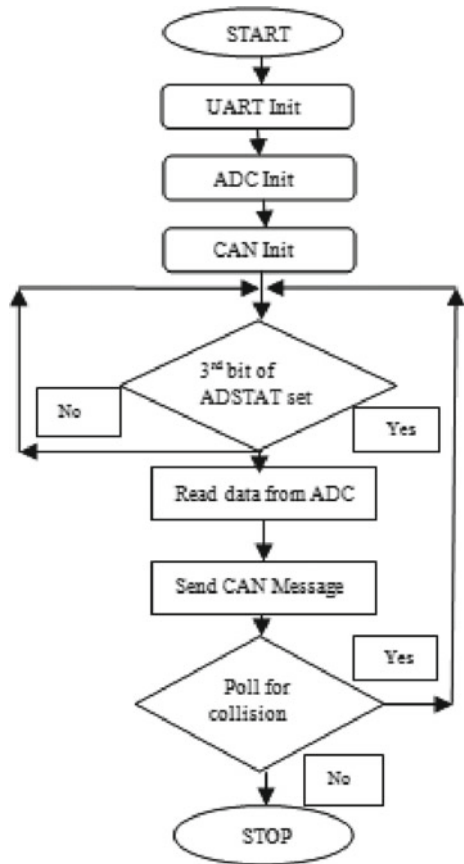
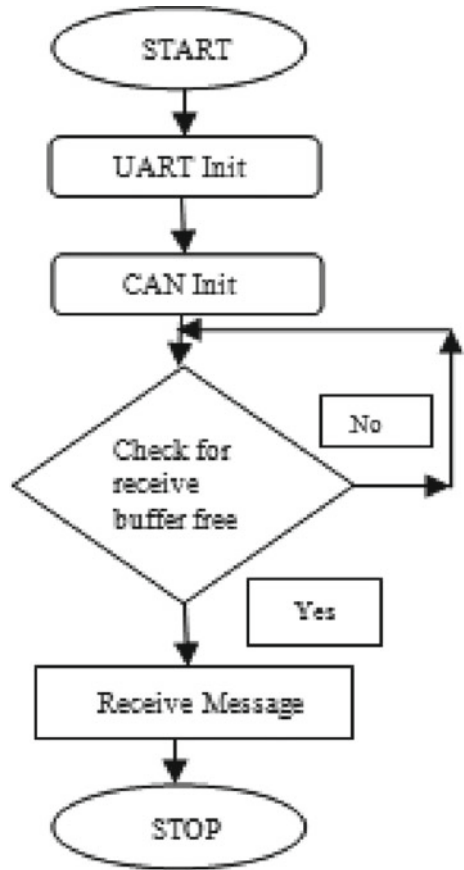


Fig. 5 Reception flow



(2) Reception flow:

The CAN Controller is initialized first. The data from one node is sent onto the bus and then received by the other node. The flowcharts of transmission and reception of data are shown [5]. The received messages are then monitored on the terminal of a personal computer.

4 Results

The real-time data can be monitored through UART on a personal computer shown in Fig. 6. The messages with corresponding ids can be seen on the terminal. A specific message can be dedicated to certain sensor data. The real-time data thus can be monitored, and corresponding controlled actions can be taken further. The

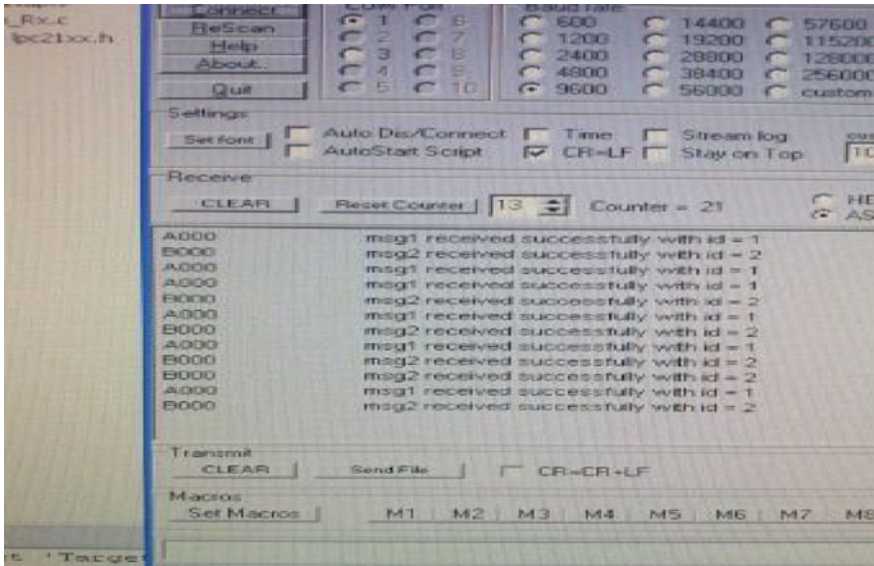


Fig. 6 Data monitored at the terminal of PC

engine temperature can be controlled by turning on a cooling fan; while the airbag deployment mechanism can be achieved by turning on a relay.

5 Conclusion and Future Scope

The paper proposes the implementation of two salient automotive applications, namely engine temperature monitoring and airbag deployment mechanisms. The engine temperature is often controlled further, which is one factor that helps to extend its efficiency. Also, the airbag deployment mechanism ensures the driver’s safety. The scope of the paper is often extended further by increasing the number of nodes like respective applications. Thus more and more automotive applications are often deployed in cars to form them as efficient as possible.

References

1. Chang-hall P, Lui C, Jul C, A design for controller area network bus real-time monitoring system. In: 20 II international conference on computer science and network technology, pp 1621–1624
2. Bo L, Tao J, The design of monitoring system based on CAN Bus. In: 2012 international conference on measurement, information and control (MIC), pp 137–140
3. Ran L, Junfeng W, Haiying W, Gechen L, Design Method of CAN-BUS Network Communication Structure for Electric Vehicle - IFOST 2010 Proceedings. 978–1–4244–1849–7/08/

4. Li R, Liu C, Luo F (2008) A design for automotive can bus monitoring system. In: IEEE vehicle power and propulsion conference (VPPC). Harbin, China
5. Quanqi W, Jian W, Yanyan W, Design of vehicle bus data acquisition and fault diagnosis system. 978-1-61284-459-6/11/

Experimental Analysis of Piezo-Beam in the Context of Vibratory Energy Harvesting



Rohan Nikam, Kanchan Bhosale, Sachin S. Pawar, Santosh B. Salunkhe, and Vaibhav S. Pawar

Abstract Vibration analysis of structures continues to be an important subject of study in the field of structural and mechanical engineering. Experimental study on piezo beams, attracted researchers since past. Conventional excitation techniques employed for vibration analysis normally require contact. In the present study, a non-contact technique for excitation of piezo beams to do the vibration analysis. An electromagnetic force was used for excitation. The vibration induced by the electromagnetic force was varied in a wide range from 20 Hz to over 50 Hz. The motion of the beam was measured along the three axes using an accelerometer. The resulting frequencies were captured using FFT constructed in LabView. This helps us to understand the response phenomenon of light weight beams such as piezo beams. Study will be useful for applications involving such beams and in energy harvesting.

Keywords Non-contact excitation · Beam · Accelerometer · LabVIEW · FFT

R. Nikam
Mechanical and Industrial Engineering Department, UIC Chicago, Chicago, USA

K. Bhosale (✉)
Indira Gandhi College of Engineering, Navi-Mumbai, Ghansoli, Maharashtra, India
e-mail: kanchan.bhosale85@gmail.com

S. S. Pawar
Mechanical Engineering Department, School of Engineering, MIT Art Design and Technology (ADT) University, Rajbaug, Loni-Kalbhori, Pune, Maharashtra, India

S. B. Salunkhe
Department of Mechanical Engineering, SVERI's College of Engineering, Pandharpur, Maharashtra, India

V. S. Pawar (✉)
Department of Mechanical Engineering, Annasaheb Dange College of Engineering and Technology Ashta, Ashta, Maharashtra, India
e-mail: vaibhavpawar3@yahoo.co.in

1 Introduction

Beams are fundamental models of structures used in many engineering applications. Vibration measurement is very needful in mechanical and electrical industries to check the machine health and to take predictive maintenance steps before failure or major fault occur. Now a day there is a need to measure vibration as the machine life is extended because of elimination of vibration. Detection of vibration is an important sensor technology for monitoring the operation of machines, bridges and buildings, warrant of security, prediction of natural disasters and more. Vibration is undesirable, unwanted energy and creating noise in circuit. Undesirable vibration may occur in electric machines, engines, or any mechanical instruments in operation. Such vibrations could be caused by not aligned in the rotating parts, uneven rubbing etc. It should be noted that in real-time applications, vibrations steady or transient in nature but source of excitation may or may not come in physical contact with vibrating structure. In this paper we attempt to study the vibrational characteristics of a beam. The cantilever beam supported on one end would be subjected to continuous forced vibrations from another end. transverse stiffness of a cantilever beam,

$$k = \frac{3EI}{L^3} \quad (1)$$

where k = stiffness, E elastic modulus, I second moment of area about the neutral axis, L is length of the beam. Novelty of the work is that non-contact excitation is used to induce the vibrations as in practical applications. The resulting acceleration and force are recorded with the help of accelerometer and force sensor attached to the beam. A beam is fixed at one end and free at other end, so fundamental natural frequencies of Beams,

$$f = \frac{K}{2\pi L^2} \sqrt{\frac{EL}{m}} \quad (2)$$

2 Literature Survey

Adali et al. [1] considered a beam problem where the maximum vertical deflection of a laminated beam was to be minimized using one pair of actuators. The distance of the actuator pair from the support was taken as the design variable. Aldraihem et al. [2] objective was to maximize the weighted controllability of a simply supported or cantilever beam. Pairs of piezoelectric actuator patches were placed such that they provide maximum controllability for weighted modes, where the weights on modes were determined by ranking their contribution to overall system response. Begg et al. [3] developed five algorithms for simultaneous design smart structures

which is based on standard linear and quadratic programming. Bruant et al. [4] optimized both sensor and actuator locations but considered them separately. The actuator length and location were found first by minimizing the mechanical energy integral, then the sensor location was found by maximizing a measure of the observability. Han and Lee et al. [5] consider a plate problem, where the steady-state controllability Grammian was used as a way to maximize the eigenvalues. A genetic algorithm was used to find the optimal locations of two actuators from a set of 99 possible rectangular areas on the plate. The optimal locations of the two sensors were then found in a second stage. Gao et. al. [6] objective was to minimize the total radiated acoustic power, so they have used location of piezoelectric patches and actuation voltages. Lu et. al. [7] developed an analytical model to optimize a plate actuator equipped with the passive corrugated core. The goal was to minimize the weight by designing the plate thickness, core member thickness, total length, and total height. A combination of graphical and sequential quadratic programming (SQP) methods was used to solve the optimization problem. Sigmund and Torquato et al. [8] employed a very similar approach in designing piezoelectric composite material microstructures. In their approach, a composite material consisting of a soft polymer material with piezoelectric rods through the thickness was assumed. The topology of the piezoelectric rods remained fixed, but their volume fraction was varied in the optimization. The objective functions were maximizing the effective hydrostatic charge coefficient. Zhao et. al. [9] studied the optimum design of piezoelectric cantilever beam under a low-frequency condition. Piezoelectric cantilever beams were designed based on the finite element method with the validation of laboratory experiments. The finite element analysis software ANSYS was used to calculate the relationship between the dimension and the natural frequencies of Two piezoelectric cantilever beams were. Zemcika et al. [10] developed a one-dimensional finite element method for the analysis of structures with applied piezoelectric sensors and actuators, i.e. smart structures, mechanical behavior of which can be controlled in real-time. The element is based on Euler–Bernoulli theory and it assumes the bilinear distribution of electric field potential. A mathematical model was implemented in a MATLAB environment. Sensitivity analysis was carried out for the case of modal analysis with and without piezo patches. Alaimo et al. [11] performed boundary element analyses on delaminated composite structure and it repaired by active piezoelectric patches. Rahman and Alam [12] developed an experimental set-up to obtain the active vibration suppression of smart beam.

This work details use of non-contact technique for the excitation of piezo beams. It executes the experiments on the beam for the vibratory energy harvesting. Piezo beam is subjected to excitation at lower frequencies from 20 to 70 Hz. Novel experimental setup is developed for the conduct of experiments which is equipped with multifaceted technologies to investigate vibratory response of smart structures. Fixtures are designed so that different end conditions can be imparted to slender structures such as beams. Piezo patch characteristics are studied accordingly and critical responses and concerned frequencies are noted from vibratory energy harvesting view point.

3 Experimental Set Up

Critical literature survey reveals that lightweight beams and plates, which have potential applications, for instance; in wipers, lightweight constructions, measuring instruments, tuners, etc. is lagging. In particular; steady-state response, the behavior of beams; under different range of frequencies (practical conditions) due to non-contact excitation which is a more practical condition need to be investigated. Present work is contributed to such key aspects. Following are the objective of the paper: (a) To investigate beam response of piezo patch equipped aluminum at different excitation frequencies via non -contact excitation; (b) To capture forces of reaction at the piezo location for different excitation frequencies; (c) To simulate dynamic response at obtained excitation frequencies, forces, and some modes Test facility has been developed which uses non-contact way of excitation.

As shown in Fig. 1, non-contact exciter receives signal through microcontroller equipped with power source which has communication with desktop. The arrangement is such that, any frequency up to 150 Hz can be possible. Thus by time pulses, frequency of excitation can be fixed. This methodology has been followed in this work. It should be noted that excitation frequency is controlled in the present work which is novelty. Further, force sensor is located near the piezo-patch below the aluminum plate (not shown in the present schematic). Accelerometer is communicated to serial ports via microcontroller. Thus accelerations in X, Y and Z directions are portrayed in the excel sheet. Same strategy was followed to capture the magnitude of the reaction force. Received signals through piezo-patch are processed via FFT to retrieve the information related to harmonics. Thus, with plenty of the information, viz. acceleration in three directions, corresponding harmonics, reaction forces etc. This information is benchmarking one and can be used for harvesting the vibratory energy. Nevertheless, vibrations can be controlled with the help of this information as well. Further, one can have number of trials to fix the position of piezo-patch and accelerometer. In the present work, focus has been kept over beam response at different excitation frequencies and thereby generating benchmark results of acceleration against vibrational frequencies. Figure 2 indicates the photograph of test set up.

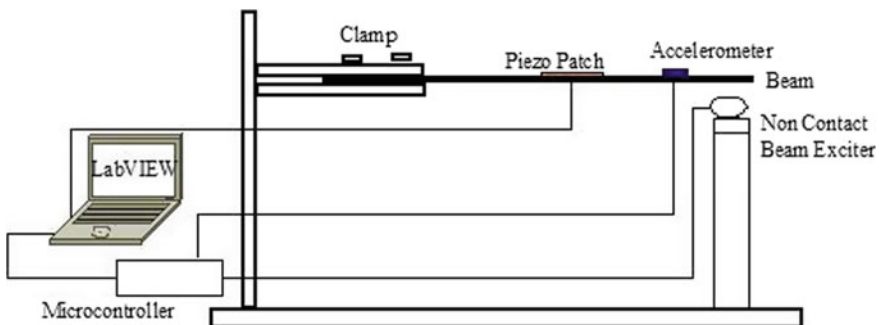


Fig. 1 Schematic of the setup used for vibration study

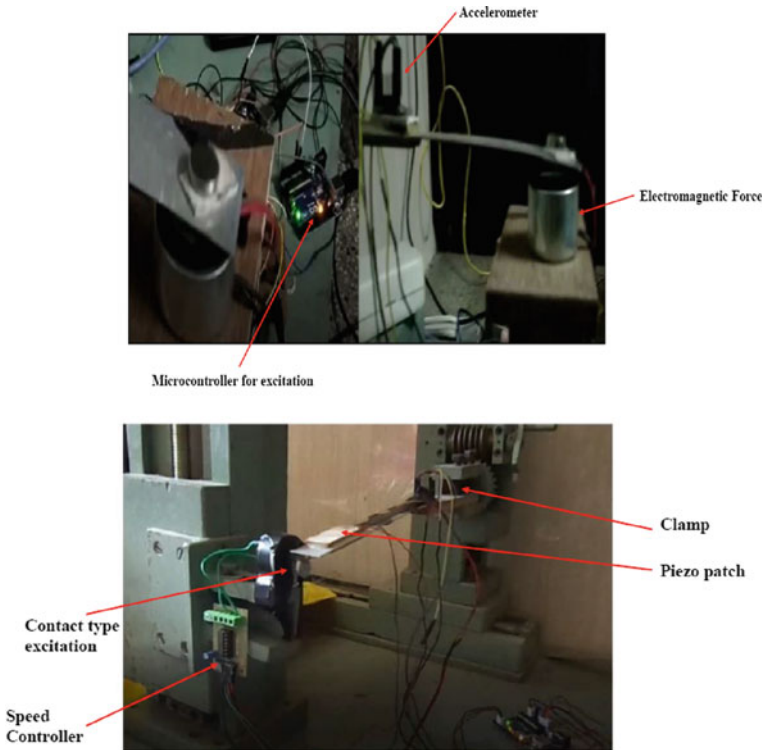
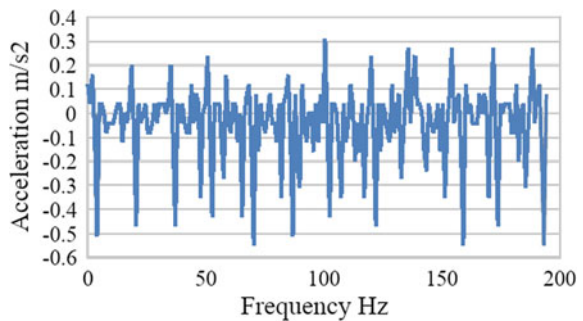


Fig. 2 Photograph of test setup

4 Result and Discussion

Acceleration response of the beam at lower frequencies is shown in Fig. 3. It can be noted that, for the chosen position of the accelerometer, the mean value observed tend to be negative. Sharp fluctuations in acceleration levels observed at lower harmonics viz. 5, 20 and 36 Hz. In the harmonic analysis, one of the natural frequency turned

Fig. 3 Experimental frequency response at excitation frequency of 20 Hz along X-axis



out to be around 34 Hz. Thus, second natural frequency was excited in the context of X -axis vibrations. As acceleration levels are too much lower, they are insignificant and immediate conclusions cannot be drawn.

Figure 4 illustrates Y-axis response for excitation frequency of 20 Hz. Dynamic amplification having absolute value of 2.25 was observed around 92 Hz, of 2 was observed at 140 and 190 Hz. Thus excitation frequency is too far from damped frequencies. Furthermore, it is interesting to note that at 190 Hz sharp changes in the Z axis acceleration magnitudes observed from 12 m/s² to -2 m/s² as in Fig. 5. As this harmonic also indicated sharp change in Y-axis acceleration, one of the natural frequency of the system might be closer to 190 Hz. It is noteworthy to mention here that damped frequency in the harmonic analysis which is briefed later, one of the natural frequency observed to be 212.26 Hz. Thus, damping offered by the system (including piezo, wooden support from bottom and top) must be around 0.4–0.45. Further, it is not necessary to have damping factor to be constant as it is governed by piezo, wooden support and aluminium combination.

At higher frequency, more fluctuations observed in the acceleration levels and they are clustered too. Thus, with appropriate filters, foundations can be set for harnessing energy in the form of mean and alternating voltage. It is to be noted here that, mean accelerations for this case are around zero, in particular for X- axis accelerations, Fig. 3. This was not the case for 20 Hz wherein mean acceleration was negative. In case of X axis response at 20 Hz frequency, suitable rectifiers can be used to harness the energy in required form.

Fig. 4 Experimental frequency response at excitation frequency of 20 Hz along Y-axis

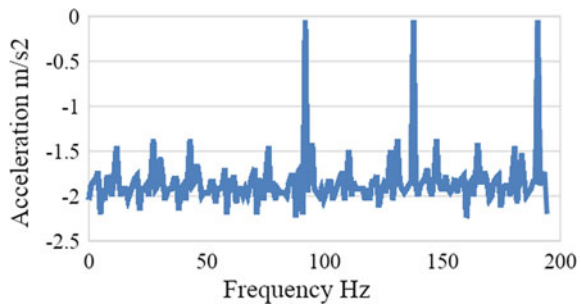
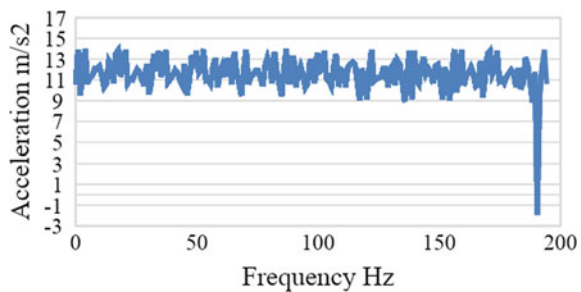


Fig. 5 Experimental frequency response at excitation frequency of 20 Hz along Z-axis



It is safe to say that for light weight applications such as present one, piezo based system is suitable for harnessing vibratory energy at low speed range quite comfortably. Further, frequencies at which peak accelerations happen to be higher can be filtered out to prevent damage to the device and harnessing circuit.

It has been observed that response is very much insensitive to excitation frequency. This clearly suggest that axial stiffness of beam structure is much higher and so also natural frequency. This is also evident from the higher peak of the acceleration observed at higher natural frequency which is well captured in the experiments conducted. Thus, we can harness the vibratory energy of similar systems, in the context of X -axis vibrations easily provided that stiffness along the X axis is alike i.e. of the higher magnitude, which is obvious.

From Figs. 6, 7 and 8, in all the cases, mean accelerations as well as fluctuations are quite high when compared to X axis and Y axis counterparts. It is noteworthy to mention here that Piezo damping is playing crucial role for the system. As a result, to different excitation frequencies, two peak frequencies (we can say that damped natural frequencies) found in general. To add to this, these frequencies observed to be shifting both towards left first and then to right with slight variation in shift. Exceptions to this trend are lower and higher excitation frequencies. Thus harnessing of the vibratory energy is crucial in this regard and filters must be programmed to accommodate frequencies in range and eliminating the others. In particular, it is appropriate to harness vibratory energy in the small to medium excitations without having much problems and with simple adjustments. It is to be noted that at this

Fig. 6 Experimental frequency response at excitation frequency of 40 Hz along X-axis

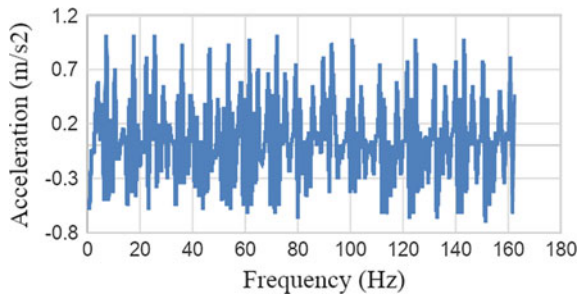


Fig. 7 Experimental frequency response at excitation frequency of 40 Hz along Y-axis

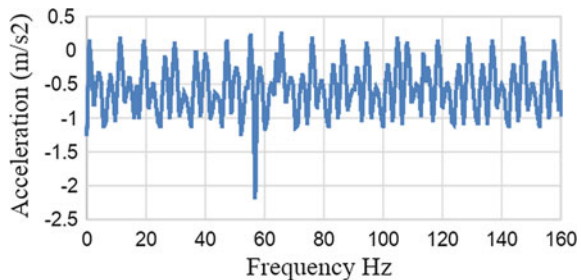
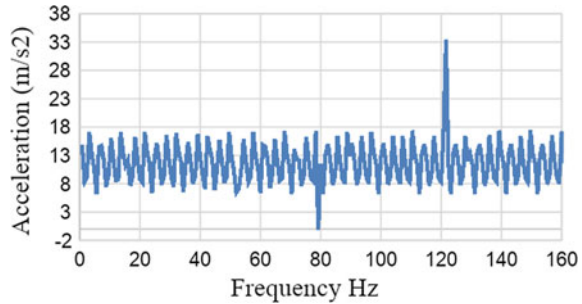


Fig. 8 Experimental frequency response at excitation frequency of 40 Hz along Z-axis



modelling of the beam is difficult as no such clear patterns observed in the experiments. As phenomenon is not clearly understood, clear inferences in the context of piezo cannot be drawn for now. Still, it can be concluded that low frequency energy, in particular below 70 Hz frequency can be harnessed properly with corresponding arrangement in place. For brevity, other results are not detailed here.

5 Conclusions

Paper detailed experimental investigation of light weight piezo beam at different excitation frequencies. For excitation, non-contact way of the excitation has been developed. Three- axis accelerations and force have been obtained using lab view and FFT interface. Following conclusions can be drawn from performed work.

1. Two peak frequencies observed as long as Z axis accelerations are considered for each excitation frequency except 20 Hz.
2. It is appropriate to harness vibratory energy in low frequency range.
3. Suitable filters can retrieve vibratory energy by eliminating certain frequencies in the context of Z axis vibrations.
4. For Y axis energy can be harnessed though of the less root mean square amplitude (RMS) by filtering out only one frequency for different excitation frequencies except 20 Hz excitation frequency.
5. For X axis vibrations, however we can harness the energy over wider range for low excitation frequency. For excitation frequency of 50 Hz, peak frequency happens to be around 160 Hz. As it is higher, we can harness vibratory energy over wide range without need of filters.
6. In simulations, modes confirm bending mode followed with twisting and axial mode did not happen.

References

1. Adali S, Bruch J Jr, Sadek I (2000) Robust shape control of beams with load uncertainties by optimally placed piezo actuators. *Str. Multi. Opt. Strl. Multi. Optim.* 19:274–281
2. Aldraihem OJ, Singh T, Wetherhold RC (2000) Optimal Size and Location of Piezoelectric Actuator/Sensors: Practical Considerations. *J. Guid. Cntl. Dyn.* 23:509–515
3. William Begg D, Liu X (2000) On simultaneous optimization of smart structures – Part II: Algorithms and examples. *Comp. Meth. App. Mech. Engg.* 184:25–37
4. Bruant I, Coffignal G, Lene F, Verge M (2001) A methodology for determination of piezoelectric actuator and sensor location on beam structures. *J. Sou Vib* 243:861–882
5. Han J-H, Lee I (2015) Optimal Placement of Piezoelectric Sensors and Actuators for Vibration Control of a Composite Plate Using Genetic Algorithms. *Smrt. Mate. Stru. Acta. Mech.* 226:3451–3462
6. Gao F, Shen Y, Li L (2000) The Optimal Design of Piezoelectric Actuators for Plate Vibroacoustic Control Using Genetic Algorithms with Immune Diversity. *Smrt. Mate. Stru.* 9:485–491
7. Lu T, Hutchinson JW, Evans AG (2001) Optimal Design of a Flexural Actuator. *J. Mech. Phys. Soli.* 49:2071–2093
8. Sigmund O, Torquato S (1999) Design of smart composite materials using topology optimization. *Smrt. Mate. Stru.* 8:365–379
9. Zhao Q, Liu Y, Wang L, Yang H, Cao D (2018) Design method for piezoelectric cantilever beam structure under low frequency condition. *Int. J. Pav. Rese. Tech.* 11(153–159):1996–6814
10. Zemčik R, Sadilek P (2007) Modal analysis of beam with piezoelectric sensors a actuators. *Appl. Compu. Mech.* 1:381–386
11. Alaimo A, Milazzo A, Orlando C, Messineo A (2013) Numerical Analysis of Piezoelectric Active Repair in the Presence of Frictional Contact Conditions. *Sens.* 13:4390–4403
12. Rahman N, Alam M (2012) Active vibration control of a piezoelectric beam using PID controller: Experimental study. *Lat. Ameri. J. Soli. Struct.* 9:657–673

Manufacturing and Fabrication Processes for Societal Applications

Ergonomic Analysis Tools for Power-Loom Industry



Somnath Kolgiri, Rahul Hiremath, and Vaishali Kolgiri

Abstract Work associated musculoskeletal disorders (WMSDs) are the most ergonomic risk elements of the power-loom industry due to repeated motions, stooping and squatting postures when operating for a long time. The purpose of this study is to determine the importance of three methods for ergonomic risk assessment, i.e. by applying the F test, RULA/REBA, and NMSQ to verify the results and find the pairwise rank of agreement among tools using Kappa analysis. The p-value is too chosen to transform $p < 0.05$, suggesting that there is statistical significance in the relationship between the REBA and Nordic questionnaires. Since the Kappa value is 0.7875, RULA / REBA shows complete agreement.

Keywords Ergonomics · WMSDs · RULA/REBA · NMSQ · Kappa analysis · Power-Loom Industry

1 Introduction

Stooped and squatting postures are commonly seen among workers in third world nations like India, particularly in small-sized sectors. The small-scale textile workers have gained less benefit since work-related health and safety provision [1]. Several studies depicted that Indian workers of small or medium scale textile industries affect from WMSDs namely carpal tunnel syndrome, forearm tendinitis, epicondylitis, bicipital tendinitis, low back ache, neck ache, shoulder ache and osteoarthritis of the knee [2]. In Indian small and medium scale textile sectors, the employees are highly vulnerable by performing cumbersome tasks such as maintaining standing work posture throughout working hours in operating loom's, handling heavy materials by pushing and moving iron beam weighing 100 kg for a distance of nearly 3 m

S. Kolgiri (✉)
SBPCOE, Pune, India

R. Hiremath
SCMHRD, Pune, India

V. Kolgiri
RVDC, Bengaluru, India

for five times in a day after wrapping the raw material, continuously monitoring with high attention if any break off on threads [3]. Several physically performed activities in such factories are conducted in uncomfortable body positions. In determining exposure to hazard elements related to WMSDs, many techniques and methods were created, that can generally be divided into three groups: questionnaire, experimental techniques, and direct estimates. Self-reports have been due to subjective drawbacks, such as ambiguity in the perception and understanding of employee exposure, despite their simple execution. The purpose of experimental techniques is to test the disclosure in the workplace by measuring employees' motor activity on paper sheets either when they notice or revisit videos taken on the spot. The RULA index is among some of the most known observational techniques, which depends on observing postures (biomechanical and postural) as load parameters to provide an exposure score to MSDs, especially over the body parts of the trunk, neck, and top joints used. REBA is being made to examine dynamic work where there is a WMSDs risk. It is to be used to examine the tasks for which RULA was not designed. RULA is a survey method which was established to be used in ergonomics examinations of the sedentary workstation where the job associated upper extremity and neck discomforts are stated [4, 5]. REBA uses the RULA posture scoring measures as a basis and is being made to additionally record risks associated with the knee positions, the loads or forces being applied, the coupling and whole body activities [6–8]. MSDs problems were evaluated using NMSQ developed [9, 10]. The NMSQ is largely utilized [11–13]. NMSQ was fundamentally categorized into 3 for the distinct regions if they were with 3 sub-measures. The respondents were told to answer the first sub-measures (NMSQ1 to NMSQ9) when they perceived listed musculoskeletal problems sustained for a week. To compare and find the pair wise level of conformity between tools RULA/REBA and NMSQ Kappa analysis is suitable. Kappa is an extensively adopted trial of inter or intra-observer consensus or reliability which rectifies for likelihood consensus. The basic percentage equation can be utilized to determine the consensus yet regardless the easiness included in its evaluation, percentages can be deceptive and do not show the actual situation because it does not consider the scores that the evaluators allot because of likelihood. Cohen's Kappa conquers this challenge since it considers the consensus prevailing randomly. The Kappa coefficient of agreement is a measure of agreement that factors out of the expected agreement [14]. Kappa varies from +1 to -1 the value of Kappa is shown in the ranges and it is converted into the moderate, slight, fair, substantial relationship also along with almost perfect agreement when the value is above 0. If Kappa value is less than 0 then the agreement is termed as less than chance agreement.

2 Purpose of the Study

The aim of the present examination was to apply three tools for ergonomic risk assessment, i.e. in the power-loom industry, RULA, REBA and NMSQ checklists and evaluate the importance of these risk assessment instruments by applying the F test

to verify the findings. Using the Kappa analysis, these techniques were distinguished and the pair-wise degree of conformity between instruments was found.

3 Materials and Methods

An investigation had been performed to collect the anthropometric and demographic data of 540 workers from 30 textile industries age spanning from 21 to 60 (Age = 32.24 ± 4.03) were selected. RULA and REBA methods are adopted in evaluating the body position, exertion and motion of the low back, neck, shoulders, trunk related to the activities of various departments, namely threading, spinning, weaving, knitting, bleaching, dyeing, printing and finishing, and to evaluate the body position, exertions utilized, kind of action, recurrence, and coupling appropriately and NMSQ were utilized to measure the magnitude and analyze the risk of WMSDs among power-loom industry women workers. SPSS software was used to perform analysis of statistics over collected data.

- Scoring for the RULA and REBA sheet is done for every task with the help of video analysis.
- The ANOVA test is performed in order to find out the connection between the risk levels of all the three methods and the reported pain by the workers. This will give the validity of each method in the power-loom industry.
- After the validity of each method has made the comparison to be made between the methods and level of agreement is found between them by the F and P value analysis for significance. Identifying the cause of the amount of concurrence between tools.

4 Result and Discussion

4.1 *RULA and REBA Scores of Various Tasks Performed by Workers in Power Loom*

The score of all the tools that were applied has been characterized into three classes of risk, i.e. low, medium, and high (Figs. 1, 2 and 3). The ambiguity of three, four and five level classification was converted to three level classifications by the author [15]. All the score is converted to the three category risk level to contrast the resulted score of the two techniques is shown in Table 1 RULA and REBA were applied for application in ergonomic investigations of job place where the job associated upper extremities discomforts are stated and which assess the locomotive and positional loading on the entire body for specific observation on the upper extremity, shoulder, trunk, and neck [16–18].



Fig. 1 Activity of guiding thread in thread formation department

Repetitive Upper Limb Assessment

File Edit Help

Task Information | **RULA Score**

Analyst: Kolgiri | Job Name: Guiding thread in bobbin | Workstation ID: Spinning

Hand

Right Side | Left Side

Wrist

Wrist Twist: In mid-range of wrist twist | At/near end of wrist twist

Lower Arms

0 to 90 | > 90 | Midline

Upper Arms

Upper arm between 21 and 45 deg. (Flexion)

<-20 | -20 to 20 | 21 to 45 | 46 to 90 | >+90

Shoulder is... | Upper arm... | Arm is sup...

Neck

Exten. | 0 - 10 | 11 - 20 | > 20

Neck is twisting | Neck is side bending

Trunk

Neutral | 0 - 20 | 21 - 60 | > 60

Leg

Legs and feet are well-supported and in an evenly balance posture | Legs and feet are not supported and in an uneven balance posture

Muscle Use

Mainly static, e.g. held for longer than 10 minutes | Repeated more than 4 times/minute

Force or Load

0 to <4 lbs intermittent load or force | 4 to 20 lbs intermittent load or force | 4 to 20 lbs static or repeated load or force | +20 lb static or repeated loads

Fig. 2 Assessment of Right Hand for the activity shown in Fig. 1 using NexGen RULA

Table 2 shows the ultimate average score for any activity if above 8 which imply an activity level of 5 that is immediate examination and modifications are needed in the current job station, with the ultimate average score for any activity if 7 which imply an activity level of 4 that is urgent examination and modifications are needed in the current job station. For any task, the average score was observed to be 5 which

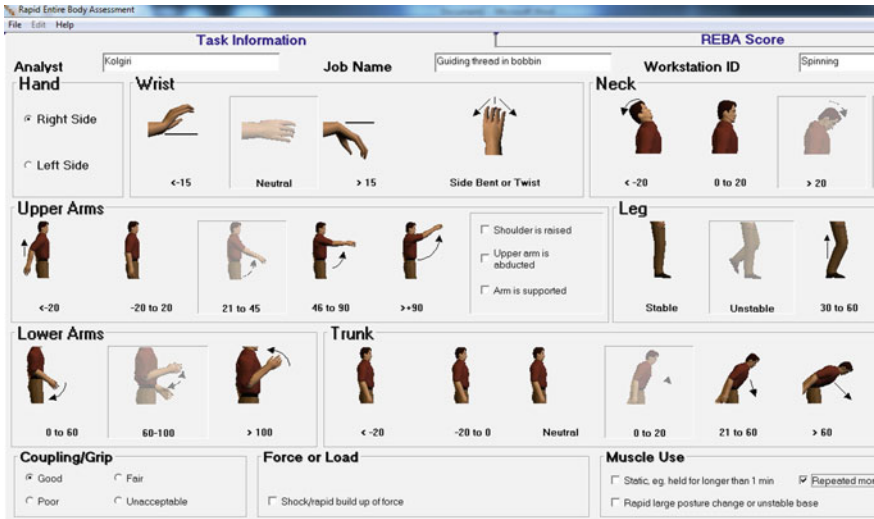


Fig. 3 Assessment of Right Hand for the activity shown in Fig. 1 using NexGen REBA

Table 1 Risk groups adapted to contrast the outcome scores from 2 techniques for evaluating MSD

Tool	Low risk	Medium risk	High risk
RULA	1–2	3–6	7
REBA	1	2–7	8–15

implies an activity level of 3 that is speedy examination and modifications are needed in the current job station.

4.2 NMSQ

NMSQs were utilized for job evaluation of work in determining body uneasiness. NMSQ is a systematized and a scrutiny instrument to determine the body parts attacked by musculoskeletal signs comparatively cheap and simple [19]. There is no requirement of some technical apparatus to carry out this analysis. SPSS software was used to perform analysis over the data collected from participants. Table 3 depicts the NMSQ scores for various main departments in the power-loom industry.

Figure 4 depicts the associated outcomes in the percentage of operator perceived distress in several parts of the body in these jobs. The larger part of the analysis, respondents, that is 34.6% have perceived the ache in the lower back while shoulder ache was perceived by 28.5%. Right wrist/hands, upper arm and upper back 28.6, 27.7 and 30.8% respectively were the second most distressing locations noticed in the examined population. The outcomes of this analysis showed that the power-loom workers occupy in sustained forward flexing body position in their operating

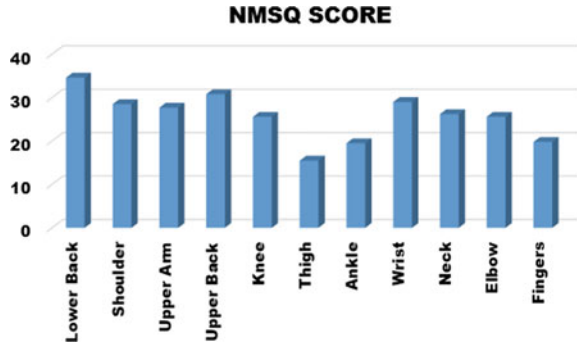
Table 2 Average RULA and REBA Scores of various tasks performed by workers in power loom industry

Sr. No	Department		Thread Formation N = 60	Spinning N = 84	Weaving N = 90	Knitting N = 96	Bleaching N = 72	Dyeing N = 54	Printing N = 48	Finishing N = 36	RULA and REBA total score
	Pain										
1	Lower back		5	4	4	3.6	4	4	3	2.8	30.4
2	Shoulder		3	3.6	4	3	3	3.6	2.7	3.6	26.5
3	Upper arm		4.8	4	4	4.3	3	4	2.1	2.8	29
4	Upper back		5	4	3	3	4	3.4	2.4	2	26.8
5	Knee		3	3	2	2	2	3	4	2	21
6	Thigh		2	2	2	2	2	2	3	3	18
7	Ankle		1	2	2	2	2	1.4	2.6	2.6	15.6
8	Wrist		4.5	4.3	2.5	2.2	2	3.7	2.6	3.1	24.9
9	Neck		2	2.2	3	3	3	2.9	2.1	3	21.2
10	Elbow		3	3	1	3	2	3	5	3	23
11	Fingers		1	1	1	1	2	1	2	3	12

Table 3 Scores are directly collected from power-loom employees using NMSQ

Sr. No	Department	Thread Formation N = 60	Spinning N = 84	Weaving N = 90	Knitting N = 96	Bleaching N = 72	Dyeing N = 54	Printing N = 48	Finishing N = 36	NMSQ total score
	Pain									
1	Lower back	5	5	5	4.8	5	4.2	3	2.6	34.6
2	Shoulder	3.4	3.6	3.6	4.1	4	4	2.6	3.2	28.5
3	Upper arm	4.8	4.2	3	4.3	3.4	3.2	2	2.8	27.7
4	Upper back	4.8	4.2	4.6	4.6	4.8	3	2.8	2	30.8
5	Knee	3.2	3	2	3.2	4.2	3	4	3	25.6
6	Thigh	2.1	1.5	1.7	2	2.6	1.3	2.3	2	15.5
7	Ankle	2.5	1.8	2	2	3.4	2	3	2.8	19.5
8	Wrist	4.5	4.2	4.8	2.8	3.3	3.4	2.8	2.8	28.6
9	Neck	2.5	2.6	4.2	4.3	3.5	3.2	2.5	3.4	26.2
10	Elbow	3	3	2.4	3.8	3.4	3.8	2.8	3.4	25.6
11	Fingers	2.6	1.6	1.8	3.4	2.8	2.8	2	2.8	19.8

Fig. 4 NMSQ Score distribution over several body parts



circumstance. The analysis showed that 47.23% part of the population on average experiencing minimum one job associated musculoskeletal distress [20].

Table 4 shows recomputed the RULA + REBA and NMSQ for 6 Body Regions, which have distinguished to three body parts are upper extremity, upper body part and lower extremity. Fractions appeared in RULA + REBA scores and NMSQ data because say for instance in the calculation of the RULA + REBA score of the upper arm of thread formation, the average of the leg of RULA + REBA scores from the rows of 5, 6 and 7 was taken i.e. $(3 + 2 + 1) / 3 = 1.5$.

Similarly, in the calculation of NMSQ value of trunks of thread formation, the average of upper back and lower back on NMSQ values of the rows of 1 and 4 (these rows were considered because trunk RULA + REBA associated with upper back and lower back, refer Table 5) was taken i.e. $(5 + 4.8) / 2 = 4.9$.

Table 6 uses statistical analysis, Student’s T and goodness of fit were performed and evaluated Pearson’s and Spearman’s correlation coefficients to find significance between scores. Following inference was observed by looking the values of correlation coefficients, there is no big difference to perform video analysis for evaluation of RULA and REBA or administer Nordic Musculoskeletal Questionnaire for finding pain in body regions. The regression equations were also found out to find NMSQ value from RULA/REBA scores.

Table 4 Obtained chart for comparing factors between RULA + REBA Wizard and NMSQ

Sr. No	RULA + REBA	NMSQ
1	Upper Arm	Shoulder + Upper Arm
2	Wrist + Wrist Twist	Wrist
3	Trunk	Upper Back + Lower Back
4	Neck	Neck
5	Lower Arm	Elbow
6	Leg	Thigh + Knee + Ankle

Table 5 Recomputed the RULA + REBA and NMSQ scores for 6 Body Regions

Sr No	Department	Thread Formation		Spinning		Weaving		Knitting		Bleaching		Dyeing		Printing		Finishing	
		RULA	NMSQ	RULA	NMSQ	RULA	NMSQ	RULA	NMSQ	RULA	NMSQ	RULA	NMSQ	RULA	NMSQ	RULA	NMSQ
1	Upper arm	3.9	4.1	3.8	3.9	4	3.3	3.65	4.2	3	3.7	3.8	3.6	2.4	2.3	3.2	3.0
2	Wrist/ Wrist twist	4.5	4.5	4.3	4.2	2.5	4.8	2.2	2.8	2	3.3	3.7	3.4	2.6	2.8	3.1	2.8
3	Trunk	5	4.9	4	4.6	3.5	4.8	3.3	4.7	4	4.9	3.7	3.6	2.7	2.9	2.4	2.3
4	Neck	2	2.5	2.2	2.6	3	4.2	3	4.3	3	3.5	2.9	3.2	2.1	2.5	3.0	3.4
5	Lower Arm	2	2.8	2.1	2.3	2	2.1	2.6	3.6	2	3.1	3.0	3.3	2.6	2.4	2.9	3.1
6	Leg	1.5	2.6	2	2.1	2	1.9	2	2.4	2	3.4	1.7	2.1	2.8	3.1	2.8	2.6

Table 6 Depicts the significance of RULA /REBA score and NMSQ score

Methods	Parameter	Thread Formation formation	Spinning	Weaving	Knitting	Bleaching	Dyeing	Printing	Finishing
Pearson's	Coefficient	0.8464	0.8763	0.8637	0.7952	0.9036	0.9032	0.87446	0.8443
	P Value	0.0126	0.0110	0.013	0.0293	0.00675	0.00610	0.01846	0.01784
Spearman's	Rho	0.88545	0.92763	0.811679	0.94286	0.92582	0.92342	0.91645	0.90546
	P -2 tailed	0.00387	0.00767	0.04986	0.0048	0.00805	0.00602	0.00544	0.00446
Student's T	T value	-6.4413	-5.23008	-7.92671	-7.71925	-6.42625	-6.5345	-6.35646	-6.85464
	P value	0.000178	0.000192	<0.00001	<0.00001	0.000038	0.00002	<0.00001	<0.00001
Regression	Equation	14.32R-10.54	19.68R-13.74	15.27R-2.638	13.69 + 10.78R	8.084 + 13.52R	8.073 + 12.24R	10.464 + 11.64R	18.54R-12.564
	R-Square	0.6456	0.7680	0.7460	0.6323	0.8164	0.8042	0.7946	0.7754
Goodness of Fit	S _{y-x}	7.787	9.877	6.504	6.417	6.417	6.417	6.504	2.753

Table 7 Tabulation for RULA and REBA

RULA/ REBA Comparison					
Count					
		REBA			Total
		High	Low	Moderate	
RULA	High	167	5	8	180
	Low	9	144	27	180
	Moderate	4	31	145	180
Total		180	180	180	540

4.3 Assessment of Level of Agreement Between the Tools

4.3.1 Kappa Analysis Among RULA and REBA

In order to compare the agreement among RULA and REBA, we first convert all the score of RULA and REBA into three levels, of the risk i.e. low, medium, high. Then the Kappa coefficient is applied in SPSS software to find the level of understanding between the two [21]. Table 7 shows the count of the RULA risk level of low, medium and high with the risk level of REBA in the tabulation. The Kappa value for the level of understanding among RULA and REBA is evaluated as 0.7875. It represents that there is an almost significant agreement among RULA and REBA. The chosen p-value $p < 0.05$ is also transformed, which means that the relationship between RULA and REBA has statistical significance.

The reason for the almost perfect level of understanding between RULA/REBA is because both the methods depend much on the angle measurement and method of achieving the score is quite similar. Since the degree of understanding between the RULA and REBA methods is almost complete, it can therefore be claimed that both methods in the power-loom industry can be used interchangeably.

4.3.2 Kappa Analysis Between RULA and NMSQ

The RULA analysis was combined into the category of medium and high risk, into the category of risk, and the category of low risk, into the category of no risk. This count for RULA risk and no risk with the questionnaire pain and no pain is shown in Table 8.

The Kappa value for the level of understanding between RULA and Nordic questionnaire as shown in Table 10 is coming out to be 0.349 which represents that there is a reasonable consensus between RULA and Nordic questionnaire. The p-value is too turned selected $p < 0.05$ which indicates that the association between RULA and Nordic questionnaire have statistical significance.

Table 8 Tabulation for RULA and NMSQ

RULA and NMSQ				
Count				
		NMSQ		
		No pain	Pain	
RULA	No risk	140	76	216
	Risk	94	230	324
Total		234	306	540

4.3.3 Kappa Analysis Between REBA and NMSQ

The REBA analysis score has been merged into its category of medium and high risk into risk category and low-risk category into no risk category. This count for REBA risk and no risk with the questionnaire pain and no pain is shown in Table 9.

The Kappa value for the level of understanding between REBA and Nordic questionnaire as Table 10 is coming out to be 0.274 which represents that there is a reasonable consensus between REBA and Nordic questionnaire. The p-value is too turned selected $p < 0.05$ which indicates that the association between REBA and Nordic questionnaire have statistical significance.

Table 9 Tabulation for REBA and NMSQ

REBA/NMSQ				
Count				
		NMSQ		
		No pain	Pain	
REBA	No risk	122	77	199
	Risk	113	228	341
Total		235	305	540

Table 10 Comparison of tool and NMSQ

Comparison of tool and NMSQ	Kappa Value	Agreement
RULA and NMSQ	0.349	Fair
REBA and NMSQ	0.274	Fair

5 Conclusion

The number of workstations in the power-loom sector has been studied and each instrument has been converted into three risk levels. The Kappa value amongst RULA and REBA, i.e. 0.7875, is the highest since the methods are very close to each other. Both use the same kind of analysis of neck, trunk, leg in one table and arm and wrist analysis another table. Both techniques are taken care of by an additional force / muscle score factor, but still, RULA and REBA do not fit much of the leg analysis in seven cases. RULA evaluates whether or not the score is accompanied by the leg and does not emphasize the angle of the leg, while REBA provides the angle in the leg and also attaches a score in the leg. That is why RULA is often used as an evaluation tool for the upper limb, while REBA is an evaluation tool for the whole body. Since the Kappa value is 0.7875, it demonstrates complete agreement between the two. Therefore, in the power-loom industry, these tools can be used interchangeably, i.e. if one tool has not introduced the other tool as both would provide synonymous results in a power-loom industry.

References

1. Metgud DC (2008) An ergonomic study of women workers in a woolen textile factory to identify problems related to health. *Ind J of Occ and Env Med* 2(1):14–19
2. Robert N, Richard W (1998) Ergonomic interventions for reducing musculoskeletal disorders: an overview, related issues and future directions, for the institute for work & health to the royal commission on workers compensation in British Columbia, (1998)
3. Kolgiri SG (2018) Implementing sustainable ergonomics for power-loom textile workers. *Int J Pharm Pharm Sci* 10(6):08–112
4. McAtamney L (2002) RULA and REBA in the REAL World. In: Proceedings of 2th conference of the New Zealand ergonomics society, Wellington, New Zealand 15–25 (2002)
5. Dockrell S et al (2012) An investigation of the reliability of Rapid Upper Limb Assessment (RULA) as a method of assessment of children's computing posture. *Appl Ergon* 43(3):632–636
6. McAtamney L, Hignett S (1995) REBA: a rapid entire body assessment method for investigating work related musculoskeletal disorders. In: Annual conference ergonomics society of Australia: proceedings of the 31st annual conference ergonomics society of Australia, 13–15 (1995)
7. Kong YK et al (2010) Development of an ergonomic checklist to examine work-related lower-limb disorders in agriculture-ALLA: lower-limb agricultural evaluation. *J Ergon Soc Korea* 29:933–942
8. Kong YK et al (2018) Comparisons of ergonomic evaluation tools (ALLA, RULA, REBA and OWAS) for farm work. *Int J Occup Saf Erg* 24(2):218–223
9. Mesquita CC et al (2011) Portuguese version of the standardized Nordic musculoskeletal questionnaire: Cross cultural and reliability. *J Pub Health* 18(5):461–466
10. Serranheira F et al (2013) Backache and work in hospital nurses. In: Proceedings of the 9th International Symposium on Occupational Safety and Hygiene (SHO), Guimaraes, Portugal, 14–15 (2013)
11. Hayes MJ et al (2009) A systematic review of musculoskeletal disorders among dental professionals. *Int J Dent Hygiene* 7:159–165
12. Feng B et al (2014) Prevalence of work-related musculoskeletal symptoms of the neck and upper extremity among dentists in China. *BMJ Open* 4:e006451

13. Descatha A et al (2007) Validity of Nordic-style questionnaires for tracking work-related upper limb musculoskeletal disorders. *Scand J Work Environ Health* 33(1):58–65
14. Cohen J (1960) A coefficient of agreement for nominal scales. *Educ Psychol Measur* 20:37–46
15. Chiasson MÈ et al (2012) Comparing the results of eight methods used to evaluate risk factors associated with musculoskeletal disorders. *Int J Ind Erg* 42(5):478–488
16. Cheon W, Jung K (2020) Analysis of accuracy and reliability for OWAS, RULA, and REBA to assess risk factors of work-related musculoskeletal disorders. *J Korea Saf Manag Sci* 22:31–38
17. Hita-Gutierrez M et al (2020) An overview of REBA method applications in the world. *Int J Environ Res Public Health* 17:26–35
18. Lee KS et al (2009) Comparisons of different evaluation tools for musculoskeletal disorders. In: *Proceedings of the fall conference of the ergonomics society of Korea, Daegu, Korea, 205–210 (2009)*
19. Kuorinka I et al (1978) Standardized Nordic questionnaires for the analysis of musculoskeletal symptoms. *App Erg* 18(3):233–237
20. Kolgiri SG et al (2018) Work related musculoskeletal disorders among power-loom industry women workers from Solapur City, Maharashtra, India. *IJETSR* 5(3):1002–1008
21. Blackman NJ, Koval JJ (2000) Interval estimation for Cohen's kappa as a measure of agreement. *Stat Med* 19(5):723–741

Role of Fillers in Controlling the Properties of Polymer Composites: A Review



K. B. Bommegowda, N. M. Renukappa, and J. Sundara Rajan

Abstract The use of polymer composites has risen tremendously over the last decade and it finds numerous applications in fields such as microelectronics, automobiles and structural applications. In this paper, an extensive review of the recent developments in polymer composites is presented. The interface and compatibility of the polymer matrix and the filler have a significant role in the ultimate properties of the composites. The basic processes like the selection of the polymer matrix, hardener, fillers and reinforcement, synthesis and dispersion of the filler and the fabrication processes are the key for developing good polymer composites. With the recent advances in hybrid fillers, polymer structure has become more complex and hence there is for a thorough of the various stages of development of polymer hybrid composites. This review summarizes different aspects like material processing techniques of polymer composites.

Keywords Polymer composites · Electrical insulation · Nano and micro fillers

1 Introduction

In recent years, there is an increasing demand for nanocomposites in the area of electrical insulation as well as in applications requiring EMI shielding, thermal barriers etc. The dominant role of nano/micro scale fillers in the polymer matrix

K. B. Bommegowda (✉)

Department of Electronics and Communication Engineering, N.M.A.M. Institute of Technology (Visvesvaraya Technological University, Belagavi) Nitte, Udipi, Karnataka, India
e-mail: bgowda_kbl@nitte.edu.in

K. B. Bommegowda · N. M. Renukappa

Department of Electronics and Communication Engineering, JSS Science and Technology University, Mysuru, Karnataka, India
e-mail: renunijagal@gmail.com

J. S. Rajan

Department of Electrical and Electronics Engineering, Siddaganga Institute of Technology, Tumakuru, Karnataka, India
e-mail: drjsrajan12@ieee.org

in the enhancement of electrical, thermal, and mechanical properties of polymeric composites [1] is evident from literature. The use of composites in High voltage insulation systems is based on its basic function of providing good insulation, in addition to having good thermal life and higher temperature class [2]. Due to its significant advantages like resistance to corrosion, lightweight, low cost and simplicity of processing, the polymer composites with fillers are slowly replacing traditional polymer composites in insulation applications and also in EMI shielding applications [3, 4] with conducting fillers. The large ratio of surface to volume of the nanofillers helps in good dispersion in a polymer matrix. However, it results in the formation of a large number of interfaces [5, 6]. The physical properties of the constituents of the polymer composites being dissimilar in nature to the physical properties of the interface area, and this induces many changes in the characteristic properties of the nanocomposites [7–9]. Since the entire process of development of nanocomposites is overly complex in nature, a thorough review of the literature was carried out to identify the key areas of concern for the development of nanocomposites.

2 Benefits of Fillers Used in Composites

Many investigations have been carried out in the last decade to highlight the benefits and disadvantages of using different micro/nanofillers, and the focus has generally been on the effects of filler particle size, concentration, and its distribution. The benefits of the individual fillers are the benchmark for improving the properties of the polymer composites. Table 1 summarizes some of the advantages of the fillers which find applications for use by the electrical industry. A small amount of well-dispersed nanofillers in a polymer matrix provides multiple advantages since the modifications of the polymer matrix resulting from the size, weight percentage (wt.%) and distribution has a huge impact of the structure of the polymer nanocomposites [10–12]. The large interaction zones created by the filler particles leads to a significant increase in localized sites of interaction between the filler and the polymer matrix, even when the filler wt.% is low. The interactions help to improve the electrical, thermal, and mechanical properties, but the complex nature of the filler-matrix interactions can lead to an improvement in some properties and deterioration in other properties which are also vital for industrial applications [13]. Hence by proper choice and combination of fillers, it is possible to achieve a balance of electrical, mechanical, and thermal properties of the nanoparticles [9]. Most of the particulate fillers have low electrical conductivity and are preferred for enhancement of electrical insulation capability [14, 15]. However, in the case of conducting fillers which are governed by electrical percolation. Thus, the incorporation of conducting filler has little effect until the formation of a continuous conducting pathway through the polymer matrix [16]. At the percolation threshold, a dramatic increase in the electrical conductivity of the composite is accomplished as shown in Fig. 1. In Figs. 2, 3 and 4 the role of the interface is graphically depicted.

Table 1 Benefits of different fillers used in polymer composites [23–26]

Filler	Advantages
Silica	Increases the breakdown strength Enhances surface and volume resistivity Increases glass transition temperature High wear resistance Improve the abrasive wear performance
Alumina	Enhances volume resistivity Increases breakdown strength Enhances dielectric constant Reduces dielectric loss Increases dissipation factor
Graphite	Sustained by high temperature Chemical resistance High thermal conductivity Improve the toughness Increases tensile strength
Cenosphers	Low water absorption
Silicon carbide	Increases hardness Reduction in dielectric constant
Molybdenum disulfide	Increases glass transition temperature Good chemical and thermal stability Increases tensile and flexural strength
Aluminium trihydrate	Improves thermal conductivity Improves permittivity
Calcium carbonate	Good dielectric properties Improves thermal conductivity Improves thermal stability Increases permittivity
Magnesium oxide	Increases dielectric strength Improves thermal conductivity Reduces dissipation factor Increases volume resistivity
Zinc oxide	High dielectric constant High thermal conductivity
Boron nitride	Absorb UV light released by partial discharges High electrical resistivity Low dielectric constant High temperature resistance

To achieve the homogeneous dispersion, the surface functionalization of nanoparticles is needed by coupling agents. The surface-treated nanofillers are more resistant to moisture absorption for shorter periods than untreated nanofillers. However, this is not true for longer periods. The surface modification of nanofiller helps to achieve a better dispersion but it harms the other properties. Better results can be obtained

Fig. 1 Percolation of electrically conductive particles [27]

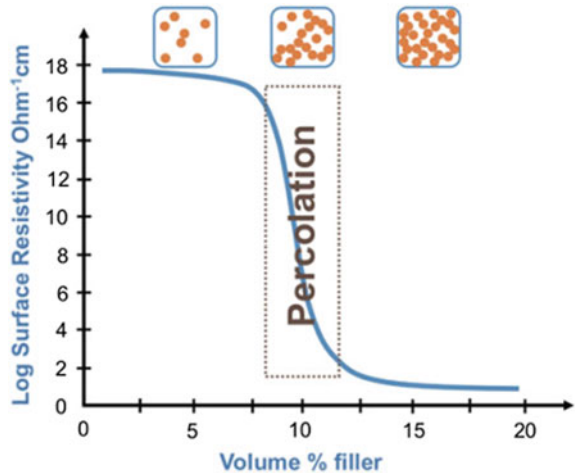
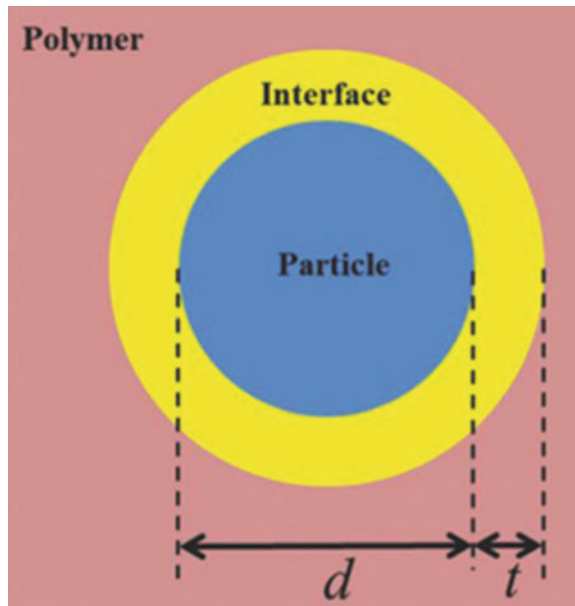


Fig. 2 Schematic of polymer interface structure in a composite [28]



for composites through the combination of micro and nanofillers and such composite performs better than nanocomposites [17]. Nano and micro filler combination is a new and innovative approach to improve the electrical insulation as well as electrical conduction in polymers. For example, nano layered silicate fillers and micro scale silica fillers in epoxy resin are used for electrical insulation. Epoxy composites with silica hybrid fillers exhibited outstanding performance under rapid rise electrical breakdown test and the composite with hybrid filler resulted in a 7% higher

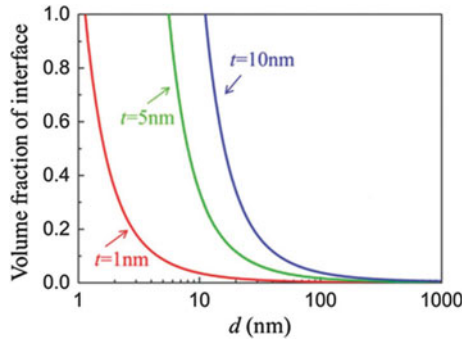


Fig. 3 Volume fraction of interface with the diameter of the filler particles and interface thicknesses [28]

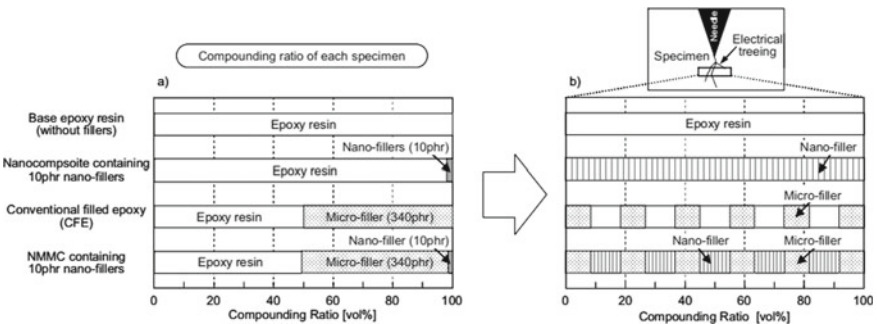


Fig. 4 Densely packed structure of nano and micro filler mixed composites [19]

electrical breakdown strength than the conventional epoxy composite. Even under the proof voltage AC dielectric test, the composite with hybrid filler exhibited vast improvement in terms of time duration for voltage withstand capability [18]. Hybrid composites with a combination of nano and micro fillers (HNC) have the advantage of the synergy that exists in the two fillers. This results in significant improvement in some of the properties of the composites. For example, the insulation breakdown occurs via electrical tree propagation under divergent electric field in epoxy composites. Fillers are used by some researchers for inhibiting the growth of electrical treeing. Nanocomposite containing 10phr of nano fillers has 98 vol.% of epoxy resin, while HNC containing 10phr of nano fillers has 50 vol.% of epoxy resin, as shown in Fig. 5. The addition of micro fillers in HNC reduces the amount of epoxy resin. Moreover, the nano fillers get dispersed between the micro fillers in the HNC and hence the nano filler particles successfully block the growth of electrical trees. Thus, the synergistic effect of nano and micro fillers helps to enhance the electrical insulation breakdown strength [19] of the composites. The composites containing both nano and micro fillers are observed to improve the endurance capability of the composites to partial discharges even if the dc parameters like volume and surface resistivity show minimal

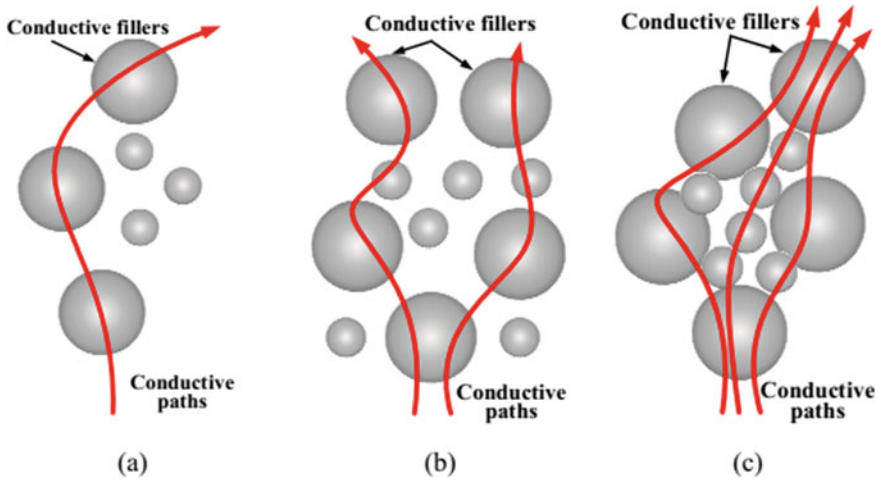


Fig. 5 Comparison between thermal conductive paths in composites. **a** Low wt.% **b** High wt.% with reduced conducting path **c** High wt.% of filler with thermal conducting network [31]

improvements [20]. With the size of the filler particle being increased, the role of the interphase regions becomes less dominant. Therefore, a considerable increase in micro filler no significant change in glass transition temperature results, as in the case of silica in the epoxy matrix [21].

The electrical breakdown strength is reduced when the epoxy resin is filled with a high proportion of the micro fillers [22]. Hence the combination of nano and micro filler in polymer composites have shown higher electrical breakdown strength and partial discharge resistance than the micro composites.

The addition of nano fillers provides an excellent approach towards increasing the dielectric breakdown strength of epoxy composites which is reduced by the presence of micro fillers [29]. The micro fillers also have a dominating role in the control of the thermal conductivity when present at lower concentrations, due to their ability to control of phonon scattering [30]. Composites with small filler particles have large interfacial areas, causing phonon scattering, resulting in reduced thermal conductivity.

The composites with large fillers have less filler/polymer interfaces and thus offer lower thermal interfacial resistance leading to improved heat conduction. The mechanism of domination of the thermal conductivity of the composites is described schematically shown in Fig. 5 [31]. Therefore, care should be exercised when the combination of micro and nano fillers are used, by the selection of the optimum ratio of micro to nano fillers.

3 Importance of Fabrication Techniques

The fabrication of conventional epoxy composites, which is the most extensively used polymer is well established over the last two decades. However, with the introduction of nanocomposites, the fabrication techniques have assumed significance because of the differences arising in the microstructure due to the adoption of different fabrication processes. The term fabrication is a general terminology which includes initial pre and post-conditioning of the polymer matrix, hardeners, and the filler, mixing of the resin with the hardener and dispersion of fillers into the polymer matrix. When reinforcement is used, the process of fabrication becomes more complex when different reinforcing materials are used. Different glass fibers, fabrics, carbon fibers and fabrics are used as reinforcements, depending upon the end-use.

Polymer processing consists of different methods. These include (1) in situ polymerization, (2) blending either by Solution blending or Melt blending. During the in-situ polymerization [32], the nanofiller is to be properly dispersed in the monomer solution before polymerization to ensure polymer matrix has a good distribution of the nanofiller. Polymerization can be initiated by heating or with an appropriate initiator. Polymers with good dispersion of nanoparticles, even at higher loading without aggregation can be achieved by this method. Organic modifiers are used to aid the dispersion of the nanoparticles and they also take part in the polymerization processes. These techniques result in better performance of polymer composites for critical applications in the industry. In the mini-emulsion polymerization method, monomer droplets are dispersed into a solution with nanoscale particles. The method of production of polymer nanocomposites is shown schematically in Fig. 6. Some of the benefits of this method are controllable particle morphology, good interfacial adhesion of the nanofillers and high transparency. With this method, it is possible to incorporate higher wt.% of the nanofillers without agglomeration.

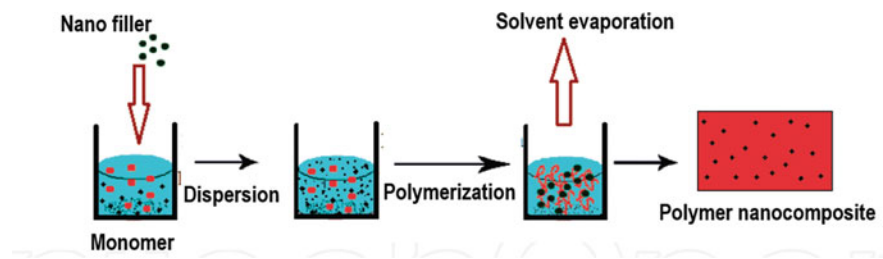


Fig. 6 Schematic of the in-situ polymerization method of fabrication [32]

3.1 Dispersion of Fillers and Fabrication of Nanocomposites

Fillers are mixed in a solution and the filler aggregates are subjected to shear stresses imparted from the medium (e.g., solvent or polymer melt). Therefore, the flow of the medium in response to an external force (either the rotation of a mixer blade or cavitation in ultrasonication) would generate local shear stresses that are responsible for the dispersion of the filler [33]. During the mixing process, delivery of mechanical energy into the solution helps to separate the aggregates. The opposing factor against the separation of aggregates is the binding energy which holds them together. Considering these two factors, the mixing criteria for good aggregate separation is that the energy from the mixing device should be greater than the binding energy of the filler aggregates. To retain the morphology of individual fillers, the energy should be less than the energy required to split the nanofillers [34]. Hence, an ideal aggregate separation technique should supply energy density which is in-between the binding energy of the aggregates and the fracture resistance of individual fillers. It is the general practice to employ a ball mill method to reduce the larger particles to nano-scales. In this method, smaller grain-sized nano-particles are produced by the collision of the milling balls [7–9]. There are numerous methods for fabricating components or laminates with fillers dispersed in the polymer. Selection of a method, therefore, will depend on the materials, design and end-use or application. Some methods have been borrowed from plastics like injection molding but many were developed to meet specific design or manufacturing challenges faced with *fiber-reinforced* polymers. The most basic fabrication method for thermoset composites is *hand layup*, which typically consists of placing layers, called plies of either dry fabrics, or prepreg (fabric pre-impregnated with resin), by hand onto a tool to form a laminate stack [35]. Resin is applied to the dry plies after layup is complete. In a variation known as a wet layup, each ply is coated with resin and *debulk*ed (compacted) after it is placed [36]. Although debulk can be done by hand with rollers, most fabricators today use a *vacuum-bagging* technique that involves placing plastic sheet materials over the layup, sealing it at the tool's edges, adding one or more ports for air hoses and then evacuating air from the space between the sheet and the layup using a vacuum pump). Debulking consolidates the layup but also removes air trapped in the resin matrix.

Several *curing methods* are available today. The most basic method is to simply to allow natural curing at room temperature which is initiated by a catalyst or hardener additive premixed into the resin. To accelerate the process, heating may be used and pressure employing a vacuum may be employed [37]. For the latter, a vacuum bag, with breather assemblies, is placed over the layup and attached to the tool and vacuum is applied to initiate curing. Autoclaves are used and are generally expensive and bit complex to operate. Computer systems today help to monitor and control autoclave temperature, pressure, vacuum, and the atmosphere, which allows unattended and/or remote supervision of the cure processes [38]. When heat is required for curing, the temperature is “ramped up” in small increments, maintained at cure level for a specified time which is specific to the resin system, and then “ramped down” to

room temperature, to avoid part distortion or warp caused by uneven expansion and contraction [39]. Electron-beam (E-beam) curing has been explored as an efficient curing method for thin laminates. X-ray and microwave curing technologies work similarly. Use of ultraviolet (UV) curing, for crosslinking has been developed. The ever-increasing demand for faster production rates has compelled the industry to replace the hand layup method with automated processes. A common alternative is the resin transfer molding (RTM), sometimes referred to as liquid molding.

4 Effect of Fillers

Different types of fillers are used to improve the properties of composite materials. However, fillers improve the dielectric strength and resistance to environmental effects, up to a certain extent and adding too much filler may worsen the properties instead of improving them. Therefore, a controlled amount of filler should be added to achieve optimum results. Fillers like silicon carbide (SiC) have revealed enhancement in mechanical properties namely the tensile strength, flexural strength, hardness and with a drastic reduction in the dielectric constant [40]. Improving thermal conductivity with fillers is more challenging especially when electrical insulation is required. Attempts are made to improve electrical insulation with fillers such as silicon carbide, alumina, and silica [41, 42]. The tensile strength of epoxy with micro silica composites is observed to reduce at higher loading of micro silica. But electrical breakdown strength is satisfactory at 50 wt.% of micro silica filler [43]. Some authors [44] have studied the effect of epoxy-micro alumina composites for microelectronics. It is reported that inclusion of micro- alumina of different weight percentages (2.5–25 wt.%) in epoxy increases the thermal conductivity and glass transition temperature but decreases the Coefficient of Thermal Expansion (CTE). The dielectric constant of epoxy composite with 25 wt.% of micro alumina is reported to be around 6 and the glass transition temperature increases from 98 to 116 °C, whereas the CTE is reported to decrease from $66 \times 10^{-6}/^{\circ}\text{C}$ to $56.2 \times 10^{-6}/^{\circ}\text{C}$. Composites with 3 wt.% of molybdenum disulphate (MoS_2) filler is reported to possess reduced mechanical strength and minimum water uptake. The tensile strength decreases by 3%, flexural strength by 18% and shear strength by 42% when 3 wt.% due to MoS_2 filler [45]. However, glass fiber reinforced epoxy composite with 4 wt.% of MoS_2 have shown different characteristics. It is also observed that there is a linear increase in the tensile strength with increase in MoS_2 filler percentage [46]. Studies are reported on epoxy composites with cenosphere which for better thermal and electrical stability with reduced electrical resistivity. The crystallinity induced by the better interaction between cenosphere and epoxy and cross-linked state facilitates increases some of the insulating properties [47]. The flexural and impact strength are observed to decrease above 50 wt.%, due to incompatibility issues [48, 49].

5 Conclusion

Nanotechnology offers tremendous scope for development of nanocomposites with optimized electrical, thermal and mechanical properties. There are many opportunities and challenges in the development of hybrid composites for different industrial applications. However, a judicious choice of the polymer matrix, fillers and processing and fabrication techniques would be required. These processes are extremely specific to the polymer matrix and the filler or filler combination used and hence more research is required for the development of novel hybrid composites.

References

1. Edison Selvaraj D, Usa S, Pugazhendhi Sugumaran C (2012) Comparative analysis of dielectric properties of enamel filled with various nanofillers such as ZrO_2 , Al_2O_3 , CNT and ZnO. *Int J Sci Eng Appl* 1
2. Nguyen MQ, Malec D, Mary D, Werynski P, Gornicka B, Therese L, Guillot Ph (2009) Investigations on dielectric properties of enameled wires with nano filled varnish for rotating machines fed by inverters. In: *IEEE electrical insulation conference*
3. Dinesh PG, Renukappa NM, Pasang T, Dinesh M, Rangananthaiah C (2014) Effect of nanofillers on conductivity and electromagnetic interference shielding effectiveness of high-density polyethylene and polypropylene nanocomposites. *Eur J Adv Eng Technol* 1(2):16–28
4. Jorice GC (2012) Samuel and stephanie lafon placette.: epoxy alumina nanocomposites: advanced materials for high voltage insulation. In: *IEEE electrical insulation and dielectric phenomena annual report conference*. pp 573–576
5. Jegatheesh G, Muniraj R (2015) Fabrication and analysis on critical parameters of nano solid dielectric material for enhancing the insulation strength. In: *IEEE international conference on innovations in information embedded and communication systems*. pp 1–5
6. Han Z, Garrett R (2008) Overview of polymer nanocomposites as dielectrics and electrical insulation materials for large high voltage rotating machines. In: *Nanotechnology Conference*, vol 2
7. Pazhanimuthu C (2012) Investigation of dielectric and thermal properties of nanodielectric materials in electrical applications. *Int J Eng Innovat Technol* 2
8. Kirkici H, Serkan M, Koppisetty K (2005) Nano-dielectric materials in electrical insulation application. In: *Annual conference of IEEE industrial electronics society*
9. Pugazhendhi Sugumaran C (2014) Experimental investigation on dielectric and thermal characteristics of nanosized alumina filler added polyimide enamel. *J Electric Eng Technol*
10. Pugazhendhi Sugumaran C, Mohan MR, Udayakumar K (2010) Investigation of dielectric and thermal properties of nano-filler (ZrO_2) mixed enamel. *IEEE Trans Dielectr Electr Insul* 17(6)
11. Diahm S, Saysouk F, Locatelli ML, Lebey T (2014) Dielectric properties of polyimide/boron nitride nanocomposites at high temperature. In: *IEEE annual report conference on electrical insulation and dielectric phenomena*
12. Das S, Gupta N (2013) Effect of thermal and humidity ageing on space charge accumulation in epoxy resin. In: *IEEE international conference on solid dielectrics*. pp 456–459
13. Saba N, Tahir PM, Jawaid M (2014) A review on potentiality of nano filler/natural fiber filled polymer hybrid composites. *J Polym*
14. Roy M, Nelson JK, MacCrone RK, Schadler LS (2005) Polymer nanocomposite dielectrics - the role of the interface. *IEEE Trans Dielectr Electr Insul* 12
15. Singha S, Joy Thomas M (2008) Dielectric properties of epoxy nanocomposites. *IEEE Trans Dielectr Electr Insul* 15

16. Pazhanimuthu C (2012) Investigation of dielectric and thermal properties of nano-dielectric materials in electrical applications. *Int J Eng Innov Technol (IJEIT)* 2
17. Paramane AS, Kumar KS (2016) A review on nanocomposite based electrical insulations. *Trans Electr Electron Mater* 17:239–251
18. Imai T, Sawa F, Nakano T, Ozaki T, Shimizu T, Kozako M, Tanaka T (2006) Effects of nano and micro-filler mixture on electrical insulation properties of epoxy based composites. *IEEE Trans Dielectr Electr Insul* 13:319–326
19. Imai T, Komiya G, Murayama K, Ozaki T, Sawa F, Shimizu T, Harada M, Ochi M, Ohki Y, Tanaka T (2008) Nano and micro filler combination enabling practical use of nanocomposite insulating materials. In: *International symposium on electrical insulating (ISEIM 2008)*. pp 299–302
20. Fabiani D, Montanari GC, Krivda A, Schmidt LE, Hollertz R (2010) Epoxy-based materials containing micro and nano-sized fillers for improved electrical characteristics. In: *IEEE international conference on solid dielectrics*. pp 1–4
21. Nguyen V, Vaughan AS, Lewin PL, Krivda A (2011) Stoichiometry and effects of nano-sized and micro-sized fillers on an epoxy based system. In: *IEEE conference on electrical insulation and dielectric phenomena*. pp 302–305
22. Abdelkarim MF, Nasrat LS, Elkhodary SM, Soliman AM, Hassan AM, Mansour SH (2014) Effect of nano fillers on electrical performance of epoxy composite insulators. *Int J Eng Tech Res (IJETR)*
23. Han Z, Wood JW, Herman H, Zhang C, Stevens, GC (2008) Thermal properties of composites filled with different fillers. *IEEE Trans Dielectr Electr Insul*
24. Calebrese C, Hui L, Schadler LS, Keith Nelson J (2011) A review on the importance of nanocomposite processing to enhance electrical insulation. *IEEE Trans Dielectr Electr Insul* 18
25. Wang Q, Chen G, Alghamdi AS (2010) Influence of nanofillers on electrical characteristics of epoxy resins insulation. In: *International conference on solid dielectrics*
26. Barber P, Balasubramanian S (2009) Polymer composite and nanocomposite dielectric materials for pulse power energy storage. *J Mater*
27. DeArmitt C, Rothon R (2017) Particulate fillers selection and use in polymer composites. *Springer Reference on Fillers for Polymer Applications*, pp 3–27
28. Luo H, Zhou X, Ellingford C, Zhang Y, Chen S, Zhou K, Zhang D, Bowen CR, Wan C (2019) Interface design for high energy density polymer nanocomposites. *R Soc Chem* 48:4424–4465
29. Li Z, Okamoto K, Ohki Y, Tanaka T (2010) Effects of nano-filler addition on partial discharge resistance and dielectric breakdown strength of micro- Al_2O_3 /epoxy composite. In: *IEEE transactions on dielectrics and electrical insulation*, vol 17. pp 653–661
30. Pugazhendhi Sugumaran C (2014) Experimental investigation on dielectric and thermal characteristics of nanosized alumina filler added polyimide enamel. *J Electr Eng Technol*
31. Wang Y, Wu J, Yin Y, Han T (2020) Effect of micro and nano-size boron nitride and silicon carbide on thermal properties and partial discharge resistance of silicone elastomer composite. *IEEE Trans Dielectr Electr Insul* 27:377–385
32. Feng Y, Yin J, Chen M, Liu X (2011) Dielectric properties of PI/BaTiO_3 with disparate inorganic content. In: *International forum on strategic technology*
33. Zou C, Fothergill JC, Rowe SW (2008) The effect of water absorption on the dielectric properties of epoxy nanocomposites. *IEEE Trans Dielectr Electr Insul* 15
34. Yang B, Zhang J (2015) Effect of nano-fillers on the thermal performance of pCBT resin. In: *7th world congress on particle technology (WCPT7) procedia engineering*
35. Wang Z, Nelson JK, Miao J, Linhardt RJ, Schadler LS (2012) Effect of high aspect ratio filler on dielectric properties of polymer composites: a study on barium titanate fibers and graphene platelets. *IEEE Trans Dielectr Electr Insul* 19
36. Stevens GC, Freebody NA, Hyde A, Perrot F, Szkoda-Giannaki I (2015) Balanced nanocomposite thermosetting materials for HVDC and AC applications. In: *Electrical insulation conference (EIC)*

37. Raju BR, Suresh B, Swamy RP, Bharath KN (2012) The effect of silicon dioxide filler on the wear resistance of glass fabric reinforced epoxy composites. *Int J Adv Polym Sci Technol* 51–57
38. Maity P, Kasisomayajula SV, Parameswaran V, Basu S, Gupta N (2008) Improvement in surface degradation properties of polymer composites due to pre-processed nanometric alumina fillers. *IEEE Trans Dielectr Electr Insul* 15
39. Singha S, Thomas MJ (2006) Polymer composite/nanocomposite processing and its effect on the electrical properties. In: Annual report conference on electrical insulation and dielectric phenomena
40. Suresha B, Chandramohan G, Renukappa NM, Siddaramaiah H (2009) Influence of silicon carbide filler on mechanical and dielectric properties of glass fabric reinforced epoxy composites. *J Appl Polym Sci* 111:685–691
41. Hussain WA, Hussein AA, Khalaf JM, Al-Mowali AH, Sultan AA (2015) Dielectric properties and a.c. conductivity of epoxy/alumina silicate NGK composites. In: Advances in chemical engineering and science, pp 282–289
42. Castellon J, Nguyen HN, Agnel S, Toureille A, Frechette M, Savoie S, Krivda A, Schmidt LE (2011) Electrical properties analysis of micro and nano composite epoxy resin materials. *IEEE Trans Dielectr Electr Insul* 18:651–658
43. Park J-J (2019) Tensile and electrical insulation properties of epoxy/micro-silica composites. *Trans Electr Electron Mater* 20:67–72
44. Agarwal A, Satapathy A (2014) Experimental investigation of micro-sized aluminium oxide reinforced epoxy composites for microelectronic applications. In: International conference on advances on manufacturing and materials engineering (AMME-2014), vol 5. pp 571–526
45. Jhansi K, Babu KN, Rao LB (2019) The effect of moisture on the properties of glass fiber polymer matrix composites with MoS₂ and CaCO₃. *Int J Eng Adv Technol* 8:4800–4806
46. Vijay BR, Srikantappa AS (2019) Physico-mechanical and tribological properties of glass fiber based epoxy composites. *Int J Mech Eng Robot Res* 8:929–934
47. Kadam P, Pawar B, Mhaske S (2013) Studies in effect of low concentration of cenosphere on mechanical, thermal, electrical, crystallinity, colorimetric and morphological properties of epoxy cured with triethylenetetramine. *J Miner Mater Charact Eng* 1:117–123
48. Kushnoore S, Varma GA, Akhil K, Jathin Ch, Reddy MM (2018) Experimental investigation on mechanical behaviour of cenosphere reinforced epoxy composites. *Int J Mech Eng Technol* 9:73–81
49. Suresha B, Chandramohan G, Renukappa NM, Siddaramaiah (2007) Mechanical and tribological properties of glass-epoxy composites with and without graphite particulate filler. *J Appl Polym Sci* 103:2472–2480

Frequency Spectrum Analysis of Various Defects in Rolling Element Bearings Used in Heavy Load and High Speed Machinery



Prashant H. Jain and Santosh P. Bhosle

Abstract Rolling element bearings are common components of any machine and defects in them are one of the most common types of the machine faults. Many vibration signal analysis techniques are available to monitor the condition of bearings. Time domain analysis technique is one of the easiest techniques widely used to know the condition of bearings. However, one of the limitations of time domain analysis techniques is that it can diagnose the severity of the bearing defect, but it cannot identify the location of defect. For this purpose, frequency domain analysis techniques are widely used. In this paper, frequency spectrum analysis of defects in cylindrical roller bearings N205 and NU205 used in heavy load and high speed machinery is carried out for different types of defects and sizes at constant speed and radial load. Inner race defect, outer race defect, roller defect are considered for analysis. The effects of localized multiple defects and defects in combination are also studied. The results show the effectiveness of frequency spectrum analysis technique for identifying bearing defects and their severity.

Keywords Frequency spectrum analysis · Bearing defects · Multiple defects · Cylindrical roller bearings

1 Introduction

Cylindrical roller bearings (CRBs) are used in machineries to support the rotating parts subjected to heavy radial loads and high speeds such as gearboxes, motors, pumps and compressors, material handling equipment, paper machines, etc. CRB consists of four main components i.e. inner race, outer race, cylindrical roller and cage. Defects in bearings are broadly categorized into two types i.e. localized and distributed defects. Localized defects include spalls, pits, cracks, dents etc. on the rolling surfaces of bearings, which are generally caused by fatigue, overloading,

P. H. Jain (✉)

Research Scholar, Maharashtra Institute of Technology, Aurangabad, Maharashtra, India

S. P. Bhosle

Principal, Maharashtra Institute of Technology, Aurangabad, Maharashtra, India

shock loading, corrosion, etc. Such defects in bearing cause undesirable vibrations in machines. Therefore, it is necessary to identify the defects in bearings in their early stages. Among vibration signal analysis (VSA) techniques, time domain analysis (TDA) is the easiest and widely used technique to monitor the condition of bearings. TDA involves representation of vibration signal into amplitude versus time graph. Several statistical parameters are used in TDA such as RMS, crest factor, skewness, kurtosis, etc. for the analysis of bearing vibration signals. These parameters can only indicate the condition of bearings i.e. good or defective and does not indicate the exact location of the defect in bearing. Also these parameters vary with the factors such as defect type, size, speed, load, etc. Frequency domain analysis is widely used for identification of defects in the bearings. In frequency domain analysis, Fourier transform is used to convert the time domain signals into frequency domain signals, which are also called as frequency spectrums. For the signal having frequency f and time t , the Fourier transform is given by following equation [1]

$$X(f) = F[x(t)] = \int_{-\infty}^{+\infty} x(t)e^{-j2\pi ft} dt \tag{1}$$

where $x(t)$ is a vibration signal in time domain and $X(f)$ is the Fourier Transform of $x(t)$ in frequency domain.

Frequency spectrum is a graphical representation of amplitude of vibration and frequency. Vibration amplitude is usually measured in terms of displacement, velocity or acceleration (G’s) by using FFT spectrum analyzer. Every bearing element has its characteristic rotational frequency and their values can be calculated from the kinematic analysis of bearing. Table 1 shows the formulae of characteristic defect frequencies of bearings [2, 3]. The defected bearing element can be identified by comparing the frequency spectrums of defected bearing and a good bearing.

Researchers used two experimental approaches to study the effects of bearing defects on vibration signals. In first approach, use the bearing under running condition

Table 1 Formulae of characteristic bearing defect frequencies

Characteristic defect frequency	Formula
Outer race defect frequency (ORDF)	$\frac{nf_r}{2} \left(1 - \frac{D_b}{D_c} \cos\varphi\right)$
Inner race defect frequency (IRDF)	$\frac{nf_r}{2} \left(1 + \frac{D_b}{D_c} \cos\varphi\right)$
Roller defect frequency (RDF)	$\frac{D_c}{D_b} f_r \left[1 - \left(\frac{D_b}{D_c} \cos\varphi\right)^2\right]$
Cage rotational frequency (CRF)	$\frac{f_r}{2} \left(1 - \frac{D_b}{D_c} \cos\varphi\right)$

where n = no. of balls/rollers, f_r = Shaft speed in rpm, D_b = Diameter of ball/roller, D_c = Diameter of cage, φ = Contact angle of ball

till the development of defects in it and then measure the vibration response. In second approach, create the defects intentionally in the bearings by scratching, spark erosion or indentation and then measure the vibration response. Finally, compare the vibration signals of defective bearings with that of good bearings to know the location of the defect. The second approach is mostly preferred by the researchers, as it is easy and requires less time.

In last two decades, many researchers published research work on application of frequency spectrums for detection of bearing defects. Tandon and Kumar [4] used overall vibration RMS velocity levels, frequency spectrums and shock pulse values for detection defects in ball bearings at different locations. They showed that the ORDs in maximum load zone can be easily detected as the vibration levels are high when ORD is in this zone and it decreases when the ORD is moved away from this zone. They also showed that the vibration levels and shock pulse value decreases with the increase in angle between two defects. Amarnath et al. [5] employed TDA, FDA and spike energy analysis to identify different defects in REBs. They showed that time waveform indicates severity of defect in bearing and frequency spectrum shows the exact location of defect in bearing. Liu et al. [6] used experimental vibration signal analysis (VSA) method and finite element analysis (FEA) method to study the effects of localized defect shapes of ball bearing on vibration amplitude. They found that the vibration amplitude produced by localized defects are greatly influenced by shape of defect and slightly influenced by the radial load, axial load and speed. Utpat et al. [7] compared various vibration parameters such as peak, peak to peak and RMS. They found that the defect detectability of outer race defect (ORD) is best followed by inner race defect (IRD) and ball defect (BD). They also found that peak to peak gives better results followed by peak and RMS. The use of spectrum analysis for bearing defect detection is recently presented by some researchers viz. Orhan et al. [8], Patel et al. [9], Patel et al. [10], Patel et al. [11], Dube [12], Shah et al. [3], Khadersab and Shivakumar [13], Jafari [14], Utpat et al. [15], Ghazaly et al. [16], Immovilli and Coconcelli [17], Rao and Ratnam [18], Jain and Bhosle [19]. From the survey on frequency spectrum analysis of bearings, it is found that very few researchers [11, 12] analyzed the multiple defects and combined defects in bearings. Hence, in this paper the frequency spectrum analysis technique is used to study the effect of localized multiple defects and defects in combination.

2 Experimental Setup and Methodology

In this paper, two types of cylindrical roller bearings N205 and NU205 of NRB make are used for analysis. From the catalogue of NRB bearing, it is observed that both the bearings have same specifications as shown in Table 2. The only difference is that; in bearing N205, the outer race is removable and in bearing NU205 inner race is removable. Figure 1 shows cross-sectional views of N205 and NU205 bearings. For all the experiments, the vibration responses have been measured for shaft speed

Table 2 Specifications of N205 and NU205 bearings

Outer diameter (D)	Inner diameter (d)	Width (B)	Pitch diameter (D_c)	Roller diameter (D_b)	No. of balls (n)	Contact angle (φ)
52 mm	25 mm	15 mm	38.5 mm	6.5 mm	12	0°

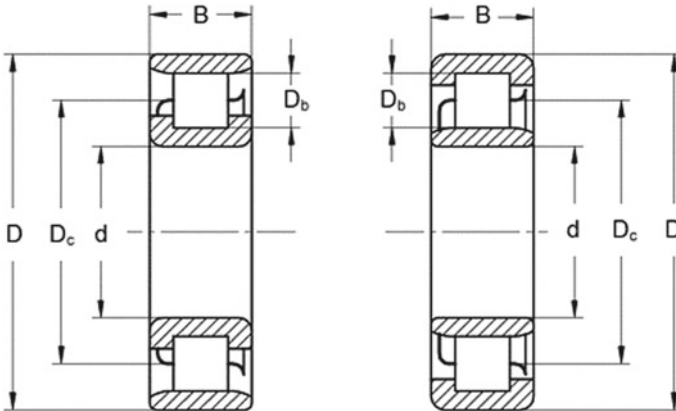


Fig. 1 Cross-sectional view of N205 and NU205

Table 3 Bearing defect characteristic frequencies for shaft speed 1735 rpm

ORDF	IRDF	RDF	CRF
144.2 Hz	202.8 Hz	166.4 Hz	12.02 Hz

1735 rpm and radial load 5 kg. Table 3 shows the bearing defect characteristic frequencies for shaft speed 1735 rpm i.e. 28.9 Hz.

The photographic view of the experimental setup is shown in Fig. 2. An induction motor of 1 H.P. is used along with belt and pulley arrangement to rotate the shaft at 1735 rpm. Load of 10 kg is applied at the center of the shaft supported in self aligned bearing and the test bearing. Therefore, the effective radial load on the test bearing is 5 kg. Self aligned bearing is used to avoid the misalignment of the shaft. To measure the vibration signals, an accelerometer NP 3120 of Ono Sokki make is placed at the top of the test bearing. Fast Fourier Transform (FFT) analyzer CF-250 of Ono Sokki make is used for the frequency spectrum analysis of bearing vibration signals. In this paper, bearings with zero defect, one defect on each element, two defects on each element and combined defects as shown in Table 4 are taken for the study. Diamond file is used to make the defects on bearing elements. Figures 3 and 4 shows different types of defects made on inner, outer and rollers of cylindrical bearings.

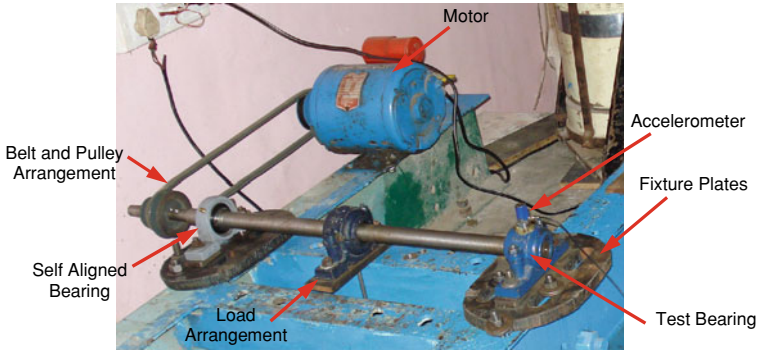


Fig. 2 Photographic view of experimental setup

Table 4 Formulae of characteristic bearing defect frequencies

Sr. No.	Bearing defects	Sr. No.	Bearing defects
1	1 defect on outer race (2 mm)	8	1 defect on outer race and 1 defect on roller (2 mm each)
2	2 defects on outer race (2 mm)	9	1 defect on outer race and 2 defects on rollers (2 mm each)
3	1 defect on inner race (2 mm)	10	2 defects on outer race and 1 defect on roller (2 mm each)
4	2 defects on inner race (2 mm)	11	2 defects on outer race and 2 defects on rollers (2 mm each)
5	1 defect on roller (2 mm)	12	1 defect on inner race and 1 defect on roller (2 mm each)
6	2 defects on rollers (2 mm)	13	1 defect on inner race and 2 defects on rollers (2 mm each)
7	1 defect on roller (4 mm)	14	2 defects on inner race and 1 defect on roller (2 mm each)
		15	2 defects on inner race and 2 defects on rollers (2 mm each)



(a) One defect on outer race of N205 bearing
 (b) Two defects on outer race of N205 bearing
 (c) One defect on inner race of NU205 bearing
 (d) Two defects on inner race of NU205 bearing

Fig. 3 Different types of defects made on inner and outer races of bearing

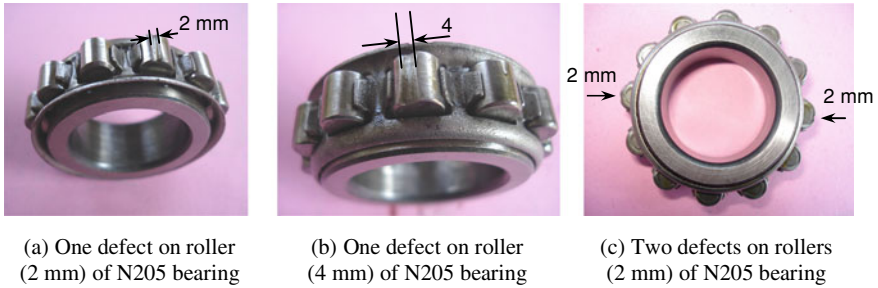


Fig. 4 Different types of defects made on rollers of bearing

3 Results and Discussion

3.1 Good Bearing

Figure 5 shows time waveform and frequency spectrum of a good bearing obtained by using FFT analyzer at 1735 rpm speed and 5 kg radial load. It is found that, in time waveform the peak value of amplitude is less than 0.1×10^2 G and in frequency

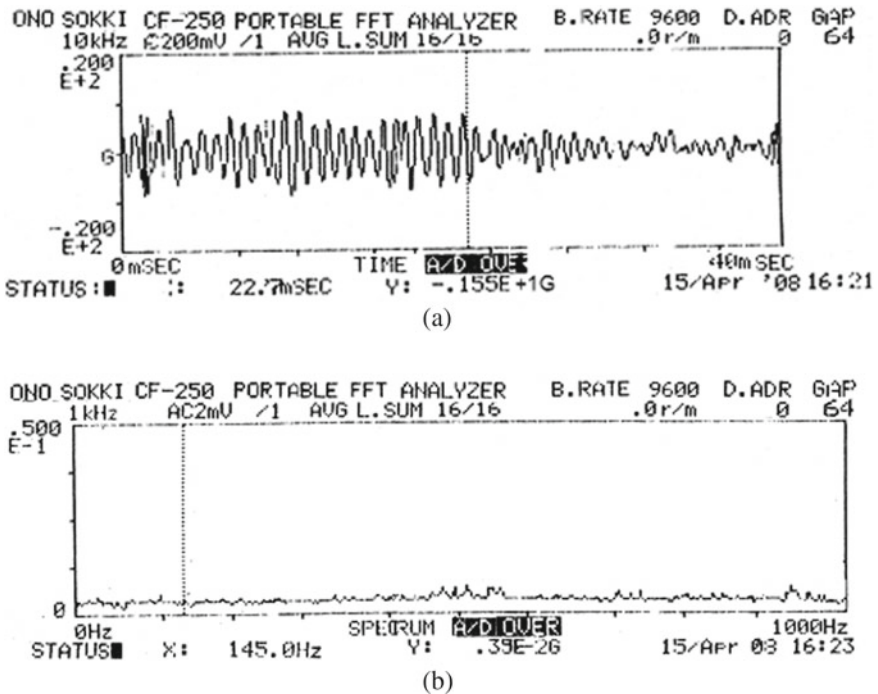


Fig. 5 a Time waveform and b frequency spectrum of a good bearing

spectrum there are no peaks found at any amplitude and the spectrum is nearly flat. This indicates that no defect is present in the bearing.

3.2 Bearings with Single Defect

Bearing with One ORD

Figure 6 shows time waveform and frequency spectrum of a CRB with one ORD of 2 mm width. It is seen that, in time waveform there is significant change in the vibration levels as compared to good bearing and the peak value of amplitude increased to 0.2×10^2 G. The frequency spectrum shows the peaks at 145 Hz and its multiples i.e. 290, 435 and 580 Hz, which are close to the fundamental ORD frequency 144.2 Hz and its harmonics. This indicates the presence of ORD in bearing. The amplitude value at first peak seen is 0.250×10^{-1} G.

Bearing with One IRD

Figure 7 shows time waveform and frequency spectrum of a CRB with one IRD of 2 mm width. It is seen that, in time waveform there is significant change in the vibration levels as compared to good bearing and the peak value of amplitude increased to 0.3×10^2 G. The frequency spectrum shows the peaks at 202.5 Hz and its multiple 405 Hz, which are equal to the fundamental IRD frequency 202.5 Hz and its harmonic. This indicates the presence of IRD in bearing. The amplitude value at first peak seen is 0.206×10^{-1} G.

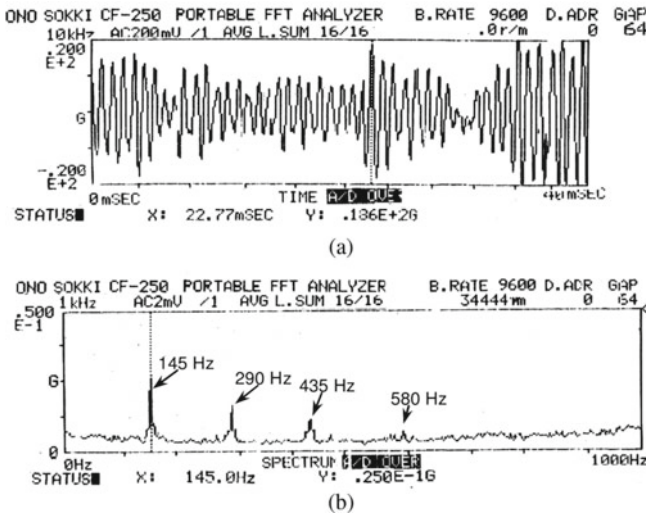


Fig. 6 a Time waveform and b frequency spectrum of bearing with One ORD

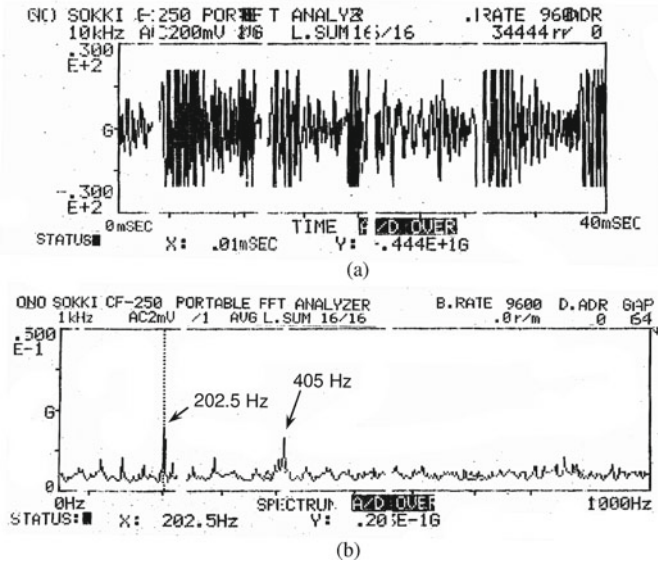


Fig. 7 a Time waveform and b frequency spectrum of bearing with One IRD

Bearings with One Roller Defect (RD)

Figure 8 shows time waveform and frequency spectrum of a CRB with one RD of

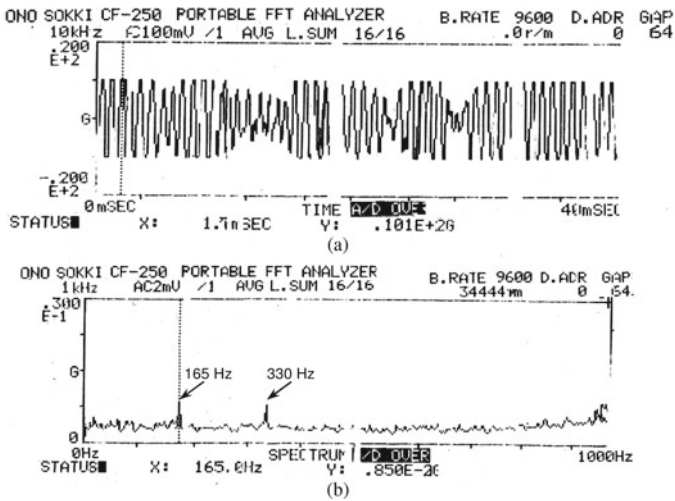


Fig. 8 a Time waveform and b frequency spectrum of bearing with One RD of 2 mm

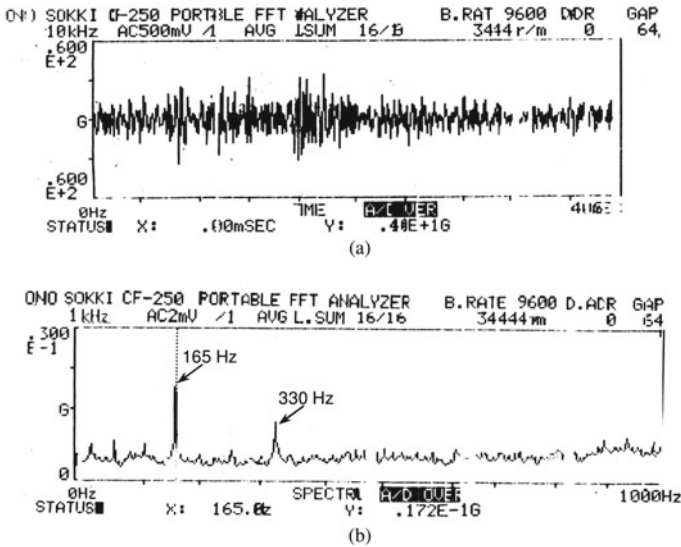


Fig. 9 a Time waveform and b frequency spectrum of bearing with One RD of 4 mm

2 mm width. It is seen that, in time waveform the peak value of amplitude increased to 0.101×10^2 G. The frequency spectrum shows the peaks at 165 Hz and its multiple 330 Hz, which are close to the fundamental RD frequency 166.5 Hz and its harmonic. This indicates the presence of roller defect in bearing. The amplitude value at first peak seen is 0.85×10^{-2} G.

Figure 9 shows time waveform and frequency spectrum of a CRB with one RD of 4 mm width. The frequency spectrum shows the peaks at 165 Hz and its multiple 330 Hz, which are close to the fundamental RD frequency 166.5 Hz and its harmonic. This indicates the presence of roller defect in bearing. Time waveform and frequency spectrum shows that in case of 4 mm RD the vibration level is increased significantly as compared to 2 mm RD. The amplitude value at first peak seen is 1.72×10^{-2} G.

3.3 Bearings with Two Defects

From the time waveforms as seen in earlier session, it can be concluded that time waveform indicates only the severity of the vibration signal but not indicate the exact location of bearing defect. Hence, from this session onwards only frequency spectrums of bearings are studied. Figure 10 shows frequency spectrums of CRBs with two ORDs, IRDs and RDs of 2 mm width. It is seen that, in each frequency spectrum the peaks are observed at their fundamental defect frequencies and their harmonics. Table 5 shows the comparison of amplitude of peaks observed in frequency spec-

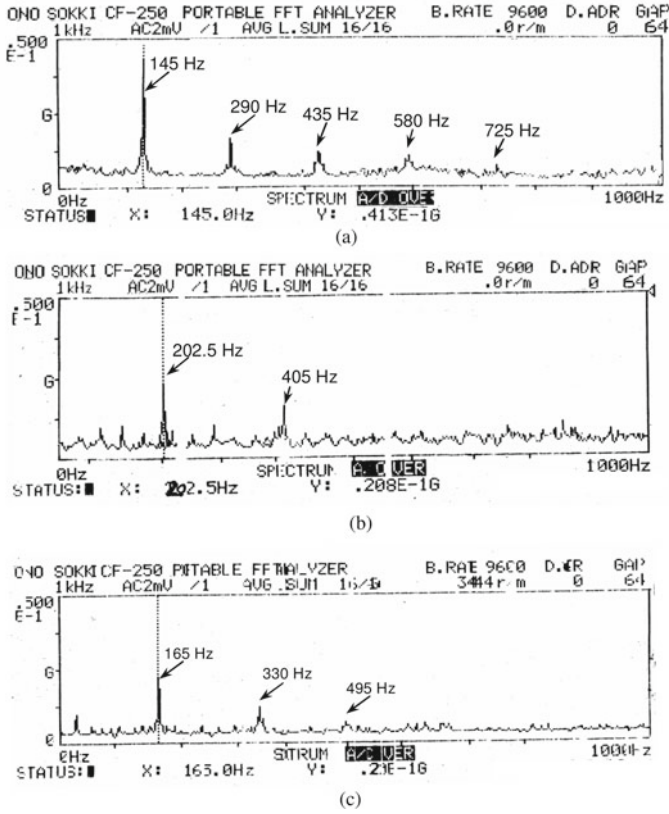


Fig. 10 Frequency spectrums of bearings with **a** two ORDs, **b** two IRDs and **c** two RDs

trums of one and two bearing defects of same type. It is observed that the amplitudes of peaks are higher than that of one defect bearings.

3.4 Bearings with Combined ORDs and Roller Defects

Figure 11 shows frequency spectrums of CRBs with combined ORDs and roller defects of 2 mm width. It is seen that, in each frequency spectrum the peaks are observed at each fundamental defect frequencies and their harmonics i.e. at 145 and 165 Hz, which correspond to ORD and RD frequencies. These frequencies confirm the presence of ORD and RD in the bearings. It is also seen that the overall vibration levels are increased as compared to individual defect bearings. Table 6 shows the comparison of amplitude of peaks observed in frequency spectrums of combined ORD and roller defects.

Table 5 Comparison of amplitude of peak for single and double bearing defects

Sr. No.	Bearing defects	Defect frequencies (Hz)		Amplitude (G)
		Calculated	Experimental	
1	1 defect on outer race (2 mm)	144.2	145	0.250×10^{-1}
2	2 defects on outer race (2 mm)	144.2	145	0.413×10^{-1}
3	1 defect on inner race (2 mm)	202.8	202.5	0.206×10^{-1}
4	2 defects on inner race (2 mm)	202.8	202.5	0.208×10^{-1}
5	1 defect on roller (2 mm)	166.4	165	0.085×10^{-1}
6	2 defects on rollers (2 mm)	166.4	165	0.250×10^{-1}
7	1 defect on roller (4 mm)	166.4	165	1.72×10^{-1}

3.5 Bearings with Combined IRDs and Roller Defects

Figure 12 shows frequency spectrums of CRBs with combined IRDs and roller defects of 2 mm width. It is seen that, in each frequency spectrum the peaks are observed at each fundamental defect frequencies and their harmonics i.e. at 202.5 and 165 Hz, which correspond to IRD and RD frequencies. These frequencies confirm the presence of IRD and RD in the bearings. It is also seen that the overall vibration levels are increased as compared to individual defect bearings. Table 7 shows the comparison of amplitude of peaks observed in frequency spectrums of combined IRD and roller defects.

4 Conclusions

In this paper, time domain analysis and frequency spectrum analysis of different types of defects in cylindrical roller bearings is carried out at constant speed and radial load. On the basis of results obtained following conclusions are made:

- (1) Time domain analysis of vibration signals shows the severity of the bearing defects; however, they cannot identify the exact location of the defect in the bearings. Frequency spectrums proved their effectiveness in finding the exact location of defects in bearing.
- (2) For each type of defect, the vibration amplitude in frequency spectrum for two defects is higher than one defect and vibration amplitude increases with increase in defect width.

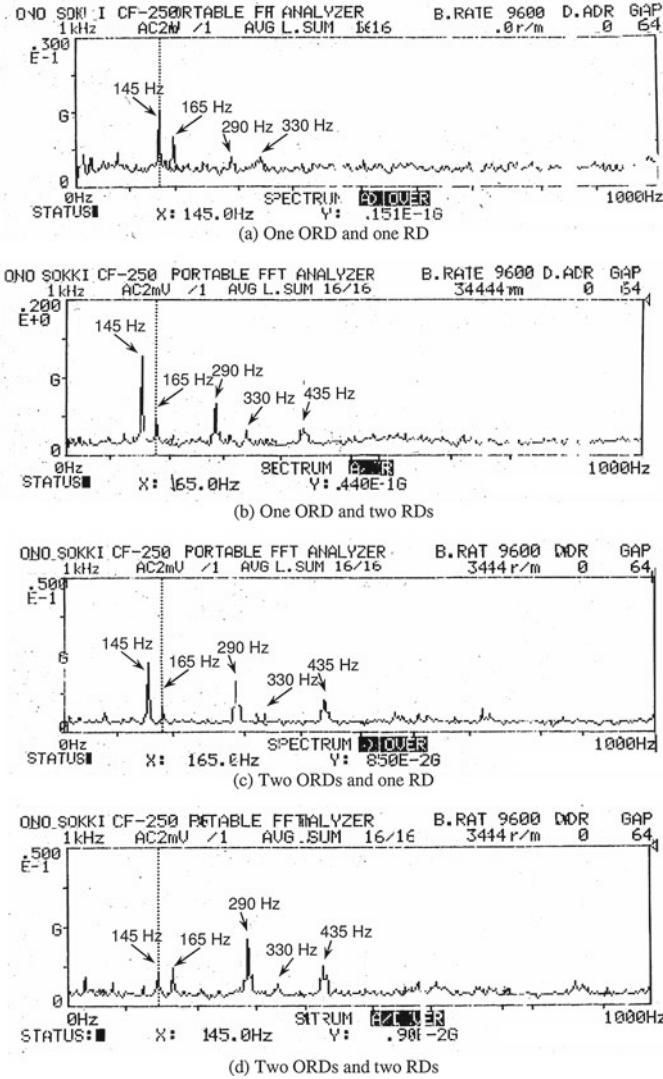


Fig. 11 Frequency spectrums of bearings with combined ORDs and RDs

Table 6 Comparison of amplitude of peak for combined ORDs and RDs

Sr. No	Bearing defects	Amplitude (G)
1	1 defect on outer race and 1 defect on roller	0.151×10^{-1}
2	1 defect on outer race and 2 defects on rollers	1.300×10^{-1}
3	2 defects on outer race and 1 defect on roller	0.240×10^{-1}
4	2 defects on outer race and 2 defects on rollers	0.250×10^{-1}

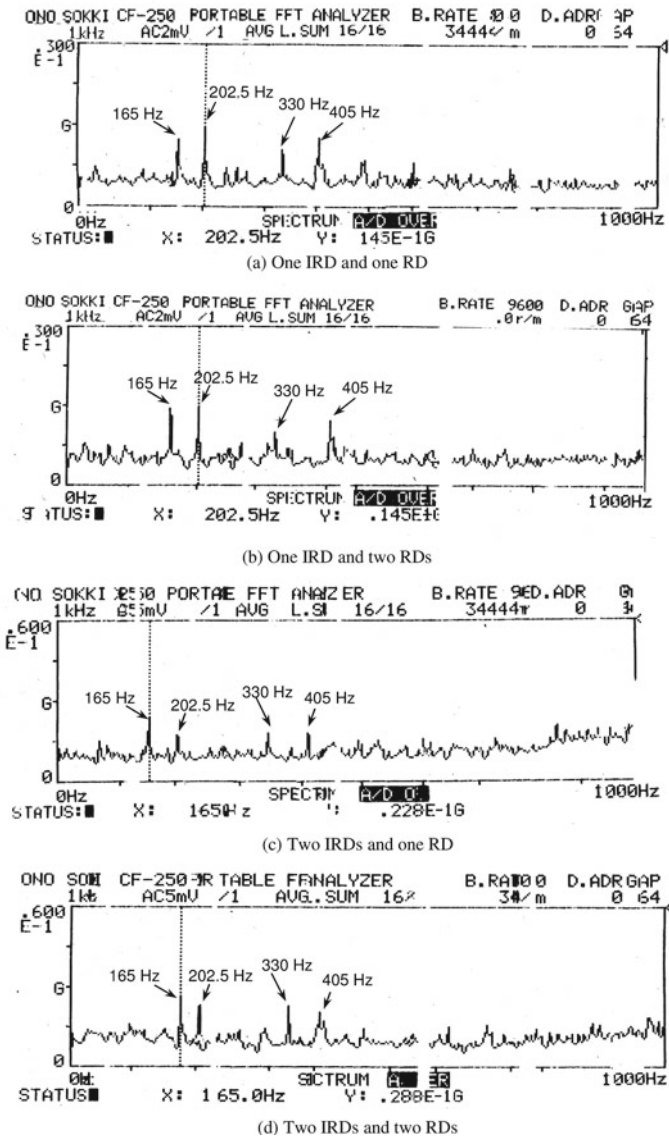


Fig. 12 Frequency spectrums of bearings with combined IRDs and RDs

- (3) Vibration amplitude in frequency spectrum for ORD is higher than IRD followed by RD for same defect size.
- (4) Defect frequencies for all types of defects calculated by kinematic analysis and found experimentally are shown in Table 8. It is found that there is a slight

Table 7 Comparison of amplitude of peak for combined IRDs and RDs

Sr. No.	Bearing defects	Amplitude (G)
1	1 defect on inner race and 1 defect on roller	0.120×10^{-1}
2	1 defect on inner race and 2 defects on rollers	0.140×10^{-1}
3	2 defects on inner race and 1 defect on roller	0.228×10^{-1}
4	2 defects on inner race and 2 defects on rollers	0.288×10^{-1}

Table 8 Comparison of defect frequencies

Sr. No.	Defect frequencies	Calculated (Hz)	Experimental (Hz)	% Difference
1	ORDF	144.2	145	0.555
2	IRDF	202.8	202.5	-0.148
3	RDF	166.4	165	-0.841

difference (less than $\pm 1\%$) in these values; this may be due to sleeping of rolling elements while running and may be due to length of defect width.

Although the analysis shown in this paper shows the effectiveness of frequency spectrum in identification of defect types in bearings for different combinations of bearing defects at constant speed and radial load, a more comprehensive analysis can be carried out for change in factors like shaft speed, load, defect depth, defect position, bearing clearance, etc. and by using other VSA techniques. The results of this analysis will help the maintenance persons to understand the effects of various types of bearing defects.

Acknowledgements The authors would like to thank to Walchand College of Engineering Sangli for providing the experimental setup facility. Authors also thank to Maharashtra Institute of Technology Aurangabad and T.P.C.T's College of Engineering Osmanabad for providing the literature survey facility.

References

1. Kim BS, Lee SH, Lee MG, Ni J, Song JY, Lee CW (2007) A comparative study on damage detection in speed-up and coast-down process of grinding spindle-typed rotor-bearing system. *J Mater Process Technol* 187–188:30–36
2. Howard I (1994) A review of rolling element bearing vibration, detection, diagnosis and prognosis. Defense Science and Technology Organization, Canberra, Australia. <https://apps.dtic.mil/docs/citations/ADA291123>
3. Shah DS, Patel VN, Darji PH (2018) Experimental vibration studies of deep groove ball bearings having damaged surfaces. *J Inst Eng (India): Ser C* 100:919–935
4. Tandon N, Kumar KS (2003) Detection of defects at different locations in ball bearings by vibration and shock pulse monitoring. *Noise Vib Worldw*
5. Amamath M, Shrinidhi R, Ramachandra A, Kandagal SB (2004) Prediction of defects in antifriction bearings using vibration signal analysis. *J Inst Eng (India)*

6. Liu J, Shao Y, Zuo MJ (2013) The effects of the shape of localized defect in ball bearings on the vibration waveform. *Proc Inst Mech Eng Part K: J Multi-body Dyn*
7. Utpat A, Ingle RB, Nandgaonkar MR (2011) Response of various vibration parameters to the condition monitoring of ball bearings used in centrifugal pumps. *Noise Vib Worldw* 42:34–40
8. Orhan S, Akturk N, Celik V (2006) Vibration monitoring for defect diagnosis of rolling element bearings as a predictive maintenance tool : comprehensive case studies. *NDT & E Int* 39:293–298
9. Patel VN, Tandon N, Pandey RK (2013) Vibration studies of dynamically loaded deep groove ball bearings in presence of local defects on races. *Procedia Eng* 64:1582–1591
10. Patel VN, Tandon N, Pandey RK (2014) Experimental study for vibration behaviors of locally defective deep groove ball bearings under dynamic radial load. *Adv Acoust Vib* 1–7
11. Patel VN, Tandon N, Pandey RK (2014) Vibrations generated by rolling element bearings having multiple local defects on races. *Procedia Technol* 14:312–319
12. Dube AV, Dhamande LS, Kulkarni PG (2013) Vibration based condition assessment of rolling element bearings with localized defects. *Int J Sci Technol Res* 2:1–7
13. Khadersab A, Shivakumar S (2018) Vibration analysis techniques for rotating machinery and its effect on bearing faults. *Procedia Manuf* 20:247–252
14. Jafari SM, Rohani R, Rahi A (2020) Experimental and numerical study of an angular contact ball bearing vibration response with spall defect on the outer race. *Arch Appl Mech*
15. Utpat A, Ingle RB, Nandgaonkar MR (2011) Identification of defects in high speed ball bearing using vibration analysis. *Int J Mech Automob Eng* 3:8–40
16. Ghazaly NM, Abd el-Jaber GT, Stojanovic N (2019) Study various defects of ball bearings through different vibration techniques. *Am J Mech Eng* 7:146–150
17. Immovilli, Cocconcelli (2016) Experimental investigation of shaft radial load effect on bearing fault signatures detection. *IEEE Trans Ind Appl* 1–9
18. Rao VV, Ratnam Ch (2015) A comparative experimental study on identification of defect severity in rolling element bearings using acoustic emission and vibration analysis. *Tribol Ind* 37:176–185
19. Jain PH, Bhosle SP (2021) Study of effects of radial load on vibration of bearing using time-domain statistical parameters. *IOP Conf Ser Mater Sci Eng* 1070:012130

Characterization of Hydroxyapatite-Titanium (HA-Ti) Samples Synthesized from Different Material Composition



Pranita Sawant, Vijaykumar Jatti, Swati Dhamale, and Meghna Gawade

Abstract Hydroxyapatite (HA) is one of the most important materials for orthopedic implants, as it has a similar chemical composition as that of the bone tissue and tooth. Hydroxyapatite is synthesized as they increase osteoconductivity, biodegradability with a significant increase in mechanical properties. But, HA cannot be applicable for bearing the load, in this situation hydroxyapatite is combined with titanium. Hydroxyapatite titanium composites possess low density, low modulus but it possesses high strength. In this study, to study the interface between hydroxyapatite and titanium, HA-Ti samples were prepared by wet precipitation method. The amount of Ti was considered as 0.05, 0.1, and 0.15 mol%. The supplier of titanium was used as Titanium isopropoxide ($\text{Ti}(\text{OCH}(\text{CH}_3)_2)_4$). The characterizations of various specimens were carried using Scanning Electron Microscope-Energy Dispersive Spectroscopy (SEM-EDS), X-Ray diffraction (XRD) and Fourier Transform Infrared (FTIR) Spectroscopy, wherein morphology, crystallography and grain size were investigated. The results induced that titanium can fulfill the required criteria along with HA in biomedical applications.

Keywords Chemical precipitation · Hydroxyapatite · Titanium · SEM-EDS · FTIR

1 Introduction

Various factors such as illness, accidents, and bone disorders nowadays make use of biomaterials; biomaterials are the materials that are allowed to function in our body which repairs the damaged and lost tissue. Thus, the thinking of humans has changed for this material that it should have increasing application in biology [1]. The main constituent of hard tissues is calcium phosphates. To give the body organs hardness and stability, this carbonated hydroxyapatite (HA) is present in bone, teeth, and tendons [2].

P. Sawant (✉) · V. Jatti · S. Dhamale · M. Gawade
Department of Mechanical Engineering, D. Y. P. COE, Pune, India

The composition of HA consists of 70% bones, 20% collagen and 10% water [2]. The naturally present component in human-animal bone and teeth is hydroxyapatite ($\text{Ca}_{10}(\text{PO}_4)_6(\text{OH})_2$, HA), which also the most important element of bioceramics. Thus, to perform the most significant osseointegration in the body HA is readily available in composites, coatings and powders, etc. [3]. In applications such as dental implants, filling bones or coatings in orthopedics as well as in partial or complete bone augmentation HA is used as bone replacement or substitution [4].

On the other hand, hydroxyapatite cannot bear the load as it has low mechanical properties related to the human bone [5]. Thus to rectify this drawback titanium makes its usage in implants. Titanium has great toughness and can withstand load-bearing applications [6]. Other than this, titanium exhibits biocompatibility as it binds with the human body as well as with tissue associated with the area beside the implants.

Thus hydroxyapatite and titanium are combined to get effective results. Synthesis and characterization of HA using chemical process is performed but HA-Ti preparations using wet chemical precipitation are very few [7]. In this present work, hydroxyapatite titanium samples were produced using the wet precipitation method at pH 9. The titanium composition was varied as 0.05, 0.10 and 0.15 M, which were sintered at 70 °C. These samples were exposed to characterizations scanning electron microscope–energy dispersive spectroscopy (SEM–EDS), X-Ray diffraction (XRD) and Fourier Transform Infrared (FTIR) Spectroscopy.

2 Materials and Method

2.1 *Fabrication of HA-Ti Samples Using Wet Precipitation Method*

Hydroxyapatite-titanium composites exhibit excellent bioactivity and biocompatibility rather than alone hydroxyapatite. These materials possess high strength, low modulus and low density [8]. To obtain HA-Ti composites, the wet precipitation method is used. The source of titanium here used is Titanium isopropoxide ($\text{Ti}(\text{OCH}(\text{CH}_3)_2)_4$). To start with the procedure as shown in Fig. 1, the overall solution of calcium phosphate, ortho-phosphoric acid, titanium and distilled water should make up to 100 ml solution. Here 3 samples (TH1, TH2 and TH3) of HA-Ti were prepared, with titanium addition as 0.05, 0.1 and 0.15 M at pH 9 by taking the composition as shown in Table 1. The experiment was carried out as shown in Figs. 2 and 3. Calcium phosphate ($\text{Ca}(\text{OH})_2$) and distilled water were added into a beaker which was stirred continuously with the help of a magnetic stirrer. Whereas ortho-phosphoric acid (H_3PO_4) and distilled water were added into burette 1 (B1). The solution in the burette 1 was added into the beaker at the rate of 20–30 drops per minute for over one hour and then from burette 2 (B2) titanium was added into the beaker drop-wise as per the composition. To adjust the pH level of the mother solution to 9, ammonia was added into the solution. The prepared solution was kept aside for 24 h and then

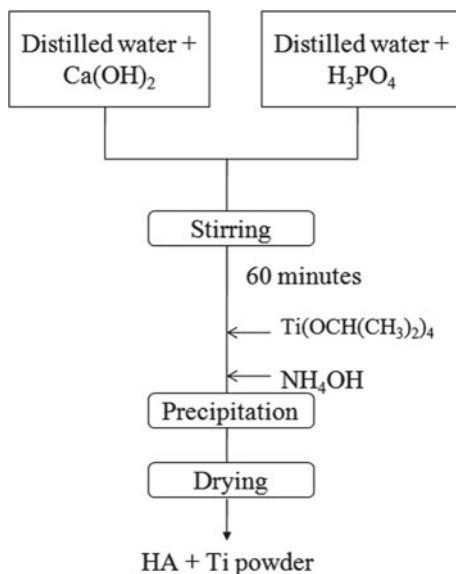


Fig. 1 Flowchart of H-Ti precipitation process

Table 1 Different parameters during HA-Ti preparation

Parameters	Sample 1 (TH1)	Sample 2 (TH2)	Sample 3 (TH3)
Ca(OH) ₂	3.04 g	7.41 g	11.11 g
H ₃ PO ₄	1.73 ml	3.478 ml	5.21 ml
Ti(OCH(CH ₃) ₂) ₄	15.16 ml	30.33 ml	45.5 ml
Ammonia	10 ml	20 ml	30 ml

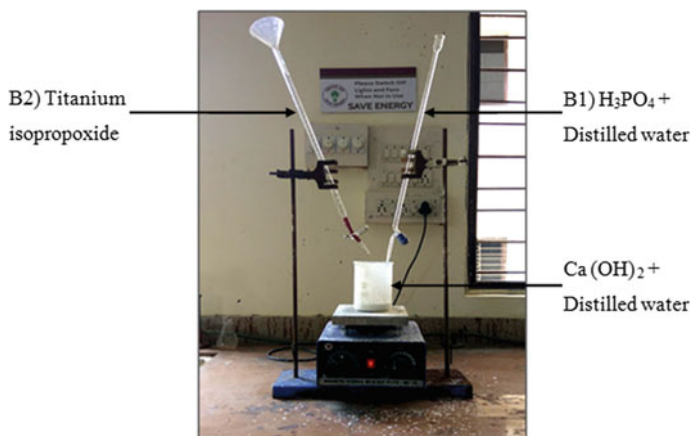


Fig. 2 Wet precipitation process



Fig. 3 Drying process in a furnace

precipitated using a filter paper. Further, the precipitated powder was kept for drying in the furnace at a temperature 70 °C.

2.2 Characterization

For morphological and topography information, samples were determined by field emission scanning electron microscope (JEOL-JSM-7600F). The scanning of the crystal surface was investigated by X-ray diffraction using Cu-K α radiation. The scanning was carried out in a range of 2θ degrees, i.e. from 20° to 80°, with a step size of 0.02°. Also, the vibrational analysis and the water molecule content were determined using FTIR.

3 3. Results and Discussion

3.1 Scanning Electron Microscope-Energy Dispersive Spectroscopy

The below figure shows the morphology of HA-Ti powder prepared at 70 °C temperature. It can be seen that at lower titanium amount in sample 1 i.e. Fig. 4a shows sharp corner edges of the grains which turn to round and spherical shaped grains as the amount of titanium increases i.e. in Fig. 4b, c. The morphology of HA-Ti depicted rods like structure which are beneficiary to the cell adsorption and cell tissue growth. Also, it is observed from images that the average size of grain decreases as the amount of titanium increases. From Fig. 5, SEM-EDS analyses show that the peaks of Ca, P and Ti exist as expected, which results in inter diffusion of HA-Ti structure and these show similar behaviour as that of hydroxyapatite. The EDS data gives the weight and atomic percentage, which is used to calculate the calcium/phosphorous ratio. For these three samples, the ratio of Ca/P was observed in the range of 1.10–2.42, which was between the acceptable criteria.

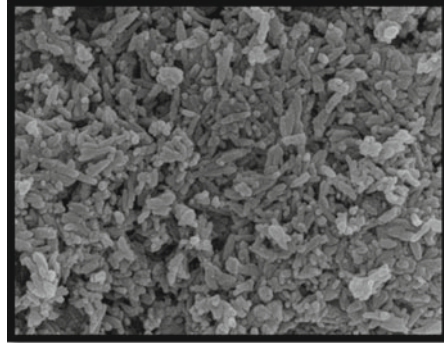
3.2 X-Ray Diffraction

Figure 6 shows the XRD pattern of HA-Ti. It can be seen that as the Ti addition increases i.e. from 0.05 to 1.5 M, there is a steady peak shifting. This XRD indicates that the samples include the presence of TiO_2 and CaTiO_3 . With the addition of 0.05 M Ti, peak shift was observed along with a decreased XRD pattern. Thus, the presence of Ti exhibits the properties of densification in a particular material. The XRD examples of HA-Ti at 70 °C show increment in force because of planes around (1 1 2), (2 2 2), (3 1 0) and (3 1 1).

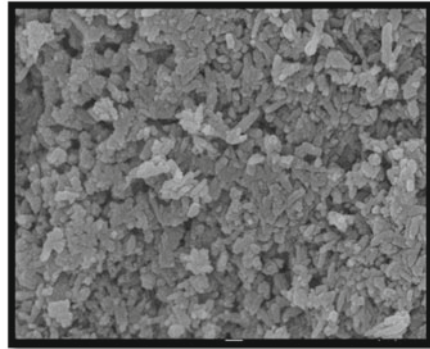
3.3 Fourier Transform Infrared Spectroscopy

The FTIR result from Fig. 7a–c represented the vibration analysis of PO_4^{3-} , CO_3^{2-} and OH^- group. The strong peaks at 962.48 and 1095.57 cm^{-1} represented PO_4^{3-} group. The region from 1415.75 to 1534 cm^{-1} demonstrated the carbonate CO_3^{2-} group, which is due to asymmetric stretching of CO_3^{2-} ion. Whereas the peaks 603.72 and 3154.30 cm^{-1} represented the hydroxyl (OH^-) group. The broadening of the OH group is due to H-bonding in absorbed H_2O and OH^- group of apatite [9]. It was also observed that with increased Ti concentration, there was a decrease in the peaks of phosphate band as well as stretching of OH^- band [8].

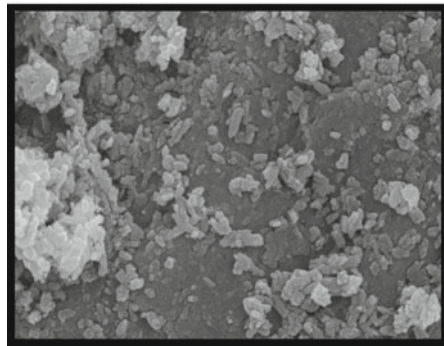
Fig. 4 **a** SEM of TH1 sample, **b** SEM of TH2 sample, **c** SEM of TH3 sample



(a). SEM of TH1 sample



(b). SEM of TH2 sample



(c). SEM of TH3 sample

4 Conclusion

In this study, hydroxyapatite-titanium samples were prepared by the wet precipitation method, wherein amount of Ti addition was 0.05, 0.1, and 0.15 mol%. The synthesis method of wet precipitation method is very easy and simple; also it conserves energy

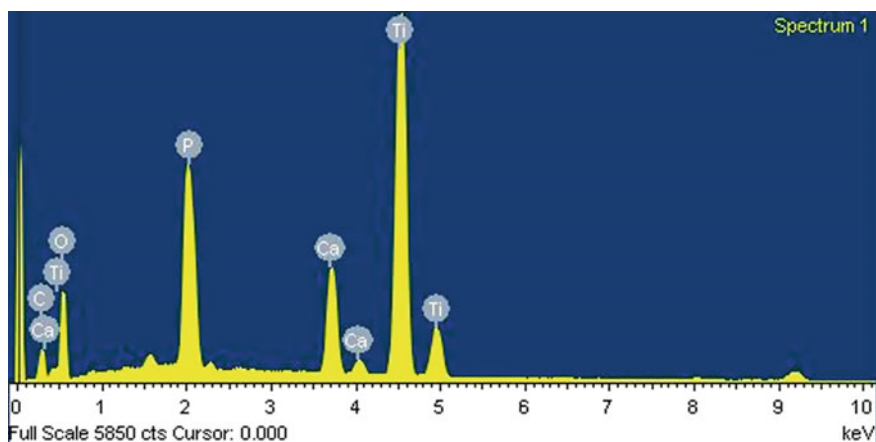
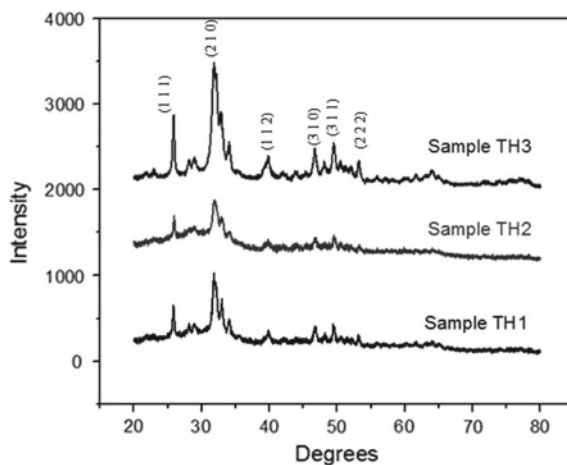


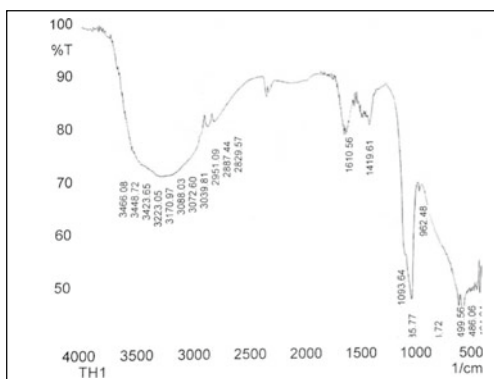
Fig. 5 EDS spectrum analysis of HA-Ti samples

Fig. 6 XRD patterns of HA-Ti samples

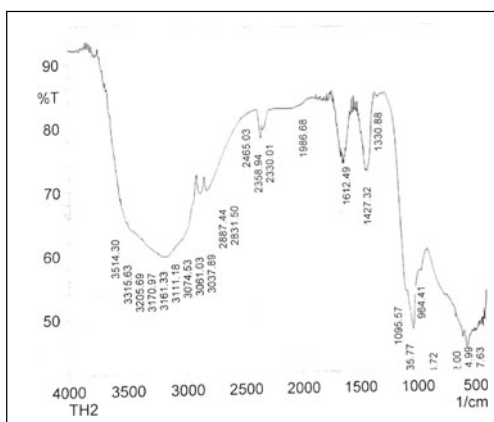


and time as compared to other methods of synthesis. The morphology of HA-Ti revealed rod-like structure which is beneficial to the cell adsorption and cell tissue growth. Also, EDS depicted an acceptable ratio of Ca/P ratio i.e. from 1.10 to 2.42. The presence of Ti from the XRD pattern exhibited properties of densification by supporting dehydration of the HA phase. FTIR results showed increase in Ti content resulted in a decrease in the peaks of OH^- as well as in phosphate bands. Thus, the results of this present work, makes Ti along with HA suitable for biomedical applications.

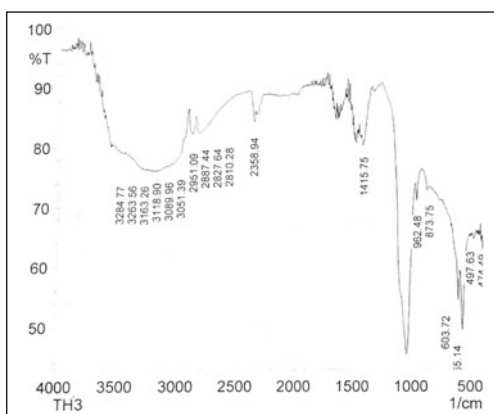
Fig. 7 a FTIR of TH1 sample, **b** FTIR of TH2 sample, **c** FTIR of TH3 sample



(a). FTIR of TH1 sample



(b). FTIR of TH2 sample



(c). FTIR of TH3 sample

References

1. Ratner BD, Hoffman AS, Schoen FJ, Lemons JE (2004) *Biomaterials science: an introduction to materials in medicine*, 2nd edn. Elsevier Academic Press, London
2. Dorozhkin SV, Epple M (2002) Biological and medical significance of calcium phosphates. *Angew Chem Int Ed* 41:3130–3146
3. Yelten A, Yilmaz S (2016) Various parameters affecting the synthesis of the hydroxyapatite powders by the wet chemical precipitation technique. *Mater Today: Proc* 3:2869–2876
4. Szczes A, Holysz L, Chibowski E (2017) Synthesis of hydroxyapatite for biomedical applications. *Adv Colloid Interface Sci* 249:321–330
5. Lin K, Chang J (2015) Structure and properties of hydroxyapatite for biomedical applications. *Woodhead Publishing Series in Biomaterials*, pp 3–15
6. Niespodziana K, Jurczyk K, Jurczyk M (2006) The manufacturing of titanium hydroxyapatite nanocomposites for bone implant applications. *International conference on advances in nanostructured materials, processing–microstructure–properties*. pp 219–229
7. Yelten A, Yilmaz S (2018) Wet chemical precipitation synthesis of hydroxyapatite (HA) powders. *Ceram Int* 44:9703–9710
8. Ozbek YY, Bastan FE, Canikoglu N, Ozsarac U (2016) The experimental study of titanium-ions into hydroxyapatite by chemical precipitation. *J Therm Anal Calorim* <https://doi.org/10.1007/s10973-016-5335-8>
9. Ye H, Liu XY, Hong H (2009) Characterization of sintered titanium/hydroxyapatite biocomposite using FTIR spectroscopy. *J Mater Sci: Mater Med* 20:843–850

Performance Evaluation of Molybdenum Disulfide Based Cutting Fluids Under Near-Dry Machining as an Environment-Friendly Technique



Shrikant U. Gunjal and Sudarshan B. Sanap

Abstract Machining is the most important process and prone to deal with many complexities in terms of surface roughness, chip formation, extreme cutting temperature, cutting forces, tool wear, and abrupt tool failure, etc. To deal with the concerned complexities; cutting fluids are widely used in industries. The application of cutting fluids minimizes the adverse effect of temperature and friction on the entire machining environment which finally results in better machining performance. The current research work is an attempt to evaluate the performance of molybdenum disulfide powder addition in water-soluble conventional oil and mineral oil during the turning of AISI 316L stainless steel under near-dry machining technique. The Taguchi orthogonal array has been used for the design of the experiment. The investigation shows better results with molybdenum disulfide addition in the cutting fluids under consideration in terms of improved surface finish and lower chip thickness.

Keywords Chip thickness · Machining · Molybdenum disulfide · Near-dry machining · Surface finish

1 Introduction

Cutting fluids are an essential part of the manufacturing industries dealing with machining operations. Challenges and issues need to be addressed attributed to machining operations using cutting fluids. Researchers are working on a compatibility check of various cutting fluids concerning the different machining processes under consideration. The selection of a machining environment is also an important task to decide as it causes several impacts on the entire performance of the process.

Literature has shown better results with near-dry machining (NDM) i.e. minimum quantity lubrication (MQL) for a wide range of materials, cutting speed, and cutting fluids, etc. MQL technique hardly uses 50–150 ml/h oil flow rate which is approximately 0.004% of conventional technique consumption; which also avoids any

S. U. Gunjal (✉) · S. B. Sanap
MIT ADT University, Rajbaug, Loni Kalbhor, Pune 412201, Maharashtra, India
e-mail: shrikant.gunjal@mituniversity.edu.in

chance of disposal issue as up to 100% cutting fluid (a mixture of cutting oil and pressurized air in MQL) is evaporated after cooling and lubrication of cutting zone. This gives the clear path of NDM i.e. MQL proving the potential solution as an environment-friendly technique for the modern industrial requirements. Researchers have noticed the improved surface finish under MQL in comparison to flood and dry machining environment. This is attributed to reduced and uniform tool wear which also promotes the tool life and higher productivity allowing higher cutting speed and feed [1–6]. Elmunafi et. al. [7] have found similar attributes of MQL performance in comparison to conventional technique during machining of AISI 420 steel material as the surface finish is improved under MQL with 50 ml/h cutting fluid. Reduction in cutting temperature under MQL leads to a reduction in tooltip damage achieving better surface quality of the material [8]. A similar trend was observed as the improvement in surface quality was noted to be 10% under MQL comparing to the flood lubrication technique as noted by Kumar et. al. [9]. Nizamuddin et. al. [10] have observed the reduced chip thickness by 11% under the MQL environment. Chip thickness is an important attribute to study in the investigation of energy consumption by the virtue of shear angle calculation based on the chip thickness measurement [11]. Reduction in temperature at tool-work interface under MQL has been noticed by Dennison et. al. [12]; which they found the influencing factor of producing better quality products. Das et. al. [13] have noted a significant reduction in dimensional deviation and auxiliary flank wear under MQL. This causes the improvement in surface integrity and machinability characteristics leading to approximately 16% cost savings.

Cutting fluid under MQL is found suitable for varied machining conditions. In addition to this, the addition of some attributed powder particles like molybdenum disulfide (MoS_2), silica (SiO_2), aluminum oxide (Al_2O_3), etc. is found useful in improving the performance of the cutting fluid under consideration. The addition of these designated particles improves the wettability characteristics of the cutting fluid along-with reduced tool wear and significant improvement in tool life comparatively [14, 15]. Koshy et. al. [16] have noticed the very special attribute of MoS_2 added cutting fluid in terms of enhanced tribological and thermophysical properties of the concerned oil. Evaluation of different cutting oil samples has been undertaken by Padmini et. al. [17], and inferred that MoS_2 addition improves the basic properties of the cutting oil; well supported by the experimental investigation for the surface finish which was improved by approximately 39% comparative to dry environment. Patole and Kulkarni [18, 19] have noted the better performance of the MQL machining environment using nanoparticle assisted cutting fluid compared to other lubrication systems, as they have noticed the improvement in surface finish comparatively. In another attempt of hard-to-cut material machining; Ravuru et. al. [20] has investigated the compatibility of Al_2O_3 assisted cutting fluid during machining of Titanium alloy using MQL. They found that MQL with Al_2O_3 assisted cutting fluid has outperformed the conventional machining environment. Literature has strong evidence to support the significant results in terms of improved surface finish, tool life, reduced tool wear, and cutting zone temperature using MoS_2 , Al_2O_3 , SiO_2 , and similar kinds of particles in varying sizes [21–23].

The exhaustive literature review indicates the potential compatibility of minimum quantity lubrication (near-dry machining) using assisted attributes of cutting fluids for different materials and machining applications.

2 Experimental Work

In the current research work, experimental investigations on AISI 316L material are revealed in terms of surface roughness and chip thickness. Figure 1 shows the photographic view of the CNC lathe in use during experimental investigations. MQL is an innovative approach termed to be near-dry machining as it consumes the least amount of cutting fluid and pressurized air mixture which serves the dual purpose of lubrication and cooling respectively.

AISI 316L material has a wide range of applications. Following Table 1 shows the chemical composition of the concerned material.

Experimental details and cutting conditions are mentioned in the following Table 2.

Molybdenum disulfide powder particles are added in varying proportions (as mentioned in Table 2) in water-soluble conventional cutting fluid and mineral-based paraffin oil concerning the comparative performance evaluation.

The design of the experiment is prepared using Taguchi (L9) orthogonal array as shown in Table 3.

Fig. 1 A photographic view of CNC lathe



Table 1 AISI 316L- Chemical composition

Element	C	Mn	Si	P	S	Cr	Mo	Ni
Content (%)	0.03	2.0	1.0	0.05	0.02	18.50	2.50	13.00

Table 2 Experimental details and cutting conditions

Parameter	Description
Workpiece material	AISI 316L
Cutting insert	Uncoated cemented carbide
Cutting speed (Vc)	150, 100, 50 (m/min)
Feed (f)	0.25, 0.2, 0.15 (mm/rev)
Depth of cut (d)	1 (mm)
MoS ₂ concentration	6, 4, 2 (wt%)
Machining environment	Near-dry machining (MQL)
Oil flow rate	50 (ml/h)
Airflow rate	6 (bar)
Nozzle angle	15°
Measuring parameters	Surface roughness, Ra (μm) & chip thickness, Tc (mm)

Table 3 Design of experiment

Experiment trial	Cutting speed	Feed rate	MoS ₂ concentration
1	50	0.15	2
2	50	0.2	4
3	50	0.25	6
4	100	0.15	4
5	100	0.2	6
6	100	0.25	2
7	150	0.15	6
8	150	0.2	2
9	150	0.25	4

3 Results and Discussion

The observations for surface roughness and chip thickness under both the cutting fluid samples are summarized for comparative performance evaluation. Following is the investigation based on experimentation work.

Figure 2 shows the effect of molybdenum disulfide assisted cutting fluid samples on the surface finish. From the figure, it is clear that the surface finish of the material is improved in direct proportion to that of MoS₂ concentration.

As the MoS₂ concentration increases, there is a significant reduction in the surface roughness. It is observed that surface roughness is at the higher side under the application of paraffin oil sample in comparison to conventional oil. Better results with conventional oil samples over mineral-based paraffin oil are noted. This is attributed to the combined effect of water-soluble conventional cutting fluid assisted by excellent tribological properties of the molybdenum disulfide. This combined effect causes

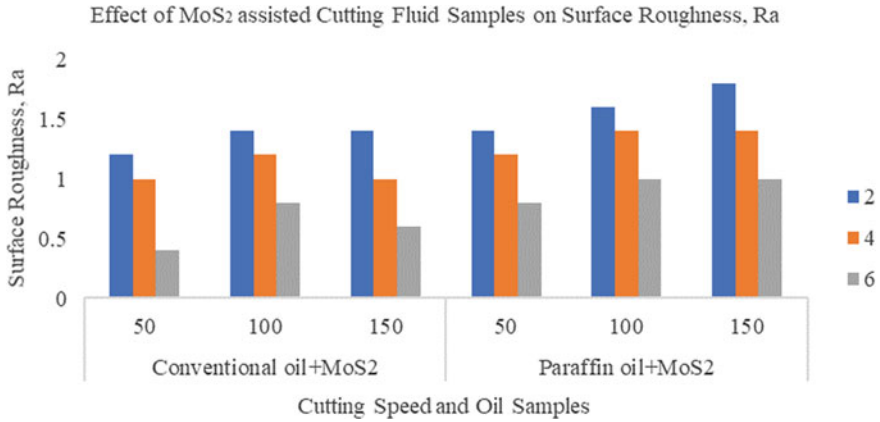


Fig. 2 Performance evaluation of varying MoS₂ concentration assisted cutting fluid samples on surface roughness

the reduced cutting zone temperature which minimizes the wear and damage to the cutting insert leading to a superior surface finish.

A similar impact on chip thickness measurement attributed to the better effect of MoS₂ assisted conventional water-soluble cutting fluid sample over the mineral-based paraffin oil is noted, as shown in Fig. 3. Conventional oil sample mixed with MoS₂ concentration helps in reducing the chances of built-up edge formation. Lower chip thickness is attributed to a maximum shear angle which means that

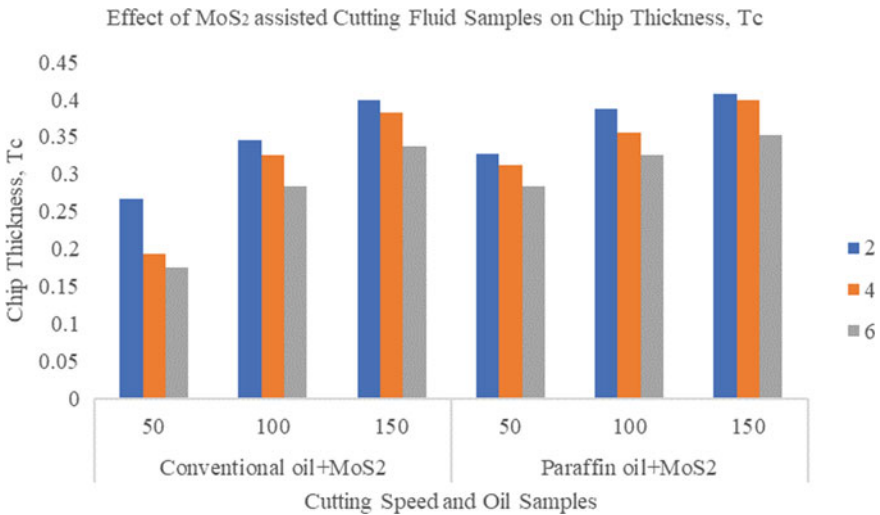


Fig. 3 Performance evaluation of varying MoS₂ concentration assisted cutting fluid samples on chip thickness

there is a reduction in power consumption and cutting forces under the application of conventional cutting fluid over a paraffin oil sample.

4 Conclusions

The current research work is an attempt to check the compatibility of molybdenum disulfide assisted cutting fluids under near-dry machining i.e. minimum quantity lubrication under consideration. We have noted the significant improvement in surface finish and similarly for the chip thickness measurement as it shows the lower thickness under MoS₂ concentration assisted conventional water-soluble cutting fluid. As the concentration of molybdenum disulfide increases it has shown a positive impact in terms of proportionate superior performance during the machining operation under consideration.

The following are the important observations:

- Surface roughness increases with an increase in feed rate under normal cutting fluid application, but the addition of molybdenum disulfide reduces the roughness significantly.
- Surface finish under conventional water-soluble cutting fluid was found to be improved approximately by average 15–20% over the mineral-based cutting fluid.
- Chip thickness is lowered under the application of MoS₂ assisted water-soluble conventional cutting fluid.

The future work scope may include the comparative evaluation of Al₂O₃ and MoS₂ under high-speed machining applications with and without coated carbide inserts under near-dry machining as an environmentally friendly approach.

References

1. Dhar NR, Kamruzzaman M, Ahmed M (2006) Effect of minimum quantity lubrication (MQL) on tool wear and surface roughness in turning AISI-4340 steel. *J Mater Process Technol* 172:299–304
2. Thakur DG, Ramamoorthy B, Vijayaraghavan L (2013) Influence of minimum quantity lubrication on the high speed turning of aerospace material superalloy inconel 718. *Int J Mach Mach Mater* 13:203–214
3. Eker B, Ekici B, Kurt M, Bakýr B (2014) Sustainable machining of the magnesium alloy materials in the CNC lathe machine and optimization of the cutting conditions. *Mechanika* 20:310–316
4. Das RK, Kumar R, Sarkar G, Sahoo S, Kumar SA, Mishra PC (2018) Comparative machining performance of hardened AISI 4340 steel under dry and minimum quantity lubrication environments. In: International conference on advances in materials and manufacturing applications. *Materials Today Proceedings*, Bangalore, pp 24898–24906

5. Gunjal SU, Patil NG (2018) Experimental investigations into turning of hardened AISI 4340 steel using vegetable based cutting fluids under minimum quantity lubrication. In: 2nd international conference on materials manufacturing and design engineering. Procedia Manufacturing, Aurangabad, pp 18–23
6. Gajrani KK, Suvin PS, Kailas SV, Sankar MR (2019) Hard machining performance of indigenously developed green cutting fluid using flood cooling and minimum quantity cutting fluid. *J Clean Prod* 206:108–123
7. Elmunafi MHS, Kurniawan D, Noordin MY (2015) Use of castor oil as cutting fluid in machining of hardened stainless steel with minimum quantity of lubricant. In: 12th global conference on sustainable manufacturing. Procedia CIRP, Johor Bahru, pp 408–411
8. Ghuge NC, Mahalle AM (2016) Performance evaluation of vegetable oil during turning of AISI4130 in terms of temperature and surface roughness. *Int J Eng Sci Comput* 6:5879–5881
9. Kumar S, Singh D, Kalsi NS (2017) Optimization of the machining performance during hard turning of AISI 4340 steel under different cutting environments using Taguchi-grey approach. *Asian J Appl Sci Technol* 1:1–5
10. Nizamuddin M, Agrawal SM, Patil N (2018) The effect of karanja based soluble cutting fluid on chips formation in orthogonal cutting process of AISI 1045 steel. In: 2nd international conference on materials manufacturing and design engineering. Procedia Manufacturing, Aurangabad, pp 12–17
11. Gunjal SU, Sanap SB, Patil NG (2020) Role of cutting fluids under minimum quantity lubrication: an experimental investigation of chip thickness. In: 2nd international conference on recent advances in materials & manufacturing technologies. Materials Today: Proceedings, Dubai, pp 1–5
12. Dennison MS, Sivaram NM, Barik D, Ponnusamy S (2019) Turning operation of AISI 4340 steel in flooded, near-dry and dry conditions: a comparative study on tool-work interface temperature. *Mech Mech Eng* 23:172–182
13. Das RK, Sahoo AK, Kumar R, Roy S, Mishra PC, Mohanty T (2019) MQL assisted cleaner machining using PVD TiAlN coated carbide insert: comparative assessment. *Indian J Eng Mater Sci* 26:311–325
14. Khandekar S, Sankar MR, Agnihotri V, Ramkumar J (2012) Nano-cutting fluid for enhancement of metal cutting performance. *Mater Manuf Process* 27:963–967
15. Settu S, Murugabalaji V, Manikandan S (2015) Vegetable oil based nano cutting fluids and its applications in reduction of tool wear - a review. *Int J Res Appl Sci Eng Technol* 3:451–457
16. Koshy CP, Rajendrakumar PK, Thottackkad MV (2015) Evaluation of the tribological and thermo-physical properties of coconut oil added with MoS₂ nanoparticles at elevated temperatures. *Wear* 330:288–308
17. Padmini R, Krishna VP, Rao GKM (2016) Effectiveness of vegetable oil based nanofluids as potential cutting fluids in turning AISI 1040 steel. *Tribol Int* 94:490–501
18. Patole PB, Kulkarni VV (2017) Experimental investigation and optimization of cutting parameters with multi response characteristics in MQL turning of AISI 4340 using nano fluid. *Cogent Eng* 4:17–25
19. Patole PB, Kulkarni VV (2018) Prediction of surface roughness and cutting force under MQL turning of AISI 4340 with nano fluid by using response surface methodology. *Manuf Rev* 5:29–36
20. Revuru RS, Posinasetti NR, VSN VR, Amrita M (2017) Application of cutting fluids in machining of titanium alloys—a review. *Int J Adv Manuf Technol* 91:2477–2498, 47–60
21. Yuan S, Hou X, Wang L, Chen B (2018) Experimental investigation on the compatibility of nanoparticles with vegetable oils for nanofluid minimum quantity lubrication machining. *Tribol Lett* 66:13–21
22. Duc TM, Long TT, Chien TQ (2019) Performance evaluation of MQL parameters using Al₂O₃ and MoS₂ nanofluids in hard turning 90CrSi steel. *Lubricants* 7:27–33
23. Das A, Patel SK, Biswal BB, Sahoo N, Pradhan A (2020) Performance evaluation of various cutting fluids using MQL technique in hard turning of AISI 4340 alloy steel. *Meas J Int Meas Confed* 150:7–13

Investigation of Lubricant Condition and Machining Parameters While Turning of Steel



L. B. Abhang, Mohd.Iqbal, and M. Hameedullah

Abstract The present work contains an experimental investigation to study the effect of various lubricant conditions and machining parameters on cutting forces and surface roughness in turning of steel. Experimental work was carried out in turning steel alloy by using tungsten carbide inserts. There were three main purposes of this study. The first was to explain and demonstrate a systematic procedure of Taguchi parameter design and applying it to the data on turning. The second was to find out the optimal combination of process parameters based on S/N ratio and to know the significance of each parameter by performing ANOVA analysis. The third important aim was to find out the effect of lubricant temperature in the tuning process on the responses (i.e. cutting forces and surface roughness). The cutting parameters namely feed rate, depth of cut, and lubricant temperature were varied to observe the effects on responses. The main conclusion drawn from this study is that a better surface finish is obtained by applying cooling lubricant. There is a trade-off between (lowering or minimizing) forces and surface finish. Even with a higher depth of cuts surface finish is improved if lubricant temperature is lowered.

Keywords Taguchi design · Anova · Lubricant · Cutting force · Surface roughness

1 Introduction

In a turning operation, it is important to select cutting parameters so that high cutting performance can be achieved. Selection of desired cutting parameters by experience or using handbook does not ensure that the selected cutting parameters are optimal for a particular machine and environment. The effect of cutting parameters is reflected on surface roughness, surface texture and dimensional deviations of the product. Surface

L. B. Abhang (✉)

Mechanical Engineering, Department of PREC, Loni, Maharashtra, India

Mohd.Iqbal

Faculty of Engineering, Universitas Syiah Kuala Banda, Aceh, Aceh, Indonesia

M. Hameedullah

Mechanical Engineering Department, Aligarh Muslim University, Aligarh, UP, India

© The Author(s), under exclusive license to Springer Nature Switzerland AG 2021

P. M. Pawar et al. (eds.), *Techno-Societal 2020*,

https://doi.org/10.1007/978-3-030-69925-3_66

roughness, which is used to determine and to evaluate the quality of a product, is one of the major quality attributes of a turning product. Surface roughness is a measure of the technological quality of a product and a factor that significantly influences manufacturing cost. It describes the geometry of the machined surfaces and combined with the surface texture. The mechanism behind the formation of surface roughness is very complicated and process dependent [1]. Nalbant et al. [1] presented an application of the parameter design of the Taguchi method in the optimization of turning operations. To select the cutting parameters properly, several mathematical models [2] based on statistical regression or neural network techniques have been constructed to establish the relationship between the cutting performance and cutting parameters. Then, an objective function with constraints is formulated to solve the optimal cutting parameters using optimization techniques. Therefore, considerable knowledge and experience are required for this approach. In this study, an alternative approach based on the Taguchi method [3, 4] is used to determine the desired cutting parameters more efficiently. In the past, several optimization methods for turning operations have been documented [3–5]. It is shown by this study that the use of the parameter design of the Taguchi method can significantly simplify the optimization procedure for determining the optimal cutting parameters in turning operations. As a result, from the practical viewpoint, the parameter design of the Taguchi method seems to be the most suitable approach to determine the optimal cutting parameters for turning operations in a machine shop [6]. Montgomery [7]. Emphasizes that Taguchi's philosophy about quality engineering is broadly applicable. He considers three stages in a product's (or process's) development: system design, parameter design, and tolerance design. In system design, the engineer uses scientific and engineering principles to determine the basic configuration. In the parameter design stage, the specific values for the parameters are determined. Usually, the objective is to specify nominal values for the parameters to minimize variability transmitted from uncontrollable (or noise) variables. Tolerance design is used to determine the best tolerances for the parameters. Taguchi suggests analyzing variation using an appropriately chosen signal-to-noise ratio (S/N). These signal-to-noise ratios are derived from the quadratic loss function, and three of them are considered "Standard" and widely applicable. They are 1 Nominal the best, 2 Larger the better and 3 Smaller the better. Factor levels that maximize the appropriate S/N ratio are optimal.

In this study, the experimental work was carried out by turning EN-31 steel alloy by using tungsten carbide inserts with minimum solid-liquid lubrication method. The reason for selecting EN-31 steel alloy as work material is that this alloy is widely used in the automotive industry for the parts made by turning operations such as roller bearing, ball bearing, spline shaft and shearing blades. There were three main purposes of this study. The first was to explain and demonstrate a systematic procedure of Taguchi parameter design in turning. The second was to find out the optimal combination of process parameters based on S/N ratio and to know the significance of each parameter by performing ANOVA analysis. The third important aim was to find out the effect of lubricant temperature using minimum quantity lubrication technique developed by author [8] in tuning process on the responses (i.e. cutting forces, surface roughness chip tool interface temperature, power prediction model formed)

and to control the chip tool interface temperature and to develop prediction models for surface roughness, cutting forces and chip tool interface temperature when the lubricant temperature was varied during test. The cutting parameters namely feed rate, depth of cut, and lubricant temperature were varied to observe the effects on responses (output) [9]. The author has also done the grey relational analysis technique and obtained the optimum turning process parameters during machining alloy steel.

During machining, test using a cutting tool with small tool nose radius, the area of contact available for conduction between the tool and workpiece is small compared with that with a higher tool nose radius [10]. The nose radius is also taken at such a value that the surface roughness is reported to be best. If the tool nose radius increases to 1.2 mm (either three times, compared to nose radius of 0.4 mm), the values of cutting temperatures, decreases (of approximately 21%) while machining with higher tool nose radius [10]. An experimental set up was designed and fabricated and calibrated in Mechanical Engineering Department AMU, Aligarh, to measure the temperature on cutting tool and workpiece junction during metal cutting on the precision lathe (LMT, LTM 20 heavy-duty engine lathe machine). The essential characteristics of boric acid (solid) for use as a lubricant are that it is readily available, cheap and environmentally safe. Abhang and Hameedullah [11] reported that by increasing boric acid, more than 10% boric acid with SAE-40 base oil does not give any performance improvement.

2 Experimental Conditions and Planning of Experiments

The experiments were performed as follows-Nine experiments were carried out with parameters at different levels (each repeated thrice). The experimental conditions so far discussed have been summarized below in the following Table 1.

Table 1 Experimental conditions

Machine tool	10 hp. Lathe LTM20
Work material	EN-31 steel, 500 mm in length and 60 mm Φ
Tool holder	WIDAX, SCLCR12FOGT3, INDIA Lit
Insert configurations	CNMA 120,412, (diamond shape), ($\alpha = 6^\circ$, $\gamma_0 = -6^\circ$, $\lambda = -6^\circ$, $Kr = 95^\circ$, $\epsilon_r = 80^\circ$, $r = 1.2$ mm)
Cutting speed	1200 rpm
Nose radius	1.2 mm
Environments	MQL(10% boric acid + SAE-40 base oil)

Fig. 1 Experimental setup

Initial cutting parameters

**Table 2** Cutting parameters and their levels

Symbol	Cutting parameter	Unit	Level 1	Level 2	Level 3
A	Feed rate	mm/rev	0.05	0.1 ^a	0.15
B	Depth of cut	mm	0.2	0.4 ^a	0.6
C	Lubricant temperature	°C	10	30 ^a	50

^aInitial cutting parameters

2.1 Selection of the Cutting Parameters and Their Levels

The initial cutting parameters were as follows: cutting speed, feed rate; and depth of cut. In the cutting parameter design, three levels of the cutting parameters were selected, shown in Table 2. Experimental set up has been demonstrated in Fig. 1.

2.2 Cutting Performance Measure

(Carl-Zeiss, Japan made lens factor is 0.89). The surface roughness was taken perpendicular to the turning direction. Cutting forces are measured with the help of strain gauge type three components lathe tool dynamometer. The surface roughness was measured on an optical microscope.

2.3 Orthogonal Array Experiment

To select an appropriate orthogonal array for the experiments, the total degrees of freedom need to be computed. The degrees of freedom are defined as the number of comparisons between design parameters that need to be made to determine which level is better and precisely how much better it is. For example, a three-level design parameter counts for two degrees of freedom. The degrees of freedom associated with the interaction between two design parameters are given by the product of the degrees of freedom for the two design parameters. In the present study, the interaction between the cutting parameters is neglected. Therefore, there are six degrees of freedom owing to there being three cutting parameters in the turning operations. Once the required degrees of freedom are known, the next step is to select an appropriate orthogonal array to fit the specific task. The degrees of freedom for the orthogonal array should be greater than or at least equal to those for the design parameters. In this study, an *L9* orthogonal array with four columns and nine rows was used. This array has eight degrees of freedom, and it can handle three-level design parameters. Each cutting parameter is assigned to a column, nine cutting-parameter combinations being available. Therefore, only nine experiments are required to study the entire parameter space using the *L9* orthogonal array. The experimental layout for the three cutting parameters using the *L9* orthogonal array is shown in Table 3. Since the *L9* orthogonal array has four columns, one column of the array is left empty for the error of experiments: orthogonality is not lost by letting one column of the array remain empty [2].

2.4 Conducting Experiments as Per Design

The experiments were conducted as per the design explained above. The three cutting forces acting on a single point cutting tool are—feed force F_x , thrust force or cutting force F_y and radial force F_z acting in x , y , z directions respectively. The responses were recorded.

2.5 Results and Discussion

a. Analysis of surface roughness

Table 4 shows the experimental results for surface roughness and the corresponding S/N ratios. Taguchi uses the S/N ratio to measure the quality characteristic deviating from the desired value. The S/N ratio η is defined as

$$\eta = -10 \log (M.S.D.) \quad (1)$$

Table 3 Experimental layout using /9 orthogonal array

Experiment no	A	B	C
	Feed rate	Depth of cut	Lubricant temperature
1	1	1	1
2	1	2	2
3	1	3	3
4	2	1	3
5	2	2	1
6	2	3	2
7	3	1	2
8	3	2	3
9	3	3	1

Table 4 Experimental results for surface roughness and s/n ratio

Exp. no	Feed rate (mm/rev)	D.O.C (mm)	T (°C)	Ra(μm)	S/N ratio (dB)
1	0.05	0.2	10	9.28	-19.35
2	0.05	0.4	30	10.2	-20.17
3	0.05	0.6	50	10.68	-20.57
4	0.1	0.2	50	11.1	-20.91
5	0.1	0.4	10	9.42	-19.48
6	0.1	0.6	30	10.34	-20.29
7	0.15	0.2	30	10.78	-20.65
8	0.15	0.4	50	11.37	-21.12
9	0.15	0.6	10	10.09	-20.08

T (°C) = lubricant temperature

There are three categories of quality characteristics, i.e. the-lower-the-better, the higher—the better, and the-nominal-the-better. The mean-square deviation (M.S.D.) for the-higher-the-better quality characteristic can be expressed as:

$$M.S.D. = \frac{1}{m} \sum_{i=1}^m \frac{1}{T_i^2} \tag{2}$$

where m is the number of tests, and Ti is the parameter. Lower the better quality characteristic for surface roughness and cutting forces should be taken for obtaining optimal cutting performance. The M.S.D for the lower, the better quality characteristic can be expressed as:

$$M.S.D. = \frac{1}{M} \sum_{i=1}^m S_i^2 \tag{3}$$

where s_i is the value of the parameter for the i th tests. We have used lower the better quality characteristic formula. S/N Response for surface roughness is shown in Table 5.

S/N graph for surface roughness is shown in Fig. 2. Thus it can be observed that A1B2C1 are the optimal levels of the design parameters for the improved surface finish which implies feed rate at a low level, depth of cut at medium level and lubricant temperature at low-level combination gives the best surface finish within the specified range. The results of the confirmation experiment are shown in Table 6.

Table 5 S/N response table for surface roughness

Symbol	Cutting parameter	Mean S/N ratio(dB)			
		Level 1	Level 2	Level 3	Max-min
A	Feed rate	-20.03	-20.23	20.62	0.59
B	Depth of cut	-20.3	-20.26	-20.313	0.053
C	Temperature of lubricant	-19.64	-20.37	-20.87	1.23

Total mean S/N ratio = -20.29 dB

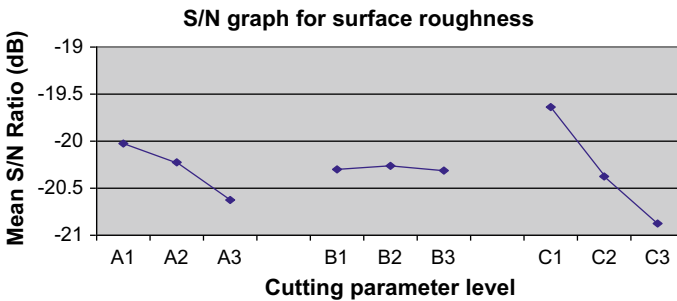


Fig. 2 S/N graph for surface roughness

Table 6 Results of the confirmation experiment

Level	Initial cutting parameters	optimal cutting parameters	
		Prediction	Experiment
Level	A2B2C2	A1B2C1	A1B2C1
Surface roughness (μ m)	11.76	9.28	9.51
S/N ratio (dB)	-21.41	-19.35	-19.57

Improvement of S/N ratio = 1.84 dB

Table 7 Results of ANOVA for surface roughness

Source	D.F	S.S	M.S	F value	P-value	% C
Feed rate	1	0.7211	0.7211	34.175	0.002 s	18.05
Depth of cut	1	0.0004	0.0004	0.0189	0.894 ns	0.01
Lubricant temperature	1	3.1683	3.1683	150.156	0.000 s	79.299
Residual error	5	0.1056	–	–	–	2.64
Total	8	3.9954	–	–	–	100

It is clear from the ANOVA Table 7 that lubricant temperature is the most significant parameter for surface roughness. Among the three design parameters, lubricant temperature contribution is the largest, i.e. 79.299% followed by feed rate whose contribution is 18.05% and then the depth of cut 0.01%. Thus within specified range effect of depth of cut on surface roughness is insignificant.

b. Analysis of thrust force:

Tables 8 and 9 shows the experimental results and S/N response table for thrust force respectively.

Table 8 Experimental results for thrust force and s/n ratio

Ex no	Feed (mm/rev)	D.O.C (mm)	Temp. of lubricant (°C)	Thrust force (N)	S/N ratio (dB)
1	0.05	0.2	10	61.17	-35.73
2	0.05	0.4	30	55.89	-34.95
3	0.05	0.6	50	48.45	-33.71
4	0.1	0.2	50	73.23	-37.29
5	0.1	0.4	10	87.35	-38.82
6	0.1	0.6	30	80.54	-38.12
7	0.15	0.2	30	116.58	-41.33
8	0.15	0.4	50	108.31	-40.69
9	0.15	0.6	10	125.48	-41.97

Table 9 S/n response table for thrust force

Symbol	Cutting parameter	Mean S/N ratio(dB)			
		Level 1	Level 2	Level 3	Max-min
A	Feed rate	-34.796	-38.08	-41.33	6.534
B	Depth of cut	-38.12	-38.15	-37.93	0.22
C	Temperature of lubricant	-38.84	-38.13	-37.23	1.61

Total mean S/N ratio = -38.07 dB

S/N response table for the thrust force is shown in Table 9. It can be observed that A1B3C3 are the optimal levels of the design parameters for low thrust force which implies feed rate at a low level, depth of cut at a high level and lubricant temperature at high-level combination keeps the thrust forces in control within a specified range of input parameters. S/N graph for thrust force is shown in Fig. 3. Thrust force is low at high temperature. Table 10 shows the results for the confirmation experiment carried out for the thrust force. It shows that there is good agreement between the predicted and experimental result and improvement of 2.19 dB is observed.

The ANOVA results for thrust force (Table 11) shows that the depth of cut is insignificant for our range of design parameters. Feed rate is the most significant factor for thrust force contributing 93.564% followed by lubricant temperature (5.303%) and then the depth of cut (0.033%).

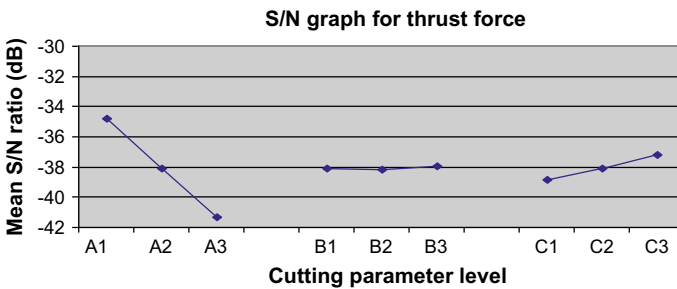


Fig. 3 S/N graph for thrust force

Table 10 Results of the confirmation experiment thrust force

	Initial cutting parameters	optimal cutting parameters	
		Prediction	Experiment
Level	A2B2C2	A1B3C3	A1B3C3
Thrust force (N)	68.13	49.06	52.95
S/N ratio (dB)	-36.67	-33.816	-34.48

Improvement of S/N ratio = 2.19 dB

Table 11 Results of Aanova for thrust force

Source	D.F	S.S	M.S	F value	P-value	%C
Feed	1	5695.5	5695.5	425	0.000 s	93.564
Depth of cut	1	2.0	2.0	0.149	0.713 ns	0.033
Lubricant temperature	1	322.8	322.8	24.09	0.004 s	5.303
Residual error	5	66.9	13.4			1.099
Total	8	6087.3	-	-	-	-

Table 12 Experimental results for feed force and s/n ratio

Ex no	Feed (mm/rev)	D.O.C (mm)	Temp. of lubricant (°C)	Feed force (N)	S/N ratio (dB)
1	0.05	0.2	10	29.43	-29.38
2	0.05	0.4	30	19.61	-25.85
3	0.05	0.6	50	9.81	-19.83
4	0.1	0.2	50	16.35	-24.27
5	0.1	0.4	10	35.97	-31.12
6	0.1	0.6	30	29.43	-29.38
7	0.15	0.2	30	42.51	-32.56
8	0.15	0.4	50	29.43	-29.38
9	0.15	0.6	10	58.86	-35.396

Table 13 S/n response table for feed force

Symbol	Cutting parameter	Mean S/N ratio(d/B)			
		Level 1	Level 2	Level 3	Max-min
A	Feed rate	-25.02	-28.26	-32.45	7.43
B	Depth of cut	-28.74	-28.78	-26.197	2.583
C	Temp of lubricant	-31.97	-31.27	-24.49	7.48

Total mean S/N ratio = -28.58 dB

c. Analysis of feed force: Experimental results and response table for feed force have been shown in Tables 12 and 13.

Table 13 and Fig. 4 clearly shows that the optimum combination in terms of feed force is A1B3C3. The improvement in S/N ratio is 1.237 dB, and there is good agreement between the prediction and confirmatory experiment as is clear from Table 14.

Among the three design parameters chosen feed rate contributes the most in feed force (49.94%) followed by lubricant temperature (45.49%). Depth of cut is an insignificant parameter for feed force as is evident from ANOVA Table 15.

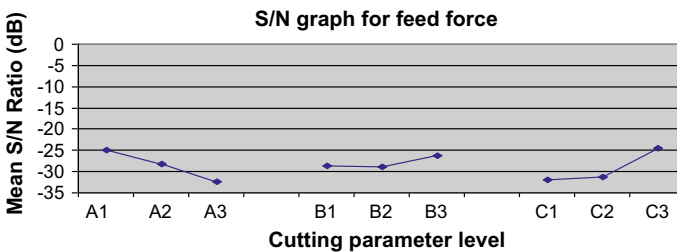


Fig.4 S/N graph for feed force

Table 14 Results of the confirmation experiment

	Initial cutting parameters	Optimal cutting parameters	
		Prediction	Experiment
Level	A2B2C2	A1B3C3	A1B3C3
Feed force (N)	28.83	23.52	25.01
S/N ratio (dB)	-29.197	-27.43	-27.96

Improvement of S/N ratio = 1.237 dB

Table 15 Results of Anova for feed force

Source	D. F	S.S	M.S	F value	P-value	%C
Feed	1	862.80	862.80	68.53	0.000 s	49.94
Depth of cut	1	16.04	16.04	1.274	0.310 ns	0.928
Lubricant temperature	1	785.93	785.93	62.425	0.001 s	45.49
Residual error	5	62.94	12.59			3.642
Total	8	1727.71	-	-	-	-

3 Conclusion

The following conclusions can be drawn based on the experimental results of this study:

1. Taguchi’s robust orthogonal array design method is suitable to analyze the surface roughness, cutting forces problem as described in this study.
2. The experimental results show that lubricant temperature and feed rate are the main parameters among the three controllable factors (feed rate, depth of cut and lubricant temperature) that influence surface roughness in turning EN-31 steel.
3. For cutting forces, the main parameters are the feed rate and lubricant temperature. For forces (Thrust and feed force), the order of significance is feed rate followed by lubricant temperature.
4. In turning:
 - (a) For minimum surface roughness, use of lower feed rate (0.05 mm/rev), medium depth of cut (0.4 mm) and low lubricant temperature (10 °C), i.e. A1B2C1 are recommended to obtain better surface roughness for the specific test range. Thus the surface finish is better if cooled lubricant is applied.
 - (b) For minimum thrust force and feed force low feed rate (0.05 mm/rev), high depth of cut (0.6 mm) and high lubricant temperature (50 °C), i.e. A1B3C3 are optimum parameters.
5. Minimum surface roughness at optimum cutting parameters is 9.51 micron, Minimum thrust force at optimum cutting parameters is 52.95 N, Minimum feed

force at optimum cutting parameters is 25.01 N. This research demonstrates how to use Taguchi parameter design for optimizing machining performance with minimum cost and time to industrial readers.

References

1. Nalbant M, Gokkaya H, Sur G (2007) Application of Taguchi method in the optimization of cutting parameters for surface roughness in turning. *J Mater Des* 28:1379–1385
2. Yang W, Tarn Y (1998) Design optimization of cutting parameters for turning operations based on the Taguchi method. *J Mater Process Technol* 84:122–129
3. Abuelnaga A, Dardiry EI (1984) Optimization methods for metal cutting. *Int J Mach Tool Des Res* 24(1):11–18
4. Chua M, Rahman M, Wong Y, Loh H (1993) Determination of optimal cutting conditions using design of experiments and optimization techniques. *Int J Mach Tools Manuf* 33(2):297–305
5. Zhou C, Wusk R (1992) An integrated system for selecting optimum cutting speeds and tool replacement times. *Int J Mach Tools Manuf* 32(5):695–607
6. Nian C, Yang W, Tarn Y (1999) Optimization of turning operations with multiple performance characteristics. *J Mater Process Technol* 95:90–96
7. Montgomery D (2010) *Statistical quality control*, 3rd edn. Wiley, New York, pp 158–169
8. Abhang L, Hameedullah M (2010) A power prediction model for turning En-31 steel using response surface methodology. *J Eng Sci Technol Rev* 3(1):116–122
9. Abhang L, Hameedullah M (2012) Determination of optimum parameters for multi-performance characteristics in turning by using grey relational analysis. *Int J Adv Manuf Technol*. <https://doi.org/10.1007/s00170.011-3857-6>
10. Abhang LB, Hameedullah M (2010) Chip-tool interface temperature prediction model for turning process. *Int J Eng Sci Technol* 2(4):382–393
11. Abhang L, Hameedullah M (2010) Control of chip-tool interface temperature for improved productivity through a new lubricating technique. *Int J Appl Eng Res* 5(14):2373–2382

A Short Spiral Conveyor Using Cut Flight Screw with Two Different Trough Cover of Different Height—A Comparative Study



Debayan Mondal

Abstract Mechanization and automation are one of the crucial areas of interest in any industry handling materials for efficient conveying and transportation. Screw conveyor is the most efficient mechanized conveying device for free-flowing or relatively free-flowing bulk solids with a moderate capacity of 1200 ton/h. And small conveying distance less than 40 m for horizontal configuration, while in case of vertical operation lifting material up-to 15 m at a rate of 50 ton/h. The application area of the screw conveyor is agricultural grains and bulk material conveying. The objective of the research work is to compare two different values of trough height (112 and 180 mm) with various screw speed along with dry, coarse sand as conveying material and type of screw as cut flight one. Hence to draw characteristics curves of volumetric capacity and loading efficiency within a predetermined speed range.

Keywords Screw conveyor · Bulk density · Loading efficiency · Trough height

1 Introduction

A cut flight type screw of unique design features is considered through experimentation with dry, coarse sand as conveying material. The unique design features involve a small notch at regular intervals in the flighting, where the material has been removed from the profile of the screw. One of the purposes of using cut flight type screw is mixing action and agitation of material in transit.

D. Mondal (✉)
Technology Campus, University of Calcutta, Kolkata 700106, India
e-mail: debayan3@rediffmail.com

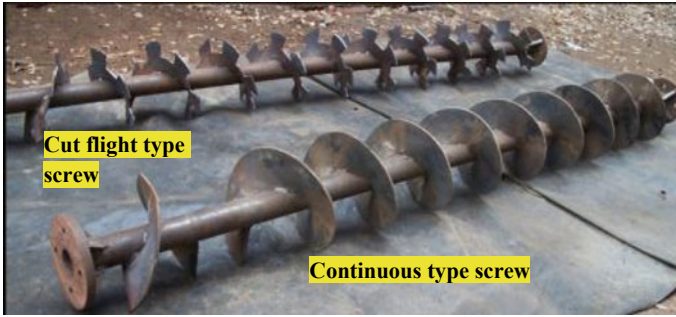


Fig. 1 Photograph of continuous and cut-flight types screw

2 Material of Screw with an Associated Manufacturing Process

The screw [1–7] are generally manufactured from 4 to 8 mm thick mild steel plate, cut into circular section [8, 9] with a hole at centre corresponding to the outer diameter of the tubular shaft. One radial slit is made in a circular plate and then formed into one pitch of the screw. The connection between shaft and screw blank is through tag welding to avoid distortion of the tubular shaft during the welding process. The no of spiral helix is connected through welding or riveting to each other to form the entire length of the shaft. The screw may also be cast integral with the shaft as shown in Fig. 1.

3 Objective of Experiment

The objective of the present experiment is to find out volumetric capacity, mass flow rate while keeping two distinct constant trough height (112 and 180 mm) and hence to study the variation of filling factor [1, 3, 5, 6] with the variation of screw speed within a predetermined range with cut flight type of screw. Hence to make a comparison in two different cases, with the variation of screw speed and to draw the characteristic curves of volumetric capacity [1–3, 5, 7] and loading efficiency versus different screw speeds with a particular type of bulk material and Screw combination. The mass flow rate [1–11, 13–15] of a transported material in a spiral conveyor depends on this loading efficiency as given by the following formula

$$Q = (\pi \times D^2 \times S \times 60 \times n \times \Psi \times \gamma \times C)/4 \text{ ton/h} \quad (1)$$

Where Q is a mass flow rate in ton/h.

Ψ is a Capacity factor or loading efficiency. (also known as Filling factor).

D is the nominal Screw diameter in m. = 0.2 m.

S is Screw pitch in m. = 0.16 m.

γ is tapped density of transported material in $\text{ton/m}^3 = 1.572 \text{ ton/m}^3$.

C is the Inclination factor, for horizontal screw conveyor its value is “one.”

4 Experimental Methodology and Set Up

The specified screw conveyor [1–11] with provision for variable speed through variable frequency Drive (VFD) [12] along with instrument panel, as shown in Fig. 2. The drive of the conveyor [1–11, 13–15] consisting of motor, worm reducer and couplings.

In case of continuous operation, the drive of the equipment needs to have some cooling arrangement to dissipate the heat generated during a long run, which is ensured through worm reducer with a provision of fan cooling.

A screw conveyor and variable frequency drive with instrument panel were installed to perform dissertation work to fulfil the need of experimentation with varying screw speed through VFD [12] in the area of material handling. At the input of the screw conveyor [1 to 15], there is a feed hopper of adequate size and capacity with a provision for shifting the hopper position along the length of the conveyor to experiment keeping the different sufficient length of the conveyor. However, the experiment was conducted keeping the constant conveying length of 1480 mm. Reading was taken for dry, coarse sand as conveying material at 4 different screw speeds of 12, 15, 21 and 26 rpm respectively, using cut flight type of screw. Two numbers of wooden buckets (Bucket No.1 and Bucket No.2) was placed side by side under the outlet spout of the conveyor to collect the conveyed material and different take for weighing purpose with a suitable digital weighing machine. A maximum speed of screw as 26 rpm with the 30-s continuous run was considered judiciously

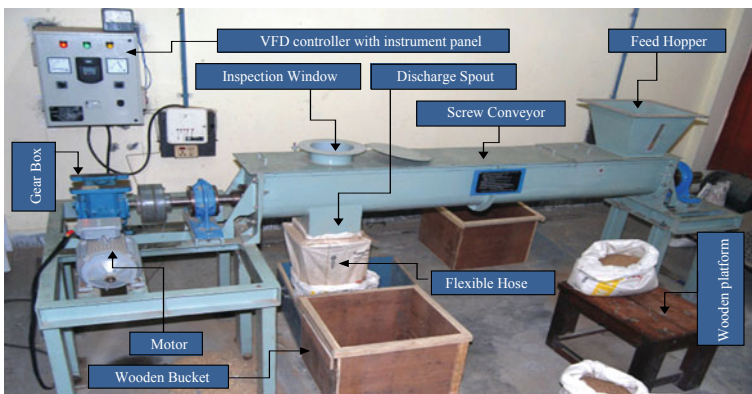


Fig. 2 Experimental setup

as experimental run for manual feeding arrangement of the conveyor. The predetermined speed range was chosen as 12, 15, 21 and 26 rpm keeping because of different result to study the effect of screw speed. Each experimental run at a particular speed was repeated for four times, and an average of the four runs was taken to minimize experimental error.

After filling the conveyor with dry sand, the screw conveyor was started and speed up to a specific speed, ensuring at a finite value of frequency through VFD [12] push button switch and allowed to run at that speed for about 5 s for stabilization purpose. The outlet of the conveyor was connected to a flexible hose, which allows to direct and collect the conveyed materials into different buckets through manual switching off the hose from one empty bucket to another. During each experimental run, one person of the three members team continuously feed the sand into the feed hopper to ensure that the hopper was always filled beyond a threshold level, confirming flood feeding condition so that the conveyor discharge rate was not influenced because of lack of material supply. During 5 s of conveyor runs, as the screw speed gets stabilized and transported material was received in the empty bucket (Bucket No.-1). At that instant, the output hose of the equipment was manually switched over to the second container (Bucket No.2) and the commencement of measurement of time was started by operating a suitable stopwatch. After the passage of 30 s for each run for the output was again transferred to another empty container and during 30 s time interval conveyed material was collected and taken further for weighing to calculate mass flow rate [1–4, 8–10, 13–15] from Eq. 1. These processes were repeated for four different speeds, and the raw data was collected.

5 Experimental Results

The experiment was conducted with dry, coarse sand using cut flight type screw and two different trough covers having trough height 112 and 180 mm respectively. Experimental data is as shown in Tables 1 and 2.

5.1 Characteristic Curves-1

A characteristic curve is being plotted based on the tabulated values showing a variation of volumetric capacity (V) with the variation of screw speed (n) in rpm for two distinct values of trough height (112 and 180 mm) with cut flight type of screw are shown in Fig. 3.

Table 1 Experimental datasheet for 112 mm trough height

Sl No	Frequency (f) in Hz	Screw speed (n) in (rpm)	Experimental run time (t) in second	Amount of material transported (kg)	The average amount of material transported (M) (kg)	Mass flow rate (Q) in ton/h	Volumetric capacity (V) in m ³ /min	Loading efficiency (Ψ)
1	10	12	30	28.720	28.28	3.39	0.04	0.60
2				27.930				
3				28.185				
4				28.280				
5	12.5	15		35.865	35.83	4.30	0.05	0.6
6				35.810				
7				35.835				
8				35.810				
9	17.5	21		52.520	51.03	6.12	0.06	0.62
10				49.910				
11				52.145				
12				49.535				
13	21.7	26		65.930	66.39	7.97	0.08	0.65
14				66.650				
15				66.115				
16				66.855				

5.2 Characteristic Curves-2

In Fig. 4 characteristic curve is plotted for variation of filling factor for variation of speed for two distinct values of trough cover height 112 and 180 mm with cut flight type of screw and conveyed material as dry, coarse sand.

6 Result Analysis and Conclusion

The result may be analyzed, and Conclusions can be made as follows from the experimental data.

- 6.1 As per experimental philosophy is a concern, the investigation is performed for a definite type of screw namely cut flight type with four numbers of different speeds 12, 15, 21 and 26 rpm respectively at two distinct trough height and hence comparison can be made.

Table 2 The experimental datasheet for 180 mm trough height

Sl No	Frequency (f) in Hz	Screw speed (n) in (rpm)	Experimental run time (t) in second	Amount of material transported (kg)	The average amount of material transported (M) (kg)	Mass flow rate (Q) in ton/h	Volumetric capacity (V) in m ³ /min	Loading efficiency (Ψ)
1	10	12	30	35.650	35.4152	4.25	0.05	0.75
2				35.527				
3				35.533				
4				34.951				
5	12.5	15		43.970	43.85943	5.26	0.06	0.74
6				43.986				
7				44.131				
8				43.350				
9	17.5	21		62.960	63.0855	7.57	0.08	0.76
10				62.897				
11				63.044				
12				63.320				
13	21.7	26		78.823	79.083	9.49	0.10	0.77
14				79.250				
15				79.049				
16				78.210				

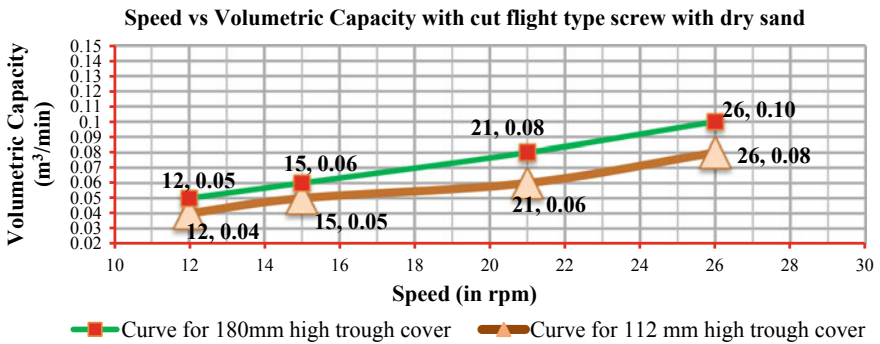


Fig. 3 A characteristic curve: volumetric capacity (V) with the variation of screw speed (n) in rpm for two different trough height

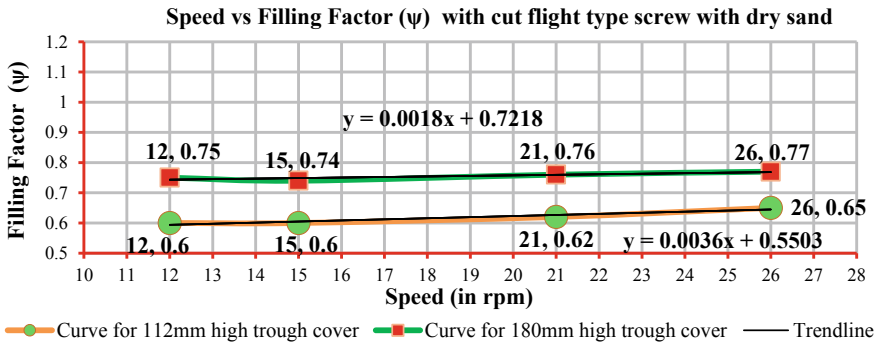


Fig. 4 Characteristic curve: variation of filling factor for variation of speed for both the values of trough height as 112 and 180 mm respectively with cut flight type of screw

- 6.2 It is observed from experimental data that with cut flight type screw for 112 mm trough cover height at four predetermined screw speeds 12, 15, 21 and 26 rpm mass flow rate are found to be 3.39, 4.30, 6.12 and 7.97 ton/h respectively and while for 180 mm trough height the values of mass flow rate are 4.25, 5.2633, 7.571 and 9.4937 ton/h respectively.
- 6.3 With cut flight type of screw for 112 mm trough height the volumetric capacity is found to be 0.04, 0.05, 0.06 and 0.08 m³/min while for 180 mm trough [8–10] height same values are 0.05, 0.06, 0.08 and 0.10 m³/min respectively at four distinct screw speeds (12, 15, 21, 26 rpm).
- 6.4 Mass flow rate as well as volumetric capacity in both the cases (112 and 180 mm trough height) increasing trends with the increase of screw speed, which can be self-explanatory from Eq. 1.
- 6.5 For constant trough height, loading efficiency varies slightly within a range of 0.6 to 0.65 and 0.74 to 0.77 with the variation of screw speed.
- 6.6 In case of the high value of trough cover height, the mass flow rate, volumetric capacity and loading efficiency are found to be higher values, which may be explained as that the higher value of filling factor is because the feeding condition was flooded feeding one and the sufficient conveying length was 1480 mm (less than 2 m), a short one. These can be further explained that use of the lower value of trough cover restricts the material height over the screw top near the loading zone and thus reduces the value of loading efficiency compared to when higher trough cover 180 mm are used. Though in both the cases 112 mm as well as 180 mm trough cover it was observed that loading efficiency was almost constant within the range of speed, however with lower trough cover, loading efficiency shows a slightly increasing trend with the variation of screw speed. These may be due to the variation of tapped density of bulk material with speeds.
- 6.7 From the characteristic’s curves of filling factor to screw speed, it was observed that for trough height 112 mm the slope of the trend line has got a positive

value with a small inclination 0.21° . In contrast, for 180 mm trough height, the slope is almost zero value for a horizontal axis.

7 Future Scope

It is to be noted that normal range of speed for 200 mm diameter screw is in between 20 and 150 rpm. The present experimental set up also allows a top speed of about 60 rpm. However, the experiment being conducted in between 12 and 26 rpm only, because of the physical limitation of manual feeding. The experiment could not be conducted at higher speeds to find out whether the loading efficiency would become constant at higher speeds or not.

In the present research work, the observations and result analysis were performed on a single screw within a single U trough [1, 2, 4, 6, 10]. However, the same type of experiment may be conducted on using a double screw with varying speeds and various type of screw combination. Hence, mass flow rate, volumetric capacity and filling factor may be investigated for the double screw.

With the cut flight type screw and two different bulk material can be introduced, and hence mixing and blending efficiency may be investigated through sieve analysis during transportation.

In the present research, the experiment was conducted with a particular type of screw with a constant helix angle. However with cut flight [2, 3, 6, 8–10] type of screw with different helix angle for particular conveying material need to be investigated and hence mass flow rate, volumetric capacity and loading efficiency [10] may be studied.

An extensive study on torque and power requirement of a screw-type conveyor for different bulk and free-flowing materials need to be investigated.

A sincere effort on helix angle [6, 8–10] of the screw and the effect of torque requirements for a particular type of bulk material need to be studied, and hence helix angle of the screw along with the torque requirements need to be investigated.

Using lining material with low dynamic friction coefficient [5–10, 14, 15] at the inner surface of the trough and its effect on torque and power requirements of screw conveyor need to be studied further.

An extensive study of various types of a screw with different types of bulk material surcharge angle [5, 7–10] may be investigated and hence to recommend the particular type of screw along with the bulk material combination is beneficial from capacity as well as torque and power requirements as concerned.

A screw feeders' performance [1–5] in the inclined configuration with the varying inclination may be further observed.

Acknowledgements The support and infrastructure Facilities of the National Institute of Technical Teacher's Training and Research, Kolkata are duly and sincerely acknowledged. The author expresses his sincere gratitude to Prof. Dr Siddhartha Ray, former Director-in-Charge, NITTR-Kolkata for his guidance, support and continuous encouragement throughout the dissertation work.

The author is also grateful to all faculty members, technical staff of Mechanical engineering department, NITTR- Kolkata and B.M Engineering Company.

References

1. Nagel G (1968) Archimedean screw pump handbook. Prepared for Ritz-Atro Pumpwerksbau GMBH Roding, Nürnberg, Germany
2. Fuchs A, Zangl H, Brasseur G (2007) Mass flow meter screw conveyor based on capacitive sensing. In: Proceedings of IEEE instrumentation and measurement technology conference (IMTC), May 1–3, 2007. Warsaw, Poland, pp 1–5
3. Fottner J (2000) Characteristics of bulk material in screw type conveyors. In: Engineering meeting of Krupp Forder technik session
4. Roberts AW (2001) Design consideration and performance evaluation of screw conveyors. Centre for Bulk Solids and Particulate Technologies, The University of Newcastle, Australia
5. Yu Y, Arnold PC (1996) Investigation into power requirements for screw feeders. In: 1996, National conference on bulk material handling. Australe
6. IS:5563 (1985) Specification of screw conveyors for industrial use, BIS
7. IS:12960 (1990) Determination of power requirements for screw feeder general requirements, BIS
8. Spivakovsky A, Dyachkov V (1985) Conveying machines, vol II, 1st edn. Mir Publishers, Moscow
9. Ray S (2008) Introduction to materials handling, 1st edn. New Age International(P) Limited Publishers, New Delhi
10. Alexandrov MP (1981) Materials handling equipment, 1st edn. Mir Publishers, Moscow
11. Kurjak A (2005) The vertical screw conveyor-powder properties and screw conveyor design. Department of Chemical Engineering, Sweden
12. Simens Homepage <https://www.siemens.com/products/drive>
13. Zareiforoush H, Mohammad Hassan K, Mohammad Reza A (2010) A review on screw conveyor performance evaluation during handling process. J Sci Rev 2(1):55–63
14. Mondal D, Ghosh N, Rudrapati R (2016) Study on filling factor of short screw conveyor with ribbon type screw at two different trough height (112 mm & 180 mm) in flood-feeding condition. Int J Curr Eng Technol E-ISSN2277–4106, P-ISSN2347–5161
15. Mondal D, Ghosh N (2018) Study on filling factor of short length screw conveyor with the flood-feeding condition. Mater Today Proc 5:1286–1291

Design Consideration of a Laboratory Size Screw Conveyor with Variable Speed for Experimentation Purpose—A Methodological Approach



Debayan Mondal

Abstract A small size horizontal screw conveyor needs to set up for conducting experiments and undertaking research in the area of materials handling. The responsibility of designing a suitable horizontal screw conveyor was entrusted to the present author. The Present work includes a methodological approach to design a small horizontal spiral conveyor with a provision for speed change through variable frequency drive (VFD) for experimental purpose. The proposed screw conveyor may be capable of conveying three different types of materials such as dry sand, crushed stone, and wheat with various speed along with three different types of screw (Continuous, Cut flight and Ribbon type) having easy replacement facility of each screw type. Design philosophy of an equipment is based on so many factors, such as overall size of the screw (which depends upon space availability of the equipment, where it is to be installed) and design capacity required and running under variable speed during experiment.

Keywords Screwconveyor · Bulk density · Loading efficiency · Progress resistance-co-efficient

1 Introduction

A screw [1–8] or spiral conveyor comprise of continuous or interrupted helical screw [9] fixed to solid or tubular shaft within a stationary U shape trough. The shaft is rotated by an electric motor through gear box and couplings to push fine grain bulk material [1–4, 8–14] through the round bottom shape trough, [10] covered with a top plate having an opening for loading. The shaft integral with screw is supported by two thrust bearings at two extreme ends. Spiral conveyors are three types [8, 9]. Horizontal or inclined (inclination up to 20°) and vertical or steeply inclined one [8]. However present work is based on horizontal screw conveyor with helix angle of 30°. Screw of different constructional design and style are used such as continuous, cut flight and ribbon type with a provision for easy replacement facilities for conducting

D. Mondal (✉)

Technology Campus, University of Calcutta, Kolkata 700106, India

experiments. Before starting actual design, procedure following information need to be collected by the researcher. (i) Primary condition of the conveyed material, including lump size and tapped density of the transported material. (ii) Quantity of conveyed material with rate of flow expressed in ton/hr. (iii) The conveying distance. Once the material conveyed and rated capacity requirement is well understood by the researcher, which guides in selecting suitable screw diameter and speed to achieve the design capacity as per IS:5563:1985 [6]. Design of a screw conveyor is an extensive job starting from requirements by considering capacity and conveying distance. Initially screw diameter and speed is being selected to achieve design capacity and hence motor power calculation and drive component selection is performed and determination of the dimension of each component like screw, trough etc. However present work restricted to selection of screw diameter, motor power calculation and drive component selection as the scope of work does not allow in detail for determination of the component's dimension.

2 Design Methodology and Procedure

The horizontal screw conveyor capable in handling various type of materials like dry sand, stone chip and wheat. Proposed conveyor must be able to run at different speed for experimental purpose, which is achieved by introducing VFD with the drive motor along with instrument panel [12]. Design methodology refers to ensure the desired performance considering critical condition with stone chip as conveying material having lump size of 15 mm, minimum nominal diameter of the screw should be 12 × 15 mm is 180 mm with continuous type of screw maximum speed is calculated 153 rpm as per empirical formula.

$$n_{\max} = \frac{A}{\sqrt{D}} \quad (1)$$

Thus in Eq. (1) A is co-efficient and D is nominal screw diameter [10].

The rotational speed n of a screw is chosen, depending on the kind of conveyed material, screw diameter selected, bulk density of material and abrasiveness of the load. The rotational speed is decreased with increase of screw diameter, density and abrasiveness of the load. In Eq. (1) D is 180 mm and A is 65 for slightly abrasive material [10].

Referring to IS:5563:1985 [6], the next higher size specified screw diameter is 200 mm. Thus the diameter D of the screw selected as 200 mm.

Pitch of the screw S is generally considered as D to 0.8 D as per IS:5563:1985 [6], the nearest recommended pitches are 160 mm and 200 mm. Pitch is selected to be 160 mm. Conveying length is generally decided from system requirement and from layout. However, keeping the space constraint in mind, the total length of the screw is taken to be 2000 mm, while maximum effective length of conveying, i.e. length

Table 1 Steps for selection of screw conveyor system [8, 9]

Screw dia, mm	150	200	250	300	400	500	600
Maximum rpm	150	150	118	118	95	95	75
Minimum rpm	23.6	23.6	23.6	19	19	19	16

between the centerline of the material feeding hopper to the nearest inner edge of the discharge spout to be 1520 mm, which is 7.6 times of the screw diameter. The total length is thus taken as 2000 mm. Above mentioned Table 1 shows the normally recommended speed range [3, 4] of operation for different size of screw, the higher speeds for nonabrasive light materials.

Based on desired capacity, speed or speed range is selected within the above speed range as per Table 1. The throughput capacity Q in ton/hr of a horizontal screw conveyor is given by the formula in Eq. (2) [8, 9]

$$Q = \frac{\pi}{4} \times D^2 \times S \times n \times 60 \times \gamma \times \psi \text{ ton/hr.} \tag{2}$$

Considering dry coarse sand as the conveying material, the following values can be put in Eq. (2):

In Eq. (2) D is the nominal diameter of screw as 0.2 m.

S is the Screw pitch of 0.16 m.

γ is bulk density dry coarse sand as 1.57ton/m³.

Ψ is loading efficiency, value of 0.64 is considered, for length of conveyor less than 2 m as short one [8].

n is theScrew speed in rpm as 150, which is the maximum recommended for 200 mm diameter screw. The capacity of the screw conveyor dry sand as transported material at 150 rpm with an assumed loading efficiency of 0.64, is as follows in Eq. (3)

$$Q = \frac{\pi}{4} \times 0.2^2 \times 0.16 \times 150 \times 60 \times 1.57 \times 0.64\text{ton/hr.} \tag{3}$$

$$Q = 45.5\text{ton/hr or}758\text{kg/min.} \tag{4}$$

This capacity Q in Eq. (4) is comparatively too high for a laboratory conveyor, where loading of material at such a high rate is physically impracticable as present experimental set up consisting with manual feeding arrangement. Therefore, the top speed of the conveyor is targeted to be around 60 rpm, at which speed the capacity of the conveyor with dry sand will be as follows.

$$Q = \frac{\pi}{4} \times 0.2^2 \times 0.16 \times 60 \times 60 \times 1.57 \times 0.64\text{ton/hr.} \tag{5}$$

$$Q = 18.18\text{ton/hr or}303\text{kg/min.} \tag{6}$$

The target top speed is thus selected as 60 rpm.

For laboratory and research work the proposed drive system should be capable to run the equipment with a variable speed to conduct experiment at different speeds. A variable frequency drive capable of speed regulation within a specified speed range must be fulfilling experimental requirement. As per technical specification of variable frequency drive Siemens make MM420 drive for 3 phase AC 200 V TO 240 V $\pm 10\%$ (0.12 kW TO 5.5 kW) output to input frequency ratio is approximately.

$$650Hz/63Hz = 10.3 = 10 \quad (7)$$

The minimum speed through a variable frequency drivespeed regulation system will be around

$$60/10 = 6rpm \quad (8)$$

The output speed range of screw will be 6 rpm to 60 rpm as per Eq. (8). This range of speed from 6 to 60 rpm is considered to be sufficient for experiments and research work and hence accepted.

Other physical dimensions of a screw conveyor like screw shaft diameter, width of the trough, clearance between trough and screw, trough height from the center of the screw shaft, thickness of trough material and nominal thickness of screw flights have been determined, as per recommendation of IS:5563:1985 [6].

Once the screw diameter, screw shaft diameter and rotational speed of screw are selected, next step is to calculation for consumed power at screw shaft and selection of motor power and selection of gearbox size.

For calculating motor power, all resistances must be considered during transportation because the load is prevented from rotating with screw by weight of the material and by the friction of the material against the wall of the trough. IS:12,960:1990 [7] has specified the general considerations and formula to be used for determination of power requirement of a screw conveyor. Some of the important factors on which the motor power requirement of a horizontal spiral conveyor depends on following factors are mentioned as below:

- (i) Friction in between conveyed material with rotating screw and material to stationary U-trough during transportation.
- (ii) Resistance between transported material while it is being rolled or mixed due to screw rotation.
- (iii) Supplementary resistance of material entrapped in between screw and U-trough.
- (iv) Friction at the thrust bearings at both the ends.

Frictional resistance as mentioned above in (i), (ii) and (iii) may be expressed as in terms of progress resistance coefficient [6–9] of the material being transported, and also depends on different properties of the bulk material.

Thus, power requirement of a Screw Conveyor for conveying material depends on the following factors.

Length of the material being conveyed, the rate at which the material is being transported mass flow rate, i.e. capacity of the conveyor.

The progress resistance coefficient λ [6-9], type of screw and properties of the material. The driving power of a loaded screw conveyor may be estimated by the formula, as indicated in IS:12,960:1990 [7], as follows:

$$\begin{aligned} \text{Total power requirement}(P) &= \text{Power necessary for conveying the material}(PH) \\ &+ \text{No load power}(PN) \\ &+ \text{Power due to inclination}(Pst) \end{aligned} \tag{9}$$

Power necessary for conveying the material

$$P_H = QL'\lambda \frac{g}{3600} \text{ kW} \tag{10}$$

$$P_H = QL'\lambda/367 \text{ kW} \tag{11}$$

Thus, in Eq. 11, Q = mass flow rate in ton/hr, L' = length of material movement in conveyor in m., λ = progress resistance coefficient [6-9]. It is generally of the order of 2 to 4. For the design the highest value is considered as 6.

$$P_H = 18.18 \times 1.48 \times 6 \frac{1}{367} \text{ kW} \tag{12}$$

$$P_H = 0.44 \text{ kW} \tag{13}$$

$$\text{No-load Power } P_N = DL/20 \text{ kW} \tag{14}$$

In Eq. (14) D is the nominal diameter of screw in m, L is the Length of screw

$$P_N = 0.2 \times 2/20 \text{ kW} \tag{15}$$

$$P_N = 0.02 \text{ kW} \tag{16}$$

$$\text{Power for an inclined conveyor } Pst = (Q \times H)/367 \text{ kW} \tag{17}$$

However, for the horizontal conveyor, H = height between inlet and out let = 0. By using the above formula we get,

$$\text{Total Power } P = P_H + P_{NkW} \tag{18}$$

(as per Eq. (9)).

Now, from Eqs. (13), (16) and (18) can be written as

$$P = 0.44 + 0.02\text{kW} \quad (19)$$

$$P = 0.46\text{kW} \quad (20)$$

So, the minimum demand power at screw shaft required to drive a loaded screw conveyor conveying dry sand is 0.46 kW, based on which motor power is selected with following considerations.

Assuming a worm reduction gear box having efficiency of 75% and out put coupling having efficiency of 97%.

Therefore, actual power required to drive above specified system is equal to.

$$= \frac{0.46}{0.75 \times 0.97} \text{ kW} = 0.63\text{kW} \quad (21)$$

Considering, screw conveyor will be driven by a 3 phase, 4 pole, AC squirrel cage inductionmotor having de-rating factor 88%

$$\text{So, Demand power at motor shaft} = \frac{\text{Actual power required to drive the system}}{\text{Motor derating factor}} \quad (22)$$

$$\text{Theoretical demand power at motor shaft} = (0.63/0.88) \text{ kW} = 0.72\text{kW}. \quad (23)$$

Motor name plate power is generally selected considering safe margin(1.5 times) on consumed power as well as on demand power on motor shaft(1.25 times),whichever higher to the fact that conveyor will be used to convey other materials with much higher progress resistance coefficient [6–9] and with other operating parameters.

$$(1.5 \times \text{consumed power}) = (1.5 \times 0.46) = 0.69\text{kW} \quad (24)$$

$$(1.25 \times \text{demand power at motor shaft}) = (1.25 \times 0.72) = 0.90\text{kW} \quad (25)$$

A motor name plate power of of 2.2 kw, 4 pole 3 phase has been chosen for conveyor drive.

3 Drive Component Selection

A motor of 2.2 kw rating 4 pole and 3 phase has been chosen. The rated speed of a 2.2 kW 3 phase 4 pole motor is 1435 rpm (Refer manufacturer's catalog). Therefore, to achieve a target speed of 60 rpm, the reduction ratio of the gear box should be

$$1435/60 = 23.91 \quad (26)$$

From the worm reducer gear box catalog, the nearest standard reduction ratio of 25:1 is selected. Worm Reducer Size CTS 3½ inch, fan cooled, under driven, with RH handing, NAW make or equivalent. Thus the top designed speed of the screw comes to

$$1435/25 = 57.4\text{rpm} \quad (27)$$

Input Coupling: Size BC2A (Fenner make or equivalent) and pin bush flexible type.

Output Coupling: Size BC4 (Fenner make or equivalent) and pin bush flexible type.

Table 2 refers to the brief specification of Screw conveyor.

4 Screw Conveyor with VFD Complete and Experimental Set Up

The specified screw conveyor with provision for variable speed through variable frequency Drive(VFD) [12] along with instrument panel as shown in the Fig. 1. In order to have a variable speed of the screw conveyor, it is proposed to introduce a variable voltage variable frequency drive, commonly known as variable speed drive (VSD). As per technical specification of variable frequency drive Siemens make MM420 drive for 3 phase AC 200 V TO 240 V ± 10% (0.12 kW TO 5.5 kW) output to input frequency ratio is 650 Hz/63 Hz = 10.3 = 10 approximately [12].

Figure 1 Shows Typical Experimental Set up including Screw Conveyor along with VFD complete.

5 Conclusions

The designed screw conveyor is suitable for conveying varieties of materials like dry sand, wheat, stone chips, and able to run at variable speeds of wide range 6 rpm to 60 rpm, which is quite inline with basic requirements of the research work and experimentation in the field of material handling. However different design of screw

Table 2 Design outcome brief specification of screw conveyor

Screw diameter [1–11, 13, 14]	200 ± 1 mm
Screw types [1–11, 15]	Different design of screw with same pitch and diameter with easy replacement facility need to be considered for experimentation purpose (As for example Continuous, Ribbon or Cut flight type of screw)
Screw length [1-6, 8–11, 13, 14]	2000 mm
Screw pitch	160 mm
Screw fixing arrangement	Fanged at both ends [7–9]
Screw shaft/Material	48.3 × 3.5 mm pipe[6]/EN-24
Thickness of screw/Material	4 mm/M.S
Screw supporting bearing [8–10]	Spherical roller bearings on both ends
Trough shape [3–6, 8–11]	U
Trough width [6, 9]	220 mm
Trough height form centre of screw	Depending on experimental requirements Different trough cover ensuring different values of trough height may be used, However the maximum height of the trough cover [1–5, 8–11, 13, 14] as 180 mm considered
Feeding hopper	Trapezoidal section, shift able over the trough
Feeding arrangement	Manual
Effective length of screw (Hopper centre line to edge of discharge spout)	1480 mm, adjustable up to maximum of 1520 mm
Drive motor	220 V, 2.2 kW, 3 Phase, 4 Pole, Foot mounted
Gear box	Worm Reducer, 25:1 ratio, Size CTS 3 ½ inch, Fan cooled
Speed controller	Frequency control drive. Speed ratio = 10:1 with frequency/rpm indicator [12]
Structural details	Fabricated structure at drive and non-drive end connected with necessary stretchers [8–10]

with easy replacement facility in combination with different height of trough cover allows to carry out various research works, changing the parameters like screw speed, screw type, trough height, effective length of conveying with different conveyed material type are very much useful to perform various experiments in the field of material handling. So the attempt of present design work is successful and unique from the laboratory and research work point of view.

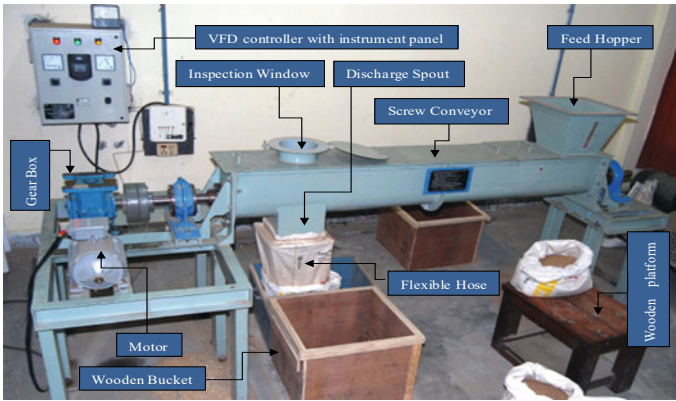


Fig. 1 Screw conveyor along with VFD complete, experimental set up

Acknowledgements The support and infrastructural facilities of the National Institute of Technical Teacher's Training and Research, Kolkata are duly and sincerely acknowledged.

The author expresses his sincere gratitude to Prof. Dr. Siddhartha Ray, former Director-in-Charge, NITTTTR-Kolkata for his guidance, support and continuous encouragement throughout the dissertation work. The author is also grateful to all faculty members, technical staff of Mechanical Engineering department, NITTTTR-Kolkata and B.M Engineering Company, Kolkata, India.

References

1. Nagel G (1968) Archimedean screw pump Handbook. Prepared for Ritz-Atro Pumpwerksbau GMBH Roding, Nu`rnberg, Germany
2. Fuchs A, Zangl H, Brasseur G (2007) Mass flow meter screw conveyor based on capacitive sensing. In: Proceedings of IEEE instrumentation and measurement technology conference (IMTC), Warsaw, Poland, pp 1–5
3. Fortner J (2000) Characteristics of bulk material in screw type conveyors. Engineering Meeting of Krupp, Forder technik session February
4. Roberts AW (2001) Design consideration and performance evaluation of screw conveyors, Centre for bulk solids and particulate technologies, The University of Newcastle, Australia
5. Yu Y, Arnold PC (1996) Investigation into power requirements for screw feeders, 1996, National Conference on Bulk Material Handling, Australia
6. I.S. 5563 (1985) Specification of screw conveyors for Industrial Use, BIS
7. I.S. 12960 (1990) Determination of power requirements for screw feeder general requirements, BIS
8. Spivakovsky A, Dyachkov V (1985) Conveying machines, vol 2, 1st edn. Mir Publishers, Moscow
9. Ray S (2008) Introduction to materials handling, 1st edn. New Age International(P) Limited Publishers, New Delhi
10. Alexandro MP (1981) Materials handling equipment, 1st edn. Mir Publishers, Moscow
11. Kurjak A (2005) The Vertical screw conveyor-powder properties and screw conveyor design. Department of Chemical Engineering, Lund Institute of Technology, Sweden
12. Simens Homepage <https://www.siemens.com/products/drive>

13. Zareiforush H, Komarizadeh MH, Alizadeh MR (2010) A review on screw conveyor performance evaluation during handling process, *J Sci Rev* 2(1):55–63
14. Mondal D, Ghosh N, Rudrapati R (2016) Study on filling factor of short screw conveyor with ribbon type screw at two different trough height(112mm&180mm) Inflood-feeding condition, *Int J Curr Eng Technol* E-ISSN 2277–4106, P-ISSN 2347–5161
15. Mondal D, Ghosh N (2018) Study on filling factor of short length screw conveyor with the flood-feeding condition, *Materials Today: Proceedings* 5(1):1286–1291

Case Study Related to Volumetric Capacity, Mass Flow Rate and Filling Factor Against a Constant Trough Height As 180 mm for a Screw Feeder with Continuous Screw



Debayan Mondal

Abstract A spiral conveyor or screw type conveyor consists of a rotating helical blade with suitable drive arrangement, a stationary U-trough, though cover, two end plates with end bearings. However, the opening on top cover can feed the material in to trough and bottom opening at the U trough allows to discharge the conveyed material. A small screw conveyor with horizontal configuration is known as screw feeder. The objective of present experimental work is to find out the volumetric capacity, mass flow rate while keeping a constant trough height (180 mm) and hence to study variation of filling factor with the variation of screw speed within a predetermined range with continuous type of screw. Hence to draw the conclusion about the inter-relation with the variation of screw speed and to draw the characteristic curves of volumetric capacity and loading efficiency verses different screw speeds under constant trough height with particular type of bulk material as dry coarse sand and Screw combination.

Keywords Screw conveyor · Bulk density · Loading efficiency

1 Introduction

Screw conveyor, as we know it today, is the descendant of the oldest form of conveyor in recorded history, utilizing the oldest mechanical device employed by mankind. Screw conveyor [1, 2] is an essential part of many conveying and storage systems dealing with powdered or granular materials. A spiral conveyor utilized for transportation, blending and mixing of two or more materials during conveying [2, 3]. The screw conveyor is suitable for mass flow rate [4–8] less than 1200 ton/h with wide varieties of material type and to convey relatively small distance of 40 m in horizontal configurations, while the limit is restricted up to 30 m for inclined [8–10] one. However screw type conveyor is not at all suitable for sticky, fragile materials and

D. Mondal (✉)
Technology Campus, University of Calcutta, Kolkata 700106, India
e-mail: debayan3@rediffmail.com

not recommended for conveying corrosive and toxic materials [8–10]. The performance characteristics [8–13] like filling factor (also known as loading efficiency) and mass flow rate associated with volumetric capacity during transportation is one of the important parameters where researches is to be concentrated on in order to have a clear understanding on this specified area. The construction of spiral type conveyor is much simple with only rotating part, the helical blade itself and also convenient for intermittent discharge [13–15]. The maintenance of the equipment is very easy, compare to other type of conveyors. The Screw type conveyor consist of a continues or interrupted helical screw fastened to a solid or hollow circular shaft, which is rotated within U- shaped stationary trough or tube to push fine grained bulk material through the pipe or trough, hence transport the material along the conveying length. The brief specification of screw conveyor is presented in Table 1.

Table 1 Brief specification of screw conveyor

Screw Diameter	200 ± 1 mm
Screw Types	Continuous
Screw Length	2000 mm
Screw Pitch	160 mm
Screw Fixing Arrangement	Flanged at both ends
Screw shaft	48.3 × 3.5 mm pipe, M. S
Thickness of Screw/Material	4 mm/M. S
Screw Supporting Bearing	Spherical roller bearings on both ends
Trough Shape	U
Trough Width	220 mm
Trough Height form Center of Screw	case study has experimented 180 mm trough cover height
Feeding Hopper	Trapezoidal section, shift-able over the trough
Feeding Arrangement	Manual ensuring flood feeding condition
Maximum effective length of Screw (Hopper center line to edge of discharge spout)	1480 mm and adjustable up to maximum of 1520 mm
Drive Motor	220 V, 2.2 kW, 3 Phase, 4 Pole
Gear Box	Worm Reducer, 25:1 ratio, Size CTS 3½ inch, FAN Cooled, under driven, Right Hand handing make
Speed controller	Frequency control drive. Speed ratio = 10:1 with frequency/ rpm indicator
Structural Details	Fabricated structure at drive and non-drive end connected with necessary stretchers

2 Objective of Experiment

The objective is to study the effect of constant trough height from center of the screw shaft to the top of the U-Trough which is kept as 180 mm and hence the study of volumetric capacity, mass flow rate and associated loading efficiency for a continuous type of screw with variation screw speed. Further objective is to draw the conclusion above volumetric capacity, mass flow rate and filling factor and to draw the characteristics curves with respect to variation predetermined of screw speeds. The mass flow rate of a transported material in a screw conveyor depends on loading efficiency as given by the following formula.

$$Q = (\pi \times D^2 \times S \times 60 \times n \times \psi \times \gamma \times C)/4 \text{ ton/h} \quad (1)$$

where is mass flow rate in ton/h.

ψ is Loading efficiency or filling factor (also known as capacity factor).

D is the nominal Screw diameter in m., value as 0.2 m.

S Represents Screw pitch in m., value as 0.16 m.

γ is Tapped density of transported material in ton/m^3 , value as 1.572 ton/m^3 .

C Represents inclination factor, for horizontal screw conveyor its value is “one”.

2.1 Mass Flow Rate or Capacity of a Screw Conveyor

Capacity or mass flow rate of a conveyor defined as mass of the conveyed material with a constant speed (rpm) during one-hour continuous operation at ambient temperature and expressed in ton/h, which may be calculated from Eq. (1). In case of continuous operation, the equipment must have some cooling system to dissipate heat, generated during operation, which is ensured through the worm reducer itself with a provision for Fan cooling.

3 Experimental Set up and Procedure

The specified screw conveyor with provision for variable speed through variable frequency Drive(VFD) [12] along with instrument panel as shown in the Fig. 1.

The screw conveyor is having rear end drive arrangement while the front end or non-drive end is connected with a Trapezoidal shaped feed hopper and provision for manual feeding arrangement only. A slit, covered by a transparent plastic sheet is to check the material fill level at feed hopper during manual feed or at the time of the experiment. The outlet spout is connected with a flexible hose to direct and collect the discharged material into wooden bucket. Two numbers of wooden buckets are placed side by side under the outlet spout of the conveyor to collect the discharged material

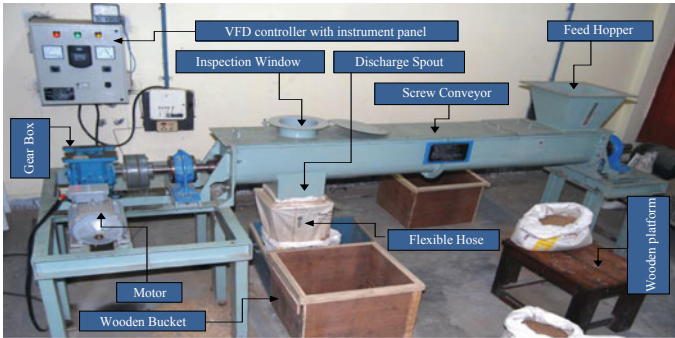


Fig. 1 Experimental set up

and further taken for weighing purpose with suitable weighing machine of 50 kg capacity and 1 gm minimum resolution. A dedicated stop watch is used measuring experimental run time. Conveyor is started with loaded condition and seeded up to a specific predetermined screw speed by controlling the VFD controller [12] push button switch and allowed to run the conveyor at that speed. Once the conveyor speed gets stabilized at that instant the output of the conveyor is manually switched over to the empty bucket and commencement of the measurement of time is started through stop watch. Researcher has set the experimental time of 30 s judiciously for each run. After 30 s the outlet spout is shifted to another wooden box. Hence the material conveyed during experimental runs of 30 s is gets collected and taken further for weighing So that the mass flow rate and hence volumetric capacity can be calculated from Eq. (1).

4 Experimental Result

Experiment was conducted with dry coarse sand as transported material with continuous type of screw and using 180 mm high trough cover and the recorded that is depicted in Table 2.

5 Characteristic Curves

Two characteristics curves are plotted based on the experimental data sheet with the variation of screw speed as follows.

Table 2 Experimental data sheet

Sl. no	Frequency (f) in Hz	Screw speed (n) in (rpm)	Operating time (t) in second	Amount of material transported (kg)	Average amount of material transported (M) (kg)	Mass flow rate (Q) in ton/h	Volumetric capacity(V) in m ³ /min	Loading efficiency (Ψ)
1	10	12	30	43.765	43.80	5.26	0.06	0.92
2				43.835				
3				42.950				
4				44.650				
5	12.5	15		54.385	54.2483	6.51	0.07	0.92
6				54.100				
7				54.260				
8				54.250				
9	17.5	21		75.815	76.095	9.13	0.1	0.92
10				75.830				
11				76.660				
12				76.075				
13	21.7	26		95.250	95.5625	11.47	0.12	0.93
14				95.875				
15				95.500				
16				95.625				

5.1 Characteristic Curve-1

A characteristic curves is being plotted based on the tabulated values showing variation of volumetric capacity (V) with the variation of screw speed(n) in r.p.m is shown in Fig. 2.

5.2 Characteristic Curve-2

In Fig. 3. characteristic curve is plotted for variation of filling factor with respect to variation of speed for 180 mm trough cover height with continuous type of screw and conveyed material as dry coarse sand.

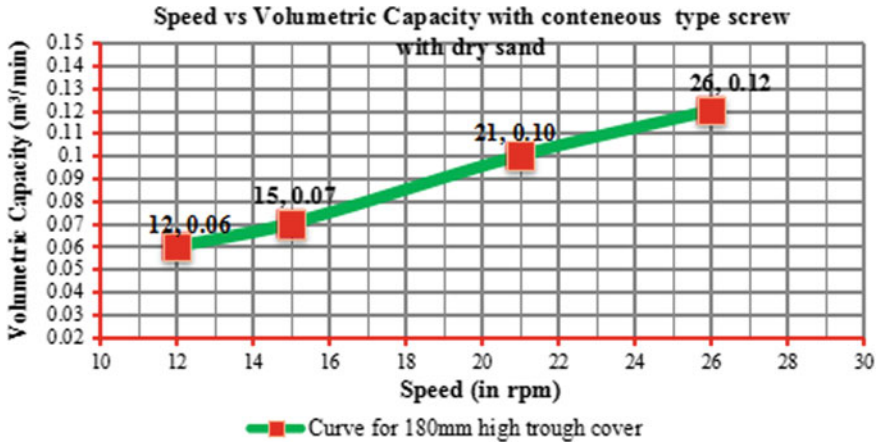


Fig. 2 A characteristic curves showing volumetric capacity (V) with the variation of screw speed(n) in r.p.m

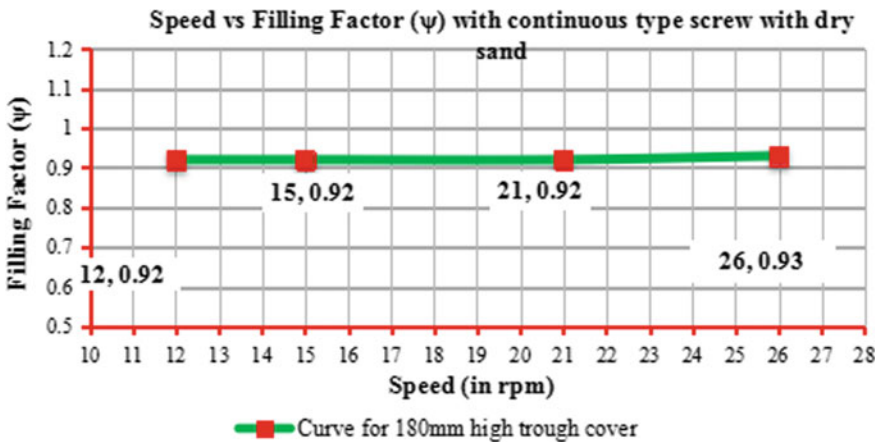


Fig. 3 Characteristic curve showing variation of filling factor with respect to variation of speed for 180 mm trough cover

6 Result Analysis and Conclusions

Result may be analyzed and conclusions can be made as follows from the experimental data.

1. From the series of experimental results, using continuous type of screw with a constant height of trough cover (180 mm) at varying speed as 12 rpm, 15 rpm, 21 rpm, 26 rpm respectively and fixed effective conveying distance (1480 mm), the volumetric capacity found to be as $0.06\text{m}^3/\text{min}$, $0.07\text{m}^3/\text{min}$, $0.1\text{m}^3/\text{min}$,

0.12m³/min respectively, which is in gradual increasing trends ensuring higher volumetric capacity at high speed of screw.

2. The mass flow rate at screw speed 12 rpm, 15 rpm, 21 rpm, 26 rpm are found to be 5.26 ton/h, 6.51 ton/h, 9.13 ton/h, 11.47 ton/h respectively, which also attributed to increasing trends of through put capacity with respect to the increase in screw speeds, which is self explanatory from the Eq. 1., considering constant value filling factor.
3. As the experiment was conducted, ensuring continuous flow of the material through feed hopper, the condition of feeding may be assumed to be as flood feeding one.
4. However for a particular type of screw, maintaining constant trough height the filling factor is almost constant as 0.92. There will be slightly increase of filling factor value (0.92 to 0.93) after screw speed of 21 rpm which can be explained further by the vortex property of conveyed material after certain speed range [3, 4].
5. The value of loading efficiency calculated from experimental result is of the order of 92% and 93%. The higher value of loading efficiency is due to associated loading condition (flood-feeding one) and the conveyor length is very short with out any hanger bearing. Result is inline with the recommended value of capacity factor of short screw conveyor without having any obstruction (about 2.0 times more than that of long one.) (Reference: Materials Handling Equipment by Alexandrov, M.P [10]).

7 Probable Source of Errors in the Experiment

1. There may be small time lag in between switching off of the screw conveyor and shifting of the outlet hose to the another empty bucket during the small interval there may be continuous discharge of conveyed material due to inertia of the rotating screw hence leads to error in mass flow rate and volumetric capacity.
2. The bulk density of conveyed material was separately found out experimentally prior to actual experimentation which was find out in a static condition. There may be chances of variation of bulk density of conveyed material in dynamic condition during experimental runs. As the calculation of volumetric capacity is based on constant values, may leads to some error.
3. Calculation of the volumetric capacity and mass flow rate is based on assuming circular cross section of the trough, however in practical the trough is of a U shaped.
4. It is assumed that the filling factor is constant through out the effective length of the screw as it is a short in length (approximately 2 m). In practical it may vary from feeding point to discharge point along the length of the conveyor and these variation was not taken into consideration.

8 Future Scope

A similar experiment may be conducted with different bulk material of different angle of repose along with angle of surcharge, hence the observation may be taken. Similar study may be performed on free flowing material like wheat and the observation may be studied. The experiment may be conducted ensuring restricted flow of the material through the introduction of rack and pinion and rod gate and the effect may be studied further. With the provision for mechanized feeding arrangement in place of manual feeding, the volumetric capacity, mass flow rate and filling factor may be observed further, if there is appreciable increase of above mentioned quantity or not with same range of speed. Same experiment may be conducted for comparatively long screw conveyor and the value of filling factor need to be study. The effect of intermediate bearing hanger on filling factor need to be investigated.

Acknowledgements The support and infrastructural facilities of the National Institute of Technical Teacher's Training and Research, Kolkata are duly and sincerely acknowledged. The author expresses his sincere gratitude to Prof. Dr. Siddhartha Ray, former Director-in-Charge, NITTTR-Kolkata for his guidance, support and continuous encouragement throughout the dissertation work. The author is also grateful to all faculty members, technical staff of Mechanical engineering department, NITTTR- Kolkata and B.M Engineering Company.

References

1. Nagel G (1968) Archimedean screw pump Handbook. Prepared for Ritz-Atro Pumpwerksbau GMBH Roding, Nu`rnberg, Germany
2. Fuchs A, Zangl H, Brasseur G (2007) Mass flow meter screw conveyor based on capacitive sensing. In: Proceedings of IEEE instrumentation and measurement technology conference (IMTC), Warsaw, Poland, May 1–3, 2007, pp 1–5
3. Fottner J (2000) Characteristics of bulk material in screw type conveyors. Engineering Meeting of Krupp, Forder technik session February
4. Roberts AW (2001) Design consideration and performance evaluation of screw conveyors. Centre for bulk solids and particulate technologies. The University of Newcastle, Australia (2001)
5. Yu Y, Arnold PC (1996) Investigation into power requirements for screw feeders, 1996. National conference on bulk material handling, AUSTRALIE (1996)
6. **IS:5563:1985** – Specification of screw conveyors for Industrial Use, BIS
7. **IS:12960:1990**–Determination of Power Requirements for Screw Feeder General Requirements, BIS
8. Spivakovsky A, Dyachkov V (1985) Conveying Machines, Volume-II, 1st edn. Mir publishers, Moscow
9. Ray S (2008) Introduction to materials handling, 1st edn. New Age International(P) Limited Publishers, New Delhi
10. Alexandrov MP (1981) Materials handling equipment, first edition. Mir Publishers, Moscow (1981)
11. Kurjak A (2005) The Vertical Screw conveyor-powder properties and screw conveyor design. Department of Chemical Engineering, Lund Institute of Technology, Sweden
12. Simens Homepage. <https://www.siemens.com/products/drive>

13. Zareiforoush H, Mohammad Hassan K, Mohammad Reza A (2010) A review on screw conveyor performance evaluation during handling process. *J Sci Rev* 2(1):55–63
14. Mondal D, Ghosh N, Rudrapati R (2016) Study on filling factor of short screw conveyor with ribbon type screw at two different trough height(112 mm & 180 mm) In flood-feeding condition. *International Journal of Current Engineering and Technology*, E-ISSN2277–4106, P-ISSN2347–5161(2016)
15. Mondal D, Ghosh N (2018) Study on filling factor of short length screw conveyor with flood-feeding condition. *Mater Today: Procee* 5(2018)1286–1291(2018)

CFD Investigation on Optimization of Pipe Pattern in Radiant Cooling System



Prashant R. Nawale, Sudesh B. Powar, and Pramod P. Kothmir

Abstract The radiative heat transfer process has so far been proven effective and efficient in the Heating, Ventilation and Air Conditioning industry and therefore it has been used for air conditioning applications. Radiant floor heating systems could be even effective over the conventional air conditioning systems as the water in motion that is used in the radiative systems have more energy carrying capacity compared to air in motion used in conventional air conditioning systems. In the present study, the computational fluid dynamics analysis of a radiant cooled room is carried out by varying the design of pipe patterns and their simulations for cooling the typical room has been carried out. Eleven such pipe patterns were analyzed for both steady and unsteady conditions. A three dimensional geometrical model of specified dimension was used for the analysis. Ordinary heat loads from the light bulb, window, floor, human and laptop are defined in the model. Different loads such as energy, buoyancy, and radiation are also included in the simulation and thermal boundary conditions are applied on ceiling and walls. Also, the effect on the analysis when the room is unoccupied and occupied was studied by considering the factors such as air velocity, inlet water temperature as constant. This study validated the difference between the inlet and outlet of water and air temperature respectively. The temperature distribution pattern in a room due to the mixed flow design pipe pattern was found to be most effective for cooling and better comfort conditions.

Keywords CFD analysis · Pipe patterns · Design of pipe pattern · Radiant cooling · Heat loads · Boundary conditions

1 Introduction

The radiative heat transfer principle is emerging technology used in the Air Conditioning system and has been proven effective. For heating and cooling application, the Hydronic systems i.e. water-based systems are practically in use. In this case, the

P. R. Nawale (✉) · S. B. Powar · P. P. Kothmir
School of Mechanical and Civil Engineering, MIT Academy of Engineering, Alandi(D), Pune
412105, India

pipes carrying water may be embedded in the building structures like floor ceilings or walls. Radiant panels are also in use which have metal pipes integrated into it. But the radiative heat transfer process may also have few limitations like a condensation of water may take place around the radiating panels.

An experiment on the building of a software firm INFOSYS Ltd has been successfully carried out in Hyderabad by Guru Prakash Sastry [1]. The building was geometrically symmetrical and hence in the one half of a building conventional air conditioning system was used and in the other half portion Radiative air conditioning system was used so that a direct comparative analysis could be done. It was found that the radiative air conditioning system consumes 33% less energy as compared to the conventional air conditioning system and other factors such as Human comfort, cost-effectiveness were also found to be more effective [2].

2 Literature Survey

The computer simulation was done by Angelo Zarella et al. [3] where the dehumidification system was used in integration with the radiative cooling system for three Italian climate zones. The conclusion was made that the partial or latent heat load is transferred to the dehumidifier and the remaining to the radiative cooling system. But in terms of the cost and space, the system may be inconvenient for practical use.

Xiazhou et al. [4] developed a simplified model by using a conduction shape factor with which surface temperature and heat transfer of radiant floor heating or cooling systems could be calculated. The graphs were plotted such as the pipe space versus thermal resistance of radiant floor and the thickness of screed versus thermal resistance of the radiant floor. It was observed that the screed thickness has no impact on the thermal resistance whereas the pipe spacing and average water temperature had a great effect on the thermal resistance. Prateek Srivastava et al. [5] analyzed the system where the radiative cooling system was used in integration with evaporative cooling systems for different Indian climate zones. Two main systems first chiller operated Radiative cooling system and second cooling tower operated radiative cooling systems were analyzed for the study. The cooling tower operating system gave 7% of annual savings in hot and dry climate followed by 11% and 20% in composite and temperate climate respectively.

Laia Haurie et al. [6] studied the fire behavior of the different fraction of the Phase change material with mortar for the radiant floor systems. With the increase in the fraction of the PCM the thermal diffusivity reduces still the PCM could be used in a radiant floor system with some protection. Jovan Pantelic et al. [7] performed an experiment in which he studied the effect of the direct solar radiation on the cooling capacity. It was observed that when the solar radiations come in direct contact with the floor the cooling capacity increases from 32 to 110 W/m². Also, the use of high-speed ceiling fans increased the cooling capacity by 12%.

Bladamir Romas Alvarado et al. [8] did a study of liquid-cooled heat sinks of microchannels used in solar cells or other electronic fuel cells. Eight different flow

channels were analyzed using ANSYS software and heat flow and distribution pattern was studied. The best effective pattern was selected as a reference for the pipe patterns used in our analysis.

In this study the main focus is to cool down the temperature of conditioned space up to or below than 24°C so that humans feel comfort inside the conditioned space. Study plans different pipe patterns being used below the floor surface so that the temperature decreases at the occupied floor. It is based on the pipe pattern as none of the researchers has not been studied the effect of pipe pattern inside the room by using computational fluid dynamics tools. The previous research says that they had done simulations by considering any of the patterns instead of fifteen Fig. 3. patterns used inside the conditioned space. This paper focused on the temperature distribution using CFD with single phase fluid, the above review shows that no such analysis for different patterns was carried out [9]. The present study focused on floor temperature and inside the thermal condition of the air and water. With the help of the CFD simulation tool, we have investigated the optimum floor pattern for temperature distribution which should be maintained in a room to get sufficient residence time to cool down the floor temperature. Also, we correlated one of the patterns concerning industrial floor surface temperature. Though, caution has to be taken on the air inlet conditions and water inlet condition.

3 Methodology

A 3D geometric CATIA model having dimensions 4 × 3 × 3 m(l × b × h) was used for the analysis. All the dimensions are in millimeters as shown in Fig. 1a.

The schematic diagram shows us an unoccupied room. This figure is essential to view the location and dimensions of the door, window, bulb, air and water inlets

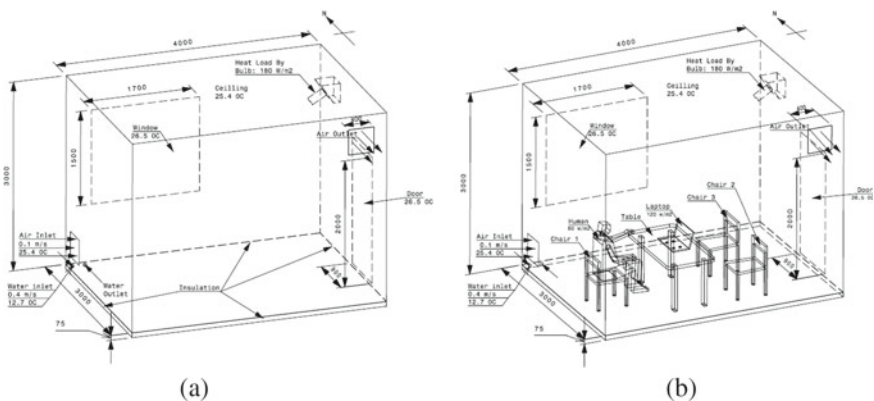


Fig. 1 Schematic Diagram of room when the room is **a** unoccupied, and **b** occupied with human, electric component, wooden chairs and table

outlets respectively. Below the floor surface, a 75 mm thick is provided to buried polybutylene pipes while construction and the insulation is given in beneath. Air is imposed into the room through a square duct of area 0.16 mm² and air is extracted with the same size of duct. Figure 1b, shows us the pattern in which the room is occupied by the Table, Human, Chairs, and laptop.

The analysis was done in two types one was of the room with no occupants and the other was with occupants. Eleven such pipe patterns were analyzed for both the above cases using the ANSYS-Fluent software. In meshing the pipe joints have more finely meshed for better results. For flexible results output, the input air and water temperatures and other ambient temperatures were considered almost constant. To get the optimum results, the inlet and outlet positions of water and air are needed to study. Refer to Tables 6 and 7 for the temperature of air and water outlets. For both occupied and unoccupied rooms, different pattern design Fig. 1. is used to get temperature distribution.

3.1 Nomenclature for Pipe Patterns

As per the shape of the pipe pattern we got different names for the eleven cases Fig. 2a. Case 1 & 8 Serpentine Pipe Pattern Case 2 Counter-flow Pipe Pattern Case 3 & 4 Double Serpentine Pipe Pattern Case 5 Mixed flow Pipe Pattern Case 6 & 7 Distributor flow Pipe Pattern Case 9 & 10 Double-wall Serpentine Pipe Pattern Case 11 Triple wall Serpentine Pipe Pattern (Fig. 3).

The distance between the two pipes in each pipe pattern is 200 mm in all the above cases and also the clearance from side walls are the same.

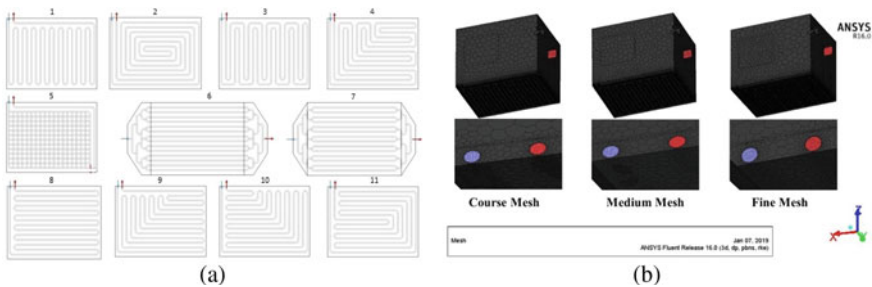


Fig. 2 a Different designs of pipe pattern for cooling water circulation through radiant pipe, b Polyhedral meshing of geometry

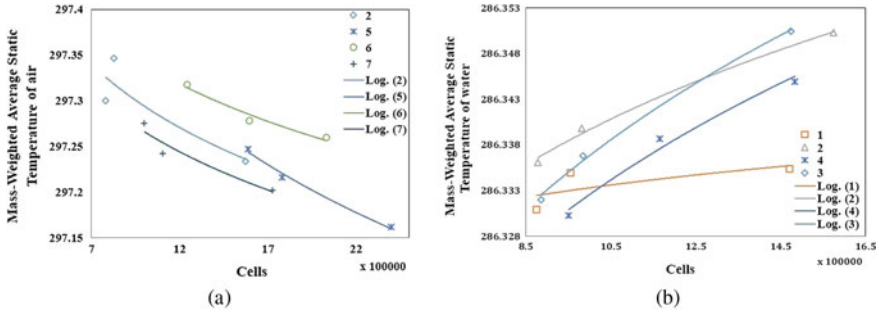


Fig. 3 Mass weighted average static temperature with cells count of pattern

3.2 Meshing of Geometry

The mesh contains polyhedral meshing elements for simulations. For 3D Fig. 1 modeling here we used CATIA V5. From Fig. 2b we can observe that water enters at the inlet this water split through holes of the distributor. The fine mesh was generated on a model with near about 4,754,286 nodes and 878,123 elements. It is performed by ANSYS workbench to get the course, medium, and fine meshing as shown in Fig. 4. Fluent is used as a solver. Tetrahedron mesh is used for this geometry. For occupied and unoccupied rooms also have a similar meshing process.

4 CFD Model

Following CFD models were analyzed using the Energy equation, viscous model and radiation model. When energy equations are activated then the temperature variations in the finite volume method are viewed. For the viscous model, two equations of the K-Epsilon model including near-wall treatment with standard wall functions for turbulence were selected [1].

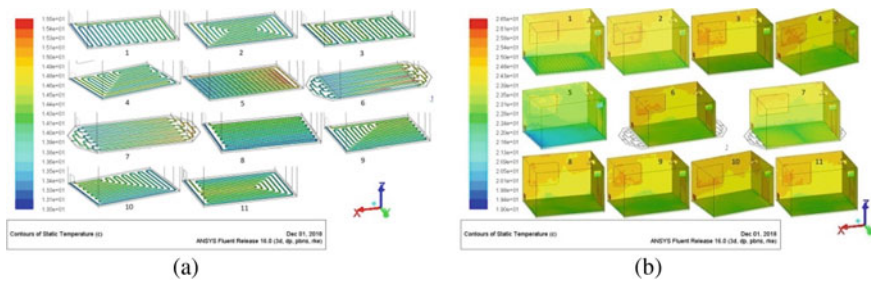


Fig. 4 Contours of temperature distribution a through pipe and b at the floor and walls of the room

The residual plot for every simulation approaches to zero as several iterations increases, therefore, the flow converges. Every simulation was carried out until the steady-state was achieved. In the residual plot after convergence, the graph of energy equations decreases below the 0.0001.

4.1 Analysis of 3D-Model

The analysis of the model was done by flow and turbulence equations. Flow converges at the same mass flow rate at inlet and outlet with the help of the continuity equation. Air inlet and outlet temperature conditions have also been considered. Temperature Distribution on the human body is shown in contours. Water temperature contours were applied for temperature distribution. The residual plot was done for the momentum equation, energy equation, and flow equation.

Planes were located at different heights z-axis for temperature gradient planes. Planes are at 0.3, 0.6, 0.9, 1.2, 1.5, 1.8 m from floor surface.

4.2 Governing Equations and Boundary Conditions

The energy conservation equation for solid regions [6], accounting for volumetric heat release can be written as:

$$K_s \left(\frac{\partial^2 T}{\partial x^2} + \frac{\partial^2 T}{\partial y^2} + \frac{\partial^2 T}{\partial z^2} \right) = 0 \quad (1)$$

The energy conservation equation for a fluid domain [5], accounting for volumetric heat release, can be written as:

$$u \frac{\partial(\rho_f C_f T_f)}{\partial x} + v \frac{\partial(\rho_f C_f T_f)}{\partial y} + w \frac{\partial(\rho_f C_f T_f)}{\partial z} = k_f \frac{\partial^2 T_f}{\partial x^2} + k_f \frac{\partial^2 T_f}{\partial y^2} + k_f \frac{\partial^2 T_f}{\partial z^2} \quad (2)$$

The fluid continuity equation [8], accounting for flow, can be written as:

$$\frac{\partial(\rho_f u)}{\partial x} + \frac{\partial(\rho_f v)}{\partial y} + \frac{\partial(\rho_f w)}{\partial z} = 0 \quad (3)$$

$$\frac{\partial(\rho_f u_i)}{\partial x_i} = 0 \quad (4)$$

The momentum equations [4] in x, y and z direction, accounting for momentum, can be written as:

$$u \frac{\partial(\rho_f u)}{\partial x} + v \frac{\partial(\rho_f u)}{\partial y} + w \frac{\partial(\rho_f u)}{\partial z} = \frac{\partial(\mu_f \frac{du}{dx})}{\partial x} + \frac{\partial(\mu_f \frac{du}{dy})}{\partial y} + \frac{\partial(\mu_f \frac{du}{dz})}{\partial z} - \frac{\partial p}{\partial x} \quad (5)$$

$$u \frac{\partial(\rho_f v)}{\partial x} + v \frac{\partial(\rho_f v)}{\partial y} + w \frac{\partial(\rho_f v)}{\partial z} = \frac{\partial(\mu_f \frac{dv}{dx})}{\partial x} + \frac{\partial(\mu_f \frac{dv}{dy})}{\partial y} + \frac{\partial(\mu_f \frac{dv}{dz})}{\partial z} - \frac{\partial p}{\partial y} \quad (6)$$

$$u \frac{\partial(\rho_f w)}{\partial x} + v \frac{\partial(\rho_f w)}{\partial y} + w \frac{\partial(\rho_f w)}{\partial z} = \frac{\partial(\mu_f \frac{dw}{dx})}{\partial x} + \frac{\partial(\mu_f \frac{dw}{dy})}{\partial y} + \frac{\partial(\mu_f \frac{dw}{dz})}{\partial z} - \frac{\partial p}{\partial z} \quad (7)$$

$$\frac{\partial(\rho_f u_i u_j)}{\partial x_j} = \frac{\partial}{\partial x_j} (-\rho u'_i u'_j) + \frac{\partial}{\partial x_j} \left[\mu \left(\frac{\partial u_i}{\partial x_j} + \frac{\partial u_j}{\partial x_i} - \frac{2}{3} \delta_{ij} \frac{\partial \mu_k}{\partial x_k} \right) \right] - \frac{\partial p'}{\partial x_i} \quad (8)$$

There are three zones: air, concrete, and water out of which concrete has a solid zone and the rest of the zones are fluid zones. For these fluid zones, we have considered the outlet as a pressure outlet and inlet as a velocity inlet. As per the referred research paper [5] the velocity between 0.3 to 0.4 m per second gives the better temperature distribution by water to the floor surface. The floor surface and water pipe surface are coupled to the solid zone and fluid zones. Kinematic Viscosity of air and water are $1.7894e^{-05}$ and 0.001003 kg/ms respectively.

4.3 Material Properties

From Table 1, these are the properties of the materials consisting of the room. After a few research surveys, the most appropriate insulation was selected based on its

Table 1 Material used and their properties

Materials	Density (kg/m ³)	Specific heat (J/kgK)	Thermal conductivity (W/mK)
Air	1.225	1006.43	0.0242
Concrete	2400	800	0.6
Glass	2531	840	0.8
Human	985	3600	1.06
Insulation	48	790	0.01
Polybutylene	940	1421	0.2741
Water	998.2	4182	0.6
Wood	700	2310	0.173

Table 2 Inlet boundary conditions of fluid zones

Zone boundary	Inlet velocity (m/s)	Inlet temperature (°)	Thermal emissivity
Air	0.1	25.4	0.9
Water	0.4	12.7	0.98

Table 3 Heat fluxes given to boundary surfaces

Heating surfaces	Boundary material	Heat flux (°)	Thermal emissivity
Bulb	Glass	180	0.9
Human	Skin properties	40	0.97
Laptop	Glass	120	0.9

density specific heat and thermal conductivity. The unit of properties is in the S.I system. Thermal emissivity for the floor surface is 0.9 and the material used is concrete. The water pipe used in the model is considered as polybutylene material and its thermal emissivity is 0.96.

4.4 Boundary Conditions

The Table 2 shows us the boundaries i.e. the contents of the room. For the boundary conditions of the heat loads (Human, Bulb, and Laptop), heat flux and thermal emissivity were considered (Tables 3, 4).

For the other objects which aren't supposed to impose a considerable heat load, for them, the average surface temperature and the thermal emissivity are described. The normal Surface area of a human being is 1.8 m², in a given model the surface area is 2 m² hence the heat flux on the human surface is up to 80 W.

Table 4 Temperatures in degree celsius given to boundary surfaces

Boundary	Material	Temperature (°)	Emissivity
Chairs (Three)	Wood	23	0.78
Ceiling	Concrete	25.4	0.92
Door	Wood	26.5	0.8
Insulation	Insulation	23	0.88
Table	Wood	23	0.78
Wall	Concrete	24.2	0.9
Window	Glass	26.5	0.85

5 Grid Independency Test

In grid independency test the mass flow rate of air and water inlet due to area varies as the number of cells increases. A smooth temperature contour plot is achieved as the cells increase but due to system specifications, we cannot increase the cells beyond the specified limit. The mass-weighted average static temperatures within the air zone and water zone versus the number of cells were plotted.

The mass-weighted average static temperature inside the water zone increases as the number of cells increases whereas the mass-weighted average static temperature inside the air zone decreases as the number of cells increases. The cross-section of inlet and outlet of water and air changes as grid size increases hence the mass flow rate changes. The cross-section of the inlet and outlet of the water pipe tends to become circular but the grid size can not increase much due to computational restrictions.

6 CFD Analysis

Figure 4, indicates the temperature distribution inside the pipes for different patterns. With the help of the color-map situated on the left side of the figure, the temperature distribution can be well understood regarding the colors. Twenty levels are used in the color map. The low-temperature field can be determined by the Blue color indication similarly for the high-temperature fields red color serves as an indication. From Fig. 6, it is seen that as the temperature of the water increases from inlet to outlet due to the heat absorbed, the color tends to change from Blue to Red.

As seen in Fig. 4b, the color pattern here helps us to understand the heat pattern inside the room for different cases. It can be seen that the floor temperature is cooler than the walls and also a quiet redness near the door and the window indicates the temperature is comparatively high. The temperature distribution on the surface of humans is shown above. The second, fifth and ninth case were found to be comfortable when the human is occupied.

As it is visible in Fig. 5, the region near the legs of the human is blue as they are situated close to the floor. This indicates that the heat removal takes place from bottom to top of the human body.

Area-Weighted Average Static Temperature at floor surface is almost 294.33 degrees Celsius this increases from floor to ceiling as shown in Table 5. Figure 6a, is a plot between temperature and length for eight patterns. The length of the pipes in all the eight cases is almost the same. This graph helps us to understand the behavior of the heat being absorbed along the length of the pipe. From Fig. 6a, it is observed that the absolute temperature at the axis is increased across the length of the pipe. The small spikes in the graph indicate the temperature at a turn in the pipe. At this turn-point due to the turbulence more heat is removed. From this, it is concluded that if we increase the number of turns more heat could be removed.

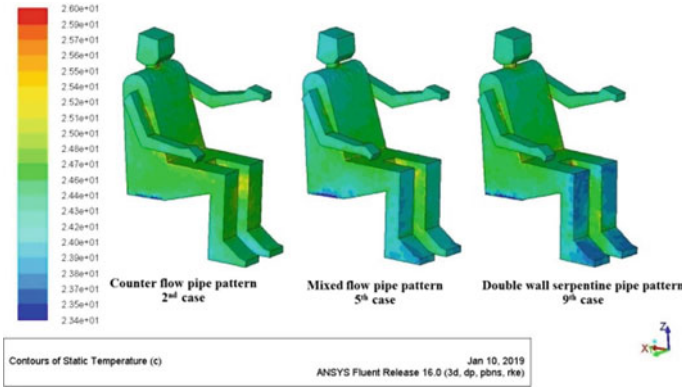


Fig. 5 Contours of temperature distribution on Human Body

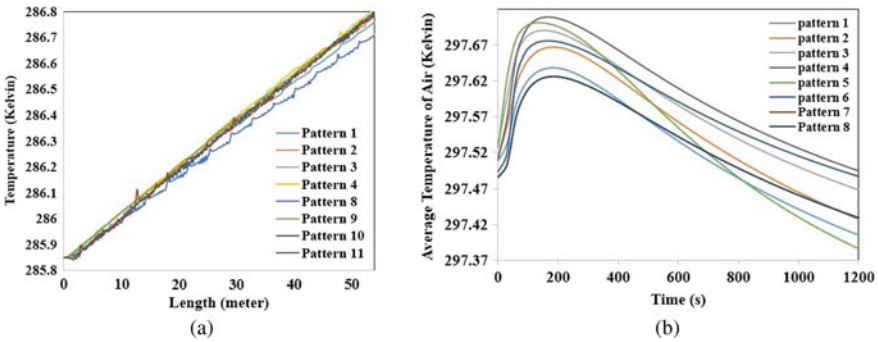


Fig. 6 Temperature at center of pipe with length of pipe and temperature of air with time

Table 5 Average temperature of the plane at different height from the floor surface

Z from Floor surface	30	60	90	120	150	180
T_{avg} (°C)	296.96	297.04	297.11	297.17	297.23	297.26

7 Results and Discussions

For the steady-state, after the convergence, the mass flow rate at inlet and outlet of air and water was achieved almost the same due to the same surface area of air and water, inlets and outlets. The mass flow rate of air is 0.01951 kg/s and the mass flow rate of water is 0.803 kg/s.

An increasing slope in the graph of Fig. 6b between 0 to 100 s indicates that the temperature increases for the first 100 s due to heating surfaces inside the room and later on the temperature tends to decrease slowly as there is no heat generation. As compared to the other patterns it is seen from the graph that the average temperature

of the air is lower than means of this pattern has been more effective in case of the heat removal with the help of water circulation. The graph of Fig. 7a, not only shows us the heat being removed with time but also serves as an analysis of the model. The unsteady state was analyzed for eight patterns following results were obtained. As concluded from Fig. 6, the avg temp of water is more during the first 100 s similar results were obtained for the air as well. A steep rise is seen in the graph at the start and later on again the slope. This means the avg temp of air is initially high and decreases as time increases. In this plot too, it is seen that the plot-line for the fifth case lies at the bottom-most position indicating that the average temperature is the lowest compared to the other cases. As the pipes are situated between the concrete the plot between the average temperatures of concrete vs time helps us to validate the above-obtained results. It would be contradictory to the previously plotted results if in this Fig. 6b plot the fifth case was not found efficient. Fortunately, Fig. 7b also shows the same results that the average temperature of the floor in the fifth pattern is the least pattern.

The average temperature of the concrete tends to decrease with the time-lapse. The average temperature seems to be reduced until a lapse of 1200 s (twenty minutes) whereas in the case of the air and water it reduces up to the first hundred seconds. Even for the concrete, the least average temperature was to be noted for the fifth case. The graph shown in Fig. 7b is the plot between the average temperatures of floor vs time. It is a natural behavior that the average temp of the floor reduces as time elapses. This graph is plotted up to 1200 s. The mass flow rate and velocity of water and air are almost considered to be constant for all the cases. The heat removal takes place mainly due to water. The negative sign in the table indicates that the heat is being added by the air. The maximum amount of heat removal takes place in the fifth case. The readings for the unsteady state were taken for two-time intervals of five and ten minutes. The unsteady state was analyzed for five patterns following result were obtained.

From Table 6, we observe that again the maximum amount of heat is being removed from the fifth case. Till the first interval maximum heat is removed and as the time increases the heat removal rate decreases because later on the heat is

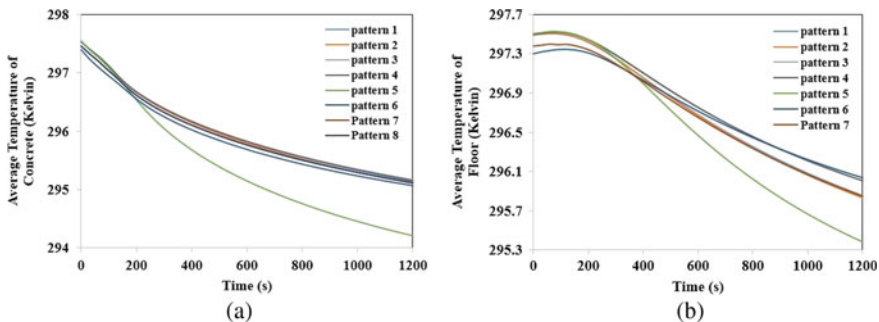


Fig. 7 Area weighted average temperature of a concrete and b floor with time of pattern

not generated by any source into the conditioned space. Following Table 7 shows the results for the steady-state when the human and other electronic component is inside the room. From the above table, it is observed that the maximum amount of heat is being removed in the fifth case. As air already has a temperature of 25.4 °C not much appreciable amount of heat is added to the room. The heat removal for the eighth case is from South to North direction. For the second case, the heat is being extracted from outwards towards the center. The third and fourth case comes under double serpentine pattern; in the third case the heat is being removed similar to the first case but here there is more equal temperature distribution observed. In the fourth case due to the arrangement of pipes, the cold and hot water pipes come in contact and a better heat transfer is achieved between them so the temperature here is equally distributed but not centralized as in the counter flow pattern. In the distributor pattern for the sixth case, the water is distributed such that the water flows parallel below the floor, but due to less surface area of the pipe below the floor, the heat removed is less. When the seventh case is studied it was found that it is better as compared to the sixth one because more turbulence takes place at the end corners of the pipes and also due to 20% more surface area.

8 Conclusions

After the analysis of eleven cases with and without occupants of pipe patterns it was found that the fifth case i.e., mixed flow pattern was more efficient than other patterns. It removes 8% more heat than other cases, because the surface area of this pattern is 30% more than other patterns. If the almost same surface area is considered for the other eight cases the second counter flow pattern is more efficient for temperature distribution inside the conditioned space because the temperature is equally distributed on the floor. Serpentine pattern included two cases: first and the eighth case, in the first case the heat is being removed from the west side to the east side that's why the temperature on the west side is less as compared to the east side. Double-wall serpentine consists of two cases ninth and tenth, wherein the ninth case the temperature is distributed from South-west corner to North-east corner and for the tenth case the heat is removed from south-east corner to north-west corner. Triple wall serpentine i.e., the eleventh simulated case the heat is being removed from all three directions and accumulated towards the west wall. But still one factor i.e., the position of the occupant is important to decide the type of flow pattern despite this fifth pattern being found more effective. Also, when the analysis was done for the occupied room the ninth case was found most effective amongst all because the occupant is located towards the southwest corner where maximum heat is removed.

Table 7 Heat Removal calculations in watt for all patterns when the room is occupied

Case	1	2	3	4	5	6	7	8	9	10	11	
Temperature (Kelvin)	(a) Air _{in}	298.5										
	(b) W _{in}	285.85										
Temperature-difference	(c) Air _{out}	285.85	296.61	296.52	296.48	296.54	296.57	296.56	296.57	296.56	296.59	296.50
	(d) W _{out}	288.26	288.18	288.18	288.23	288.42	288.19	288.24	288.09	288.21	288.06	288.21
	(e)-(a)	-1.91	-1.99	-1.98	-1.91	-1.98	-2.01	-2.01	-2	-2.4	-1.97	-2.12
	(d)-(b)	2.30	2.34	2.37	2.29	2.47	2.41	2.41	2.36	2.37	2.34	2.32
Heat removed by air (w)	-38.34		-39.95	-39.78	-38.53	-40.45	-40.45	-40.45	-40.33	-48.31	-39.57	-42.76
Heat removed by water (w)	7713.6		7848.4	7944.4	7689.8	8287.6	8085.2	8085.2	7910.6	7956.1	7865.6	7803.4

References

1. Sastry G (2012) First radiant cooled commercial building in india—critical analysis of energy, comfort and cost. *Environmental and Social Management*
2. Younsi LKZ, Cherif Y, Naji H (2017) Numerical investigation and analysis of indoor air quality in a room based on impinging jet ventilation. *Energy Procedia* 139:710–717
3. Zarrella A, De Carli M, Peretti C (2014) Radiant floor cooling coupled with dehumidification systems in residential buildings: A simulation-based analysis. *Energy Convers Manage* 85:254–263
4. Wu X, Zhao J, Olesen BW, Fang L, Wang F (2015) A new simplified model to calculate surface temperature and heat transfer of radiant floor heating and cooling systems. *Energy Build* 105:285–293
5. Srivastava P, Khan Y, Bhandari M, Mathur J, Pratap R (2018) Calibrated simulation analysis for integration of evaporative cooling and radiant cooling system for different Indian climatic zones. *J Build Eng* 19:561–572
6. Haurie L, JavierMazo, MónicaDelgado, BelénZalba (2014) Fire behavior of a mortar with different mass fractions of phase change material for use in radiant floor systems. *Energy Build* 84:86–93
7. Pantelic J, Schiavon S, Ning B, Burdakis E, Raftery P, Bauman F (2018) Full scale laboratory experiment on the cooling capacity of a radiant floor system. *Energy Build* 170:134–144
8. Ramos-Alvarado B, Li P, Liu H, Guerrero A (2011) CFD study of liquid-cooled heat sinks with micro channel flow field configurations for electronics, fuel cells, and concentrated solar cells. *Appl Therm Eng* 31:2494–2507
9. Ahmed AQ, Gao S (2017) Numerical investigation of height impact of local exhaust combined with an office work station on energy saving and indoor environment. *Build Environ* 122:194–205

Design and Simulation of Multiband, Circular Microstrip Patch Antenna for Wireless Applications



Manoj Deshmukh, Ashish Jadhav, Nagashettappa Biradar, Husain Bhaldar, Mahesh Mathpati, and Renuka Wadekar

Abstract This article summarizes the detailed design of a circular-shaped microstrip patch antenna. This antenna is designed to radiate at 10 different frequencies that can be used for advanced wireless communication. The proposed antenna can be used in Bluetooth, BLE, Wi-Fi, Zigbee, 2G 3G 4G LTE, and 5G communication. This antenna can radiate at 10 different frequencies such as 3.26, 5.36, 7.45, 9.65, 11.79, 13.20, 13.20, 13.72, 15.32, and 19.1 GHz. These are specially designed frequencies on which the proposed antenna should work. That means this antenna can be modified and redesigned to work for a dedicated application operating between the ranges of 3.26 to 19.1 GHz. The at all the 10 frequencies mentioned above, they observed values of s parameter are below -10 dB. The voltage standing wave ratio at about resonating frequencies observed to be between 1 and 2. Since it shows narrow bands at the designed frequencies; this antenna can be used for a specific application with a specific frequency without interference with other systems.

Keywords Antenna · Circular antennas · Microstrip Patch antenna · Multiple band antennas · Multi-frequency antennas · Reflection coefficient

M. Deshmukh (✉) · A. Jadhav · H. Bhaldar · R. Wadekar

Department of Electronics and Telecommunication Engineering, Shri Vithal Education and Research Institute's College of Engineering, Pandharpur, PAH Solapur University Solapur, Solapur, India

e-mail: madeshmukh@coe.sveri.ac.in

A. Jadhav · H. Bhaldar · M. Mathpati · R. Wadekar

Department of Electronics and Communication Engineering, Bheemanna Khandre Institute of Technology, Bhalki, Visvesvaraya Technological University Jnana Sangama, Belagavi, Karnataka, India

N. Biradar · R. Wadekar

Department of Electronics and Communication Engineering, Bheemanna Khandre Institute of Technology, Bhalki, India

M. Mathpati · R. Wadekar

GNDCE Bidar, Visvesvaraya Technological University Jnana Sangama, Belagavi, Karnataka, India

1 Introduction

Multiband Antennas are the Antennas that can radiate the signals in the form of electromagnetic waves at multiple frequencies. Today, as far as advanced wireless communication systems are concern, the multiband antenna plays a very vital role. Because a single handheld device such as a mobile phone is enabled with many wireless features such as Bluetooth, Wi-Fi, Zigbee, infrared, in addition to data and voice communication over GSM, 3G, 4G, and 5G in some cases.

Multiband antenna with small size structure plays important role in modern mobile communication systems. In the last decade, millimeter-wave antennas are rapidly developed and employed in the advanced generation of mobile communication [1].

Still, this development is spontaneous because of being increased functionality of Advanced wireless devices. And multiband antenna is the backbone of any wireless communication system [2].

Also for vehicle-to-vehicle communication, multi-functional of any communication system is needed. Hence share the proposed antenna can work at 10 bands of frequencies. And the hypothetic study says 10 different applications can operate this single antenna at the same time.

2 Review of Literature

The comparison of simulation work carried out and presented in this article with the existing work reported in other literature is done in Table 1. In [1], the Hepta band antenna with the composite mode is described which can radiate at three Subband and frequencies such as 6, 28, and 38 GHz. A Monopole antenna with hybrid polarization is described in [2], this antenna is manufactured using flame retardant 4 with a dielectric constant of 4.4 and a thickness of 1.6 mm. It is designed for three different bands of frequencies having dimensions of 70 mm × 45 mm. Magnetolectric dipole antenna reported in [3], designed for 1.86 to 1.92 GHz, 2.30 to 2.65 GHz, 3.40 to 3.80 GHz, and 5.30 to 6.92 GHz. Designed antenna having a size of 100 mm × 100 mm for 2G, 3G, 4G, and 5G applications. Single port dual-band patch antenna reported in [4], in having the capability of offering different radiation properties at 3500 and 2485 MHz with peak gains of 1.98 and 8.46 dBi, respectively. An innovative bianisotropic Omega frequency-selective antenna is presented in [5], this antenna is fabricated to operate at C band and K band at 14.312 GHz.

In [6], reported the MIMO antenna that can be used at 2.51 GHz, 4.15 GHz, 6.04 GHz, 2.36 GHz, 3.68 GHz, and 5.47 GHz frequencies. This MIMO antenna is designed by using multiple patches on a single ground plane, separated by Isolator. In [7], triple band MIMO antenna reported that operate at 2.37 GHz, 3.94 GHz, and 5.96 GHz frequencies. This antenna is designed by using multiple slots on a single patch, separated by calculated distances. Improvement in VSWR, Directivity, and Gain can be achieved by using a microstrip patch antenna. The return loss of

Table 1 Comparison between this antenna design and the other designs

References	Technique	Substrate and ϵ_r	Operating frequency band (s)	Overall dimensions	S-parameters	Reference impedance	VSWR	Applications mentioned
[1]	Hepta-band mode-composite antenna	NA	6, 28, and 38	110 mm × 80 mm	Below -10 dB	Theoretically 50 Ω	NA	LTE and 5G
[2]	Monopole antenna with hybrid polarization	FR4 with $\epsilon_r = 4.4$, thickness = 1.6 mm	(1.478–1.714 GHz) (2.54–2.72 GHz) (4.29–4.89 GHz)	70 mm × 45 mm	Under -10 dB	Theoretically 50 Ω	NA	GPS, LTE, and Satellite Applications
[3]	Magneto-electric dipole antenna	NA	1.86–1.92 GHz, 2.30–2.65 GHz, 3.40–3.80 GHz, 5.30–6.92 GHz	100 mm × 100 mm	Below -10 dB	NA	NA	2G, 3G, 4G, 5G, wireless area network (WLAN)
This work	Multiband, circular microstrip patch antenna	FR4 with $\epsilon_r = 4.4$, thickness = 1.6 mm	10 bands: 3.26, 5.36, 7.45, 9.65, 11.79, 13.20, 13.20, 13.72, 15.32, and 19.1 GHz	40 mm × 55 mm	-20.85, -12.74, -31.64, -22.76, -34.54, -13.87, -15.73, -21.95, -24.35, and -24.06 dB, resp.	56 Ω	1–2 for all bands	Bluetooth, BLE, Wi-Fi, Zigbee, 2G 3G 4G LTE, and in 5G

Designed MIMO is below -10 dB and VSWR are between 1 and 2 at 2.37, 3.94, and 5.96 GHz. Fabrication of this triple band MIMO antenna and validation of results is done in [8].

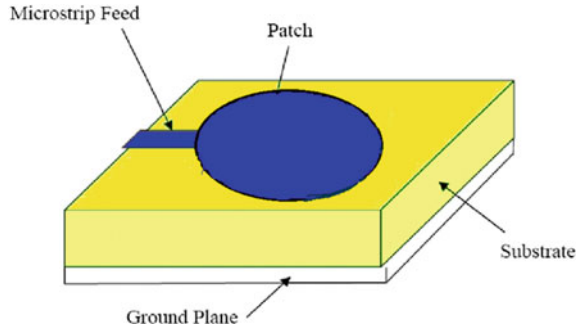
Snehal Surwase et al. [9], The 4 element Multiple Input Multiple Output (MIMO) Microstrip Patch Antenna that has 4 ports, has been designed and implemented. The proposed antenna consists of four ports with all the four patches operates at LTE and WLAN frequencies 1.8, 2.8, 3.3 GHz.

The antenna is fabricated on an inexpensive FR4 material of a dielectric constant of $\epsilon = 4.4$, with the thickness of the substrate that is 1.6 mm and the thickness of the patch is 0.035 mm. From the practical results of Dhanashree Yadav et al. [10], it is concluded that the increase in the number of patches on the substrate, data rate, and radiation pattern gets increased. The Proposed design is of 3 bands which is resonating at three frequencies and that are 1.8, 2.8, and 3.3 GHz and it gives VSWR in the range of 1 to 2 and the values of S Parameters which are less than -10 dB. Kartiki Gaikwad et al. [11], demonstrated two-element slotted patch antenna for two different applications that are Wi-Fi (wireless fidelity) and LTE (long term evolution) which operates on the frequency 2.4 and 2.6 GHz. Ashish A. Jadhav et al. [12], Comparison of various methodologies of antenna design and different software tools used for simulation is done to propose powerful techniques to proceed in the field of Microstrip Patch Antenna Design for implementation of MIMO systems. Antenna system with the high data rate, high gain, wider bandwidth, improved signal quality, higher spectral efficiency, reduced mutual coupling, low cost, and small size is the need of today's wireless communication engineering. MIMO antenna systems will also be used for next-generation wireless terminals, i.e. 5G and beyond. For every new wireless generation, the data rates and channel capacities are growing. Hence, a very large leap is expected by the year 2020 where data rates in the ranges of tens of gigabits per second are expected from mobile terminals and other compact devices. In this paper, a novel compact two element MIMO array is developed resonating at 5.4 GHz with a reduced mutual coupling of -31 dB. These characteristics are well suitable for applications, using which high data rates can be obtained. We can further improve the channel capacity by employing more number of antennas in the system [13]. A good design of antenna can improve the performance of the system. In [14], authors have proposed an inverted U-shaped patch antenna which produces dual-band of frequencies resonates at 2.8 and 6.4 GHz with an excellent return loss of -25 dB. Hence from the results, it is concluded that this antenna is well suited for wireless (WLAN) and satellite communications.

3 Methodology

The circular-shaped microstrip patch antenna is the key technology that is used to implement this design. A microstrip patch antenna is a low profile small size antenna in which a small radiating patch, dielectric substrate, and the ground plane

Fig. 1 Microstrip patch antenna



are sandwiched. The radiating patch may any shape such as rectangular, triangular, circular, elliptical, etc.

To get high directivity at a designer frequency, a circular shaped patch antenna is preferred. This circular patch is made up of conducting material such as copper. The microstrip line feeding technique is used to excite the circular patch. This feed line is also made up of conducting material. The feedline is made tapered near to the patch just to broaden the bandwidth and make the antenna resonating at different frequencies. Commonly used circular patch antenna is shown in Fig. 1.

To design this antenna, commercially available flame-retardant 4 (FR4) materials are used as a dielectric substrate with dielectric constant 4.4 and substrate thickness of 1.6 mm. Both sides of this FR4 material are coated with a conducting layer of copper with a thickness of 0.035 mm. On one side of this copper layer, the circular patch with a tapered feed line is etched.

4 Design Considerations and Steps

Sample of various design steps involved in the design of the circular-shaped patch antenna is described below;

4.1 Design Considerations

Resonating Frequency (F_r) = 2.4 GHz, Permittivity $\epsilon_r = 4.4$, Speed of Light (C) = 3×10^8 m/s, Substrate Height (h_s) = 1.6×10^{-3} m, Height of Ground/Patch (h_t) = 0.035 m.

4.2 Step 1 Calculation of Radius (a)

$$a = [F/\{1 + 2h/\sqrt{\epsilon_r F(\ln(\sqrt{F/2h} + 1.7726))}^{1/2}]$$

$$a = 15.28 \text{ mm}$$

4.3 Step 2 Calculation of Length of Ground (L_g)

$$L_g = (6 \times h) + L$$

$$L_g = 39.04 \text{ mm}$$

4.4 Step 3 Calculation of Width of Ground (W_g)

$$W_g = (6 \times h) + W$$

$$W_g = 47.64 \text{ mm.}$$

4.5 Step 4 Calculation of Length of Fed Line (F_i)

$$F_i = \frac{6 \times h}{2}$$

$$F_i = 4.8 \text{ mm}$$

4.6 Step 5 Gap Between the Circular Patch and the Inset Feed (G_{pf}) is Usually 1 mm

The remaining dimensions of the multiband circular-shaped microstrip patch antenna are given in Table 2.

The design of the proposed multiband circular-shaped microstrip patch antenna is shown in Fig. 2, and ground plane is shown in Fig. 3.

Table 2 Dimensions of microstrip patch

Name	Expression	Value	Description	Type
Gap	= 1.4	1.4	Feedline gap	Length
h	= 0.035	0.035	Thickness of Patch	Length
hs	= 1.6	1.6	Thickness of Substrate	Length
Lf	= 10.33	10.33	Length of tapered section	Length
Lg	= 55	55	Length of Ground Plane	Length
Ltapper	= 11.7	11.7	Length of taper	Length
R	= 13	13	Radius of circular patch	Length
Wf	= 3.1	3.1	Width of Feedline	Length
Wg	= 40	40	Width of Ground Plane	Length
Wt	= 1.8	1.8	Width of Feedline Throat	Length

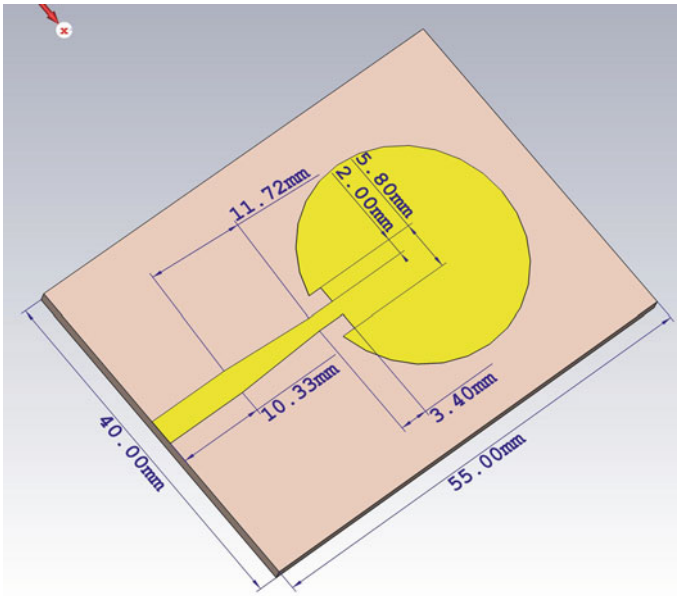


Fig. 2 Design of multiband, circular microstrip patch antenna

5 Results and Descussions

5.1 Scatering Parameter

The scattering parameter of any antenna indicates how efficiently the antenna can radiate in free space. It is a measure of radiation of electromagnetic waves in the

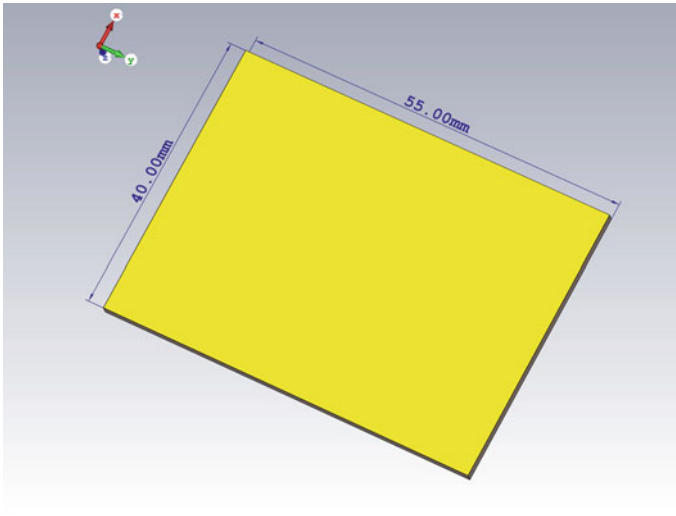


Fig. 3 The ground plane of the multiband, circular microstrip patch antenna

air without reflection. The S parameter value of any antenna should be less than -10 dB. For the antenna design here operating at 10 different frequencies viz 3.26, 5.36, 7.45, 9.65, 11.79, 13.20, 13.20, 13.72, 15.32, and 19.1 GHz, the S-Parameter values observed are -20.85 , -12.74 , -31.64 , -22.76 , -34.54 , -13.87 , -15.73 , -21.95 , -24.35 , and -24.06 dB, respectively and shown in Fig. 4.

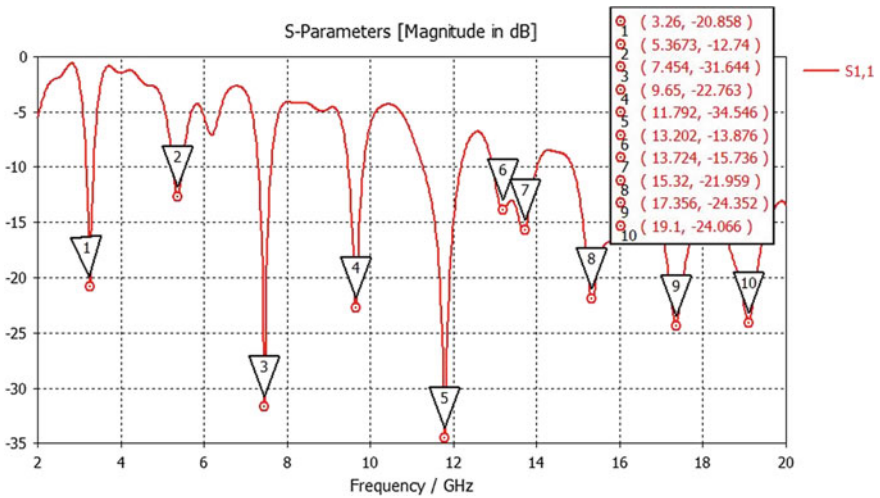


Fig. 4 S-Parameter of the multiband, circular microstrip patch antenna

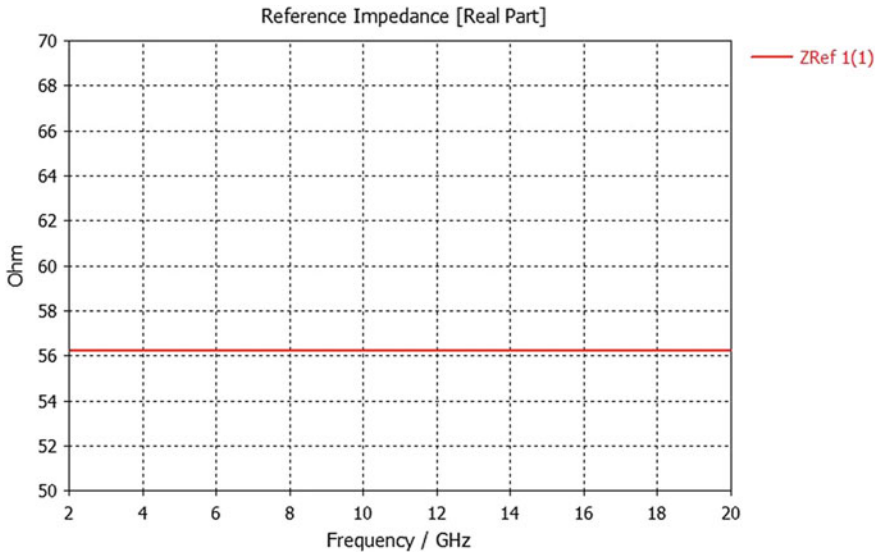


Fig. 5 Reference impedance (Zref) of the multiband, circular microstrip patch antenna

5.2 Reference Impedance

The reference impedance of an antenna is to be matched with the impedance of transmitter or receiver circuitry. It is the necessary and sufficient condition for maximum power transfer in the form of electromagnetic waves. The standard value of Reference impedance is 50 Ω in most of the wireless applications and 75 Ω some of the times. This antenna is designed in such a way that it should provide a reference impedance of 50 Ω. The observed value of reference impedance is as shown in Fig. 5.

5.3 Voltage Standing Waves Ratio (VSWR)

The voltage standing wave ratio is one of the key parameters that should be observed during the design of the antenna. VSWR is the measure of the amount of Impedance mismatch. If impedance mismatch is higher than the VSWR value will be more. Ideally, the value of VSWR must be between 1 and 2. VSWR value for multiband, circular-shaped microstrip patch antenna is observed on the EM solver and shown in Fig. 6.

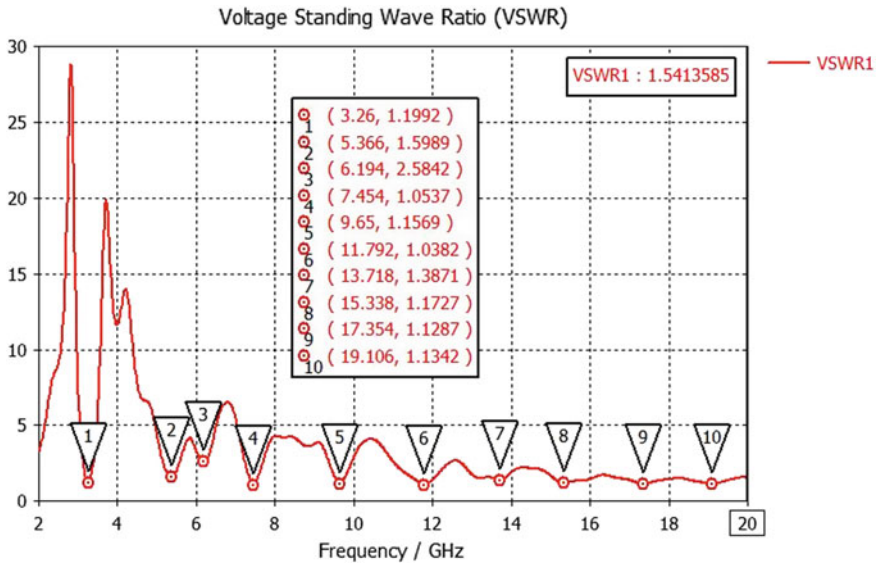


Fig. 6 VSWR of the multiband, circular microstrip patch antenna

6 Conclusions

This paper proposes an innovative approach to design a multiband antenna with a circular-shaped microstrip patch as a radiating element. The circular patch is able to radiate at 10 different frequencies (3.26, 5.36, 7.45, 9.65, 11.79, 13.20, 13.20, 13.72, 15.32, and 19.1 GHz). This antenna can be utilized in some dedicated applications where a narrow band of frequency is required without having any interference with other wireless communication systems. The obtain the S parameter values for all of these frequencies is less than -10 dB. Also, voltage standing wave ratios of all those 10 frequencies are between 1 and 2. Also, the reference impedance measured is around 56Ω that means it can radiate maximum power when implemented in a wireless application.

References

1. Liu Y, Li Y, Ge L, Wang J, Ai B (2020) A compact hepta-band mode-composite antenna for sub (6, 28, and 38) GHz applications. *IEEE Trans Antennas Propag* 68(4):2593–2602
2. Al- MA, Salim AJ, Ali JK (2020) A compact multiband printed monopole antenna with hybrid polarization radiation for GPS, LTE, and satellite applications. *IEEE Access* 1:110371–110380
3. Yang G, Zhang S, Li J, Zhang Y, Pedersen GF (2020) A multi-band magneto-electric dipole antenna with wide beam-width. *IEEE Access* 16:68820–68827
4. Yang X, Ji Y, Ge L, Zeng X, Yongle Wu, Liu Y (2020) A dual-band radiation-differentiated patch antenna for future wireless scenes. *IEEE Antennas Wirel Propag Lett* 19(6):1007–1011

5. Ahmed F, Hassan T, Shoaib N (2020) A multiband bianisotropic FSS with polarization insensitive and angularly stable properties. *IEEE Antennas Wirel Propag Lett* . <https://doi.org/10.1109/LAWP.2020.3020949>
6. Jadhav AA, Biradar N, Bhaldar H, Mathpati MS, Inamdar SA (2020) Design of miniaturized, two elements 6-band MIMO antenna with patch isolator. *Int J Sci Technol Res* 1(1):3492–3496
7. Jadhav AA, Biradar N, Bhaldar H, Mathpati MS, Wadekar R (2020) Design and analysis of triple band miniaturized antenna for wearable application. *Int J Innov Res Comput Commun Eng* 7(12):4262–4269
8. Jadhav AA, Biradar N, Bhaldar H, Mathpati MS, Wadekar R (2020) Design, simulation and implementation of triple band miniaturized antenna for wearable application. *IJSRD Int J Sci Res Dev* 7(11):538–542
9. Surwase S, Yadav D, Shinde S, Prof Jadhav A (2018) Design and simulation of 4 element MIMO antennas for wireless application. *Int J Innov Res Comput Commun Eng* 6(2)
10. Yadav D, Surwase S, Atkale D, Prof Jadhav A (2018) Fabrication of 4 element MIMO antenna for wireless applications. *IJSRD Int J Sci Res Dev* 6(04). ISSN (online):2321–0613
11. Gaikwad K, Thorat K, Gend G, Nakate P, Prof Jadhav A (2019) Common element MIMO antenna system for Wi-Fi/LTE access point. *IJSRD—Int J Sci Res Dev* 7(02):30–33. ISSN (online):2321–0613
12. Prof Jadhav AA, Prof Mathpati MS, Dr Biradar N (2019) A systematic analysis of existing methodologies, tools, materials and EM solvers used in design of MIMO antennas for wireless applications. *IJSRD—Int J Sci Res Dev* 7(01):1696–1700. ISSN (online):2321–0613
13. Satya Mitra et al YVSS (2016) Design of a novel microstrip MIMO antenna system with improved isolation. *Int J Antennas (JANT)* 2(2)
14. Krishna TM (2015) Design of an inverted U-shaped MIMO patch antenna for dual-band applications. *Int J Innov Res Electr Electron Instrum Control Eng*

Portable UV-C 360 Degree Disinfection Chamber



Dattatraya Anarse, Anjali Sakurkar, Mahadev Kadam, and Sonali Kale

1 Introduction

A novel coronavirus known as COVID-19 emerged at the end of the year 2019 and continued putting human health and the worldwide economy at risk. The World Health Organization (WHO) has declared this situation as a global pandemic. The combat against this virus follows three major Points: The first to detect the infection, the second to develop drugs, vaccines and therapies and the third to develop technologies to inactivate and suppress the virus's spread. Worldwide researchers are engaged in developing detection methods for COVID-19 and searching for drugs, vaccines and therapies to cure patients for this novel virus. It is now well known that COVID can be spread through water droplets and air ejected during talking, coughing and sneezing, also through contact with patients [1, 2]. Hence, the third point needs to be focused more to reduce the exposure of people to the virus and hence the pressure on required health care infrastructure. The study reported that COVID-19 virus remains on various surfaces for several hours [3]. The airborne respiratory water droplets (containing coronavirus) ejected will be adsorbed on various surfaces and further transmitted to others. This crisis has highlighted the importance of disinfection to minimise the possibility of the virus being carried away to different locations. Ethyl alcohol is the main ingredient in alcohol-based hand sanitisers (ABHS), which is volatile and flammable at room temperature, hence needs to be stored safely. In contrast, UV-C light is chemical-free and is suitable for hospitals to disinfect different surfaces, such as medical equipment [4].

This paper has reported a UV-C disinfection chamber design, suitable for disinfection of electronics products, vegetables, and materials that can not be sanitised by liquid sanitisers. This device provides an option to disinfect objects where alcohol-based liquid sanitisers are not suitable.

D. Anarse (✉) · A. Sakurkar · M. Kadam · S. Kale
Pimpri Chinchwad College of Engineering, Nigdi 411044, India
e-mail: dattatraya.anarse@pccoepune.org

2 About Work

2.1 *Ultraviolet Light*

Natural ultraviolet (UV) radiations emitted from the sun are only 10% of total sunlight. It is the part of the electromagnetic spectrum that lies between visible light and the X-ray radiation. The wavelength of invisible ultraviolet radiation lies between 1000 and 4000 Å°.

Ultraviolet radiations are divided into three types:

UV-A from 3150 Å° to 4000 Å°—large wavelength.

UV-B from 2800 Å° to 3150 Å°—medium wavelength.

UV-C from 1000 Å° to 2800 Å°—short wavelength.

2.2 *Design of the UV- C Disinfection Chamber*

Researchers reported that COVID-19 virus could live on different surfaces up to 48 hrs. [3] It is also proved that the UV-C sanitizers can disinfect viruses, including novel COVID-19. Recently alcohol-based sanitisers are being used to disinfect the coronavirus. But these are consumable and due to frequent use may affect skin and also not suitable for vegetables, masks, electronic devices, etc. Hence to overcome these problems we have developed an UV-C light-based portable disinfection chamber at a low cost of Rs.3650 /- to disinfect different products to minimize COVID-19 risk. The low pressure mercury lamp (UV-C) used to disinfect virus has a good life time of 9000 h. The developed prototype chamber can be used to disinfect mobile phones, masks, wallets, keys, spectacles, bags, papers, vegetables and parcels, etc. in 1 min to minimize the risk of COVID-19. The structure of the chamber is like a cuboid with dimensions ($l = 27$ cm, $b = 27$ cm, $h = 30$ cm) and is made up of wooden board of thickness 1 cm as shown in Fig. 1. The chamber is an opaque wooden frame with inner surface covered with a layer of aluminium foil to increase reflectivity as well as to prevent UV-C light leakage. Two Philips UV-C lamps each of 11 W are fitted at top and bottom surface to provide UV-C light exposure to the object and these lamps are connected with door operated switch, which prevents human body exposure to UV-C radiation. The object is placed on a thin mesh tray provided at the centre of the chamber for sanitization and 360° UV-C light exposure. The UVC lamps are operated on 230 V AC power supply and to regulate power supply lamps are connected with choke. The electrical connections are as shown in Fig. 2. The specifications of the chamber are as follows.

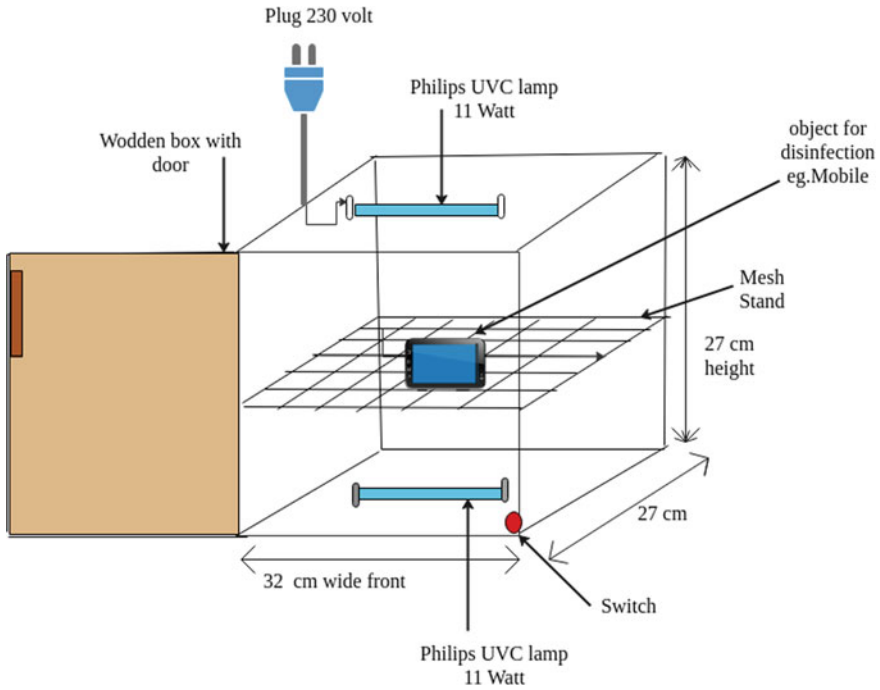


Fig. 1 Design of the UV-C disinfection chamber

2.3 Design

See Fig. 1.

2.4 Specifications

- Capacity: 21 L
- Philips UVC lamps: 2 nos
- Outer Dimensions: 27 × 27 × 30 cm
- Output Wavelength: 254 nm UV-C light
- Operating Power: 11 W each lamp
- Operating Voltage: 230 ~ 240 V, AC-50 Hz
- User UV-C protection: Door operated ON/OFF switch
- Power Cable: 2 pin 5A, 1 m
- Operating Temperature: 0–45 °C
- Chamber Frame: Wooden
- Mesh Stand: Metallic

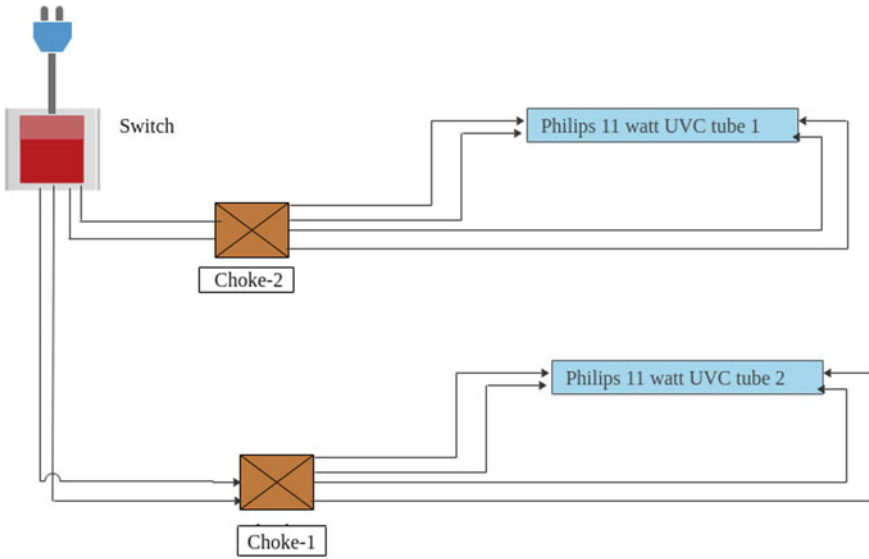


Fig. 2 Electrical connections of UV-C lamp

Distance Between Mesh and Lamp: d 13 cm

2.5 Electrical Connections of UVC Lamp

See Fig. 2.

2.6 Actual Images

The actual photographs of the designed UV-C disinfection chamber are shown in Fig. 3.

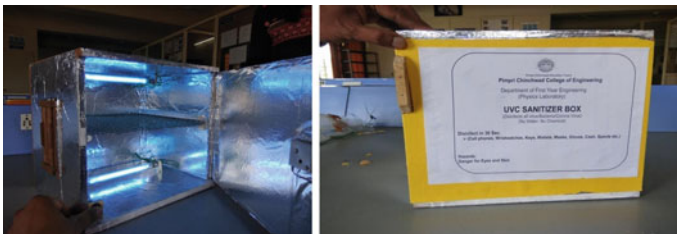


Fig. 3 Setup of disinfection chamber developed at PCCoE, Engineering Physics laboratory

2.7 Overall Cost of UV-C Disinfection Chamber

- Philips UV-C lamps: 2 nos (11 W) = 750/- (each) × 2 = Rs.1500/-
- Chamber Wooden Frame (Dimensions: 27 × 27 × 30 cm) = Rs. 1600/-
- Door operated ON/OFF switch = Rs. 50/-
- Power Cable: 2 pin 5A, 1 m = Rs. 50/-
- Metallic Mesh Stand = Rs. 100/-
- Tube holder and wiring = Rs.100/-
- Aluminium Foil = Rs. 50/-
- Spray paint = Rs. 200/-

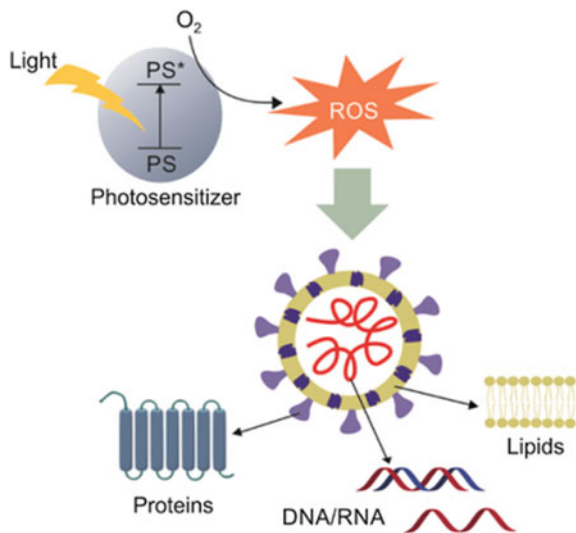
Total amount = Rs. 3650/- (Cost can be reduced for multiple chambers).

3 Operation of UV-C Sanitizer Chamber

3.1 How Does UV-C Destroy Viruses?

The disinfection mechanism of viruses using UV-C is shown in Fig. 4. RNA and DNA of the virus absorb UV-C light,when exposed to it. High energy of UV-C

Fig. 4 Mechanism of disinfection of virus (Reproduced from [9])



radiation destroy nucleic acids in RNA and DNA, and restrict the growth of virus and its replication by damaging its molecular structure. This process is known as photodimerization [5].

Heilingloh et al. [6] demonstrated that SARS-CoV-2 virus could be completely inactivated by UV-C exposure as compared to UV-A and UV-B. [7] Even though UV-A is weakly absorbed and less effective, it can damage genes by producing reactive oxygen species [8].

3.2 Operating UV-C Disinfection Chamber

- Turn ON the main Switch.
- Place the object on the mesh tray at centre inside the UV-C disinfection chamber.
- Close the door. Closing the door switches the light ON inside the chamber.
- Allow the exposure of UV-C radiation for 30 s–1 min.
- Opening the door will switch OFF the light. Take out the disinfected object outside.
- Turn OFF the main switch.

4 Conclusion and Future Scope

For disinfection of different non living things, UV-C radiation can be effectively used. The designed compact, portable and low cost UV-C disinfection chamber will help to prevent the spread of COVID-19 virus through electronic gadgets, vegetables, masks, groceries, etc.

In future,

1. The designed product can be made available in the market to serve sanitization needs at homes, offices, shops, restaurants, etc.
2. The product can be modified for disinfection of conference rooms, interior of car.
3. Currently it is not operated on solar and battery backup however in future, provision will be made to operate the chamber on solar energy and battery, when electricity from mains is not available

References

1. Miriam ER, Darnell K, Subbaraob SM, Feinstone D, Taylor R (2004) Inactivation of the corona virus that induces severe acute respiratory syndrome. SARS-CoV, J Virol Methods 121:85–91
2. Kumar D, Sonawane U, Gohil MK, Anand SRP, Reema P, Avinash M, Agarwal K (2020) Design and development of a portable disinfectant device. Trans Indian Nat Acad Eng 5:299–303

3. van Doremalen N, Bushmaker T, Morris DH, Holbrook MG, Gamble A, Williamson BN, Tamin A, Harcourt JL, Thornburg NJ, Gerber SI, LloydSmith JO, deWit E, Munster VJ (2020) Aerosol and surface stability of SARS-CoV-2 as compared with SARS-CoV-1. *New Engl J Med* 382:1564–1567
4. Casini B, Tuvo B, Cristina ML, Spagnolo AM, Totaro M, Baggiani A, Privitera GP, (2019) Evaluation of an ultraviolet C (UVC) light-emitting device for disinfection of high touch surfaces in hospital critical areas. *Int J Environ Res Pub Health* 16:3572(1–10)
5. Beck SE, Rodriguez RA, Hawkins MA, Hargy TM, Larason TC, Linden KG (2015) Comparison of UV-induced inactivation and RNA damage in MS2 phage across the germicidal UV spectrum. *Appl Environ Microbiol* 82(5):1468–1474
6. Silke C, Aufderhorst HUW, Schipper L, Dittmer U, Yang OWMDDY, Zheng X, Sutter K, Trilling M, Alt M, Steinmann E, Krawczyk A (2020) Susceptibility of SARS-CoV-2 to UV irradiation. *Am J Infect Control* 48:1273–1275
7. Perdiz D, Grof P, Mezzina M, Nikaïdo O, Moustacchi E, Sage E (2000) Distribution and repair of bipyrimidine photoproducts in solar UV-irradiated mammalian cells. *J Biol Chem* 275:26732–26742
8. Tyrrell JL, Douki T, Cadet J (2001) Direct and indirect effects of UV radiation on DNA and its components. *J Photochem Photobiol B* 63:88–102
9. www.uvdisinfection.philips.com

Eco-friendly Soldering Technique



Puskaraj D. Sonawwanay  and V. K. Bupesh Raja 

Abstract Since the start of electronics, soldering has been studied a dynamic activity in the design of hi-tech microelectronic circuitry, and substantial improvement in soldering practices is perceived in the near future. Concentrated solar energy (CSE) is being used for material treating. In this study, CSE is utilized for soldering and named as the “Concentrated Solar Energy Soldering (CSES) technique.” A Fresnel lens accompanied by a two-axis sun tracker to concentrate the solar energy needed for soldering is used. CSES technique, a green technology, is discovered to be promising. The CSES technique can be used to solder on-site electronics apparatuses used in nuclear, space, automobiles, computer hardware, electronic circuits used in process equipment’s, etc. Exclusively, in the secluded areas, CSES will be beneficial to solder numerous components, circuits, etc.

Keywords Concentrated solar energy · Soldering · Ecofriendly · Environment · Solder joint · Sun

1 Introduction

Soldering is the oldest technique of joining two pieces of metal together. There are three joining methods: welding, hard soldering (or brazing), and soft soldering. With both hard and soft soldering, the joint gap is filled with a molten alloy, which has a lower melting point than the joint members themselves, but which is capable of wetting them and, on solidifying, of forming a firm and permanent bond between them. The basis of most hard solders is copper, with additions of zinc, tin and silver. Most hard solders do not begin to melt below 600 °C/1100 °F, which rules them to make conductive joints in electronic assemblies. Soft solders for making joints

P. D. Sonawwanay (✉)

School of Mechanical Engineering, Dr. Vishwanath Karad MIT World Peace University, Pune 411038, India

V. K. Bupesh Raja

School of Mechanical Engineering, Sathyabama Institute of Science and Technology, Chennai 600119, India

on electronic assemblies were by tradition, until recently, alloys of lead and tin, which begin to melt at 183 °C/361 °F. This comparatively modest temperature makes them suitable for use in the assembly of electronic circuits, provided heat-sensitive components are adequately protected against overheating [1].

For electronic devices, proper solder material and soldering method ensure good integration of mechanical and electric connections. For the past few decades, lead–tin solders were extensively used. They have a distinctive amalgamation of adequate mechanical properties, including decent resistance to corrosion, low cost and excellent wettability. The use of lead is banned by the “European Reduction of Hazardous Substances(RoHS)” in July 2006 [1, 2]. Different researchers are working on developing novel lead-free solder alloy. Because of environmental concerns of Sn–37Pb eutectic solder, Sn–Ag–Cu solder is being developed as a substitute solder alloy. Because of good solder properties and reasonably good mechanical properties, SAC305 solder is commonly used in microelectronic applications [1, 2].

2 Handsoldering

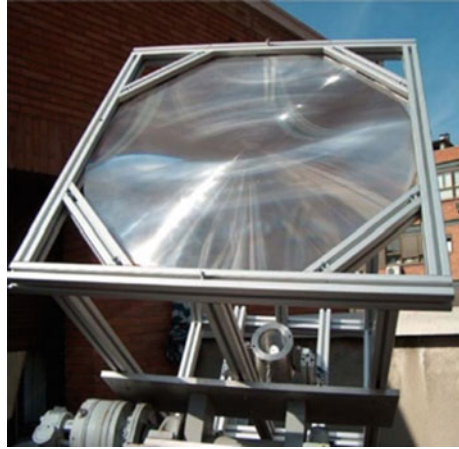
With hand soldering, the heat basis is the tip of a soldering iron, which is heated to 300–350 °C/570–660 °F. A small quantity of flux is applied to the joint members. The assembled joint is heated by employing the tip of the soldering iron on it. Solder and flux are then applied jointly, in the arrangement of a solder wire, which carries a core of flux. As soon as its temperature has reached about 100 °C/200 °F, the rosin softens and runs out of the solder wire into the joint. Subsequently, the joint temperature rises beyond 183 °C/361 °F; the solder also starts to melt and follows the flux into the joint gap. As soon as the joint is reasonably filled, the soldering iron is raised, and the joint is permitted to solidify [1, 2].

3 Solar Energy for Soldering

At present, we are finding the usage of solar energy for numerous purposes. As there is noticed inadequacy of fossil fuel, unending works are being taken to explore a substitute energy source [3–5]. For surface hardening of steel, usage of Concentrated Solar Energy (CSE) is located to be reasonable in relationship to established practices. With an economic Fresnel lens arrangement, CSE was commissioned for surface alterations, as shown in Fig. 1 [6]. Materials treatment was accomplished in minutes since in a few seconds, the temperature was elevated to 1500–2000 K [6].

For materials treating, Concentrated Solar Energy is a strong alternative. CSE is a nature-friendly technology as it is non-contaminating. As the processing efficiency of CSE is more, CSE provides decent quality of altered surface in a smaller treatment period. Solar furnaces are employed in numerous materials treating by means of

Fig. 1 Fresnel installation at CENIM [6]



concentrating solar energy. For material treating with CSE, small and economic Fresnel lens setups are also being used [7].

In the literature, it was located that nobody has studied for employing CSE for soldering purposes. No literature is available on CSE using cost-effective and compact Fresnel lens installations for soldering applications. The purpose of this study is to apply CSE (by using a Fresnel lens) to lead-free soldering applications and establish this eco-friendly technology [7].

4 Concentrated Solar Energy Soldering (CSES)

In this study, concentrating solar energy is utilized for soldering and named as the “Concentrated Solar Energy Soldering (CSES) technique”. A two-axis sun tracker is used with a Fresnel lens to concentrate the solar energy required for soldering, as shown in the virtual prototype of the experimental setup of the Concentrated Solar Energy Soldering (CSES) technique (refer Fig. 2).

CSES setup has a Fresnel lens supported by the base frame to concentrate solar energy. Soldering is done on a soldering fixture, as shown in Fig. 3, which is movably mounted on a base frame under the Fresnel lens. The Fresnel lens in amalgamation with the soldering fixture is utilized to attain a focal length for the accomplishment of the required temperature for soldering. The arrangement to fix and regulate the space between the substrates is created for appropriate soldering. The arrangement for solder wire to go into the gap between substrates is also made. The fixture can be moved to adjust the exact location of a focal point of the Fresnel lens, to achieve the temperature at a focal point to heat solder wire to facilitate soldering [8].

The CSES setup also comprises sensors mounted on the frame for sensing east–west & north–south direction of the sun and achieves two-axis solar tracking. A controller unit is provided to assist in solar tracking with the help of sensors and

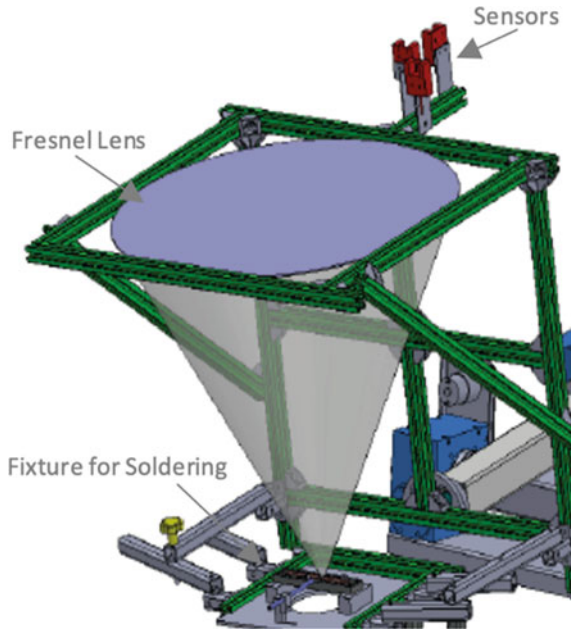


Fig. 2 Virtual prototype of experimental setup of ‘Concentrated Solar Energy Soldering’ (CSES) technique [8]

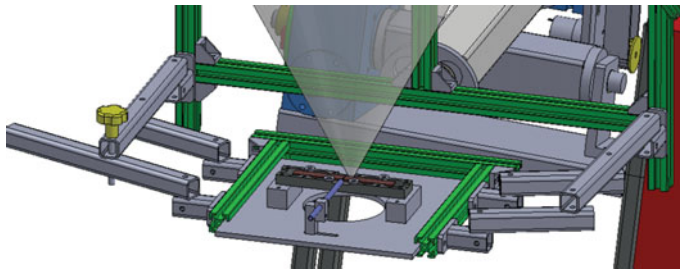


Fig. 3 Virtual prototype of special fixture for soldering with ‘Concentrated Solar Energy Soldering’ (CSES) technique

motors [9]. The Fresnel lens concentrates the solar energy required for soldering, as shown in Fig. 4.

The CSES technology discussed in this paper is patented with patent application No: 201721009049 [10] and can be used to solder on-site electronics components used in nuclear, space, automobiles, computer hardware, electronic circuits used in process equipment’s, etc. Specifically, CSES can be used in remote areas to solder various components, circuits, etc.

Fig. 4 Experimental setup of ‘Concentrated Solar Energy Soldering’ (CSES)



5 Conclusion

1. In this research work, Concentrated Solar Energy (CSE) is utilized for soldering and named as the “Concentrated Solar Energy Soldering (CSES) technique”.
2. A two-axis sun tracker with a Fresnel lens is used to concentrate the solar energy needed for soldering.
3. CSES technique was found to be encouraging ecofriendly technique.

References

1. NaiS ML, Wei J, Gupta M (2008) Effect of carbon nanotubes on the shear strength and electrical resistivity of a lead-free solder. *J Electron Mater* 37(4):515–522
2. Sonawane PD, Raja VKB (2019) Advances in lead-free solders. *Int J Mech Eng Technol* 10(2):520–526
3. Thirugnanasambandam M, Iniyan S, Goic R (2010) A review of solar thermal technologies. *Renew Sustain Energy Rev* 14:312–322
4. Sonawane PD, Raja VKB (2017) An overview of concentrated solar energy and its applications. *Int J Ambient Energy* 1–6
5. Francis AJ, Raja VKB (2015) An overview of concentrated solar power (CSP) and its applications. *Int J Appl Eng Res* 10(5):1755–1761
6. Sierra C, Vazquez AJ (2005) High solar energy concentration with a Fresnel lens. *J Mater Sci* 40:1339–1343
7. Sonawane PD, Raja VKB (2018) Concentrated solar energy in materials processing. *Int J Ambient Energy* 1–7
8. Sonawane PD, Raja VKB (2019) Novel “concentrated solar energy soldering (CSES) technique—a feasibility study.” In: *Proceedings of the IEEE 5th international conference on science, technology, engineering and mathematics (ICONSTEM 2K19)*, pp 401–407

9. Sonawane PD, Raja VKB, Gupta M (2020) Microstructure, mechanical, and electrical properties and corrosion analysis of lead-free solder CSI joints on Cu substrate using novel concentrated solar energy soldering (CSES) method. *Adv Mater Sci Eng* 1–16
10. Sonawane PD, Raja VKB (2017) Portable “Solar Welding Kit”, Indian patent, 201721009049

Friction Drilling an Emerging Technique in Hole Making Process



Mathew Alphonse and V. K. Bupesh Raja

Abstract Friction drilling is identified as a new way of hole making process, which is also known as nontraditional drilling method. The traditional drilling process has been covering in 90% of the machining process and it is not suitable for sheet metal application. Researchers are focusing on nontraditional drilling process for completing the drilling on sheet metal. This method is more preferable for automotive and aeronautical applications. Friction drilling is a hole making process which completes the process in five steps, the advantage of friction drilling is a chipless hole making process. The chips melt due to heat and pushed due to tool movement into top and bottom of the material called bushing. Bushing is used for support, threading etc. In this review emerging technique friction drilling in the drilling process has been reviewed and throws light on sheet metal hole making process.

Keywords Friction drilling · Bushing height · Coated tool · Uncoated tool · Surface roughness

1 Introduction

Friction drilling a nontraditional way of make hole process. Heat produced in-between the tool and work piece has used for the piercing tool into the work piece. It is a five step hole making method [1, 2]. Due to the heat developed, the metal melts and tool plunged into the work piece, the metal pushed and pulled to top and bottom side of the work piece material called as bushing [3]. This has more advantages like support, threading etc. [4]. In recent years enormous effort has been taken for research on studying of bushing height formation. From the researches it has observed that bushing height depends upon various factors like material thickness, work material,

M. Alphonse (✉)

Department of Mechanical Engineering, Sathyabama Institute of Science and Technology, Chennai 600 119, Tamil Nadu, India

V. K. Bupesh Raja

School of Mechanical Engineering, Sathyabama Institute of Science and Technology, Chennai 600 119, Tamil Nadu, India

spindle speed, feed rate and machining condition [5, 6]. Roughness of the surface is another key factor in friction drilling process. In friction drilling process the tool is pierced into the material, depends upon the heat produced in between tool and the material. While comparing with conventional method the temperature developed is very high, this may affect roughness of the drilled surface Ozek et al. [7] has compared work material aluminum and stainless steel and tool material high speed steel and tungsten carbide in the investigation. Surface roughness of aluminum is more because aluminum is softer than steel. The roughness of the surface can be controlled by feed rate and spindle speed.

Another solution of decreasing the surface damages has been identified is pre-drilling process. For aluminum plate at several feed rate and spindle speed have verified with and without pre-drilling. From the survey it has been identified that predrilled hole cracks were less and petal also formed better than normal friction drilling process [8]. Latif Ozler [9] has investigated the impact of surface roughness and bushing height with fixed and variable feed rate. It has been found that the variable feed rate 50–100 mm/min has lesser surface roughness and higher bushing height, which is compatibility better for friction drilling process. In recent years enormous effort has taken for studying the formation of bushing height. Bushing height depends upon the material thickness, material nature, tool and input parameters. The chips formed in traditional drilling method is formed as bushing in nontraditional drilling process [10, 11]. Bushing is formed in a single step [12]. Dehghan et al. [13] has taken effort to study the effect of bushing height produced. They used titanium alloy as tool material. Depends upon the process parameters the bushing height also varied. Petals are formed that depends upon spindle speed, feed rate and tool material. It has concluded that lower feed rate and higher spindle speed plays a vital role in bushing height. Latif Ozler et al. [14] experimentally proved the formation of bushing height depends upon various factors like spindle speed, feed rate, friction cone angle and drilling conditions. They have used tungsten carbide as tool material and concluded that during machining time the conditions varied depends upon above said factors. Due to the change in temperature the chances of varying bushing height also differs. At lower spindle speed and lower feed rate the temperature produced is more and the bushing height produced is very less, whereas at higher spindle speed and lower feed rate the bushing produced is more. Somasundaram et al. [15] conducted experiment based on bushing height formation; they have concluded that at lower temperature the bushing height produced is improper, this is also because of lesser softening and ductility. Boopathy et al. [16] has evaluated the temperature difference while machining process going on. Aluminum, Brass and Stainless steel has been compared. It has concluded that at initial stage of drilling temperature is very less, but while dept of cut increases the temperature increases. For stainless steel temperature is more than other two materials.

Optimization techniques are utilized to find the best result. The response and significance can be analyzed using ANOVA [17–19, 21]. Wei–Liang Ku et al. [17] has observed the friction drilling tool with various factors like feed rate, spindle speed and friction contact area ratio (FCAR). ANOVA tool were used to find the significance of result. It has been observed that smooth roughness and maximum

bushing height is observed for 50% FCAR tool. Response Surface Methodology (RSM) is the best tool identified for optimization. Without losing the accuracy the most possible solution can be identified from RSM [15].

The aim of this review is to focus on the emerging technique of friction drilling process. Majority of the manufacturing field uses drilling process. But the major drawback of the drilling technique is to make a hole in sheet metal. This nontraditional technique has filled the space in sheet metal hole making process. In this review the process, advantages and limitations is covered.

2 Experimental Setup

Friction drilling is a five step hole making process, were tool plunged into the work material with the help of heat generated due to high rotation of spindle speed as shown in Fig. 1. Initially tool is kept in contact with the work piece then due to the heat, metal starts melting, at the same time the tool starts piercing into the work piece. The conical area of the tool plunged into the work piece in next stage. Further the cylindrical portion of the tool smoothen the drilled hole. The metal is pushed top and bottom side of the work material called bushing. Finally the tool is retracted to its original position.

The tool is rotated at higher rpm. The thrust force and torque developed is very high, which depends upon the material and tool. A high power machine is only capable of withstanding all the above said issues. Vertical machining centre (VMC) is used for drilling process. Friction drilling setup is shown in Fig. 2. Dynamometer is attached to the vice in the VMC machine. It is to evaluate thrust force and torque.

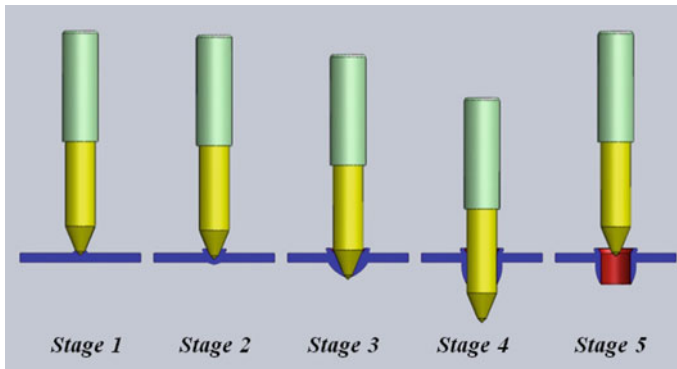


Fig. 1 Friction drilling stages (Source [20], p. 321)



Fig. 2 Setup for friction drilling

2.1 Selection of Tool

The tool geometry is shown in Fig. 3. The nomenclature is chosen depends upon the results produced. In Table 1 shows different dimensions chosen by different researchers.

The center portion of the tool has key role in friction drilling process. Initial punching of the tool into the material is initiated by center portion. Conical portion

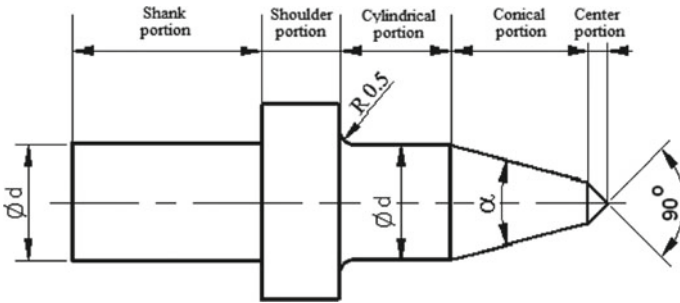


Fig. 3 Tool geometry (Source [14], p. 471)

Table 1 Dimensions of previous research work for a friction drilling tool

Dimensions	Mathew et al. [2]	Miller et al. [10]	Somasundaram et al. [15]
Diameter (d)	4 mm	5.3 mm	5.3 mm
Center angle (α)	90°	90°	90°
Conical angle (β)	18°	36°	36°
Center height (h_c)	0.8 mm	0.940 mm	1 mm
Conical height (h_n)	10 mm	5.518 mm	10 mm
Cylindrical height	10 mm	7.043 mm	15 mm

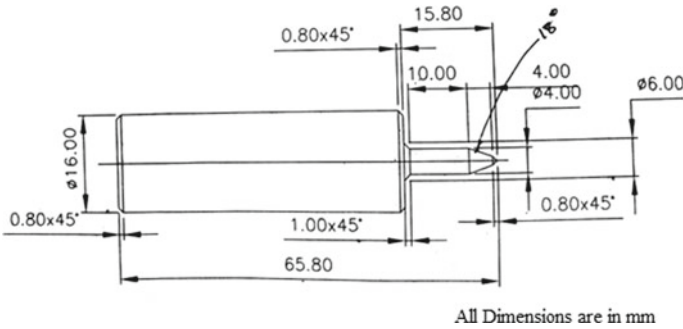


Fig. 4 Preferable tool dimension for friction drilling (Source [22], p. 471)

of the tool helps to plunge the tool into the work piece. Cylindrical portion of the tool polishes the surface in forward movement as well as retraction movement of tool.

Friction drilling tool with the dimensions best suited for drilling operation is shown in Fig. 4. The dimensions are chosen from various literature surveys. The conical area is mainly involved in cutting the work material. The maximum allowable work piece thickness is 4 mm for work piece.

In tool geometry two different profile exits conical and straight profile exits. From the literature survey it is noted that hole quality is best found for conical profile, because the conical profile find easy to pierce into the work piece initially. But in a straight profile tool stress is more to get tool pierced into the work pierce.

3 Observations

Friction drilling is a newer technology in machining process, though this process exists before. Many challenges are facing in this field, in this review few issues that make challenges in this friction drilling process are brought forward. Observations are based on literature survey.

Figure 5 shows tool wear. Tungsten carbide tool has used as friction drilling tool material. Low carbon steel has used as work material. Tungsten carbide tool has very good property for its hardness. Initially the tools have lesser wear, but wear increases after so many drills only while using a tungsten carbide tool. It has been observed that tool has unique property to withstand wear. At 11,000 drilled hole only the tungsten carbide tool started to wear. Optical microscope is use for capturing the image.

The Edax and SEM image of friction drilling tool is shown in Fig. 6. It is observed that large flow of material is transferred to tool. C, Si, and Fe are deposited into the tool material, from the work material.

The bushing height developed in various feed rate and angle is shown in Fig. 7. It is noted that higher rpm, lower feed rate and minimum angle produces better quality

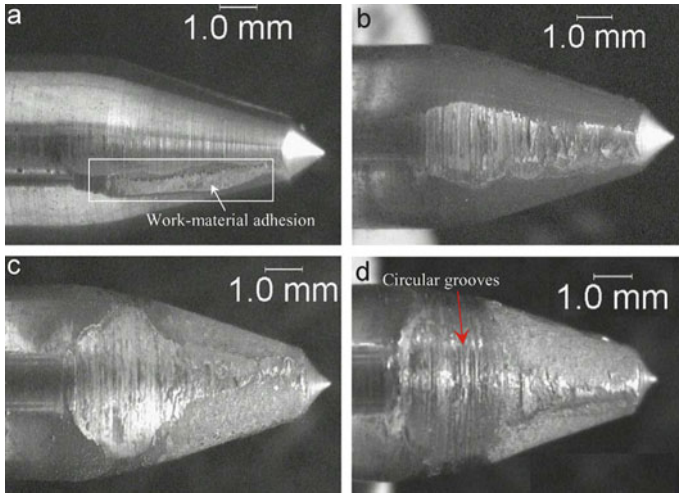


Fig. 5 Tool wear (Source [10], p. 1641)

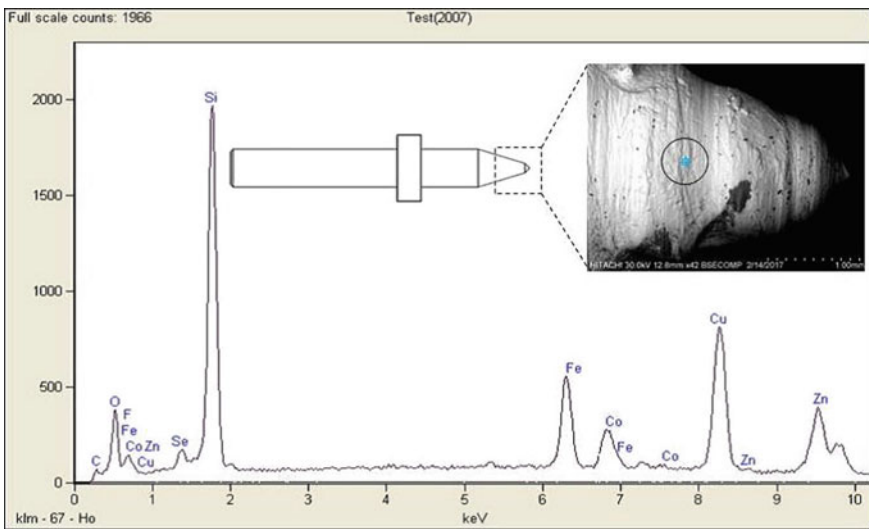


Fig. 6 Tool wear (Source [23], p. 100)

hole. At higher feed rate and angle the parent material also gets bending, but in lower spindle speed the bushing height produce is less compactly.

It is important to increase the tool life. The chances of wear is very high in friction drilling process, because of temperature is very high in this process. In Fig. 8 uncoated, titanium aluminum nitride coating and aluminum chromium nitride coating is compared. Figure 8a shown number of holes versus maximum wear. In Fig. 8b

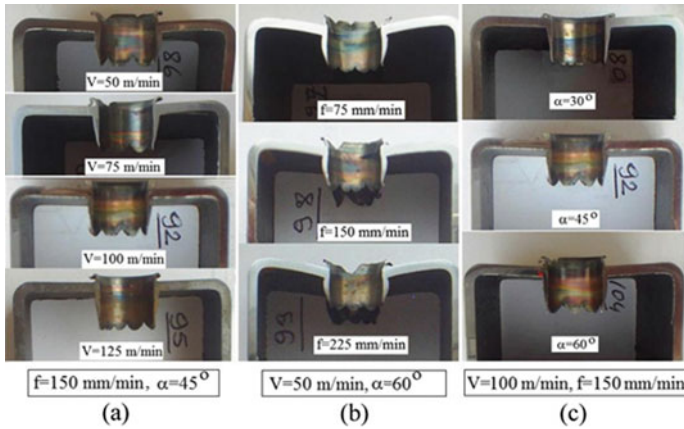


Fig. 7 Bushing height (Source [14], p. 474)

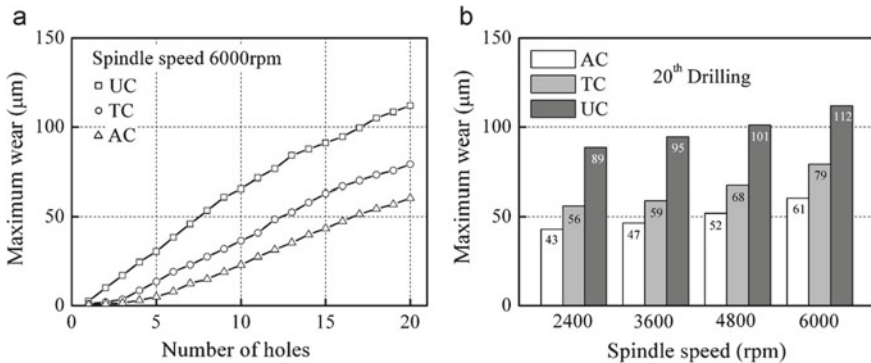


Fig. 8 Wear analysis of different types of drill (Source [24], p. 84)

shown, comparison between spindle speed and wear. In both the cases it has noted that uncoated tool has maximum wear. Whereas PVD AlCrN coating exhibit lesser wear that PVD TiAlN coating.

4 Conclusion

The overview of emerging friction drilling technique has been reported in this review. The following points has been drawn from the experience of review.

1. The key highlighting factor is bushing height in sheet metal, the maximum bushing height produced depends upon the tool, material and input parameters used.

2. Coated friction drilling tool helps to reduce wear and improve tool life.
3. Friction drilling is suitable for only material less than 4 mm thickness.
4. Surface roughness can be reduced that depends upon input parameters, coated tool and work piece material.
5. Selection of tool material is another major criteria. The tool material should be based on hardness, wear resistance and higher temperature resistance.

Reference

1. Alphonse M, Raja VKB, Gupta M (2020) Investigation on tribological behavior during friction drilling process—a review. *Tribol Ind* 42(2):200–213
2. Alphonse M, Raja VKB, Gupta M, Logesh K (2020) Optimization of coated friction drilling tool for a FML composite. *Mater Manuf Process* 1–10
3. Jesudoss NR, Kumar HR (2017) Process optimization for maximizing bushing length in thermal drilling using integrated ANN—SA approach. *J Braz Soc Mech Sci Eng* 39:5097–5108
4. Raja VKB, Rajasekaran R, Francis AJ (2014) An overview of non traditional drilling process. *IJAER* 9(23):23145–23153
5. Kilickap E, Huseyinoglu M, Yardimeden A (2011) Optimization of drilling parameters on surface roughness in drilling of AISI 1045 using response surface methodology and genetic algorithm. *Int J Adv Manuf Technol* 52(1–4):79–88
6. Rawat S, Attia H (2009) Characterization of the dry high speed drilling process of woven composites using machinability maps approach. *CIRP Ann—Manuf Technol* 58(1):105–108
7. Ozek C, Demir Z (2013) Investigate the surface roughness and bushing shape in friction drilling of A7075-T651 and st 37 steel. *TEM J* 2(2):170–180
8. Demir Z, Özok C (2014) Investigate the effect of pre-drilling in friction drilling of A7075-T651. *Mater Manuf Process* 29(5):593–599
9. Özler L (2019) The influence of variable feed rate on bushing and surface roughness in friction drilling. *J Braz Soc Mech Sci Eng* 41(8):1–9
10. Miller SF, Blau PJ, Shih AJ (2007) Tool wear in friction drilling. *Int J Mach Tools Manuf* 47(10):1636–1645
11. Miller SF, Shih AJ (2007) Thermo-mechanical finite element modeling of the friction drilling process. *J Manuf Sci Eng* 129(3):531–538
12. Raju BP, Swamy MK (2012) Finite element simulation of a friction drilling process using deform-3D. *Int J Eng Res Appl* 2(6):716–721. ISSN 2248–9622
13. Dehghan S, Ismail MIS, Ariffin MKA, Baharudin BTHT (2018) Experimental investigation on friction drilling of titanium alloy. *Eng Solid Mech* 6(2):135–142
14. Ozler L, Dogru N (2013) An experimental investigation of hole geometry in friction drilling. *Mater Manuf Process* 28(4):470–475
15. Somasundaram G, Rajendra Boopathy S, Palanikumar K (2012) Modeling and analysis of roundness error in friction drilling of aluminum silicon carbide metal matrix composite. *J Compos Mater* 46(2):169–181
16. Boopathi M, Shankar S, Manikandakumar S, Ramesh R (2013) Experimental investigation of friction drilling on brass, aluminium and stainless steel. *Procedia Eng* 64:1219–1226
17. Ku WL, Hung CL, Lee SM, Chow HM (2011) Optimization in thermal friction drilling for SUS 304 stainless steel. *Int J Adv Manuf Technol* 53(9–12):935–944
18. Davim JP, Reis P, António CC (2004) Experimental study of drilling glass fiber reinforced plastics (GFRP) manufactured by hand lay-up. *Compos Sci Technol* 64(2):289–297
19. Waleed WA, Chathriyan A, Vimal RSS (2018) Experimental investigation on the influence of process parameters in thermal drilling of metal Matrix Composites. *FME Trans* 46(2)

20. BB, HKA, Kaya MT, Aktas A (2014) An experimental study on friction drilling of ST 12 steel. *Trans Can Soc Mech Eng* 38(3):320–329
21. Alphonse M, Raja VKB, Logesh K, Murugu Nachippan N (2017) Evolution and recent trends in friction drilling technique and the application of thermography. *IOP Conf Ser Mater Sci Eng* 197(1):1–15
22. Alphonse M, Raja VKB, Gupta M (2020) Materials today: proceedings optimization of plasma nitrided, liquid nitrided & PVD TiN coated H13-D2 friction drilling tool on AZ31B magnesium alloy. *Mater Today Proc* 2–10
23. Zurrayen M et al (2018) Characterization of tool wear in friction drilling. *J Tribol* 17(April):93–103
24. Lee SM, Chow HM, Huang FY, Yan BH (2009) Friction drilling of austenitic stainless steel by uncoated and PVD AlCrN—and TiAlN-coated tungsten carbide tools. *Int J Mach Tools Manuf* 49(1):81–88

Statistical and Multi-attribute Analysis in Hardened Steel Turning Under Vegetable Oil-Based MQL



A. A. Chavan and V. G. Sargade

Abstract This research discusses statistical and multi-attribute analysis in hard machining of AISI 52100 steel by using TiSiN-TiAlN coated carbide tool with three different vegetable oils based minimum quantity lubrication (MQL) environment. These vegetable oils are coconut oil, soyabean oil, and palm oil. Moreover, these three vegetable oil-based MQL results are compared with dry machining. The full factorial method of design experiments is used. To analyze the results statistical technique, main effects plot and analysis of variance (ANOVA), and multi-attribute grey relational analysis (GRA) approaches were used. The feed exhibits direct proportionality with chip thickness ratio, surface roughness, and cutting forces, on the contrary, the cutting speed shows a reverse trend. Besides, the results show that optimum process parameters obtain are at low feed (f : 0.08 mm/rev) and medium cutting speed, (V_c : 140 m/min), in the soyabean oil-based MQL.

Keywords Hard turning · MQL · Vegetable oil · ANOVA · GRA

1 Introduction

The medium and high plain carbon steel is heat treatable steel, which forms a metastable martensite phase in the hardened state that helps to an improved desirable hardness of workpiece. The typical properties of hardened steels are resistant to wear, excellent corrosion resistance against chemical environments, higher abrasion resistance for severe sliding purpose, and durability [1, 2]. Due to these properties of hardened steels are extensively used in many industries for making different geometrical parts, including gear shaft, main axis, valve rod, connecting rod, aircraft bearing, mandrel bars, punching, and machine tools. In the advancement of the machining process, hardened steel turning has replaced as a grinding process because the grinding process required more considerable machining time and has a limited shape of parts produced capability [3]. Hence, to improve metal removal rate with

A. A. Chavan (✉) · V. G. Sargade
Mechanical Engineering Department, Dr. Babasaheb Ambedkar Technological University,
Lonere, Raigad 402103, Maharashtra, India
e-mail: ajaychavan@dbatu.ac.in

acceptable surface quality and dimensional accuracy in hard turning, a single point cutting tool inserts are adopted in industrial applications [4]. But it generates high temperature at high cutting speed and feed at the tool-workpiece interface in high hardness steel [2]. Due to this, the tool rigidity and strength get reduces which affects the life of tool insert, especially in coated carbide tool [3, 5]. The effective cooling and lubrication are beneficial to improve the performance of coated carbide tools while hard machining. But flood cooling is health hazards and costlier one in comparison with the near-dry technique [6, 7].

Researchers enlighten the machinability of various hardened steel in hard turning by using cost effective coated carbide tool in sustainable machining environments. Li et al. [8] studied the effect of various coated carbide tool in high-speed milling of hardened AISI 4340 steel. In which the TiN/TiCN/TiAlN carbide tool shows effective performance in comparison with others. Panda et al. [9] explored the performance and practicability of the cemented carbide insert in hard turning of AISI 52100 steel. The performance is analyzed through development of statistical regression model for flank wear, surface roughness and chip morphology which is adequate at a 95% confidence interval. Sredanivic and Lacic [10] studied performance of carbide tool coated with TiSiN/TiAlN in hard turning of AISI 52100 steel under high-pressure jet cooling technique. They found higher tool life, improved productivity, and low surface roughness. Chinchankar et al. [11] modeled surface roughness of AISI 52100 steel in hard turning under dry, vegetable oil, and water-based cutting fluid. They found that at higher cutting speed, coconut oil shows lower surface roughness.

Alok and Das [12] used multi-objective optimization technique, desirability function, for AISI 52100 steel turning by a new carbide HSN2 coated tool. They observed optimized results were found at low level of feed, medium level of cutting speed, and low level of depth of cut. Awale and Inamdar [13] done high speed turning of AISI S7 steel in hardened state and optimized process parameters by applying multi-objective analysis GRA. Optimized turning parameters were cutting speed Vc: 450 m/min, nose radius: Rn: 1.2 mm, depth of cut dc: 02 mm and feed Vf: 0.05 mm/rev.

The aforesaid analysis indicates that the past research work mainly focused on machining of hardened steels using coated carbide tools in dry and near-dry condition, specially the MQL technique. But, limited studies are done on the comparative performance of different vegetable oil-based MQL. Besides, multi-objective optimization for the selection of proper vegetable oil with appropriate cutting parameters is not reported. Therefore, this study focused on statistically analysis and GRA based multi-objective optimization in AISI 52100 steel hard turning by PVD coated carbide tool inserts in to the various vegetable oils based MQL environments.

2 Methodology

2.1 Statistical Analysis

The statistical analysis is done by using ANOVA and the main effects plot. The ANOVA is a technique used to check a significant difference between means of two or more factors. It checks the impact of the parameter by comparing all the sample's mean.

2.2 Multi-Attribute Analysis (GRA)

The ultimate aim of the industry is maximum manufacturing from minimum resources. However, the researcher has developed various techniques in this regard. GRA is one of the techniques which trying to full fill this aim by optimizing multiple objectives to provide the best solution. This technique is applied in the turning process by researchers who specified detailed steps accordingly [12–15]. The GRA optimization technique is explained step by step as follow:

Step I: Selection of Parameter, Experimental Run and Response Measurement.

This step is the primary process of full factorial design, which includes the selection of parameters, actual experimental runs, and measurement of response. The measured responses are considered for further analysis of GRA.

Step II: Normalization of Responses.

A normalization of measured output from the experimental run to convert the original sequence into a comparable sequence. This linearity of the sequence is normalized by analysing the nature of sequence in two conditions; larger-the-better and smaller-the-better. Hence, to transfer the sequence of original to sequence of comparable in 'smaller-the-better' condition, Eq. 1 is considered.

$$x_i^*(k) = \frac{\max x_i^{(o)}(k) - x_i^{(o)}(k)}{\max x_i^{(o)}(k) - \min x_i^{(o)}(k)} \tag{1}$$

Similarly, to convert the original sequence in comparable form of larger-the-better condition Eq. 2 used.

$$x_i^*(k) = \frac{x_i^{(o)}(k) - \min x_i^{(o)}(k)}{\max x_i^{(o)}(k) - \min x_i^{(o)}(k)} \tag{2}$$

Step III: Deviation in Sequences, ($\Delta 0_i(k)$), Calculation.

The variance between a sequence of reference, $x_0^*(k)$, and sequence of comparable, $x_i^*(k)$, afterward normalization is known as deviation in sequence, $\Delta 0_i(k)$. It is calculated from Eq. 3. However the value of $x_0^*(k)$ was 1.

$$\Delta 0_i(k) = |x_0^*(k) - x_i^*(k)| \tag{3}$$

Step IV: Grey Relational Coefficient Calculation.

The variation in between higher and real normalized response parameter is a grey relational coefficient (GRC) of a particular sequence. The Eq. 4 represents GRC.

$$\gamma(x_0(k), x_i(k)) = \frac{\Delta \min + \zeta \Delta \max}{\Delta 0_i(k) + \zeta \Delta \max} \tag{4}$$

Step V: Grey relational grade, (GRG), determination,

The GRG is the final output of this analysis, which provides an optimum condition for experiments. It GRG is calculated from Eq. 5.

$$\gamma(x_0, x_i) = \frac{1}{m} \sum_{i=1}^m \gamma(x_0(k), x_i(k)) \tag{5}$$

Step VI: Determination of optimum parameters.

A post-analysis step to get more optimize conditions of sequence. The GRC of each sequence considered as output for the next analysis. The higher value indicates better performance. Therefore, larger-the-better function is used for the GRG analyses.

3 Experimental Details

3.1 Workpiece

A hardened AISI 52100 bearing steel (59 ± 2 HRC) is considered as work material in this analysis. The nominal chemical composition is presented in Table 1.

Table 1 Chemical Composition in wt. % for work material

Elements	C	P	Ni	Cr	S	Mn	Mo	Si	Fe
Contents (wt. %)	0.41	0.012	0.11	1.10	0.0290	0.74	0.170	0.26	Balance

3.2 Cutting Tool

The cutting insert, PVD coated TiSiN/TiAlN carbide (make: SECO, Code TH1000), was mounted on tool holder, PCLNL2525M12, make widia, are used in this analysis.

3.3 Parameter Selection and DOE

Four strategies are planned based on a summary of the literature review. These are (1) Dry (2) MQL1 using coconut oil (3) MQL2 using soybean oil (4) MQL3 using palm oil environment. To perform a systematic experiment design of experiment is the best method to plan. Hence, the experiment was designed using a full factorial design matrix. In this design, two machining factors, cutting speed and feed, having three-level and four different machining environment were considered. The process parameters and their levels are indicated in Table 2.

Table 2 Controlled and constant parameters with their levels

Factors	Parameter	Levels			
		i	ii	iii	iv
Control	Feed, f (mm/rev)	0.08	0.14	0.2	–
	Cutting Speed, V_c (m/min)	80	140	200	–
	Machining Environment	Coconut oil MQL1	Soyabean oil MQL2	Palm oil MQL3	Dry
Constant	Depth of Cut: 0.3 mm				
	MQL Flow Rate: 100 ml/hr				

Table 3 Experimental layout

Exp. No	Machining Environment	Feed (mm/rev)	Cutting speed (m/min)
01	Dry	0.08	80
02		0.14	80
03		0.20	80
04		0.08	140
05		0.14	140
06		0.20	140
07		0.08	200
08		0.14	200
09		0.20	200

However, Table 3 shows experimental design layout for selected cutting parameters, feed and cutting speed, for dry machining environment. Same design layout is repeated for MQL1, MQL2 and MQL3 machining environment. Hence total no of experiment is 36 with all combination.

3.4 Experimental Setup

The experimental setup consists of an MQL system (Fig. 1a) and its setup, i.e., nozzle positioning on tool turret near to rake face of the tool (see Fig. 1b). A workpiece of AISI 52100 steel rod (\varnothing 90 mm and 210 mm long) was clamped on 3-jaw chuck of CNC turning lathe, Jobber XL (Make: Micromatic-ACE). The three-component cutting force dynamometer, KISTLER 9257BA, is used to measure cutting forces on tooltip during turning. For each experiment, the new cutting edge of the insert is used. The machining length was kept 30 mm for each experiment. The roughness of machined surface was measured by MITUTOYO SJ-301 surface roughness tester after each experiment by taking 3 readings around the *circumference* of the machined surface considering 0.8 mm as a cut-off length.

4 Results and Discussion

The findings are evaluated and discussed using the statistical approach and the GRA multi-objective optimization methodology.

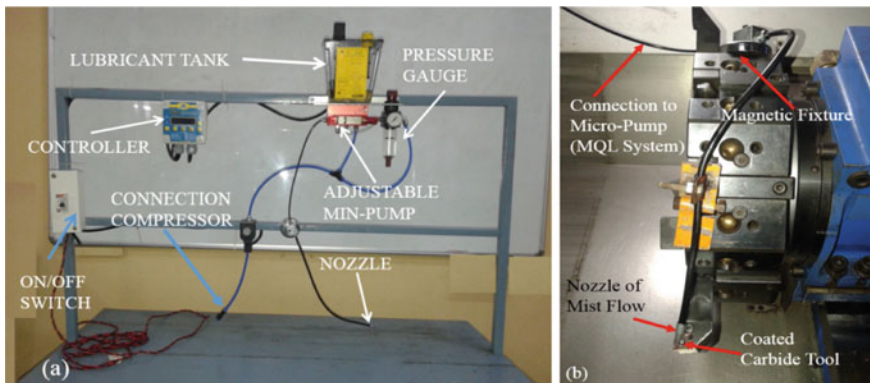


Fig. 1 Photographic view of **a** MQL system **b** Experimental Set-up

Table 4 ANOVA for Chip thickness ratio in different machining environment

Parameters	DF	Adj. SOS	Adj. MOS	F	P	% Contribution
Machining Environment	03	0.2678	0.089264	11.70	0.000	29.58
Cutting Speed	02	0.1574	0.078714	10.32	0.000	17.39
Feed	02	0.2664	0.133203	17.46	0.000	29.73
Error	28	0.2137	0.007630			
Total	35	0.9053				

4.1 Statistical Analysis

The results were presented using main effects plot and ANOVA, to determine significance of input factor on output parameters.

4.1.1 Chip Thickness Ratio

The cutting ratio or chip thickness ratio is the critical characteristic of machinability, which represents the consumed energy by plastic deformation in metal cutting. It is the ratio of unreformed chip (ac) to the chip after the cut (ao). The ANOVA results for the chip thickness ratio has been tabulated in Table 4. The effect of cutting speed, feed and machining environment is on the chip thickness ratio is represented main effects plots, Fig. 2. From ANOVA, it indicates that the machining environment, cutting speed, and feed substantial influence on chip thickness ratio. The P-value of the machining environment, cutting speed, and feed is lower than 0.05 which indicates the confidence level of parameters is 95%. The percentage contribution is 29.58% for the machining environment, 17.39% for feed, and 29.73% for cutting speed.

The main effects plot indicates that soyabean oil MQL2 shows higher CTR. The chip thickness ratio is higher at lower cutting speed and low for high cutting speed. At lower cutting speed, the thin chips produced due to a shorter share plane. However, at higher cutting speed, thicker chips are formed due to the long share plane. The feed represents a reverse trend than cutting speed. As feed increase CTR increase, because un-cut chip thickness is a directly promotional to feed. The chip thickness ratio is optimum at low cutting speed V_c : 80 m/min, and high feed f : 0.2 mm/rev in soyabean oil MQL2 environment.

4.1.2 Cutting Forces

Cutting force provides essential information for selection of cutting tool inserts in terms of cutting conditions which calculates the productivity through power requirements. The ANOVA results indicates effect of machining parameters and machining environment on cutting force are represented in Table 5 and Fig. 3 shows the main

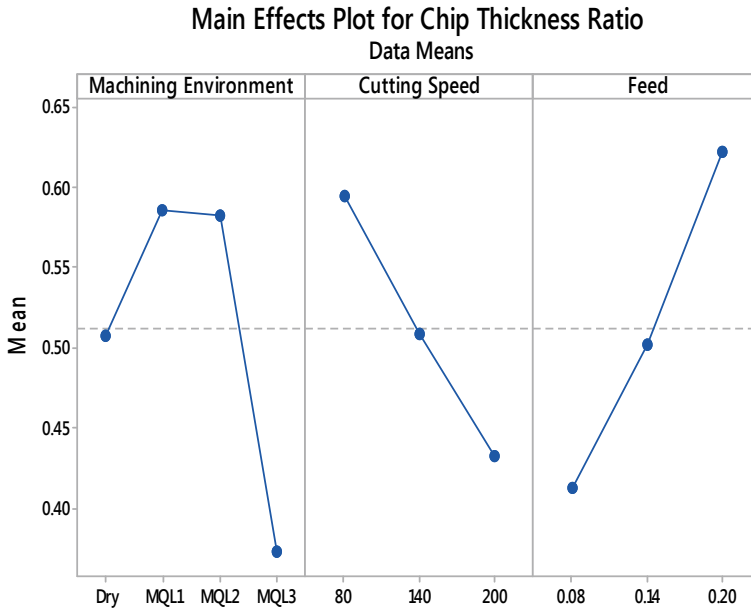


Fig. 2 Main effects plot for chip thickness ratio

Table 5 Analysis of variance (ANOVA) for cutting force

Parameters	DF	Adj. SOS	Adj. MOS	F	P	% contribution
Machining Environment	03	285,101	95,034	51.72	0.000	57.73
Cutting Speed	02	14,130	7065	3.85	0.033	02.86
Feed	02	143,145	71,573	38.96	0.000	28.99
Error	28	51,445	1837			
Total	35	493,821				

effects plot. It observed from ANOVA that machining environment, feed, and cutting is a significant parameter for the cutting force at confidence level of 95%. However, the percentage contribution of machining environment, feed, and cutting speed is 57.73%, 28.99% and 2.86%, respectively.

The main effects plot indicates an increase in cutting speed tends to decrease cutting forces. This is done because workpiece material is getting softened ahead of the cutting tool due to an increase in the temperature at the cutting zone at high cutting speed. Further, it is observed that cutting forces have a higher value at a higher feed. Also, the main effects plot indicates that cutting forces are higher in dry machining environment and decreasing in MQL environments. Palm oil MQL3 shows the lowest value of cutting forces as compared to MQL1 and MQL2. The soybean oil MQL3 provides better lubrication and cooling as compared to other MQL environments and dry environments.

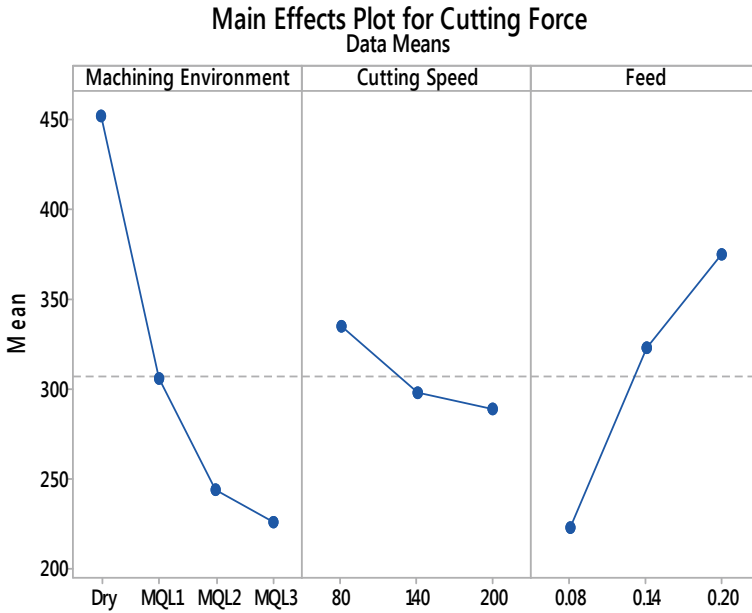


Fig. 3 Main effects plot for cutting force (N)

4.1.3 Surface Roughness R_a

Surface roughness is a crucial parameter in expectance and rejections of components in the quality section as it affects the fatigue strength, corrosion resistance, coefficient of friction, and services life of the machined product. The ANOVA results, Table 6, for surface roughness indicates that the feed and machining environment are significant. The P-value of the machining environment and feed is less than 0.05 at a 95% confidence level. The machining environment contributes 51.50% and feed at the second-highest, 36.86%. The cutting speed does not present statistical significance on the obtained surface roughness because of their smaller F-value; also, its percentage contribution is below 1.

Table 6 ANOVA for Surface Roughness, R_a

Parameters	DF	Adj SOS	Adj. MOS	F	P	% Contribution
Machining Environment	03	18.689	6.22983	42.20	0.000	51.50
Cutting Speed	02	0.0863	0.04314	00.29	0.749	0.24
Feed	02	13.379	6.68985	45.31	0.000	36.86
Error	28	4.1340	0.14764			
Total	35	36.289				

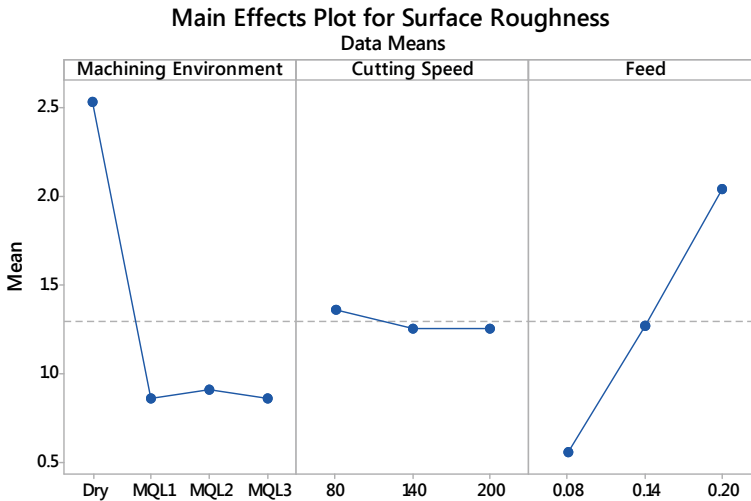


Fig. 4 Main effects plot for surface roughness R_a (μm)

The surface roughness increased with increasing the feed rate and decreasing cutting speed, shown in Fig. 4. The reason behind this is a basic formulation of surface roughness, i.e., at a constant nose radius of a single-point cutting tool, the square of feed is directly preproportional to surface roughness. Cutting speed shows a reverse tendency, that increase in cutting speed tends to decrease in surface roughness. However, the dry machining environment shows high surface roughness in compression with the MQL machining environment. All MQL environment shows a similar effect on surface roughness. The optimum condition for lower surface roughness form the main effect plot is at 200 m/min and 0.08 mm/rev in the coconut oil MQL1 environment.

4.2 Multi-Attribute Analysis-GRA

A multi-attribute analysis by GRA is applied to response parameters in sequence. The responses are cutting force, surface roughness, and chip thickness ratio to evaluate machinability. Lower cutting forces and surface roughness with a higher chip thickness ratio is an indication of good machinability. Hence cutting forces and surface roughness are categorized under smaller-the-better condition, and the chip thickness ratio in higher-the-better. The normalization of responses, cutting forces, surface roughness and chip thickness, are done by using Eq. 1 and Eq. 2. Then, Eq. 3 is used to evaluate the deviation sequences. In the next step distinguishing coefficient, $\zeta = 0.5$ was substituted in Eq. 44 to calculate the grey rational coefficient. Then, by considering the equal weight to response parameters in the process, the grey relational grade (GRG) has been determined by using Eq. 5. The highest value of GRG indicates

Table 7 Average GRG value of each processing parameters with a rank

Factor	Level				Max–Min	Ranking
	I	II	III	IV		
Cutting Speed	0.631	0.626	0.626	–	0.005	3
Feed	0.713	0.631	0.573	–	0.140	2
Cutting Environment	0.479	0.665	0.703	0.665	0.224	1

optimal condition where objective of every response are fulfilled. The experiment number 22, f:0.08 mm/rev and Vc:140 m/min for soyabean oil-based MQL environment, has the highest GRG value (0.787) in all experimental. The optimum response for expt. number 22 is cutting force (168.86 N), surface roughness (0.397 μm), and chip thickness ratio (0.478).

The averaging of GRG value of each input parameter at every level is calculated. Then maximum to minimum difference is calculated in average value of GRG for each level. For example, machining environments, the average GRG value for each level dry, coconut oil MQL1, soyabean oil MQL2, and palm oil MQL3 calculated by averaging the GRG of experiments run 1–9, 10–18, 19–27, 28–36 respectively. Similarly, it is formulated for other parameters also. Then the difference between maximum GRG value to minimum GRG value of each parameter are calculated, which provides a ranking of input parameters, as shown in Table 7.

The ANOVA has been performed to find the significance of cutting speed, feed, and machining environment, on GRG. Table 8 indicates ANOVA results for GRG, in which the P-value machining environment and feed are less than 0.05. It means to feed, and the machining environment has a significant contribution to the multi-objective performance of the machining process. ANOVA of GRG also stated a similar order of rank got by machining parameters.

The main effects plot of GRG, Fig. 5, shows the influence of input parameters on multi-objective performance GRG. The plot indicates that soyabean oil MQL2 has higher GRG, and the dry environment has lowered one: coconut oil and palm oil MQL show equal performance. The low feed shows higher GRG and high feed low GRG. Medium cutting speed indicates higher GRG. The optimum parametric conditions are indicated by higher value of GRG in the main effect plot, at medium

Table 8 ANOVA for GRG

Source	DF	Adj. SOS	Adj. MOS	F	P
Machining Environment	03	0.275383	0.091794	67.99	0.000
Cutting Speed	02	0.000210	0.000105	00.08	0.925
Feed	02	0.134653	0.067327	49.87	0.000
Error	28	0.037802	0.001350		
Total	35	0.448048			

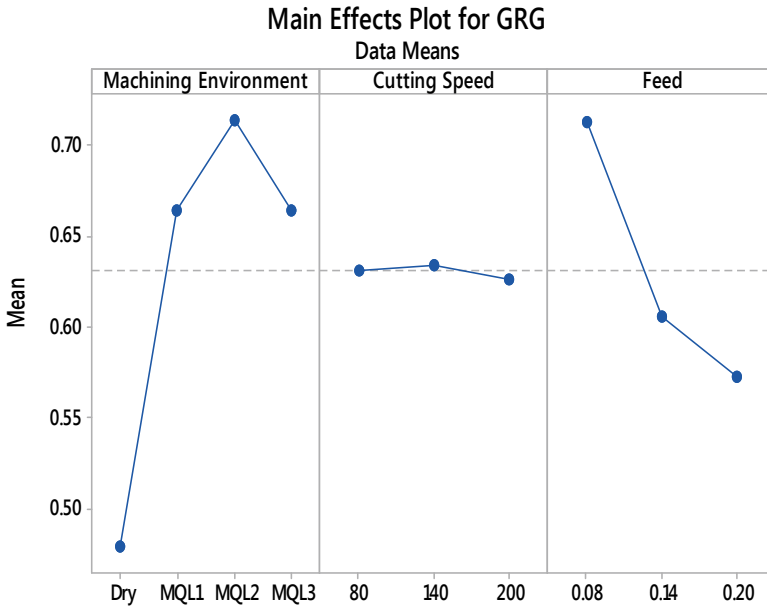


Fig. 5 Main effects plot for GRG

low feed (0.08 mm/rev) and cutting speed (140 m/min) in the MQL2 environment, is an optimum parametric combination.

5 Conclusion

The analysis of effect of input parameters and multi-attribute analysis of hardened AISI 52100 steel turning using coated carbide tool under three different vegetable oils based minimum quantity lubrication (MQL) environment on cutting force, chip thickness ratio and surface roughness shows following findings.

1. The lower cutting forces are observed at higher cutting speed (200 m/min), and lower feed (0.08 mm/rev) in palm oil based MQL environment.
2. The surface roughness, R_a , has a lower value at higher cutting speed (200 m/min), and lower feed (0.08 mm/rev) in coconut oil based MQL environment.
3. The chip thickness ratio scores higher value at low cutting speed (80 m/min), and high feed (0.20 mm/rev) in soyabean oil based MQL environment.
4. MQL environment shows excellent performance as compared to the dry environment.
5. The multi-objective optimization GRA indicates experimental run 22, medium cutting speed (140 m/min) and Low feed (0.08 mm/rev), in soyabean oil

based MQL environment, gives a higher value of GRG (0.809). The optimum responses for this experiment are cutting force (168.86 N), surface roughness (0.397 μm), and chip thickness ratio (0.478).

References

1. Satelkar DS, Jogi BF, Thorat SB, Chavan AA (2020) Activated pulsed-tungsten inert gas welding of DSS 2205. *Techno-Societal* 2018:511–521
2. Bartarya G, Choudhury SK (2012) State of the art in hard turning. *Int J Mach Tool Manuf* 53:1–14
3. Shihab SK, Khan ZA, Mohammad A, Siddiquee AN (2014) A review of turning of hard steels used in bearing and automotive applications. *Prod Manuf Res* 2:24–49
4. Thorat S, Sadaiah M (2019) The effect of residual stresses, grain size, grain orientation, and hardness on the surface quality of Co–Cr L605 alloy in Photochemical Machining. *J Alloys Compd* 804:84–92
5. Chinchanikar S, Choudhury SK (2015) Machining of hardened steel Experimental investigation performance modeling and cooling techniques: A review. *Int J Mach Tools Manuf* 89:95–109
6. Chavan A, Sargade V (2020) Surface integrity of AISI 52100 steel during hard turning in different near-dry environments. *Adv Mater Sci Eng* 2020:1–13
7. Liew PJ, Shaaroni A, Sidik NAC, Yan J (2017) An overview of current status of cutting fluids and cooling techniques of turning hard steel. *Int J Heat Mass Transf* 114:380–394
8. Li Y, Zheng G, Cheng X, Yang X, Xu R, Zhang H (2019) Cutting performance evaluation of the coated tools in high-speed milling of aisi 4340 steel. *Materials (Basel)* 12:1–16
9. Panda A, Sahoo AK, Rout AK (2017) Statistical regression modeling and machinability study of hardened AISI 52100 steel using cemented carbide insert. *Int J Ind Eng Comput* 8:33–44
10. Sredanović B, Globočki Lakić G (2017) Hard turning of bearing steel AISI 52100 with carbide tool and high pressure coolant supply. *J Brazilian Soc Mech Sci Eng* 39:4623–4632
11. Chinchanikar S, Salve AV, Netake P, More A, Kendre S, Kumar R (2014) Comparative evaluations of surface roughness during hard turning under dry and with water-based and vegetable oil-based cutting fluids. *Procedia Mater Sci* 5:1966–1975
12. Alok A, Das M (2019) Multi-objective optimization of cutting parameters during sustainable dry hard turning of AISI 52100 steel with newly develop HSN2-coated carbide insert. *Meas J Int Meas Confed* 133:288–302
13. Awale A, Inamdar K (2020) Multi-objective optimization of high-speed turning parameters for hardened AISI S7 tool steel using grey relational analysis. *J Brazilian Soc Mech Sci Eng* 42:356 <https://doi.org/10.1007/s40430-020-02433-z>
14. Nipanikar S, Sargade V, Guttedar R (2018) Optimization of process parameters through GRA, TOPSIS and RSA models. *Int J Ind Eng Comput* 9:137–154
15. Sonawane GD, Sargade VG (2019) Evaluation and multi-objective optimization of nose wear, surface roughness and cutting forces using grey relation analysis (GRA). *J Brazilian Soc Mech Sci Eng* 41:1–13

Technology For Rural and Agricultural Employment Generation

Design and Analysis of Automated Detaching of Coconut and Branches from Tree Using a Robot



Ayush Narayan Malviya, Gokul Kumar Vishwanathan, Tejas walke, and Rahul K. Patil

Abstract The motivation of this paper is to make the robot interact with surrounding and cut the coconut autonomously. As technology is getting advanced things are getting simpler for us. By the mean of Autonomous it is possible to increase productivity and get things easier. The robot consists of hexagon chassis of two segments, in between two segments three motors and wheels are assembled. For automatic arrangement of robot with tree diameter, lead screw mechanism is used. The chassis is designed with the help of CAD software and analysis was done considering maximum load factor. For rotation robot about tree axis, motor mount is made such that it can rotate up to 90°. The motion of robot is manually controlled from ground using remote. For cutting of Coconuts robotic arm is used, on which cutting plate is mounted. Webcam mounted on robotic arm is used for giving feedback to controller. Motor driver, raspberry pi used for giving motion to robot.

Keywords Limit switch · Webcam · DC motor · Robotic arm · Threaded rod/lead screw mechanism

1 Introduction

Coconuts and coconut parts are used in wide applications in our daily needs. India produces near to 25% of the world's coconut meat and fiber, which produces oil, shampoo, rope, and doormats. To get coconuts laborers required much effort to get

A. N. Malviya (✉) · G. K. Vishwanathan · T. walke · R. K. Patil
Department of Mechanical Engineering, School of Mechanical and Civil Engineering, MIT
Academy of Engineering, Alandi, Pune 412105, India
e-mail: anmalviya@mitaoe.ac.in

G. K. Vishwanathan
e-mail: vgkumar@mitaoe.ac.in

T. walke
e-mail: tswalke@mitaoe.ac.in

R. K. Patil
e-mail: rkpatil@mitaoe.ac.in

it from a tree. India produces maximum coconuts all over the world. But the farmers get a lot of problems in getting coconuts manually from the tree. All over the world farmers have difficulties to harvest coconuts. By now in maximum areas, farmers climb the tree to detached coconuts. As the growth of India is growing economically, numbers of workers are also moving to do jobs. Cutting of coconuts manually is a risky job, there are chances of getting an accident. By the survey it is found that the person who climbs tree get skin infection after some year. As we know that there are lots of challenges faced while picking the coconut by climbing the tree. The user used to climb the coconut tree without any safety instruments and also it was time-consuming. So we came up with a solution that will make the user do the job with more safety and also in very less time with help of the robot that is designed below. To harvest coconuts, a better solution has to come, since it is difficult to detached coconuts. So to reduce farmer effort this paper is to provide a solution for them to detach coconut by the mean of Robot. The robot is controlled from the ground with the help of a remote. It will easily touch at top of the tree which of any irregular shape without any slippage. The robot is capable to rotate about three axes. The cost of a robot will be easily payable by rural area workers.

Here there is no risk of human life since the user will be directly controlling this via his Mobile App. The robot will also consist of Raspberry pi camera which will help in live streaming of coconut. This will help the user to identify the position of coconut through is Mobile App. Then the bot will be controlled accordingly to cut the coconut.

Dubey [1] a robot has 2 layers hexagonal chassis and working is done by using a lead screw mechanism. Calculation of power and Torque required to climb is done. Robot and cutting arm is controlled by wired controller. Jacob [2] autonomous tree climbing and pesticide spraying robot. The robot analyses and climb on the tree autonomously. Tree climbing Robot works on a principle of human pole climbers and relies on wheel mechanism to ensure smooth and fast climbing motion. The robot has made using 3D software and implements successfully. Electronic parts were accommodated on the electronic board perfectly. Calculation of power required to, upward force, and torque are done. This robot has been only a single-layer hexagonal structure hence it is not dynamically stable and the degree of freedom of robot is 2, which restricts its motion. Senthil [3] in this paper focuses on the designing and automated tree climbing robot, Tree robot which doesn't require human labor to the accompany the device but only to control it from the ground using a remote control. Widanagamage [4] has design Autonomous Tree Climbing Robot Utilizing the Four Bar Linkage System designed by the work was presented in this paper, it taken into focuses on designing Tree Robot. The mechanical structure is designed to move the structure upwards against the gravitational forces in the successive upper body and lower body movements similar to a tree climber. Yoon and Rus [5] this project is consist of making autonomous robot that will climb many large civil and industrial structures (e.g. bridges, towers, communication antennas, and construction scaffolds) and space structures (e.g. space station components and solar panel supports.). All the structural parts consist of PCB boards. A 6-DOF manipulator composed of two 3-DOF Shady3D modules and a passive truss element. The robot is able to move in

all the directions, one side is get fixed with another bar and another side get removed to attached with another bar. “Robot Modeling and Control” written by Spong et al. [6]. Explained detailed about robot kinematics, motion planning, dynamic algorithm, trajectory optimization, and control of robots is explained.

Hence by studying and analyzing the issues and drawbacks faced by the above mentioned research papers, we came to a solution which we will be explaining below.

2 Design of Robot

The working of a robot overall depends on the design of the robot. Design of robot consists of three different branches:

1. Mechanical
2. Computer
3. Electronics.

Mechanical

The overall performance depends on the mechanical design of the robot. It consists of frame/chassis, selection of Chassis is done by the analysis of a given factor:

- Maximum load
- Material
- Weight
- Area constraints
- Stability.

After analyzing different frames, the hexagonal frame is selected as shown in Fig. 1a. Which consists of 2 stages, 2 stages are used for increased stability and to mount different components. Three opposite side is used for a motor mount. Two adjacent

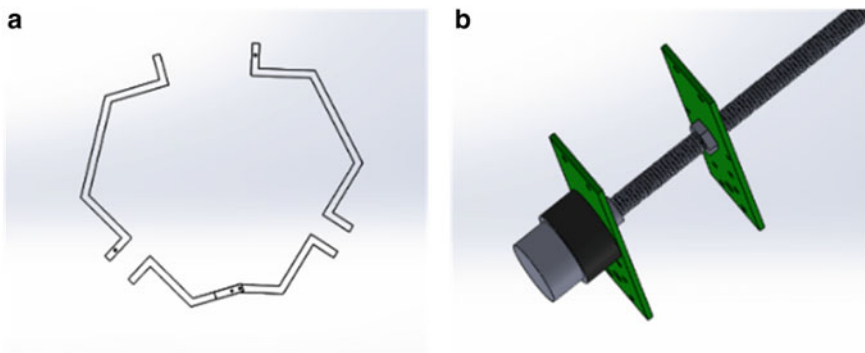


Fig. 1 a Hexagonal frame. b Lead screw mechanism

sides are used for the lead screw mechanism for variable length as required. And the front side is used for installation to a tree. With the help of the lead screw mechanism, the robot diameter adjusted with the help of remote such that robot will be fitted to a tree as shown in Fig. 1b.

Figure 2a, b shows the Isometric and the top view.

To reduce weight and simple manufacturing motor mount is made by a 3D printer using PLA material. The motor mount is assembled on a 3 mm Aluminum plate, and the Aluminum plate is attached with a frame with the help of springs. To maintain friction between wheels and trees, springs are used.

As shown in Fig. 3a spring attached with the plate and motor mount used to maintain contact with a tree. Initially, the robot is assembled with a tree manually by the worker. Then as per diameter worker will be fixed the plate with the help of a screw. As there are many holes, the hole are use as per requirement, shown in Fig. 3b.

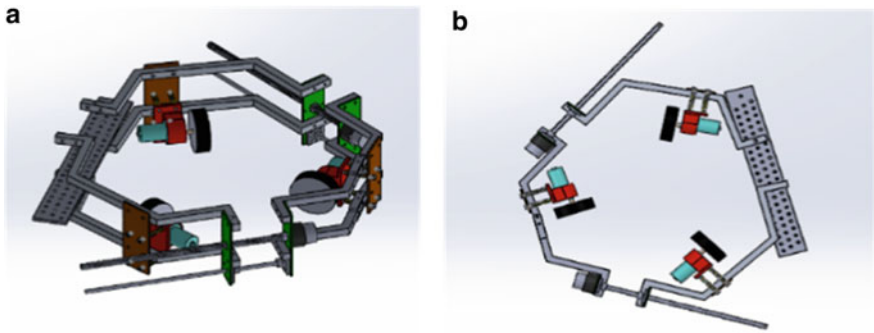


Fig. 2 a Isometric view. b Top view

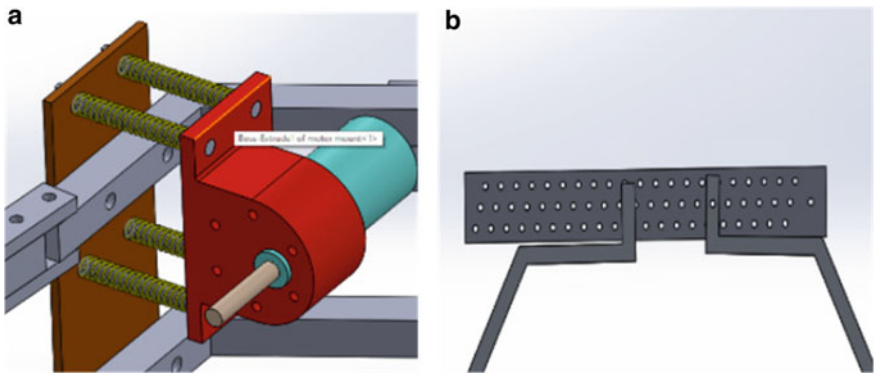


Fig. 3 a Motor mount. b Variable sizing plate

2.1 Dimensions

Design of robot is done such that, as per requirement of diameter of tree, bot will adjust accordingly. As shown Fig. 4a, b minimum diameter that robot can cover is 150 mm and maximum diameter of 400 mm. To increase diameter of bot, side motors will rotate in Clockwise direction and to decrease diameter of bot motor will rotate in anticlockwise direction.

Properties of material used (Aluminum) for making frame/chassis given (Table 1).

After defining material to all different parts and considering the load of electronic parts, the center of Mass of final assembly comes at the center of the robot i.e. ($X \approx 0, Y \approx 0, Z \approx 0$). So that robot remains balanced at the time of its working. The Analysis was done on Solid Works software which is given below.

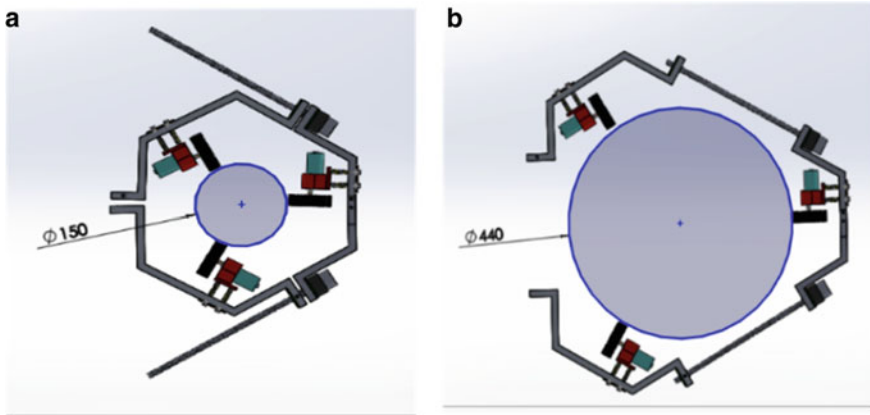


Fig. 4 a Minimum diameter. b Maximum diameter

Table 1 Properties of materials

Property	Value	Units
Elastic modulus	69000	N/mm ²
Poisson's ratio	0.33	N/A
Shear modulus	27000	N/mm ²
Mass density	2700	Kg/mm ³
Tensile strength	68.9356	N/mm ²
Compressive strength	-	N/mm ²
Yield strength	27.5742	N/mm ²
Thermal expansion coefficient	2.4×10^{-5}	/K
Thermal conductivity	200	W/(m k)

2.2 Mass Properties

Mass = 2279.35 g

Volume = 1432001.88 mm³

Surface Area = 554386.90 mm²

Center of Mass (considering center as origin):

$X \approx 0.0$

$Y \approx 0.0$

$Z \approx 0.0$

Principal axes of inertia and principle moments of inertia: (gram*mm⁴) Principal axes of inertia and principle moments are taken at the center of mass:

$$I_x = (-0.26, -0.06, 0.96)P_x = 49930131.81$$

$$I_y = (0.97, 0.00, 0.26)P_y = 57558033.50$$

$$I_z = (0.01, 1.00, 0.05)P_z = 95039916.56$$

Components used

1. 3 wheels
2. 3 motor mount
3. 12 springs
4. 2 threaded rod
5. 3 + 2 Johnson geared motor (2 kgcm, 200 RPM)
6. Aluminum 12.7 × 12.7 mm² bar.

Stress Analysis

Various Loads acting on Chassis are:

1. Load acting due to Cutting arm
2. Load when robot climb tree
3. Load acted by Electronic components.

Efficiency of robot Depends on capability to sustain maximum external Load. For that weight reduction plays an important role.

We have done analysis for different materials (considering its self-load). After analysis maximum efficiency and productivity comes out of Aluminum bars.

Below shows Total Deformation and Equivalent Stress (Von Mises stress) analysis of robot under single and double stages:

The selection of Chassis is done through the analysis of different orientated chassis. Design of chassis is done on SolidWorks software, and stress analysis is done on Ansys Software. Figure 5a, b shows Total deformation of single stage chassis and double stage respectively.

Maximum deformation

$$\text{One stage chassis} : 2.7645 \times 10^{-7} \text{m} \tag{1}$$

$$\text{Two stage chassis} : 1.05 \times 10^{-7} \text{m} \tag{2}$$

From Eqs. 1 to 2, it is concluded that 2 stage chassis is more acceptable.

From Fig. 6a, b, Equivalent stress:

One stage chassis: 44.276 MPa from Fig. 6a

Two stage chassis: 19.370 MPa from Fig. 6b

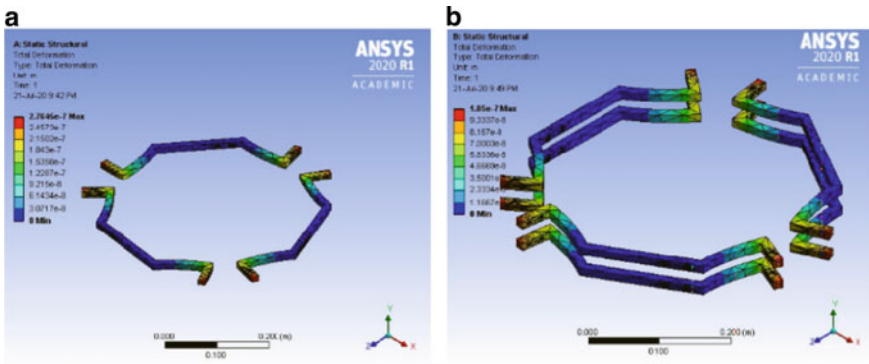


Fig. 5 Total deformation. a Total deformation of one layer. b Total deformation of one layer

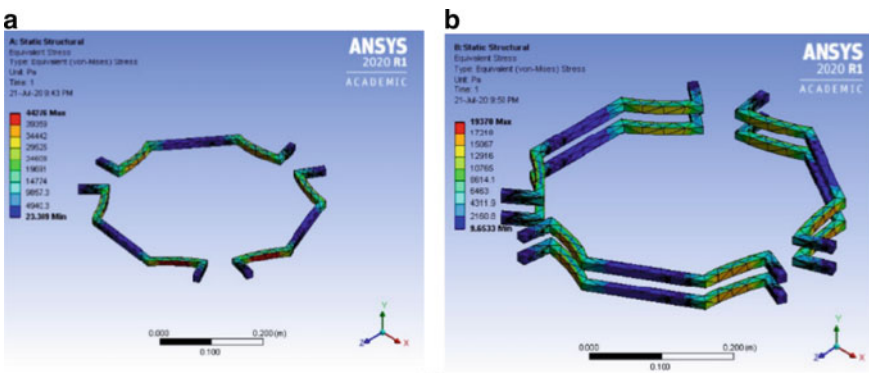


Fig. 6 Equivalent stress. a Equivalent stress of one layer. b Equivalent stress of one layer

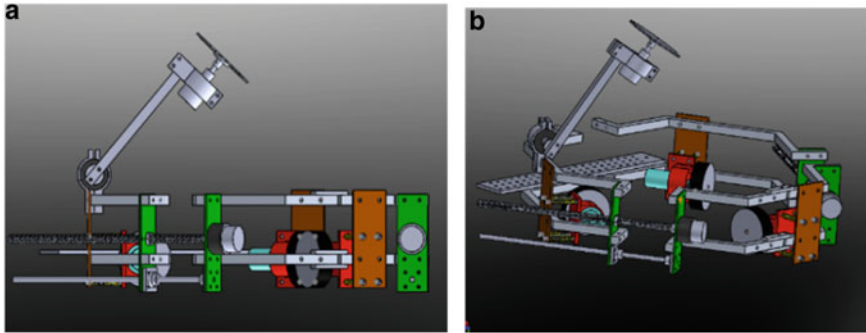


Fig. 7 Design of arm. **a** Side view. **b** Isometric view

From stage one to stage two equivalent stress reduced to half, which defines that selection of two stage chassis is better than single layer chassis.

Design of Arm

Design of final assembly of robot shown in Fig. 7a, the Degree Of Freedom (DOF) of mechanism is 3. To reduce the overall weight we have modified the solid aluminum to hollow aluminum bar of dimensions $12.7 \times 12.7 \text{ mm}^2$ with thickness of 2 mm^2 bar. The motion of arm is controlled remotely by Wi-Fi of Raspberry pi. If in case coconut is situated on the opposite of the arm, then the bot has a facility to rotate itself along periphery of the tree. By this the user can easily navigate the robot. The cutting mechanism of coconut is done by using DC Motor, coupled with motor which is attached with frame. The motor has rating of 12 V which rotates at max 1200 rpm.

2.3 Electronics

1. Raspberry pi:

Raspberry pi is used for processing the inputs received from the components, in form of voltage or current, and converting it into readable signals or voltage. Also it is used for image processing in order to convert the image into grayscale, which later on is further processed to tensor flow for image recognition. The processed image is being displayed to the user, who is controlling the robot, via android device. Since it has inbuilt Wi-Fi, also the number of pins required for the functioning of the bot is present in this module we preferred to use this module.

Wi-Fi (inbuilt in Raspberry pi): (Purpose)

- In order to control the bot while climbing the tree.

- Also to control the actuators needed to pluck the coconut and cut the branches that are required.
- Also to give the live stream of the camera attached to the Raspberry pi.

2. L298N:

Motor driver which can sustain a voltage up-to 30 V can be used for delivering stable voltage and current to the motor. The workings of 7 different motors are done by Four L298N H bridge motor controllers. Three motors are attached with frame for up and down motion. Two stepper motors are used for arm controlling and two motors for adjustment of the diameter of the bot according to the tapering diameter of the tree. If there is any slippage then, the side motor will rotate in clockwise direction to avoid any discontinuity in motion.

3. Lithium Polymer (Li-Po) battery:

To provide power supply to motor controller and Raspberry pi, we have used two Li-Po battery, each of 12 V i.e. total power of 24 V is provided. We had an option for lithium ion battery but instead of that we have used Li-Po battery.

Given below advantages of Li-Po battery:

- Lightweight
- Retains charging capacity better than Li-ion battery
- Conversion rate: 80–90%
- Charging duration is comparatively shorter than Li-ion battery
- Li-Po battery is safer, less chance of explosion compare to Li-ion battery.

Control algorithm flow chart

Here we use Arduino and Raspberry Pi for controlling a robot. Arduino is used for controlling the L298 motor driver, which is used to control BLDC Motor (Lead-screw mechanism), High torque motor for climbing, and Arm motor. With the help of Raspberry, Pi video is shown on a display of controller using Pi camera, communication between Raspberry Pi and controller is done by using Wifi Module. Which makes a robot friendly useable. There is no difficulty while cutting coconuts. Figure 8a shows detail about the flow of working of robot.

3 Conclusion

From the research finding it is observed that hexagonal chassis is the most efficient in terms of stress distribution and also provides an advantage for maintaining a good contact between the tree and the wheels. As the bot moves upwards it automatically configures the diameter and doesn't lose the contact, which is achieved by controlling

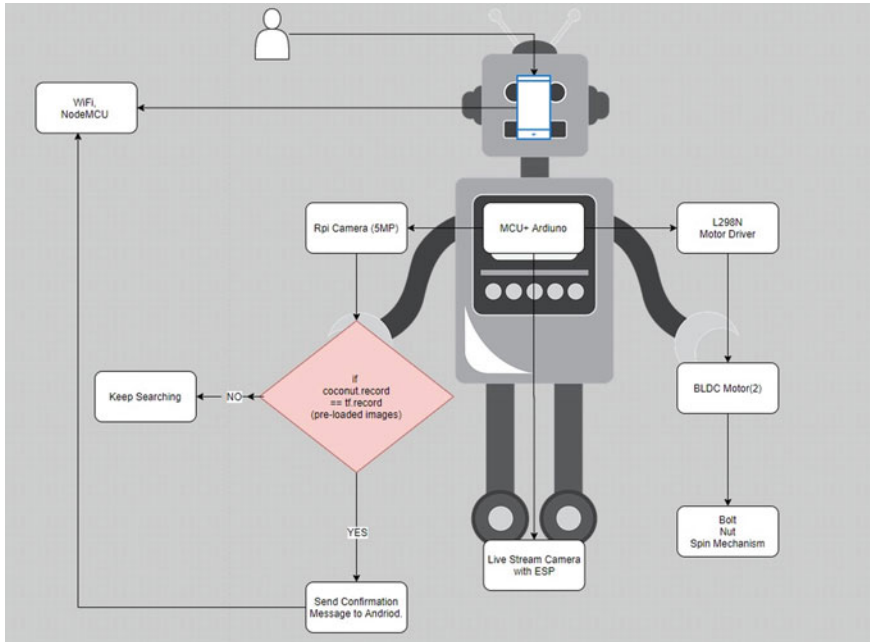


Fig. 8 a Flowchart of working

the lead screw mechanism. From the finite element analysis it is observed that the double layered chassis structure of robot is having lowest deformation as compared to the single layered chassis robot. The results have been compared and is well suited with our project objectives.

Acknowledgements First we would like to thank our parents for their constant guidance and endurance throughout our research. We thank our guide Assistant Professor. Rahul K Patil, for guiding us throughout the project and The Robocon Team for technical assistance. We also wish to express our appreciation to our lecturers and the Dean, School of the Mechanical and Civil Engineering, MIT Academy of Engineering, Alandi for their continuous support and guidance.

References

1. Dubey AP, Pattnaik SM, Banerjee A, Sarkar R Autonomous control and implementation of coconut tree climbing and harvesting robot. In: International conference on computational modeling and security. CMS
2. Jacob E, Haridasan VP (2015) Development of an autonomous tree climbing robot. In: IRF international conference, Chennai, India. ISBN: 978-93-82702-83-2
3. Senthilkumar SK, Srinivas A, Kuriachan M, Sibi SM, Veerabhadhran VB, Sundar Ganesh CS (2015) Development of automated coconut harvester prototype

4. Widanagamage BC, Gallege TN, Salgado S, Wijayakulasooriya J (2014) Treebot: an autonomous tree climbing robot utilizing four-bar linkage system. In: SAITM research symposium on engineering advancements 2014
5. Yoon Y, Rus Shady D (2007) 3D: a robot that climbs 3D trusses. In: IEEE international conference on robotics and automation, Italy
6. Sponge MW, Hutchinson S, Vidyasagar M, Robot dynamics and control, 2nd edn

An Economic Method for Fabrication and Calibration of Five-Hole Pressure Probes



Shrikant B. Taware and Chandrakant L. Prabhune

Abstract The multi-hole probes are less expensive and accurate devices for measurement of velocity in three-dimensional flow field. In order to measure absolute velocity and its inclination with reference direction at the inlet and outlet of water turbine runner two five-hole angle tube probes were designed, fabricated and calibrated with low expenditure. The yaw-pitch calibration device was designed to set the probe tip at different angles in yaw and pitch planes. The calibration data was prepared and graphs plotted by using MATLAB R12014. The correction factor for each probe was found out to give real values of velocities measured by probes. The range of flow angularity in yaw and pitch planes is between -30 and $+30^\circ$. During application flow angles, total and static pressure at probe tip, velocity and its components can be computed from measured values of pressures at five ports and calibration data.

Keywords Multi-hole probes · Flow angularity · Calibration · Fabrication

1 Introduction

Many techniques had been developed for measurement of flow velocity like Laser Doppler Velocimetry (LDV), Particle Image Velocimetry (PIV), hot wire anemometry and multi-hole probes. Among these techniques LDV, PIV and multi-hole probes are suitable for the water flow field. The LDV and PIV techniques are effective but, are costly. Multi-hole pressure probes are becoming popular due to their simple and robust construction. Their application is relatively cheap also probe requires only a few pressure transducers and post processing devices.

S. B. Taware (✉)

Department of Mechanical Engineering, Research Scholar, Dr. D.Y. Patil Institute of Technology, Pimpri, Pune 411018, India

C. L. Prabhune

Department of Mechanical Engineering, Zeal College of Engineering and Research, Pune 411041, India

The calibration procedure comprises identifying non-dimensional pressure coefficients. These non-dimensional pressure coefficients are functions of flow angles and calculated from pressure readings at five ports of probe. The readings were taken in steady flow for different flow angles in yaw and pitch plane, ranging between -30 and $+30^\circ$.

The five hole probe can be used in two ways nulling and non-nulling mode. The space limitations and other considerations make nulling technique impractical. In such situations non-nulling method is employed. In a nulling mode probe is rotated until the direction sensing port aligned with the direction of flow. In the second method, the probe is fixed and flow direction is determined from correlation based on the relation between probe pressure and flow direction.

Krause and Dudzinski [1] found that indicated dynamic pressure formed by the difference between indicated total pressure and the averaged value of the four indicated static pressures corresponding to surrounding four ports was a satisfactory normalising parameter. Pien [2] described theory used in developing a five hole probe to measure three dimensional flow. The procedure of analyzing the test data presented in their report is useful and used in the present work. Treasure and Yocum [3] stated that there exists a relation between measured pressures at five ports and true local total and static pressure. This relationship usually expressed as dimensional pressure coefficients which are functions of flow angularity. The cylindrical and spherical Pitot tubes were developed to measure flow velocity direction in Taylor Basin Model [4]. Janes described Pitot tubes having spherical sensing elements and consisting of 5 and 13 orifices. He found that there is correlation between pressure head difference in central orifice and average head at the remaining orifices. They found that results were accurate when angularity of flow was small.

Ostowari et al. [5] described new calibration method for calibrating a five hole probe for extending the useful measurement range up to flow angularities of 85° . Morrisison [6] presented refined calibration technique which reduced the effects of bad calibration points.

While designing probe size and shape of the sensing element and distance of sensing element from the support which affects the sensitivity of the probe are considered [7, 8]. Calibration of five hole probe consists of preparing data which are useful for plotting three graphs; i.e. (i) Yaw pressure coefficient versus. Pitch pressure coefficient (ii) Static pressure coefficient versus. Pitch angle (iii) total pressure coefficient versus. Pitch angle. With the help of these graphs and measured values of four coefficients flow angles are determined. Flow velocity is determined from total and static pressure values. The neural network method consists of a series of series of simple and highly interconnected processing elements. The interconnection between neurons approximates the arbitrary functions. As the data in the calibration of five hole probe are non-linear it can be suitably processed by using neural network method [9].

Homan et al. [10] employed artificial neural network method for the prediction of flow parameters for calibration of multi-hole pressure probes and compared with the commonly used polynomial functions. Their results showed that ANN with high interpolation capacity is beneficial to reduce experimental efforts.

1.1 Theory

The shape of the probe tip is hemispherical. The probe was placed in a potential flow. The theory of the five-hole probe is based on energy equation between point on free stream and point on the surface of sphere. As shown in Fig. 1, there are five ports on the tip one is at centre and other four surrounding this central port. The plane containing axis of holes 2, 3 and 4, 5 intersects each other at right angle. Axis of central hole is at intersection of these planes. The holes 2 and 3 are lying in yaw plane. The holes 4 and 5 are lying in pitch plane (Table 1).

Applying Bernoulli’s equation along a streamline, passing through point on free stream and point on a spherical surface of the probe.

$$p + \frac{1}{2}\rho V^2 = p_n + \frac{1}{2}\rho V_n^2 \tag{1}$$

where p is pressure at a point on free stream, V is free stream velocity, V_n is velocity at point n , pressure at point n becomes:

$$p_n = p + \frac{1}{2}\rho V^2 \{1 - (V_n/V)^2\} \tag{2}$$

The relation in Eq. (2) reveals that pressure at point ‘ n ’ on a sphere is a function of angle of V_n with reference direction. The Eqs. (3–6) give four dimensionless

Fig. 1 Pitch and yaw plane

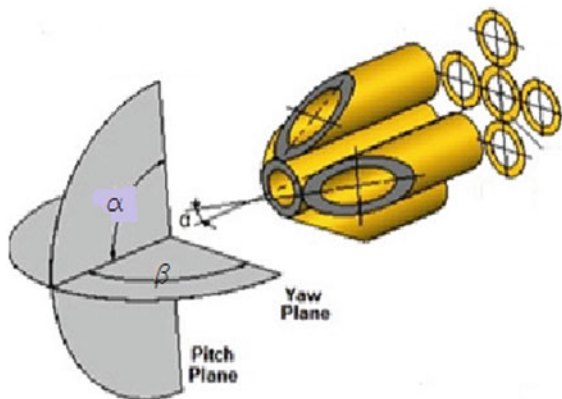


Table 1 Nomenclature

p_1 —Indicated total pressure at central port	p_2 —Pressure at port 2
p_3 —Pressure at port 3	p_4 —Pressure at port 4
p_5 —Pressure at port 5	$p_{av} = (p_1 + p_2 + p_3 + p_4)/4$
u —velocity component in x-direction(axial)	α —pitch angle
v —velocity component in y-direction(radial)	β Yaw angle
w —velocity component in y-direction(tangential)	p_t —Total pressure
Cp_{yaw} -dimensionless yaw pressure coefficient	Cp_{pitch} -dimensionless pitch pressure coefficient p_s —Static pressure
Cp_{total} -dimensionless total pressure coefficient	V —Absolute or total velocity
Cp_{static} -dimensionless static pressure coefficient	ρ —density of fluid
p —free stream pressure	

coefficients which are functions of yaw angle (b) and pitch angles (a) [3].

$$Cp_{yaw} = (p_2 - p_3)/(p_1 - p_{av}) \quad (3)$$

$$Cp_{pitch} = (p_4 - p_5)/(p_1 - p_{av}) \quad (4)$$

$$Cp_{total} = (p_1 - p_t)/(p_1 - p_{av}) \quad (5)$$

$$Cp_{static} = (p_1 - p_s)/(p_1 - p_{av}) \quad (6)$$

2 Methodology

2.1 Calibration

In this work angle tube five-hole probes were designed and fabricated. A probe consists of five hypodermic stainless steel tubes of diameter 1.6 mm, inserted through a 6 mm dia. stainless steel tube. At the tip of these probes hypodermic tubes of dia. 1.27 mm and length 22 mm were inserted through 1.6 mm dia. tubes. The joint was made leak proof using soft solder. As shown in Fig. 2 probe has four equally spaced ports in an annular circular configuration around a central port. The outside holes

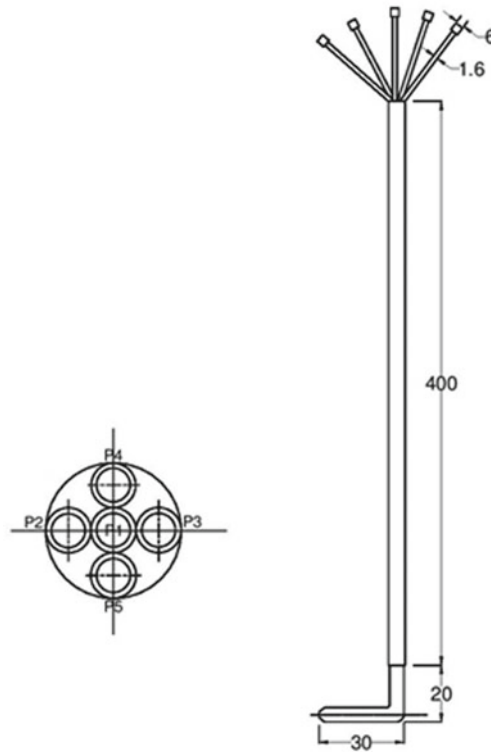


Fig. 2 Five hole probe

are located on planes which make 45° angles to the plane containing the axis of the central tube. This geometry is suitable for flow measurement in turbo machines [11].

A yaw-pitch calibration device as shown in Fig. 3 was designed and fabricated. It was used for calibration of probes. Yaw-pitch calibration device consist of yaw and pitch angle setting. The scales were provided to measure angular movement of the probe tip. The yaw scale reads the angular movement of probe tip around the probe axis with reference to zero. The rotation of the probe in a clockwise sense is taken as a negative yaw angle and that in anticlockwise sense as a positive. The pitching movement of probe tip was measured with respect to pipe axis or flow direction. The limiting range of yaw and pitch angle is between -30° and $+30^\circ$.

An equal and constant pressure was maintained at the other ends of manometer tubes. Before taking readings the probe reference line corresponding to zero yaw and pitch angles was determined by nulling or balancing pressures p_2 with p_3 and p_4 with P_5 respectively. The total pressure was measured with Pitot tube whose tip was placed in potential core and at the same radial distance as five-hole probe tip. Static pressure was measured by the wall pressure tap.

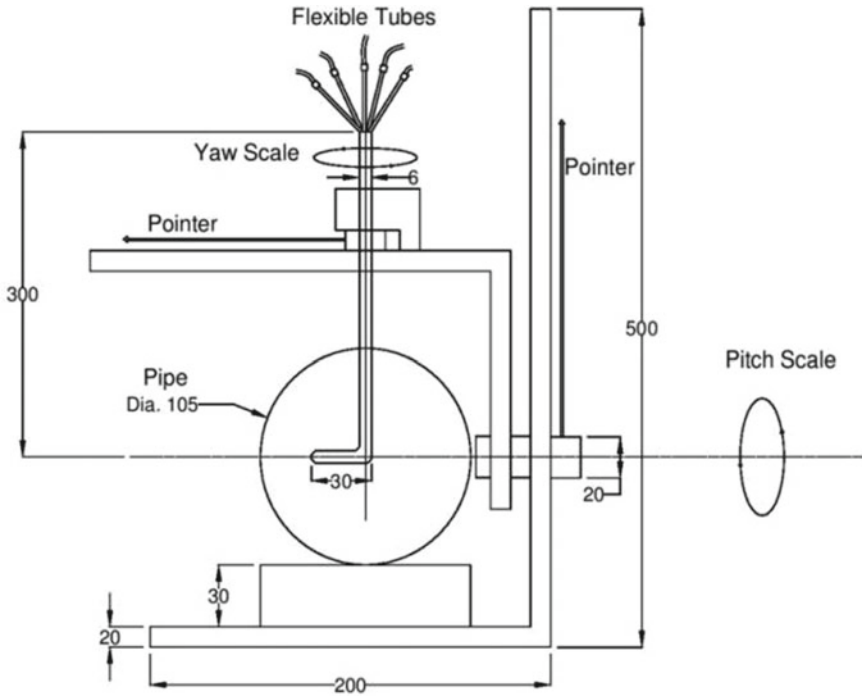


Fig. 3 Yaw pitch calibration device

The probe was positioned at one of the yaw angles and pitch angle was varied at an increment of 10° . For each yaw angle seven pressure readings were measured and recorded. Both yaw and pitch angles were set with a range of -30 to $+30^\circ$, corresponding to pitch angles (Fig. 4). The dimensionless coefficients were computed by using relations given in Eqs. (3–6).

The values of all pressure coefficients for the corresponding values of α and β were tabulated. While taking readings the mean values of observed quantities were recorded. The graphs were plotted using MATLAB R2014 software.

2.2 Computation for Velocity

The differential pressure indicated by Δp_i is the difference between subject pressure ‘i’ and reference pressure. From equation ‘7’ total pressure value can be obtained.

$$Cp'_{total} = (\Delta p_1 - \Delta p_t) / (\Delta p_1 - \Delta p_{av}) \tag{7}$$

$$p_{total} = p_{ref} + \Delta p_1 - Cp'_{total} (\Delta p_1 - \Delta p_{av}) \tag{8}$$



Fig. 4 Actual experimental set up

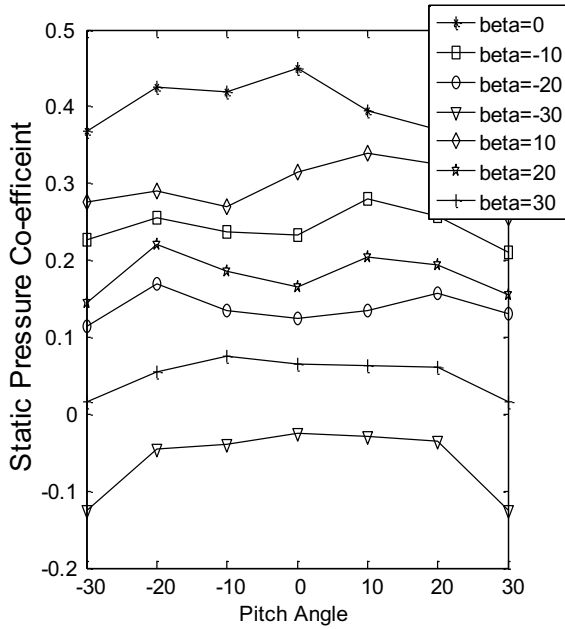


Fig. 5 A plot of static pressure coefficient versus pitch angle (probe-I)

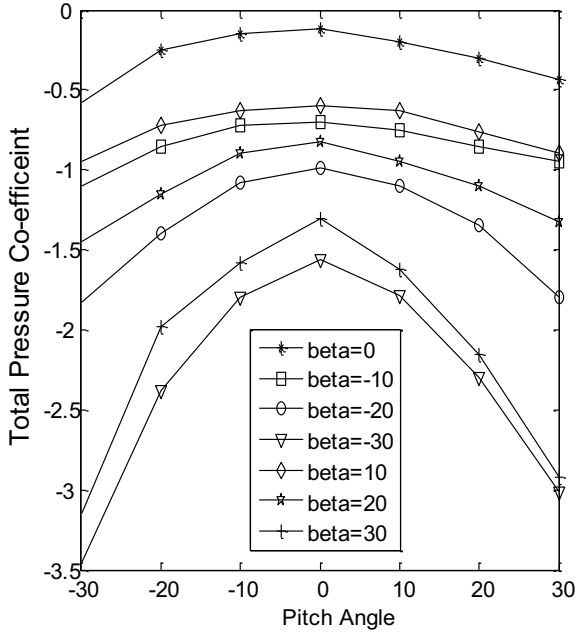


Fig. 6 A plot of total pressure coefficient versus pitch angle (probe-I)

Cp'_{total} is to be determined from calibration data. Similarly, static pressure is,

$$p_{static} = p_{ref} + \Delta p_{av} - Cp'_{static} (\Delta p_1 - \Delta p_{av}) \tag{9}$$

In the above equations experimental coefficients are represented by “primed” superscripts i.e. Cp'_{total} and Cp'_{static} . Using Bernoulli’s equation local total velocity can be found out as:

$$V = \sqrt{[2(p_{total} - p_{static})/\rho]} \tag{10}$$

Components of velocity along x, y and z axis can be found by following relations [3].

$$u = V \cos\beta \cos\alpha$$

$$v = V \cos\beta \sin\alpha$$

$$w = V \sin\beta$$

The interpolation procedure is to be used to obtain intermediate values. The actual values of a and b corresponding to measurement can be found from a calibration grid of Cp_{yaw} versus Cp_{pitch} . A double interpolation is required as values to be determined are functions of two independent variables. The values of actual pitch and yaw angles can be found by interpolation. Actual total and static pressure coefficients can be found from second and third calibration grids.

3 Results and Discussion

3.1 Verification of Velocity Relation and Correction Factor

For probe-I

Discharge passing through the pipe was measured by using calibrated venturimeter.

Average velocity of flow through pipe = $0.012892397/8.007 \times 10^{-3} = 1.61$ m/s.

From calibration data of probe no. 1, at a = 0, b = 0, $Cp_{static} = 0.45$,

$Cp_{total} = -0.1125$. Measured pressure head difference between central hole and average of 5 holes $(\Delta p_1 - \Delta p_{av})/\rho g = 7.75$ cm of water.

Hence the total velocity, by using the Eq. (10) is = 1.5413 m/s.

Reynold's number based on the pipe diameter, $Re = 1.5413 \times 10^5$. The flow is turbulent. Turbulent velocity distribution across a circular flow section is given by power law [8].

Power law,

$$\frac{V_{av}}{V_{max}} = (1-r/R)^{1/7}$$

Probe tip was placed at pipe center where $r = 0$. Hence, $V_{av} = V_{max}$.

Percentage error in actual measurement and calculated average velocity based on discharge is

$$\% \text{ error} = (1.61 - 1.5413) \times \frac{100}{1.61} = 4.267\%.$$

With reference to literature review [5] the percentage error is 2.4% within the range of angles $\pm 20^\circ$, whereas the percentage error in this probe calibration within the range of angles $\pm 30^\circ$ is 4.267%.

The Correction factor for probe I = $1.61/1.5413 = 1.04475$

For probe-II

Discharge = 0.01281112 m³/s, Average velocity of flow through pipe = 1.442 m/s. From calibration data of probe no. 2, at a = 0, b = 0, $(\Delta p_1 - \Delta p_{av})/\rho g = 5.82$ cm of water, $C_{p_{static}} = 0.215$, $C_{p_{total}} = -0.83$.

Hence the total velocity, $V = 1.5281$ m/s. Reynold's number of flows, $Re = 1.5281 \times 10^5$, the flow is turbulent.

Percentage error in actual measurement and calculated values is 4.493%.

With reference to literature review [5] the percentage error is 2.4% within the range of angles $\pm 20^\circ$, whereas the percentage error in this probe calibration within the range of angles $\pm 30^\circ$, is 4.493%.

The Correction factor for probe II = 1.6/1.5281 = 1.047

The graphs between yaw pressure coefficient and pitch pressure coefficient (Figs. 7 and 10) are nearly symmetric about the x axis and y axis. Nonlinear distribution of points is observed. The lines joining points of the constant yaw angle are a complex curve similar to spline curve. Negative angle represents an angle measured in a clockwise direction and positive angle in anticlockwise sense. The nature of the curves obtained for static pressure coefficient versus pitch angle and total pressure

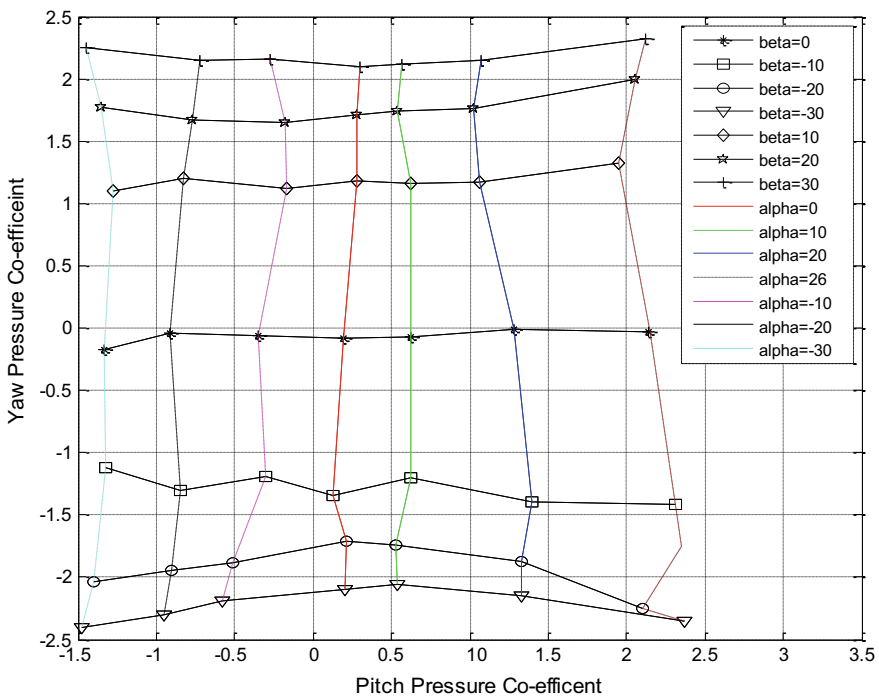


Fig. 7 A plot of yaw pressure coefficient versus pitch pressure coefficient (probe-I)

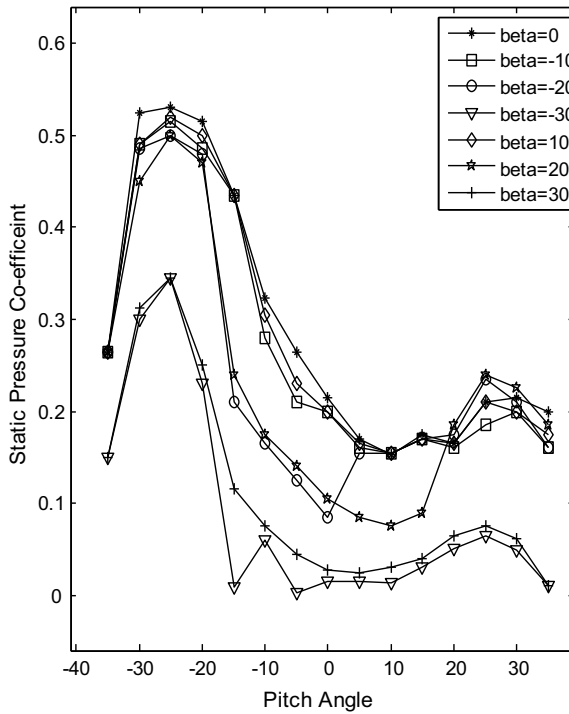


Fig. 8 A plot of static pressure coefficient versus pitch angle (probe-II)

coefficient versus pitch angle are nearly symmetric about vertical axis (Figs. 5, 6 and 9). It is observed from Fig. 8 that exceeding value of pitch angle beyond 30°, corresponding to the yaw angle 30° graph changes drastically means results not accurate beyond angle ±30°. The values of flow angles α and β , static and total pressure coefficients can be easily found out by proper interpolation.

The 5 hole probe calibration problem can be solved finding a matrix equation. This approach was applied by Morrison et al. [6]. They have expressed flow velocity parameters using third order polynomials or polynomial ratios. Georgiou and Mili-donis [4] also found similar solutions. However, there is complexity in finding a governing equation of the probe.

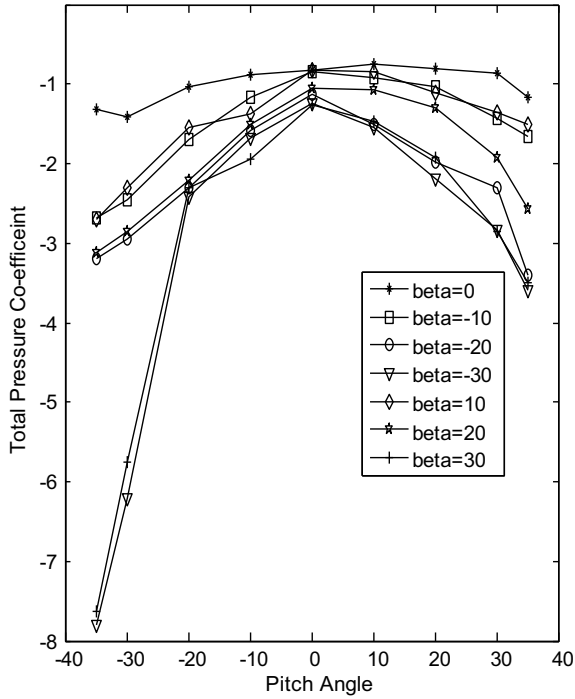


Fig. 9 A plot of total pressure coefficient versus pitch angle (probe-II)

4 Conclusion

The calibration of two angle tube probes was satisfactory. The graphs plotted are useful for the application of probes in three-dimensional flow fields. The calibration of first and second probe was performed at constant average velocities. The correction factors for first and second probe are 1.04475 and 1.047 respectively. Effect of wall proximity and Reynolds number were neglected during the calibration of probes.

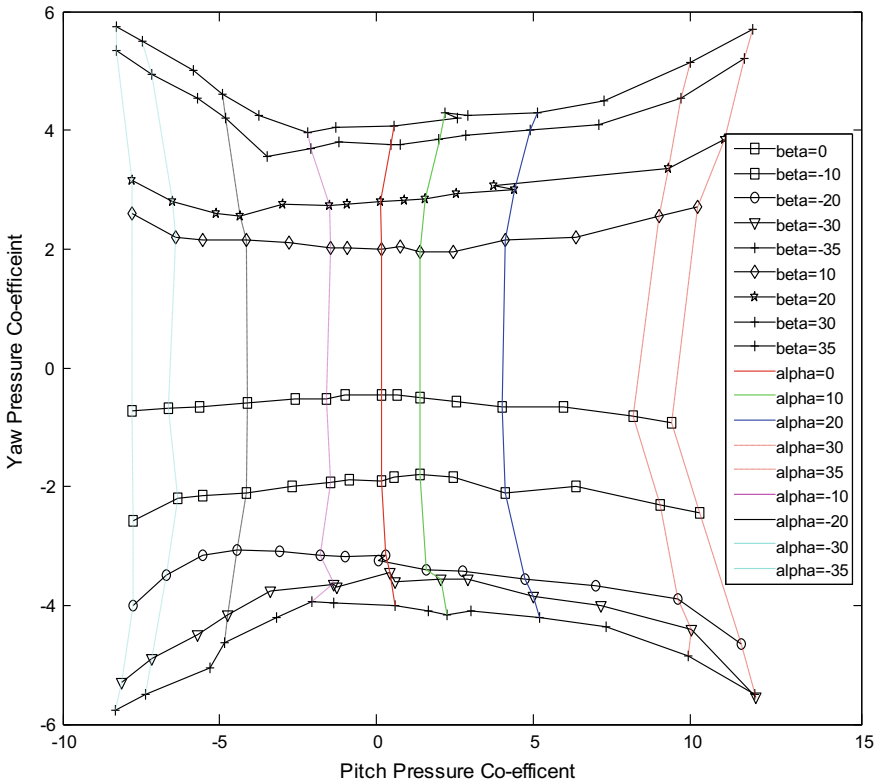


Fig. 10 A plot of yaw pressure coefficient versus pitch pressure coefficient (probe-II)

References

1. Dudzinski TJ, Krause LN (1969) Flow direction measurement with fixed-position probe. NASA Report TM X-1904
2. Pien PC (1958) Five-hole spherical pitot tube. Report No. 1229, published by U. S. Navy
3. Treaster AL, Yocum AM (1978) The calibration and application of five-hole probes. In: 24th ISA transactions, vol 18, no 3, pp 23–34
4. Janes CE (1982) Instruments and methods for measuring the flow of water around ships and ship models. Report No. 487, Published by U. S. Navy
5. Ostwari C, Wentz WH (1983) Modified Calibration Techniques of a five-hole probe for high flow angles. *Exp Fluids* 3:166–168
6. Morrison GL, Schobeiri MT, Pappu KR (1998) Five-hole pressure probe analysis technique. *Flow Meas Instrum* 3:153–158
7. Nowack CFR (1970) Improved calibration method for a five-hole spherical pitot probe. *J Phys E: Sci Instrum* 3(1):21–66
8. Fox, McDonald, Pritchard (2014) *Fluid mechanics*. Wiley
9. Lee H-H et al (2014) Application of ANFIS method to the nonnulling calibration of multi-hole pitot tube. *Int Conf Procedia Eng* 79:125–132

10. Homan NS et al (2020) A novel approach based on artificial neural network for calibration of multi-hole pressure probes. *Flow Meas Instrum* 73
11. Town J, Camci C (2011) Sub-miniature five-hole probe calibration using a time efficient pitch and yaw mechanism and accuracy improvements. In: *Proceeding of ASME turbo expo turbine technical conference*, Vancouver, Canada

Lab Scale Batch Reactor Design, Fabrication and Its Application for Biodiesel Production



Niraj S. Topare, Kiran D. Patil, Satish V. Khedkar, and Nilesh Inamdar

Abstract In order to produce biodiesel, mechanically agitated lab-scale reactor vessels have been developed and fabricated. It has been recognized that in the synthesis of biodiesel the use of batch stirred reactor is a primary mode. As the development process from sunflower waste cooking oil has been tested for the reliability of the reactor vessels, transesterification routes have been selected. The laboratory scale reactor makes the flow residence time with an enhanced mass turbulence distribution and heat transfer and offers precise mixing control with agitator geometry, making operation simple. Parameter such as reactor dimensions and physical properties of reactants must be taken into account in accordance with the philosophy of reactor design before design work has recently been initiated. Control logic also developed to run a reactor. The reactor design involves the use of two software such as PVElite for mechanical thickness calculation and Solidworks for 3D modeling. Results show that produced biodiesel from sunflower waste cooking oil (SWCO) was within the recommended standards of biodiesel fuel. The transesterification reaction using sodium hydroxide (NaOH) catalyst was effective in the designed lab-scale batch reactor. The yield and conversion of produced biodiesel from SWCO oil by using NaOH catalysts in the lab-scale reactor at 70 °C are 94% and 96% respectively at 3 wt%.

Keywords Biodiesel · Reactor design · Sunflower · Waste cooking oil

N. S. Topare (✉) · K. D. Patil
School of Chemical Engineering, Dr. Vishwanath Karad MIT World Peace University, Pune 411 038, India
e-mail: niraj.topare@mitwpu.edu.in

S. V. Khedkar
Department of Chemical Engineering, College of Engineering & Technology, Akola 444 104, India

N. Inamdar
Patpert Teknow Systems, Pvt., Ltd, Pune 411 048, India

1 Introduction

The monoalkyl esters of fatty acids derived from animal fats or vegetable oils shall be classified as biodiesel. In a simple way, biodiesel is produced when animal fat or vegetable oil is chemically reacted with a catalyst (homogeneous and heterogeneous) and alcohol to produce a fatty acid alkyl ester [1]. For biodiesel production is needed a homogeneous catalyst, such as sodium hydroxide (NaOH) or potassium hydroxide (KOH), and glycerol is produced in a byproduct formulation. Recycled cooking oils are the best suitable feedstock for biodiesel along with plant oils, animal fats. The pure type of biodiesel or mix it with petroleum diesel at any stage can be used to create a biodiesel blend since it contains no petroleum. The diesel motor needs very little to no motor modification because biodiesel has similar properties to gasoline diesel. It is the most widely used diesel engine [2, 3]. It needs no separate infrastructure and can be stored as petroleum diesel fuel. As biodiesel has virtually no aromas, it contains around 10% oxygen that helps burn entirely, and no sulphur, it is known as safe fuel. It increases the ignition efficiency due to its higher cetane number even when mixed into petroleum diesel [4].

A single or two stage batch transesterification process is the most regular and suitable method to generate biodiesel [5]. Batch methods require greater reactor volume, which results in a large expenditure of capital. In contrast with ongoing processes, it has suffered some drawbacks. Afterward, a continuous process in producing biodiesel from animal fats or vegetable oils or waste cooking oils has been developed by some innovative researchers to reduce a higher cost and improving reactants mixing in order to increase reaction rates [6]. The main aim of this research, design and fabricate a lab-scale batch reactor that is applicable for efficient sunflower waste cooking oil development of biodiesel. The experiment was conducted with homogeneous catalysts in the designed and fabricated lab-scale batch reactor for bio-diesel production from the SWCO. SWCO contains high FFAs so that a transesterification of alkalis is done using methanol and NaOH catalysts. It evaluated the effect of operating parameters such as reaction temperature 70 °C, the reaction time of 2.5 h, and loading of the catalyst 1, 2, and 3 wt% at 5:1 methanol/oil ratio.

2 Design Method for Lab Scale Batch Reactor

The geometric configuration is an approached to design a lab-scale batch reactor by maintaining the dynamic similarity followed by the application of other empirical design correlations using various dimensionless groups.

2.1 Geometry Detail of Reactor Parts

The lab scale batch reactor consists of shell $530 \times 210 \times 3$ mm with Shell Jacket $603 \times 165 \times 2$ mm. The total volume of the reactor is 5 L and the actual working volume is 3.5 L. The agitator is used for mixing having shaft dimension 8 mm diameter and 210 mm length, Blades used having dimensioned $16 \times 12 \times 2$ mm. We also provide a provision for air spurge. For the heating purpose, we designed a new type of heater having heating coil 10 mm diameter. The material used for the fabrication of lab scale

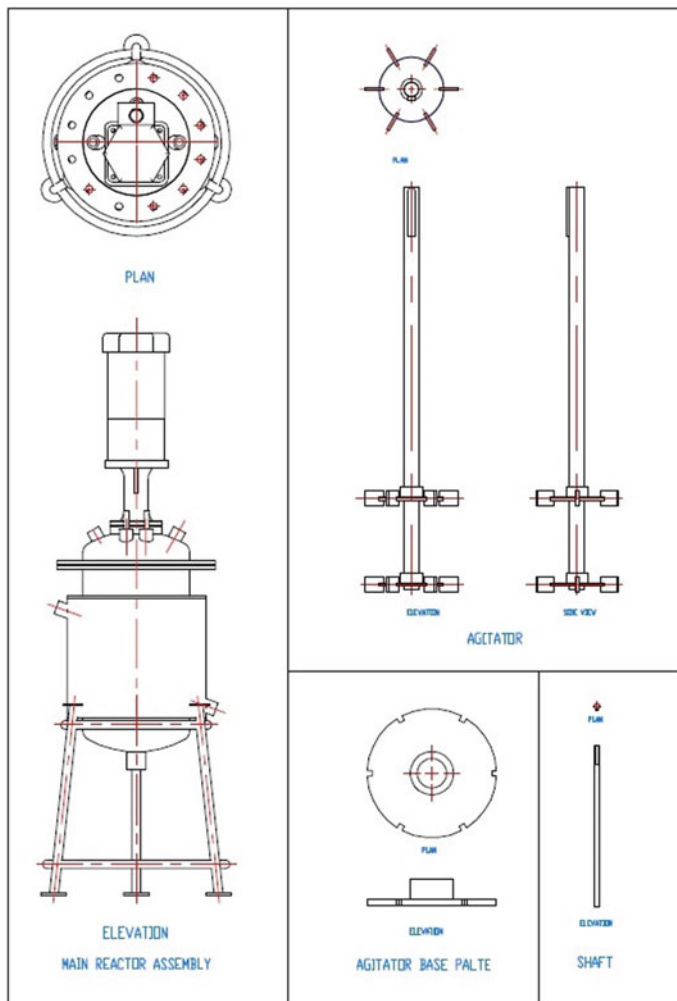


Fig. 1 Technical drawings-1 of each part with the assembly of batch reactor of laboratory scale

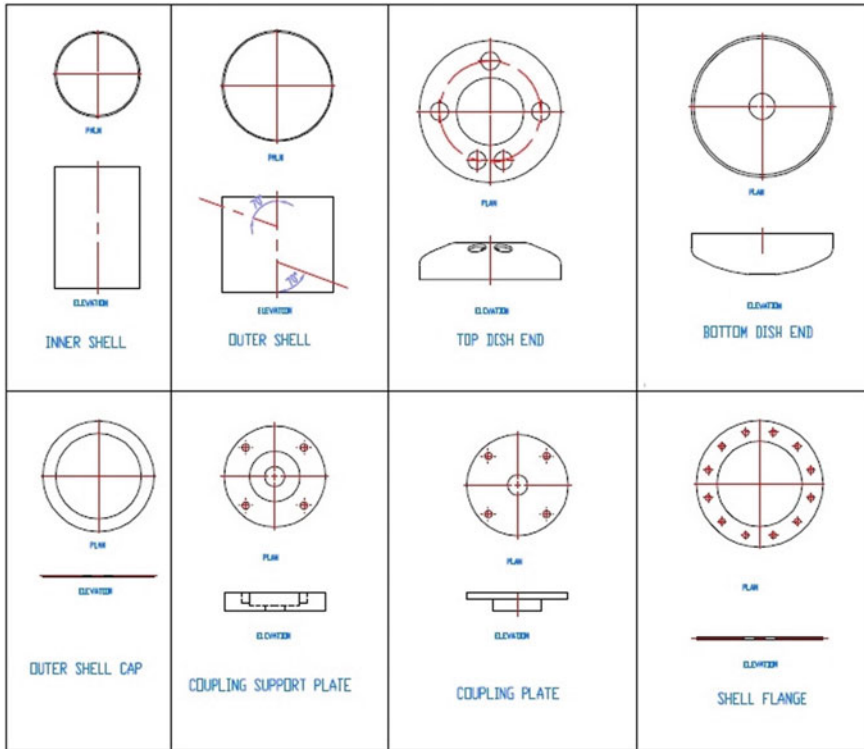


Fig. 2 Technical drawings-2 of each part with the assembly of batch reactor of laboratory scale

batch Reactor is SS 316. The following Figs. 1 and 2, show the technical drawings –1 and 2 of each part with the assembly of batch reactor of laboratory scale.

2.2 Software Used

2.2.1 SolidWorks Software

A mechanical design automation programme, SolidWorks CAD software enables developers to rapidly draw up ideas, test features and measurements, and generate modeling, simulation and informative drawings. A SolidWorks model is composed of a component or assembling document in 3D solid geometry. Usually start with a sketch, construct a basis function and then add more characteristics to our model (can also start with a solid geometry or imported surface). It can enhance our architecture with the addition, alteration or reorganization of functions. In combination with parts, assemblies and sketches, modifications to a document or view are made automatically for all other documents and views. At any point in the design process it can produce

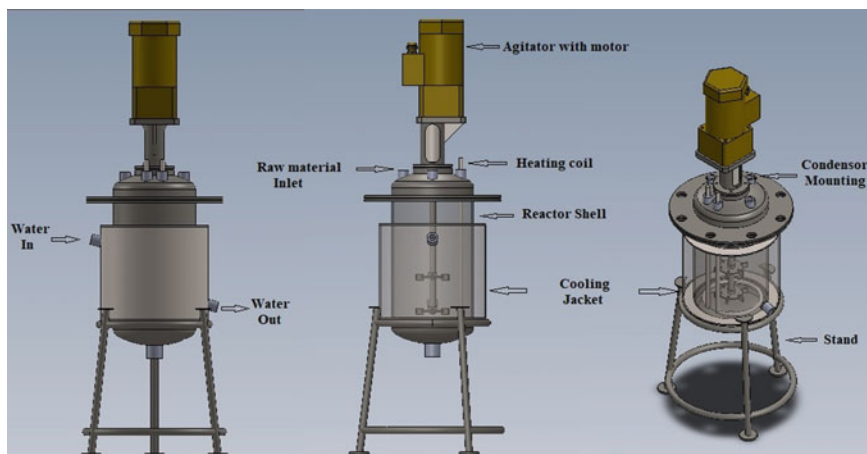


Fig. 3 3D model design of lab scale batch reactor by using SolidWorks software

sketches or assemblies [8]. Figure 3, shows that the 3D model designs of lab-scale batch reactor by using SolidWorks software. In general, the design process includes the following steps:

- Determine the model specifications
- Conceive the model according to the needs defined
- Design the concept-based model
- Review of the model
- The model prototype
- Build the model
- If required, edit the model.

2.2.2 PV-Elite Software

PV-Elite offers developers, designers, suppliers, estimators, and a graphical, easy-to-use software programme, and tall towers, horizontal vessels, individual vessels and heat exchangers with full design capabilities inspectors. In compliance with the rules of ASME Sect. 8, Division 2, Canadian NBC, EN-13445 and PD5500, PV Elite may be used in the design, submission or re-rated of a wide range of vessels and vessel components. The Interface, which gathers the definition of the model, ensures that the pattern is accurate. The analysis is easily shown on the computer interactively with the intermediate findings. Instant technical assistance for each data field offers context sensitive support. For each phase of the study, the outcome is shown in an organised and succinct format with the reports available. PV-Elite is also designed for engineering like other Intergraph programmes [9, 10]. Compare the manually and PV-ELITE shell software, the ellipse head and the straight flange, respectively compare thickness, maximum allowable working pressure (MAWP) and

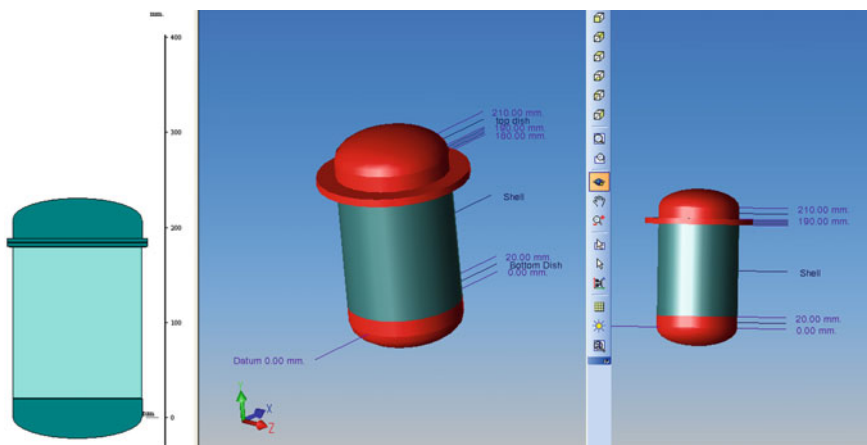


Fig. 4 Lab scale batch reactor part thickness calculation by using PV-Elite software

maximum allowable pressure (MAP). The variations in the results are well within the permissible range. Figure 4, shows that the lab-scale batch reactor part thickness calculation by using PV-Elite software.

2.3 Control Logic

For carried out an operation some instruments were used i.e. temperature Controller, temperature Sensor, agitator, and Heater. We have developed control logic for controlling processes carried out in a lab-scale batch reactor. Figure 5, shows the detail flow diagram of control logic.

2.4 Experimental Method and Setup

The transesterification of sunflower waste cooking oil can be expressed as follows by the use of methanol:



For each mole of waste cooking oil a stoichiometric reaction requires three methanol moles and is an equilibrium reaction. The methanol/oil molar ratio is 3:1, as the literature suggests that it is the optimum ratio for transesterification of vegetable oil [7]. The transesterification reaction was carried out in the designed and fabricated lab-scale reactor with a mechanical stirrer. Figure 6, shows the actual experimental setup.

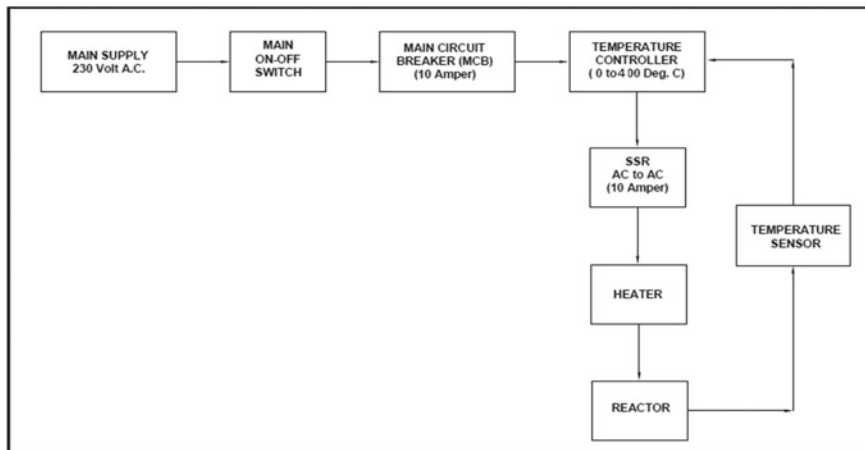


Fig. 5 Schematic representation of control logic

Fig. 6 Actual experimental setup (Lab scale batch reactor)



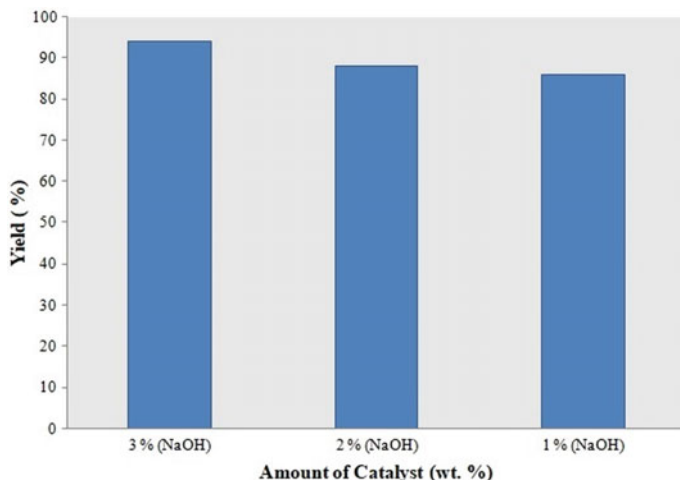


Fig. 7 Percentage yield of waste cooking soybean oil into biodiesel

Raw SWCO as feed was made free from water, as any water or moisture in the system will consume some of the catalysts and slow the transesterification reaction. The transesterification process was studied for catalyst 1, 2, and 3 wt% of NaOH at reaction temperature 70 °C, the reaction time of 2.5 h, 5:1 methanol/oil ratio and at atmospheric pressure. At a temperature lower than the boiling point of methanol, the reaction occurs at atmospheric pressure, i.e. at 70 °C to ensure conversion only depends on reactor concentrates and avoid vaporization of the methanol. After the reaction ended the product was taken through the outlet at the bottom of the reactor then put in the separating funnel for separation. With the density difference, two phases are formed as a result of the transesterification reaction. The upper layer consisted of methanol, biodiesel, soap and glycerin, impurities and catalyst with traces of unreacted oil composed the lower layer. The upper layer has been cleaned by removing methanol through the maintenance of the mixture at a high temperature of 80 °C and the removal soap was rendered with warm water. Figures 7 and 8 shows the percentage yield and conversion of waste cooking soybean oil into biodiesel.

3 Conclusion

In accordance with design requirements and specifications, the lab-scaled batch reactor for the transesterification process for biodiesel production was successful. Design values were also calculated using PV-Elite and the results were compared. Manual calculation of thickness is about 8% more while working pressure calculation is about 10% less when compared with PV-ELITE software output. Biodiesel produced by reactors from sunflower waste cooking oil yields good results. Results

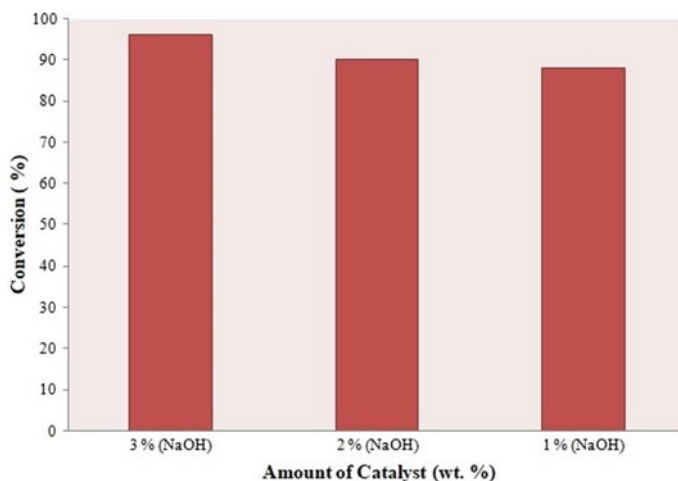


Fig. 8 Percentage conversion of waste cooking soybean oil into biodiesel

show that produced biodiesel from SWCO was within the recommended standards of biodiesel fuel and also observed that the transesterification reaction using the NaOH catalyst was effective. The yield and conversion of produced biodiesel from SWCO by using NaOH catalysts in a lab-scale batch reactor at 70 °C are 94% and 96% respectively at 3 wt%. There have been some changes and technological adjustments to the development in the laboratory-scale reactor batch.

Acknowledgements Authors (NST, KDP & SVK) acknowledge the support provided by Mr. Nilesh Inamdar, Director, Patpert Teknow Systems, Pvt., Ltd, Pune through the academic collaboration for the Reactor fabrication

References

1. Sani W, Hasnan K (2009) Development of the mini scale biodiesel reactors. In: Proceedings of MUCET, vol 20, pp 1–3
2. Topare NS, Chopade SG, Raut SJ, Renge VC, Khedkar SV, Bhagat SL (2011) Biodiesel production from *Jatropha curcas* oil. *Int J Chem Sci* 9(4):1607–1612
3. Ibrehem AS, Al-Salim HS (2009) Advanced mathematical model to describe the production of biodiesel process. *Bull Chem React Eng Catal* 4(2):37–42
4. Yunus R, Yaw TCS, Azhari TI, Mohd. Ghazi MFM, Resul G (2008) Preliminary design of oscillatory flow biodiesel reactor for continuous biodiesel production from *jatropha triglycerides*. *J Eng Sci Technol* 3(2):138–145
5. Hosseini M, Nikbakht AM, Tabatabaei M (2012) Biodiesel production in batch tank reactor equipped to helical ribbon-like agitator. *Mod Appl Sci* 6(3):40–45
6. Abdulla Yusuf H, Elkanzi EM, Hossain SMZ, Alsaedi AM, Alhindy AH, Ebrahim E (2020) Design and performance assessment of an in-house fabricated microreactor for enzyme-catalysed biodiesel synthesis. *Arab J Basic Appl Sci* 27(1):239–247

7. Topare NS, Raut SJ, Attar SJ (2012) 3D model design and simulation of photocatalytic reactor for degradation of dyes using solidworks software. *Int J Chem Sci* 10(2):808–816
8. Degenstein JC, Kamireddy S, Tucker MP, Ji Y (2011) Novel batch reactor for the dilute acid pretreatment of lignocellulosic feedstocks with improved heating and cooling kinetics. *Int J Chem React Eng* 9:1–9
9. Topare NS, Khedkar SV, Renge VC, Deshmukh N, Hazarika S, Charhate A, Pal U (2012) MUR system for biodiesel production. *Chem Eng World* 47(10):76–78
10. Vivekanandan M, Venkatesh R, Sathish T, Dinesh S, Ravichandran M, Vijayan V (2019) Pressure vessel design using PV-ELITE software with manual calculations and validation by FEM. *J Eng Technol* 8(1):425–433

Pest Management System Using Agriculture Robot



Anup S. Vibhute, Krishna R. Tate Deshmukh, Ravikant S. Hindule,
and Sharad M. Sonawane

Abstract Detection of pests or insects is a common problem in the field of agriculture. Therefore strong action should be taken to save the crop from the infestation as well as reducing the use of pesticides. Monitoring of pests infestation depends on resources used by human being however, an automatic monitoring system has been developing to reduce efforts and errors made by human. This project proposes the development of system in which image processing approaches are to be establishing for an automated detection and extraction system for detecting pest densities in agriculture fields. We have precisely developed a multipurpose robot, depending upon the densities of infestation robot decides spraying on infected area by sprayer or removes the part of crop by cutter infected by pest with an accuracy of 93% pest detection and 95% of decision making. So, it gives protection to crops, which can finally give better management and production of the crop.

Keywords Raspberry-Pi · Image processing · Robotics · PMS

1 Introduction

Pest detection of the crop is necessary in the field of agriculture. When crops are attacked by different kinds of pests or insects then there quality as well as quantity is going to be reduce. Hence, it is higher priority to find out efficient techniques to minimize the level of their infestation in agriculture fields. This project presents an approach for careful detection of pests and handling to prevent the crops from heavy losses. Mealybugs lesion case is considered for this project.

Earlier in traditional way gummed traps are normally used for collection of the pests. Then those insects are taken to the laboratory or workshop to count as well as to identify manually. After that, crop experts identify and separate out the insects manually based on their genus and count the visible pests separately. After getting count, that count gives estimation about pest density in agriculture field.

A. S. Vibhute (✉) · K. R. Tate Deshmukh · R. S. Hindule · S. M. Sonawane
SVERI's College of Engineering, Pandharpur, India
e-mail: asvibhute@coe.sveri.ac.in

Although, cover the larger area and continuously counting of pests is time consuming and difficult process for the crop expertise. This results in minimum accuracy and time delays for better results. This proposed project extends the development of system using various techniques of image processing for detection and extraction of insects and uses robotics for the advancement by developing an automated detection and extraction system on the robot for getting accurate results of pest detection on crops in agriculture field.

After detection and extraction of pest, with the help of the controller, it will give the command to the robot for spraying on infected area or cutting of infected leaf.

2 Literature Survey

Srisuphab and Silapachote [1] proposes, an efficient technique to detect the flying insects and to observing number of insects in an open field. For that purpose, they use various image processing techniques as well as computer vision technique. Firstly, they point out an interested region as well as point out locations where the rover needs not to go. For the completion of mapped mission, the execution of path finding algorithm is to be done and rover is programmed in such a way that it can execute unmanned. In this the rover successfully covers the entire selected region and achieves the target. Then they evaluated the accuracy, and they achieved accuracy of the insect detection of 89.43% which is very much efficient.

Lagad and Karmore [2] used the web camera which is having better resolution for taking the images and in the segmentation they produce the binary image depends on gray level threshold segmentation and after that isolating of the band is finished, In band separation they watch different color band image. At that point they apply masking process for color image segmentation which enhance quality and classify it.

Thomas [3] proposed, monitoring and bomb diffusion by using a haptic arm technique placed on unmanned ground vehicle (UGV). In this model they used mechanism of four fingered which is having less weight, more convenient, and easily operated with reduction in difficulty. For the advancement they make use of new haptic arm which is wireless and self-reliant interfaced on the arm for doing flexible motion of the robot. This haptic arm is not limited with moves of finger sizes; also, this system can provide a better accuracy and smoothness for robot control. Due to this type of provision the system is more suitable for bomb detection and diffusion mechanism.

Pawar [4], proposed a system in which the image of the infected leaf is taken and therefore the image pre-processing is finished taking the histogram equalization is applied to extend the contrast in low contrast image. K-means clustering algorithm used for segmentation, which classifies objects supported a collection of features into K number of classes, and eventually, classification is performed using Neural-network. Thus, image processing technique is employed for detecting diseases on cotton leaves is straightforward and accurately.

Miranda [5] presented an automatic detection and extraction system for the pest present in captured image, for that purpose they use different image processing techniques, for detection of pests within the captured image they use modelling of background. And to remove the noise present in captured image due to various lightning condition they use a median filter which works efficiently. Then objects in the captured image are extracted through algorithm of feature extraction which is very much easier to understand. Then scanning of image has been done in row and column wise manner for working on coordinates.

Li et al. [6] proposed, the techniques which works very much efficiently for detection of pest also for finding position of that pest. The system uses binocular stereo vision technique for giving proper location of pest, with the help of that position of pest the robot can automatically spray on pest location. By using color feature, they separate out the pest from leaf and this extraction is done by image segmentation technique. With the help of outputs from image segmentation stage and binocular stereo stage 3D position of pest is determined. For displaying common object, they embraced centroid matching technique into position locating technique. Also, they revised the formula which is used to calculate distance and it supports a binocular stereo vision technique.

Martin and Moisan [7] they promoted early bio-aggressor detection in greenhouse crops to scale back pesticide use. Static analogy vision systems make use in greenhouse analysis have limited by their spatial and temporal sampling potential. By analyzing video and explication of scenes coming from multi camera data they describe early pest detection. This constructive and defensive approach will allow quick corrective decisions from manufacturer.

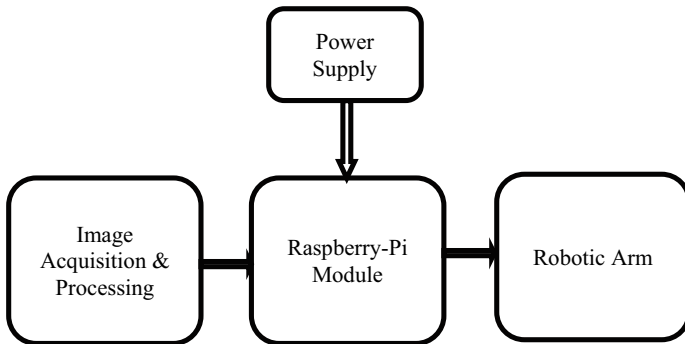


Fig. 1 Block diagram of proposed work

3 Methodology

The Fig. 1 Shows the block diagram of the proposed pest management system (PMS) using robot. The hardware part consist of Micro-controller based system i.e. RaspberryPi model along with Robotic arm. The input to the system is an image which is captured directly from farm and processes using image processing algorithm as follows.

- Input Image or image acquisition
- Pre-processing and Normalization
- Segmentation
- Features Extraction
- Decision Making (Pesticide spraying or cutting leaf).

3.1 Image Acquisition

In this technique we capture input image of leafs from the crop through pi camera which interfaced with raspberry pi. This camera is very much compatible with the latest version of Raspbian which is mostly preferred OS of Raspberry Pi, and this is capable of capturing static images having 2592×1944 pixels. It has 5-megapixel native resolutions. Hence it will detect the pest on the leaf very easily.

3.2 Image Preprocessing

After images have been captured using Pi camera, then that are taken for the preprocessing for the better results, in that for removing noise of background and also for filtering unwanted reflections because of illumination system, so that firstly captured image is taken for filtration with the help of median filter. For the proper filtration we have designed one mask which is compatible with the any kind of input images. The distortions come from acquisition system are corrected through image restoration technique which helps in improving the quality of image. Also, in preprocessing we can convert the RGB image into Gray image.

3.3 Image Segmentation

After completion of all the processing we have a target to calculate the area of leaf, for that only one leaf is to be separated out from multiple leaf so we use edge detection technique then we get multiple leaf after that we use algorithm for numbering those out of those multiple leaf we select one leaf and process on it. For

removing the background from the image, we use thresholding type of segmentation technique which has given a very much perfect result. By using binary segmentation technique, we convert only green part as white part so that we will get only leaf part and remaining part made as black part.

3.4 Feature Extraction

It involves reducing the amount of information required to describe a large set of data correctly. Samples of features include size, position, contour measurement and texture detection. In this we use the simple white color detection algorithm which help us to detect the mealybugs on the leaf, after applying the algorithm we get result as showing mealybugs as it is image and the remaining all part of image made as black. After that we can easily count the exact count of mealybugs affected area by counting white pixel, also we are counting the area of leaf. Depending upon leaf and mealybugs affected area on that leaf, then we calculating the affected percentage.

3.5 Decision Making

When the feature is extracted i.e. mealybugs or pest are detected the area is to be calculated which is further compared with the threshold value set by user then according to the result came from thresholding function robot module has been ordered to spraying that area by sprayer or cutting that leave by cutter and this important decision making is done by the system. The robotic arm will move towards defected leaf which is detected in image processing with the help of distance sensor which calculate the distance between set position of the robotic arm and position of the defected leaf with the help of image processing techniques which calculates X–Y position of objects. Here we are keeping two threshold values one is lower threshold value and another is higher threshold value. If the affected area is in between first and second threshold value then we are going to spray on that leaf or affected area and if the affected area is more than higher threshold value then we are going to remove this affected area by cutting this leaf with the help of robotic arm.

Advantages

- Reduces chemical and labor cost.
- Reduces workload of farmer.
- Minimize environmental damage.
- Avoid chemical effect on human health.
- Improve quality & quantity.

4 Results

Images are captured with the help of web camera for mealybug pest and the percentage of infection is predicted over the total leaf area. The thresh has been decided as 50%. If the affected area is above 50% then the decision of leaf cut is taken and robot arm is instructed to cut the leaf else the spraying action is initiated. The Fig. 2a, b is the captured image of leaf which is affected by mealybug pest. The segmentation algorithm (Fig. 3) is used to find the total pixels in the form of affected area and area is calculated on the basis of white pixels in the image as shown in Fig. 4. The flowchart shown in Fig. 6 gives the idea of decision making algorithm used for pest management system Fig. 5.



Fig. 2 Image of leaf and preprocessing

Fig. 3 Segmentation of bug

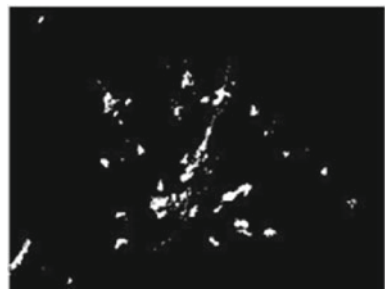


Fig. 4 Area estimation

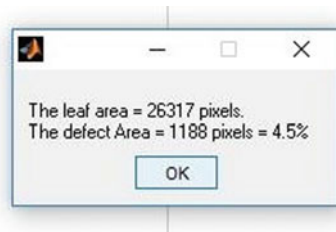


Fig. 5 Robotic structure



The model of robot with arm is as shown in Fig. 5 which consist two parts one is cutting arm and spray nozzle. The activation of cutting or spray depends on the percentage of affected area.

Flowchart

Images captured are preprocessed, segmented and white pixels are counted to calculate the area affected so that decision of either cutting or spraying is to be taken. Once one decision is taken then the robot is moved and the process is repeated. The results obtained gives the accuracy of 93% in bug detection and 95% accuracy in decision making.

5 Conclusion

This paper is effectively experimented & implemented for effective detection and measurement of the pest with accuracy of 93% on the crops and prevention of crops by using robot which also consist robotic arm with decision making capacity of accuracy of 95.5, which helps to easy handling with the pest on the crops.

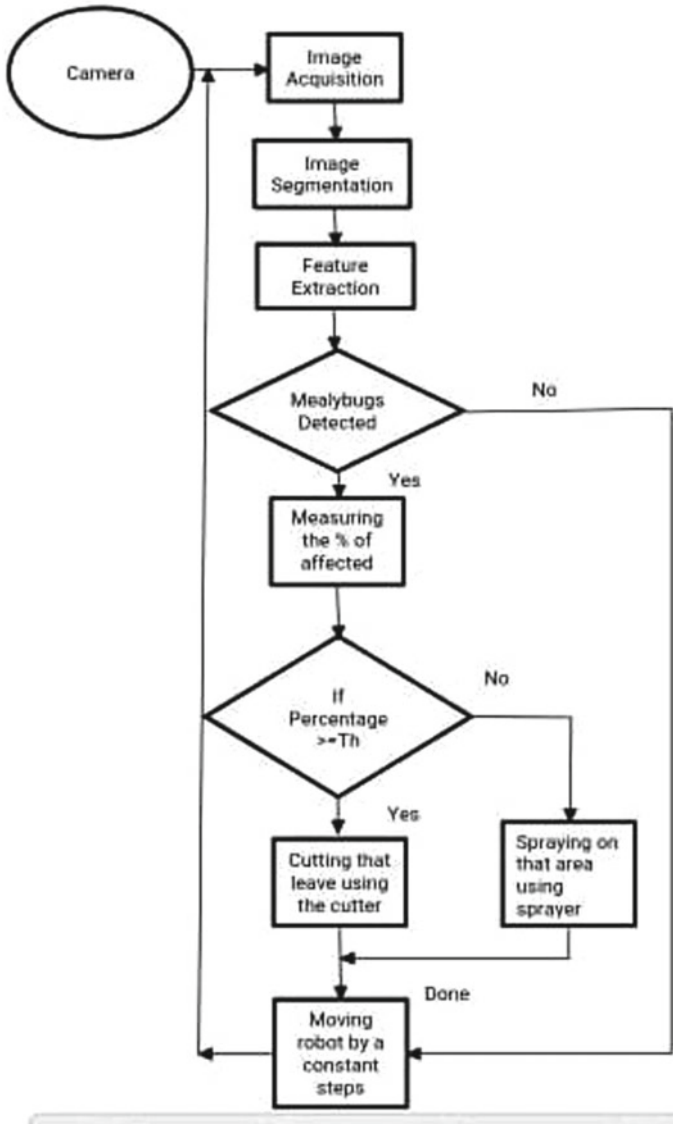


Fig. 6 Flowchart of working of PMS

References

1. Srisuphab A, Silapachote P (2018) Insect detection on an unmanned ground rover. In: Proceedings of TENCON 2018–2018 IEEE region 10 conference
2. Lagad S, Karmore S (2017) Design and development of agrobot for pesticide spraying using grading system. In: 2017 International conference on electronics, communication and aerospace

technology ICECA

3. Thomas S (2017) Design and implementation of unmanned ground vehicle (UGV) for surveillance and bomb detection using haptic arm technology. In: 2017 IEEE international conference on innovations in green energy and healthcare technologies
4. Bhong VS, Pawar PBV (2016) Study and analysis of cotton leaf disease detection using image processing, 3(2):1447–1454
5. Miranda JL, Gerardo BD, Tanguilig BT (2014) Pest detection and extraction using image processing techniques. *Int J Comput Commun Eng* 3(3)
6. Li V, Xia C, Lee J (2009) Vision-based pest detection and automatic spray of greenhouse plant. In: IEEE international symposium on industrial electronics (ISIE 2009) Seoul Olympic Parktel, Seoul, Korea
7. Martin V, Moisan S (2008) Towards a video camera network for early pest detection in greenhouses. In: ENDURE international conference

A Profound Approach Towards Rural Empowerment with the Aid of Solar Drying Technology



Asiya S. Pendhari, Nilprabha N. Yadav, M. Kaif R. Bagsiraj, Rajmati M. Patil, and Avesahemad S. N. Husainy

Abstract In recent years it is growing need to think about development of rural areas by creating the source of income to villagers with the use of simple and user-friendly technology which reduces their losses and creating way to do business as well as employment for villagers. In this paper attempt has been given on reducing post harvesting losses and developing solar dryer as approach to increase the income in rural area. In the given work different type of drying techniques are studied and found the research gap with consideration of objective and design the solar dryer to overcome all the lacunas found. The experimentation had done at Yadrav (Maharashtra) which has latitude 16.7140° N and longitude 74.4882° E in the month of May and June. The research mechanism is designed for 30 kg capacity for fruits and vegetables. The innovations make dryer fully renewable, user-friendly with well-maintained drying condition which gives perfectly dried product suitable for international markets. The main innovations are of desiccant bed and recirculation pipe in this experiment removes moisture. Also efficiency increases and drying time decreases. Maximum efficiency occur 36.64% and product dried in 30 days for minimum mass flow rate of 0.01484 kg/s.

Keywords Solar dryer · Food safety · Desiccant bed · Recirculation mode · Rural development · Moisture content · Mass flow rate

1 Introduction

Protection of agricultural products is necessary action to make sure the availability of product for longer duration and to decrease post-harvest losses. The drying is one of the most useful preservation techniques from last few decades. Solar drying is very helpful because it useful for decrement of large issues faced by all growing countries. Solar dryers remove moisture from solar wet products with the help of

A. S. Pendhari (✉) · N. N. Yadav · M. K. R. Bagsiraj · R. M. Patil
UG Students, Department of Mechanical Engineering, SITCOE, Yadrav, Maharashtra, India

A. S. N. Husainy
Assistant Professor, Mechanical Engineering Department, SITCOE, Yadrav, Maharashtra, India

sun energy and it gives a large range of benefits like (i) superior quality of dried products, (ii) process speed, (iii) losses reduction (iv) Controls process and (v) less space requirement [1, 2]. Therefore indirect type solar dryer is the best option to control the matter occurred as above mentioned [3].

Moisture content reduction to safe level is main aim of drying so the products can safely store for long interval of time without any failure. The less moisture content is beneficial because it prevents from microorganisms like moulds, bacteria, and yeasts, etc. [4]. The reduction of mass and volume also takes place so the least packaging is possible, storage can be easy, and transportation cost also reduces [5]. Now a days, lots of alternative methods found for drying purposes like electrical dryer, oven dryer, different types of solar dryers, freeze dryer etc. Also, continuous development and improvement is done by researchers. The aim of research is design and development of experimental set up of Forced convection Photo Voltaic operated solar dryer. To get a good quality of dried product with high nutrient value to protect fruits from toxic and contaminated nature to study the cost analysis and decide best design, cut the drying time as compare to other conventional dryers. Also, there are lots of solar dryers are available such as natural convection solar dryer, forced convection solar dryer and mixed mode solar dryer with including various innovations in different types like energy storage, PV cell, collector, etc.

1.1 Need and Scope of Solar Drying Technology

The Agriculture is seasonal and it is mostly depends on rain [7]; so rural farmers face lots of problems regarding unemployment in summer. So energy is mostly needed factor and it is continuously growing day by day. Many investigations are done on renewable energy. So it is important point of research [6, 8, 9]. Considering all these factors, solar drying technology is best suitable game changing technology for large amount of production. This technology is most advantageous for poor people and farmers [7]. Farmers in the rural area face lots of problems regarding unemployment in summer season [10]. Sun dried meat products are produced by solar drying technology and it will increases employment and profit gaining with the use of livestock, and so it provides income source all over the world. Therefore, it is most important modern drying technology and it is more useful for villagers and they earn maximum profit from this source is the main point [11]. India is the largest meat producer and it produces about 5.94 million tons of meat [12] in which, 20–30% of meat is wasted per year because of minimum storage facilities and wastage can be minimize by using this technology. So, products are storable for longer time and for further use [13].

1.2 Principle of Drying

Drying is a technique of expulsion of fluid by dissipation to make it solid. Mechanical techniques for isolating a fluid from a rigid aren't contemplated. For the given segment an effort is make to give a succinct diagram for the major standard of drying measure for rural items. These standards are enforced to convectional drying with concerned essentially for solar i.e. sun powered drying. As a rule it should be noticed that the traditional drying fundamentals and theories are fully based on kind of energy utilized [14]. It gives a complete analysis of basics and approach to controlling the drying process. The conversion of fluid mist to vapor is the main part of energy saving in between drying process (2258 kJ/kg at 101.3 kPa). Water may be present in different states like free wetness or bound structure which impacts on rate of drying.

$$X_w = m_w / (m_w + m_d), \text{ kg/kg of mixture} \tag{1.1}$$

Furthermore, X_d is dry premise, communicated with proportion of water content to the moisture weight/unit of wet material.

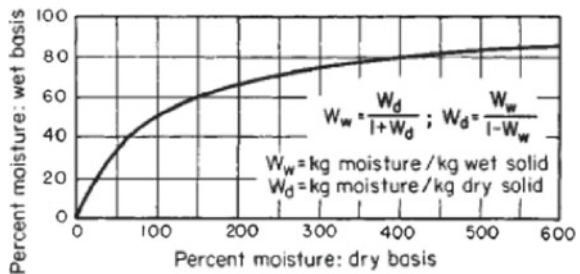
$$X_w = m_w / m_d \tag{1.2}$$

Figure 1 shows the connection between dry-weight and wet- weight even though this is a best way to show wetness for numerical determinations on dry basis however for farm products wetness content is normally shown in wet basis.

2 Literature Survey

Poonia et al. [16] focused on plan and assembling of solar grape dryer. The dryer is mainly points on commercial value of farmers. Solar dryer is the best and affordable path for protection and to expand the income of villagers and farmers. The best development in this dryer is paraffin max PCM storage which diminishes the time of drying. Components like Flat plate collector, UV sheet and blower are utilized for high performance and good quality of product. This dryer is manufactured for 30 kg

Fig. 1 Relationship between wet-weight and dry-weight basis [15]



which requires absolute 49 mJ of energy for drying in 35 h. The efficiency of dryer is 36.64% with mass stream pace of 0.01484 kg/s. Çiftçioglu et al. [17]. An agricultural product gets wasted because of factors like fungus, insects, and micro-organisms in rural areas. The paper gives information about smart agriculture design for drying brilliant farming plan for drying which is cost-effective and flat plate solar collector. The entire system depends on air heated flat plate solar collector safeguard sanctioned ease of warmth for example utilizing solar sustainable power is determined and contrasted and petroleum derivative fuel sources like flammable gas, power and LPG. Since quite a while ago run of time examination shows that, solar energy is best. Regarding Payback period, it's a lot of speedy. Udomkun et al. [18] the paper mainly focused on various types of solar dryer which can be employed in these continents. The solar dryers is having two types those are natural convection dryers and forced convection dryers. Additionally further they are delegated is direct sun based dryers, circuitous sun powered dryers and cross breed sun based dryers. In this paper for additional subtitles, a contextual analysis has been done through different nations like India, china, Indonesia, Thailand, The Philippines, Burkina Faso, Kenya, Uganda and DR of cargo. Therefore, they found that this advanced innovation displays parcel of potential as an eco-accommodating strategy and will decrease post reaping misfortunes in low income rural regions. It's with referencing here that this innovation will clearly enable provincial zones in surprising way. Varalakshmi [19] the research paper focuses the use of conventional energy in rural area development in India. It is the innovation which benefits residents by methods for contributing less and gaining more. The innovation is eco-friendly and subsequently, it doesn't hurt nature. By study, assumption is done with the limit of 50 kg/day which is skilled for little families in rural settlements. For crude material and end result 15 days is accepted as capacity period and continuing task development is expected as six days. Furthermore, half of deals are considered as approval. By considering all this aspects it can be concluded that this solar drying technology is the most profitable and efficient as compared to others. Husainy et al. [20] in this paper, literature had done experimentation on solar dryer for drying turmeric and concludes that turmeric dried in less time with perfect moisture content. There is also mentioned the process of turmeric is drying with different mass flow rate and conclude that decrease in mass flow rate, increase the efficiency and get final moisture content reduced from 84 to 15% and complete drying cycle attend within 47 h by using mixed mode forced convection solar dryer.

3 Experimentation and Methodology

The project works on the principle of recirculation mode of forced convection Solar Tunnel drying technology. This method utilizes solar panel with solar tracking which provides sufficient amount of energy available by sunlight and stored it in battery. This energy is further used to run the fan for air circulation. Product which is to be kept at drying chamber in which solar energy is used. There are two trays on



Fig. 2 Experimental setup

which the product is to be placed for drying purpose. UV protected sheet is used for drying chamber to protect product quality from excess solar energy. The hot air with moisture content from drying chamber is drawn by using fan and it is supplied to the desiccant bed. In desiccant bed silica gel is used as moisture remover. The main purpose of desiccant bed is to remove the moisture content present in hot air. This hot air is again circulated in a drying chamber. It is used to record Moisture content, weight of product, drying time etc. Figure 2 shows the experimental setup.

For reduction of economic losses in raisin formation, is one of the great methods. For performing experiment, indirect sun drying method issued. For drying of grapes, firstly grapes dipped in chemical which dissolves the grape skin and improves drying rate. Then these grapes are taken out from chemical and further placed on trays in the drying chamber based on the calculation which are recorded. The conditions of drying chamber are recorded to conduct trial on experimental setup under controlled drying conditions of air velocity, air temperature and humidity. After two hours, readings of temperature in drying chamber are taken. Then the dried grapes (resins) from chamber are taken out and further transferred for checking moisture content and nutritional value. Studied the results of the experimentation for the different flow rates $M1 = 0.014 \text{ kg/s}$, $M2 = 0.0156 \text{ kg/s}$, $M3 = 0.0165 \text{ kg/s}$ and $M4 = 0.0172 \text{ kg/s}$ and found the conclusion, which are useful in future research for grape drying. Dimensions of dryer is total height 135.5 cm with 40 W Capacity of solar panel and chamber length 15 cm i.e. Overall dimensions of the drying chamber are: Length \times Width \times Height = 150 cm \times 121 cm \times 61.5 cm.

3.1 Design Calculation for Drying Chamber

For removing moisture content from grape, energy is required. For that, moisture content testing is taken in lab for different grapes like wet grapes and dry grapes available in market. Finally reports found that final and initial moisture content as 110 g/80 g and 100 g/20 g respectively. By using all the data calculation had done.

Suppose,

Amount of wetness = 80% and 20% for dry grapes respectively.

Moisture removed from grapes

$$m_w = \frac{m_p(m_i - m_f)}{(100 - m_f)} = 18.75 \text{ kg of water}$$

Here,

- m_p mass of grape
- m_i Initial moisture
- m_f Final moisture
- m_w moisture content.

$$\text{Amount of heat required to evaporate water} = Q = m_w \times h_{fg} \quad (3.1)$$

$$h_{fgw} = 4186(597 - 0.56 \times T_p) = 2.35 \text{ MJ/kg} \quad (3.2)$$

T_p initial temperature of grape

Quantity of heat required to evaporate water = $Q = m_w \times h_{fg} = 44.06 \text{ MJ}$

Suppose 10% heat loss occur in drying chamber

Heat need to be supply = $44.06 \times 1.1 = 48.460, \text{ MJ} \approx 49 \text{ MJ}$

4 Results and Discussion

As mentioned in the methodology, experiments are performed on solar dryer takes place and then results are obtained. After that for the study of different parameters graphs were plotted like variation of moisture versus time, Variation of intensity versus solar radiation also for finding the effect of mass flow rate on drying time etc.

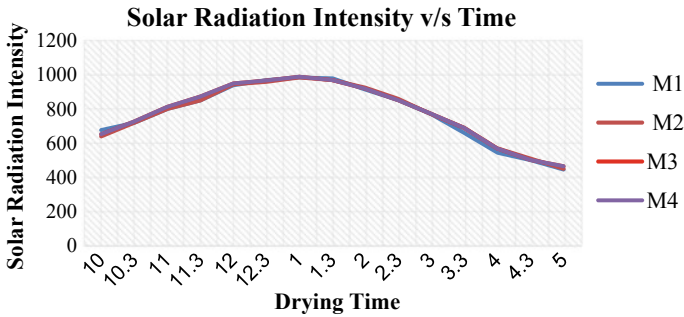


Fig. 3 Variation of intensity of solar radiation versus time for different mass flow rate. M1 = 0.0148 kg/s, M2 = 0.0156 kg/s, M3 = 0.0165 kg/s, M4 = 0.0172 kg/s

4.1 Variation of Intensity of Solar Radiation with Time

On each first day of experimentation intensity of solar radiation was measured at day time for finding the variation, on that basis graphs were plotted on intensity of solar radiation versus time for finding the variation in the intensity for different mass flow rates. The examinations were directed for a couple of working days, usually in understanding to examination of solar intensity emission upon the experimental trial day; pyrometer is used for solar intensity measurement and plotted against the every trial timing. The assortment of force of sunlight based radiation when the examination was carried by utilizing for four different mass flow rate of 0.0148, 0.0156, 0.0165 and 0.0172 kg/s.

Along these lines, from the above charts clearly the solar intensity radiation remained around same for the throughout the times of the test examination. Figure 3 shows the variation of intensity of solar radiation versus time for different mass flow rate.

4.2 Variation of Moisture Content on Dry Basis with Time

The examination of change in the content of wetness on wet premise is completed by drawing the graph of content of wetness decided on dry premise versus time for Fig. 4. And wet premise versus time for Fig. 5. The wetness change is determined for the supposed mass flow rates, and also presents a concept of impact of mass stream rate on rate of drying. Graph of content of wetness on wet and dry reason for mass flow rate of M1 = 0.0148 kg/s, M2 = 0.0156 kg/s, M3 = 0.0165 kg/s and M4 = 0.0172 kg/s versus the time of drying. The impact of flow rates on the drying time are describes simply from graphs.

From the over the two graphs of wetness (i.e. moisture) content on dry reason and wet reason exclusively grapes versus time of four different mass stream rates,

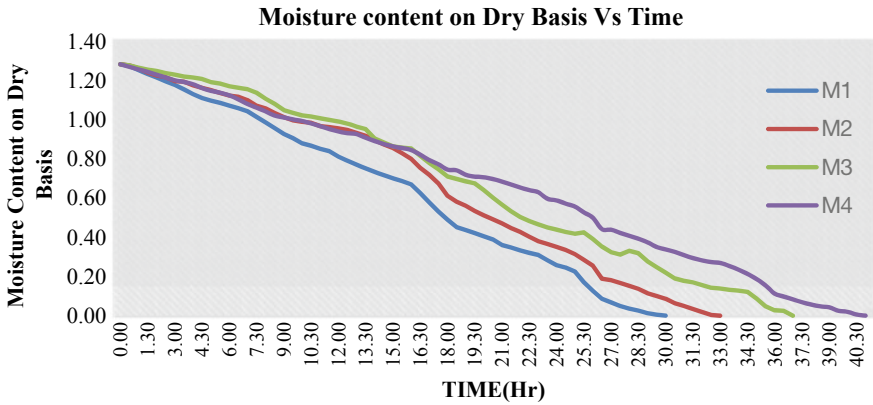


Fig. 4 Variation in moisture content (dry basis) versus time for grapes

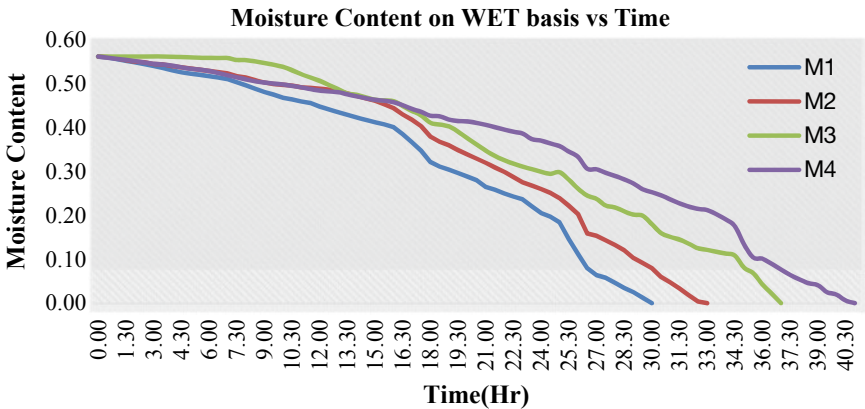


Fig. 5 Variation in moisture content (wet basis) versus time for grapes

it is successfully characterized that wetness content diminishing significantly with increment in the mass stream pace of air for dry premise and moisture content decline extensively with diminishes in the mass flow rate of air for wet premise.

4.3 Moisture Ratio Versus Drying Time

The graph in Fig. 6 of moisture proportion during drying period are plotted against the drying time. The moisture proportion in the grapes differed with the adjustment in mass stream amount of the air. The readings for the moisture proportion were

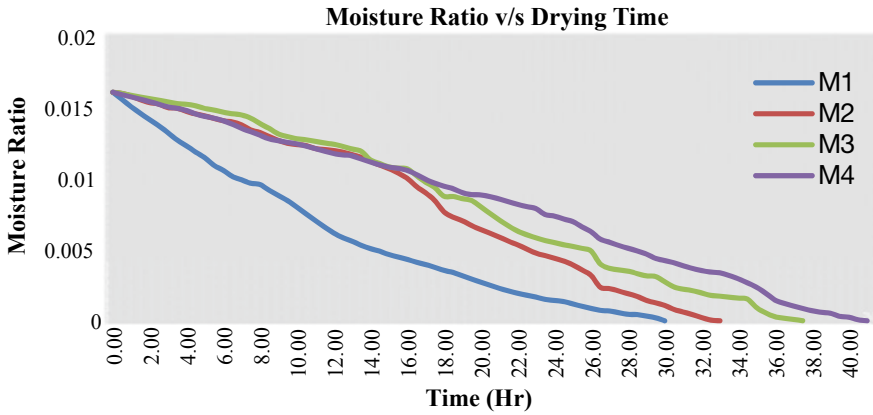


Fig. 6 Variation in moisture content versus time for grapes

done for the depicted approaches (for M1 = 0.0148 kg/s, M2 = 0.0156 kg/s, M3 = 0.0165 kg/s and M4 = 0.0172 kg/s, for grapes).

4.4 Drying Rate Variation with Time

The Graph in Fig. 7 show changes in the drying rate (regarding gram of water misfortune to kg of dry item every hour) as opposed to drying time. The drying rate for the grapes is at its pinnacle esteem at first and continues diminishing with time and after a significant stretch appears to have come to stop. The drying rate is the capacity of the measure of moisture staying in the grapes. Drying rate intensely depends on the nature of the air provided.

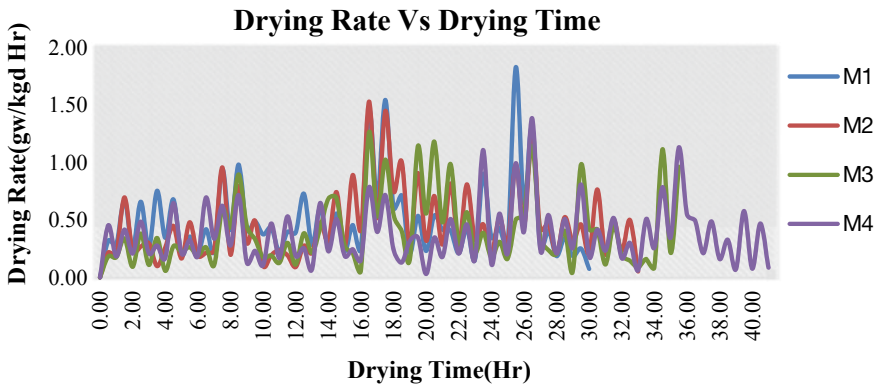


Fig. 7 Variation in drying rate and drying time

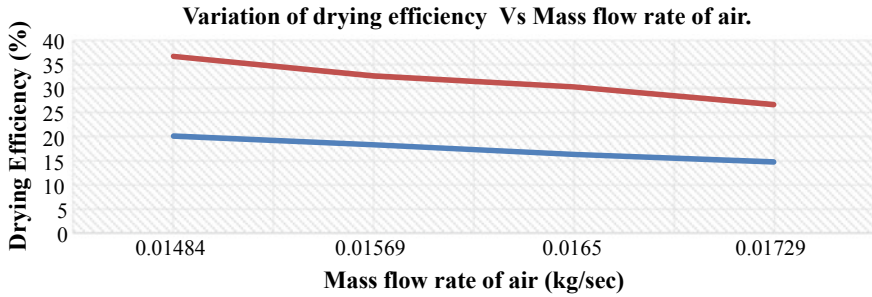


Fig. 8 Variation in drying efficiency versus mass flow rate

4.5 Variation of Drying Time for Performed Test Methodologies

The variation in the time of drying for different mass stream rates of the air is computed in the below graph.

The graph in Fig. 8 declares changes in dryer efficiency and mass stream rate of air. The time of drying was reduces with reduction in mass flow rate thus it improves the efficiency of drying. When the mass flow rate of air is increases, the temperature of air outside the collector can reduces and it can also decrease the temperature and time of drying.

5 Conclusion

This paper examines the role of solar drying technology in rural areas focusing on economically backward people in the sense of cost affordability and overall reliability. As a result, it's worth mentioning here that it will overcome lacunas like inadequate or extra drying of product, microbial infestation, and improper post-harvesting factors like impaired test and decreased nutritional value. This system is flexibly transportable because of its systematic design considerations which reduce any type of fatigue during handling. Following are the conclusions of examination, for the mass flow rate of 0.0148, 0.0156, 0.0165 and 0.0172 kg/s in the current work on the solar grape dryer.

- The solar radiation intensity remained equal for ordinary and normal sunlight based Radiation force considered for the energy figuring is 800 W/m^2 .
- For the low mass flow rate of 0.0148 kg/s only 30 days required to drying and for maximum mass flow rate of 0.0172 kg/s there are 41 days required i.e. mass flow rate is directly proportional to drying time.
- Drying rate is high during the peak temperatures and lowers with the variation in the temperatures and also the amount of atmospheric humidity.

- Efficiency of dryer occurred is 37% for the mass flow rate of air 0.0148 kg/s for minimum mass flow rate high efficiency obtained.
- This system avoids excess drying As well as uncontrolled drying. It is the most effective way to grow income of villagers.
- With the use of Recirculation mode and Desiccant Bed drying time decrease by 1½ to 2 h also moisture content in drying chamber is removed which make chamber in controlled condition.

References

1. Prakash O, Kumar A (2013) Historical review and recent trends in solar drying systems. *Int J Green Energy* 10(7):690e738
2. Vijayan S, Arjunan TV, Kumar A (2016) Mathematical modeling and performance analysis of thin layer drying of bitter melon in sensible storage based indirect solar dryer. *Innov Food Sci Emerg Technol* 36:59e67
3. Mustayena AGMB, Mekhilef S, Saidur R (2014) Performance study of different solar dryers: a review. *Renew Sustain Energy Rev* 34:463–470
4. Bahnasawy AH, Shenana ME (2004) A mathematical model of direct sun and solar drying of some fermented dairy products (Kishk). *J Food Eng* 61:309–319
5. Akpınar EK (2006) Mathematical modelling of thin layer drying process under open sun of some aromatic plants. *J Food Eng* 77:864–870
6. Zhang H, Gowing T, Degreve J, Leadbeater T, Baeyens J (2016) Use of particle heat carriers in the stirling engine concept. *Energy Technol* 4(3):401–408
7. <http://nsdl.niscair.res.in/jspui/bitstream/123456789/554/1/Concepts%20of%20rainfed%20agriculture%20-%20Formatted.pdf>. Accessed 10 Nov 2015
8. Yılan G, Kadirgan MAN, Çiftçioglu GA (2020) Analysis of electricity generation options for sustainable energy decision making: the case of Turkey. *Renew Energy* 146:519–529
9. Sevencan S, Altun-Çiftçioglu G, Kadirgan N (2011) A preliminary environmental assessment of power generation systems for a stand-alone mobile house cradle to gate approach. *Gazi Univ J Sci* 24(3):487–494
10. Jain D, Tiwari GN (2003) Thermal aspects of open sun drying of various crops. *Energy* 28:37–54
11. Ladipo JK, Ossai GEA, Olunloyo OA (1986) Food science and technology in national development: entrepreneurship in the food industry. *Niger Food J* 4:3–11
12. <http://dahd.nic.in/dahd/WriteReadData/FINAL%20ANIMAL%20AR%202013-14%20FOR%20WEB.pdf>. Accessed 6 Oct 2015
13. APEDA: Export of agro and processed food products including meat and meat products (2008) Agricultural and Processed Food Products Export Development Authority. Ministry of Commerce, Government of India
14. Mujumdar AS (2007) Handbook of industrial drying, Part-I. Taylor and Francis group, UK
15. Perry JH (2007) Chemical engineering handbook, 8th edn. McGraw-Hill, New York, p 28
16. Poonia S, Singh AK, Santra P, Mishra D (2018) Design, development and performance evolution of a low-cost solar dryer. In: Concentrated solar thermal energy technologies. Springer, Singapore
17. Çiftçioglu GA, Kadirgan F, Kadirgan MAN, Kaynak G (2020) Smart agriculture through using cost-effective and high-efficiency solar drying. *Heliyon* 6
18. Udomkun P, Romuli S, Schock S, Mahayothee B, Sartas M, Wossen T, Njukwe E, Vanlauwe B, Müller J (2020) Review of solar dryers for agricultural products in Asia and Africa: an innovation landscape approach. *J Environ Manage* 268:

19. Varalakshmi K (2016) Role of conventional energy in rural development in India: feasibility analysis of solar drying technology. *Int J Energy Environ Eng* 7(3):321–327
20. Husainy ASN, Pujari S, Wale G (2018) Experimental investigation of mixed mode forced convection solar dryer for turmeric (*Curcuma longa*). *Asian Rev Mech Eng* 7(1):1–6

Chemical and Physical Processes

An Experimental Study of Dynamic Adsorption of Polymer in Alkaline Surfactant Polymer (ASP) Flooding for Heavy Oil



Siraj Bhatkar and Lalitkumar Kshirsagar

Abstract Problems associated with the recovery of heavy viscous oil are key challenges for the upstream industry. In this research work, systematic experimental studies of chemical flooding were conducted for heavy crude reservoir. Alkali-Surfactant-Polymer (ASP) flooding in the reservoir may enhance the crude oil recovery; it may lead to adsorption of flooded chemicals. These flooded chemicals are very expensive and high rate of adsorption will make the recovery uneconomical. Analysis of petroleum core flood effluent has to be done, to study dynamic adsorption. This experimental work shows the selectivity of ASP flooding for heavy oil and increase in percentage recovery of heavy oil with optimizing ASP concentrations. The results also show that polymer flooding is quite effective at low oil saturation.

Keywords Chemical flooding · ASP flooding · Dynamic adsorption · Heavy oil · Enhanced

Abbreviations

ASP	Alkali Surfactant Polymer
HCPV	Hydrocarbon pore volume
A	Alkali
RRF	Residual resistance factor
LCDE	Linear core displacement efficiency
HCPV	Hydrocarbon pore volume
W/F	Water flood
RF	Resistance factor
ETP	Effluent treatment plant

S. Bhatkar (✉) · L. Kshirsagar
School of Petroleum Engineering, Dr. Vishwanath Karad MIT World Peace University, Pune 411 038, India

L. Kshirsagar
Department of Petroleum Engineering, Maharashtra Institute of Technology, Pune 411 038, India

1 Introduction

Problem with heavy viscous crude oil is that it has adverse mobility which causes a more rapid decline in production rate during the primary recovery period [1–5]. Heavy oil recovery is very difficult; the rate of oil recovery is between 10 to 20% and mostly less than 20% [6–8]. In case of heavy oil recovery, thermal methods can be used easily. But in cases where there are thin pay zones, the method of thermal recovery becomes difficult [9–12]. For thin pay zones where heavy viscous crude oil is present, chemical flooding can be done for enhancing the recovery of oil effectively [13–17]. Thermal methods of Enhance oil recovery can be used but it does not suit thin pay zones as thermal methods affects the nearby formation of pay zones [18, 19]. Dynamic adsorption of polymer in ASP flooding needs to be well understood depending upon case to case [20].

Chemical flooding, alkali-surfactant-polymer (ASP) flooding can be best suited for reservoirs having less than 10 m thickness and having heavy crude with high viscosity, in such cases thermal recovery fails to recovery maximum oil [21–23].

In this experimental work the field under study has thin pay zone with heavy viscous crude. This experimental work deals with ASP flooding for heavy oil and increases in percentage recovery of oil with optimizing ASP concentrations. Dynamic adsorption of polymer in ASP flooding needs to be monitored and based on this result selectivity of polymer needs to be done. The results also show that polymer flooding is quite effective at low oil saturation. The pay zone under study is a thin pay zone having heavy viscous crude. By water flooding the overall recovery is very less which needs to be improved. Screening of polymer, Alkali and surfactant samples was done in this work. For screening of polymers, compatibility study, thermal stability study, screen factor, rheological study was done in laboratory. For screening of alkali and surfactant, IFT measurements and phase behaviour study was carried out. Physico-chemical analysis of water samples was carried out along with SARA analysis of crude oil. Mineralogical analysis of formation core was very useful. After screening study for ASP is done, displacement studies on core/sand pack was carried out successfully in the laboratory.

2 Experimental

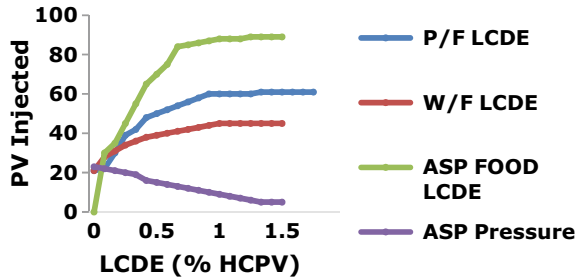
Chemicals used: Commercial grade Partially Hydrolyzed Polyacrylamide (PHPA) used as PSR Polymer (Avg. Mol. Wt. = 3,000,000), Associate polymer used as SPP, FPS and DXX is a polymer with protective package these polymers are water soluble, low shear degrading, non-biodegradable polymers manufactured by Meta form Well Tech.

All the polymer samples in Table 1 were found thermally stable as their retention of flow time was found more than 90 after 6 days.

Table 1 Thermal stability (percentage retention) data in tube well water

Thermal stability (% retention) data in tube well water						
Sr. no	Name of the polymer	Day 0	Day 2	Day 6	Day 15	Day 30
1	PSR	100	95.2	85.3	80	80
2	SPP	100	99.6	99.6	87.2	58.3
3	FPS	100	82.3	78.9	70.4	57
4	DXX	100	99.1	86.4	68.7	58.1

Fig. 1 PV injected versus LCDE



2.1 Core Flood

XZ Sand-I of ABC field is an unconsolidated formation. The study was carried out on the most representative core sample of XZ-I sand in ABC#121. The experiment was conducted by preparing 20 cm long native sand pack. The sand pack was then saturated with crude oil (Viscosity 262 cP at 70 °C). The initial oil saturation was 72.3% PV. Oil permeability at irreducible water saturation (S_{wr}) was 4522 mD.

Polymer flooding was conducted by injecting 1 PV of 2000 ppm PSR solution followed by tube well water as chase water till there was no oil production. Polymer flood displacement efficiency was found 63.2% of HCPV. Incremental displacement efficiency was 19.3% of HCPV over water flood. Figure 1 shows PV injected versus LCDE where AS flood has maximum LCDE.

2.2 Polymer Flood

For a given flow rate, resistance Factor (RF) is a measure of the decrease in mobility of polymer solution compared to injection water. As per literature, RF of about 10 is sufficient. A higher value may lead to high injection pressure and hindrance in the field. The RF was found 12 based on core flood studies. Residual Resistance Factor (RRF) is the amount of reduction in permeability of the porous media caused by the flowing of the polymer solution through the rock. It means reduction in effective

Table 2 Polymer Slug size = 1 PV (2000 ppm) PSR + Chase water

Total volume injected, PV	Displacement efficiency in % HCPV	Water cut (%)	Polymer produced (% of original Conc.)	Polymer produced in mg
0.16	24.7	0.0	0.0	0.0
0.21	29.1	40.0	–	–
0.36	39.2	58.1	–	–

water permeability. Table 2 shows that total PV volume injected will increase the displacement efficiency but water cut will also increase simultaneously.

2.3 Fractional Flow Curve

Fractional flow curves were generated using the fraction of oil and water using end face saturation curves versus water cut, during displacement studies. Polymer controls the mobility ratio of injected water by changing the viscosity of injected water and due to change in relative permeability of water and of oil. The fractional flow curves were generated and it shows that the curve shifts in the correct direction in the case of polymer flood and ends at 0.70 Pore volume of water saturation as against of 0.63 Pore volume of water saturation while water flood at 96% water cut. From Fig. 2 we understand that 0.13 Pore volume of oil can be produced extra over and above water flood by means of chemical flooding using polymer.

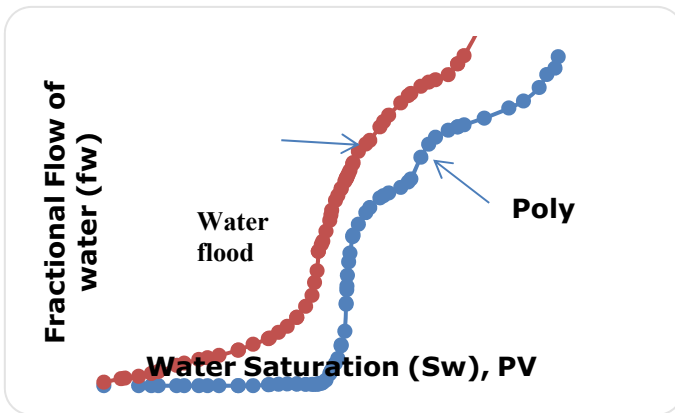
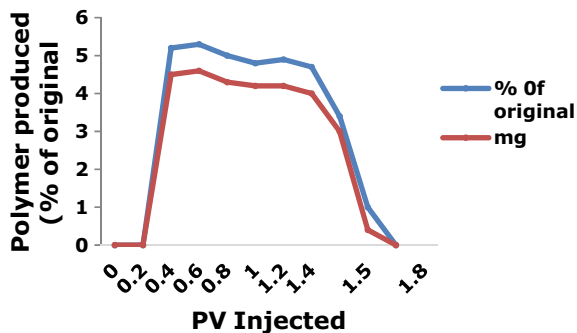


Fig. 2 Fractional flow curve for polymer flood and water flood

Fig. 3 Dynamic adsorption of polymer



2.4 Dynamic Adsorption

On the solid surface, Polymer gets retained in permeable formation because of adsorption. Polymer gets trapped within smaller pores. Loss of polymer from solution occurs because of Retention, this can lead to mobility control effect to be lost, particularly pronounced effect at low polymer concentration. The dynamic adsorption of the polymer was calculated by analyzing the produced fluid obtained during displacement experiment. Separation of oil and aqueous phase was carried out. Polymer concentration was calculated by measuring the flow time using Cannon–Fenske viscometer. Figure 3 shows the polymer produced % of original and polymer produced in mg versus PV Injected, average adsorption of polymer on the rock after the injection of 1.5 PV was 1180 ppm as per experimental result. Dynamic adsorption value was 0.32 mg/gm of rock.

Table 3 summarizes all four core flood experiments result data, in which first three core food experiment runs are done only for Polymer flooding and fourth experiment run is for ASP flooding. In the table below initially basic data for all core flood experiments is summarized, then results related to WF Displacement Efficiency, Polymer /ASP Disp. Efficiency are shown.

3 Result and Discussion

Based on the screening studies of four polymer samples, one Polymer PSR 2000 ppm concentration was found suitable for core flood studies. Screening tests for alkali and surfactants indicated Alkali (Sodium Carbonate) of 3.0 wt % and surfactant (Sulfodet L-38) of 2800 ppm as suitable for core flood studies. Based on the above experiment, polymer slug of 1.0 PV of PSR can be considered as optimum. The results also show that polymer flooding is quite effective at low oil saturation, but experiment no 4 shows maximum oil recovery as remaining oil saturation is 10% and has maximum linear core displacement efficiency. ASP flooding: One number of native sand pack studies experiments were carried out for ASP flooding at oil

Table 3 The summary of result of all core flood experiments for ABC field (XZ-I)

Important parameters	Experiment run no. 1	Experiment run no. 2	Experiment run no. 3	Experiment run no. 4
Sand pack details	Type of core: sand pack, XZ#111; Core length (cm) = 20; Cross sectional area (cm ²) = 7.8; Bulk volume (ml) = 148			
Pore volume (ml)	55	55	56	58
Oil permeability at Swr, mD	4310	4310	3811	3842
Oil saturation (Soi) (% PV)	73.1	73.1	68.6	68.6
Water permeability at Sor, mD	266	266	223	223
Oil viscosity at 70 °C, cP	262	262	262	262
<i>WF displacement efficiency</i>				
Water flood LCDE (% HCPV)	43.9	43.9	43.1	43.1
<i>Polymer/ASP disp. efficiency</i>				
LCDE (% HCPV)	60.3	53.7	57.9	87.6
Remaining oil saturation S _{orc} , % PV	26	31	29	10
Stage at which polymer/ASP used	Secondary	Secondary	After Water break through	Secondary
Resistance factor (RF)	12	14	11	–
Residual resistance factor (RRF)	8	9	8.1	–
Dynamic adsorption of polymer (mg/gm of rock)	0.32	0.31	0.26	0.21

saturation by injecting 0.40 PV of ASP slug consisting of Alkali -3 wt%, surfactant-3000 ppm, and Polymer-2000 ppm followed by 0.30 PV of Graded Mobility Buffer with an average concentration of 1100 ppm. At 68.6% saturation, LCDE = 43.1% HCPV over W/F (43.7% HCPV). Significant improvement in displacement efficiency of ASP Flooding is due to the synergistic effect of ASP components and favorable crude characteristics.

Dynamic adsorption of the polymer solution was found in the range of 0.21–0.32 mg/gm of rock. For alkali and surfactant, it was found to be 2.68 and 0.26 mg/gm of rock respectively. The adsorption values of all three components were found more

due to the presence of clay and Fe-rich minerals. However, alkali helps in reducing adsorption of polymer on the rock.

4 Conclusion

In this work it was observed that, Alkali-Surfactant-Polymer (ASP) flooding enhances the heavy crude oil recovery as LCDE (% HCPV) is 87.6% which is maximum for ASP, compared to polymer flooding. Dynamic Adsorption of Polymer (mg/gm of rock) is low for ASP; it shows that ASP is very effective as compared to polymer flooding. Remaining oil saturation S_{orc} , for polymer is high as compared to ASP i.e. 10 % PV. Hence, the overall displacement efficiency of ASP is very high as compared to polymer flooding and increase in percentage recovery of heavy oil can be achieved by optimizing ASP concentrations. Thus, ASP flooding is very effective and successful method of heavy oil recovery in thin pay zones with viscous oil.

References

1. Giri V, Vecchiolla D (2018) Bubble–bubble pinch-off in symmetric and asymmetric microfluidic expansion channels for ordered foam generation. *Soft Matter* 14:9312–9325
2. Zeng Y, Xiao E, Vavra S, Hirasaki G (2018) Microfluidic devices for characterizing pore-scale event processes in porous media for oil recovery applications. *JoVE*
3. Xiao S, Xiao E, Vavra S, Hirasaki G (2018) Destabilization, propagation, and generation of surfactant-stabilized foam during crude oil displacement in heterogeneous model porous media. *Langmuir* 34:739–749
4. Alzahid Y, Payman M, Warkiani M, Armstrong R, Joekar V (2017) Alkaline surfactant polymer flooding: what happens at the pore scale? (Society of Petroleum Engineers, Houston, 2017).
5. Alzahid Y, Mostaghimi P, Walsh S, Armstrong R (2019) Flow regimes during surfactant flooding: the influence of phase behaviour. *Fuel* 236:851–860
6. Dong P, Puerto M, Ma K, Bourdarot G, Bourrel M, Biswal S, Hirasaki G (2018) Low-IFT foaming system for enhanced oil recovery in highly heterogeneous/fractured oil-wet carbonate reservoirs. *SPE J* 23:2243–2259
7. Telmadarreie A, Trivedi J (2018) Static and dynamic performance of wet foam and polymer-enhanced foam in the presence of heavy oil. *Coll Interfaces* 2:38
8. Baek K, Francisco J, Okuno R, Sharma H, Upali P (2018) An experimental study of emulsion phase behavior and viscosity for athabasca bitumen/diethylamine/brine mixtures. *SPE Reservoir Eval Eng*
9. Sheng K, Argüelles-Vivas F, Okuno R (2018) An experimental study of emulsion flow in alkaline solvent coinjection with steam for heavy-oil/bitumen recovery (Society of Petroleum Engineers, Houston, 2018)
10. Amirmoshiri M, Zeng Y, Chen Z, Singer P, Puerto M (2018) Probing the effect of oil type and saturation on foam flow in porous media: core-flooding and nuclear magnetic resonance (NMR) imaging. *Energy Fuels* 32:11177–11189
11. Boruah DM (2014) Polity and petroleum making of an oil industry in Assam, 1825–1980. Ph.D. thesis, Indian Institute of Technology, Guwahati
12. Brown MA, Goel A, Abbas Z (2016) Effect of electrolyte concentration on the stern layer thickness at a charged interface. *Angew Chem Int Ed* 55(11):3790–3794

13. Das BM, Gogoi SB (2015) Relating IFT with oil recovery with special reference to bhogpara porous media of upper Assam basin. *J Petrol Eng Technol* 5(1):1–8
14. Das BM, Gogoi SB (2015) Adsorption study of a natural product into the oil producing porous media of upper Assam Basin. *Int J Res Eng Appl Sci* 5(6):20–30
15. Erincik MZ, Qi P, Balhoff MT et al (2018) New method to reduce residual oil saturation by polymer flooding. *SPE J* 23:1–944
16. Fan JC, Wang FC, Chen J et al (2018) Molecular mechanism of vis-coelastic polymer enhanced oil recovery in nanopores. *R Soc Open Sci* 5:180076
17. Gogoi SB (2014) Effluent as surfactant for enhanced oil recovery. *J Innov Energy Polic* 3(1):40–50
18. Gogoi SB, Kakoty M (2017) A study of CO₂ flooding on wave velocities in the Naharkatiya oil reservoir of upper Assam basin. *Resour Effic Technol* 3(1):101–112
19. Hazarika K, Yadav R, Gogoi SB et al (2018) Characterization of crude oil for enhanced oil recovery: a study with anionic surfactant. *Int J Ambient Energy* 39(2):1–12
20. S Sarmah, S B Gogoi, J Barman, et al. (2017) Study on the effects of the rheological properties for flow behaviour of assam crude oil with various chemicals. In: *Proceedings of the 1st GeoM East international congress and exhibition, Egypt 2017 on sustainable civil infrastructures*, pp 148–168
21. Torrealba VA, Johns RT (2017) Coupled interfacial tension and phase behavior model based on micellar curvatures. *Langmuir* 33(47):13604–13614
22. Torrealba VA, Johns R, Hotiet H (2018) Curvature-based equation of state for microemulsion-phase behavior. *SPE J* 24(2):1–13
23. Torrealba VA, Johns R, Hotiet H (2018) Description of micellar radii for phase behavior and viscosity modeling of aqueous surfactant solutions and microemulsions. *Langmuir* 34(50):15327–15334

Analyzing Corrosion Prediction and Dose Optimization of Corrosion Inhibitor in Oil Field Production



Siraj Bhatkar, Niraj S. Topare, and Bashique Ahmed

Abstract Oil and gas field produced water disposal is very serious issue in hydrocarbon industry. Corrosion occurred by this produced water from oil industry is very difficult to be predicted. Produced water reinjection, treatment and disposal are a huge problem in onshore as well as offshore fields. As the reservoir depletes, mostly the water cut increases up to 90%, thus increasing the chances of corrosion of the surface and subsurface equipment. In this experimental work corrosion studies were undertaken on steel tubular at reservoir temperature. It is essential to remove the dissolved oxygen to control corrosion. The dissolved oxygen content in effluent was found to be high. The dose of sodium sulphite as oxygen scavenger after treatment of the injection water in the laboratory is optimized. Dissolved oxygen may vary from time to time; therefore the dose of oxygen scavenger may be changed accordingly for effective removal of oxygen. Sodium sulphide requires a catalyst like Cobaltous chloride. For dose optimization of corrosion inhibitor, laboratory treated effluent after filtration with 0.45- μ filter was used for this study. The water was treated with different concentrations of corrosion inhibitors (WIN). The rate of corrosion for different doses of corrosion inhibitor along with oxygen scavenger needs to be optimized. Corrosion plays a very important role in reducing the life of tubulars, Completion equipment, handling and treating equipment. Corrosion studies needs to be carried out in order to optimize the dose of oxygen scavenger and corrosion inhibitor. In this research work the corrosion studies were undertaken on N-80 steel tubular coupons at 88 °C. This paper discusses the laboratory fluid compatibility, scale and corrosion prediction analysis and treatment for injection water utilization while providing an insight into the potential impact of scale and corrosion risks associated with raw produced water.

Keywords Corrosion · Optimization · Inhibitor · Reinjection

S. Bhatkar (✉) · B. Ahmed

School of Petroleum Engineering, Dr. Vishwanath Karad MIT World Peace University, Pune 411 038, India

e-mail: siraj.bhatkar@mitwpu.edu.in; siraj.bhatkar@mitpune.edu.in

N. S. Topare

School of Chemical Engineering, Dr. Vishwanath Karad MIT World Peace University, Pune 411 038, India

© The Author(s), under exclusive license to Springer Nature Switzerland AG 2021

861

P. M. Pawar et al. (eds.), *Techno-Societal 2020*,

https://doi.org/10.1007/978-3-030-69925-3_82

Abbreviations

DO	Dissolved oxygen
TDS	Total dissolved solids
GAB	General Aerobic Bacteria
SRB	Sulphate reducing bacteria
USD	United States Dollar
ETP	Effluent treatment plant
CWIP	Central water injection plant
GGs	Group gathering station
TSS	Total suspended solid
NTU	Nephelometric turbidity unit
mpy	Mils per year
N 80	Steel Grade
SI	Scale Inhibitor

1 Introduction

The oil and gas industry faces tremendous amount of corrosion related problems. These problems are very crucial to identify the basic cause and remedial solution for these corrosion related problems [1–3]. Corrosion if not controlled on time may lead to permanent damage to the formation, equipments involved in process, tubing, well head, pipelines, handling components etc. [4]. Research indicates that total spending on corrosion inhibitor every year by industry is approximately USD 6.5 Billion.

Mainly in oil & gas export pipelines and production systems, to reduce the corrosion rates by a minimum of 90%, corrosion inhibitors are commonly used [5]. Deliverability of treatment is by either continuously pumping corrosion inhibitor into the system or in batch treatment depending on basic process requirements and its condition. The required dosing rates are between 10-50 ppm (parts per million), depending on total fluids which is basically required during continuous injection [6]. In the selection process, a number of test procedures that are required needs to be followed before the selection of a particular inhibitor [7]. These things are of vital importance as any mistake or negligence in corrosion inhibitor design can result in significant rise in flow assurance problems, for e.g., non compatibility of chemicals, emulsification problems, foaming tendency of crude & water etc. [8]. Hence, selecting a corrosion inhibitor which is suitable for entire facility is very important step to minimize overall costs, dosage optimization, increasing in corrosion inhibitor efficiency and reduction in overall cost related to corrosion [9].

The laboratory test are conducted keeping constant field conditions, which can indicate the same rate of corrosion as the temperature and pressure are maintained as per field conditions [10]. Field crude and synthetic brines can be used to ensure that the corrosion inhibitor is tested near to field conditions. The corrosiveness present

in the system needs to be identified. Other non performance test conditions are utilized to confirm that designed treatment is very effective [11]. Partial pressures of H_2S and CO_2 are mostly replicated in the laboratory [12]. Additional consideration such as water cuts, shear stress, temperature, crude type and materials are mostly built into testing patterns [13]. Testing in laboratory of any chemical for process requirement depends on process conditions, critical requirement of the component and its application [14].

The optimum dose for corrosion inhibitor chemical has been selected for the field application as per the process requirement [15]. There are different stages involved in the selection of a corrosion inhibitor, very stage is basically designed to specifically select and identify corrosion inhibitor based on its performance [16]. Screening of corrosion inhibitors involves basic physical properties identification. For a desired process even compatibility tests needs to be carried out to make sure that there is no adverse effect during application of corrosion inhibitor. Selection of corrosion inhibitor may depend and may vary by viscosity pH, thermal stability measurements, emulsion forming, foaming and gunking properties of corrosion inhibitor chemicals.

2 Background of Field Data Under Study

Presently, about 1200–1300 m^3/d of effluent is received and initially treated at ETP-I, XZ. Effluent is dispatched to CWIP-I, where it is subjected to filtration followed by chemical treatment. Finally injection water is dispatched to various GGS's through manifold for onward transmission to injectors. Out of total treated effluent, presently about 550 m^3/d is injected in Y-VII sand through 15 injector wells. An assessment of existing water parameters has shown very poor quality of injection water in terms of vital parameters such as TSS, turbidity and oil & grease content and presence of prolific bacterial activity. Similar observations were recorded in the surveillance studies carried out by lab.

2.1 Details of Fluid, Core and Chemical Samples

The following water, oil, native core samples and treatment chemicals were collected.

- Effluent water- raw and treated effluent from ETP-I, XZ
- Injection water – XZ- CWIP-I, GGS-VI, well head XZ#622
- Formation water - XZ# 649 (XZ-VII pay sand)
- Oil sample – XZ#649
- Core samples – XZ#408 (XZ-VII pay sand)
- Coagulant – Alum
- Flocculant – PE (Poly Electrolyte)
- Scale inhibitor $CaCO_3$ type SI

Table 1 Quality parameters of injection water

Sr. no.	Parameter	Unit	Desired limit	Achieved
1	pH	–	6.5–8.5	8.20
2	Turbidity	NTU	<0.5	0.27
3	TSS	Mg/l	<2.5	1.71
4	Filterability	L/30 min	>5.0	5.65
5	Oil & grease	mg/l	<10	Nil
6	Scaling tendency	% fall in hardness	<10	5
7	Rate of corrosion	mpy	<1	0.60
8	Total iron	Mg/l	0.1	

- Corrosion inhibitor- WIN (supplied by M/s Venus chemicals).

Table 1 shows quality parameters of injection water where pH achieved is in desired limit along with other parameters, which indicates that water used for injection is satisfied with the desired limit for all parameters.

2.2 Physicochemical Characterization of Raw Effluent

The ionic composition and physical parameters of raw effluent collected at ETP-I was analyzed and results are shown in Table 2. The water sample is of alkaline nature with high turbidity of 98 NTU. The chloride and salinity content of water are 4260 and 7020 mg/l respectively. Calcium and magnesium contents are on the lower side. Presence of high suspended solids (106 mg/l) and oil & grease (114 mg/l) has contributed to low filterability of raw effluent (0.610 L/30 min). Chlorine demand of effluent water is of the order of 4.8 ppm. Residual chlorine of 0.4 ppm is required to be maintained in the treated injection water to prevent deterioration in its quality. It may be mentioned that the chlorine demand of effluent water may vary from time to time. Therefore, dose of chlorine should be decided based on periodic onsite monitoring of chlorine demand maintaining residual chlorine of 0.4 ppm. Raw effluent has GAB of the order of 1–110 and SRB counts are found to be nil. Table 2 shows the Physico-chemical analysis of raw effluent without any treatment. pH, turbidity, TSS, bicarbonate, chloride, sodium, TDS has to reduced in order to make this water fit for injection.

2.3 Ionic Composition of Formation Water from XZ#649

The formation water of XZ #649 (pay sand XZ-VII) was collected and analyzed for ionic composition.

Table 2 Physico-chemical analysis of raw effluent ETP-I, XZ

Sr. no.	Parameters	Unit	Raw effluent
1	pH	–	8.34
2	Turbidity	NTU	98
3	Filterability	L/30 min	0.61
4	TSS	mg/l	106
5	Carbonate	mg/l	150
6	Bicarbonate	mg/l	1586
7	Chloride	mg/l	4260
8	Sulphate	mg/l	Nil
9	Calcium	mg/l	16
10	Magnesium	mg/l	20
11	Sodium	mg/l	3450
12	Salinity (as NaCl)	mg/l	7020
13	TDS	mg/l	9482
14	Iron (total)	mg/l	0.1
15	Oil & grease	mg/l	114
16	Chlorine demand	ppm	4.8
17	Dissolved oxygen	ppm	5.1
18	GAB	Counts/ml	1–110
19	SRB	Counts/ml	Nil

Table 3 shows ionic composition of formation water indicating high TDS, salinity, sodium, chloride and bicarbonate content, which may result in increase in corrosion rate and salt deposition. Primary salinity (S1) 74.97% (strong acids combining with primary bases), Primary alkalinity (A1) 21.32% (weak acids combining with

Table 3 Ionic composition of formation water of XZ#649

Sr. no.	Parameters	Unit	Results
1	pH	–	7.67
2	Carbonate	mg/l	Nil
3	Bicarbonate	mg/l	2806
4	Chloride	mg/l	4864
5	Sulphate	mg/l	2
6	Calcium	mg/l	84
7	Magnesium	mg/l	29
8	Sodium	mg/l	4051
9	Salinity (as NaCl)	mg/l	8015
10	TDS	mg/l	11836
11	Iron	mg/l	0.1

primary bases), Secondary Alkalinity (A2) 3.59% (weak acids combining with secondary bases), Water is Bicarbonate-Sodium type as per Sulin's classification. Anions such as chloride, bicarbonate, sulphate are being balanced by sodium, calcium and magnesium cations.

3 Experimental

3.1 Dose Optimization of Oxygen Scavenger

The corrosion studies were undertaken on N-80 steel tubular coupons at 88 °C. The dissolved oxygen content has a direct bearing on the rate of corrosion, it is essential to remove the dissolved oxygen to control corrosion. The dissolved oxygen content in effluent was found to be 5.1 ppm. The dose of sodium sulphite (as oxygen scavenger) after treatment of the injection water in the laboratory is optimized to be 60 ppm. It may be mentioned that the dissolved oxygen concentration may vary from time to time; therefore the dose of oxygen scavenger may be changed accordingly for effective removal of oxygen. The sodium sulphite requires a catalyst like Cobaltous chloride in about 0.22 ppm dose.

3.2 Dose Optimization of Corrosion Inhibitor

The laboratory treated effluent after filtration with 0.45 μ filter was used for this study. The water was treated with different concentrations of corrosion inhibitors (WIN). The rate of corrosion for different doses of corrosion inhibitor along with oxygen scavenger is shown in Table 4.

4 Result and Discussion

Experimental work done at reservoir temperature of 88 °C proves that corrosion rate is minimum of 0.66 mpy for maximum volume of 15 mg/ml WIN. Dose optimization was done where existing dose of sodium sulphite (oxygen scavenger) of 50 mg/ml and suggested dose was 60 (8–10 mg/l of actual per ppm of dissolved oxygen). For Corrosion inhibitor (WIN), where existing dose was 10 mg/ml and suggested dose is 12 mg/ml. Sodium sulphite with a dose of 60 ppm along with 12 ppm of WIN is likely to control corrosion activity in the system. Table 5 shows the existing and suggested dose of treatment chemicals where dose for oxygen scavenger has to be increased from 50 to 60 mg/l.

Table 4 Dose optimization of oxygen scavenger & corrosion inhibitor at temperature 88 °C, Duration 96 h, Material N-80

Sr. no.	Treatment	Corrosion rate, mpy
1	Blank	2.01
2	Effluent + 50 mg/l oxygen scavenger	1.88
3	Effluent + 60 mg/l oxygen scavenger	1.52
4	Effluent + 70 mg/l oxygen scavenger	1.50
5	Effluent + 60 mg/l oxygen scavenger + 5 mg/l WIN	1.32
6	Effluent + 60 mg/l oxygen scavenger + 8 mg/l WIN	1.11
7	Effluent + 60 mg/l oxygen scavenger + 10 mg/l WIN	0.60
8	Effluent + 60 mg/l oxygen scavenger + 15 mg/l WIN	0.66

*0.22 mg/l Cobaltous chloride was added in all the sets, The rate of corrosion observed in treated effluent is found to be 2.01 mpy which is above the permissible limit of 1 mpy. From the data, it is evident that sodium sulphite with a dose of 60 ppm along with 12 ppm of WIN is likely to control corrosion activity in the system. Table 4 shows decrease in corrosion rate by increasing the dose of corrosion inhibitor and oxygen scavenger in the treatment, optimized dose of 10 mg/l WIN with 60 mg/l oxygen scavenger gives 0.60 mpy of corrosion rate

Table 5 Existing and suggested dose of treatment chemicals

Sr. no.	Treatment	Existing dose (mg/l)	Suggested dose
1	Sodium hypochlorite for initial concentration	40	5.2 ppm (residual chlorine of 0.4 ppm to be maintained)
2	Alum	300	250 mg/l
3	Poly electrolyte	5	1 mg/l
4	Sodium sulphite (oxygen scavenger)	50	60 (8–10 mg/l of actual per ppm of dissolved oxygen)
5	Cobaltous chloride	0.1	0.22 mg/l
6	Scale inhibitor	20	15 mg/l
7	Corrosion inhibitor (WIN)	10	12 mg/l

5 Conclusion

The proposed injection water is corrosive (2.01 mpy) in nature at reservoir temperature. For removal of dissolved oxygen, 12 mg/l of sodium sulphite *(oxygen scavenger) per ppm of dissolved oxygen with 0.22 mg/l Cobaltous chloride as catalyst is required. The system requires removal of dissolved oxygen followed by treatment with corrosion inhibitor (WIN) in the dose of 10 mg/l. actual dose of oxygen scavenger may be worked out periodically by monitoring DO content at the site. As existing injection water is corrosive in nature at reservoir temperature, if proper dose optimization is not done for the existing injection water then it will result in high rate of corrosion of well equipments which will reduce life of the well.

References

1. Savaloni H, Modiri F (2020) A study of the corrosion of stainless steel 304L coated with a 190 nm-thick manganese layer and annealed with nitrogen flux in a 0.4-mole solution of H_2SO_4 at different temperatures. *J Theor Appl Phys* 14:21–35
2. Wang M, Zhou Z, Wang Q, Liu Y, Wang Z, Zhang X (2019) Box-behnken design to enhance the corrosion resistance of plasma sprayed Fe-based amorphous coating. *Results Phys* 15, Article ID 102708
3. Tripathy DB, Murmu M, Banerjee P, Quraishi MA (2019) Palmitic acid based environmentally benign corrosion inhibiting formulation useful during acid cleansing process in MSF desalination plants. *Desalination* 472, Article ID 114128
4. Alibakhshi E, Ramezanzadeh M, Haddadi SA (2019) Persian liquorice extract as a highly efficient sustainable corrosion inhibitor for mild steel in sodium chloride solution. *J Clean Prod* 210:660–672
5. Saha SK, Murmu NC, Banerjee P (2019) Amine cured double schiff base epoxy as efficient anticorrosive coating materials for protection of mild steel in 3.5% NaCl medium. *J Mol Liq* 278:521–535
6. Mahato P, Mishra SK, Murmu M, Hirani H (2019) A prolonged exposure of Ti-Si-B-C nanocomposite coating in 3.5 wt. % NaCl solution: electrochemical and morphological analysis. *Surf Coat Technol* 375:477–488
7. Morozov Y, Calado LM, Shakoor RA et al (2019) Epoxy coatings modified with a new cerium phosphate inhibitor for smart corrosion protection of steel. *Corros Sci* 159, Article ID 108
8. Shehata MF, El-Shamy AM, Zohdy KM, Sherif SM, Zein El Abedin S (2020) Studies on the antibacterial influence of two ionic liquids and their corrosion inhibition performance. *Appl Sci* 10:1444–1453
9. Hussein ME, Senousy AS, Abd-Elsalam WH (2019) Roselle seed oil and its nano-formulation alleviated oxidative stress, activated Nrf2 and downregulated m-RNA expression genes of pro-inflammatory cytokines in paracetamol-intoxicated rat model. *Rec Nat Products* 14:1–17
10. Chengduan W, Chuan L, Bin X, Xiaogang G, Dong F, Bin L (2018) Corrosion inhibition of mild steel in HCl medium by S-benzyl-O, O'-bis (2-naphthyl) dithiophosphate with ultra-long lifespan. *Results Phys* 10:558–567
11. Salman T, Al-Azawi K, Mohammed I, Al-Baghdadi S, Al-Amiery A, Gaaz T (2018) Experimental and quantum chemical simulations on the corrosion inhibition of mild steel by 3-((5-(3,5-dinitrophenyl)-1,3,4-thiadiazol-2-yl)imino)indolin-2-one. *Results Phys* 10:291–296
12. Zeino A, Abdulazeez AI, Khaled M, Jawich M, Obot I (2018) Electrochemical corrosion performance of aromatic functionalized imidazole inhibitor under hydrodynamic conditions on API X65 carbon steel in 1 M HCl solution. *J Mol Liq* 250:50–62
13. Umoren S, Eduok U (2016) Application of carbohydrate polymers as corrosion inhibitors for metal substrates in different media: a review. *Carbohydr Polym* 140:314–341
14. Hu K, Zhuang J, Zheng C, Ma Z, Yan L, Gu H, Zeng X, Ding J (2016) Effect of novel cytosine-l-alanine derivative based corrosion inhibitor on steel surface in acidic solution. *J Mol Liq* 222:109–117
15. Srivastava M, Tiwari P, Srivastava S, Prakash R, Ji G (2017) Electrochemical investigation of Irbesartan drug molecules as an inhibitor of mild steel corrosion in 1 M HCl and 0.5 M H_2SO_4 solutions. *J Mol Liq* 236:184–197
16. Mahmoodian M, Qingi C (2017) Failure assessment and safe life prediction of corroded oil and gas pipelines. *J Pet Sci Eng* 151:434–438

A Study of Process Parameters for Adsorption of Textile Industry Wastewater Using Low-Cost Adsorbent (Bamboo Activated Carbon)



Shantini A. Bokil, Niraj S. Topare, and Satish V. Khedkar

Abstract This study involves the Adsorption of Secondary treated Textile industry wastewater (dye) employing activated carbon (AC). Adsorption activity of adsorbent such as produced from Bamboo through chemical activation method has been investigated. Phosphoric acid (H_3PO_4) was used for the development of AC from Bamboo as a chemical activating agent under condition (temperature of 400 °C for 1 h). An attempt was made to research the effect of process parameters on the removal of dye by quantity of adsorbents, initial dye concentration, pH, contact time, temperature, and agitation speed. The experiments were carried out by the varying amount of adsorbents (0.5, 1, 1.5, 2, 2.5 g/L), initial concentration of dye (200, 400, 600, 800 mg/L), pH (3, 5, 7, 9, 11), contact time (1, 2, 3, 4, 5, 6, 7, 8 h.), Agitation speeds (100, 200, 300 rpm) and temperature (30, 40, 50 °C). The acceptable adsorbent dose was found to be 2 g/l of 200 mg/L Bamboo Activated Carbon (BAC) for dye. The maximum rate of removal was observed in the basic medium at pH11 with agitation speed 200 rpm at 30°C for BAC. The removal of dye by using BAC has been found to be a low-cost, eco-friendly, effective process.

Keywords Activated carbon · Bamboo · Process parameters · Phosphoric acid

S. A. Bokil

School of Civil Engineering, Dr. Vishwanath Karad MIT World Peace University, Pune 411 038, India

N. S. Topare (✉)

School of Chemical Engineering, Dr. Vishwanath Karad MIT World Peace University, Pune 411 038, India

e-mail: niraj.topare@mitwpu.edu.in

S. V. Khedkar

Department of Chemical Engineering, College of Engineering & Technology, Akola 444 104, India

1 Introduction

The textiles industry, which consumes a significant amount of water in various processes and releases equal volumes of waste water containing various pollutants is one of the water-intensive industries [1]. In large amounts the textiles industry discharges in waste water sources heavy metals, salts, suspended solids, and colour elements [2]. At present, there are over 100000 dyes for commercial use, and Annual production of approximately 700 MT of dyestuffs [3]. The main challenge facing the textile sector nowadays is changing and developing alternative, environmentally-friendly and economical methods of production [4]. In addition, the use for the treatment units of safer dyes and chemicals would minimise waste treatment and disposal costs [5]. This research work's ultimate goal is to evaluate the most suitable treatment technology for water reuse in the textile industry. Among the various advanced treatment methods, tertiary polishing treatment processes like adsorption are very effective [6]. This study intends to throw light on the fact that, both by modifying certain treatment processes and by integrating conventional and innovative technologies of wastewater treatments, A considerable reduction in water consumption can be achieved and the treated effluent can be recycled and reused [7, 8].

This study was initiated to determine the most effective low-cost agricultural waste activated carbon as a final polishing treatment to remove contaminants from secondary treated effluents. This research is therefore aimed at observing the influence of operating parameters such as the amount of adsorbents (0.5, 1, 1.5, 2, 2.5 g/L), initial concentration of dye (200, 400, 600, 800 mg/L), pH (3, 5, 7, 9, 11), contact time (1, 2, 3, 4, 5, 6, 7, 8 h.), Agitation speeds (100, 200, 300 rpm) and temperature (30, 40, 50 °C) on removal capacity of dye. However, compared with other conventional adsorbents the adsorption activity of BAC for removal of dye water has been less reported.

2 Experimental

2.1 Materials

The raw material (Bamboo) required for the preparation of AC was collected from the local area. Bamboo was washed to remove dirt, dried and crushed sieving through a 60-mesh sieve. The chemical activator for the production of Bamboo AC was phosphoric acid (H_3PO_4). The grade of analytical chemicals (AR) was used and the glassware washed with distilled water.

2.2 Methods

2.2.1 Chemical Activation

The material was carbonized at a temperature of 200 °C for two hours and cooled in the room. Per sample 250 grams is combined with 250 ml H₃PO₄ after preparation of the sample. The samples have been impregnated for 1 h at 400 °C in the muffle furnace. Cleaning the basic contents of the AC, the samples were washed. The washing process continued up to pH7. In order to remove moisture content, at 100 °C in an oven samples were dried.

2.3 Batch Adsorption Study

The experiments have been conducted to investigate the adsorption of bamboo activated carbon (BAC) as an adsorbent. Batch adsorption studies are conducted using different important parameters such as the amount of adsorbents (0.5, 1, 1.5, 2, 2.5 g/L), initial concentration of dye (200, 400, 600, 800 mg/L), pH (3, 5, 7, 9, 11), contact time (1, 2, 3, 4, 5, 6, 7, 8 h.), Agitation speeds (100, 200, 300 rpm) and temperature (30, 40, 50 °C). The experiments on adsorption were performed with a completely mixed batch reactor (CMBR) technology. Pre and post-adsorption concentrations of dye in the supernatant solution were calculated by using the appropriate wavelength UV-visible spectrometer. It was measured with a normal calibration curve for a dye concentration. [9]. The adsorption amount at equilibrium, q_e (mg/g), has been determined by,

$$q_e = \frac{(C_0 - C_e)V}{X} \quad (1)$$

where, q_e = Adsorbed dye per unit of adsorbent mass (mg/g), C_0 = Original dye concentration (mg/L), C_e = Final dye concentration (mg/L), V = Solution Volume (ml), X = Dose of dry adsorbent used (gm).

2.4 Adsorption Isotherm

2.4.1 Langmuir Isotherm

Many researchers have extensively employed adsorption Langmuir isotherm on activated carbon of heavy metals, dyes and organic contaminants. The isotherm model of Langmuir estimates the maximum adsorption ability provided on adsorbent surface by complete single-cover coverage [10, 11]. Langmuir model's linear form is given by,

$$\frac{C_e}{q_e} = \frac{C_e}{q_{\max}} + \frac{1}{q_{\max}K_L} \quad (2)$$

where, C_e = Dye solution equilibrium concentration (mg/L), q_e = Equilibrium capacity of dye on the adsorbent (mg/g), q_{\max} = Adsorbent Adsorption Capacity (mg/g), K_L = Langmuir (L/mg) constant is correlated with adsorption free energy.

2.4.2 Langmuir Isotherm

The model of Freundlich emphasizes the concept that the metal ions on a heterogeneous surface are adsorbed and are not limited to monomolecular layer formation [12]. Freundlich model can be expressed as follows in the linear form,

$$\ln q_e = \ln K_F + \frac{1}{n} \ln C_e \quad (3)$$

where, K_F and n (dimensionless constants) are Freundlich isothermal adsorption constants that indicate adsorption capability and intensity, respectively.

3 Result and Discussion

3.1 Prepared Adsorbent Characterization

BAC adsorbents used in the present investigation. A Physico-chemical characteristic of adsorbents used for their characterization includes proximate analysis, bulk density, elemental analyses, surface area, and particle size. Table 1 illustrates the physico-chemical characteristics of the adsorbents.

3.1.1 Result of XRF Analysis

The nature and concentration of the crystallographic structure of the elements was investigated by XRF analysis. The result shows eight elements which contribute to an improvement in the adsorption process when AC is an adsorption. Table 2 shows the elemental analysis of AC produced from bamboo by the XRF method. The data indicate the concentration of different elements present in each sample, which may be used for the adsorption study.

Table 1 Characteristics of the BAC

Sr. no	Properties	BAC
<i>Typical properties</i>		
1	Specific surface area (m ² /g)	316.20
2	Total pore volume (cm ³ /g)	0.27
3	Average pore diameter (Å)	34.95
4	Bulk density (g cm ⁻³)	0.60
<i>Proximate analysis</i>		
1	Moisture content (wt%)	9.39
2	Volatile matter (wt%)	25.57
3	Fixed carbon (wt%)	63.37
4	Ash content (wt%)	1.67
<i>Ultimate analysis</i>		
1	C	61.74
2	H	1.37
3	N	5.63
4	S	9.33
5	O (by difference)	21.96

Table 2 Elemental analysis of adsorbents by XRF method

Sr. no.	Element	Symbol	Weight percentage
1	Carbon	C	48.08
2	Oxygen	O	43.97
3	Aluminum	Al	0.12
4	Silicon	Si	1.91
5	Phosphorus	P	4.92
6	Iron	Fe	0.33
7	Copper	Cu	0.39
8	Zinc	Zn	0.26

3.1.2 Results of XRD Analysis

The XRD diagrams of bamboo AC show the extreme high point indicating the existence of a strongly ordered rhombohedral-carbon crystalline structure. The crystalline structure improves dyes' adsorption to prepared AC. X-ray diffractogram for AC prepared from bamboo is shown in Fig. 1. The intensity of peaks indicates the presence of structure of carbon with respect to the range of degrees, indicating the existence of the crystalline form of carbon present in activated carbon.

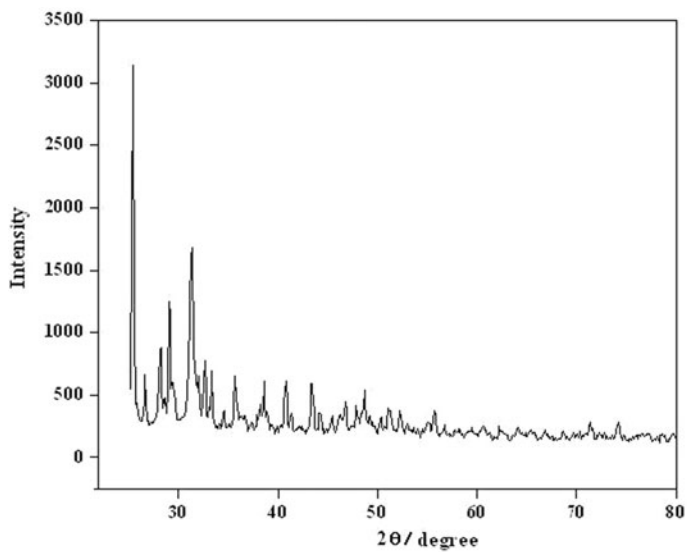


Fig. 1 X-ray diffractogram for AC prepared from bamboos

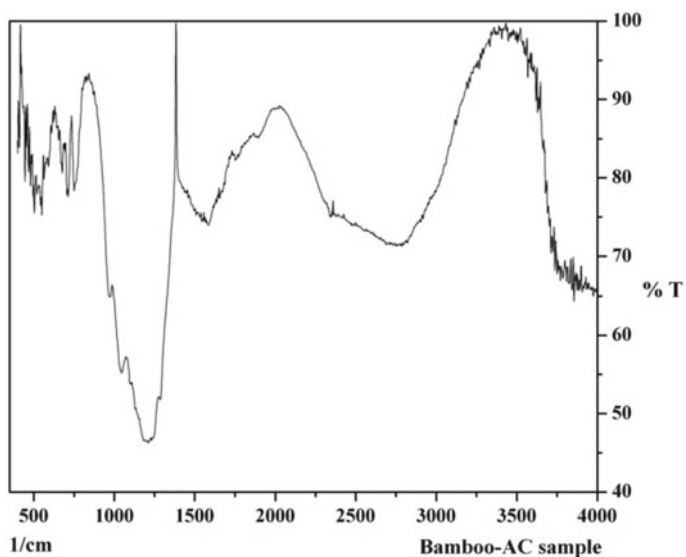
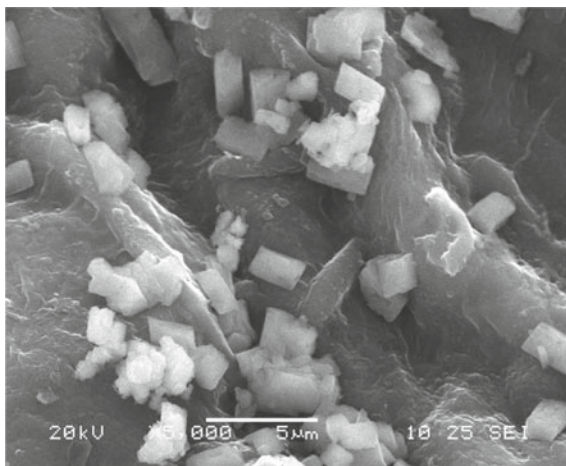


Fig. 2 FTIR for AC prepared from bamboo

Fig. 3 SEM image of AC prepared from bamboo



3.1.3 Results of FTIR Analysis

The FTIR spectroscopic study of the AC prepared from bamboo is shown in Fig. 2. The sample showed four main bands of absorption at 2500–3100, 1000–1500, 900–1300 and 400–600 cm^{-1} for BAC. The graphical representation indicates the percentage of functional groups. The carbon-oxygen functional groups present, one of the most critical parameters on the carbon surface affecting dye adsorption by activated carbon. This study shows that the lactone with frequency feature groups 1460.81 cm^{-1} and C–O at 1293.03 cm^{-1} and aromatic C–H at 845.63 cm^{-1} was found in AC prepared from bamboo. In this analysis, activation of H_3PO_4 produced an oxygen-rich carbon surface.

3.1.4 Results of SEM Analysis

The technique of SEM was used for analysis the AC type bamboo surface physical morphology. Figure 3 show the SEM image of AC prepared from bamboo. It indicates that the AC contains homogenous and open macro-pores on the external surface. Further, it is obvious that the AC has an irregular and highly porous surface.

3.2 Study of Batch Adsorption

3.2.1 Effect of Adsorbent (BAC) Dose

The adsorbent dosage is important as it defines the capacity of adsorbent for a certain initial dye concentration. The adsorbent dosages impact on dye removal in BAC was

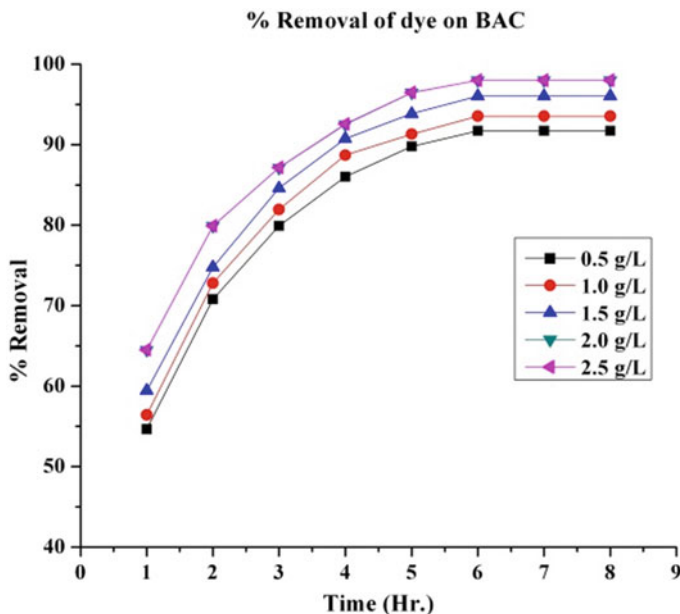


Fig. 4 Effect of adsorbent dose on removal of dye on BAC

investigated by maintaining a constant concentration of all other experimental conditions at 200 mg/L. In Fig. 4, the adsorbent dose effect upon the dye removal percentage was shown to be increasing to the adsorbent 2 g/L dosage and then remaining almost constant. This can be influenced by the increase in adsorption levels, which increases the surface area for adsorption, thereby making more adsorption sites more accessible. At low concentrations, equilibrium was found to be achieved more easily. Therefore 2 g/L was selected as an adsorbent dose for dye adsorption onto BAC. At 2 g/L adsorption dose, all adsorption experiments on the BAC were carried out.

3.2.2 Effect of Initial Concentrations of Dye

At different initial dye concentrations (200, 400, 600, 800 mg/L) the experiments were performed at a set dose of adsorbent (2 g/L) at different intervals, with a rpm of 200 rpm and a rpm of agitation speed at a pH 7. The removal rate is shown in Fig. 5 of dye at different concentrations of dye solutions on BAC and it is noted that the dye is rapidly absorbed for the first 04 h and then slows and eventually saturates. This can be clarified by rapid outward surface adsorption and slow adsorption within the pores. Due to the fact that nearly all dye molecules were easily adsorbed on the outside surfactants at lower concentrations, original concentration of dye increased between 200 and 800 mg/L, which indicate that the equilibrium removal of dye decreased from 98.90 to 90.90%. Initial dye concentration increased however further leading

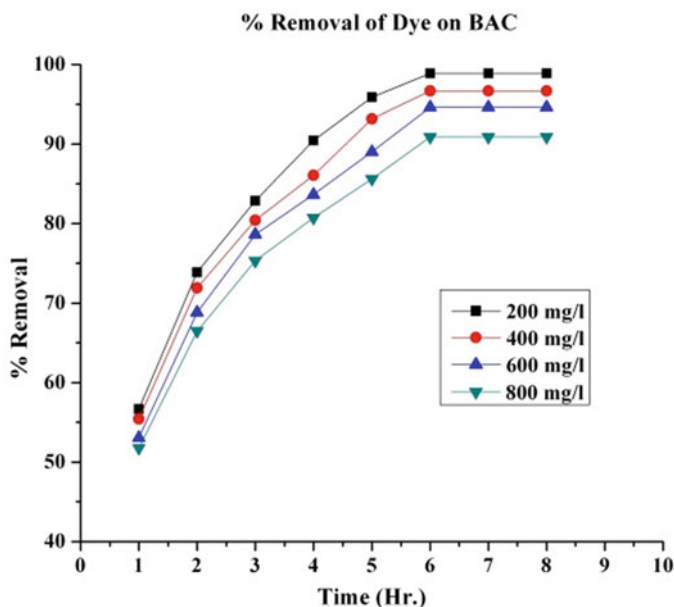


Fig. 5 Effect of initial concentration onto BAC

to the rapid saturation of the BAC surfaces. Thus most dye adsorption slowly took place within pores. The time of equilibrium has been observed regardless of the initial concentration of dye. However it takes 6 h to reach equilibrium. To ensure complete equilibrium, experimental data were calculated up to 8 h.

3.2.3 Effect of PH

Experiments were performed with different p H values from 3, 5, 7, 9 and 11 to measure the influence of pH on the percentage removal. 250 mL dye solution with different pH values (3–11) of 50 mg/l with 2 gm BAC with water-bath shaker at 30 °C is agitated during this experiment. Stirring took place at 200 rpm for 8 h, which was more than enough time to maintain equilibrium at the constant agitation speed of 200 rpm. Similar experiments were carried out with adsorbent. The pH has been adjusted by using a pH metre with 0.1 N NaOH and 0.1 N HCl solutions. Figure 6 show the percentage removal of dye as a function of pH. At a higher pH, dye removal is favorable. With the pH increased from 3 to 5, the removal efficiency is insignificant. The removal of dye increases significantly with pH above pH5. The maximum removal of dye was observed to be at pH11. However, there is a sharp increase in dye uptake for dye from pH7 to 9 and then after there is little increase in dye uptake as the pH is further increased from 9 to 11. The best pH range was therefore

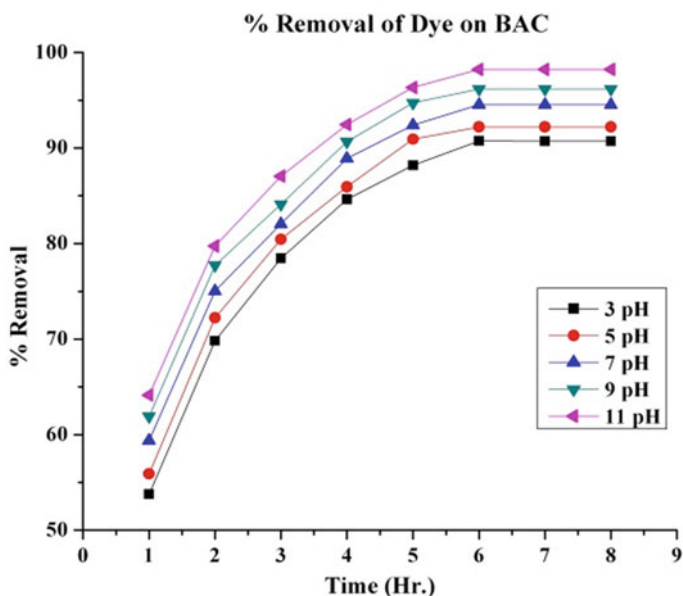


Fig. 6 Effect of pH onto BAC

7–11 for dye adsorption. No effect of pH on equilibrium time, which remained around 6 h, was observed.

3.2.4 Effect of Agitation Speed

In order to keep pH, dye concentration, temperature and all other operating parameters constant, varying agitation speeds from (100, 200, 300 rpm) were analyzed by the effect of agitation rate on dye uptake. The results achieved are shown graphically in Fig. 7, and equilibrium dye concentration was influenced by low agitation in the solid phase. These findings showed that the absorption of dye increases from 89.75 to 97.45% for adsorption onto BAC with an increase in rotational speeds from 100 to 300 rpm. However the uptake of the dye has not been significantly affected by the further increase in agitation speed from 200 to 300 rpm. In contrast to low-speed agitation, however, higher agitated speed equilibrium was achieved.

3.2.5 Effect of Temperature

Adsorption experiments took place at various temperatures (30, 40 and 50 °C) and were conducted at initial 200 mg/l dye concentrations at pH7 and a 200 rpm agitation speed. Figure 8 demonstrates the effects of time-rate studies for dye adsorption by

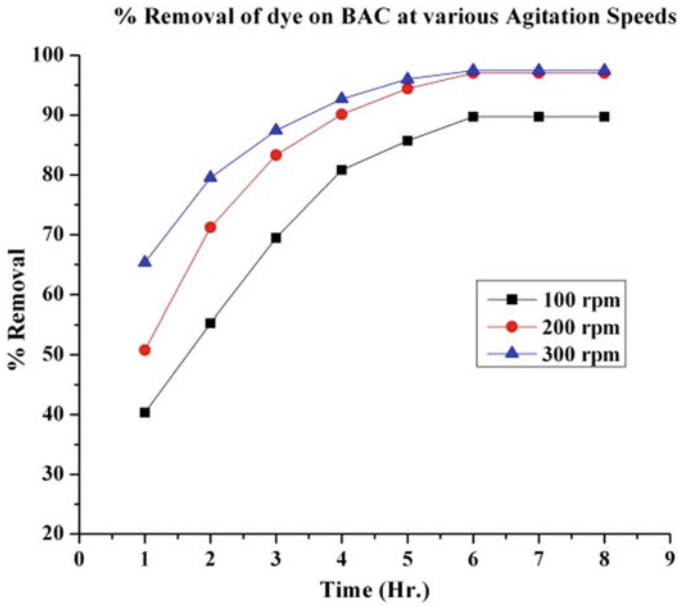


Fig. 7 Effect of agitation speeds onto BAC

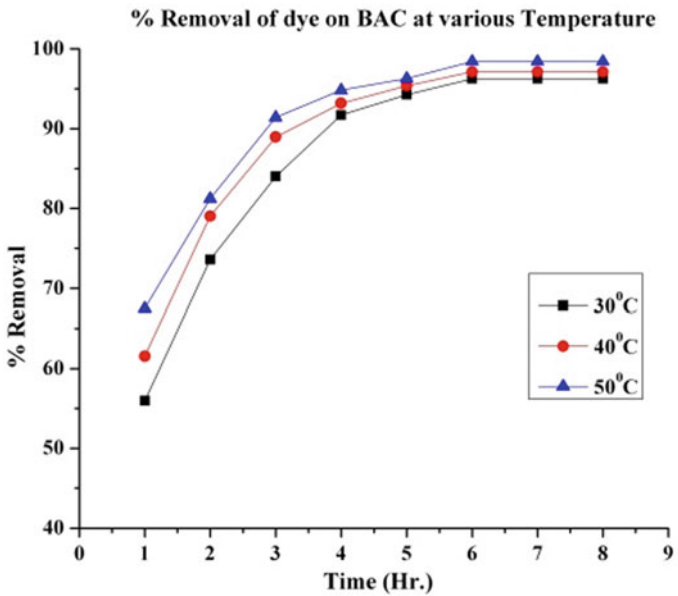


Fig. 8 Effect of temperature onto BAC

different adsorbents (BAC) at various temperatures (30, 40 and 50 °C) and Shows that with temperature increase removal by BAC adsorbent increases. The percentage removal of by BAC adsorbent increases from 96.25 to 98.44% as an adsorbent with the rise of temperature from 30 to 50 °C at 200 mg/l. There is negligible uptake of dye with an increase in temperature from 30 to 50 °C in view of this all the experiments in the batch mode were carried out at 30 °C.

4 Conclusion

Process variables, such as the amount of adsorbents, dye initial concentration, pH, contact time, temperature, and agitation speeds significantly affect the process of adsorption. Also, the production of AC from Bamboo using Phosphoric acid (H_3PO_4) was done successfully. The results of this research indicate that AC preparation is feasible with relatively high surface areas from bamboo by chemical activation method and experimental results indicate that the removal of dye is facilitated in the presence of prepared adsorbents. The maximum percentage removal (98.90%) was observed in the basic medium at pH11 with agitation speed 200 rpm at 30 °C and at 2 g/L for BAC dose. The adsorption activity of prepared adsorbent (BAC) has clearly indicated that these processes were efficient in the removal of dye.

References

1. Srinivasakannan C, Bakar MZA (2004) Production of activated carbon from rubber wood sawdust. *Biomass Bioenergy* 27:89–96
2. Sivakumar B, Kannan C, Karthikeyan S (2012) Preparation and characterization of activated carbon prepared from balsamodendron caudatum wood waste through various activation processes. *Rasayan J Chem* 5(3):321–327
3. Khan AM, Ansari R (2009) Activated charcoal: preparation, characterization and applications: a review article. *Int J Chem Tech Res* 1(4):859–864
4. Kanan N, Sundaram MM (2001) Kinetics and mechanism of removal of methylene blue by adsorption on various carbons a comparative study. *Dyes Pigment* 51:25–40
5. Topare NS, Attar SJ, Manfe MM (2011) Sewage/wastewater treatment technologies: a review. *Sci Revs Chem Commun* 1(1):18–24
6. Hameed (2007) Adsorption of basic dye (methylene blue) onto activated carbon prepared from rattan sawdust. *Dyes Pigments* 75:143–149
7. Chandrakant D, Shendkar RC, Torane KS, Mundhe AA, Bhave NR, Deshpande (2012) Characterization of activated carbon prepared from *Achyranthes aspera* Linn. by X-ray fluorescence spectroscopy (XRF). *J Nat Prod Plant Resour* 2(2):295–297
8. Topare NS, Chopade SG, Khedkar SV, Renge VC, Bhagat SL (2011) Production of activated carbon from sugarcane bagasses. *Int J Adv Eng Technol* 2(3):356–358
9. Al-Husseiny HA (2014) Adsorption of methylene blue dye using low cost adsorbent of sawdust: batch and continues studies. *J Bab Univ Eng. Sci* 22(2):296–310
10. Ali I, Asim M, Khan TA (2012) Low cost adsorbents for the removal of organic pollutants from wastewater. *J Environ Manage* 113:170–180

11. Topare NS, Joshi P (2015) Characterization of activated carbon prepared from citrus sinensis (Orange) Peels by X-ray fluorescence Spectroscopy (XRF). *Emer Tre Chem Eng* 2(3):49–51
12. Bharathi KS, Ramesh ST (2013) Removal of dyes using agricultural waste as low-cost adsorbents: a review. *Appl Water Sci* 3:773–790

Photodetection Performance of Sb^{3+} Doped $\text{Cd}_{0.92}\text{Hg}_{0.08}\text{S}$ Based Electrochemical Cells



S. A. Lendave, S. T. Pawar, and L. K. Bagal

Abstract The present investigation deals with the preparation of Sb^{3+} doped (from 0.01 to 1 mol%) $\text{Cd}_{0.92}\text{Hg}_{0.08}\text{S}$ thin films onto the well polished and cleaned stainless steel substrates. The previously optimized conditions were used for the deposition. The electrochemical photosensing cells were fabricated out of these series of Sb^{3+} doped $\text{Cd}_{0.92}\text{Hg}_{0.08}\text{S}$ photoactive electrodes and sulphide/polysulphide (0.2 M) as an electrolyte. The cells were then characterized through the various properties and their performance has been studied with a special reference to the Sb^{3+} doping concentration. The cells were illuminated with a white light of (13 mW/cm^2) intensity and the cell parameters such as photocurrent (I_{ph}), photo voltage (V_{ph}), the electrochemical conversion efficiency (η), fill factor (ff) etc., have been determined. It is found that I_{ph} , V_{ph} , $\eta\%$ and $\text{ff}\%$ have been boosted significantly with Sb^{3+} doping concentration up to 0.1 mol% and then decreased. Typically, I_{ph} enhanced from 0.152 to 0.214 mA/cm^2 and that V_{ph} from 297 to 391 mV whereas η increased from 1.27 to 2.41% and ff from 36.44 to 38.65%. The junction ideality factors were determined and indicated that the recombination mechanism is dominant at the electrode/electrolyte interface. The capacitance—voltage measurements showed V_{fb} to be enhanced from -1.068 to -1.297 V (Vs SCE). Barrier potential measurements determined Pool—Frenkel type conduction mechanism. Overall the photovoltaic detector performance has been found to be boosted significantly at 0.1 mol% Sb^{3+} doping concentration in $\text{Cd}_{0.92}\text{Hg}_{0.08}\text{S}$ electrode.

Keywords $\text{Cd}_{0.92}\text{Hg}_{0.08}\text{S}:\text{sb}$ photoelectrode · Photo voltage · Photocurrent · Efficiency · Fill factor

S. A. Lendave (✉) · S. T. Pawar
SVRI's College of Engineering, Pandharpur, Solapur 413304, MS, India

L. K. Bagal
Department of Physics, K. B. P. College Pandharpur, Pandharpur 413304, MS, India

1 Introduction

Presently, the world energy consumption is 10 terawatts (TW) per year, and by 2050, it is projected to be about 30 TW. The world will need about 20 TW of non-CO₂ energy to stabilize CO₂ in the atmosphere by mid-century. The simplest scenario to stabilize CO₂ by mid-century is one in which photovoltaics (PV) and other renewables are used for electricity (10 TW), hydrogen for transportation (10 TW), and fossil fuels for residential and industrial heatings (10 TW) [1]. Thus, PV will play a significant role in meeting the world future energy demand. The present is considered as the “tipping point” for PV [2].

Photovoltaic devices are based on the concept of charge separation at the interface of two materials of different conduction mechanism. A typical type of the photocurrent-generator device has a semiconductor in contact with an electrolyte, and this is often referred as photoelectrochemical cells. A photoelectrochemical cell consists of a photoactive semiconductor working electrode (either n- or p-type) and a counter electrode made of either metal (e.g. Pt) or treated graphite or semiconductor. Both electrodes are immersed in the electrolyte containing a suitable redox electrolyte. The electrochemical photovoltaic cells are used to realize the direct energy transfer from photons to chemical species and therefore provide an economic chemical route for trapping solar energy [3]. A possible direction of semiconductor research is the search for novel materials with tailored properties for significant applications. Wide-bandgap II–VI compounds are expected to be one of the most vital materials for high-performance optoelectronic devices [4]. Additionally, the high ionicity of these compounds makes them good candidates for high electro-optical and electromechanical couplings [5, 6]. They are good photoconductors have high absorption coefficients and their materials properties can be engineered and improved by forming higher order compounds [7].

A variety of methods such as spray pyrolysis, electrodeposition, metallic chemical vapor deposition, thermal and flash evaporation, chemical bath deposition (CBD) [8–12], etc. have been employed for the synthesis of thin chalcogenide films and possible reaction mechanisms and growth kinetics have been suggested. All most all these technologies require the use of sophisticated equipments and process instrumentation that budget to higher production costs. Further the processes are clumsy, tedious and time consuming. Solution-based chemical bath deposition methods, however, do not require the costlier systems and can be used to fabricate large area thin films on a variety of substrates such as glasses, semiconductors, metals, plastics, etc. It is a method by which thin semiconductor films of metal-chalcogenides can be deposited on the substrates immersed in the dilute solutions containing metal ions and a source of chalcogen ions [12]. Therefore, an energy efficient, faster in response and more reliable environmentally friendly system (LPCBD) was used for the fabrication of Sb³⁺ doped (0.01–1 mol%) Cd_{0.92}Hg_{0.08}S thin films [12]. It has proved to be capable of controlling the size and morphology of materials by deposition conditions and reaction parameters such as bath temperature, reaction pH, deposition duration and

solvent concentration, etc. Many unusual hierarchical structures of inorganic materials with high complexity and structural specialties can be created using the CBD method [12].

Through these investigations therefore, it is proposed to dope the $\text{Cd}_{0.92}\text{Hg}_{0.08}\text{S}$ electrode material with a varying Sb^{+3} doping concentration and to observe its reflections on the electrochemical photovoltaic performance of a cell devised out of these electrodes. The observed results have been predicated and supported by the microscopic and optical characteristics of the electrode material.

2 Experimental Techniques and Processes

Antimony (III) doped (0.01–1 mol%) $\text{Cd}_{0.92}\text{Hg}_{0.08}\text{S}$ thin films were grown by a modified CBD technique onto the well polished and thoroughly cleaned stainless steel substrates using equimolar solutions of cadmium sulphate, mercury chloride and thiourea as the precursors. Sufficient quantity of ammonia and triethanolamine was used as the complexing agents. Solutions were prepared using analytical-grade reagents. For deposition of the films, the preparative parameters namely temperature, deposition time, pH and speed of the substrate rotation were kept as optimized (60°C , 90 min, 10.8 ± 0.2 and 70 ± 2 rpm) [13, 14]. The experimental and procedural details are reported elsewhere [13, 14].

The electrochemical cells were then fabricated using undoped and doped $\text{Cd}_{0.92}\text{Hg}_{0.08}\text{S}$ thin films as the photoactive electrode and sensitized graphite as the counter electrode. The electrodes are kept 0.3 cm apart. The redox electrolyte used was aqueous 1 M NaOH–1 M Na_2S –1 M S. A 200 W tungsten filament lamp was used as the source of light. Cell heating was prevented using a water filter (circulated) interposed between the lamp and the cell. The cells were given an input of constant intensity (13 mWcm^{-2}) and the power output characteristics were recorded. The dynamic I–V and C–V characteristics in dark were obtained potentiometrically for all the cells. Three electrode systems were used for recording the capacitance-voltage measurements. The reverse saturation current of the various cells at 300 mV was then noted as a function of the cell temperature (300–373 K) and the built-in-potentials were calculated. The photocurrents and photovoltages were also noted for various input illumination intensities to determine lighted ideality factors of the various junctions. The currents and voltages were measured by a 6, 1/2 digit HP and 4, 1/2 digit HIL multimeters, respectively whereas the junction capacitance was noted with the 4, 1/2 digit capacitance meter (Aplab Make). A Lutron 101—Luxmeter was employed to measure the input intensity. The surface morphology was observed through a scanning electron microscope, EDAX FEI QUANTA 200 and the optical characteristics were determined by an UV-Vis-NIR photospectrometer Varian Cary 5000.

3 Results and Discussion

In a semiconductor-electrolyte junction, the potential drop occurs on the semiconductor side as well as on the solution side. The charge distribution at the electrode/electrolyte interface is such that a space charge region is created in the semiconductor at the interface. If the semiconductor-electrolyte interface is illuminated with a light of energy greater than the bandgap of the semiconductor, the photogenerated electrons and holes are separated from the space charge; the holes arrive at the semiconductor electrode surface whereas electrons move and accumulate at the back of the semiconductor constituting an electric current that flows through the external circuitry causing electrochemical reaction with the redox electrolyte at the counter electrode [3].

In these investigations the electrochemical cells set in a glass cuvette with $\text{Cd}_{0.92}\text{Hg}_{0.08}\text{S}:\text{Sb}$ active photoelectrodes of varying Sb^{3+} doping concentration and a sulphide/polysulphide electrolyte as a conducting medium were devised and illuminated by a white light of intensity 13 mW/cm^2 . The electrochemical characterization of these cells has been carried out and their photovoltaic output performance is examined with a special reference to the Sb^{3+} doping concentration in the $\text{Cd}_{0.92}\text{Hg}_{0.08}\text{S}$ electrode.

3.1 Effect of Sb^{3+} —Doping on the Photodetection Output Performance

The electrochemical photovoltaic cells were devised with the $\text{Cd}_{0.92}\text{Hg}_{0.08}\text{S}$ electrodes doped with various concentration of Sb^{3+} and were illuminated by a constant illumination intensity of 13 mW/cm^2 . The short circuit current (I_{sc}) and open circuit voltage (V_{oc}) for each of the cells were measured. It has been found that both V_{oc} and I_{sc} boosted from 297 to 391 mV and 0.152 to 0.214 mA/cm^2 as the concentration of Sb^{3+} in $\text{Cd}_{0.92}\text{Hg}_{0.08}\text{S}$ was increased from 0 to 0.1 mol%. For higher doping levels, both V_{oc} and I_{sc} decreased. This is shown in Fig. 1.

The power output curves were also obtained for all these cells under the same illumination intensity and analyzed to determine the various characteristic properties of the cells. Typically, we have determined power conversion efficiency (η), fill factor (ff) and series and shunt resistances (R_s , R_{sh}), etc. These are cited in Table 1. Figure 2 shows power output curves for five representative photoelectrode compositions.

Table 1 shows that η and ff% vary significantly with electrode composition (x); maximized at 0.1 mol% Sb^{3+} doping concentration and then decreased for further increase of doping concentration. The enhancements in V_{oc} , I_{sc} , η and ff% have been understood to be due to the following observations on the cell and electrode materials properties.

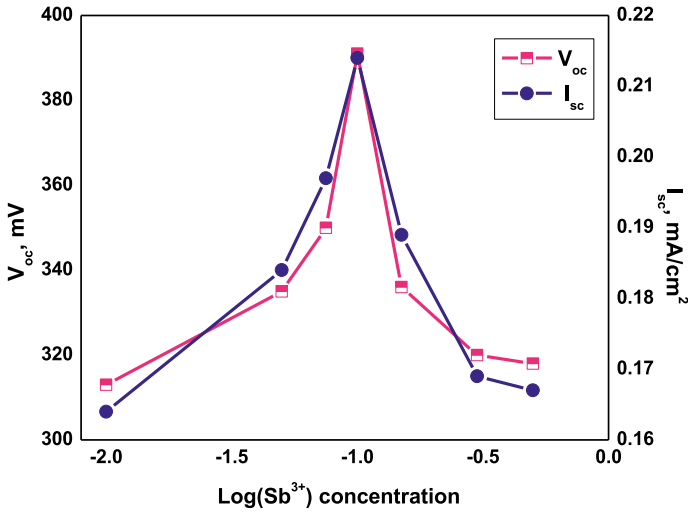


Fig. 1 Variation of V_{oc} and I_{sc} with Sb³⁺ doping concentration in Cd_{0.92}Hg_{0.08}S photoelectrode

Table 1 Table showing electrochemical performance of the detector cells formed with Sb³⁺ doped Cd_{0.92}Hg_{0.08}S electrodes

Doping Sb %	R _s Ω	R _{sh} KΩ	η (%)	ff (%)	n _d	n _L	Φ _B (eV)	V _{fb} (V)
0	892	7.56	1.27	36.44	2.14	2.94	0.470	-1.068
0.01	830	8.27	1.45	36.72	2.08	3.17	0.485	-1.138
0.05	757	8.94	1.70	37.15	1.98	3.44	0.499	-1.196
0.075	654	9.29	2.02	38.17	1.73	3.67	0.521	-1.232
0.1	603	9.77	2.41	38.65	1.52	3.92	0.537	-1.297
0.15	617	9.54	1.68	34.39	1.57	3.63	0.523	-1.280
0.3	673	9.22	1.52	36.42	1.61	3.52	0.518	-1.238
0.5	714	9.03	1.47	36.11	1.63	3.50	0.507	1.220

3.2 Attributes to the Output Performance

The enhancements in the above cell characteristics can be correlated to the observed changes in the flat band potential of a cell, effective barrier height at electrode/electrolyte interface and observation of the incident light by the electrode material. The capacitance—voltage (vs CSE) and current—voltage characteristics in dark were therefore obtained and analyzed for the series of cells. The current—voltage characteristics were analyzed to determine the junction ideality factors, which determines the extend of carrier recombination at the electrode/electrolyte interface. The values of ideality factor (>1) listed in Table 1 show that the electrode/electrolyte interfaces in our case been much influenced by a recombination mechanism effect.

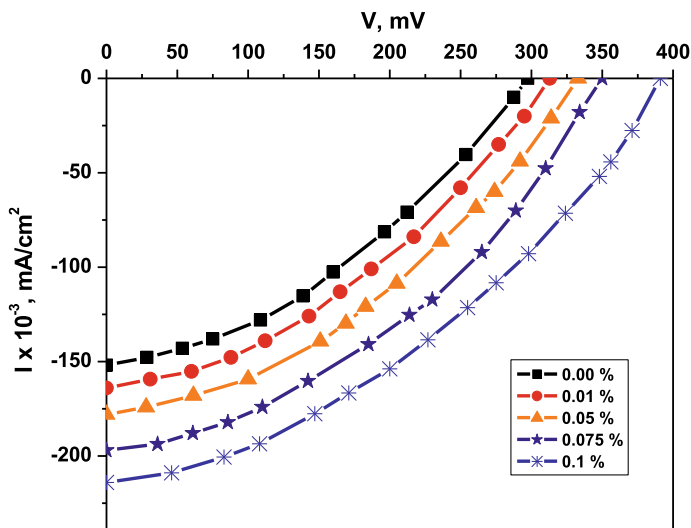


Fig. 2 Power output curves for the various cells with $\text{Cd}_{0.92}\text{Hg}_{0.08}\text{S}$ photoelectrode of varying Sb^{3+} doping concentration

However, the effect is least for a cell devised 0.1 mol% Sb^{3+} doped $\text{Cd}_{0.92}\text{Hg}_{0.08}\text{S}$ electrode supporting the maximum values of I_{sc} and V_{oc} at this doping level due to maximum trapping of the charge carriers. Similar reports are available in the photoelectrochemical literature and that has become now an universally accepted mechanism for the electrode/electrolyte based solar cell [3, 15–16].

A second important characteristics of an electrode/electrolyte interface is its voltage dependent space charge layer capacitance. This characteristics gives an important insight about the relative positions of the Fermi levels of both the species (semiconductor and an electrolyte) that determine band bending at the interface which is a measure of the flat band potential and consequently the maximum value of the open circuit photovoltage (V_{oc}). The flat band potential (V_{fb} 's) were therefore determined for all the cells of different electrode composition by measuring the space charge layer capacitance under a reverse bias voltage (vs SCE). The C^{-2} versus V (vs SCE) plots were then constructed (Fig. 3) for all the cells and extrapolated to the voltage axis to give the flat band potentials. The as-obtained values of V_{fb} are shown in Table 1. It is notable that V_{fb} enhanced considerably with Sb^{3+} doping concentration, attained a maximum value of 0.1 mol% Sb^{3+} doping in $\text{Cd}_{0.92}\text{Hg}_{0.08}\text{S}$ electrode and then decreased for higher doping levels. The increase in V_{fb} is caused mainly due to the additional donor levels which effectively shift the Fermi level in upward direction contributing to the increased V_{oc} of a cell whereas the decrease in V_{fb} at higher doping levels can be attributed to pinning of the Fermi level [16].

The measurements of built-in potential (ϕ_{B}) also support these observations. The ϕ_{B} 's were therefore measured for all the cell configurations. For this the reverse saturation currents of the various cells were measured for 300–373 K of temperature

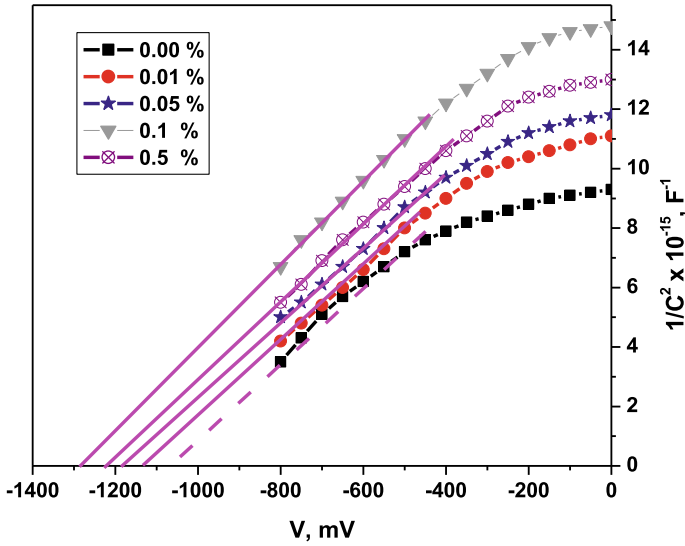


Fig. 3 Mott–Schottky plots for the cells with Cd_{0.92}Hg_{0.08}S photoelectrodes of various Sb³⁺ doping concentration

range. ϕ_B 's were then determined from the variation of $\text{Log } I_0/T^2$ versus $1/T$ for five typical cell configurations (Fig. 4). ϕ_B 's are listed in Table 1. The enhancement in short circuit current (I_{sc}) can also be attributed to the increased photon absorption volume as a result of the increased photoelectrode thickness due to Sb³⁺ doping. The variation of an electrode thickness with log Sb^{3+} electrode doping concentration is shown in Fig. 5. The increase in thickness causes a considerable enhancement in the grain size that enhances both I_{sc} and V_{oc} of a cell. This is made clear from the surface micrographs (Fig. 6) of the typical electrode structures.

4 Conclusions

1. Many usual/unusual structures of inorganic materials with high complexity and structural specialties can be created using the CBD method.
2. The terminal layer thickness of the as-grown electrode varied nonlinearly with the increasing Sb³⁺ doping content in electrode film.
3. A maximum conversion efficiency of 2.41% is made feasible by the Cd_{0.92}Hg_{0.08}S electrode doped with 0.1 mol% Sb³⁺ doping concentration (at our experimental conditions).
4. Microscopic investigations showed enhanced grain—growth after Sb³⁺ doping.

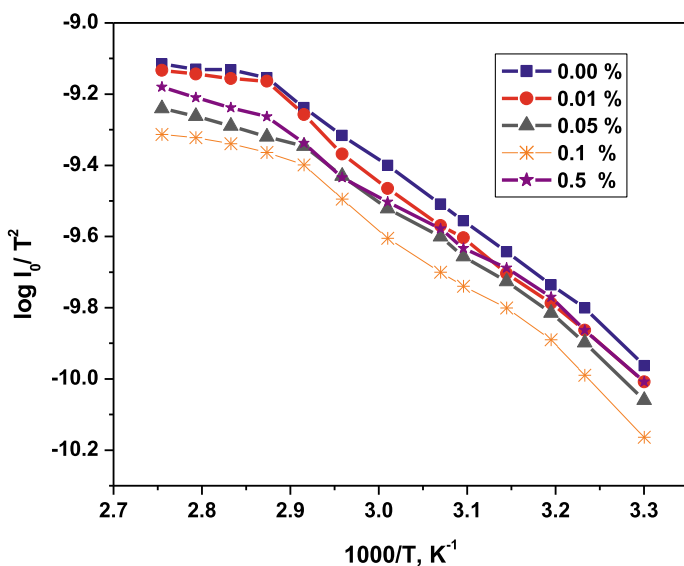
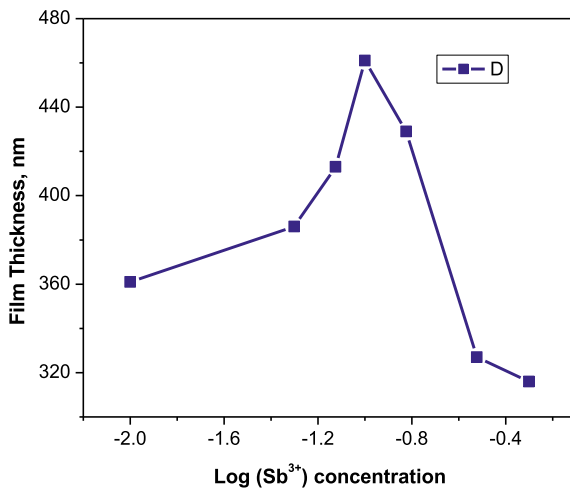


Fig. 4 Plots showing the variation of $\text{Log} I_0/T^2$ with $1/T$ for the cells with $\text{Cd}_{0.92}\text{Hg}_{0.08}\text{S}$ photoelectrodes of various Sb^{3+} doping concentration

Fig. 5 Variation of electrode thickness with Sb^{3+} doping concentration



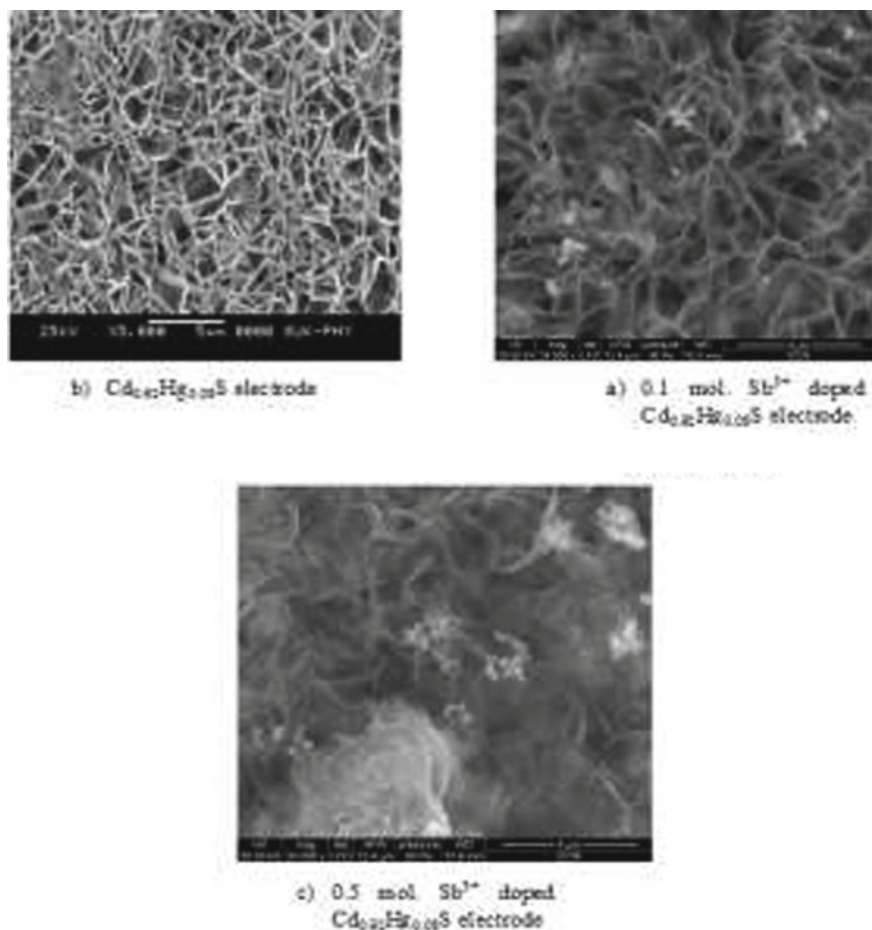


Fig. 6 SEM images of the: **a** $\text{Cd}_{0.92}\text{Hg}_{0.08}\text{S}$ electrode, **b** 0.1 mol. Sb^{3+} doped $\text{Cd}_{0.92}\text{Hg}_{0.08}\text{S}$ electrode and **c** 0.5 mol. Sb^{3+} doped $\text{Cd}_{0.92}\text{Hg}_{0.08}\text{S}$ electrode

References

1. Von Roedern B, Zweibe K, Ullal HS (2005) The role of polycrystalline thin film PV technologies for achieving mid-term market-competitive PV modules, IEEE PVSC-31. Orlando USA 2005:1635–1638
2. Kazmerski LL (2006) Solar photovoltaics R & D: at the tipping point: a 2005 technology overview. *J Electron Spectroscop* 150:105–135
3. Wei Di, Amaratunga Gehan (2007) Photoelectrochemical cell and its applications in optoelectronics. *Int J Electrochem Sci* 2:897–912
4. Song SH, Wang JF, Lalev GM, He L, Isshiki M (2003) *J Cryst Growth* 252:102–106
5. Chopra KL, Paulson PD, Dutta V (2004) Thin-film solar cells: an overview. *Prog Photovolt Res Appl* 12:69–92
6. Green MA, Emery K, King DL, Igari S, Warta W (2003) Solar cell efficiency tables (version 21). *Prog Photovolt Res Appl* 11:39–45

7. Razykov TM, Ferekides CS, Morel D, Stefanakos E, Ullal HS, Upadhyaya HM (2011) Solar photovoltaic electricity: current status and future prospects. *Sol Energy* 85:1580–1608
8. Tepantlan CS (2008) Structural optical and electrical properties of CdS thin films obtained by spray pyrolysis. *Revista Mexicana de Fisica* 54(2):112–117
9. Rashwan SM, Abdul-Wahab SM, Mohammed MM (2007) Electrodeposition and characterization of CdSe semiconductor thin films. *J Mater Sci: Mater Electron* 18:575–585
10. Chu TL, Chu SS, Britt J, Ferekides C, Wu CQ (1991) Cadmium zinc sulfide films and heterojunctions. *J Appl Phys* 70:2688–2693
11. Shreekanthan KN, Rajendra BV, Kasturi VB, Shivakumar GK (2003) Growth and characterization of semiconducting cadmium selenide thin films. *Cryst Res Technol* 38:30–33
12. Hodes Gary (2007) Semiconductor and ceramic nanoparticle films deposited by chemical bath deposition. *Phys Chem Chem Phys* 9:2181–2196
13. Lendave SA, Karande VS, Deshmukh LP (2010) Optical and microstructural properties of chemically deposited mercury cadmium sulphide thin films. *J Surf Eng Appl Electrochem* 46:462–468
14. Lendave SA, Karande VS, Deshmukh LP (2010) Structural and transport characteristics of $Hg_xCd_{1-x}S$ thin composite films: a correlation. *J Metall Mater Sci* 52:363–370
15. Chopra KL, Paulson PD, Dutta V (2004) Thin-film solar cells: an overview prog. *Photovolt: Res Appl* 12:69–92
16. Deshmukh LP, Shahane GS (1997) $CdS_{1-x}Se_x$ thin film electrode: an electrochemical photovoltaic study. *Int J Electron* 83:341–347

Facile Synthesis and Characterization of Pentanary Zn(Co, Cd, S)Se Semiconductor Thin Films



S. T. Pawar, S. A. Lendave, G. T. Chavan, V. M. Prakshale, S. S. Kamble, L. K. Bagal, and P. C. Pingale

Abstract This work, reports the synthesis of $Zn_{1-x-y}Co_xCd_yS_zSe_{1-z}$ thin films by a vacuum-free, low temperature, inexpensive, easiest modified chemical route. The wettability studies indicated the hydrophobic nature of as-grown samples. The energy dispersive spectroscopic analysis revealed the addition of Co, Cd, and S in the ZnSe host. Further, the chemical analysis confirmed the oxidations states of constituents as Zn^{2+} , Co^{2+} , Cd^{2+} , S^{2-} and Se^{2-} . The Fourier transform spectroscopy was used to identify the existing bond structure in the films. The morphology of the as-grown thin films showed a distribution of globular grains over the surface of elongated multi-faceted crystallites.

Keywords Chemical route · Thin films · Wettability studies · XPS · Morphology · Oxidations states

S. T. Pawar (✉) · S. A. Lendave
SVERI'S College of Engineering Pandharpur, Solapur 413304, MS, India
e-mail: stpawar@coe.sveri.ac.in

G. T. Chavan
College of Information and Communication Engineering, Sungkyunkwan University, Suwon 440-746, South Korea

V. M. Prakshale
Thin Film and Solar Studies Research Laboratory, School of Physical Sciences, Punyashlok Ahilyadevi Holkar Solapur University, Solapur 413255, MS, India

S. S. Kamble
Government Polytechnic, Vikramgad 401605, MS, India

L. K. Bagal
Department of Physics, K. B. P. College Pandharpur, Pandharpur 413304, MS, India

P. C. Pingale
Department of Physics, T.C. College Baramati, Pune, MS, India

1 Introduction

CuInSe₂ thin films and its quaternary and pentenary compounds, such as CuIn(Se, S)₂, Cu(In, Ga)Se₂, and Cu(In, Ga)(Se, S)₂ are favorable absorber materials for low-cost solar cells [1]. The frontrunners in thin film photovoltaic (PV) materials such as CIGS, CdTe, and Cu₂ZnSn (S, Se)₄ (CZTSSe) were emerging owing to its suitable material characteristics. The toxicity of Cd as well as the insufficiency of Ga and In elements are the shortcomings for large scale manufacturing, and utilization PV devices rely on CIGS and CdTe. Therefore, focusing on the future demand of the PV industry, it is crucial to discover environment-friendly earth-abundant materials [2].

Alloying of semiconductor compounds, resulting in quaternary or pentenary compounds allows modifications in material characteristics as a function of composition variation [3] such as Cd_{1-x}Zn_xS_ySe_{1-y} [4], Co_{1-x-y}Zn_xCd_yS [3], Cd_{1-x-y}Zn_xCu_ySe [5] and pentenary CuGa_{1-x}In_x(S_ySe_{1-y})₂ [6]. The modulation in the synthesis process of multinary metal chalcogenides with controlled morphology, structure and composition alteration is currently a burning research topic [5].

Out of the available thin film deposition methods, chemical routes are most promising since it does not involve luxurious vacuum condition simplicity, low cost, and large-scale applications [7]. Particularly, chemical bath deposition (CBD) technique, a chemical method at inexpensive for large area deposition and doping of the impurity atoms via this route is a simple process to achieve desired properties in the aqueous environment. This technique is suited for smoother, homogenous, and stoichiometric thin film deposition [7]. In this article, we report the preparation of pentenary compound Zn_{1-x-y}Co_xCd_ySe_{1-z}S_{-z} by chemical bath deposition (CBD) technique, the effect of Co²⁺, Cd²⁺ and S²⁻ concentration on the surface, compositional and morphological properties were studied.

2 Synthesis and Characterizations of Zn_{1-x-y}Co_xCd_yS_zSe_{1-z} Thin Films

2.1 Synthesis

Zn_{1-x-y}Co_xCd_yS_zSe_{1-z} thin films of various compositions were deposited on the micro glass-substrates from an aqueous medium [7]. The precursors used were AR grade zinc sulfate, cobalt sulfate, cadmium sulfate, sodium selenosulphate, and thiourea in an appropriate volumetric ratio. Optimized quantities of triethanolamine (0.3 ml), hydrazine hydrate (6 ml), and ammonia (17 ml) were used. The deposition temperature was (80 °C), deposition time (90 min), speed of substrate rotation (60 ± 1 rpm), and reaction pH (10.5 ± 0.1) were taken as optimized. The preparation parameters, x and y, were changed from 0.5 to 0.15, and z was varied from 0.1 to 0.3.

2.2 Characterizations

Wettability measurement was done using a Rame-Hart Inc (model-10) micro-syringe with a CCD camera. The morphological and compositional analyses of as-deposited thin films were visualized using FESEM, JEOL, JSM-7000 (20 kV) model. The oxidation states of the targeted elements were explored via X-ray photoelectron spectroscopy (XPS, VG Multilab 2000, Thermo Scientific, UK) model. The FTIR measurement was done by the Perkin Elmer spectrophotometer.

3 Results and Discussion

a. Contact angle

The wettability is the result of interaction between immiscible liquid and solid surface. It is known that the wettability varies with the surface free energy and surface roughness [8]. In our case, the solid-water contact angle was used to characterize the sample surface. It was observed that (Fig. 1), the as-grown $Zn_{1-x-y}Co_xCd_yS_zSe_{1-z}$ thin film surfaces are hydrophobic.

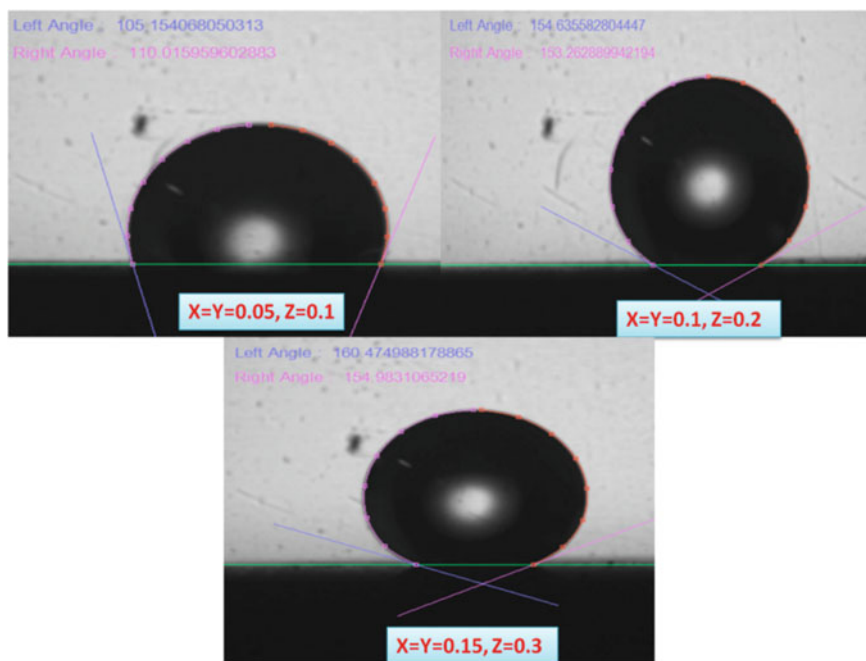


Fig. 1 Variation in the contact angle as a function of the composition

Table 1 Chemical composition of different $Zn_{1-x-y}Co_xCd_ySe_{1-z}S_z$ thin films measured by EDS

Composition parameter		Average contact angle (θ°)	Atomic %					Se/Zn ratio (%)
(x and y)	z		Zn	Co	Cd	S	Se	
0.05	0.1	107.58	36.49	35.38	6.49	10.49	11.15	31
0.1	0.2	153.94	33.48	36.86	7.85	11.05	10.76	32
0.15	0.3	157.73	29.74	37.11	8.34	13.65	11.16	38

b. EDS analysis

The composition of $Zn_{1-x-y}Co_xCd_yS_zSe_{1-z}$ thin films was examined using energy dispersive spectroscopy (EDS) and their composition is reported. The result indicated the existence of anticipated elements in as-obtained $Zn_{1-x-y}Co_xCd_yS_zSe_{1-z}$ thin films. The variation in atomic % of Zn, Co, Cd, S and Se contents are documented in Table 1. From Table 1, it is observed that the amount of Zn element decreases with increasing Co and Cd content suggesting the partial replacement of Zn by Co/Cd. In the case of S and Se content, a small increase in S was observed with as light decrease in Se content. The Se/Zn ratio was found to vary from 31 to 38% with increasing composition parameter x, y, and z.

c. XPS analysis

The oxidation state of all five elements in the Zn, Se, S, Co, and Cd in as-deposited thin films was detected from X-ray photoelectron spectroscopy (XPS). Figure 2 shows the XPS survey spectra of the as-obtained thin film sample. The XPS survey spectra was deconvoluted on the separate elements to study the oxidation states of existing elements. The zinc appears as a doublet of $2p^{3/2}$ and $2p^{1/2}$ peaks at 1026.17 eV and 1051.49 eV respectively, with splitting energy of 25.32 eV which is the characteristic of divalent zinc [9, 10]. The cobalt also splits into a doublet of $2p^{3/2}$ and $2p^{1/2}$ located at 784.35 and 804.41 eV with a doublet with 20.06 eV splitting, which is good consonance with the standard of 15.88 eV, confirms chemical state as Co^{2+} [9, 10]. The $Cd3d^{5/2}$ and $Cd3d^{3/2}$ peaks were found at 401.0 and 408.70 eV, respectively. The peak separation of 7.68 eV indicates the 2^+ oxidation state of Cd. Whereas, $S2p$ core level has a binding energy of 171.69 eV which is consistent with the S^{2-} chemical state. The $Se3d$ peak was located at 65.85 eV indicating presence of Se^{2-} [4].

d. FTIR

The FTIR spectra of $Zn_{1-x-y}Co_xCd_yS_zSe_{1-z}$ thin films are as shown in Fig. 3. The sharp peak corresponding to Zn–Se stretching mode was detected at $\approx 746\text{ cm}^{-1}$ – 757 cm^{-1} . FTIR spectrographs also show absorption bands at $\approx 833\text{ cm}^{-1}$ – 903 cm^{-1} which correspond to Se–O or Zn–Se bending and stretching vibrations. The peaks detected at around 1400, 1500, and 2100 cm^{-1} corresponds to C–H, H–OH, C–N,

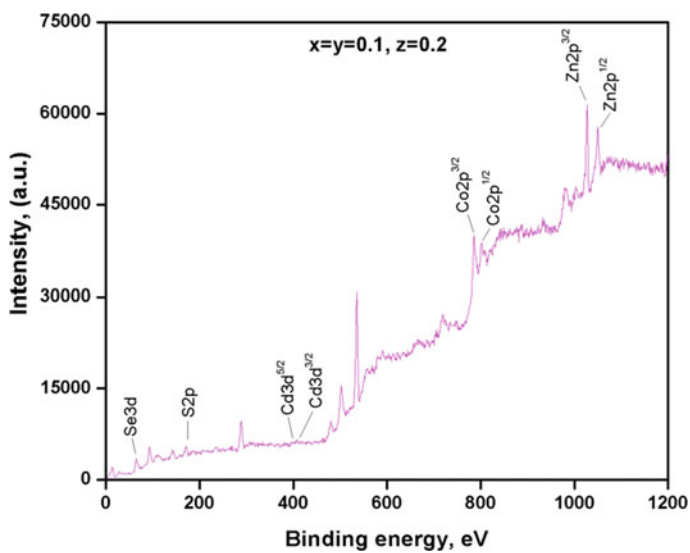


Fig. 2 XPS spectra of $\text{Zn}_{1-x-y}\text{Co}_x\text{Cd}_y\text{Se}_{1-z}\text{S}_z$ ($x = y = 0.1$, $z = 0.2$) thin films

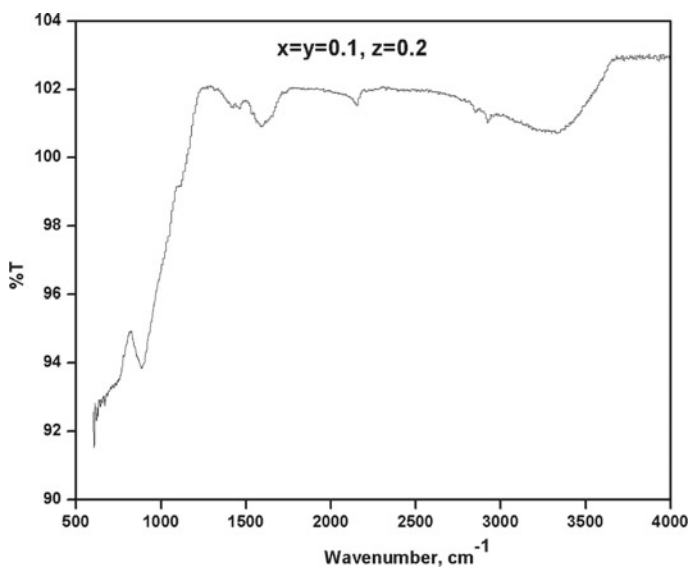


Fig. 3 FTIR spectra of $\text{Zn}_{1-x-y}\text{Co}_x\text{Cd}_y\text{Se}_{1-z}\text{S}_z$ ($x = y = 0.1$, $z = 0.2$) thin films

and H–N–H group. The small peaks found at $\approx 2840 \text{ cm}^{-1}$ – 2880 cm^{-1} and $\approx 2915 \text{ cm}^{-1}$ – 2928 cm^{-1} are the bending typical vibrations of Zn–Zn and Zn–Se in the as-deposited sample [9].

e. SEM observations

Figure 4 shows micrographs of $\text{Zn}_{1-x-y}\text{Co}_x\text{Cd}_y\text{S}_{1-z}\text{Se}_z$ thin films with different composition parameters, x , y , and z . It is witnessed that, the substrate surface is covered with almost spherical and randomly distributed crystallites with the elongated fuzzy multi-facets. The micrographs also revealed a continuous decrease in inter-crystalline spacing with an increase in the composition parameter x , y , and z . It is further viewed that, the globular grains are being grown on the surface of elongated fuzzy multi-faceted crystallites.

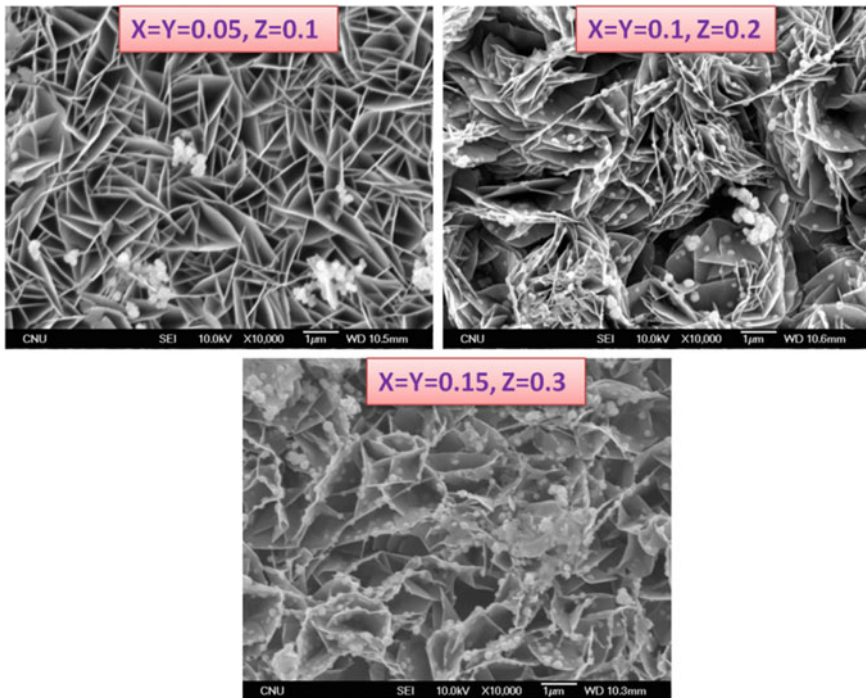


Fig. 4 The SEM micrographs of $\text{Zn}_{1-x-y}\text{Co}_x\text{Cd}_y\text{S}_{1-z}\text{Se}_z$ thin films deposited at different composition

4 Conclusions

In summary, spherical and elongated fuzzy multifaceted crystallites of $\text{Zn}_{1-x-y}\text{Co}_x\text{Cd}_y\text{S}_z\text{Se}_{1-z}$ thin films were successfully synthesized by chemical deposition. The $\text{Zn}_{1-x-y}\text{Co}_x\text{Cd}_y\text{S}_z\text{Se}_{1-z}$ thin film surfaces are hydrophobic. The compositional and chemical analysis revealed the presence of Zn, Co, Cd, S, and Se elements in the $\text{Zn}_{1-x-y}\text{Co}_x\text{Cd}_y\text{S}_z\text{Se}_{1-z}$ thin film samples. The growth of globular grains on the surface of elongated fuzzy multifaceted crystallites was observed in morphological studies.

References

1. Dejene FB (2010) Material and device properties of Cu(In, Ga)Se₂ absorber films prepared by thermal reaction of InSe/Cu/GaSe alloys to elemental Se vapor. *Curr Appl Phys* 10:36–40
2. Santos IMDL, Courel M, Mathews NR, Mathew X (2017) Study on the effect of annealing under pressure on the material properties of Cu₂ZnSn(S, Se)₄ thin films. *Mater. Sci Semicond Process* 68:68–75
3. Kamble SS, Sikora A, Deshmukh SL, Chavan GT, Karande VS, Pawar ST, Tarwal NL, Deshmukh LP (2016) Quaternary $\text{Co}_{1-x-y}\text{Zn}_x\text{Cd}_y\text{S}$ thin films: a facile synthesis approach and its aptness for the applications in micro-devices. *Mater Lett* 167:61–64
4. Chavan GT, Pawar ST, Prakshale VM, Sikora A, Pawar SM, Chaurane NB, Kamble SS, Maldar NN, Deshmukh LP (2017) Quaternary schematics for property engineering of CdSe thin films. *Appl Surf Sci* 426:466–479
5. Chavana GT, Sabah FA, Kamble SS, Prakshale VM, Pawar ST, Patil S, Sunhwa Lee A, Sikora LP, Deshmukh S, Cho Y, Cho E-C, Yi J (2020) Novel synthesis method for quaternary Cd(Cu, Zn)Se thin films and its characterizations. *ceramics international* 46:74–80
6. Bar M, Bohne W, Rohrich J, Strub E, Lindner S, Lux-Steiner MC, Fischer CH, Niesen TP, Karg F (2004) Determination of the band gap depth profile of the pentenary $\text{Cu}(\text{In}_{(1-x)}\text{Ga}_x)(\text{S}_y\text{Se}_{(1-y)})_2$ chalcopyrite from its composition gradient. *J Appl Phys* 96:3857
7. Pawar ST, Kamble SS, Pawar SM, Chavan GT, Prakshale VM, Deshmukh SL, Chaurane NB, Maldar NN, Deshmukh LP (2016) Constraints for ZnSe thin film growth and stoichiometry regulation. *J Mater Sci: Mater Electron* 27:10582
8. Zheng Y, Zaoui A (2017) Wetting and nanodroplet contact angle of the clay 2:1 surface: the case of Na-montmorillonite (001). *Appl Surf Sci* 396:717–722
9. Pawar ST, Chavan GT, Prakshale VM, Sikora A, Pawar SM, Kamble SS, Maldar NN, Deshmukh LP (2017) Physical, structural and topographical aspects of $\text{Zn}_{1-x}\text{Co}_x\text{Se}$ thin films. *Mater Sci Semicond Process* 61:71–78
10. Shatnawi M, Alsmadi AM, Bsoul I, Salameh B, Alna'washi GA, Al-Dweri F, El Akkad F (2016) Magnetic and optical properties of Co-doped ZnO nanocrystalline particles. *J Alloy Compd* 655:244–252

Corrosion Prevention Study by Using Nano and Micro NiCrAlY Coating Over SA213 T22 Boiler Tube



Madhab Chandra Ghosh and Bappa Mondal

Abstract Failure of the boiler tube is the main reason for forced outages at the coal fired thermal power plants. With increasing the demand for electricity, it is very necessary for the power plants to generate electricity without forced outages. Boiler tube failure accounts for a 4% annual loss in large fossil unit availability on a national basis. A significant amount of engineering and technical effort has been expended to prevent boiler tube failure. The present work is concerned with the prevention of the corrosion failure of boiler tube by using High Velocity Oxy-Fuel (HVOF) NiCrAlY coating. An experimental analysis has been carried out with the nano-crystalline (nc) and micro-crystalline (mc) NiCrAlY coating over T22 (2.25 Cr–1 Mo) specimen subjected to high temperature cyclic oxidation at 700 °C in presence of air to investigate its oxidation kinetics. A comparative study has been conducted to study the effect of nano-crystalline (nc) and micro-crystalline (mc) NiCrAlY coating over T22. A good impact is observed for nano-crystalline NiCrAlY coating from the current work.

Keywords HVOF · Micro-crystalline · Nano-crystalline · NiCrAlY · T22

1 Introduction

Thermal power plants contribute about 75% to all India installed capacity of electric power generating stations. In the worldwide energy sector, about 37% of electricity is produced by combusting coal. Most of the Indian industrial boilers has been a prominent problem of boiler tube failure (BTF). Successful and reliable operation of steam generating equipment needs the use of the best available methods to prevent scale and corrosion. Once leakage from tube occurs, it will not only bring about unscheduled shutdown that leads to economic loss but also develop into major accidents. The

M. C. Ghosh (✉)

Department of Industrial Engineering & Management, Maulana Abul Kalam Azad University of Technology, West Bengal, India

B. Mondal

Department of Mechanical Engineering, National Institute of Technology Silchar, Silchar, India

safe running of the tubes in a boiler depends on the assurance of many aspects, such as steel material quality, design reasonableness, manufacturing process, installation skill, and running and overhaul levels [1]. The boiler tubes are interacted at a harsh environment through inside steam and outside flue gases. One common reason of the boiler tube failure is higher the tube metal temperature than the specified temperature [2]. The temperature rise may be due to the development of scale on the internal and/or external surfaces with prolonged exposure at elevated temperature [3]. These failures can be grouped under six major causes such as stress rupture, fatigue, water side corrosion, erosion, fire side corrosion, and lack of quality.

Metal and alloys get oxidised when they are heated to elevated temperatures in air or highly oxidising environments, such as a combustion gas with excess of air or oxygen [4]. They often rely on the oxidation reaction to develop a protective oxide scale to resist corrosion attack, such as sulphidation, carburisation, ash/salt deposit corrosion etc. That is why oxidation is considered to be the most important high-temperature corrosion reaction. Further the rate of oxidation for metals and alloys increases with increasing temperature [5].

Thermal barrier coating (TBC) are widely used to increase the efficiency and protection of metallic components that suffer degradation due to corrosion, oxidation, or excessive heat load during service in thermally drastic environments. Some of its main applications are on gas turbines engines and also in aerospace and aircraft applications [6, 7]. The most common TBC-systems consist of a nickel-base super alloy as substrate, a MCrAlY layer (M: Ni, Co, Fe, or combination of these elements) as bond coat. MCrAlYs are one of the most important protective coating materials applied to gas turbine parts [8, 9]. NiCrAlY coating protect the components against high temperature oxidation and hot corrosion attack, typically deposited by Vacuum Plasma Spray (VPS) or Low-Pressure Plasma Spray (LPPS), by Air Plasma Spray (APS), and recently by High Velocity Oxy-Fuel process (HVOF). However, the HVOF thermal spray is a highly cost-effective method to add properties and performance qualities over these surfaces [10].

This paper shows the experimental study of the impact of using high Velocity Oxy-Fuel Spray (HVOF) NiCrAlY coating on T22 (2.25 Cr–1 Mo) materials for the prevention of boiler tube failure due to high temperature corrosion. The experiment has done on the microcrystalline (mc), nanocrystalline (nc) NiCrAlY coating and uncoated T22 specimens. Based on the study, the effect of micro and nano size NiCrAlY coating on its life has been discussed.

2 Experimental Details

2.1 Methodology

The applied methodology for the experimental study of the impact of using high velocity oxy-fuel spray (HVOF) NiCrAlY coating over SA213 T22 boiler tubes is

discussed in details. The major used apparatuses for the current work are precision analytical balance, high temperature vertical tube furnace, metallurgical trinocular optical microscope, and field emission scanning electron microscope. The detail has been discussed one by one. The study is conducted in the following sequences:

- First the T22 material was coated by NiCrAlY coating using HVOF coating technique.
- Oxidation studies were conducted on uncoated as well as high velocity oxy-fuel and mc coated T22 specimen in air at 700 °C under cyclic conditions. Each cycle consisted of 30 min of holding time at 700 °C and then decreased the temperature to 400 °C in 75 min (4 °C/min). The cycles repeat for 10 times.
- The specimen's weight gain was measured with precision analytical balance.
- Mold was made by cold mounting process using cold mounting resin and liquid for post analysis.
- The specimens were examined in optical microscope and Field Emission Scanning Electron Microscope (FESEM) with EDS Attachment for mapping the powder particle.

2.2 Specimen Preparation

The material used for the investigation is T22 (2.25 Cr–1 Mo) steel plate of 6 mm thickness. The chemical composition is reported in Table 1. Rectangular specimen of 20 mm × 20 mm are prepared from plates. Some of the specimens are kept in uncoated bare substrate for experimental investigation. Some are coated with high velocity oxy-fuel coating.

2.3 NiCrAlY Coating Powder

The NiCrAlY powder is characterized with a Scanning Electron Microscope (SEM). The powder morphology of NiCrAlY powder is shown in Fig. 1 and the chemical composition of the coating is shown in Table 2. Before the application of the coating, the specimens are subjected to the grit blasting by alumina powder (Al_2O_3) in Pressure blasting machine. Grit blasting is a process in which the substrates are blasted with abrasive particles. These particles remove surface oxides and contaminants stuck to the surface of the substrates. Grit blasting also roughness the surface, thereby promoting increase adhesion of the deposited coating. For thermal spraying

Table 1 Chemical composition of T22

C	Mn	Si	S	P	Cr	Mo	Fe
0.11	0.51	0.19	0.008	0.012	2.07	0.95	Balance

Fig. 1 SEM photomicrograph of NiCrAlY coating

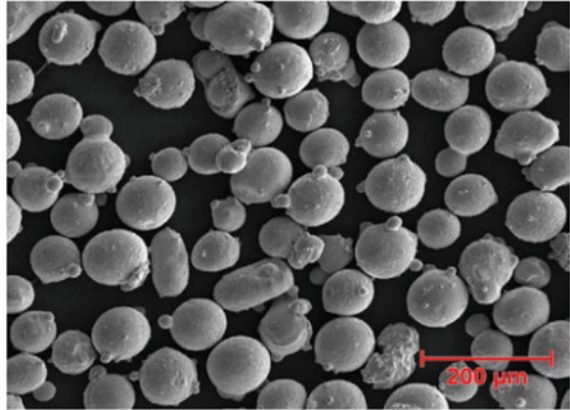


Table 2 The chemical composition of the NiCrAlY coating

Ni	Cr (%)	Al (%)	Y (%)
Bal%	22	10	1

aluminum oxide grit is typically used. Grit blasting is done in a closed chamber where the grit pellets are projected at a high speed through a nozzle towards the substrate. The grit size of the alumina powder is 16 mesh size and Air pressure during blasting is 6 kg/cm². The blasting distance is maintained 90 mm.

2.4 Oxidation Study

Oxidation studies were conducted on uncoated as well as high velocity oxy-fuel nc and mc coated over T22 specimen. The specimen was kept in the presence of air at 700 °C under cyclic conditions with a high temperature vertical tube furnace which is shown in Fig. 2. Each cycle consisted of 30 min of holding time at 700 °C and then the temperature is reduced to 400 °C. This phenomenon was completed within 75 min (4 °C/min). The cycle repeats for 10 times.

2.5 Corrosion Results

The nc and mc NiCrAlY coated and uncoated specimens are examined under 700 °C. The result is shown in the Table 3 and the weight gain per area of each cycle are given in the Table 4.

Fig. 2 High temperature vertical tube (HVOF) furnace



Table 3 Corrosion growth rate of nano, micro size NiCrAlY coating and uncoated Specimens

Sl. no.	Description	Nano size NiCrAlY coated T22	Micro size NiCrAlY coated T22	Uncoated T22
1	Area (cm ²)	8.12	8.08	7.6
2	Initial weight (gm)	9.0649	9.8712	8.6133
3	Final weight (gm)	9.07795	9.8918	8.6477
4	Weight gain (mg)	130.5696	206.1	314.032
5	Weight gain/area after 10 cycle (mg/cm ²)	16.08	25.38	41.32

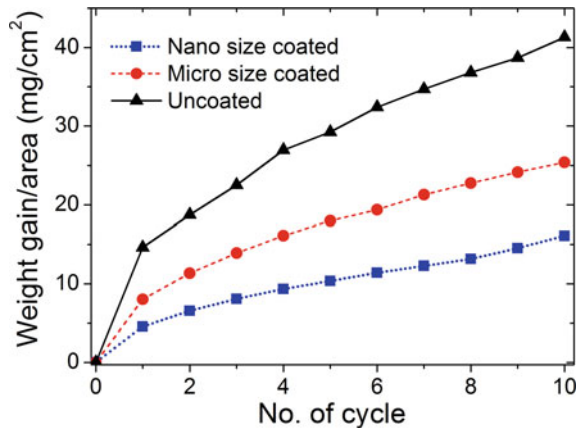
2.6 Reaction Kinetics and Oxidation Behavior of Nano, Micro Size NiCrAlY Coated and Uncoated T22 Specimens

The result has been presented in Fig. 3. It is observed from the figure that weight gain per area of uncoated T22 is higher compare to nano and micro size NiCrAlY coated T22. The nano crystalline NiCrAlY coating exhibit superior high temperature corrosion resistance in air due to the formation of adherent, non-porous, and uniform protective scales such as NiCr₂O₄, Al₂O₃, Cr₂O₃ etc. when compared to mc coating.

Table 4 Weight gain/area(mg/cm²) for nano, micro size NiCrAlY coating and uncoated T22 specimens

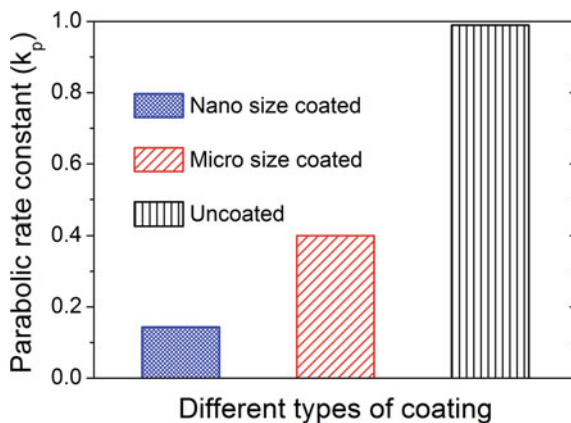
No. of cycle	Weight gain/area (mg/cm ²) for nano size NiCrAlY coated T22	Weight gain/area (mg/cm ²) for micro size NiCrAlY coated T22	Weight gain/area (mg/cm ²) for uncoated T22
1	4.56	8.04	14.62
2	6.58	11.35	18.73
3	8.09	13.9	22.51
4	9.34	16.12	26.96
5	10.37	17.96	29.25
6	11.42	19.36	32.42
7	12.29	21.28	34.7
8	13.17	22.75	36.82
9	14.54	24.14	38.69
10	16.08	25.38	41.32

Fig. 3 Reaction kinetics and oxidation behavior compare between nano size, micro size coated and uncoated specimens



On the other hand, the protective scales formed over the mc coating are non-uniform, discontinuous which provides relatively less protection in the corrosive environment compare to nano crystalline. The mechanisms of nano size effect on the rapid formation of protective scale, through high diffusivity of alloying elements, in nc coating are proposed. The experiment is done for the 10 no. of cycle.

Fig. 4 Parabolic rate constants for nano, micro size NiCrAlY coated and uncoated T22



2.7 Parabolic Rate Constants of of Nano, Micro Size NiCrAlY Coated and Uncoated T22 Specimens

The parabolic rate constants were calculated by the following equation

$$(\Delta W/A)^2 = k_p t \quad (1)$$

where, $\Delta W/A$ is the weight gain per unit area (mg cm^{-2}), k_p is the parabolic rate constant ($\text{mg}^2 \text{cm}^{-4} \text{s}^{-1}$) and t is the time in seconds. The parabolic rate constant (k_p) of nc, mc coated and uncoated specimens are plotted in the Fig. 4.

The parabolic rate constant (k_p) of nc, mc coated and uncoated specimens were found to be $0.1436 \text{ mg}^2 \text{cm}^{-4} \text{s}^{-1}$, $0.400158 \text{ mg}^2 \text{cm}^{-4} \text{s}^{-1}$, $0.98918 \text{ mg}^2 \text{cm}^{-4} \text{s}^{-1}$ respectively. It was observed that lower the value of k_p means higher the corrosion resistance property. It was clear that the value of k_p for the steel had decreased significantly after the deposition of the coating.

2.8 FESEM and EDS Analysis

Figure 5 shows the FESEM micrograph of top scale morphology of nano size, and micro size formed after 10 cycles of oxidation in air 700°C . For nano and micro coated T22 indicate mainly white crystalline phase rich in Al_2O_3 , irregularly dispersed in the black phase (matrix) rich in Ni_3Al . While FESEM micrograph of top surface of the scale in case of uncoated T22 indicates inter granular cracks, which mainly contain Cr_2O_3 and NiO , in Fig. 5. Fine globules (white) are mainly dispersed in the black matrix, along with the presence of some coarse globules (Ni_3Al). Further, FESEM micrographs point out similar morphologies of the oxide scales for both the

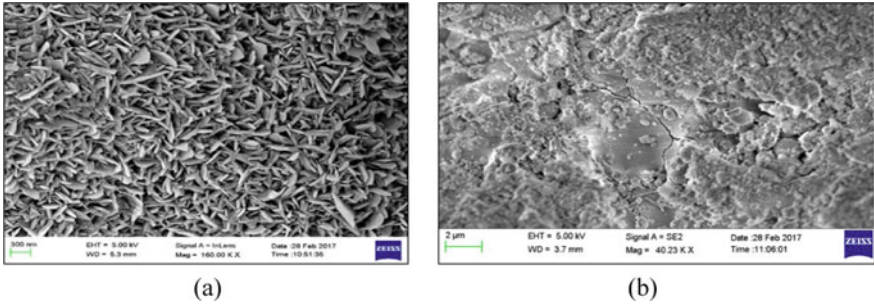


Fig. 5 Top scale morphology of **a** nano size **b** micro size

NiCrAlY coated superalloys. FESEM/EDS shown in Fig. 5 for the coated T22 indicates that the oxide scale contains mainly Ni₃Al with little amount of oxides of Cr. Whereas in case of uncoated specimen, white (Fe₂O₃) can be observed to be dispersed in the scale. The presence of Fe₂O₃ indicates the probable diffusion of Fe and Si from the base materials.

Figure 6 shows the surface morphologies and EDS analyses of the scales formed on the HVOF NiCrAlY coating after isothermal oxidation at 700 °C for 10 cycle, respectively. The FESEM images show that the morphologies of the coating are different with each other. No spallation was observed on the coating. For nc coating, the oxides are a mixture of small round grains and some large nodules. EDS analysis indicated that the large nodules in spectrum1 mainly consisted of Ni (55.84%, molar fraction), Cr (20.21%) and/or Al (12.9%) and O (9.19%), while the small round grains in spectrum 2 are rich in Al (18.58%) and O (18.92%). However, only small round grains formed on the ground coating.

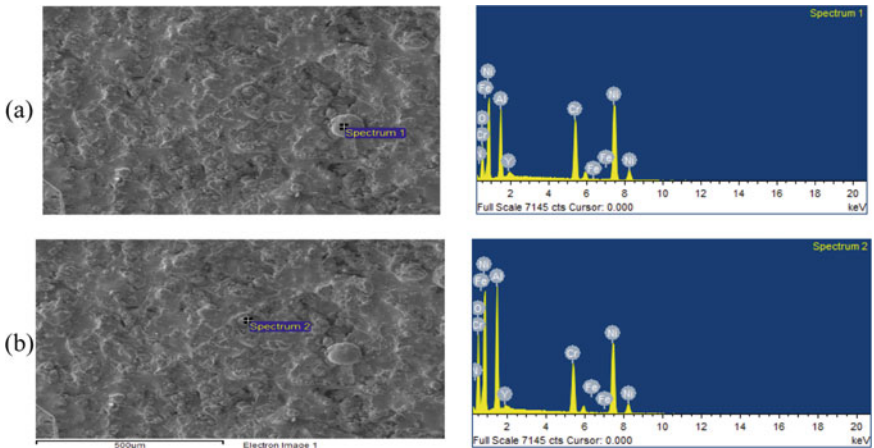
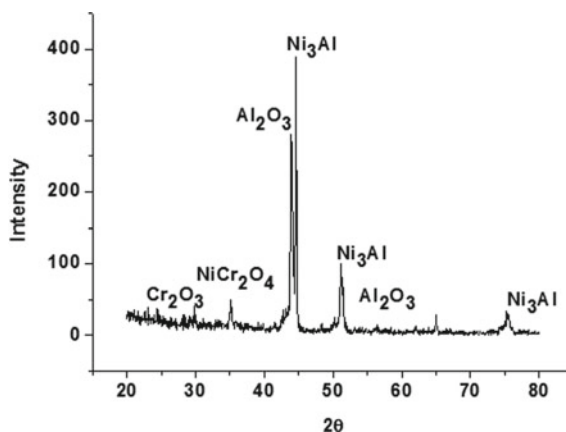


Fig. 6 EDS elemental mapping of powder particle NiCrAlY **a** on spectrum 1, **b** on spectrum 2

Fig. 7 XRD patterns of the coatings after 10 cycle oxidations in air at 700 °C



XRD diffractograms for the uncoated and coated T22 after exposure to air at 700 °C for 10 cycles are depicted in Fig. 7 on reduced scales. As is clear from the diffractograms in Fig. 7 NiO, Cr₂O₃ and NiCr₂O₄ are the phases which are found to be present in both the oxidised mc and nc coated T22, whereas Fe₂O₃ is revealed in uncoated T22. Further, it can be seen from the diffractograms, that both the NiCrAlY coated T22 have indicated the formation of NiO, Al₂O₃ and NiCr₂O₄ as main phases after oxidation along with some relatively weak peaks of Cr₂O₃.

The result indicates formation of thicker scale of the uncoated specimen are consists of mainly Fe₂O₃ and Fe₃O₄ phases. The presence of Cr₂O₃ as weak phases indicates that the absence of strong protective layer of NiCr₂O₄. In case of the scale consists of Nickel chromium rich oxide and some nickel oxide as a result of which thin compact adherent scale formed on the substrate.

3 Conclusion

The main aim of the present work is to study the effect of High Velocity Oxy-Fuel (HVOF) nano size and micro size NiCrAlY coating over SA213 T22 boiler tube. The main findings from the present work can be summarized as follows:

- The application of NiCrAlY coating over T22 (2.25 Cr-1 Mo) steel improves the resistance rate to significant extent in comparison to the uncoated T22.
- The corrosion resistance is improved up to 59.08% for nano-crystalline and 40.57% for micro-crystalline NiCrAlY coating.
- The outer scale of post corroded uncoated specimen shows extensive cracking and spallation. Further the cracked and spalled scale act as easy diffusion path for outer cation and inner anion migration and corrosion rate is increased.

- The outer scale of post corroded coated specimen shows adherent scale without scale cracking and spallation, which resists the migration of outer cation and improves the corrosion resistance to significant extent.

References

1. Sijacki Z, Bakic G, Djukic M (2010) Contemporary maintenance management of power plant life exhaustion components. *Tech Technol Educ Manage* 5(3):431–436
2. French DN (1993) *Metallurgical failures in fossil fired boilers*, 2nd edn. Wiley, New York Inc
3. Clark KJ, Paterson SR, Rettig TW (1988) *Remaining life assessment of superheater and reheater tubes*. Aptech Engineering Services Inc, CA (USA)
4. Higuera HV, Belzunce JV, Carriles AM, Poveda SM (2001) High temperature erosion wear of flame and plasma-sprayed nickel – chromium coatings under simulated coal-fired boiler atmospheres. *J Wear* 247:214–222
5. Lai GY (1990) *High temperature corrosion of engineering alloys*. ASM International Pub. vol 15
6. Khoddami AM, Sabour A, Hadavi SMM (2007) Microstructure formation in thermally-sprayed duplex and functionally graded NiCrAlY/Yttria-stabilized Zirconia coatings. *Surf Coat Technol* 201(12):6019–6024
7. Lima CRC, Guilemany JM (2007) Adhesion improvements of thermal barrier coatings with HVOF thermally sprayed bond coats. *Surf Coat Technol* 201(8):4694–4701
8. Zhao L, Lugscheider E (2002) High velocity Oxy-fuel spraying of a NiCoCrAlY and an intermetallic NiAl-TaCr alloy. *Surf Coat Technol* 149(2–3):231–235
9. Lugscheider E, Herbst C, Zhao L (1998) Parameter studies on high-velocity Oxy-fuel spraying of MCrAlY coatings. *Surf Coat Technol* 108(3):2577–2584
10. Haoliang T, Guob J, Erbao L, Fuyuan W, Changliang W, Mengqiu G, Junguo G, Yongjing C (2020) Preparation and performance of thermal barrier coatings made of BNwcontaining modified Nd₂O₃-Doped Yttria-stabilized Zirconia. *Ceram Int* 46:500–507

Design and Development of Water Cooling System for Copper Mold



Shashikant S. Jadhav, Avinash K. Parkhe, Subhash V. Jadhav, and Samadhan J. Shinde

Abstract This research presents an overview of the cooling system used to cool the FeSiMg alloy in one Industry. The traditional cooling system being used requires 20 min for the solidification of FeSiMg alloy. The Magnesium present in the alloy reacts with oxygen forming a layer of Magnesium oxide at the top surface of the alloy. The formation of the Magnesium oxide leads to wastage of the material. Thus, there is a need to minimize the solidification time of FeSiMg alloy to minimize the alloy wastage, and hence there is a need to design an efficient cooling system. The cooling system uses water for taking out the heat from the molten alloy. Therefore, efficient cooling system design is basically applied to improve the heat transfer coefficients (h) from FeSiMg alloy to the cooling water. The experimental analysis is performed to optimize the parameters like mass flow rate of water, water inlet temperature, so the cooling is achieved in less time. The experimental analysis revealed the optimized parameters resulting in a reduction in the solidification time, i.e., 8 min. Thus, with the reduction in the solidification time, the loss of alloy is reduced from 5 to 3.5%, i.e., the saving of material is 1.5% of the total material.

Keywords Alloy · FeSiMg · Oxide · Solidification

1 Introduction

One Industry is producing the FeSiMg alloy. The molten alloy FeSiMg is produced using a furnace and is poured into the Copper alloy mould which is then allowed to solidify. The solidified alloy is in the form of a thick plate of size 8×5 feet approximately. This alloy plate is then broken down to small pieces and is used as the raw material in different Industry like Tata steel, Mahindra and Mahindra, and many more. The industry is facing a problem that the Magnesium Oxide is formed readily during the solidification of alloy. In usual practice, the solidification of alloy requires 20 min which is a higher time and thus leads to the formation of Magnesium

S. S. Jadhav (✉) · A. K. Parkhe · S. V. Jadhav · S. J. Shinde
SVERI's College of Engineering, Pandharpur, MH, India
e-mail: ssjadhav@coe.sveri.ac.in

Oxide. The formation of Magnesium Oxide leads to wastage of FeSiMg alloy. To maintain the desired quality of the alloy, the solidification time of FeSiMg alloy is to be minimized.

So, we aim to reduce the solidification time so that contact of magnesium with oxygen is reduced. For the solution of the said problem cooling system is designed in which water is used as a coolant. The cooling system is fabricated of copper. In the cooling system involves the use of baffles to make the water flow more manageable in a particular path due to which cooling is achieved effectively.

2 Literature Survey

The interfacial heat transfer coefficient (IHTC) for vertically upward unidirectional solidification of a eutectic Al–Si casting on water-cooled copper and steel chills was measured during solidification. A finite difference method (FDM) was used for the solution of the inverse heat conduction problem (IHCP). Six computer-guided thermocouples were connected with the chill and casting, and the time-temperature data were recorded automatically. The thermocouples were placed, located symmetrically, at 5, 37.5 and 75 mm from the interface. As the lateral surfaces are very well heated isolated, the unidirectional solidification process starts vertically upward at the interface surface. The measured time-temperature data files were used by an FDM using a precise technique. A heat flow computer program has been written to estimate the transient metal–chill IHTC in the IHCP. The experimental and calculated temperatures have shown excellent agreement. The IHTC during vertically upward unidirectional solidification of an Al–Si casting on copper and steel chills have varied between about 19–9.5 kW/m² K and 6.5–5 kW/m² K, respectively.

Our calculated results have shown that the applied model for determination of the metal casting–chill IHTC in one-dimensional heat flow is achieved successfully, and the following conclusions can be summarized as follows:

1. A satisfactory FDM to evaluate the IHTC at the Al–Si eutectic metal casting at both the copper and steel chill interfaces has been achieved for one-dimensional heat flow.
2. The numerical calculated and experimental temperature values have shown excellent agreement and, consequently, a high-reliability grade for the IHTC.
3. The IHTC values during the vertically upward unidirectional solidification of a eutectic Al–Si casting have varied between about 19–9.5 kW/m² K and 6.5–5 kW/m² K on copper and steel chills, respectively. These values have shown good agreement with those in the literature.
4. The results have shown that the receding of the casting from both the copper and steel chill surfaces does not occur during the solidification.
5. The IHTC could be affected mainly by the contact position and area between the casting and chill surfaces roughness. Future investigation should, therefore, consider these effects [1].

3 Research Objectives

Some researchers have studied the problem of measuring the transient metal–chill IHTC during unidirectional solidification [2, 3]. These studies show that the heat transfer coefficient becomes a high value in the initial stage of solidification and then declines to a low steady value because the casting contracts from the chill surface, creating an interfacial gap [4, 5]. Several significant studies have applied mathematical models to understand the thermal and mechanical behaviour of single-piece tube moulds for casting steel billets. This behaviour was found to be very important to heat transfer, dimensional accuracy, strand quality, and life of the billet mould tubes [6, 7].

So, the number of research work is done on different cooling methods for cooling the high-temperature molten metal so the suggest and design a better cooling method for the cooling FeSiMg alloy and analyse the system. So, the objectives of the study are listed below.

1. To decrease the solidification time to reduce the thickness of oxides on casting.
2. To suggest a cooling system for required copper mould (i.e. for 20 kg FeSiMg alloy)
3. Design & analysis of the cooling system.
4. Study the effect of variation in parameters of the cooling system on solidification time.
5. To calculate the mass flow rate of water flowing through the mould for cooling 20 kg of FeSiMg alloy, the following parameters are being considered.

4 Design and Development of the System

To calculate the mass flow rate of water flowing through the mould for cooling 20 kg of FeSiMg alloy, the following parameters are being considered. This parameter we have considered from the analysis of 1 kg FeSiMg alloy system. We have made a setup for the 1 kg FeSiMg alloy from that setup we get the approximate values for the 20 kg of FeSiMg alloy system. According to this, we have calculated the required mass flow rate by using a lumped analysis [3]. Mass flow rate for 20 kg FeSiMg alloy, Density of the FeSiMg alloy is 4600 kg/m^3 , and Volume mass/density, Volume of FeSiMg alloy is 4347 cm^3 , Heat present in 1 kg FeSiMg alloy is 85800 J is calculated using Eq. (1).

$$Q = m C_p dt \tag{1}$$

Heat present in 20 kg FeSiMg alloy is given by Eq. (2) and is 17160000 J

$$Q = m C_p dt \tag{2}$$

But $Q = h A dt$ means Q is directly proportional to Area. Therefore, the area required for 20 g FeSiMg alloy is 0.2 m^2 . From that suitable dimensions for the systems are Length of the system is 65 cm, Width of the system is 35 cm, Thickness of collar is 2.5 cm Thickness of copper mould is 4 cm and Height of water cavity is 6 cm. The surface area of copper mould is 0.18 m^2 , the volume of Cu mould is 0.0072 m^3 , Cross-section area of the water cavity is 0.018 m^2 and Hydraulic diameter (D_h) is 0.1 m. By lumped system analysis equation is calculated as $604 \text{ w/m}^2\text{k}$. Similarly, By Dittus Boelter equation Nu is calculated, and Eq. (3) is as follows and velocity calculated is 0.125 m/s and mass flow rate calculated is 2.25 lpm. Therefore for 20 kg, FeSiMg alloy mass flow rate of water required is 135 lpm.

$$Nu = 0.023 Re \left(\frac{4}{5} \right) Pr^{0.4} \tag{3}$$

5 Result and Discussion

We have made the setup of the experiment and measured temperatures of different locations by using thermocouples. Experimentally we get the values of temperature for the different mass flow rates.

Reading and graph for the mass flow rate of water versus Time required for solidification of FeSiMg alloy. From the readings of the solidification time of FeSiMg alloy for a different mass flow rate of water is as shown in Table 1. The design model of copper cooling system is shown in Fig. 1. Also the actual setup of copper cooling system along with temperature measuring devices shown in Figs. 2, 3 below.

From the readings, the graph for the mass flow rate of water versus solidification time is as shown in Fig. 4. From the above Fig. 4, it is seen that if the mass flow rate of water increases then solidification time is reduced. So the water as a coolant is efficient for cooling the alloy.

Table 1 Reading for the mass flow rate of water versus time required for solidification of FeSiMg alloy

A mass flow rate of water (lpm)	The time required for solidification of FeSiMg alloy (s)
80	402
115	380
135	364
180	338

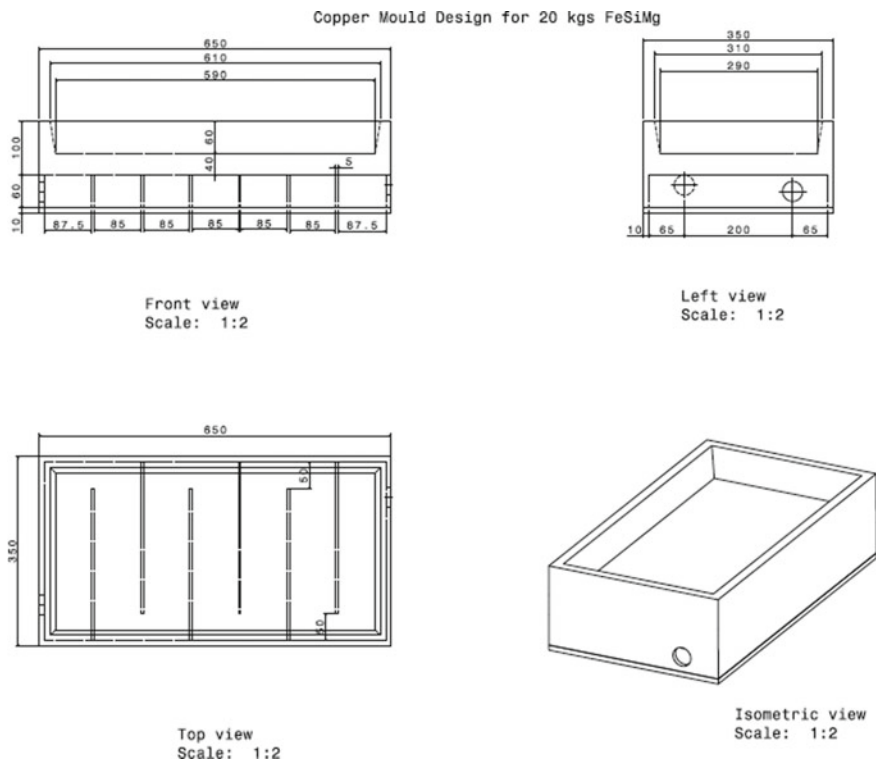


Fig. 1 Copper mold design for 20 kg FeSiMg alloy

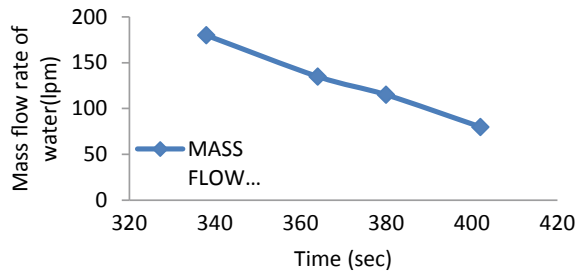


Fig. 2 Development of copper mold for 20 kg FeSiMg alloy



Fig. 3 Measurement of temperatures (Thermocouples)

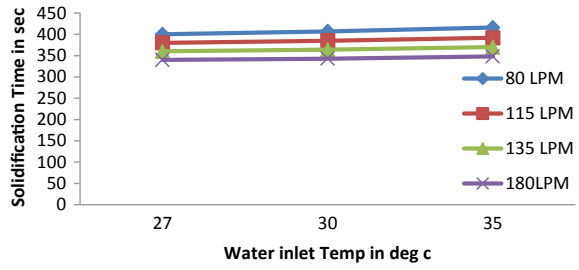
Fig. 4 Graph for the mass flow rate of water versus solidification time



5.1 Graph for the Variation of Solidification Time of Alloy and Water Inlet Temperature

The mass flow rates of water considered for calculating solidification time of alloy is 80,115,135,180 lpm, and the same is plotted in Fig. 5. From the above graphs if the water inlet temperature increases solidification time also increases, so the less inlet water temperature is suitable for the system. If water inlet temperature is less, then solidification of alloy takes place in less time.

Fig. 5 Graph for the solidification time of alloy and water inlet temperature for 80,115,135,180 lpm



5.2 Variation of Alloy Temperature with Time for Different Mass Flow Rates of Water

For the mass flow rate of water of 80 lpm values obtained are plotted in Fig. 6 and for the mass flow rate of water of 115 lpm values obtained are plotted in Fig. 7. For the mass flow rate of 135 and 180 lpm, values obtained are plotted in Figs. 8 and 9.

Fig. 6 Variation of alloy temperature with time for 80 lpm mass flow rate of water

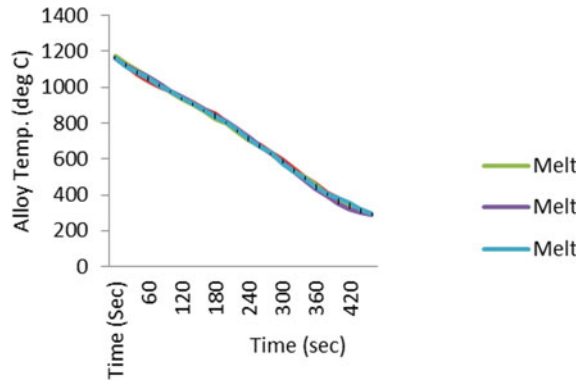


Fig. 7 Variation of alloy temperature with time for 115 lpm mass flow rate of water

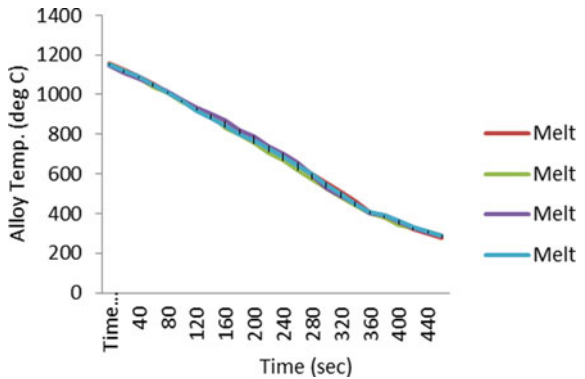


Fig. 8 Variation of alloy temperature with time for 135 lpm mass flow rate of water

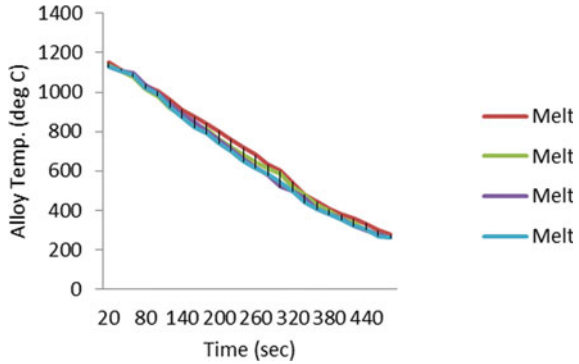
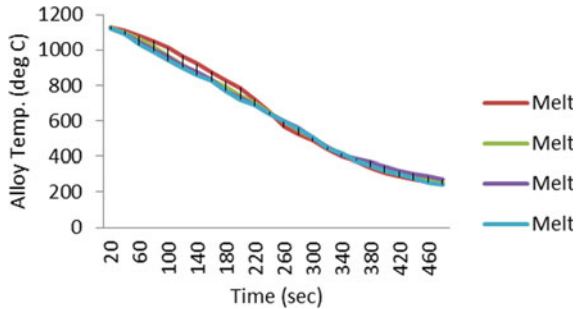


Fig. 9 Variation of alloy temperature with time for 180 lpm mass flow rate of water



From the above graph of the alloy temperature versus the time it is clear that the temperature of the alloy is continuous decreases with time i.e., the cooling is carried out by using the water which is continuously passing at the bottom of the copper mould. So that by using water as coolant the alloy temperature is continuously decreasing.

6 Conclusion

The Industry is manufacturing the FeSiMg alloy being used as flux material for the steel plants. The molten alloy FeSiMg is produced using the furnace and is poured into the Copper alloy mould which is then allowed to solidify. This alloy plate is then broken down to small pieces and is used as the raw material in different Industry like Tata steel, Mahindra and Mahindra, and many more. The industry is facing a problem that the Magnesium Oxide is formed readily during the solidification of alloy. In regular practice, the solidification of alloy requires 20 min which is a higher time and thus leads to the formation of Magnesium Oxide. The formation of Magnesium Oxide leads to wastage of FeSiMg alloy. To maintain the desired quality of the alloy, the solidification time of FeSiMg alloy is to be minimized.

A cooling system to operate on the optimized parameter is designed for reducing the solidification time of the alloy. The parameters of prime importance are the mass flow rate of water, the inlet temperature of the water. The effect of the inlet mass flow rate of water and the inlet temperature of the water are critically studied. Several important conclusions are drawn from the present study and are as follows:

1. If the mass flow rate of water is increased, then the solidification time of alloy is reduced.
2. The increase in water inlet temperature increases the solidification time.
3. By using the water as a coolant, the temperature of the alloy continuously decreases with time.
4. The experimental analysis revealed the optimized parameters resulting in a reduction in the solidification time, i.e., 8 min.
5. With the reduction in the solidification time, the loss of alloy is reduced from 5 to 3.5%, i.e., the saving of material is 1.5% of the total material.

7 Future Scope

1. The numerical model and simulation can be done for the cooling system for a wide range of operating parameters.
2. CFD analysis can be performed to study the effect and behaviour of the system to optimize the heat transfer coefficient.

References

1. Cheung N, Ferreira IL (2009) Melt characteristics and solidification growth direction for gravity affecting the interfacial heat transfer coefficient of chill castings. *Mater Des* 30:3592–3601
2. Sahin HM, Kocatepe K, Kayikci R, Akar N (2006) Determination of unidirectional heat transfer coefficient during unsteady-state solidification at metal casting-chill interface. *Energy Convers Manage* 47:19–34
3. Griffiths WD (2000) A model of the interfacial heat-transfer coefficient during unidirectional solidification of an aluminium alloy. *Metall Mater Trans B* 31:85–95
4. Abed EJ (2011) The influence of different casting method on solidification time and mechanical properties of AL-Sn castings. *Int J Eng Tech* 11(6):110806–7474
5. Thomas BG, Li G, Moitra A, Habing D (1997) Analysis of thermal and mechanical behavior of copper molds during continuous casting of steel slabs. *Mechanical and Industrial Engineering Dept., University of Illinois, Urbana, IL 61801(217):333–6919*
6. Guejjman SF, Schvezov CE (2010) Vertical and horizontal directional solidification of Zn–Al and Zn–Ag diluted alloys. *Mater Trans* 51(10):1861–1870
7. Kovacevic L, Terek P, Kaka D (2012) A correlation to describe interfacial heat transfer coefficient during solidification of Al–Si alloy casting. *J Mater Process Technol* 212:1856–1861

Characterization of Calophyllum Oil Biodiesel—Alternative Fuel to Diesel Engines



Rahul Krishnaji Bawane, Chetan Choudhary, A. Muthuraja,
and G. N. Shelke

Abstract A preliminary investigation on the fitness of Calophyllum (non-edible) oil for the development of its fractions for biodiesel/Calophyllum Oil Methyl Ester and its characterization is carried out. The Calophyllum seeds considered, which shows the second-highest productivity (after palm) of 4680 kg oil per hecter. According to the oil yield, Calophyllum was identified as the future potential feedstock for biodiesel with the productivity of 4680 lit oil per hecter, the second-highest after palm oil. The highest biodiesel yield 67% was found at 1.5:1 oil to methoxide ratio at reaction temperature 50–60 °C among the ratio of 1:1, 1.5:1 and 2:1 for the temperature range 40–50, 50–60 and 60–70 °C. The investigation revealed that the fatty acid methyl ester of Calophyllum seed oil met all the major biodiesel requirements in the USA ASTM D 6751-02, ASTM PS 121-99, European Union EN 14214, Germany DIN V 51606 and Indian Standards IS 1448. And in fuel blend, the increase in content of biodiesel, there is increases in density, kinematic viscosity at the same time there is reduction in calorific value, cetane number, flash point and fire point.

Keywords Biodiesel · Blend · Calophyllum · Characterization · Transesterification · Yield

1 Introduction

Now a day government stringent emission regulations with adopting BS-IV emission norms which were already adopted in developed countries as Euro 6 norms to minimize the emissions from automobiles, also fuel crisis in the upcoming years enforced to search for unconventional sources of fuel. Many countries are critically dependent on petroleum fuels for agricultural machinery and transportation sector,

R. K. Bawane (✉)

Department of Mechanical Engineering, Sandip University, Nashik, MS, India

e-mail: rahul.bawane@pccoer.in

C. Choudhary · A. Muthuraja · G. N. Shelke

Department of Mechanical Engineering, Sandip Institute of Engineering and Management, Sandip Foundation, Nashik, MS, India

few countries together geared up to the bulk of petroleum and this leads to high price variation and uncertainties in supply for the remaining countries. India mainly depends on the import of petroleum and about 2/3rd of its demand met through imports and the emissions from their use have an opposing impact on the environment and human health [1, 2]. In such a scenario, biomass is become known as one of the promising environmental friendly renewable energy substitutes, if the conventional energy sources, petroleum oils, coal, and gases happen to exhaust. This biomass treated thermo-chemically or biologically and converted into liquid and gaseous biofuels [3]. In the recent decade, biodiesels are gained importance and recognition due to their biodegradability, renewability, and environment-friendly [4]. However, biodiesel from such vegetable/crops inherently contains oxygen 10–45% by mass which is not available in the case of petroleum fuel. This promotes chemical reaction, better and complete combustion of biodiesel. Also, biodiesels reported very low sulfur content and many have a low nitrogen level which makes it more environmental friendly [2, 3]. There has been greater wakefulness on biodiesel in developing countries these days, along with boosting the economy, especially in rural areas. Biodiesel is a renewable and biodegradable fatty acid methyl ester extracted from various kinds of vegetable oil and animal fats. Edible oils to be used as fuel is not significant due to food crops are more expensive and terrific demand in food/cooking uses. Therefore researchers are made their research focused on extracting biodiesel from non-edible oil crops, non-edible oils established themselves as promising crude oils in the area of alternative fuel to the conventional petroleum diesel fuel [5]. Biodiesel has features like compatible with the diesel engine systems without any modification, also it can be blended with petroleum diesel fuel in any proportion and can be extended to neat biodiesel, and it shows a higher flash point, improved cetane number and lesser harmful emissions [1].

India is producing about 6.73×10^6 tons of non-edible oils such as Linseed, Castor, Karanja, Neem, Palash, Kusum and many more other plant-based forests derived oils which may have a much higher production potential. The present work is focused on non-edible vegetable oil from *Calophyllum* and characterization and formulating its properties to study to see that the modified fuels can be utilized in the existing diesel engine without any substantial hardware modifications [6]. However, *Calophyllum* (Beauty Leaf Tree) is a large evergreen tree in the family Caryophyllaceae and widely available in countries like India, Australia, and East Asia. It is commonly cultivated in all tropical regions of the world. Because of its decorative leaves, fragrant flowers, and spreading crown, it is best known as an ornamental plant. This tree often grows in coastal regions, as well as nearby lowland forests. However, it has also been cultivated successfully in inland areas at moderate altitudes. It tolerates varied kinds of soil, coastal sand, clay, or even degraded soil. In India it is found in Andaman & Nicobar Islands, Lakshadweep, Karnataka, Kerala, Odisha, Maharashtra, and Tamil Nadu [6]. The average oil yield is 11.7 kg oil/tree which is about 4680 kg oil per hectore, which is second highest after palm (Fig. 1).

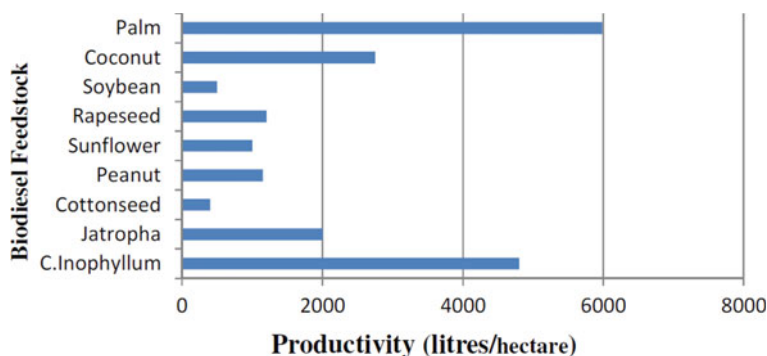


Fig. 1 Biodiesel feedstock oil productivity yield

2 Material and Method

Calophyllum species extensively dispersed in tropical Asia (India, Srilanka, Thailand, Indonesia, Malaysia, Philippines), including the Hawaiian and other Pacific Islands [7]. In Maharashtra state Calophyllum available in the wild region of Kokan (Dapoli, Ratnagiri, Harihareshwar) [8], and seeds are collected mostly from May to August. The fresh seeds contain moisture 12%, therefore, fruits/seeds are dried in sunlight for 2–3 days. It was found that after drying oil yield is 1 lit per 100–150 seeds. These dried seeds are heated at 105 °C for 24 h, the kernel was then separated from the shell, and then oil yield is found to be around 70% [7, 8].

Calophyllum oil can be extracted from the seed kernel by either Full Press Extraction method wherein an electric powered screw press used or chemical oil extraction method wherein n-hexane as the solvent is used (Fig. 2).

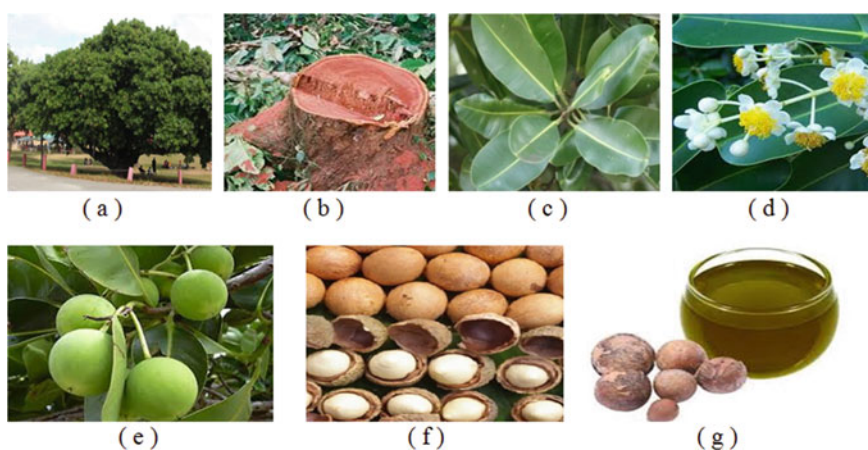


Fig. 2 Calophyllum and parts; **a** tree, **b** bark, **c** leaves, **d** flowers, **e** fruits, **f** seeds, **g** oil [4, 9]



Fig. 3 Oil extraction; **a** Mechanical Screw Press, **b** chemical process [2, 3]

The Full Press Extraction Process where mechanical screw presses are used to extract the oil by squeezing the oil under high pressure. In the Chemical Oil Extraction Process where a solvent is mixed with the material to separate the oil, in this method, dried seed kernels were ground to a fine consistency, then this powder were put into conical flasks in which hexane was added at a ratio of two parts of hexane and one part of kernel powder, this mixture is then placed on the orbital mixer and left to run for at least eight hours. The hexane-oil mixture was collected, filtered and decanted into aluminum foil containers for solvent evaporation when hexane had been fully evaporated, the oil was transferred into containers for analysis [3] (Fig. 3).

The Full Press Extraction Process is generally used for the smaller capacity process, typically under 200 tons per day, and the Solvent Extraction Process is generally used for larger capacity systems.

The fresh extracted Calophyllum oil is greenish-yellow and it gets darkened during the storage and it having disagreeable odor and bitter taste (Table 1).

3 Experimentation and Procedure

The Calophyllum Oil Methyl Ester (biodiesel) conversion is made by using transesterification of raw Calophyllum oil, and it is carried out as,

- Preparation of methoxide solution
- Sample preparation of raw Calophyllum oil with methoxide
- Reaction under Heating and continuous stirring
- Separation of biodiesel and glycerol
- Removal of excess methanol
- Biodiesel washing and drying
- Test Sample/Fuel Blends.

Table 1 Characteristics of calophyllum oil

Description	ASTM method	Unit	Calophyllum oil				Author
			Jahirul et al. [2]	Chavan et al. [8]	Atabani et al. [10]	Sahoo and Das [11]	
Density at 40 °C	D1298	kg/m ³	964	910	924.9	896	944.3
Kinematic viscosity at 40 °C	D445	cSt	56.74	38.17	55.478	71.98	65.29
Cloud point	D2500	°C	–	–	–	–	–
Pour point	D97	°C	–	–	–	–	9
Flash point	D93	°C	–	224	236.5	221	216
Calorific value	–	MJ/kg	38.10	32.50	38.51	39.25	38.37
Refractive index at 25 °C	–	°C	–	–	–	–	1.3–1.5
Iodine value	–	–	–	–	–	–	14.207
Saponification value	–	–	–	203	–	–	81.72
Peroxide value	–	–	–	–	–	–	4.01
Acid value	–	–	36.26	–	–	44	70 max

The raw/crude Calophyllum oil which is contributed by Keynote International, Mumbai, and as a catalyst is Potassium Hydroxide (KOH), Methanol. The expected product is Calophyllum Oil Methyl Ester and the by-product is Glycerol [12] (Fig. 4).

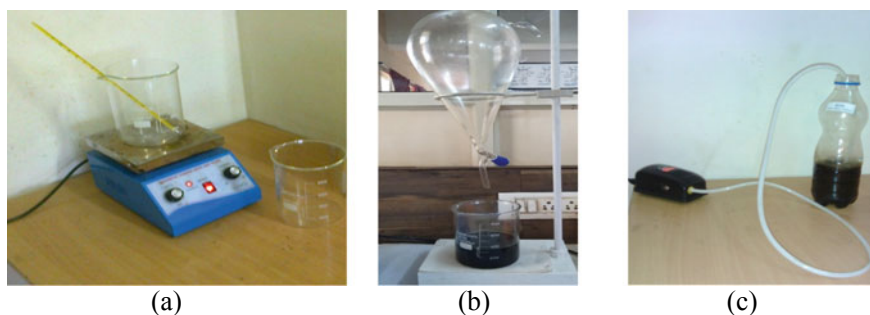


Fig. 4 Transesterification setup; **a** hot plate with magnetic stirrer, **b** separating funnel, **c** air bubbler [12]

Table 2 Test sample prepared [Author]

Sr. no.	Sample	Ratio	Description	Total mixture (ml)
1	Sample-1	1:1	1000 ml Calophyllum oil + 1000 ml Methoxide	2000
2	Sample-2	1.5:1	1500 ml Calophyllum oil + 1000 ml Methoxide	2500
2	Sample-3	2:1	2000 ml Calophyllum oil + 1000 ml Methoxide	3000

3.1 Preparation of Methoxide Solution

Most commonly NaOH or KOH are used as catalyst to speed up reaction and reduce transesterification time, and the concentration of the catalysts to methanol is maintained 0.5 to 1% by weight, as on increasing concentration it will raise the Total Acid Number also this reduces the yield of biodiesel conversion [13–15]. However, each crude oil transesterification reaction got its optimum catalyst concentration, if exceed then it participates in saponification which reacts with triglyceride to form soap and water and lead to a reduction in biodiesel yield.

In the present study, 0.1% by weight KOH catalyst is used, thus 0.79 gm of potassium hydroxide (KOH) pellets were added to 1 lit (0.791 kg) 99% pure methanol (CH₃OH) and stirrer until KOH pellets get dissolved completely into methanol and form the Methoxide Solution.

3.2 Sample Preparation

Test sample were prepared where the raw Calophyllum oil is mixed with the methoxide solution in three different ratios as (Table 2).

3.3 Reaction Under Heating and Continuous Stirring

A raw Calophyllum oil is preheated up to 40 °C using a heating plate with a magnetic stirrer, and then methoxide solution is poured into it and continue stirring with heating for 90 min. under the varying temperature ranges from 45 ± 5, 55 ± 5, and 65 ± 5 °C. During the experiment, the author found below 40 °C and above 70 °C, the reaction could not complete to the level where the separation of biodiesel and glycerol take place. Table 3, shows sets of parameters used and findings of the experiments carried.

Table 3 Characterization of biodiesel yield [Author]

Ratio	Temp. range (°C)	Total mixture (ml)	Yield	
			Biodiesel (ml)	%
1:1	40–50	2000	400	40
	50–60		550	55
	60–70		520	52
1.5:1	40–50	2500	530	35
	50–60		1000	67
	60–70		870	58
2:1	40–50	3000	300	15
	50–60		480	24
	60–70		370	18.5

3.4 Separation of Biodiesel and Glycerol

After transesterification reaction time 90 min. the mixture prepared is transferred to separating funnel to settle down, within 10 min. biodiesel separation is observed, but for complete separation, it took for 24 h. wherein the separated upper layer is of biodiesel and the bottom layer is of glycerol. Glycerol is separated out and thus biodiesel is collected for the further treatment of purification.

3.5 Removal of Excess Methanol

The biodiesel may have content of excess methanol which is removed out by using the thermostatic bath or rotary evaporator at a temperature 60–65 °C

3.6 Biodiesel Washing and Drying

The biodiesel is then washed with the help of warm water to remove any residual methanol, catalyst and glycerol traces from the saponified reaction. Water wash was carried out in successive steps to avoid trapping any air bubbles, washed water due to higher density get collected at bottom and biodiesel separated at the top layer which is then separated. The finished biodiesel was heated again to about 50 °C in the oven for 15-20 min. to remove any moisture traces left during water washing. In some cases, air washing is also preferred.

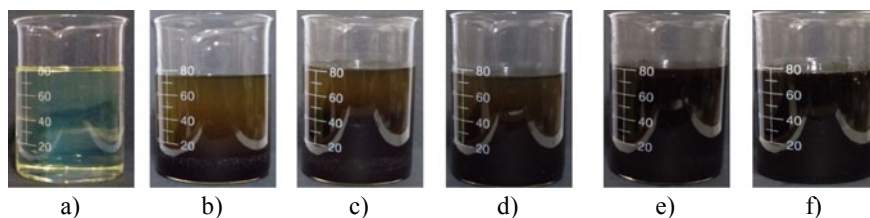


Fig. 5 Fuel samples blends; a B00, b B20, c B40, d B60, e B80, f B100

3.7 Test Samples/Fuel Blends

The Calophyllum oil biodiesel (COME) thus produced is used to prepared test fuel samples as, B00—this is neat diesel, B20—this is the biodiesel blend where mixture of 80% diesel and 20% COME, B40—this is the biodiesel blend where mixture of 60% diesel and 40% COME, B60—this is the biodiesel blend where mixture of 40% diesel and 60% COME, B80—this is the biodiesel blend where mixture of 20% diesel and 80% COME and, B100—this is neat biodiesel (Fig. 5).

The specific gravity reduces after transesterification, viscosity of raw Calophyllum oil from 65.29 cSt to COME 3.7 cSt, which is acceptable as per ASTM norms for Biodiesel. Flash point and fire point are important temperatures specified for safety during storage, handling and transport. The flash point and fire point of biodiesel was found to be 142 °C and 34 °C respectively. Flash point of Calophyllum oil 216 °C observed decreases after transesterification, which shows that its volatile characteristics had developed and it is also safe to handle.

4 Result and Discussion

4.1 Biodiesel Yield

The variation Calophyllum oil biodiesel yield influence by solution temperature maintained during transesterification process. In this experiment temperature ranges in three categories as 40–50, 50–60 and 60–70 °C and the raw oil and methoxide solution ratio varies from 1:1, 1.5:1 and 2:1. The Fig. 6 and Table 3, shows that Calophyllum oil biodiesel yield is found highest 67% at 1.5:1 oil to methoxide ratio at reaction temperature 50–60 °C for a time period of 90 min (Table 4).

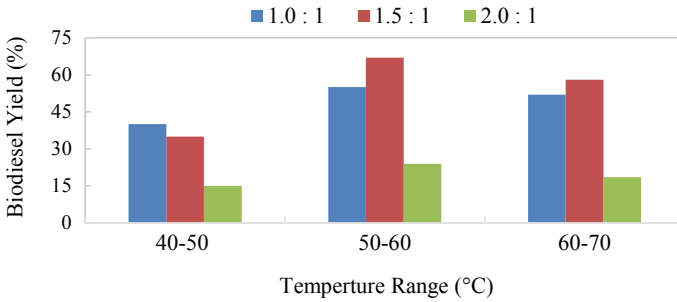


Fig. 6 Variation of biodiesel yield

4.2 Characteristics of Calophyllum Oil Biodiesel

Density is the very important property of any fuel and its combustion efficiency. For any liquid, density can be defined as the mass per unit volume and measured in the unit kg/l. The density of fuel in compression ignition engine play a key role because of it gives the signal of the delay between the fuel injection and combustion of the fuel in a compression ignition engine and also indicate the energy per unit mass of fuel. As in compression ignition engine, fuel injection and system are worked on the volume and thus higher density fuel result in more mass injected than required and vise-versa. Therefore the Calophyllum oil biodiesel blend and its property variations are discussed below.

Variation of Kinematic Viscosity. Table 5 shows the properties of Calophyllum Oil Methyl Ester as per ASTM standards, wherein, viscosity plays important role in fuel injection characteristics, it may disturbs the operation of fuel injector especially at low temperature conditions. High kinematic viscosity result in poor fuel atomization which lead to the more engine deposits and formation of soot The vegetable oil shows highest values and it is important to control it within the acceptable level to avoid adverse effect on fuel injector system and performance. The author found kinematic viscosity of the biodiesel derived is 3.7 cSt which is closed to the diesel value.

The increase of biodiesel content in fuel blend with diesel, the kinematic viscosity increases, also there is increase in density of the fuel blend (Fig. 7).

The relationship between kinematic viscosity and density is shown by the regression equation,

$$KinematicViscosity = 0.0282 * Density - 20.974$$

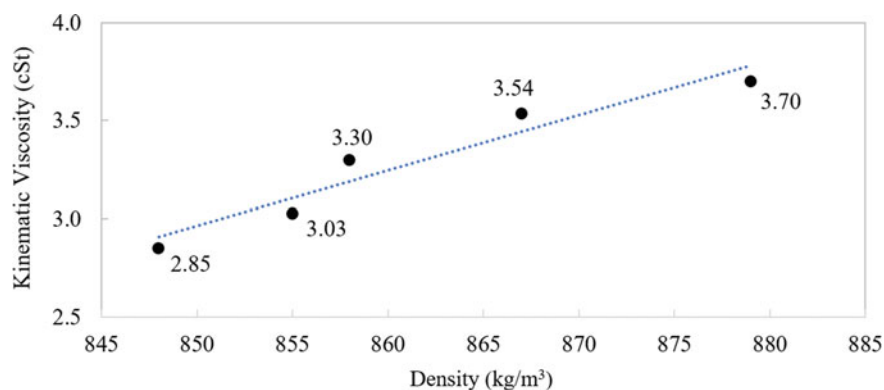
Variation of Calorific Value. The calorific value is the major parameter in the selection of a fuel. It indicates is the amount of heat energy present in the fuel, which is determined by the complete combustion of specified quantity at constant pressure and in normal conditions. Table 5 shows the value of calophyllum oil biodiesel is

Table 4 Characterization of Calophyllum Oil Methyl Ester (Biodiesel)

Description	ASTM method	Unit	ASTM limits [10, 16]	Diesel	COME			Author			
				Ashok et al. [17]	Atabani et al. [10]	Sahoo and Das [11]	SathyaSelvabala et al. [18]		Sahoo et al. [19]	Rizwanul Fattah et al. [20]	Ashok et al. [17]
Density @ 40 °C	D1298	kg/m ³	820-900	815	877.6	880.6	-	-	864	879.1	
Kinematic viscosity @ 40 °C	D445	cSt	1.9-6.0	2.3	5.54	5.72	4	4.92	4.71	5.58	3.7
Cloud point	D2500	°C	-	-	12	-	13.2	13.2	10	-	12
Pour point	D97	°C	-	-	13	-	-	4.3	8	-	-
Flash point	D93	°C	55-101	53	162.5	151	140	140	141.5	160	142
Calorific value	-	MJ/kg	-	42.5	39.51	-	-	38.66	38.39	39.8	37.24

Table 5 Characterization of calophyllum oil biodiesel blends [Author]

Properties	Unit	B00	B20	B40	B60	B80	B100
Density @ 15 °C	kg/m ³	840	847.6	854.6	857.5	867.3	879.1
Kinematic viscosity @ 40 °C	cSt	3.12	2.85	3.03	3.3	3.54	3.7
Flash point	°C	57	179	172	163	154	142
Fire point	°C	66	188	180	171	163	151
Calorific value	MJ/kg	44.34	43.86	41.21	40.13	39.02	37.24
Cetane number	–	48	56	55	54	53	52

**Fig. 7** Variation of Kinematic viscosity

37.24 kJ/kg which is lesser than diesel because of inherently vegetable oil having lesser carbon content, thus lower energy density.

The increase of biodiesel content in fuel blend with diesel, the calorific value of fuel blend decreases, along with the increase in density of the fuel blend (Fig. 8).

The relationship between calorific value and density is shown by the regression equation,

$$\text{Calorific Value} = -0.1988 * \text{Density} + 211.57$$

Variation of Cetane Number. Cetane number is an inverse function of a fuel ignition delay which is the time period between the start of injection and the first identifiable pressure increase during combustion of the fuel. In a particular diesel engine, higher cetane fuels will have shorter ignition delay periods. Cetane number is used to measure of ignition quality of diesel fuels. It influences both gaseous and particulate emissions. The fuels with higher auto ignition temperatures are more likely to cause diesel knock.

Table 5 shows the cetane number of neat biodiesel is 52 and on increasing of biodiesel content in fuel blend, the value of cetane number goes on decreasing for

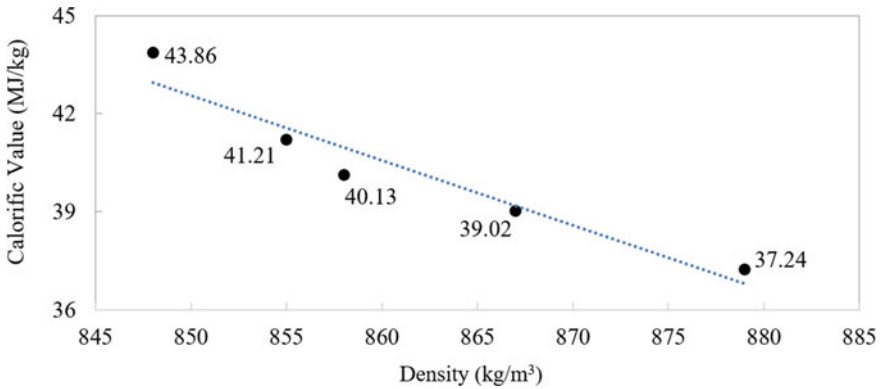


Fig. 8 Variation of calorific value

the fuel blend, also it is observed that the increase of biodiesel content increases density of the test fuel blend (Fig. 9).

The relationship between cetane number and density is shown by the regression equation,

$$CetaneNumber = -0.1291 * Density + 165.21$$

Variation of Flash Point. This is the property that indicates the lowest temperature at which fuel ignites when it is exposed to a flame. From Table 5, the flashpoint of neat biodiesel reported by the author is 142 °C which is higher than petroleum diesel, which favors safe transportation.

The increase of biodiesel content in fuel blend with diesel, the flash point value of fuel blend reduces, along with the increase in density of the fuel blend (Fig. 10).

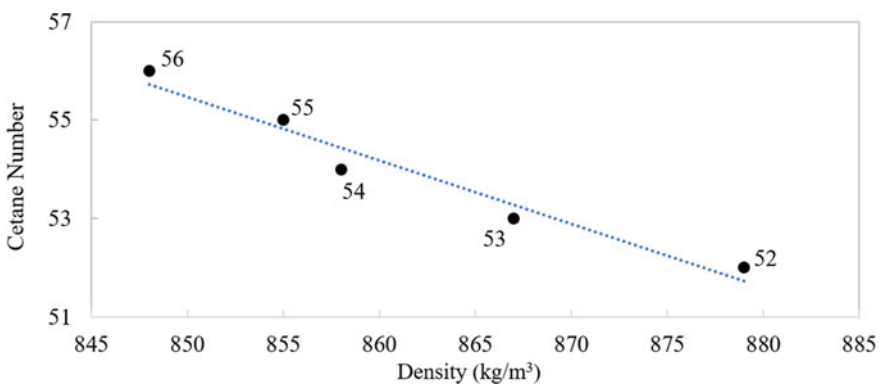


Fig. 9 Variation of cetane number

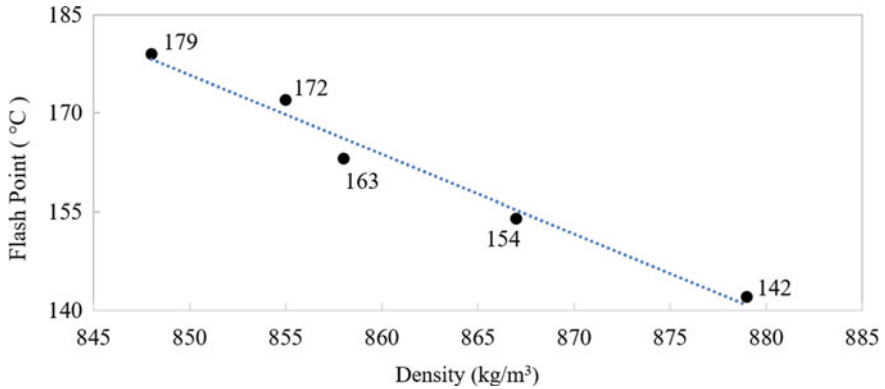


Fig. 10 Variation of flash point

The relationship between calorific value and density is shown by the regression equation,

$$FlashPoint = -1.2073 * Density + 1201.9$$

Variation of Fire Point. The fire point is the lowest temperature at which the vapors keep burning after the ignition source is removed. It is higher than the flash point, because at the flash point more vapor may not be produced fast enough to sustain combustion.

From the Table 5, the fire point of the neat biodiesel is 151 °C. The increase of biodiesel content in fuel blend with diesel, the fire point of the fuel blend reduces, also it is observed that there is increase in the density of the fuel blend (Fig. 11).

The relationship between calorific value and density is shown by the regression equation,

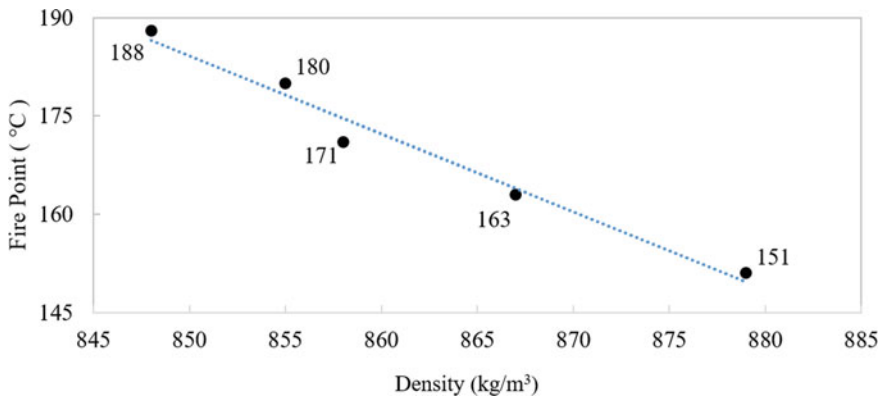


Fig. 11 Variation of fire point

$$\text{Fire Point} = -1.1902 * \text{Density} + 1195.8$$

5 Conclusions

- The analysis shows that Calophyllum oil biodiesel met the major biodiesel requirements as per standards ASTM D 6751-02, ASTM PS 121-99, EN 14214, DIN V 51606 and IS 1448.
- Highest triglyceride conversion rate of 67% was achieved after 90 min. of reaction at temperature 50–60 °C with 1.5:1 molar ratio.
- Transesterification of Calophyllum oil help to reduce the kinematic viscosity to 3.7cSt, density to 879.1 kg/m³.
- Alcoholises of Calophyllum oil lower its calorific value from 43.86 to 37.24 MJ/kg.
- Calophyllum oil biodiesel reported cetane number 52, flash point 142 °C, and fire point 151 °C.

References

1. Elangovan T, Anbarasu G, Jeryraj Kumar L (2016) Development of Calophyllum Inophyllum biodiesel and analysis of its properties at different blends. *Int J Chem Tech Res* 9(4):220–229
2. Jahirul MI, Brown RJ, Senadeera W, Ashwath N, Rasul MG, Rahman MM, Hossain FM, Moghaddam L, Islam MA, O'Hara IM (2015) Physio-chemical assessment of beauty leaf (Calophyllum inophyllum) as second generation biodiesel feedstock. *Energy Rep* 1:204–215
3. Jahirul MI, Brown JR, Senadeera W, Ashwath N, Laing C, Leski-Taylor J, Rasul MG (2013) Optimisation of bio-oil extraction process from beauty leaf (Calophyllum Inophyllum) oil seed as a second generation biodiesel source. *5th BSME Int Conf Therm Eng Procedia Eng* 56:619–624
4. Ashok B, Nanthagopal K, Sakthi Vignesh D (2018) Calophyllum inophyllum methyl ester biodiesel blend as an alternate fuel for diesel engine applications. *J. Alexandria Eng.* 57:1239–1247
5. Demirbas A (2009) Characterization of biodiesel fuels. *Energy Sour Part A: Recover Util Environ Eff* 31(11):889–896
6. Agarwal AK, Das LM (2001) Biodiesel development and characterization for use as a fuel in compression ignition engines. *J Eng Gas Turbines Power* 123:440–447
7. Sarnaik J (2014) Resource assessment of high biodiversity value species with a biofuel potential in Northern Western Ghats of India. A report of the Conservation and sustainability. Applied Environmental Research Foundation (AERF) India
8. Chavan SB, Kumbhar RR, Deshmukh RB (2013) Callophyllum Inophyllum Linn (“honne”) oil, a source for biodiesel production. *Res J Chem Sci* 3(11):24–31
9. Hathurusingha S, Potential of beauty leaf tree (Calophyllum inophyllum L) as a biodiesel feedstock. A thesis for the degree of Doctor of Philosophy. Centre for Plant and Water Science, Faculty of Science, Engineering & Health, CQ University Rockhampton Australia
10. Atabani AE, Mahlia TMI, Masjuki HH, Badruddin IA, Yussof HW, Chong WT, Teong LK (2013) A comparative evaluation of physical and chemical properties of biodiesel synthesized

- from edible and non-edible oils and study on the effect of biodiesel blending. *Energy* 58:296–304
11. Sahoo PK, Das LM (2009) Process optimization for biodiesel production from *Jatropha*. *Karanja Polanga Oils Fuel* 88:1588–1594
 12. Bawane RK, Muthuraja A, Shelke GN, Gangele A (2020) Impact analysis of calophyllum inophyllum oil biodiesel on performance and emission characteristic of diesel engine under variation in compression ratio, engine load, and blend proportion. *Int J Amb Energy*. <https://doi.org/10.1080/01430750.2020.1730955>
 13. Hossain ABMS, Mazen MA (2010) Effects of catalyst types and concentrations on biodiesel production from waste soybean oil biomass as renewable energy and environmental recycling process. *Aus J Crop Sci* 4(7):550–555
 14. Efavi JK, Kanbogtah D, Apalangya V, Nyankson E, Tiburu EK, Dodoo-Arhin D, Onwona-Agyeman B, Yaya A (2018) The effect of NaOH catalyst concentration and extraction time on the yield and properties of *Citrullus vulgaris* seed oil as a potential biodiesel feed stock. *South Afr J Chem Eng* 25:98–102. <https://doi.org/10.1016/j.sajce.2018.03.002>
 15. Kai T, Kubo A, Nakazato T, Takanashi H, Uemura Y (2012) Influence of the acid value on biodiesel fuel production using a two-step batch process with a homogeneous catalyst. *Int J Biomass Renew* 1:15–20
 16. The Worldwide Fuel Charter Committee (2009) Biodiesel guidelines. automobile and engine manufacturers. Members; European Automobile Manufacturers Association, Belgium. Alliance of Automobile Manufacturers, Washington DC. Engine Manufacturers Association, Chicago IL. Japan Automobile Manufacturers Association. Tokyo
 17. Ashok B, Nanthagopal K, Jeevanantham AK, Bhowmick P, Malhotra D, Agarwal P (2017) An assessment of calophyllum inophyllum biodiesel fuelled diesel engine characteristics using novel antioxidant additives. *Energy Convers Manage* 148:935–943. <https://doi.org/10.1016/j.enconman.2017.06.049>
 18. SathyaSelvabala V, Selvaraj DK, Kalimuthu J, Periyaraman PM, Subramanian S (2011) Two-step biodiesel production from calophyllum inophyllum oil: optimization of modified B-zeolite catalyzed pre-treatment. *Biores Technol* 102:1066–1072. <https://doi.org/10.1016/j.biortech.2010.08.052>
 19. Sahoo PK, Das LM, Babu MKG, Naik SN (2007) Biodiesel development from high acid value polanga seed oil and performance evaluation in a CI Engine. *Fuel* 86:448–454. <https://doi.org/10.1016/j.fuel.2006.07.025>
 20. Rizwanul Fattah IM, Kalam MA, Masjuki HH, Wakil MA (2014) Biodiesel production, characterization, engine performance, and emission characteristics of malaysian alexandrian laurel oil. *R Soc Chem* 4:17787–17796. <https://doi.org/10.1039/c3ra47954d>

Performance and Emission Characteristics of CI Engine by Using Aluminium Nano Oxides with B40 Blended Bio Diesel in Diesel Fuel



Swapnil Vijay Ghogardare and Sanjeev Reddy K. Hudgikar

Abstract A huge power claim has focused to discover the finest way of using conventional energy. Nearly all current energy requirements in India are being met with fossil fuels. Because of this alternative fuels for engines should be made from available local resources. Due to less availability of diesel fuel and its inflated cost as well as harmful emissions emitted by CI engine, the use of biodiesel and its mixture has gained significance over the last twenty years due to its environmental and cost-effective benefits. On the basis of obtained experimentation results the use of biodiesel in diesel boost up engine performance and lowers hazardous emissions. The requisite to reduce hazardous emissions at the least level is to make sure safety for the mankind and also to the engine. Nanoparticles have been found to be well capable in hazardous emission control. Using optimized mixture of biodiesel and diesel will reduce some considerable amount of the world's dependence on fossil fuels without variation of CI Engine.

Keywords Undi oil · Biodiesel · Nanoparticles · CI engine · Combustion · Emissions · Pollution

1 Introduction

Largest energy requirement creating awareness to identify most suitable way of conventional energy usage. Therefore, enhancement of fuels is necessity of upcoming days. Due to rapid growth of automobiles the demand for petroleum products expected to rise to more than 240 million metric tonnes by 2021–22 [2]. The maximum consumption of this fossil fuel has a indecorous result on the atmosphere

S. V. Ghogardare (✉)

Research Scholar, Visvesvaraya Technological University, Jnana Sangama, Belagavi, Karnataka, India

e-mail: ghogardare10@gmail.com

Assistant Professor, D.Y. Patil College of Engineering, Akurdi, Pune-44, Maharashtra, India

S. R. K. Hudgikar

Lingaraj Appa Engineering College, Gornalli, Bidar, Karnataka, India

through its polluting output. Biodiesel is an alternate fuel for diesel. Biodiesel will be blend with diesel fuel at various proportions, as it has almost same properties but lesser emissions. Biodiesel fuel has better properties than those of diesel such as renewable, environment friendly, safe, and mainly sulphur free. The recent advances in nano science and nanotechnology proved that the nano energetic materials have great advantages over micro sized materials [1]. The use of crude oil is related with pollutants such as CO₂, CO, NO_x, SO_x, and PM, which are at present the uppermost global reason of pollution. Many of experimentations shown that use of biodiesel in CI engines can diminish various emissions. The ongoing study in nano science proved that the nano oxides have greater reward over micro sized materials. Ignition delay and ignition temperatures are the significant parameters to illustrate the performance of a CI engine. The metal based additives diminish CI engine emissions and fuel consumption standards. The cause for reduction in emission is that the metal reacting with water to create hydroxyl radicals, which advance soot oxidation. From the study, nano-oxides can perform as a burning rate catalyst as when mixed into liquids they increases the burning rate and does dirt free burning, also PM and CO are reduced. Due to absolute burning of fuel, emissions like CO, CO₂ and NO_x are appreciably lowered.

2 Methodologies

2.1 Preparation of Biodiesel

The process of biodiesel preparation is as follow.

The transesterification of biodiesel is as below.

1. lit. of Undi oil is taken in a container and then energized up to a temperature of 60 °C.
2. A mug is filled with 200 ml of methanol and then about 3.5 g of Potassium Hydroxide is mixed as a catalyst.
3. The container is closed and then stirred for about twenty minutes and Potassium Meth oxide is produced as a result.
4. The heated oil is taken into a separate pot and then the Potassium Meth oxide solution is mixed along with the heated oil.
5. The mixture is allowed to settle for about ten hours and then the biodiesel is produced along with glycerin, deposited at the bottom as shown in Fig. 1.
6. At the end biodiesel is separated from the container by using the separating funnel and then it is mixed in the precise proportions along with the diesel fuel for the experimental verifications by putting aluminum oxide.

Fig. 1 Pure biodiesel

2.2 Blending of Aluminum Oxides in Biodiesel

For mixing of aluminum oxide (Al_2O_3) nanoparticles in biodiesel, trial of 1 lit biodiesel and 0.025 gm of Al_2O_3 form of nanoparticles is mixed to make dosing level of 20 ppm. The quantity level of 20 ppm is 0.020 gm/lit, likewise. After mixing of Aluminum oxide, it is mixed well and taken into mechanical homogenizer container where it is kept for about 30 min in an ultrasonic vibrator making consistent distribution. It is shaken well before the use for better results.

Figure 2 shows below mentioned biodiesel blends:

1. Raw Undi Oil
2. Transesterified Oil (top biodiesel, bottom glycerol layer)
3. H00: 100% Diesel
4. H30: 30% Biodiesel + 70% Diesel
5. H40: 40% Biodiesel + 60% Diesel.

**Fig. 2** Biodiesel blends

Table 1 Diesel engine specification

Type	Vertical, water cooled, four stroke
Number of cylinder	One
Bore	87.5 mm
Stroke	110 mm
Compression ratio	17.5:1
Maximum power	3.7 kw
Speed	1500 rev/min
Dynamometer	Electrical
Injection timing	230

3 Experimental Setup

The experiments are conducted on Kirloskar AVI, four Stroke and single cylinder diesel engine. The rated power of the diesel engine is 3.7 kW. The engine was run at a constant Speed of 1500 rpm by maintaining the pressure from 250 to 500 kgf/cm². The first step of procedure is engine is run initially with pure diesel and corresponding readings are taken. Graphs are plotted for brake thermal efficiency (BTE) and brake specific fuel consumption (BSFC) versus given load of the engine. In this experiment B40 blend is used to carry out test on diesel engine. BTE and BSFC results are calculated for taken blend. In engine performance analysis graphs of BTE Vs Power, BSFC versus Power has been plotted for diesel fuel and B 40 biodiesel blend.

Table 1 shows engine specifications. Electrical dynamometer was used for changing load of the engine. The AVL smoke meter was attached to measure the smoke present in the exhaust. AVL five-gas analyzer was taken to determine HC, CO and NOx emissions. Pressure and heat release rate inside of cylinder was calculated by using data acquisition system interfaced with dual core computer. In Fig. 3 experimental set-up is shown.

4 Experimental Results

Observation Data

Speed rpm	Load kg	Comp ratio	T1 °C	T2 °C	T3 °C	T4 °C
1552.0	3.29	18.00	34.58	40.29	34.58	36.41
1547.0	4.67	18.00	34.71	41.19	34.71	37.47
1534.0	5.67	18.00	34.85	41.88	34.85	38.36

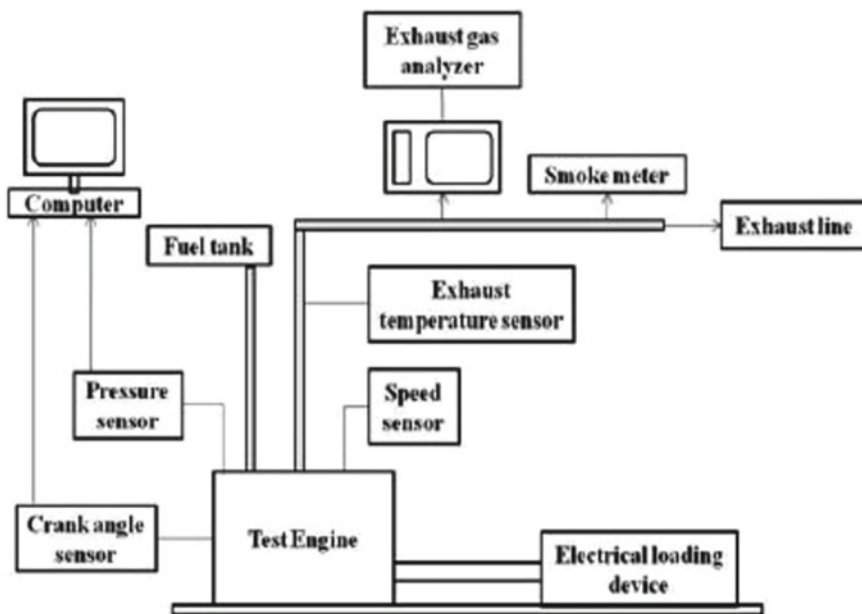


Fig. 3 Diesel engine

Observation Data

T5 °C	T6 °C	Air mmWC	Fuel cc/min	WFlow Eng lph	WFlow Cal lph
189.90	138.00	78.03	11.59	300.00	75.00
209.92	154.64	79.24	13.25	300.00	75.00
225.87	167.81	73.70	14.01	300.00	75.00
245.42	182.23	77.24	16.00	300.00	75.00

Result Data

Torque Nm	BP Kw	FP Kw	IP Kw	BMEP bar	IMEP bar	BTHE %	ITHE %	MechE %
5.97	1.12	1.32	2.44	1.31	2.97	15.24	33.18	45.94
8.48	1.43	1.17	2.60	1.68	3.06	19.36	35.22	54.95
10.29	1.99	1.14	3.12	2.35	3.62	23.07	36.27	63.62

Result Data

Air Flow kg/hr	Fuel Flow kg/hr	SFC Kg/Kw-Hr	Vol.%	A/F	HBP %	HGas %	HJW %	RAD %
28.77	0.58	0.56	80.45	49.85	15.24	21.70	29.56	48.75
28.99	0.66	0.44	80.51	43.94	19.36	21.53	29.39	49.08
27.96	0.70	0.37	74.38	40.07	23.07	21.39	30.11	48.50

5 Result Graphs

With the help of above result data below graphs are plotted. In Fig. 4 its shows results of IP, BP & FP versus Load. Figure 5 gives details about IMEP, BMEP, FMEP versus Load. Figure 6 shows graph of Torque, Mech Eff., Vol. Eff. versus Load. In Fig. 7 we will get graph of Air, Fuel versus Load. Figure 8 shows IThEff, BThEff, SFC versus Load. In Fig. 9 HBP, HJW, HGas versus Load graph is plotted.

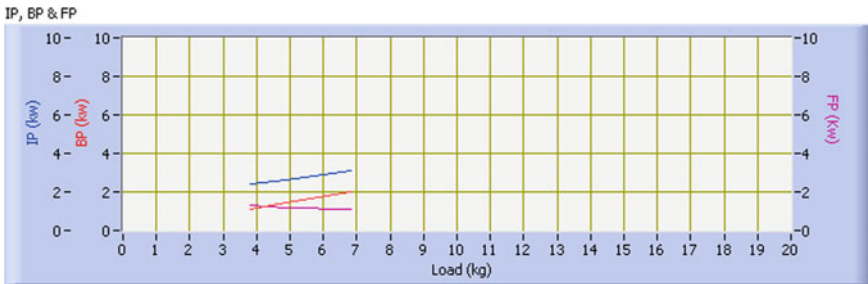


Fig. 4 IP, BE, FP versus load



Fig. 5 IMEP, BMEP, FMEP versus load



Fig. 6 Torque, Mech Eff., Vol. Eff. versus load

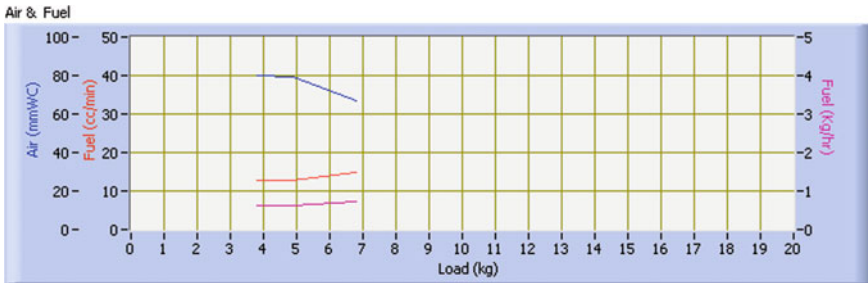


Fig. 7 Air, Fuel versus load

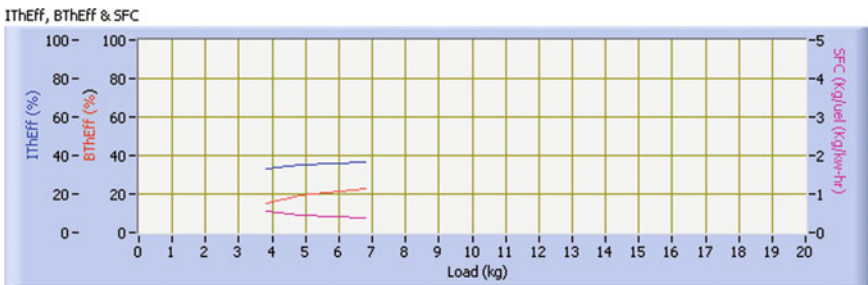


Fig. 8 IThEff, BThEff, SFC versus load

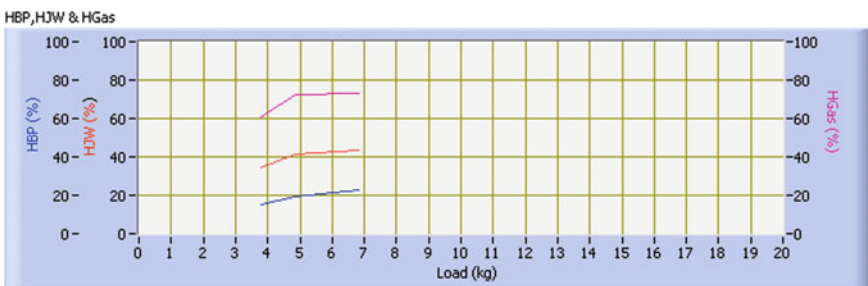


Fig. 9 HBP, HJW, HGas versus load

6 Conclusion

The performance and emission characteristics of diesel and undi oil blends with the mixing of aluminum oxide nanoparticles are studied to calculate the emission reduction on the single cylinder CI engine. The nano-oxides act as combustion medium which reduce delay period and encourage complete burning when added in undi oil to diesel fuel and hence improved efficiency of engine and reduced brake specific fuel consumption.

Specific fuel consumption is decreased for undi oil biodiesel in diesel fuel mixed with aluminum oxide at 20 ppm. As this undi oil quantity is abundant in coastal region of India. This will promote increase of wealth of the people residing in such area with significant reduction in emissions.

References

1. Syed A, Saravanan CG, Kannan M (2015) Experimental investigation on CRDI system assisted diesel engine fuelled by diesel with nanotubes. *Am J Eng Appl Sci* 8(3):380–389
2. Soni G, Rathod P, Goswami J (2015) Performance and emission characteristics of CI engine using diesel and biodiesel blends with nanoparticles as additive—a review study. *IJEDR* 3(4):2321–9939
3. Alli A, Bafghi T, Bakhoda H, Khodaei F, Chegeni (2015) Effects of cerium oxide nanoparticle addition in diesel and diesel-biodiesel blends on the performance characteristics of a CI engine. *World Acad Sci Eng Technol Int J Mech Aerosp Ind Mechatron Manuf Eng* 9(8)
4. Mehta RN, Chakraborty M, Parikh PA (2013) Nanofuels: combustion, engine performance and emission. *Fuel* 120:91–97
5. Bawane R, Chanapattana SV, Pawar AA (2014) Performance test of CI engine fuelled with undi oil biodiesel under variation in blend proportion, compression ratio & engine load. *Int J Sci Eng Technol Res (IJSETR)* 3(8)
6. Ghogardare SV, Hudgikar S, Reddy K (2020) Performance and emission characteristics of ci engine by using aluminum nano oxides with B20 blended bio diesel in diesel fuel. *Int J Sci Technol Res* 9(4)

Energy Recovery in Domestic Stove Using Thermosyphon



**Balaji D. Kshirsagar, Zakeer S. Baig, Bait Shubham Ramesh,
and Bagul Rahul Prakash**

Abstract Energy in the form of heat can be restored and later can be used is need for today's situation. Preserving any form of energy is important to save the environment and protect global warming. In present research heat recovery from domestic gas is carried out and can be used for different purposes also it is used on large scale also. In turn, we save electric consumption and fuel used for heating water and cooking purposes. Therefore the proposed design will actually use the heat of the emitted stream (that was previously just discarded to the atmosphere by the chimneys), and consume a considerable amount of the electrical units (kWh) and the LPG fuel that was being used to heat up water for various residential purposes. After the design, the model is tested several times for various flames such as low medium and high flame and by the experimental observations and the theoretical calculations the efficiency of the system is calculated.

Keywords Thermosyphon · Heat recovery · Energy · Domestic stove

1 Introduction

In our day to day life, we come across to see various processes that involve the emission of heat, and we term this emitted heat as Waste heat [1]. Waste Heat Recovery is actually a mechanism which involves the method of transferring or exchanging the amount of heat of a certain emitted stream with a certain component [2].

Since most of the waste heat is being transferred or released to the environment, so using the amount of energy of that waste heat is practically an economical idea [3, 4]. It is also observed that most of the modern kitchens have gas stove as primary equipment and electric chimneys as its secondary equipment [5, 6]. If we go into the engineering aspect the heat energy released by the LPG through gas stove is used for cooking. As we all know the whole of the heat cannot be used therefore is wasted to the kitchen atmosphere and further to the environmental atmosphere with the help of the chimneys. In order to remove this excess heat, we install chimneys [7].

B. D. Kshirsagar (✉) · Z. S. Baig · B. S. Ramesh · B. R. Prakash
JSPM'S Rajarshi Shahu College of Engineering, Tathawad, Pune, India

The idea behind the proposed project is to use this so-called waste heat, heat up water, and use it for various residential purposes.

Objectives

- To recover the waste heat generated during the cooking.
- To convert this recovered heat into useful applications such as water heating.
- To minimize the heat losses.

2 Method and Preparation

2.1 Working of Waste Heat Recovery Model

The model below shows the waste heat recovery a model consisting of the evaporator, condenser working in a thermo syphon (Figs. 1 and 2) [9].

The waste heat recovery model consists of mainly three sections as

- Evaporator section

Fig. 1 Waste heat recovery model





Fig. 2 Evaporator section

- Condenser section
- Coolant filling arrangement.

2.2 Evaporator Section

In the evaporative section, there is the evaporation of coolant i.e. water is done by heat exchange between the high-temperature burner flames waste heat and coolant. Due to this heat exchange, there is evaporation of water and formation of high-temperature vapors is done then these high temperature vapors are carried to the heat exchanger section through a vertical copper tube closed in a cycle forming thermosyphon with a thermal insulation to avoid heat losses.

2.3 Condenser Section

In this section the hot vapors carried from heat exchanger part with low temperature are cooled with the help of shell and tube water-cooled heat exchanger. Due to the heat exchange between the hot surface of the tube and cold water the latent heat is transferred to the water and water gets heated and the coolant gets cooled and moves to the evaporator by gravity (Figs. 3 and 4) [9].



Fig. 3 Condenser coil and condenser

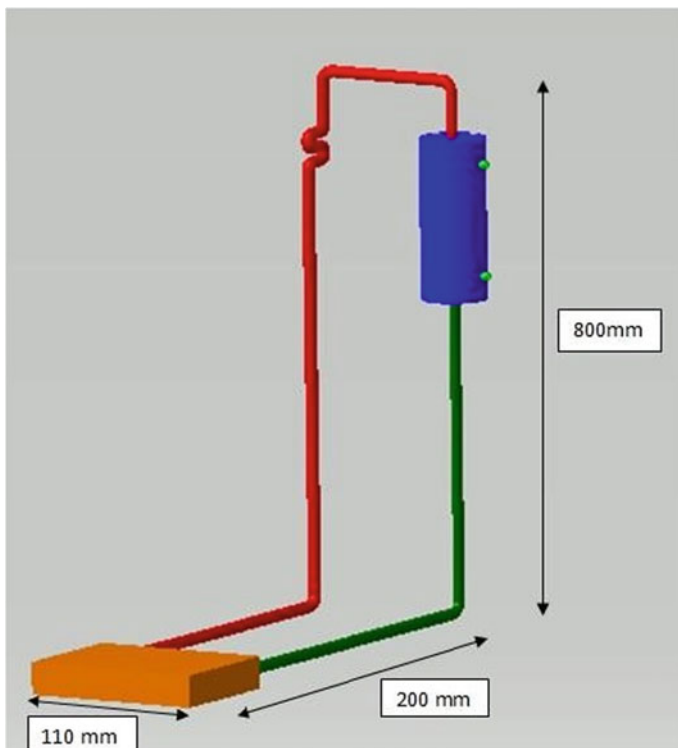


Fig. 4 Design model of waste heat recovery system

2.4 Theoretical Heat Analysis

$$\text{Thermal conductivity : } k = (\Delta T) \quad (1)$$

$$\text{Thermal resistance : } R = \Delta T/q = L/k \quad (2)$$

$$\text{Thermal conductance : } C = q/\Delta T = L/k \quad (3)$$

A thermal resistance may also be associated with heat transfer by convection at a surface. From Newton's law of cooling,

$$q = hA(T_s - T_\infty) \quad (4)$$

The thermal resistance for convection is then

$$R_{\text{conv}} = (T_s - T_\infty)/q = 1/hA \quad (5)$$

Applying thermal resistance concept to the plane wall, the equivalent thermal circuit for the plane wall with convection boundary conditions.

In terms of the overall temperature difference ($T_s - T_\infty$), and the total thermal resistance R_{tot} , the heat transfer rate may also be expressed as

$$q = (T_s - T_\infty)/R_t \quad (6)$$

Since the resistance is in series, it follows that

$$R_t = \text{Thermal resistance due to} \\ (\text{Convection (air)} + \text{Conduction} + \text{Convection (water)})$$

$$R_t = \sum(\text{all resistances}) = 1/h_a A + L/kA + 1/h_w A \quad (7)$$

where,

- h_a Convective heat transfer coefficient for air
- k Thermal conductivity of medium
- h_w Convective heat transfer coefficient for water [8].

2.5 Data

k = 400 W/mK (for copper), h_a = 50 W/m²K (for air), h_w = 700 W/m²K (for water),
Do = 9.5 mm, Ao = 18095 mm², Di = 7.7 mm, Ai = 13571 mm²

Solution: Waste heat recovery from the gas stove at evaporator,

$R_t = (\text{Resistance due to air convection} + \text{resistance due to material conduction} + \text{resistance due to coolant convection})$

Resistance Due to,
Convection due to air,

$$R_{ca} = 1/haA = 1/(50 * (1.8095/2)) = 0.0221 \text{ K} - \text{m}^2/\text{W}$$

Conduction,

$$R_{cond} = L/ka = (2 * 10^{-3})/(400 * (1.5833/2)) = 6.3 * 10^{-6} \text{ K} - \text{m}^2/\text{W}$$

Convection due to water,

$$R_{cw} = 1/hwA = 1/(700 * (1.3571/2)) = 2.1 * 10^{-3} \text{ K} - \text{m}^2/\text{W}$$

$$R_t = 1/(50 * 1.8095/2) + (2 * 10^{-3})/(400 * 1.5833/2) + 1/(700 * 1.3571/2)$$

$$R_t = 0.0241 \text{ K m}^2/\text{W}$$

$$Q_r = (T_s - T_\infty) / R_t = (70 - 30) / 0.0241$$

$$Q_r = 1659.75 \text{ W}$$

2.6 Design Check

A) Thin cylinder Analysis:

$$D_o = 9.63 \text{ mm}$$

$$D_i = 7.8 \text{ mm, Thickness}(t) = 1.8 \text{ mm}$$

$$S_{ut}(\text{copper}) = 420 \text{ MPa, FOS} = 2$$

$$\sigma_{all} = S_{ut}/\text{FOS} = 420/2 = 210 \text{ MPa,}$$

from data sheet σ_{all} is,

$$\sigma_{all} = P_i D_i / 2t = (0.03 * 7.8) / (2 * 1.8) = 65 \text{ MPa}$$

Hence, selected tube dimensions of material are correct.

2.7 Practical Calculations Heat Recovery

1. Heat supplied by the gas stove = mf = 175 g/h,

$$CV = 46.1 * 106 \text{ J/Kg}$$

$$Q_s = mf * CV = (0.175/3600) * (46.1 * 106) = 2240.97 \text{ J/s}$$

2. Heat Gain at the evaporator:

$$mc = 1\text{kg}, C_p = 4.187 \text{ KJ/Kg } T_f = 70 \text{ }^\circ\text{C}, T_i = 37 \text{ }^\circ\text{C}$$

$$Q_g = mc * C_p * (T_f - T_i) = 1 * 4.187 * (70 - 37) = 1315.9 \text{ J/s}$$

3. Heat recovery:

$$Q_r = Q_s - Q_g = 2240.97 - 1315.9 = 925.07 \text{ J/s}$$

4. Efficiency:

$$\begin{aligned} \eta &= \frac{\text{Practical Heat recovery}}{\text{Theoretical heat recovery}} \\ &= \frac{925.07}{1659.7} \\ \eta &= 55.87\% = 56\% \end{aligned}$$

3 Observations and Calculations

For mass flow rate and experimental hat transfer coefficient in condenser, $C_p = 4187 \text{ J/kg k}$ (Table 1).

4 Result and Discussion

Graph of Mass Flow Rate versus Temperature

From Fig. 5, it is clear that

1. As we are reducing the mass flow rate, the outlet temperature at the condenser goes on increasing.
2. Thus optimum mass flow rate should be selected to get better results.

So we get a higher temperature at the outlet of the condenser at the higher flame as compared to medium and low flame.

Graph of Heat Gained at Condenser versus Temperature

From Fig. 6, it is clear that

Table 1 Observation and calculation

Flame type	Sr.no	Mass flow rate (m), (ml/sec)	Ti (°C)	To (°C)	Q = m*Cp* ΔT (J/s)	Expt. heat transfer coeff. (h) (W/m ² K)
High	1.	10.16	30.2	47.69	732.6	41.87
	2.	9.01	30.2	49.60	731.4	37.70
	3.	8.45	30.2	52.04	731.7	33.50
	4.	7.3	30.2	55.02	732.4	29.53
Medium	1.	10.16	30.2	43.88	573.2	41.90
	2.	9.01	30.2	45.43	574.07	37.69
	3.	8.45	30.2	47.33	573.93	33.50
	4.	7.3	30.2	49.77	573.67	29.31
Low	1.	10.16	30.2	39.39	387.05	42.57
	2.	9.01	30.2	40.48	387.81	37.72
	3.	8.45	30.2	41.17	388.12	35.38
	4.	7.3	30.2	42.87	387.39	30.57

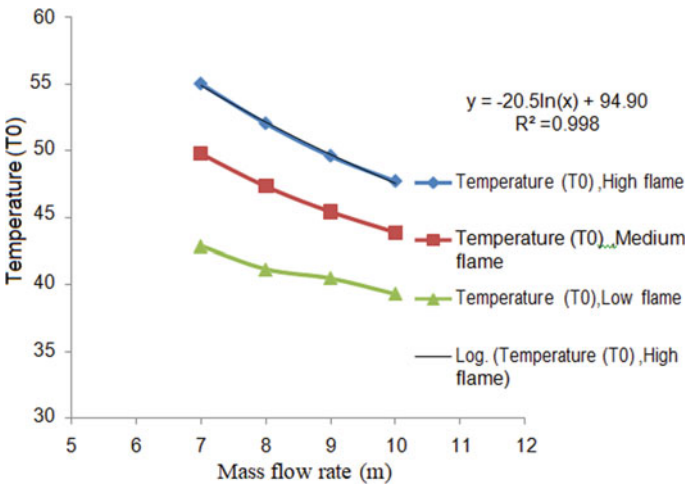


Fig. 5 Mass flow rate versus temperature

At the higher flame, heat gained by the condenser fluid which we get at the outlet is higher as compared to low and medium flame.

There is no considerable amount of change in heat gained at the outlet of the condenser with a change in the mass flow rate [10].

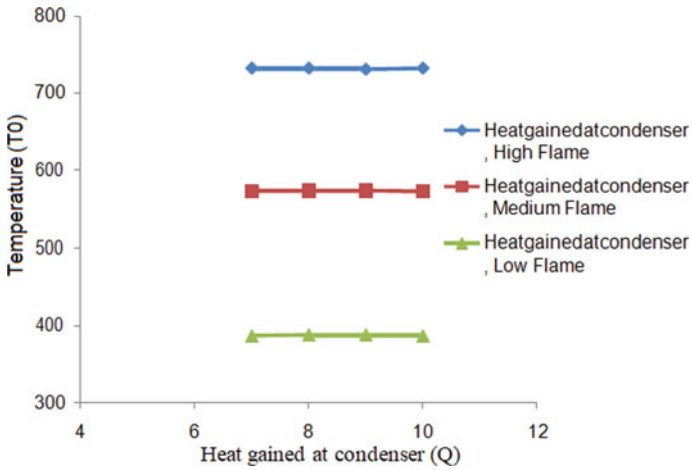


Fig. 6 Heat gained at condenser versus temperature

Graph of Mass flow rate versus convective heat transfer coefficient

From above Fig. 7, we come to know that as mass the flow rate of condenser fluid increases, the convective heat transfer coefficient also increases.

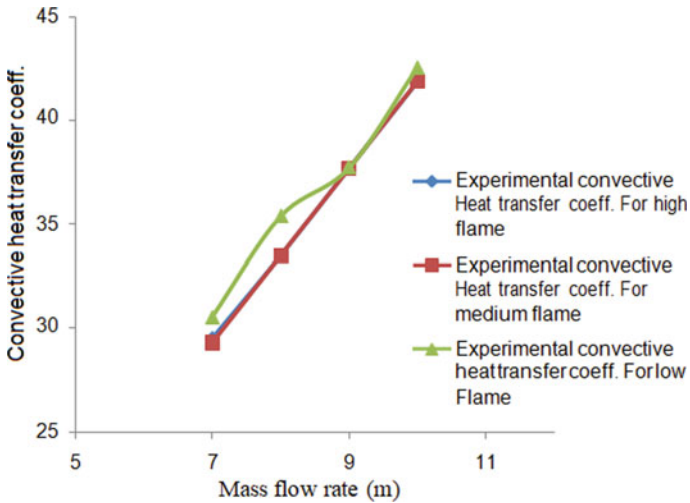


Fig. 7 Mass flow rate versus convective heat transfer coefficient

5 Conclusion

Heat pipe technology plays an important role in the optimization and performance of the heat pipe. The heat pipe is more efficient, reliable, and cost-effective for passive operations and manufacturing is easy.

By using thermosyphon as the thermal transport device may offer savings by lowering energy consumption, equipment cost, maintenance cost, however current industrial applications and technologies aren't fit for domestic use or small scale use in terms of cost and ergonomics.

Using specific correlations for thermosyphon condensers, together with a mass flow rate calculated from experimental results it was possible to determine heat transfer coefficient into the condenser region.

The method devised by us by mathematical model and the physical model shows that it can be used for domestic purposes therefore it can be concluded that the methodology used in the development, test, and analysis of thermosyphon proved to be feasible.

References

1. Liu LB, Fu L, Jiang Y (2010) Application of an exhaust heat recovery system for domestic hot water. *J Energy* 35:1476–1481. <https://doi.org/10.1016/j.energy.2009.12.004>
2. De Paepe M, Theun E (2003) Heat recovery system for dishwashers. *J Appl Therm Eng* 23:743–756. [http://dx.doi.org/10.1016/S1359-4311\(03\)00016-4](http://dx.doi.org/10.1016/S1359-4311(03)00016-4)
3. Lukitobudi R, Akbarzadeh A, Johnson PW, Hendy P (1995) Design, construction and testing of a thermo syphon heat exchanger for medium temperature heat recovery in bakeries. *J Heat Recovery Syst CHP* 15:481–491. [https://doi.org/10.1016/0890-4332\(95\)90057-8](https://doi.org/10.1016/0890-4332(95)90057-8)
4. Colangelo G, de Risi A, Laforgia D (2006) Experimental study of a burner with high temperature heat recovery system for TPV applications. *Energy Convers Manage* 47:1192–1206. <http://dx.doi.org/10.1016/j.enconman.2005.07.001>
5. Noie-Baghban SH, Majideian GR (2000) Waste heat recovery using heat pipe heat exchanger (HPHE) for surgery rooms in hospitals. *J Therm Eng* 20:1271–1282. [http://dx.doi.org/10.1016/S1359-4311\(99\)00092-7](http://dx.doi.org/10.1016/S1359-4311(99)00092-7)
6. El-Baky MAA, Mohamed MM (2007) Heat pipe heat exchanger for heat recovery in air conditioning. *J Appl Therm Eng* 27:795–801. <https://doi.org/10.1016/j.applthermaleng.2006.10.020>
7. Kearton WJ, Steam turbine theory and practices
8. Fadhl B, Wrobel LC, Jouhara H (2013) Numerical modeling of the temperature distribution in a two-phase closed thermosyphon. *Appl Therm Eng* 60:122–131
9. Kalogirou SA, Papamarcou C (2000) Modelling of a thermosyphon solar water heating system and simple model validation. *Renew Energy* 21:471–493
10. Mantelli MBH, Angelo WB, Borges T (2010) Performance of naphthalene thermosyphons with non-condensable gases—theoretical study and comparison with data. *Int J Heat Mass Transf* 53:3414–3428

Synthesis and Characterization of Copper(II), Cadmium(II) and Nickel(II) Complexes Containing 3-Amino-2-Methyl-4(3H)Quinazoline and Triphenylphosphine as Ligands



Panchsheela Ashok Ubale, Amit Arvind Kamble,
Maina Machindra Awatade, and Vasant Baburao Helavi

Abstract Some copper(II), cadmium(II) and nickel(II) complexes of the formula $[\text{Cu}(\text{L})(\text{PPh}_3)_2\text{H}_2\text{O}]$, $[\text{Cd}(\text{L})(\text{PPh}_3)_2\text{H}_2\text{O}]$, $[\text{Ni}(\text{L})(\text{PPh}_3)_2\text{H}_2\text{O}]$ ($\text{C}_1\text{--C}_3$) [where $\text{L} = (\text{Z})\text{-3-(2,5-Dimethoxybenzylideneamino)-2-methylquinazolin-4(3H)-one}$; $\text{PPh}_3 =$ triphenylphosphine] have been synthesized and characterized on the basis of IR, UV–Vis, $^1\text{H-NMR}$ spectral studies, mass spectroscopy as well as on the basis of X-ray diffraction (XRD) analysis, elemental analysis and conductance data. The results revealed that the bidentate ligand (L) coordinated to the metal center through the lactum oxygen and the azomethine nitrogen. The powder X-ray diffraction studies showed that $\text{Cu}(\text{II})$, $\text{Cd}(\text{II})$ and $\text{Ni}(\text{II})$ complexes of schiff base ligand (L) exhibited triclinic crystal system.

Keywords 3-quinolin-4(3H)-one · Metal complexes · Spectral studies

Electronic supplementary material The online version of this chapter (https://doi.org/10.1007/978-3-030-69925-3_91) contains supplementary material, which is available to authorized users.

P. A. Ubale (✉) · V. B. Helavi
Department of Chemistry, Rajaram College, Kolhapur 416004, Maharashtra, India
e-mail: panchsheela_ubale@rediffmail.com

P. A. Ubale
N.K. Orchid College of Engineering and Technology, Solapur 413002, Maharashtra, India

A. A. Kamble
Bharatratna Indira Gandhi College of Engineering, Solapur 413002, Maharashtra, India

M. M. Awatade
Department of Chemistry, Sveri's College of Engineering and Sveri's College of Engineering (Poly), Pandharpur 413304, Maharashtra, India

1 Introduction

Co-ordination compounds play vital role in biochemistry, medicinal chemistry, biology, function of many enzymes, their metabolisms, and also in many industrial processes in the development specially designed of materials with unbelievable properties [1, 2]. A good class of organic compounds Schiff base ligands with oxygen or nitrogen donor atoms is capable of coordinating to different metal ions with interesting biological and non-biological properties and very popular. [3, 4]. These Schiff base ligands (SB) can be easily synthesized by simple condensation reaction of aldehydes with a primary amines [5]. The versatile role of transition metal complexes of Schiff base ligands in metallo-organic, inorganic and biochemistry have gained considerable attention because of their extensive use in a wide range of areas [6, 7]. From last decades it has been found that transition metal complexes of quinazolinone derivatives have wide exposer because of their exquisite colors, co-ordination geometries, spectroscopic properties, technical application depends on molecular study and their mysterious medical applications [8–12]. Metal complexes of ligands containing mixed electron donors have been studied extensively due to their potent applications as molecular materials [13–16]. In recent years, considerable research has focused on synthesis and properties of metal complexes of hybrid ligands because they can provide new materials with useful properties such as magnetic exchange [17, 18], photoluminescence [19], electrical conductivity [20], antimicrobial activity [21], non-linear optical properties [22] etc.

Herein, we report the synthesis and characterization of Cu(II), Cd(II) and Ni(II), complexes using a Schiff base ligand derived from the condensation of 3-amino-2-methyl-4(3*H*)quinazolinone and 2,5-Dimethoxybenzaldehyde. The synthesized ligand, (L) was particularly characterized by spectral techniques viz., UV-Vis, IR, ¹H-NMR and MS. Similarly, the complexes (C₁–C₃) were characterized by spectral, elemental, conductivity data and thermal studies. Further, all the complexes were characterized by using powder X-ray diffraction technique.

2 Experimental

2.1 Materials and Methods

3-amino-2-methyl-4(3*H*)-quinazolinone was purchased from Sigma Aldrich and was used as received. 2,5-Dimethoxybenzaldehyde, metal salts and solvents were commercially available on high purity and used as it is. The completion of reaction was monitored by spotting the reaction mixture by thin layer chromatography (TLC) method and spots were visualized by UV irradiation. Melting point of the compounds was determined by the open capillary method. The IR spectra were recorded with Perkin Elmer FT-IR spectrometer in between the frequency range 4000–400 cm⁻¹.

The $^1\text{H-NMR}$ spectra were recorded on Bruker AC (300 MHz for $^1\text{H-NMR}$) spectrometer using TMS as an internal standard in $\text{DMSO-}d_6$ for Cd(II) and Ni(II) metal complexes. Chemical shifts (δ) are expressed in ppm. Mass spectra were recorded on Agilent 7890B GC system, Agilent 5977B MSD Mass spectra of complexes were recorded on Agilent technology (HP) 5973 mass spectrometer operating at an ionization potential of 70 eV. Ultraviolet and visible spectra of Schiff base and its complexes were recorded on Shimadzu UV-3600 electronic spectrometer using quartz cells at room temperature in range 200–1000 nm. Elemental analysis has been calculated on Thermo Finnigan Flash EA 1112 CHN analyzer. Molar conductivity data was recorded on conductivity meter Model No. EQ-660A. The X-ray powder analysis was obtained using an X-ray diffractometer (Rigaku Model-Mini Flex II) with monochromatized Cu $K\alpha$ X-ray beam of wavelength 0.15418 nm operated at 30 kV and 15 mA.

2.2 Synthesis of Metal Complexes (C_1 – C_3)

Synthesis of ligand 3-[[(E) -(2, 5-dimethoxyphenyl)methylidene]amino]-2-methylquinazolin-4(3H)-one is reported as earlier [23]. To an ethanolic solution (25 mL) of appropriate metal salts (($\text{CuCl}_2 \cdot 2\text{H}_2\text{O}$ (0.170 g) or 1 mmol $\text{CdCl}_2 \cdot 2\text{H}_2\text{O}$ (0.219 g) or $\text{NiCl}_2 \cdot 6\text{H}_2\text{O}$ (0.238 g) or), solution of ligand (L) in dichloromethane (25 mL) (1 mmol L (0.323 g)) was added followed by addition of triphenylphosphine (1 mmol, 0.278 g) in 1:1:1 (M: L: PPh_3) ratio. The resultant mixture was stirred under reflux for 6 h. The green colored product obtained of the Cu(II) and Ni(II) complexes and white colored product obtained of the Cd(II) complexes were filtered, washed off with ethanol and dried under vacuum over CaCl_2 . Molecular formula of the obtained complexes: C_1 : $\text{C}_{36}\text{H}_{34}\text{CuN}_3\text{O}_4\text{P}$; C_2 : $\text{C}_{36}\text{H}_{34}\text{CdN}_3\text{O}_4\text{P}$; C_3 : $\text{C}_{36}\text{H}_{34}\text{N}_3\text{NiO}_4\text{P}$ (Scheme 1).

3 Results and Discussion

The synthesized metal complexes (C_1 – C_3) were stable at room temperature and soluble in common solvents like DCM, DMSO etc. The elemental analysis of metal complexes are found in agreement with the proposed structure of the metal complexes (C_1 – C_3) are listed in Table 1.

3.1 $^1\text{H-NMR}$ Spectral Analysis

Figure 1 shows $^1\text{H-NMR}$ spectra of the complex (C_2) were recorded in $\text{DMSO-}d_6$ to elucidate the structure of Cd(II) complexes (C_2). The $^1\text{H-NMR}$ spectra of the

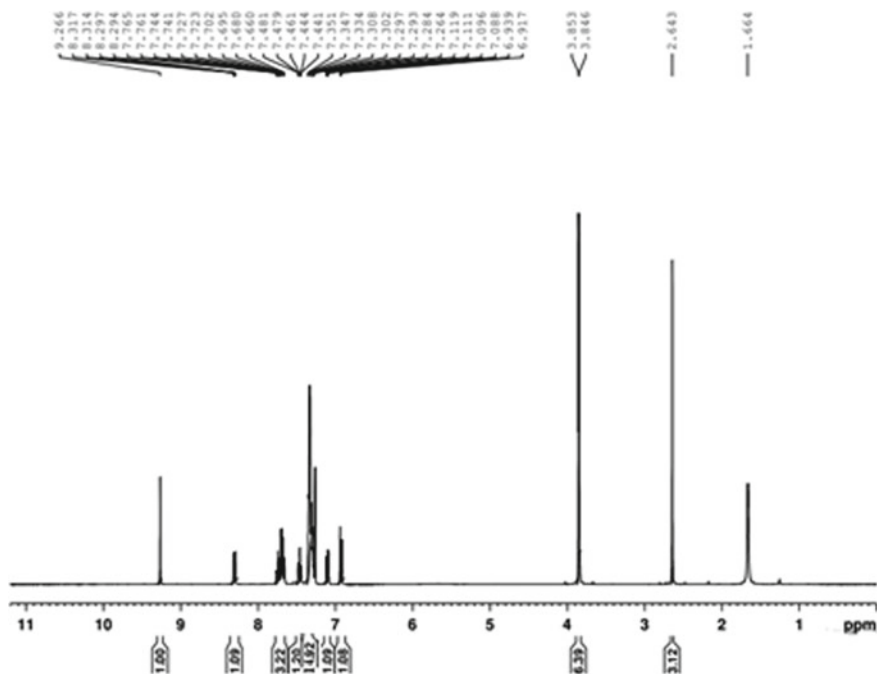


Fig. 1 $^1\text{H-NMR}$ of C_2 complex

C_2 complex show the resonance of ligand overlap to the protons of PPh_3 (Fig. S1). However, a broad multiplet observed in the range δ 6.91–8.32 ppm for C_2 complex was assigned to the phenyl group of PPh_3 together with the ring proton of schiff base ligand (**L**). The peak appears at δ 9.27 ppm due to azomethine proton group. In the ligand, peak appears at δ 3.857 and 3.851 due to methoxy protons is assigned in between δ 3.840–3.86 of methoxy proton of metal complexes. The signals observed at δ (2.5) are due to methyl protons that remain almost unaffected in Cd(II) and Ni(II) complexes indicating the nonparticipation of these groups in coordination [24].

3.2 FT-IR and UV-Visible Spectral Studies

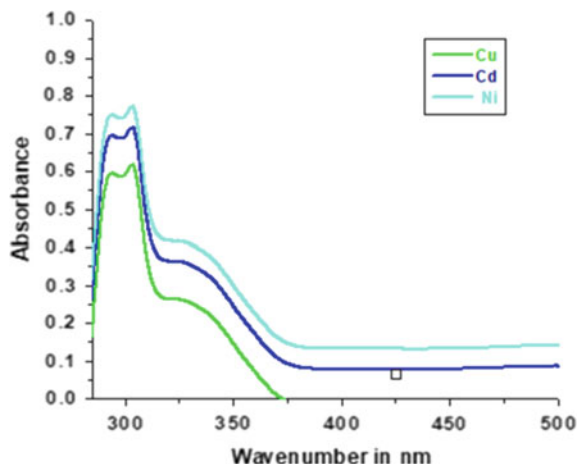
Table 2 shows the characteristic absorption of IR spectra of Schiff base ligand (**L**) and its complexes (C_1 – C_3). The comparison of infrared spectral data of ligand (Fig. S2) and its complexes confirmed that complexation has occurred as significant shifts in the band of azomethine group $\nu(\text{CH}=\text{N})$ and lactum $\nu(\text{C}=\text{O})$ groups were observed. The Schiff base ligand has interacted with metal ions (Cu(II) , Cd(II) and Ni(II)) via coordination of the metal ions to azomethine nitrogen group and lactum oxygen (Figs. S3–S4). The medium and strong band appears in the IR spectra of the metal complexes

Table 2 Important IR spectral bands of metal complexes

Compound	$\nu(\text{C}=\text{O})$	$\nu(\text{HC}=\text{N})$	$\nu(\text{M}-\text{O})$	$\nu(\text{M}-\text{N})$
L	1668	1603	–	–
C ₁	1621	1540	598	426
C ₂	1620	1556	513	418
C ₃	1645	1586	627	419

showed characteristic imine band in the region 1540–1588 cm^{-1} , shifted to lower frequency from 1603 cm^{-1} observed in ligand due to metal coordination. A sharp band in the ligand at 1668 cm^{-1} is due to $\nu(\text{C}=\text{O})$ was shifted to lower frequencies in complexes in the region 1620–1645 cm^{-1} . However, this was also supported by the appearance of the weak bands of $\nu(\text{M}-\text{O})$ and $\nu(\text{M}-\text{N})$ were observed at 513–627 cm^{-1} and 418–426 cm^{-1} .

The UV-Visible spectra of metal complexes were recorded in DMSO solutions between 200 and 800 nm at room temperature. The UV-Visible spectra of metal complexes were shown in Fig. 2. Two bands were observed in between 285 and 306 nm, which are attributed to $\pi - \pi^*$ transition of the quinazoline moieties and $n - \pi^*$ transition of the azomethine group, respectively. The electronic absorption spectra of Cu(II) shows d–d band at 712 nm which is assigned to ${}^2\text{E}_g \rightarrow {}^2\text{T}_{2g}$ transition. This prefers the distorted octahedral geometry of C₁. The Ni(II) complex (C₂) shows the absorption band at 690 nm assigned to ${}^3\text{A}_{2g}(\text{F}) \rightarrow {}^3\text{T}_{2g}(\text{F})$ and ${}^3\text{A}_{2g}(\text{F}) \rightarrow {}^3\text{T}_{1g}(\text{F})$ corresponds to octahedral geometry. The cadmium(II) complexes did not show any d–d bands.

Fig. 2 UV-Vis spectra of complexes (C₁–C₃)

3.3 Mass Spectra

The formation of metal complexes (C_1 – C_3) was further confirmed by mass spectroscopic analysis. The molecular ion peaks observed at $m/z = 668$, 718 and 663 corresponds to the mass value of C_1 , C_2 , and C_3 , respectively. Furthermore, all the experimental mass values are in well agreement with the theoretically calculated values (Figs. S5, S6 and S7).

3.4 Powder X-Ray Diffraction Analysis

As crystals for single crystal X-ray diffraction studies were unable to be obtained, therefore X-ray powder diffraction studies were carried out on the samples (C_1 – C_3). The X-ray powder diffraction patterns were obtained in the range of 10 – 80° in steps of 0.0200 . X-ray powder diffraction analysis of metal complexes (C_1 – C_3) was carried out to determine the type of crystal system, lattice parameters and the cell volume. As shown in (Figs. S8, S9 and S10), the XRD patterns indicate a crystalline nature for complexes (C_1 – C_3). For (C_1 – C_3) complexes d values, FWHM and relative intensities are listed in Tables S1, S2 and S3. From the indexed data, average crystallite size were also calculated and are listed in Table 3. The full width at the half-maximum (FWHM) of the diffraction peaks obtained from the refinement was used to calculate the particle size. The average size of the samples was calculated with the help of the Debye-Scherrer equation,

$$D = \frac{0.90\lambda}{(\beta \cos\theta)}$$

Table 3 Unit cell parameters, volume and crystallite size of metal complexes

Compound	Lattice constants	Volume (\AA^3)
C_1	$a = 17.7378$, $b = 6.3000$, $c = 15.0881$ $\alpha = 90.0000$, $\beta = 104.1133$, $\gamma = 90.0000$	1891
C_2	$a = 8.8956$, $b = 16.6380$, $c = 7.4000$ $\alpha = 90.0000$, $\beta = 90.0000$, $\gamma = 90.0000$	1095
C_3	$a = 16.8665$, $b = 9.2000$, $c = 10.0200$ $\alpha = 90.0000$, $\beta = 108.2903$, $\gamma = 90.0000$	1554

where λ is the wavelength ($\text{Cu K}\alpha$), β is the full width at the half maximum (FWHM) and θ is the diffraction angle. The diffraction peaks indicate that the synthesized materials are in the nanometer range.

4 Conclusions

In summary, the series of Cu(II), Cd(II) and Ni(II) complexes were successfully synthesized using Schiff base ligand 3-[[*E*-(2, 5-dimethoxyphenyl)methylidene]amino]-2-methylquinazolin-4(3H)-one is prepared. The molecular structure of metal complexes (C_1 – C_3) has been determined by UV-Vis, FT-IR, $^1\text{H-NMR}$, mass spectroscopy as well as on the basis of elemental analysis and conductance data. The Schiff base ligand (L) behaves as a bidentate ligand and reacts with metal ions to yield mononuclear complexes (C_1 – C_3). The electronic absorption of the ligand and complexes were investigated in DMSO- d_6 solution, which exhibit that the bands shifted to longer wavelength in the complexes is due to the coordination of the ligand with the metal ions. The powder XRD analysis of all the complexes is also carried out. The results revealed that all the complexes show triclinic system. This information could be useful in complementing the experimental data as the starting point for the development of new therapeutic drugs based on these molecules.

Acknowledgements Authors are thankful to the Director, Institute of Sciences, Mumbai for providing analytical facilities. PAU is thankful to Principal, N.K. Orchid college of Engineering and Technology, Solapur.

References

1. Yousif E, Majeed A, Al-Sammarrae K, NadiaSalih JS, Abdullah B (2017) Metal complexes of schiff base: preparation, characterization and antibacterial activity. Arab J Chem 10:S1639–S1644
2. Annapoorani S, Krishnan C (2013) Synthesis and spectroscopic studies of trinuclear N4 Schiff base complexes international. J Chem Tech Res 5:180–185
3. Liu Y-T, Sheng J, Yin D-W, Xin H, Yang X-M, Qiao Q-Y, Yang Z-J (2018) Ferrocenyl chalcone-based Schiff bases and their metal complexes: highly efficient, solvent-free synthesis, characterization, biological research. J Organomet Chem 856:27–33
4. Lashanizadegan M, Shayegan S, Sarkheil M (2016) Copper(II) complex of (\pm)trans-1,2-cyclohexanediamine azo-linked Schiff base ligand encapsulated in nanocavity of zeolite-Y for the catalytic oxidation of olefins. J Serbian Chem Soc 81:153–162
5. Yu H, Zhang W, Yu Q, Huang F-P, Bian H-D, Liang H (2017) Ni(II) complexes with schiff base ligands: preparation, characterization. DNA/Protein Interact Cytotox Stud Mol 22:1772
6. Ganguly R, Sreenivasulu B, Vital J (2008) Amino acid containing reduced schiff bases as the building blocks for metallasupramolecular structures. Coord Chem Rev 252:1027–1050

7. Golcu A, Tumer M, Demirelli H, Wheatley RA (2005) Cd and Cu complexes of polydentate Schiff base ligands: synthesis, characterization, properties and biological activity. *Inorg Chim Acta* 153:1785–1797
8. Tolazzal M, Tarafder H, Ali M, Juan D (2000) Complexes of a tridentate ONS schiff base. Synthesis and biological properties. *Trans. Metal Chem* 25:456–460
9. Khojasteh R, Matin SJ (2015) Synthesis, characterization and antimicrobial activity of some metal complexes of heptadentateschiif base ligand derived from acetylacetone. *Russ J Appl Chem* 88:921–925
10. Hou SH, Jihui J, Huang X, Wang X, Ma L, Shen W, Kang F, Hiang Z-H (2017) Silver nanoparticles-loaded exfoliated graphite and its anti-bacterial performance. *Appl Sci* 7:852
11. Lee J, Purushothaman B, Li Z, Kulsli G, Song JM (2017) Synthesis, characterization, and antibacterial activities of high-valence silver propamidine nanoparticles. *Appl Sci* 7:736
12. Wang SX, Zhang FJ, Feng QP, Li YL (1992) Synthesis, characterization, and antibacterial activity of transition metal complexes with 5-hydroxy-7,4?-dimethoxyflavone. *J Inorg Biochem* 46:251–257
13. Mohamed G (2001) Metal complexes of antibiotic drugs. Studies on dicluxacillin Complexes of Fe(II), Fe(III), Co(II), Ni(II) and Cu(II). *Spectrochim Acta A* 57(8):1643–1648
14. Panchal PK, Patel MN (2004) Synthesis, structural characterization, and antibacterial studies of some mixed-ligand first rowd-transition metal complexes. *Synth React Inorg* 34(7):1277–1289
15. Mashaly MM, Ramadan AT, El-Shetary BA, Dawoud AK (2004) Synthesis and characterization of new transition and actinide metal complexes of a hydrazone ligand. mixed-ligand complexes, pyrolysis products, and biological activity. *Synth React Inorg* 34(8):1319–1348
16. Masoud MS, Amira MF, Ramadan AM, ElAshry GM (2008) Synthesis and characterization of some pyrimidine, purine, amino acid and mixed ligand complexes. *Spectrochim Acta A* 69(1):230–238
17. Puthilibai G, Vasudhevan S, Rani SK, Rajagopal G (2009) Synthesis, spectroscopic characterization, electrochemical behaviour and antibacterial activity of Ru(III) complexes of 2-[(4-N,N'-dimethylaminophenylimino)-methyl]-4-halophenol, *spectrochim. Acta A* 72(4):796–800
18. Kulkarni AD, Bagihalli GB, Patil SA, Badami PS (2009) Synthesis, Characterization, Electrochemical and invitro Antimicrobial Studies of Co(II), Ni(II) and Cu(II) Complexes with schiff bases of Formyl coumarin derivatives. *J Coord Chem* 62(18):3060–3072
19. Gupta K, Sutar AK (2008) Catalytic activities of schiff base transition metal complexes. *Coord Chem Rev* 252(12–14):1420–1450
20. Shiri-Yekta Z, Yaftian MR (2010) Anion control selectivity of neutral N4-type schiff base extractants towards transition metal ions. *Iran J Chem Chem Eng* 29(2):11–17
21. Shivakumar L, Shivaprasad K, Revanasiddappa HD (2012) Synthesis, spectroscopic characterization, antimicrobial, DNA binding and oxidative-induced DNA cleavage activities: new Oxovanadium(IV) complexes of 2-(2-hydroxybenzylideneamino)isindoline-1,3-dione. *Spectrochim Acta A* 97659–666
22. Kumar R, Mani G (2015) Exhibitionofthe Brønsted acid-base character of a schiff base in Palladium(II) complex formation: lithium complexation, fluxional properties and catalysis of suzuki reactions in water. *Dalton Trans* 44(15):6896–6908
23. Ashok UP, Kollur SP, Arun BP et al (2020) In vitro anticancer activity of 4 (3H)-quinazolinone derived Schiff base and its Cu (II), Zn (II) and Cd (II) complexes: preparation, X-ray structural, spectral characterization and theoretical investigations. *Inorganica Chimica Acta* 511:119846
24. Badiger DS, Hunoor RS, Patil BR, Vadavi RS, Mangannavar CV, Muchchandi IS, Gudasi KB (2012) Synthesis, physico-chemical characterization and antimicrobial activities of 3-methoxysalicylaldehyde-2-aminobenzoylhydrazone and its transition metal complexes. *J Mol Struct* 1019:159–165

Analysis of Heat Transfer and Pressure Drop for Pressure Driven Flow of Non-Newtonian Fluids Through a Serpentine Channel: Influence of Prandtl Number



Sumit Kumar Mehta and Sukumar Pati

Abstract We investigate numerically the thermo-fluidic behaviors for laminar flow of non-Newtonian fluids through a serpentine channel. The temperature and velocity fields, Nusselt number, and performance factor have been investigated by varying the Prandtl number (Pr), power-law index (n) and Reynolds number (Re) in the range of $0.72 \leq \text{Pr} \leq 100$, $0.5 \leq n \leq 1.5$ and $50 \leq \text{Re} \leq 500$, respectively. The size of recirculation zone depends on both Re and n . For $\text{Re} = 50$, average Nusselt number (\overline{Nu}) decreases with n for smaller Pr, while opposite trend is observed for higher Pr. For $\text{Re} = 500$, \overline{Nu} monotonically decreases with n for all Pr. It is found that for higher Pr and Re, the performance factor is greater than unity for all n .

Keywords Non-Newtonian fluid · Wavy channel · Nusselt number · Performance factor

1 Introduction

The efficient thermal systems and devices are the need of the hour for many industrial applications. Normally, heat transfer enhancement techniques can be classified into three types [1–7]. First one is the passive technique, which includes surface modifications, metallic porous media, and nanofluids. The second one is the active technique, which requires external energy sources other than the driving energy. The third one is the compound technique, which includes either two or more than one active, passive, or both techniques.

The addition of waviness is a common practice for the augmentation of heat transfer [8]. Wang and Chen [1] numerically analyzed the heat transport rate for flow through a symmetric wavy channel. Pati et al. [3] compared the performance parameters for flow through serpentine and raccoon channel.

S. K. Mehta (✉) · S. Pati

Department of Mechanical Engineering, National Institute of Technology Silchar, Silchar 788010, Assam, India

e-mail: sumit_rs@mech.nits.ac.in

The types of working fluid and fluid rheology have a considerable influence on the transport phenomena [4, 9]. The working fluids like water-carboxymethyl cellulose, water-carbopol solution [10], hybrid nanofluid-carboxymethyl cellulose-water [11], hybrid nanofluid-water and ethylene [12], water-corn starch and water-glass beads mixtures [13] exhibit the non-Newtonian behavior. These fluids have either shear-thinning or shear-thickening behavior. The Prandtl number varies in the range of 65–90 for water and 0.05% carbopol solution, more than 85 for 0.5% carboxymethyl cellulose water solution, 5–100 for ethylene glycol–water mixtures for the different fraction of ethylene glycol and working temperature [14], less than 1 for metallic liquids, and 0.72 for the air [1]. The thermal transport phenomena for the flow of non-Newtonian fluid squeezed and extruded between two parallel plates were investigated by Kaushik et al. [15] in the laminar regime. They have considered power-law model and the flow field and Nusselt number have been analyzed for $Pr = 10$ and $0.4 \leq n \leq 1.4$. Shubham et al. [4] analyzed the flow of non-Newtonian fluids through a wavy channel at $Pr = 6.93$. They reported a higher performance factor for shear-thinning fluids. Mehta and Pati [7] analyzed the effect of Pr ($0.72 \leq Pr \leq 100$) for flow through a wavy channel for $5 \leq Re \leq 200$ and found that the performance factor monotonically increases with Pr at higher values of Re , while non-monotonic trend is observed at lower values of Re .

From the existing literature, it is apparent that the fluid rheology and Prandtl number for different types of fluid affect the heat transfer characteristics significantly [10–13]. The use of the wavy channel enhances the heat transfer rate [2–7]. The effects of fluid rheology and different fluids on the transport performance for flow through serpentine channel are not available. Accordingly, aim of the current work is to analyze the thermal transport phenomena for pressure driven flow of non-Newtonian fluids through a serpentine channel at different Pr .

2 Theoretical Formulation

The schematic diagram of the domain is shown in Fig. 1. The normalized profiles of the top and bottom wavy walls are $S_{Top}(X) = 0.3 \sin(\pi(X - 3))$ and $S_{Bottom}(X) = 0.3 \sin([\pi(X - 3)] + \pi)$, respectively [2]. The flow is incompressible and steady. To predict the fluid rheology, power-law model is taken into consideration. The

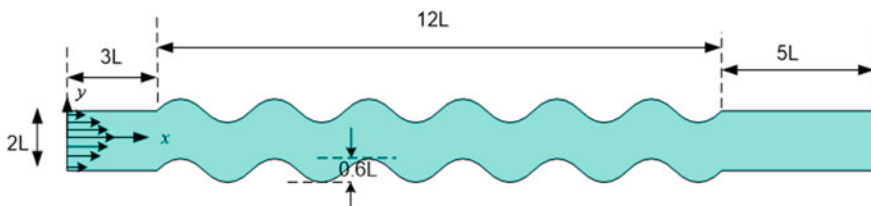


Fig. 1 Computational domain for an asymmetric wavy channel

dimensionless governing transport equations are as follows [4]:

$$\nabla \cdot \mathbf{U} = 0 \tag{1}$$

$$(\mathbf{U} \cdot \nabla)\mathbf{U} = -\nabla P + (1/\text{Re})\nabla\tau_{ij} \tag{2}$$

$$\mathbf{U} \cdot \nabla\theta = (1/(\text{Re} Pr))\nabla \cdot \nabla\theta \tag{3}$$

Here, $\mathbf{U} = (U\hat{i} + V\hat{j}) = (u\hat{i} + v\hat{j})/u_r$, u_r is the reference velocity, $\nabla = (\hat{i}\partial/\partial X + \hat{j}\partial/\partial Y)$, $X = x/L$, $Y = y/L$, $\theta = (T - T_{inlet})k/qL$, $\tau_{ij} = \tau_{ij}^*/(\mu_r u_r/L)$ is the dimensionless deviatoric stress tensor, $\mu_r = m(u_r/L)^{n-1}$, $\text{Re} (= (\rho u_r L)/\mu_r)$ is the Reynolds number, and $\text{Pr} (= (\mu_r c_p)/k)$ is the Prandtl number. For the non-Newtonian power-law model, the deviatoric stress tensor can be written as:

$$\tau_{ij}^* = 2\eta\varepsilon_{ij} \tag{4}$$

Here, $\varepsilon_{ij} (= (\partial u_i/\partial x_j) + (\partial u_j/\partial x_i))$, η is the generalized viscosity that can be represented as [4]:

$$\eta = (\mathbf{I}_2/2)^{\frac{n-1}{2}} \tag{5}$$

Here, $\mathbf{I}_2 = \sum_i \sum_j \varepsilon_{ij}\varepsilon_{ji}$, n is the power-law index, and m is the flow consistency index.

It is to be noted that η can also be expressed in terms of shear rate ($\dot{\gamma}$) as [4]: $\eta = m|\dot{\gamma}|^{n-1}$. The reference viscosity can be written as $\mu_r = m(u_r/L)^{n-1}$.

To solve the above governing transport equations, the following boundary conditions are imposed.

At the inlet

$$U(Y) = ((2n + 1)/(n + 1))(1 - |Y|^{\frac{n+1}{n}}); \theta = 0. \tag{6}$$

At the wall

$$U = 0; \partial\theta/\partial\Omega = 1 \text{ for } 3 \leq X \leq 15; \partial\theta/\partial Y = 0 \text{ for } X < 3 \text{ and } X > 15. \tag{7}$$

Here, Ω is the dimensionless normal to the wall.

At the outlet

$$\partial\theta/\partial X = 0; P_G = 0. \tag{8}$$

The local heat transfer can be represented as [2]:

$$Nu = qL/(k(T - T_{inlet})) \tag{9}$$

Using Eq. (9), one can write $Nu = 1/\theta_{wall}$. The mean Nusselt number can be represented as [2]:

$$\overline{Nu} = 0.5 \left(\int_{X=3}^{X=15} NudS|_{Top} + \int_{X=3}^{X=15} NudS|_{Bottom} \right) / \int_{X=3}^{X=15} dS \tag{10}$$

The relative augmentation in heat transfer to the pressure-drop in wavy channel as compared to plane channel is termed as performance factor, represented as [5]:

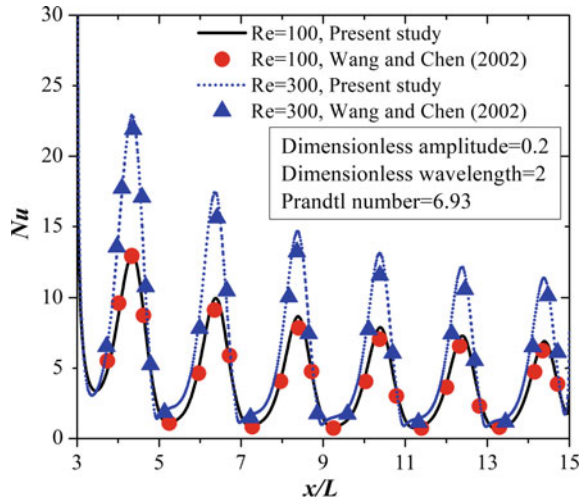
$$PF = \left((\overline{Nu})_{wavy} / (\overline{Nu})_{plane} \right) / \left((\Delta P)_{wavy} / (\Delta P)_{plane} \right)^{1/3} \tag{11}$$

3 Numerical Methodology

The finite element method based numerical solver has been used to solve the governing equation numerically. The details of the numerical technique can be seen in [5]. The non-uniform mesh is used with dense ones near the wall. The grid sensitivity analysis has been performed by calculating the \overline{Nu} for different mesh system at $Re = 500$ and $Pr = 100$, although, not presented here. The selected \overline{Nu} mesh system has a number of elements of 152,148 and the percentage difference of \overline{Nu} in comparison to extremely fine mesh is less than 1%.

Validation has been made by comparing Nu with the results of Wang and Chen [1] for flow through a symmetric sinusoidal channel at $Re = 100$ and 300 (Fig. 2). The good agreement of the results confirms the correctness of the numerical methodology used for the present work.

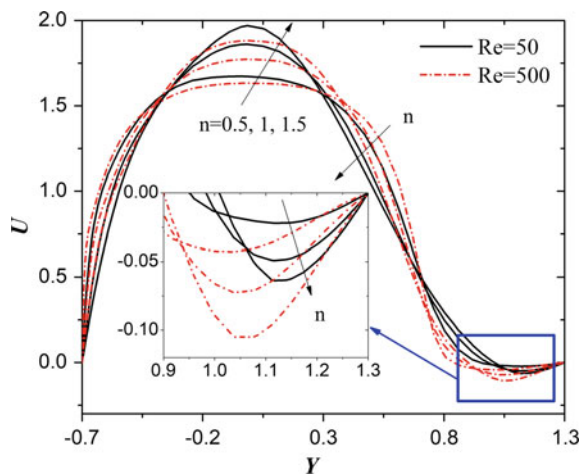
Fig. 2 Comparison of Nu with the results of Wang and Chen [1]



4 Results and Discussion

The transport phenomena for flow of non-Newtonian fluids through a serpentine channel are analyzed for $50 \leq Re \leq 500$, $0.72 \leq Pr \leq 100$, and $0.5 \leq n \leq 1.5$ [4–7, 10–13]. To explain the effect of fluid rheology on the flow field, the variation of dimensionless flow velocity (U) at different n is presented in Fig. 3 for $Re = 50$ and 500. It is seen that the negative flow velocity (shown in rectangle) is induced due to the momentum loss near the concave wavy surface [16–19]. Near the convex surface, the favourable negative pressure-gradient [5–7, 16] allows flow to take place in the downstream direction. The flow velocity near the convex surface decreases with n

Fig. 3 Variation of velocity (dimensionless) at $X = 7.5$ for different n with $Re = 50$ and 500



due to increase in effective viscosity [4]. The maxima of flow velocity in the core region increases with n to satisfy the mass conservation. The magnitude of reversed flow velocity increases with n as the enhancement in effective viscosity enhances the momentum loss. It is also observed that the enhancement in Re allows to increase the maxima of flow velocity as well as the magnitude of reversed flow velocity due to the increase in inertia forces. The size of the recirculation zone enhances with Re as the length of reverse flow velocity region enhances (see the zoomed view of Fig. 3). It can be noted this length of reversed flow zone decreases with the increase in n because of the higher core region velocity for the higher n suppresses the size of the zone of recirculation.

The variation of dimensionless temperature (θ) is presented in Fig. 4a and b near the wavy wall ($X = 6$ to 9) for $n = 0.5$ and 1.5 , respectively for $Re = 500$. The local maxima and minima of θ exist in the recirculation zone hot fluid region and higher velocity gradient region near the heated wall, respectively [5–7]. The increase in Pr decreases θ and the same is in line with [7]. It can be noted that the minima of θ (exists near the convex part) increases with n because of the decrease in velocity

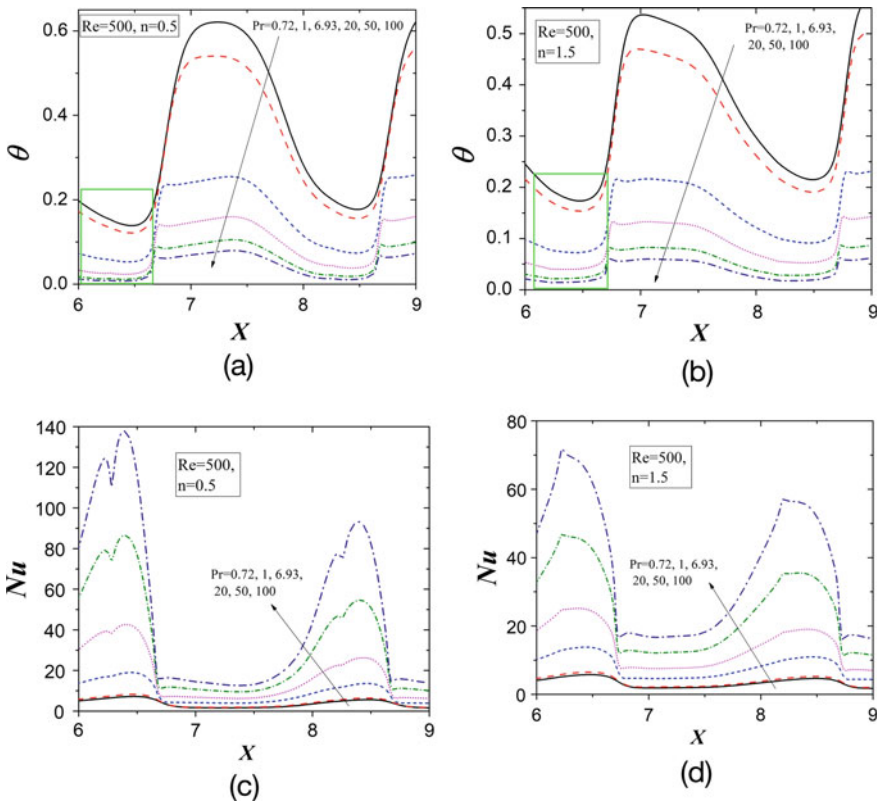


Fig. 4 Variation of θ and Nu at different Pr for $Re = 500$

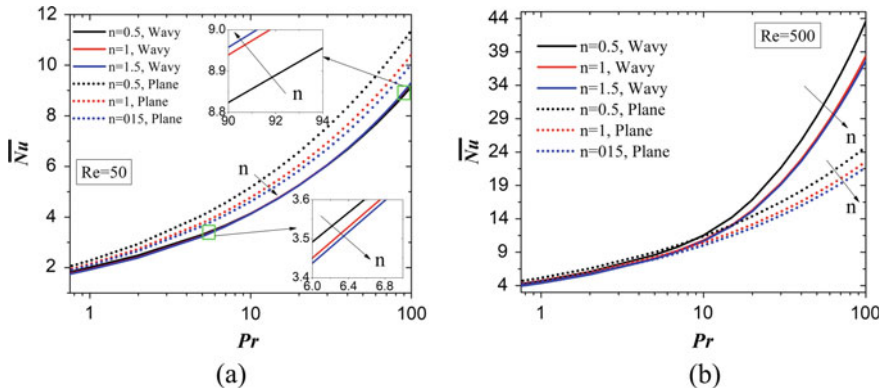


Fig. 5 Variation of \overline{Nu} with Pr for the wavy and plane channel

gradient (Fig. 3), while the maxima of θ (exists near the recirculation zone) decreases with n as the enhancement in reversed flow convection strength allows a decrease in hot-spot intensity (Fig. 3). The axial variation of Nu is presented in Fig. 4c and d in the region $X = 6$ to 9 for $n = 0.5$ and 1.5, respectively at $Re = 500$. The trend the variation of Nu is just reverse of θ with the change in Pr and n .

The variation of \overline{Nu} is presented in Fig. 5a and b for $Re = 50$ and 500, respectively for the wavy and plane channel, respectively. The increase in Pr enhances the value of \overline{Nu} . It can be noted that for $Re = 50$, \overline{Nu} decreases with n for smaller values of Pr, while the opposite effect is observed at higher values of Pr for wavy channel. It is because of the dominance of the decrease in maxima of Nu with n at lower Pr thus decreasing \overline{Nu} for wavy channel (Fig. 4). While for higher values of Pr, the diffusion dominated heat transfer allows more heat removal due to the larger core velocity for shear thickening fluid (Fig. 3). Hence, for higher values of Pr, \overline{Nu} enhances with n for wavy channel. For $Re = 50$, \overline{Nu} is always higher for the plane channel as compared to the wavy channel. For the plane channel, \overline{Nu} monotonically decreases with n for both $Re = 50$ and 500, due to the monotonic decrease in velocity gradient near the wall with n . For higher Re (=500), the value of \overline{Nu} decreases with n for all Pr. The dominance of convection strength allows a significant decrease in maxima of Nu with n (Fig. 4).

The variation of PF is presented in Fig. 6a, b for $Re = 50$ and 500, respectively. For $Re = 50$, PF decreases with Pr up to the critical Pr (Pr_{cri}) (as shown by rectangle) and thereafter PF increases with Pr for all n . It is because of the decrease in relative enhancement in wavy channel as compared to the plane channel with Pr for smaller Pr, and increase at higher Pr. For smaller Pr, PF increases with n . For higher values of Pr, the relative increase in \overline{Nu} (Fig. 5a) and pressure-drop with n in wavy channel allows a non-monotonic variation of PF as shown in Fig. 6a. For higher Re (=500), PF monotonically increases with Pr and n . The decrease in relative pressure-drop (pressure-drop ratio) in wavy channel as compared to the plane channel with increase

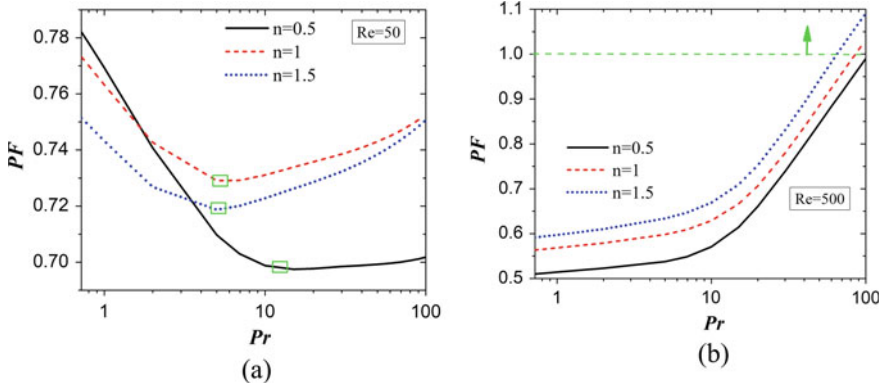


Fig. 6 Variation of PF with Pr

in n is the reason for it. The enhancement in heat transfer with Pr at a given pressure-drop monotonically enhances PF with Pr as shown in Fig. 6b. The value of PF is larger than unity at the higher Pr .

5 Conclusions

The thermal transport phenomena for flow of non-Newtonian fluids through a serpentine channel are analyzed by varying the Re , Pr and n in the range of $50 \leq Re \leq 500$, $0.72 \leq Pr \leq 100$, and $0.5 \leq n \leq 1.5$, respectively. The important findings are summarized as follows:

- The size of the recirculation zones formed in the wavy passages increases with Re and decreases with an increase in n .
- For lower Re ($=50$), the average Nusselt number decreases with n for smaller Pr , while the opposite trend is observed at higher values of Pr . For higher Re ($=500$), the average Nusselt number monotonically decreases with n .
- For smaller Re ($=50$), the variation of performance factor (PF) is non-monotonic with Pr as well as n at higher Pr . For higher Re ($=500$), PF increases monotonically with Pr and n . The performance factor is greater than unity for higher Pr and Re for all n .

References

1. Wang CC, Chen CK (2002) Forced convection in a wavy-wall channel. *Int J Heat Mass Transf* 45(12):2587–2595
2. Mehta SK, Pati S (2021) Thermo-hydraulic and entropy generation analysis for magnetohydrodynamic pressure driven flow of nanofluid through an asymmetric wavy channel. *Int J Numer Meth Heat Fluid Flow* 31(4):1190–1213. <https://doi.org/10.1108/HFF-05-2020-0300>
3. Pati S, Mehta SK, Borah A (2017) Numerical investigation of thermo-hydraulic transport characteristics in wavy channels: comparison between raccoon and serpentine channels. *Int Commun Heat Mass Transfer* 88:171–176
4. Shubham, Saikia A, Dalal A, Pati S (2018) Thermo-hydraulic transport characteristics of non-Newtonian fluid flows through corrugated channels. *Int J Therm Sci* 129:201–208
5. Mehta SK, Pati S (2019) Analysis of thermo-hydraulic performance and entropy generation characteristics for laminar flow through triangular corrugated channel. *J Therm Anal Calorim* 136(1):49–62
6. Mehta SK, Pati S (2018) Effect on non-uniform heating on heat transfer characteristics in the wavy channel. In: *Proceedings of the 5th international conference on computational methods for thermal problems (THERMACOMP 2018)*, ISSN: 2305–6924, IISc Bangalore, India, pp 498–501
7. Mehta SK, Pati S (2020) Numerical study of thermo-hydraulic characteristics for forced convective flow through wavy channel at different Prandtl numbers. *J Therm Anal Calorim* 141:2429–2451. <https://doi.org/10.1007/s10973-020-09412-5>
8. Rush TA, Newell TA, Jacobi AM (1999) An experimental study of flow and heat transfer in sinusoidal wavy passages. *Int J Heat Mass Transf* 42(9):1541–1553
9. Boruah MP, Pati S, Randive PR (2019) Implication of fluid rheology on the hydrothermal and entropy generation characteristics for mixed convective flow in a backward facing step channel with baffle. *Int J Heat Mass Transf* 137:138–160
10. Huang M-J, Huang J-S, Chou Y-L, Chen C-K (1989) Effects of Prandtl number on free convection heat transfer from a vertical plate to a non-Newtonian fluid. *J Heat Transfer* 111(1):189–191
11. Hojjat M, Etemad SG, Bagheri R, Thibault J (2011) Rheological characteristics of non-Newtonian nanofluids: experimental investigation. *Int Commun Heat Mass Transfer* 38(2):144–148
12. Bahrami M, Akbari M, Karimipour A, Afrand M (2016) An experimental study on rheological behavior of hybrid nanofluids made of iron and copper oxide in a binary mixture of water and ethylene glycol: non-Newtonian behavior. *Exp Thermal Fluid Sci* 79:231–237
13. Marn J, Ternik P (2006) Laminar flow of a shear-thickening fluid in a 90° pipe bend. *Fluid Dyn Res* 38(5):295–312
14. Bohne D, Fischer S, Obermeier E (1984) Thermal, conductivity, density, viscosity, and Prandtl-numbers of ethylene glycol-water mixtures. *Ber Bunsenges Phys Chem* 88(8):739–742
15. Kaushik P, Mondal PK, Pati S, Chakraborty S (2017) Heat transfer and entropy generation characteristics of a nonNewtonian fluid squeezed and extruded between two parallel plates. *J Heat Transf* 139:022004.
16. Mondal B, Mehta SK, Patowari PK, Pati S (2019) Numerical study of mixing in wavy micromixers: comparison between raccoon and serpentine mixer. *Chem Eng Process-Process Intensif* 136:44–61
17. Mehta SK, Pati S (2021) Effect of non-uniform heating on forced convective flow through asymmetric wavy channel. In: Pandey KM et al (eds) *Recent Advances in Mechanical Engineering*. Lecture Notes in Mechanical Engineering. Springer Nature Singapore Pte Ltd. https://doi.org/10.1007/978-981-15-7711-6_34

18. Mehta SK, Pati S (2020) Thermo-hydraulic characteristics for MHD forced convective flow through raccoon channel. ISBN 978-93-83660-56-8. Jadavpur University, Kolkata, India, pp 501-504
19. Mehta SK, Pati S, Mondal PK (2021) Numerical study of the vortex induced electroosmotic mixing of non-Newtonian biofluids in a non-uniformly charged wavy microchannel: effect of finite ion size. *Electrophoresis*. <https://doi.org/10.1002/elps.202000225>

Study of Transference Number and Dc Electrical Conductivity of Polianiline Composite



Sarika A. Khapre, Ramdas Biradar, and Sushil Deshpande

Abstract The polymer compound can change from an insulator to a semiconductor over a very small filtration range. In the present work the ionic/electronic transfer rate (ition/te) was measured using the dc polarization process proposed by Wagner and Wagner 1957. The number of ionic transference number for all samples was found to be 0.952 to 0.973 and the temperature dependence of conductivity is measured by two-probe method, in which the sample resistance measured dc conductivity is found to be $4.00464 \times 10^{-06} \text{Scm}^{-1}$. The further increase in LiCl causes a decrease in high salinity filtration, a decrease in mobility may be due to the increasing influence of ion pairs, ion triplets, and high ion concentrations, which reduces overall travel and freedom level.

Keywords Polyaniliane · PEO · LiCl · Dc conductivity · Transference number

1 Introduction

Traditionally polymers are considered good electrical protectors and most of their applications relied on their protective properties [1]. However, until the last thirty years researchers have shown that a certain class of polymers exhibits semiconducting properties [2]. Condensing polymers are highly integrated molecules: they can be exchanged with one and two bonds. In these molecules, electrons are able to move from one side of the polymer to the other through an expanded p-orbital system [3]. In p-conjugated polymers such as polyacetylene, polyaniline, poly (p-phenylenevinylene), or polythiophene, the exchange of single and double bonds in the polymer spine leads to different energy circuits and electrons transfer through the spine. Polyaniline is a standard polymer based on phenylene with a group of chemical variants—NH in a polymer chain with each side with a phenylene ring. The protonation, deprotonation and various other physico-chemical properties of polyaniline are due to the presence of this group -NH-. Compared to electrical conductivity

S. A. Khapre (✉) · R. Biradar · S. Deshpande

Department of Engineering Physics, Dr. D.Y. Patil Institute of Technology Pimpri, Pune 411018, India

and polyaniline reaction product, polished by four different oxidizing agents and at different aniline/oxidant ratios. These authors conclude that the redox power of the oxidizing agent is not a prominent parameter in the chemical synthesis of aniline; most oxidizing agents have given similar results. Abd Razak et al. [4] studied the structure and properties of active polyaniline compounds. He studied the cost of compounding, Composite melt viscosity and frequency. They have a large number of applications such as LED display, solid phase control unit, sensors, transducer, optical storage, plastic batteries etc.

Nagarajan et al. [5] studied poly block copolymers (ethylene glycol) (PEG) containing various vinyl monomers acrylonitrile (AN), acryl amide (AAm), methyl methacrylate (MMA) and Methacrylic acid (MAA) is synthesized using Ce^{4+} -PEG and Mn^{3+} -PEG redox system in an acidic liquid environment. He found that the formation of block copolymers confirmed chemical experiments and fractional precipitation, as well as FT-IR, 1H & ^{13}C FT-NMR spectroscopy. The triblock type is established by the cracking of the ether connection of the PEG components.

Chunhui Yang et al. [6] prepared Polyaniline/ Fe^3O_4 nanoparticle composite by polymerizing aniline in the presence of Fe^3O_4 nanoparticles in the use of H_2O_2 as an oxidant. The polymerization was monitored by visible spectroscopy to absorb ultraviolet absorption. The microstructure structure of the composite exposed by electron transfer microscopy. The resulting cellular polyaniline cell structure was investigated by both Fourier transform infrared spectroscopy and X-ray photoelectron spectroscopy, while the magnetic properties of the compound were detected by vibration of the sample magnetometer. The current study focuses on the investigation of ionic and electronic performance and dc electrical conductivity of PANI-PEO-LiCl films. The Wagner polarization method is a simple and well-known method for estimating the number of polymeric film transfer. The transfer number provides details of the size of the ionic and electronic contribution level for full performance [7].

2 Materials

The aniline monomer was A.R. The grade reagent obtained from M/S S.D. Good Chem. (India). The chemical ammonium persulfate $[(NH_4)_2S_2O_8]$ was recovered from M/S LobaChemie India and used as such. Acid i.e., hydrochloric acid is a concentrated solution found in M/S SD Good Chem. (India). PEO (polyethylene oxide) acquired by Merck company. Solvents NMP (1-methyl 2-pyrrolidone) water mixed with methanol used after purification, LiCl was received from M/S LobaChemie India and used as such.

Table 1 Weight percentage of PANI-PEO-LiCl

Percentage (%)	Polyaniline (PANI)	Polyethylene oxide (PEO)	Li-salt (LiCl)
3	0.1879	1.9	0.064574
5	0.1879	1.9	0.109889
7	0.1879	1.9	0.157154
9	0.1879	1.9	0.206496
11	0.1879	1.9	0.26398

2.1 Preparation of Samples

Polyaniline was synthesized in a normal wetland environment using HCl-like acid as a dopant ion and oxidizing agent ammonium persulfate ($(\text{NH}_4)_2\text{S}_2\text{O}_8$), as a precursor. Aniline monomer, acid dopant and oxidizing agent were taken in a molecular ratio of 1: 1: 1.1. Hydrochloric acid was taken from refined water where aniline monomer was added and stirred to obtain an aniline-acid complex stored in a freezer component to obtain a reaction temperature of 0–5 °C. In another beaker $(\text{NH}_4)_2\text{S}_2\text{O}_8$ was dissolved in distilled water and stored in a portion cold. After both solutions received the heat of the reaction, they were mixed together and stored for six hours for the reaction. Polyaniline powder is filtered, rinsed thoroughly with water to remove excess salt and dried under a machine (10 –3 torr) for 24 h to reduce moisture. Sreejith [8] PANI, PEO and LiCl were added to NMP (1-methyl 2-pyrrolidone) which was stirred for 30 min [9]. Films containing PANI, PEO and LiCl (Lithium chloride) were obtained by freezing the mixture at 75 for 24 h. Film included in Teflon sheet. To make it easier to remove the film. Only in this case Li-salt varies and PANI and PEO remain constant. Shown in Table 1 no.

2.2 Transference Numbers

The transference number gives quantitative information for the total conductivity of the ionic and electronic contributions. Ionic/electronic transition numbers ($t_{\text{ion}}/t_{\text{e}}$) are measured by Wagner and Wagner 1957 using DC polarization methods. A polymer electrolyte is sandwiched between a blocking (graphite) and a non-blocking electrode (silver). A constant DC potential (1 V) with the polarity shown is applied throughout the sample. Current in a circuit is measured as a function of time. A specific current versus time plot is obtained.

2.3 Dc Conductivity Measurement

The dc conductivity of the samples is measured in the form of two probes, where the sample resistance is measured. The sample under test was a sandwich between the two electrodes of the sample holder. A constant dc voltage was applied to the sample and the current correlation was noted. Ohm's law provides resistance to samples. Some objections are listed as,

$$\rho = \frac{RA}{t} \quad (1)$$

where, ρ = resistivity of the sample, A = cross-sectional area, R = resistance of the sample, t = thickness, σ = conductivity of the sample.

3 Results and Discussion

3.1 Transferecenumbers

The number of ionic transference is limited to every wt% of the LiCl PANI-PEO-LiCl mixture by Wagner's polarization process using electrode blocking. Figure 1a–e shows the current variation as a time function. The current value represents both ionic current (I_{on}) and electric current (i_e). The ionic transfer number was obtained using the standard formula.

$$t_{ion} = (i_t - i_e)/i_t \quad (2)$$

The total current performance is approximately three hours indicating that the mobile ions in the PANI-PEO-LiCl compound, given the external dc power, are completely separated. Ionic transfer numbers for all samples were found in the range 0.952–0.973 from the observations it is clear that the PANI-PEO-LiCl combination shows ionic conductivity. Estimated values of the composite films are listed in Table 2. From the table, it is clear that the ionic transfer rate increases and decreases after 9 wt% of LiCl i.e. 7 wt% of LiCl has a higher transfer rate and higher conductivity which has already been reported in DC conductivity.

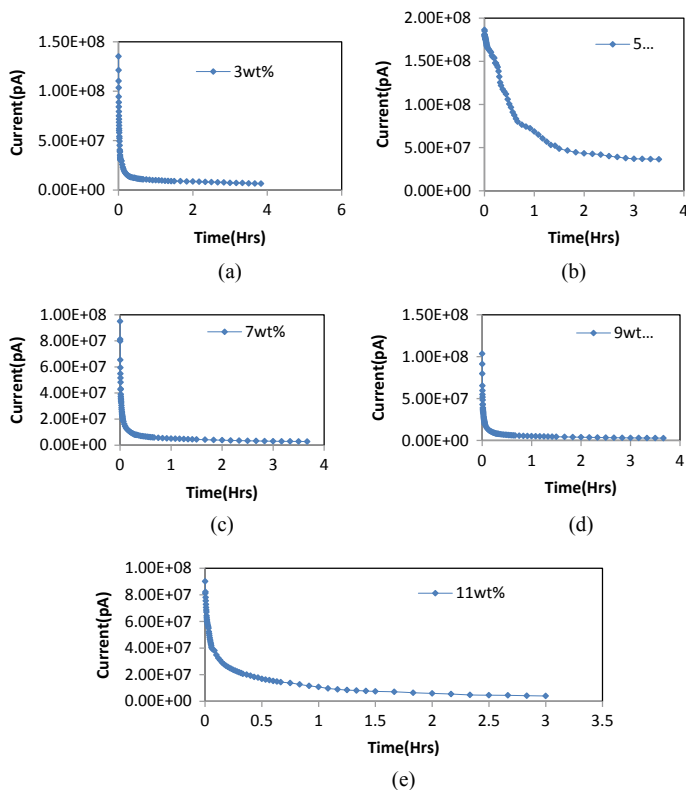


Fig. 1 Current variation as a time function of **a** 3 wt% **b** 5 Wt% **c** 7 wt% **d** 9 wt% **e** 11 wt% of the PANI-PEO-LiCl combination

Table 2 Ionic transference number for the PANI-PEO-LiClblend

wt % of LiClfor PANI-PEO- LiCl blend (Wt%)	Ionic transference no	Electronic transference no
	t_{ion}	t_{elec}
3	0.952	0.0478
5	0.804	0.1951
7	0.97	0.0294
9	0.973	0.0266
11	0.955	0.0445

3.2 DC Behavior

Variation of dc electrical conductivity by temperature ($\log \sigma$ Vs $1/T$) of all PANI-PEO-LiCl films combined at a temperature range of 308–333 K is shown in Fig. 2. As the temperature increases the electrical conductivity of these films increases indicating

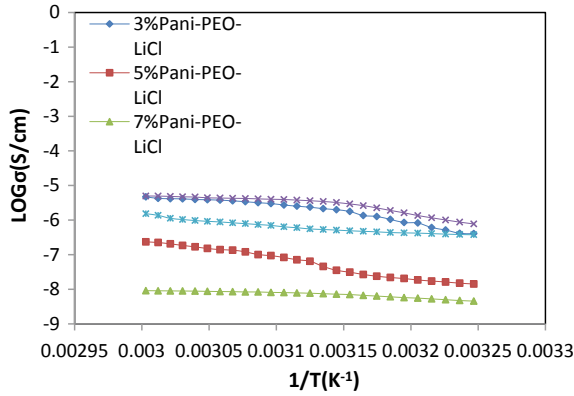


Fig. 2 Temperature dependence of dc electrical conductivity of PANI- PEO- LiCl composite film of different wt %

negative thermal resistance (NTC) resistance. This shows the nature of the films. The polymer becomes more comfortable with the movement of most of the chains as the temperature rises. In addition to this the rotation of the side groups becomes easier. The position of $\log \rho$ against $1/T$ in the case of PANI-PEO- LiClwt% indicates that ρ in this region indicates an active character in relation to the relationship.

$$\sigma = \sigma_0 \exp(-\Delta E / KT) \tag{3}$$

where ΔE is the operational force, K is Boltzmann’s consistent and σ_0 -pre-exposure feature including charge flow and state stability.

Jeon et al. [10] showed that ionic conductivity was improved almost equally in relation to rising temperatures despite the slight curvature of the zones. They also explained that as the temperature rises, the polymer release rate increases and thus free volume is produced.

Figure 3 shows the conductivity of the PANI-PEO- LiClblend with a different concentration. With the addition of lithium salt (LiCl) the ionic conductivity of the polymer film increases. High efficiency is achieved with the addition of 9 wt% of

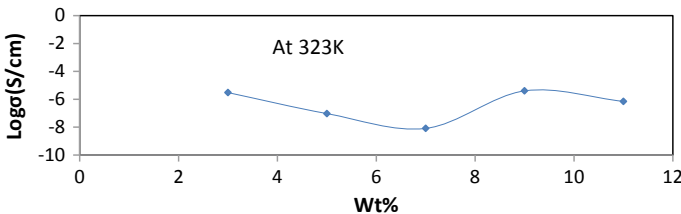


Fig. 3 Variation of $\text{Log}\sigma(\text{S/cm})$ with LiCl wt% concentration for PANI-PEO-LiClblend at 323 K

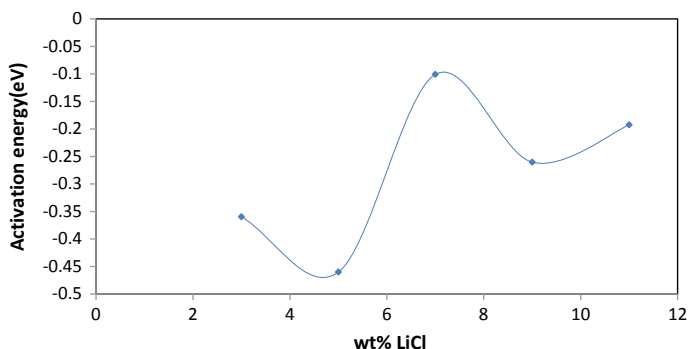


Fig. 4 Variation of activation energy for D.C. electrical conductivity with LiClwt% concentration for PANI-PEO- LiClblend

Table 3 Activation energy and pre-exponential factor for the PANI-PEO- LiCl blend

wt % of LiCl for PANI-PEO- LiCl blend (Wt%)	Activation energy, E_a (eV)	Pre-exponential factor, σ_0
3	0.3597	3084.053
5	0.46014	31,257.042
7	0.10085	0.01374
9	0.2604	81.9410
11	0.19255	3.20913

PANI-PEO- LiCl gives a conductivity values $4.00464 \times 10^{-06} \text{Scm}^{-1}$. An additional increase in LiCl causes a decrease in conductivity due to high salt concentration, a decrease in mobility may be due to the increasing influence of ion pair, ion triplets, and high ion aggregation, reduce overall mobility and level of freedom.

Figure 4 shows the variation in activation energy through the concentration of LiCl. The values of activation energy and pre-exponential factor are calculated from the Arrhenius structure using the $\sigma = \sigma_0 \text{Exp}(-E_a/kT)$ relationship. Summarized in Table 3 it can be seen that 9 wt% LiCl included samples with high dc power and low E_a .

4 Conclusion

PANI-PEO- LiCl composite film prepared using different concentrations of LiCl shows ionic conductivity. The Theionic transference number for all samples was found in the range of 0.952–0.973. The electrical conductivity of all PANI-PEO-LiClcomposite films is calculated at a temperature range of 308–333 K by measuring sample resistance. The electrical conductivity of these films increases with increasing

temperature, indicating negative temperature coefficient (NTC) of resistance. This shows the semiconducting nature of the films. Activation energy values are calculated from $\log \sigma$ vs $1/T$ plots and are found to be in the range 0.10085–0.46014.

References

1. Epstein AJ, Ginder JM, Zuo F, Bigelow RW, Woo H, Tanner DB, Richter AF, Huang W, MacDiarmid GA (1987) Insulator-to-metal transition in polyaniline effect of protonation in emeraldine. *Synth Met* 303–309
2. Heeger A (2001) Semiconducting and metallic polymers: the fourth generation of polymeric materials. *J Ger Chem Soc* 2591–2611
3. Rahman M, Kumar A, Su-Park D, Shim Y (2008) Electrochemical sensors based on organic conjugated polymers. *Sensors* 8:118–141
4. Abd Razak SI et al (2013) Polyaniline and their conductive polymer blends: a short review. *Malays J Fundam Appl Sci* 9(2):74–80
5. Nagarajan S, Sudhakar S, Srinivasan KSV (1998) Poly(ethylene glycol) block copolymers by redox process: Kinetics, synthesis and characterization. *Pure Appl Chem* 70(6):1245–1248
6. Yang C, Du J, Peng Q, Qiao R, Chen W, Xu C, Shuai Z, Gao M (2009) Polyaniline/ Fe_3O_4 nanoparticle composite: synthesis and reaction mechanism. *J Phys Chem* 113:5052–5058
7. Wagner JB, Wagner C (1957) Electrical conductivity measurements on cuprous halides. *J Chem Phys* 26:1597
8. Sreejith V (2004) Structure and properties of processible conductive polyaniline blends. *Polymer science and engineering chemical engineering Division NCL, Pune* 1–267
9. Zhang X-W et al (2002) Composite doped emeraldine–polyethylene oxide-bonded lithium-ion nano-tin anodes with electronic–ionic mixed conduction. *Center for electrochemical systems and hydrogen research*, pp 843–3402.
10. Jeon JD, Kwak SY, Cho BW (2005) The effects of ceramic fillers on PMMA-based polymer electrolyte salted with lithium triflate, LiCF_3SO_3 . *J Electrochem Soc* 152–1583

Functionalization of Graft Copolymers of Poly (Ethyl Acrylate) and Cellulose by Post Polymer Reactions to Develop Reactive Metal Ion Sorbents



Suresh Kumar

Abstract In present work an attempt has been made to synthesize polymeric stationary phase for metal ion sorption by polymer analogous reactions by post reacting the graft copolymers. Cellulose was graft copolymerized with EAc [hereafter called Cell-g-poly (EAc)] by redox initiation method using Ce^{+4} ions following the earlier reported scheme at the optimum grafting conditions worked out for grafting of Acrylonitrile (AN) onto Hydroxyethyl cellulose(HEC). The graft copolymer was further functionalized by post reacting it to poly (hydroxamic acid) [cell-g-poly (CONHOH)] to generate chelating (-CONHOH) groups for metal ion sorption. Functionalization was achieved by refluxing known weight of grafted sample with 20% $NH_2O^-K^+$ in distilled methanol (50 mL) for 6 h at 60–70 °C followed by the equilibration of product with 0.5 N HCl. Functionalized graft copolymer was characterized by Elemental analysis and FT-IR to establish the qualitative and quantitative aspects of polymer conversion. Since functionalization was never upto 100% the resultant polymer was a copolymer of parent and functionalized polymer [cell-g-poly (EAc-co-CONHOH)]. An attempt was also made to report the sorption behaviour of some metal ions like Fe^{+3} , Co^{+2} , Cu^{+2} , Ca^{+2} and Mg^{+2} on candidate polymer in order to explore selectivity in metal ion sorption. Effect of structural aspects of the functionalized graft copolymer on sorption behaviour was also investigated to define its end uses in more specific way.

Keywords Graft copolymer · Post polymer reaction · Sorption · Functionalization

1 Introduction

Functionalization of graft copolymers by post polymer reactions is another technique to affect their properties in a marked manner to obtain polymeric materials with wide spectrum of end uses. Novel reactive polymers can thus be synthesized by simple reactions as substitutions, hydrolysis and also by co-grafting of two or more

S. Kumar (✉)

Associate Professor, Department of Chemistry, Government P. G. College Una, Una 174303, Himachal Pradesh, India

monomers simultaneously from the monomer mixture in the grafting system and these polymers can be used as polymer supports with functional groups attached to perform specific functions as catalysts, reagents and polymer substrate and are often referred as functional or reactive polymers. In polymer analogous reactions the polymer reacts in similar manner as its simple low molecular weight analogue as reactivity is independent of molecular size, however, the reaction rate and yield may be low. In present study an attempt has been made to synthesise polymeric immobile phase for separation, enrichment and purification of metal ions by way of polymer analogous or post polymer reactions. Cellulose was graft copolymerized with EAc [hereafter called Cell-g-poly (EAc)] following the earlier reported scheme [1] and graft copolymer was further functionalized to poly (hydroxamic acid) [cell-g-poly (CONHOH)] to generate reactive (-CONHOH) groups for metal ion sorption [2]. Functionalization was carried out by refluxing known weight of grafted sample with 20% $\text{NH}_2\text{O}^- \text{K}^+$ in distilled methanol (50 mL) in 250 mL round bottom flask for 6 h at 60–70 °C [3]. Functionalized product was then equilibrated with 0.5 N HCl to substitute K^+ for H^+ ions. Functionalized graft copolymer was characterized by Elemental analysis and FT-IR to establish the qualitative and quantitative aspects of polymer conversion. Since functionalization was never upto 100% the resultant polymer became a co-polymer of parent and functionalized polymer [cell-g-poly (EAc-co-CONHOH)]. An attempt was also made to report the sorption behaviour of some metal ions like Fe^{+3} , Co^{+2} , Cu^{+2} , Ca^{+2} and Mg^{+2} on candidate polymer in order to establish trend in metal ion sorption. Effect of structural aspects of the functionalization of graft copolymer on sorption was also investigated.

2 Experimental

2.1 Materials

Hydroxylamine hydrochloride, potassium hydroxide (S.D., Fine), methanol and hydrochloric acid (Merck), copper sulphate, cobaltous chloride, calcium chloride, magnesium chloride and ferric chloride (all analytical grades, CDH, Mumbai) were used as they received. Known weights of Cellulose (Merck, Germany), its graft copolymer [cell-g-poly (EAc)] and functionalized co-polymer [cell-g-poly (EAc-co-CONHOH)] were taken for metal ion sorption studies.

2.2 Methods

2.2.1 Synthesis of Cell-g-poly (EAc-co-CONHOH)

Cell-g-poly (EAc) was functionalized to cell-g-poly (EAc-co-NHOH) by the following procedure. Potassium salt of hydroxyl amine (NH_2OK) was prepared using an earlier reported scheme. Hydroxylamine hydrochloride (69.5 g) was dissolved in hot distilled methanol (300.0 mL) with constant stirring. Potassium hydroxide (113 g) was also dissolved in hot distilled methanol (400.0 mL) in separate vessel. Two solutions were mixed and kept overnight to ensure complete precipitation of potassium chloride. The product thus obtained contains 20% NH_2OK in methanol and it was filtered and used as such. Cell-g-poly(EAc) (1 g, $P_g = 64.6$) was taken in 50 mL methanol in 250 mL round bottom flask to it was added 20% NH_2OK (20 mL). The reaction flask was refluxed at 60–70 °C for 6 h with occasional shaking. The product thus obtained was filtered and washed with methanol followed by distilled water to remove any traces of unreacted NH_2OK . The functionalized polymer was then equilibrated with 0.5 N hydrochloric acid to replace potassium ions by hydrogen ions. Equilibrated product was again washed with distilled water, and dried at 40 °C in an air oven [2].

2.2.2 Characterization of Polymers

Cellulose, its graft copolymer and functionalised copolymer were characterized by FT-IR spectroscopy using KBR pallets on RKIN ELMER spectrophotometer. Grafted and functionalized polymers were also analysed for nitrogen content (recorded on Carlo Erba EA-1108) to quantify the extent of polymer conversion.

2.2.3 Sorption of Metal Ions by Cellulose, Cell-g-poly (EAc) and Cell-g-poly (EAc-co-CONHOH)

Metal ion sorption has been thoroughly investigated on hydrogels of cellulose modified with various acrylamides for sorption of Cr^{+6} , Cu^{+2} and Fe^{+2} ions [4–8]. Some cellulose graft copolymers with acrylates modified to poly (hydroxamic acid) have been successfully used for recovery or removal of heavy metal ions in aqueous phase [9–14]. In present study Sorption of metal ion was carried by immersing a known weight of polymer in 50 mL aqueous solution of known concentration of each ion for 24 h. Amount of metal ion incorporated onto the polymer was obtained from standard calibration curve that was plotted between the optical density and concentration of ion, recorded on Elico Colorimeter. Aqueous solutions of known concentrations of copper sulphate (Cu^{+2} ions), cobaltous chloride (Co^{+2} ions) and ferric chloride (Fe^{+3} ions) were prepared. To obtain a standard calibration curve different known concentrations of each ion were made and optical density at each concentration

was recorded by selecting a suitable filter. A graph was then plotted between optical density and concentration. A known weight of polymer (100 mg) was then immersed for 24 h in 50 mL solution of each ion, the resulting solution was filtered and optical density of filtrate of each was recorded at the selected filters. The concentration of rejected ion was then obtained from the calibration curve. Amount of metal ion retained by polymer was calculated by subtracting the concentration of rejected ion from its original value. The amounts of Ca^{+2} and Mg^{+2} ions were obtained by titrimetric method using standard solutions of EDTA. The percent metal ion uptake was expressed as [5]:

$$P_u = \frac{\text{Amount of metal ion in feed (mg)} - \text{amount of metal ion rejected(mg)}}{\text{Amount of metal ion in feed (mg)}} \times 100$$

3 Results and Discussions

In polymer analogous reactions the polymer reacts in similar manner as its low molecular weight analogue without affecting its chain length. The reactivity of functional group is independent of molecular size but reaction rates and extent of conversion observed in polymer reactions differ significantly from the corresponding low molecular weight analogue. Reaction rates and their yields in polymer reactions may be low due to many factors, viz low accessibility of reacting species, crystallinity, and electrostatic and neighbouring effects. Since the reaction in polymer is not up to 100% so the resultant polymer becomes a co polymer of the parent polymer that is reacted and the polymer that is obtained after the analogous reaction.

3.1 Synthesis of Cell-g-poly (EAc-co-CONHOH)

In present study, the ester group ($-\text{COOC}_2\text{H}_5$) of EAc in cell-g-poly (EAc) was partly converted to hydroxamic acid function($-\text{CONHOH}$) after the synthesis, and the graft copolymer became cell-g-poly(EAc-co-CONHOH) i.e., on the cellulose now two monomers were incorporated, one by grafting and the other was by way of nucleophilic substitution from the N: of NH_2OK that was later changed to $-\text{NHOH}$ with HCl. Substitution of $-\text{OC}_2\text{H}_5$ by $-\text{NHOH}$ results in weight loss that was observed in present case as well. Quantification of polymer conversion done on the basis of %N analysis revealed 15.8 percent mole conversion.

Table 1 Elemental analysis of graft and functionalized co-polymers

Polymer	P _g	Obs		
		%C	%H	%N
Cell-g-poly(EAc)	64.6	49.49	7.10	0.40
Cell-g-poly(EAc-co-CONHOH)	–	25.9	6.38	1.26

Obs. = observed.

3.2 Characterization of Polymers by Elemental Analysis and FT-IR

3.2.1 Elemental Analysis of Cell-g-poly (EAc) and Cell-g-poly (EAc-co-CONHOH)

The graft copolymers of Cell-g-poly(EAc) have been analysed for C,H and N content from which 49.49% C,7.10% H and 0.40% N have been found in the polymer. The observed N in the grafted polymer was due to the incorporation of initiator, ACN and the same was carried to the functionalized graft copolymer. The %N observed in functionalized polymer i.e., cell-g-poly (EAc-co-CONHOH) was 1.26 (Table 1).The increase in %N from 0.4 to 1.26 was due to partial conversion of ester moiety in cell-g-poly (EAc) to nitrogen containing -CONHOH group. The increase of 0.86% N was corresponding to incorporation of 0.03685 g or 0.614×10^{-3} mol of poly(-CONHOH) which were obtained from 0.062 g or 0.614×10^{-3} mol of poly(EAc), thus out of 0.392 g or 0.00388 mol of poly(EAc) available per gram of cell-g-poly(EAc) [P_g = 64.6], only 0.614×10^{-3} mol were converted to -poly (-CONHOH) affording 15.8% conversion. Since the polymer conversion was only up to 15.8% so the resultant polymer was a co polymer of EAc and hydroxamic acid i.e., cell-g-poly (EAc-co-CONHOH). Mole percent conversion correlated to %N is reported in Table 2.

3.2.2 FT-IR Analysis

FT-IR spectra of cellulose, cell-g-poly (EAc) and functionalized cell-g-poly (EAc-co-CONHOH) are given in Figs. 1, 2 and 3 respectively and results are presented in Table 3. FT-IR spectra of cellulose exhibited prominent peaks around 3345.1 cm^{-1} , 2899.9 cm^{-1} , 1403.4 cm^{-1} , 1373.4 cm^{-1} , 1318.2 cm^{-1} , 1281.7 cm^{-1} , 1113.3 cm^{-1} , 1059.5 cm^{-1} corresponding to O–H, C–H stretching O–H bending and C–O–C stretching respectively. In FT-IR spectrum of cell-g-poly(EAc), in addition to the peaks due to stretching and bending of cellulose functionalities, a sharp peak at 1735.2 cm^{-1} due to C = O stretching of ester groups provides evidence of grafting of ethyl acrylate on cellulose. Besides, other base peaks due to cellulose, FT-IR spectrum of cell-g-poly (EAc-co-CONHOH) exhibited broad peaks in the region 1654.2 cm^{-1} and 1563.8 cm^{-1} , and a reduced peak at 1735.2 cm^{-1} . The peaks in the

Table 2 Elemental analysis and conversion percent of poly (EAc) graft copolymers

Polymer	Obs. %N	Weight of poly(EAc) (g)	Moles of poly(EAc)	Moles of poly(EAc)	Weight of poly(CONHOH) (g)	Moles of poly(CONHOH)	%C
Cell-g-poly (EAc)	0.4	0.392		0.0038	-	-	15.8
Cell-g-poly (CONHOH)	1.26	-			0.03685	0.614×10^{-3}	

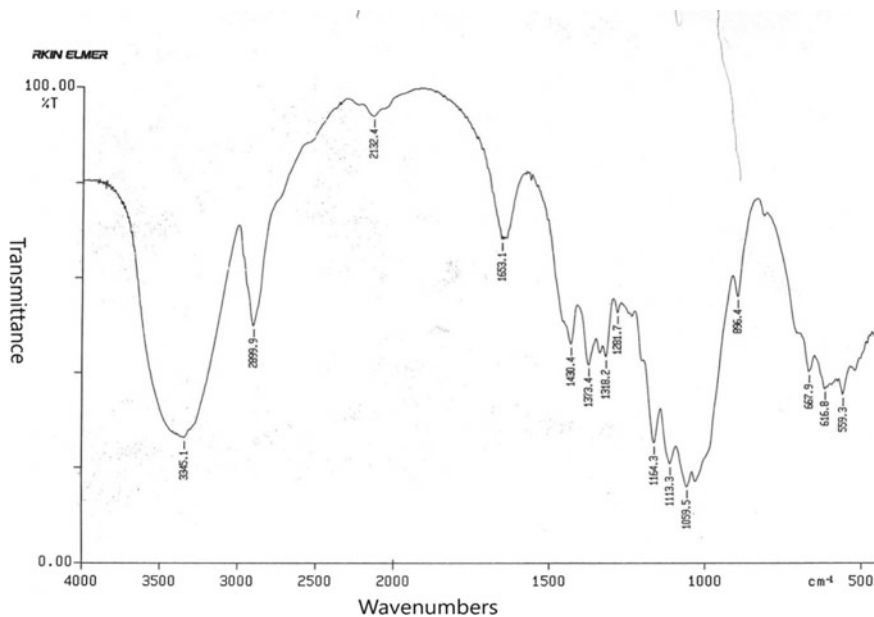


Fig.1 FT-IR spectrum of cellulose

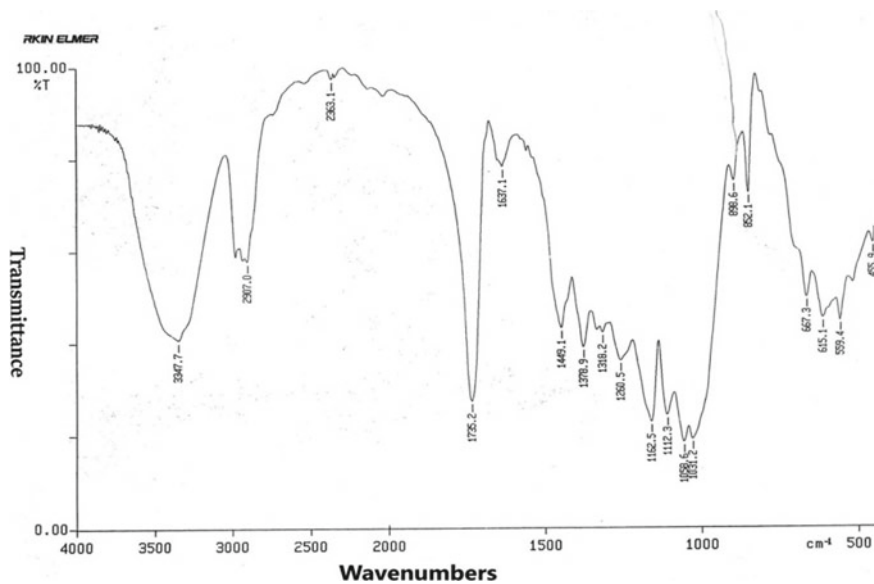


Fig.2 FT-IR spectrum of cell-g-poly (EAc)

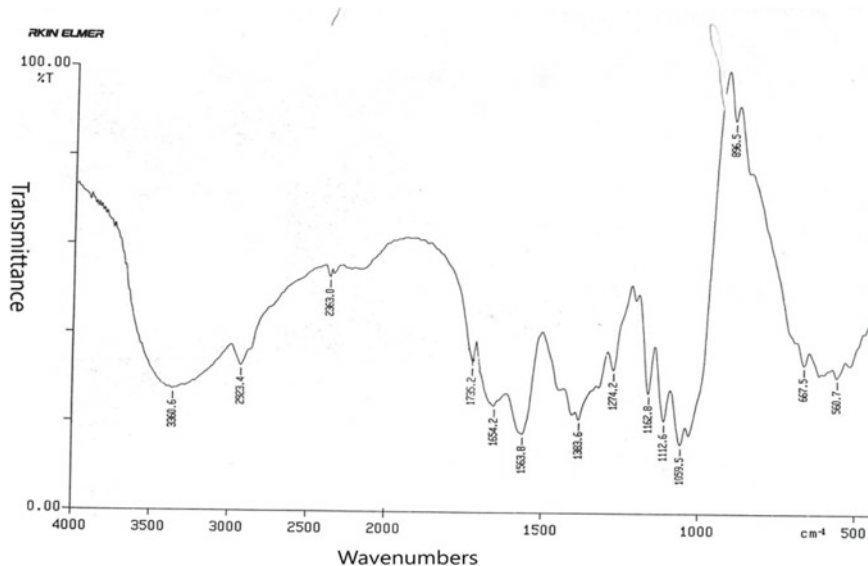


Fig. 3 FT-IR spectrum of cell-g-poly (EAc-co-CONHOH)

Table 3 FTIR analysis of cellulose, cell-g-poly (EAc) and cell-g-poly (EAc-co-CONHOH)

P _g	Vibration frequencies (cm ⁻¹)		
	OH Str	C–O–C Str. /OH Ben	C = O/C = N Str
<i>Cellulose</i>			
–	3345.1	1059.5, 1113.3, 1164.3 1281.7, 1318.2 1373.4, 1430.4	–
<i>Cell-g-poly(EAc)</i>			
64.6	3347.7	1058.6, 1112.3, 1162.5 1260.5, 1318.2 1378.9, 1449.1	1735.2
<i>Cell-g-poly(EAc-co-CONHOH)</i>			
–	3360.6	1059.5 1112.6, 1162.8, 1274.2, 1383.6	^a 1664.2 ^b 1735.2 ^c 1563.8

Str. = Stretching, Ben. = Bending, ^a = C = O str. of CONHOH, ^b = C = O str. of ester, ^c = C = N Str. of C = NH-OH

region 1654.2 cm⁻¹ and 1563.8 cm⁻¹ are characteristics of C = O/C = N stretching and N–H and O–H bending vibrations of –CONHOH and its tautomeric –C = NOH group. The peak at 1735.2 cm⁻¹ was ascribed to C = O stretching of ester moiety.

Thus from FT-IR spectra it can be further inferred that post functionalization of cell-g-poly (EAc) to generate poly (-CONHOH) is partial and the resulting polymer is a copolymer of functionalized and parent graft copolymer on the cellulose backbone.

3.3 Metal Ion Sorption by Cell-g-poly (EAc-co-CONHOH)

Sorption is a common term to express the nature of metal ion uptake by ion exchange, chelation and adsorption on targeted groups, and in the bulk of polymer. Metal ions are effectively distributed between polymer and solution phase and retention capacity of polymer is tremendously affected by affinity of the polymer backbone and monomer for a particular metal ion, and also by hydrophilic/hydrophobic balance of the polymer. Incorporation of unique metal ion active groups like -CONHOH on grafted polymer by post polymer reactions is expected to enhance metal ion uptake. In case of cell-g-poly(EAc-co-CONHOH), 100 mg of sample when charged with metal ions feed: $\text{Ca}^{+2} = 97.4$ mg, $\text{Mg}^{+2} = 64.8$ mg, $\text{Cu}^{+2} = 63.5$ mg, $\text{Co}^{+2} = 60$ mg and $\text{Fe}^{+3} = 56$ mg, afforded metal ion uptake: $\text{Ca}^{+2} = 19.9$ m g, $\text{Mg}^{+2} = 16.8$ mg, $\text{Cu}^{+2} = 28.2$ mg, $\text{Co}^{+2} = 17$ mg and $\text{Fe}^{+3} = 21$ mg. The percent ion uptake, P_u was found to be: $\text{Ca}^{+2} = 20.43$, $\text{Mg}^{+2} = 25.92$, $\text{Cu}^{+2} = 37.48$, $\text{Co}^{+2} 28.33$ and $\text{Fe}^{+3} = 37.5$. Thus the following order of selectivity in metal ion binding onto functionalized polymer was established: $\text{Fe}^{+3} = \text{Cu}^{+2} > \text{Mg}^{+2} > \text{Ca}^{+2}$. The trend in sorption (P_u) of these ions onto cellulose was observed as: $\text{Mg}^{+2} > \text{Ca}^{+2} > \text{Fe}^{+3} = \text{Co}^{+2} > \text{Cu}^{+2}$. As reported earlier the grafting of hydrophobic monomers like acrylates lowered metal ion sorption relative to cellulose [2], whereas functionalization of later by post polymer reaction to generate desired -CONHOH groups had markedly enhanced the metal ion uptake. Thus structure of polymer backbone, its modification by grafting and functionalization by post reactions affected the metal ion sorption behaviour appreciably that can be viewed from the percent ion uptake of functionalized graft copolymer relative to cellulose. Results of metal ion sorption are presented in Table 4.

4 Conclusions

On the basis of evidences collected from FT-IR and Elemental analysis studies it can be concluded that functionalization of Ethyl acrylate based graft copolymers of cellulose by post polymer reaction was successful, however, the extent of polymer conversion was low as expected. Polymer conversion up to 15.8% as achieved in present case was quite significant to modify the properties of the grafted polymer to impart the targeted metal ion sorption behaviour. The resultant polymer was a noble combination of two functional groups on the cellulose backbone as if two monomers with diverse properties were grafted onto it. Further, from the results of

Table 4 Sorption of metal ions by cellulose and cell-g-poly (EAc-co-CONHOH)

Metal ion	Metal ion in feed (mg)	Metal ion rejected (mg)	Metal ion sorbed (mg)	P _u
Cell-g-poly (EAc-co-CONHOH)				
Ca ⁺²	97.4	77.5	19.9	20.43
Mg ⁺²	64.8	48.0	16.8	25.92
Cu ⁺²	63.5	39.7	23.8	37.48
Co ⁺²	60.0	43.0	17.0	28.33
Fe ⁺³	56.0	35.0	21.0	37.5
Cellulose				
Ca ⁺²	97.4	87.0	10.0	10.67
Mg ⁺²	64.8	56.0	8.8	13.50
Cu ⁺²	63.5	61.0	2.5	3.90
Co ⁺²	60.0	54.5	5.5	9.10
Fe ⁺³	56.0	50.9	5.1	9.10

metal ion sorption it can be concluded that sorption of metal ions has been significantly increased in the functionalized polymer relative to the native cellulose, and in addition to other ions Fe⁺³ and Cu⁺² ions have been sorbed in substantial amounts. These polymers therefore can serve as good materials for water based technologies.

References

1. Chauhan GS, Singh B, Kumar S (2004) *J Polym Mater* 21:89–98
2. Chauhan GS, Singh B, Kumar S, Chinkara A (2005) *Polym Polym Compos* 13(5):467–478
3. Chauhan GS, Singh B, Kumar S (2005) *J Appl Polym Sci* 98:373–382
4. Chauhan GS, Kumar S, Verma M, Sharma R (2005) *Polym Polym Compos* 13(1)
5. Chauhan GS, Mahajan S (2002) *J Appl Polym Sci* 86:468
6. Chauhan GS, Bansal M, Ram B, Kaushik A. (2018) *Int J Biol Macromol* 112:728–736
7. Sharma RK, Kumar R (2019) Functionalized cellulose with hydroxyethyl methacrylate and glycidyl methacrylate for metal ions and dye adsorption applications. *Int J Biol Macromol*. <https://doi.org/10.1016/j.ijbiomac.2019.05.059>
8. Ghanshyam C, Hem SJ, Sunita R, Dharmender K (2020) *Sep Purif Technol* 239:116513
9. Junior OK, Gurgel LVA, de Freitas RP, Gil LF (2009) Adsorption of Cu(II), Cd(II), and Pb(II) from aqueous single metal solutions by mercerized cellulose and mercerized sugarcane bagasse chemically modified with EDTA dianhydride (EDTAD). *Carbohydr Polym*. <https://doi.org/10.1016/j.carbpol.2009.02.016>
10. Zampano G, Bertoldo M, Bronco S (2009) Poly(ethyl acrylate) surface-initiated ATRP grafting from wood pulp cellulose fibers. *Carbohydr Polym*. <https://doi.org/10.1016/j.carbpol.2008.06.005>.
11. Kiani GR, Sheikhloie H, Arsalani N (2011) Heavy metal ion removal from aqueous solutions by functionalized polyacrylonitrile. *Desalination*. <https://doi.org/10.1016/j.desal.2010.11.012>
12. Rahman ML, Sarkar SM, Yusoff MM, Abdullah MH (2015) Efficient removal of transition metal ions using poly(amidoxime) ligand from polymer grafted kenaf cellulose. *RSC Adv*. <https://doi.org/10.1039/c5ra18502e>.

13. Abdel-Raouf MS, Abdul-Raheim ARM (2016) Removal of heavy metals from industrial waste water by biomass-based materials: a review. *J Pollut Eff Control*. <https://doi.org/10.4172/2375-4397.1000180>
14. Jiao C, Zhang Z, Tao J, Zhang D, Chen Y, Lin H (2017) Synthesis of a poly(amidoxime-hydroxamic acid) cellulose derivative and its application in heavy metal ion removal. *RSC Adv*. <https://doi.org/10.1039/c7ra03365f>

Effect of Finishing Chemicals on Fastness Properties in Reactive Dye of Cotton Fabric



Tushar A. Shinde, Sachin M. Munde, Leena N. Patil, K. K. Gupta, and Jitendra Sonawane

Abstract In present research work, cotton fabric was dyed with reactive dye using primary colors like red, green, blue after evaluate the fastness properties of the dyed sample via, fastness to washing, fastness to water, fastness to rubbing were evaluated by standard method. Using the non-formaldehyde based fixing agent in reactive dyes. It is also pointed out that the non-formaldehyde based fixing agent is eco-friendly and meets the environmental norms and all fastness result are good. In continuation after dyeing applying the various concentration of silicone softener and polyethylene softener which increases in tearing and tensile strength.

Keywords Cotton fabric · Reactive dye · Primary color · Fastness properties · Fixing agent · Silicone softener

1 Introduction

The National accreditation board for testing and calibration laboratories (NABL) is an autonomous body under the aegis of department of science and technology, government of India, and is registered under the societies act. Government of India has authoresses NABL as the sole accreditation body for testing and calibration laboratories [1]. In discussion with developments in reactive dyes and methods of dye fixation which involved; (i) major trends (ii) novel chromophores (iii) reactive group chemistry (iv) dyes containing two reactive groups (v) polyfunctional dyes (vi) dyes with improved environmental performance (vii) effects of chemical and physical agencies on dyes [2].

Proper technical evaluation requires the use of technical expert who can assess the laboratories against internationally accepted criteria. These criteria embraced globally in a document called ISO/IEC 17,025. Additional technical requirement for

T. A. Shinde (✉) · K. K. Gupta · J. Sonawane
Centre for Textile Functions, MPSTME, NMIMS University, Shirpur Campus, India

S. M. Munde · L. N. Patil
Department of Engineering Sciences, SOET, Sandip University, Nashik, India
e-mail: leena.patil@sandipuniversity.edu.in

evaluating a laboratory, as per requirement of different technical fields. In conventional reactive dyeing methods is used to dye all ranges of shades that can be obtained with reactive dyes through various dyeing processes on all cellulosic fibres such as cotton, viscose, Tencel and linen. With the economic and ecological merits offered by this process in comparison with other continuous dyeing methods [3]. General requirements for the competence of testing and calibration laboratories, was first issued in 1999 by the International Organization for Standardization (ISO) and the International Electro-technical Commission (IEC). It is the single most important standard for calibration and testing [4]. The Cellulose fibres may be dyed with reactive dyes in the absence of added electrolyte under neutral to slightly acidic conditions provided the fibre is modified to include cationic sites [5]. The manufacture product comparable to international standard, to be customer focused and globally competitive through better quality, latest technology and continuous innovation [6]. In the electrolyte-free reactive dyes which high exhaustion rate and high fixation rate with good build-up properties on cotton. The fastness properties were also very good. The optimal dyeing process of these electrolyte-free dyes for cotton fibre was 60 °C with 20 g/l sodium carbonate [7]. The cationized cotton samples were dyed with different reactive dyes containing various reactive groups. Then the results showed that the wash and dry rubbing fastness of the cationized cotton dyed with different reactive dyes are similar to those of the untreated cotton [8].

The textile substrate and dye molecule, not necessarily should have of homogeneous characteristics to combine with each other. In such case, we require some catalyst to facilitate dyeing action on fabric. Salt plays this crucial role of catalyst. Salt has an extremely high affinity for water [9]. In the chemistry and application of reactive dyes which comprise an enormous subject. This offered one of the two principal reactive groups used in reactive dyes for textile fibres: activated pi-bonds. The other topics were determined by his own particular interests or by a close relationship to the main area. This attempt has also been made to address new developments in reactive dyeing [10]. The dyeing was evaluated through colour measurements and standard wash, light and rub fastness tests. Generally, mordanting process known for many centuries and connected with the textile dyeing resulted in an improvement in dye absorption and fastness properties mainly for the cotton samples, as is concluded from the tests and measurement assessments [11]. The optimization concentration of salt as exhausting agent for reactive dyeing of cotton fabric. The resulting washing fastness and color strength observed this was obtained after dosing of reduced salt concentration simultaneously [12]. In reactive dyeing process E-control dyeing is most ecological and economical process of dyeing which introduced to provide textile dyers to the dyeing system with rapid method for cellulosic fibers with minimum chemical use. In every reactive dyeing of cotton alkali plays an important role which is used as per depth of shade, but the PH of all the reactive dyes is not same so requirement of alkali is also different from dye to dye and also as per shades [13]. In Reactive dyeing process, the fixation of a color yield of dyed cellulosic fiber significantly depends on the rate of dye diffusion extent into the fiber polymer matrix. In the case of pad-drying process dye diffusion exerts more significant influence on dye fixation. Consequently, color yield takes place [14]. A softener's main purpose is

Table 1 Standard test conditioning and parameters

Sr. No	Method	Temp	Humidity (%)	Time (In hours)
1	AATCC	21–23 °C	65–67	04.00
2	ASTM	21–23 °C	65–67	04.00
3	ISO	21–23 °C	65–67	04.00
4	M&S	21–23 °C	65–67	04.00

to improve the aesthetic properties of textiles bearing in mind that terry material is widely used for towels, home textile products, headgears, slippers, children's clothes, hygiene products for babies [15]. Softening is important process in the finishing operations. Softeners have achieved great important in finishing, almost all pieces of textile leaves production are being treated with softeners these softening treatments is to give textiles the required handle to make the next procedure easier and also improve the handling properties, soft handle often for buying a textiles and therefore vital importance for marketing many textiles [16].

Purpose of Testing: (i) To check up quality and durability of fabric, it is directly affected by the quality of fiber. (ii) The purpose of testing is to satisfaction of customer requirement and analysis to make sense of the results. (iii) To eliminate faulty production in future and so provide a better-quality product. Testing is an important part for textile production. (iv) The primary purpose of textile testing and analysis is to assess textile product performance and to use test results to make predictions about product performance. Need of testing: During textiles testing the variation of a fiber or fabric i.e., length, color, fineness, is detected properly. Thus, proper raw materials are selected properly. It is help full for maintained to control increase of waste, rise of cost, we can easily detect the faults of machinery and materials during test of textiles, Process Development, Test of the textiles helps the authority to decide the next route etc. Testing is the process or procedure to determine the quality of a product (Table 1).

2 Material and Method

Material: We used 100% cotton woven fabric (RFD) which was procured by Birla century, Jhagadia, Bharuch, Gujrat.

Machines: Padding machine, Gyro washing machine (James H Heal), Crock Meter (James H Heal), Spectrophotometer Color I- match (version 7.0), and Dyer.

Method: Color fastness to washing: AATCC 61, Color fastness to Rubbing: AATCC -8, Color fastness to Water: AATCC -107, Tensile Strength: ASTM D 5034, and Tear Strength: ASTM D 1424.

Chemicals for Cold Pad Batch Dyeing: Dispersing agent, Resist salt, Wetting agent, Solubility of dyes, and Anti-migrating agent. All chemicals were of analytical grade and used as received without further purification.

Chemicals for E-control Dyeing: Resist salt, Wetting agent, Solubility of dyes, Green acid, Soap and Anti-migrating agent. All chemicals were of analytical grade and used as received without further purification.

3 Result and Discussion

[A] Color fastness to Washing:

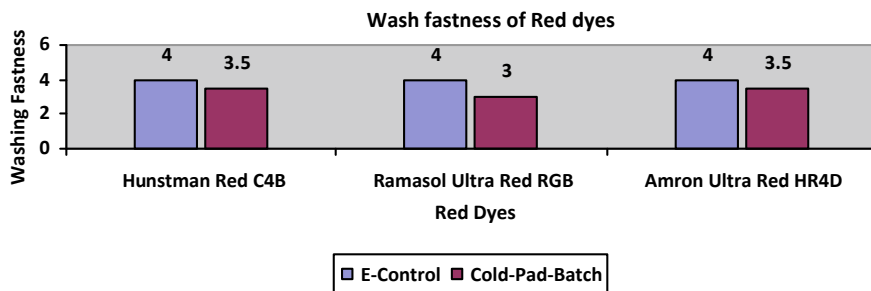
- (1) **Color fastness to Washing in Red Dyes:** To check the washing fastness of E-CONTROL and CPB dyed fabric with Red dyes (Table 2).

Discussion: From the above Graph 1 which shows that the difference in washing fastness properties in E-Control process and Cold-Pad-Batch (CPB) with respect on Red dyes. As on graph we observed that in E-Control process which gives better washing fastness of all threes red dyes compare to Cold-Pad-Batch (CPB). So the E-control process gives better fastness properties than the CPB.

- (2) **Color fastness to Washing in Blue Dyes:** To check the washing fastness of E-CONTROL and CPB dyed fabric with Blue dyes (Table 3).

Table 2 Wash fastness of red dyes

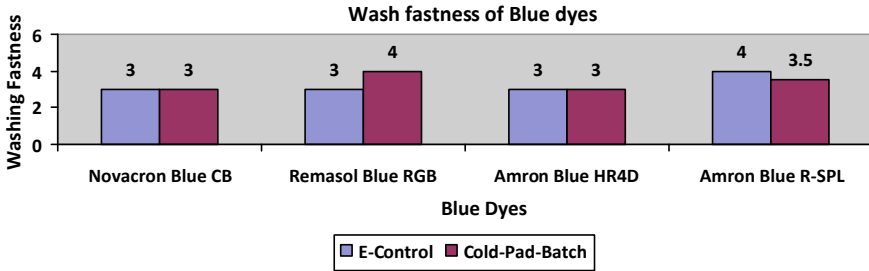
Sr. No	Red dye	E-control	Cold-pad-batch
1	Huntsman red C4B	4	3.5
2	Remasol ultra red RGB	4	3
3	Amron ultra red HR4D	4	3.5



Graph 1 Effect of different dyeing process route on fastness

Table 3 Wash fastness of blue dyes

Sr. No	Blue dye	E-control	Cold-pad-batch
1	Novacron blue CB	3	3
2	Remasol bue RGB	3	4
3	Amron blue HR4D	3	3
4	Amron blue R-SPL	4	3.5



Graph 2 Effect of different dyeing process route on fastness

Discussion: The Graph 2 is concluding that the washing fastness of E-CONTROL machine shows moderate Rating than CPB dyeing. So with the help of E-CONTROL. We can give the proper control for dyeing process with respective to fastness properties concerned.

- (3) **Color fastness to Washing in Yellow Dyes:** To check the washing fastness of E-CONTROL and CPB dyed fabric with Yellow dyes (Table 4).

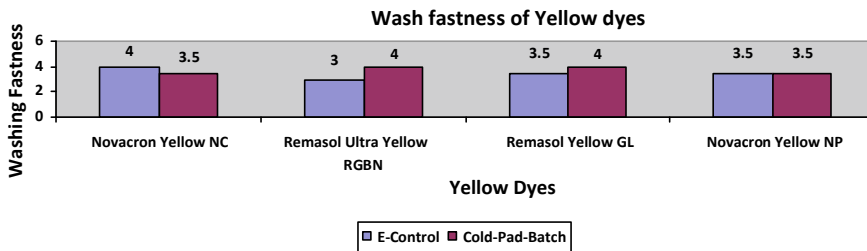
Discussion: The Graph 3 is concluding that the washing fastness of E-CONTROL machine shows moderate Rating than CPB dyeing. With the help of E-CONTROL. We can give the proper control for dyeing process with respective to fastness properties concerned.

[B] **Color Fastness to Rubbing:**

- (1) **To check Rubbing fastness of E-CONTROL and CPB dyed fabric of Red Dye:** Table 5 shows Rubbing fastness of Red dyes.

Table 4 Wash fastness of yellow dyes

Sr. No	Yellow dye	E-control	Cold-pad-batch
1	Novacron yellow NC	4	3.5
2	Remasol ultra yellow RGBN	3	4
3	Remasol yellow GL	3.5	4
4	Novacron yellow NP	3.5	3.5



Graph 3 Effect of different dyeing process route on fastness

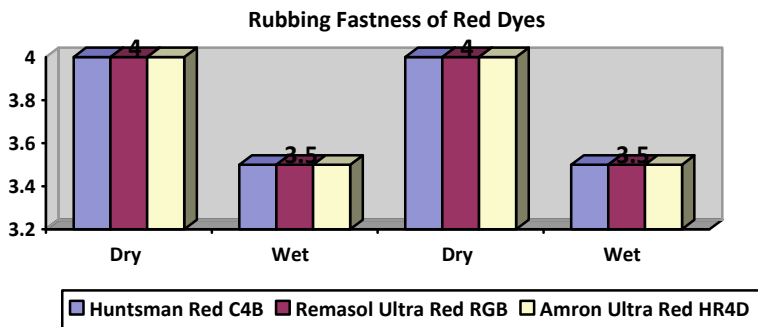
Table 5 Rubbing fastness of red dyes

Sr. No	Red dye	E-control		Cold-pad-batch	
		Dry	Wet	Dry	Wet
1	Huntsman red C4B	4	3.5	4	3.5
2	Remasol ultra red RGB	4	3.5	4	3.5
3	Amron ultra red HR4D	4	3.5	4	3.5

Discussion: The Graph 4 concluded that the Rubbing of Dry and Wet condition of E-CONTROL dyeing is moderate to good rating as well as CPB dyeing so with the help of E-CONTROL. We can give the proper control for dyeing process with respective to fastness properties concerned.

- (2) **To check Rubbing fastness of E-CONTROL and CPB dyed fabric of blue dye:** Table 6 shows Rubbing fastness of Blue dyes.

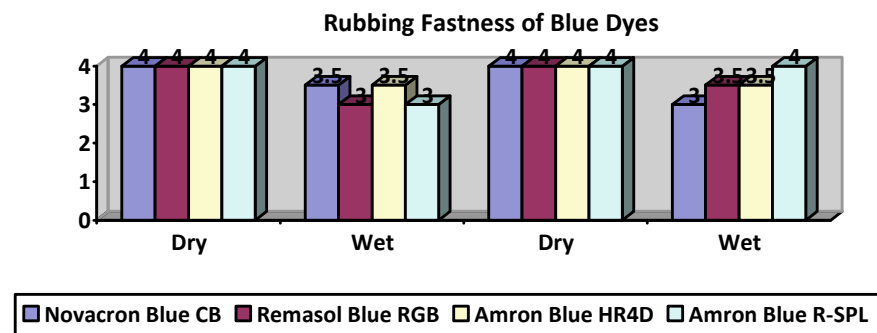
Discussion: The Graph 5 concluded that the Rubbing of Dry and Wet condition of E-CONTROL dyeing is moderate to good rating as well as CPB dyeing. So with the help of E-CONTROL. We can give the proper control for dyeing process with respective to fastness properties concerned.



Graph 4 Effect of Different dyeing process route on fastness

Table 6 Rubbing fastness of blue dyes

Sr. No	Blue dye	E-control		Cold-pad-batch	
		Dry	Wet	Dry	Wet
1	Navacron blue CB	4	3.5	4	3
2	Remasol blue RGB	4	3	4	3.5
3	Amron blue HR4D	4	3.5	4	3.5
4	Amron blue R-SPL	4	3	4	4

**Graph 5** Effect of different dyeing process route on fastness

- (3) **To check Rubbing fastness of E-CONTROL and CPB dyed fabric of yellow dye:** Table 7 shows Rubbing fastness of Yellow dyes

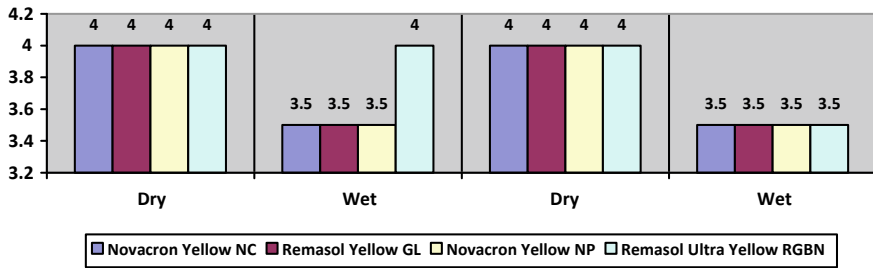
Discussion: The Graph 6 concludes that the Rubbing of Dry and Wet condition of E-CONTROL dyeing is moderate to good rating as well as CPB dyeing. With the help of E-CONTROL. We can give the proper control for dyeing process with respective to fastness properties concerned (Graph 7).

[C] Color Fastness to Water:

- (1) **To check Water fastness of E-CONTROL and CPB dyed fabric of red dye:** Table 8 shows Water fastness of Red dyes.

Table 7 Rubbing fastness of yellow dyes

Sr. No	Yellow dye	E-control		Cold-pad-batch	
		Dry	Wet	Dry	Wet
1	Novacron yellow NC	4	3.5	4	3.5
2	Remasol yellow GL	4	3.5	4	3.5
3	Novacron yellow NP	4	3.5	4	3.5
4	Remasol ultra yellow RGBN	4	4	4	3.5



Graph 6 Effect of different dyeing process route on fastness

Sr. No.	Polyethylene Softener	Before finish	After Finish		
			5 GPL	10GPL	15GPL
		Weft	Weft	Weft	Weft
1.	Ceralube PEPE	15.81	15.90	16.33	17.23
2.	Silone PEM-2	15.81	17.43	16.68	17.25
3.	Ultrafab RTS	15.81	16.29	17.89	16.1

Graph 7 Effect of Softener on Dyed fabric for strength properties

Table 8 Water fastness of red dyes

Sr. No	Red dye	E-control	Cold-pad-batch
1	Huntsman red C4B	4	3.5
2	Remasol ultra red RGB	4	3
3	Amron ultra red HR4D	4	3.5

Discussion: The graph is concluding that the color fastness to water of CPB machine is show moderate rating and E-CONTROL machine shows good rating. With the help of E-CONTROL. We can give the proper control for dyeing process with respective to fastness properties concerned.

(2) **To check Water fastness of E-CONTROL and CPB dyed fabric of blue dyes:** Table 9 shows water fastness of blue dyes.

Table 9 Water fastness of blue dyes

Sr. No	Blue dye	E-control	Cold-pad-batch
1	Novacron blue CB	3	3
2	Remasol blue RGB	3	3
3	Amron blue HR4D	3	3
4	Amron blue R-SPL	4	3.5

Table 10 Water fastness of yellow dyes

Sr. No	Yellow dye	E-control	Cold-pad-batch
1	Novacron yellow NC	4	3.5
2	Remasol yellow GL	4	3.5
3	Novacron yellow NP	3.5	3.5
4	Remasol ultra yellow RGBN	3.5	3.5

Discussion: The graph is concluding that the color fastness to water of CPB machine is show moderate rating and E-CONTROL machine shows good rating. With the help of E-CONTROL. We can give the proper control for dyeing process with respective to fastness properties concerned.

- (3) **To check Water fastness of E-CONTROL and CPB dyed fabric of Yellow dyes:** Table 10 shows water fastness of Yellow dyes.

Discussion: The graph is concluding that the color fastness to water of CPB machine is show moderate rating and E-CONTROL machine shows good rating. With the help of E-CONTROL. We can give the proper control for dyeing process with respective to fastness properties concerned.

[D] **To Check Tensile Strength:**

- (1) **To check the Tensile Strength of E-CONTROL and CPB dyed fabric using Silicon Softener:** Table 11 shows Tensile strength of silicone softener in various concentrations.

Discussion: The graph shows that the application of various concentrations of silicon softener decrease the tensile strength of fabric. It may be due to action of softener on fiber/fabric surface.

- (2) **To check the Tensile Strength of E-CONTROL and CPB dyed fabric using Silicon Softener:** Table 12 shows Tensile strength of silicone softener in various concentration.

Table 11 Tensile strength of silicone softener in various concentrations

Sr. No	Silicon softener	Before finish	After finish		
			5 GPL	10GPL	15GPL
		Warp	Warp	Warp	Warp
1	Rucofine SIQ	33.69	32.61	32.24	31.77
2	Hydrosil	33.69	31.76	32.13	32.6
3	Rucofine GSQ	33.69	32.69	30.89	32.45

Table 12 Tensile strength of silicone softener in various concentration

Sr. No	Silicon softener	Before finish	After finish		
			5 GPL	10GPL	15GPL
		Weft	Weft	Weft	Weft
1	Rucofine SIQ	15.81	14.13	14.84	13.47
2	Hydrosil	15.81	13.7	14.52	14.63
3	Rucofine GSQ	15.81	14.82	13.75	13.58

Discussion: The graph shows that the application of various concentrations of silicon softener decrease the tensile strength of fabric. It may be due to action of softener on fiber/fabric surface.

- (3) **To check the Tensile Strength of E-CONTROL and CPB dyed fabric using Polyethylene Softener:** Table 13 shows Tensile strength of Polyethylene softener in various concentrations.

Discussion: The graph shows that the application of various concentrations of silicon softener increase the tensile strength of fabric. It may be due to action of softener on fiber/fabric surface.

See Table 14.

Discussion: The graph is shows that the applying of various concentrations of silicon softeners hence increase the tensile strength of fabric. Due to compact of fiber or coating of fabric. It may be due to action of softener on fiber/fabric surface.

Table 13 Tensile strength of polyethylene softener in various concentrations

Sr. No	Polyethylene softener	Before finish	After finish		
			5 GPL	10GPL	15GPL
		Warp	Warp	Warp	Warp
1	Ceralube PEPE	33.69	34.14	33.98	35.87
2	Silone PEM-2	33.69	33.52	34.35	35.25
3	Ultrafab RTS	33.69	35.89	34.09	34.11

Table 14 Tensile strength of polyethylene softener in various concentration

Sr. No	Polyethylene Softener	Before finish	After finish		
			5 GPL	10 GPL	15 GPL
		Weft	Weft	Weft	Weft
1	Ceralube PEPE	15.81	15.90	16.33	17.23
2	Silone PEM-2	15.81	17.43	16.68	17.25
3	Ultrafab RTS	15.81	16.29	17.89	16.1

Table 15 Effect of concentration of silicon softener on tearing strength of fabric

Sr. No	Silicon softener	Before finish	After finish		
			5 GPL	10 GPL	15 GPL
		Warp	Warp	Warp	Warp
1	Rucofine SIQ	817	1163	1043	1123
2	Hydrosil	817	1016	1097	1156
3	Rucofine GSQ	817	1116	1163	1083

[E] To Check Tear Strength:

- (1) **To check the Tear Strength of E-CONTROL and CPB dyed fabric using Silicon Softener of warp wise:** (Table 15).

Discussion: The graph is shows that the applying of various concentrations of silicon softeners hence increase the tear strength of fabric. Due to compact of fiber or coating of fabric. It may be due to action of softener on fiber/fabric surface.

- (2) **To check the Tear Strength of E-CONTROL and CPB dyed fabric using Silicon Softener of weft wise:** (Table 16).

Discussion: The graph is shows that the applying of various concentrations of silicon softeners hence increase the tear strength of fabric. Due to compact of fiber or coating of fabric. It may be due to action of softener on fiber/fabric surface.

- (3) **To check the Tensile Strength of E-CONTROL and CPB dyed fabric using Polyethylene Softener using warp wise:** (Table 17).

Discussion: The graph is shows that the applying of various concentrations of silicon softeners hence increase the tear strength of fabric due to compact of fiber or coating of Fabric. It may be due to action of softener on fiber/fabric surface.

- (4) **To check the Tensile Strength of E-CONTROL and CPB dyed fabric using Polyethylene Softener using weft wise:** (Table 18).

Discussion: The graph is shows that the applying of various concentrations of silicon softeners hence increases the tear strength of fabric due to compact of fiber or coating of Fabric. It may be due to action of softener on fiber/fabric surface.

Table 16 Tear strength of silicone softener in various concentrations

Sr. No	Silicon softener	Before finish	After finish		
			5 GPL	10 GPL	15 GPL
		Weft	Weft	Weft	Weft
1	Rucofine SIQ	754	1016	969	996
2	Hydrosil	754	1023	962	900
3	Rucofine GSQ	754	1110	982	1003

Table 17 Tear strength of polyethylene softener in various concentration

Sr. No	Polyethylene softener	Before finish	After finish		
			5 GPL	10 GPL	15 GPL
		Warp	Warp	Warp	Warp
1	Ceralube PEPE	817	928	893	982
2	Silone PEM-2	817	1016	982	1009
3	Ultrafab RTS	817	900	838	893

Table 18 Tear strength of polyethylene softener in various concentrations

Sr. No	Polyethylene softener	Before finish	After finish		
			5 GPL	10 GPL	15 GPL
		Weft	Weft	Weft	Weft
1	Ceralube PEPE	754	825	811	818
2	Silone PEM-2	754	989	845	859
3	Ultrafab RTS	754	858	831	817

4 Conclusion

From the above experimental data, we conclude that the red, green and blue color are the primary color. The dyeing process with using two different dyeing techniques viz. cold pad batch and E-control. The dyed sample of E-control technique gives good fastness properties comparatively with cold pad batch dyeing. In continuation of after dyeing process the fabric passes at finishing stage, the silicon softener and polyethylene softener is applied on the fabric sample in various concentration then evaluate the effect on tensile and tearing strength. When polyethylene softener is applied on fabric then tearing and tensile is increases due to binding of fiber. In another hand silicon softener is used then tensile strength is decreases due to slippage of fabric is observed. From the study we observed that in light shade is obtained 1–15 gpl, medium shade is 15–40 and dark shade is obtained 40–60 in concentration.

References

1. Vickerstaff T (1957) Reactive dyes for textiles. *J Soc Dye Color* 73(6):237–245
2. Taylor JA (2000) Recent developments in reactive dyes. *Rev Prog Color Relat Top* 30:93–108
3. Shinde BBT, Raichurkar P (2018) An assessment of pad-dry-pad-steam, E-control and cold-pad-batch-dyeing processes. *Asian Dyer* 15(4):47–50
4. Zhang S et al (2015) Continuous dyeing of cationized cotton with reactive dyes. *Color Technol* 121(4):183–186
5. Lewis DM, Lei XP (1991) New methods for improving the dyeability of cellulose fibres with reactive dyes. *J Soc Dyers Colour* 107(3):102–109

6. Blackburn RS, Burkinshaw SM (2002) A greener approach to cotton dyeing's with excellent wash fastness. *Green Chem* 4(1):47–52
7. Zheng C et al (2012) Dyeing properties of novel electrolyte-free reactive dyes on cotton fibre. *Color Technol* 128(3):204–207
8. Montazer M, Malek MRA, Rahimi A (2007) Salt free reactive dyeing of cationized cotton. *Fibers Polym* 8.6:608–612 (9. E Bohnert - The remasol linkage journal of the Society of Dyers and Colourists-1959)
9. Shinde TA, Patil LN, Patil R, Nadiger VG, Raichurkar PP (2020) Effect of Glauber salt on PDPS Dyeing. *Asian Dyer* 16:58–60
10. Renfrew A, Hunter M (1999) Reactive dyes for textile fibres. *Soc Dye Colour* 169
11. Zarkogianni M et al (2011) Colour and fastness of natural dyes: revival of traditional dyeing techniques. *Color Technol* 127(1):18–27
12. Swati k, Tushar S, Pramod R (2018) To optimize exhaustion and maximize fixation of reactive dyes. *Colourage* 37–42
13. Dhobi S et al (2018) To study the effect of alkali concentrations on E-control dyeing. *Colourage* 35–42
14. Mali H, Shinde TA, Rajput TA, Chandurkar P, Kolte P, Raichurkar PP (2019) Optimization of dye migration property in pad-dry process. *Man-Made Textiles India* 47(6)
15. Shinde TA., Dhangar Y, Patil LN, Patil SP (2020). To study the effect of finishing chemicals on physical and chemical properties in terry towel. *Man-Made Textiles India* 48(5)
16. Chavan PR, Shinde TA, Daberao AM, Dr PP, Raichurkar RS (2018) Effects of finishing chemicals on shade. *Int Dyer* 4(5):44–47

Village Level Information System in South Solapur Tahsil Using Geoinformatics Approach, Maharashtra, India



Prashant L. Unhale, D. D. Kulkarni, and R. S. Pawar

Abstract Village information system (VIS) is a geographical information system (GIS) based application, which provides detailed information pertaining to demography, Infrastructure and natural resource for every village, district and state. It displays geo-referenced maps of virtually any political boundary in India from village to a district, a state or the entire country. Users can create, query and print their own map through interactive maps. They can also download readymade thematic map. Any one visiting a village for the first time wants to first hand information about location of village, approach to the village, general idea about the topography of the village, its Population and available facilities, name of the government functionaries, etc.

Keywords Village information system · Geographical information system · Application · Solapur · etc.

1 Introduction

In Solapur district total 11 Talukas and south Solapur is one of them. There are 91 villages in Solapur South Taluka as per the Census of India in 2011. South Solapur Taluka, with population of about 2.6 lakh is Solapur district's the third least populous sub-district, located in Solapur district of the Maharashtra state in India. Kumbhari is one of the most populous villages with population of about thirty one thousands and Bandalgi is the least populous village with the population of seventy seven thousand. Telgaon Mandrup is one of the biggest villages in the sub-district with an area of about 94 km² and Indiranagar is the smallest with 1 km². Solapur South Taluka has 51,230 households, population of 2, 60,897 of which 1, 34, 206 are males and 1,26,691 are females. The children population in between age 0–6 is 34,842 which are 13.35% of the total population. The sex-ratio of South Solapur Taluka is

P. L. Unhale (✉) · D. D. Kulkarni
Punyashlok Ahilyadevi Holkar Solapur University, Solapur, Maharashtra, India

R. S. Pawar
SVERIs College of Engineering Pandharpur, Solapur, Maharashtra, India

around 944 compared to 929 which is average of state of Maharashtra. The literacy rate of South Solapur Taluka is 63.62% out of which 71.79% Males are literate and 54.96% females are literate. The total area of Solapur South is 1,189.57 Sq. km with population density around 219 per sq.km. There are 13.47% Scheduled Caste (SC) and 4.52% Scheduled Tribe (ST) of total population In South Solapur Taluka [1].

2 Study Area

South Solapur Taluka is located in Solapur district of Maharashtra. The geographical Extension of South Solapur 17° 30' 00" N to 17° 50' 00"N, and latitude to 75° 40' 00" E to 76° 20' 00" E longitudes. There are 91 villages in Solapur South Taluka As per the Census India 2011. South Solapur Tahsil, with population of about 2.6 lakh is Solapur district's the third most populous sub-district, located in Solapur district of the Maharashtra state in India [2, 3] (Fig. 1).

3 Materials and Methods

Data is soul of any system. Any kind of analysis or result mainly depends upon reliability; and accuracy and performance of any information system highly depend on nature and availability of data.

Toposheets: the study area lies in the survey of India (SOI) toposheet no 47O/10, 47O/11, 47O/13, 47O/14, 47O/15, 56C/01, 56C/02, 56C/03 are used for drainage analysis and road network analysis. Attribute data for different types of layer have been collected from toposheet map. field like Name point, Line and polygon i.e. village Name, Drainage line, Road line, Railway Line, post office have been collected in *html format (in Google Earth). Soil data is collected from NBSS.

Database Design for the integrated development as basically two components, i.e. spatial and non-spatial data. The geographical information system (GIS) package is the heart of the data for handling the two sets of data. This study is a standard GIS package is the heart of the data for handling the two set of data in the present study a standard GIS package has been employed as the main tool to design, organization, storage, retrieval, analysis and generation of cartographic output [4].

The geodatabase is the common data storage as well as management framework for Arc GIS. It combine "geo" with "database" to create a central data repository for spatial data storage and management It is the primary mechanism used to organize and use geographic information in Arc GIS The geodatabase contain three primary dataset types: (1) Feature classes (2) Raster datasets (3) tables [5]. The available south Solapur map was encompassed in single sheet, these sheets was then register from SOI Toposheet with the same projection system of topographic map. The toposheet is georegisterd, resample by geographical coordinate system i.e. Everest Modified.prj.

and reproject on WGS1984 complex UTM Zone 43 N projection system. Then digitized the georeference sheet and we get the town /village wise boundary layer of south Solapur taluka. These can be imagined as Dot on a map. The dots may represent anything which is located is one place such as village, town, school place, tourist place, etc. It will immediately be noted that, whether or not a feature can be represented as point, which depends on the scale of the map on which it may be shown.

4 Result and Discussion

In simple words, cropping pattern means the proportion of the area under various Crops at a time. It is a dynamic concept, because of no cropping pattern can be said to be Ideal for all times. It changes, in space and time and is governed largely by the physical as Well as cultural and technological factors. The change in cropping pattern in a particular span of time clearly indicates the changes that have taken place in the agricultural Development. “In most of the situations, the physical environment reduces the choice of the venture, either by prohibiting the growth of certain crops altogether or by reducing their level.” The situations like climate and physiographic are relatively suitable for Cultivation of different crops. The cultivated crops are classified into different categories like cereals, pulses oilseeds, cash crops and vegetables, etc. in Solapur district. In this research work, attempts have been made to study the production of major crops in the area under study. In the recent years, including fallow land more than 60% area is Cultivated under various crops. It shows that there is more scope for cultivation and Agricultural development.

The major crops that are grown in the region under study may be grouped into two categories as below:

1. Food Crops - The food crops include the production of rice, wheat, Jawar, Bajra, Pulses, Sugarcane and other crops.
2. Non Food Crops - The non-food crops include the production of different Crops such as ground nuts, oil seeds (fruits, vegetables etc.).

The Tehsil wise trends during 2000–01 to 2010–11 of cropping pattern under various food grains and non food grain crops of South Solapur tahsil, which is analyzed by the researcher the changes in cropping pattern over time period? The changes in agricultural pattern also depend upon the Traditional practices of the people in a particular region mentioned in Table 1 and Fig. 2.

The religion-wise information of study area is mentioned in Table 2. Hindu's contribute 85% of the total population are the largest religious community in the sub-district followed by Muslims which contributes 14% of the total population. Female Sex ratio per 1000 male in Hindu is 941 and in Muslim is 966.

South Solapur has 46% i.e. about 1.2 lakh population engaged in either main or marginal works are shown in Table 3 and Fig. 3. Working population of male and

Table 1 Changes in agricultural pattern of study area

Crop	Changes in agricultural pattern			
	2000–01	%	2010–11	%
Jawar	72,560	9.98	67,737	10.06
Wheat	5777	12.18	5692	11.76
Bajra	545	1.97	785	3.13
Rice	733	31.3	22	4.63
Maize	141	0.97	1266	4.67
Sugarcane	4685	6.99	3592	5.47
Cotton	180	4.17	38	0.87
Pulses	8422	7.61	5330	7.6
Oil crops	14,596	10.42	4834	8.26
Vegetables	959	6.83	1023	8.36
Fodder crops	321	4.15	1731	8.38

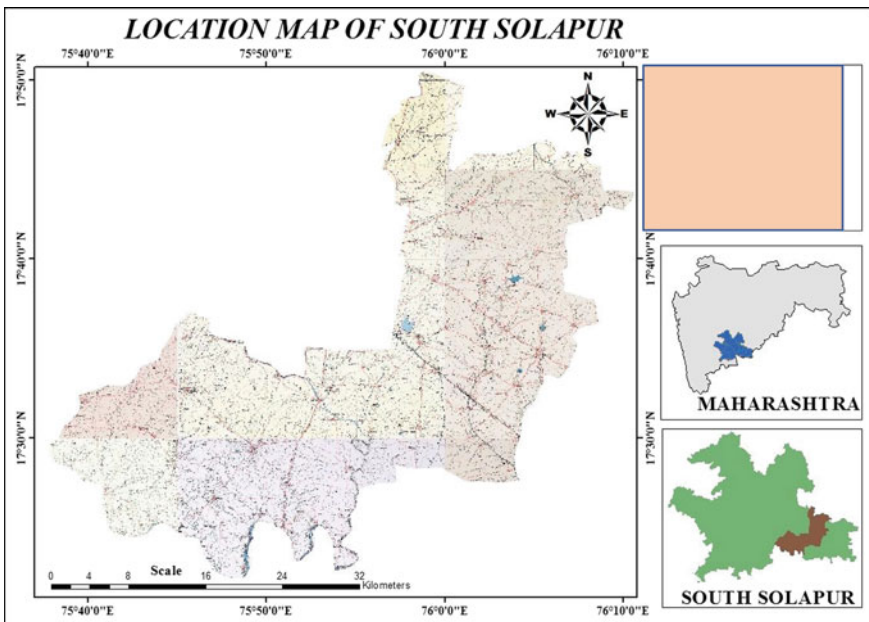


Fig. 1 Location map of the study area

female of study area is 56% and 36% respectively. Full time or main total male population is 53% workers and marginal (part time) workers are 3%.

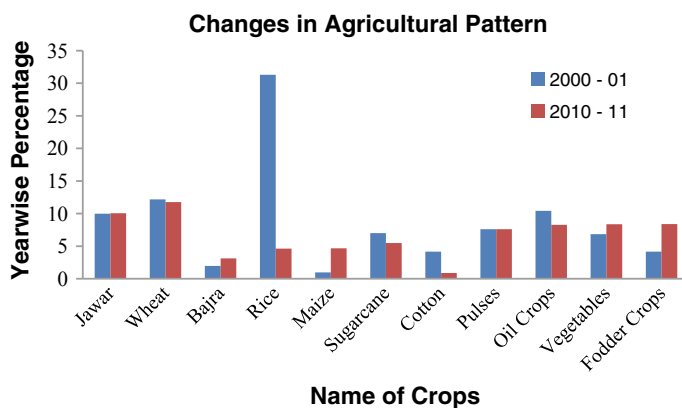


Fig. 2 Graphical representation of changes in agricultural pattern

Table 2 Religion-wise information of study region

Description	Population	Percentage
Hindu	2,22,381	85.24
Muslim	36,042	13.81
Buddhist	1,423	0.55
Jain	398	0.15
Religion not stated	375	0.14
Christian	223	0.09
Sikh	50	0.02
Other religions and persuasions	5	0
Total	2,60,897	100

Table 3 Workers profile of study area

Types of worker	Male	Female	Total
Cultivators	24,243	9153	33,396
Agricultural labours	25,152	22,345	47,497
Household industries	1376	3655	5031
Other workers	20,514	4874	25,388
Marginal workers	3804	6094	9898
Non working	59,117	80,570	1,39,687

4.1 Population Density

Following table shows village name, area of village in number of population information of study region. After observing this data out of total population 2, 60,897 the third least populous sub district, located in Solapur district of the Maharashtra state in

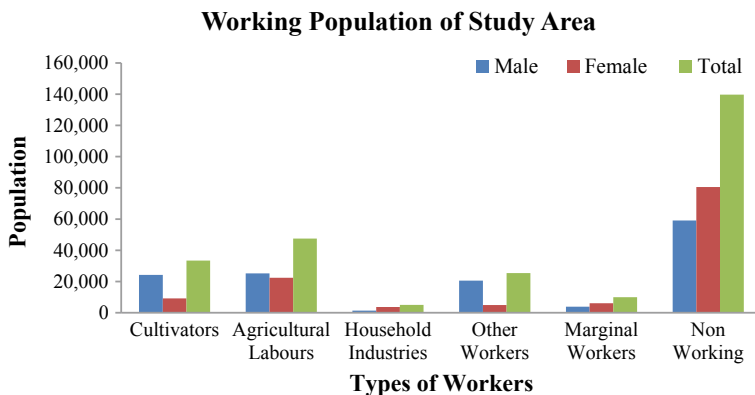


Fig. 3 Graphical representation of workers population of study area

India. There are ninety one villages in the sub-district, among them Kumbhari is the higher populous village with the population of about thirty one thousand and Bandalgi is the less populous village with the population of seventy seven. Telgaon Mandrup is the biggest village in the sub-district with an area of 94 km² and Indiranagar is the smallest with 1 km² [6].

The male population is 1, 34,206 (51.44%) & female population is 1, 26,691 (48.56%) so this tahsil having highest population density in south Solapur (MCI) i.e. -31.7 (Indiranagar) and Lowest population density in -0.11 (Bandalgi) (census of India in 2011) shown in Fig. 4. The total area of Solapur South is 1,189.57sq.km with population density of 219 per sq.km.

4.2 Transportation

The south Solapur is well connected by all the means of transport viz. Airways, Trains and Roadways. Mostly the Rail track and Roadways are used for transport. South Solapur is well connected by Road with major cities of Maharashtra. The National Highways viz. NH-9, NH-13, NH-211 and NH-204 passes through city connected Solapur to other important cities in Maharashtra and other state shows in Fig. 5. There are two Railway Junctions in the district, Kurduwadi and Hotgi. The Solapur division is an important division connecting South India to western and North West India Air Services are considered the fastest means of transport. Solapur Airport is located to the south Solapur city currently it has no scheduled services.

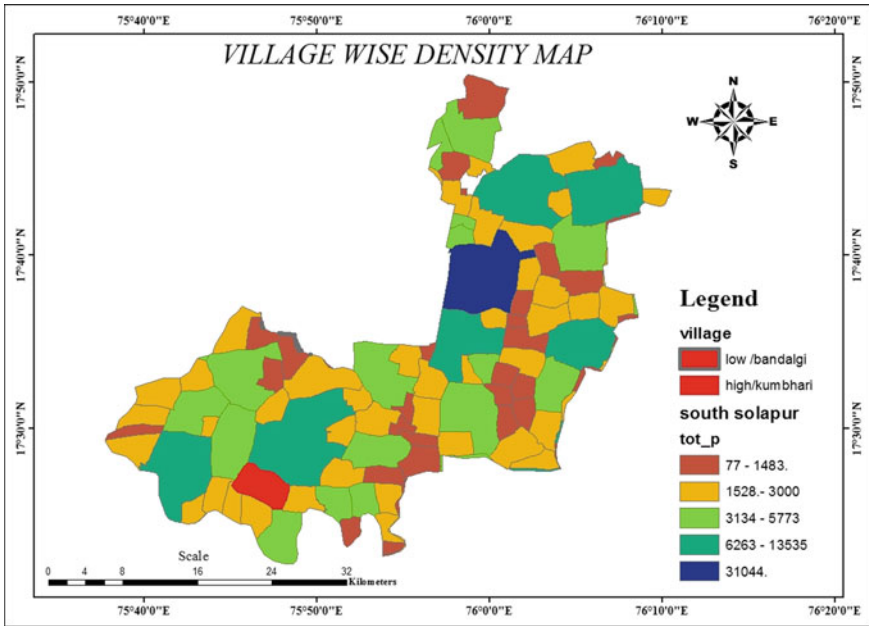


Fig. 4 Village-wise density map of study area

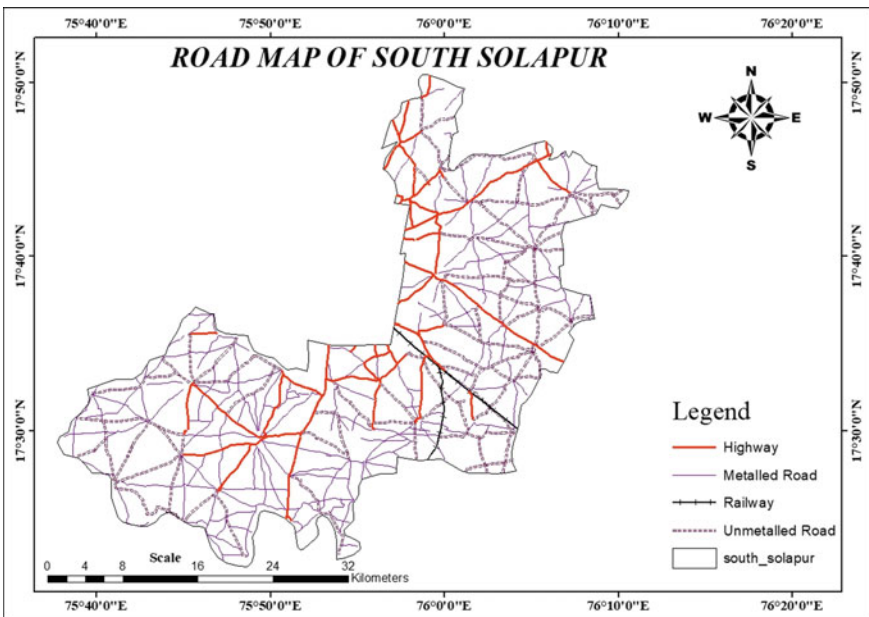


Fig. 5 Road map of study area

4.3 Drainage

The river Bhima drains in the central part of the district, comprises the greater part of Karmala, Madha, Malshiras, Pandharpur, Mangalweda, Mohol and south Solapur tahsils. The river Bhīma is one of the main feeders of river Krishna. The river Bhīma rises from the Bhimashankar plateau in Pune district and runs south east direction and enters into Solapur district near Jinti village of Karmala tahsil and flows through the district of Pune, Ahamadnagar and Solapur in Maharashtra and Bijapur district in Karnataka and it falls into Krishna River about 25 km North of Raichur in Karnataka State. The Bhīma has an overall length of 289 km within the limit of the district of Solapur it has separated Mangalweda tahsil on the right they it turns towards south for about 10 km forming the boundary between south Solapur tahsil shows in Fig. 6. The River Sina rises twenty two kilometer west of Torana in Ahamadnagar district of Maharashtra state and enters the Solapur district near Alijapur village Karmala tahsil. It is largest left bank feeder of the river Bhima. It runs south-east through Ahamadnagar and Solapur district and meets with the river Bhīma near Kudal about 25 km south of Solapur city [7].

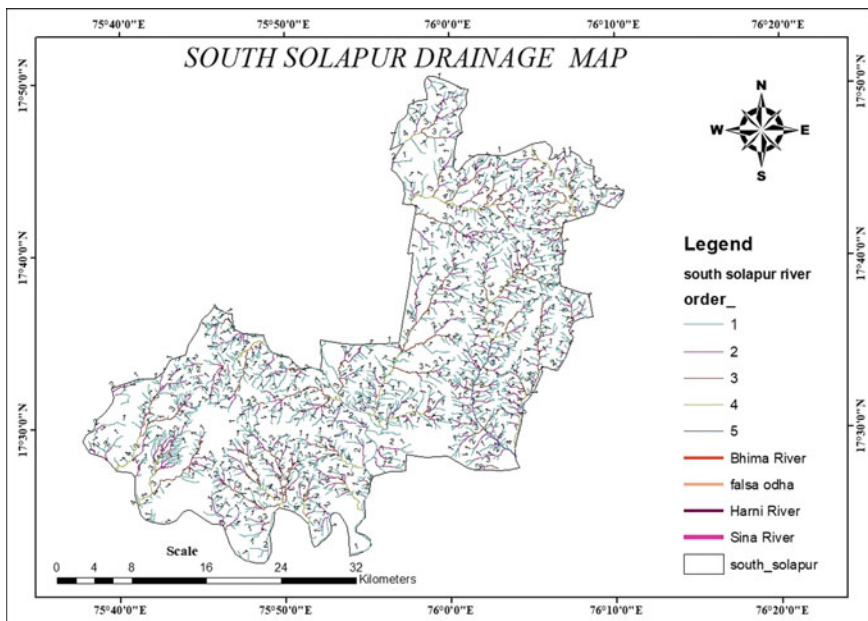


Fig. 6 Drainage map of study area

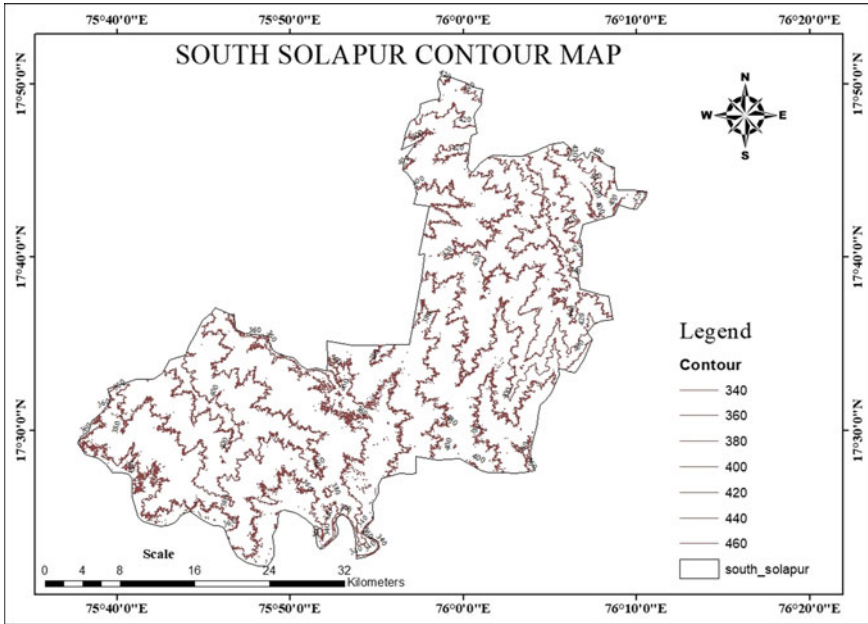


Fig. 7 Contour map of study area

4.4 Contour

Contour lines of functions of two variables are a curve along which the function has a constant value. In cartography, a contour line (contour) joins points of equal elevation. Topographic maps on the other hand do deal with the third y dimension busing contour lines to show elevation changes on the surface of the earth. In Fig. 7 shows lowest contour of 340 m and highest contour ... of 460 m with 20 m contour interval [8].

4.5 Literacy

The literacy rate of Solapur South Taluka is 63.62% out of which 71.79% males are literate and 54.96% females are literate. The lowest literacy of village is a Guardehali (49.36), medium of Ahervadi (63%) and highest is Dargnhali (79.22%) as shown in Fig. 8.

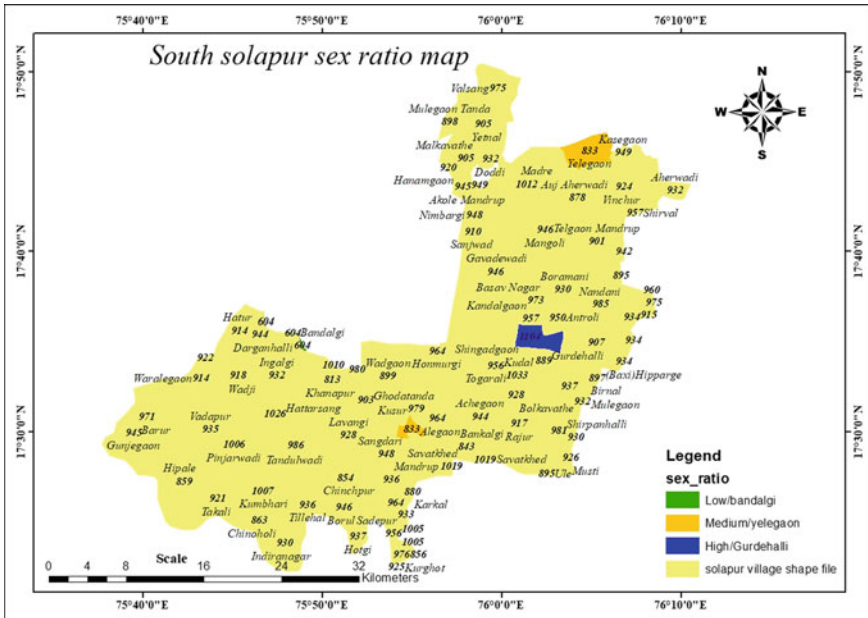


Fig. 9 Sex ratio map of study area

References

1. Purbasthali-I. <https://indikosh.com/subd/335833/purbasthali-I-22>
2. Pawar RS, Panaskar DB (2014) Characterisation of groundwater in relation to domestic and agricultural purposss, Solapur Industrial Belt, Maharashtra, India. J Environ Res Dev (JERAD) 9(01):102–112
3. Panaskar DB, Wagh VM, Pawar RS (2014) Assessment of groundwater quality for suitability of domestic and irrigation from Nanded Tehsil, Maharashtra India. SRTMUs J Sci 3(2):71–83
4. Pawar RS, Unhale PL, Kulkarni DD, Deshpande SM (2017) Remote sensing and GIS application to assess the rainwater harvesting potential in North Solapur Tahsil, Solapur District, Maharashtra. Int J Res Biosci Agric Technol (IJRBAT) V(3):192–195
5. Integrated Regional Water Management Program. <https://inyo-monowater.org/resources/gis/what/>
6. Introduction to Topographic Maps. https://geology.isu.edu/wapi/geostac/Field_Exercise/topomaps/topo_map.html
7. Collins FC, Bolstad PV (2000) A comparison of spatial interpolation techniques in temperature estimation. https://www.ncgia.ucsb.edu/SANTA_FE_CD-ROM/sf_papers/collins_fred/collins.html
8. National Drought Mitigation Center. www.drought.unl.edu/whatis/concept.html

Room Temperature Chemiresistive Properties of polypyrrole/Tin Oxide Hybrid Nanocomposites



R. D. Sakhare, Y. H. Navale, Y. M. Jadhav, R. M. Mulik, and V. B. Patil

Abstract The current research article deals with the study of preparation of polypyrrole-tin oxide (PPy/SnO₂) hybrid nanocomposites, with an addition of SnO₂ from 10 wt% to 50 wt% in PPy matrix by a solid state method, and their nitrogen dioxide (NO₂) sensing activity. The casting solution prepared by dispersing the composite powder in m-cresol solvent was used for obtaining composite films on glass substrate which were characterized for their structures, crystallinities, morphologies, and binding energies with various measurements. Room temperature chemiresistive performance of the hybrid nanocomposite sensors were studied towards ethanol, methanol, hydrogen sulfide, NO₂, ammonia, and chlorine gases. From the tested gases, PPy/SnO₂ (50 wt%) composite sensors demonstrated a highest selectivity towards NO₂ gas (~53% response to 100 ppm) together with reproducibility kinetics. So the studies are focused on same material for better clarity.

Keywords Polypyrrole · Tin oxide · Nanocomposites · Chemiresistive properties

1 Introduction

The improved human life style uses huge amount of fuel consuming equipments as well as the chemicals, pharmaceuticals, and agricultural industries through a large amount of polluting gases in the environment. The generation of electricity from the coal or gases generally produces sulfur dioxide gas which is heavily odor and easily reacts with other substances to form the harmful compounds. Carbon monoxide is basically colorless, odorless and tasteless gas. It is slightly less dense than air and hazardous above 35 ppm concentration. Ammonia is also a colorless gas with characteristic pungent odor having chemical formula NH₃, which is hazardous above 25 ppm. The poisonous chlorine gas causes illness; it can affect the respiratory system causing difficulty to breath and cough. Nitrogen dioxide is a chemical compound with chemical formula NO₂ among the NO_x family, which is biting odor and prominent

R. D. Sakhare · Y. H. Navale · Y. M. Jadhav · R. M. Mulik · V. B. Patil (✉)
Functional Materials Research Laboratory, School of Physical Sciences, Solapur University,
Solapur 413255, MS, India

pollutant. The direct contact of NO_2 with skin causes various irritation and burning problems. For example 10–20 ppm NO_2 gas causes mild irritation of throat and nose, 25–50 ppm NO_2 gas causes edema which leads to bronchitis or pneumonia and the NO_2 above the 100 ppm concentration can plug the death penalty due to asphyxiation from the fluid in lung. The ground level detection and control of a particular gas within its hazardous limit is the challenge in front of researchers. To fulfill this challenge the researchers around the world are continuously engaged in searching the sensor materials which is reproducible, have short response and recovery time values, must be stable for long time, and detect gas below its hazardous concentration at room temperature. Polymeric materials are largely used as gas sensors because of availability of easy, cost-effective and ambient temperature operable synthesis methods and high selectivity. But, performance of polymeric sensors is humidity, temperature and ageing effect dependent. Also the long time stability is a major drawback of polymers; which restrict their uses in gas sensor applications. Metal oxides have also been envisaged for the gas sensing applications but because of their high resistivity, they operate at high temperatures and consume more power compared with polymer-based sensors.

Composite materials, obtained on mixing the conducting polymers with metal oxides, overcome the drawbacks of individual constituents by providing the high surface-to-volume ratio, due to this the rate of reaction with the response of the composite sensor materials increases. The current research article consists of synthesis of composite polypyrrole, from the conducting polymer family and SnO_2 , from the metal oxide family. Polypyrrole, due to its best environmental stability, high conductivity and easy synthesis, has been so far mostly investigated material in research and industry. Since last few decades, it has been used in gas sensors [1], batteries [2], biosensors [3], and nerve tissue engineering scaffold [4]. Tin oxide (SnO_2) is also another promising material in gas sensing applications [5]. Most of the authors have reported SnO_2 as a NO_2 sensor operating at high temperatures [6]. At high temperatures, sensing material degrades and lowers the sensing performance. Also, for an efficient operation of gas sensor at elevated temperatures separate heating assembly is essential; therefore, the use of more power is unavoidable which eventually increases the fabrication cost of gas sensor. The combination of two different materials as a composite leads synergy effect and helps to improve the gas sensing properties such as thermal stability, sensitivity, reproducibility, enhance response and recovery signatures and operate at room temperature. Bandgar et al. prepared PAni/ $\alpha\text{-Fe}_2\text{O}_3$ hybridnanocomposite by solid state synthesis and in-situ polymerization methods [7, 8] where enhanced response, stability, reproducibility and short response and recovery signatures were documented for composites than that of single counterparts.

The work presented in the current paper, i.e. synthesis of PPy/ SnO_2 hybrid nanocomposites, is carried out through solid state synthesis method. Gas sensing characteristics of PPy/ SnO_2 hybrid sensors were measured towards various target gases at room temperature. The prepared PPy/ SnO_2 composite sensor materials showed better responses as compared to individual PPy and SnO_2 sensors. To the best of our knowledge and literature we come across, no reports on the solid state

synthesis of PPy-SnO₂ hybrid nanocomposites and their NO₂ gas sensing applications are reported. Improved gas response, response and recovery time values, stability and reproducibility etc., were obtained and reported, showing synergistic effect of SnO₂ in PPy matrix.

2 Experimental Details

PPy was synthesized by chemical oxidative polymerization of pyrrole using ammonium persulphate as an oxidant [9]. Tin oxide (SnO₂) was synthesized by sol-gel synthesis of stannic chloride hexahydrate using methanol as solvent [10]. The schematic in the Fig. 1 shows the synthesis route used for the preparation of PPy/SnO₂ hybrid nanocomposites. An appropriate amount of (10–50 wt %) of SnO₂ was mixed evenly in to the polypyrrole matrix to form PPy/SnO₂ hybrid nanocomposites [10]. The composite powder was dispersed in m-cresol and drop casted on glass substrate. As-fabricated composites films were used for characterization and gas sensing study.

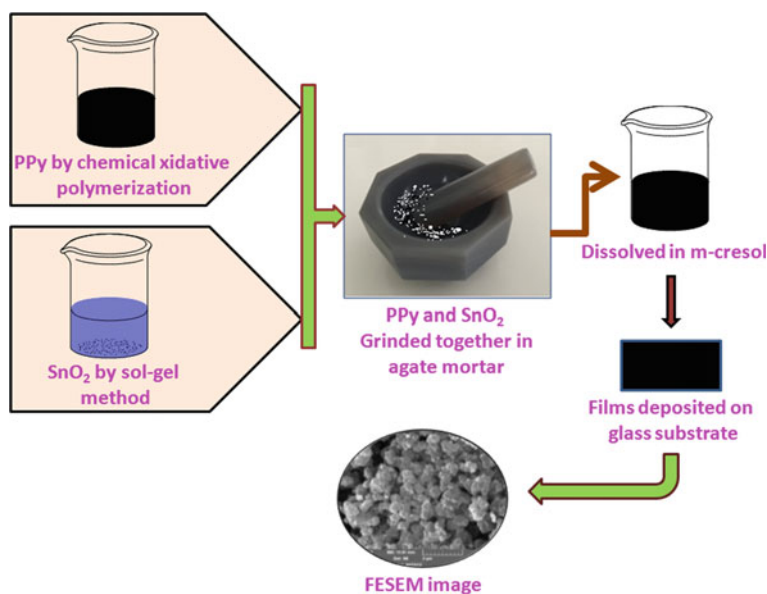


Fig.1 Schematic represents the synthesis route of PPy-SnO₂ nanocomposite sensor films

3 Gas Sensing Measurement

Gas sensing properties were studied using a homemade gas sensor unit interfaced with computer by KEITHLEY 6514 Electrometer. NH₃, NO₂, Ethanol, Methanol, H₂S and Cl₂ gases were purchased from space cryo gases pvt. Ltd. Mumbai. The response was measured in case of change in resistance by injecting NO₂ gas into sensor housing. The response was calculated using the formula,

$$\text{Response S (\%)} = \frac{|R_g - R_a|}{R_a} * 100 \tag{1}$$

where R_g and R_a are resistances of PPy/SnO₂ hybrid nanocomposite sensor in gas and air respectively.

4 Results and Discussion

4.1 Structural, Compositional and Morphological Studies

Figure 2a shows the XRD patterns of PPy/SnO₂ (10–50 wt %) hybrid nanocomposites, indicating amorphous (PPy) and crystalline (SnO₂) phases are combined together. All the observed diffraction peaks are well-indexed to the tetragonal phase of the SnO₂, signifying that the structure of SnO₂ cannot be modified in presence of PPy [9]. The XRD patterns of PPy/SnO₂ hybrid nanocomposite clearly demonstrates a bump of PPy at 2θ = 20–30° range, indicating the mixture of both the phases of

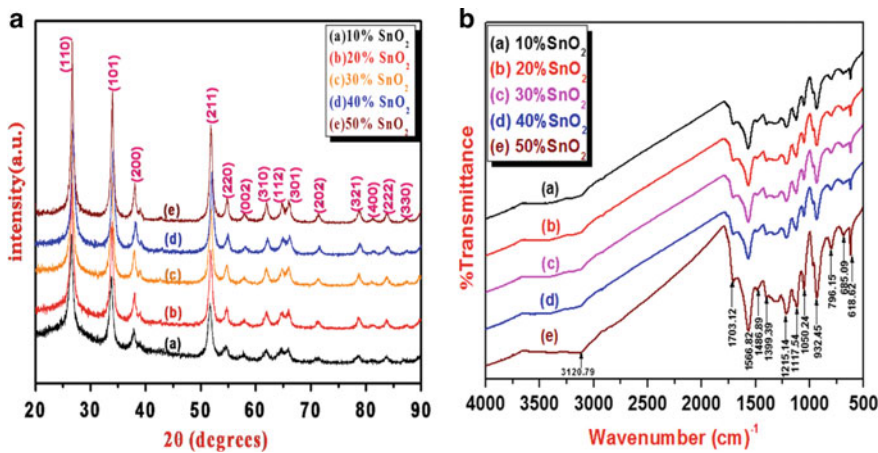


Fig.2 a XRD pattern and b FTIR spectra of PPy/SnO₂ hybrid nanocomposite

amorphous PPy and crystalline SnO₂. The observed broad peak of PPy is found to flattened upon increasing content of SnO₂ from 10 wt% to 50 wt%. To confirm the presence of SnO₂ in the hybrid nanocomposites and to observe its association with PPy, FTIR measurements were carried out and presented in Fig. 2b. The peak observed at 619 cm⁻¹ is due to the antisymmetric and symmetric vibrations of Sn–O–Sn [11]. The peaks positioned at 685 cm⁻¹ and 796 cm⁻¹ are due to the out of plane C–H bending vibrations [12]. The characteristic peaks located at 932 cm⁻¹ and 1050 cm⁻¹ corresponds to the bipolaron in PPy and = C–H in-plane vibration [13–17]. The peak at 1215 cm⁻¹ is the characteristic of the C–N stretching vibration [18]. Whereas, the peaks at 1487 cm⁻¹ and 1567 cm⁻¹ are of PPy [13–17]. All obtained data support for the formation of PPy/SnO₂ composite structures [11–17].

Figure 3a shows the FESEM images of PPy/SnO₂ (50 wt%) hybrid nanocomposite film. FESEM micrographs demonstrate fairly a uniform coverage of composite nanoparticles. The SnO₂ nanoparticles are found to dispersed in PPy matrix. The nanocomposite particles are so close to each other that the separation between them is undistinguishable, indicating the significance of the synthesis method. Several air voids are seen between the crystallites of PPy/SnO₂ nanocomposite film surfaces that can provide high surface-to-volume ratio and more interaction sites for adsorbing

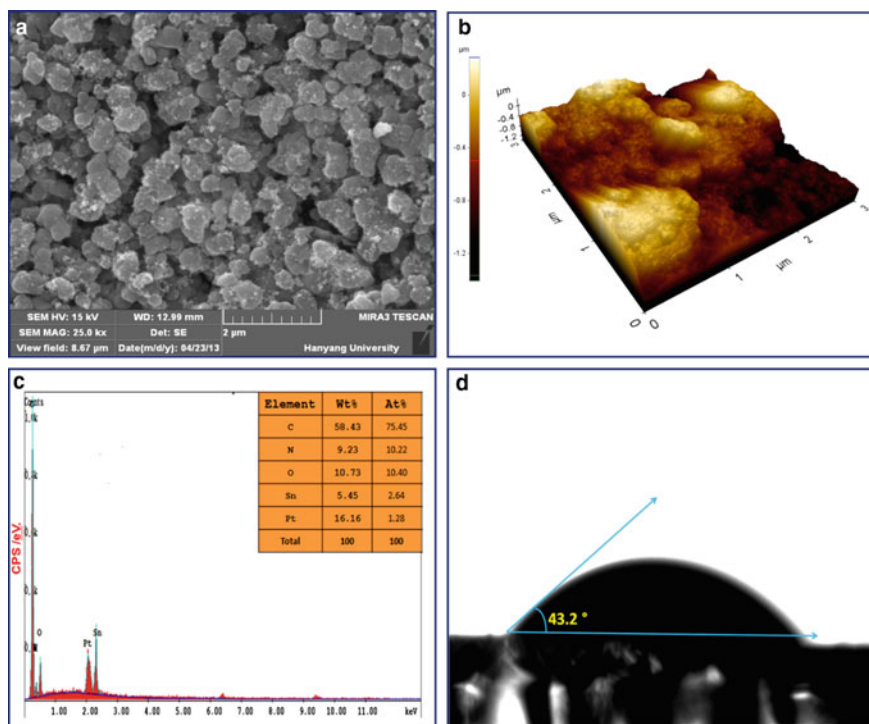


Fig.3 a FESEM image b 3D AFM image, c EDX spectra and d Contact angle of PPy/SnO₂ (50%) nanocomposite

the gas molecules for enhanced performance. Figure 3b present 3D AFM image of representative PPy/SnO₂ (50 wt%) hybrid nanocomposite film. Surface topography obtained from the AFM image confirms the rough surface along with some pores that can be useful for adsorption of gas molecules. The root mean square roughness calculated from the 3D AFM image is ± 39 nm. EDX was employed to characterize the surface atomic composition of PPy/SnO₂ (50%) hybrid nanocomposite. The element content and weight percent are given as insets of Fig. 3c. The characteristic peaks of Sn, C, N and O along with Pt from the supporting grid was observed. The result indicates the existence of Sn from SnO₂ and C, N and O elements from PPy. However, the absence of any other peak except Sn, C, N and O has evidenced the formation of PPy/SnO₂ hybrid NCs without any elemental impurities. Figure 3d shows the water contact angle image of PPy/SnO₂ (50%) hybrid nanocomposite thin film. It is observed that for the PPy/SnO₂ (50%) sample, the water droplet flats on the surface, which means it is hydrophilic in nature with observed water contact angle of 43.2°, which is favorable for gas adsorption [19–24].

5 Gas Sensing Studies

5.1 Selectivity

Selectivity of particular gas is important parameter to behave sensor as a good sensor. To investigate the selectivity of PPy/SnO₂ (50%) hybrid nanocomposite, measurements were performed towards oxidizing and reducing gases like NO₂, Cl₂, ethanol, methanol, H₂S and NH₃ gases. Figure 4a shows the plot of response of PPy/SnO₂ (50%) hybrid nanocomposite sensor film for corresponding gas. The selectivity study was carried out at 100 ppm of each gas and sensor showed highest response of 53.69% towards NO₂ gas compared to other test gases showing the selectivity. The response of PPy/SnO₂ (50%) hybrid nanocomposite for NO₂ gas is higher compared to pure PPy [25] and SnO₂ [26] sensor. The possible reasons for the higher response of composite sensor are the improved morphology of PPy due to the addition of SnO₂ observed from the FESEM. It can provide maximum surface to volume ratio and provides easy path for the movement of electrons in gas sensing mechanism [27, 28].

5.2 Dynamic Response

NO₂ sensing behavior of PPy/SnO₂ hybrid nanocomposite was determined by measuring change in response values with respect to the concentration of gas as shown in Fig. 4b. Before exposing the sensor to NO₂ gas, sensor resistance was stabilized in air ambient. After resistance stability the sensor film was exposed sequentially for

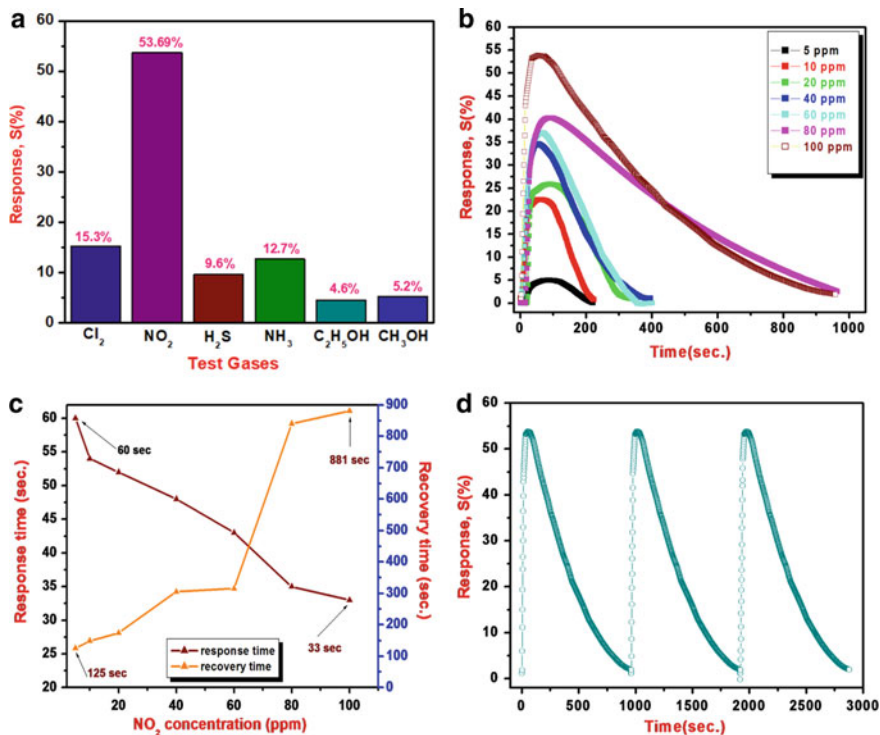


Fig.4 **a** Selectivity plot, **b** dynamic response at different NO₂ concentrations, **c** Response-Recovery characteristics, **d** Reproducibility of PPy/SnO₂ (50%) hybrid nanocomposite

the concentrations of 5 ppm, 10 ppm, 20 ppm, 40 ppm, 60 ppm, 80 ppm, 100 ppm respectively. The dynamic response curve shows variation in the response values with respect to the concentration of NO₂ gas. When sensor is exposed to gas, response changes immediately, reaches highest value, become stable and starts to decrease on decreasing the concentration of NO₂. The response obtained for 100 ppm NO₂ gas concentration was 53.69% with short response time of 33 s. and slightly longer recovery time of 881 s.

5.3 Response/Recovery Characteristics

In order to use PPy/SnO₂ hybrid nanocomposite as NO₂ gas sensor, it is important to know the rate of variation of response to the variation of gas concentration. The response and recovery characteristics of sensor were measured by monitoring the change in resistance for varying concentration of NO₂ gas from 5 ppm to 100 ppm. According to the definition response and recovery times are defined as the time required reaching 90% of the final value. As seen from the Fig. 4c response/recovery

time characteristics of PPy/SnO₂ hybrid nanocomposite sensor concludes that, for the low concentration (5 ppm) of NO₂ gas concentration, sensor takes maximum time (60 s) to reach its peak amplitude while its exposure to air takes slightly longer time (125 s) to come its baseline value. The composite sensor exposure to higher concentration (100 ppm) of NO₂ gas takes very short time (33 s) to reach at its highest amplitude value whereas its recovery time is very high (881 s).

5.4 Reproducibility

Reproducibility is an important parameter to work as an excellent sensor. Reproducibility study of PPy/SnO₂ hybrid nanocomposite sensor was measured for three cycles of NO₂ gas exposure. Plot in Fig. 4d for the investigation of reproducibility of PPy/SnO₂ sensor demonstrates that response values with constant amplitude showing excellent reproducibility. Return of resistance to its initial baseline states the ability of sensor to restore its initial energy level. From the response recovery plot, it is concluded that the PPy/SnO₂ hybrid nanocomposite sensor is reusable.

6 Conclusions

In this work, PPy/SnO₂ nanocomposites were prepared using solid state synthesis method by the addition different wt% of SnO₂ nanoparticles in PPy matrix. The structural study supports to the formation of PPy/SnO₂ nanocomposite and indicating the interaction between PPy and SnO₂. The gas sensing results revealed the better performance for PPy/SnO₂ (50%) nanocomposite sensors than that of individual PPy and SnO₂ sensors. As-fabricated PPy/SnO₂ (50 wt%) nanocomposite sensor shows good selectivity, response reproducibility and stability kinetics to NO₂ at room temperature.

Acknowledgements Prof. V. B. Patil is thankful to the CSIR (India), for financial support through scheme no. 03 (1319)/14/EMR-II. Authors also would like to thank DAE-BRNS for the financial support through scheme no. 34/14/21/2015-BRNS and RUSA Maharashtra for the financial support through scheme no. RUSA /R&I/2016/267.

References

1. Patois T, Sanchez JB, Berger F, Rauch JY, Fievet P, Lakard B (2012) *Sens Actua B: Chem* 171–172:431–439
2. Veeraraghavan B, Paul J, Haran B, Popov B (2002) *J Power Sources* 109(2):377–387
3. Guimard NK, Gomez N, Schmidt CE (2007) *Progr Poly Sci* 32(8–9):876–921
4. Lee JY, Bashur CA, Goldstein AS, Schmidt CE (2009) *Biomaterials* 30(26):4325–4335

5. Zhang J, Wang S, Wang Y, Wang Y, Zhu B, Xia H, Guo X, Zhang S, Huang W, Wu S (2009) *Sens Actuators B: Chem* 135(2):610–617
6. Kaur J, Roy SC, Bhatnagar MC (2007) *Sens Actuators B: Chem* 123(2):1090–1095
7. Bandgar DK, Navale ST, Mane AT, Gupta SK, Aswal DK, Patil VB (2015) *Synth Meta* 204:1–9
8. Bandgar DK, Navale ST, Naushad M, Mane RS, Stadler FJ, Patil VB (2015) *RSC Adv* 5:68964
9. Sakhare RD, Khuspe GD, Navale ST, Mulik RN, Chougule MA, Pawar RC, Lee CS, Sen S, Patil VB (2013) *J Alloys Comput* 563:300–306
10. Sakhare RD, Navale YH, Navale ST, Patil VB (2017) *J Mater Sci: Mater Electron* 28:11132–11141
11. Fujihara S, Maeda T, Ohgi H, Hosono E, Imai H, Kim SH (2004) *Langmuir* 20:6476
12. He C, Yang C, Li Y (2003) *Synth Met* 139:539
13. Cheng QL, Pavlinek V, Li CZ, Lengalova A, He Y, Saha P (2006) *Appl Surf Sci* 253:1736
14. Ballav N, Biswas M (2006) *Mater Lett* 60:517
15. Zhang WX, Wen XG, Yang SH (2003) *Langmuir* 19:4420
16. Xu J, Li XL, Liu JF, Wang X, Peng Q, Li YD (2005) *J Polym Sci Part A* 43:2892
17. Chen AH, Xie HX, Wang HQ, Li HY, Li XY (2006) *Synth Met* 156:346
18. Jang J, Bae J (2007) *Sens Actua B* 122:7–13
19. Lokhande CD, Barkschat A, Tributsch H (2003) *Sol Energy Mater Sol Cells* 79:293
20. Bakri MM (1966) *J Chem Phys* 44:2488
21. Chen W, Fadeev AY, Hsieh MC, Oner D, Youngblood J, McCarthy TJ (1999) *Langmuir* 15:3395
22. Yoshimitsu Z, Nakajima A, Watanabe T, Hashimoto K (2002) *Langmuir* 18:5818
23. Miwa M, Nakajima A, Fujishima A, Hashimoto K, Watanabe T (2000) *Langmuir* 16:5754
24. Li S, Li H, Wang X, Song Y, Liu Y, Jiang L, Zhu D (2002) *J Phys Chem B* 106:9274
25. Chougule MA, Pawar SG, Patil SL, Raut BT, Godse PR, Sen S, Patil VB (2011) *IEEE Sens J* 11(9):2137–2141
26. Khuspe GD, Sakhare RD, Navale ST, Chougule MA, Kolekar YD, Mulik RN, Pawar RC, Lee CS, Patil VB (2013) *Ceram Inter* 39(8):8673–8679
27. Lou XW, Archer LA, Yang Z (2008) *Adv Mater* 20:1
28. Sun SM, Li XL, Li YD (2006) *Chem Eur J* 12:2039

Hydrothermally Synthesised ZnO Nanostructure: Highly Sensitive Towards NO₂ Gas



P. R. Godse, Y. H. Navale, Y. M. Jadhav, R. N. Mulik, and V. B. Patil

Abstract ZnO nanorods structures with low dimensions were prepared by aqueous solution monitored through self-assembled hydrothermal method. The hydrothermally grown ZnO nanorods were explored by primarily X-ray diffraction (XRD), field-emission scanning electron microscopy (FESEM) and contact angle. The ramification conveys that the ZnO nanorods were collected of high-aspect-ratio nanorods. Additionally, measurement of gas-sensing properties carried out for various concentration of gas viz 5–100 ppm, which validates that the ZnO nanorods were of good selectivity and response to poisonous NO₂ and could set out for NO₂ sensor to detect low-concentration NO₂.

Keywords ZnO · FESEM · Low dimensional nanostructures · NO₂ detection

1 Introduction

Disturbed environment due to rise of venomous gases such as NH₃, F₂, CO, Cl₂, CH₄, NO₂, CO₂, SO₂, and NO₂ in the environment is a utmost worry in the world. Gases emitted by vehicles, burning of agriculture products, volcanic activity etc., are reasons for environmental pollution. In addition, due to day to day modifications in the system of industrialization causes the rise in the emission of harmful gases is one of the reasons of pollution. Out of the emission gases, NO₂ gas shows major contribution of pollution and attempts are being made worldwide for its detection and control. For this issue, efforts have been made to produce high quality NO₂ gas sensors for detection of the emission gases [1–5].

As high surface to volume ratio materials, ZnO has been extensively scrutinized for its dormant applications [6]. Outstandingly it can be utilized in harmful, poisonous and highly flammable gas sensors [7–9]. For gas sensor applications, ZnO is one of

P. R. Godse · Y. H. Navale · Y. M. Jadhav · V. B. Patil (✉)

Functional Materials Research Laboratory, School of Physical Sciences, Solapur University, Solapur 413255, M.S., India

R. N. Mulik

D.B.F. Dayanand College of Arts and Science, Solapur, M.S, India

© The Author(s), under exclusive license to Springer Nature Switzerland AG 2021

1031

P. M. Pawar et al. (eds.), *Techno-Societal 2020*,

https://doi.org/10.1007/978-3-030-69925-3_98

the inexpensive, nontoxic, auspicious materials. Additionally, ZnO materials have a roomy band gap 3.38 eV, [10, 11] which can be used as a dormant material on gas-sensing devices. ZnO with assorted morphologies, nanostructures have been synthesized using a wide range of synthesis techniques [12, 13]. Out of these techniques, the self-assembled hydrothermal technique is an apt alternative because of its environment friendly, low cost, intelligibility and duplicability, is striking substantial curiosity [14].

The aim of the current work is to create the low dimensional ZnO nanostructures based gas sensor by straightforward, hydrothermal method. A gas sensing study disclose the potential of low dimensional ZnO nanorods to sight NO₂ gas at lower ppm with optimized operating temperature. The properties of one low dimensional ZnO nanorods such as structural, morphological and gas sensing recital are orderly carried out and obtained results expressed.

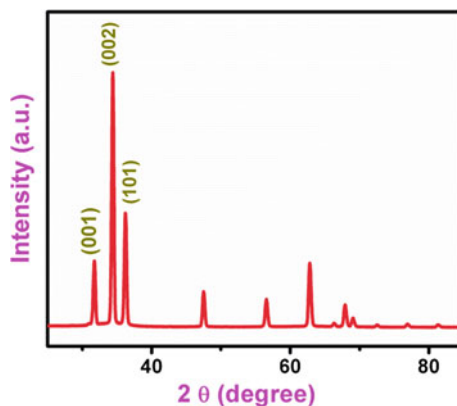
2 Experimental Details

The low dimensional ZnO nanostructures were prepared by hydrothermal method on inspected glass substrate. In the procedure the precursor solution was stirred continuously for 10 min. Then the solution was poured into 100 ml Teflon autoclave. The glass substrates were neatly inserted in the Teflon autoclave. The hydrothermal reaction was carried out for 3 h at 170° processing temperature. The structural study of the produced ZnO nanorods films were examined by X-ray diffraction process with CuK_α source and morphological study for surface carried out using FESEM (field emission scanning electron microscopy). To examine the gas sensing properties of low dimensional ZnO nanorods, conventional gas sensor unit was used [15]. The electrical parameter viz. resistance, was changed to study the response of ZnO nanorods sensor to detect toxic gases and which is conceived by programmable electrometer (Keithley 6514 System), interfaced with computer and gas sensor unit. The response S (%) of the low dimensional ZnO nanorods sensor for a test gas was decided by an equation as [15]

$$\text{Response (s) \%} = \frac{|R_g - R_a|}{R_a} * 100 \quad (1)$$

Herein, Ra and Rg are the resistance of the tested sensor in the absence of gas (i.e. atmospheric air) and in presence of test gas respectively.

Fig. 1 XRD spectrum of 1D ZnO nanorods



3 Results and Discussion

3.1 Structural Revelation

Figure 1, Shows recorded XRD spectrum of hydrothermally grown low dimensional ZnO nanostructures. Standard JCPDS card no. #36–1451 resembles values for the peaks [16]. The obtained peaks in diffraction pattern support the formation of ZnO material with a hexagonal wurtzite crystal structure without impurity.

Calculation of the average crystallite size of the hydrothermally grown ZnO sample is 47.18 nm, were carried out by Scherer relation ($D = 0.9\lambda/\beta\cos\theta$). In addition, another structural factor of ZnO nanorods like stacking fault value (SF) 0.15259, micro-strain (ϵ) 0.0735 and dislocation density (δ) 0.000449163 were obtained by the using following relations;

$$SF = \frac{2\pi^2}{45(3\tan\theta)^{\frac{1}{2}}}\beta \quad (2)$$

$$\epsilon = \frac{\beta\cos\theta}{4} \quad (3)$$

$$\delta = \frac{1}{D^2} \quad (4)$$

3.2 Morphological Analysis

Figure 2 a, b shows FESEM micrographs with different magnifications which evince that formation of low dimensional ZnO nanostructures grown on the glass substrate

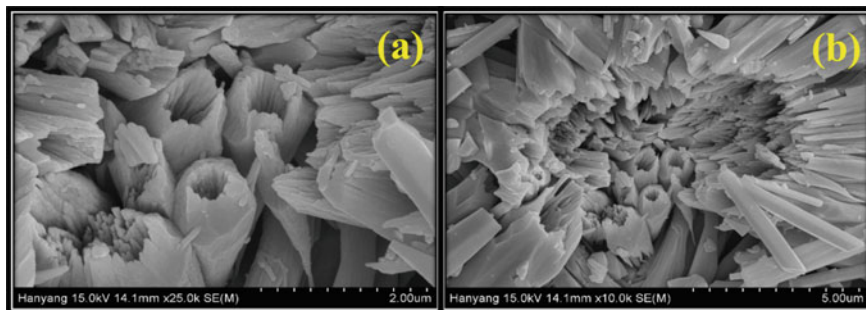


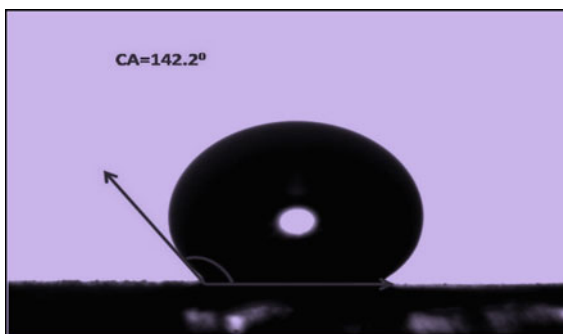
Fig. 2 a and b Different magnification FESEM images of ZnO nanostructures

with a usual diameter of 783 nm and 3.9 μm in length. These films clearly affirm the unique porous structure which boosts adsorption of test gas lead to increase in sensing of a sensors [17].

3.3 Contact Angle Measurements

Figure 3, shows contact angle measurement for a hydrothermally grown low dimensional ZnO thin film Hydrophobicity of thin film samples was determined by measuring the contact angle of a water droplet contacting a surface. Measurement Hydrophobic surfaces exhibit water-repellency, with water droplets residing on them with contact angle greater than 90° [18]. The prepared sample having contact angle of 142.2° proves hydrophobic nature which enhances strength of sensing for sensor.

Fig. 3 Contact angle measurements



3.4 Gas Sensing Assets

In gas sensing study we have obtained unique response of 505% for the prepared sensor on the exposure of 100 ppm NO_2 gas at 200 °C operating temperature compared with other operating temp, shown in Fig. 4a. The Fig. 4b. clearly indicates that prepared sensor is selective for NO_2 gas among other target gases under gas sensing study. Furthermore Fig. 4c. shows response obtained at various gas concentrations viz 5, 10, 20, 40, 60, 80 and 100 ppm. The graph manifest that as concentration of gas increases consequently response by sensor also increases. Figure 4d, shows the stability graph of gas response carried out at 100 ppm of gas as a function of time in days. Initially, the rate of gas response decreases quickly and after 30 days speed of gas response was slowed down and response becomes firm by getting 85.74% stability. This is due to initially ZnO sensor may encounter interface adaptation throughout the process and then obtain the stable state.

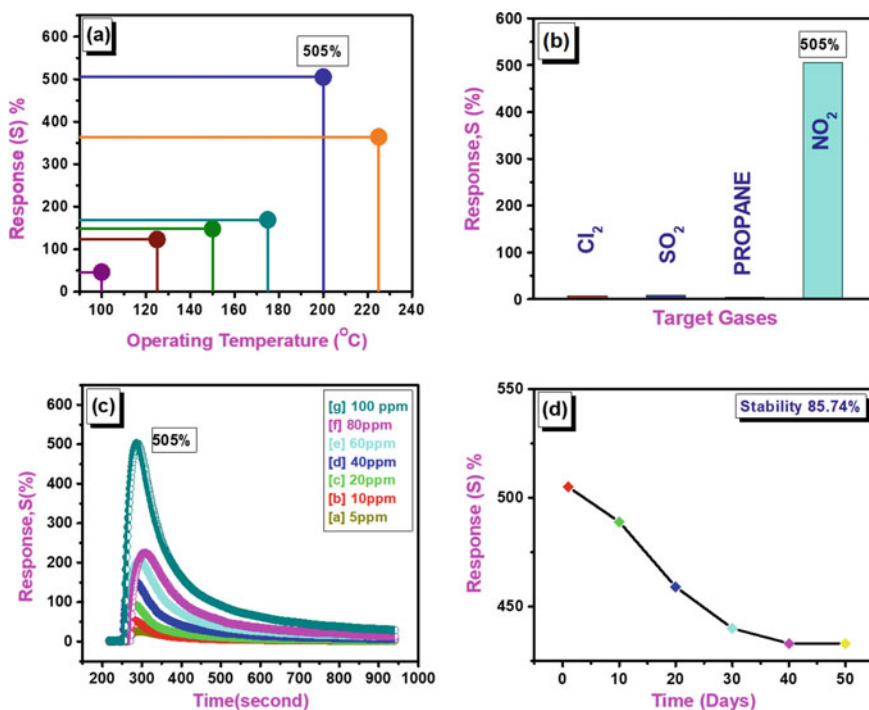


Fig. 4 a Operating temperature, b Selectivity, c Dynamic response and d Stability study of low dimensional ZnO sensors

4 Conclusions

Synthesis of low dimensional ZnO nanostructure was successfully carried by using easy hydrothermal method and applied for the detection of toxic NO₂ gas. The crystal structure and surface morphological scrutiny exposed that the formation ZnO with hexagonal wurtzite structure and nanorods with 783 nm in diameter. The contact angle of sample is 142.2°. Gas sensing dimensions express that the as-prepared sensor shows the highest response of 505% towards NO₂ gas. Hence, hydrothermally prepared ZnO have outlook to the growth of simple, low-cost NO₂ gas sensor.

Acknowledgements Prof. V. B. Patil would like to thank DAE-BRNS (scheme no. 34/14/21/2015-BRNS) for the financial support.

References

1. Julia S, Yulianto B, Nugraha B (2011) The 4th nanoscience and nanotechnology symposium
2. Boudiba A, Zhang C, Bittencourt C, Umek P, Marie-Georges O, Snyders R, Debligny M (2012) SO₂ gas sensors based on WO₃ nanostructures with different morphologies. *Proc Eng* 47:1033
3. Trung DD, Hoa ND, Tong PV, Duy NV, Dao T, Chung H, Nagao T, Hieu NV (2014) Au sensitized ZnO nanorods for enhanced liquefied petroleum gas sensing properties. *J Hazard Mater* 265:124
4. Wang Q, Dong X, Pang Z, Du Y, Xia X, Wei Q, Huang F (2012) Ammonia sensing behaviors of TiO₂-PANI/PA6 composite nanofibers. *Sensors* 12:17046–17051
5. Snyder C, Bruulsema TW, Jensen T, Fixen P (2009) Review of greenhouse gas emissions from crop production systems and fertilizer management effects. *Agric Ecosyst Environ* 133:247
6. Xu JQ, Chen YP, Chen DY, Shen JN (2006) Hydrothermal synthesis and gas sensing characters of ZnO nanorods. *Sens Actuators B* 113:526–531
7. Pradel KC, Wu W, Zhou Y, Wen X, Ding Y, Wang ZL (2013) Piezotronic effect in solution-grown p-type ZnO nanowires and films. *Nano Lett* 13:2647–2653
8. Ren L, Tian TT, Li YZ, Huang JG, Zhao XJ (2013) High-performance UV photodetection of unique ZnO nanowires from zinc carbonate hydroxide nanobelts. *ACS Appl Mater Interfaces* 5:5861–5867
9. Deng JN, Yu B, Lou Z, Wang LL, Wang R, Zhang T (2013) Facile synthesis and enhanced ethanol sensing properties of the brush-like ZnO–TiO₂ heterojunctions nanofibers. *Sens Actuators B* 184:21–22
10. Wang MJ, Li S, Zhang P, Wang YF, Li HQ, Chen Z (2015) A modified sequential method used to prepare high quality perovskite on ZnO nanorods. *Chem Phys Lett* 639:283–288
11. Xu CX, Sun XW (2003) Field emission from zinc oxide nanopins. *Appl Phys Lett* 83:3806–3808
12. Zhang P, Li S, Liu CH, Wei XB, Wu ZM, Jiang YD, Chen Z (2014) Near-infrared optical absorption enhanced in black silicon via Ag nanoparticle-induced localized surface plasmon. *Nanoscale Res Lett* 9:519
13. Sohn JI, Jung YI, Baek SH, Cha S, Jang JE, Cho CH et al (2014) A low temperature process for phosphorous doped ZnO nanorods via a combination of hydrothermal and spin-on dopant methods. *Nanoscale* 6:2046–2051
14. Zhen Cao, Yong Wang, Zhanguo Li, Naisen Yu et al (2016) Hydrothermal synthesis of ZnO structures formed by high-aspect-ratio nanowires for acetone detection. *Nanoscale Res Lett* 11:1–6

15. Navale YH, Navale ST, Stadler FJ, Ramgir NS, Debnath AK, Gadkari SC, Gupta SK, Aswal DK, Patil VB (2017) Thermally evaporated copper oxide films: a view of annealing effect on physical and gas sensing properties. *Ceram Int* 43:7057–7064
16. Akhtar MJ, Ahamed M, Kumar S, Khan MM, Ahmad J, Alrokayan SA (2012) Zinc oxide nanoparticles selectively induce apoptosis in human cancer cells through reactive oxygen species. *Int J Nanomedicine* 7:845
17. Gao T, Wang TH (2005) Synthesis and properties of multipod-shaped ZnO nanorods for gassensor applications. *Appl Phys Mater Sci Process* 80:1451–1454
18. Roach P, Shirtcliffe NJ, Newton MI (2008) *Soft Matter* 4:224–240

Indian Rural Challenges

The Challenge of Unemployment and Entrepreneurship Before Rural India and Its Solution Through the Foundry Business Using Traditional Indian Knowledge System



Ashutosh Dandekar, Akhilesh Joshi, Indraja Dandekar, Narayan Hargude, Amod Shrotri, and Satish Kulkarni

Abstract The traditional Indian knowledge system has always encouraged skill-based learning, wherein entrepreneurs played a key role in society. As per the ancient Indian culture, there are thirty-two streams of 'Vidyas; (Knowledge) and Sixty-four types of the 'Kalas' (Arts). Every Indian village was a self-dependent and smart village in those times. There was a system called 'Bara Balutedars', which was implemented to drive the routine administration as well as the economy of the village. The system could be considered as the backbone of the rural economy. However, after the nineteenth century, it was disintegrated gradually. Especially, after globalization, the condition of Indian villages worsened and the prolonged effect of the policies adopted at that time can be observed even today. The rural population in India is facing difficulties regarding education, healthcare, and entrepreneurship. Today, the rural Indian economy is mostly based on agriculture. Other businesses associated with agriculture like poultries, dairies, cattle-farming, etc. are also contributing. However, apart from agro-based industries, the establishment of other industries is necessary to boost the entrepreneurship in rural areas. The purpose of this article is to put forth the facts about traditional Indian knowledge system and how the traditional products like cow products can be helpful in foundry businesses to encourage entrepreneurship in rural India.

Keywords Entrepreneurship in rural area · Foundry business · Ancient Indian technology · Heat treatment

A. Dandekar (✉) · A. Joshi · I. Dandekar · N. Hargude · A. Shrotri · S. Kulkarni
Department of Mechanical Engineering, PVPIT-Budhgaon, Budhgaon, Maharashtra, India
e-mail: ardandekar@pvpitsangli.edu.in

A. Shrotri
e-mail: apshrotri@pvpitsangli.edu.in

S. Kulkarni
e-mail: kulsat@pvpitsangli.edu.in

1 Introduction

As per the online report of <https://tradingeconomics.com>, India has approximately 66% population, which is living in the rural area. This figure signifies that the settlement in villages is quite high. The economy of the Indian villages is highly dependent on Agriculture and allied small scale businesses. Indian government is taking efforts to encourage the development of the Indian villages through the schemes like 'Unnat Bharat Abhiyan' [1] or Smart village drive, although some villages are still deprived of the reach of such schemes. The statistical data generated by <https://unemploymentinindia.cmie.com/> shows that the unemployment rate in the rural India is around 7% in the month of August 2020. Following could be the possible reasons due to which the rural population is facing severe problem of unemployment [2].

- (1) The industries are picking the locations which are nearer to the highways or the cities, having airports facility for the establishment of the Industry. Very few plants are located in the rural region due to the lack of connectivity and limited means of transportation.
- (2) Farming is the main business in rural area. But in many cases it is seasonal. And the allied businesses like dairy, poultry are not sufficient to run the economy for the population of entire village.
- (3) Even though the formal education has reached the rural area there is no system that provides the proper education of business and management. There are no institutions that can help marketing of rural products so that they can be brought into main stream.
- (4) The tendency of new generation of rural area is to migrate to the city; this is also affecting the rural employment.

To reduce the unemployment in the area, entrepreneurship is an important tool. But it should be utilized in the smart way. The businesses which are fully or partially dependent on local resources and having potential to attract the customers in cities should be encouraged by providing proper guidance.

2 Scenario of Rural Entrepreneurship

Rural entrepreneurship can play crucial role in the economic progress of the India. It will be also helpful in the reduction of the poverty rate in the rural area. This is the only way to prevent the migration of the rural population to the metro cities, which will be helpful to maintain the demographic balance [3]. However there are some factors which are affecting rural entrepreneurship negatively. They are as follows [4]:

- (1) **Funding and Finance:**-Finance or capital is essential to run the business smoothly. Most of the rural entrepreneurs are unsuccessful in availing the loan due to the rules and regulations of the agencies. Even some times they are not aware about funding opportunities and other facilities available for them.
- (2) **Absence of marketing chain:**-Most of the rural products are attractive and useful for urban customers, but it is not possible for the rural entrepreneurs to establish a marketing chain which can drive their products smoothly to the customers without a middle man.
- (3) **Infrastructure and facilities:** - Unlike the urban areas, it is not easy to develop the infrastructure in the villages. If village is located in the remote area, then cost of the transportation, cost of raw material can consume significant share in the working capital. If the land is designated as agricultural as per records, critical procedures are there to convert it in to nonagricultural land. The other facilities like electric connection, water supply, telephone etc. are also difficult to avail.
- (4) **Problem of skilled workers:**-Generally the tendency of people is to migrate from village to city for better wages. And the educated or technical experts in the urban areas are not willing to shift to the rural areas. Hence the rural entrepreneurs have to run the unit with the available workforce.
- (5) **Problem of Internet connectivity:** - Today any business transactions cannot be enjoyed without the proper internet facility. Indian government has promised to provide the broadband internet in all the villages by 2022. There is satisfactory increment in rural internet customers. Still, there are problems of bandwidth and connection.
- (6) **Cultural, Social and Political issues:**-The rural cultural, political and social environment is little different than urban sectors. Sometimes it can create the hurdle for the rural entrepreneur.

3 The Solution for the Problem

The definition and objectives of the rural entrepreneurship should be reformed. Unconventional ways to do so are explained as under [5]:

- (1) Traditionally, businesses associated with farming are considered as rural businesses. But the business-like foundry industry, machine shop, IT Park can also become the backbones of the rural industry. The model shall be established in that direction.
- (2) Currently, it is essential for rural entrepreneurs to establish the marketing chain for the product in the urban areas. But if we change the concept of business, the people in the cities will approach to the rural area to purchase the products.
- (3) Every time it is not essential to build the infrastructure by purchasing the raw material from urban areas. Establishment of the new methods can promote the utilization of the local resources.

- (4) Using the traditional cultural entities in rural settlements (like cow) the entrepreneurship can be developed.
- (5) Establish a business which can provide the employment to the rural population through this traditional way of living.
- (6) Make perfect combination of traditional cultural aspects and modern technologies like Internet of the Things to boost the business in rural area. To establish these solutions in actual practice, we have to move back the traditional Indian knowledge system or Ancient Indian Engineering.

4 Ancient Indian Techniques Useful for the Foundry Business

Some ancient Indian texts like Rigveda or Yajurveda are providing the references related to the extraction and processing of the metal works. The first hymn in the first verse of the Rigveda states that [6].

१. ॐ अग्निमीळे पुरोहितं यज्ञस्य देवमृत्विजम् । होतारं रत्नधातमम् ॥ १ ॥

The simple meaning of this verse is that with the help of Agni (Furnace) one can get metals and gems. There is more detailing about this in the Yajurveda.

३. अग्निना रयिमभ्वत् पोषमेव दिवेदिवे । यशसं वीरवत्तमम् ॥ ३ ॥

The third rhyme in the first verse in Rigveda is talking about the 'Yash' (Zinc). The Zinc which is heated at elevated temperature becomes harder.

१३३०. युवं धेनुं शयवे नाधितायापिन्वतमश्विना पूर्याय ।
अमुञ्चतं वर्तिकामंहसो निः प्रति जङ्घां विश्पलाया अद्यत्तम् ॥८ ॥

Above verse states that Ashwinikumar have attached the iron leg to the Queen Vishpala by operation. Probably it indicates the joining or alloying process.

१६२. अश्मा च मे मृत्तिका च मे गिरयश्च मे पर्वताश्च मे सिकताश्च मे वनस्पतयश्च मे हिरण्यं च मेयश्च मे श्यामं च मे लोहं च मे सीसं च मे त्रपु च मे यज्ञेन कल्पन्ताम् ॥१३ ॥

The verse in Yajurveda is saying that 'Yajna' is useful to obtain the metals like gold, iron, lead and tin. More interesting information is provided in the book of Agnikarma [7].

अशमरुद्भ्यो धातूनां
शोधनं सुलभं स्मृतम् ॥

This verse implies that with the help of Agni (Fire) and Marut (Air or Wind) it is easy to get the metals. Agni means furnace and air means the action of blowing. These are just glimpses in the old texts which are explaining that the one application of the 'Yajna' processes is to obtain the purified form the metals. Also, there are processes of heat treatments like hardening, softening of the metals. In the books based on 'Rasshastra' there are details of the different types of the furnaces. In all the procession of the Yajna, cow products like milk, curd, and ghee are important as these products are utilized in the heat treatment process.

5 The Utilization of Cow and Herbal Products for the Foundry Business

श्वरे कदल्या मथितेन युक्ते दिनोषिते पायितमायसं यत् ।
सम्यक् शितं चाश्मनि नैति भङ्गं न चान्यलोहेष्वपि तस्य कौण्ड्यम्

The verse is from Brihatsamhita of Varahmihir. A chapter in this book explains the characteristics of the good sword. The ingredients which we are using in the worshipping procedure are actually the material required for the heat treatment. Prepare the paste of plantains and butter milk. Apply the paste on iron object for twenty four hours. It will sharpen the metal (increases the hardness).

आर्कं पयो ह्रुद्विषाणमषीसमेतं
पारावतासुशकृता च युतः प्रलेपः ।

The metal can be also hardened by applying the mixture of Sesame oil and juice of Arka plant. In the Dhanurveda (Book on the tool and techniques of the war) by Sage Jamdagni following verses are present which are explaining how the tempering process can be carried out by using the cow urine.

शिखिग्रीवानुवर्णामं तप्तपीतं तथौषधं ॥
ततस्तु विमले तोये पाययेत् शस्त्रमुत्तमं ॥

The translation can be as: Prepare the paste of cow urine, Pimpali, Rock salt and Saussurea Lappa. Apply the paste on the surface of the steel specimen and heat it till

the color of the specimen becomes yellow. And finally quench the specimen in to the iron pyrite water (Vimal Toy). In the Vishvamitra Dhanurveda (book composed) by sage Vishvamitra the tempering process is explained [8].

पिप्पली सैधवी कुष्ठं गोमूत्रेण च पेषयेत् ॥
 अतिशीतमनाविद्धं पीतं नष्टं तथौषधं ॥
 अनेन लेपयेत्फालं लिप्तं चाग्नौ प्रतापयेत् ॥
 ततो निर्वापितं तैले पाथितं तद्विशिष्यते ॥
 पंचभिर्लवणैः पिष्टं मधुसिक्तैः ससर्षपैः ॥
 एभिः प्रलेपयेत् शस्त्रं लिप्तं चाग्नौ प्रतापयेत्

Prepare the paste of five salts, mustards seeds and honey, cow urine. Coat the specimen with the paste. Heat the specimen in the fire till the color turns in to blue and then quench it in to the water. Unlike the hardening and tempering the processes of the metal softening are also mentioned in the ancient texts. In the text ‘Rasratnakara’, a section is there named as ‘Dhatumrudukaranam’. Different processes of metal softening are explained there. Some methods are briefly described here.

- (1) Immerse the heated metal in the liquid of Sesbana grandiflora to soften it.
- (2) Prepare the mixture of Mahuwa, Banana root, ghee, honey, goatmilk, jaggery, sesame oil by taking all the components in the equal proportions. Heat the metal and immerse it in the mixture, it will become soft. Apart from the heat treatment processes the cow product like cow dung is utilized to construct the ‘Putra’ furnaces. There are many types of furnaces in the texts of ‘Rashshastra’. Particularly the text ‘Rasjalnidhi’ there is interesting description about the furnaces. ‘Mahaputam’, ‘Gajputam’, ‘Varahaputam’, ‘Kapotputam’, ‘Kukkutputam’ are the some furnaces which are explained in ‘Rasjalnidhi’. All the furnaces are using naturally available resources and herbals for the constructions. In modern days the furnaces are operated by using coal, oil or electrical energy. The construction of Mahaputam (Grand sized furnace) is interesting. First create a pit of cubical shape. Fill the entire pit with dried cow dung balls. Fill the crucible with the raw material that you want to melt, tightly cover it with the cow dung cakes. Provide the heat to it. This is called as ‘Mahaputam’. For Gajputam, fill the pit up to the edge with cow dung cakes. Put the raw metal in the crucible and place it on the cow dung cake. Half numbers of the cow dung cake which are required to fill the pit shall be placed above the crucible. Provides heat to the upper layer of the cow dung. ‘Gomayaputa’, in which the cubical pit is fully filled with the cow dung cakes. Through some research we can modify the design of the old furnaces to meet the modern-day requirements.



Fig. 1 a Paste b Coated Specimen and c Heated specimen

6 Results and Discussions

The paste of herbs was prepared as per above verse as shown in Fig. 1. The specimen was coated by using the paste. The specimen was then heated in muffle furnace and quenched in water. There was 41% increase in hardness value (BHN before test 214, and BHN after test 363). However more input on the proportions of the herbs, soaking time of the specimen, heating time and quenching medium is needed, which can affect the result. Work is presently being carried out which will provide positive results. Researchers have already conducted the research on the heat treatment by using the milk products. A.A. Kumar et-al. have investigated the case hardening by using the herbs, ghee, and curd and banana tree trunk. Particularly he worked on the carburizing process [9].

The microstructure of the specimen has been observed by the team after heat treatment. The hardness was also tested. After plotting the result they found that the ancient method of case hardening is equally efficient as modern method. An attractive and effective model of entrepreneurship can be created by using the Indian traditional knowledge.

7 Entrepreneurship Model Based on Indian Traditional Knowledge

Cow is the inherited part of the rural Indian culture and economy. The Indian cattle breed is considered as a qualitative one due to its features. ‘Khillari’, ‘Gir’, ‘Kathiawari’ are some famous Indian brands. The demand of the milk of Jersey cow has increased as it is now preferred, but for the heat treatment processes, milk of the Indian cow is useful. Hence, it is essential to establish the research center which will work on the parameters of the milk of the Indian cow. The second important part is to create the nursery of the herbals which are required for the heat treatment. Encourage

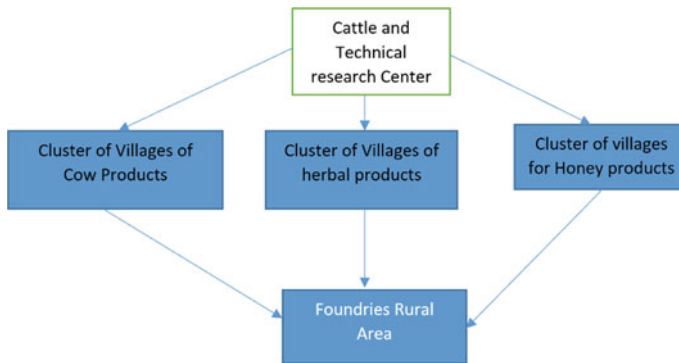


Fig. 2 Alternate industrial model for foundry business

the startups which are based on the cow products. Encourage them to produce the good quality by-products like buttermilk, ghee and curd. Also, encourage the startups which are based on the products of Honey. By conducting the research on the milk products, the parameters like time required for quenching, quantity required for the heat treatment can be modified. There will be a huge boost for the business of cow dung cakes as it is the essential material required for the furnace. The customers in the Industrial belt who are related to the foundry business can be attracted by live demonstration and presentation of the model. With the help of government and NGOs who are interested in rural area, tie ups can be established with industries. Using the modern technology like IoT the cluster of the villages in the same area can be created for the effective administration. The network of foundries which are willing to utilize traditional products shall be established. The IoT techniques can be utilized for the transaction between these cluster of such foundries and industries in urban area. Alternate Industrial Model for foundry business is shown in Fig. 2.

8 Difference Between Existing and Alternate Model of Foundry Business

Following are the differences between the existing and alternate model of foundry business as shown in Table 1.

9 Conclusion

The contribution of rural India in the GDP of the nation is remarkable. However, the village population in India is facing the challenge regarding entrepreneurship and hence employment. This situation is in-turn affecting the national economy in direct

Table 1 Comparison of business models

Sr. No	Parameter	Existing model	Alternate model
1	Furnaces	Coal operated, oil and electrical furnaces	Cow dung discs is significant component
2	Material for heat treatment	Chemicals or artificial resources	Milk products and natural herbs
3	Initial investment	Huge initial investment required	Can be started with minimum capital
4	Pollution	Pollution is the significant problem	Nonpolluting systems

or indirect manner. The migration of the people from rural area to urban areas is creating pressure on administration and infrastructure authorities. On the other hand, there is no effective utilization of available resources in the rural India. Establishing the modern businesses in villages can eliminate the problem of employability but it can create the issues like shortage of drinking water and pollution of atmosphere and other resources. The alternative model for foundry Industry will definitely eliminate the maximum existing issues. It is totally based on natural sources and the available facilities in rural area. Hence, thereby it is useful to resolve the issues of pollution. Also, the knowledge related to cow and dairy activities is inherited among rural masses. Their skills in this domain can be utilized in effective way. The foundries in the rural area can provide job opportunities to the local population. Also, the industries will be hardly dependent on the external supply. Hence the issue of the migration will be definitely sorted out. Also there will be the major boost for the dairy industry too. This model will definitely help to drive the economy of the rural area and enhance the standard of living of rural population at large. The model of foundry business created with the help of traditional Indian knowledge can change the scenario of rural India.

References

1. Prabhakaran V, Muthu Kumaran CK (2019) Impact on Unnat Bharath Abhiyan scheme on rural development Of India. *Int J Res Cult Soc* 3(5). ISSN: 2456–6683
2. Kushalakshi D, Raghurama A (2014) Rural entrepreneurship: a catalyst for rural development. *Int J Sci Res* 3(8):51–54. ISSN2319–7064
3. Sathya I (2019) Rural entrepreneurship in India. *Res Explor Blind Rev Ref Q Int J* 7–12. ISSN: 2250–1940 (P) 2349–1647 (O)
4. Jaydatta S (2017) Major challenges and problems of rural entrepreneurship in India. *J Bus Manag*. ISSN 2278–487X, Volume19-Issue 9, Ver.II pp. 25–44
5. Rao KV (2020) Rural development through sustainable business practices: juxtaposition of private and public initiatives (abstract). Book sustainable business practices for rural development the role of intellectual capita, online. ISBN978–981–13–9298–6. https://doi.org/10.1007/978-981-13-9298-6_2 (2020)
6. Public Library of India. <https://archive.org/details/RigvedInHindi>

7. PublicLibraryofIndia. https://archive.org/details/yajurvedawithhinditranslationsriramsharmaacharya_202003_591_Y
8. Vaze KV (1934) Prachin Yuddhvidy (Techniques of ancient warfare), Publisher:-Damodar Savalaram (Shree Sayaji Granthmala)
9. Kumar AA , Siva SV, Reddy KVS, Reddy ASN, Vamsi N (2017) Investigation of ancient Indian case hardening methods by using herbals and plantain ashes. Int J Mater Sci 12(2):359–370. ISSN 0973–4589

Performance Investigation of Mitticool Refrigerator



Nishigandha Patel, O. Mindhe, M. Lonkar, D. Naikare, S. Pawar, V. K. Bhojwani, and Sachin Pawar

Abstract The mitticool refrigerator works on the principle of evaporative cooling which keeps the fruits, vegetables and dairy products fresh. Mitticool refrigerator works well in hot and dry weather without electricity. The current study investigates the efficiency of mitticool refrigerator with decrease in inner temperature with respect to outer wind velocity and relative humidity. The study is further extended to different compartments and walls of the refrigerator to calculate the performance of the mitticool refrigerator for different seasons. The results showed that the refrigeration effect achieved in the mitticool refrigerator depends on ambient temperature and humidity. The maximum refrigeration effect achieved in summer is 4.5 °C due to high Dry bulb temperature (DBT). The minimum refrigeration effect achieved in winter is 2.5 °C due to low DBT. It is also observed that in the rainy season, refrigeration effect is 3 °C due to high relative humidity. The refrigeration effect at day is higher and at night is slightly lower. Mitticool refrigerator gives better performance in the summer season.

Keywords Evaporative cooler · Seasonal effect · Refrigeration effect · DBT · Mitticool refrigerator

1 Introduction

Cooling means the reduction in temperature called evaporation. It is an ancient way of cooling based on the conversion of sensible heat to latent heat [1, 2]. Hot and dry air is forced to flow over wetted pads that are replenished with water from a reservoir or porous walls. The air imparting on porous walls have low humidity due to which some of the water gets evaporated. There by transferring the sensible heat of air to water leading to evaporation due to latent heat. The latent heat follows the water

N. Patel (✉) · V. K. Bhojwani · S. Pawar
MITSOE, MITADTU, Pune, India
e-mail: nishigandha.patel@mituniversity.edu.in

O. Mindhe · M. Lonkar · D. Naikare · S. Pawar
JSCOE, Pune, India

vapor and diffuses into the air. Dry-bulb temperature is reduced and relative humidity of the air is increased due to evaporation [3, 4]. Evaporation cooling is dependent on the condition of the air and it is necessary to determine the weather condition that may be encountered to properly evaluate the possible effectiveness of evaporative cooler. On the other hand, the amount of water vapor that can be taken up and held by the air is not constant: it depends on two factors: the first is the temperature of the air [5], which determines the potential of the air to take up and hold vapor [6]. The second involves the availability of water: if little or no water is present, the air will be unable to take up very much amount of water [7].

In industrialized countries, due to improper storage, the problem of food wastage occurs due to post-harvest losses. In areas like Sub-Saharan Africa, the burden of food losses falls on the smallholder farmers and families. Electricity is not available to most of the people living in rural areas. That's the reason there was a huge amount of food spoilage which was resulting in low wealth and health issues. The mitticool refrigerators can be used in such areas for preserving the vegetables and fruits. These refrigerators are cheap and don't require any electrical input [8]. Also, they are eco-friendly and don't use toxic refrigerants. The study aims at performance investigation of the mitticool refrigerator [9]. The variation of inside temperature with surrounding air condition and its dependency is seen on various parameters like wind velocity, relative humidity, ambient temperature [10].

It is seen in most of the study's author has carried out experiments that explain temperature variation only. Most of the analyses were not considered temperature variation with specific wind velocity and relative humidity. The results of seasonal testing were then used to determine the variation of inside temperature with ambient temperature, the relative humidity of surrounding air, and air velocity. The results were then used to analyze the behavior of different walls and compartments and finding out the ideal conditions for maximum cooling effect .

2 Methodology

To check the performance of the mitticool refrigerator various tests were done. In the first stage, the seasonal testing was done to check the dependency of inside temperature on different surrounding conditions [11]. The results of seasonal testing were then used to determine the variation of inside temperature with ambient temperature, the relative humidity of surrounding air, and air velocity [12] (Fig. 1).

The results are then used to analyze the behavior of different walls and compartments and finding out the ideal conditions for maximum cooling effect.

2.1 Model Specifications

See Fig. 2.



Fig. 1 Performance testing methodology for mitticool refrigerator

1. Size: 50 liter
2. Length: 8.9inch
3. Width: 8.9
4. Height: 3.6
5. Brand: Mitticool
6. Color: white
7. Door No: Single Door



Fig. 2 Working model of mitticool refrigerator

2.2 Working Principle

It is based on the principle of evaporative cooling which is nothing but the conversion of sensible heat to latent heat. In this experimentation porous walls of the refrigerator are replenished from the upper reservoir of water and hot, dry outside air is forced to pass over the walls [13]. As outside air is dry which means has low humidity, water gets evaporated by gaining some latent heat. The sensible heat of the air is transferred to the water. The latent heat follows the water vapor and diffuses into the air. Dry-bulb temperature decreases and relative humidity of the air increases due to the evaporation effect [14]. In the mitticool refrigerator, the water into the upper reservoir drips into the clay walls and occupies the pores in the clay walls. This water in the pores absorb heat from the refrigerated space and evaporates. This leaves the refrigerator space at a lower temperature. The temperature difference depends on the humidity and velocity of air [15] (Fig. 3).

The water gets equally distributed through the medium and diffuses into the air, till the relative humidity is lower. Due to which water will also keep spreading equally throughout the material if it is porous enough. The mitticool refrigerator’s outer surface is kept relatively moist due to which evaporation will continue until there is no water left in the material or until the air has an equal or higher relative humidity. For evaporation of water either requires heat or energy. This heat is taken from the

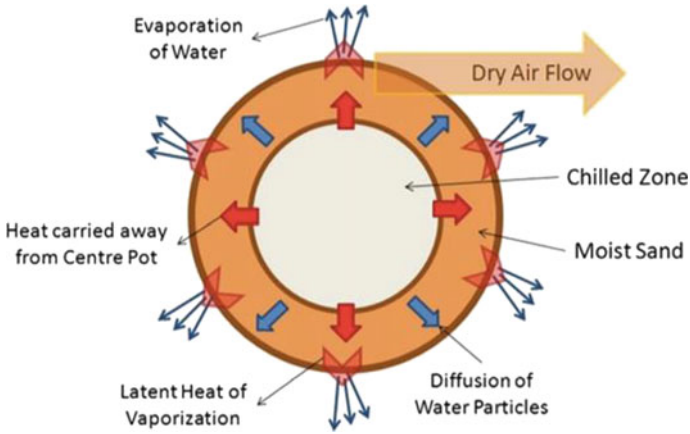


Fig. 3 Working principle of mitticool refrigerator [16]

water still on the surface and inside the body that it is leaving, making the water decrease in temperature, and there of cooling the body [17, 18].

3 Experimental Observations

The tests were done for the seasonal testing of a mitticool refrigerator. It was done to check the dependency of inside temperature on different surrounding conditions [19].

3.1 Seasonal Testing (Inside Laboratory)

See Fig. 4.

NO	Lower Compartment	NO	Upper Compartment
TC17	Thermocouple Inside vessel	TC20	Thermocouple Inside vessel
TC19	Thermocouple outside vessel	TC23	Thermocouple outside vessel
TC24	Thermocouple Inside Water Tank	TC31	Thermocouple in Atmosphere

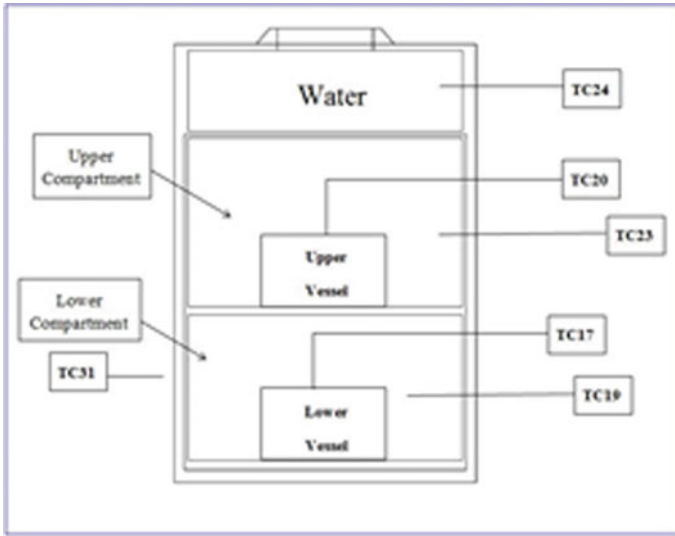


Fig.4 Locations of thermocouples (TC)

4 Results and Discussions

4.1 Testing During the Rainy Season

The test was done during the rainy season to check the performance of the mitticool refrigerator. Temperatures were continuously recorded for 72 h. The temperature of each wall and compartment was recorded. A data Acquisition system was used to record the temperatures. Two steel containers each containing 250 ml of water was kept in upper and lower compartments. The temperatures inside and outside the containers were recorded to study the cooling effect.

It is seen from Fig. 5 that temperature difference in rainy season for lower compartment between outside and ambient temperature is 3 °C whereas between Inside and ambient temperature is 2 °C. For the Upper compartment, the temperature difference seen in Fig. 6 between outside and ambient temperature is 3 °C whereas between Inside and ambient temperature is 2 °C. The resultant temperature difference between ambient and outside the container kept in the refrigerator is 3 °C for the rainy season.

4.2 Testing During the Winter Season

The test was done during the winter season to check the performance of the mitticool refrigerator. Temperatures were continuously recorded for 72 h. The temperature of each wall and compartment was recorded. A data acquisition system was used

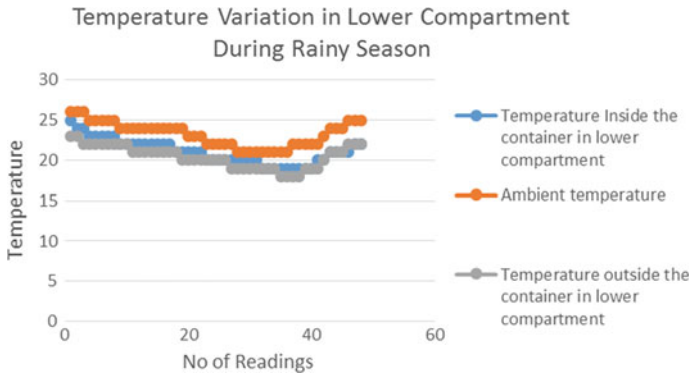


Fig.5 This is a graph between the temperature outside and inside the container in the lower compartment, ambient temperature, and time for the rainy season

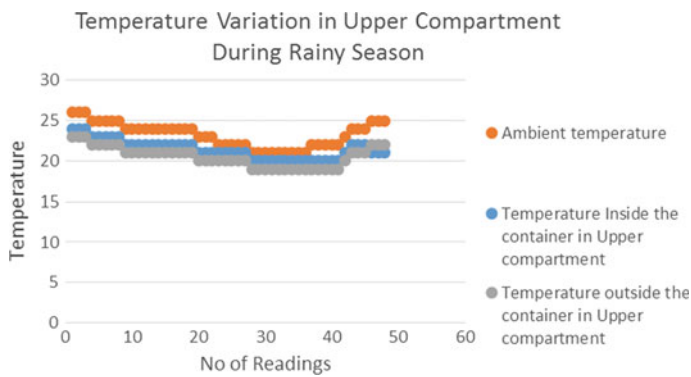


Fig.6 This is a graph between the temperature outside and inside the container in the upper compartment, ambient temperature, and time for the rainy season

to record the temperatures. Two steel containers each containing 250 ml of water was kept in upper and lower compartments. The temperatures inside and outside the containers were recorded to study the cooling effect. The below readings are taken for 72 h after every half an hour. It is seen from Fig. 7 that temperature difference in rainy season for lower compartment between outside and ambient temperature is 2.5 °C whereas between Inside and ambient temperature is 2 °C. For the Upper compartment, the temperature difference seen in Fig. 8 between outside and ambient temperature is 2.5 °C whereas between Inside and ambient temperature is 2 °C. The resultant temperature difference between ambient and outside the container kept in the refrigerator is 2.5 °C for the winter season.

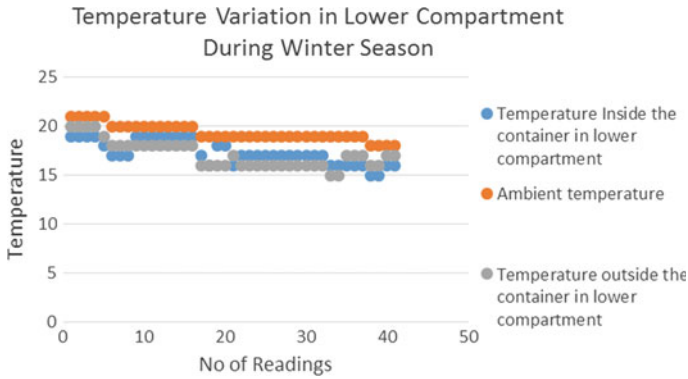


Fig.7 This is a graph between the temperature outside and inside the container in the lower compartment, ambient temperature, and time for the winter season

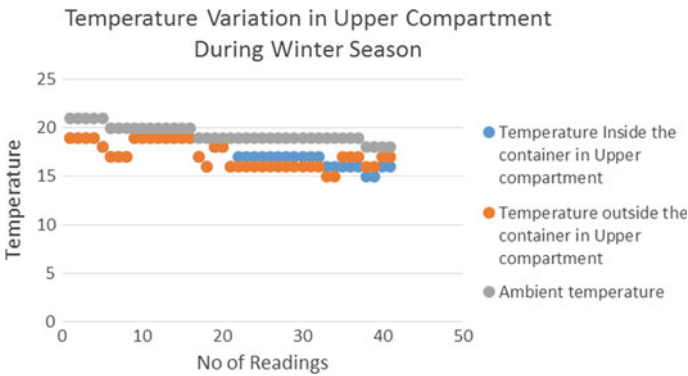


Fig.8 This is a graph between the temperature outside and inside the container in the upper compartment, ambient temperature, and time for the winter season

4.3 Testing During the Summer Season

The test was done during the summer season to check the performance of the mitticool refrigerator. Temperatures were continuously recorded for 72 h. The temperature of each wall and compartment was recorded. A data Acquisition system was used to record the temperatures. Two steel containers each containing 250 ml of water was kept in upper and lower compartments. The temperatures inside and outside the containers were recorded to study the cooling effect. The below readings are taken for 72 h after every half an hour.

It is seen from Fig. 9 that temperature difference in rainy season for lower compartment between outside and ambient temperature is 4 °C whereas between Inside and ambient temperature is 3 °C. For the Upper compartment, the temperature difference seen in Fig. 10 between outside and ambient temperature is 5 °C whereas between

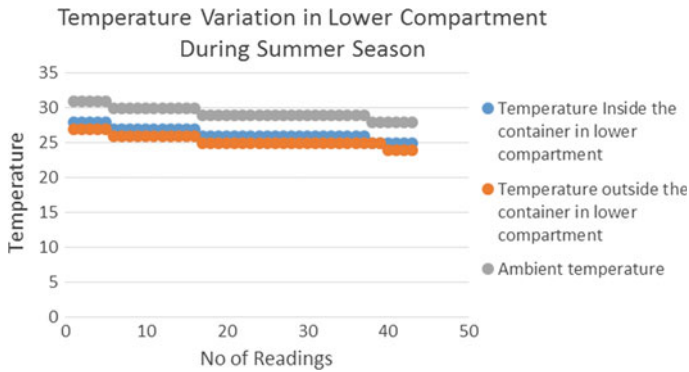


Fig.9 This is a graph between the temperature outside and inside the container in the lower compartment, ambient temperature, and time for the summer season

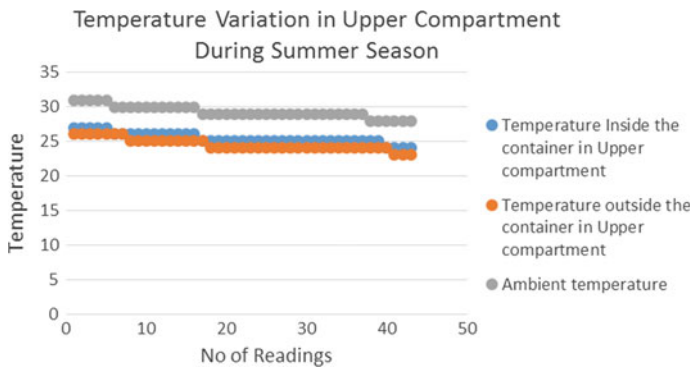


Fig.10 This is a graph between the temperature outside and inside the container in the upper compartment, ambient temperature, and time for the summer season

Inside and ambient temperature is 4 °C. The resultant temperature difference between ambient and outside the container kept in the refrigerator is 4.5 °C for the summer season.

4.4 Effect of Relative Humidity on Cooling Effect

From the results (Reffer Figs. 11, 12), it was found that the cooling effect is highly dependent on the relative humidity of the surrounding air. The DBT and WBT were recorded during the seasonal testing and the corresponding relative humidity was determined using the psychrometric chart [19, 20]. These results show that the temperature difference between inside and ambient temperature (cooling effect) decreases with an increase in the relative humidity. This is due to the air with higher relative

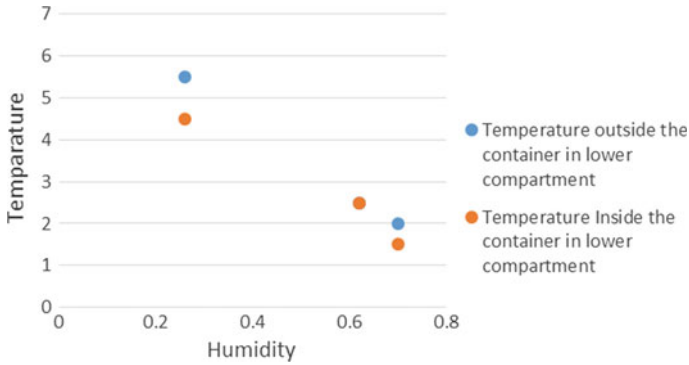


Fig.11 Plot of humidity versus inside and outside temperature of the container in the lower compartment

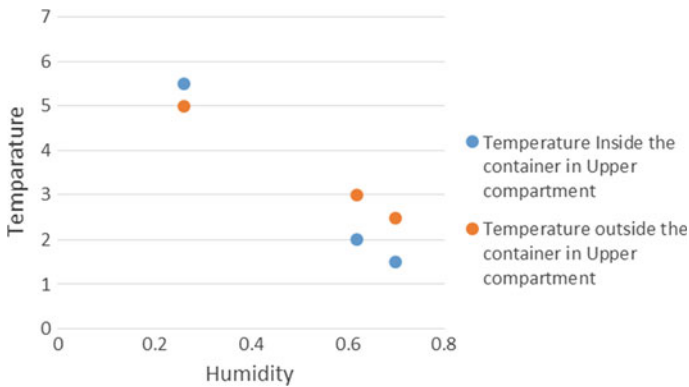


Fig.12 Plot of humidity versus inside and outside temperature of the container in upper compartment

humidity has lesser water carrying capacity. The moisture content in the air with higher relative humidity is more. Due to this the evaporation rate decreases and reduces the cooling effect. So the cooling effect achieved during the rainy season (higher relative humidity) is lesser than that achieved during summer (higher relative humidity). The variation of ΔT with relative humidity Φ is shown in the graphs below.

5 Conclusion

From the above results, it is concluded that the refrigeration effect achieved in the mitticool refrigerator depends on ambient temperature and Relative humidity. The maximum Refrigeration effect is achieved in summer is 4.5 °C due to high DBT. The minimum refrigeration effect is achieved in winter is 2.5 °C due to low DBT. Rainy season's refrigeration effect is 3 °C due to high relative humidity. The refrigeration effect at day is higher and at night is slightly lower. The Mitticool refrigerator gives better performance in the summer season.

References

1. Damle R, Date A (2015) Heat and mass transfer in a clay-pot refrigerator: analysis revisited. *J Energy* 37:11–25
2. Lal Basediya A, Samuel DVK, Beera V (2013) Evaporative cooling system for storage of fruits and vegetables - a review. *J Food Sci Technol* 50(3):429–442. <https://doi.org/10.1007/s13197-011-0311-6>. Accessed 5 Feb 2011
3. Harish H, Gowda YK, Krishne T (2014) Thermal analysis of clay pot in pot refrigerator. *IJMER* 4(9). ISSN: 2249–6645
4. Ndukwu MC, Manuwa SI (2014) Review of research and application of evaporative cooling in preservation of fresh agricultural produce. *Int J Agric Biol Eng* 7(5):85
5. Chinenye NM (2011) Development of clay evaporative cooler for fruits and vegetable preservation. *Agric Eng Int: CIGR J* (Manuscript No.1781) 13(1):1–6
6. Raghavan GSV (2008) Design and testing of an evaporative cooling system using an ultrasonic humidifier. *Dep Bioresour Eng*
7. Inamdar SJ, Junghare A, Kale P (2019) Performance enhancement of evaporative cooling by using bamboo. *Int J Eng Adv Technol (IJEAT)* 8(6S). ISSN: 2249–8958
8. Daniel P (2016) Developing the insulation sheet of luffa cylindrical for mitticool fridge. *Int J Sci Res Manag (IJSRM)* 4:4514–4524 ISSN (e): 2321–3418
9. Sai Dutt P (2016) Experimental comparative analysis of clay pot refrigeration using two different designs of pots. *Dep Mech Eng Glob Acad Technol India* 2(1). ISSN: 2454–5031. Accessed 2 Feb 2016
10. Harish HG, Krishne Gowda YT (2014) Thermal analysis of clay pot. *Indian J Eng Res Technol (IJERT)* 3(10)
11. Amer O, Boukhanouf R, Ibrahim HG (2015) A review of evaporative cooling technologies. *Int J Environ Sci Dev* 6(2)
12. Warke DA, Deshmukh SJ (2017) Experimental analysis of cellulose cooling pads used in evaporative coolers. *J. T. Mahajan College of Engineering, Jalgaon, India* 3(4). ISSN: 2381–7267 ISSN (online): 2321–0613
13. Armarkar JSPMS, Deshpande AMN (2017) Design and analysis of solar wind chill refrigeration system. *J.D.C.O.E.M, Nagpur, India* 4(11)
14. Govekar MN, Bhosale MA, Yadav AM (2015) Modern evaporative cooler. *International Int J Innov Eng Res Technol [IJIERT]* 2(4). ISSN: 2394–3696
15. Tiwari K, Dinesh Kumar B, Reddy NV, Sultana S (2017) Theoretical analysis of air-cooling by using concept of zeer pot refrigeration. *IJCRT*. ISSN: 2320–2882, ©
16. Prabodh Sai Dutt R, Thamme Gowda CS (2015) An investigation review on recent development in refrigeration by evaporation cooling. *Indian J Eng Trend Technol (IJETT)* 23:291–292
17. Ndukwu MC, Manuwa SI, Bennamoun L, Olukunle OJ, Abam FI (2018) In-situ evolution of heat and mass transfer phenomena and evaporative water losses of three agro-waste evaporative cooling pads: an experimental and modeling study. *Waste Biomass Valorization*

18. Chinenye NM (2011) Development of clay evaporative cooler for fruits and vegetable preservation. Agric Eng Int: CIGR J 13(1)
19. Arora CP (2000) Refrigeration and air conditioning. Tata McGraw-Hill Education
20. Arora SC, Arora SC, Domkundwar S (2017) A course in refrigeration and air-conditioning. Dhanpat Rai & Company

Impact of the COVID-19 Outbreak on Different Stakeholders of Hospitality and Tourism Management



Brajesh Kumar Kanchan, Guddakesh Kumar Chandan, Roma Kumari, and Ojaswi Gautom

Abstract Hospitality management has a crucial role in the success of any events or parties especially in hotels, cruise ships, and many similar events. Furthermore, the tourism environment is a direct function of hospitality management. Additionally, these industries were largely hit by the COVID-19 outbreak. A requirement of holistic employee training was never more needed than before for the survival of these industries. The present study addresses this gap and presents the recommendation of the case study. It is observed from the study that COVID-19 negatively impacted the customer traveling pattern by 53% in the Indian subcontinent. Additionally, online meeting frequency increased by 61% due to this pandemic. Furthermore, Customer preferred hotel type is improved by 18% due to getting higher safety standards. Moreover, staying with relatives is also preferred. Our study also revealed that education and experience positively impact the covid-19 training score. Further regression analysis is also performed. The readership of this research work is management trainees and societal committees and hospitality and tourism managers.

Keywords Hospitality management · Holistic training · COVID-19 · Lean philosophy

1 Introduction

India is a place of enriched hospitality and tourism sector from ancient times as several traders and students were visiting this land for trade and education. India is believing in the ideology of “Vasudhaiva Kutumbakam” meaning “the world is one family” [1]. A report published by the Indian brand equity Foundation (IBEF) reported that

B. K. Kanchan (✉) · G. K. Chandan

Department of Mechanical Engineering, National Institute of Technology, Silchar 788010, India

R. Kumari

Department of Management, Maulana Mazharul Haque Arabic and Persian University, Patna 800001, India

O. Gautom

Department of Management, Indian Institute of Management, Ranchi 834008, India

© The Author(s), under exclusive license to Springer Nature Switzerland AG 2021

1063

P. M. Pawar et al. (eds.), *Techno-Societal 2020*,

https://doi.org/10.1007/978-3-030-69925-3_101

tourism and hospitality management contribute to 12.38% of employment and US\$ 91.27 billion to Indian gross domestic product (GDP) showing the importance of this sector to the Indian market [2]. India declared lockdown on 25th March 2020 for 21 days and then continuous lockdown extends in 4 phases till 31st May 2020 due to the COVID-19 pandemic [3]. As per the world health organization (WHO) warning, the end of COVID-19 cannot be predicted [4]. On the world level, the pandemic significantly declined the demand in hospitality industries [5]. That means the tourism and hospitality sector not only have to sustain their existence but also found new ways for their business.

2 Literature

The requirements of training to hospitality and tourism staff were investigated for the last 30–40 years. Khan and Olsen [6] investigated the study where they show how the hospitality sector supports the educational program. Demetriadi [7] emphasized the requirement of exploration in many topics and subject areas in hospitality management. Ingram [8] provided prominent areas where greater attention is required in the hospitality and tourism sector. Guerrier and Deery [9] showed that most of the ideas implemented in the hospitality sector are extensions of core business ideas. In recent times, training in the hospitality and tourism sector is diverse. Cabral et al. [10] signified the relationship between green training and environmental performance, the effect of green competencies, maturity of proactive environmental management, and environmental commitment. Chang and Busser [11] concluded that mentoring functions viz. career development and psychosocial behavior can affect promotional probabilities. Manoharan and Singhal [12] emphasized the requirement of diversity in the hospitality and tourism sector. Yao et al. [13] worked on error management in the hospitality sector and shows that it is a strong function in providing higher service to customers. Zhao and Ritchie [14] investigated the relationship between leadership and tourism research in academic institutes. Furthermore, Ballantyne et al. [15] scrutinized content analysis and reported that qualitative research increased in the tourism sector. Tsionas [16] reported that government subsidies are required for sustaining the hotel business. Lean philosophies can help in mapping the customer value and thus can enhance the customer experience [17]. The COVID-19 pandemic situation worsens the condition of the hospitality and tourism sector and the time line of this pandemic could not be predicted by the world health organization. Furthermore, it is also not possible to predict that this type of pandemic situation cannot happen in the future. Therefore, to reach the ideal condition of the hospitality and tourism business, this sector not only has to go for its prime service but also add a secured environment for its customers. Additionally, the management teams also have to look for other sustainable initiatives in giving services for their customers. It is imperative to note that the training requirement in the case of pandemic and extreme life-threatening situations is largely overlooked by the researchers and needs an in-depth investigation. Further more, extensive training would be required for hotel and

tour staff members for sustaining the market. The present work addresses this gap by proposing a holistic training method for hospitality and tourism sector workers. A case study approach is investigated in the alignment of the proposed methodology. This work highlights the common issues of employees and employers in the tourism and hospitality sector. Further, it collects the voice of customers of their understanding of using these services during and after pandemic times.

3 Hypothesis Testing

The hypothesis that is addressed under the scope of the present study are:

1. COVID-19 changes the traveling pattern of an individual.
2. Higher educated and experienced staff can handle the situation better.

4 Research Methodology

The research methodology consists of case company selection, questionnaire formation, data collection, and data analysis as illustrated in Fig. 1.

Questionnaire Formation

Questionnaires distributed among three stakeholders:

- Customers
- Tourism and Hospitality workers
- Tourism and Hospitality management administrators.

Data Collection

The questionnaire response data were collected over google form. Voice of customers is collected from college students, professors, IT professionals, businessmen, etc. A total of 112 responses were collected from 348 requests for the questionnaire. In Hotel and tourist worker questionnaire, hotels from Bihar, Jharkhand, West Bengal, Maharashtra, Tamilnadu, and Karnataka were assessed. A total of 86 responses were

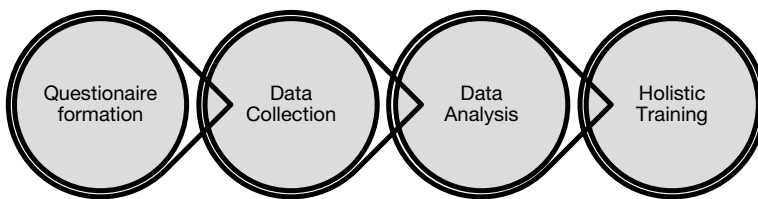


Fig. 1 Proposed research methodology

gathered from 494 requests. In the administrator questionnaire, a total of 41 responses were collected from 118 requests.

Voice of Customer

It can be observed from Table 1 that most of the individual is between age 21–50 years which are less critical in concern of COVID-19.

It can be observed from Table 2 that the frequency of outing in hotel decreases significantly even for a less critical group. That means people are following lockdown one way or another.

It can be observed from Table 3 that the frequency of online meetings increases significantly. That means people are following lockdown and working from home.

It can be observed from Table 4 that the preferred choice of hotels shifts from low rating hotels before lockdown to high rated hotels. This can be attributed to the fact that people are looking for high security and services in the corona period. Furthermore, people are preferring to stay in a relative's house over staying in a hotel.

Employer Analysis

It can be observed from Table 5 that most respondents of employer questionnaires are from high rated hotels and the tourism industry. Further, Table 6 shows that a larger section of the workforce is from the age group 21 to 50.

Table 1 Response of customer age

Age range	10–20	21–30	31–40	41–50	51–60	Above 60
Response received	10	52	25	12	9	4

Table 2 Response to hotel frequency

Frequency of hotel range	0	1–2	3–4	5 or above
Response received before covid-19	4	47	40	21
Response received after covid-19	20	67	24	2

Table 3 Response to the online meeting in a month

Frequency of online meeting	0–3	4–6	7–9	10 or above
Response received before covid-19	45	34	25	8
Response received after covid-19	4	47	37	24

Table 4 Response of preferred choice of hotel

Preferred choice of hotel	1	2	3	4	5
Response received before covid-19	40	31	20	14	7
Response received after covid-19	21	35	26	18	12

Table 5 Response to the company rating

Company rating range	1	2	3	4	5
Response received	1	12	22	44	7

Table 6 Response of employer age

Age range	10–20	21–30	31–40	41–50	Above 50
Response received	2	37	25	18	4

Table 7 Response to work experience

Experience range	0	1–2	3–4	Above 4
Response received	4	47	26	9

Table 8 Response of employer education

Education range	12 or below	Diploma	Graduation	Post-graduation
Response received	20	41	24	1

It can be seen from Table 7 that most employers are having prior experience and further Table 8 shows a significant percentage are having graduation and post-graduation degree.

It can be seen from Table 9 that most of the employers are knowing more than 2 languages.

Table 10 illustrated that a significant section of the workforce does not receive any specific training for COVID-19.

Employee's Analysis

It can be observed from Table 11 that most companies are highly rated companies and further it is comprehended by Table 12 where it is illustrated that annual turnover is high for more than half of the respondents.

The management team managers also acknowledge that they have provided sufficient training for COVID-19 as illustrated in Table 13 Additionally, it

Table 9 Response of known language

Experience range	1	2–3	4–5	Above 5
Response received	20	47	17	2

Table 10 Response of specific training on COVID-19

Specific training received	Yes	No
Response received	31	55

Table 11 Response to the company rating

Company rating range	1	2	3	4	5
Response received	1	9	18	11	2

Table 12 Response to the annual turnover

Annual turnover range	Below 50 Lakh	51 Lakh- 2 Crore	2 Crore to 50 crores	Above 50 crore
Response received	18	14	7	2

Table 13 Response of specific training on COVID-19

Response range	Yes	No
Specific training received	29	12
Thermal scanner availability	36	5
COVID-19 test random sampling	15	26
Aarogyasetu mandatory tracking	18	23
Contact tracing: phone number verification	30	11

also shows that the thermal scanner is mostly available. The use of random sampling tests and aarogyasetu is not much popular. The managers also confirm that a contact tracing facility can be availed for the government if the situation arises and phone number verification is significantly maintained. The joint secretary of the health ministry informed the media that the fatality rate is 75.3% for the age group above 60 years [18].

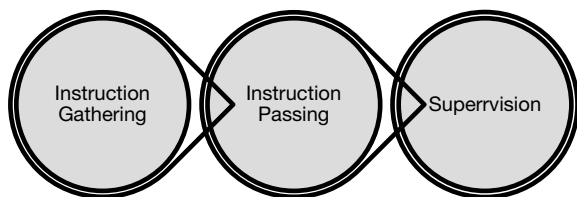
Holistic Training

The holistic training consists of instruction gathering, passing of these instructions, and supervision as shown in Fig. 2.

Instruction Gathering

Some of the significant instruction sites for the COVID-19 situation can be used for following the rules and regulations monitored by the government of India.

Fig. 2 Holistic training methodology



- <https://www.mha.gov.in/>
- <https://www.mohfw.gov.in/>
- <https://www.who.int/india>.

Further, the authors recommend tracking the instructions given by the district magistrate on their official website or handle.

Instruction Passing

The team of hospitality and tourism management needs to have smooth information flow as the COVID-19 pandemic times the various information has flowed from different sites. The maximum of takt time for information flow should be of minimum to avoid legal disputes.

Supervision

The supervision of COVID-19 information needs to be strictly maintained to avoid legal difficulties. A quantitative study of employee effectiveness is measured in terms of the COVID-19 training score is conducted. Furthermore, the supervision ensures customer satisfaction and customer services at the maximum.

5 Results and Discussion

The different hypotheses tested under the scope of the present investigation regarding the change in the travel behavior of customers after COVID-19, education and experience significantly affect the COVID-19 training scores of employees. A questionnaire with its responses is well covered in Sect. 4. In this section, a detailed discussion of hypothesis testing will be evaluated with statistic tools.

Hypothesis 1:COVID-19 Changes the Traveling Pattern of an Individual

The hotel frequency is considered as a parameter to understand the change in the travel behavior of customers. From Table 2, a bar chart is prepared to conceptualize the point and then discuss it in detail as shown in Fig. 3.

Before the COVID-19 outbreak, it is well seen that very few people were not traveling to the hotel in the month. Furthermore, the highest prioritize frequency is one to two. Furthermore, it can be seen that with the increase in hotel frequency, a considerable drop in the magnitude of the frequency. However, when the COVID-19 pandemic is going on, all of sudden the behavior of customers shifts towards the left side of the plot and is found to have a sharp increase in zero frequency. It is well expected as most of the states in India are suffering from lockdown. Furthermore, most world administration is following the lockdown. A sharp decrement in higher frequency is also expected by having Corona case growing and lockdown extension. The empirical study reported a decrement of 53% traveling behavior after the COVID-19 outbreak.

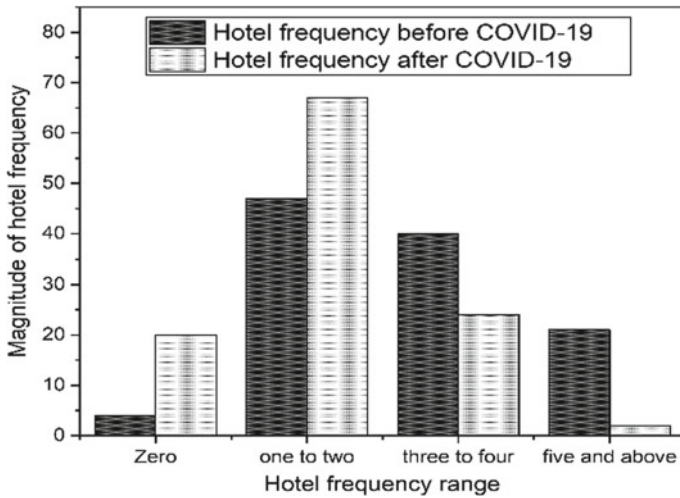


Fig. 3 Response of hotel frequency from VOC

An interesting result is also obtained from Table 3 in terms of online meeting frequency as shown in Fig. 4. The frequency of online meetings was very less significant before the COVID-19 outbreak as it can be seen that a sharp decrement of the magnitude of online meeting frequency as the frequency increase. It is well expected as the physical meeting was the most preferred mode before the COVID-19 outbreak.

However, when COVID-19 impacted our way of leaving, most of the work is done from home and online meetings are becoming the most prominent used. Our study

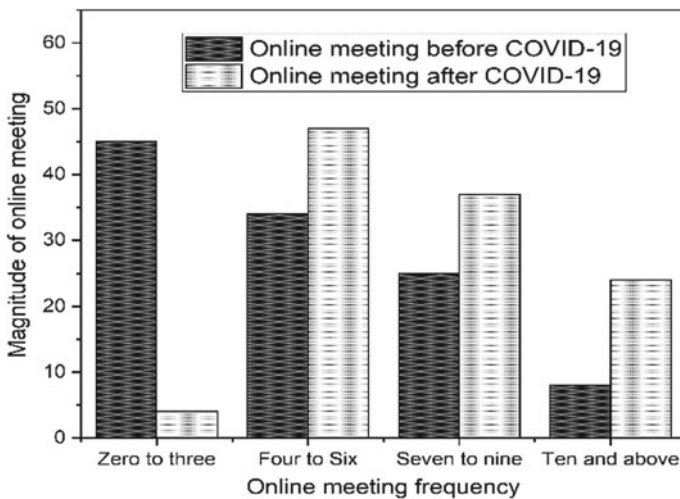


Fig. 4 Response of online meeting frequency from VOC

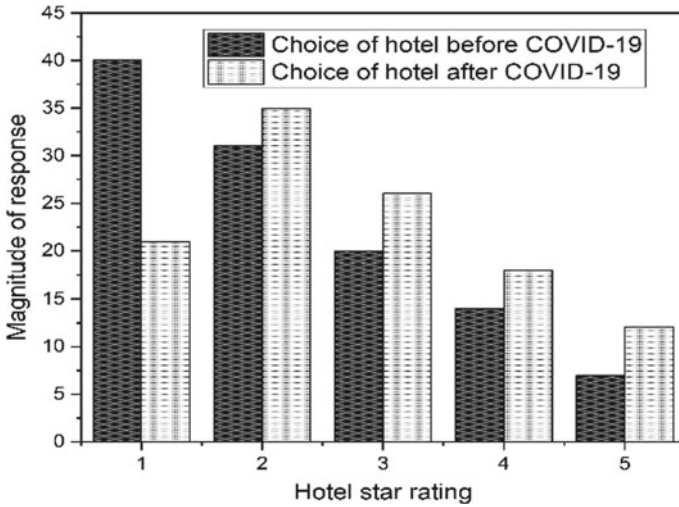


Fig. 5 Response of hotel star selection from VOC

reported an increase in 61% of online meetings once corona shattered our way of living. Additionally, the selection of hotels is also found to have significant impacts on COVID-19 from Table 3. Our study analyses the results and is illustrated in Fig. 5.

The magnitude of hotel star selection depicts that with increment in the star of the hotel eventually, the cost of the hotel increases, the magnitude decrease before the COVID-19 pandemic starts. After the pandemic, a sharp increment of 18% in customer behavior where the customer wants higher safety value and thus justifying the increment in hotel rating response.

Hypothesis 2: Higher Educated and Experienced Staff Can Handle the Situation Better

The training score of the employee after holistic training becomes the most critical part of assessing the effectiveness of the employer in the COVID-19 pandemic area. Furthermore, it is equally important to get the correlation between training score and experience in years and maximum education. Therefore, an illustration of the training score with its correlation of experience in years and maximum education is presented in Fig. 6.

It can be easily seen that the training score increases with an increase in maximum education as well as experience in years. It is further verified by statistical tools. The regression analysis shows that function of the curve is:

- Training score with experience in years: $y = 0.0462x + 3.5721$
- Training score with maximum education $y = 0.3925x + 4.6093$.

It can be seen from the regression analysis that training scores have a significant impact from experience in years and maximum education. When these parameters

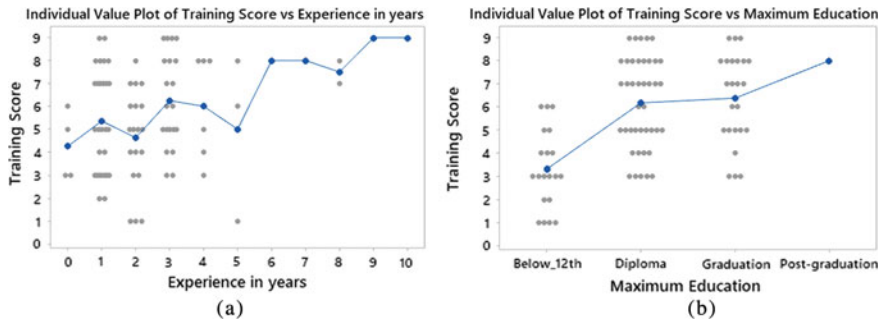


Fig. 6 Scatter diagram of training score with a correlation of **a** experience in years **b** maximum education

are studied in comparative mode, the level of impact is high for maximum education is high as illustrated in the above-mentioned equations.

6 Conclusion

Some of the notable conclusions drawn from the present study are as follows:

- COVID-19 negatively impacted the customer traveling pattern by 53% in the Indian subcontinent. Additionally, online meeting frequency increased by 61% due to this pandemic.
- Customer preferred hotel type is improved by 18% due to getting higher safety standards. Furthermore, staying with relatives is also preferred.
- Education and experience positively impact the covid-19 training score. Further regression analysis is also performed.
- As the fatality rate among the age range between 25–50 is less, and these are the prime market share of the hotel industries, still, people in this range are working with caution. Special restriction needs to be imposed who are not in this age range.

References

1. Hattangadi S (2000) “(Maha Upanishad)” (PDF) (in Sanskrit). Accessed 9 May 2020
2. IBEF (2018) Tourism & hospitality industry in India
3. Sardar T, Nadim SS, Chattopadhyay J (2020) Assessment of 21 days lockdown effect in some states and overall India: a predictive mathematical study on COVID-19 outbreak. [arXiv:2004.03487](https://arxiv.org/abs/2004.03487)
4. This Virus May Never Go Away?: WHO Says It’s Impossible To Predict End Of Covid-19, Outlook India. <https://www.outlookindia.com/website/story/world-news-this-virus-may->

- [never-go-away-who-says-its-impossible-to-predict-end-of-covid-19/352727](#). Accessed 30 June 2020
5. Bartik AW, Bertrand M, Cullen ZB, Glaeser EL, Luca M, Stanton CT (2020) How are small businesses adjusting to COVID-19? Early evidence from a survey (No. w26989). *Natl Bur Econ Res*
 6. Khan MA, Olsen MD (1988) An overview of research in hospitality education. *Cornell Hotel Restaur Adm Q* 29(2):51–54
 7. Demetriadi J (1995) Academic research in hospitality and tourism: a WHATT-CD user's view. *Int J Contemp Hosp Manag* 7(7):3
 8. Ingram H (1996) Clusters and gaps in hospitality and tourism academic research. *Int J Contemp Hosp Manag*
 9. Guerrier Y, Deery M (1998) Research in hospitality human resource management and organizational behaviour. *Int J Hosp Manag* 17(2):145–160
 10. Cabral C, Jabbour CJC (2019) Understanding the human side of green hospitality management. *Int J Hosp Manag* p. 102389
 11. Chang W, Busser JA (2017) Hospitality employees promotional attitude: findings from graduates of a twelve-month management training program. *Int J Hosp Manag* 60:48–57
 12. Manoharan A, Singal M (2017) A systematic literature review of research on diversity and diversity management in the hospitality literature. *Int J Hosp Manag* 66:77–91
 13. Yao S, Wang X, Yu H, Guchait P (2019) Effectiveness of error management training in the hospitality industry: impact on perceived fairness and service recovery performance. *Int J Hosp Manag* 79:78–88
 14. Zhao W, Ritchie JB (2007) An investigation of academic leadership in tourism research: 1985–2004. *Tour Manag* 28(2):476–490
 15. Ballantyne R, Packer J, Axelsen M (2009) Trends in tourism research. *Ann Tour Res* 36(1):149–152
 16. Tsionas MG (2020) COVID-19 and gradual adjustment in the tourism, hospitality, and related industries. *Tour Econ* p.1354816620933039
 17. Kanchan BK, Chandan GK, Rajenthirakumar D (2016) A framework for implementing just in time in a valve manufacturing industry. *Int J Eng Res* 5(4):303–307
 18. Coronavirus: 75% cases of deaths in patients aged 60 yrs and above, 83% have co-morbidities, India Today. <https://www.indiatoday.in/india/story/coronavirus-india-health-ministry-pc-deaths-comorbidities-percentage-total-cases-1668391-2020-04-18>. Accessed 30 June 2020

Characterization of Groundwater Quality for Agricultural Purpose from Akkalkot MIDC, Solapur, Maharashtra, India



A. D. Pathare, D. B. Panaskar, V. M. Wagh, S. B. Salunkhe, and R. S. Pawar

Abstract For the present study, ten samples from the Solapur Industrial Area have been collected and subjected to Physico-chemical analysis. In this paper, the results have discussed in detail. Most of the parameter like EC (100%), TDS (100%), TH (100%), Ca (90%), Mg (80%), Cl (70%), etc. shows their contents above maximum permissible limit given by WHO. The groundwater from the Solapur industrial area has classified for irrigation purpose based on Sodium Absorption Ratio (SAR), Soluble Sodium Percentage (SSP), Kelly's Ratio (KR), Residual Sodium Carbonate (RSC), Percent Sodium (%Na) and Permeability Index (PI). The values of SAR, KR, SSP, RSC and %Na of the groundwater samples are within permissible limit indicating excellent water quality for irrigation purpose. The PI values of the groundwater, indicating unsuitable water quality for irrigation purpose. As per Richards's [15] classification, all groundwater samples fall in Poor/Bad water class.

Keywords Groundwater · Wastewater · Discharge · Agricultural purpose · etc.

1 Introduction

The fast growth of the industry has resulted in severe environmental problems, especially from the textile units. Hence there is evidence to suggest that these units extract the considerable quantity of groundwater from the peripheral areas and discharge the effluent without adequate treatment. The discharge of effluents has caused severe pollution of surface water, groundwater and soil in the study area. Groundwater contamination is the result of polluted water infiltrating through the soil and rock and eventually reaching the groundwater. This process might take many years and

A. D. Pathare (✉)

Pravara Rural Engineering College, Loni, Maharashtra, India

D. B. Panaskar · V. M. Wagh

School of Earth Sciences, S.R.T.M. University, Nanded, Maharashtra, India

S. B. Salunkhe · R. S. Pawar

SVERIs College of Engineering Pandharpur, Solapur, Maharashtra, India

e-mail: rspawar@coe.sveri.ac.in

might take place at a distance from the well where the contamination has found. Once any pollutant contaminates the groundwater, it is difficult to remediate [1]. Untreated water near the point of the disposal site, create a bad odour and foul smell [2]. This bad odour is due to decomposition of floating solids present in untreated sewage. The net result is massive scale pollution of the water bodies which may act as a source of water supply for domestic use of inhabitants of localities. This loss of water quality is causing severe health hazards and death of human, livestock as well as aquatic lives, crop failure and loss of aesthetics [3]. Solapur is one of the major city in the State of Maharashtra, India. Being one of the important industrial cities, Solapur is a leading centre for cotton mills and power-looms. Various textile products like bed-sheets, terry-towels and chaddars etc. have exported to different countries in different parts of the world which have earned international fame and reputation due to their novel designs, attractive colours and durability.

2 Study Area

The study area has located between 17° 38' to 17° 41' N latitude and 75° 55' to 75° 58' E longitude shows in Fig. 1. The Solapur is situated on the south-east fringe of Maharashtra State and lies entirely in the Bhima and Seena river basin. Solapur is one of the major cities in the State of Maharashtra. It has located on the borders of the Karnataka and Andhra Pradesh state. The temperature the study area varies in a range of maximum up to 46° C and minimum up to 9 °C. The average rainfall of the Solapur is about 545 mm and stands last in list of cities in the Maharashtra state. The soil of the area is broadly classified into three types i.e. Black, Coarse grey and reddish. The major crops in study area are mainly sugarcane, jawar, wheat, chana, tur, groundnut etc. The Photos 1 and 2 shows the discharge of effluent in to environment without any treatment [4].

3 Materials and Methods

Water samples for physicochemical analysis have collected directly into the clean 1-L plastic can. The samples of groundwater from the depths ranging from 80 to 150 m have collected for the analysis. Temperature and pH were measured at a sampling station, using a thermometer and digital pH meter, respectively. All the samples have analysed for physicochemical constituents. The laboratory analyses have undertaken by adopting the standard procedures given by APHA [5] and Trivedy and Goel [6]. The concentration of Sodium (Na^+) content and potassium (K) contents have analyzed by flame photometer. All the results presented are in milligram per litre (mg/L) unless otherwise indicated [7].

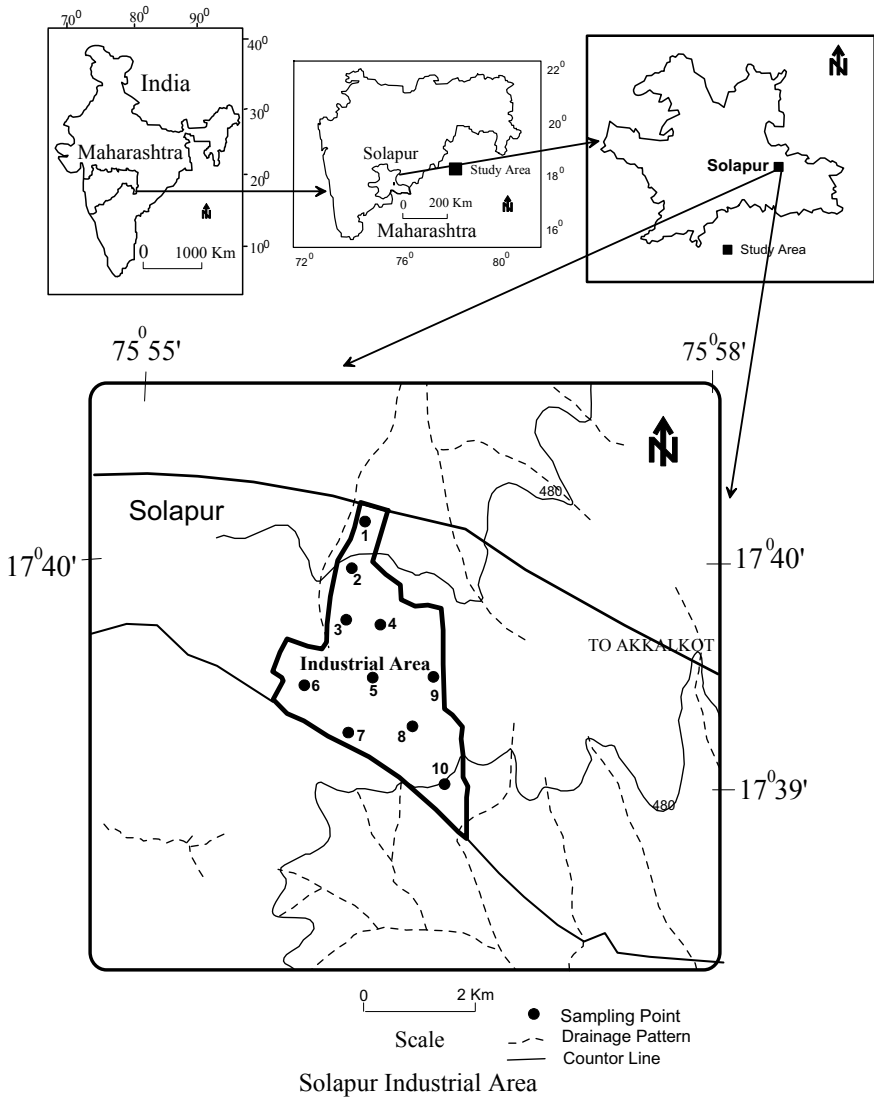


Fig. 1 Location map of the study area

4 Result and Discussion

The quality of groundwater is essential because it is the main factor which decides its suitability for domestic, industrial and agricultural purpose. Results of the Groundwater samples (Table 1) have compared with the World Health Organization (WHO)



Photo 1 Discharged untreated effluent in environment



Photo 2 Mixing of acidic and alkaline wastewater

guidelines for drinking water [8]. The concentrations that are above the guideline values have identified and discussed.

4.1 Classification of Groundwater for Agricultural Purposes

The characteristic ratios of the groundwater in the Solapur industrial belt are shown in Table 2. These ratios like Sodium Absorption Ratio (SAR), Kelly's Ratio (KR), Soluble Sodium Percentage (SSP), Residual Sodium Carbonate (RSC), Percent

Table 1 Physico-chemical characteristics of groundwater of solapur industrial area

Parameters	Unit	Min	Max	Average	STDEV
pH	-	7.6	8.2	7.91	0.213
Temp	°C	28	30	28.8	0.788
EC	μS/cm	37,950	217,800	137,180	56,607.3
TDS	mg/l	24,288	139,392	87,795.2	36,228.7
TH		900	3540	1946	752.8
Ca		160.3	889.8	490.4	195.7
Mg		48.8	292.4	176.6	80.5
Na		13.5	39.1	27.5	8.44
K		3.2	5.6	3.66	0.69
HCO ₃		170	490	340.5	92.41
Cl		167.6	2273.4	1047.3	661.33
Acidity		20	97.5	61.75	25.95

Table 2 Characteristics ratio of groundwater of solapur industrial area

Sample No	SAR	KR	SSP	RSC	% Na	PI
S ₁	0.21	0.022	2.15	-43.84	2.43	6.31
S ₂	0.24	0.026	2.56	-38.45	2.75	7.79
S ₃	0.36	0.041	4.02	-31.79	4.23	10.32
S ₄	0.44	0.067	6.31	-17.90	6.67	14.93
S ₅	0.56	0.094	8.61	-9.99	9.01	22.98
S ₆	0.39	0.053	5.03	-22.21	5.29	13.20
S ₇	0.26	0.029	2.87	-33.56	3.08	9.05
S ₈	0.21	0.025	2.48	-27.72	2.72	9.82
S ₉	0.16	0.016	1.65	-43.04	1.83	6.53
S ₁₀	0.10	0.008	0.85	-65.67	0.98	3.26
Max	0.56	0.09	8.61	-9.99	9.01	22.98
Min	0.1	0.008	0.85	-65.67	0.98	3.26
Average	0.29	0.03	3.65	-33.42	3.9	10.42
STDEV	0.142	0.0262	2.38	15.69	2.45	5.55

Sodium (%Na), and Permeability Index (PI), evaluate the groundwater quality for the irrigation purposes [7].

4.2 Sodium Absorption Ratio (SAR)

The SAR is an essential parameter for the determination of the suitability of irrigation water because it is responsible for the sodium hazard [9]. The SAR values of the groundwater samples range from 0.10 to 0.56. The water having $SAR \leq 10$ are excellent quality, 10–18 are good, 18–26 are fair and above 26 are unsuitable for irrigation purpose [10]. The SAR values for groundwater of the study area are less than 10 and therefore indicate excellent quality for irrigation purpose.

4.3 Kelly's Ratio (KR)

The KR values of the groundwater samples range from 0.008 to 0.094. The water having $KR \leq 1$ has considered being of good quality for irrigation, on the other hand, KR of more than one has deemed to be unsuitable for irrigation, and it causes alkali hazards to the soil [11]. The KR values for groundwater of the study area are less than one and therefore indicate excellent quality for irrigation purpose.

4.4 Soluble Sodium Percentage (SSP)

The SSP values of the groundwater samples range from 0.85 to 8.61. The SSP values of ≤ 50 indicate good quality and if it is more than 50 it indicates the unsuitable water quality for irrigation purpose. The SSP values for groundwater of the study area are less than 50 and therefore indicate excellent quality for irrigation purpose.

4.5 Residual Sodium Carbonate (RSC)

The excess of Carbonate and Bicarbonate of water is denoted as residual sodium carbonate [9]. The RSC values of the groundwater samples range from -65.67 to -9.99 . If the RSC values are $\leq .25$ indicates safe water quality, 1.25–2.5 indicates marginally suitable and if it is more than 2.5 then it is unsuitable for irrigation purpose. The RSC values for groundwater of the study area are less than 1.25 and therefore indicate excellent quality for irrigation purpose.

4.6 Percent Sodium

Sodium concentration is an essential parameter in classifying irrigation water because sodium reduces the permeability of soil. Excess Sodium in water is responsible in changing soil properties and reducing soil permeability [12]. In all-natural waters percent of Sodium content is a parameter to evaluate its suitability for agricultural purposes [13], Sodium combining with carbonate can lead to the formation of alkaline soils, while Sodium combining with Chloride forms saline soils. Alkaline as well as saline soils do not help the plants for their growth. Sodium content is expressed in terms of Percent Sodium (%Na). The calculated value of percent sodium ranges from 0.98 to 9.01. According to standards, a maximum of 60% sodium in water is allowed for agricultural purposes. The % Na values for groundwater of the study area are less than 60% and therefore indicate excellent quality for irrigation purpose.

4.7 Permeability Index (PI)

The soil permeability is affected by long term use of irrigation water and is influenced by bicarbonate, magnesium, calcium and sodium contents of the soil. The PI, as developed by Doneen [14] indicates the suitability of water for irrigation. According to permeability indices the waters may be divided into Class I, Class II and Class III types. Class I and Class II water types are suitable for irrigation with 75 percent or more of maximum permeability and Class III type water with 25% maximum permeability. The PI values for the groundwater samples range from 3.26 to 22.98. Based on the Doneens chart all the groundwater samples in the study area are unsuitable for irrigation purpose.

4.8 Salinity

The Na and EC concentrations are significant in classifying irrigation water. The electrical conductivity (EC) values range from 37,950 to 217,800 $\mu\text{S}/\text{cm}$. The high salt content in irrigation water leads to the formation of saline soil. Also affects the salt intake capacity of the plants through their roots. Based on electrical conductivity (EC) values, Richards [15] has classified irrigation water into four groups (Table 3).

The salinity can also be measured in terms of electrical conductivity. The occurrence of saline water is more frequent in all sampling points. Saline water is generally associated with alluvial aquifers which in general, yield water of higher salinity. Moreover, the bicarbonates contamination from the salt, which is mixed with the dyes from the textile industries found to increase the electrical conductivity (EC) of the water [1]. As per Richards's [15] classification, all groundwater samples fall

Table 3 Irrigation water quality classification (after Richard [15])

Water class	Salinity hazard		Alkali hazard	
	EC $\mu\text{S}/\text{cm}$	No. of samples	SAR	No. of samples
Excellent	Up to 250	–	Up to 10	10
Good	250–750	–	10–18	–
Fair/Medium	750–2250	–	18–26	–
Poor/Bad	>2250	10	>26	–

in Poor/Bad water class. Excess salinity reduces the osmotic activity of plants and interferes with the absorption of the water and nutrients from the soil [16].

5 Conclusion

From the detailed hydro-chemical study of the groundwater, it is observed that the pH of the groundwater has remained alkaline in the study area. Based on EC, all of the groundwater samples represent bad water class. All groundwater samples show very high TDS values than maximum desirable limit indicating mixing of effluent water in the aquifer and thereby contaminating the groundwater. All the groundwater samples are very hard. Majority of the groundwater samples Ca (90%) and Mg (80%) content higher than the maximum desirable limit. The chloride content of most of the groundwater samples (70%) is above maximum desirable limit, which indicates that the mixing of sewage waste and industrial waste in the groundwater. The groundwater from the study area have classified for irrigation purpose based on Sodium Absorption Ratio (SAR), Kelly's Ratio (KR), Soluble Sodium Percentage (SSP), Residual Sodium Carbonate (RSC), Percent Sodium (%Na) and Permeability Index (PI). The all groundwater samples SAR, KR, SSP, RSC and %Na values for the groundwater are within permissible limit indicating excellent for irrigation purpose. The only PI values of all the groundwater samples are unsuitable for irrigation purpose.

References

1. Geetha A, Palanisamy PN, Sivakumar P, Ganesh Kumar P, Sujatha M (2008) Assessment of underground water contamination and effect of textile effluents on Noyyal River basin in and around Tiruppur Town, Tamilnadu. *E-J Chem* 5(4):696–705
2. Kulkarni GJ (1997) Water supply and sanitary engineering, 10th edn. Farooq Kitab Ghar, Karachi, p 497
3. Nasrullah RN, Bibi H, Iqbal M, Durrani MI (2006) Pollution load in industrial effluent and ground water of Gadoon Amazai Industrial Estate (GAIE) Swabi, NWFP. *J Agric Biol Sci Asian Res Publ Netw* 1(3):18–24

4. Pawar RS, Panaskar DB (2014) Characterisation of groundwater in relation to domestic and agricultural purpos, Solapur Industrial Belt, Maharashtra, India. *J Environ Res Dev (JERAD)* 9(01):102–112
5. APHA (1985) Standard methods for the estimation of water and wastewater, Washington D.C., pp 6–187
6. Trivedi RK, Goel PK (1986) Chemical and biological methods for water pollution studies. Environmental publication, Karad
7. Panaskar DB, Wagh VM, Pawar RS (2014) Assessment of groundwater quality for suitability of domestic and irrigation from Nanded Tehsil, Maharashtra, India. *SRTMUs J Sci* 3(2):71–83
8. World Health Organization (WHO) (2002) Guideline for drinking water quality, 2nd edn. Health criteria and other supporting information. World Health Organization, Geneva., pp 940–949
9. U.S. Salinity Laboratory Staff (1973) Diagnosis and improvement of saline and alkali soils. U.S. department of agriculture hand book. No.60, 2nd ed
10. U.S. Salinity Laboratory Staff (1954) Dignosis and improvement of saline and alkali soils, U.S. department of agriculture hand book. No.60, 160p
11. Karanth KR (1987) Groundwater assessment, development and management. Tata McGraw-Hill Publishers, New Delhi
12. Kelly WP (1940) Permiability composition and concentration of irrigated waters. In: *Proceedings of the American society of civil engineers*, vol 66, pp 607–613
13. Wilcox LV (1955) Classification and use of irrigation water. USDA, Washington DC
14. Doneen LD (1964) Notes on water quality in agriculture, published as a water science and engineering, paper 4001. Department of water science and engineering, University of California, Davis
15. Richards LA (1954) Diagnosis and improvement of saline and alkali soils. US Salinity Laboratory Staff, US Department of Agriculture, Washington DC
16. Raju JN, Ram P, Dey S (2009) Groundwater quality in the lower Varuna river basin, Varanasi district, Uttar Pradesh. *J Geol Soc India* 73:178–192

Classification of Groundwater Quality for Drinking Purpose Concerning Industrial Effluent from Akkalkot MIDC, Solapur, Maharashtra, India



D. V. Pathare, D. B. Panaskar, V. M. Wagh, S. B. Salunkhe, and R. S. Pawar

Abstract The growth of the industry has resulted in severe environmental problems, especially from the textile units. The discharge of effluents has caused serious pollution of surface water, groundwater and soil in the study area. Groundwater contamination is the result of polluted water infiltrating through the soil and rock and eventually reaching the groundwater. Solapur is one of the major city in the state of Maharashtra and is a leading centre for cotton mills and power looms. Various textile products like bed-sheets, terry-towels, and chaddars etc. have exported to different countries which have earned international reputation and fame due to their novel design, attractive colours and durability. For the present study, ten samples from the Solapur Industrial Area have been collected and subjected to physicochemical analysis. In this paper, the results have been discussed in detail. Most of the parameter like EC (100%), TDS (100%), TH (100%), Ca (90%), Mg (80%), Cl (70%), etc. shows their contents above maximum permissible limit given by WHO.

Keywords Industrial effluent · Groundwater · Wastewater · Discharge

1 Introduction

The wastewater discharges have not avoided in the process of industrial developments which lead to the pollution of water. The water bodies are becoming major sinks for industrial pollutants. The establishment of industries or any manufacturing unit accelerates the development and helps to increase employment opportunities but unintentionally pollutes the environment, especially through the release of effluent

D. V. Pathare (✉)

Padmashri DVVP Institute of Technology and Engineering (Polytechnic) College, Pravaranagar, Loni, Maharashtra, India

D. B. Panaskar · V. M. Wagh

School of Earth Sciences, S.R.T.M. University, Nanded, Maharashtra, India

S. B. Salunkhe · R. S. Pawar

SVERIs College of Engineering Pandharpur, Solapur, Maharashtra, India

e-mail: rspawar@coe.sveri.ac.in

and emissions. Such impact of industrial development is highly complex and many times, unintentional. The industrial discharges from various units contain different types of pollutants like phenols, oils, plastics, suspended solids, traces of heavy metals as well as pesticides etc. These pollutants released to lead to the pollution of surface water, groundwater and the soils directly or indirectly. Release of industrial effluent is a major environmental issue related to the textile industries, steel industries, pharmaceuticals, leather industries, etc. These industries discharge large volumes of wastewater with varying amount of highly polluting contaminants into the environment.

Natural and anthropogenic activities reflect spatial variations in the physicochemical parameters of the groundwater. The difference of dissolved ions concentration in the groundwater is generally, governed by velocity, lithology and quantity of groundwater flow, the solubility of salts, nature of geochemical reactions and human activities [1]. Suitable quality and quantity of groundwater become a more essential alternative resource to meet the drastic increase in agriculture, social and industrial development and to avoid the expected deterioration of groundwater quality due to heavy abstraction for various uses [2].

2 Study Area

The study area has located between 17° 38' to 17° 41' N latitude and 75° 55' to 75° 58' E longitude (Fig. 1). The Solapur have situated on the southeast fringe of Maharashtra State and lies entirely in the Bhima and Seena river basin. It is one of the major city in the Maharashtra state. Temperature of the study area varies in the range of maximum up to 46° C and minimum up to 9° C. The average rainfall of the Solapur is about 545 mm and stands last in the list of cities in the Maharashtra state. The soils of the area can be broadly classified into three types i.e. reddish, coarse gray and Black. The major crops in the study area has mainly sugarcane, jawar, wheat, chana, tur, groundnut etc.

The study area has located in the southern part of Solapur city. There are about 648 industries out of which about 461 industries are in working conditions and others are in non-working condition. In this industrial belt there are 334 textile mills. Most of these are in working conditions with very few in temporary non-working conditions. The total industrial area in the possession is 216.48 hector land, under residential and commercial use is about 5368 m² and the net area under industrial use is about 2,111,632 m² [3, 4].

3 Materials and Methodology

Water samples for physicochemical analysis have collected directly into clean 1-L plastic can. The samples of groundwater from the depths ranging from 80 to

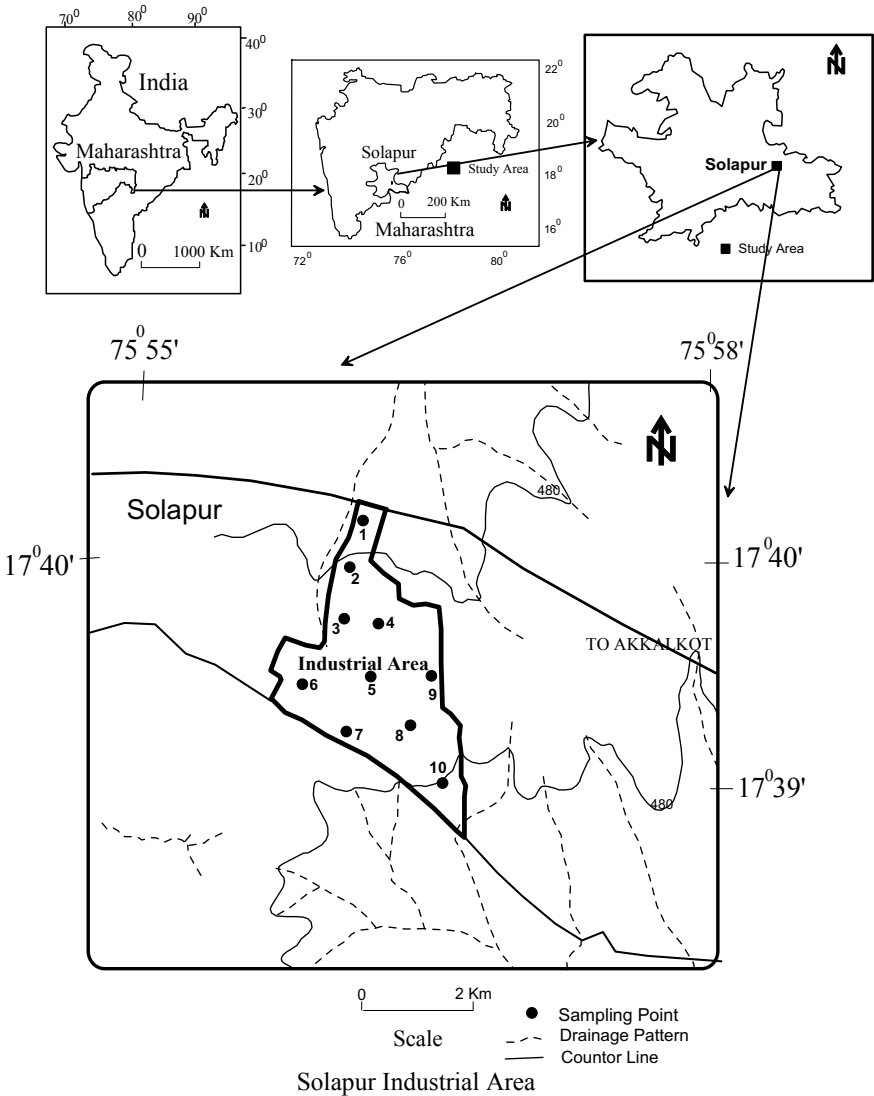


Fig. 1 Location map of the study area

150 m has collected for the analysis. Temperature and pH were measured at sampling station, using a thermometer and digital pH meter, respectively. All the samples have analysed for physicochemical constituents. The laboratory analyses have undertaken by adopting the standard procedures given by APHA [5] and Trivedy and Goel [6]. The concentration of Sodium (Na^+) content and potassium (K) contents have analyzed by flame photometer. All the results presented are in milligram per liter (mg/L) unless otherwise indicated [3, 4].

4 Result and Discussion

The quality of groundwater is very essential because it is the main factor which decides its suitability for domestic, industrial and agricultural purpose. The characteristics of main drain effluent in the Solapur industrial area have shown in the Table 1. Results of the Groundwater samples in Table 2 have compared with the World Health Organization (WHO) guidelines for drinking water [7]. The concentrations that are above the guideline values have identified and discussed.

4.1 Characteristics of Industrial Effluent

The pH of the effluent in the Solapur industrial area is within the limit i.e. 8.5. The EC of the effluent is 157000 $\mu\text{S}/\text{cm}$ in the industrial area. The EC value of the effluent is very higher than the maximum permissible limit. The extremely high values for EC are attributable to high levels of anion and cations [8]. The TDS of effluent is 100480 mg/l; this value higher than the maximum permissible limit. DO of the industrial effluent sample is 1.2 mg/l. The total hardness (TH) content of the effluent in the industrial area is 1700 mg/l, this indicates very hard water. The calcium (Ca) content of the effluent is 316.6 mg/l. This value is higher than the maximum permissible limit. The magnesium (Mg) content of the effluent is 221.7 mg/l. This value is higher than the maximum permissible limit. The chloride (Cl) content of the effluent is 1959.6 mg/l; this value is higher than the maximum permissible limit. The sodium (Na) content of the effluent is 68.8 mg/l. The Potassium (K) content of the effluent is 42.8 mg/l. The alkalinity of the effluent is 1070 mg/l. The acidity is 95 mg/l of the effluent in the industrial area [9].

Table 1 Characteristics of main drain effluent from the Solapur Industrial area

Parameters	Unit	Main drain effluent
pH	–	8.5
Temp	$^{\circ}\text{C}$	30
EC	$\mu\text{S}/\text{cm}$	157,000
TDS	mg/l	100,480
DO		1.2
TH		1700
Ca		316.6
Mg		221.7
Na		68.8
K		42.85
HCO_3^-		1070
Acidity		95

Table 2 Physico-chemical characteristics of groundwater of Solapur Industrial area

Parameters Sam. No	pH	Temp	EC	TDS	TH	Ca	Mg	Na	K	HCO3	Cl	Acidity
S1	7.7	28	181,400	116,096	2400	561.1	243.6	24.3	5.6	255	167.6	20
S2	7.8	29	169,200	108,288	2200	481	243.7	26.7	3.3	340	693	42.5
S3	8.1	28	138,330	88,531.2	1900	440.9	194.9	36.7	3.3	380	580.8	85
S4	7.7	28	89,600	57,344	1100	160.3	170.6	34.1	3.6	250	1498	30
S5	8.2	29	37,950	24,288	900	280.6	48.8	39.1	3.4	490	464.3	72.5
S6	7.9	30	107,700	68,928	1400	408.9	92.6	34.2	3.2	355	616.2	97.5
S7	8	29	172,700	110,528	2000	593.2	126.7	27.3	3.5	395	1069.2	85
S8	8.2	28	78,720	50,380.8	1720	513.1	107.2	20.2	3.4	410	1368.9	65
S9	7.9	29	178,400	114,176	2300	575.1	246.3	18.9	3.6	360	1742.4	75
S10	7.6	30	217,800	139,392	3540	889.8	292.4	13.5	3.7	170	2273.4	45
Min	7.6	28	37,950	24,288	900	160.3	48.8	13.5	3.2	170	167.6	20
Max	8.2	30	217,800	139,392	3540	889.8	292.4	39.1	5.6	490	2273.4	97.5
Average	7.91	28.8	137,180	87,795.2	1946	490.4	176.6	27.5	3.66	340.5	1047.3	61.75
STDEV	0.213	0.788	56,607.3	36,228.7	752.8	195.7	80.5	8.44	0.69	92.41	661.33	25.95

Unit—mg/L, except pH, Temperature—°C, EC—µS/cm

4.2 Characteristics of Groundwater

The groundwater quality classified for domestic and irrigation purposes. The physicochemical parameters of the Solapur industrial area are shown in Table 2. The results indicate, quality of water considerably varies from location to location. This wide variation is mainly due to dissolved material and salinity from the nearby dyeing and bleaching of textile industries in the study area [10].

4.3 Classification of Groundwater for Domestic Purposes

4.3.1 pH, EC and TDS

It can be seen that pH of groundwater has remained alkaline in study area. The minimum pH value of groundwater is 7.6 and maximum value is 8.2. The EC value of groundwater samples ranges from 37,950 to 217,800 $\mu\text{S}/\text{cm}$. All samples show EC values above 2250 $\mu\text{S}/\text{cm}$ representing poor/Bad water class and very highly saline nature of water. The TDS values of the groundwater samples range from 24,288 to 139,392 mg/l. All groundwater samples show high TDS values than maximum desirable limit given by WHO [11] indicating mixing of effluent water in the water body, aquifer and thereby contaminating the groundwater Fig. 2. According to the Fetter's [12] classification of waters based on the TDS, all groundwater samples come under brackish water (TDS > 1000 mg/l) categories. High TDS values in groundwater are generally not harmful to humans but these may affect persons, who are suffering from kidney, heart disease and cause laxative or constipation effects.

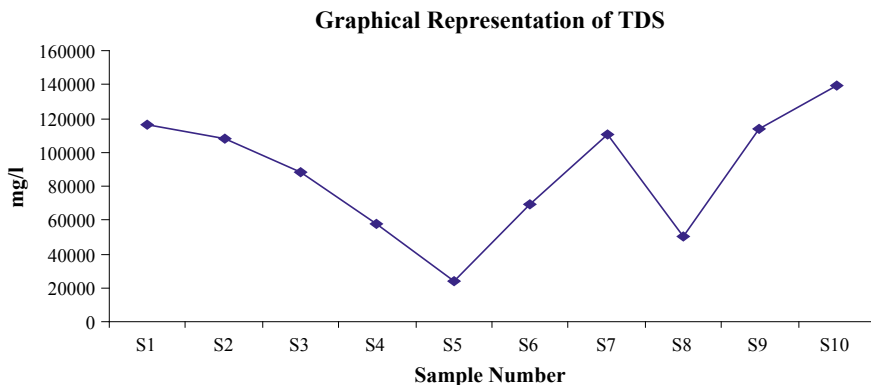


Fig. 2 Graphical representation of TDS in the study area

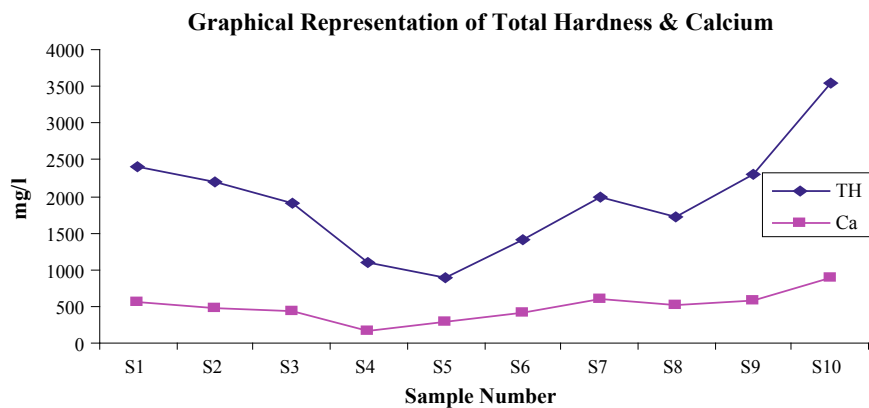


Fig. 3 Graphical representation of TH & Ca in the study area

4.3.2 TH, Ca and Mg

The Hardness value of the groundwater samples range from 900 to 3540 mg/l. The average Hardness (TH) value of the groundwater is 1946 mg/l. Hardness concentrations, with respect to their classifications, all the groundwater samples indicate the study area characterized by very hard water (>300 mg/l) Fig. 3. The important source of calcium is the dissolution of small quantities of carbonate compounds from textile industries. The Calcium value of the groundwater samples range from 160.3 to 889.8 mg/l. The average Calcium (Cl) value of the groundwater is 490.4 mg/l. Majority of the groundwater samples (90%) show calcium content higher than the maximum desirable limit. Magnesium usually occurs in lesser concentration than calcium due to fact that the calcium is more abundant in the earth's crust and that of dissolution of magnesium-rich minerals is slow process [13]. The Magnesium value of groundwater samples range from 48.8 to 292.4 mg/l. The average Magnesium (Mg) value of the groundwater is 176.6 mg/l. Majority of the groundwater samples (80%) show Magnesium content higher than the maximum desirable limit. Besides domestic wastes, the silicate minerals (plagioclase, feldspar and augite) could also have contributed towards sources of sodium, calcium and magnesium in basaltic host rock [14].

4.3.3 Na and K

The sodium value of groundwater samples range from 13.5 to 39.1 mg/l. The average sodium (Na) value of the groundwater is 27.5 mg/l. Sodium contents of all groundwater samples are below the maximum permissible limit. The Potassium concentration varies within very small ranges, from 3.2 to 5.6 mg/l in the industrial belt area.

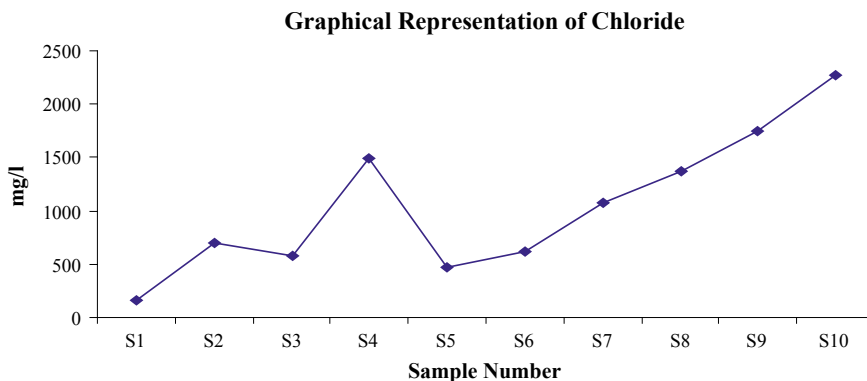


Fig. 4 Graphical representation of chloride in the study area

4.3.4 Alkalinity, Chloride and Acidity

The main cause of alkalinity in natural water is due to the presence of bicarbonates, carbonates and hydroxides [10]. The total alkalinity of the groundwater samples range from 170 to 480 mg/l. Alkalinity within considerable ranges in the area elaborates alkaline water type. The high alkalinity imparts water an unpleasant taste and may be deleterious to human health along with the high pH, TDS and TH [15]. Chloride is a wide distributed element in all type of rocks. Cl affinity towards sodium (Na) is high. Therefore, its concentration is high in groundwater, where the rainfall is less and the temperature is high. Soil porosity and permeability have a key role in building up the chlorides concentration. The chloride values of the groundwater samples ranges from 167.6 to 2272.4 mg/l. The avg. chloride (Cl) value of the groundwater is 1047.3 mg/l Fig. 4. It may be due to the continuous usage of chloride salts in the industries, preferably in dyeing and bleaching. An excess of chloride (Cl) in water is usually taken as an index of pollution and considered as a tracer for groundwater contamination [16]. The chloride content of most of the groundwater samples (70%) is above the maximum desirable limit, which indicates that mixing of sewage waste and industrial waste in the groundwater. Increase in chloride level is injurious to people suffering from diseases of heart and kidney [7]. Acidity varies from 20 to 97.5 mg/l in the industrial belt.

5 Conclusion

From the detailed hydro chemical study of the industrial effluent, it is observed that the pH of the effluent has remained alkaline. The EC, TDS, TH, Ca and Mg content of the effluent is higher than the maximum desirable limit; this indicates effluent water is highly polluted and affected to the groundwater, soil and natural environment.

From the detailed hydro chemical study of groundwater it is observed that the pH of the groundwater has remained alkaline in the study area. Based on EC, all of the groundwater samples represent bad water class. All groundwater samples show very high TDS values than the maximum desirable limit indicating mixing of effluent water in aquifer and thereby contaminating the groundwater. All the groundwater samples are very hard. Majority of the groundwater samples Ca (90%) and Mg (80%) content higher than the maximum desirable limit. The chloride content of most of the groundwater samples (70%) is above maximum desirable limit, which indicates that mixing of sewage waste and industrial waste in the groundwater.

References

1. Bhatt KB, Salakani S (1996) Hydrogeochemistry of the upper Ganges River, India. *J Geol Soc India* 48:171–182
2. Elkraill A, Shu L, Kheir O, Zhenchun H (2003) Hydrochemical evaluation of groundwater in Khartoum State, Sudan. *Map Asia 2003 conference, environmental planning*
3. Pawar RS, Panaskar DB (2014) Characterisation of groundwater in relation to domestic and agricultural purpos, Solapur Industrial Belt, Maharashtra, India. *J Environ Res Dev (JERAD)* 9(01):102–112
4. Panaskar DB, Wagh VM, Pawar RS (2014) Assessment of groundwater quality for suitability of domestic and irrigation from Nanded Tehsil, Maharashtra, India. *SRTMUs J Sci* 3(2):71–83
5. APHA (1985) Standard methods for the estimation of water and waste water, Washington D.C., pp 6–187
6. Trivedi RK, Goel PK (1986) Chemical and biological methods for water pollution studies. Environmental publication, Karad
7. World Health Organization (WHO) (2002) Guideline for drinking water quality. Health Criteria and other supporting information, 2nd edn. World Health Organization, Geneva, pp 940–949
8. Kale SS, Kadam AK, Kumar S, Pawar NJ (2009) Evaluating pollution potential of leachate from landfill site from the Pune metropolitan city and its impact on shallow basaltic aquifers. *Environ Monit Assess* 2010(162):327–346
9. Yusuff RO, Sonibare JA (2004) Characterization of textile industries' effluents in Kaduna, Nigeria and pollution implications. *Global Nest: Int J* 6(3):212–221
10. Geetha A, Palanisamy PN, Sivakumar P, Ganesh Kumar P, Sujatha M (2008) Assessment of underground water contamination and effect of textile effluents on Noyyal River basin in and around Tiruppur Town, Tamilnadu. *E-J Chem* 5(4):696–705
11. World Health Organization (WHO) (1998) International standards for drinking water quality- Geneva, WHO
12. Fetter CW (1990) Applied hydrogeology, 2nd edn. CBS Publishers and Distributors, New Delhi, 592p
13. Varadarajan N, Purandara BK (2003) *Environment and conservation* 9(3):253–262
14. Hem JD (1985) Study and interpretation of the chemical characteristics of natural water. USGS water supply paper 2254
15. Pawar NJ (1993) Geochemistry of carbonate precipitation from the ground waters in basaltic aquifers: an equilibrium thermodynamic approach. *J Geol Soc India* 41:119–131
16. Loizidou M, Kapetanios EG (1993) Effect of leachate from landfills on underground water quality. *Sci Total Environ* 128:69–81

Assessment of Rainwater Harvesting Potential in Tuljapur Tahsil, Osmanabad District, Maharashtra India Using Remote Sensing and GIS



R. S. Pawar, S. A. Gosavi, S. V. Pathare, M. R. Chougule, and D. D. Kulkarni

Abstract Rain Water Harvesting (RWH) and its Conservation, is the activity of direct collection of rainwater and collected rainwater can be recharged into the Ground Water or can be store for immediate use. The main aim of the RWH is to reduce the flow of Rain Water through Drains/Streams/Nalas to the rivers without any use of the same. It is a well-known fact that the Ground Water level is depleting and going down and down in the last 2–3 decades. Thus Rain Water Harvesting and Conservation aims at optimum utilization of the natural resource, which is the first and clean source of water that everybody knows in the water cycle and hence is a first or primary source of water for the human being. The lakes, rivers and groundwater harvesting and conservation, we all depend entirely on such secondary sources of water for all-purpose. In the process, it is forgotten that the final source of feed for these secondary sources is rainwater. The value of this essential primary source of water must not be lost.

Keywords Rainwater · Harvesting · Potential · RS and GIS · Etc.

1 Introduction

Water is the most essential for maintaining an ecosystem and environment conducive to sustaining life. Water plays a vital role not only in satisfying basic human needs for health and life as well as in socio-economic development. It is crucial to conserve and manage this precious and limited resource. As the primary source of water is rain, so it becomes necessary for us to use or harvest it effectively, we can maximize the storage and minimize the wastage of rainwater [1].

R. S. Pawar (✉) · S. A. Gosavi
SVERIs College of Engineering Pandharpur, Solapur, Maharashtra, India
e-mail: rspawar@coe.sveri.ac.in

S. V. Pathare · M. R. Chougule
Department of Geology, Rajaram College, Kolhapur, Maharashtra, India

D. D. Kulkarni
School of Earth Sciences, PAH Solapur University, Solapur, Maharashtra, India

According to GSDA, Tuljapur tahsil is received less amount of rainwater during monsoon season; hence groundwater is highly depleted due to receive less amount of water from rain. The Tuljapur tahsil is a dry area and belongs to over exploited category. This will increase demand and pressure on previously depleted water resource many folds. Studies need to be conducted for identification of catchment areas with good storage recharge potential and groundwater aquifers with good retention and community level projects be developed and implemented, so that sustainability of water resources can be assured [2].

2 Study Area

Tuljapur is a city located in the south-eastern region of the Indian state of Maharashtra. Tuljapur is located on major road and rail routes between Solapur and Osmanabad, with a branch line to the cities of Bidar and Gulbarga in the neighbouring state of Karnataka. It is well known for Tulja Bhavani temple. Tuljapur tahsil lies between 17°39' N to 18°60' N latitude and 75°50' E to 76°25' E longitude ref. Figures 1, 2 [3 and 4].

3 Materials and Methods

3.1 Material Used

The study area lies in the geological survey of India (GSI) toposheet no. 56 B/4, 56 B/8, 56 C/1, 56 C/2, 56 C/3, 56 C/5, 56 C/6 and 47 N/16. All toposheets are 1:50,000 scale with contour interval of 20 m. Used Software - ERDAS Imagine-11 has been used for mosaic and their classification. ArcGIS Desktop 10.1 for Vector and Raster based analysis such as Map Overlay, Proximity Analysis, Local and Zonal Function, Rainfall Interpolation, and for generating Flow Accumulation map, Raster Stream Network and Stream Order map. Google Earth has been used for digitizing settlements, water body, pediments and hills [5]. Used datasets are given below.

1. Landsat 8 image, May 2015; band – 3, 4, 5; resolution 30 m.
2. CARTOSAT –DEM, resolution 30 m.
3. Soil Map, Hydrological Map, Rainfall data of Maharashtra has been collected from Govt. officials.
4. Field data has been collected using GPS for ground truth.

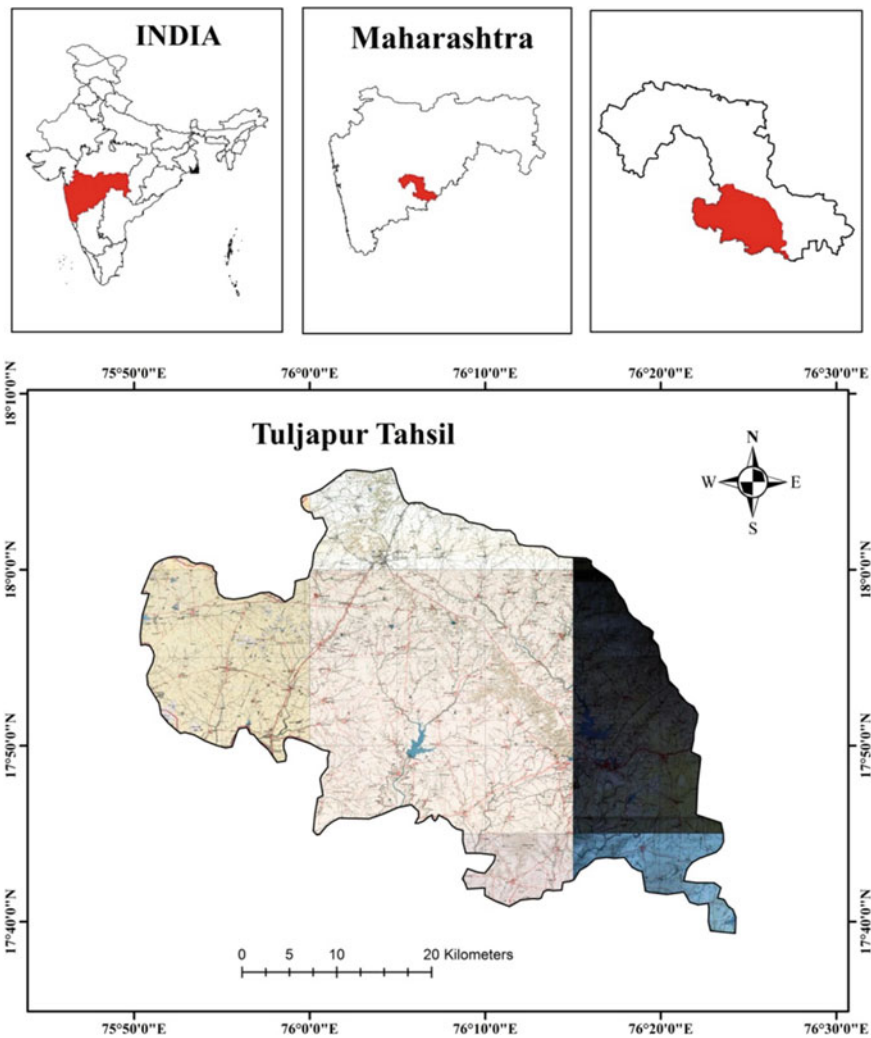


Fig. 1 Location map of the study region

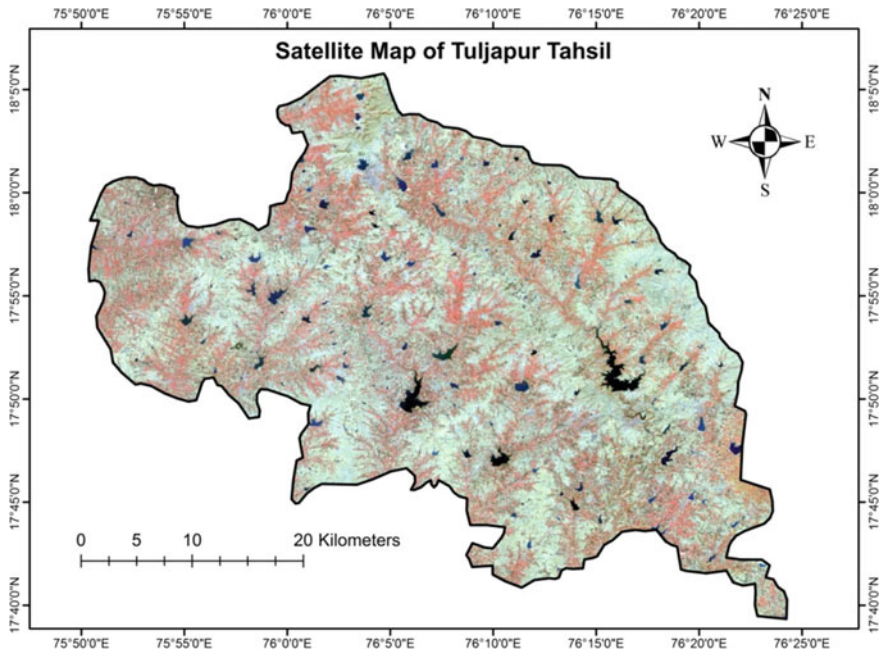


Fig. 2 Satellite image of the study region

3.2 Methodology

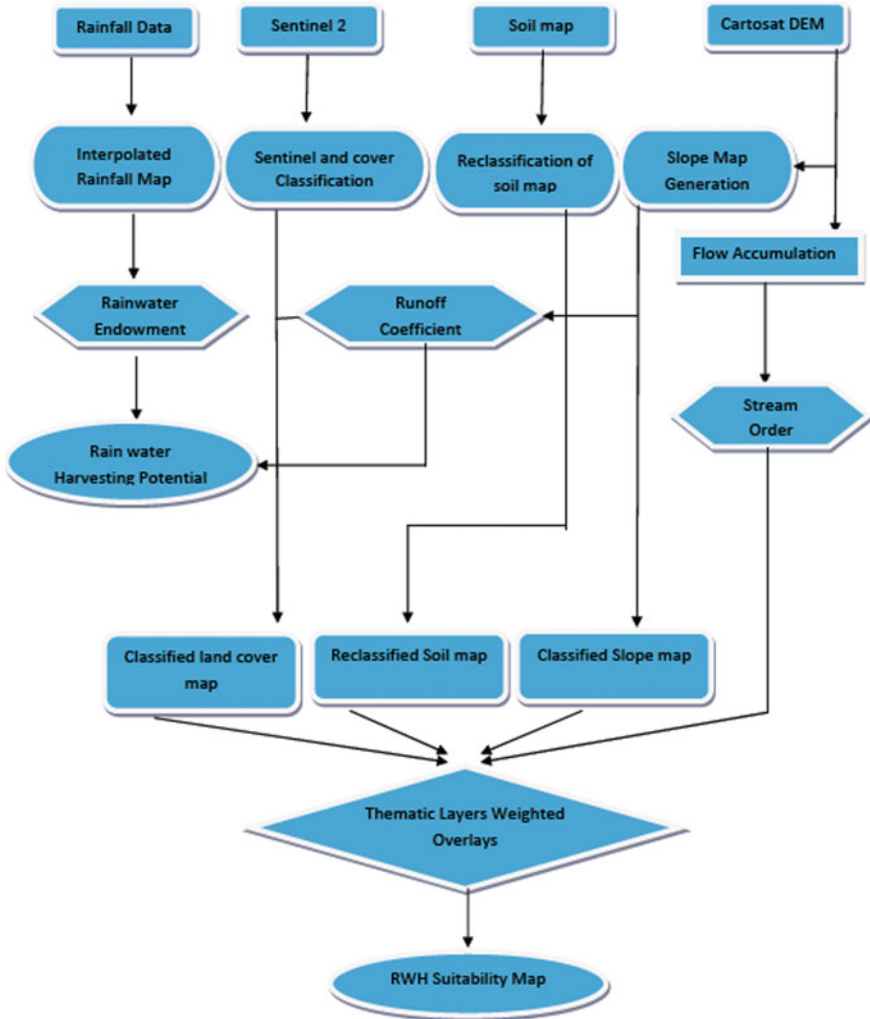
The methodology used in the present research work has summarized in Flow Chart 1.

3.3 DEM Hydro-Processing

It involves the extraction of drainage parameters from DEM. In the present study, Flow Accumulation Raster, Flow Direction Raster, Stream Raster, Strahler Stream Order, etc. Hydrological parameters have extracted from Hydrological tools of ArcGIS 10.0 (Figs. 3, 4, 5, 6, 7, 8, 9) [6].

3.4 Rain Water Harvesting Potential (RWHP) Calculations

The total amount of water i.e. collected or received in the form of rainfall over a region is called the Rain Water Endowment (RWE) of that region. Out of this, the total amount that can effectively harvest called the Rain Water Harvesting Potential [7, 8].



Flow Chart 1 Summarized Flow Chart of Used Methodology

$$RWHP = \text{Rainfall Endowment Area} \times \text{Runoff Coefficient} \times \text{Constant Coefficient}$$

4 Results and Discussion

The data such as LULC, Slope map, Drainage etc. have generated using ArcGIS software. In the present research work, Runoff Coefficient value for different land

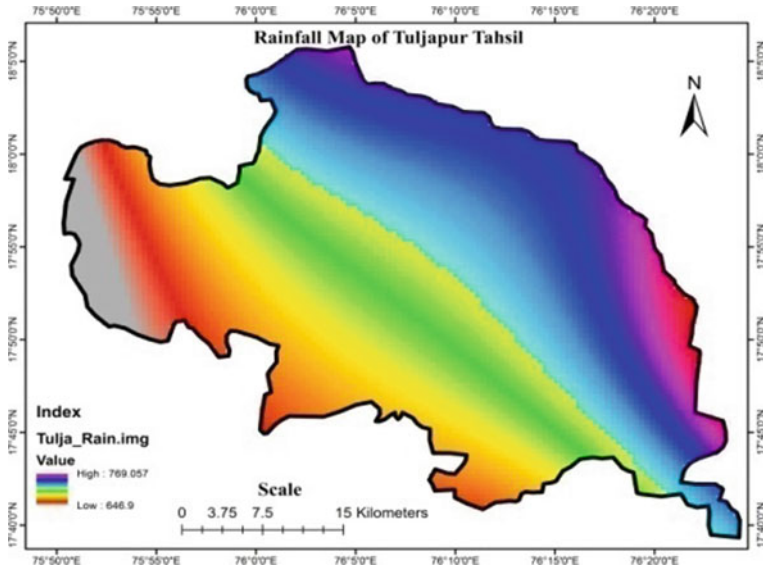


Fig. 3 Annual rainfall (cm) map

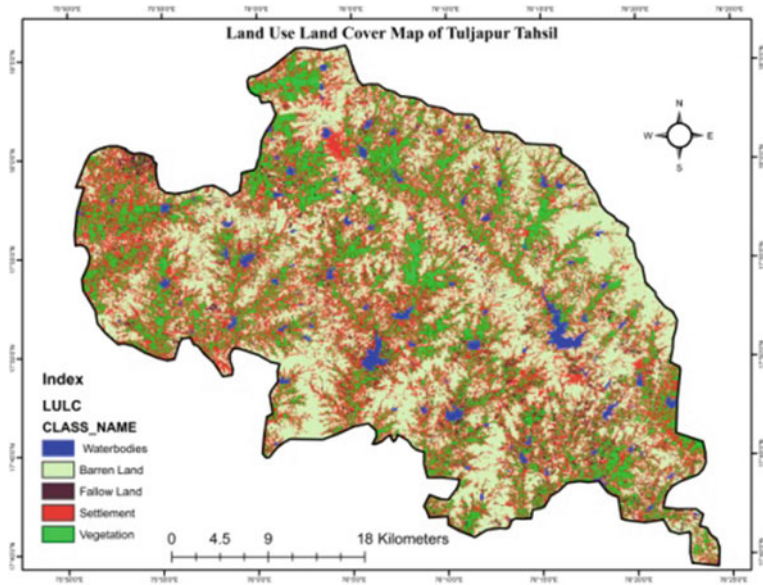


Fig. 4 LULC map

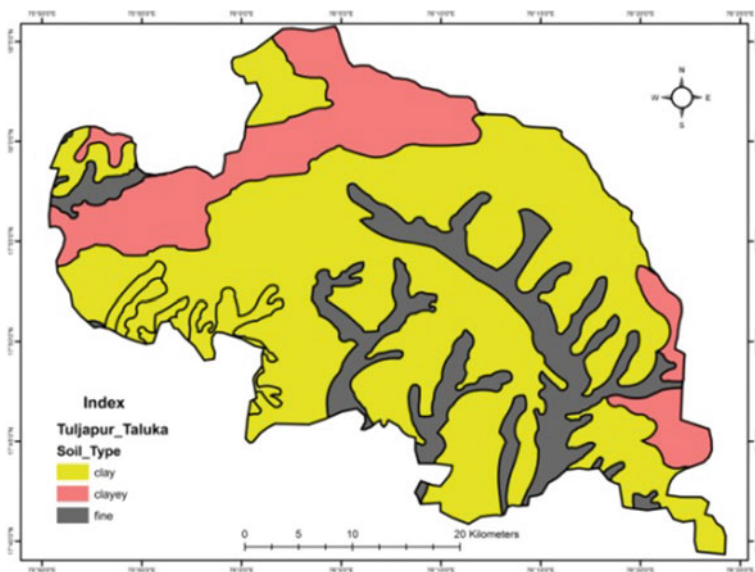


Fig. 5 Soil types map

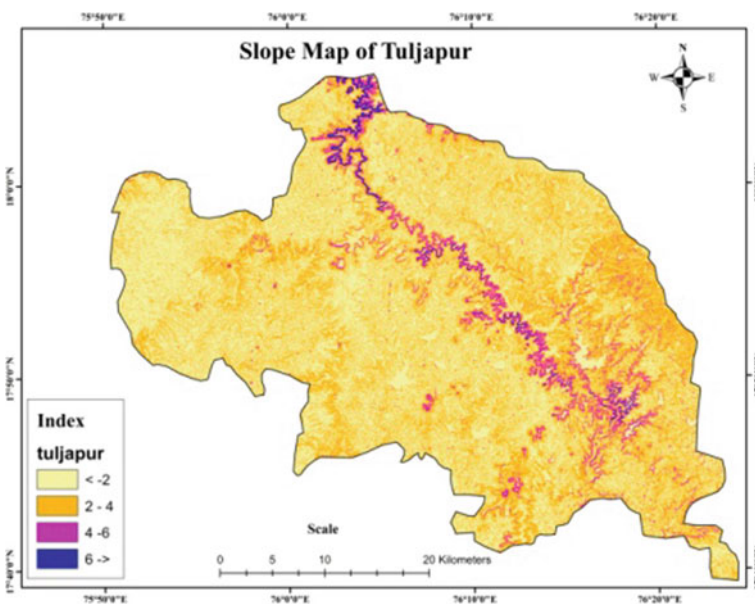


Fig. 6 Slope map

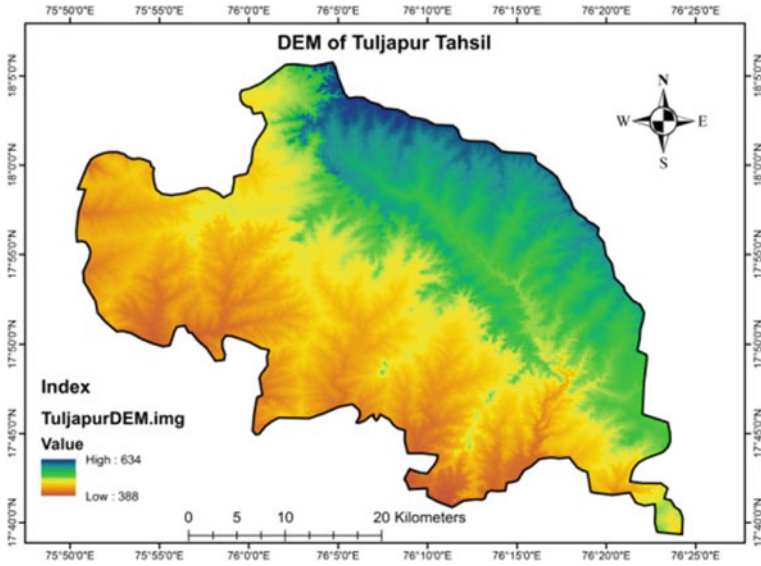


Fig. 7 DEM (meter) map

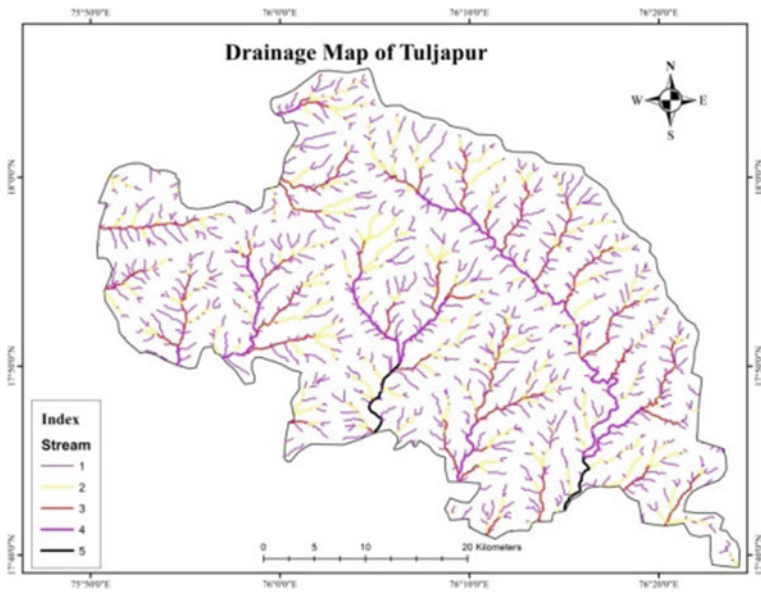


Fig. 8 Drainage map

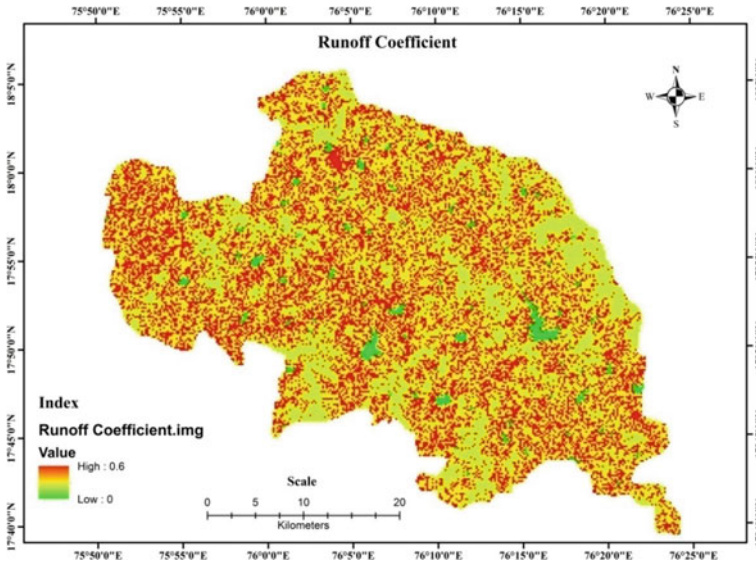


Fig. 9 Runoff coefficient map of study area

use, watershed slopes and Soil. Runoff Coefficient raster is created by combining a thematic layer of Slope Map and LULC Map and then assigning respective values. By putting this Raster Layer and Rainwater Endowment raster layer into formulae, Rain Water Harvesting Potential Map has generated, and the total potential has calculated ref Table 1. The weighted overlay techniques create RWHP map ref Fig. 10a. Total RWE of the study area is as given Table 1 and Fig. 10b.

Table 1 Classification of LULC area (sq. Km), runoff coefficient and total rainwater endowment of study area

Class	Area (sq. Km)	Runoff coefficient	RWHP (cubic meter)
Vegetation	311.4826	0.35	76,313.24
Barren Land	593.9867	0.32	133,053.02
Fallow Land	75.7425	0.34	18,026.72
Built-up	532.8978	0.60	223,817.08
Waterbody	30.7828	0	21,547.96
Total	1544.8924	—	472,758.02

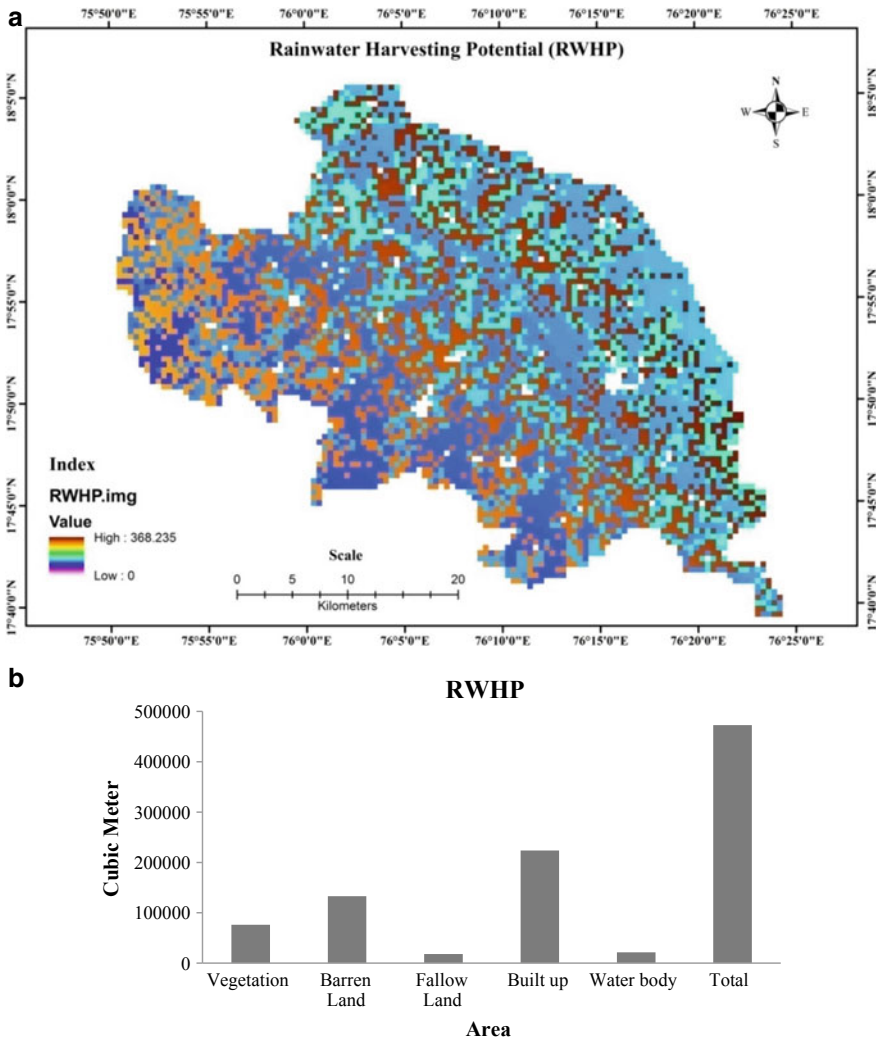


Fig. 10 a Rainwater harvesting potential (RWHP) map of study area, b Total rainwater endowment of the study area

5 Conclusions

Due to the speedy population explosion, urbanization, as well as industrialization in the study area demand for water consumption, has increased at day by day. Statistics on water availability in the study region has already revealed that the water table of study has gone down remarkably in the last 2 to 3 decades. The area has sufficient potential to feed on the ever-increasing demand of water if harvest and conserve

properly. Site selection for Rain Water Harvesting is carried out by overlying the Soil, slope, land use/land cover and buffered stream order maps. The study region is having full scope for farm ponds, check dams and percolation tanks. The Produced map will be helpful for the selection of the best suitable location of harvesting structures and help in water conservation in water depleted area. RWHP map has created by the weighted overlay method. The RWHP of the study area is useful for the collection and percolating the rainwater which is received from the southwest monsoon. The total rainwater endowment of the study area is 472758.02 m³. Such a tremendous amount of water will fulfill the agricultural, industrial, domestic, commercial and many other purposes.

References

1. Litoria PK, Singh D, Singh JP (2009) Selection of suitable sites for water harvesting structures in Soankhad water, Punjab using remote sensing and geographical information system (RS & GIS) approach- a case study. *J Indian Soc Remote Sens* 37:2135. <https://www.indiaenvironmentportal.org.in/files/Soankhad.pdf>
2. CPWD, Govt. of India. Manual on rain water harvesting and conservation. Chapter 1, 2002.
3. Pawar RS, Panaskar DB (2014) Characterisation of groundwater in relation to domestic and agricultural purposs, Solapur Industrial Belt, Maharashtra, India. *J Environ Res Dev (JERAD)* 9(01):102–112
4. Panaskar DB, Wagh VM, Pawar RS (2014) Assessment of groundwater quality for suitability of domestic and irrigation from Nanded Tehsil, Maharashtra, India. *SRTMUs J Sci* 3(2):71–83
5. Padmavathy AS, Raj KG, Yoearajan N, Thangavel P, Chandrashekhar MG (1993) Check dam site selection using GIS approach. *Adv Space Res* 13(11):123–212
6. Arnold P, Adrian C (1989) *Rainwater Harvesting: the collection of rainfall and runoff in rural areas*. Intermediate Technology Publications, London
7. Rukesh RPS, Rastogi AK (2008) Rainwater Harvesting in hostel 12 and hostel 13 of IIT bombay. *Indians Soc Hydraul J Hydraul Eng*
8. <https://www.rainwaterharvesting.org>

Women Journalists in India's Rural Areas: Social and Economic Conditions



Md. Afsar and Suman Kumari

Abstract In the recent years, the growth of women journalists in India has been at a considerable rate. This growth includes women journalists from both urban and rural areas. However, involvement of women journalists belonging to rural areas as compared to the women journalists in urban areas is not that much noticeable in mainstream news media. But this is also a fact that the number of women journalists in rural areas has been substantially improved. Hence, the study of rural women journalists becomes significant to be explored. In this paper, we focus on the study and analysis of the social and economic conditions of female journalists in news media in India's rural areas.

Keywords Women journalist · Rural · Social · Economic

1 Introduction

At present, news media is being seen as a commercial medium instead it should be used to create and transmit the information to masses keeping the common people in mind. However, India's news media is busy in covering the matters which are in some way or the other related to the benefits of the news media organizations [1, 2]. Generally, rural issues are supposed to generate lesser profits and are lesser attractive for the dominant economic hubs. This result in giving a smaller amount of space in news media for the issues related to the rural areas than the issues related to urban people. In essence, Indian news media organizations are not performing their duty to protect the fourth pillar of our nation because they are not protecting the democratic rights of the rural people to highlight their issues and problems. Indian news media should be responsible to conduct political debates and seek the attention of the government towards the most underprivileged sections living in the rural areas

Md. Afsar (✉) · S. Kumari
FMeH, MRIIRS, Faridabad, India
e-mail: afsar11@rediffmail.com

S. Kumari
e-mail: suman.fmeh@mriu.edu.in

[3, 4]. For this reason, rise of the regional or local news media started to happen to present the news stories covering the problems related to rural issues.

Over the years, female journalists of rural areas have been successful in seeking the attention of the news media toward the rural areas issues. Rural women journalists have been successful in highlighting the issues of women living in rural areas of our country in the mainstream news media [5, 6].

Rural news media have substantially risen over the last few years. Khabar Lahariya is an example of the successful rural news media [7]. The newspaper has been efficiently raising the voices of the rural people for their rights such as education, equality for women and civil rights [8, 9]. These issues have not been given space in the mainstream news media and therefore, the importance of the rural news media can be easily seen.

In the mainstream news media, men generally overpower the women in terms of the designations and news coverage which is visible. However, women journalists have been able to represent themselves, to some extent, to remove the patriarchy in this profession [10, 11].

Women should be allowed to decide their own role in the society and also should be given equal opportunities which men get in the society in terms of the profession. This will enable women to stand hand to hand with men in the society. This will help in eroding the social and cultural constraints on women especially for the rural women [12, 13]. Rural women journalists have been trying to remove these barriers over the past few years [14]. Therefore, the study of rural female journalists is important in order to analyze their working conditions that have been successful in eroding the patriarchal thinking in rural areas of our country. In this paper, the focus is to provide an insight into the social and economic status of rural female journalists. In order to understand their living conditions, we have taken telephonic interviews and also done their interviews in person of the rural women journalists. Questionnaire has been used to comprehensively study their current status. The methodology used is provided in detail in the Sect. 2 of the paper.

Paper is organized in the following sections. Section 2 presents the analysis and detailed study of the social and economic status of the rural women journalists. Section 3 presents a literature review of the work done by the researchers related to this area. In Sect. 4, we present the paper conclusion.

2 Social and Economic Status of Rural Women Journalists

Journalism is now no more a male dominated profession because of the active participation of the women journalists. Women journalists are also now aware of the importance of their career. But still rural women journalists need to have more exposure to the mainstream news media [15, 16].

This is also a fact that rural women are far less educated as compared to women journalist in urban areas in our country. As compared to men, women are half in number; only 1 out of 100 girls pursue graduation that live in rural areas in India

(ASER report 2014). Forty seven percent of women in our country are married before the age of 18 (source: National Statistical Organization). Lack of education and awareness leads to worse situation in rural areas and in turn increase this percentage.

Women living in rural areas who complete their education pursue career of their choice. These women are more aware of their deserved positions and work in their organizations. Also, in their personal lives, they want to have their space in the decision making and not limit themselves as a in the family. Female journalists from rural areas have started to make their individual stories of success [17, 18]. But then, the number of these women is very low. Their social and economic conditions may be the cause behind these low numbers [19]. Thus, it becomes significant to comprehensively study the social and economic status of rural women journalists.

Social status of rural women journalists: In this section, we present those aspects which helps in analyzing the social status of rural women journalists in our country.

- Gender discrimination: In rural areas, doing job by women is considered as a bad thing to do which in turn stop them from pursuing their career. Male in rural areas generally do not favor this freedom of women. Men have a perception that the women are not capable of taking decisions of the family and also of their professional lives [20]. Rural women are constrained to take part in discussions, elections and social activities.
- Ill behavior of spouse: Spouses of rural women are generally addicted to alcohol. This is also considered as the main reason for their ill behavior towards female in their families. They will blame the women in their families for ignoring the traditions and not follow the social and cultural values [21]. This results in domestic fight and family problems in rural areas.
- Social class hierarchy: Rural women who belong to the suppressed and most underdeveloped classes undergo a high amount of social pressure when they go out in rural areas in order to cover the news stories. The old and rigid hierarchies in our society which are based on caste and religion [22]. Rural women of lower caste or class are generally involved in cultivation activities.
- Poor health care: In rural areas in our country, health facilities are not adequate in terms of the equipment, doctors and also the distance of hospitals from the residential areas in the rural areas. Rural areas do not have sanitation and thus, rural women are highly prone to infections and illnesses [23]. Also, they do not get adequate nutrition which in turn results in their poor health. This affects their activeness and involvement in professional lives.
- Low education and facilities: These two factors lead to their low confidence. Also, they are not aware of their potential due to these two factors. In rural areas, technology is not used to do daily household work by women, for example, washing machine, LPG gas etc. Hence, they are overburdened by house work which impacts their professional life. The societal pressure and lack of education are the two main reasons for early pregnancy in rural women. Early motherhood diverts them from their professional goals and they bound themselves to only the personal lives.
- Physical unrest: Because of the hectic schedule, rural women journalists get to spent less time with their children and family members. They feel physically

exhausted as they have to manage both family work and also their professional work [24].

Economic status of rural women journalists: We now present the aspects which will be used to determine the economic status of rural women journalists.

- Income partiality: It is generally seen that men do get higher salary than women journalists which in turn makes them dependent on men economically.
- Job insecurity: As compared to men, women generally feel insecure in terms of the job security and continuation of their services in the organization [25].
- Increment and Bonus: In holidays also, female journalists agree to work and also they do not feel bad while working for extra hours. It is expected from their organizations that they give them the adequate money for the extra hours and work which they do [26]. They also expect bonus and increments on yearly basis.
- Economic independence: Rural women feel that they are independent in terms of finance when they start to pursue their career. In this way, they are free to earn their livelihood in her own way [27, 28].

Next, the methodology used is described.

- Research design: In our research, we have conducted case study and descriptive study.
- Area of study: We have considered four states for our research: UP, Bihar, Chhattisgarh and Jharkhand.
- Data collection: We collected the data from the rural female reporters and correspondents by using the questionnaire.
- Data analysis: After collecting the data, we performed the data analysis in order to study the status of rural women journalists.

Some of the questions of our questionnaire are listed below.

- (1) Do you feel discriminated based on your gender at your workplace?
- (2) Does your family support your career in news media?
- (3) Does your husband quarrel over your pursuit of job?
- (4) Are you provided with basic amenities at your home to lower your day today household work?
- (5) Do you get your expected salary in your organization?
- (6) Do you get any incentives apart from your salary?

The data collected and its analysis for rural women journalists is presented in Figs. 1 and 2 regarding the social and economic status. Social factors which are important to analyze the social status are shown on horizontal axis in Fig. 1 while economic factors which are important to analyze the economic status are shown on horizontal axis in Fig. 2. In both figures, the percentage of the rural female journalists corresponding to high, average and low categories for each social or economic factor listed is shown on the vertical axis.

The social status of rural women journalists is shown in Fig. 1 using the six factors. The percentage of the rural female journalists which agree that they suffer

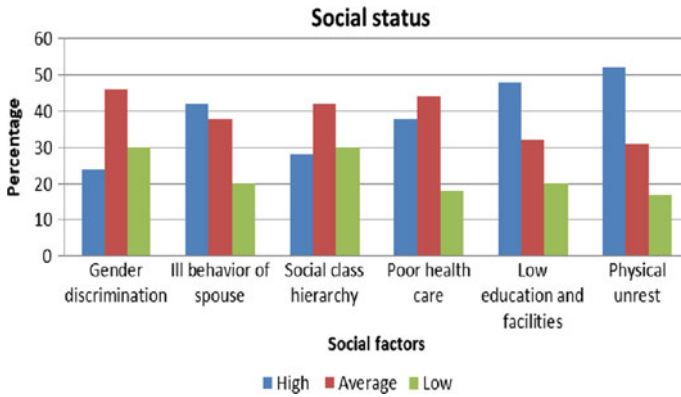


Fig. 1 Social status of rural women journalists



Fig. 2 Economic status of rural women journalists

from gender discrimination on and off when they are on field and are present in their organization is 46%. There are 42% rural women journalists who feel that they get bad treatment from their family members including their spouses and say that the reason behind this ill treatment is the patriarchal thinking of the society. The rural female journalists suffer from a lot of discrimination based on their class, caste and religion. 80% of the rural women journalists agree that they do not get adequate healthcare facilities. Total of 48% them say that they do not get good education facilities which enable them to be aware of their rights and also the job opportunities. Total of 52% say that they have to perform their household and professional duties side by side and therefore, they suffer from tremendous physical exertion.

The economic status of rural women journalists is presented in Fig. 2 on the basis of four factors. Total of 48% of the rural women journalists agree on the heavy

discrimination as compared to men. This discrimination is based on income in the organizations in which they work. Unexpectedly, a total of 46% of the rural women journalists feel that they feel insecurity in their job. The percentage of the rural women journalists who feel that get low incentives, bonus and increments is 50%. A total of 46% of the rural women journalists say that they feel that they are, to some extent, quite economically independent and do not need to be dependent on the men in their families for their basic household things.

Keeping in mind the above analysis regarding the current social and economic status of rural women journalists, we propose some of the measures that could be adopted by the government in order to enhance their visibility and involvement in the local as well as in the mainstream news media.

- New educational schemes and the necessary facilities related to providing education especially to the rural women should be started by the government.
- The government should also start initiatives to enhance the vocational skills for the rural women journalists, eg. technical programme trainings etc.
- In order to increase the self-belief in rural women journalists, their families should be the first. They should give all the freedom them e.g. encourage them to take decisions for the family etc.
- To help them in growing in their professional lives, the government and nonprofit groups may start counseling to eliminate psychological causes like lack of self-confidence and success panic which will help to succeed in news media.

Also, to see the progress, all the above measures and programs should be supervised on a regular basis in order.

3 Related Work

In this paper, we have presented the research gap which we have found while studying the related research work done in this area.

The work done in [6] argues on how to apply the theory of liberal feminism on women journalists. In this paper, it is said that whether it is male or female, everyone deserves equal rights. Preconceptions and social system are the two major reasons which limit the opportunities for women in their profession.

Author in [16] says that in the world, participation of women in India is among the lowest. It has been seen that count of female in the electronic news media is quite higher than the count of female journalists in the print news media in our country. The fact remains the same that the female journalists are still confined to soft news beats such as news/feature writing.

In [17], author states the news media profession was considered as the men dominated career, but female representation has increased in this profession over the years. However, it is also emphasized in the paper that women from the backward classes should be more encouraged to be involved in news media profession.

An 'All women' radio station has been started which is known as Sangham Radio which involves only women on all positions e.g., editors, program producers, managers and radio jockeys. It has become a good example of how an organization can give opportunity to the women who come from all diverse sections of the society to start and succeed in their career. The working women in the station have become fully economically independent [29, 30].

In the paper [31], the author has studied the status of women journalists in metropolitan cities in our country. The research done is on the women correspondents in print news media. Author has also given suggestions to start the schemes which could help in enhancing the work culture for females in the news media organizations. Research done in this paper also states that upper designations in news media organizations are not generally offered to the female as compared to men [32].

A very famous today's newspaper known as Khabar Lahariya is a rural news media organization which is run by only women [33].

In paper [34], it is stated that women in any profession is generally easily exploited. Women in generally are treated as a presentable thing not as a professional worker especially in the news media. Instead, in the professional lives, women must be treated equally and as a coworker by men. In this way, we can help women to improve their social and economic status.

It can be easily seen from the above study that there is a gap in the research which has been done so far regarding rural women journalists which study their status. Therefore, we intend to conduct a study in order to fill this research gap to analyze the social and economic status of the rural women journalists in India.

4 Conclusion

In the past years, women journalists have been able to mark their visibility in the news media. But the fact remains that, rural women journalists in our country are comparatively far less visible to the urban women journalists [35]. Over the years, women from the rural areas have started to opt journalism as their career. Therefore, we have conducted research in this paper on the social and economic status of the women journalists living in the rural areas of our country. The research was done in four states. A sample questionnaire has been used in the study. A series of telephonic and personal interviews have been conducted to study their status. In the paper, we have analyzed that the present social and economic status of the rural female journalists can be improved.

References

1. Bennett A (2005) *Jlsm Women: Pract Guid* 8405:2005
2. Deuze M (2005) What is journalism? Professional identity and ideology of journalists reconsidered. *Journalism* 6(4):442–464
3. Diwaker G (2013) Empowerment and transformation: a case study of communication skills of dalit women in India. *Pan-Commonwealth Forum* 7 (PCF7)
4. Bhandare Usha V (2015) Women exploitation in media. Volume 4(2):11–20
5. Narayana UR (2015) Mainstreaming women in news-myth or reality? *Pragyaan: J Mass Commun* 13(1):22–26
6. Patowary H (2014) Portrayal of women in Indian mass media: an investigation. *J Educ Soc Policy* 1(1):84–92
7. Gang IN, Sen K, Yun MS (2008) Poverty in rural India: caste and tribe. *Rev Income Wealth J* 54(1):50–70
8. Ammu J, Sharma K (eds) (2006) *Whose news? The media and women's issues*, Sage
9. Joshi U, Pahad A, Maniar A (2006) Images of women in print media—a research inquiry. *Indian Media Stud J* 1.1:39–51
10. <https://scroll.in/article/838263/how-the-internet-is-empowering-assams-rural-women>
11. Aggarwal VB (2002) *Media and society, challenges and opportunities*. Concept Publishing Company
12. Hendricks JA (ed) (2010) *The twenty-first-century media industry: economic and managerial implications in the age of new media*. Lexington Books, Maryland
13. Vidura AR (1990) Should Women Opt *Jlsm* 27(1):18–19
14. Prithvis C (1996) Outstanding women journalists. *Vidura* 33(2):11–13
15. Bhatnagar V (1996) *Development dynamics of press and journalism*. Printwell Publication, Jaipur
16. National Conference on Women and Media (2002) A report, social welfare April 49(1):120;
- Natranjan SA (1981) *History of the press in India*” Asia Publishing House, New York, pp 140–141 (Nitz, M., Reichert)
17. Prasad K (2005) *Women and media: challenging feminist discourse*. The Women Press
18. Tomar R (2009) Women in media like ice on cake. *Media Vimarsh, Annual issue, Oct-Dec. Bhopal. 2009. pg 74*
19. Bruce T (2002) Supportive or hostile? Teasing or professional? Women sportswriters categorize locker room interaction. *Women Sport Phys Act J* 11(1):49–61
20. Zameer Ahmad Bhat (2014) Gender bias and socioeconomic problems of women in India. *Abhinav Natl Mon Ref J Res Art Educ* 3:8–13
21. MarutiAdin R, Singhe MS (2016) Socioeconomic conditions of women domestic workers in Mangalore City. *Int J HumIties Soc Sci Res* 2:19–21
22. Ghose MALINI, Mullick DISHA (2012) Empowerment in educational processes: feminist re-appropriations. *More Powerful Literacies* 147
23. Prasad K (2006) Cracking the glass ceiling: rural women making news in India. *Media Asia* 33(3–4):229–233
24. Kandpal E, Baylis K, Arends-Kuenning M (2012) Empowering women through education and influence: an evaluation of the Indian Mahila Samakhya program
25. Rao L (2001) Facets of media and gender studies in India. *Fem Media Stud* 1(1):45–48
26. Shaw IS (2015) *Business journalism: a critical political economy approach*. Routledge
27. Singh N (2016) Analysing status of women journalists in Indian TV news channels. *J Res Arts Educ. ISSN 2277–1182*
28. Roy S (2011) Television news and democratic change in India. *Media Cult Soc* 761–777
29. *Women welfare and empowerment in India: Vision for 21st century* by RameshwariPandya (20) New Century Publications 2008
30. Sivanesan R (2013) A study on socioeconomic conditions of women workers in cashew industries of Kanyakumari district. *Int J Manag Res Bus Strat* 2:90–112

31. Tomar R Khabar Lahariya: a feminist critique of mainstream hindi print media. About SubVersions
32. Thomas PN (2011) Negotiating communication rights: case studies from India. SAGE Publications India
33. The fight within, The Hindu, 14 September, 2017 The Better India. <https://www.thebetterindia.com/37228/khabar-lahariya-women-journalists/> (2016)
34. Saltzman J (2003) Sob sisters: the image of the female journalists in popular culture. University of Southern California
35. Vaishali HB, Shivram GP (2016) Changing face of women journalists in leading Kannada television channels: a study. Int J Sci Res 4.8

Assessment of Godavari River Water Quality of Nanded City, Maharashtra, India



P. R. Shaikh, Girish Deore, A. D. Pathare, D. V. Pathare, and R. S. Pawar

Abstract Water resources are sources of water that useful or potentially useful to humans. Uses of water are including domestic, agricultural, industrial, recreational as well as environmental activities. Virtually, all these human uses require fresh water. The water samples from the Godavari River of the five sampling site are taken and analyzed for the physicochemical parameters such as Colour, Odour, Temperature, pH, Electrical Conductivity (EC), Total Solids (TS), Total Dissolved Solids (TDS), Total Suspended Solids (TSS), Total Hardness (TH), Calcium (Ca), Magnesium (Mg), Chloride (Cl), Alkalinity (TA), Dissolved Oxygen (DO), Chemical Oxygen Demand (COD), Biological Oxygen Demand (BOD) and Turbidity, etc. parameters in seven weeks. Godavari River water is one of the important sources of water in Nanded city. As the Nanded is drought-prone area alteration within major or minor in the characteristics of River water results in great attention of day to day life of citizens of Nanded. There are 5 samples taken weeks of March and April months of Godavari River to access the quality of water and the results are compared with WHO standards.

Keywords River water · Quality · Nanded · Characteristics · etc.

P. R. Shaikh (✉)

School of Earth Sciences, S.R.T.M. University, Nanded, Maharashtra, India

G. Deore

Matoshri College of Engineering, Nanded, Maharashtra, India

A. D. Pathare

Pravara Rural Engineering College, Loni, Maharashtra, India

D. V. Pathare

Padmashri DVVP Institute of Technology and Engineering (Polytechnic) College, Pravaranagar, Loni, Maharashtra, India

R. S. Pawar

SVERIs College of Engineering Pandharpur, Solapur, Maharashtra, India

e-mail: rspawar@coe.sveri.ac.in

1 Introduction

Water is well known as a natural solvent. Before, it reaches the consumer's tap, it comes into contact with different pollutants, including organic and inorganic matter, chemicals, and other contaminants which pollute them. Many public water systems, treated water with chlorine to kill disease-producing contaminants that may be present in the water. Although disinfection is an important step in the treatment of potable water, the taste and odor of chlorine is objectionable. The disinfectants that are used to prevent disease can create byproducts which may pose significant health risks. The water cycle explains interactions between the atmosphere, hydrosphere, and lithosphere. The water or hydrologic cycle is a major driving force on our planet. A river is a natural watercourse, usually freshwater, flowing towards an ocean, a lake, a sea, or another river. In a few cases, a river simply flows into the ground or dries up completely at the end of its course, and does not reach another body of water [1].

1.1 Background of the Study

In recent years, because of continuous growth of population, rapid industrialization and the technologies involving waste disposals, the rate of discharge of the pollutants into the environment is far higher than the rate of their purification. The implications of deteriorating quality of the receiving waters are considerable both in the immediate situation and over the longer term. In this context, water quality assessment is critical for pollution control and the protection of surface and ground waters. In India, disposal of untreated domestic sewage from cities, towns and villages is the major source of pollution of surface water bodies leading to the outbreak of water borne diseases. Biodegradable organic matter is the contaminant of concern for dissolved oxygen concentration which is the principal indicator of pollution of surface water. According to world health organization (WHO), about 80% of water pollution in developing countries like India is caused by domestic wastes [2].

2 Study Area

The district is situated on Maharashtra-Karnataka-Andhra Pradesh boundary. Nanded is the second largest city in the Marathwada region of Maharashtra state. It is an important holy place for the Sikh faith and is famous for the Hazur Sahib Gurudwara. It is the district headquarters once very famous as district of Sanskrit poets. Nanded is a town of great antiquity and famous for Muslim Sufi shrines. This district of great antiquity is important for the Hindu faith and is known for the Renukadevi temple at Mahur. The official languages are Marathi, Hindi, Urdu and Panjabi. The sampling locations plotted in the map of Godavari River in Nanded City (Fig. 1) [3, 4].

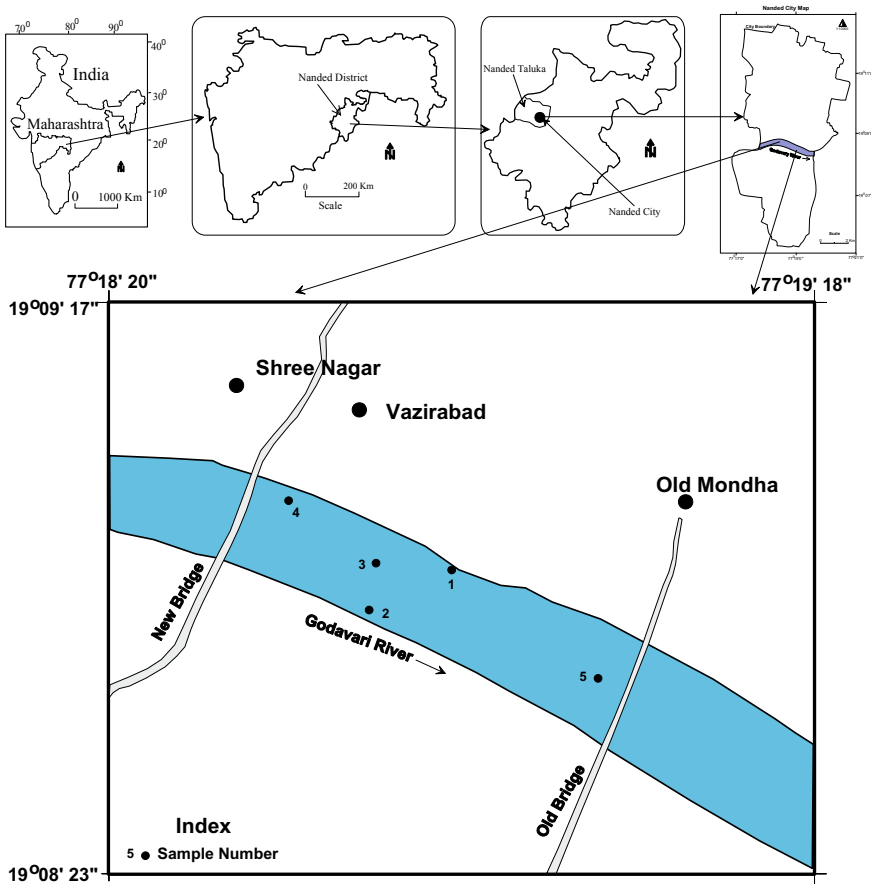


Fig. 1 Location map of the study area

3 Materials and Methods

For the study of River water quality we have select the Godavari River at Nanded city because the growth and development of the city affect the water quality of this River. As Nanded city is situated in Marathwada region of Maharashtra (draught zone). Population of this city is mainly dependent on the River water to sustain. Therefore any major alteration in the physico-chemical characteristics of River water of this region affects the day to day activities of peoples in this region adversely.

3.1 Sample Collection

There are 5 locations selected as per the pollution sources and total 7 times (Weeks of March and April Months) water samples were collected from the study of River water quality. Samples are collected in the polythene bottles. The collected samples are transfer to the laboratory for further analysis. The physico-chemical parameters such as Colour, Odour, Temperature, pH, Electrical Conductivity (EC), Total Solids (TS), Total Dissolved Solids (TDS), Total Suspended Solids (TSS), Total Hardness (TH), Calcium (Ca), Magnesium (Mg), Chloride (Cl), Alkalinity (TA), Dissolved Oxygen (DO), Chemical Oxygen Demand (COD), Biological Oxygen Demand (BOD) and Turbidity, etc. are analysed. The physico-chemical parameters are checked by the titrometric method [3, 5].

4 Result and Discussion

The water samples from the Godavari River of the five sampling site are taken. The samples are filtered with the help of filter paper and analyzed for the physico-chemical parameters such as Colour, Odour, Temperature, pH, Electrical Conductivity (EC), Total Solids (TS), Total Dissolved Solids (TDS), Total Suspended Solids (TSS), Total Hardness (TH), Calcium (Ca), Magnesium (Mg), Chloride (Cl), Alkalinity (TA), Dissolved Oxygen (DO), Chemical Oxygen Demand (COD), Biological Oxygen Demand (BOD) and Turbidity, etc. parameters in seven weeks as shown in the Table 1.

The all samples show the greenish colour, which is the indicator of algal blooms. The odour is objectionable, because of the mixing of sewage in the River water. The temperature is varies from 35 to 38 °C. It is increases because of the summer season.

4.1 pH

The pH of samples in seven weeks of March and April months is ranges from 7.4 to 7.8. The pH value of all the weeks of two months falls in Neutral category. The average and standard deviation of pH is 7.52 and 0.1 respectively. The pH of sample no. 1 is higher as compare to the other samples of first three weeks Fig. 2.

4.2 Electrical Conductivity

The EC of samples in seven weeks of March and April months is ranges from 1952 to 2178 $\mu\text{S}/\text{cm}$. The average and standard deviation of EC is 2080.9 and 77.12 respectively. The EC of sample no. 1 is higher as compare to the other samples and

Table 1 Physico-chemical parameters of Godavari River water samples in the weeks of March and April months

Parameters	Unit	Min	Max	Avg	StDev
pH	–	7.4	7.8	7.52	0.1
EC	μS/cm	1952	2178	2080.9	77.12
TS	mg/l	2253	3394	2743.2	520.6
TSS		1000	2000	1411.4	489.76
TDS		1249	1394	1331.4	49.35
TH		154	302	191.2	33.8
Ca		36.07	84.17	47.18	11.31
Mg		16.52	25.33	20.23	2.4
Cl		99.4	205.9	148.97	21.89
TA		130	150	137.57	5.86
DO		3.2	5	3.81	0.43
COD		78	128	104.71	12.25
BOD		31	51	41.66	4.84
Turbidity	NTU	220	663	370.09	81

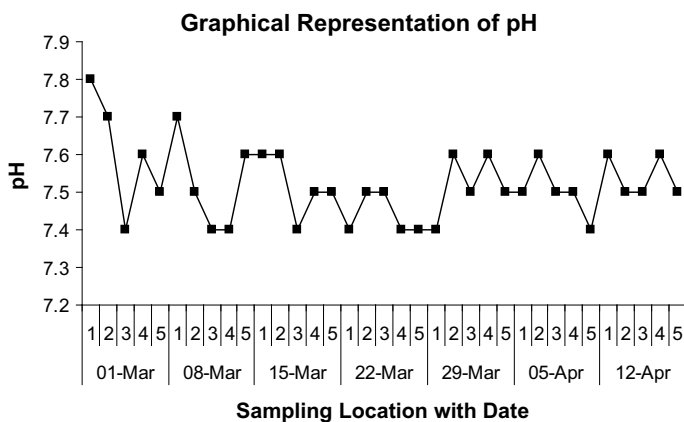


Fig. 2 Graphical representation of pH

lower in sample no. 5 of all the sampling weeks. From the Fig. 3 it is seen that the EC is gradually increased during the sampling periods.

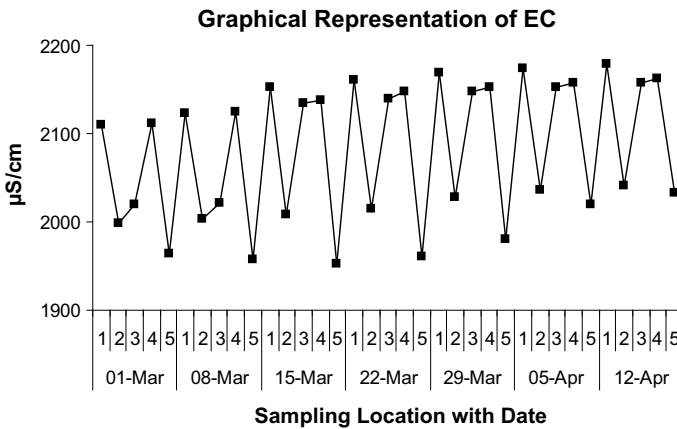


Fig. 3 Electrical conductivity

4.3 Solids (TS, TSS and TDS)

The TS of samples in seven weeks of March and April months is ranges from 2253 to 3394 mg/l. The average and standard deviation of TS is 2743.2 and 520.6 respectively. The TSS of samples in seven weeks of March and April months is ranges from 1000 to 2000 mg/l. The average and standard deviation of TSS is 1411.4 and 489.76 respectively. The TDS of samples in seven weeks of March and April months is ranges from 1249 to 1394 mg/l. The average and standard deviation of TDS is 1331.8 and 49.35 respectively. All the samples are falls in above the highest desirable limit, but below the maximum permissible limit given by WHO [6, 7]. From the Figs. 4, 5 and 6 it is seen that the TDS is gradually increased during the sampling periods.

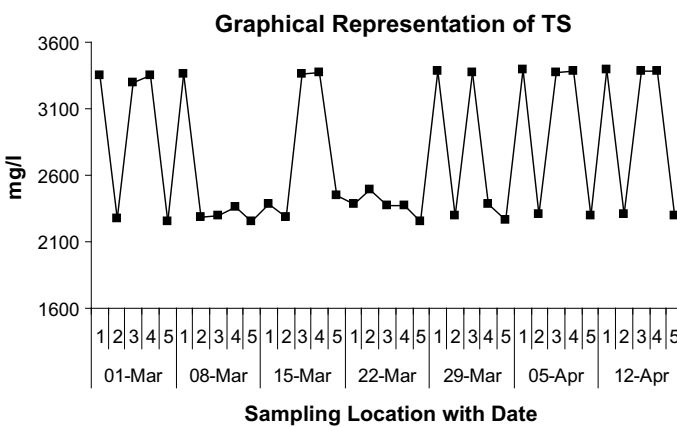


Fig. 4 Graphical representation of TS

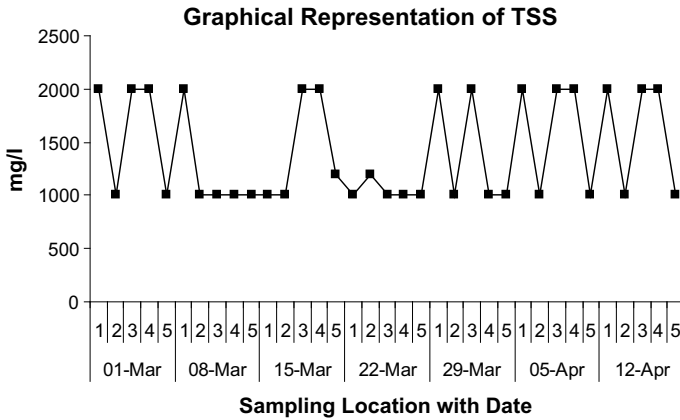


Fig. 5 Graphical representation of TSS

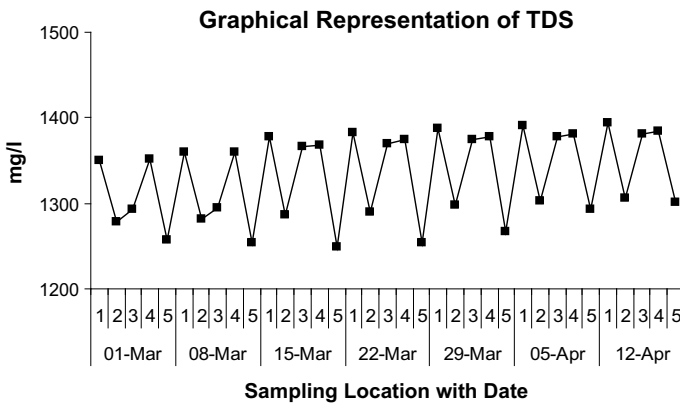


Fig. 6 Graphical representation of TDS

4.4 Total Hardness (TH)

The TH of samples in seven weeks of March and April months is ranges from 154 to 302 mg/l. The average and standard deviation of TH is 191.2 and 33.8, respectively. The all samples falls hard water category. According to WHO [6, 7], all samples falls above the highest desirable limit, but below the maximum permissible limit except one sample. It can be seen that the river water samples are more total hardness content because of mixing of sewage. From the Fig. 7 it is seen that the TH is gradually increased during the sampling periods. The sample no. 4 TH content is higher in the 8 march, 15 march and 22 march sampling period and in the sample no 2, TH content is higher in next all sampling periods.

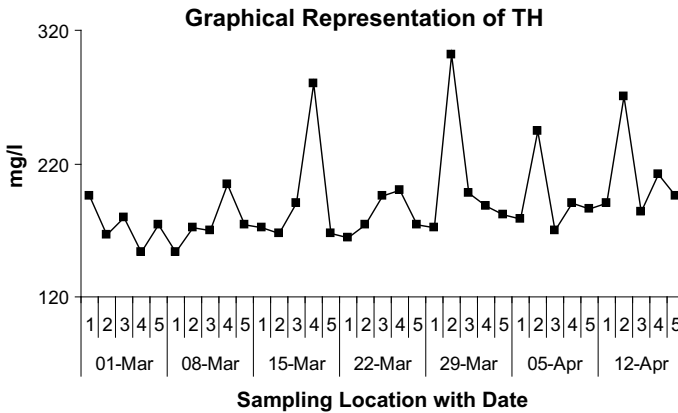


Fig. 7 Graphical representation of TH

4.5 Calcium (Ca)

The Ca of samples in seven weeks of March and April months is ranges from 36.07 to 84.17 mg/l. The average and standard deviation of Ca is 47.18 and 11.31 respectively. All samples falls below the highest desirable limit, only two samples falls above the highest desirable limit but below the maximum permissible limit given by WHO [6, 7]. From the Fig. 8 it is seen that the Ca is gradually increased during the sampling periods. The sample no. 4 Ca content is higher in the 8 march, 15 march and 22 march sampling period and in the sample no 2, Ca content is higher in next all sampling periods.

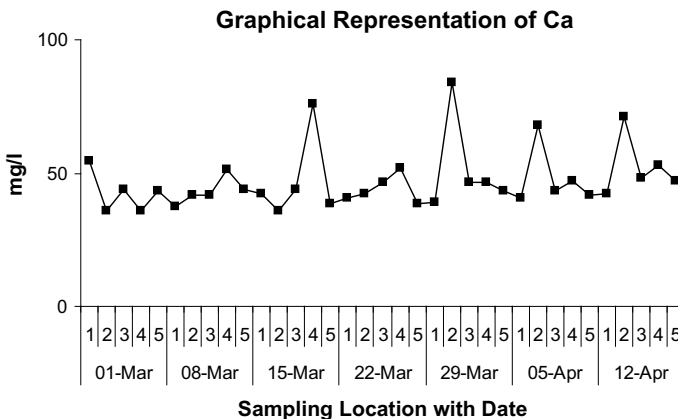


Fig. 8 Graphical representation of Ca

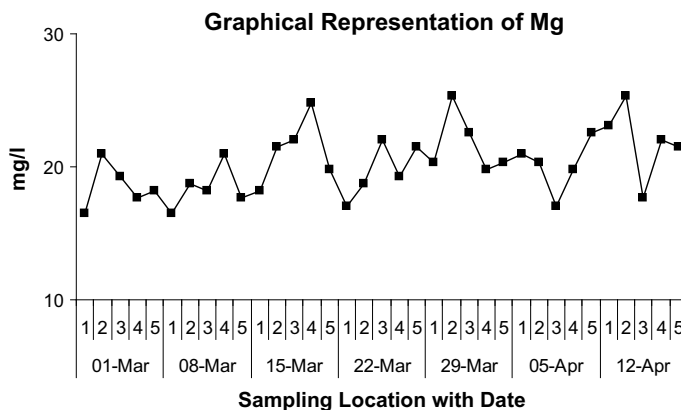


Fig. 9 Graphical representation of Mg

4.6 Magnesium (Mg)

The Mg of samples in seven weeks of March and April months is ranges from 16.52 to 25.33 mg/l. The average and standard deviation of Mg is 20.23 and 2.4 respectively. All samples falls below the highest desirable limit given by WHO [6, 7]. From the Fig. 9 it is seen that the Mg is gradually increased during the sampling periods. The sample no. 4 Mg content is higher in the 8 march, 15 march and 22 march sampling period and in the sample no 2, Mg content is higher in next all sampling periods.

4.7 Chlorides

The Cl of samples in seven weeks of March and April months is ranges from 99.4 to 205.9 mg/l. The average and standard deviation of Cl is 148.97 and 21.89 respectively. According to WHO, all samples falls below the highest desirable limit except one sample. It can be seen that the river water samples are more chloride content because of mixing of sewage. From the Fig. 10 it is seen that the Cl is gradually increased during the sampling periods. The sample no. 5 Cl content is higher except first 2 sampling periods.

4.8 Total Alkalinity

The TA of samples in seven weeks of March and April months is ranges from 130 to 150 mg/l. The average and standard deviation of TA is 137.57 and 5.86 respectively. From the Fig. 11 it is seen that the TA is gradually decreased during the sampling

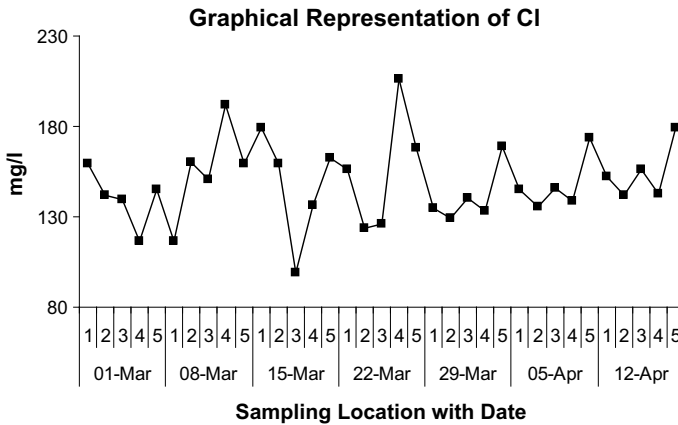


Fig. 10 Graphical representation of Cl

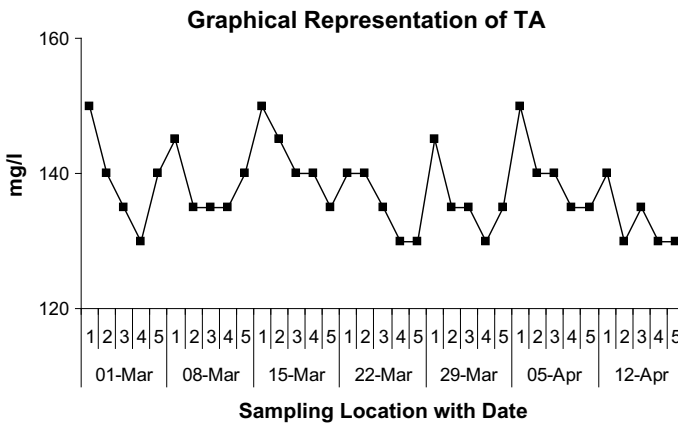


Fig. 11 Graphical representation of TA

periods.

4.9 Dissolved Oxygen (DO)

The DO of samples in seven weeks of March and April months is ranges from 3.2 to 5 mg/l. The average and standard deviation of DO is 3.81 and 0.43 respectively. From the Fig. 12 it is seen that the DO is gradually decreased during the sampling periods. The sample no. 5 DO content is higher in the first 4 sampling period and in sample no 3, DO content is higher in next all sampling periods.

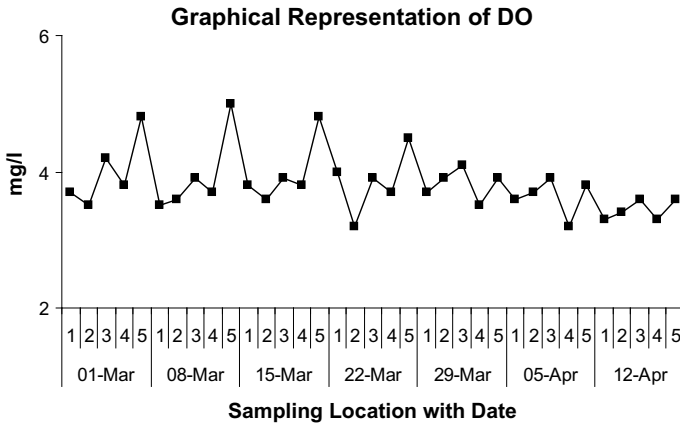


Fig. 12 Graphical representation of DO

4.9.1 Chemical Oxygen Demand (COD)

The COD of samples in seven weeks of March and April months is ranges from 78 to 128 mg/l. The average and standard deviation of COD is 104.71 and 12.25 respectively. According to WHO [6, 7], all samples falls below the maximum permissible limit. From the Fig. 13. it is seen that the COD is gradually increased during the sampling periods.

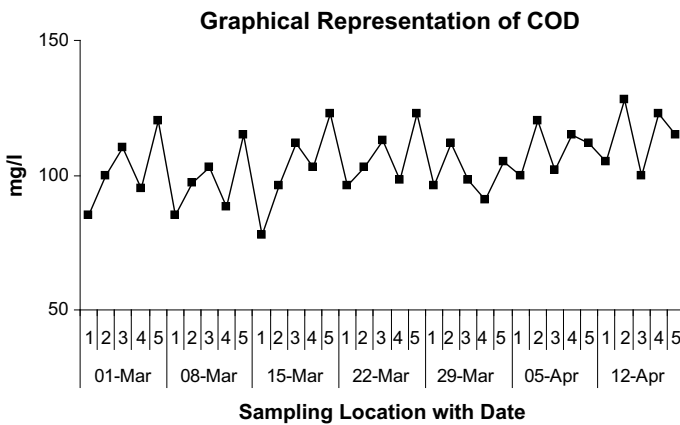


Fig. 13 Graphical representation of COD

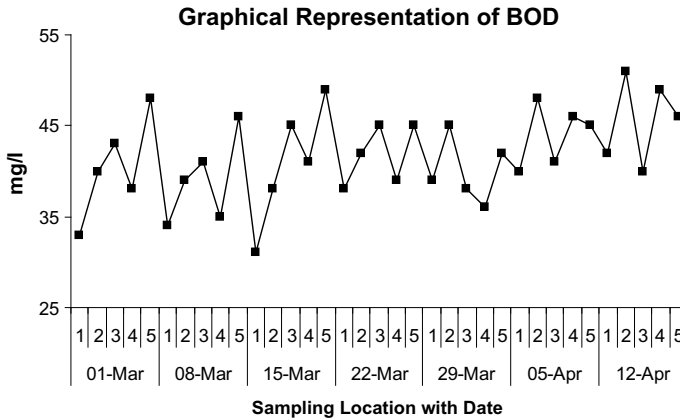


Fig. 14 Graphical representation of BOD

4.9.2 Biological Oxygen Demand (BOD)

The BOD of samples in seven weeks of March and April months is ranges from 31 to 51 mg/l. The average and standard deviation of BOD is 41.66 and 4.84 respectively. According to WHO [6, 7], all samples falls below the maximum permissible limit. From the Fig. 14 it is seen that the BOD is gradually increased during the sampling periods.

4.9.3 Turbidity

The Turbidity of samples in weeks of March and April month is ranges from 220 to 663 mg/l. The average and standard deviation of Turbidity is 370.09 and 81 respectively Fig. 15.

5 Conclusion

Godavari River water is one of the important sources of water in Nanded city. As the Nanded is drought prone area alteration within major or minor in the characteristics of River water results in great attention of day to day life of citizens of Nanded. There are 5 samples taken weeks of March and April months of Godavari River to access the quality of water and the results are compared with WHO standards. All the values are found within limit (except EC, TDS, and TH). The Chloride value is found little higher. This indicates that River water is contaminated with sewage pollution, fecal matter. Probable solutions are suggested to avoid the further contamination.

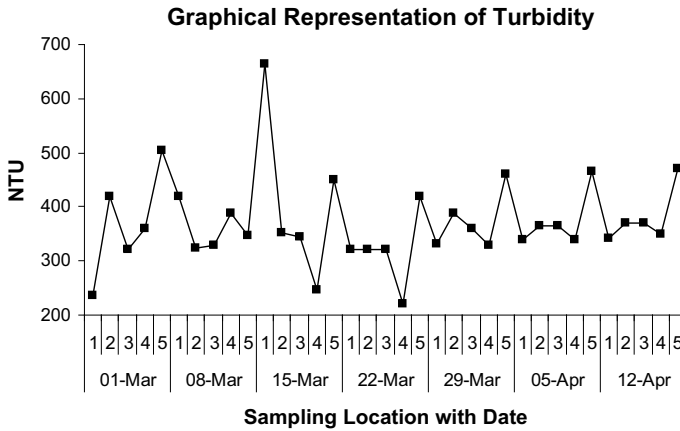


Fig. 15 Graphical representation of turbidity

1. Analysis of physico- chemical parameters of water shows that all the parameters are within (except EC, TDS, and TH) Standard limit provided by WHO.
2. River water of this region is contaminated with sewage waste
3. Disposal site for sewage waste should be out of the premises of the city to avoid further contamination of River water of the area.

References

1. Verma S (2009) Seasonal variation of water quality in Betwa river at Bundelkhand region, India. *Glob J Environ Res* 3(3):164–168
2. Srivastava A, Kumar R, Gupta V, Agarwal G, Srivastava S, Singh I (2011) Water quality assessment of Ramganga river at Moradabad by physico-chemical parameters analysis. *VSRD-TNTJ* 2(3):119–127
3. Panaskar DB, Wagh VM, Pawar RS (2014) Assessment of groundwater quality for suitability of domestic and irrigation from Nanded Tehsil, Maharashtra, India. *SRTMUs J Sci* 3(2):71–83
4. Pawar RS, Panaskar DB (2014) Characterisation of groundwater in relation to domestic and agricultural purpose, Solapur Industrial Belt, Maharashtra, India. *J Environ Res Dev (JERAD)* 9(01):102–112
5. APHA, AWWA, WEF (1985) Standard methods for the Examination of water and wastewater, 16th edn. American Public Health Association, Washington DC, pp 6–187
6. World Health Organization (WHO) (1998) International standards for drinking water quality. Geneva, WHO
7. World Health Organization (WHO) (2002) Guideline for drinking water quality. Health criteria and other supporting information, 2nd edn. World Health Organization, Geneva, pp 940–949

Land Use Land Cover Detection from Naldurg Area of Osmanabad District, Maharashtra, India



D. D. Kulkarni, Vijay Waghmare, A. D. Kokate, G. S. Pawar, and R. S. Pawar

Abstract LULC mapping is one of the most important applications of remote sensing. Land use widely used in the development of groundwater resources. The hydrogeological processes such as Infiltration, evapotranspiration, surface runoff etc. were controlled by land use. Surface cover provide roughness to the surfaces, reduce discharge there by increases the infiltration. In the forest areas, infiltration will be higher and runoff will be less whereas in urban areas rate of infiltration may decrease. Remote sensing techniques will give detailed information with respect to spatial distribution of land use and vegetation type in minimum time and low cost in comparison to other conventional data. Land Use Land Cover of study area has been analyzed for 2018 LISS III image. The investigated area shows that major portion in land use is Vegetation and Agriculture land 81%, Barren land covering area 14.12%, water body covering area 2.60% and settlement covering area 1.53%.

Keywords Land use · Land cover · Detection · Satellite image · Toposheet · DEM · etc.

1 Introduction

Development of potential of groundwater in any area requires large amount data sources. Hence, features like rainfall, infiltration, evapo-transpiration are well studies for generating a groundwater potential model of study area. Nowadays exploration of groundwater is important in drinking purposes, agricultural and other domestic uses. Despite the advancement in research and technology, groundwater study remained more risky as there is no direct method to facilitate observation of water below the surface.

D. D. Kulkarni (✉) · V. Waghmare · A. D. Kokate
School of Earth Sciences, PAH Solapur University, Solapur, Maharashtra, India

G. S. Pawar · R. S. Pawar
SVERIs College of Engineering Pandharpur, Solapur, Maharashtra, India
e-mail: rspawar@coe.sveri.ac.in

Its presence or absence can be ascertained by studying the geological and surface parameters. Integration of remote sensing with GIS for preparing various thematic layers, such as lithology, drainage density, lineament density, slope, soil and land-use with assigned weightage in a spatial domain will support the identification of potential groundwater zones [1]. Therefore, the current study focuses on the assessment of LULC in Naldurg area of Osmanabad district, Maharashtra using the highly developed technology of remote sensing and GIS.

1.1 Study Area

It lies between latitudes $17^{\circ}32'$ to $17^{\circ}42'$ and longitudes $76^{\circ}15'$ to $76^{\circ}25'$ as shown in Fig. 1 and forms part of Survey of India toposheet No. 56 C/5 on the scale 1:50,000. The area is located about 6.4 kms east of Akalkot town. The Bori River is 5th order stream originates in the Balaghat ranges in the northern part of the area and flows towards south. The National highway NH-65—(Bombay—Pune—Hyderabad) passes from west to east through the area. The area under study falls in the drought prone region and is characterized by arid to semiarid climatic conditions. The mean annual rainfall is about 700 mm and 80% of which is received in southwest monsoon, while the remaining is generally due to retreating monsoon. In general, rain fall distribution in the region is scanty and erratic [2, 3].

2 Literature Review

Waikar and Nilawar, [4] made an attempt to determine the groundwater potential zones within the Parbhani district of Maharashtra, thematic layers have been generated by using digital satellite image and ancillary data. The potential zones have been obtained using weighted overlay analysis, the ranking given for each individual parameter of each thematic map and weights were assigned according to their influence. Murugesan Bagyaraj et al. [5] have carried out groundwater study in the Dindigul district of Kodaikanal hills, which is a mountainous terrain in the Eastern Ghats of Tamilnadu. Groundwater potential zones have been demarcated with the help of remote sensing and Geographical information (GIS) techniques. Mukherjee et al. [6] studies ground water potential zone in Kuchcha region by using weighted overlay, ranking etc. techniques. Preeja et al. [7], work on applications in groundwater study, especially in the identification of ground water potential zones in Ithikkara River Basin, Kerala, India. They gathered information from Landsat ETM + data and SOI toposheets. He pointed out that the groundwater occurrence is controlled by geology, structures, slope and landforms of the area.

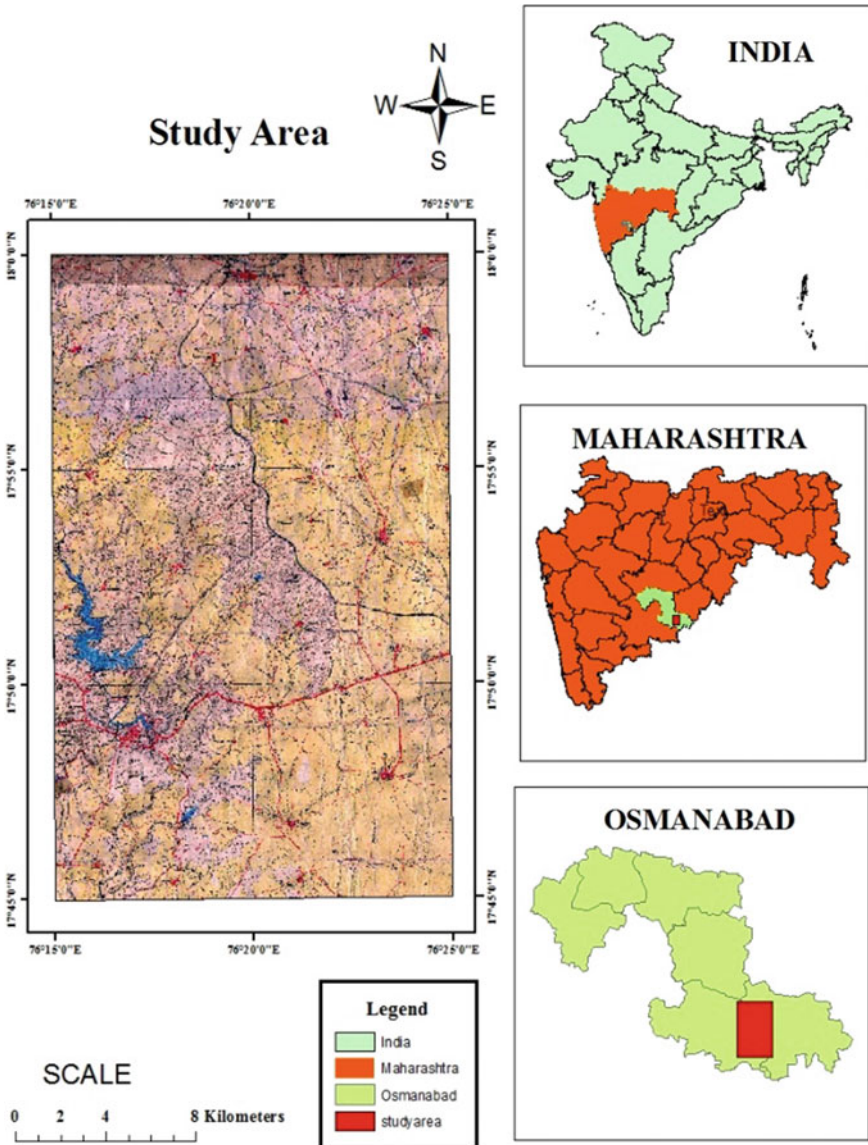


Fig. 1 Location map of the study area

3 Materials and Methods

Methods of study include various activities such as digitization of base maps, preparation various thematic maps and finally LULC map of the area by using ArcGIS software. First step includes development of spatial data base by using Survey of India

(SOI) toposheet on a 1: 50,000 scale and Bhuvan LISS III satellite data. Variety of thematic maps with reference to groundwater by understanding various geomorphic and morphometric aspects were prepared by using GIS and remote sensing techniques. Additionally, the geologic maps, Land Utilization Survey Database maps and on site investigation are adapted to quantitatively and qualitatively describe the hydrogeological conditions of the area. The second step involved preparation of digital elevation model (DEM) by interpolating contour map which are obtained from digitizing SoI toposheet. In the third step, digital image processing of the satellite data is done through geo-referencing and geometric corrections. This is followed by creation of various thematic layers using ArcGIS 10.1 software. All the attributes from the collected data added to create the buffer map for agriculture area forest land, fallow land, barren land and settlement area [8].

4 Data and Result

LULC mapping is one of the most important application of remote sensing. Land use plays a remarkable role in the development of groundwater resources. It controls many hydrogeological processes in the water cycle viz., evapotranspiration, surface runoff, infiltration, etc. Surface cover provide roughness to the surface, reduce discharge there by increases the infiltration. In the forest area, infiltration will be more and runoff will be less whereas in urban areas rate of infiltration may decrease shown in Table 1.

Remote sensing provides excellent information with respect to spatial distribution of vegetation type and land use in less time and low cost in comparison to conventional data. LULC of study area has been analyzed for 2018 LISS III image. The investigated area shows that major portion in land use (81%) is Vegetation and Agriculture land, barren land covering area 14.12%, water body covering area 2.60% and settlement covering area 1.53% and the same is depicted in Figs. 2 and 3.

Table 1 Land use land cover classification

Sr. No	Classes	Area (in sq. Km)	Percentage (%)
1	Vegetation	398.71	81
2	Barren land	68.93	14.12
3	Water body	12.68	2.60
5	Settlement	7.50	1.53

Land use Land cover map of study area in percentage

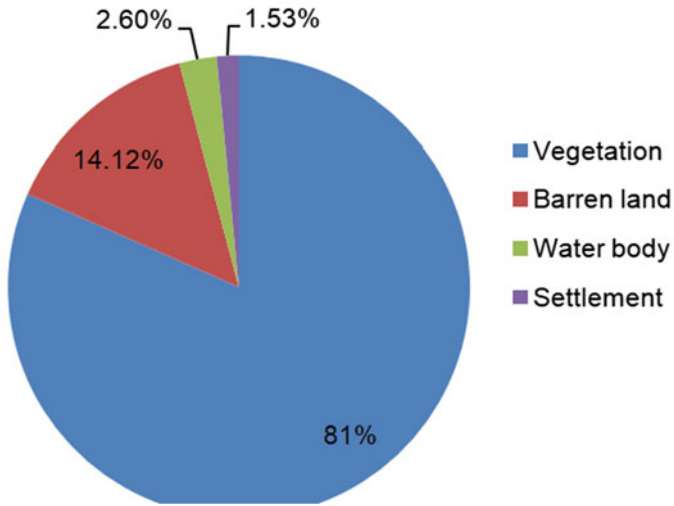


Fig. 2 Land use land cover map of study region

5 Conclusion

Various thematic maps have been overlaid in terms of weighted overlay method using spatial analytical tool on Arc GIS 10.1 platform. Economic and social progress of any region is dependent on development of natural resources – agriculture, mineral and the agronomical practice is based on ground scope that has bearing on soil erosion processes. Land use land cover is also a manifestation of many integral processes vegetation and agricultures practices is reflection of good water resources of a region. Hence, higher weightage is allotted to this category. Barren land is due to poorer water resources. Therefore, the weightage given here is lowest. Remote sensing provides excellent information with respect to spatial distribution of vegetation type and land use in less time and low cost in comparison to conventional data. LULC of study area has been analyzed for 2018 LISS III image. The investigated area shows that major portion in land use is Vegetation and Agriculture land 81%, Barren land covering area 14.12%, water body covering area 2.60% and settlement covering area 1.53%.

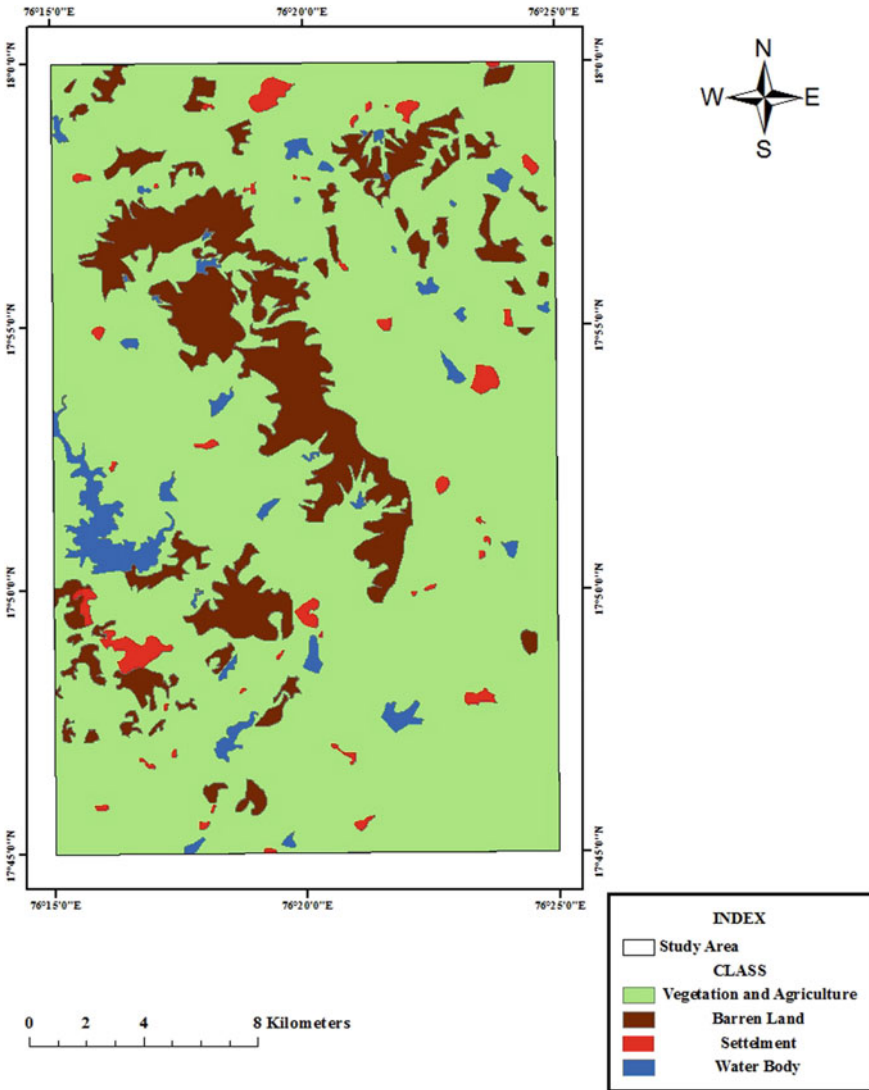


Fig. 3 Digitized land use land cover (LULC) map of study region

References

1. Manjare BS (2014) Identification of groundwater prospecting zones using remote sensing and GIS techniques in upper vena river watersheds Nagpur district, Maharashtra, India. In: 15th ESRI India user conference
2. Pawar RS, Panaskar DB (2014) Characterisation of groundwater in relation to domestic and agricultural purposss, Solapur Industrial Belt, Maharashtra, India. *J Environ Res Dev (JERAD)* 9(01):102–112

3. Panaskar DB, Wagh VM, Pawar RS (2014) Assessment of groundwater quality for suitability of domestic and irrigation from Nanded Tehsil, Maharashtra, India. *SRTMUs J Sci* 3(2):71–83
4. Waikar ML, Nilawar AP (2014) Identification of groundwater potential zone using remote sensing and GIS technique. *Int J Innov Res Sci Engg Tech* 3(5):12163–12174
5. Bagyaraj M, Ramkumar T, Venkatramanan S, Gurugnanam B (2012) Application of remote sensing and GIS analysis for identifying groundwater potential zone in parts of Kodaikanal Taluk, South India. *Front Earth Sci* 7:65–75
6. Mukherjee P, Singh CK, Mukherjee S (2011) Delineation of groundwater potential zones in arid region of India. A remote sensing and GIS approach. *Water Resour Manag* 26:2643–2672
7. Preeja KR, Joseph S, Thomas J, Vijith H (2011) Identification of groundwater potential zones of a tropical river basin (Kerala, India) using remote sensing and GIS techniques. *J Indian Soc Remote Sens* 39(1):83–94
8. Pawar RS, Unhale PL, Kulkarni DD, Deshpande SM (2017) Remote sensing and GIS application to assess the rainwater harvesting potential in North Solapur Tahsil, Solapur District, Maharashtra. *Int J Res Biosci Agric Technol (JRBAT)* V(3):192–195